

Hong Jiang *Editor*

---

# Proceedings of The 20th Pacific Basin Nuclear Conference

Volume 2



 Springer

The Springer logo, which consists of a white chess knight piece on a pedestal, followed by the word 'Springer' in a white serif font.

# Proceedings of The 20th Pacific Basin Nuclear Conference

Hong Jiang  
Editor

# Proceedings of The 20th Pacific Basin Nuclear Conference

Volume 2



 Springer

*Editor*  
Hong Jiang  
China Nuclear Power Engineering Co., Ltd  
Beijing  
China

ISBN 978-981-10-2316-3                      ISBN 978-981-10-2317-0 (eBook)  
DOI 10.1007/978-981-10-2317-0

Library of Congress Control Number: 2016954597

© Springer Science+Business Media Singapore 2017

This work is subject to copyright. All rights are reserved by the Publisher, whether the whole or part of the material is concerned, specifically the rights of translation, reprinting, reuse of illustrations, recitation, broadcasting, reproduction on microfilms or in any other physical way, and transmission or information storage and retrieval, electronic adaptation, computer software, or by similar or dissimilar methodology now known or hereafter developed.

The use of general descriptive names, registered names, trademarks, service marks, etc. in this publication does not imply, even in the absence of a specific statement, that such names are exempt from the relevant protective laws and regulations and therefore free for general use.

The publisher, the authors and the editors are safe to assume that the advice and information in this book are believed to be true and accurate at the date of publication. Neither the publisher nor the authors or the editors give a warranty, express or implied, with respect to the material contained herein or for any errors or omissions that may have been made.

Printed on acid-free paper

This Springer imprint is published by Springer Nature

The registered company is Springer Nature Singapore Pte Ltd.

The registered company address is: 152 Beach Road, #22-06/08 Gateway East, Singapore 189721, Singapore

# Organising Committee

## TPC:

Track	Chair	Co-chair	Secretariat
1	Tianmin Xin	Jiejuan Tong, Guowei He, Guohan Chai, Zhegang Ma, Jean Marie Mattei, Hussein S. Khalil, Jordi Roglans-Ribas	Denghua Chen, Yuchen Jiang
2	Tao Zhang	Yamin Miu, Tunfeng Qi, Tan Hong, Chuming Zhang, Xi Zhao, Chris Dawes, Pierre Tremblay, Chunkuan Shih	He Zhang
3	Chunning Jing	Zhiwei Zhou, Shenjie Gu, Donghui Zhang, Patrick Mariteau, Cecilia Martin-del-Campo, Takashi Takata	Wanjue Wang
4	Guoqing Deng	Yawei Mao, Shengdong Zhang, Anxi Cui, Xinhua Liu, Ju Wang, Stephane Barges, Pascal Chollet, Chilton Huang, Gerd-Michael Burow	Chuan Zhang
5	Ming Li	Jianshe Chai, Zhaohua Chi, Liming Fan, Xingqiang Zhou, Hottelart Herve, Jenq-Hornq Liang, King Lee	Chan Zhou
6	Guoan Ye	Jing Chen, Qingnuan Li, Shuming Peng, Jean Pierre Gros, Christophe Poinssot, Temitope Taiwo, Kazuhiro Suzuki	Jiali Xiong
7	Danrong Song	Xuru Duan, Dongsheng Li, Hadid Subki, Dan Ingersoll, Joel Guidez, Alain Becoulet, Marco E. Ricotti	Jing Lei, Tuo Shao
8	Changhong Yuan	Bo Yang, Tao Li, Yun Lou, Sichao Tan, Laura Hermann, Mimi Limbach, Pascal Chollet	Xiaoqing Liu, Jia Yang
9	Xiaozhe Ling	Jiang Hu, Chunhua Lu, Daguang Zhu, Jianfeng Wang	Xiangting Chen
10	Zuoxiang He	Sijin Li, Yongxue Zhang, Zhifu Luo, Yaming Li, Yuejin Hua, Henry Bom	Qingxin Xia
11	Suyuan Yu	Liangming Pan, Tomio Okawa, Igor Pioro, Sama Bilbao y Leon, Hyoung Kyu Cho	Cheng Chen

# Contents

## Part I Operation and Maintenance

<b>A Study of AP1000 Nuclear Power Plant SGTR Event Processing Strategy</b> . . . . .	3
Zhang Jintang and Ai Chen	
<b>A Summary of the Guidelines on the Evaluation of V&amp;V Tools for Safety Digital I&amp;C Software in Nuclear Power Plant Systems</b> . . . . .	15
Nan Wang, Lingpo Li, Ruidong Dai and Chun Guo	
<b>Analysis and Handling of Turbine Eccentricity Anomaly</b> . . . . .	23
Qiaochan Zhou	
<b>Analysis and Summarization of Continuous Spray Test on Pressurizer of Fuqing Nuclear Power Plant Unit 1</b> . . . . .	31
Zeng Bin and Zhao Yang	
<b>Analysis of the CRDM Coils Current Interference and the Abnormal Display of Rod Position in RGL System</b> . . . . .	39
Yue Cheng and Huanhuan Jiao	
<b>Application of Key Interlock in HUALONG-I 3rd Nuclear Unit</b> . . . . .	49
Zhijian Wang and Cuicai Dong	
<b>Charpy Impact Properties of Electron Beam Welded V-4Cr-4Ti Alloy</b> . . . . .	57
Shuang Yang, Pengfei Zheng, Jiming Chen, Xing Miao and Ran Wei	
<b>Conclusion of the Test of Fujian Fuqing Nuclear Power Plant Unit 1 Determination of Reactor Coolant Flow on the Basis of the Heat Balance</b> . . . . .	67
Dongjia Zheng	

<b>Exceptional Shut Down During Load Test of Emergency Diesel Generator . . . . .</b>	75
Ri Zhao and Yafei Li	
<b>Fangjiashan Auxiliary Transformer Low-Voltage Side of Three-Phase Voltage Imbalance Analysis . . . . .</b>	81
Anman Luo	
<b>Design for High Level Layout and Control of Nuclear Island HVAC Based on DCS Technique . . . . .</b>	93
Yong Liu, Jiru Chu, Xiaochuan Ding and Chen Shang	
<b>Improvements to CANDU6 Reactor Power Control Programs . . . . .</b>	101
Gongzhan Wang, Ligen Xu, Tan Hong, Yongxiang Zheng, Mingjun Chen, Jianxin Sheng and Yang Liu	
<b>Main Control Room Design of Advanced Nuclear Reactor . . . . .</b>	113
Huiyu Deng and Dayong Zhou	
<b>Material Substitute Research of the Main Pipeline Bracket Protection Cushion in CPR1000 NPP . . . . .</b>	121
Ai-qun Ren	
<b>Nuclear Steam Generator Water Level Control Based on DFNN . . . . .</b>	135
Junying Hong and Hong Xia	
<b>Performance Analysis and Optimization of Fang Jiashan DCS Level 2 System . . . . .</b>	153
Ping Tan	
<b>Pickering Generating Station Primary Heat Transport Pressure Control Analysis During Boiler Steam Relief Valve Testing . . . . .</b>	167
Polad Zahedi	
<b>Pressurizer Water Level Control by Makeup and Letdown Flows Operating in Discontinued Model . . . . .</b>	181
Jie-qiong Zhang and Chu-hua Tang	
<b>Qinshan 300 MW Nuclear Power Unit Condensed Water Dissolved Oxygen on the High Side Cause Analysis . . . . .</b>	189
Zengwei	
<b>Research and Application of RtCM Techniques in CPR1000 Nuclear Power Plant . . . . .</b>	201
Chen Yu, Zhang Sheng and Yang Xiaojin	
<b>Research on Technical Transformation of Lifting Equipment in Nuclear Power Plants . . . . .</b>	215
Xiaodong Bao, Jinbao Zhou, Fa Yang and Yi Li	

**Surface Corrosion Analysis of QF Control Rod Nitriding Tube . . . . .** 223  
Ligang Li

**The Corrosion Protection of Drum Strainer in Fuqing Nuclear Power Plant . . . . .** 231  
Gujian Ma and Xingbao Zhao

**The Development of HOLLY Code and Single-Point Ex-core Detectors Calibration Method . . . . .** 237  
WenHuai Li and Chao Wang

**The Reasons for the Frequently Exceeded Pressure Drop of Resin Bed in Steam Generator Blowdown System . . . . .** 247  
Shunlong Yang, Heng Liu, Hui Liu, Huaqiang Wu, Xiangmeng Hu, Kunfeng Yang, Jun Deng and Dawei Zhang

**The Research of High-Voltage Auxiliary Power System Neutral Point Grounding Modes Between the Nuclear Power Plant and Conventional Fossil Fuel Power Plant . . . . .** 257  
HouRong Pan and Yunfeng Zhang

**The Research of Selecting Scope of Maintenance Rule in the Key System of New Nuclear Power Plant . . . . .** 277  
Chaojun Li, Jiaxu Zuo, Yan Chen, Wei Song and Peng Zheng

**The Research on the Model of Condense Regenerate Heater Under Off-design Conditions . . . . .** 285  
Quan Wang, Rongyi Huang and Wei Chen

**The Study of Extending AP1000 Spent Fuel Racks’ Storage Capacity . . . . .** 295  
Yu Zhang, Weidong Rong, Shiwei Wang, Zheng Zheng and Wenbin Wei

**Valves Maintainability Study on Nuclear Power Plant Design Stage . . .** 307  
Xiaohu Yang, Jiao Deng, Hong Jiang, Lifei Yang and Wen Chen

**Part II Supply Capability and Quality Control**

**An Improved Welding Process of Instrumentation Tubes on Nuclear Reactor Pressure Vessel . . . . .** 317  
Ruifeng Guan, Hong Chen, Bin Zhang and Wenbin Zhong

**Analysis of the Development of Nuclear Power Plant Construction Management Model and Management of Engineering Company and Owners . . . . .** 327  
Keteng Ma and Bin Hou



<b>Components Qualification for the Safe Operation of Nuclear Power Plants</b> . . . . .	337
Holger Schmidt, Martin Betz, Ingo Ganzmann, Achim Beisiegel, Thomas Wagner, Emmanuel Peter, Darryl Gordon and Gong Yufeng	
<b>How to Build EQ System for Safety Classed Electrical Equipment Under the Modal of AE.</b> . . . . .	351
Shiquan Zhan	
<b>Modal Analysis of Anchored Cylindrical Liquid Storage Tanks</b> . . . . .	363
Zimin Zhan	
<b>Quality Control of Application Research on Supervision Planning of Hualong #1 Emergency Diesel Generator</b> . . . . .	369
Junxiao Li and Wenxi Ge	
<b>Quality Control of Sub-suppliers in EDG</b> . . . . .	383
Wang Wei	
<b>Research on Identification Test for Sealing Performance of Equipment on Containment Pressure Boundary</b> . . . . .	393
Xiao-xuan Wang	
<b>Research on Problems of Ultrasonic Test for Reactor Vessel Internal During Manufacturing Process.</b> . . . . .	403
Yingpeng Liao	
<b>Risk Analysis on Holes Machining and Inspecting of RVI as One of the Main Equipments in Nuclear Island.</b> . . . . .	413
Yingpeng Liao	
<b>The Disbonding Mechanism Research of Submerged Arc Stainless Steel Strip Cladding.</b> . . . . .	425
Chengdong Yang, Weibao Tang and Maolong Zhang	
<b>Welding Process and Welding Consumable of Generation III Nuclear Island Main Equipment</b> . . . . .	435
Ju-wen Yang, Shuang-yan Li, Mao-long Zhang, Li-li Wang and Wen-yang Zhang	
<b>Part III Fuel Cycles</b>	
<b>Application of Man–Machine System Analysis in the Process Control of Nuclear Fuel Manufacturing</b> . . . . .	453
Xiaolin Gu and Shibo Wang	
<b>Decisioneering on Short- to Long-Term Nuclear Energy System Strategies DANESS v7.1</b> . . . . .	463
Luc Van Den Durpel	

**Determination of Boron in ThO<sub>2</sub> Powder by ICP-AES After Matrix Separation Using Solvent Extraction** . . . . . 477  
 He Shuhua, Li Xiaoyun, Han Ling, Luo Yan, Cao Changqing and Lin Jun

**Development and Validation of Methodology for Depletion Analysis of FHR at Equilibrium State** . . . . . 485  
 Haibo Tang, Jianlong Han, Xiangzhou Cai and Jingen Chen

**Effects of Compressing Strength of Core Ball on Crushing Strength of Spherical Fuel Element** . . . . . 493  
 Jiucheng Tian, Ming Gao, Wenjie Yu, Yu Zhang and Huimin Shi

**Flow Effect on Core Burnup in a Molten Salt Reactor** . . . . . 503  
 Jianhui Wu and Jingen Chen

**Key Parameter Measurements of the Low-Pressure Gas Discharge Plasmas Used for Studying the Ion Extraction Process** . . . . . 521  
 Heping Li, Qiuhui Chu, Xin Wang, Peng Wang, Junjie Chai and Zhanxian Li

**Online Nondestructive Testing of Gadolinium Containing Fuel Rods** . . . . . 533  
 Liu Ming, Yuan Ping and Zhang Lei

**Optimization of Thorium Utilization in Fluoride Salt-Cooled High-Temperature Reactor (FHR)** . . . . . 551  
 Xiaoxiao Li, Jingen Chen and Yonghan Fang

**Preparation of Zr-Doped ThO<sub>2</sub> Ceramic Microsphere By Sol-Gel Method** . . . . . 561  
 He Huang, Jun Lin, Yan Chao, Peng Wang, Fengxia Wang, Changqing Cao and Zhiyong Zhu

**R&D Base for Nuclear Fuel Manufacturing—CNNFC** . . . . . 569  
 Wang Shibo

**Research and Discussion of Development of Reliability Program About Nuclear Fuel Cycle** . . . . . 573  
 Hong Shen, Xiaowei Yang, Chunlong Zhang and Yuntao Liu

**Role and Position of PHWR in Nuclear Fuel Cycle in China** . . . . . 581  
 Zhenhua Zhang, Gang Qiao and Shen Fan

**Shielding Calculation Model and Simplified Analysis of the Spent Fuel Pool** . . . . . 591  
 Yaoquan Zhou, Pinghui Zheng, Xiuge Ma, Puzhong Zhang and Lin Qiu

**PBNC—2016 Technology Evolutions in MOX Fuel Reprocessing Plants** . . . . . 601  
 Christopher Dane

**The First AP1000 Fuel Fabrication Line in China** . . . . . 609  
 Shuangqing Shi and Zhigang Wang

**The Important Aspects on the Protection of Occupational Exposure of the Spent Nuclear Fuel Reprocessing Facility** . . . . . 617  
 You Wei, Long Lin, Tian Yingnan, Mi Aijun and Gao Guiling

**The Method to Ascertain Time-Control Parameters of Reverse Fluidic Device Based on Level Feedback of Supply Tank** . . . . . 627  
 Bao Yin, Liu Yu and Guo Xiao-Fang

**The Microstructure and Characteristic Analysis of USW Welding** . . . . . 639  
 Pengbo Ji and Junfeng Sun

**Ultrasonic Test for Typical Defect of Zirconium Alloy Tube used in Nuclear Fuel Assembly** . . . . . 655  
 Jiangwu Ou

**Part IV New Technology and New Applications**

**A Deconvolution Algorithm for Gamma Spectrum Based on Energy Resolution Calibration** . . . . . 667  
 Rui Shi, Xianguo Tuo, Honglong Zheng, Huailiang Li and Junyu Zhou

**A Potential Way of Co-60 Production in CANDU6 Reactors** . . . . . 679  
 Jinqi Lyu, Mohammad Abdul Motalab, Younwon Park and Yonghee Kim

**Base-Isolation Technology Investigation for SMR Nuclear Island Building** . . . . . 691  
 Chen Jian and Ma Jia

**Conceptual Design of High Temperature Water-Cooled Divertor Plasma-Facing Unit for Fusion Reactor** . . . . . 705  
 Xin Mao, Xuebing Peng, Xiaobo Chang, Xinyuan Qian and Ping Liu

**Corrosion Resistance of Oxide Dispersion Strengthened Steel in Supercritical Water** . . . . . 715  
 Kaiju Yin, Wu Tang, Hao Wang, Xiaofeng Hong, Shaoyu Qiu, Rui Tang and Yong Chen

**Design of a Thin-Film Neutron Detector Used for Personnel Dosimeter** . . . . . 725  
 Wenming Xia, Junjun Gong and Junjun Chen

**Development and Verification of Liquid-Fueled Molten Salt Reactor Analysis Code Based on RELAP5** . . . . . 731  
 Chengbin Shi, Maosong Cheng and Guimin Liu

**Emergency Strategy Research of MSLB Accident with Loss of Passive Residual Heat Removal for Small Modular Reactor** . . . . . 741  
 Yuqi Wang, Aimin Yu and Tao Tang

**Evaluation and Analysis of Forced Convection Heat Transfer Correlations for Supercritical Carbon Dioxide in Vertical Tubes** . . . . . 753  
 Sheng-hui Liu and Yan-ping Huang

**Experimental Study on the Effects of Temperature and pH on the Deposition of Corrosion Products in Fusion Reactor** . . . . . 769  
 Yan Ma, Jinyun Lei, Xin Xu, Yun Fu, Yixue Chen and Arslan Muhammad

**Large-Fluence Laser-Driven Ion Beam for Inertial Fusion Ignition** . . . . . 775  
 Suming Weng, Zhengming Sheng, Masakatsu Murakami, Min Chen, Lule Yu and Jie Zhang

**Lead Cooled Fast Reactor Core Physics Parameters Calculation Based on Monte Carlo Method** . . . . . 783  
 Yang Lyu

**Neutron Activation Analysis of Candidate Materials for High-Temperature Reactors** . . . . . 793  
 Ramy Tannous, Chary Rangacharyulu, Dave Guzonas and Laurence Leung

**Physics Analysis of Alternative Fuel Options for HTGR** . . . . . 801  
 Hangbok Choi, Robert Schleicher and Myunghee Choi

**Preliminary Design of Oxygen Control and Purification System in Lead-Alloy Cooled Reactors** . . . . . 813  
 Xian Zeng and ShuBin Sun

**R&D of the In-Vessel Materials for Future Magnetic Confinement Fusion Reactors at SWIP** . . . . . 825  
 Xiang Liu, Jiming Chen, Kaiming Feng, Pengfei Zheng, Youyun Lian, Penghuai Wang, Xiaoyu Wang, Yongjin Feng, Xuru Duan and Yong Liu

**Research on Ionizing Effects in  $\gamma$ -Ray-Irradiated CMOS Pixel Image Sensor** . . . . . 839  
 Shou-Long Xu, Shu-Liang Zou and You-Jun Huang

**Scheme Research of Mars Surface Nuclear Reactor Power** . . . . . 853  
 Chengzhi Yao, Shouzhi Zhao, Gu Hu, Jiachun Xie, Jian Guo and Jian Gao

**Seawater Desalination Technology Route and Analysis of Production Capacity for Large Commercial Nuclear Power Plant** . . . . . 865  
 Hong-mei Yan, Cheng-yan Cao, Gang Bai and Wei Bai

**Structural Design and Verification of the CNFC-HTR New Fuel Transport Container** . . . . . 873  
Ning Li, Hongjun Zhang and Xiaogang Xu

**Structure Design of Calorimeter of EAST-NBI System Using Thermal Inertia with Cooling Water** . . . . . 883  
Ling Tao, Chundong Hu and Yuanlai Xie

**Study of the Tritium Breeding Blanket in an Hybrid Fusion–Fission Transmutation System** . . . . . 895  
Juan-Luis François, Cecilia Martín-Del-Campo and Aldo Fierro

**Tagged Neutron Method Analysis: A Technique for Explosives Detection and Identification** . . . . . 905  
Shi-wei Jing, Gui-fu Yang, Yong Guo, Huan-yu Li, Xuan Liu, Yan Zheng, Yu-lai Zheng, Qiang Wang and Guo-bao Wang

**Using Traveling Wave Reactor (TWR) Technology to Provide Globally Scalable and Sustainable, Carbon-Free Energy** . . . . . 919  
Kevan D. Weaver, John R. Gilleland and Robert Petroski

**Part I**  
**Operation and Maintenance**

# A Study of AP1000 Nuclear Power Plant SGTR Event Processing Strategy

Zhang Jintang and Ai Chen

**Abstract** As a key equipment in nuclear power plant, steam generator (SG) serves for both primary and secondary systems. As the pressure boundary of primary system during plant operation, when SG tubes experience rupture (SGTR), primary coolant could flow into secondary system, causing loss of coolant in primary system and radioactive materials enter into second system. If loss of offsite power happens or turbine condenser steam dump is unavailable during the accident, radioactive materials may release to atmosphere through steam relief valve or safety valve. Therefore, when dealing with SGTR, loss of primary coolant should be stopped in a timely manner, radioactivity release should be prevented as well. As the third generation advanced nuclear power plant, Passive Pressurized Water Reactors (PPWR) adopts a series of measures in design to fully satisfy the utility' requirements (URD) when face of SGTR. This paper compares the differences in regard to SGTR management between M310 and PPWR, and performs simulation verification using the latter's full-scope simulator on conditions that with/without intervention from operators, it turns out that PPWR units can mitigate radioactive consequences of SGTR effectively; its management of SGTR reflects features of advanced nuclear power plants defined by the U.S. NRC.

**Keywords** SGTR · Advanced nuclear power plant · Existing nuclear power plant · M310 · PPWR

---

Z. Jintang (✉) · A. Chen  
Shan Dong Nuclear Power Company, Haiyang, Shandong, China  
e-mail: zhangjintang@sdnpc.com

A. Chen  
e-mail: aichen@sdnpc.com

## 1 Introduction

Steam Generator Tube Rupture (SGTR) of Pressurized Water Reactor (PWR) Nuclear Power Plant (NPP) is an accident occurred due to the complete rupture of heat transfer tube resulted in the decrease of coolant water inventory. Being one of the design basis accidents that might happen within the life period of a PWR NPP, it features in a comparatively high frequency of occurrence and severe consequence of radioactivity. When accident occurs, multiple SG tubes would be ruptured due to shear fracture. The flow passing through this rupture would be significantly higher than the leakage rate under normal conditions due to differential pressure of primary and secondary systems. As coolant leaks to secondary side which has a lower pressure at a comparatively fast flow rate, water in secondary side would be contaminated. If condenser is inoperable at this time, contaminated steam might go into atmosphere directly via power-operated relief valve (PORV), resulting in radioactive contamination of the environment. Therefore, the focus of SGTR management is to maintain the coolant inventory of primary system while preventing damaged SG to be overfilled. When dealing with SGTR, existing NPPs mainly rely on operators' active intervention to prevent SG from overfilling and avoid large release of radioactive materials through PORV or safety valve; however, the Generation III passive advanced nuclear power plants represented by AP1000, taking Human Factors Engineering into consideration during the design stage, could significantly reduce the dependency on operators, namely, SG would never be overfilled even without operators' intervention, what is more, the amount of radioactive materials being released to the atmosphere is also acceptable. Currently, AP1000 and M310 are two major reactor types being constructed and operated in China. By comparing their different management strategies in response to SGTR, this paper introduces the management concept and methods of SGTR of the advanced NPPs.

## 2 SGTR Management Strategy of M310

In order to prevent radioactive materials from releasing into atmosphere during SGTR, the management strategy of M310 in response to SGTR is to assume that operators identified the failure of SG 10 min after reactor scram and then performed intervention. Intervention actions are as follows:

- Identify and completely isolate the damaged SG.
- Cool down and depressurize Reactor Coolant System (RCS). Using the relief valve of the integrated SG to cool down RCS with a speed rate as close as possible to 56 °C/h.
- Depressurization by auxiliary spray.



- Maintain adequate degree of subcooling during transient, and complete the transition from safety injection to primary system filling.
- When pressure at secondary side equals that of primary side, leakage stops.

After SGTR occurs, coolant from primary system leaks to the SG of secondary system, leading to the reduction of coolant water inventory in primary system; in order to compensate the lost coolant, an automatic actuation safety injection signal is set in M310 to actuate scram and start safety injection system to make up for primary system.

The SGTR accident sequence of M310 is as follows:

1. SGTR occurs during power operation, RCS coolant leaks to SG.
2. Pressurizer (PZR) low pressure signal actuates reactor scram and turbine trip.
3. PZR low 2 pressure signal actuates the start of SI Injection Pump (Train 2).
4. Operators' intervention per A3 procedure: stop Train 1 Injection Pump, and primary system starts to depressurize and cool down (56 °C/h).
5. Train 2 SI Injection Pump stops.
6. Pressure at primary side of the damaged SG equals to that of secondary side.

After analysis of the accident sequence of M310, the following features of its accident management strategies are identified:

- Operators' active intervention is required and should be in place within 10 min after SGTR occurs.
- Safety injection to feed primary system should be stopped in a timely manner to prevent too much coolant flow into SG.
- Cool down and depressurize primary system should be rapid to balance the pressure between primary and secondary system. Cooldown should be performed prior to depressurization to maintain adequate subcooling degree of primary system coolant.
- Without operators' intervention, pressure between primary and secondary system cannot be balanced, causing SG to be overfilled which would result in radioactive materials' constantly release into atmosphere.

### **3 SGTR Management Strategy of PPWR**

The requirements of URD (Utility's Requirements Document) from the U.S. NRC to advanced nuclear power plant (passive light water reactors) in regard to accident management have emphasized that adequate response time margins should be reserved for operators to intervene (at least 72 h after initial event occurs which requires actions, no manual interventions from operators are necessary), and adequate safety margins should also be guaranteed in design. In order to meet such requirement of URD, PPWR gives more space to PZR and SG in design, a series of

automatically controlled protection configuration are also designed to prevent excessive loss of primary system coolant and SG's overfilling even without intervention from operators, which is almost impossible to happen.

### ***3.1 The Automatic Process to Deal with SGTR of PPWR***

- PZR low pressure and low level are actuated to start or increase the uprush flow of CVCS and heating capacity of PZR electric heater to try to maintain PZR's water level and pressure. In SG secondary side, SG level increases because of the flow through ruptured tube from primary side to secondary side, leading to the decrease of main feedwater flow of the damaged SG.
- Alarms from Condenser Deaeration Radioactivity Release Monitor, SG Blowdown Radioactivity Detector/Main Steam Line Radioactivity Monitor indicate increase of radioactivity in secondary system.
- Continuous loss of reactor coolant inventory would actuate PZR overpressure or over temperature  $\Delta T$  signal and in turn trip the reactor. After reactor trips, further decrease of reactor coolant pressure and PZR level would be offset somewhat as CVCS compensates the flow and PZR electric heater goes into operation. PZR Low-3 pressure signal would actuate "S" signal which starts CMT and PRHR heat exchanger. "S" signal would also automatically shut off normal feedwater and reactor coolant pumps, and terminate power supplied from PZR electric heater. Startup feedwater system is started by SG narrow range low level signal, and SG level would be maintained at the setpoint of this level.
- Turbine would be tripped automatically after reactor trips. If offsite power is available, steam dump valve opens to allow steam dump to condenser. Under accident conditions of loss of offsite power or failure of condenser, steam dump valve automatically closes to protect condenser. SG pressure would increase rapidly, forcing steam dump to atmosphere through SG PORV or safety valve.
- As reactor trips, CMT and PRHR put into operation, PRHR heat exchanger would go into operation, together with startup feedwater flow, boric flow of CMT and flow of CVCS, heat sink is provided for the removal of decay heat. The quantity of SG steam as well as steam bypassed to condenser would be reduced.
- Flow from CVCS and CMT would stabilize RCS pressure and PZR level, RCS pressure would approach an equilibrium value with the total injected flow equals to flow from the ruptured tube.
- As pressure between primary and secondary system temporally approaches to balance, CVS makeup water would be isolated and PZR electric heater be shut off to reduce the recovery of primary system pressure.
- Startup feedwater system would be automatically isolated to prevent SG from overfilling due to its failure and continuous makeup occurs.

### 3.2 Simulator Verification on PPWR's Automatic Disposition of SGTR

PPWR full-scope simulator is supplied by NI supplier, who is responsible for the design and manufacture of simulator hardware, design and development of plant system simulation software. Taken Unit 1 of an PPWR NPP as reference, the simulated process is mainly as follows: Initial condition: 100 % power operation; PZR pressure at 15.41 MPa, water level at 46.8 %; SG pressure at 5.52 MPa, water level at 58.6 %; Feedwater flows of 2 SGs equal to steam flow at 99.8 %; The unit is at stable condition with offsite power available. The simulated result is as follows:

1. 0s: One SG tube ruptures with a leakage area of 1.88 cm<sup>2</sup>.
2. 5s: SG N-16 high radioactivity alarm in and instrument saturation.
3. 240s: CVS water makeup actuated.
4. 760s: Control rod insertion, Tavg rises.
5. 1200s: PZR water level decreases to 20 %, electric heater is removed.
6. 2010s: PZR water level decreases to 10 %, CMT actuated.
7. 2040s: PZR pressure reduces to 12.5 MPa, S signal actuated.
8. Around 15000s: Pressure between primary system and SG1 are balanced, leakage stops (Figs. 1, 2 and 3).

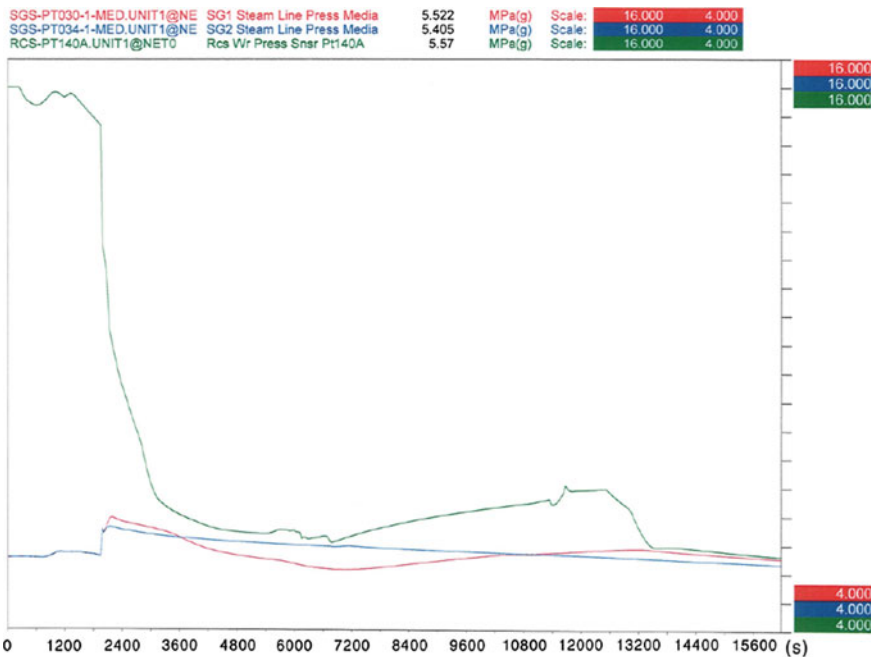


Fig. 1 Pressure of RCS and SG secondary side

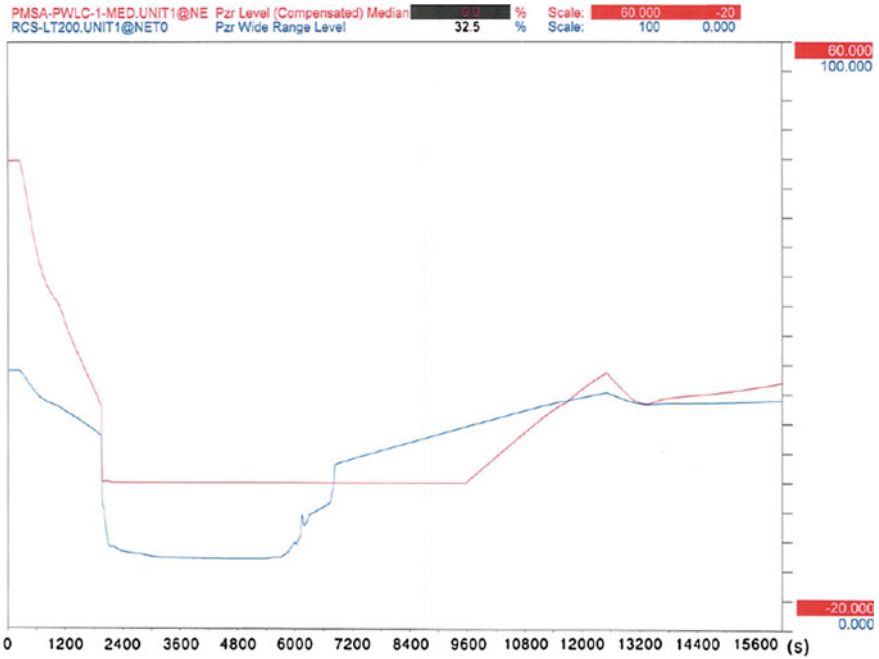


Fig. 2 Narrow/wide range level of PZR

Simulated result has showed that: pressure between primary and secondary system reaches equilibrium automatically, and water inventory in primary system is guaranteed so that SG will not be overfilled. During accident evolution, the maximum pressure of damaged SG is 6.6 MPa, therefore, PORV and main steam dump valves will not open.

### 3.3 Operators' Intervention and Simulator Verification of SGTR

After SGTR occurs, by accident diagnosis, operators can adopt recovery measures to trip the reactor in a timely manner before automatic protection system is actuated so that leakage from primary side to secondary side can be stopped and NPP be maintained at a stable condition. According to Abnormal Operating Procedure (AOP) and Emergency Operating Procedure (EOP), operations are as follows:

1. Identify the damaged SG in a timely manner by SG radioactivity alarm and chemistry sampling.

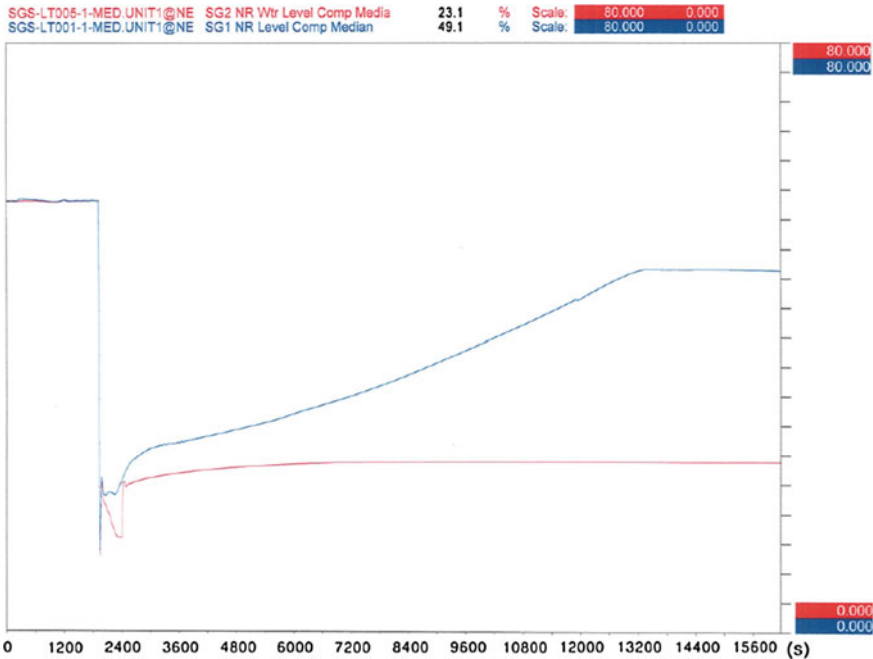


Fig. 3 Level variation of SG1 and SG2

2. Manually trip the reactor and actuate S signal per procedure after SG leakage rate ( $49.05 \text{ m}^3/\text{h}$ ) exceeds the maximum makeup capacity ( $39.7 \text{ m}^3/\text{h}$ ) of CVS is determined.
3. Operators ensure Engineered Safety Features (ESF) motion is normal using about 20 min, during which time 5 min will be used to go to EOP (SGTR).
4. Isolate the damaged SG and provide maximum makeup water to primary system; startup feedwater is in operation to supply water to the integrated SG, check if the pressure of primary system is lower than the value to allow S signal blocking, or to depressurize primary system until it is below the value.
5. Block S signal, cool down RCS via integrated SG, depressurize RCS by auxiliary spray.
6. Maintain the level of damaged SG is above the minimum flooding level of heat transfer tube, and maintain the level of integrated SG at zero power setpoint.
7. 50 min after SGTR occurs, pressure between primary system and the damaged SG balances out, and the leakage is stopped.
8. Stop unnecessary plant equipment, isolate CMT.
9. Maintain the saturation of PZR to ensure pressure control of primary system, restore letdown and operation of RCP, and isolate ACC.

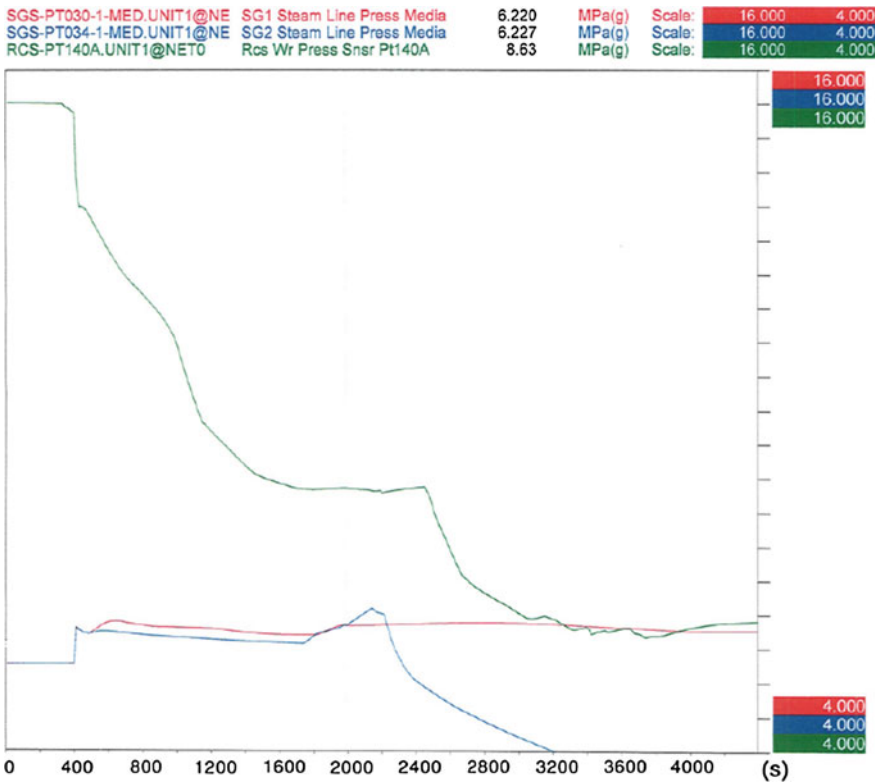


Fig. 4 Secondary side pressure of RCS and SG

- 10. Depressurize the damaged SG, put RNS into operation, establish normal feed to RCS and isolate PRHR.
- 11. Maintain cold shutdown.
- 12. The simulated result is as follows (operators intervened 20 min after accident occurs) (Figs. 4, 5 and 6).

Simulated result has showed that: even if operators begin intervention 20 min after the accident occurs, pressure between primary and secondary system could still be balanced after 50 min; water inventory of primary side can be maintained and SG will not be overfilled; under the condition that offsite power and condenser are available, main steam power-operated valve (MSPORV) will not release radioactivity to atmosphere.

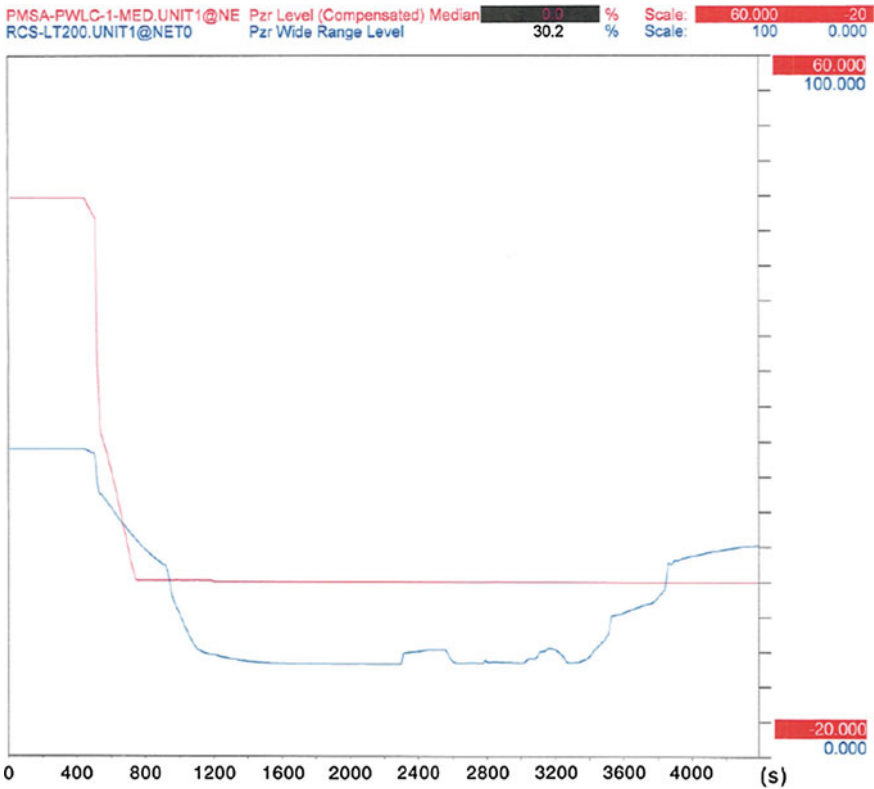


Fig. 5 Narrow/wide range level of PZR

### 3.4 Summary

PPWR is designed to use bigger PZR and SG to buy more time for operators to respond after SGTR occurs; the application of passive safety injection system, residual heat removal system and the more reliable automatic control system has simplified operators' intervention, and can avoid the overfill of SG even without any intervention.

## 4 Comparison

Although the mitigation strategy of PPWR to SGTR is similar to that of M310, its outstanding features are indicated in specific mitigation measures (including the automatic response of systems); major differences can be concluded as to key mitigation measures or outcomes:

Items compared	M310	PPWR
Necessary intervention from operators	YES	NO
Dependency on AC power	YES	NO
Safety injection mode	Active	Passive
Cooling mode of primary system	Manual/active	Automatic/passive
Risk of primary system overpressure	YES	NO
Risk of SG overfill	YES	NO
Risk of PORV open	YES	NO

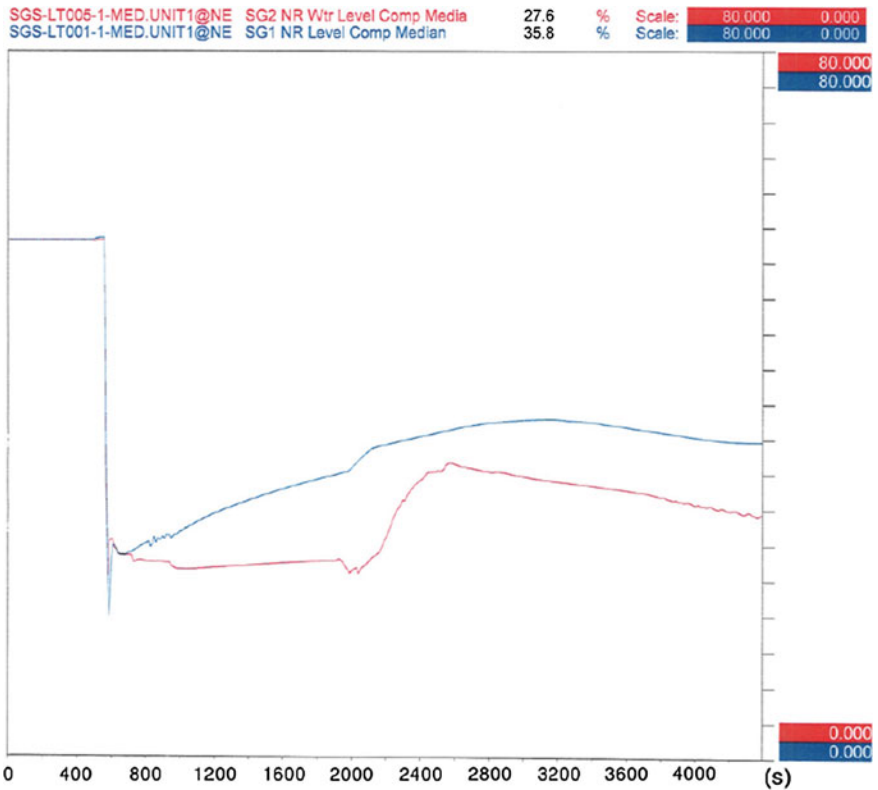


Fig. 6 Level variations of SG1 and SG2



## 5 Conclusion

Nine technical features of advanced NPPs were put forward in Suggested Management Policies of Advanced Nuclear Power Plant issued in 1985 by the U.S. NRC, including:

- Reactor trip and residual heat removal system of high reliability and less complexity; inherent and passive methods are encouraged to be adopted to achieve this goal.
- Longer event coefficient and adequate instrumentation to allow more diagnosis and disposition in case of safety system is challenged/key equipment are exposed to adverse conditions.
- As far as possibly simplified systems to reduce necessary actions from operators; for equipment in face of adverse conditions and parts necessary to maintain a safety reactor trip condition, simplified system should be beneficial for operators to understand, and also in favor of reliable system functions as well as more direct construction analysis.

The analysis of SGTR management strategy of PPWR has showed that the large capacity of PZR and SG, the application of passive safety injection system and residual heat removal system as well as the design of multifunctional automatic control of PPWR have reflected the technical features of advanced nuclear power plants.

# A Summary of the Guidelines on the Evaluation of V&V Tools for Safety Digital I&C Software in Nuclear Power Plant Systems

Nan Wang, Lingpo Li, Ruidong Dai and Chun Guo

**Abstract** With the rapid development of the digitalized instrumentation and control (I&C) systems, computer-based and software-driven systems have been employed in nuclear power plant on a large scale. Automated tools take a crucial role in the software verification and validation (V&V) process. However, defects in the tools may bring uncertainty, risk, and even failures to the safety software if the tools are not well designed, carefully developed, effectively tested, and appropriately used. Therefore, it is critical that automated tools should be evaluated and tested for the reliability, accountability, and feasibility before they are used in the software V&V process. However, there is no widely accepted method to evaluate the tools. Many methods for tool evaluation have been proposed by different organization, including nuclear industry and other high reliability industry. This study is a survey of the current practice and standards related to the evaluation of tools for safety-related digital Instrumentation and Control (I&C) software for nuclear power plants. Standards and documents from organizations such as IEEE, IAEA, and NRC Regulations are collected and analyzed in this paper. By summarizing and analyzing the related standards and practice, this study intends to explain what should be done for the evaluation of the tools, which may be used in the self-reliance process of nuclear industry in China.

**Keywords** Digital I&C · V&V · Software tools · Standards · Regulatory guidance

## 1 Introduction

With the advanced nuclear power reactors under development, the demand for safety I&C system is urgent. The tools used for the evaluation of the developed product should have high reliability and accountability. In terms of verification and

---

N. Wang (✉) · L. Li · R. Dai · C. Guo  
State Nuclear Power Automation System Company, Shanghai, China  
e-mail: wangnanb@snpas.com.cn

validation process, automated software tools are frequently used. Uncertainty and even risks should be controlled in an acceptable level so that tools will not affect the feasibility and reliability of the whole system.

This paper does a survey of the current regulations, guides, and standards that are relevant to the V&V process. A summary of the information related to the software tools is listed. Based on the information, a detailed guideline to the V&V work is pictured.

## **2 Discussion and Survey Summary**

### **2.1 *RG 1.152***

Regulatory Guide (RG) 1.152, Revision 3 [1], provides a method for “promoting high functional reliability, design quality, and a secure development and operational environment (SDOE) for the use of digital computers in the safety systems of nuclear power plants”, which is accepted by NRC. This regulatory guide takes hardware, software, firmware, and interfaces into account based on waterfall life cycle.

Section 2.2 describes the requirement of predeveloped software and systems. It is emphasized that unnecessary or extra requirement and codes should be prohibited.

Section 2.3 describes the software tool requirement of design phase. Predeveloped software shall guarantee the safety of the operating environment. Special measurements should be taken if unwanted features are introduced.

Section 2.4 describes the software tool requirement of implementation phase. Due to the fact that most of the COTS software is confidential, reviews cannot be conducted directly because of uncertainty. Developers are required to ensure the COTS software will not threaten the operating environment.

The conclusion reached from the (RG) 1.152, Revision 3 [1], is that development and operating environment must be ensured, for the sake of preventing unnecessary and unauthorized code. Besides, the review of COTS and predeveloped software should be considered carefully.

### **2.2 *RG 1.168***

RG 1.168, Revision 2 [2], provides a method for software V&V and review, which is accepted by NRC. There is not much information related to software tools.

Section C 3 requires that if the product will be introduced in a safety-related system, the licensee shall be responsible for assuring that the V&V and software

quality meet the NRC's requirements for reliability. The independence of V&V software tools should comply with regulations and laws.

Section C.4 requires that the acceptance of preexisting software shall be based on RG 1.152.

Section C.6 describes the requirement of safety-related system software tools. "V&V tasks of witnessing, reviewing, and testing are not required for software tools, provided the software that is produced using these tools is subject to V&V activity that will detect flaws introduced by the tools."

### **2.3 *RG 1.169***

RG 1.169, Revision 1 [3], discusses the method of configuration management, which is accepted by NRC.

Section C.6 requires that configuration items or controlled documents shall include all the supportive software during development phase and codes used during testing.

Section C.7 requires commercial software dedication for safety-related systems shall comply with the recommendation of EPRI TR-106439.

Section C.8 requires that all the software that is used during development phase shall be managed according to IEEE 7-4.3.2-2003. Besides, software tools during development phase should be treated as a configuration item.

### **2.4 *RG 1.170***

RG 1.170, Revision 1 [4], discusses the test documentation of safety-related digital computer software in a nuclear power plant. It requires that the minimum documentation package shall include all the elements that are essential for completing the task, including environmental conditions, special controls, equipment, tools and instrumentation.

### **2.5 *RG 1.172***

RG 1.172, Revision 1 [5], discusses the software requirement specification of the digital I&C system in a nuclear power plant. If representation tools are used to express the requirements, the traceability between the representations and natural language descriptions of the software requirements needs to be maintained.

## **2.6 *RG 1.173***

RG 1.173, Revision 1 [6], discusses the process of software life cycle. This guide has little relevance with software tools. It mainly focuses on the acceptable process of COTS software evaluation.

## **2.7 *DI&C-06***

DI&C-06 requires dedicating COTS and predeveloped software tools for safety-related systems based on EPRI TR-106439.

## **2.8 *NUREG-0800***

NUREG-0800 [7] BTP 7-14 requires that software tools shall be reviewed according to their rigidity. Methods, techniques, and tools shall be verified to an acceptable degree.

NUREG-0800 Appendix 7.1-D requires that the system shall meet single-failure criterion. Software tools shall not violate single-failure criterion, especially compilers and linkers. Section 5.3 of this appendix discusses the usage of software tools. Review of software tools shall comply with the content in IEEE 7-4.3.2-2003 and IEC 60880-2. “If, however, it cannot be demonstrated that defects not detected by software tools or introduced by software tool will be detected by verification and validation (V&V) activities, the software tool should be designed as safety-related software itself, with all the attendant regulatory requirements for safety software.”

## **2.9 *NUREG/CR-6421***

NUREG/CR-6421 [8] proposes an approval process for COTS software employed in nuclear power plant safety systems. Section 1.3 states that the system software tools are important for safety. Therefore, they shall be classified as critical software tools. The safety category classification of COTS software is category A, B, C, or unclassified.

## **2.10 IEEE Std 7-4.3.2**

IEEE Std 7-4.3.2-2010 [9] Sect. 5.3.2 discusses the usage of software tools, which contains two criteria. The first one is that the output of the software needs to be verified and validated based on the same safety degree of the software. The second one is that development and commercial dedication shall be conducted according to quality assurance requirement in 10 CFR 50 Appendix B.

## **2.11 IEEE Std 603-2009**

IEEE Std 603-2009 [10] provides the minimum functional design for the safety system in a nuclear power plant. Two important proposed concepts are the isolation between safety and non-safety systems and the single-failure criterion. It also accounts common cause failure, which is defined as “loss of function to multiple structures, systems, or components due to a shared root cause”. Software tools evaluation should take single-failure criterion and common cause failure into account.

## **2.12 IEEE Std 1012**

IEEE Std 1012 [11] extends the definition description of the software tool by different revisions. IEEE Std 1012-2012 requires that “If the tool cannot be verified and validated, then the output of the tool shall be subject to the same level of V&V as the software element”.

## **2.13 IEEE Std 14102**

IEEE Std 14102-2010 [12] defines the process and features of CASE tool selection. This standard can be used during the process of software tools technical evaluation and selection. The process of tool selection includes preparation, definition, evaluation, and selection. The subsequent documentation can demonstrate the quality of selected tools.

### **2.14 IAEA NS-G-1.1**

IAEA NS-G-1.1 [13] describes the planning, documentation, selection, and qualification of software tools. This guide considers all categories of software: preexisting software (e.g., an operating system), software developed for the project (testing software tools).

Section 3 requires that software based on computer systems shall hold diversity and variety. Software tools shall commensurate within different phases. Based on the function in the development phase and the safety-related requirement, software tools need to be dedicated accordingly.

Section 10 [13] focuses on the software verification and validation. Software verification and validation tools will not introduce defects to the system. However, it also may not detect defects. For tools including V&V tools, it is necessary to have adequate safety features to ensure overall safety. During the V&V process, test operators shall keep adequate records (including tools, input, setup etc.) in order to demonstrate that the process of V&V tests can be repeated.

## **3 Conclusions**

Regarding to software tools, guides and standards surveyed in this paper directs that

1. Software tool verification and validation shall be conducted based on application methods and functions to assure the accuracy.
2. Configuration management is essential.
3. Commercial software that is directly used in nuclear power plants shall conduct the CGI dedication.

Detailed explanation is as following (e.g., test signal generating devices):

1. According to IEEE 1012-2012, it is regarded as tool without codes. Therefore, verification needs to be done to ensure the correctness of the function.
2. According to IAEA NS-G-1.1, it is regarded as a V&V tool. It is required to figure out the function and effect on the environment and then start the evaluation task accordingly.
3. According to IEEE 7-4.3.2-2003, a V&V program needs to be developed to demonstrate that the tool can be function correctly as the requirement states.
4. According to IAEA NS-G-1.1, based on testing requirement, clear and adequate records are demanded, as well as calibration and standardization of the tool periodically.
5. In addition, it shall comply with the basic quality assurance requirement. Development phase documentation of the tool is also required.

## References

1. Regulatory Guide 1.152, Revision 3
2. Regulatory Guide 1.168, Revision 2
3. Regulatory Guide 1.169, Revision 1
4. Regulatory Guide 1.170, Revision 1
5. Regulatory Guide 1.172, Revision 1
6. Regulatory Guide 1.173, Revision 1
7. NUREG-0800
8. NUREG/CR-6421
9. IEEE Std 7-4.3.2-2010
10. IEEE Std 603-2009
11. IEEE Std 1012-2012
12. IEEE Std 14102-2010
13. IAEA NS-G-1.1



# Analysis and Handling of Turbine Eccentricity Anomaly

Qiaochan Zhou

**Abstract** This article found out that inappropriate mounting gap between the key phase sensor and corresponding key phase marker was the main cause of excessive turbine eccentricity which occurred in TQNPC, put forward an improved mounting method of key phase sensor which not only avoids the fault recurring, but also can be used as work reference to similar rotary mechanism.

**Keywords** Turbine · Eccentricity · Installation of key phase sensor · Threshold voltage · Hysteresis

There is no doubt that the turbine as an energy convertor plays a very important role in a power plant. For safety reason, the eccentricity of the turbine always considered a vital parameter to assess the whole device operation status. It is an indicator of rotor, which is observed while on turning. It is defined as the variation between the outer diameter of a shaft surface and the true geometric center line of the shaft. This variation, called shaft bow, can be a fixed mechanical bow, a temporary thermal or gravity bow, or some combination of each. The eccentricity is useful in determining shaft attitude angle, which is an indicator rotor stability, this makes the rotor eccentricity monitoring a must-do to evaluate the rotor bow. Based on the result previously mentioned, the operators can take appropriate actions accordingly. Therefore, reckless turbine speedup and further serious damage can be totally avoided.

When the turbine runs under low speed, it can be called rotor static bow and is used as one turbine startup restrictive condition. When the turbine rotate speed reaches 600 rpm and beyond, the rotor will deflect and drift significantly thanks to the exciting force it received. For the time being the parameters that the eccentricity transducer conducts including shaft vibration, rotor deflection and original swing but no real eccentricity, since then the eccentricity monitoring loses its fundamental meaning.

---

Q. Zhou (✉)  
CNNO, Jiaxing, Zhejiang, China  
e-mail: zhouqc@cnp.com.cn

## 1 Introduction

The turbine that running in TQNPC modeled TC4F-52 with a full power 728 MW and a rated speed 1500 r/min is supplied by Hitachi. The whole shafting of the turbine unit consists of one high-pressure rotor, two low-pressure rotors, and one generator rotor. The Eccentricity Monitoring system consists of the following components and is manufactured by Shinkawa, a Japanese company: Probe and Driver, installed in the Turbine; Eccentricity monitor with two input ports mounted labeled Channel 1 and Channel 2, installed in the Control Equipment Room.

There are two eddy sensors working collaboratively to perform the turbine eccentricity monitoring, one is a VK-202A eddy sensor which can be found in the front box and is used as a eccentricity detector, another is a VK-202A eddy sensor which is located between the HP and LP which acts as the key phase detector, both sensors are 8 mm probes. For the key phase detecting part, the key phase marker is designed as a projection sized 38 mm × 14 mm × 9 mm (L × W × H), therefore care must be taken when adjusting the gap between the marker and the top of the sensor to make sure it in the  $1.3 \pm 0.05$  mm tolerable range without damaging the sensor.

The input signal to the monitor from the eccentricity transducer is split into two channels designated as direct and peak to peak channels. Direct measurement is the gap between the sensor tip and the rotating surface. The peak to peak measurement is the summation of the upper and lower peaks of shaft radial motion during a complete shaft revolution. Of which, the direct measurement derived from the key phase transducer enters the monitor through channel 1 and the peak to peak measurement derived from eccentricity transducer through channel 2. As we know, the key phase sensor produces a nonstandard pulses with amplitude ranges from  $-10$  to  $-21$  Vdc as the shaft spins, the nonstandard pulses then get rectified by the monitor previously mentioned and used as the time base to achieve the real-time peak to peak eccentricity in that revolution. Furthermore, the pulses are counted to calculate the real-time turbine speed. As we discussed in the second paragraph, once the turbine speed reaches 600 rpm, the eccentricity signal will be cut off by the turbine speed control signal.

Since the key phase signals (event) come from key phase transducer cannot be used directly (see preceding paragraph), it is necessary to rectify them to standard ones (see Fig. 1). To achieve this goal, a circuit loop fabricated in the monitor unit provides a reference voltage to compare the key phase inputs and triggers out standard pluses. For this process and in case of noises-induced accidental action, two key parameters are needed to configure carefully to get appropriate signals, they are called Threshold and Hysteresis, respectively, here Threshold is the voltage level in the input signal where the trigger out pulse turned on, and Hysteresis is the difference between the level where the trigger out pulse turns on and the level where it turns off. Since different configuration could lead to different results, that is why

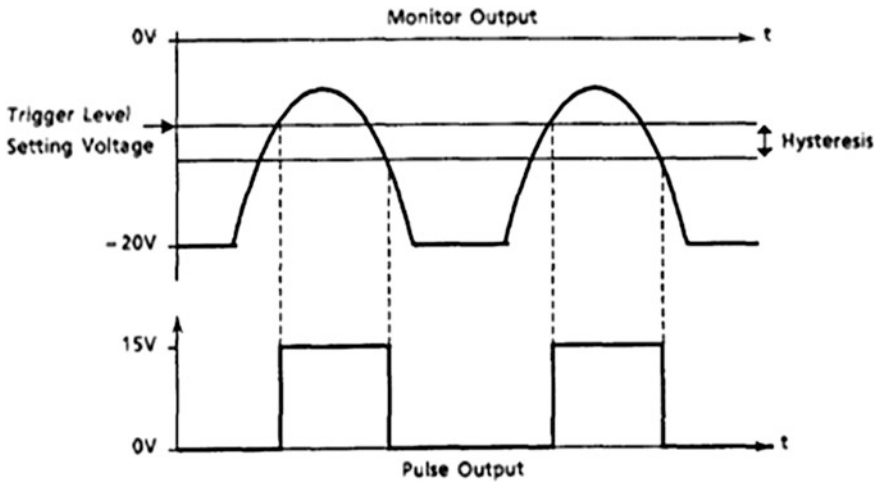


Fig. 1 Key phase pulses rectifying [1]

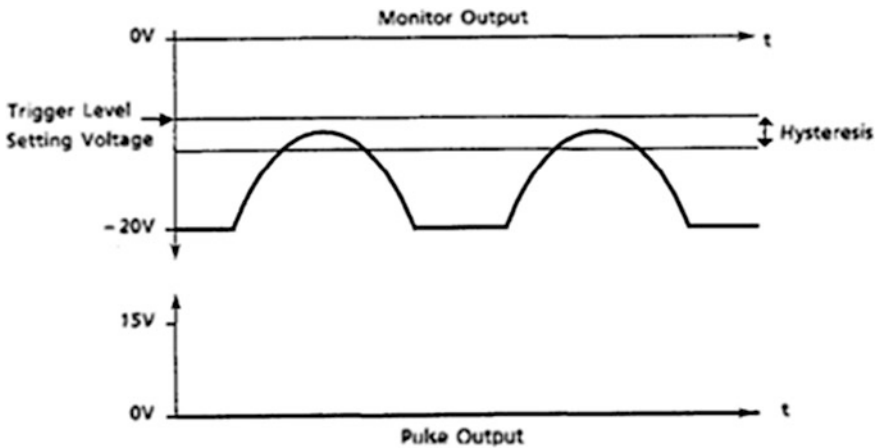


Fig. 2 If threshold selected too high [1]

the two parameters must be taken seriously, the following two scenarios should always keep in mind, (1) too high threshold value selected could mean no trigger out pulses at all (see Fig. 2), and (2) too small hysteresis value selected could mean too many trigger out pulses (noises could become effective pulse, see Fig. 3).

The trigger out pulses first buffered then output through BNC connector on front panel of the monitor unit and terminal bar on the backplane.

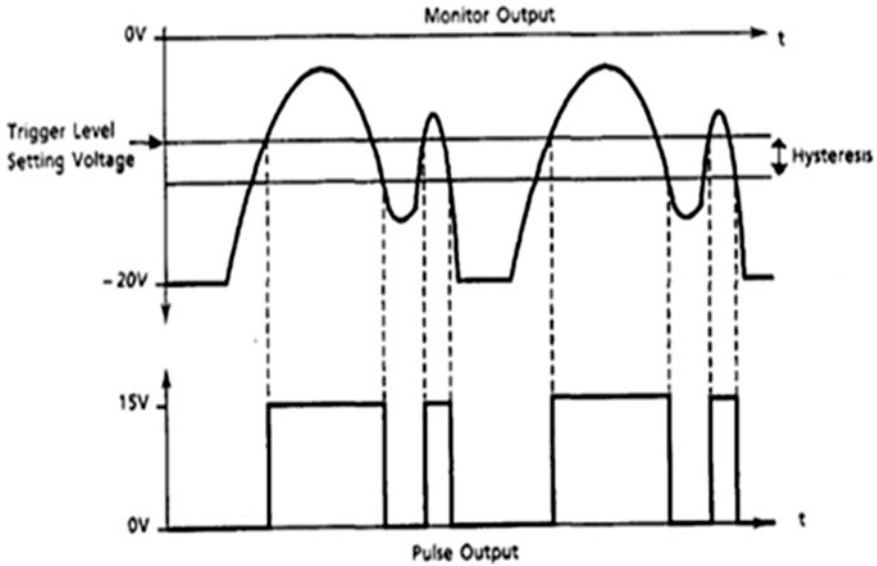


Fig. 3 If hysteresis selected too small [1]

## 2 A Case of Historic Fault

On February 7th, 2015 in TQNPC, the operators were implementing Main Control Valves stroke periodic test as plan, at 15:32 a alarm message issued by TSI system warning that the turbine eccentricity high while the MCV No. 2 test was underway, but no such messages occurred on MCV No. 1s and No. 3s due. According to the Turbine Monitoring Trend, the maximum eccentricity value peaked at 0.028 mm (see Fig. 4, in green), and other turbine monitoring parameters showed that the turbine power (in cyan), rotor position (in yellow), low-pressure cylinder differential expansion (in red), high-pressure cylinder differential expansion (in purple) all had different degrees of change then.

## 3 Root Cause Analysis

The turbine was running at rating when the fault occurred and as we know from the introduction, this fault should not occur at all, the turbine speed control signal would cut off the eccentricity monitoring signal once the turbine speed reached 600 rpm and beyond, but in fact the eccentricity signal still took effect and issued a eccentricity high alarm message, therefore we could make a conclusion that the turbine speed signal derived from key phase transducer must be wrong, in other

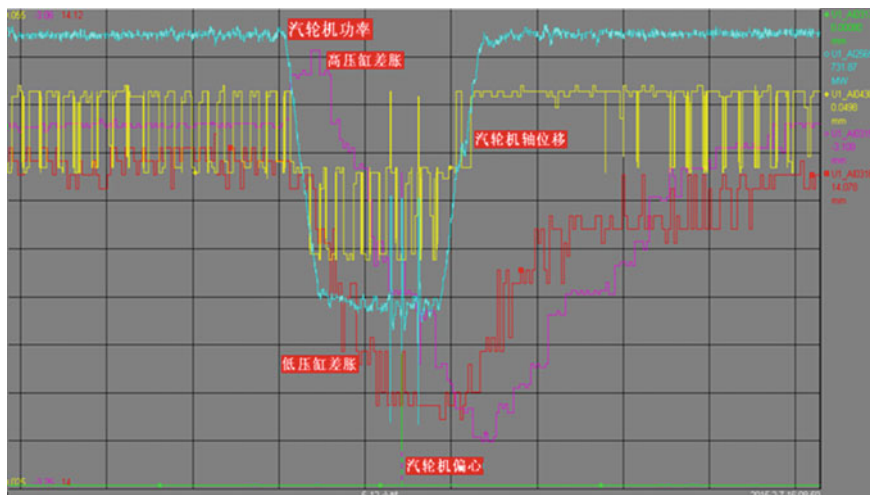


Fig. 4 Turbine monitoring trend (Color figure online)

words, some key phase pulses must be lost. Here are the causes related to key phase transducer signal missing:

1. Key phase transducer precision out of tolerance;
2. Eccentricity monitor precision out of tolerance;
3. Nonstandard key phase pulses rectifier malfunction;
4. Threshold or Hysteresis inappropriate configuration or key phase marker improper mounting (the original key phase pulses could not be fully rectified);
5. Unit operation state changed.

When the turbine runs at high speed, the data detected by the eccentricity sensor is complicated. This means the eccentricity transducer signal cannot simply be used to judge the unit operation state. When the alarm is issued, according to other turbine monitoring parameters trend, the turbine vibration, journal bearing metal temperatures, journal bearing drain oil temperature are all in normal ranges, the trend of shaft vibration from the point near the No. 1 bearing went smoothly and kept stable (especially the trend of turbine shaft No. 1 vibration near the eccentricity measuring point was smooth and kept stable.), and then the control valve was in the closing phase, all the factors which the shaft drifted axially and the steam flow at the nozzle outlet changed continually combined to reach a conclusion, all the factors changed and made the eccentricity value become larger, but no serious damage sign such as shaft excessive bow, dynamic unbalance, rotor-stator collision, etc. Now, the turbine can continue power operation.

If the unit operation state changes, the culprit for the missing key phase pulses would be the marker with a short length. When the shaft drifts axially, the key phase sensor is dislocated from the marker, making it difficult to get accurate measurements. But back then the alarm sounded, high-pressure cylinder differential

expansion and low-pressure cylinder differential expansion were both very tiny, especially the former only changed 0.22 mm, that was too small to compare the marker length of 38 mm, therefore the cause 5 can be taken off the table.

## **4 Troubleshooting and Handling**

### ***4.1 Temporary Handling During Unit Normal Operation***

Since the problem was not the sign of serious damage, it was economically and better to handle it during the unit outage, and before that the maintenance staff could implement some routine checks that would not influence operation of the unit.

Based on this principle, the maintenance staff first checked the key phase transducer signal and eccentricity transducer signal but no anomalies found, then checked the eccentricity monitor and noticed its status LED kept on normally, and initiate the user-invoked self-test with no any error code available. After these steps, an oscilloscope was connected to the key phase trigger out pulse output port to check if there were some pulses missing. The record finally confirmed that there was something wrong with key phase transducer loop.

### ***4.2 Final Handling During Unit Outage***

#### **4.2.1 The Work Done During OT108**

1. Key Phase transducer calibration: before the key phase transducer calibration, it was confirmed the precision of the transducer still in acceptable range, this possible cause was then eliminated.
2. Eccentricity monitor calibration: one card in the monitor unit used for handling eccentricity signals was checked for its precision before calibration and confirmed it was still acceptable. a signal generator connected to the card for 2 days to simulate the eccentricity signal and key phase signal, no any problems found. The possible cause 2 therefore was deleted.
3. Parameters threshold and hysteresis were checked and confirmed that both of them were configured as recommendation. Dynamic eccentricity signal and key phase signal were both simulated at the monitor unit input ports and corresponding indicator were checked, and the results showed both indicators were totally fine, so the possible cause 3 and part of cause 4 (inappropriate threshold and hysteresis configuration) could not stand any more.

From the checks and analysis listed above, what was the cause left was what the cause really existed. So here we can say the improper marker mounting must be the very root cause.

The key phase marker is designed as a sleeve as we mentioned in the overview part, the key phase sensor must always align with the marker when mounting the sensor and adjusting the gap, otherwise it is very possible to cause the two to collide and break the sensor when the turbine runs.

#### 4.2.2 Stereotype Mounting Method of Key Phase Sensor in TQNPC

Following is the stereotype mounting method of key phase sensor used in TQNPC before.

First use the smooth shaft surface as the datum line, adjust the gap voltage of the sensor and key phase marker to the range of  $-11 \pm 0.5$  Vdc (gap  $\approx 1.40 \pm 0.06$  mm), then screw out the sensor of length equals to the key phase marker height, and last fasten the sensor to finish the work.

The stereotype mounting method of key phase sensor still is used in the corresponding work in OT108 of TQNPC, but in the turbine turning stage the key phase sensor gap voltage measured is from  $-15$  to  $-16$  Vdc, which was very close to the threshold setting in the eccentricity monitor. If the shaft drifts even a little bit, the gap voltage will exceed the Threshold, and the monitor unit will not be able to fully trigger out standard pulses (see Fig. 2). In the early years of plant operation, this scenario did not become so obvious which can reduce to two possible causes below

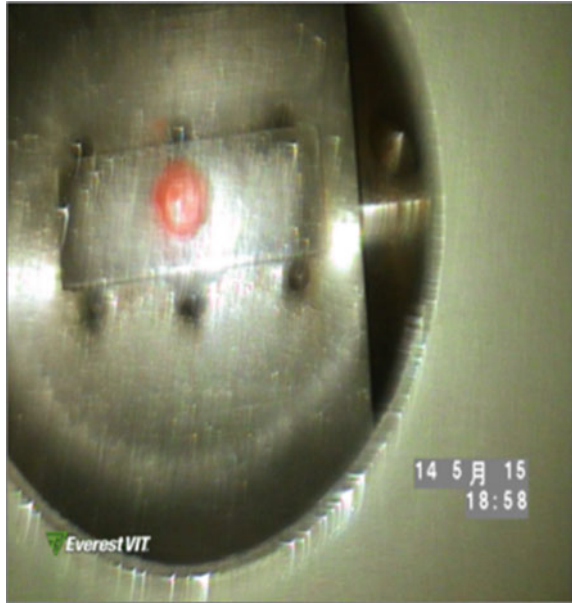
1. If rust or oil stains found on the key phase marker during turbine overhaul with the case opened, grinding works are needed, and it is inevitable to reduce the marker height (original height is 9.5 mm, measured 8.9 mm at OT105). The work staff mounted the key phase sensor according to the later height and made the gap bigger than their expectation.
2. Subconsciously the work staff thinks the smaller the gap, the bigger risk of breaking the top of the key phase sensor, and this prone to cause the gap bigger than requirement according to human thinking.

### 4.3 Solution

Optimize the mounting method of key phase sensor. Change the datum line from the shaft surface to the upper surface of the key phase marker.

Following is the new improved key phase sensor mounting method. First the mechanical work group turns the rotor at speed of  $1/3$  r/h until the upper surface center of the key phase marker aligns with the sensor mounting hole, then inks the top of the sensor and screws it in until it touches the marker. Withdraw the sensor

**Fig. 5** Use an endoscope to check the ink position



and check the ink position on the marker upper surface with an endoscope. If the ink is at the very center (see Fig. 5), the aligning is done, otherwise return the rotor and try again. After the aligning job finished, use the marker upper surface as datum line to mount the key phase sensor. Through this method, the key phase pulse triggers out rightfully, and eccentricity high problem never recurred.

## 5 Conclusions

The key phase signal which derived from the key phase transducer plays a very important role in the turbine eccentricity acquisition. Improper mounting of the key phase sensor will affect eccentricity value directly. This paper made an in depth analysis on the root cause of an abnormal turbine eccentricity alarm of TQNPC, put forward an improved and suitable key phase sensor mounting method which is not only simple, but also highly reliable, and can be used as reference to peer power plants.

## References

1. VM-5 SERIES MONITOR MODEL VM-5C ECCENTRICITY MONITOR INSTRUCTION MANUAL SHINKAWA Sensor Technology. Inc.



# Analysis and Summarization of Continuous Spray Test on Pressurizer of Fuqing Nuclear Power Plant Unit 1

Zeng Bin and Zhao Yang

**Abstract** Pressurizer is the primary equipment on pressure control of primary loop, and spray valves are concerned with pressurizer pressure control. In order to control the pressurizer pressure, spray valves play a vital role, the continuous spray flow rate adjusted to the design value, in order to reduce the thermal stress and shock when spray valves automatically open, and help to maintain the pressurizer uniformity of chemistry and temperature inside water, during reactor power changes, in order to maintain a uniform boron concentration, adjusting the polarization spray flow. Taking Fujian Fuqing Nuclear Power Plant as a reference nuclear power plant, this test describes how to measure heat loss of pressurizer, how to adjust the flow rate to compensate for the continuous spray of heat loss, and the polarization spray flow regulation and verification, providing a reference and guidance for the follow-up spray valve experiment.

**Keywords** Spray valve · Heater loss · Continuous spray · Polarization spray

## 1 Preface

Pressurizer pressure control system is mainly designed to maintain pressurizer at 15.5 MPa (absolute), not cause scram at normal transient, and stabilize pressurizer safety valve. Surge line in the lower portion of the Pressurizer is connected with the circuit 1 heat pipe, thus the control of the pressurizer pressure is to control the pressure of the reactor and the primary coolant in the loop. On a broader scale, the pressurizer displays, records, abnormal pressure alarm, allow and scram signal, and outputs analog signal to the relevant system, also serve as the functions of the pressurizer pressure control system. In addition, the control to spray valve is the so-called “polarization” control.

---

Z. Bin (✉) · Z. Yang  
Fujian Fuqing Nuclear Power Co., Ltd., Fuqing 350318, Fujian, China  
e-mail: jianghong@cnpe.cc

When the RCP (Reactor Coolant System) pressure exceeds the threshold value of pressurizer safety valve, the safety valve opens automatically to discharge steam from within to the pressurizer relief tank so as to relieve pressure of RCP. Preventing coolant system pressure exceeds the designed value.

Pressurizers shall be designed to adjust the pressure fluctuation due to the load instantaneous fluctuation that is able to maintain the balance of water and steam under saturation. The designed capacity volume of it must contain sufficient water and steam volume.

## **2 Spray Valves Overview**

### ***2.1 Introduction of Pressurizer Spray Pipe***

Pressurizer spray pipes are respectively connected with cooling section of two circuits on primary loop (Unit 1 connected with 1, 2 circuit, Unit 2 connected with 1, 3 circuit). There is an automatic control of pneumatic valves on each line, which is equipped with a small link stopper, keeping a small continuous spray flow.

At one terminal of spray pipe equipped with a spray head in the pressurizer. The opposite spoon-shaped terminal is set in primary loop to use the speed of the fluid in the loop to increase the driving force of spray head.

At the end of common pipe RCP001VP/002VP of spray pipes nearing the top section is arranged with a water seal to prevent steam gathering behind the spray valve, causing water hammer when opening the spray valve.

Spray valve downstream is connected with the auxiliary spray pipe (supply water by RCV, chemical and volume control system) to control pressure when main pump outage or cool the pressurizer when reactor shutdown, spray flow rate is up to 9.5 m<sup>3</sup>/h.

### ***2.2 Pressurizer Continuous Spray***

RCP001VP and 002VP spray valve are equipped with a lower limiting stopper, when the valve is closed, the lower limit sets the valve at a slightly open state, a certain leakage flow rated at 230 L/h is kept as a continuous spray, function of the continuous spray is as follows:

- Maintaining uniformity of water temperature and chemical composition in the pressurizer;
- Limiting heat stress and thermal shock to the spray pipes when mass flow spray activated;
- Balancing boron concentration in pressurizer and primary loop, to keep the ratio of electric heater adjusting at a base value.

Each spray pipe is equipped with a temperature measuring device, lower temperature indicates insufficient continuous spray flow.

### ***2.3 Pressurizer Polarization Spray***

The so-called spray valve polarization running means: inputting on-off electric heater RCP001RS and 002RS first and turning the spray valve up to a preset aperture (22 %, preset by RCP401MS) 10 s later, if the needed aperture of the analog adjustment channel exceeds the preset one, the aperture of the spray valve will still be decided by analog adjustment channel. Polarization running helps keeping uniformity of the boron concentration in the pressurizer and primary loop, and avoiding coolant in primary loop flowing backwards to pressurizer by surge line, to reduce thermal shock when changing load. Therefore, spray valve polarization running should be activated in the following two situations:

- Adjusting the boron concentration in reactor coolant loop by dilution or adding boron;
- Turbine up-loading running at a more prominent tilt coefficient.

## **3 Process and Results Analysis**

Continuous spray adjustment is arranged during hot functional test and first critical test, here takes the heat function test as example. Pressurizer liquid level control placing in automatic mode, pressure control placing in automatic mode, the ratio electric heater powering in and adjusting by the controller (RCP401KU on KIC, Plant Computer Information & Control System, setting in automatic mode), breaking on-off electric heater and setting the controller in automatic mode, spray valves setting in automatic mode; pressurizer safety valves available, the pressurizer liquid level, pressure and temperature measuring instruments available, spray pipe and surge line temperature measurement channel available, the alarm value setting at designed value; polarization running valve initial aperture setting at 8 %. Before the hot function test, adjust the initial aperture of RCP002VP and RCP001VP at 10 % by adjusting mechanical shutter.

### ***3.1 Pressurizer Heater Loss Measurements***

Setting aperture of valve RCP001VP and RCP002VP at 0 % manually via KIC, confirming no P7 signal in RPR system, stop running two reactor coolant pumps

**Table 1** Pressurizer heat loss calculation

Electric heater	RCP 003 RS	RCP 004 RS
Control signal C	GD1	GD2
	33 %	33 %
Heater signal (aperture) $X_{RS}$	33.2 %	33.4 %
Voltage between phases $U$	392.8 V	394 V

which are connected with spray pipes (restart the reactor coolant pump at the end of the outage), then monitoring RCP003RS and RCP004RS heat signal.

30 min after stable working conditions (all parameters must meet the operating standards in the stable condition) notify electrician reading out and record the following data on the ratio electric heat plate cabinet Table 1.

Actual power  $P_{380}$  of each group electric heat

$$RCP_{003RS} : 216.45 \text{ kW} \quad RCP_{004RS} : 216.60 \text{ kW}$$

Heater rating formula of each group ratio heater compensates heater loss:

$$P = X_{RS} \times P_{380} \times \left[ \frac{U}{380} \right]^2$$

Each group ratio heat compensates heater loss

$$P_{003RS}; 76.78 \text{ kW} \quad P_{004RS} : 77.77 \text{ kW}$$

Pressurizer heater loss  $P_L$

$$P_L = P_{003RS} + P_{004RS} = 154.55 \text{ kW}$$

Thus, continuous spray is indispensable to compensate the inevitable pressurizer heater loss, on the basis of the known heat loss, adjustment to continuous spray is necessary.

### 3.2 Continuous Spray Flow Regulation

First, set the valve RCP001VP and RCP002VP in manual mode and keep it turned off, then alternately adjusting (up) valves RCP001VP and RCP002VP slowly to obtain the following working conditions by adjusting continuous spray flow: pressurizer constant pressure 15.4 MPa g; temperature constancy and approximately equal of two spray pipes; no triggering alarm of spray pipes and surge lines; the ratio electric heater stabilizing at 50 % heater power (KDO indication). 30 min after stable working condition, recording the data (in the meantime aperture of

**Table 2** Continuous spray adjustment

Spray pipes temperature	RCP002MT (Circuit 2)	RCP003MT (Circuit 1)
	268.4 °C	270.0 °C
Pressurizer pressure and water level	RCP014MP	RCP 007/008/011MN
	15.4 MPa g	-4.05 m
Electric heater	RCP 003 RS	RCP 004 RS
Control signal C	GD1	GD2
	50 %	50 %
Heater signal (aperture) $X_{RS}$	50.9 %	50.5 %
Voltage between Phases $U$	387.5 V	391.2 V

RCP001VP and RCP002VP should be marked at the site to set following-up stopper aperture) Table 2.

Actual power  $P_{380}$  of each group electric heater

$$RCP_{003RS} : 216.45 \text{ kW} \quad RCP_{004RS} : 216.60 \text{ kW}$$

Heater rating formula of each group ratio heater compensation heater loss

$$P = X_{RS} \times P_{380} \times \left[ \frac{U}{380} \right]^2$$

Got each group ratio heater compensation heater loss

$$P_{003RS} : 114.56 \text{ kW} \quad P_{004RS} : 115.93 \text{ kW}$$

Thus aggregate power of electric heater

$$P_T = P_{003RS} + P_{004RS} = 230.49 \text{ kW}$$

Continuous spray flow relevant power

$$P_T - P_L = 75.94 \text{ kW}$$

Allowed continuous spray flow calculation

$$M_S = \frac{P_T - P_L}{\Delta H}$$

( $\Delta H$ : Enthalpy drop of pressurizer saturation water and spray water,  $P_L$ : pressurizer heater loss)

Spray pipes average temperature (RCP002 MT + RCP003 MT)/2: 269.2 °C

Spray water enthalpy: 1181.03 kJ/Kg

Pressurizer water enthalpy (considered to be 15.4 MPa g corresponding saturation water enthalpy): 29.85 kJ/Kg

$$\Delta H = 448.82 \text{ kJ/Kg}$$

$$M_s = 0.1692 \text{ Kg/s}$$

Mechanical staffing setting RCP001VP and RCP002VP stroke stopper position continuous spray flow depends on the valve stroke stopper position, locking the two valves at fully closed position, then re-calibrated the corresponding 4–20 mA range, in the meantime stop the running loop reactor coolant pump corresponding to relevant valves. Therefore, at this time, even if the valve aperture indication is zero, there still is a small continuous spray flow to compensate pressurizer heater loss.

### ***3.3 Polarization Spray Flow Regulator***

First, keep the pressurizer control device in automatic position, set electric heaters RCP001RS and RCP002RS at manual position, put them into operation, adjust RCP401KU, set electric heaters RCP003RS and RCP004RS at 50 % power; then open the valves RCP001VP and RCP002VP alternately, when the pressure is stabilized at 15.4 MPa g, check the aperture consistency of the two spray valves, which are 9 %. Reset polarization aperture of the two spray valves to 9 %.

Then turn off valves RCP001VP and RCP002VP slowly and alternately, reset to auto state, outage RCP001RS and RCP002RS and resume the auto position.

Verify polarization aperture: set RCP063 Kg at polarization spray, confirm RCP001RS and RCP002RS electrified, and 10 s later, open the polarization valves RCP001VP and RCP002VP to polarization running aperture; confirm ratio heater RCP003RS and RCP004RS at 50 % power after parameter keeps stable, if not close RCP063 Kg. To ensure the test accuracy, repeated tests are necessary to adjust RCP401MS. Close RCP063 Kg finally.

## **4 Conclusions and Recommendations**

During the test, stable working conditions are necessary, but they will be hard to obtain for the sluggish fluctuation of actual state (temperature, pressure, etc.), at this time we have to adjust spray valves slowly and patiently to be better conditions. To get optimum data, rough adjustment is inadvisable.

Through above experiments, pressurizer heater loss was got during heat functional test of Fuqing Nuclear Power Unit 1, readjusted the off position of spray valves, ascertained the continuous spray flow rate, and obtained the 9 % of the polarization spray aperture, which was quite different with the theoretical 22 %. Referring to other plant test results, certain deviation of polarization spray aperture exists between different unit and power plant. It is not fixed but related with field environment, pressurizer heat preservation effect, and differences in devices.

## References

1. Duan Yong Qiang, Zhao Yu, Su Rong Fu, < The SCP of RCP > A CFC, Nuclear Power Institute of China, 2011-03-04
2. Jin Xiao Feng, < The Manual of RCP > A CFC, Nuclear Power Institute of China, 2008-08

# Analysis of the CRDM Coils Current Interference and the Abnormal Display of Rod Position in RGL System

Yue Cheng and Huanhuan Jiao

**Abstract** RGL is a rod control and monitor system, which is used to lift or insert the control rod sets, and to monitor the position of each control rod sets. This paper mainly discusses the problems of the CRDM coils current interference and the big leap in the rod position measuring during the commissioning of a nuclear power plant.

**Keyword** RGL · Coil · Current · Interference · Leap

## 1 Introduction

Rod Control and Monitor System (RGL) is used to lift or insert or hold control rod sets, and to monitor the position of each control rod set. As the main reactor control system, its main function is, according to the changes of the load, regulating the reactivity of the core by lifting or inserting the control rods, so as to control the core temperature and the nuclear power. When the reactor is running stably, the core reactivity is in a state of dynamic equilibrium, for the moving of the control rods compensate the fast change of the core reactivity, which is due to the temperature effect and the power effect and the xenon-poison effect caused by the fast load change. When the reactor is in unstable running state, Rod Control and Monitor System can promote the reactor from zero power to full power in reactor start-up phase, and implement reactor trip during normal shutdown phase or accidental circumstance, so as to protect the reactor and ensure safety of reactor core.

---

Y. Cheng (✉) · H. Jiao  
Commissioning Department, China Nuclear Power Engineering Co., Ltd.,  
Beijing, Haidian, China  
e-mail: chengyue@cnpe.cc

H. Jiao  
e-mail: jiaohh@cnpe.cc; jiaohh@foxmail.com



In nuclear power plant, RGL system is very important in economic and security aspects. Any phenomenon that does not meet the design standards must be highly valued.

## 2 Control Rod CRDM Coil Current Interference

### 2.1 Issue Discovering

During the commissioning of a nuclear power station, the output current waveform of the power supply cabinet is not in accordance with the design standard when the time sequence of the rod bundle is recording. The most prominent defects is in the lifting waveform of every rod, so is the transferring and the holding module, occasionally. According to the recorded current waveform sent to the CRDM, when the lifting coil current is changing from small current to zero current, the waveform jitters every time no matter in lifting sequence or inserting sequence.

The unexpected waveform is as follows. (The waveforms respectively stand for lifting, transferring and holding coil from top to bottom, and the C2 rod set have only 1 rod) (Fig. 1a, b).

In lifting sequence, when the high current of lifting coils and holding coils is reduced to low current, there is one or more pulses which peak current are more than 50 % of the difference between the high current and the low current. To find the fault reason, by lifting the 33 rods 5 steps, respectively, the results showed that all 33 rods have such problems. See the Fig. 2.

### 2.2 Fault Investigation

According to the analysis of RGL module's theoretic diagram, this fault is because of the lower limit set of the power cabinet, so the commissioning team presents a parameter modification solution:

Falling edge: 0.5–0.8 (V)

Offset: -7 to -7.1 (V)

Triangle wave: 3.6–3.5 (V)

The above parameters modification solution was tried, and the zero current interference problem had been resolved largely, but the interference of high current to low current still exists. But when the commissioning team plugs the recorder's test pen to the square wave test hole of the lifting cabinet's phase shift module A/B/C (see Fig. 3), it was found that the unexpected waveform became normal, and no matter which rod set, as long as the recorder's test pen were plugged to the

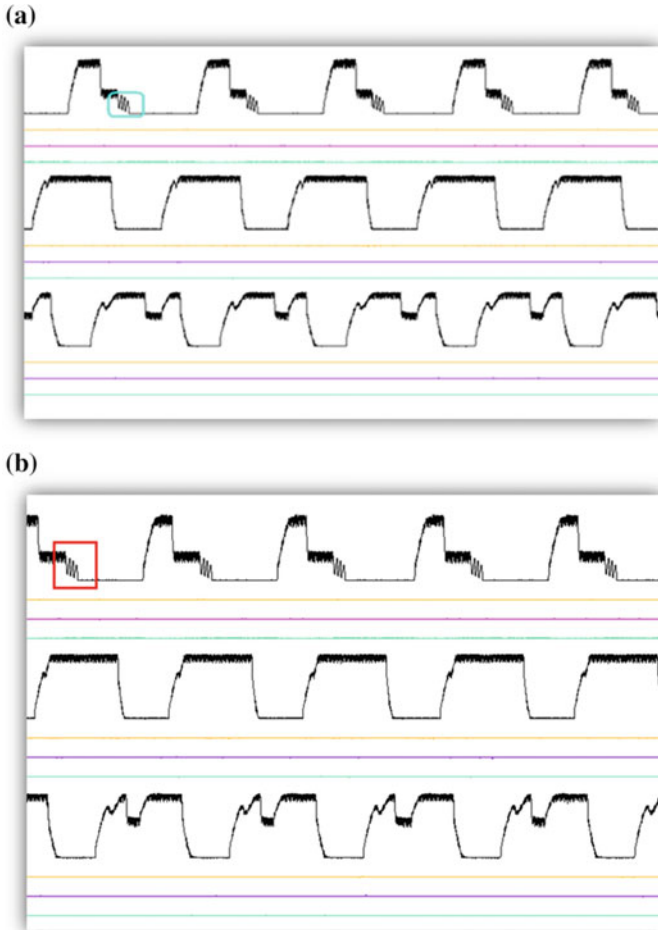


**Fig. 1** a Lifting waveform (C2 rod set). b Inserting waveform (C2 rod set)

square wave test hole of the lifting cabinet's phase shift module A/B/C, the waveform is normal. Then the following tests were performed:

1. Connecting with a charged oscilloscope, waveform is standard;
2. Connecting with an uncharged oscilloscope, waveform is standard;
3. Only plug the test pen, without oscilloscope, waveform is standard.

Final conclusion is that, as long as the recorder's test pen was plugged to the square wave test hole of the lifting cabinet's phase shift module A/B/C, the waveform is as standard as normal. Therefore, resistance and capacitance test were performed, and the results are respectively infinite and  $0 \mu\text{F}$ .

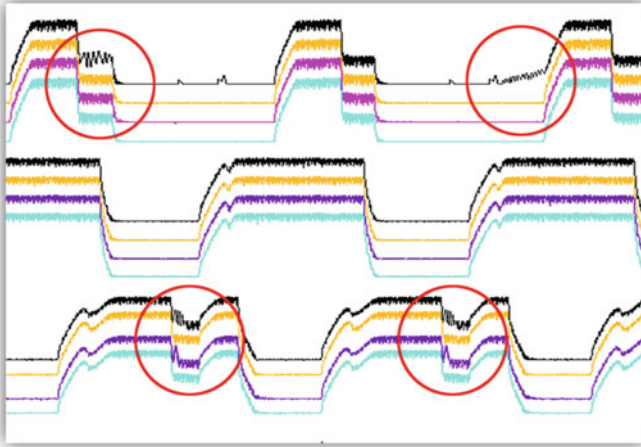


Fig. 2 Lifting waveform (one of other rod sets)

Fig. 3 Front of phase shift module A/B/C

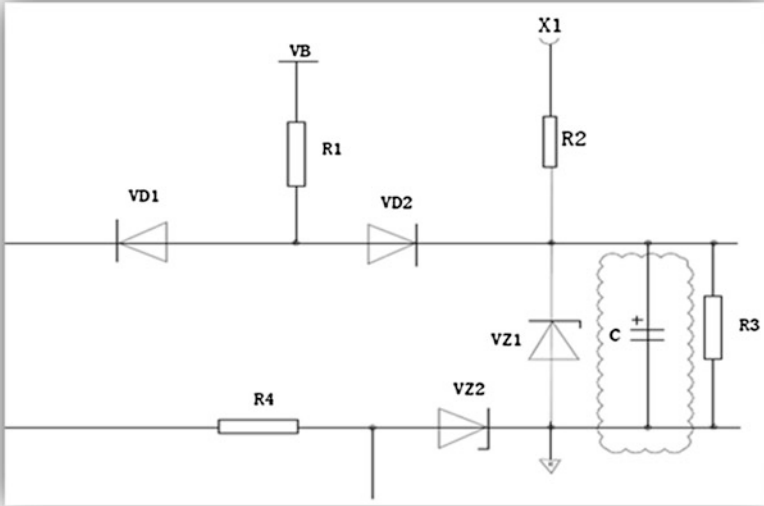


### 2.3 Solution

According to the phenomena found in the search process and the phase-shifting module circuit schematic diagram, plugging a test pen in the square wave measuring hole is like connecting a capacitor to the output of the square wave.

Therefore, the decision is made; add a 1000 pF capacitor (see Fig. 4a) to the output (X1) of phase-shifter's square wave, and add a 680 pF capacitor to the adjusting module's current feedback side (X1) (see Fig. 4b).

(a)



(b)

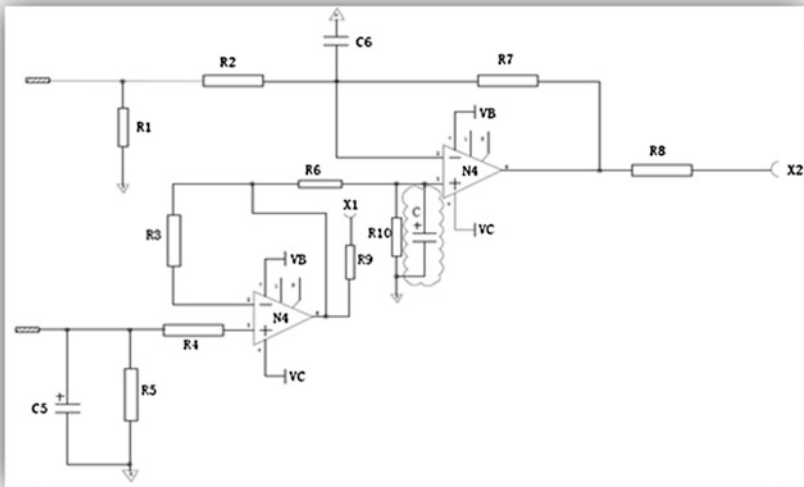
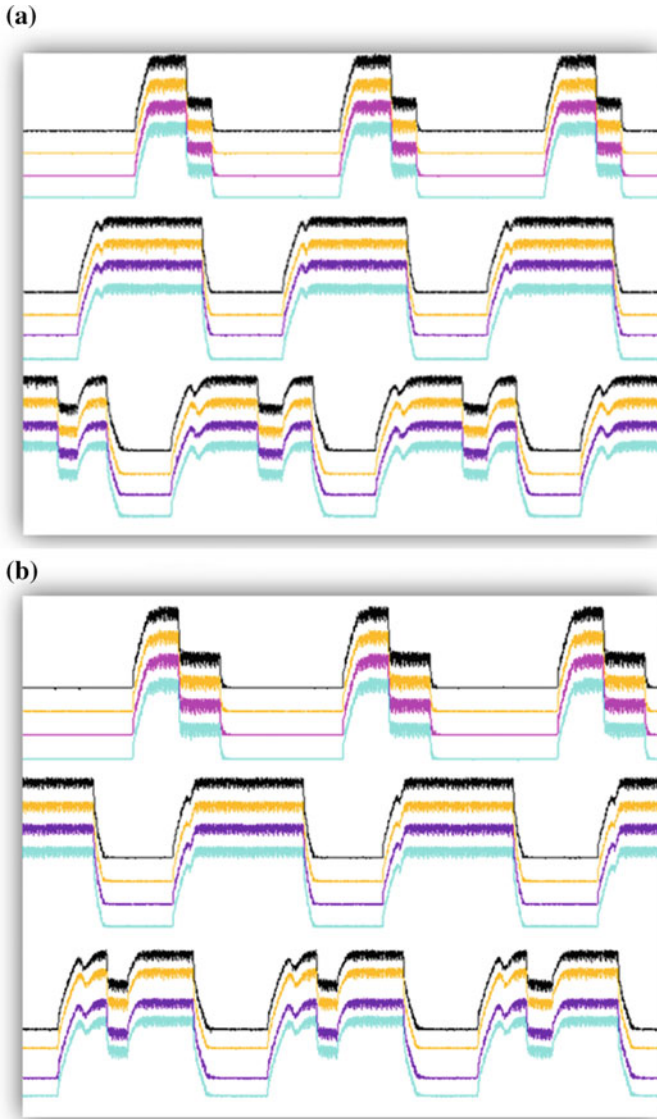


Fig. 4 a Add a 1000 pF capacitor. b Add a 680 pF capacitor

### 2.4 Effect

After all the capacities are welded to every module, the commissioning team performed all the lifting and inserting test again, and all results are in accordance with the standard. See Fig. 5a, b.



**Fig. 5** a One lifting waveform of the rod sets. b One inserting waveform of the rod sets

By analyzing the lifting sequence of lifting coils and transfer coils, fault occurred when high current turned into low current. High current is used to lift the rods, and low current is used to keep the rod where it is. The interference, which is strong enough to harm the coil, will decrease the hardware performance.

Solving this problem might promote the reliability of the whole RGL system.

### **3 Big Unexpected Leap in Rod Position Display the of the Rod Position Measuring System**

#### ***3.1 Issue Discovering***

During the RGL's Gray Code commissioning, when the lifting test of the B rod bundles (include B1-1–B1-4 and B2-1–B2-4 eight rod bundles) was performed; there is a big leap in lifting process of the B2-2 rod bundle, while the other rod bundles appear good and smooth. As soon as this issue was discovered, commissioning team tried adjusting the parameters of the C-Code and D-Code to avoid this problem but failed.

#### ***3.2 Fault Investigation***

After the failed attempt, the commissioning team pulled out the cabinet and module, ensured that every part of the module was in accordance with the circuit schematics. After an analysis, the initial suspicion is a rod position detector failure or an abnormal operation. Then the commissioning team used a recorder to sample and analyze all A, B, C, D, E code of the B2-2 rod bundle's coil, meanwhile they sampled and analyzed other normal bundle's data as a control group. The difference of these waveforms are shown in Fig. 6a, b.

From the waveforms above, we can clearly find that there is a failure happened at B2-2's C- and D-code (from top to bottom, they're A, B, C, D, E code, and wide line means 1 while narrow line means 0). By excluding other possible failure reasons, such as module fault, wrong wiring, wrong devices model, etc., the conclusion is that the first coils of B2-2's C-code and D-code were wound in a wrong way.

#### ***3.3 Solution***

Because the fault happened inside the Rod Position Detector, which is an integral device, the only way to solve this problem is to replace this detector directly, and have the faulted one returned to its manufactory and disintegrated and repaired.

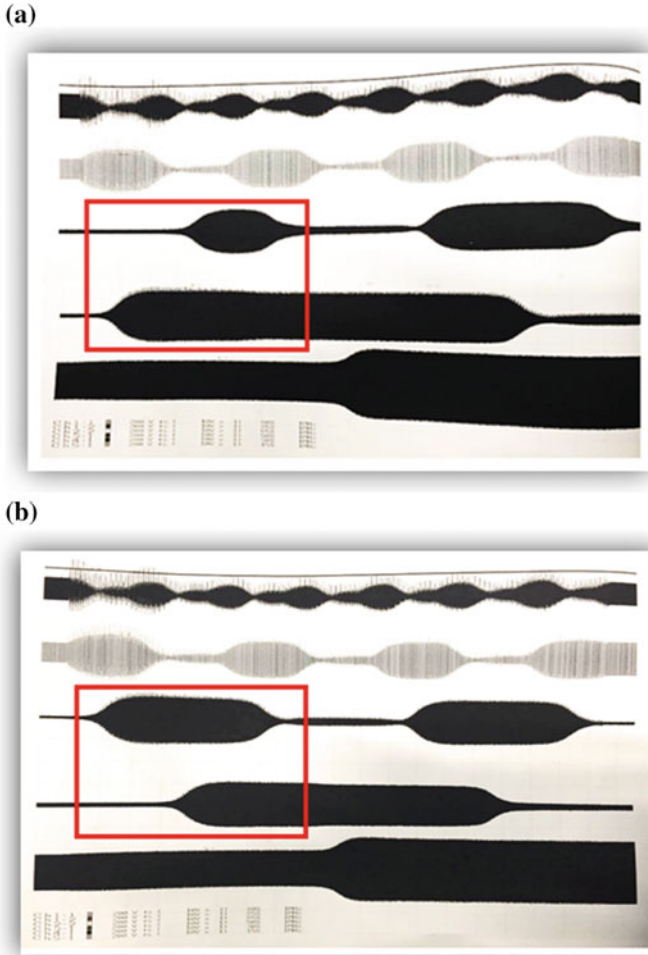


**Fig. 6** **a** The sample of B2-2 rod bundle. **b** The sample of any other rod bundle

When the commissioning team found this problem and came to the decision of replacing the detector, the nuclear power plant's unit is in a hot state, of which the temperature was 290.8 °C, and the pressure was 15.4 MPa. Referring to other nuclear power plant, which had similar experience, the final decision is to reduce the temperature and pressure to 60 °C and 2.5 MPa, then implement the replacing work.

### 3.4 Effect

After the B2-2 Rod Position Detector's replacement, the commissioning team redoes the lifting test and monitors the whole process with both official displayer of

rod position and the recorder used to record the waveform when the rod bundles were lifting. As expected, the B2-2 rod bundle's position was displayed as well as all the other rod bundles. No step-leap happened again.

## **4 Conclusions**

RGL is one of the most important control systems of core control, its performance stability directly affects the safe operation of units. If the current interference through the CRDM coils exists for a long time, there will be a certain impact on the performance of the coils. The deviation of the display of the rod position also affects the judgment of the core state of the operating personnel. Therefore, the problems found and the experimental data in commissioning must be recorded, analyzed, and processed by rigorous attitude, and effective solutions should be proposed. This paper discusses two reliable thoughts when such problems happened in similar nuclear power plants.



# Application of Key Interlock in HUALONG-I 3rd Nuclear Unit

Zhijian Wang and Cuicai Dong

**Abstract** Key interlock system is a significant measure to protect power system operation safety and reliability in nuclear plant. In this paper, working principle and system structure of key interlock are introduced at the beginning. And then, key interlock scheme of plant power distribution system in an example HUALONG-I 3rd nuclear unit is deeply discussed and studied. The result shows that the key interlock system makes an outstanding effect on preventing human error, improving the reliability of power system, protecting the personal safety of electrical operator, and promoting the economic benefit of nuclear power station.

**Keywords** Key interlock · Power system · HUALONG-I · Reliability · Nuclear station

## 1 Introduction

Safety operation of nuclear power plant is extremely important. As one of the main parts of the system, the electrical power system plays the key role in nuclear safety. During the normal operation and maintenance period, manual operations are frequently involved due to the huge amount of electrical equipment within the nuclear power plant. How to avoid electrical accident and hazard caused by human error becomes an important nuclear safety issue for power system reliability. HUALONG-I 3rd nuclear unit, which is the completely independent intellectual property right of China, continuously employs the key interlock system with partial improvement, expecting to guarantee the reliability of electrical system within the nuclear power plant [1].

---

Z. Wang (✉) · C. Dong  
China Nuclear Power Engineering Co., Ltd., Beijing, China  
e-mail: wangzj@cnpe.cc

## **2 Key Interlock and Classification**

### **2.1 Key Interlock**

Key interlock is achieved by the combination of “key” and “lock,” which is designed to follow the correct operation logic sequence. The manual operation could be ensured in the correct operational mode using this “key” and “lock” combination.

The personal safety of operators can be guaranteed with utilization of key interlock in electrical power system. Mis-entrance of electrified gap, on load operation of disconnector and charged closing of earth switch, charging of earth switch and mis-operation of circuit breaker can be avoided to eliminate the mis-operation of electrical equipment and mis-entrance of dangerous region to guarantee the safety of electrical system.

### **2.2 Type of Key Interlock**

According to the demand variety, the key interlock can be classified as the following types in nuclear power plant:

1. Permission of Key Isolation (PI)  
Permission of Key Isolation means that it is allowed to move equipment from operating position, equipment would not be charged when PI is locked. The key could only be released when equipment on the operating position.
2. Certified Key Isolation (POI)  
The key could only be released when the circuit breaker or disconnector is removed from the operating position, or the stationary breaker or switch is disconnected completely.
3. Permission of Earthing Key (PE)  
Permission of Earthing Key means that the earth switch could only be closed when the key is plugged in and the key could only be released after disconnection of earth switch.
4. Certified Earthing Key (POE)  
Certified Earthing Key means the key could only be released after earth switch is closed and the key could only be removed when earth switch is locked on the earthing position.
5. Permission of Access  
The equipment could only be accessed when key is plugged in. The equipment is not allowed to be charged when the key is locking on the door lock. Key could only be released till all the access points are locked.

### 3 Key Interlock System Design Case Study

#### 3.1 Demand of Electrical Design

The simplified subsystem electrical wiring diagram of one “HUALONG-I” 3rd nuclear power unit can be shown as in Fig. 1.

Indicated as Fig. 1, 10 kV medium voltage busbars ESS and EST are designed in this subsystem, which is equipped with inlet circuit breaker 001JA, 002JA, and busbar cabinet 001PT and 002PT. According to the electrical design demand, the mechanical key interlock system is designed to achieve the logic of “3 for 2” with 001JA, 002JA, and 003JA. So that the safety of personal and electrical equipment can be ensured by avoiding the mis-entrance of electrified gap, on load operation of disconnecter, and closing of earth switch, charging of earth switch, and mis-operation of circuit breaker.

#### 3.2 Key Interlock Design Analysis

Based on the electrical wiring diagram from Fig. 1, the electrical demands are analyzed individually. Corresponding key interlock methods are collected and the final key interlock scheme has been set to satisfy the electrical operation demand as well as the insurance of personal and equipment safety.

With the preliminary analysis, the logical designs which require the setting of key interlock can be listed as below:

1. Preventing mis-entrance of electrified gap, preventing charging of earth switch, and preventing circuit breaker mis-operation. The cabinet door of 001JA can only be opened for maintenance operation after the disconnection of medium voltage feeder line circuit breaker from upstream, earthing of earth switch and

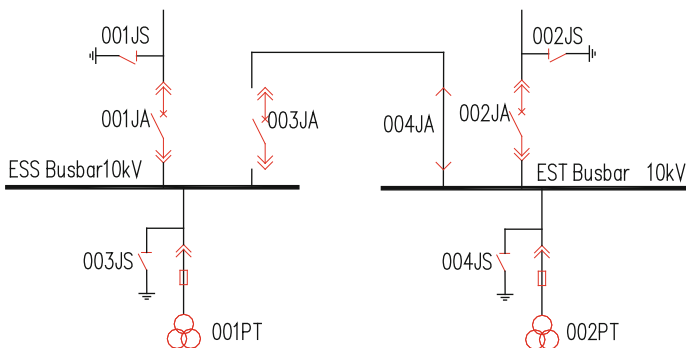


Fig. 1 Simplified main electrical wiring diagram of plant power subsystem

- earthing of local side earth switch are confirmed. The circuit breaker closing operation can only be implemented when the earth switches from upstream and downstream are both disconnected.
2. Preventing onload operation of disconnector. The disconnector can only be operated when 003JA is disconnected or not in the operating position, and the busbar is not charged.
  3. Preventing charged closing of earth switch. Take 003JS as an example, the earth switch of 003JS can only be closed when 001JS is earthed, 003JA is not in the operating position, 001PT is withdrawn, and busbar EES discharged completely.
  4. “3 for 2” Logic for 001JA, 002JA, and 003JA. When busbar circuit breaker 003JA is closed on operating position, the “3 for 2” key interlock logic needs to be set to prevent the simultaneously power supply of 001JA and 002JA.

### 3.3 Key Interlock Schematic Design

With the analysis from 3.2, the schematic design of key interlock for this plant power subsystem can be shown as Fig. 2.

Key types are listed in Table 1.

Considering the schematic design diagram from Fig. 2 and key type information table from Table 1, it can be found that:

Busbar earth switch 003JS is designed with key interlock 7SA to prevent the mis-closing operation of charged earth switch. When the busbar ESS needs to be maintained, the key coded of 7SA needs to be obtained and plugged into the Lock 003JS. Thus, 003JS can be closed to earth. The key of 7SA is located in key exchange box 002CV. In order to obtain and take off Key 7SA, the Key 1GS, 8SA, 6SA of 002CV need to be collected. The acquirement for these above three keys

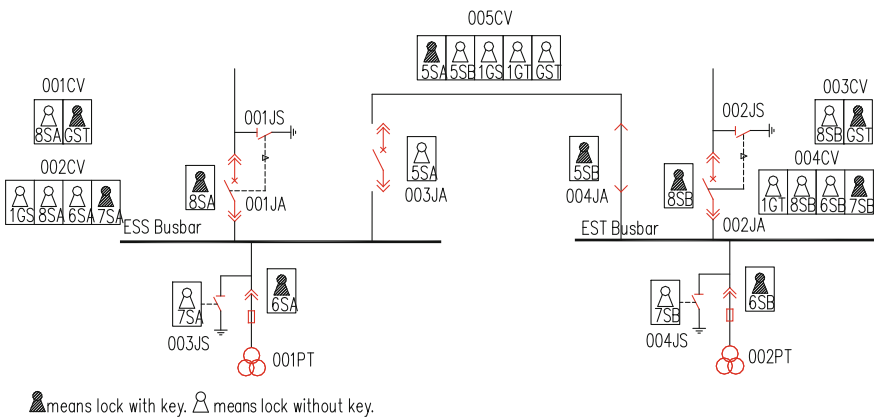


**Fig. 2** Schematic design diagram of key interlock

**Table 1** Key type information table

Name	Description	Function	Key A = release T = trap F = Free	Name	Description	Function	Key A = release T = trap F = Free
Key exchange box 001CV							
8SA	ESS incoming BREAKER	POI	A	8SB	EST incoming BREAKER	POI	A
GST	ESS EST 3 for 2	POI	T	GST	ESS EST 3 for 2	POI	T
Key exchange box 002CV							
8SA	ESS incoming breaker	POI	A	8SB	ESS incoming breaker	POI	A
6SA	ESS busbar PT	POI	A	6SB	EST busbar PT	POI	A
7SA	ESS busbar earthing key	PE	T	7SB	EST busbar earthing key	PE	T
1GS	Free key	POI	F	1GT	Free key	POI	F
Key exchange box 005CV							
GST	ESS EST 3 for 2	POI	A	5SA	From 005CV	POI	T
1GS	Free key	POI	F	5SB	From 005CV	POI	F
1GT	Free key	POI	F				

would be tracked in the following. Key 8SA is located in the interlock of 001JA, POI would be triggered if Key 8SA needs to be obtained, which indicate that 001JA should not be set in operating position or disconnect the switch of 001JA. In other words, the inlet switch should be disconnected. Key 6SA is located in Cabinet 001PT, it can be obtained by withdrawing the truck PT from the cabinet, which means PT would not be discharged for the remaining voltage of busbar ESS. Key 1GS is a unique free key, if Key 1GS is plugged into 002CV, 005CV cannot be occupied by 1GS simultaneously. Without Key for 005CV means that 003JA cannot locate on the operating position. Not charge for the busbar for this condition and the reason would be explained in the following. As illustrated from Fig. 2, the power supply loops are disconnected and busbar connection ESS can be confirmed with no charge when the Key 7SA is obtained after the acquisition of Key 1GS, 8SA, 6SA. Earthing operation can be safely implemented with closing of earth switch after plugging of Key 7SA.

Same interlock principle applies for busbar EST. The implementation of logic “3 for 2” interlock scheme for 001JA, 002JA, and 003JA. Lock 5SA is set on the position of busbar connection 003JA. No key exists for this lock and 003JA would set in testing position in normal condition. Only under the condition that Key 5SA is obtained and plugged into Lock 5SA, 003JA can be pushed into operating position for switching operation. From key exchange box 005CV, it can be found that Key 5SA can only be acquired after the collection of Key 5SB, 1GS, 1GT, and 1GST. The key acquisition method for these four keys would be analyzed individually in the next. Key 5SB, type of certified key isolation, is located in disconnecter 004JA. It can be obtained when disconnecter 004JA in the operating position. 1GS is a unique free key, but with two Locks 002CV and 005CV. If Lock 005CV is plugged with Key 1GS, Lock 002CV cannot be opened, which means busbar ESS is not connected to the earth and can be operated with charge. Same principle for Key 1GT and 1GS. Key 1GST has two copies in 001CV and 003CV. Disconnection of inlet circuit breaker 001JA from ESS or 002JA from EST can unlock Key 1GST. Thus, if Key 1GST is plugged into Lock 005CV, it means that at least one inlet circuit breaker between 001JA and 002JA is disconnected. Key 5SA can only be accessed after the collection of above keys, and 003JA would be pushed to close switch in operating position. From the above interlock, the “3 for 2” logic of 001JA, 002JA, and 003JA can be achieved effectively, which ensures that the busbar ESS and EST are both earthed and the mis-operation for earth switch charging can be eliminated.

Five-preventing interlock should be set in medium voltage cabinet between each circuit breaker and its corresponding earth switch. Earth switch can only be closed to earth after the circuit breaker disconnection. Thus, charged closing of earth switch can be prevented. In addition, with the installation of interlock, the cabinet door of circuit breaker gap can only be opened after the earth switch is closed to ground. Mis-entrance of electrified gap can be avoided.

The key interlock between medium voltage earth switch and downstream power distribution transformer cabinet door can be installed according to the demand. The key located in earth switch can be obtained and used to open front and rear door of

power disconnected transformer cabinet when medium voltage cabinet earth switch is closed to ground and the upstream is confirmed to be discharged.

## **4 Conclusions**

The key interlock system involved in “HUALONG-I” 3rd nuclear unit can prevent personal hazard of operators, mis-entrance of electrified gap, on load operation of circuit breaker, closing of charged earth switch, charging of earth switch, preventing of circuit breaker mis-operation, which means that this system can effectively eliminate mis-operation of electrical equipment and mis-entrance of dangerous region caused by human error. Thus, the nuclear safety and electrical system reliability can be guaranteed.

## **Reference**

1. IEC 61497-2006, Nuclear Power Plants—Electrical Interlock for Functions Important to Safety

# Charpy Impact Properties of Electron Beam Welded V-4Cr-4Ti Alloy

Shuang Yang, Pengfei Zheng, Jiming Chen, Xing Miao and Ran Wei

**Abstract** Due to many advantages over other candidate materials, V-4Cr-4Ti alloys are considered as leading candidate structural materials for liquid Li blanket of fusion reactors in the future. To develop the joining technology of this alloy, a V-4Cr-4Ti alloy plate has been welded by electron beam and characterized at Southwestern Institute of Physics (SWIP). The Charpy impact properties, Vickers hardness, and microstructure of specimens machined from welded plates after different heat treatments were investigated. Different post-weld heat treatments (PWHT) were applied and reviewed to recovering the mechanical property of V-4Cr-4Ti after welding. TEM observation were also conducted to investigate the effect of Ti-C, N, O precipitates on the property degradation.

**Keywords** V-4Cr-4Ti · Charpy impact · Electron beam weld · Post-weld heat treatment

## 1 Introduction

Due to many advantages over other candidate materials, V-4Cr-4Ti alloys are considered as leading candidate structural materials for liquid Li blanket of fusion reactors in the future [1–3]. In the application of vanadium alloys in fusion reactors, joining is a widely used technique that the materials form a component, however, the mechanical properties would be degraded. Thus, it is necessary to investigate the degradation due to joining and optimize a post-welding treatment to recover it [4–9]. This work focuses on the study of electron beam weld of V-4Cr-4Ti alloy. The main purpose is to investigate the DBTT of weld metal and propose a suitable post-weld heat treatment (PWHT) to increase the ductility of this alloy weld. Microstructural examinations by SEM and TEM were also conducted.

---

S. Yang (✉) · P. Zheng · J. Chen · X. Miao · R. Wei  
Southwestern Institute of Physics, Chengdu, Sichuan, China  
e-mail: yangs@swip.ac.cn



## 2 Experimental Procedure

The investigated alloy is SWIP-30 which was fabricated in 2010 in China by electron beam welding with high purity [10]. Table 1 summarizes the chemical composition of main elements and impurities in SWIP-30 vanadium alloy [10]. The oxygen concentration is 270 wppm and the total C, O, N concentration is 420 wppm which is close to other widely studied V-4Cr-4Ti alloys, such as NIFS-HEAT-1,2 and US832665,832664 [11]. The welded vanadium plates were vacuum annealed at 1000 °C for 2 h, which is a standard heat treatment for high purity V-4Cr-4Ti alloys. The alloy plates were bead-on-head welded by electron beam under vacuum condition better than  $5 \times 10^{-3}$  Pa. Weld belts are placed perpendicularly to the rolling direction of the plates.

Charpy impact specimen were machined from the weld plate by 1/3 size ( $3.3 \times 3.3 \times 25.4$  mm) with V-notch (0.66 mm in depth, angle of 30, and root radius of 0.06 mm) placed in the weld metal. The impact test of welds was carried out by means of drop weight impact tester with a striker velocity of 3.45 m/s. The test temperatures were from  $-196$  to  $120$  °C. Vickers hardness was measured across the weld joint in the middle of coupon samples under the loading of 200 gf for 30 s.

Optical, scanning electron microscopes (OM and SEM), and transmission electron microscopes (TEM) were utilized in order to characterize the morphology of zones of weld joints in as-welded condition and character of fracture mode after impact tests.

Post-welded heat treatment (PWHT) was done to recover the DBTT of welded metal. The PWHT conditions were listed in Table 2.

**Table 1** Chemical compositions of SWIP-30 V-4Cr-4Ti (wt%) [11]

Cr	Ti	C	N	O	S
3.81	3.92	0.013	0.0020	0.027	0.0020
Al	Si	K	Fe	Mg	Ca
0.010	0.059	<0.005	0.0053	0.0022	0.0067
Ge	Mo	Na	Ta	Zr	Ni
<0.001	0.0035	<0.005	<0.001	<0.001	0.0082

**Table 2** Postweld heat treatment (PWHT) of V-4Cr-4Ti electron beam welds

#	SA (°C)	Time (h)	Aging (°C)	Time (h)
STD	1000	2		
SA	1100	1		
SA + A(500)	1100	1	500	20
SA + A(600)	1100	1	600	20
SA + A(700)	1100	1	700	20

STD standard heat treatment, SA solid annealing, A aging

### 3 Results and Discussion

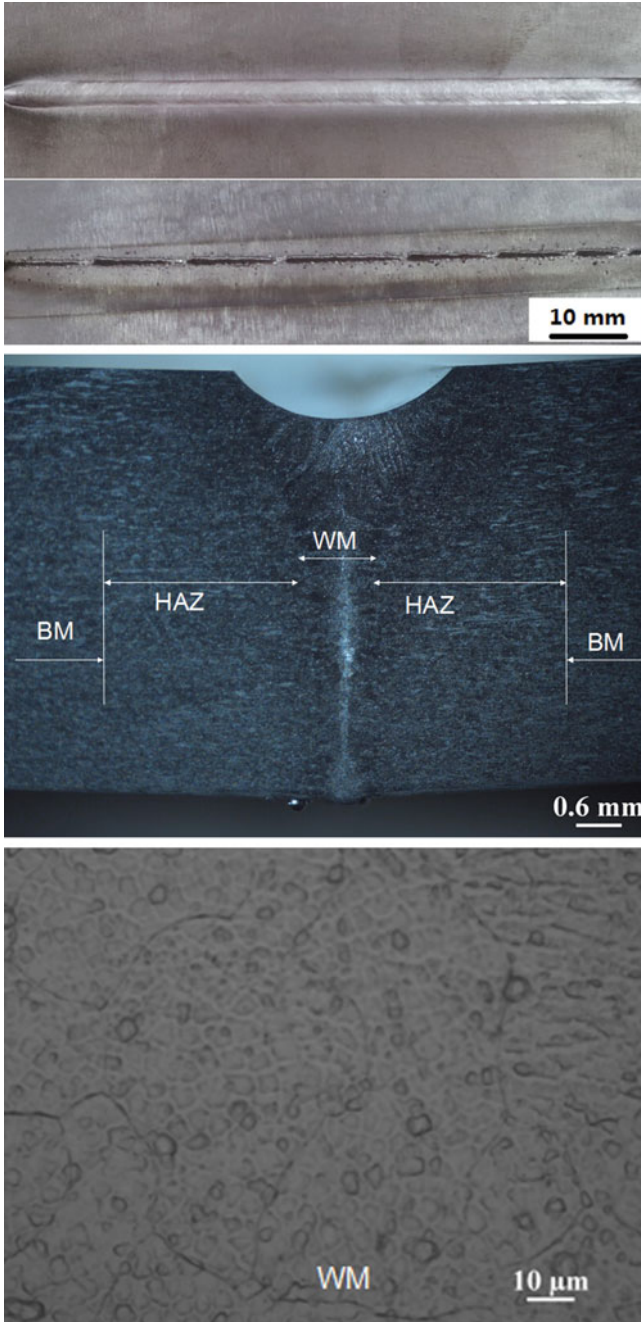
#### 3.1 *Microstructure of Weld Zones*

Figure 1 shows the appearance of V-4Cr-4Ti electron beam welds and optical microstructures of base metal (BM), heat affected zone (HAZ), and weld metal (WM). Both the appearance and microstructures show that there are no obvious weld defects. The thickness of weld metal is about 1 mm and the heat affected zone is about 4 mm thick. The grain size of WM, HAZ, and BM are all around 15  $\mu\text{m}$ .

#### 3.2 *Impact Tests and Vickers Hardness Tests*

Figure 2 shows the results of Charpy impact test V-4Cr-4Ti alloy before and after electron beam welded and post-weld heat treatment. Ductile to brittle transition temperature (DBTT) was defined as the temperature where absorbed energy was 3.55 J, which is half of the upper shelf energy 7.1 J. DBTT of vanadium alloy before weld is  $-110\text{ }^{\circ}\text{C}$  which is fairly low, but after welding the DBTT increased to  $-28\text{ }^{\circ}\text{C}$ . The samples before and after welding absorbed energy as high as upper shelf energy at room temperature, which shows good ductility. But the DBTT after welding has increased much and show brittleness at low temperature. The possible reasons for this should be the residual stress caused by electron beam welding. Therefore, some PWHT were proposed to recover the DBTT of vanadium alloy after welding. PWHT methods were listed in Table 2. The results of STD ( $1000\text{ }^{\circ}\text{C}$ , 2 h) and SA ( $1100\text{ }^{\circ}\text{C}$ , 1 h) show almost the same impact results as welded condition. For the results of SA plus A (aging), the specimens seem to have bigger DBTT than the welded condition which is out of expectation. The potential reason could be the absorption of oxygen during aging process which leads to severe material brittleness.

Figure 3 shows the hardness change of welded plates before and after PWHT at different conditions. The Vickers hardness test results shows that for the base metal the hardness in different areas is more or less around 148 HV, while that of the weld metal, HAZ (heat affected zone), base metal show different harness results with the highest on the weld metal area. This is reasonable because after the electron beam welding, the metal is cooled immediately with coarse grain structure produced. Residual thermally induced stresses could be another reason for this. After PWHT, this welding center hardening phenomenon is gone for three different PHWT and the average hardness value is around 150–180 HV which is above the before welded condition.



**Fig. 1** Light optical microstructures of electron beam welded V-4Cr-4Ti plates

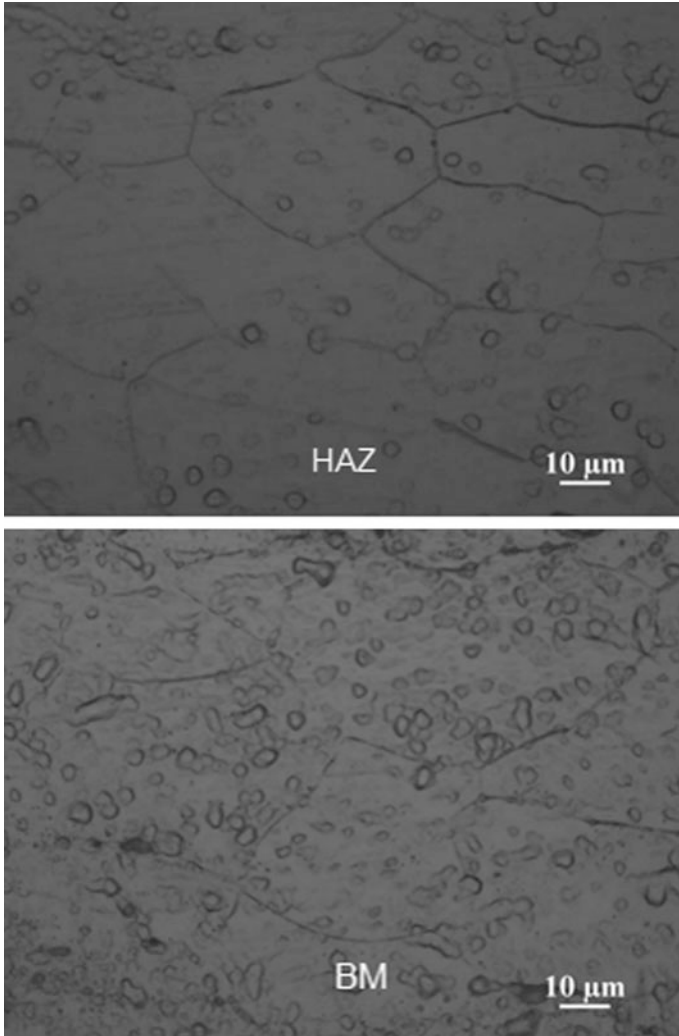


Fig. 1 (continued)

### 3.3 Fracture Morphology

Figure 4 shows the SEM fracture morphology of SWIP-30 after Charpy impact properties test. The specimen fracture images were taken from the impact specimen tested at room temperature, and for the before and after weld condition the absorbed energy is close to the upper shelf energy values with good ductility which could be

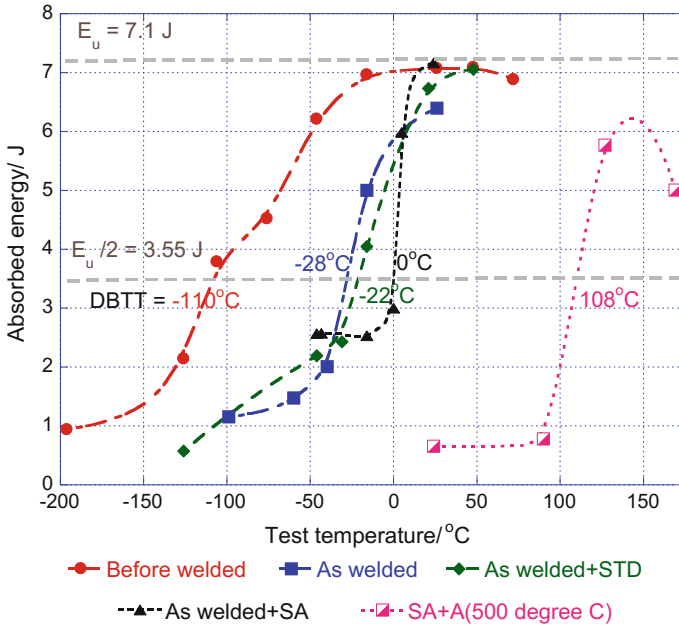


Fig. 2 Charpy impact tests of V-4Cr-4Ti alloy before and after electron beam welded and post-weld heat treatment

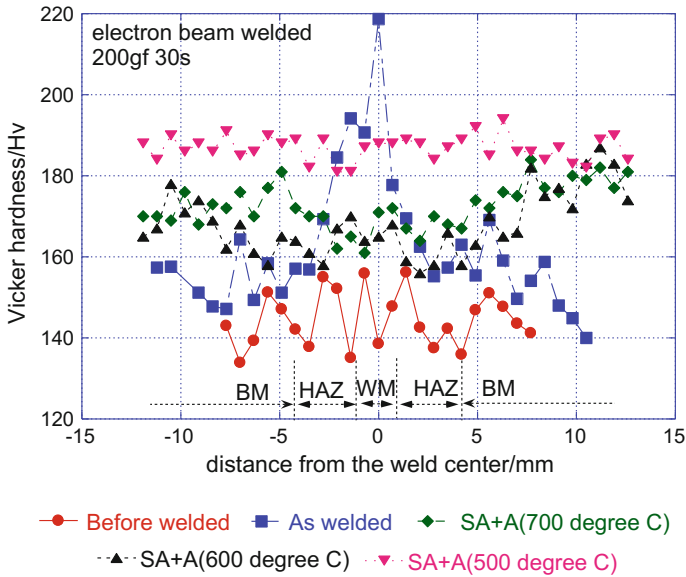
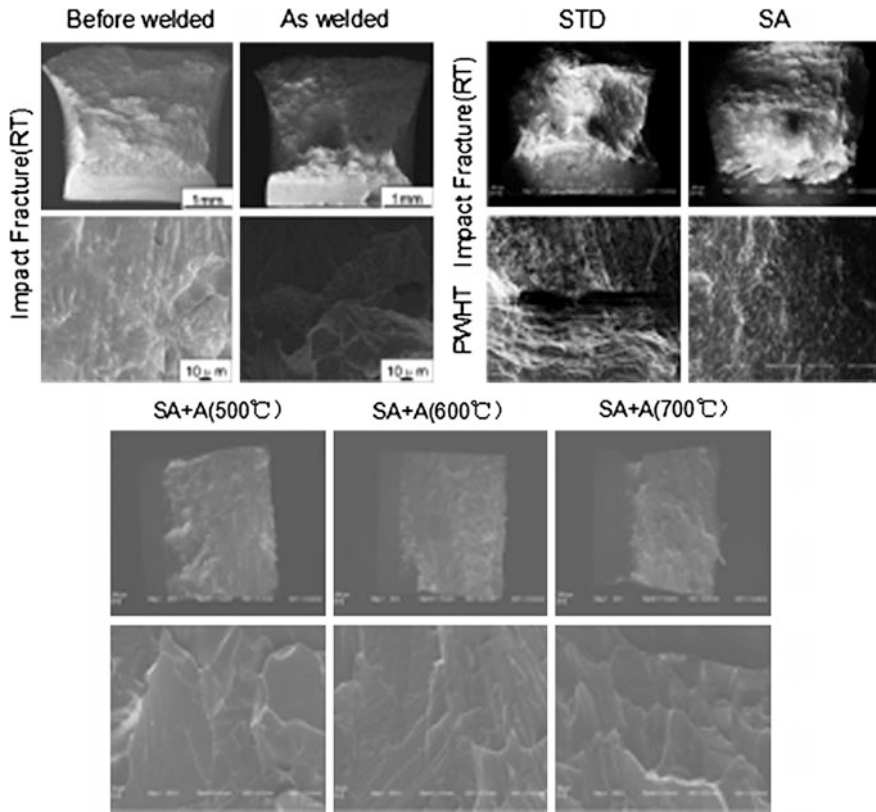


Fig. 3 Vickers hardness results of V-4Cr-4Ti under different conditions



**Fig. 4** SEM images of Charpy impact test specimen fracture morphology of V-4Cr-4Ti alloy before, after welding, and PWHT

also concluded from the SEM results. For the PWHT of STD and SA, the fracture mode is still ductile while for SA plus A the results show all brittle fracture mode.

### 3.4 TEM Observation

Figure 5 shows the TEM images of V-4Cr-4Ti welds. From the results, we find the precipitates density is quite low and for some specimen we even found no precipitates which show no direct effect for the increase of DBTT after PWHT. The density is quite low and the average size the precipitates are 100 nm which is much larger the mechanical alloyed products.

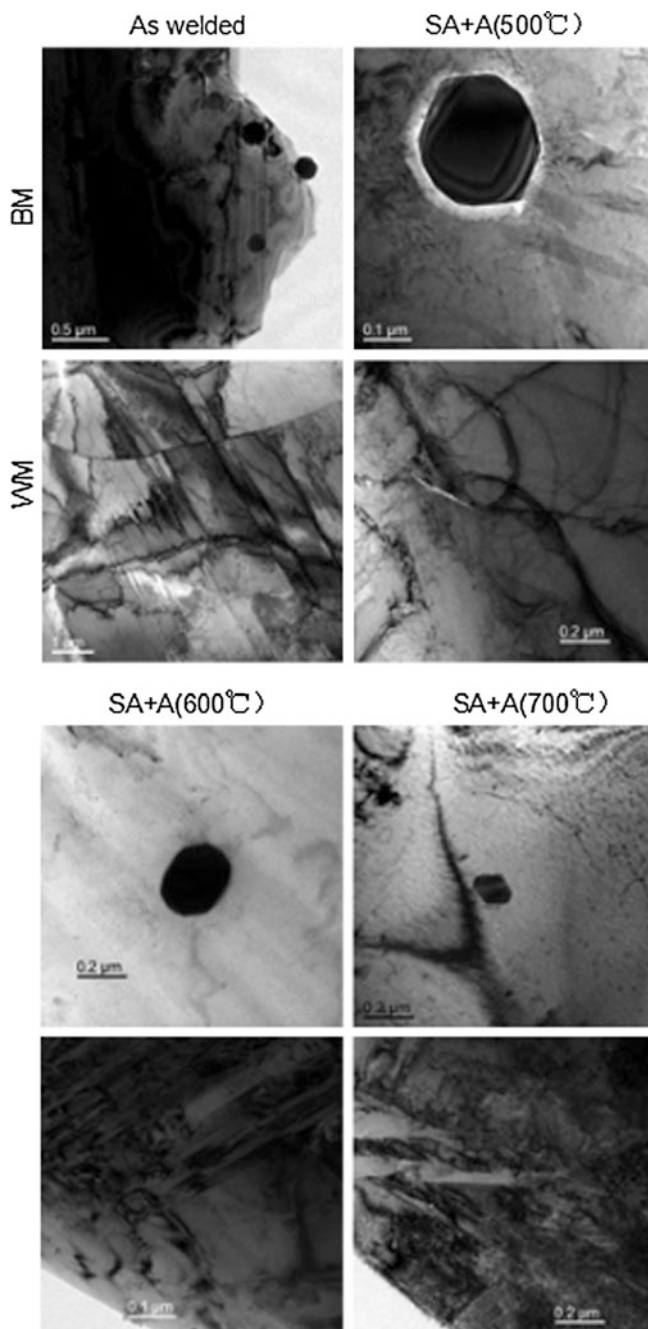


**Fig. 5** TEM images of V-4Cr-4Ti alloy morphology and precipitates different after different PWHT in BM and WM

## 4 Conclusions

This sample is illustrated to help your understanding on the paper format. We are looking forward to seeing you at the PBNC-2016. The hardness, impact of SWIP-30 vanadium alloy before welding and after welding were tested and microstructure observation were done before and after test. The following conclusions were obtained:

1. Electron beam welding caused hardening of material in the welding center and PWHT can eliminate this phenomenon;
2. The DBTT of V-4Cr-4Ti after welding increase much and the applied PWHT methods did not recover the DBTT and some other PWHT should be tried;
3. The precipitates number is limited in the weld metal and has no remarkable effect on the DBTT change of V-4Cr-4Ti.

**Acknowledgments** This study was supported by the Chinese Nuclear Energy Development Program (H6600003-13-2) and National Natural Science Foundation of China (No. 51341005). The authors are grateful for the technical support of TEM observation from Dr. Xiaona Li and Beibei Jiang in Dalian University of Technology.

## References

1. T. Muroga, J.M. Chen, V.M. Chernov, R.J. Kurtz, M. Le Flem et al. / Journal of Nuclear Materials 455 (2014) 263–268
2. J.M. Chen, V.M. Chernov, R.J. Kurtz, T. Muroga. Overview of the vanadium alloy researches for fusion reactors, J. Nucl. Mater. 417 (1–3) (2011) 289–294
3. R.J. Kurtz, K. Abe, V.M. Chernov, et al. Recent progress on development of vanadium alloys for fusion[J]. Journal of nuclear materials, 329, (2004) 47–55
4. M. Le Flem, J.M. Gentzittel, P. Wident, Assessment of a European V–4Cr–4Ti alloy – CEA-J57, J. Nucl. Mater. 442 (2013) S325-S329
5. T. Muroga, T. Nagasaka, A. Iiyoshi, A. Kawabata, S. Sakurai, M. Sakata, J. Nucl. Mater. 283–287 (2000) 711–715
6. T. Nagasaka, M.L. Grossbeck, T. Muroga, J.F. King, Fus. Technol. 39 (2001) 664
7. T. Muroga, T. Nagasaka, A. Iiyoshi, A. Kawabata, S. Sakurai, M. Sakata, J. Nucl. Mater. 283–287 (2000) 711
8. T. Nagasaka, T. Muroga, M. Imamura, S. Tomiyama, M. Sakata, Fus. Technol. 39 (2001) 659
9. T. Nagasaka, T. Muroga, M.L. Grossbeck, T. Yamamoto, J. Nucl. Mater. 307–311 (2002) 1595–1599
10. H.Y. Fu, J.M. Chen, P.F. Zheng, T. Nagasaka, T. Muroga, Z.D. Li, S. Cui, Z.Y. Xu, J. Nucl. Mater. 442 (Suppl. 1) (2013) S336-S340
11. T. Muroga et al, Journal of Nuclear Materials 30–311 (2002) 547–554



# Conclusion of the Test of Fujian Fuqing Nuclear Power Plant Unit 1 Determination of Reactor Coolant Flow on the Basis of the Heat Balance

Dongjia Zheng

**Abstract** Determination of reactor coolant flow on the basis of the heat balance test results the reactor thermal power through the heat balance of the primary loop and secondary loop of nuclear power plant, and then calculates the flow through the primary pump and the pressure vessel, verifies that whether the primary pump flow and pressure vessel flow satisfy the safety standard at full power platform. Fuqing nuclear power plant Unit 1 flow tests in each power platform exist the phenomenon that the loop flow or pressure vessel flow exceeds the mechanical design flow. Analyzing the influence factors of flow measurement results, improving the main factors to the impact, the overflow degree has a certain improvement. Understanding the Guangdong Nuclear Power M310 units also have the common problems of overflow, finally give the conclusion that the overflow has no effect on the safe and stable operation of units.

**Keywords** KME · Heat balance · Flow · Overflow · Primary pump · The mechanical design · Flow · Temperature

## 1 Introduction

KME Test Instrumentation System is supported by the primary loop reactor thermal power of the heat balance of nuclear power plants based on the primary loop and secondary loop, data acquisition from the instrumentation installed on the main water supply system are, the main steam system VVP, the steam generator blow-down system APG systems, such as the accuracy of these instruments high, and different that installed in the reactor as a loop-line instruments affected by the reactor irradiation, therefore KME nuclear reactor thermal power calculation is the most accurate method of computing power. Based on the KME calculated thermal

---

D. Zheng (✉)  
Fujian Fuqing Nuclear Power Co., Ltd., Fuqing 350318, China  
e-mail: zhengdj@fqnp.com

power and the relationship between the power and the flow, get the loop flow and the reactor pressure vessel flow.

The enthalpy balance on each steam generator gives the following equation:

$$W_{SGi} = H_v Q_v + H_p Q_p - H_e Q_e$$

$$Q_v = Q_e - Q_p$$

where

- $W_{SGi}$  (kW) thermal power exchanged with steam generator;  
 $Q_e$  (kg/s) feedwater flow rate;  
 $Q_p$  (kg/s) blowdown flow rate;  
 $Q_v$  (kg/s) steam flow rate;  
 $H_e$  (kJ/kg) feedwater enthalpy;  
 $H_p$  (kJ/kg) blowdown enthalpy;  
 $H_v$  (kJ/kg) wet steam enthalpy.

Thermal power of each loop gives the following equation:

$$W_i = W_{SGi} - W_{RCP} \approx W_{SGi} - W_P = W_{SGi} - \eta_m \times W_e$$

where

- $W_i$  (kW) loop i thermal power;  
 $W_{RCP}$  (kW) power transferred to reactor coolant system;  
 $W_P$  (kW) thermal power transferred to pump thermal barrier;  
 $W_e$  (kW) reactor coolant pump electrical power;  
 $\eta_m$  (fraction) reactor coolant pump motor efficiency.

The reactor coolant pump flow is:

$$Q = \frac{3600 \times v \times (W_{SG} - W_{RCP})}{\Delta H}$$

or:

$$Q_i = \frac{3600 \times v_i \times W_i}{H_{hi} - H_{ci}}$$

where

- $v_i$  (m<sup>3</sup>/kg) water specific volume in cold leg  $i$ ;  
 $H_{hi}$  (kJ/kg) reactor coolant water enthalpy at steam generator inlet in loop  $i$ ;  
 $H_{ci}$  (kJ/kg) reactor coolant water enthalpy at pump outlet inlet in loop  $i$ .

Enthalpy value is determined by the pressure and temperature. The temperature data is obtained by measuring the resistance of a loop installed in the hot and cold sections alternate bypass channel temperature.

The reactor vessel flow is:

$$Q_V = Q_1 + Q_2 + Q_3.$$

## 2 TP RCP64 Test

Fuqing Nuclear Power Unit 1 commissioning tests TP1RCP64 determination of reactor coolant flow on the basis of the heat balance test (hereinafter referred to as “flow test”) is executed at 30 %FP, 50 %FP, 75 %FP, 87 %FP, and 100 %FP, and the results of the tests on each platform are shown in Table 1. The objectives of this test are: ① to get more accurate calculation of reactor coolant flow through the heat balance than online flow instrument; ② to check online flow instrument; ③ 100 % FP test to verify that reactor coolant flow to meet safety standards. The specific acceptance criteria is: given the uncertainty factor, the measured loop flow should be between the thermo hydraulic flow of 22,840 m<sup>3</sup>/h and the mechanical flow of 24,740 m<sup>3</sup>/h; given the uncertainty factor, the measured vessel flow should be between three times the thermo hydraulic flow (68,520 m<sup>3</sup>/h) and three times mechanical flow (74,220 m<sup>3</sup>/h). ④ to provide flow date to TP1RCP60 reactor coolant flow coast down test.

As can be seen from the experimental results, without considering the uncertainty, 30 %FP and 50 %FP loop 2 flow exceeds the mechanical design flow. After considering the uncertainty, 30 %FP flow test three loop flow and the vessel flow exceeded mechanical design flow; in 50 %FP, 75 %FP, 87 %FP, 100 %FP except that loop 2 flow exceeds mechanical design flow, the loop 1, the loop 3 and the

**Table 1** Fuqing nuclear power unit 1 TP1RCP64 test results

Power	30 %FP	50 %FP	75 %FP	87 %FP	100 %FP
Loop flow (m <sup>3</sup> /h)	24,097	24,192	24,055	24,259	24,318
	25,474	24,659	24,899	24,490	24,584
	24,325	24,076	24,187	23,948	23,929
Vessel flow (m <sup>3</sup> /h)	73,896	72,927	73,141	72,698	72,832
Loop flow uncertainty (m <sup>3</sup> /h)	1375	514	374	340	309
	1489	563	386	342	312
	1408	514	374	334	301
Vessel flow uncertainty (m <sup>3</sup> /h)	2468	919	655	587	532
Loop flow consider positive uncertainty (m <sup>3</sup> /h)	25,472	24,706	24,429	24,599	24,630
	26,963	25,221	25,285	24,833	24,896
	25,733	24,590	24,561	24,282	24,230
Vessel flow consider positive uncertainty (m <sup>3</sup> /h)	76,364	73,846	73,796	73,284	73,364

vessel flow were to meet the design requirements. As the uncertainty of Low-power platform was larger, then flow over a large difference; as power increases, the uncertainty decreases. This was because the low-power platform specific volume error, than the uncertainty error and an evaporator enthalpy of errors, etc., leading to large total uncertainty. As power increases, the instrument measurement results more accurate, uncertainty decreases.

## 2.1 Analysis of the Overflow

According to the principle of the test, there are factors that affect power flow calculation, KME power calculating temperature, pressure, and so the main pump delivery. Where in the main pump power delivered approximately equal in each platform, as shown in Table 2, it can ignore its impact on the flow calculation. Comparative enthalpy pressure, specific volume is negligible. Therefore, the main factors affecting the flow temperature and KME computing is computing power. Further traffic tolerance is the common problem of domestic counterparts M310 power plant units, flow test acceptance criteria, and therefore is reasonable also to be discussed.

### 2.1.1 Temperature Influence

Temperature during the test requirements are: average primary coolant temperature at the reference temperature  $\pm 1$  °C, and maintained within a predetermined temperature range of  $\pm 0.5$  °C. Analysis of temperature change on each test platform 0.1 °C for flow.

Table 3 shows that a great influence of temperature on the flow calculation itself, especially in low-power platform, if the temperature fluctuations measured 0.1 °C, namely temperature difference increases or decreases 0.1 °C, the flow rate will be 10 % tolerance -50 about% of improvement or deterioration, and therefore, the temperature measurement is particularly important. The current design practice documents and CGN were installed in temperature by measuring the shunt resistor obtain alternate detector temperature, although this method avoids the error signal conversion and instrument display, but increases the risk of the test, such as data read, recording errors, and plug in the terminal block error cause reactor shutdown events. The test results were analyzed using online thermometer data into the traffic flow error and spare thermometer error introduced substantially equal, it is recommended that

**Table 2** The power that the primary pump transferring to the reactor coolant system

Power	30 %FP	50 %FP	75 %FP	87 %FP	100 %FP
Pump power (kW)	5963	5966	5969	5968	5981
	5947	5945	5963	5960	5969
	5971	5962	5991	5988	5999

**Table 3** The influence of temperature

Power	30 % FP	50 % FP	75 % FP	87 % FP	100 % FP
Flow impacted by that hot leg bypass temperature increase 0.1 °C (m <sup>3</sup> /h)	-238	-124	-105	-97	-92
	-283	-145	-109	-98	-94
	-243	-143	-105	-96	-90
Flow impacted by that hot leg bypass temperature decrease 0.1 °C (m <sup>3</sup> /h)	242	166	94	86	74
	236	153	98	87	75
	248	144	94	84	72
Flow impacted by that cold leg bypass temperature increase 0.1 °C (m <sup>3</sup> /h)	239	122	97	87	80
	260	163	100	88	79
	243	141	97	86	78
Flow impacted by that cold leg bypass temperature decrease 0.1 °C (m <sup>3</sup> /h)	-233	-157	-88	-81	-70
	-253	-126	-94	-82	-72
	-240	-137	-90	-79	-67

the follow-up test to select online thermometer data calculations. As can be seen from Table 1, 30 %FP traffic tolerance is the most serious, and external factors in addition to low-power platform above flow analysis easy tolerance, the data processing selected data interval is 1 min, selected interval subsequent data processing platform two seconds of data traffic over the extent of the difference has been greatly improved. Therefore follow regardless of which method should be selected to eliminate large amounts of data random error trials.

**2.1.2 KME Power Calculation Influence**

Fuqing Nuclear Power Unit 1 KME system to ensure accurate results than 30 % FP. TP1RCP64 in thermal equilibrium measurements for each test platform is shown in Table 4. At 87 %FP ago, loop 2 flow ratio flow loop 1 and loop 3 is large, larger than the loop 1 and loop 3 loop 2 traffic flow phenomenon does exist according to the debugging experience CGN M310 units, but because of Fuqing unit 1 nuclear power flow over loop 1 loop 2 and loop 3 more traffic, so in 87 %FP test before KME system for in situ measurements (namely, water pressure, water flow, water temperature, evaporator outlet pressure, etc.) were recalibrated. 75 %FP Loop 1 and Loop 3 power substantially equal loop 2 power tolerance up to 20 MW, the second evaporator power calibration after a significant improvement, 87 %FP, 100 %FP loop 2 power tolerance improved to 10 MW, flow rate on up to 200 m<sup>3</sup>/h. Therefore, before the follow-up unit commissioning tests should first confirm whether the instrument needs to be calibrated to ensure the accuracy of the measuring instruments KME data collection (Table 4).

**Table 4** Fuqing nuclear power plant unit 1 heat balance measurement

Power	30 %FP	50 %FP	75 %FP	87 %FP	100 %FP
SG power (MW)	281.199	482.188	728.197	828.634	948.592
	289.215	476.527	751.766	837.485	958.923
	279.618	481.725	736.948	825.425	946.7

### 2.1.3 Acceptance Criteria

Test acceptance criteria introduced in Sect. 2③, in the Fuqing nuclear power units 1 and 2 Final Safety Analysis Report FSAR Chapter 15 [1] introduces the analysis of accidents, such as the large break loss of coolant accident, the small break loss of coolant accident, the main water supply start feedwater and auxiliary feedwater completely lost, containment spray pump or low pressure safety injection pump failure, power plant auxiliary equipment for nonemergency AC power loss, loss of normal feedwater flow analysis assumes that all other accidents using thermal design flow calculation, but not the best Estimation of traffic. From the M310 unit flow tolerance of common problems, the acceptance criteria of the mechanical design flow are not appropriate. Currently, CGN NNSA has made an application to modify the acceptance criteria ceiling until after the application by China Guangdong Nuclear, Fuqing will also apply.

## 2.2 Effect of the Overflow

Fuqing Nuclear Power Unit 1 100 %FP flow measurement loop 2 test results for mechanical design traffic flow exceeds 0.63 %, according to the Nuclear Power Institute of Fuqing Nuclear Power Plant Unit 1 and 2 thematic review of the final safety analysis report will be a work order to answer a single dialogue (FQ12-FLW3-11) made Fuqing 1,2 unit RCP flow gauge the impact preanalysis [2], it was found Fuqing unit 1 red river flow gauge is below 1.63 % overrun value that the test results are acceptable of. The report notes that the flow gauge with minimal impact on the main pump, steam generators, fuel assemblies, core design, and the like.

## 3 Conclusion

Factors affecting the flow test are: ① the accuracy of the measuring instruments measured KME; ② measurement methods; ③ acceptance criteria. Therefore, before the follow-up unit commissioning and production trials, we should first confirm whether KME measuring instrument needs to be calibrated, and second on the measurement method should be introduced to avoid human error, it is

recommended to test directly select the output temperature detectors DCS system, reducing the flow measurement own error, error analysis when considering the data from the temperature sensor to the display through the various aspects of the introduction of an error, this method avoids the risk of operating the terminal block because the error caused by the shutdown of the reactor. On acceptance criteria, M310 unit calculated according to the heat balance of the reactor coolant flow test there is the phenomenon of ultra-poor, indicating the presence of the acceptance criteria unreasonable, China Guangdong Nuclear Power is proposing to modify the acceptance criteria apply to the NNSA, Fuqing will continue tracking.

## References

1. FSAR of Fujian Fuqing Nuclear Power Plant Unit 1 and unit 2, part 15
2. NPIC. Fujian Fuqing Nuclear Power Plant Unit 1 and unit 2 justification of primary overflow, 2014-3-20

# Exceptional Shut Down During Load Test of Emergency Diesel Generator

Ri Zhao and Yafei Li

**Abstract** A study of the Exceptional shut down during load test of emergency diesel generator (EDG) was performed for M310 unit (1000 mW). An EDG protection shut down was executed during the EDG load test after finishing synchronizing with power grid in an M310 unit, generator circuit-breaker (GCB) opened automatically, but no protection shut down signal or alarm had been recorded except low lube oil pressure alarm. The reason of the protection shut down was analyzed in this article, modification was introduced to reduce the risk of damaging EDG.

**Keywords** Nuclear power plant commissioning · EDG · Emergency diesel generator · Diesel engine · M310

## 1 Introduction

For a typical M310 PWR unit, LHA/B emergency bus is energized by LGB/C bus, when offsite power is lost, emergency auxiliary power will begin to work, LHA/B emergency bus is energized by EDG. The primary diagram of the LHA/B emergency bus is shown as Fig. 1. Each M310 PWR unit is equipped with two EDG sets, which are designed to be highly reliable, and independent to the power plant. LHA/LHB bus provides power to several emergency pumps for nuclear power plant, thus it is very critical for nuclear safety. This article will discuss MTU-20V956TB33 type EDG.

EDG consists of engine, generator, and several subsystems, such as compressed air start system, coolant system, fuel supply system, lube oil system, and exhaust gas system. Parameters of EDG can be monitored on SIMATIC WinCC (Windows

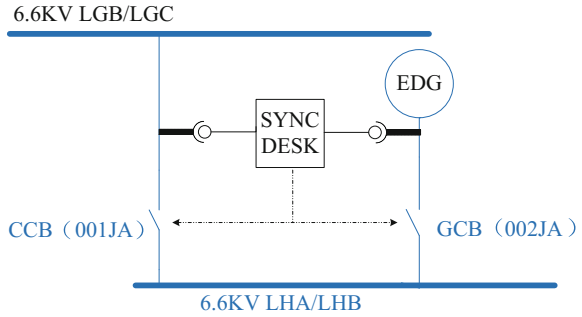
---

R. Zhao (✉) · Y. Li  
China Nuclear Power Engineering Co., Ltd., Beijing, China  
e-mail: zhaori@cnpe.cc

Y. Li  
e-mail: liyff@cnpe.cc



**Fig. 1** Primary diagram of emergency bus



Control System) on LCP (Local Control Panel). WinCC is a software which is installed on Windows. The software is capable of performing two-way communication between PC and PLCs, configuring a user interface with all the parameters of EDG, allowing operators to input commands to PLC with PC I/O devices, providing data saving, trends, alarms, and user access functions. Its capability provides significant convenience to the EDG operation.

## 2 Shut Down During the Load Test

The procedure of the EDG load test was as follows:

1. Incoming current circuit-breaker (CCB) was always closed during the test;
2. Started EDG manually, until EDG was stabilized;
3. Mobile Synchronizing Desk synchronized the EDG to emergency bus (LHA/LHB);
4. Increased the load of EDG to 4.5 MW;
5. EDG executed the emergency shutdown, GCB open;
6. Local control panel showed no alarm or protection shut down triggered during above operation;
7. A few seconds later, local control panel showed “lube oil pressure low” alarm and triggered protection shut down.

## 3 Analysis

In the test mode, following signals shall result in the protection shut down of EDG:

1. Manually emergency shut down;
2. Generator stator windings temperature high;
3. Lube oil temperature high;

4. Either one of the two air flaps closed;
5. Coolant temperature high;
6. Engine rotation speed don't reach 350 rpm after 6 s since startup;
7. Generator protection shut down signal;
8. Engine over speed;
9. Exhaust gas temperature high;
10. Generator crank bearing temperature high;
11. Lube oil pressure low;
12. Engine lube oil tank level high;
13. Day fuel tank level low;
14. Coolant tank level low.

According to all the status messages recorded by WinCC software on LCP, No. 1–10 of the shutting down signals were not the reason of the exceptional shut down. The alarm of 11 lube oil pressure low had been triggered during the test. Analysis shall be given in the next part of this article.

The lube oil pumps are driven directly via a gear train and draw oil from the oil pan. Lube oil pressure should be nearly proportional to the engine rotation speed, which is shown in Fig. 2.

- $t_1$  EDG reacted to the shutting down signal, pumps stopped pumping fuel to cylinder stators and GCB opened, engine rotation speed raised due to load shedding, at this time no alarm had been triggered;
- $t_2$  EDG rotation speed and lube oil pressure reached the maximum point;
- $t_3$  Lube oil pressure reached minimum set point ( $P > 5$  bar);

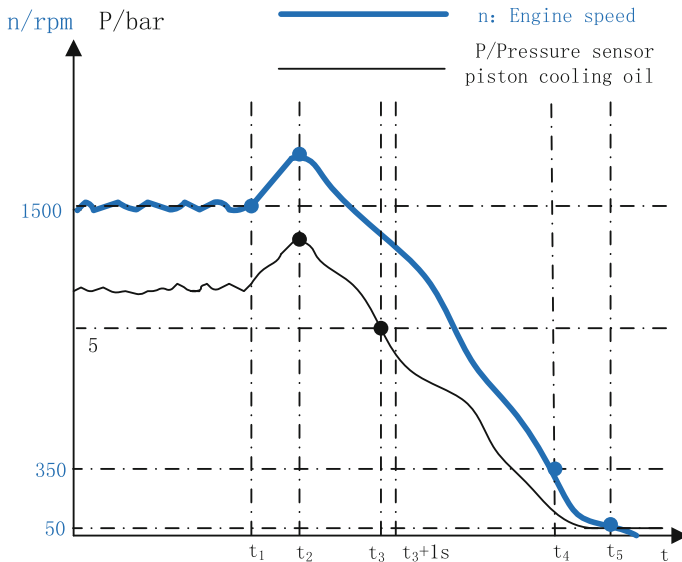


**Fig. 2** Trends of lube oil pressure and engine speed during shutdown procedure

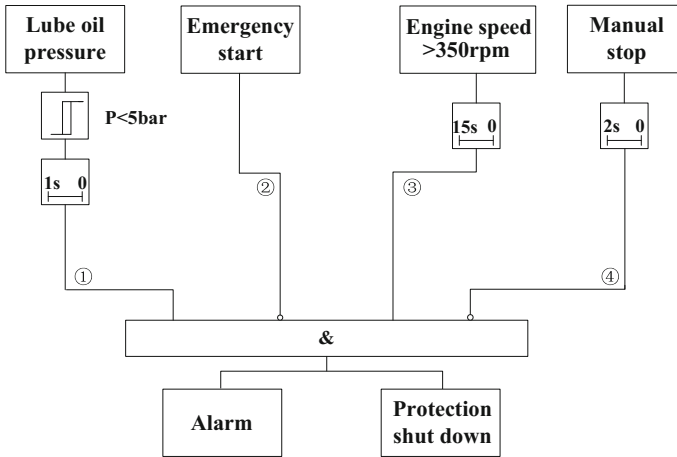


**Fig. 3** Control logic of lube oil pressure protection shut down

- $t_3 + 1s$  Lube oil pressure low shutting down signal had been triggered;
- $t_4$  EDG rotation speed reached 350 rpm, Lube oil pressure low shutting down signal disappeared;
- $t_5$  EDG rotation speed reached 50 rpm, which means the shutting down was complete, pre-lubrication pump was reactive.

Logic of EDG I&C cabinet which is relevant to this case is shown in Fig. 3. Signal ① is “1” if lube oil pressure is below 5 bar for longer than 1 s, so it was “0” until  $t_3$ . EDG was operating with load in testing mode, which means it was not operating in emergency mode, signal ② was always “0” in this case. Signal ③ is “1” if engine rotation speed is above 350 rpm for longer than 15 s, so it was “0” until  $t_4$ . Signal ④ was never triggered in this case due to neither manual stop order had been given nor start failure had taken place.

Given all of four signals considered, the lube oil pressure low protection shut down signal was true since  $t_3 + 1s$  until  $t_4$ , at this time the shut down order had already been given, so it can be concluded that shutting down was not caused by lube oil pressure low in this case. Thus each time the EDG shut down, a lube oil pressure low alarm will appear on the LCP screen.

No. 12–14 of the shutting down signals shall be discussed in the next part of the article.

Another module is installed in the cabinet, which is designed to monitor lube oil tank level sensor (151-MN). This module is part of 1E cabinet, it is independent to the PLC and WinCC and able to function properly after losing of offsite power. During another startup in other test, the sensor showed that the lube oil tank level reading was not stable, sometimes it suddenly changed to more than 300 mm, which triggered protection shutdown, relevant logic diagram is showed in Fig. 4a.

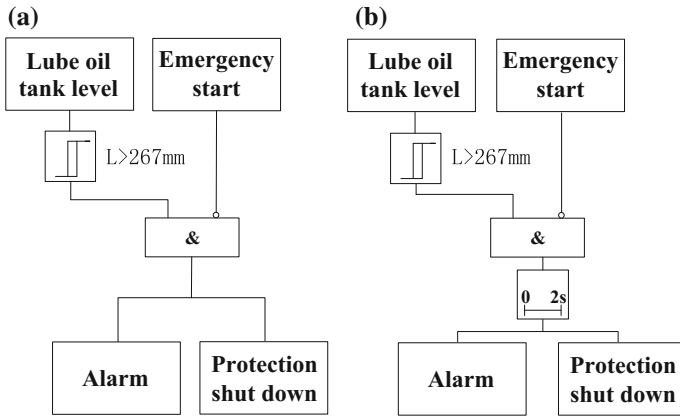


Fig. 4 Control logic of lube oil tank level protection shut down

WinCC software is designed to monitor multiple PLC input/output signals via an I/O connector between Siemens PLCs and PC. Both analog and digital signals can be monitored in the same time. But in the meantime, all the signals are not monitored or recorded continuously due to the inadequate PC processing capability, there is a small time difference between every two signal picking up, the time deference can be set ranging from milliseconds to minutes. In this case the time difference was set to 2 s (default value of the configuration).

If a short pulse signal is sent to the WinCC software right in this time gap, it would not be recorded in the WinCC software. However, PLCs are designed to process short pulse signals, relevant logic programs shall still process regardless whether WinCC software pick up the signal or not. In this case, EDG reacted to the lube oil tank high shutting down order, which is processed in PLC, but no messages or relevant data were recorded on LCP.

The running of EDG causes severe vibration, such vibration may affect analog signal transmission loosing connection. After replacing the lube oil tank level sensor (151-MN), the reading of lube oil tank level was much more stable.

Serious problem may be caused by the unstable output of the lube oil tank level sensor. If a false lube oil tank low-level alarm triggered during engine running, lube oil tank refilling pump will begin to work. As the refilling pump working, the actual oil level in the tank will be raising to critical level which is very dangerous to the safety of the EDG. If a false lube oil tank high-level alarm triggered during engine running, a protection shut down shall be triggered while EDG is running in test mode as the incident discussed in this article.

An improvement to avoid such unpredicted protection shut down are suggested in this article. A schematic diagram is showed in Fig. 5, an additional small tank which is installed on the engine next to the lube oil tank, these two tanks are connected via two hose tubes, which making a communication vessel. Level sensor is installed in the additional leveling tank. An improvement is suggested to reduce

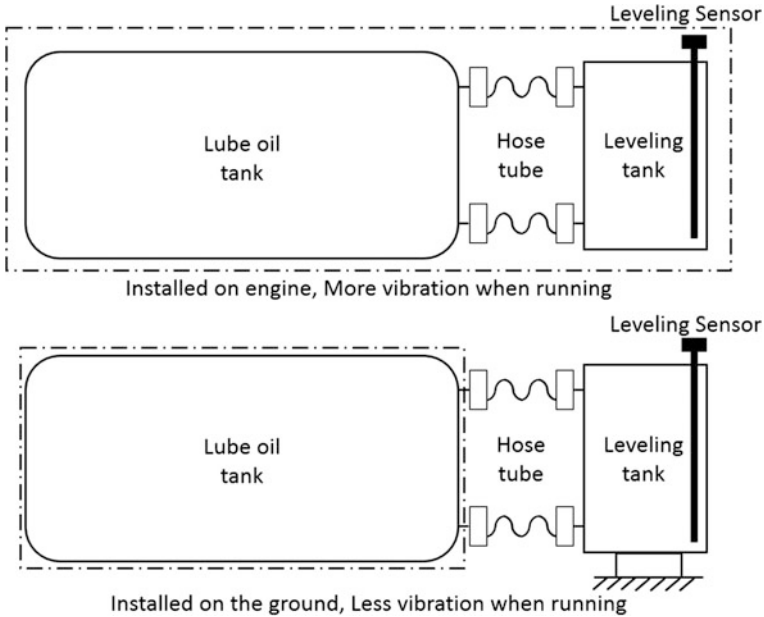


**Fig. 5** An improvement aiming to remove the effect of vibration during engine running

the vibration of the sensor by simply removing the leveling tank from the engine and reinstalling the tank on the ground. Therefore, the output of the analog signals can be stabilized during the running of EDG. In the meanwhile, an off-delay relay should be added in the protection shutting down logic of the lube oil tank level high, which is shown in Fig. 4b.

## 4 Conclusions

Based on the analyses given in this article, conclusions can be given as follows.

Lube oil level tank sensor's reading was unstable during the test, which triggered an unpredicted protection shut down of EDG. The shutting down signal was executed by PLCs but not recorded by the WinCC software on the monitoring PC. The running of EDG caused severe vibration, which lead such unstable analog output of the sensor.

A modification is introduced to minimize the risk in this article.

## References

1. Zamfirescu. «Logic Diagram of I&C Cabinet EDG» (C), 2014
2. Kueck. «Equip operation and maintenance manual Genset EDG» (A), 2014

# Fangjiashan Auxiliary Transformer Low-Voltage Side of Three-Phase Voltage Imbalance Analysis

Anman Luo

**Abstract** Fangjiashan nuclear power engineering 9LGR auxiliary power system during the commissioning phase, it occurs to the voltage imbalance seriously when the auxiliary transformer empty punch test, comparing some common causes of system of three-phase voltage imbalance by a more detailed description and the corresponding treatment measures, combing with 9LGR auxiliary power system which had designed a system architecture design drawings, carry out the analysis of the auxiliary transformer low voltage side of three-phase voltage imbalance, conclusion: resonant frequency cause the reason of phase auxiliary transformer low-voltage side of the three-phase voltage imbalance, according to the practical operation characteristics, offer some proposals to avoid the three-phase voltage unbalance in running process.

**Keywords** Fangjiashan · Auxiliary transformer · Three-phase voltage · Imbalance

## 1 Preface

The case of Fangjiashan nuclear power engineering of the auxiliary power supply system (9LGR) for the outer grid and generator are de-energized, mainly for LGB and LGC systems powered by the system in order to supply power to emergency and public works equipment, the plant used external power plant equipment for the public Fangjiashan 2 units, equipped with two auxiliary transformer, the capacity of each auxiliary transformer is 34 MVA [1].

Appeared in Fangjiashan Nuclear Power Engineering 220 kV power transmission air rushed down the overvoltage test issue, after the impact of stability, the C-phase voltage of transformers 9LGR101TU reaches 10 kV, the A phase voltage of transformers 9LGR201TU reaches 9.6 kV, approximately rated phase voltage of

---

A. Luo (✉)

Department 2, CNNP Nuclear Power Operations Management Co., Ltd.,  
Jiaxing, Zhejiang, China  
e-mail: jianghong@cnpe.cc

2.6 times [2], there has been a serious three-phase voltage imbalance, phase voltage imbalance can lead to shortened system load, transformers, and other electrical or mechanical equipment greatly shorten life; similarly, the three-phase voltage imbalance will occur directly increase the system line loss [3]. Therefore, it is necessary to analyze the three-phase voltage imbalance occurs, and to take timely measures to prevent the emergence of three-phase voltage imbalance, improve auxiliary power system stability and security.

## **2 Auxiliary Power System Introduction**

### ***2.1 One-Time Diagram of Auxiliary Power System***

According to Fangjiashan nuclear power engineering main electrical wiring diagram of the auxiliary power supply section, 9LGR auxiliary power supply system can be a simplified schematic diagram shown in Fig. 1, including the deputy bus, circuit breakers, switches, auxiliary transformers, common enclosure busbar, two part buses, 9LGR PT and bus line PT, highlighting several key equipment, is a clear need for further analysis of the object.

### ***2.2 Important Equipment***

#### **2.2.1 Auxiliary Transformer**

Auxiliary transformer model for the SFZ-34000/220, three-phase double-winding power transformer load tap changer, belonging power plants transformer, iron core is three-phase three-column miter nonporous structure, choke with low magnetic steel belt tensioning column by banding with banding, the upper and lower clamps coupled with low magnetic steel plate, between the core level part support by a round wooden, 30ZH120 electrical steel is the core design material. Regarding the high-voltage coil, in order to change the bottom transposition tangled style, it adopts with the three helical for low-voltage coil, double helical one for balance coil, the spiral one for the regulator coil. The oil tank is with the bell type. Between the main coil insulation using a thin paper tube small oil-gap structure, with insulation plate [1]. The body of the arrangement from inside to outside as follows: core-balance coil-low voltage coil-a high-voltage coil-tap winding. The high-pressure side is connected using cable bushing, tap wires have connected using cable carrier switch, the low pressure side and the balance winding using by the copper lugs and sleeves connected, taking into account the low pressure side of the auxiliary transformer is ungrounded system, adds a  $\Delta$  wiring balance windings.

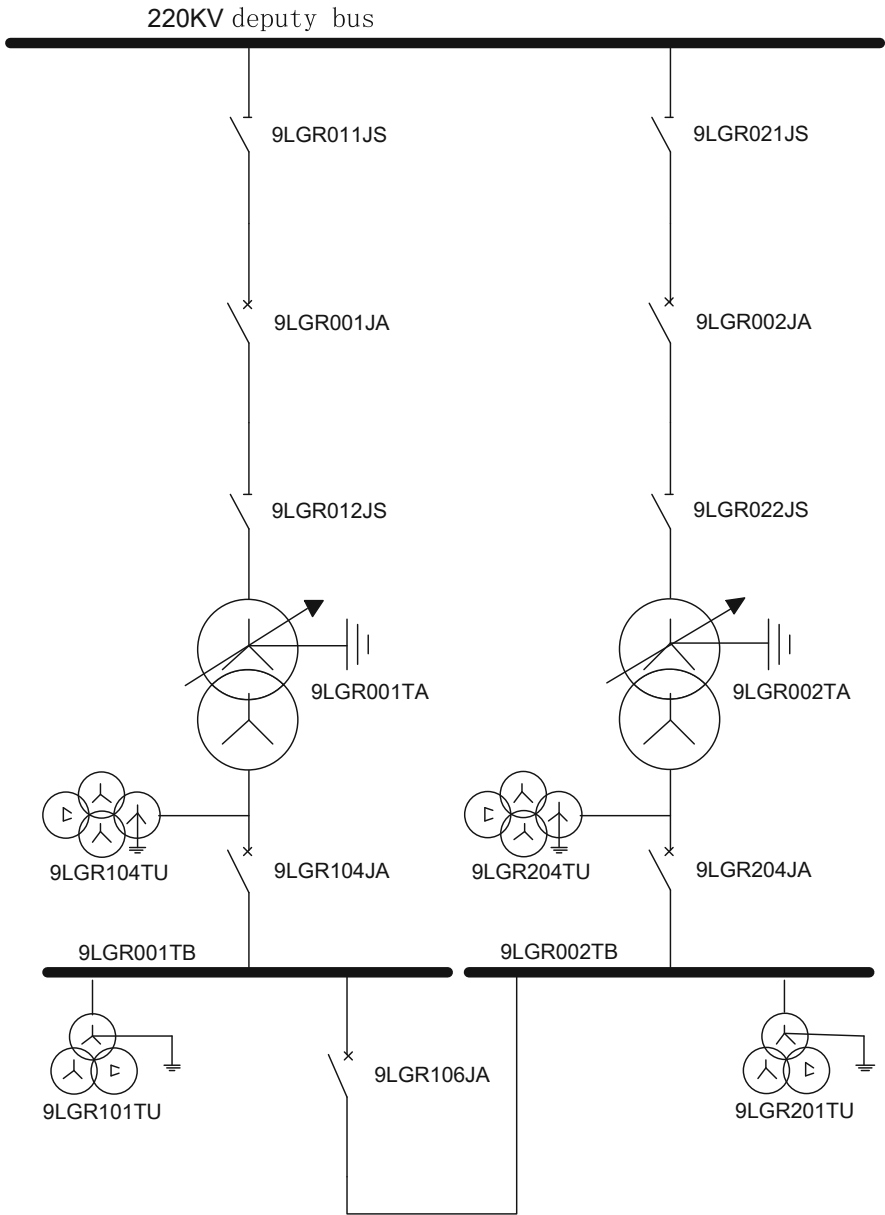


**Fig. 1** Simplified one-time diagram of auxiliary power system

Auxiliary transformer rated capacity of 34 MVA; rated frequency of 50 Hz; connection group for the YN, yn0 + d (i.e.: high side and low side are star-connected, wherein the high-pressure side of the neutral point grounding, the low pressure side is not grounded, with another a delta winding for balance one);



high side rated voltage of 220 kV, rated current is 89.2 A; low-voltage side rated voltage of 6.9 kV, rated current is 2845 A; no-load loss  $\leq 35$  kW rated frequency rated voltage, rated voltage load loss (75 °C)  $\leq 135$  kW; under normal circumstances, the top oil temperature rise limit of 55 K, average winding temperature rise limit of 65 K, tanks, core, and metal structure temperature limit of 80 K [4].

### 2.2.2 The Common Enclosure Busbar

Common Enclosure Busbar is produced by Zhenjiang East China power equipment factory, model BGFm-10/513500-Z, the total purchasing length of the contract is 40 m [5], based on the file “total Common Enclosure Busbar Support Arrangement Drawings” in the labeling, the length of total Common Enclosure Busbar connection can be calculated between two auxiliary transformer and JX plant building, total Common Enclosure Busbar length about 11 m for auxiliary transformer one to JX plant building, total Common Enclosure Busbar length is about 29 m [6], between the auxiliary transformer II to JX plant building, construction drawings provided in the file “TD outdoor cable channel and a total Common Enclosure Busbar support base construction program” in the dimensioned to be about determining the total length [7], for total Common Enclosure Busbar bus of actual construction process installed.

## 3 The Reasons Leading to the Three-Phase Voltage Imbalance

Ungrounded systems and small current grounding system used to run a dynamic change in the way, so there are voltage imbalance is a very common anomaly. Through the analysis of ungrounded same voltage imbalance, it can help abnormality factor determination system, easy to find fault and to take measures to eliminate the fault.

Causes the system appears voltage imbalance generally include the following, namely: a three-phase asymmetric load, voltage transformer fuse blown, PT internal fault and failure, PT wiring error, single-phase ground fault, and iron A magnetic resonance [8]. Voltage transformer fuse blown fuse can be divided into high-pressure, low-voltage fuses blown, special circumstances may arise voltage transformer neutral point of breakdown of insurance breakdown voltage imbalance based on actual operating experience. Single-phase ground into a nonmetallic and metallic ground grounding. Partakers ferromagnetic resonance frequency resonance frequency resonant and the resonant frequency three cases. The following sections describe these types of voltage imbalance causes.

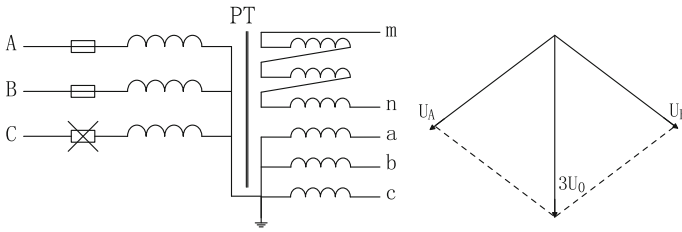


Fig. 2 High-voltage fuse blown

### 3.1 High-Voltage Fuse Blown

When the single-phase high-voltage fuse blows, because the voltage transformer-induced voltage, the voltage of the faulted phase will be reduced, but not reduced to zero, and the remaining two-phase voltage is normal, the vector angle of  $120^\circ$  in open delta PT will appear at zero-sequence voltage, generating a ground signal (Fig. 2).

PT high voltage fuse breaking phenomenon can occur in single-phase fuse blown, two-phase, and three-phase Insurance blown fuse are blown, the characteristics shown in Table 1.

### 3.2 Low-Voltage Fuses Blown

When single-phase voltage fuses blown, as is the PT secondary side fuse is blown, so the voltage of the fault phase will be reduced, but it will not be reduced to zero, non-fault phase voltage is normal, the vector angle of  $120^\circ$ , zero-sequence voltage at PT open triangle generate, it will not produce ground signal, the primary side voltage is normal (Table 2).

Table 1 The characteristics of PT high voltage fuse breaking

$U_a$	$U_b$	$U_c$	$U_{ab}$	$U_{ac}$	$U_{bc}$	Zero-sequence	Phenomenon	Fault category
Down	Down	Down	Down	Down	Keep	Up	Ground fault, PT disconnection	A phase high voltage fuse blown
Down	Down	Keep	Down	Down	Down	Up	Ground fault PT disconnection	A B phase high voltage fuse blown
Down	Down	Down	Down	Down	Down	Keep	PT disconnection	Three phases high voltage fuse blown

**Table 2** The characteristics of PT low voltage fuse breaking

$U_a$	$U_b$	$U_c$	$U_{ab}$	$U_{ac}$	$U_{bc}$	Zero-sequence	Phenomenon	Fault category
Down	Keep	Keep	Down	Down	Keep	Keep	PT disconnection	A phase low voltage fuse blown
Down	Down	Keep	Down	Down	Down	Keep	PPT disconnection	A B phase low voltage fuse blown
Down	Down	Down	Down	Down	Down	Keep	PT disconnection	Three phases low voltage fuse blown

### 3.3 Occurred Metallic Ground

When a metallic ground point occurred on the line or live equipment, the grounded phase voltage is the same with the earth potential, two normal phase-to-ground voltage value increased to line voltage, resulting in the displacement of the neutral point, PT open delta voltage 100 V emergence occurred ground signal. When the ground appears to a nonmetallic, grounding phase voltage is less than the phase voltage, and nonzero, and the remaining two-phase voltage increases, but less than the line voltage, PT open delta voltage occurring at less than 100 V, issue a ground signal. No negative sequence voltage when single-phase ground, only positive and zero-sequence voltage.

### 3.4 Ferroresonance

Another important reason leading to voltage imbalance is resonant, resonance generally occurs in the small current grounding system running on under-compensation or full compensation for small ground current system, the ferromagnetic resonance occurs due to voltage transformer primary winding connected into a star, the neutral point directly to ground, each relative to the magnetizing inductance  $L_1$ ,  $L_2$ ,  $L_3$ , and the system ground capacitance  $C_0$  between each form an independent oscillator circuit, when the parameter matches within a certain range ( $\omega L = 1/3\omega C_0$ ) occurs parallel resonance, there might inspire ferromagnetic resonance. When resonance, it will form a high neutral point displacement voltage and overvoltage, thereby endangering the equipment insulation. Resonance phenomenon for three-phase voltage was some kind of law change, and accompanied by a phase or two-phase voltage is high or low, and because of higher residual voltage, it may start grounding device, issued a ground signal. Ferromagnetic resonance can be divided into the resonant frequency, high-frequency resonant, and the resonant frequency of three forms.

**Table 3** The amount of voltage divider resonance characteristics

$U_a$	$U_b$	$U_c$	$U_{ab}$	$U_{ac}$	$U_{bc}$	$3U_0$	Phenomenon	Failure category
Up			Keep	Keep	Keep	Up	Ground signal	The resonant frequency

### 3.4.1 Subfrequency Resonance

When the system is 1/2 times harmonics, will open delta PT overvoltage, such as the B phase as the reference phasor, the opening of voltage:

$$\begin{aligned}
 U_{mn} &= U_a + U_b + U_c \\
 &= U_m \sin \frac{1}{2} \omega(t + 120^\circ) + U_m \sin \frac{1}{2} \omega t + U_m \sin \frac{1}{2} \omega(t - 120^\circ) \\
 &= U_m \left[ \sin \frac{1}{2} \omega(t + 60^\circ) + \sin \frac{1}{2} \omega t + \sin \frac{1}{2} \omega(t - 60^\circ) \right] \\
 &= 2U_m \sin \frac{1}{2} \omega t \\
 &= 2U_b
 \end{aligned}$$

1/2 visible when harmonic resonance occurs, the voltage at the secondary side of PT open delta voltage is phase 1/2 times 2 times the harmonic component when this component is large enough, it will cause at the open triangle voltage relay, resulting in single-phase ground illusion. When a division resonance characteristics as shown in Table 3.

When the resonant frequency at the same time the three-phase voltage increases, the neutral point of zero-sequence voltage, due to the significant decline in PT inductance, the excitation current increases rapidly, can reach 10 times the number of ratings, causing PT burned or blown fuse.

### 3.4.2 High-Frequency (Third Harmonic) Resonance

When the system harmonic resonance to the third harmonic resonance, for example, where the voltage sine wave third harmonic component contained in the B phase as the reference phasor, PT open delta voltage is:

$$\begin{aligned}
 U_{mn} &= U_a + U_b + U_c \\
 &= U_m \sin^{\frac{1}{2}} 3\omega(t + 120^\circ) + U_m \sin^{\frac{1}{2}} 3\omega t + U_m \sin^{\frac{1}{2}} 3\omega(t - 120^\circ) \\
 &= U_m(2 \cos 2\pi\omega + 1) \sin 3\omega t = U_b(2 \cos 2\pi\omega + 1) \\
 &= 3U_b
 \end{aligned}$$

**Table 4** Characteristics of high-frequency resonant voltage

$U_a$	$U_b$	$U_c$	$3U_0$	Phenomenon	Failure category
Elevated high			Elevated	Ground signal	Frequency (third harmonic) resonance

Visible third harmonic resonance occurs when the voltage in the secondary side of PT open delta voltage is phase three times in the third times harmonics, when this component is large enough, it will cause a voltage relay open delta, causing single-phase ground illusion, caused by PT burned or blown fuse. When the high-frequency resonance characteristics as shown in Table 4.

At the same time the high-frequency resonance-phase voltage increases, the neutral point appears high residual voltage.

### 3.4.3 Resonance Frequency

When the two-frequency resonant system relative voltage increases, another relative voltage drop; or two opposite voltage is lowered, another relative voltage rises. Maximum voltage rise of not more than 3 times the phase voltage, the same voltage drop is not reduced to zero.

## 4 Fangjiashan Auxiliary Transformer Low Voltage Side of the Three-Phase Voltage Imbalance Analysis

### 4.1 Field Test Data

Transformer factory and field test data as follows:

According to the manufacturer's test report shows: auxiliary transformer A low-voltage winding three-phase capacitor 20.25 nf, equivalent to a single relatively capacitance is 6.75 nf. According to the actual measurement data field, the common enclosure busbar connected to the auxiliary transformer A closed bus (included the into line PT) single relatively capacitance is 3 nf, in addition, single bus capacitance relative 1 nf, 9LGR002TB single bus capacitance relative 1 nf. According to pour power transmission field sent back 9LGR101TU and voltage waveforms 9LGR201TU, and after the impact of stability, the voltage of transformers 9LGR101TU C phase reaches 10 kV, the voltage of transformers 9LGR201TU A phase reaches 9.6 kV [2].

## 4.2 Cause Analysis

According voltage transformer measurement data of 9LGR101TU and 9LGR201TU, you can learn A-phase voltage and C-phase voltage are with respect to the rated phase voltage was increased, the voltage rise no more than three times the rated phase voltage, the characteristics consistent with ferromagnetic resonance frequency, in addition, voltage transformer failure and kind of single-phase-to-ground fault did not occur during the test, so you can make the following inference, since the voltage three-phase transformer core by different incentives and showing a different saturation, the extent of each phase inductance voltage transformer has also undergone a change, each phase inductance values are not the same, the neutral point is displaced emerged residual voltage. During the impact, the voltage transformer core magnetic saturation gradually, when  $\omega L$  and  $1/\omega C$  close to induce the ferromagnetic resonance, and with overvoltage generate, eventually leading to the three-phase voltage imbalance.

In “9LGR resonance treatment program seminars Minutes,” the program two on increasing the capacitance section concerning the derivation, the main consideration of the six kinds of situations. Were briefly describe (1) When the 6.6 kV line circuit breaker open, only put into the line PT, this time the ratio of capacitance and inductance of 0.36, not far from the resonant frequency time base area; (2) When the 6.6 kV circuit breaker closing, put into the line PT and bus PT, section breaker open, 6.6 kV bus not load, the ratio of the capacitance and inductance is 0.63, not far from the resonance frequency of the time base area; (3) When the 6.6 kV circuit breaker keep closing, put into the line PT and bus PT, section breaker closing, 6.6 kV bus not load, the ratio of the capacitance and inductance is 0.73, from the area close to the resonant frequency of the time base; (4) When 6.6 kV line breaker closing, put into the line PT and bus PT, sub-breaker closing, the current LGR001TB to 1LGB bus in the charged state, the ratio of the capacitance and inductance is 0.0135, very far from the resonant frequency of the time base area, basically does not produce resonance; (5) When 6.6 kV line breaker closing, put into the line PT and bus PT, section breaker closing, LGR001TB to 1LGB bus cables and bus cables LGR002TB to 1LGC state of charge, then the ratio of capacitance, and inductance is 0.0088, far away from the resonance region, does not return to resonate; (6) When 6.6 kV line breaker closing, put into the line PT and bus PT, segmentation trip is closing, 6.6 kV connect one generating units with 9LGIA and LHB bus, 3-band bus are running with load, capacitance, and inductance ratio at this time was 0.0106, very far away from the resonance region, the basic does not produce resonance. These six cases, three front can produce ferromagnetic resonance, three are back away from the resonance region, the difference is behind the three cases are related to the LGC and LGB’s cable, this cable is longer, the earth capacitance larger, allows the system to be taken into account to avoid the resonance.

For reasons more vivid representation frequency resonance occurs, it can directly assume a single auxiliary transformer relatively capacitance 3 nf, so to third case is calculated as follows:

$$X_{C03} = \frac{1}{\omega C} = \frac{1}{2\pi f C} = \frac{1}{2 \times 3.14 \times 50 \times 8 \times 10^{-9}} = 398,089.17 \Omega$$

$$X_{m3} = X_{mj1} // X_{mm1} // X_{mm2} = 369,600 \Omega$$

$$\frac{X_{C03}}{X_{m3}} = \frac{398,089.17}{369,600} = 1.077$$

Wherein the  $X_{C03}$  represents the system capacitive reactance,  $X_{m3}$  is the system inductance values, from the calculation results can be clearly seen when assuming the value of the capacitor is small underground inductance capacitance extremely close, this time just to meet frequency resonance conditions.

## 5 Several Measures to Eliminate the Ferromagnetic Resonance

Elimination of ferromagnetic resonance should consider two aspects, one is to change the inductance, capacitance parameter, the second is the resonance energy consumption. There are several points on which the harmonic elimination of measures:

1. the selection of the excitation characteristics of a good voltage transformer or switched capacitor voltage transformer.  
If the PT voltage characteristics are very good, the PT possible general over-voltage will not enter the deep saturation region, thereby constituting less susceptible to the resonance parameter matching; switch capacitor voltage transformer, changing the parameters of the system. In a sense, this is a fundamental measure to eliminate the ferromagnetic resonance.
2. in the PT primary side of the neutral point grounding resistor in series.  
PT primary side is directly grounded neutral point of the original, in order to limit resonance, to ground via a resistor, this approach is equivalent to every relative parallel resistance or PT open delta secondary winding resistance as access, can play a consumption energy and suppress resonance effects.
3. the primary side of the neutral point of the PT series single-phase voltage transformer.  
This approach enables the voltage has two PT share, equivalent to improve the excitation characteristics of PT, so easy saturated PT, but PT withstand high voltage neutral point, not entirely eliminate resonance.

4. in an open delta PT secondary access damping resistor or harmonic elimination device.

The damping resistor is equivalent to the power transformer neutral point, in the three-phase voltage imbalance, the port will open delta winding generates a voltage, damping resistors on port junction will consume energy, damping resistor smaller energy consumption the more, the more it can suppress the occurrence of resonance.

5. access certain size on the bus capacitors, capacitance, and inductance so that the ratio is less than 0.01.

This method is based on the study of the resonance region and proposed increases when each relatively capacitance, so that the ratio of capacitance and inductance of less than 0.01, you can prevent resonance. This is a more direct approach, with a simple and efficient features, however, increasing the capacitance to ground, the single-phase ground current increases, it may cause arc grounding overvoltage and capacitance converted to PT open delta across the capacitor is large, capacitance is very small, when the single-phase ground, prone to over-current and burn PT.

6. the installation of the system neutral point arc suppression coil.

Petersen coil inductance than PT magnetizing inductance several orders of magnitude, the equivalent of PT short circuit, to avoid matching the resonance parameters. This approach eliminates the resonator has significant advantages, disadvantages are the large investment, as well as if Petersen coil compensation of inappropriate, still there will be a voltage imbalance, because Petersen coil grounding system accessible or full compensation arc suppression coil form.

7. using the principle of automatic tuning ground compensation device.

Such automatic compensation device consists of five parts, grounding transformers, electric arc suppression coil, computer control section, the damping resistor section dedicated transformer neutral and nonlinear resistors. Grounding transformer is used as artificial neutral point arc suppression coil access. Petersen coil current through the load switching regulator and realize remote automatic control, use and adjust the way, that is, in the normal operation mode case, according to changes in the system at any time to adjust the parameters of the arc suppression coil tap into the best position. The use of microcomputer control its automatic tracking and automatic tuning. By measuring the phase displacement voltage and neutral current and voltage, can accurately calculate, judge, issued a directive to automatically adjust the parameters display (capacitive currents, the inductor current, residual current, and displacement voltage, etc.).

8. the system then gapless zinc oxide arrester (MOA).

MOA has good nonlinear, large flow capacity, superior general arrester protection performance. It is a sequence of zero discharge of three relatively capacitance charge on nonlinear resistor to achieve this purpose. Studies have shown that the best harmonic elimination MOA is combined with other measures to effectively inhibit the ferromagnetic resonance, MOA as a backup



protection, on the one hand the use of other harmonic elimination measures will greatly improve operating conditions in the MOA ferromagnetic resonance, the other in the other When the measure failed to effectively suppress overvoltage, MOA can effectively play its superior performance overvoltage protection.

## **6 Fangjiashan Auxiliary Transformer Low Voltage Side of the Three-Phase Voltage Imbalance Workaround**

Since the inverted power transmission throughout the Fangjiashan project is still in the commissioning phase, JX plant to LX cable has not been laid down on the other hand in order to ensure the progress of power transmission test, and do not have major improvements to the system, using a temporary increase in the capacitance program: that two transformers 6.6 kV line-side installation of a micro-capacitance of each group. After the installation of a micro-capacitance method, the system can guarantee inductance capacitance at a voltage of less than 0.01 times the line voltage is applied, the damage frequency resonance condition occurs, the effective solution of the auxiliary transformer low-voltage side of the three-phase imbalance. After the formal operation, it can bring LGR to 6.6 kV cable LGB and power transmission LGC segment were together, except on the breakers LGR electric boiler, both in the closed state, LGR to LGB and LGC are also always 6.6 kV cable is charging running, this operating mode reference power plant in Daya Bay and Ling Ao namely nuclear power plant has been verified.

## **References**

1. The auxiliary power system (9LGR) System Manual, Beijing, 2011
2. LGR resonance treatment program summary seminars, Haiyan, 2011
3. Liu chao Hua, of the three-phase voltage unbalance and harmonics on power system operation hazards, China Electric Power Education, 2007: 292–293
4. The auxiliary transformer operation and maintenance manuals, Baoding, 2010
5. The Qinshan Nuclear Power Plant Expansion Project (Fang Shan nuclear power engineering) common box busbar factory acceptance outline, 2010
6. The common box busbar support arrangement drawings, 2010
7. TD outdoor cable channel and a common box busbar support base construction plan, 2011
8. CaoyaXu, ungrounded system voltage unbalance analysis and processing, the Tenth China Association annual meeting, 2008

# Design for High Level Layout and Control of Nuclear Island HVAC Based on DCS Technique

Yong Liu, Jiru Chu, Xiaochuan Ding and Chen Shang

**Abstract** At present, most of Chinese Nuclear Power Plants (NPPs) in operation and under construction adopt Digital Control System (DCS). As a result, the special High Level Layout and Control Function based on DCS platform are required to fulfill the normal and accident operation tasks. As the supporting systems of safety and safety-related systems, the Heating, Ventilation, and Air Conditioning (HVAC) systems are responsible for shielding the radioactive productions and maintaining the environment temperature in the acceptable scope for the staffs and the important equipments. Considering that the HVAC systems have been involved frequently during normal and accident operating, the special High Level Layout and Control Functions (HLLCF) for HVAC should be designed to present the advantages of DCS platform, but also assist the operators to implement the operating procedures quickly and improve the safety of NPPs.

**Keywords** DCS · NI HVAC · High level layout and control functions (HLLCF)

## 1 Introduction

### 1.1 *Emergency Operating Procedures*

The NPP operation is support by a series of operating procedures, which contains Operating Technical Specification (OTS), Normal Operating Procedures (NOPs), Abnormal Operating Procedures (AOPs), Emergency Operating Procedures (EOPs), and Severe Accidents Management Guideline (SAMG). EOPs are essential for maintaining fundamental safety functions and preventing core damage during design basis accidents and beyond design basis accidents in a NPP.

---

Y. Liu · J. Chu (✉) · X. Ding · C. Shang  
Communist Party, Beijing, China  
e-mail: chujr@cnpe.cc; 435711745@qq.com

## **1.2 *Ni HAVC***

The main function of NI HAVC is to provide a comfortable environment for all staffs, maintain the environment condition in an acceptable scope for all important equipments, and shield the radioactive productions, by the way of controlling and regulating the air temperature, ventilation pressure, filtration efficiency, air humidity, and air change frequency.

## **1.3 *HLLCF***

Refer to a typical PWR, the paper format procedures should be changed to the computerized procedures due to DCS technology, therefore the development and the design tasks of HLLCF are imperative under the situation. With this technology, the necessary control means, information layout and status surveillance will be provide to the operators. As a result, the computerized procedures implementation efficiency could be increased meanwhile the human factor failure could be decreased.

# **2 Analysis and Design for Ni HVAC HLLCF**

The operator is able to control the reactor to a safe status by operating and monitoring the ventilation systems and main processing systems according to accident operation procedures when accident occurs. The operation sequence and content for NPP ventilation systems are complicatedly and precisely required in this process.

## **2.1 *Analysis of Operation and Monitoring Content***

Base on EOP, the function list of each ventilation system which is required to be designed could be obtained through the analyses of operation and monitoring content step by step. Equipments and parameters required to be operated or monitored to realize specified functions in EOP should be included in function list. Meanwhile, those requirements of operating and monitoring some equipments and parameters that the accident operation procedures do not mention can also be added to the list according to operation experience.

## ***2.2 Determination of Frequency and Correlation***

The operating content in all NPPs EOP should be analyzed one by one, so that the operation frequency and sequence of ventilation systems served in accident operation procedures can be counted and ventilation systems with high operation frequency and sequence correlation can be preliminarily selected.

## ***2.3 Selection for Operation and Monitoring Content***

The operation for a function of ventilation system is diverse from different EOP, hence the function information for ventilation systems should be integrated and important information benefit for conducting operation should be selected in order to form high level layout and control content.

## ***2.4 Division and Classification***

Each HLLCF should be layout in one screen in order to facilitate operation and decrease the number of switching screens. Owing to the quantity limitations of information, ventilation systems should be classified. On one hand, not only the preliminarily selection for ventilation systems with high operation frequency and sequence correlation, but also selection of operating and monitoring content for ventilation systems should be taken in consideration. On the other hand, ventilation systems that involved to accident operation procedures need to be divided and classified in consideration of the correlation between systems in processing design. Meanwhile, HLLCF is classified and distributed comply with the rules of processing system design. As to ventilation systems which would hardly used in accident operation procedures, relative operation can be mentioned at individual system layout pages.

## ***2.5 Optimization***

Each HLLCF of ventilation system differs from complexity, type, and importance, so it needs to optimize the information in the layout and control function:

- Analyze the frequency, importance, and correlation of every single ventilation system of all accident procedures. First of all, removal information that is not important and less emerged according to its frequency and importance, and then increase information that is closely related to the importance of operation and monitoring when information cannot be centralized in one screen;

- Optimize equipments and relevant process flow information with HLLCF of ventilation system by the restriction for the amount of information of every single function;
- The experience feedback of operating personnel and operating habits must be taken into consideration for the design and composition of HLLCF of ventilation system.

The above analysis and design process is shown in Fig. 1.

### **3 Analysis and Design Example for HVAC HLLCF**

This chapter takes the NI HVAC system of a typical NPP adopting DCS system as an example to introduce the analysis and design process of ventilation modules.

The NPP uses Emergency Operating Procedures to deal with accidents, which mainly contains the ventilation system of Control Room Air Conditioning System, Electrical Cabinet Room Ventilation System, Charging Pump Room Emergency Ventilation System, Fuel Building Ventilation System, Containment ring Gallery Ventilation System, and Containment Continuous Ventilation System.

#### ***3.1 Frequency and Correlation***

All the operations in the EOPs should be collected to determine the control equipment and monitoring information during accidents, and the operation frequency and correlation of related components could then be determined.

After analysis, components of Charging Pump Room Emergency Ventilation System/Fuel Building Ventilation System/Containment ring Gallery Ventilation System are used often and related during accidents.

#### ***3.2 Determining Components of Each System***

The components of Charging Pump Room Emergency Ventilation System/Fuel Building Ventilation System/Containment ring Gallery Ventilation System should be detailed further. The final component lists should be based on the requirements of EOPs.

For different EOPs, needed components are different. The most important and necessary components should be kept, and be modified after users' experience feedback.

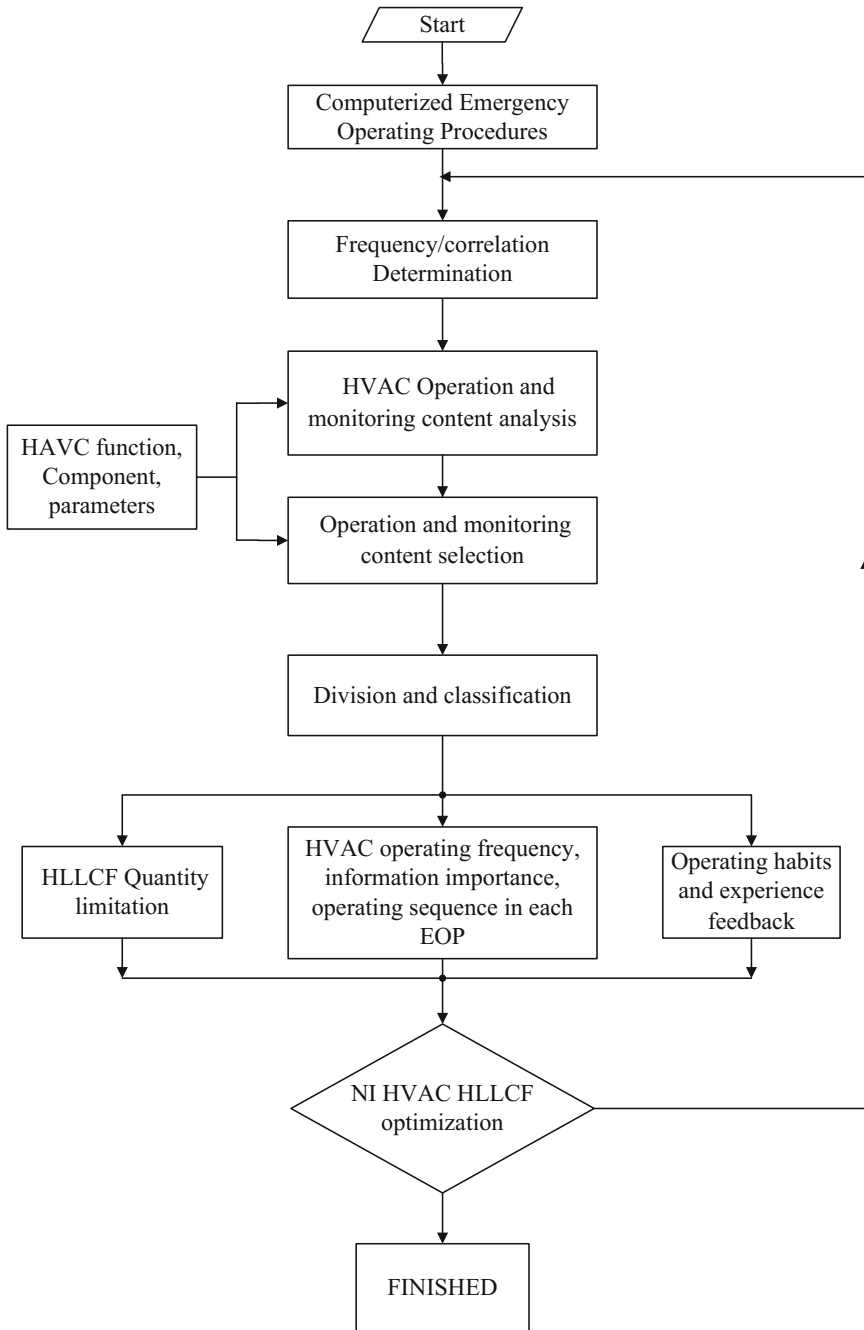


Fig. 1 HVAC modules analysis and design process in the CEOP

### 3.3 Partition and Classification of HVAC HLLCF

Under the precondition that the information on one high level layout/control function been restrained, interrelated HVAC functions have been partitioned and classified on one layout, so as to reduce the time of screen exchanges. The Charging Pump Room Emergency Ventilation system, the Fuel Building Ventilation system and the Annulus Ventilation System which have been picked out according to the high controlled frequency and conversant controlling order relation as described above paragraphs should be lay out on the same one high level layout/control function display.

In addition, the Nuclear Auxiliary Building Ventilation system is also lay out on the same display with The Charging Pump Room Emergency Ventilation system, Fuel Building Ventilation system, and Annulus Ventilation System, as the Nuclear Auxiliary Building Ventilation has conversant relation with the three systems and the information on the display can be restrained.

### 3.4 Optimization

The HLLCF which is designed above with analyze contain four systems: the Charging Pump Room Emergency Ventilation system, the Fuel Building

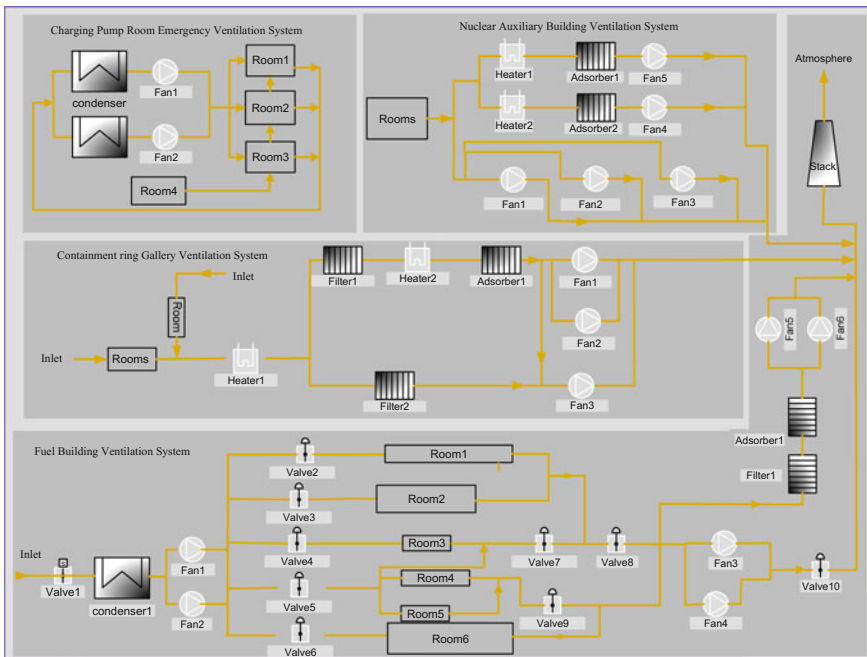


Fig. 2 Example of HVAC HLLCF

Ventilation system, the Annulus Ventilation System, and the Nuclear Auxiliary Building Ventilation system. The final high level layout/control function shown in Fig. 2 can be ascertained with information optimized according to the system layout tenet, function list, the essentiality of the control information, and feedback from operating experience.

## 4 Conclusions

Most of Chinese Nuclear Power Plants (NPPs) in operation and under construction adopt Digital Control System (DCS), so as to improve the economics and the safety. The Emergency Operating Procedures (EOPs) which are essential for maintaining fundamental safety function after accident should be computer designed and been cooperating with DCS. This paragraph depicts the analyze method, design process, and example of the HVAC high level layout/control function (HLLCF) according to the Event Oriented Procedure which will be used in the under construction NPP. The use of modularized layout/control function will exert the advantage of the DCS and improve the enforcement efficiency of EOP. This paragraph can also be used for reference for the design of the layout/control function modularization for other computerized procedure.

## References

1. Fan Xin-ju. Application of DCS system in nuclear power plant [J]. Mechanical and Electrical Information, 2010(24) (in Chinese)
2. Wang Cui-fang, Ren Yong-zhong. Application of DCS in HVAC System of Nuclear Power Plant [J]. Process Automation Instrumentation, 2010 (in Chinese)
3. Liu Fei, Zhang Zhi-jian, Peng Min-jun. Development of Computerized Procedures System for Nuclear Power Plants [J]. Nuclear Power Engineering, 2007 (in Chinese)
4. Li Peng-cheng, Zhang Li, Dai Li-cao. Effects of Digital Human-Machine Interface Characteristics on Human Error in Nuclear Power Plants [J]. Nuclear Power Engineering, 2007 (in Chinese)
5. Fang Zhou. Application of Human Factors Engineering to Computerized Procedure Operating System in Nuclear Power Plants [J]. Modern Computer, 2013 (in Chinese)



# Improvements to CANDU6 Reactor Power Control Programs

Gongzhan Wang, Ligen Xu, Tan Hong, Yongxiang Zheng,  
Mingjun Chen, Jianxin Sheng and Yang Liu

**Abstract** CANDU6 reactor power control programs include flux mapping programs and reactor power regulation programs. For reactor power control, the step of reactor power set point change is redoubled as the step is calculated by the slow program and executed by the fast program; this affects the reactor power control precision. For flux mapping, due to logic error and inappropriate initial setting, failure of a single flux signal may result into a wide range of signals reporting failure, or overflow at specific reactor power levels. This paper studies the causes of these problems and correspondent improvements made to solve these problems.

**Keyword** CANDU6 · Reactor power · Software · Precision · Overflow

---

G. Wang (✉) · T. Hong · Y. Zheng · M. Chen · J. Sheng · Y. Liu  
China National Nuclear Power Operations Management Company Limited,  
Haiyan, Zhejiang, China  
e-mail: wanggz@cnp.com.cn

T. Hong  
e-mail: hongt@cnp.com.cn

Y. Zheng  
e-mail: zhengyx@cnp.com.cn

M. Chen  
e-mail: chengmj@cnp.com.cn

J. Sheng  
e-mail: shengjx@cnp.com.cn

Y. Liu  
e-mail: liuyang@cnp.com.cn

L. Xu  
Fuqing Nuclear Power Company Limited, Fuqing, Fujian, China  
e-mail: xulg@fqnp.com

## 1 Introduction

CANDU6 nuclear power plant uses Digital Control Computer (herein after “DCC”) to control the main processes of the plant, including reactor power, steam generator level and pressure, primary heat transport system pressure and inventory, moderator temperature, etc. DCC system has two duplicated computers, named DCCX and DCCY, respectively. DCC is a 16-bits centralized control computer, programmed with assemble language.

Reactor power control function is jointly realized by several programs, such as Reactor Regulation Slow program (herein after “RRS”), Reactor Regulation Fast program (herein after “RRF”), Flux Mapping program (herein after “FLX”), and Step-back program. This paper will analyze the problems encountered with reactor power control function, and the correspondent improvements made in our plant.

## 2 Improvement to Control Precision of Reactor Power

### 2.1 Precision Problem of Reactor Power Control

Reactor power regulation function is realized by RRS and RRF together, in which RRS carries out background calculations, such as calculation of thermal power and calibration factors, RRF calculates the neutron power and control signals and send them out to field control equipment. RRS executes every 2 s, whilst RRF executes every 0.5 s. The purpose of this design is to realize the control function with high efficiency.

When reactor power is to be changed, new set point (\$PRA, \log\$ power) and power change rate (RRA, \$\log\$ power/second) are inputted into RRS through a man-machine interface. RRS calculates a power change step (RSP, \$\log\$ power per 0.5 s) for RRF with formula (1), in which PLOG is the current reactor \$\log\$ power:

$$RSP = \text{Minimum}(RRA/2, (\$PRA - PLOG)/2/4) \quad (1)$$

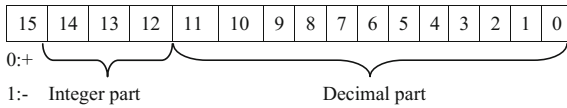
RRF uses RSP to calculate demand \$\log\$ power PDLOG with formula (2) in its every execution:

$$PDLOG = PDLOG + RSP \quad (2)$$

The difference between PLOG and PDLOG, as shown in formula (3), is the reactor power error, which will be used later to calculate reactor power control signals:

$$EP = PLOG - PDLOG \tag{3}$$

In RRS and RRF, PLOG, PDLOG, and RSP are all stored as variables of one word, i.e., 16 bits length. The functions of the 16 bits are defined as the following (the number of bits of the integer part is called B-Scaling, and in this case it is B3):



The highest precision value could be stored with this format is 1 at bit0, which is equal to  $1 * 2^{-12}$ , this is also the minimum change step RSP from RRS to RRF could be. As RRF will execute for four times after each RRS execution, the minimum PDLOG change will be  $4 * 2^{-12}$ , i.e., 0.0009765625. This is a log power value, converted to a percentage power value it is  $10^{0.0009765625} = 1.00225$ , which means the actual minimum power change stage is 0.225 %. If the sign bit is 1, means negative, the minimum power change stage will be -0.225 %.

In normal operation, reactor power should be controlled at full power; this means that the hourly average thermal power (AX377, FP) should be close but not over 100 %FP. Operators check AX377 on every shift, and if it is found over 100 %FP, reactor power will be lowered by entering a new reactor power set point \$PRA with an appropriate change rate RRA. As the minimum change stage is -0.225 %, ideally reactor power will be lowered to a value between 100 %FP and 99.775 % FP, and the long-term average value is 99.89 %FP. There is a space of 0.11 %FP to the full power, equivalent to >0.8 MWe in CANDU6 reactor power plant.

On the other hand, the existing man-machine interface only allows the operator to input percentage power value, which will be converted into log power by RRS and then used for control. Precision will be further lost during this process. Together with the relatively big minimum change stage, it is not an easy and straightforward work for operators to maneuver reactor power to an expectant level.

## 2.2 Improvement of Control Precision

To solve this problem, a new approach was designed to improve the feasibility and precision of reactor power maneuvering, in which RRS is bypassed and PDLOG in RRF is changed directly. To ensure reactor safety, the range of PDLOG allowed to be directly changed is limited to a small but enough scope around \$PRA, with a set of conditions checked before carrying out the change.

A new man-machine interface, as shown in Fig. 1, was added to enable this operation.



Fig. 1 Interface of RRS set point fine maneuver

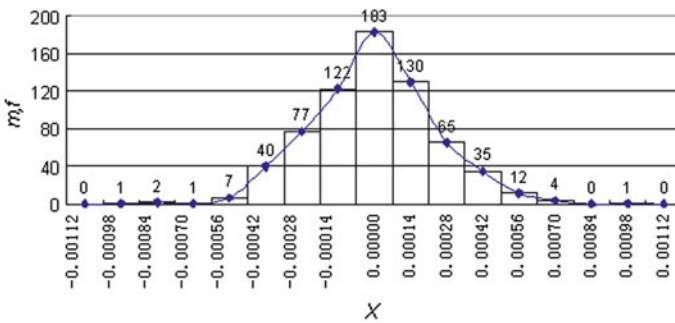


Fig. 2 Statistic of hourly average reactor power oscillation

After the new approach was provided, its maneuver scheme must be decided, too. Statistics result of 680 h oscillation of hourly average reactor power is shown in Fig. 2. The pattern satisfies a normal distribution as shown in formula (4):

**Table 1** Reactor power set point maneuver scheme

Hourly average power (FP)	Adjustment (FP)	PDLOG count adjustment
1.00056–1.00113	–0.00113	–2
1.00000–1.00056	–0.00056	–1
0.99944–1.00000	0	0
0.99888–0.99944	+0.00056	+1
0.99832–0.99888	+0.00112	+2
0.99775–0.99832	+0.00168	+3
0.99719–0.99775	+0.00225	+4
0.99950–0.99719	+0.00281	+5

$$f(x) \approx \frac{1}{\sqrt{2\pi}0.000245} e^{-\frac{x^2}{2(0.000245)^2}} \quad (4)$$

Therefore, we established the following rule to adjust \$PRA in order to control the average reactor power close to but not exceed the full power (Table 1).

After this modification, reactor power has been controlled at a more stable level through an easier approach. The average thermal power at full power operation was also raised to 99.972 %FP accordingly.

### 3 Modifying Default Estimation Values of FLX

#### 3.1 Main Function and Flowchart of FLX Program

CANDU6 reactor core is big and subject to power oscillation, that is why it is divided into 14 zones and controlled independently to maintain the stability of reactor power throughout the core. However, thermal power could only calibrates overall reactor power, therefore 102 vanadium detectors are installed to measure local reactor power precisely, and FLX program is introduced to calculate zonal power calibration factors.

The calculation and correction logic of FLX is shown in Fig. 4.

#### 3.2 Problem Description

On June 8, 2004, FLX program was turned on at 5 %FP during reactor startup, but it reported 88 Vanadium detectors failed. Actually there were only two detectors, #74 and #78 failed. There were still 65 detectors reported failed by FLX on the next

morning. FLX program was turned off and on again at 8:51 AM of June 9, and correct result was reported until 14:15, 5.5 h later.

### 3.3 Problem Analysis and Solution

From the flowchart we can see, if a detector reading is found irrational, its previous estimation value will be used as FC for the calculation of FINT. However, if a detector is found irrational on the first execution after FLX being turned on, 1 is used as the default FC value as there is no previous estimation value available. In the aforementioned event, 1 was far from the actual value at 5 % FP, therefore it affected the estimation results of all the rest detectors as this 1 was involved in the estimation of all detectors.

To solve this problem, a better estimation of the initial default values is needed. Flux is fitted with a set of 15 plus flux modes, in which the first mode M1 is the basic mode and its coefficient is close to the actual reactor power level in most cases. Therefore, it is reasonable to use the basic mode and the actual reactor power to calculate the default estimation values as formula (5):

$$[\text{FDEST}]_{\text{def}} = [\text{M1}] * P \quad (5)$$

In which:

$\text{FDEST}_{\text{def}}$  is the initial default estimation values of vanadium detectors

M1 is the basic fitting mode of flux mapping

$P$  is the actual percentage reactor power

Simulation shows that under the same event conditions, FLX could achieve correct results immediately after been turned on without spreading failure to other detectors. Another prerequisite of this solution is to turn on RRS before FLX to provide  $P$  for the calculation of  $\text{FDEST}_{\text{def}}$ .

## 4 Overflow Problem

### 4.1 FLX Problem Description

Since March, 2013, during refueling of unit #2, a series of flux mapping corruptions and reactor power transients occurred. For example, at 19:19:27 of June 4, just after reactor power was raised back to full power following a fuel channel refueling, FLX program suddenly reported too many detectors bad, actually there were only two detectors that failed since several months ago. The alarms returned to normal around 2 min later automatically. The relative messages are as follows:

A FLX 155 DET LIFETIME TOTAL NOT UPDATED	19:19:27
A FLX 153 FLX PRGM BAD: MANY DET BAD	19:19:27
N FLX 155 DET LIFETIME TOTAL NOT UPDATED	19:21:36
N FLX 153 FLX PRGM BAD: MANY DET BAD	19:21:36
RRS RATE INDEX CHANGED FROM 0 TO 1	19:24:24
RRS SETPOINT CHANGED FROM 99.89 TO 99.0 % FP	19:24:24
RRS 712 ALT. MODE—HOLD POWER REQUESTED	19:24:37

Some relative parameters are shown in Fig. 3, in which we can see the zonal calibration factors from FLX program changed quickly when the alarms were issued, and the zonal powers were also affected by the calibration factors too.

### 4.2 FLX Problem Analysis and Solution

In a similar event, a set of DELK was printed, and the amplitude of M1 was found around -1. As its normal value should be around +1 at full power level, overflow was suspected as the cause of the problem.

After careful studying of the source code, a logic mistake was detected which could result in overflow of DELK. In FLX, DELK was calculated out as shown in formula (6):

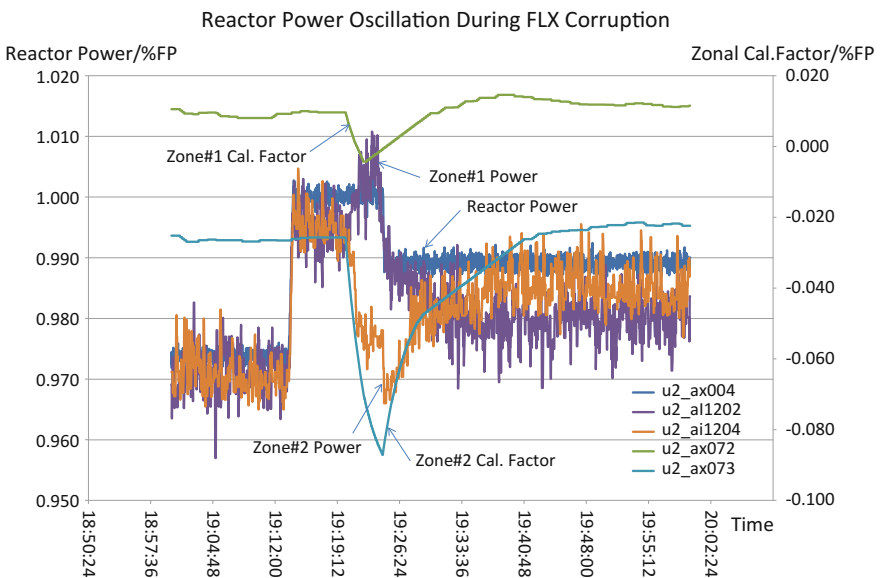


Fig. 3 Reactor power and zonal calibration factors during FLX corruption event

$$[\text{DELK}] = [\text{MDX}] \times [\text{FC}] * \text{FACT} = [\text{TLA}] * \text{FACT} \quad (6)$$

In which:

DELK is the amplitude of fitting modes

MDX is the generalized inverse matrix of fitting modes matrix MX

FC is the readings of vanadium detectors

FACT is the coefficient adopted to improve calculation precision, its value is related with MDX

TLA is an intermediate vector

Each intermediate TLA value is stored in two words, TLA and TLA+1. To improve product precision, TLA is shifted left until bit 14 becomes 1 for a positive value (codes of line 575–592). Afterward, the program checks TLA+1, if its bit 14 is found 1, TLA will be rounded up with an instruction of IAR (codes of line 618–621). In this case, if TLA is already 077777, TLA will overflow and become a negative value, and DELK will also become negative. The directly involved program codes of FLX1 are listed as below, and the italic lines are the trouble instructions.

575 ROWSCN	LDX	COLCNT
576	CALL	INNERX
577	LDX	BTA14
578	LDA	TLA
579	LDB	TLA+1
580	JIF	AEQ0+BEQ0, RNDWN2
581	JAP	PR3
582	BTA0	14, PR6
583 * USE BIT 13 FOR NEG NUMBERS IN CASE A & B ARE ALL ONE'S		
584	LDX	BTA13
585 PR3	STX	PR4
586 PR4	BTA1	14, PR6
587	LASL	1
588	INR	SHFT
589	JMP	PR4
590 *		
591 PR6	STA	TLA
592	STB	TLA+1
...		
618	LDA	TLA
619	LDB	TLA+1
620	BTB0	14, RNDWN1

(continued)



(continued)

621	IAR	
622 RNDWN1	TAB	
623	TZA	
624	MUL	FACT
625 PR10	BSS	1
626	BTB0	14, RNDWN2
627	IAR	
628 RNDWN2	STAE*	VECASN

**Table 2** Possible overflow cases

B-scaling	TLA1 (077777)	DELK1	Overflowed value
B3	7.9997558	0.97626301	-0.9762928
B2	3.9998779	0.48813150	-0.4881464
B1	1.9999389	0.24406575	-0.2440732
B0	0.9999694	0.12203287	-0.1220366
B-1	0.4999847	0.06101643	-0.0610183
...	...	...	...

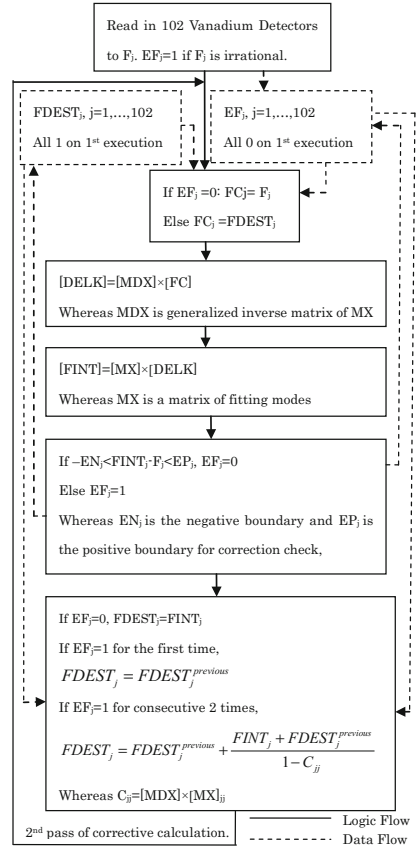
Normally FLX uses mode set 1 for fitting and FACT equals to 0.1220366; When TLA is octal 077777, its possible binary scaling may be 3, 2, 1, 0, -1 ... according to the then power levels. As  $DELK1 = TLA1 * FACT$ , its corresponding values and overflowed values are listed in Table 2.

DELK1 is normally close to the reactor power value, therefore, when reactor power is around 97.63 %FP, an overflow may occur. That is why the FLX corruptions always occurred during refueling, as DELK1 was passing by the trigger value when the power was changing between a little lower value and the full power. This is only one of the possible values that may trigger overflow. Any value that satisfies the aforementioned logic may trigger overflow.

Actually this problem has been there since very beginning, but has resulted into no consequence as there was no failed detector(s). According to Fig. 4, if an overflow occurs while there is no failed detector, all  $EF_j$  will become 1. But it is for the first time that EFs become 1, FDEST will be replaced by the previous FDEST and the second corrective calculation will avoid overflow.

If there is one failed detector already, its  $EF_j$  should be kept at 1. Under this situation, as soon as an overflow occurs, its  $EF_j$  will satisfy the condition of two consecutive 1 s, instead  $FDEST_j$  will be calculated with formula (7) immediately. Therefore, negative  $FINT_j$  spreads to  $FDEST_j$  and then to all FDEST.

**Fig. 4** Estimation and correction logic of FLX program



$$FDEST_j = FDEST_j^{\text{previous}} + \frac{FINT_j + FDEST_j^{\text{previous}}}{1 - C_{jj}} \quad (7)$$

The error logic locates in the module of inner product calculation, which is used for all the three sub-programs of FLX program. To solve this problem, an extra check was added before rounding up TLA: if it is already 077777, then no round up will be carried out.

### 4.3 RRS Problem Description

During the commissioning period, when RTD transmitters were calibrated at very low reactor power, reactor power indication suddenly dropped by  $-0.3$  decade and

started to raise back. One operator pressed Hold Power button immediately and reactor power was stabilized.

#### 4.4 RRS Problem Analysis and Solution

The cause of this event was a combination of human error and software flaw. When the RTD was calibrated, its signal was not disconnected from DCC, therefore the simulated calibration signal was sent to RRS program. After complex screening logic, the wrong RTD was used to calculate reactor RTD power, and the result was over 10 % FP, much higher than the actual power. Afterward when the RTD power was divided by ion chamber power to calculate calibration factor, an overflow occurred due to the big difference between them. The calibration factor became a big negative value and was limited to  $-0.3$  and added up to the ion chamber power, therefore the calibrated reactor power dropped by  $-0.3$  decade whilst the actual power did not change at all. The directly involved program codes of RRS are listed below, and the italic line is the trouble instruction.

2615 LDA	PTH KI = PTH/PIUFLL (B2)
2616 ASRA	2 MAKE PTH B3 TO ALLOW DIVISION
2617 DIV	PIUFLL
2618 TBA	
2619 CALL	LIMIT, 0.5 B2, 2 B2 LIMIT TO (0.5, 2)

The event analysis deemed it is necessary to check the calibration factor calculation against overflow in RRS and set it to a safe value if overflow occurred. A software modification was installed, to reset overflow flag before division, and check it again after division. If overflow flag was found set, the calibration factor will be set to a safe value, which is  $+0.3$  decade.

## 5 Summary

This paper summarizes the main improvements made to reactor power control programs at Qinshan III nuclear power plant. All of these problems are common to all CANDU6 nuclear power plants. From the problems, we could see that programming with assemble language is a big challenge to software correctness and robust. Many instructions such as division, add, subtract, and register increase are subject to overflow. Overflow is not easy to detect as it will only appear under specific conditions. Therefore it is necessary to pay more attention to these instructions, add boundary check, and overflow check accordingly.

The old programming style also limits the precision of reactor power control. By introducing a new approach to precisely maneuver reactor power set point, reactor power control became easier and more stable, economic benefit was also achieved.

## References

1. RFSP Program Description, 1995, AECL
2. RRS Program Listing, 1999, AECL
3. FLX program Listing, 1999, AECL

# Main Control Room Design of Advanced Nuclear Reactor

Huiyu Deng and Dayong Zhou

**Abstract** Thorium Melt Salt Reactor (TMSR) is the fourth generation reactor; it is the strategic science and technology project of Chinese Academy of Sciences. The main control room (MCR) is the important role of the TMSR. The stability and reliability of the reactor depends on the design and construction of the MCR. The MCR is designed to enable the operator to detect and address design basis faults. The paper introduces the design of MCR from two aspects. The principal objectives of the MCR design are to provide the operator with accurate, complete, and timely information regarding the functional status of the reactor systems. First, the technology design of the console room is provided, the layout of the console room is given, the objective of the console room construction function guarantees the equipment of the MCR is operated regularly. Second, the design principles are introduced. Third, human factors engineering is considered as a major role in the MCR design. Fourth, the MCR design is discussed including control equipment layout, environment conditions, control and information equipment. The design shall allow for all operation states, including normal and accident conditions, optimize the tasks and minimize the workload required to monitor and control the reactor and provide safe, available and reliable operation of plant. At last, the preliminary MCR design scheme is introduced.

**Keywords** Main control room · Thorium melt salt reactor · Human factors engineering · Control equipment layout

---

H. Deng (✉) · D. Zhou  
Shanghai Institute of Applied Physics, Chinese Academy of Science, Shang Hai, China  
e-mail: denghuiyu@sinap.ac.cn

© Springer Science+Business Media Singapore 2017  
H. Jiang (ed.), *Proceedings of The 20th Pacific Basin Nuclear Conference*,  
DOI 10.1007/978-981-10-2317-0\_13

113

## 1 Introduction

Thorium Melt Salt Reactor (TMSR) is the fourth generation reactor, the main control room (MCR) is the important role of the TMSR, the stability and reliability of the reactor depend on the design and construction of the MCR. The construction of MSR is high technology and comprehensive basic engineering.

## 2 Function Requirement of MRC

MCR is the main place for the operators to monitor and control the reactor facility and other reactor system (including safety system) during the reactor normal and abnormal operation period. MCR provides the main control equipment for the operators to operate the reactor in the normal、abnormal and accident condition [1, 2]. According to the two former generations of the main control room, the MCR of TMSR is the third digital control system [3]; its technical characteristics are illustrated in Table 1.

The design of MCR is introduced from two aspects. First, the technology condition of architectural structure design is introduced to satisfy the MCR work; second, the installation equipment of MCR is introduced to satisfy the reactor control requirement.

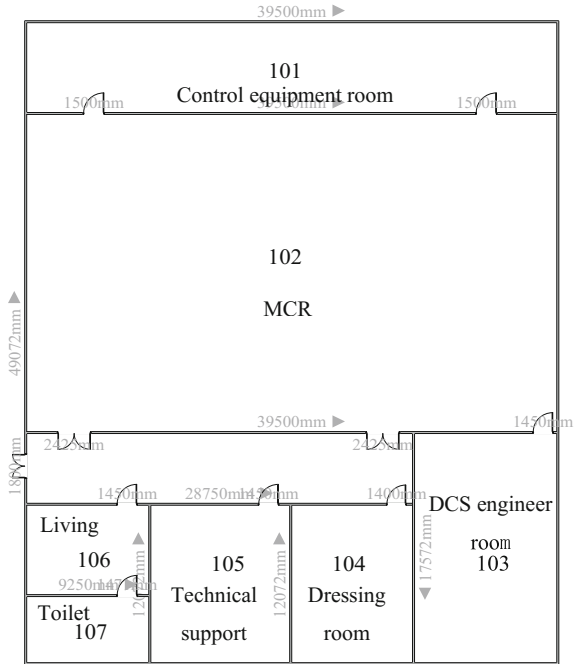
## 3 Technology Condition of MCR Architectural Structure Design

There are two operators and an officer in the MCR when the reactor operates. So, the operators must have necessary working area. The main architectural structure layout is illustrated in Fig. 1. The MCR is the main work area of the operators, DCS

**Table 1** Technical characteristics of MCR development

Technical characteristics	First generation	Second generation	Third generation
Type	Analog control room	Half digital control room	Digital control room
Conventional instrument	Many instruments	Some instruments	No
Cable connecting line	Several thousands of cables	Less cables	Few, only dozens of cables
Net cable	No	Part net cables	Main net cables
Hardware controller	Many controllers	Less controllers	Few
Operator	Many	Less	Few, only two or three operators

**Fig. 1** The main architectural structure layout drawing



system engineers configurate and debug system in the DCS engineer room; technical support center provides work area for technical personnel in emergency response. Control room operators have a rest in living room during normal operation period, the living room provides the basic life support for operators and technical support personnel in emergency period.

The design of the MCR accords to the national standard:  
GBT 13630-1992 the design standard of nuclear plant station control room.  
GBT 13631-1992 the design standard of nuclear plant station auxiliary control point.

## 4 MCR Design Principle

### 4.1 Security Operation Principle

The control room must guarantee the reactor monitor and operation function safely, the reactor is stopped safely in operation period, including normal operation, normal operation departure, design base accident, and super design reference accident.

## ***4.2 Usability Principle***

Accident power and shutdown probability is reduced because of the operator mistake, I& C system failure and fault as much as possible to minimize.

## ***4.3 Operating Management Principle***

The operator equipment and training are part of MCR system design and operating management, the MCR design must provide equipment operator number and professional skills requirement.

## ***4.4 Defense in Depth Principle***

The reactor digital I&C system provides more defense in depth ways.

## ***4.5 Human Factors Engineering Principle***

In human factors engineering principle, as the third digital MCR, human and operation machine function must be divided reasonably. This opinion is specially emphasized so that all human and operation machine could develop design ability. The MCR design is considered human factors engineering principle fully to reach the optimal allocation of human and operation machine efficiently. The MCR detail design must according to human characteristics and ability [4].

# **5 MCR System Design**

## ***5.1 System Technology Design Content***

MCR system design research includes the following contents:

(1) MCR function requirement, ergonomia and human ergonomics principles implement; (2) MCR system configuration static design; (3) Display information requirements of safety monitor; (4) MCR internal channel entity separation requirements should satisfy the electrical equipment entity separation requirements, especially using multichannel controller (5) Seismic design requirements of safety display and operation equipment [5, 6].



## ***5.2 Technical Route***

Large information and safety displays (1E) are used to display reactor system flow flat, CRT, small hard wired backup switches and controllers are used to normal control and protection operation, MCR is connected with safety system, control system, and information display system by fiber optic serial and network interface.

## ***5.3 Application of Human Factors Engineering Principle in Console Design***

Human factors engineering principle must be considered in console structure design. According to the human characteristics of the operator and repair personnel, the console structure should satisfy the function application. Under this premise, the console structure design satisfies the human engineering principle and beautiful technology performance. The console design accords to the following design principle:

1. The length of the console meets the use function, the detail size is designed according to human engineering requirements, all angles and edges are arc transitions. This design scheme guarantees operation safety and convenience.
2. The console guarantees electrical safety, the equipment layout should be easy to operate. Materials and color schemes that present an attractive display that is compatible with central control room carpet, wall, and other colors.

The console has the following characteristics:

1. A quiet, office type environment (noise from CPU fans and other sources abated as much as possible)
2. Almost all cabling hidden from view, easy access phone, business network, control network, test network, and AC power outlets to the operator area and the equipment compartment.
3. Completely open foot-space in the front (operator area). An operator work area that allows both keyboards and standard size loose leaf notebooks, laptop, computers, etc. in front of the monitor screens.
4. Easy access to cable area where cabling can be added or rearranged when needed.
5. Other than the work area in front of the screens, horizontal surfaces that attract clutter should be minimized.

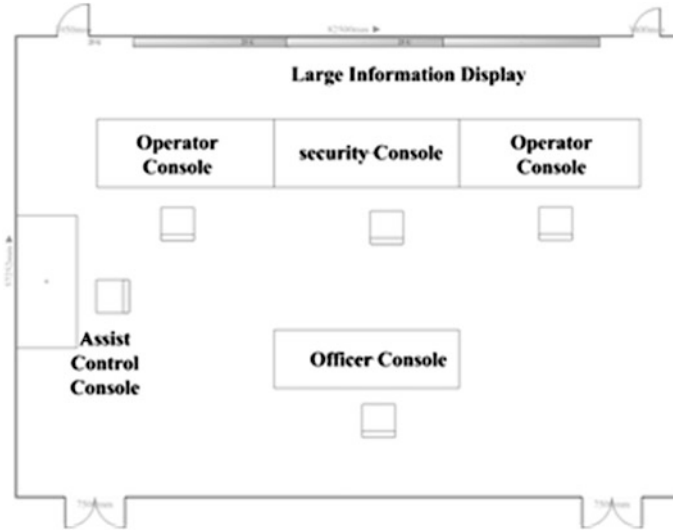


Fig. 2 MCR layout drawing

## 6 MCR Preliminary Design

### 6.1 MCR Layout

The MCR layout drawing is showed in Fig. 2. The MCR includes large information display, operator console, leader monitor console, special-purpose security panel, and assist control panel.

### 6.2 Large Information Display System Design

There are four 80 inch large displays system in MCR, the display image of the large system is provided by the video conversion matrix, the input signal of the video conversion matrix is computer display screen signal.

The controller of the large display system has network interface, it could control the equipment by Internet. At the same time, it has split screen card, every big display system is divided into  $2 * 2$  video matrixes, every matrix has different video image.

### 6.3 Equipment Design Requirement of the Display System

Four display screens are equipped in the special-purpose security panel console, two computers control the four display screens. Every computer controls two

display screens. The controller buttons are equipped in the special-purpose security panel console. The different color distinguishes the special-purpose security panel console from the operator console. The special-purpose security panel console has two working positions.

Four display screens are equipped in every operator and leader monitor console. Every computer controls two display screens. Every console has two working positions.

The output images of the special-purpose security panel, operator and leader monitor console are connected to the input of the video conversion matrix.

## **6.4 Cable Layout**

All cable trends of nonstandard equipment in the consoles are designed reasonably, which avoids the mutual interference. Fiber cable need separate line slot. The detail implement schedule is refined further after the cooperative equipment supplier is confirmed.

## **7 Conclusions**

The MCR of the fourth nuclear reactor is the third digital main control room; it is the further development trend of reactor I&C system. Human factors engineering design improves the MCR comfortable and provides better working condition for the operators. Operation is simplified and the operator workload is reduced, which improves safety and reliability of the reactor. The MCR design of TMSR is investigated fully in early stage. On the basis of the national standard and principle, the concept design, design principle, and preliminary plan design of the MCR are carried out, which lays the good foundation for further work.

## **References**

1. Jun Su Ha, Poong Hyun Seong, Myeong Soo Lee, and Jin Hyuk Hong. Development of Human Performance Measures for Human Factors Validation in the Advanced MCR of APR-1400. IEEE TRANSACTIONS ON NUCLEAR SCIENCE, VOL. 54, NO. 6, DECEMBER 2007:2687–2700
2. Inseok Jang, Ar Ryum Kim, Mohamed Ali Salem Al Harbb, Seung Jun Lee, Hyun Gook Kang, Poong Hyun Seong. An empirical study on the basic human error probabilities for NPP advanced main control room operation using soft control. Nuclear Engineering and Design. 2013(257) 79–87
3. ZHENG Mingguang, ZHANG Qinshun, XU Jijun, NING Zhonghe, LIN Zhijian, SHEN Zengyao. The Development of NPP Advanced Main Control Room and Self Design Research

- Objectives. Chinese Journal of Nuclear Science and Engineering. 2000, Dec, Vol. 20, No. 4: 297–303
4. Dhong Hoon Lee, Dai Il Kim, Choong Huei Chung. Regulatory Approach on Human Factors Engineering of Main Control Room Modernization: A Case of Kori-1 Nuclear Power Plant in Korea. Joint 8th IEEE HFPP/13th HPRCT:66–69
  5. CHEN Gang, YAN Min. Research of Design and Testing Method For Main Control Room Consoles and Panels Based on Human-machine Ergonomic. Equipment Manufacturing Technology. 2013(8):119–224
  6. MA Yuanrui ZHU Yizhou WANG Chihu XIE Yongcheng. Research and project practice in AP1000 nuclear plant MCR assemblies seismic test. Nuclear Technology. 2013. Vol. 36, No. 4:1–4

# Material Substitute Research of the Main Pipeline Bracket Protection Cushion in CPR1000 NPP

**Ai-qun Ren**

**Abstract** The purpose of this article is to try to find one kind of material to substitute the protection cushion material of bracket which is used in CPR1000 for preventing throwing off the main pipeline. The original material of the cushion is X2CrNi18-9, which should be substituted by the new material of 022Cr19Ni10 because the less output of the X2CrNi18-9 and it is difficult to purchase. We study the standard and do some test, to validate the feasibility of that 022Cr19Ni10 can substitute X2CrNi18-9.

**Keywords** CPR1000 NPP · Bracket of preventing throwing off the main pipeline · Substitute material

## 1 Preface

As many of the materials used in the design are foreign brands, there often occur some questions such as the higher procurement prices, longer procurement cycle, and not guaranteed procurement quality. From the point view of technology, a lot of material, especially small batch special materials, which already can be produced in domestic. In order to verify the actual situation of domestic materials whether that meets the alternative requirements or not, it is necessary to research on the domestic material properties. In this paper, we analysis some parts of the substitution materials, the results can be the foundation for the follow-up to the supplementary test, for the material replacement feasibility analysis, and for the domestic materials application.

---

A. Ren (✉)  
CNPEC, Room309, Dayabay Nuclear Power Station,  
Da Peng District, Shen Zhen 518124, Guangdong, China  
e-mail: renaiqun@cgnpc.com.cn

## 2 Anti-Rejection Profile Protective Pad Synopsis of the Main Pipe

Main pipeline anti-rejection plate of the protective bracket is the anti-swing bracket component, the raw materials is X2CrNi18-9. It plans to use 022Cr19Ni10 as the alternative material, material type is plate. Material conditions are required for the normal operation of the equipment condition, test conditions, in a rare accident situation and the unlikely situation.

## 3 Standard Scope of Application

The applicable scope of X2CrNi18-9 steel reference standards and standards are as follows:

- Standard code: BS EN 10088-2-2005: Stainless Steels—Part 2: Technical Delivery Conditions for Sheet/Plate And Strip of Corrosion Resisting Steels for General Purposes.
- Application scope: suitable for anti-corrosion of stainless steel standard grade and special grades of hot-rolled or cold-rolled sheet and strip for general purposes, does not apply in the deep processing of the above products.

022Cr19Ni10 stainless steel reference standard and standard applicable scope are as follows:

- Standard code
  - GB/T 3280-2007: cold-rolled stainless steel sheets and strips
  - GB/T 4237-2007: hot-rolled stainless steel sheets and strips
- Application scope
  - GB/T 3280-2007: Suitable for corrosion resistant stainless steel cold-rolled wide steel strip and its roll cut fixed length steel plate, longitudinal shear cold-rolled wide strip and roll cut fixed length steel strip, cold-rolled narrow strip and its roll cut fixed length steel strip, also applies to the single rolled steel plate.
  - GB/T 4237-2007: Suitable for reversible rolling mill rolling resistance to corrosion of stainless steel hot rolling thick steel plate and a continuous rolling mill rolling resistance corrosion of stainless steel hot-rolled wide strip and roll the cut steel ruler, slitting width of the strip. It is also used in resistance to corrosion of stainless steel hot-rolled narrow strip and roll the cut set steel tape.

**Table 1** Chemical composition (Wt %)

Element	Ladle analysis		Remark
	X2CrNi18-9	022Cr19Ni10	
C	≤ 0.03	≤ 0.03	The high limit value of S in 022Cr19Ni10 stainless steel is higher than that of S in X2CrNi18-9 steel;
Mn	≤ 2.00	≤ 2.00	
Si	≤ 1.00	≤ 0.75	The high/low limit value of Cr in 022Cr19Ni10 stainless steel is higher than that of Cr in X2CrNi18-9 stainless steel;
P	≤ 0.045	≤ 0.045	
S	≤ 0.015 <sup>a</sup>	≤ 0.030	The high limit value of Ni in 022Cr19Ni10 stainless steel is higher than that of Ni in X2CrNi18-9 steel
Cr	17.5–19.5	18.0–20.0	
Ni	8.0–10.5	8.0–12.0	
N	≤ 0.11	≤ 0.10	

<sup>a</sup>Except the carbon content of the low carbon steel can be 0.001 % of the deviation, the carbon content of other steel can be 0.01 %

## 4 Chemical Composition

Stainless steel chemical composition (ladle analysis) requirements of the X2CrNi18-9 and 022Cr19Ni10, see Table 1.

## 5 Mechanical Properties and Sampling

### 5.1 Batch Definition

The batch definition in BS EN 10088-2-2005 is as follows:

Batch refers to the same ingot, the same nominal thickness and deviation ( $\pm 10\%$ ), the same final heat treatment system (i.e., the same heat treatment and/or the same degree of cold treatment) of steel.

The batch definition in GB/T3280-2007 and GB/T 4237-2007 is as follows:

Batch refers to the same grade, the same number of furnace, the same thickness, and the same heat treatment system of steel plate or steel stripe.

### 5.2 Sampling

The sampling position of X2CrNi18-9 stainless steel and 022Cr19Ni10 stainless steel are shown in Table 2, and the sampling quantity is in Table 3.

### 5.3 Tensile Property

The tensile properties of X2CrNi18-9 steel and 022Cr19Ni10 stainless steel are shown in Table 4, and the yield strength at high temperature is shown in Table 5.

Table 2 Sampling position

Grade	Sampling position	Remark
X2CrNi18-9	<ol style="list-style-type: none"> <li>1 Tensile test: for hot-rolled plate, the weight of each batch is no more than 30,000 kg, the quantity is no more than 40; one sample from each batch, which can be obtained from the heat treatment state board that the length does not exceed 15 mm; another sample from the longest heat treatment state board of a group of length more than 15 m heat treatment state boards, and sampled in the tail</li> <li>2 The sampling method of the tensile test is cut along the length of the sample and half of the axis. If the strike test is required, the sampling position is the same as the tensile test</li> <li>3 For hardness testing of steel with corrosion resistance requirements, the sampling position is the same as the tensile test</li> <li>4 Samples should be obtained from the delivery products, if agreed, that can be obtained before flattening, but also can be obtained from a similar heat treatment products (annealing, hardening and tempering)</li> <li>5 For tensile test and striking test, the sample is cut from axis when width &lt;300 mm, or from orientation when width <math>\geq</math> 300 mm</li> <li>6 For the striking sample, the size can be 1/10 of the thickness</li> </ol>	<p>The specimen of 022Cr19Ni10 should be cut from orientation; the specimen of X2CrNi18-9 should be cut from axis when its width &lt;300 mm; and the European standard and the national standard has a greater difference</p>
022Cr19Ni10	<ol style="list-style-type: none"> <li>1 Tensile property test samples from the orientation of the test specimens, the specific reference to GB/T 2975</li> <li>2 The tensile, bending and striking samples should be cut at the width of the steel plate 1/4;</li> <li>3 For longitudinal steel plate, when the product standard is not specified in the direction of sampling, it should be cut in the width of the steel plate 1/4; if the width of the steel plate is not enough, the sample can be moved inside the center</li> <li>4 The tensile sample should be in the direction of steel plate thickness</li> <li>5 When the striking sample is cut from the steel plate thickness direction, the sampling position is selected according to the product standard or the agreement contract</li> <li>6 For hardness testing of steel, the sample can be cut from any one or any of the volumes</li> </ol>	



**Table 3** Sampling Quantity

Grade	Item	Sampling quantity requirement	Remark
X2CrNi18-9	Tensile properties at room temperature	One per batch	There is no impact performance and high temperature tensile property sampling quantity requirement for 022Cr19Ni10
	Hardness property	One per batch	
	Impact performance	Three per batch	
	High temperature tensile property	One per batch	
022Cr19Ni10	Tensile property	One per batch	
	Hardness property	One per piece or roll	

**Table 4** Tensile property

Tensile property	X2CrNi18-9 <sup>a</sup> (solid solution annealing)	022Cr19Ni10 (by solid solution treatment of austenitic type)	Remark
Room temperature yield strength (MPa)	Hot-rolled steel plate: $t \leq 75$ mm Lateral: $Rp0.2 \geq 200$ $Rp1.0 \geq 240$ <sup>b</sup>	Lateral: $Rp0.2 \geq 170$	The lower yield strength of the austenitic stainless steel 00Cr19Ni 10 stainless steel is lower than the lower limit of the yield strength of X2CrNi18-9 0.2 %;
Tensile strength at room temperature Rm (MPa)	$t \leq 75$ mm: 500–700	Lateral: $\geq 485$	The room temperature tensile strength of the austenitic stainless steel 00Cr19Ni 10 stainless steel is lower than that of X2CrNi18-9, and the upper limit value of tensile strength is not specified in the 00Cr19Ni 10 stainless steel;
elongation after fracture A (%)	Lateral <sup>c</sup> : A80 $t < 3$ mm, $\geq 45$ A <sup>d</sup> $t \geq 3$ mm, $\geq 45$	Lateral: $\geq 40$	The elongation limit of 022Cr19Ni10 stainless steel was lower than the lower limit elongation X2CrNi18-9

<sup>a</sup>The thickness of the sample is less than 75 mm for hot-rolled plate, thickness of more than 75 mm products, its mechanical properties are still applicable

<sup>b</sup>仅作为指导,对于连续热轧产品, 比Rp0.2最小值高20 MPa或比Rp1.0最小值高10 MPa可以在采购时按协议接受;

<sup>b</sup>Only as a guide for continuous hot-rolled products, Rp0.2 minimum value higher than 20 MPa or higher than Rp1.0 minimum value of 10 MPa can be accepted at the time of purchase agreement

<sup>c</sup>If rolling sample strip <300 mm, the longitudinal specimens, minimum reduction as follows: yield strength reduce 15 MPa, elongation rate for fixed standard distance from the size of the reduction of 5 %, elongation rate and the proportion of the underlying distance from the size of the reduction of 2 %. The size of the sample is marked 80 mm, width 20 mm, but also the distance 50 mm width 12.5 mm

<sup>d</sup>Sample size is  $5.65 \sqrt{S_0}$

**Table 5** Yield strength at high temperature

Temperature (°C)	X2CrNi18-9 <sup>a</sup> (solid solution annealing)	022Cr19Ni 10 (by solid solution treatment of austenitic type)	Remark
100	Rp0.2 ≥ 147, Rp1.0 ≥ 181	/	The lower limit values of 022Cr19Ni10 and Rp0.1 of Rp0.2 stainless steel are not specified at high temperature
150	Rp0.2 ≥ 132, Rp1.0 ≥ 162		
200	Rp0.2 ≥ 118, Rp1.0 ≥ 147		
250	Rp0.2 ≥ 108, Rp1.0 ≥ 137		
300	Rp0.2 ≥ 100, Rp1.0 ≥ 127		
350	Rp0.2 ≥ 94, Rp1.0 ≥ 121		
400	Rp0.2 ≥ 89, Rp1.0 ≥ 116		
450	Rp0.2 ≥ 85, Rp1.0 ≥ 112		
500	Rp0.2 ≥ 81, Rp1.0 ≥ 109		
550	Rp0.2 ≥ 80, Rp1.0 ≥ 108		

## 5.4 Act Performance

Impact performance requirements of X2CrNi18-9 steel and 022Cr19Ni10 stainless steel are shown in Table 6.

## 5.5 Hardness Property

X2CrNi18-9钢与022Cr19Ni10不锈钢硬度性能要求见表7.

X2CrNi18-9 steel and 022Cr19Ni10 stainless steel hardness performance requirements see Table 7.

**Table 6** Act performance

	X2CrNi18-9 <sup>a</sup>	022Cr19Ni10	Remark
KV	The longitudinal impact energy is greater than or equal to 100 J Sample: transverse impact power is more than 60 J	/	022Cr19Ni10 stainless steel does not specify the lower impact performance

<sup>a</sup>Specimen thickness greater than 10 mm

**Table 7** Hardness property

X2CrNi18-9	022Cr19Ni10	Remark
Not explicitly specified value; Test method: The hardness of the reference ISO6506-1 EN ISO 6508-1 EN with reference to the hardness of the Vivtorinox hardness reference ISO6507-1 EN	Brinell hardness $\geq 201$ Rockwell hardness $\geq 92$ Vivtorinox hardness $\geq 220$	/

**Table 8** Heat treatment

X2CrNi18-9	022Cr19Ni10	Remark
Heat treatment symbol +AT; Solid solution annealing temperature 1000–1100 °C; Cooling: water cooling or rapid air cooling	heat treatment temperature: $\geq 1040$ °C Cooling: water cooling or other ways of cooling	022Cr19Ni10 stainless steel heat treatment temperature lower than the lower limit of X2CrNi18-9 heat treatment, while not required to limit the temperature of heat treatment

## 6 Heat Treatment and Delivery Status

### 6.1 Heat Treatment Process

The heat treatment process of X2CrNi18-9 steel and 022Cr19Ni10 stainless steel is required in Table 8.

### 6.2 Delivery Status

Delivery status of X2CrNi18-9 steel and 022Cr19Ni10 stainless steel is shown in Table 9.

## 7 Nondestructive Testing

Non-destructive testing requirements of X2CrNi18-9 steel and 022Cr19Ni10 stainless steel are shown in Table 10.

## 8 Intergranular Corrosion

Table 11 is required for intergranular corrosion of X2CrNi18-9 steel and 022Cr19Ni10 stainless steel.

**Table 9** Delivery status

Grade	Delivery status	Remark
X2CrNi18-9	Referring to the processing technology, the two sides agreed to purchase agreement	/
022Cr19Ni10	<p>1 Cold-rolled sheet: After cold rolling, the steel plate and the steel strip can be treated by heat treatment and acid washing or similar treatment According to the requirement of steel sheet and strip according to different cold hardening state of delivery For precipitation hardening steel heat treatment, the buyer should specify the kinds of heat treatment in the contract and shall state that is to strip, plate itself or the samples of heat treatment When necessary, straightening, leveling or grinding can be carried out</p> <p>2 Hot-rolled plate: Plate, sheet and strip after hot rolling, after heat treatment and pickling or similar treatment delivery. If the buyer agrees to, save pickling treatment For precipitation hardening steel heat treatment, the buyer should be in the contract indicate the kinds of heat treatment of steel plate or sample, strip, or sample, if not specified, in the solid solution state delivery</p>	

## 9 Delivery Dimension

The delivery dimension of X2CrNi18-9 steel and 022Cr19Ni10 stainless steel is shown in Table 12.

## 10 Variance Analysis

Above each section, apart from the chemical composition, mechanical properties, sampling requirements, heat treatment technology, nondestructive detection, intergranular corrosion, delivery size of X2CrNi18-9 steel and 022Cr19Ni10 stainless steel for comparative analysis and gather the information shown in Table 13.

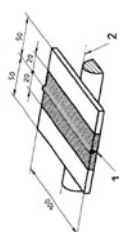
## 11 Conclusions and Recommendations

According to the requirement 4237-2007 en 10088-2-2005 and GB/T3280-2007 and GB/T, the X2CrNi18-9 steel and 022Cr19Ni10 stainless steel by comparative analysis, combined with the main pipeline anti-rejection protection bracket plate

**Table 10** Nondestructive testing

Grade	Nondestructive testing	Remark																																								
X2CrNi18-9	<p>1 Products should not have an impact on the performance of internal defects, for the thickness of more than 6 mm of austenitic or austenitic ferritic stainless steel plate in accordance with the order of the ultrasonic testing, the specific reference to EN 10307;</p> <p>2 Inspection methods: Reflection method;</p> <p>3 Testing equipment: a display manual ultrasonic testing device, the dead area of single crystal probe as close as possible to the small, such as the use of 15 % or 15 mm thickness, double crystal probe focus area can use the product thickness, probe the maximum size range for 10–35 mm, frequency rate range for 1–5 MHz. For the dominant frequency range that can be used in automatic or semiautomatic test 1–5 MHz probe, using a double probe, between two probe scanning direction (angle of 45 DEG to 90 DEG);</p> <p>4 By using the double crystal probe 4. The product is less than or equal to 6 mm thickness &lt;60 mm, product is less than or equal to 60 mm thickness &lt;200 mm, using double-crystal probe or single-crystal probe</p> <p>5 General coupling medium is water, the supplier can also choose other coupling medium;</p> <p>6 Manual scanning speed is not more than 150 mm/s;</p> <p>7 Flat product thickness <math>t</math> Zone width</p> <table border="1" data-bbox="635 970 764 1375"> <thead> <tr> <th>规格</th> <th>厚度 <math>t</math></th> <th>最大面积 <math>S_{max}</math> (mm<sup>2</sup>)</th> <th>量</th> </tr> </thead> <tbody> <tr> <td>E1</td> <td>50</td> <td>1000</td> <td>5</td> </tr> <tr> <td>E2</td> <td>40</td> <td>500</td> <td>4</td> </tr> <tr> <td>E3</td> <td>30</td> <td>100</td> <td>15</td> </tr> <tr> <td>E4</td> <td>20</td> <td>50</td> <td>10</td> </tr> </tbody> </table> <p>mm  <math>6 \leq t &lt; 50</math> 50  <math>50 \leq t &lt; 100</math> 75  <math>100 \leq t &lt; 200</math> 100</p> <p>8 Supply and demand sides agreed to determine the standard reference is as follows:</p> <table border="1" data-bbox="776 970 882 1375"> <thead> <tr> <th>级别</th> <th>最大尺寸 <math>L_{max}</math> (mm)</th> <th>最大面积 <math>S_{max}</math> (mm<sup>2</sup>)</th> <th>量</th> </tr> </thead> <tbody> <tr> <td>E1</td> <td>50</td> <td>1000</td> <td>5</td> </tr> <tr> <td>E2</td> <td>40</td> <td>500</td> <td>4</td> </tr> <tr> <td>E3</td> <td>30</td> <td>100</td> <td>15</td> </tr> <tr> <td>E4</td> <td>20</td> <td>50</td> <td>10</td> </tr> </tbody> </table> <p>Note for the thickness is greater than or equal to 60 mm products, continuous calculation using the characteristic curve of 11, 8, 5 mm hole; E3 discontinuous defect echo amplitude between 8 and 11 mm diameter hole characteristic curve range; 3; E4 discontinuous defect echo amplitude between 5 and 8 mm diameter hole area characteristic curve Wai: 3</p>	规格	厚度 $t$	最大面积 $S_{max}$ (mm <sup>2</sup> )	量	E1	50	1000	5	E2	40	500	4	E3	30	100	15	E4	20	50	10	级别	最大尺寸 $L_{max}$ (mm)	最大面积 $S_{max}$ (mm <sup>2</sup> )	量	E1	50	1000	5	E2	40	500	4	E3	30	100	15	E4	20	50	10	<p>Nondestructive testing methods and criteria for 022Cr19Ni10 stainless steel</p>
规格	厚度 $t$	最大面积 $S_{max}$ (mm <sup>2</sup> )	量																																							
E1	50	1000	5																																							
E2	40	500	4																																							
E3	30	100	15																																							
E4	20	50	10																																							
级别	最大尺寸 $L_{max}$ (mm)	最大面积 $S_{max}$ (mm <sup>2</sup> )	量																																							
E1	50	1000	5																																							
E2	40	500	4																																							
E3	30	100	15																																							
E4	20	50	10																																							
022Cr19Ni10	<p>According to the requirement, can be added</p>																																									

**Table 11** Granular corrosion

Grade	Granular corrosion	Remark
X2CrNi18-9	<p>1 Refer to EN ISO 3651-2</p> <p>2 Samples of surface area of 15–35 cm<sup>2</sup>, if the sheet thickness exceeds 6 mm, the maximum thickness of the sample is 6 mm, also need to retain a rolling surface;</p> <p>3 For the plate specimen, if possible, use the following dimensions: 2–6 mm in thickness, the width of at least 10 mm, length of at least 50 mm;</p> <p>4 Welding test specimen: two about 100 mm long and 50 mm wide plate welded together, in accordance with the cut;</p>  <p>5 Test method: 16 % sulfuric acid copper sulfate corrosion test (austenitic stainless steel containing Cr amount more than 16 % and Mo content 3 %), 35 % sulfuric acid copper sulfate corrosion test (austenitic stainless steel containing Cr content more than 20 % and Mo content in the range of 2–4 %), 40 % sulfuric acid iron sulfate corrosion test (austenitic stainless steel containing Cr amount contribution that 17 % and Mo content exceeds 3 %, test cycle for 20 h</p> <p>6 Corrosion after bending test: Wrought plate specimen must be in corrosion test, bending test, specimens have to bend at least 90 degrees, mind bending radius of not more than the sample thickness, for casting products, mind bending radius does not exceed two times the thickness of the product, curved specimens at low magnification factor (10×) instrument on crack detection</p>	<p>Test method for corrosion of 022Cr19Ni10 stainless steel intergranular and determine the standard is not consistent with X2CrNi18-9 stainless steel</p>

(continued)

Table 11 (continued)

Grade	Granular corrosion	Remark
022Cr19Ni10	<p>1 Steel corrosion resistant testing method of performance negotiated by both parties and specified in the contract, no indication, can not test;</p> <p>2 The position of sampling and test methods of corrosion resistance of the 2 test according to GB/T 4334;</p> <p>3 The use of stainless steel in sulfuric acid iron corrosion test method, 65 % nitric acid corrosion test of stainless steels, stainless steels nitric hydrofluoric acid corrosion test method and stainless steel sulfuric acid sulfuric acid copper corrosion test method, steel sheet or strip thickness &lt;4 mm, sampling along the rolling direction, steel plate or steel strip thickness &gt;4 mm, sampling along the rolling direction, a sample from a processing to the sample thickness, another sample from the other side processing to sample thickness;</p> <p>4 10 % oxalic acid etching test is suitable for screening test of austenitic stainless steel intergranular corrosion and to test for solid solution treatment (delivery) products sample after 10 % of the oxalic acid solution in electrolytic etching, under a microscope observation surface microstructure, after etching groove-shaped structure, choose sulfuric acid corrosion of iron or copper sulfate sulfuric acid corrosion acid heat test; after etching groove structure, concave organization II, choose 65 % nitric acid corrosion acid heat test;</p> <p>5 The reduction of iron corrosion test of 5 sulfuric acid - sulfuric acid: Test status: sensitizing treatment; corrosion reduction: negotiation</p> <p>6 65 % reduction of nitrate corrosion test corrosion: Test status: sensitizing treatment; corrosion reduction: negotiation</p> <p>7 Test status: sensitizing treatment; bending surface state: no intergranular corrosion cracks</p> <p>8 As the requirement and indicate the salt corrosion test in the contract, the test method according to the provisions of GB/T 10125</p>	

**Table 12** Delivery dimension

X2CrNi18-9	022Cr19Ni10	Remark
1 Allow dimensions and deviations agreed by mutual agreement in order; 2 For single size hot-rolled plate according to EN 10029, the thickness tolerance for B, and for the continuous hot-rolled plate, according to EN 10051	1 Dimensions and allowable deviation of specific requirements should be consistent with the requirements of GB/T708 2 Cold-rolled plate: The nominal size, thickness deviation, allowable width deviation, length deviation, roughness, camber, cutting slope in accordance with the requirements, this does not specify 3 Hot-rolled plate: The nominal size, thickness deviation, allowable width deviation, length deviation, roughness, camber, etc., in accordance with the requirements, this does not specify	/

usage analysis, conclusion pipeline anti-rejection protection bracket plate can be used after solution annealing of austenitic 022Cr19Ni10 so alternative X2CrNi18-9 corrosion resistant austenitic stainless steel, but need to meet the following conditions:

1. Chemical analysis test for 022Cr19Ni10 stainless steel, S, Ni, verify the content of Cr in line with the European standard;
2. According to the EN 10088-2-2005 required for 022Cr19Ni10 stainless steel samples test sample selection criteria;
3. For stainless steel 022Cr19Ni10 of room temperature tensile test and verify the yield strength, tensile strength, and fracture elongation rate are in-line with the requirements of EN 10088-2-2005;
4. For 022Cr19Ni10 stainless steel by high temperature tensile test, verify the high temperature yield strength meet EN 10088-2-2005 requirements;
5. For 022cr19ni10 stainless steel impact performance test, verify the impact properties are consistent with the requirements of 10088-2-2005 EN
6. According to the [1] EN 10088-2-2005 requirements for 022Cr19Ni10 stainless steel to intergranular corrosion, nondestructive testing, verify the intergranular corrosion, nondestructive detection performance conforms to the EN requirement of 10088-2-2005;
7. In the procurement of technical specification for the material delivery in accordance with the requirements of 10088-2-2005 EN size can be made clear.



**Table 13** Variance analysis

Item	X2CrNi18-9 steel and 022Cr19Ni10 stainless steel contrast
Chemical composition	The content of S was higher than the upper limit of X2CrNi18-9 steel in the upper limit value of S content in 022Cr19Ni10 stainless steel; The content of 022Cr19Ni10 stainless steel Cr in the upper and lower limits were higher than those of X2CrNi18-9 steel Cr in the upper and lower limit value; The maximum content of 022Cr19Ni10 stainless steel Ni in the upper limit of content is higher than the value of Ni in X2CrNi18-9 steel
Sample	022Cr19Ni10 stainless steel were not specified number of sampling impact and high temperature tensile properties; The provisions of 022Cr19Ni10 stainless steel and X2CrNi18-9 stainless steel transverse specimens, the rolling width is less than 300 mm from the longitudinal sample, and has a larger difference between the European standard and national standard
Tensile property	The 00Cr19Ni type austenitic 10 stainless steel solid solution at room temperature yield strength lower than X2CrNi18-9 0.2 % of the yield limit; The tensile strength limit of 00Cr19Ni type austenitic 10 stainless steel solid solution below room temperature tensile strength of X2CrNi18-9, at the same time, 00Cr19Ni 10 stainless steel were not specified tensile strength limit; The elongation limit of 022Cr19Ni10 stainless steel was lower than the lower limit elongation X2CrNi18-9; 022Cr19Ni10 stainless steel is not prescribed lower yield strength at high temperature and Rp0.2 value of Rp0.1
Impact properties	022Cr19Ni10 does not specify the impact performance limit of stainless steel
Heat treatment process	022Cr19Ni10 stainless steel heat treatment temperature lower than X2CrNi18-9 heat treatment temperature limit, and no limit of heat treatment temperature
Delivery status	
Intergranular corrosion	Test method for corrosion of 022Cr19Ni10 stainless steel intergranular and determine the standard is not consistent with X2CrNi18-9 stainless steel
Nondestructive testing	022Cr19Ni10 stainless steel is not specified NDT methods and criteria

## References

1. 压水堆核电站核岛主设备材料和焊接 主编:上海发电设备成套设计研究院 出版社: 上海科学技术文献出版社 2008年12月第1版
2. 900 MW压水堆核电站系统与设备 广东核电培训中心编 原子能出版社出版 2007年1月第2版 2008年10月第2次印刷

# Nuclear Steam Generator Water Level Control Based on DFNN

Junying Hong and Hong Xia

**Abstract** Steam generator is a major component in a nuclear power plant (NPP). Properly controlling the water level of it is very important to guarantee the security of a NPP. In this paper, aimed at the shortcomings of steam generator water level system with time-variation and complex nonlinearity, the precision of traditional control method was low and the adaptive capacity was poor, a novel dynamic fuzzy neural network (DFNN) was put forward. It gave full play to the advantage of PID control and increased the abilities of self-learning and deal with quantitative data by combining fuzzy neural network with PID. For the key issue of how to confirm the fuzzy rules and the network structure, it dynamically constructed the fuzzy neural system online based on the sampling data through the DFNN algorithm. Then the fuzzy neural PID controller was designed to control the water level. The simulations show that it performs wonderfully in anti-jamming, fast and steadily responding, rapid convergence and small static error. The self-adaptation and robustness of these systems are good.

**Keywords** Steam generator · Water level control · DFNN · Adaptive capacity · Anti-jamming

## 1 Introduction

A major component in a NPP is Steam Generator (SG); it supplies needful steam to generate electricity. To ensure safety, dependable and operation economically of the NPP, the stability and valid water level control of the SG is particularly significant.

The control of the water level is too hard, due to a highly complicated, nonlinear, time-varying and non-minimum phase of the SG. Generally, the water level control

---

J. Hong (✉) · H. Xia  
Harbin Engineering University, Harbin, China  
e-mail: y-paopao@qq.com

H. Xia  
e-mail: xiahong@hrbeu.edu.cn

of the SG of reactor mainly depends on the manual operation of experts based on their experience. Most of the water level control is modulating control system based on traditional PID controller. To obtain well-controlled result in variable working situation, the parameters and gain of PID controller must be changed. However, the traditional controller always cannot satisfy the requirement of automation control of nuclear power plant under the instantaneous condition. Hence, all kinds of methods are studied to realize the water level online control of SG at home and abroad like GA optimize control [1], fuzzy control [2], neural network control [3] and fuzzy neural network control [4] and so on. They all acquired some achievements.

Fuzzy Neural Network (FNN), a combination of fuzzy system and neural network, which has become the research focus has well stability of studying and the fusion of system information [5]. And FNN based on Takagi-Sugeno model is adopted in this paper. Easy computation and convenient mathematics analyses are the advantages of T-S fuzzy system [6]. Also it is easier to combine with PID and adaptive control to design controller which owns the ability of optimization and adaption. According to the features of T-S fuzzy method, it is feasible to combine it with neural network and design the FNNC system which can study adaptively.

In fact, the FNN is also one kind of neural network. From the point of neural network, generalization ability is a core index to evaluate the stand or fall. Although the generalization ability is deeply associated with the choice of initialization and the strategy of study, the main factor is still the choice of the structure of the neural network. And there are still some problems to determine the initial parameters, the neural network structure, and the fuzzy rules. If the number of nodes is too little, the learning error will be great and likely to have the overtraining problem. If the number of the nodes is too much, it will appear over-fit phenomenon. Both of them will deeply reduce the generalization ability of the neural network. To deal with the problems above, dynamic fuzzy neural network (DFNN) is proposed here [7]. The controller proposed in this paper can model, get fuzzy neural network structure parameters, and obtain fuzzy rules automatically and the expert knowledge in this field will not need anymore.

In this paper, a novel dynamic FNN is used to control the water level of a SG. The novel control algorithm can give full play to the merits of the fuzzy control and the neural network; it dynamically constructed the fuzzy neural system online based on the sampling data through the DFNN algorithm. Then the fuzzy neural PID controller is designed to control the steam generator water level.

## 2 Mathematical Model of Steam Generator

This paper uses the simplify SG mathematic model given by Irving [8] and its state equations are as follows:

$$\begin{aligned} \dot{x}(t) &= Ax(t) + B_1u(t) + B_2q_v(t) \\ y(t) &= Cx(t) \end{aligned} \tag{2.1}$$

Therein,  $x(t)$  is the state variable;  $u(t)$  is the feed water flow, is control input of the system;  $y(t)$  is the water level of SG;  $q_v(t)$  is the exit steam flow of SG.

$A, B_1, B_2, C$  are as follows:

$$A = \begin{bmatrix} 0 & 0 & 0 & 0 \\ 0 & -\tau_2^{-1} & 0 & 0 \\ 0 & 0 & -2\tau_1^{-1} & 1 \\ 0 & 0 & -(\tau_1^{-2} + 4\pi^2 T^{-2}) & 0 \end{bmatrix},$$

$$B_1 = \begin{bmatrix} G_1 \\ -G_2\tau_2^{-1} \\ G_3 \\ 0 \end{bmatrix}, \quad B_2 = \begin{bmatrix} -G_1 \\ G_2\tau_2^{-1} \\ 0 \\ 0 \end{bmatrix}, \quad C = [1 \quad 1 \quad 1 \quad 0]$$

where,  $G_1, G_2, G_3, \tau_1, \tau_2$  and  $T$  is relative with the power.

We consider that Irving’s model as four piecewise linear parameters varying with the system according to the operating power as follows:

- Region I is  $0 \% \leq \text{power} \leq 15 \%$ ,
- Region II is  $15 \% \leq \text{power} \leq 30 \%$ ,
- Region III is  $30 \% \leq \text{power} \leq 50 \%$ ,
- Region IV is  $50 \% \leq \text{power} \leq 100 \%$ .

It is assumed that the model in each region is linear varying offline (Table 1).

**Table 1** The dynamic parameters of Irving’s model

$p$	5 %	15 %	30 %	50 %	100 %
$q_v(kg. s^{-1})$	57.4	180.8	381.7	660.0	1435.0
$G_1(p)$	0.058	0.058	0.058	0.058	0.058
$G_2(p)$	9.63	4.46	1.83	1.05	0.47
$\tau_2(p)$	48.4	21.5	4.5	3.6	3.4
$\tau_1(p)$	41.9	26.3	43.4	34.8	28.6
$T(p)$	119.6	60.5	17.7	14.2	11.7
$G_3(p)$	0.181	0.226	0.310	0.215	0.105

### 3 Dynamic Fuzzy Neural Network

#### 3.1 Structure of DFNN

The DFNN is a patulous RBF neural network in the structure, and is equivalent to a T-S fuzzy system [9]. The specific structure is shown as Fig. 1.

In Fig. 1,  $x_1, x_2, \dots, x_r$  is the linguistic variable of the input,  $y$  is the system output,  $MF_{ij}$  is the  $j$ th membership function of  $x_i$ .  $R_j, N_j$  mean the  $j$ th fuzzy rule and normalized node, and  $w_j$  represents the THEN-part (resulting parameters) or weight of the  $j$ th rule,  $u$  means the number of membership functions, which is the same with the system total rules. Detailed description of the network is presented as follows.

Layer 1: The input layer. Every point expresses an input variable. The number of input is  $r$ .

Layer 2: The subordinate function layer. Every point in this layer shows a subordinate function which is as the Gaussian functions

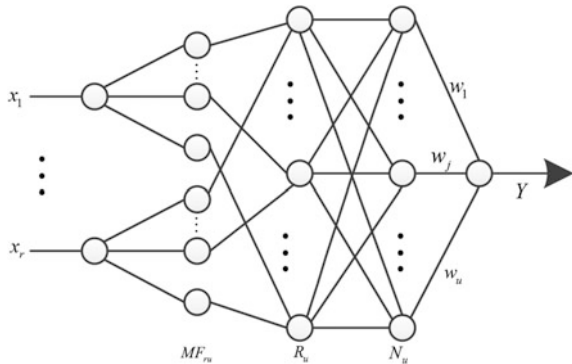
$$\mu_{ij}(x_i) = \exp \left[ -\frac{(x_i - c_{ij})^2}{\sigma_j^2} \right], \quad i = 1, 2, \dots, r, \quad j = 1, 2, \dots, u \quad (3.1)$$

Therein,  $\mu_{ij}$  is the  $j$ th subordinate function of  $x_i$ ,  $c_{ij}$  and  $\sigma_j$  is the center and the width of the  $j$ th Gaussian subordinate function of  $x_i$ ,  $u$  is the subordinate functions number, the same with the number of the system total rules.

Layer 3: The bound norm layer. Every point expresses a possible section of fuzzy rules. The output of the  $j$ th rule is

$$\phi_j = \exp \left[ -\frac{\sum_{i=1}^r (x_i - c_{ij})^2}{\sigma_j^2} \right] = \exp \left[ -\frac{\|X - C_j\|^2}{\sigma_j^2} \right], \quad j = 1, 2, \dots, u \quad (3.2)$$

**Fig. 1** The structure of the DFNN



Therein,  $C$  is the center of the  $j$ th RBF unit. It shows that every point expresses an RBF unit.

Layer 4: The uniformized layer. Evidently, the number of points is the same with the number of fuzzy rules. And the output is as follows

$$\varphi_j = \frac{\phi_j}{\sum_{k=1}^u \phi_k}, \quad j = 1, 2, \dots, u \quad (3.3)$$

Layer 5: The output layer. Every point expresses an output variable of DFNN. In the paper, we used a single-output. The output is as follows

$$y(X) = \sum_{k=1}^u \omega_k \cdot \varphi_k \quad (3.4)$$

where,  $y$  is the output,  $\omega_k$  is the weight of the  $k$ th rule, which is displayed as follows

$$\omega_k = a_{k0} + a_{k1}x_1 + \dots + a_{kr}x_r, \quad k = 1, 2, \dots, u \quad (3.5)$$

Take formulas (3.2), (3.3), (3.5) into formula (3.4), we can conclude

$$y(X) = \frac{\sum_{i=1}^u \left[ (a_{i0} + a_{i1}x_1 + \dots + a_{ir}x_r) \exp\left(-\frac{\|X-C_i\|^2}{\sigma_i^2}\right) \right]}{\sum_{i=1}^u \exp\left(-\frac{\|X-C_i\|^2}{\sigma_i^2}\right)} \quad (3.6)$$

### 3.2 The Learning Algorithm of the DFNN

#### 1. Guidelines of generating rules

##### (a) systematic error

Obviously, if the number of the rules is too little, the system will not be able to fully contain the input-output state space. The performance of DFNN will be very poor. For another, if the rules number is too much, it will not only increase complexity of the system, but also increases the calculation burden hardly and cause a deterioration of the generalization ability of DFNN. Hence, systematic error is the crux point to decide whether a new rule should join in.

Define

$$\|e_i\| = \|t_i - y_i\| \quad (3.7)$$

If

$$\|e_i\| > k_e \tag{3.8}$$

It means that a new rule should be generated.  $\frac{\partial E}{\partial c_{ij}} = -\delta_{ij}^{(2)} \frac{2(x_i - c_{ij})}{\delta_{ij}}$  represents a predefined error parameter.

Figure 2 shows the flow of DFNN learning algorithm.

(b) Accommodation boundary

If a new sample exists at some Gaussian function cover range (accommodation boundary), it can be represented by exist Gaussian function that do not need to generate a new rule. Accommodation boundary criterion is as follows:

For the  $i$ th point  $(X_i, t_i)$

$$d_i(j) = \|X_i - C_j\|, \quad j = 1, 2, \dots, u \tag{3.9}$$

Therein,  $u$  shows the existing fuzzy rules number.

Find

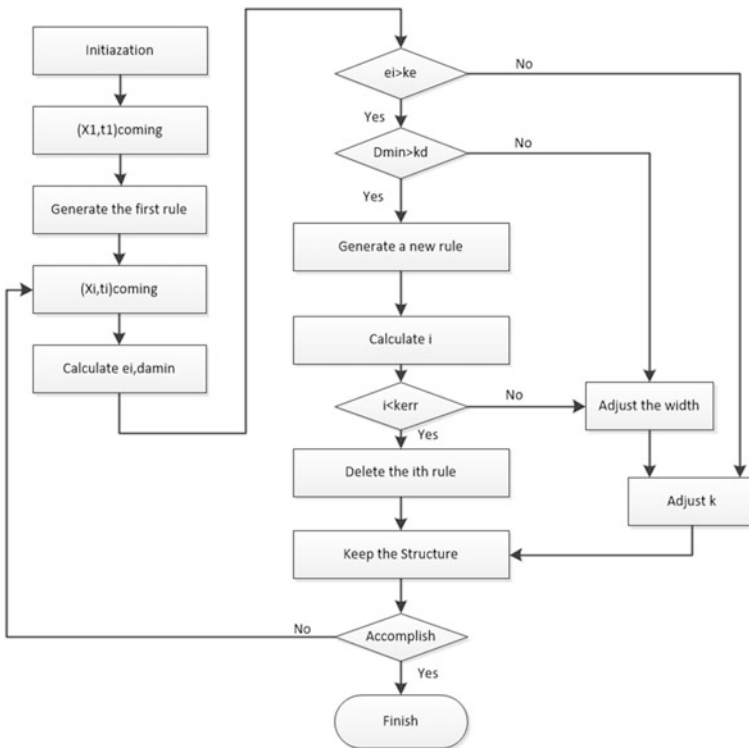


Fig. 2 The flow of DFNN learning algorithm



$$d_{\min} = \arg \min(d_i(j)) \quad (3.10)$$

If

$$d_{\min} > k_d \quad (3.11)$$

It means that a new rule should be generated; or observation data  $x_i$  can be showed by a recent existing RBF unit. Therein,  $k_d$  represents a predefined valid radius.

## 2. Hierarchical learning

“Hierarchical learning” was first presented in reference [10]. Its main idea is that the accommodation boundary of each RBF unit is not fixed but dynamically adjusts according to the following way [10]. According this idea, we proposed a simple method, that is, gradually decrease to the valid radius of per unit of RBF and error index based on the monotone decreasing function. That is to say,  $k_e$ ,  $k_d$  in formulas (3.8) and (3.10) are not constant and it is determined as follows:

$$k_e = \max[e_{\max} \times \beta^i, e_{\min}] \quad (3.12)$$

$$k_d = \max[d_{\max} \times \gamma^i, d_{\min}] \quad (3.13)$$

Therein,  $e_{\max}$ ,  $e_{\min}$  are predefined maximum error and required accuracy of an DFNN output,  $\beta(0 < \beta < 1)$  is a restrain constant. And  $d_{\max}$  is the largest width of the input space,  $d_{\min}$  is the smallest.  $\gamma(0 < \gamma < 1)$  is a delay constant.

## 3. Parameter adaptive

While a fuzzy rule is generating, how to decide its parameters becomes a problem. For generalization, the width of every RBF unit is important.

So we can distribute a new RBF unit as follows:

$$C_i = X_i \quad (3.14)$$

$$\sigma_i = k \times d_{\min} \quad (3.15)$$

Therein,  $k(k > 1)$  represents an overlap parameter.

When a first observed data  $(X_1, t_1)$  comes, DFNN has not been set up yet. Therefore, the data will be selected as the first fuzzy rule:  $C_1 = X_1$ ,  $\sigma_1 = \sigma_0$ , where  $\sigma_0$  is a preset constant.

In short, only when  $\|e_i\| > k_e$ ,  $d_{\min} > k_d$ , we need to generate a new rule.

## 4. Pruning techniques

In the paper, the error rod rate (ERR) is adopted as the pruning strategy. Given  $n$  pairs of input-output  $\{X(i), t(i), i = 1, 2, \dots, n\}$ .

$$Y = W \times \psi \quad (3.17)$$

$$E = \|T - Y\| \quad (3.18)$$

Considered formulas (3.17) and (3.18), as a special circumstances of a linear regression model

$$D = H\theta + E \quad (3.19)$$

where,  $D = T^T \in R^n$  is an expected output,  $H = \psi^T = (h_1 \cdots h_v) \in R^{n \times v}$ ,  $v = u \times (r + 1)$ .

Known as the regression vector,  $\theta = W^T \in R^v$  contains laboratory parameters and assume  $E \in R^n$  is an error vector uncorrelated with regressor  $h_i$ .

For every matrix  $H$ , if the number of lines is greater than the columns through the QR decomposition, then:

$$H = QA \quad (3.20)$$

$H$  can be transformed to a set of orthonormal base vectors  $Q = (q_1, q_2, \dots, q_v) \in R^{n \times v}$ , its dimension is same with  $H$ , each column  $q_i$  constitute orthogonal basis, and  $A \in R^{v \times v}$  is a upper triangular matrix. Through this transformation is on the cards, the calculation each individual's contribution to the desired output energy through each base vector.

Take formula (3.20) into formula (3.19)

$$D = QA\theta + E = QG + E \quad (3.21)$$

The least-square solution of linear system  $G$  is

$$G = (Q^T Q)^{-1} Q^T D \quad (3.22)$$

or

$$g_i = \frac{q_i^T D}{q_i^T q_i}, \quad i = 1, 2, \dots, v \quad (3.23)$$

And  $G$ ,  $\theta$  satisfy the following equation:

$$A\theta = G \quad (3.24)$$

If  $i \neq j$ , as  $q_i$  orthogonal to  $q_j$ , the quadratic sum of  $D$  could be given

$$D^T D = \sum_{i=1}^v g_i^2 q_i^T q_i + E^T E \quad (3.25)$$

After get rid of the mean, variance of  $D$  can be given by the following formula:

$$n^{-1}D^T D = n^{-1} \sum_{i=1}^v g_i^2 q_i^T q_i + n^{-1}E^T E \quad (3.26)$$

We can see that  $\sum g_i^2 q_i^T q_i/n$  is a part of the expectation output variance caused by regressor  $q_i$ . Therefore, the error drop rate can be defined as follows:

$$\text{err}_i = \frac{g_i^2 q_i^T q_i}{D^T D}, \quad i = 1, 2, \dots, v \quad (3.27)$$

Take formula (3.23) into formula (3.27):

$$\text{err}_i = \frac{(q_i^T D)^2}{q_i^T q_i D^T D}, \quad i = 1, 2, \dots, v \quad (3.28)$$

Suppose  $\varphi_i$  is the angle of vector  $q_i$  and  $D$ , then

$$\cos^2 \varphi_i = \text{err}_i = \frac{(q_i^T D)^2}{q_i^T q_i D^T D} \quad (3.29)$$

If  $\varphi_i = 0$ ,  $\text{err}_i = 0$ , shows that  $q_i$  has a great effect on  $D$ . Otherwise, if  $\varphi_i = 90^\circ$ ,  $\text{err}_i = 0$ , two vectors are orthogonal, shows that  $q_i$  has no effect on  $D$ .

Rearrange the new  $\text{err}_i(1, 2, \dots, (r+1)u)$  for matrix  $\Delta = (\delta_1, \delta_2, \dots, \delta_u) \in R^{(r+1)u}$ , the  $i$ th column of  $\Delta(\delta_i)$  is the  $(r+1)$ th error drop rate related with the  $i$ th rule. We can define as follows:

$$\eta_i = \sqrt{\frac{\delta_i^T \delta_i}{r+1}} \quad (3.30)$$

Then,  $\eta_i$  shows the importance of the  $i$ th rule.

If

$$\eta_i < k_{\text{err}} \quad (3.31)$$

where,  $k_{\text{err}}$  is the preset threshold, then the  $i$ th rule will be rejected.

## 4 Fuzzy Neural Network Controller

### 4.1 Structure of FNN

This paper used the FNN based on Takagi-Sugeno fuzzy system. The specific structure we can see as Fig. 1.

Layer 1: The input layer. Every point expresses an input variable. The number of input is  $r$ .

Layer 2: The subordinate function layer. Every point in this layer shows a subordinate function which is as the Gaussian functions

$$\mu_i^j(x_i) = \exp\left[-\frac{(x_i - c_{ij})^2}{\sigma_j^2}\right], \quad i = 1, 2, \dots, r, \quad j = 1, 2, \dots, u \quad (4.1)$$

Therein,  $\mu_{ij}$  is the  $j$ th subordinate function of  $x_i$ ,  $c_{ij}$  and  $\sigma_j$  is the center and the width of the  $j$ th Gaussian subordinate function of  $x_i$ ,  $u$  is the subordinate functions number, the same is with the number of the system total rules.

Layer 3: The bound norm layer. Every point expresses a possible section of fuzzy rules. The output of the  $j$ th rule is

$$\alpha_j = \min\{\mu_1^{i_1}, \mu_2^{i_2}, \dots, \mu_n^{i_n}\} \quad (4.2)$$

Therein,  $C$  is the center of the  $j$ th RBF unit. It shows that every point expresses an RBF unit.

Layer 4: The uniformized layer. Evidently, the number of points is the same with the number of fuzzy rules. And the output is as follows:

$$\bar{\alpha}_j = \frac{\alpha_j}{\sum_{k=1}^u \alpha_k}, \quad j = 1, 2, \dots, u \quad (4.3)$$

Layer 5: The output layer. Every point expresses an output variable of DFNN. In the paper, we used a single output. The output is as follows:

$$y(X) = \sum_{k=1}^u \bar{\alpha}_k \cdot \varphi_k = \sum_{k=1}^u \bar{\alpha}_k \cdot (p_{j0}^i + p_{j1}^i x_1 + \dots + p_{jr}^i x_r). \quad (4.4)$$

## 4.2 Online Adjustment Algorithm

Adopt the delta learning rule to fix the adjustable parameters and define the cost function of the error as follows:

$$E = \frac{1}{2}(t - y)^2 \quad (4.5)$$

Therein,  $t$  and  $y$  are expect output and actual output.

The adjustment algorithm of coefficient matrix  $P$  is as follows:

$$\frac{\partial E}{\partial p_{ji}^l} = \frac{\partial E}{\partial y_l} \frac{\partial y_l}{\partial y_{ij}} \frac{\partial y_{ij}}{\partial p_{ji}^l} = -(t_l - y_l) \bar{\alpha}_j x_i \tag{4.6}$$

$$p_{ji}^l(k+1) = p_{ji}^l(k) - \beta \frac{\partial E}{\partial p_{ji}^l} = p_{ji}^l(k) + (t_l - y_l) \bar{\alpha}_j x_i \tag{4.7}$$

Take the intermediate variable calculation results are as follows:

$$\delta_i^{(5)} = t_i - y_i, \quad (i = 1, 2, \dots, n) \tag{4.8}$$

$$\delta_j^{(4)} = \sum_{i=1}^r \delta_i^{(5)} y_{ij}, \quad (j = 1, 2, \dots, m) \tag{4.9}$$

$$\delta_j^{(3)} = \delta_j^{(4)} \sum_{\substack{i=1 \\ i \neq j}}^m \alpha_i / \left[ \sum_{i=1}^m \alpha_i \right]^2, \quad (j = 1, 2, \dots, m) \tag{4.10}$$

$$\delta_{ij}^{(2)} = \sum_{k=1}^m \delta_k^{(3)} e^{-\frac{(x_i - c_{ij})^2}{\delta_{ij}^2}}, \quad (i = 1, 2, \dots, n; \quad j = 1, 2, \dots, m_i) \tag{4.11}$$

So the adjustment algorithm of the blurred layer base width vector is:

$$\frac{\partial E}{\partial c_{ij}} = -\delta_{ij}^{(2)} \frac{2(x_i - c_{ij})}{\delta_{ij}} \tag{4.12}$$

$$c_{ij}(k+1) = c_{ij}(k) - \beta \frac{\partial E}{\partial c_{ij}} \tag{4.13}$$

The adjustment algorithm of the blurred layer central vector is:

$$\frac{\partial E}{\partial \delta_{ij}} = -\delta_{ij}^{(2)} \frac{2(x_i - c_{ij})^2}{\delta_{ij}^3} \tag{4.14}$$

$$\delta_{ij}(k+1) = \delta_{ij}(k) - \beta \frac{\partial E}{\partial \delta_{ij}} \tag{4.15}$$

Therein, the learning rate  $K_P = 0.4, K_I = 0.005, K_D = 0,$   
 $i = 1, 2, \dots, n; \quad j = 1, 2, \dots, m_i.$

## 5 General Design of System

In this paper, DFNN was used first for offline training in order to decide the fuzzy rules number and the network structure parameters of the fuzzy neural network controller. And then, use the BP algorithm to adjust and optimize the parameters of the FNN online. We improve the FNN self-learning ability and robustness of the control system by combining the two methods. Figure 3 is the specific structure of control system.

In Fig. 3, the input is the error of the SG water level setting value and actual value,  $K_P = 0.4, K_I = 0.005, K_D = 0$  is the change rate of the error,  $u$  is the output of the controller. We get the initial network structure parameters of the fuzzy neural network controller through the offline learning of DFNN, and then control the SG water level online based on the parameters learned.

## 6 Simulation Results

In this part, a nest of simulations is presented to appraise the performance of the system proposed above.

### 6.1 DFNN Offline Learning

In this part, the main of the simulations is the performance of DFNN offline training.

The training parameters were chosen as below

$$K_P = 0.4, \quad K_I = 0.005, \quad K_D = 0,$$

the DFNN given parameters are

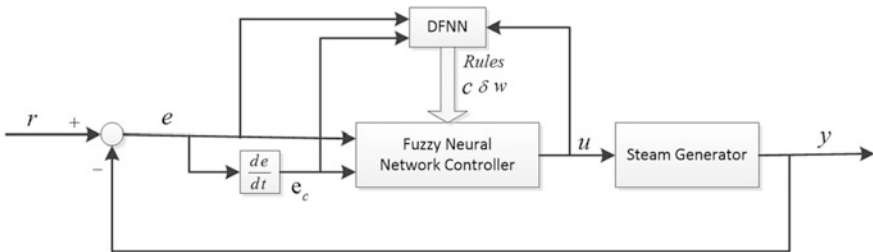


Fig. 3 The structure of control system

$$e_{\max} = 1, \quad e_{\min} = 0.1, \quad d_{\max} = 25, \quad d_{\min} = 0.1, \quad \gamma = 0.97,$$

$$\beta = 0.95, \quad \sigma_0 = 12, \quad k_s = 0.7, k_w = 1.1, \quad k_{\text{err}} = 0.0005.$$

The simulations are shown as Figs. 4 and 5. Therein, Fig. 4 showed the fuzzy rules number of DFNN while identifying the SG model and controlling the water level. In the figure, we can see that the number of fuzzy rules remained as seven from about 17 s to the end. And Fig. 5 shows the root mean squared error (RMSE) of DFNN while identifying the SG model, which converged to zero fast.

After the training, the network structure parameters were given as follows:

$$C_0 = \begin{bmatrix} -1.9724 & 11.3162 \\ 6.1005 & 8.0729 \\ -8.7302 & -14.8307 \\ -8.0393 & 0.6910 \\ -10.984 & -8.3874 \\ -9.8730 & -12.3829 \\ -5.8042 & -10.2918 \end{bmatrix}.$$

$$B_0 = [7.7736 \quad 6.0900 \quad 12.5137 \quad 5.9699 \quad 4.7782 \quad 1.8910 \quad 2.6613]$$

$$P_0 = \begin{bmatrix} 0.000 & 0.000 & 0.000 & 0.000 & 0.000 & 0.000 & 0.000 \\ 0.005 & 0.005 & 0.005 & 0.005 & 0.005 & 0.005 & 0.005 \\ 0.600 & 0.600 & 0.600 & 0.600 & 0.600 & 0.600 & 0.600 \end{bmatrix}$$

where,  $C_0$  is the Gaussian function center,  $B_0$  is the Gaussian function width,  $P_0$  is the coefficient matrix.

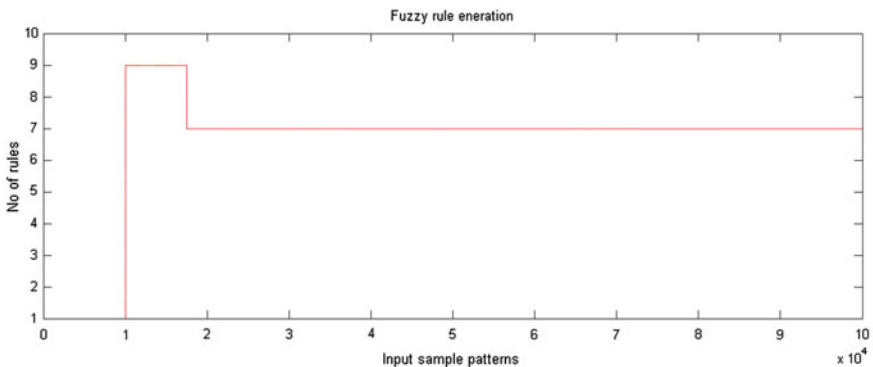
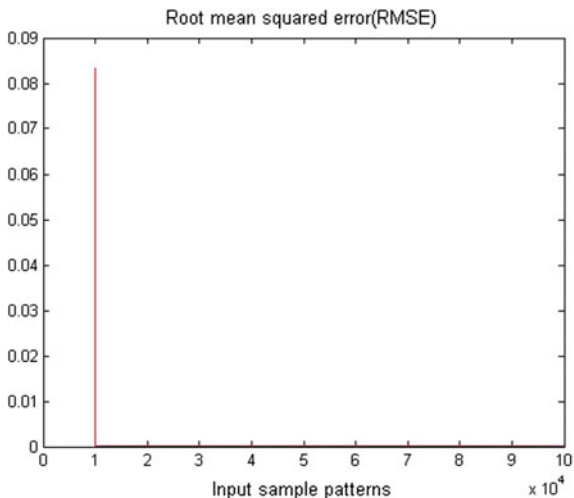


Fig. 4 The fuzzy rules of DFNN

**Fig. 5** The RMSE of DFNN



### 6.2 FNN Online Control

In this part, the main of the simulations is the performance of the FNN online controller with the trained parameters at the two typical power levels.

In the system, the feed water flow is taken as input, the steam flow is the interfering signal, and sampling time is 1 ms, join 15 % steam flow disturbance to the system at  $t = 10 s$ .

The simulation results are shown as the below figures.

Where, Figs. 6 and 8 show the expression of the traditional PID controller, Figs. 7, 9 show the expression of the proposed new controller. We can see that the overshoot on low power level is larger than on high power level, and the settling

**Fig. 6** SG water level control of PID controller (positive step)

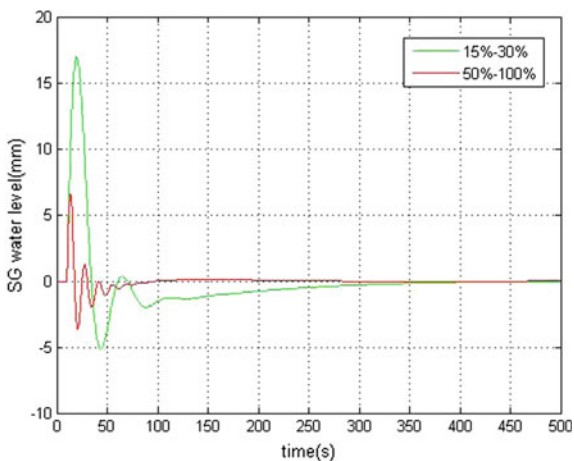




**Fig. 7** SG water level control of trained FNNC (positive step)

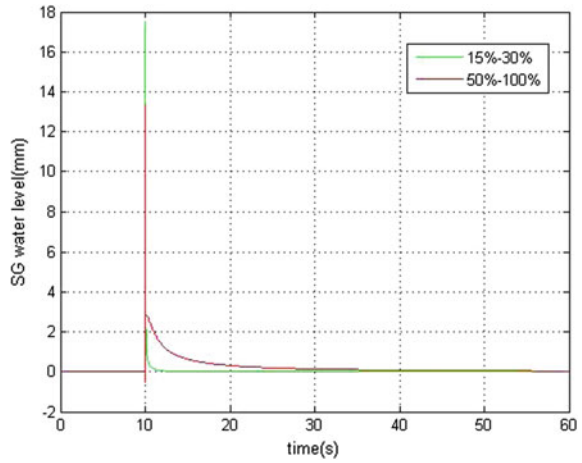
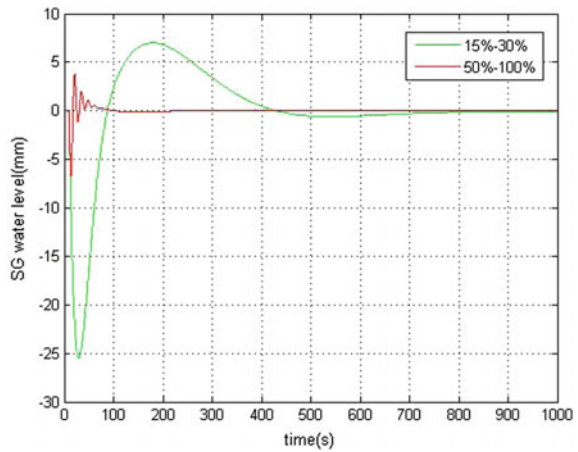
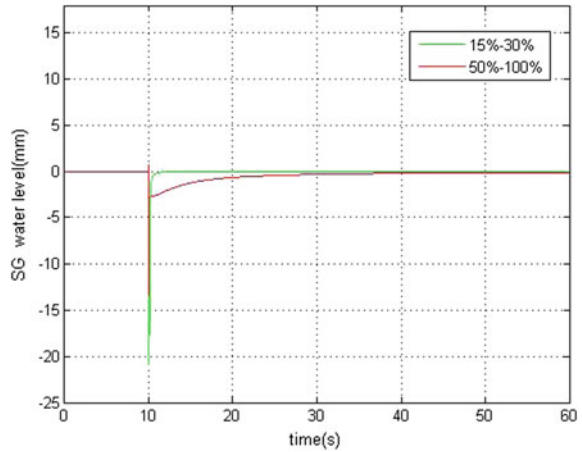


**Fig. 8** SG water level control of PID controller (negative step)



time is also longer. It is observed that SG water level control of trained FNNC can get stability in a short time and solved the change hysteresis and falsity of the water level effectively. It is satisfactory in the expression while the steam flow distraction at both of low power level and high power level.

**Fig. 9** SG water level control of trained FNNC (negative step)



## 7 Conclusions

In the paper, a novel dynamic fuzzy neural network (DFNN) was used for the water level control of a steam generator. The novel control algorithm can give full play to the merits of the fuzzy control and the neural network; it dynamically constructed the fuzzy neural system online based on the sampling data through the DFNN algorithm. Then the fuzzy neural PID controller was designed to control the steam generator water level. This method supplies a high-performance controller on the system. Also, it is simple to put into effect the practical applications. The simulation results show that it is available in SG water level control system and performs wonderfully in anti-jamming, fast and steadily responding, rapid convergence and small static error. The self-adaptation and robustness of these systems are good.

## References

1. Ye Jun, Zhang Xinhua. "Design for PID Controller Based a New Genetic Algorithm", Control Engineering of China. 9(3): pp. 51–52. 2002
2. Suzhen Duan, Naiyao Zhang, Zhenhua Cui. "Design Method of PWR Steam Generator Water Level Fuzzy Controller", Journal of Tsinghua University(natural science).46(9).2006
3. Wangdou Wang, Guangfu Zhang. "BP neural network-adjusting PID control and simulation for the water levelin the nuclear steam generator", Ship Ocean Engineering. 174(5): pp. 78–81.2006
4. Sudath R. Munasinghe, Min-Soeng Kim, Ju-Jang Lee. "Adaptive Neuro Fuzzy Controller to Regulate USTG Water Level in Nuclear Power Plants". IEEE Transaction on nuclear science. 5(2): pp. 421–429.2005
5. Habibiyani H, Setayeshi S, Arab-Alibeik H. "A fuzzy-gain-scheduled neural controller for nuclear steam genera-tors". Annals of Nuclear Energy, 31: pp. 1765–1781.2004

6. Chen Zhi, Liao Longtao, Liu Lixin, Li Wei. "Study on Application of T-S Fuzzy Neural Method in Once Through Steam Generator Feedwater Control", Nuclear Power Engineering. 33(4); pp. 20–23.2012
7. Er M J, Wu S Q, Gao Y. "Dynamic Fuzzy Neural Networks: Architecture, Algorithms and Applications". McGraw-Hill, Singapore, 2003
8. E Irving, C Miossec, J Tassart. "Toward Efficient Full Aromatic Operation of The PWR Steam Generator with Water Level Adaptive Control". Proceeding of 2nd International Conference on Boiler Dynamics and Control in Nuclear Power Stations London: British Nuclear Energy Society, pp: 309–329. 1980
9. Er M J, Wu S Q. "A Fast Learning Algorithm for Parsimonious Fuzzy Neural Systems", Fuzzy Sets and Systems.126,pp:337–351.2002
10. Lee S, Kil R M. "A Gaussian Potential Function Network with Hierarchically Self-Organizing Learning", Neural Networks. 4. pp:207–224.1991

# Performance Analysis and Optimization of Fang Jiashan DCS Level 2 System

Ping Tan

**Abstract** This paper is based on the experience of Fang Jiashan DCS level 2 system optimization project. Level 2 system is the essential part in the whole DCS system as it is responsible for monitoring and controlling the plant operation. Its performance affects the stability and economic efficiency of the plant operation directly. This paper briefly describes the architecture of Fang Jiashan Nuclear Power DCS level 2 system and the way of signal exchanging among the different levels of DCS. It also describes how the signal scanning and processing mechanism affect level 2 system performance, and demonstrates in detail why there were signals delayed during the major test-like disconnection from grid test at the 100 % power level. This paper also proposes optimization methods to enhance the performance for the level 2 system in multiple aspects including hardware upgrade, signal scan rate optimization, internal calculation process mechanism improvement, system task scheduling mechanism improvement and system architecture optimization. The methods for performance optimization discussed in this paper have been applied to DCS level 2 system updating project of Fang Jiashan NPP and Fuqing NPP 1&2 successfully, which have been proved feasible and effective, the schemes are valuable for new plant DCS design and construction or for old plant DCS refurbishment in certain aspects.

**Keyword** DCS performance analysis optimization · Performance · Analysis · Optimization

## 1 Brief Introduction

This paper is based on the experience of Fang Jiashan DCS level 2 system optimization project. The Fang Jiashan (FJS) I&C (Instrumentation & Control) system is designed into four different levels, level 0 is the field processing system interface

---

P. Tan (✉)

CNNC Nuclear Power Operations Management Co. Ltd, Jiaxing, Zhejiang, China  
e-mail: tanp@cnnp.com.cn

level, mainly containing transmitters, sensors, actuators etc. Level 1 is the automatic control level, mainly containing Field Bus Module (FBM, Level 1 acquisition module) and Field Control Processor (FCP, Level 1 processing units), Level 2 is the monitoring and controlling level (ADACS\_N, a product of Atos), mainly containing information treating servers, operator workstations and Level 3 is the information management level, mainly containing the different information systems interface with DCS Level 2. Level 1 and Level 2 are the scope of the DCS of FJS I&C system. The DCS Level 2 product “ADACS\_N” is supplied by Atos which is a French company and they provide the first whole digital level 2 system in the world called “N4”. ADACS\_N is a product evolved from N4 which has been applied to eight nuclear power units in China: Fangjiashan NPP unit 1 and 2, Fuqing NPP unit 1, 2, 3, and 4, and Hainan NPP unit 1 and 2. ADACS\_N is the target system to be referred in this paper

Fig. 1 shows the DCS structure of FJS nuclear power plant, the whole data flow chain are as below: the level 0 signals are transmitted into FCP through FBM module and after processing, these level 1 signals are transmitted to level 1 Application Interface server (API, Level 1 interface server) which is responsible for interacting with DCS level 2 through Level 1 network (MESH network). Correspondingly in Level 2, there is a frontier server (CFR, Level 2 interface server) interfacing with Level 1 API server to retrieve the Level 1 data with regular polling mechanism, then CFR transmitted these Level 1 data to the Central Calculation and Treatment server (CCT, Level 2 main processing server). After calculation by CCT, the site equipment signals are digitalized and finally displayed in the Operator Workstation Place (OWP, Operator Workstation in the main control

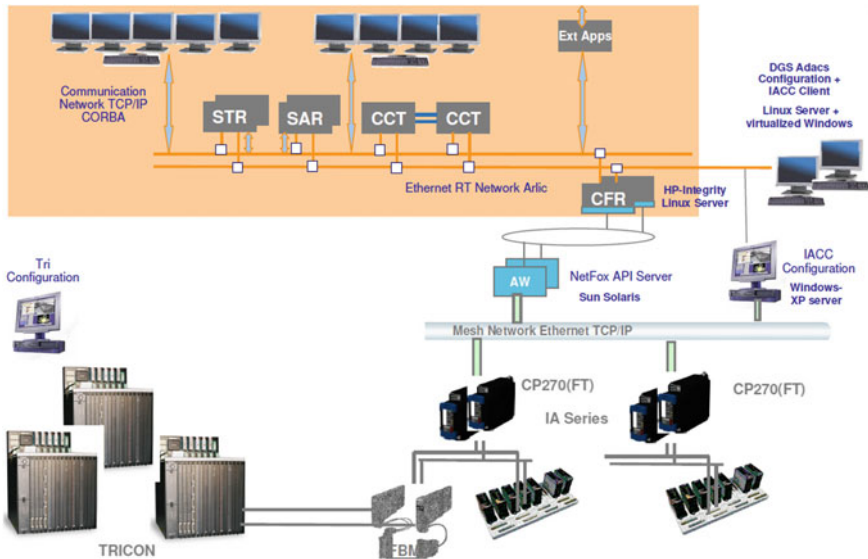


Fig. 1 Overview of DCS

room) through the Real-Time server (STR, real-time server) and data archive server (SAR, data archive server) [1].

### 1.1 DCS Level 2 Signal Transmitting Sequence

The DCS level 2 acts as the terminal of the whole digital control system for the operator to monitor and control the plant operation; it takes over the responsibility of both monitoring and controlling function. Fig. 2 shows the DCS signal transmitting sequence, two data channels presented in Fig. 2 (from arrow 1 to 4, it shows a complete sequence of the signal), one is sending a command to motivate the local equipment and the other is receiving the local equipment signals or feedback, a command is sent first from a OWP by the operator clicking on a command button, the real-time server STR is receiving this signal and passes it to the CCT for treatment. After calculation, CCT sends the command to CFR, CFR passes the command to level 1 for executing. After the command execution or any action from the local equipment, the level 0 signals are sent to CFR through level 1, after receiving the signal, CCT will perform calculation based on the signal type; then these signals can be digitalized and displayed in the OWP after further processing by STR and SAR server.

In the data transferring structure, CFR acts as a frontier server only responsible for receiving data from level 1 and transferring data to CCT, then receiving

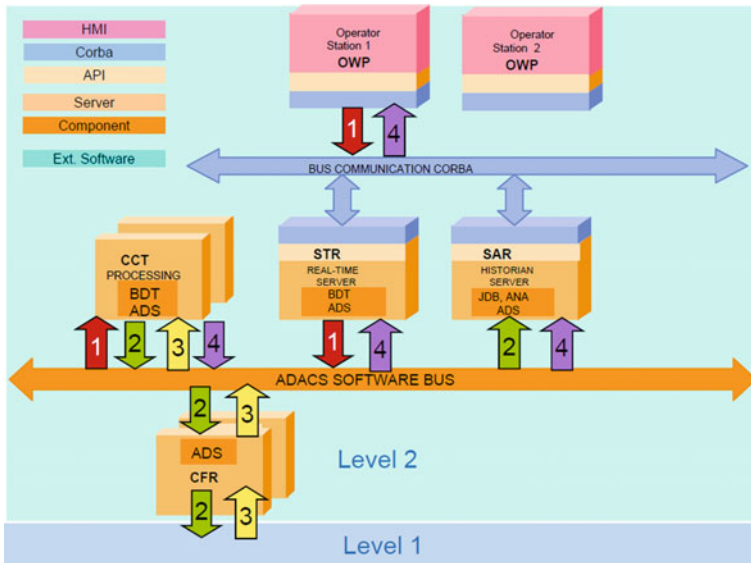


Fig. 2 Process of signal exchanging

command from CCT and transferring command to Level 1. STR is only responsible for real-time data exchanging with OWP. But CCT acts as a central calculation server who is responsible for the equipment status monitoring, data invalidity calculation, real-time data calculation, level 2 internal data calculation, alarm information treatment, besides, CCT is also responsible for the level 2 equipment management including scheduling the tasks for all level 2 servers and workstations, server redundancy monitoring and server failover treatment. The signal exchanging process shown in Fig. 2 is supported and monitored by the CCT, it is the brain of the whole level 2 structure; thus the performance of CCT has decisive influence on the DCS level 2 performance.

## ***1.2 Performance Influence Caused by Signal Acquisition and Processing***

There are totally three types of signals acquired by DCS level 2 system: binary values, analog values, signal validity (quality bit). Different types are acquired and treated differently, for example, CCT is only triggered for calculation when there are status changes for the binary signals. For the analog signals, these signals are acquired and treated periodically by scan time. In the CCT, there is one term named TOX (Treatment Of Exploitation) to measure the CCT calculation frequency per second, any treatment activated by receiving an external signal or level 2 internal calculation requirement is recognized as a TOX activation. The number of TOX activation per second is a real key element to judge the performance and load of the CCT.

No matter what, equipment has a limited processing ability. There is also a limited TOX activation value for CCT to handle the signals. Therefore, system designers and dataset configuration engineers have to balance and control the indicator in a reasonable range, especially for analog values, the value changing is slow (temperature, flow, etc.) in normal status, if the scan rate is unreasonably high, it is possible that level 2 acquired too much useless signal change. It will lead to a very fast filling-in for the archiving server which makes no sense, meanwhile, CCT is under heavy loading status (that is under high TOX activation) for a long time, the consequence is that level 2 system has bad performance.

## **2 Performance Issue**

The data refresh on the level 2 display during the FJS NPP Unit 1 disconnection from grid test has been found significantly delayed, on December 9 2014. Another event is that Fuqing NPP Unit 1 level 2 system stopped due to CCT performance issue in September 21 2015. There was one common feature in the two events: the

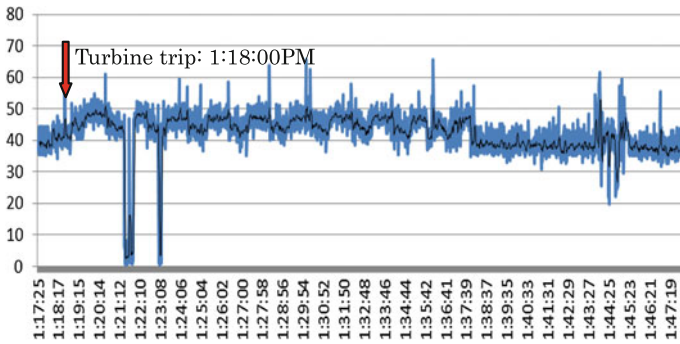


**Fig. 3** CPU load during the disconnection from grid test at the 100 % power level on FJS NPP 1

CPU usage of CCT server was overloaded. Take the disconnection from grid test of FJS NPP Unit 1 as an example. Fig. 3 shows the CPU usage during the whole test. Through the trends, it is apparent to see that the CPU usage is between 40 and 50 % during 20 min of the test. From the CPU usage, it conforms to the requirement of the technical specification which describes clearly. The average CPU load should be below 40 % in normal condition, below 50 % in busy condition, but allows to exceed 50 % in a short time. The reality was that, level 2 system had latency while receiving data from the equipment or sending command to the equipment which is unacceptable.

Only regarding the load values, it is in a low level and has no reason leading to the display frozen or sending command in delay. The root cause leading to the result above is because the server uses two cores CPU, the curve shows in the records above is based on average load value of the two cores. While using “TOP” Linux command in the CCT server (ref. Fig. 4), the CCT1 application (core processing application of the CCT server) reaches 89.3 %, regarding the delayed display refreshment, the peak value of the CCT1 application approached 100 %. Furthermore, CCT1 is responsible for all the calculation of the level 2 system, the consequence is that CCT1 is not able to treat the other tasks or respond to any further requests, CCT1 application jumped into a race-condition context. As a result, the display refreshment slowed and sent command to level 1 in delay.

### 3 Root Cause Analysis

#### 3.1 Unreasonable Scan Rate Configuration

During the major tests (e.g., disconnection from grid), the DCS system will be in high load due to the massive amount of plant equipment status changing. In order to further analyze the root cause for the high load of CCT CPU, the following data are measured during FJS NPP Unit 2 disconnection from grid. Through the internal



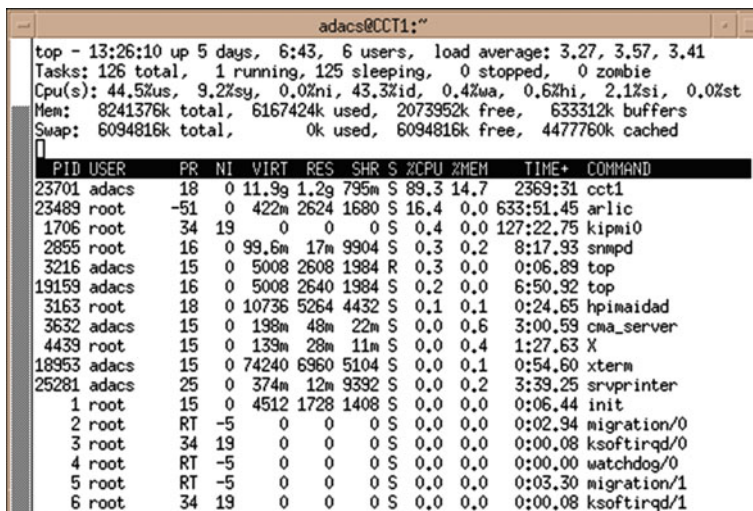


Fig. 4 CCT1 core process CPU load

Table 1 TOX for each type

Data type	TOX activation value
<u>ANALOG_INPUT_FQ</u>	344158
<u>ANALOG_INTERNAL_FQ</u>	288724
<u>BINARY_INTERNAL</u>	54521
LOOP_CONTROL	25484
MULT_ANA_INPUT	13210
LOOP_VALVE_FC	9554
LOOP_VALVE_FO	7332
REDUNDANT_SENSOR	6966
BINARY_INPUT	1088
GENERAL_INFO	866

CCT system measure tool, it has been recorded for a period of 500 s, CCT was doing huge amount of calculations, the calculation are divided and ordered into types. Table 1 shows the TOX activation (calculation times) and its related Process Object Type (POT). A POT is modeling in terms of data, and reflex treatments an acquired signal, a computed complex analog or logic expression, an equipment and so on.

Figs. 5 and 6 show the trend of total TOX and also the trends of TOX activations for four critical data types. 8 h 55 min 00 s is the beginning point of disconnection from grid. From Fig. 5, the recorded TOX disperses in the range 1500–2000 in four minutes when CCT was in busy condition, inside, the Analog Input and Analog Internal data contribute the most TOX to CCT, especially, the TOX activation of

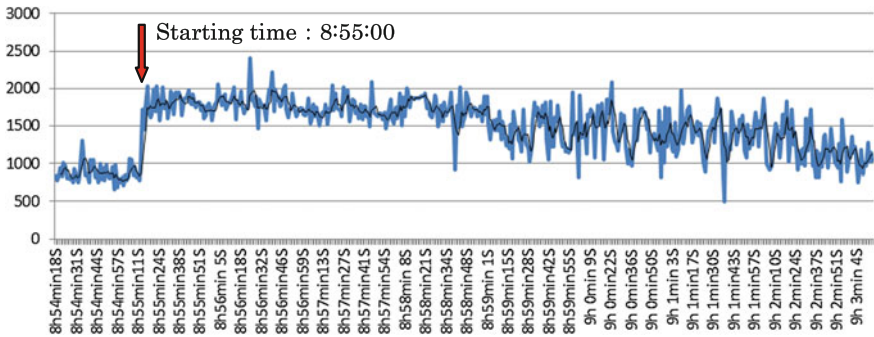


Fig. 5 Total TOX

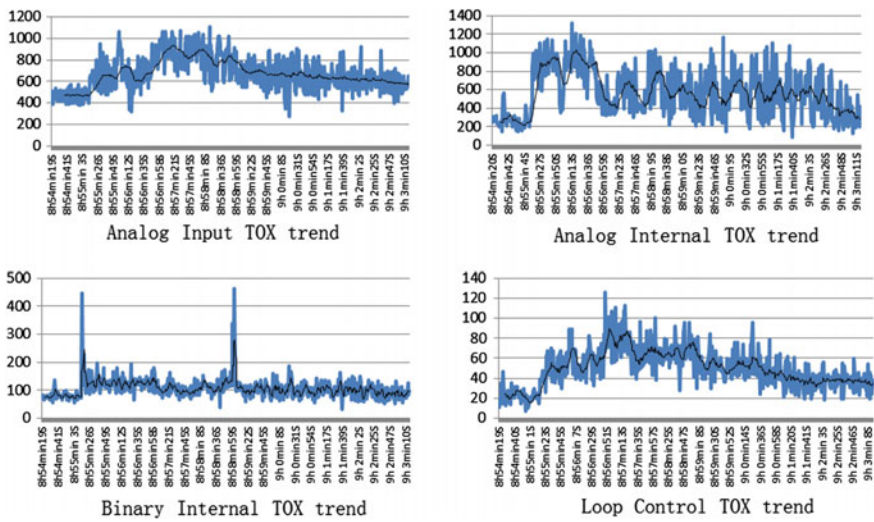


Fig. 6 Critical data type TOX

Analog Internal data type increased sharply in 2 min from the start point (see Fig. 6).

As mentioned in the previous paragraphs, the treatment for the analog data are closely related to the processing frequency and scan rate, the default scan rate configuration for analog data is 100 ms, the data variation rate is set to 0.1 % of the range by default. According to the operation experience from other power plant in service, the current scan rate configuration of FJS site is too small and probably leads to server resource over-consuming which is harmful to the system performance. Therefore, tuning the scan rate is an important method for enhancing the DCS level 2 system performance.

### 3.2 Unreasonable CCT Heap Configuration and Scheduling Mechanism

Figure 7 shows the CCT data processing diagram. As a central calculation treating server, CCT processing application is responsible simultaneously for treating plant real-time data acquired from field equipment and monitoring ADACS\_N system equipment status. In the CCT processing application, there are specific heap to stock temporarily the request for real-time data treatment and KIC monitoring request. During the disconnection from grid test, CCT processing application received an avalanche of data from DCS level 1 in the short time, which brought extremely heavy load for CCT application. This heavy load made the CCT to not treat all the requests timely and these requests were all stocked in the heap, the situation last around a few minutes or longer, the internal heap of CCT became saturated quickly, therefore, the level 2 system shows slow response.

In order to simulate the delayed response issue under the situation of disconnection from grid test, extensive avalanche data stress test have been simulated from level 1 (a script which can stimulate huge amount of data changes for Binary and Analog type has been used), the purpose was to identify the bottle neck of the CCT processing ability. Figure 8 shows the trends for 1KIC101KM (the trends should be displayed as triangle wave curve in normal status) from the OWP, but actually the curve has about 2 min delay, it means the data refreshment from the OWP is not normal.

Table 2 shows during this stress test, the heap buffer SYSCOM\_EXTERNE\_RECEPTION was decreased to nearly use out, from the predefined 5120000 to 301016 byte (that is the heap size reduction of free memory to 5.8 % of the total size).

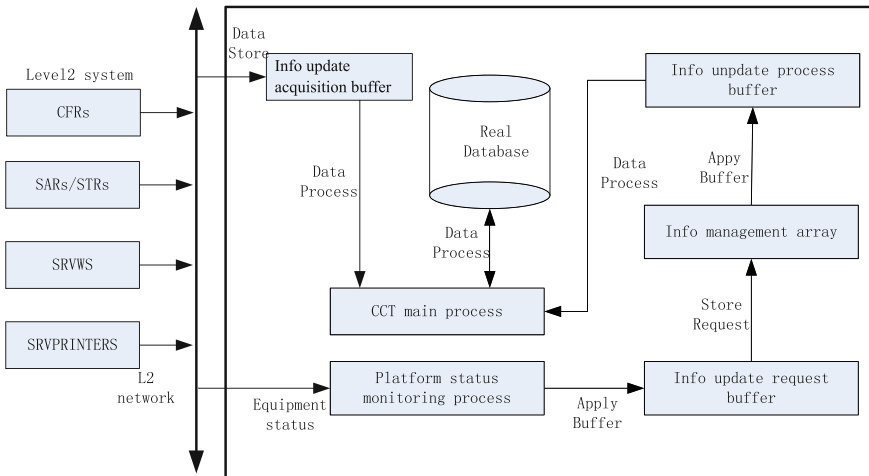


Fig. 7 CCT data process diagram

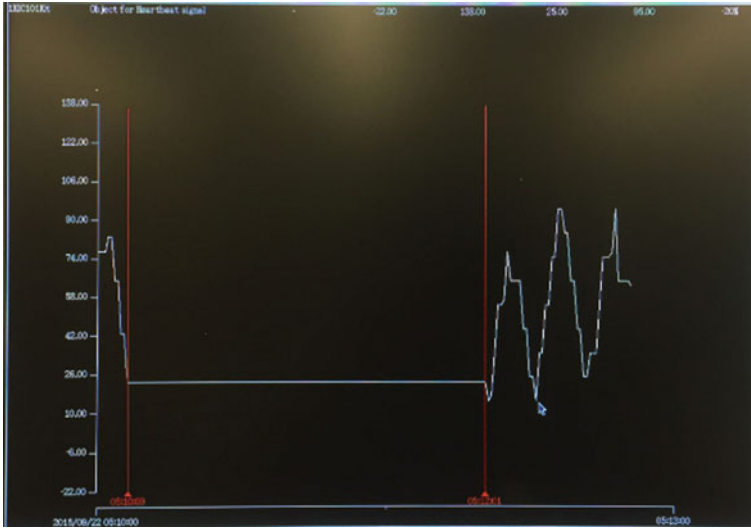


Fig. 8 1KIC101KM trend frozen under stress test

## 4 Improvement

### 4.1 System Hardware Upgrade

The technology of industrial computer evolves very quickly, the previous hardware structure was proposed by Atos six years ago. Nowadays, the industrial computer reaches into a new technical level, there are more advanced, matured, stable hardware in the market, thus, it has a good basis to upgrade the hardware. This solution will large improve the processing ability for the whole level 2 system. For the hardware upgrade or replacement, it will have no impact for the stability and availability of the current level 2 system because the software is coded in a normalized, mature, and portable programming language. Besides, accompany with the hardware aging, several stops occurred because of hardware failure. It is necessary to have the performance margin from the hardware perspective in order to increase the reliability and ability to handle the extreme plant situation. Table 3 shows the parameter comparison between new server and old server [2].

Under the same avalanche condition (a script which can stimulate huge amount of data changes for Binary and Analog type has been used), the average CPU load of the old server model is 10 % (see Fig. 9) while the new server model is only 2 % (see Fig. 10), Obviously, the performance of optimized system is five times better than the previous system [3, 4].

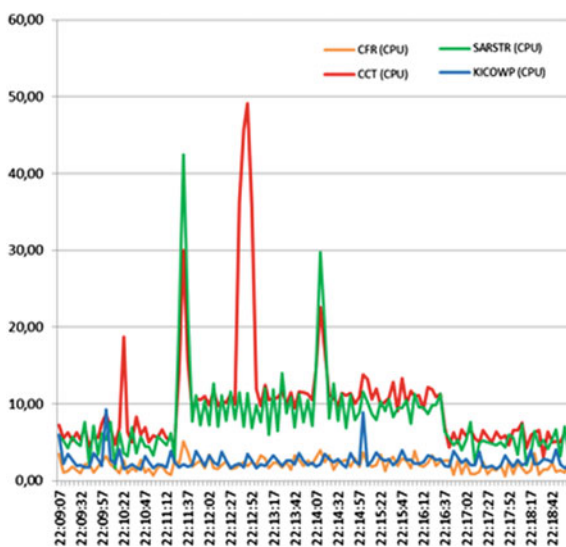
**Table 2** The internal heap size decreased

Heap tag	Global heap size	Available heap size	Nb of holes	Minimum size hole	Maximum size hole
BDT	536870912	266214168	1	266214144	266214144
<u>SYSCOM_EXTERNE_RECEPTION</u>	<u>5120000</u>	<u>301016</u>	79	8	79776
SYSCOM_EXTERNE_EMISSION	15360000	15039168	1	15039144	15039144
SYSCOM_INTERNE_PROCESSUS	307200000	307199960	1	307199936	307199936
SYSCOM_INTERNE_TACHE	1048576	1038056	3	2824	1029872

**Table 3** New server versus old server

Parameter Server type	CPU clock speed	Memory	Hard driver type
HP DL380G9 (after upgrade)	3.40 GHz	32G DDR4	Solid state disk
HP RX2660 (before upgrade)	1.60 GHz	8G DDR2	Mechanical hard disk

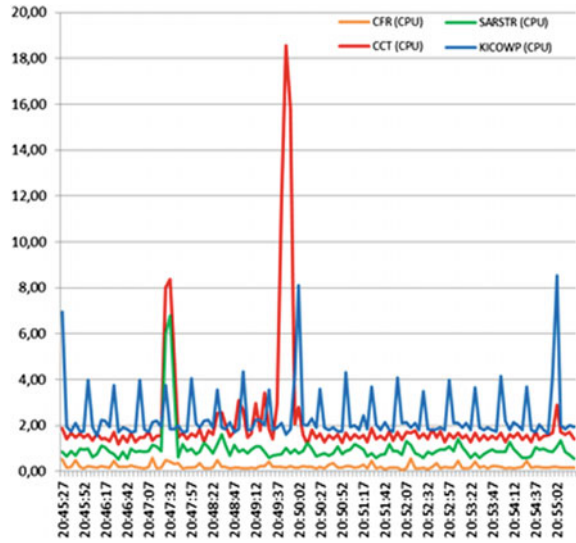
**Fig. 9** Average CPU load (before optimization)



#### 4.2 Scan Rate, Dead Band and Internal Calculation Optimization

According to the feedback from supplier as they have provided control system for different countries, the scan rate configuration for analog data as below:

**Fig. 10** Average CPU load (after optimization)



Scan rate: 1–120 s

Dead band: 0.1–1.0 % of the physical range

Input data type includes Binary Input and Analog Input, for Binary input values, the values are acquired based on change, therefore, no more optimization can be done. The optimizations are mainly conducted regarding analog values, as below:

1. Analog Input scan rate optimization

The level 2 default scan rate configuration is set to 100 ms, but the change rate for most of analog signals cannot reach such high frequency in reality. Therefore, a huge improvement can be done for the analog value acquisition by level 2. Based on the experience from FJS Unit 1 and FJS Unit 2, the optimization method has been proved to be effective.

2. Analog Input acquisition precision optimization

For most of the intermediate values for analog data, the trivial change for these intermediate values can be ignored. Based on this feature, the intermediate values for analog data has to be analyzed to increase the dead band. This method can not only further improve the analog data to be processed, but also makes the value trends smoother. FJS adopts the precision according to the real needs of site.

Figure 11 shows the CPU usage during the disconnection from grid in FJS NPP Unit 2 after the optimization of scan rate and dead band. It shows that the high CPU usage lasts about five minutes which is significantly decreased than that in FJS NPP Unit 1. Besides, the CPU usage before the disconnection from grid of Unit 2 is also lower than that in Unit 1. It proves the effectiveness of the optimization, but the high load period is still long so the system needs further improvement.

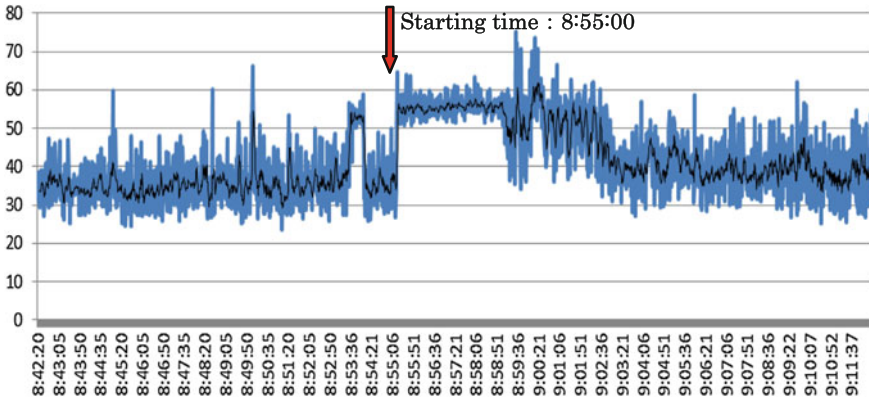


Fig. 11 CPU load during the disconnection from grid test at the 100 % power level on FJS NPP 2

### 3. Optimization for internal variables process mechanism

Two kinds of internal variables are used in the current level 2 system, which are simple internal variable and complex internal variables. The two kinds of variable are distinguished by its complexity of the expressions. In the initial design of the Atos DCS system, the size of the expressions are constrained to a limit, thus the complex internal variables have to be split to several simple internal variables, during the treatment of these complex internal variables, CCT has to spend extra efforts to treat these embedded internal variables, if the change rate of these variables reaches a certain level, large part of the resources of CCT are occupied by the treatment to these internal variables and other real-time task are delayed. This explains why the TOX curve rushed into a peak during the experiment of disconnection from grid. It also explains why the responsive time of the level 2 is largely delayed. So, the internal variable optimization will improve the DCS level 2 system performance significantly.

### 4.3 Increase CCT Heap Size and Scheduling Mechanism Improvement

From the root cause analysis of Sect. 3.2, it can be found that the volume of the internal heap buffer can affect the system tolerance rate, therefore, inside the CCT, the heap buffer size should be increased to improve the tolerance rate for CCT in busy condition. In the other side, while the heap buffer is approaching saturation, the lower priority task such as KIC internal system monitoring task and printers' status monitoring tasks should be suspended till the completion of the higher priority task such as real-time data from level 1. With this method, the CCT can be guaranteed to treat the tasks in priority order, then to ensure the system stability.

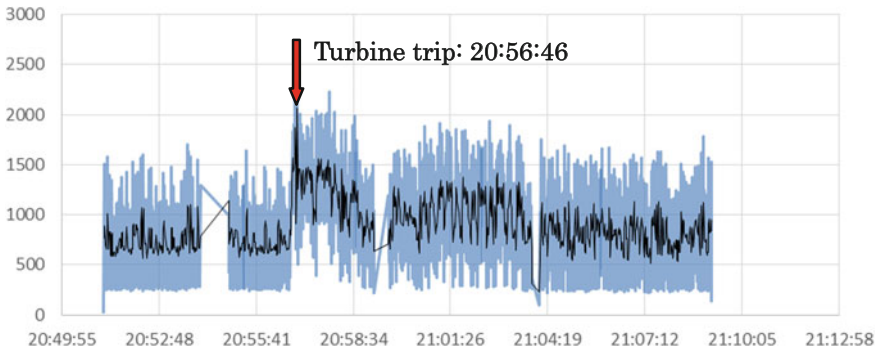


Fig. 12 CCT TOX trend during the turbine trip without reactor trip in Fuqing NPP 2

During the turbine trip without reactor trip on September 11 2015 of Fuqing NPP unit 2, the level 2 system of Fuqing Unit 2 site has been optimized for the aspects of scan rate optimization, internal variable improvement and CCT scheduling optimization, from the result of the test, the system performance had been improved largely and DCS level 2 has apparent improvement. Figure 12 shows the TOX trends of CCT of the whole test, the feedback from the operators reflected positive result (e.g., no command latency during the whole test), it shows clearly that before the test, the TOX level is 700 and increased to 1000–1500 three minutes after the test starts. At that moment, the level 2 system operated smoothly. Figure 13 shows the CPU load trends of CCT during the test, it can be seen that the result improved a lot.

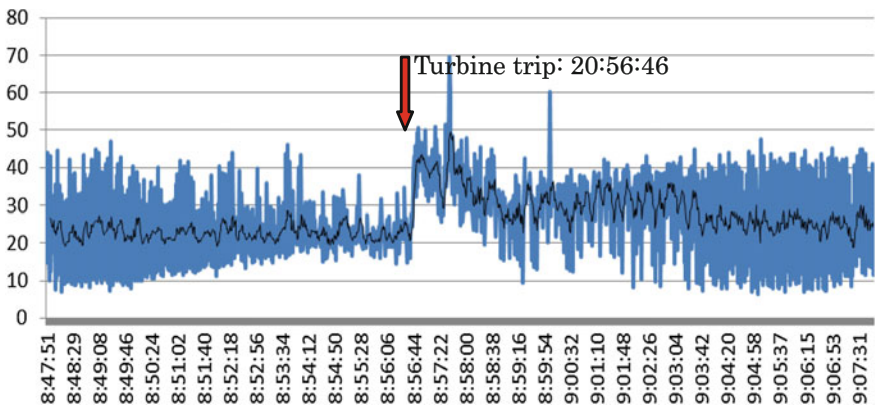


Fig. 13 CCT CPU usage during the turbine trip without reactor trip in Fuqing NPP 2



#### **4.4 System Structure Optimization**

Regarding the current system level 2 structure, data processing and system administration are highly centralized in the single application of the CCT server. Therefore, during system design, the distributed calculation conception should be applied into the CCT application implementation; the CCT function can be distributed to multiple process and multiple cores. The scheduling application can be optimized to eliminate the bottle neck from structure aspect.

Due to the limitation of time, risk, and economy, it has not been studied and implemented in the current optimization project, but the perspective of the system structure optimization has valuable significance for both research and implementation, especially to the software supplier.

### **5 Conclusions**

The paper analyzes in detail for the DCS level 2 slow down phenomenon during disconnection from grid test under 100 % power level for Fang Jiashan nuclear plant, it consolidates the Fang Jiashan site DCS level 2 upgrade project and extensive performance tests done on site. This paper also proposes multiple solutions from the aspects of hardware, scan rate, internal calculation treatment, main processing application task scheduling, and system structure, and also provides the final experiment result of these optimization solutions, the optimization ways provided guarantee for the safe plant operation. The solutions mentioned in this paper which have been proved to be successful and are valuable for the similar level 2 system during design or implementation phases, it has been implemented in Fang Jiashan Unit 1 and 2, also in Fuqing Unit 1 and 2. In addition, the solution will be also referred by Hainan Chang Jiang Unit 1 and 2 level 2 system upgrade.

### **References**

1. Atos world grid, Fang Jiashan KIC hardware and software design, 2011:48–53
2. Tan ping, Detail design of the Fang Jiashan optimization project. CNNC Nuclear Power Operations Management Co. Ltd. Zhejiang, China, 2015
3. Atos world grid, DCS V5 Performance Tests Synthesis. 2014.9:18–20
4. Atos world grid, DCS V6 Performance Tests Synthesis. 2015.10:28–31

# Pickering Generating Station Primary Heat Transport Pressure Control Analysis During Boiler Steam Relief Valve Testing

Polad Zahedi

**Abstract** During recent boiler steam relief valve (SRV) test on units 1 and 4 in Pickering generating stations, several incidences of heat transport system liquid relief valve (LRV) opening were experienced due to an overshoot in primary heat transport (PHT) system pressure. This specific LRV has a lower setpoint compared to the other PHT LRVs. The test requires opening six boiler SRVs, one at a time. This LRV only opens on some SRV openings on some occurrences of the tests. Based on simulations performed using the Pickering Training Simulator and hand calculations, it can be qualitatively concluded that increasing the bleed capacity by means of readjusting the bleed valve travel stops and recalibrating the valve strokes can reduce the magnitude of pressure overshoot experienced during the tests and can consequently reduce the chance of the LRV opening during such tests. However, there are issues associated with increasing the bleed capacity. These issues include possible pipe vibrations due to the increased flow through the bleed valves and reduced IX column effectiveness due to possible operation of purification circuit relief valve. Alternatively, based on the fact that the opening of this LRV during large pressure transients is the original design intent, maintaining the current configuration, accepting occasional LRV opening during the tests in conjunction with careful investigation, and monitoring of valve life cycle for the LRV, preventative maintenance, and pipe integrity can also be considered. Investigating the above issues and analyzing each potential solution are the main focus of this paper. Quantitative analysis and plant transient simulations are used in deriving conclusions. Operations and maintenance priorities and concerns are then considered to formulate a recommendation and path forward. In this case, considering all of the above, the approach of reducing the SRV opening time was taken to dampen the effect of PHT pressure oscillation. This approach satisfactorily resolved the issue eliminating LRV opening in subsequent SRV tests.

**Keywords** Process control · Primary heat transport · Steam relief valve test · Simulation · Plant modification

---

P. Zahedi (✉)  
Ontario Power Generation, Toronto, Ontario, Canada  
e-mail: polad.zahedi@opg.com

# 1 Problem Statement

During the recent E-012 tests on units 1 and 4, several incidences of heat transport system liquid relief valve (LRV) CV2 opening were experienced due to an overshoot in PHT system pressure. CV2 has a lower setpoint compared to the other primary heat transport (PHT) LRVs.

# 2 Background

The E-012 test requires opening six boiler steam relief valves (SRVs), one at a time. CV2 only opens on some SRV openings on some occurrences of E-012 tests. During the E-012 test on February 10, 2012, the opening of two of the SRVs caused CV2 to lift while the other four SRVs did not lift CV2. The Yokogawa data for this test is shown in Figs. 1, 2, 3, 4, 5, and 6.

Several contributing factors were originally considered as the cause of CV2 lifting during the E-012 tests:

1. Speeder Gear Rate Increase: during a recent modification, the speeder gear rate was increased from 200 to 600 RPM. The speeder gear rate increase, without a corresponding boiler pressure controller (BPC) gain change, can increase the overall steam pressure loop gain. In general, a large loop gain increase may contribute to some controllability issues such as overshoot and undershoot. Boiler pressure is linked closely to PHT pressure and a pressure overshoot in boiler can consequently cause a pressure overshoot in the PHT system.

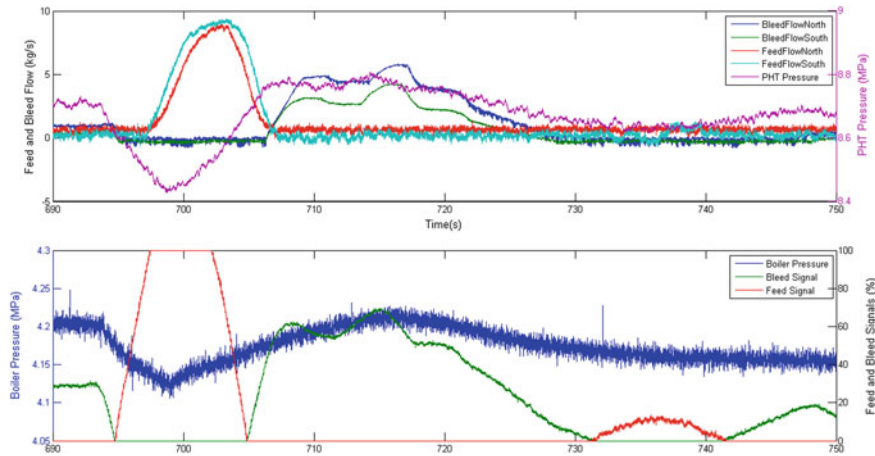


**Fig. 1** E-012 test—MV37 (Note that the Yokogawa boiler pressure data had a different time stamp in compare to the other variables and was synchronized by visual inspection)

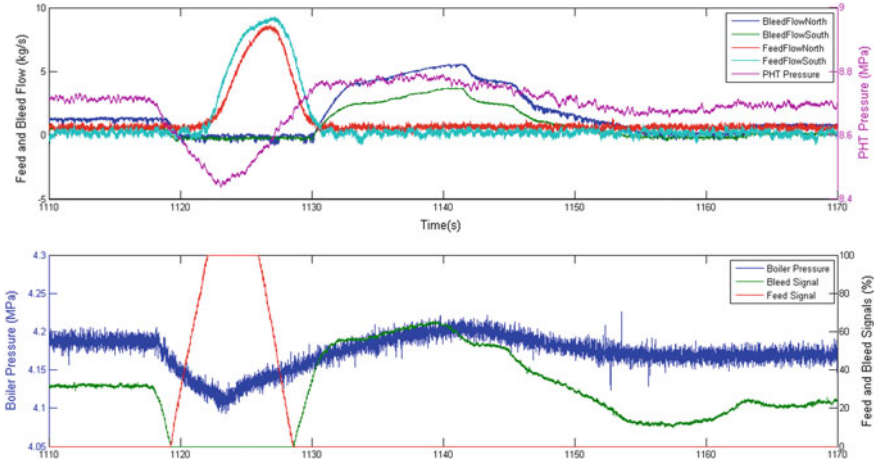


**Fig. 2** E-012 test—MV43 (Note that the Yokogawa boiler pressure data had a different time stamp in compare to the other variables and was synchronized by visual inspection)

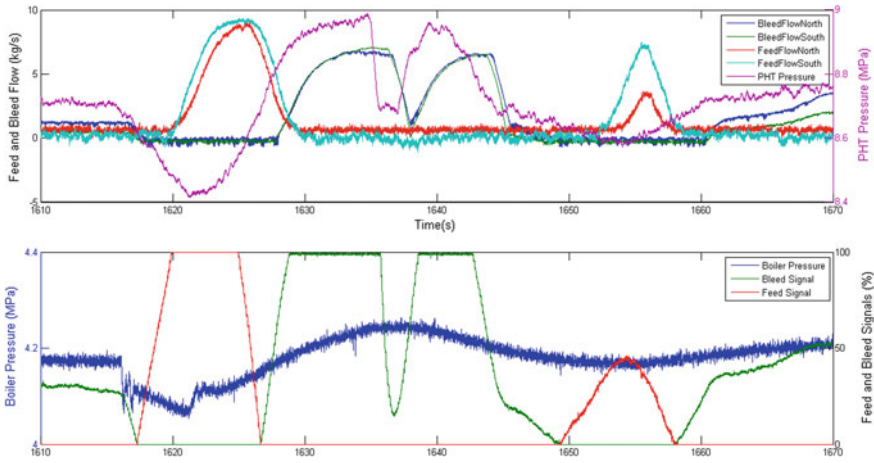


**Fig. 3** E-012 test—MV40 (Note that the Yokogawa boiler pressure data had a different time stamp in compare to the other variables and was synchronized by visual inspection)

2. CV2 Setpoint Reduction: It was realized that one of the LRVs (CV2) has considerably lower setpoint compared to the other LRVs (CV1, CV3, and CV4). It was suspected that the CV2 setpoint difference was introduced during a modification to the PHT system.
3. SRV Opening Time: As previously mentioned, the boiler and PHT pressures are closely linked. The magnitude of a transient in boiler can directly impact the magnitude of the corresponding pressure transient in the PHT system. Due to

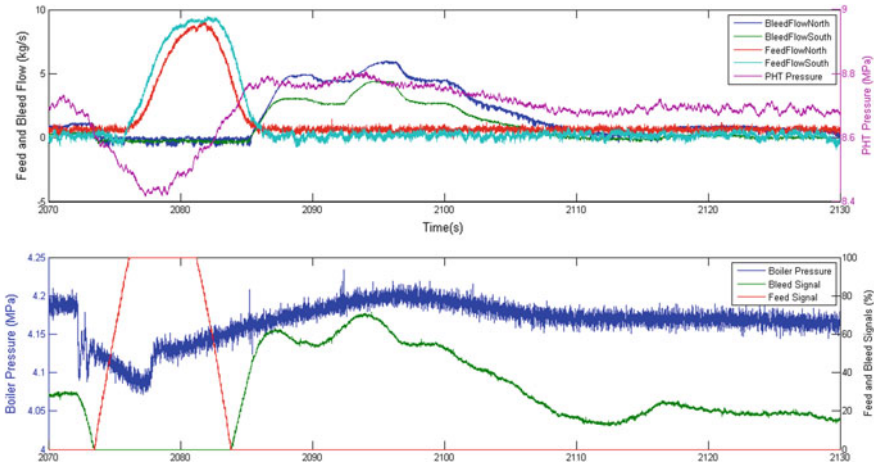


**Fig. 4** E-012 test—MV41 (Note that the Yokogawa boiler pressure data had a different time stamp in compare to the other variables and was synchronized by visual inspection)

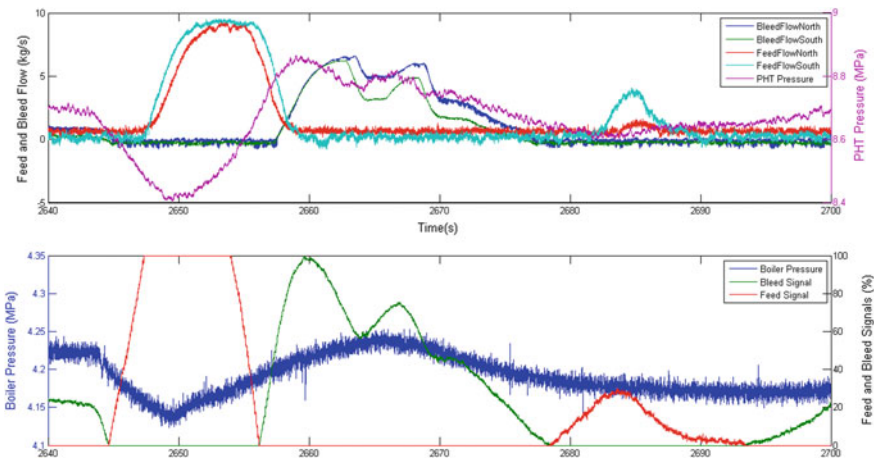


**Fig. 5** E-012 test—MV38 (Note that the Yokogawa boiler pressure data had a different time stamp in compare to the other variables and was synchronized by visual inspection)

this close link, the duration of time for which each of the SRVs was open at the time of E-012 test was considered as one of the contributing factors. The longer the time an SRV is open, the larger is the drop in boiler pressure which leads to lower PHT pressure. The lower PHT pressure leads to increased feed to correct the pressure which effectively increases PHT mass. The longer the SRV is open, the more feed may be added. Eventually, when SRV is closed, boiler pressure increases and with inadequate bleed capacity, PHT pressure increases causing CV2 to lift.

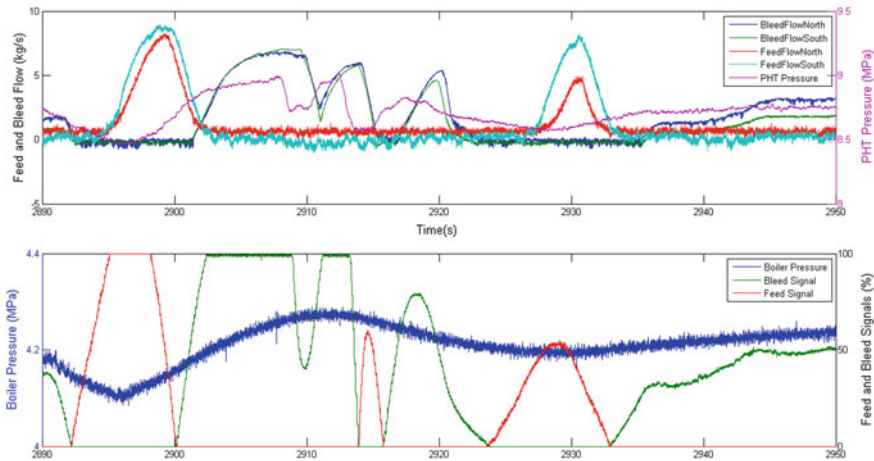


**Fig. 6** E-012 test—MV39 (Note that the Yokogawa boiler pressure data had a different time stamp in compare to the other variables and was synchronized by visual inspection)

4. **Bleed Valve Flow Restriction:** It was discovered, based on the valve stoke tests, that the PHT bleed valves are calibrated to a travel of 5/8". Based on the manufacturer’s specification, the total travel for the PHT bleed valves is 3/4". It is also suspected that these valves have mechanical travel stops installed that restricts their travel to 5/8". This travel restriction can cause bleed flow restriction when the valves are called to fully open for maximum bleed flow. A reduction in bleed capacity in PHT can cause a reduced effectiveness of the bleed circuit to reduce pressure and consequently dampen a PHT pressure overshoot.

### 3 Findings

The followings are the findings with regard to the above suspected contributing factors:

1. It was suspected that reducing the speeder gear rate to its original value or an intermediate value can reduce the boiler pressure overshoot and as a result reduce the PHT pressure overshoot. Based on the Pickering a turbine speeder gear control analysis, the original speeder gear rate (i.e., 200 RPM) limits the impact of the pulse from BPC on the governor valves and consequently on the boiler and PHT pressure. This would impact the BPC effectiveness during a reactor setback and require manual intervention to ensure a reactor setback does not lead to a reactor trip. In addition, although an intermediate speeder gear rate (i.e., 400 RPM) may be satisfactory during a reactor setback in preventing a

reactor trip, the PHT pressure can drop to 7.9 MPa, which is lower than that allowed by current practice [1].

2. Based on the original PHT design manual issued in 1972 (legacy document), the original design intent was to have one LRV (CV2) with a lower pressure set-point (i.e., 8.96 MPa) compared to the other CVs. The original design manual indicates that during maximum system maneuvering conditions, an increase in bleed capability is required to avoid a spurious high-pressure trip due to system pressure overshoot. This increase is obtained by including one relief valve within the bleed capability. When the heat transport pressure reaches this reduced setpoint, valve CV2 opens to increase the bleed capability [2].
3. The time for which each of the SRVs were open in the February 10, 2012 E-012 test is listed in Table 1. It can be concluded from Table 1 that the SRV open time does not have a strong correlation with CV2 lifting. Although MV40 which has the highest open time is one of the SRVs which lift CV2, MV39, the only other SRV which lifts CV2, has a lower open time than MV41 and MV38 which do not cause CV2 lifting.
4. Based on our communication with the valve manufacturer, the PHT bleed valves purchased in 1970 had 3/4" port size and 3/4" total travel. They also indicated that the travel stop of 5/8" was installed on the bleed valves at the time they were supplied. However, the Pickering plant design confirmed that the bleed valves currently have a port size of 1" [3]. This change in port size introduces a 59.8 % increase in valve flow coefficient ( $C_v$ ). It is suspected that this modification was performed in an attempt to increase the bleed capacity.

Increasing the valve total travel by means of adjusting the travel stop and recalibrating the valve can increase effective valve  $C_v$  and as a result increase the total bleed capacity. However, there are issues that need to be considered before execution of such modification.

- (a) There is a relief valve upstream of the purification circuit which has been provided to prevent overpressure of the IX columns. With the west bank of columns being used and with the bleed filter in the dirtiest tolerable condition (i.e., 25 psid at 180 Igpm) the relief valve will lift when the purification flow is increased to about 206 Igpm. This corresponds to a bleed flow of 174 Igpm (a gland return flow of 12 Igpm and leakage collection returns flow of 20 Igpm makes up the remainder). For the same bleed flow with a clean filter, the flow pressure at the relief valve will be nearly 30 psi below the opening

**Table 1** SRV open time during February 10, 2012 E-012 test

SRV name	Open time	LRV lifted?
MV 37	5.43	No
MV 43	5.32	No
MV 40	7.47	Yes
MV 41	5.89	No
MV 38	6.20	No
MV 39	5.55	Yes

pressure so that if the bleed filters gradually clog up while operating steadily at 174 Igpm bleed flow, the “high  $\Delta P$ ” alarm on the bleed filter will come in before the relief valve opening pressure is reached, thus allowing the other bank of columns to be valved in and the dirty filter cartridge replaced without bypassing any of the bleed around the purification columns. Thus the recommended maximum bleed flow with one bank of IX columns is 174 Igpm. This is within the capacity of one feed pump and gives a contact time of about 11 s in the IX columns [4]. The bleed flow limitation should be considered prior to any bleed capacity increase.

- (b) It is suspected that the bleed line may experience vibrations if the bleed flow through the bleed lines is increased. The possible bleed line vibration, given an increased bleed line flow, should be considered prior to any bleed line capacity increase.

## 4 Calculations

In order to increase the PHT bleed capacity through valve travel stop adjustment and recalibration, the impact of this adjustment on PHT pressure should be modeled and studied.

The PHT bleed valve travel stop adjustment will change the effective valve  $C_v$ . The change in effective valve  $C_v$  will impact the flow characteristic throughout the entire valve opening range since the valve will be recalibrated for the new total travel. In addition, the total excess pressure present in the PHT in case of a pressure overshoot following an E-012 test SRV opening should be predicted. The valve travel stop should be adjusted such that the excess bleed flow from the adjustment compensates for the predicted excess pressure in the PHT.

The excess pressure during an E-012 test pressure overshoot is defined as the amount of pressure which if eliminated through additional bleed flow could prevent CV2 from lifting. The elimination of this excess pressure will ensure that the PHT pressure does not exceed CV2 pressure setpoint (i.e., 8.96 Mpa). This excess pressure is shown as the area in yellow in Fig. 7. This area is constructed assuming a linear increase in PHT pressure from 1633 s up to the boiler pressure peak. It is assumed that the PHT pressure would increase with boiler pressure if CV2 did not lift. So, the yellow area in Fig. 7 presents the excess pressure that is needed to be relieved up to the boiler pressure peak to prevent CV2 from lifting:

$$\begin{aligned} \text{EPTI} &= \frac{(P_{\text{Peak}} - P_{\text{Set}}) \times (t_{\text{Peak}} - t_{\text{Set}})}{2} \\ &= \frac{(8997.5 - 8960) \times (1637 - 16312)}{2} \\ &= 97.13 \end{aligned}$$



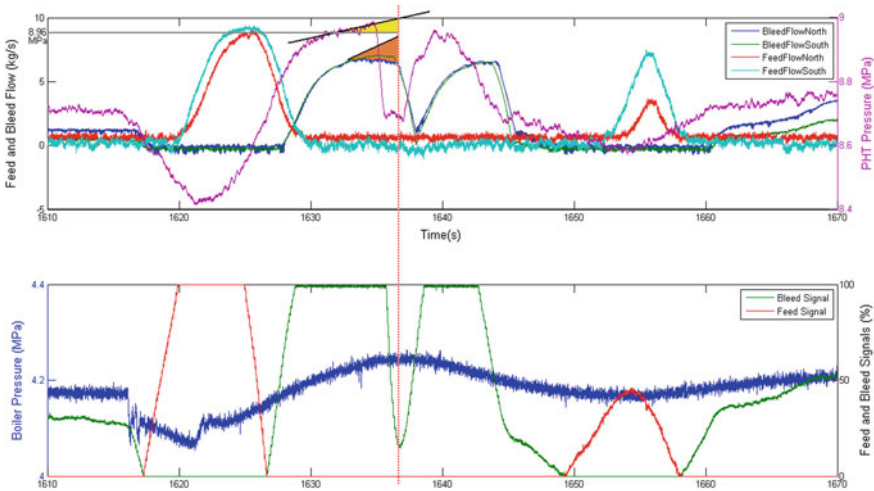


**Fig. 7** Bleed valve  $C_v$  calculation

where

- EPTI = Excess Pressure\_Time Integral (kpa. s)
- $P_{Peak}$  = Predicated Peak Pressure with no CV2 lift (kPa(g))
- $P_{Set}$  = CV2 Pressure Setpoint (kPa(g))
- $t_{Peak}$  = Time of Predicated Peak Pressure with no CV2 lift (s)
- $t_{Set}$  = Time of Reaching CV2 Pressure Setpoint (s)

The excess heavy water mass in the PHT is defined as the amount of heavy water that needs to be removed from the PHT circuit through an increased bleed capacity to prevent CV2 from lifting.

Based on the heat transport system design manual, one  $ft^3$  ( $0.028 m^3$ ) of heavy water added to one half of the heat transport system raises its pressure by about 33.5 psid (231 kPa(d)) or, if one cross connection between the two halves of the system is open, the whole system pressure is raised about 17 psid (117 kPa(d)) [4]:

$$CC_{PHT} = \frac{\Delta m}{\Delta P} = \frac{0.028 \times 800}{117} = 0.1932$$

where

$\Delta m$  = Added Heavy Water Mass (kg)

$\Delta P$  = Pressure rise corresponding to added Heavy Water Mass (kPa(d))

$CC_{PHT}$  = PHT Compressibility Coefficient  $\left(\frac{Kg}{kPa}\right)$

$$EMPT = EPTI \times CC_{PHT} = 97.13 \times 19.32 \times 10^{-2} = 18.77$$

where

$EMTI = \text{Excess Mass\_Time Integral}(Kg\ s)$

$$EHWM = \frac{EPTI}{(t_{Peak} - t_{Set})} = \frac{18.77}{(1637 - 1631.82)} = 3.62 \tag{1}$$

where

$EHWM = \text{Excess Heavy Water Mass (kg)}$

The excess bleed flow from the valve travel stop adjustment should be calculated in such a way as to relieve the predicted required excess heavy water mass. For this purpose, it is assumed that if the valve travel was increased, there would be a linear increase in bleed flow from the point that the original valve saturates up to the point that the predicted PHT pressure peak is reached (shown as the brown area in Fig. 7). In this case, the valve characteristic is calculated such that maximum opening is reached at the peak predicted PHT pressure. This is a conservative assumption since it assumes that the valve will not reach its maximum opening before the PHT pressure peak. The bleed valve takes about 5 s to reach its current maximum opening. Assuming that the valve opening time is linear throughout the range, it will take less than one second for the valve to travel from the current maximum valve opening to the new maximum opening:

$$\frac{(W_{NewMax} - W_{OldMax}) \times (t_{NewMax} - t_{OldMax})}{2} \times 2 = EHWM$$

$$\frac{(W_{NewMax} - 6.72) \times (1637 - 1633.04)}{2} \times 2 = 3.62$$

$$W_{NewMax} = 7.63$$

where

$W_{\text{NewMax}}$  = Maximum Flow with adjusted valve travel stop  $\left(\frac{\text{kg}}{\text{s}}\right)$

$W_{\text{OldMax}}$  = Maximum Flow with original valve travel stop  $\left(\frac{\text{kg}}{\text{s}}\right)$

$t_{\text{NewMax}}$  = Time of Reaching Maximum Flow with adjusted valve travel stop (s)

$W_{\text{OldMax}}$  = Time of Reaching Maximum Flow with original valve travel stop (s)

Note that the left-hand side of Eq. 1 has been multiplied by two to account for both north and south loop bleed flows.

The valve flow coefficient is calculated using the following equation:

$$C_v = F \sqrt{\frac{SG}{\Delta P}}$$

where

$C_v$  = Flow Coefficient of valve

$F$  = Rate of Flow  $\left(\frac{\text{kg}}{\text{s}}\right)$

$\Delta P$  = Pressure Drop Across valve (Pa)

$SG$  = Specific Gravity of Fluid  $\left(\frac{\text{kg}}{\text{m}^3}\right)$

Assuming that the specific gravity of heavy water and pressure difference between the two ends of the PHT bleed valve remains constant for different valve openings, the following can be assumed:

$$C_v = FK$$

where  $K$  is a proportionality constant ( $k = \sqrt{(SG/\Delta P)}$ )

The effective current  $C_v$  for the PHT bleed valves can be obtained based on information provided in Table 2. Based on a valve body size of 1", port size of 1" and original total travel of 3/4" the valve  $C_v$  can be obtained. 5/8" travel stop amounts to a valve opening of 83.33 %. Through interpolation the effective valve  $C_v$  is calculated to be 10.97. Based on the Yokogawa data the maximum bleed flow through one of the bleed valves is 7 kg/s:

$$K = \frac{C_v}{F} = \frac{10.97}{7} = 1.57$$

Table 2 Bleed valve flow coefficients

Micro-Form					Equal Percentage Characteristic										
Body Size (In.)	Port Diameter		Total Travel		Valve Opening—Percent of Total Travel										F <sub>L</sub> *
	In.	mm	In.	mm	10	20	30	40	50	60	70	80	90	100	
<b>C<sub>v</sub></b>															
1	1/4	6.4	3/4	19	.086	.124	.166	.227	.305	.426	.601	.867	1.23	1.59	.95
	3/8	9.5	3/4	19	.125	.194	.294	.431	.627	.890	1.25	1.74	2.40	3.06	.98
	1/2	12.7	3/4	19	.276	.432	.621	.870	1.21	1.65	2.25	3.03	4.05	4.97	.98
	3/4	19.1	3/4	19	.332	.600	.978	1.50	2.18	3.28	4.64	6.40	7.52	8.01	.95
	1†	25.4†	3/4	19	.690	1.09	1.65	2.52	3.70	6.11	8.62	10.5	11.9	12.8	.95
2	1/4	6.4	3/4	19	.075	.114	.161	.221	.304	.422	.593	.845	1.20	1.58	.95
	3/8	9.5	3/4	19	.094	.156	.249	.378	.568	.830	1.20	1.71	2.41	3.23	.98
	1/2	12.7	3/4	19	.249	.401	.571	.813	1.16	1.68	2.38	3.28	4.48	5.60	.98
	3/4	19.1	3/4	19	.425	.678	1.04	1.55	2.30	3.36	5.02	7.37	9.68	11.8	.92
	1	25.4	3/4	19	.673	1.08	1.67	2.53	3.88	5.90	8.87	13.4	17.3	19.9	.87
	1-1/4	31.8	3/4	19	.980	1.39	1.90	2.88	4.73	8.17	14.0	19.8	23.9	26.7	.89
		1†	25†	...	...	...	...	...	...	...	...	...	32.0	.89	
<b>X<sub>T</sub></b>															
1	1/4	6.4	3/4	19	.887	.707	.674	.673	.672	.675	.672	.671	.674	.671	...
	3/8	9.5	3/4	19	.859	.859	.859	.777	.681	.636	.624	.638	.696	.793	...
	1/2	12.7	3/4	19	.854	.754	.654	.611	.588	.602	.622	.662	.715	.830	...
	3/4	19.1	3/4	19	.613	.461	.408	.472	.629	.593	.653	.592	.685	.747	...
	1†	25.4†	3/4	19	.860	.752	.662	.617	.593	.456	.551	.685	.699	.715	...
2	1/4	6.4	3/4	19	.873	.873	.756	.706	.642	.575	.490	.408	.385	.413	...
	3/8	9.5	3/4	19	.847	.374	.344	.352	.343	.351	.370	.397	.437	.463	...
	1/2	12.7	3/4	19	.737	.657	.663	.614	.589	.532	.531	.567	.610	.719	...
	3/4	19.1	3/4	19	.649	.600	.559	.555	.540	.540	.514	.522	.573	.648	...
	1	25.4	3/4	19	.544	.505	.554	.593	.568	.566	.537	.519	.576	.654	...
	1-1/4	31.8	3/4	19	.559	.582	.623	.578	.509	.526	.651	.711	.714	.715	...
		1†	25†	...	...	...	...	...	...	...	...	...	...	.686	...

Based on  $W_{NewMax}$  and  $K$ , new flow coefficient can be calculated:

$$C_v = W_{NewMax} \times K = 7.63 \times 1.57 = 11.98$$

This  $C_v$ , based on Table 2, corresponds to 90.89 % or 0.682" valve opening. From the above calculation, it can be concluded that adjusting the valve travel stop from 0.625" (current value) to 0.682" can provide enough additional bleed capacity to potentially eliminate the CV2 lifting.

## 5 Simulations

The concept of adjusting the bleed valve travel stop to increase bleed capacity was also tested on the training simulator. For this purpose, two test cases were simulated. In the first test case, the simulator was set up based on the current plant configuration while an E-012 test was performed. CV2 lift was confirmed. In the second test case, the bleed valve travel stop was adjusted, by trial and error, to eliminate CV2 from lifting during an E-012 test (through increased bleed capacity).

In order to construct the first test case, the feed and bleed valve characteristics were matched to body size of 1", port size of 3/4" and total travel of 3/4" valve data from the manufacturer. This data can be found in Table 2. It was also ensured that stem position stops were placed at 5/8". The feed and bleed lines were then sized through adjustment of their conductance, so as to yield the same maximum feed and

bleed flow as the Yokogawa data. Figures 8, 9, and 10 show the results of the first test case. Based on Yokogawa data, the E-012 test caused reactor outlet heater (ROH) pressure to drop to approximately 8.4 MPa(g). In order to cause the same pressure drop in the training simulator, the SRV had to be opened for 22 s. This resulted in a boiler pressure drop of approximately 0.1 MPa and resulted in the CV2

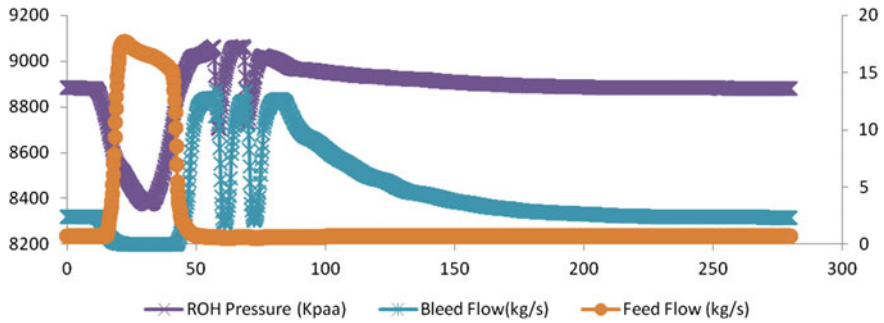


Fig. 8 Test case #1

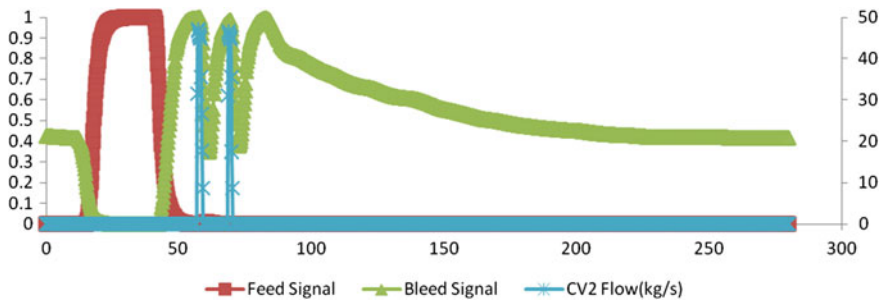


Fig. 9 Test case #1

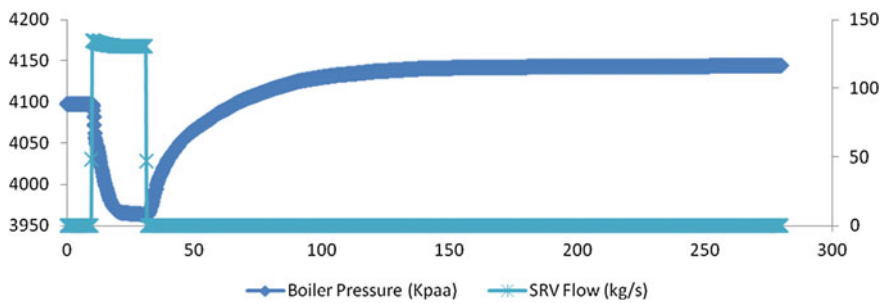


Fig. 10 Test case #1

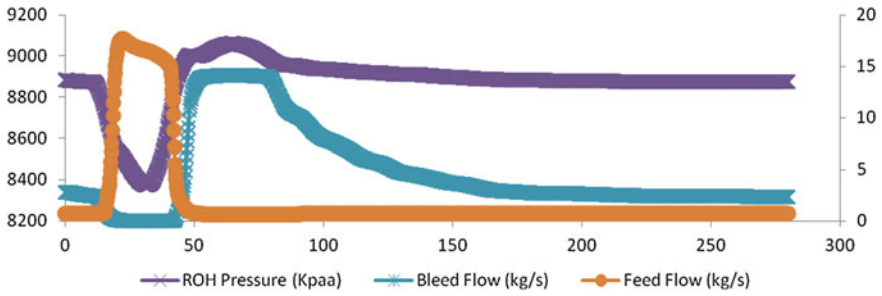


Fig. 11 Test case #2

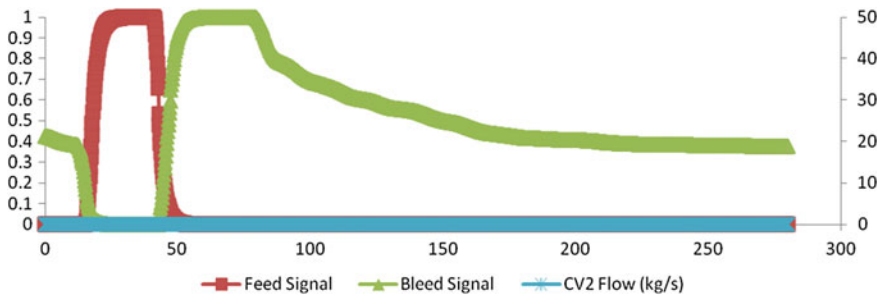


Fig. 12 Test case #2

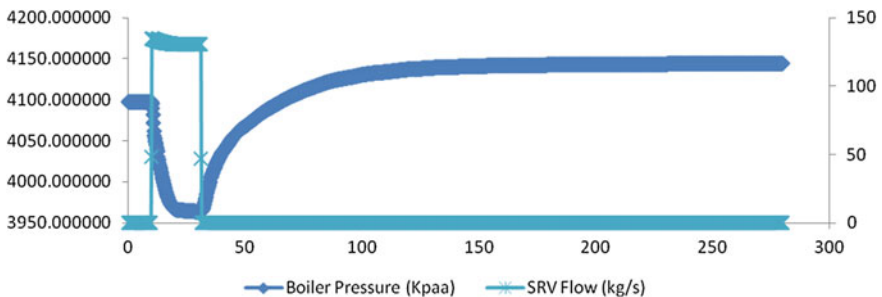


Fig. 13 Test case #2

lifting twice. Similar effect can be seen in MV39 E-012 test on February 10, 2012 where CV2 lifts twice as shown in Fig. 6.

Figures 11, 12, and 13 show the results of the second test case. With bleed valve travel stop adjustment from 0.625" to 0.69" CV2 lifting was eliminated.

Note that the difference between the magnitude of ROH pressure in the simulation plots and PHT pressure in the Yokogawa plots is mainly due to difference in pressure presentation convention. Simulator plots use absolute pressure and Yokogawa plots use gauge pressure.

## 6 Conclusion

Based on the calculations and simulation test cases, it can be qualitatively concluded that adjustment of PHT bleed valve travel stop can increase overall bleed capacity. This increase in bleed capacity can potentially dampen the pressure overshoot during E-012 test to a level sufficient to eliminate CV2 lifting. However, some considerations should be made with regards to increasing PHT bleed capacity. For instance, bleed line pipe vibrations and IX column effectiveness are some of these considerations.

Alternatively, based on the fact that the opening of CV2 during large pressure transients is the original design intent, maintaining the current configuration, accepting occasional CV2 opening during E-012 tests in conjunction with careful investigation, and monitoring of valve life cycle for CV2, preventative maintenance, and pipe integrity can also be considered.

Several other possible solutions to the CV2 lifting issue were studied. It was concluded that execution of these solutions would either deviate the plant configuration from its design values or would introduce adverse effects on other interconnected systems. In this case, considering all of the above, the approach of reducing the SRV opening time was taken to dampen the effect of PHT pressure oscillation. This approach satisfactorily resolved the issue eliminating LRV opening in subsequent SRV tests.

## References

1. Pickering A Turbine Speeder Gear Control Analysis; March 2008
2. Heat Transport System Feed, Bleed and Relief Systems (Legacy Documents); October 1974
3. Size 1" Design DBQ 2" SCH 80 ANSI Butt Weld End Diaphragm Actuated Control Valve Assy; July 1982
4. Heat Transport System Feed, Bleed And Relief Systems; December 2007

## Author Biography

**Polad Zahedi** is an assistant technical engineer/officer in the Computers and Control Department of Ontario Power Generation Inc. His primary research area is process control analysis, dynamic modeling, and simulation. Polad obtained his masters of applied science from the Mechanical Department of University of Toronto. His thesis was on Tritium Removal Facility process control analysis and modeling. Polad obtained his undergraduate degree in computer engineering from the University of Western Ontario. His undergraduate thesis was on CANDU Boiler Level Control Optimization.

# Pressurizer Water Level Control by Makeup and Letdown Flows Operating in Discontinued Model

Jie-qiong Zhang and Chu-hua Tang

**Abstract** The function of pressurizer water level control is to maintain a programmed water level in the pressurizer during its automatic operation [1, 2]. The system maintains the water level in the pressurizer, and indirectly maintains reactor coolant system inventory, within operating bounds and reduces the potential for pressurizer going water-solid and heater discovering. This paper proposes an optimized control method for pressurizer water level controlling by analysis and calculating the relationship between reactor coolant average temperature and pressurizer water level. The control method will simplify control strategy and obviously reduce the frequency of actuator operating for pressurizer water level controlling by makeup and letdown flows operating in discontinued.

**Keywords** Pressurizer · Water level · Control · Makeup · Letdown

## 1 Introduction

The pressurizer water level control system maintains the water level in the pressurizer, and indirectly maintains reactor coolant system inventory, within operating bounds and reduces the potential for pressurizer going water-solid and heater discovering [3]. The system controls the pressurizer water level by makeup and letdown flows, makeup when actual pressurizer water level is lower than programmed level and letdown when actual pressurizer water level is higher than programmed level [3]. This paper proposes an optimized control method for pressurizer water level controlling by analysis and calculating the relationship between reactor coolant average temperature and pressurizer water level. The control method will simplify control strategy and obviously reduce the frequency of actuator operating for pressurizer water level controlling by makeup and letdown flows operating in discontinued module.

---

J. Zhang (✉) · C. Tang  
China Nuclear Power Engineering Co., Ltd, Beijing, China  
e-mail: zhangjq-38112@163.com



## 2 Overview

The two main functions of pressurizer water level are reducing the makeup and letdown flow of coolant for declining the load of waste and keeping more space of steam for main system pressure control especially for discontinuous running mode of makeup and letdown [4].

To explain the pressurizer water level control function, the basic control method used in current PWR is introduced first, then programmed water level set-points is analyzed and calculated by actual parameter of AP1000, and finally an optimized pressurizer water level control strategy is proposed by analyzing the relationship of calculated water level set-points and engineering design for discontinuous running mode of makeup and letdown.

Attention should be paid to the water level control method that is proposed in this paper which is only for automatic running after the bulb is established in the pressurizer and mainly for power operation.

## 3 Level Control Mode

The reactor coolant system controls the pressurizer water level by makeup and letdown flows, operating in continued or discontinued mode, which is determined by used main pump [1].

Discontinuous makeup and letdown flows are applied in the AP1000 pressurizer water level control system due to the shielded main pump. Figure 1 presents the control strategy during power operating. The AP1000 pressurizer water level is controlled in a wide level band, which is about  $\pm 10\%$  bias to programmed level. Manual control is needed when the coolant temperature is less than  $290\text{ }^{\circ}\text{C}$  or above  $300\text{ }^{\circ}\text{C}$ , which means that manual control is needed when the reactor power is outside the bound of 0–100 % thermal power.

**Fig. 1** AP1000 makeup and letdown [3]

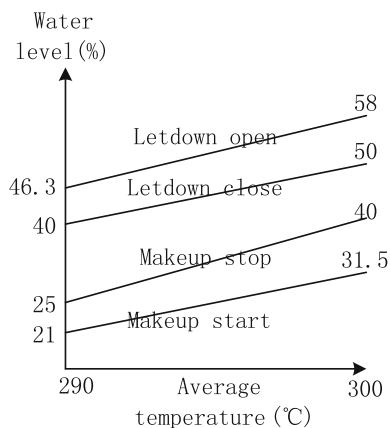


**Fig. 2** M310 pressurizer program set-points [5]

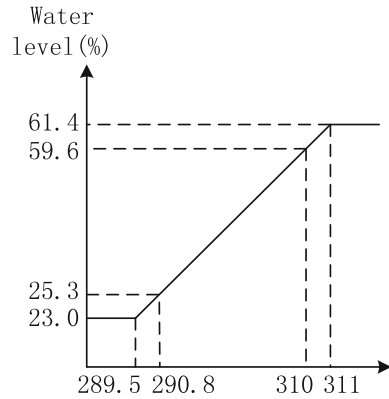


Figure 2 presents the control strategy for the M310 pressurizer water level control system. The pressurizer water level is strictly controlled to programmed level, and automatic control is switched as soon as the bulb is established in the pressurizer (Fig. 2).

#### 4 Programmed Level Set-Points

There are two basic target should be achieved by the pressurizer water level control system, one is the coolant should be involved as much as possible in the reactor coolant system during thermal power changes, which will result coolant volume change; the other is bulb in the pressurizer should be maintained as bigger as possible under the condition of undiscovering of heater tube, which is 14 % set-point of the total pressurizer water level.

To achieve the pressurizer water level control target, the basic relationship should be built between the coolant temperature and the pressurizer water level after bulb is established in the pressurizer. As the relationship is related to design parameters of the reactor coolant system, the AP1000 related system parameters is adopted to calculate and analyze the trend. It should be noted that the vessel volume changes is not contained in calculation during the coolant temperate changes, which make the actual pressurizer water level should be less than the calculated one.

For the AP1000, the total volume of the reactor coolant system is 299 m<sup>3</sup>, the pressurizer is 12.776 m high, 2.54 m in diameter, and the total volume of the pressurizer is 59.4 m<sup>3</sup> [1]. It is assumed that the bulb is established in the pressurizer at 230 °C of the coolant temperature, the reactor coolant system pressure is 9 MPa, and the initial pressurizer water level is 40 % when it is switched to automatic mode. By the parameters, it can be calculated that the initial coolant volume is 263.36 m<sup>3</sup>, the initial coolant mass is 216276.59 kg, the initial bulb mass is 1739.81 kg, and the initial total mass is 218016.40 kg in the reactor coolant system.

**Table 1** AP1000 average temperature versus water level

Temperature (°C)	Liquid level (%)	Temperature (°C)	Liquid level (%)
289.574	31.62	295.836	41.46
290.496	33.04	296.697	42.85
291.408	34.45	297.549	44.24
292.311	35.86	298.394	45.63
293.205	37.27	299.231	47.00
294.091	38.67	300.06	48.38
294.968	40.07		

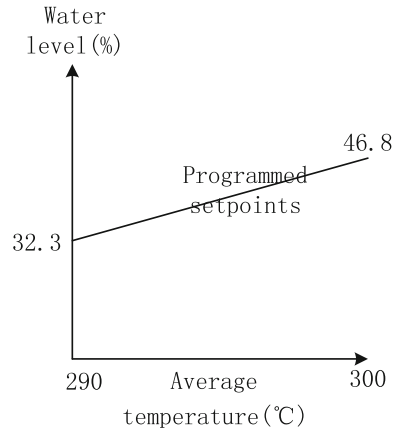
As the coolant temperature increase, the volume of the coolant will expand as the mass of the coolant maintains its initial quantity. The volume will expand to 297.6 m<sup>3</sup> when the reactor coolant temperature increases to 290 °C and system pressure increase to 15.5 MPa, which means that the pressurizer bulb nearly disappeared, if there is no makeup or letdown maneuver introduced. The volume of pressurizer bulb should be controlled to about 1/3–2/3 of the total volume of the pressurizer in favor of controlling of the pressurizer pressure; so many times of letdown maneuver should be needed to maintain the volume of bulb. The pressurizer water level will adjust to 32.3 % by manual operation eventually at 290 °C of the coolant temperature, and then the control system is switched to auto mode. It can be easily calculated that the coolant volume is 258.79 m<sup>3</sup>, the coolant mass is 186933.39 kg, the initial bulb mass is 3957.68 kg, and the initial total mass is 190891.07 kg in the reactor coolant system at the state of the zero thermal power. Table 1 presents the values of the pressurizer water level as the coolant temperature ascends from 290 to 300 °C at about 1 °C intervals.

The pressurizer water level data indicates a strong linear relationship with the reactor coolant temperature. The pressurizer water level increases to 48.38 from 32.3 % when the reactor coolant temperature ascends from 290 to 300 °C, and the slope is about 1.6 %/°C. The actual water level is about 46.8 %, because the calculated water level ignores the vessel swell which may introduce 1.58 % water level error.

Similarly, the relationship between the pressurizer water level and the coolant temperature is calculated for the M310. The pressurizer water level increases to 57.9 from 25.3 % when the reactor coolant temperature ascends from 290.8 to 310 °C, and the slope is about 1.67 %/°C.

Figure 3 shows the programmed the pressurizer water level set points. To simplify the control strategy, the programmed level set points is set linear to the coolant temperature with a slope of about 1.6 %/°C, and the initial pressurizer water level is set to 32.3 % for the pressurizer heater tube undiscovering consideration.

**Fig. 3** AP1000 pressurizer programmed set points



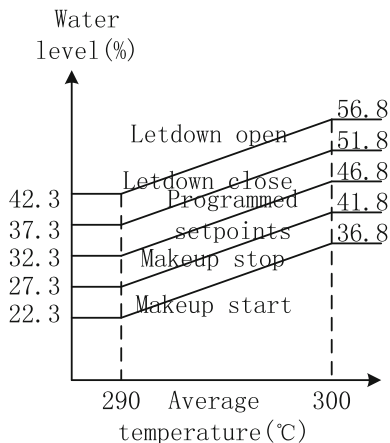
### 5 The Analysis of Problem and Solution

The process of makeup and letdown is controlled by the difference between actual level and set points. The pressurizer water level will change about 15 % as the reactor coolant temperature changes when the reactor thermal power ascends from 0 to 100 % for AP1000. There is enough space to control the pressurizer in a wide band, and so the discontinuous running mode of makeup and letdown is figured out. This method is simple and efficient, but the current control mentrol is much complicated for it should calculate and adjust water level difference on every power. This paper proposes a simplified control method without change performance of the system by a fixed water level difference.

It can be seen from Fig. 1 that the pressurizer water level ascends from 46.3 to 58 % when the reactor coolant temperature ascends from 290 to 300 °C which represents 0 and 100 % reactor thermal power in AP1000, and it can be calculated that the slope of letdown open line is 11.7 %/°C. For other control lines, the slope of letdown close line is 10 %/°C, the slope of makeup stop line is 15 %/°C, and the slope of makeup start is 10.5 %/°C. The slope of the program level set points is 14.5 %/°C in Fig. 3, the water level difference between each control line and program level set points will change with different coolant temperature changes, then the control methodology will be much more complicated to accomplish the control strategy which is unnecessary for the function of the pressurizer water level control.

The slope of four control lines is set to 14.5 %/°C and keep consistent with that of program level set points, then the water level difference will be fixed as the reactor coolant temperature ascends from 290 to 300 °C, and the methodology is much simplified and more efficient than before. It will be much suitable by setting the water level difference between start set points of makeup and letdown and program level set points to ±10 % and the water level difference between stop set

**Fig. 4** Optimized control strategy



points of makeup and letdown and program level set points to  $\pm 5\%$  considering the lowest and highest pressurizer water level needed. Then the optimized pressurizer water level control strategy is shown in Fig. 4.

Figure 4 broadens the control scope which is much convenient for reactor operation. The control strategy alleviating the burden of operator during coolant temperature ascends from the coolant temperature when the bulb of the pressurizer is established to  $290\text{ }^{\circ}\text{C}$  by substituting manual control mode with automatic one, and so as to overpower operation condition. It is much better to adjust pressurizer water level to program level set points after each maneuver of dilution and boronation before switching to automatic mode, though it is not necessary.

## 6 Conclusion

The optimized pressurizer water level control strategy is proposed by simplifying the control methodology and broadening the automatic control scope, which is based on calculation on the relationship between reactor coolant temperature and pressurizer water level. The optimized control strategy alleviates the burden of operator during coolant temperature ascending from the coolant temperature when the bulb of the pressurizer is established to  $290\text{ }^{\circ}\text{C}$  by substituting manual control mode with automatic one, and so as to overpower operation condition.

## References

1. AP1000 Nuclear power station system and equipment, Atomic Energy Press, 2010.
2. 900 MW Nuclear power station system and equipment, Atomic Energy Press, 2010.
3. Chemical and volume control System-System Specification Document.
4. Reactor coolant System-System Specification Document.
5. RRC system manual.

# **Qinshan 300 MW Nuclear Power Unit Condensed Water Dissolved Oxygen on the High Side Cause Analysis**

**Zengwei**

**Abstract** Qinshan 300 MW nuclear power unit is introduced in the winter when the condensate **water** of operation under low load, and the mechanism of dissolved oxygen on the high side. Combined with the unit operation mode, the condensate dissolved oxygen changes trend analysis of condenser vacuum system and related system, equipment, temperature, etc. The causes of the unit water dissolved oxygen on the high side. Developed detailed screening measures, and puts forward the follow-up discussion, provide reliable guarantee for safe and economic operation of the unit.

**Keywords** Condensed water · Dissolved oxygen · On the high side

## **1 Foreword**

Water dissolved oxygen is one of WANO chemical performance index calculation parameters of 300, 300 MW WANO content on the high side will affect chemical performance index control and accelerate the condensate system pipeline corrosion of equipment.

In view of the steam generator the pipe rupture is the probability of large nuclear accident, the need for the steam generator design and manufacture of taking preventive measures of stress corrosion cracking at the same time, on the operation and management, strict control and management of water quality in secondary circuit, tend to have a great contribution to prevent the pipe burst. Qinshan 300 MW nuclear power unit of the pipe steam generator using Incoloy—800, the operation rules need to condense the water content of dissolved oxygen (O<sub>2</sub>) control in less than 5 μg/L value. Units in normal operation, the condenser in the normal vacuum condition, the condensate should be qualified, the dissolved oxygen is leaking due

---

Zengwei (✉)

CNNP Nuclear Power Operations Management Co., Ltd., Haiyan, Zhejiang, China  
e-mail: jianghong@cnpe.cc

to the condenser vacuum negative pressure system, filling water system and hydrophobic system design aspects of reasons, unqualified water dissolved oxygen on the high side and long-term problems.

## **2 The Dangers of 300 MW Unit Water Dissolved Oxygen on the High Side**

1. Because oxygen and metal can produce electrochemical corrosion, water dissolved oxygen content sharply higher or unqualified for a long time, accelerates the condensate pipeline corrosion and thermal system. The production of iron scale affects the service life of the auxiliary equipment and reduces the reliability of unit operation. Qinshan 300 MW unit adopted regenerative cycle system, when the water through heat recovery system with high oxygen content of equipment and its accessory line, can accelerate the condenser to the deaerator equipment corrosion in the system, increase the burden of deaerator equipment, affect the deaerating effect.
2. High water dissolved oxygen content will aggravate the burden to remove oxygen from the water, often causing water dissolved oxygen unqualified, causing high pressure feed water system of oxygen corrosion and increase the iron content in feed, speed up the evaporator of the heat pipe, heating surface fouling, reduce the heat transfer efficiency of the evaporator, may cause the evaporator U the pipe burst, influence the safe operation of the evaporator. Condensate of high oxygen content also increases the steam iron content, speed up the scale of turbine blade, a threat to blade, reduce the operating efficiency of the steam turbine, and affect the safe operation of steam turbine.
3. Unit condenser running in the high vacuum state, if it is too much air leakage to the steam side of the vacuum unit, will reduce. Increase in the volume of the air inside the condenser to be gathered together, increase the ejector work burden, not within the condenser condensate gas cannot pull out, a further increase in the volume of the air inside the condenser to be gathered, thereby reducing the condenser in thermal efficiency, improve the operation of the condenser pressure, lower thermal efficiency of the unit.

## **3 The Mechanism of the Water Dissolved Oxygen**

Water dissolved oxygen mechanism is in accordance to the law of gas dissolved (Henry's law): at a certain temperature and pressure, the solubility of a gas in a liquid is proportional to the balance of the gas pressure. So clear air leakage quantity increases, increasing the partial pressure of air, water dissolved oxygen content increases, the condensate supercooling degree increased, the water



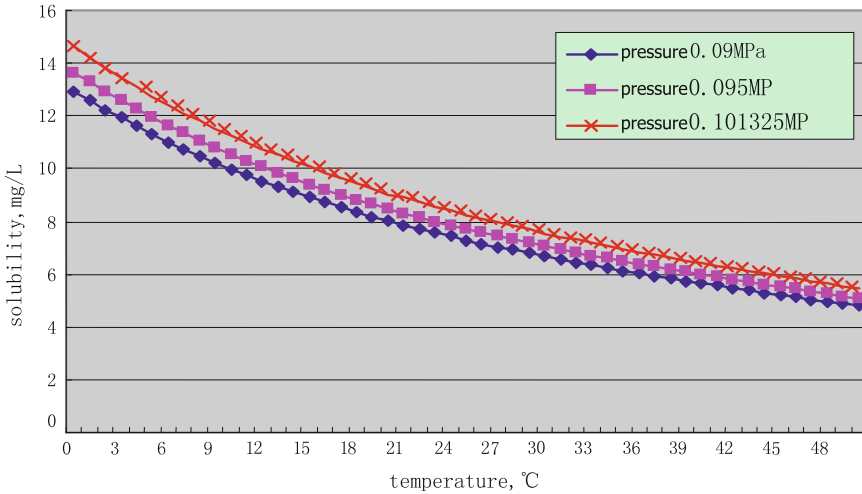


**Fig. 1** Different pressure of oxygen in the air is saturated solubility in water

dissolved oxygen also will increase, if not to leak into the air and supercooling degree zero, oxygen solubility in the liquid tends to zero, as shown in Fig. 1. The two factors influencing the water dissolved oxygen is the condensate supercooling degree and the leak into the air [1].

### 3.1 Air Leakage into the Reason

Air leakage into the condenser increases the air pressure, thus increasing the air in the water, solubility of the condensation water dissolved oxygen content increases. The water dissolved oxygen content increases with the increase of air leakage into the amount.

The cause of the 300 MW unit of air leakage into the: steam turbine vacuum system cannot be absolutely tight, in the vacuum state of steam turbine low pressure exhaust steam, there will always be the condenser tube and valve, air leak is so pure that the steam entering the condenser in fact is not steam but gas mixtures. The pressure inside the condenser is the sum of the partial pressure of the mix. Ejector efficiency of high and low smoke and empty area design is reasonable and directly affect the oxygen content of the condensate, in certain cases no condensation gas extraction of gas amount is much, the dissolved oxygen in condensate, and vice versa. The steam is condensed in the air and other gas separated from steam in the process of steam condensation was siphoned off, so the condensate of dissolved oxygen on the high side should mainly come from the negative pressure of the frozen water area. Condenser leakage of corrosion or cracking, bulging leakage circulating water leakage into the hot well, not only affect the water quality but also

influences the water dissolved oxygen, although the dissolved oxygen is very high, but circulating water leakage quantity is small and the risk of leakage is small. All kinds of hydrophobic recovery into oxygen, such as main feed water pump shaft seal back (to the pump shaft seal water tank back through the atmosphere), steam generator domestic sewage recycling, sewage sampling boxes on atmospheric), such as direct access to the condenser hot well.

### ***3.2 The Reason of Supercooling***

The condensate supercooling degree of [2] is the condensate in the condenser hot well under cooling degree of condensate hot well export water temperature and the condenser in the exhaust steam pressure corresponding saturation temperature difference is called supercooling degree. Modern device for the condenser to supercooling degree of not more than 0.5–1 °C. Supercooling degree increased, the water dissolved oxygen also will increase.

300 MW unit too cold reason: as the steam from the exhaust mouth to lower flow resistance, lower steam pressure is lower than the upper pressure, the lower water temperature was lower than those of the upper, and had a cold, in addition, the steam is cooled into droplets flow between the condenser cooling water pipe, due to the droplet temperature higher than the cooling water pipe wall temperature, water cooled below the saturation temperature thereby, had a cold, and leak into the air, air pressure, steam partial pressure is relatively lower, the steam condenses, are still under pressure from their own points make the water temperature is lower than the exhaust temperature, had a cold, if ejector not out in time, increase the heat transfer resistance, also make supercooling degree increases, thus make the condenser dissolved oxygen increases; the condenser hot well water is higher than the normal range, titanium tube, cooling water and take away heat and cooling, part of the condensate supercooling degree increasing, the condensate increase dissolved oxygen; circulating water temperature was low and circulating water is too large, the condensate by excessive cooling, supercooling degree increases, the relative increase dissolved oxygen.

## **4 Water Dissolved Oxygen Content Is the Reason Analysis**

### ***4.1 Dissolved Oxygen Changes Analysis of Condensate Pump Discharge***

The condensate system since the condenser to the condensate pump area, the condensate is in negative pressure area, is the most important occurrence area water dissolved oxygen on the high side. Prior to October 25, 2013, condensate pump

export value has been dissolved oxygen control is good (below 2  $\mu\text{g/L}$ ), this may be related to the last time during overhaul, condenser water leak for a long time, again to funnelled to ensure that the condenser for getting rid of rigor have certain relations. But with the increase of 2013 running time, temperature and water temperature gradually reduce, the content of dissolved oxygen in condensate increased: October 25, 2013 up to about 6  $\mu\text{g/L}$  in the future, on November 18 2013 condensate pump export 10  $\mu\text{g/L}$ , dissolved oxygen in February 2014, 13 condensate pump outlet dissolved oxygen more than 18  $\mu\text{g/L}$ . visual check during condenser and condensate pump suction negative pressure zone, without exception. Show that: with the lengthen of time, the equipment operation because of condensing equipment is often the effect of thermal stress and mechanical stress, its rigor gradually decline, air infiltration quantity increase gradually, cause water dissolved oxygen increased as shown in Fig. 2.

Because of the condensate pump is to adopt the way of packing seal and seal water seal, at the same time under the water pump is in a state of negative pressure operation, to seal the seal water is the pressure of the pump discharge into the water, so when the pump in standby state, easily lead to bad sealing water sealing, which can lead to air leakage into the pump, condensate oxygen content on the high side. According to the mechanism of the water dissolved oxygen, eliminate the influence of the temperature (because of the dissolved oxygen content is inversely proportional to the temperature), theoretically, the winter water dissolved oxygen content on the high side main reason: doubt condensate pump body parts (especially the negative pressure and positive pressure alternating section) and sealing parts have air leakage into the water, or condenser rigor fuel cycle is slightly worse than ever, the condensate system pressure section, flanges, valves and other equipment, untight seal water vacuum system may be unchecked to funnelled, and some cannot

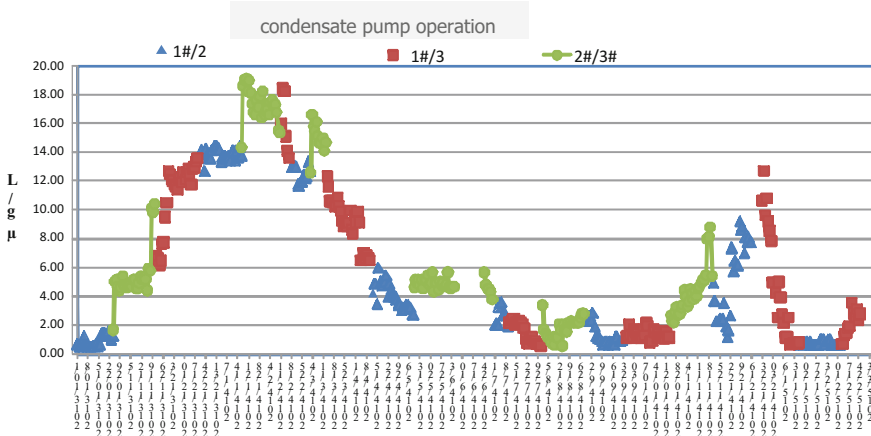


Fig. 2 October 2013 to February 2015, dissolved oxygen content in the tendency of the export of condensate pump figure [3]

through the condenser water filling method for leak inspection equipment such as pump shaft seal water tank funnelled back.

#### ***4.2 Steam Generator Domestic Sewage Recycling to the Condenser***

After minor repair unit in 2014, January 1, 2015 after the full power of unit steam generator domestic sewage by emissions cut directly to the condenser recycling, steam generator prominence on January 1, 2015 domestic sewage recycling to the condenser, if dissolved oxygen online table is normal work, the oxygenated water saturation add instrument is still used in condenser in 2.5–4  $\mu\text{g/L}$ . On January 14–22, 2015, the steam generator domestic sewage from condenser recycling cut to direct emissions (condenser hydrating about 20 t/h), dissolved oxygen content in the tendency of the export of condensate pump diagram as shown in Fig. 2, show that the saturation oxygen add water into the condenser had no significant effect of condensate pump outlet dissolved oxygen content.

#### ***4.3 The Condenser Vacuum Effects on Water Dissolved Oxygen***

Of the condensate water temperature in the same circumstances, condenser vacuum degree is relatively high, low points, condensation water dissolved oxygen content is relatively low. C14 loop in November 2012 to February 2013, condenser vacuum, 740–746 mmHg (1.86–2.66 kPa), dissolved oxygen content in the condensate pump exports—19  $\mu\text{g/L}$ . C15 loop in November 2013 to February 2014, condenser vacuum, 743–757 mmHg (0.40–2.26 kPa), condensate pump outlet dissolved oxygen content is 4.0–11  $\mu\text{g/L}$ . C14 cycle condenser vacuum is higher than C15 cycle 11 mmHg, condensate pump outlet dissolved oxygen content is relatively lower around 8  $\mu\text{g/L}$ .

#### ***4.4 Circulating Water Flow's Influence on Water Dissolved Oxygen***

Due to the condenser device runs for a long time, the condenser and condensate pump in the vacuum state, it is hard to avoid air infiltration of condensate water, with the seasons, the temperature drops, the condensate will be excessive cooling,

oxygen in the air is gradually increasing solubility in the water, cause water dissolved oxygen content gradually increased as shown in Figs. 1 and 2.

After switching cycle pump, circulating water flow increase, the circulating water outlet butterfly valve opening, the condensate by excessive cooling, super-cooling degree increases; (winter and is especially significant load down during Spring Festival) makes the condensate by excessive cooling, the condenser inlet exhaust temperature lower (low temperature, increase the solubility of oxygen in the water), result in slight increase in water dissolved oxygen content.

#### ***4.5 The Influence of Water Supply Water to the Water Dissolved Oxygen***

The qinshan 300 MW condenser filling water without oxygen is in addition to salt water, fill the water, the greater the more oxygen into the condenser. In addition to the brine in salt water tank through the condenser water inlet valve automatically or add in addition to salt water pump directly into the condenser. Because in addition to salt water tank placed outside, in addition to the brine temperature basically for the environment temperature, below the condensation water tank water temperature, dissolved oxygen concentration and 20 °C environment water at about 7000–9000  $\mu\text{g/L}$  (see Fig. 1), equivalent to 1000 times the condensation of oxygen content in water. Add in addition to salt water reaches the saturation temperature under corresponding exhaust back pressure, the dissolution of precipitation, air and may cause excessive water dissolved oxygen. But the summer temperature rise, the increase of the condenser water supplement, condenser vacuum has a certain degree of decline, the water dissolved oxygen content here is relatively lower than 5  $\mu\text{g/L}$ , it is concluded that the increase of the condenser water supplement, condensate pump outlet dissolved oxygen content had no obvious change as shown in Fig. 2.

## **5 Have Done Screening Measures**

### ***5.1 1# Condensate Pump Switch Test***

In order to prevent the backup system of the condensate pump leak caused water dissolved oxygen content is higher, 1# condensate pump the switch test, field observation three condensate pump seal water pump body, found that 1# condensate pump seal water is minimal. Condensate pump outlet dissolved oxygen content in 1# condensate pump operation condition was lower than those of 1# condensate pump stop working about 3–4.7  $\mu\text{g/L}$  as shown in Table 1.

**Table 1** 1# condensate pump condensate pump outlet dissolved oxygen changes before and after the switch

Condensate pump switch time	Condensate pump switch	Condensate pump before and after the switching time	Water dissolved oxygen (μg/L)
2014-03-03	1# → 3# (2, 3#)	2014-03-02	13.8
		2014-03-04	18.5
2014-03-14	2# → 1# (1, 3#)	2014-03-13	14.6
		2014-03-15	11.5
2014-05-09	1# → 3# (2, 3#)	2014-05-08	3.03
		2014-05-10	6.03

### 5.2 1# Condensate Pump Shut Down

In order to find the 1# condensate pump shut down during the rising reason, dissolved oxygen on March 5, 2014 for 1# condensate pump isolation: 1# condensate pump power, close #1 condensate pump inlet/outlet valve, air valve, bearing cooling water valve, doubt 1# condensate pump body parts (especially the negative pressure and positive pressure alternating section) and sealing parts have air leakage into the water. After isolation of 1# condensate pump condensate pump outlet dissolved oxygen levels drop about 3 μg/L as shown in Fig. 3.

### 5.3 The Condenser Leak Test

In the condenser leakage detection device of vacuum pump and vacuum pump water valve of a stainless steel tee indirectly, and on the stainless steel pipe by one

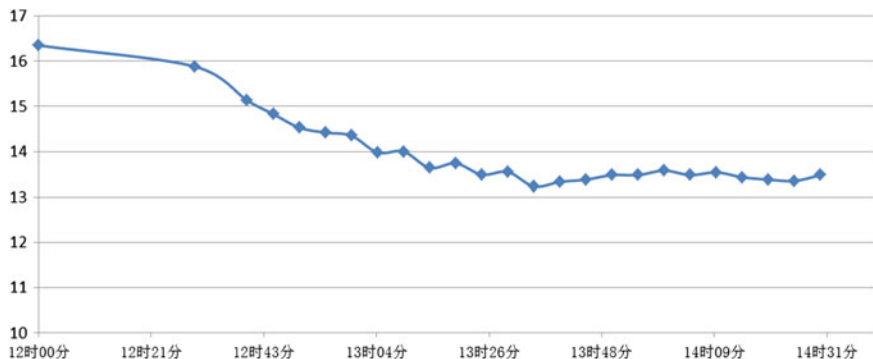


**Fig. 3** 1# import and export of condensate pump valve isolation condensate pump outlet dissolved oxygen before and after the change

ball valve, or needle valve for artificial detection condenser hot well dissolved oxygen content. Condenser pressure part flanged valves and flange pipe change form for welding, water (gas) and secondary valves, all valves to the good sealing valve or add sealing water (necessity), arrange the inspection below the condenser hot well water pipe weld and pipeline external corrosion (especially wall part, implement accessibility). Isolation #1, #2 condenser hot well leakage, and 1#, 2# condenser leakage detection device A side, B side inlet valve closing, dissolved oxygen (do) the basic no change.

#### ***5.4 Implementation of the “Helium Leak Detection Technology in the Steam Turbine Plant Condenser Condensate System Solution”***

Helium mass spectrometry vacuum spray helium sampling method, spray on the measuring point by helium, helium mass spectrometer in the vacuum system vent continuous monitoring sampling to determine whether were leaking. Near the leak scope: pump connected pipeline equipment and system and condensate pump suction pipe wall; condensate pump water sealing conditions (each pump in the operation and shutdown state test, run with switching condensate pump); flange of equipment and system (including manhole flange, blasting valve, corrugated pipe, filters, piping and equipment flange, etc.); other mechanical seal, such as screw thread interface, level gauge, etc. Condenser expansion joint area exists vacuum leakage phenomenon, pipe valve flange and valve packing. Butter and package for these regions cling film after temporary treatment, dissolved oxygen content peak declined.

## **6 The Latest Water Dissolved Oxygen Jump Events**

On April 24, 2015, 9 began to water dissolved oxygen began to rise, on April 26, up to 66  $\mu\text{g/L}$ , condenser vacuum is normal, confirm condensate pump discharge and water supply online oxygen monitoring instrument is normal; check vacuum sealing water pressure and water level is normal, the condenser water, expansion joint seal of dissolved oxygen without easing trend; on April 27, his—he has opened the 1#, 3# condensate water drain valve of cooling water pump bearing (GYS-26 fv, GYS-28 fv) of 1#, 3# condensate pump condensate pump bearing cooling water cooling water bearing detection of dissolved oxygen, “condensate pump outlet dissolved oxygen from 60  $\mu\text{g/L}$  fell rapidly, and now back to normal level 1.3  $\mu\text{g/L}$ .”

The 7 April 29 condensate pump outlet dissolved oxygen in 20  $\mu\text{g/L}$  ups and downs, up to 32  $\mu\text{g/L}$ , the main feed water pump shaft seal water tank back to

420 mm, the main feed water pump shaft seal water pump back to shut down the state, the main feed water pump shaft seal water tank level control valve back PFS-07 v valve position is 40 %, check for normal vacuum sealed tank, shaft and liquid level is normal, check the blowdown sampling boxes level is normal, sewage sample return pump is not running, at 10 down PFS-06 v will give the pump shaft seal water level back up to 600 mm, keep watch two hours, dissolved oxygen, no ease trend, returned to normal. Passion—15:00 successively opened 3#, 1#, 2# condensate water drain valve of cooling water pump bearing (GYS-28 fv, GYS-26 fv GYS-27 fv) of 3#, cooling water pump bearings, 1#, 2# condensate pump bearing cooling water condenser cooling water pump bearing detection, dissolved oxygen for condensate pump export from 48.5  $\mu\text{g/L}$  fell rapidly, dissolved oxygen and resumed to 1.78  $\mu\text{g/L}$  in summer.

30 April 4 when condensate pump exports begin to rise, dissolved oxygen on-site inspection main pump shaft seal water level back to normal, take turns to switch GYS-26 fv/GYS-27fv/GYS-28 fv and observed trends, dissolved oxygen dissolved oxygen has no obvious improvement, the rising trend 9:40, in turn, open GYS-28 fv, GYS-26 fv, GYS-27 fv 10 min after closing, as condensate pump outlet dissolved oxygen from 54 to 1.78  $\mu\text{g/L}$ , on May 1, condensate pump discharge at 7:40 dissolved oxygen from 20 to about 40  $\mu\text{g/L}$ , at 10:00 on GYS-28 fv, measurement of 3# condensate pump bearing cooling water dissolved oxygen <16.1  $\mu\text{g/L}$ ; At 10:30 closed GYS-28 fv, open GYS-26 fv, measuring 1# condensate pump bearing cooling water dissolved oxygen <2.90  $\mu\text{g/L}$ ; Himself condensate pump outlet dissolved oxygen from 40  $\mu\text{g/L}$  quickly fell to 1.53  $\mu\text{g/L}$  (certain pressure-out measures in the process of dissolved oxygen measurement.).

The abnormal fluctuations condensate pump outlet dissolved oxygen, and the condensate pump export decline in dissolved oxygen was associated with a condensate pump bearing cooling water dissolved oxygen detection, preliminary conclusions are as follows:

#1–#3 condenser cooling water pump bearing of water drain valve (GYS-28 fv, GYS-26 fv, GYS-27 fv) each operation, the condensate pump outlet dissolved oxygen content will change, then condensate pump 1# condensate pump, in particular, the negative pressure parts, shaft seal or bearing cooling water in small funneled, in a sealed balance has been broken or inhaled oxygen air, rising high condensate pump outlet dissolved oxygen ratio.

## 7 Conclusion

Nuclear power because of its special design requirements of chemical limit of water dissolved oxygen is lower than 5  $\mu\text{g/L}$ , it is also a limit WANO indicators. Water dissolved oxygen levels is a comprehensive problem, through the above analysis it can be seen that the condenser volatility and dissolved oxygen rise phenomenon possible reason is: condensate pump body parts (especially negative pressure and



positive pressure alternating section) and water sealing parts, bearing return pipe is air leakage into the cooling, etc. Therefore put forward the follow-up to discuss:

1. air leakage into the point search: focusing on condensate water cooling water pump bearing, seal and return it along the pipeline, equipment, valves, including to the pump shaft seal water tank liquid level, the operation condition of the pump, etc., and switch 1# 3# condensate water drain valve of cooling water pump bearing, observe the change of the condensate pump outlet dissolved oxygen.
2. increase in condensate pump discharge pipe line after multiple instrument or joint on through the switching of drain pipe (interface for 3/8 or 1/4), use the portable dissolved table scan the dissolved oxygen content, and compared with online dissolved oxygen table data, so as to determine the online condensate pump discharge line whether there is funnelled dissolved oxygen table. Test run of the condensate water dissolved oxygen content of the mixed bed, to verify that the condensate pump outlet dissolved oxygen content is indeed on the high side.
3. query condensate pump mechanical seal in 2007 before the change of packing seal condensate pump export fluctuation change slightly and dissolved oxygen in under 10  $\mu\text{g/L}$ , since 2009 to fluctuations of more than 10  $\mu\text{g/L}$ , suggested that condensate pump mechanical seal changed back.
4. lower water temperature and dissolved oxygen during more than 5  $\mu\text{g/L}$ , adjusted for seawater circulating water flow, open valve adjusting flow HQS-012. By HQS-012 is valve gate, should not be used for the flow control, need to change to butterfly valve; or increase the circulation pump run the numbers increase in seawater circulating water flow.

## References

1. Jing Chang Cai. Steam turbine high dissolved oxygen the cause analysis and countermeasures of frozen water. *North China electric power technology*, 2002, no. 4, 44–45.
2. Li Xiao Yong. The effect of condensate supercooling degree of unit and countermeasures [J] *power station auxiliary equipment*, 2004, 90(3):12–14, 16.
3. CNNP Nuclear Power Operations Management Co. 4# condensate pump export dissolved oxygen on the high side. Ten defects report material-04, 201502.

# Research and Application of RtCM Techniques in CPR1000 Nuclear Power Plant

Chen Yu, Zhang Sheng and Yang Xiaojin

**Abstract** By combining reliability-centered maintenance (RCM) analysis approach, which has been implemented by domestic and international nuclear power plants for years and the development of related maintenance optimization techniques, this article analyzes deficiencies of traditional RCM analysis and provides the improved RtCM to strengthen technical analysis and improve analysis efficiency and quality. This article also provides cases in which RtCM is applied into CPR1000 nuclear power plant. It has the extraordinary significance for establishing a sound maintenance management program and maintenance optimization program in nuclear power plants and improving the safety, reliability, and economic benefits of plant's operations. Meanwhile, this paper provides an important direction and thought for the development of domestic and international maintenance optimization techniques.

**Keywords** RCM · RtCM · CPR1000 · Plants · Maintenance optimization · Reliability

## 1 Introduction

After the Fukushima Daiichi nuclear power plant explosion, plant safety issues have attracted more and more attention from the world's nuclear power field. Based on the experience gained from Fukushima Daiichi nuclear power plant explosion, it is of importance to develop the technical research of plant reliability assurance and improve plant safety and reliability level. With the vigorous development of domestic

---

C. Yu (✉) · Z. Sheng · Y. Xiaojin  
Suzhou Nuclear Power Research Institute Co., Ltd., Shenzhen, Guangdong, China  
e-mail: chenyu@cgnpc.com.cn

Z. Sheng  
e-mail: zsheng@cgnpc.com.cn

Y. Xiaojin  
e-mail: yangxiaojin@cgnpc.com.cn

nuclear power units, the higher requirement for production safety and equipment reliability is proposed. Maintenance has a very close relationship with equipment reliability, because maintenance program, maintenance planning, maintenance process, maintenance skills, maintenance quality, etc., are directly or indirectly connected with equipment reliability. Among them, maintenance program, which is run through the whole maintenance activities, is the source and guide file in the field of maintenance and its reasonability has a critical effect on the safety, economic benefits, and reliable operations of plant units. Currently, the development of plant maintenance activities is mainly based on preventive maintenance program, which is a significant plant formal specification. Due to the limitation of historical conditions, the main benchmark of maintenance program is equipment operation maintenance manuals along with a little experience feedback and the contents prioritize the periodic disassembly maintenance. However, the scientific data and maintenance practice tell us that the maintenance program, which prioritizes the periodic disassembly maintenance, cannot meet requirements of system and equipment reliability improvement and maintenance cost-saving. The maintenance program that prioritizes periodic disassembly maintenance focuses more on scheduled maintenance intervals. In many cases, it leads to the equipment well operating their intended functions have to be implemented disassembly maintenance at their scheduled maintenance intervals, not only wasting manpower and materials resources but also often causing new failures after maintenance, while some equipment, which should have been repaired, is not repaired on time due to the limitation of maintenance program. Since there has not been the scientific approach to grasp maintenance requirements, plants have set up more and more periodic disassembly maintenance projects, and thus maintenance cost has become higher and higher. So far, when most plants make traditional RCM analysis, they mostly use the primary analysis approach which is characterized by big workload, low analysis efficiency, strong subjective judgment, and requires extensive manpower and materials resources.

Based on the above situations, a part of domestic nuclear power utilities have already made a research on and imported reliability maintenance techniques. The research on traditional RCM has been developed and successfully applied into practice in part of domestic nuclear power plants. The achievements are significant. However, since traditional RCM approach is widely used in different industry fields, it means its technique steps and decision logic are not designed only for nuclear power plants. Meanwhile, as for the seven standard RCM questions, the answers to several questions lack effective technical strategies. Therefore, the research on RCM techniques improvement is required by circumstances.

## **2 Chapter 1 Basic Definitions on RCM**

Reliability-centered maintenance (RCM) is a systematic technical approach, which is generally used internationally to determine equipment preventive maintenance requirements and optimize maintenance system [1]. According to the State military

standard GJB 1378-92 “Equipment Preventive Maintenance Program Planning Requirement and Approach,” RCM is defined as “it is a process or an approach to determine equipment preventive maintenance requirements according to the principle of using minimum resources to keep equipment reliability and safety.” The process analyzes functions and failures and determines failure consequences, and then determines the preventive action for effects of all failures, and also further determines the maintenance strategy to optimize system by on-site failure data statistics, expert assessment, and quantitative modeling and reaching the goal of minimizing trip loss and resources consumption. RCM analysis determines what the user needs to do to ensure that the equipment can continue to do what the user needs it to do. Or in another way, it determines what the plant needs to ensure that the equipment can meet requirements of the plant. In a simple way, RCM determines which maintenance strategy a plant needs to keep the equipment to normally perform its intended function.

The result of RCM analysis is to put forward preventive maintenance projects, specific maintenance intervals, maintenance strategies, and the implementation department. As for SSCs in plants, the result of RCM analysis is to put forward preventive maintenance program for the equipment. Preventive maintenance program is a summarized document to set preventive maintenance requirements of SSCs and is also a general arrangement on equipment preventive maintenance requirements. Its main contents include:

- The equipment which needs preventive maintenance (WHAT)
- Implemented maintenance strategy (HOW)
- Maintenance intervals (WHEN)
- Maintenance level (WHERE)

### **3 Chapter 2 RtCM Techniques (Improved RCM)**

Based on the experience of RCM implementation in domestic and international nuclear power plants in several years, traditional RCM has the following deficiencies:

- Lack of analysis approach to general equipment  
Traditional RCM considers system as the analysis subject. Equipment in the system is an important part for functional support and failure analysis and is also the end subject of maintenance strategy implementation. In a plant, there often are a large number of equipment with the same manufacturer and model or components are installed in the same or similar operating circumstances. According to RCM analysis experience, the maintenance strategies for the equipment are often similar. Using the traditional analysis approach, the analysis efficiency and strategy application efficiency are not high.

- **Lack of effective technical criteria to determine status monitoring**  
 The sixth RCM question needs to determine the predictive or preventive maintenance task to manage failure modes. According to RCM, the first is to determine status monitoring. However, the point is whether there is a proper status monitoring task? How to implement the status monitoring task? Status monitoring is determined by the judgment and determination of failure P-F features and failure criteria in RCM analysis. Lack of effective technical criteria and approach results in that it is difficult for RCM analysis working group to put forward proactive action to identify and predict failures.
- **Lack of reasonable equipment classification management**  
 Although the traditional RCM analysis classifies failure consequences, it just classifies failure consequences from the nonobjective perspective and the consequences are classified as four types: safety degradation, environment degradation, availability degradation, and availability nondegradation. Considering the more complicated and diversified equipment in the modern society and limited enterprise input resources, this classification does not present Pareto Principal. That is to manage the most critical minority. Therefore, it does not put significant management and maintenance resources into the enterprise management priorities. For plants that have strict requirements for quality assurance system, it is much more important to use limited resources to manage critical equipment.
- **Lack of effective quantitative analysis modeling of preventive maintenance intervals**  
 When using traditional RCM to make maintenance strategy, many utilities are bothered by determining status monitoring intervals and periodic maintenance intervals. The seven RCM questions do not put forward good technical strategies to solve these issues.  
 Additionally, although traditional RCM can analyze the failure modes of different equipment, for enterprises owning complex instrumentation and control equipment, like nuclear power plants, considering analysis intervals, traditional RCM analysis approach does not make the further analysis of instrumentation and control components. Therefore, the general maintenance strategies for instrumentation and control equipment focus more on signal channels function checking, probe checking, etc. With the development of modern science and technology, instrumentation and control, and intelligent control design become more and more complex and diversified. Plant's design is much more complex. It is necessary to make an effective analysis of its instrumentation and control equipment.  
 After over 10-year research about RCM, CGN equipment reliability application working group has proposed new RtCM (reliability and technique-centered maintenance) concept by adding techniques analysis (frequencies, failures probability, operation environment, etc.) based on RCM process. RtCM not only optimizes analysis process and procedure but also the technical implementation

of the whole maintenance strategy. RtCM complies with the following nine questions and answers:

1. In the current operating environment, the user needs the system to provide what function and what are the related performance criteria? (function)
2. What are all performance forms of functional failures? (functional failures)
3. What failure consequences are caused by functional failures? By combining effects of functional failures on units safety, environment and economic benefits (like radioactive leakage, shutdown, and load down), classify functional failure consequences as Category Y (critical, unacceptable) and Category N (non-critical, acceptable). Category Y functional failure consequences are considered to lead to unacceptable consequences and need to list all equipment that may lead to functional failures. (find equipment to be managed)
4. What causes functional failures of equipment to be managed? (failure modes)
5. What effects would be caused by failure modes? (failure effects)
6. What kind of failure consequences it belongs to? (failure consequences)
7. How about the operating environment, service frequency and failure probability? (reliability analysis)
8. How to prevent or predict the failure modes? (preventive and predictive)
9. If there is no approach to prevent or predict the failure modes, how to manage the consequences? (manage failure consequences) (Chart 1)

## **4 Chapter 3 Application of RtCM Techniques on CPR1000**

This article takes ASG of LNPS Phase II as example. Ling Ao Phase II Nuclear Power Plant adopted CGN's self-reliant brand Chinese evolutionary PWR (CPR1000) with  $2 \times 1080$  mW class PWR units. Each unit is installed with one set of ASG, including a cistern, a set of pump system (capacity of  $2 \times 100\%$ , including two units of motor pump with capacity of  $2 \times 50\%$ , two units of pneumatic pump with capacity of  $2 \times 50\%$ ) and a set of feed water line, which is installed with flow-control valves and connects with a boiler. Additionally, two units share 8ASG deoxygenated equipment to offer deionized and deoxygenated water to water tank of 3ASG, 4ASG, and REA. The flowchart is in Chart 2.

### **4.1 Boundaries Determination**

ASG system boundaries are classified by related flow chart.

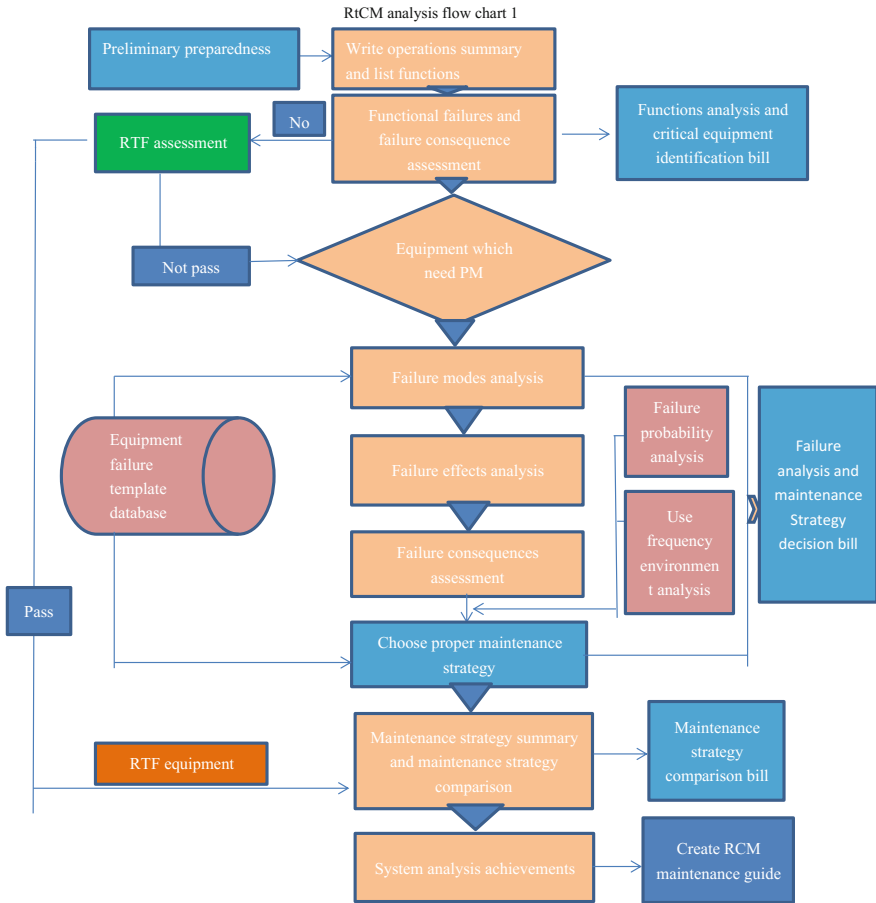


**Chart 1** RtCM analysis flow chart

1. Process boundary

Regard equipment boundary and functional position code in the flow chart as basis. Functional position code includes mechanical and electric equipments of ASG system, which includes flange valve or weld.

When boundary equipment belongs to ASG system, boundary equipment and two-side flange or weld is included in the analysis range. When boundary equipment does not belong to ASG system, boundary equipment is not included in the analysis range, while the related ASG flange or weld is included in the analysis range.

2. Power supply system boundary

Power supply system boundary is included in power cables, including cables.

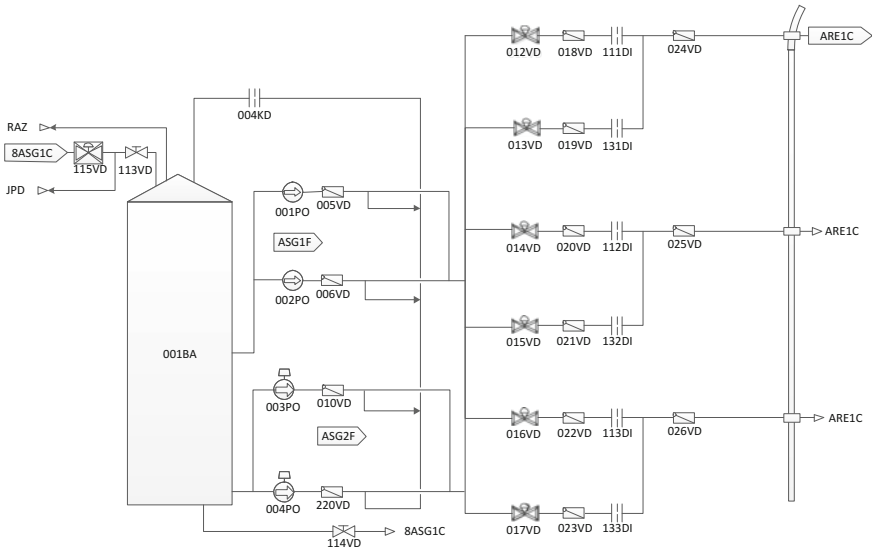


**Chart 2** ASG system flow chart

3. DCS boundary

DCS boundary is included in signal cables of local junction box, including cables.

4. Mechanical and instrumentation and control boundary

It is included in instrumentation one-time isolation valve, including one-time isolation valve. It belongs to electric–mechanical major.

5. Piping hanger is managed according to piping hanger program and is outside of boundary.

**4.2 System’s Main Functions**

According to system design manual, ASG system function is defined as: ASG is the backup system to feed water to boiler secondary loop when the main feedwater system fails to perform its function. It can replace main feedwater system to feed water to SG secondary side in the following situations:

- Reactor start-up and reactor coolant system heatup
- Hot shutdown
- Reactor cooling until RRA can be in operation status

Use auxiliary feedwater motor pump to feed water to boiler secondary side (primary feedwater and refeed water after cold shutdown).



When feedwater system is unable to start up, operators can use auxiliary feedwater motor pump or pneumatic pump instead to maintain water level of a boiler's secondary side. ASG deoxygenated equipment is used to offer deionized and deoxygenated water to ASG water tank and REA system cistern.

ASG system is one of the specific safety equipment systems. When one of the normal feedwater systems (APA, APD, ARE) is failure to function, ASG is operated for residual heat removal until RRA system can be in the operation status. The heat removed from RCP is transferred to secondary system by boiler that is supplied water by ASG. Secondary system is cooled by GCT system.

### ***4.3 Function Analysis and Identification of Critical Equipment***

Analyze and list ASG system functions and functional failures. Analyze the functional failure consequences and classify functional failure consequences as Category Y (serious, unacceptable) and Category N (not serious, acceptable) by combining effects of functional failure consequences on units safety, environment and economy. For Category Y functional failure consequences, equipment failures will lead to unacceptable consequences. List all equipment that may lead to functional failures (it refers to critical equipment) and analyze failure modes and failure consequences by equipment classification. For Category N functional failure consequences, list the corresponding equipment and implement run to failure (RTF) assessment (like industrial safety, environment, radiation safety risk and economic cost, etc.). N-RTF equipment, which does not pass RTF assessment, needs maintenance strategy like critical equipment to analyze failure modes and failure consequences. No need to implement maintenance strategy analysis for equipment that passes RTF assessment. Implement corrective maintenance strategy for the equipment instead of analyzing failure modes and failure consequences. The achievements are ASG system function bill and ASG system function analysis and critical equipment identification bill.

The equipment that is worth managing includes two kinds of equipment. One is the equipment that can directly lead to serious functional failure consequences. This kind of equipment needs maintenance strategy analysis. The other is the equipment that does not pass RTM assessment. This kind of equipment also needs maintenance analysis and management. Besides, no need to implement maintenance strategy analysis for other equipment.

The specific implementation process can be divided into three parts: functional failure consequence analysis and severity level assessment, identification of equipment with functional failures, RTF assessment.

#### **1. Functional failure consequence analysis**

Functional failure consequence analysis is aimed at analyzing consequences of the functional failure and the severity level and providing input for identifying the

**Table 1** Functional failure types

Type	Assessment criteria
I	For safety/environment: failures result in nuclear safety degradation, industrial safety risk and affect important redundancy For production loss: failures result in a reactor trip and load down For non-production loss: failures result in sharp increase of maintenance cost
II	Other functional failure consequences except those which have been categorized in Category I can be considered as Category II

related equipment that can lead to serious functional failures. Functional failure consequences description focuses on the effects on units’ safety, environment, and economy, like radioactive leakage risk, shutdown, load down, etc.[2].

Analysts list all functional failure consequences according to functional failures and judge the level of functional failures (Category I or Category II in Table 1).

2. Identification of equipment with functional failures (for equipment considered as Category I)

As for the identification of equipment with functional failures, first, we need to have an overall understanding of system functions. Then analyze what can result in functional failures according to equipment failure modes signs. Supervisors need to draft bills and failure signs analysis in advance and check and confirm them with team members in meetings and sort out critical equipment bills. Exclude critical equipment from system function analysis bills and the rest is non-critical equipment bill, which can be considered as RTF assessment input.

3. RTF assessment

The goal is to classify non-critical equipment as N-RTF equipment and RTF equipment according to RTF assessment criteria. N-RTF equipment still has maintenance requirement as critical equipment. Analyze their failure modes and consequences by types and set up the corresponding maintenance strategy. No need to analyze the maintenance requirement of the equipment that pass RTM assessment. RTM assessment criteria for nuclear power plants are as below [3]:

- Equipment failures can result in the unacceptable risk increases, like individuals, industrial safety, environment, radiation safety risk, etc.
- Equipment needs the unacceptable high cost for maintenance, replacement, or operations.
- Equipment is out of time or short of supply while it takes high cost or long time to repair or replace.
- Equipment failures can lead to other equipment failures or affect the operation of other functional equipment.
- Equipment failures can result in power transient and downgrade of required redundancy or defense in depth.
- Equipment failures can result in limited consequences, like violating related regulations.

- Equipment failures will affect or result in critical components cannot be repaired in time.
- Comparing with maintenance or replacement after failures, PM is more economic.

If one of the above criteria can apply and the related equipment is non-critical but needs to be analyzed, there is the need to analyze failure modes and failure consequences. If any one of the above criteria cannot apply, the equipment shall be considered as RTF equipment and there is no need to set up maintenance strategy.

#### ***4.4 Identification of Maintenance Strategy***

It is applied for the equipment critical to system function analysis and screened by equipment classification. Analyze failure modes, failure consequences, and maintenance strategy by equipment categorization. Analyze the failure modes that may result in system functional failures in the following three directions:

- Failure modes that already happened to the same or similar equipment.
- Failure modes that have been marked to prevent in existing maintenance program.
- Other failure modes have not happened so far, but they may happen.

Failure modes, as the basis of this chapter, are all events that result in equipment functional failures. Failure consequences are a series of events that may happen when failures happen and they are mainly used for RtCM judgment. On this basis, make a detailed description of failure consequences and lay the foundation for managing failure modes, failure consequences and frequencies. According to effects of equipment failures, classify failure consequences as apparent and inapparent, related with safety, environment, production, etc. According to service frequency, environment, failure probability and restoration time, implement maintenance integrated technical analysis. According to different technical feathers and status monitoring, periodic refurbishment, periodic replacement, periodic test, corrective maintenance, and sequence of change and retrofit, choose maintenance strategy, manage the consequences of failure modes, and determine maintenance contents and frequency and implementation department [4]. The achievement is ASG system equipment maintenance strategy bill.

#### ***4.5 Maintenance Summary***

On the basis of equipment maintenance strategy identification, summarize all related maintenance tasks. Fill in RtCM task statements and assign the specific tasks to the related implementation units according to RtCM task statements.

The implementation units can change maintenance program, maintenance process, periodic test process, walkdown process, etc., according to RtCM task assignment. The achievement is ASG system maintenance summary.

#### **4.6 Analysis Achievements**

After the summary of maintenance tasks, compare RtCM summary with the previous equipment maintenance program, confirm RtCM analysis of system or equipment has already covered all contents of the previous maintenance program and ensure all information is not missing. The achievement is ASG system maintenance program comparison before and after RtCM analysis. Main changes (achievements) of ASG system before and after RtCM analysis are as below:

1. Extend check cycle of 003/004PO total disassembly 3C → 7C  
Keep 3C disassembly check for 003/004PO protection shutoff valve and entry modulating valve
2. Extend press set and check cycle of 176/177/182VD214VZ safety valve 2Y → 3Y
3. Extend disassembly check cycle of 126VZ water tank breather valve 1C → 3C
4. Extend disassembly check cycle of 145VZ valves 3C → 7C
5. Extend 001DZ internal check cycle 5Y → 6Y
6. Extend replacement and check cycle of 012/013/014/015/016/017VD vulnerable components 6C → 7C
7. Extend cycle of 001 RF internal check, flushing loop and cooler 5Y → 6Y
8. Extend cleaning cycle of 001/002MO oil and grease of 3C → 6C
9. Cancel 5Y daily lubricating of 051/052/053VD (chemical samples' instrumentation isolation valve)
10. Cancel 5Y daily lubricating of 833/834/835/836/838/839/840/841/843/844/845/846VD (instrumentation isolation valve)
11. Cancel 5Y daily lubricating of 144/244VV (separator 001/003ZE air vent valve), 953/951/952/252/128/129/130VD (ASG pump upstream and downstream air vent valve), 511VD (ASG pump minimum flow line air vent valve), 803VD (001BA level measuring water tank air vent valve), 510/540/570VD (ASG pump discharge line drain air vent valve) and 801/802/804/808VZ (001BA nitrogen isolation valve)
12. Cancel 7C disassembly of 199/299VD valves and check whether the upstream and downstream lines are blocked
13. Add 001DZ hydraulic test 12Y, periodic in-service check 6Y
14. Add 001RF hydraulic test 12Y, periodic in-service check 6Y
15. Add 005/006/010/220VD valve visual inspection, check whether valves are leaked, mechanical vulnerability, etc. 1C
16. Add check on 001/002MO electric-mechanical heater, check on temperature-controller setting, check on terminals in wiring box and cleaning 4C

17. Add 001/002PO cooler tube 7C
18. Add 002BA hydraulic test 12Y, periodic in-service check 6Y
19. Extend 001/002PU disassembly check cycle 1C → 2C
20. Add 001/002MO sampling disassembly 10C

#### ***4.7 Comparison with Periodic Test Surveillance Program***

After RtCM analysis, compare RtCM analysis result with the existing updated periodic test surveillance program and ensure that the safety criteria that are required by the existing periodic test surveillance can be complied with.

By comparison, the analysis result of ASG system completely complies with the requirements of periodic test surveillance program.

#### ***4.8 Benefit Assessment of System Analysis***

The main purpose of RtCM analysis is to manage the possible failure consequences of system by integrating maintenance contents, frequency, and implementation methods into maintenance program so as to improve equipment reliability and availability and reduce maintenance or repair cost. The benefit assessment of ASG system analysis is as below:

##### **1. Direct benefits**

The analysis cancels many unnecessary periodic PM projects, which cost time and money with few effects and adds some necessary PM projects to improve equipment reliability and reduce maintenance cost.

The obvious benefits which are caused by RtCM analysis are as below:

- Cancel some unnecessary periodic PM task.
- Prevent the failure mode that was not prevented before and has the significant failure consequences. Reduce the failure probability and improve equipment reliability [5].

##### **2. Indirect benefits**

- Ensure system reliability and reduce maintenance cost

The analysis cancels many unnecessary PM tasks and adds some necessary PM tasks to improve equipment reliability and reduce maintenance cost.

- Set up the basis of maintenance strategy and build the base of continuous maintenance strategy optimization

RtCM analysis sets up the maintenance guide, which is the upstream file of ASG system maintenance program, and establishes the maintenance

strategies according to failure consequences and failure modes, which is good for the right feedback and continuous maintenance program optimization.

- Standardize the description of the program and ensure the completeness and standardization of the program project. Further optimize the description of the program and ensure the completeness and standardization of the program project.
- Systematically sort of site equipment/technical documents and timely feedback the questions to push the solution.

RtCM analysis systematically sorts of site equipment, design manual, maintenance manual, flow chart, function chart, operation procedure, maintenance procedure, etc., and timely feedback the questions and push the solution.

- Good cooperation among all departments and promotion of RtCM idea

RtCM analysis group members are from maintenance department, equipment management department, operations department, etc. Thus, they can fully make use of their advantages and make up their shortness in the discussion and find out repetitive, missing, or wrong part in the previous maintenance, operations documents and reasonably assign equipment maintenance task to all departments in order to improve the overall working efficiency [6].

- Improvement of staff's skills.
  - Staff has a further understanding of the equipment.
  - It is good to improve their ability of equipment failure analysis, judgment, and handling.
  - Staff can better understand equipment functions, failure modes, and failure effects, which is helpful to find more reasonable management strategies and approaches.

## 5 Website

### 5.1 Website of PBNC2016

The website of PBNC2016 is <http://www.pbnc2016.org/>. For more information please visit the website.

## 6 Conclusion

The application of RtCM techniques on nuclear power plant's equipment management and maintenance management has reduced the situation in which the traditional RCM analysis results in resources are highly occupied and has improved

analysis efficiency. It is significant to establish sound maintenance management system and maintenance optimization system in plants and improve operations safety, reliability, and economic benefits in plants. In terms of domestic RtCM techniques application for several years, the improved RtCM techniques have strengthened technical analysis and made maintenance strategies more feasible and convincing. Meanwhile, the reliability analysis is introduced to provide an important reference to establish PM intervals. General RtCM software and maintenance template database are planned to develop in order to improve RtCM analysis efficiency and quality and better support RtCM system analysis. It has the positive effect on the improvement of equipment reliability and cost-saving of maintenance. The research achievements in this paper are helpful to improve RtCM analysis efficiency and quality, strengthen the scientificity, and reliability of RtCM analysis and better direct nuclear power plants and other enterprises to promote reliability maintenance techniques.

## References

1. Moubray J. Reliability-Centered Maintenance (M). Translated by Shi Lei & Gu Changning, Beijing: China Machine Press. 1995
2. EPRI. Streamlined Reliability-Centered Maintenance (SRCM) Program for Fossil-Fired Power Plants [R]. TR-109795, 1998
3. EPRI-GEN.Streamlined Reliability Centered Maintenance (SRCM) Implementation Guidelines [R]. TR-1097952, 1998
4. EPRI, Reliability and Preventive Maintenance- Balancing Risk and Reliability, December 2002
5. EPRI, Maintenance Engineer Fundamentals Handbook, December 2007
6. EPRI, PMBD 2.1 (Preventive Maintenance Basis Database)

# Research on Technical Transformation of Lifting Equipment in Nuclear Power Plants

Xiaodong Bao, Jinbao Zhou, Fa Yang and Yi Li

**Abstract** There are a lot of problems in the use of lifting equipment, such as wrong design, harsh environment, higher standards, obsolete spare parts, inadequate performance, and so on. If these problems are not properly handled, they will inevitably affect safety and reliability of lift equipment. The standards and requirements of lifting equipment in nuclear power plants are different from other plants due to the special nature of nuclear power plants. Some problems are never encountered in general plants, such as high radiation workshop and humid and highly salty environment. It is necessary to generalize various types of problems that appear during operation of lifting equipment in nuclear power plants. To solve these problems, specific technical transformation will be implemented in order to meet high standards and requirements in nuclear power plants.

**Keywords** Lifting equipment · Nuclear power plants · Technical transformation

## 1 Foreword

According to the domestic plan to beef up nuclear power plants, the next few years there will be more nuclear power plants in operation. With nuclear power plants that have been put into operation, the number of lifting equipment in nuclear power plants will be running more and common problems are more widespread. Based on technical transformation of lifting equipment in Qinshan II nuclear power plant, this paper has a brief introduction of different types of technical transformation and precautions about design, environment, standard, spare parts, and performance. Qinshan II nuclear power plant has four sets of 650 MW PWR nuclear power units. Units 1 and 2 are China's first commercial nuclear power plant of self-designed,

---

X. Bao (✉) · J. Zhou · F. Yang · Y. Li  
CNNC Nuclear Power Operations Management Co., Ltd.,  
Haiyan, Zhejiang, China  
e-mail: 89524678@qq.com



self-built, self-managed, and self-operated, and therefore problems of lifting equipment appeared in the operation are special and have the reference value.

## **2 Design**

### ***2.1 Design of the Plant***

Since the actual situation of nuclear power plant is extremely complex, during the design and arrangement of lifting equipment, technical personnel do not have intuitive view of the positional relationship between lifting equipment and other devices. Also among the different types of work, changed information cannot be delivered in time, so it is easy that design and installation do not actually coincide. Often lifting equipment cannot achieve its original design function. For example, lifting height is not enough, the path of moving cannot lift devices, or even no lifting equipment is installed above some devices.

#### **2.1.1 Lifting Height**

Lifting height of some lifting equipment does not meet the requirement and there are two kinds of situations. (1) Lifting height of lifting mechanism is limited. For example, designer only consider devices on the platform and miss devices below the platform or holes, so lifting height of lifting mechanism is not enough. In this case, technical transformation of lifting mechanism can be implemented to add the range of lifting. (2) Lifting height of lifting mechanism is satisfied, but the track of lifting equipment is so low that lifting height is not enough. For example, the track of lifting equipment is so close to devices below lifting equipment that the lifting height is very limited. If there are other devices near the device that need to be lifted out, other devices must be first removed that there is enough space for move the device. This is a waste of time and affects other devices. In particular, during unit operation period, other devices cannot be removed, so the device that needs maintenance cannot be lifted out and unit safety will be affected. In this case for lifting maintained device and not affecting operation of other devices, technical transformation is considered to raise the track of lifting equipment or use low headroom lifting equipment.

#### **2.1.2 The Path of Moving**

There are three kinds of situations that the path of moving cannot lift devices. (1) Lifting points of devices are not in the path of moving. If the deviation is very small, it is possible to lift devices. If the deviation is too large to lift devices safely,

it is possible to install temporary lifting equipment. It is a waste of time and human, and also causes a waste of lifting equipment. In this case, it is considered that the track of lifting is transformed to make the lifting point of devices in the path of lifting. (2) The track of lifting equipment is not long enough that the hook cannot achieve above the device or the hook can achieve above the device but cannot achieve above the ground. In this case, technical transformation is considered to increase a range of the track. (3) Devices are installed on the pack of moving, so the hook of lifting equipment cannot travel fully. In this case, it is first considered to move devices. If devices are difficult to move, technical transformation is considered to move lifting equipment to avoid devices. It is also considered to increase lifting equipment, so devices can be lifted separately.

### **2.1.3 No Lifting Equipment**

During the design and installation phase of nuclear power plants, there is no lifting equipment installed above some devices. Also the space is extremely narrow in some places and temporary lifting equipment cannot be installed, but these devices must be lifted out. In this case, it is considered to add lifting equipment and two kinds should be considered. (1) Above devices is there bearing beam that can load desired weight? (2) Is there enough space to install lifting equipment? According to the space, appropriate lifting equipment should be selected. If the space is insufficient, pipes, brackets, and other devices need to be moved to make space for installing lifting equipment.

## ***2.2 Design of Lifting Equipment***

### **2.2.1 Wrong Design**

There are also errors during the design and manufacture phase in the factory. For example, on a bridge crane there is interference between the hoisting rope and the plate of trolley when the hook runs to close to the upper limit position. After a long-term operation, it has caused rope broken. In this case, it is necessary to communicate with the factory of lifting equipment. Technical transformation can be implemented with a clear reason, at the same time without any effects on the structure of lifting equipment.

### **2.2.2 Inappropriate Design**

During the design stage of lifting equipment, the weight of devices should be taken full account and then suitable tonnage of main and auxiliary hook is selected. After this work efficiency can be improved greatly, for example, in units 1 and 2 of

Qinshan II nuclear power plant, the auxiliary hook of ring crane is designed to 10 tons but the weight of many devices is a little bit more than 10 tons. In order to avoid overloading, the main hook that is 190 tons is selected to lift devices and its speed is very slow, so it will waste a lot of time. Because the technical transformation of ring crane is very difficult, with the limit of time and other conditions, there is no way to transform ring crane. Drawing on this experience, in Units 3 and 4, the auxiliary hook is designed to 20 tons. This improves work efficiency and greatly reduces the maintenance period, so it makes a very considerable economic benefit.

### **3 Environment**

#### **3.1 Radiation**

In nuclear power plants, the radiations from some room are very high and some lifting equipment is located above the room due to work. At that time, the control boxes of many lifting equipment are installed on lifting equipment and they move with lifting equipment. If this lifting equipment breaks down in the highly radioactive area, maintenance staff may need a scaffold to reach the control box and carry out maintenance. In this case, maintenance staff will be exposed to radiation and receive a lot of radiation doses. According to the principle of optimization of radiation protection, radiation doses of staff should be minimized as low as reasonably practicable. It is necessary to transform this lifting equipment so that the control box is far away from high radiation point or placed behind a shielding wall. Of course, the control box is preferably installed close to the ground and maintenance staff can reach the control box without any scaffold. It will reduce radiation doses to staff but also help to find and deal with failure quickly.

#### **3.2 Humidity**

Since nuclear power plants are always located near the sea, the air is very humid and salty. Devices are easily corroded. Because some lifting equipment has low usage, if there is not enough maintenance, after several years, corrosion is extremely serious and even some have lost their hoisting function. According to design requirements of nuclear power plants, in case of an accident you must ensure that it can be put into operation in time, although this lifting equipment is not used once. You must keep it in a safe and usable state. In this case the maintenance of lifting equipment must be strengthened against mild corrosion and technical transformation should be carried out against heavy corrosion. Corrosion resistance of lifting equipment should be focus in transformation process. Whenever possible,

anti-corrosion materials should be used, such as marine cables, stainless steel parts and other materials. It is also a good way to reduce the opening portion of lifting equipment. After technical transformation, reasonable maintenance cycle should be formulated, focusing on corrosion. Lifting equipment that has low usage should be regularly sent to run and maintain in the best condition.

## **4 Standard**

Relevant standards of lifting equipment have been being updated, so some lifting equipment that can get acceptance during the installation of nuclear power plants has been unable to pass inspection at present. More importantly, this lifting equipment has potential safety hazard and is likely to cause damage or casualties. There are several aspects: (1) Operating handle must have an emergency power-off switch. (2) Control power supply must use 36 V. (3) The power supply circuit must have short-voltage or loss-voltage protection. (4) The hook must be equipped with anti-decoupling device. (5) The necessary electrical chain must be set. (6) Overload protection device must be fitted. (7) Must there is other protection, including: over-current protection, short circuit protection, limit protection, phase sequence protection. Before these transformations are implemented, it is best to make a survey on lifting equipment, and then transformations can be implemented systematically.

## **5 Spare Parts**

Due to the age and product upgrade, some spare parts of lifting equipment cannot be bought on the market and the new products can not completely replace the old products. In this case, technical transformation of replacement should be considered in time, so as not to delay maintenance period and even affect safety of nuclear power plants.

## **6 Performance**

Due to the technical conditions at that time, the performance of some lifting equipment can barely meet production needs. With operational requirements continuously increasing, technical transformation is urgently required to meet the new requirements.

## **6.1 *Adjusting Speed***

Many original adjusting speed systems of lifting equipment use multi-speed motors, rotor series resistance or stator voltage regulation to adjust speed. There are many problems with these adjusting speed systems, such as speed range small, current impact large, start and brake jitter large, equipment loss serious and so on. These seriously affect their quality and efficiency of daily maintenance work. Therefore, reliable adjusting speed system is very important. Compared with conventional adjusting speed system, variable frequency adjusting speed system has high operation efficiency, good adjusting speed performance, simple external control circuit, less maintenance, perfect protection function and so on. In totally, it is a good way to improve adjusting speed performance by transformation of frequency conversion.

## **6.2 *Positioning Accuracy***

For some lifting equipment in nuclear power plants, there are high demands positioning accuracy, even in the millimeter-level requirements. If positioning is not accurate, it will easily damage device and influence maintenance quality. To avoid risks and improve maintenance quality, technical transformation of lifting equipment is implemented to improve positioning accuracy. There are two kinds of situations. (1) Such as refueling machine in nuclear island and remote control crane in QT facilities (solid waste transit storage), this lifting equipment has many positioning coordinate points and requires more precise positioning. But this lifting equipment generally only achieves positioning accuracy of  $\pm 5$  mm, due to the technical conditions at that time. With current domestic and foreign mature PLC technology as well as servo controller, inverter, CNC systems and other control mode, lifting equipment can achieve positioning accuracy of  $\pm 1$  mm. (2) Such as lifting equipment that is used to cooperate with the main pump overhaul in AC workshop (radioactive integrated workshop), this lifting equipment needs very little movement to achieve precise positioning requirements, but under normal conditions they need high-speed operation to improve efficiency. During the design phase, only normal operation is taken into account. In this case, it is considered for bridge and trolley to increase a micro-drive mechanism, connected with bridge and trolley drive mechanism through an electromagnetic clutch. The micro-drive mechanism can be operated by controlling the special control box. During normal operation, the clutch is opened, and the micro-drive mechanism is not connected with bridge and trolley drive mechanism, so bridge and trolley can be high-speed operation to improve efficiency.

These technical transformations are intended to improve the performance of lifting equipment, so the cost of transformation and the actual situation should take into account together. It is not desirable to increase the cost for useless high performance.

## **7 Summary**

Lifting equipment in the nuclear power plants will not directly affect the operation of nuclear power plants, but they are essential in the operation and maintenance period. Therefore, it is very important that technical transformation of lifting equipment is safe and reliable in nuclear power plants. This paper lists the various types of transformation. The situation is different for each nuclear power plant, but ideas of transformation are in common. There is a certain reference value for other nuclear power plants about design, installation and operation of lifting equipment.

# Surface Corrosion Analysis of QF Control Rod Nitriding Tube

Ligang Li

**Abstract** In September 2014, when core PIT in QF1, Fuel manager found some yellow settling matter around the nozzle of FA guide tube. The rod cluster control assembly (referred to as RCCA) had slung up for visual inspection in 1KX, there were more corrosion products found on the RCCA rods' surface. When wiped with absorbent cotton cloth, they were disappeared. Then manager inspected backup RCCAs (include backup black control rod assembly and backup gray control rod assembly) stored in the new fuel storage rack (Dry Storage),  $\Phi 0.5\text{--}\Phi 3$  mm rust-colored flecks were found on some RCCA rods' surface with irregular distribution. Fuel manager analyzed several kinds of aspects those maybe the cause of RCCA nitriding tube surface corrosion, including raw material, machining, storage and application environment, analysis of the sensitive source, and he also dis some tests, drew a conclusion and gave the suggestion about how to reduce the surface corrosion of control rod nitriding tube.

**Keywords** RCCA · Nitriding tube · 316L · Corrosion · CrN

## 1 Introduction

In September 2014, when core PIT in QF1, fuel manager found some yellow settling matter around the nozzle of FA guide tube. In Fuqing unit 1, we found the same situation, as shown in Fig. 1. The RCCA had be slung up for visual inspection in 1KX, there were more corrosion products be found on the RCCA rods' surface. Wiped with absorbent cotton cloth, they were disappeared, as shown in Fig. 2. After wiping, where matching the water hole of FA guide tube found the obvious signs of corrosion accumulation, shown in Fig. 3. Then fuel managers inspected backup RCCAs (include backup black control rod assembly and backup gray

---

L. Li (✉)  
Core & Fuel Management Department, CNNP,  
Haiyan, Zhejiang, China  
e-mail: lilg@cnp.com.cn



Fig. 1 Fuqing nuclear power guide tube mouth yellow precipitate

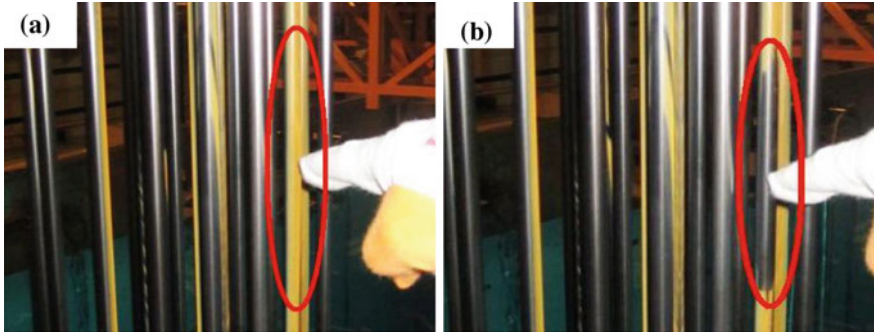


Fig. 2 Control rod surface corrosion, wipe before (a), after wiping (b)

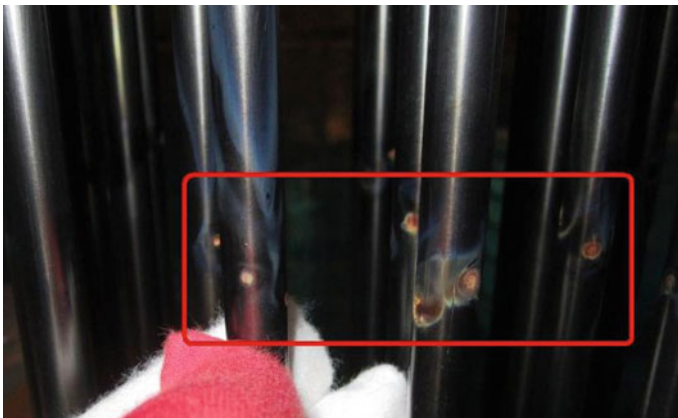


Fig. 3 Control rod corrosion traces



control rod assembly) those stored in the new fuel storage rack (Dry Storage). In some rod, there were 0.5–3 mm diameter red-brown rust spots with irregular distribution. After the corrosion product sampled for testing, the main component was found to be Fe oxides.

## 2 The Control Rod

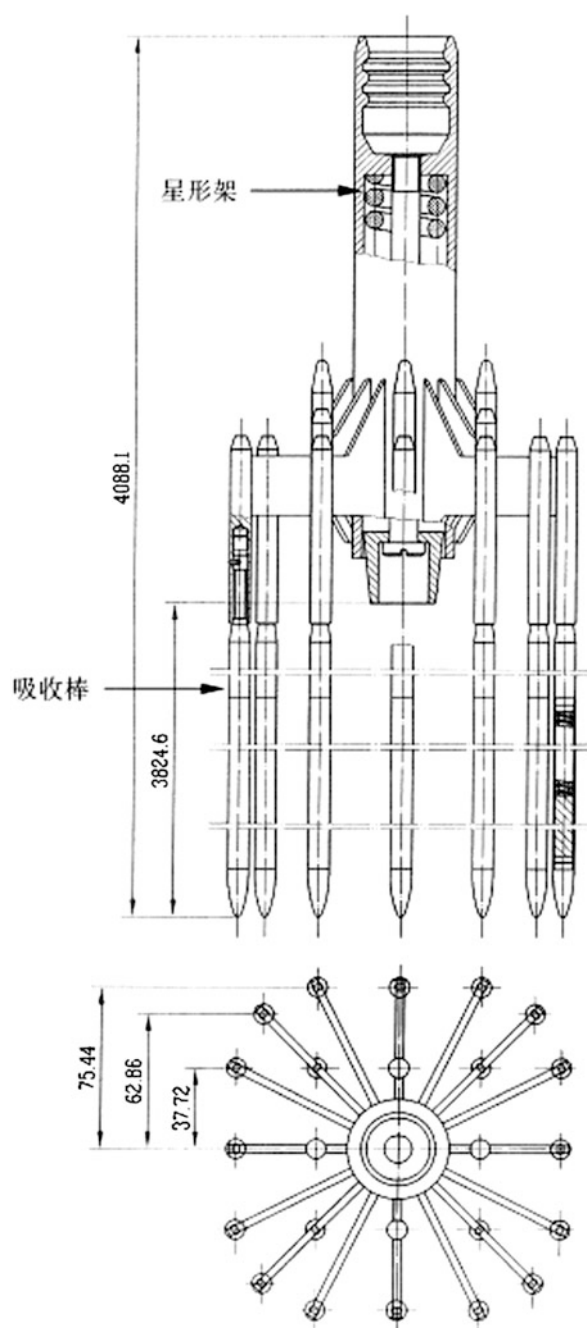
RCCA is mainly used to control the rapid reactivity changes and shutdown. Upper ends of a bundle of neutron absorbed rods are fixed to the common star rack, the RCCA, as shown in Fig. 4. In order to improve the wear resistance of control rod, control rod tube outer surface and bottom plugs were treated by ion nitriding treatment. The diameter of the control rod tube is  $\Phi 9.68$  mm, thickness is 0.47 mm, made of AISI316L (nitrided). The technical conditions of RCCA required nitrogen-enriched control rod tubes with a thickness of  $\geq 12$   $\mu\text{m}$ .

## 3 Nitriding Process

Control rods ion nitriding: work pieces put in the thin atmosphere with nitrogen, hydrogen, and hydrocarbons; a potential difference of about 500–1000 V was applied between the reactor wall and the work pieces; when glow discharged, active nitrogen separated from the gas mixture is infiltrated into the surface by ion bombardment and other principles; and then under the same temperature, nitrogen-atoms diffusion into inside of these work pieces. A minimum of nitriding layer thickness guarantee the Anti-wear strength.

After reviewing the literature, we found that nitriding of 316L stainless steel can form hardness greater than 1400 HV, thickness greater than 200  $\mu\text{m}$  nitride hardened layer. However, due to the precipitation of chromium nitride in the nitride layer, resulting in a stainless steel matrix of chromium reduction, it would reduce the corrosion resistance. In 1985, Zhang and Bell invented the low-temperature plasma nitriding process. Stainless steel nitriding at 450  $^{\circ}\text{C}$ , dozens of  $\mu\text{m}$  hardened layer can be obtained. It is not only high hardness, but high corrosion resistance, as shown in Fig. 5a. Currently, the process widely used in Europe, and plays an important role in project. France applied Nivox2 process on austenitic stainless steel rods ( $\Phi 9.7$  mm thin wall pipe) as shown in Fig. 6. Each capable of processing = 100. After the treatment, obtain a uniform nitrogen S-phase [1].

Fig. 4 RCCA diagram



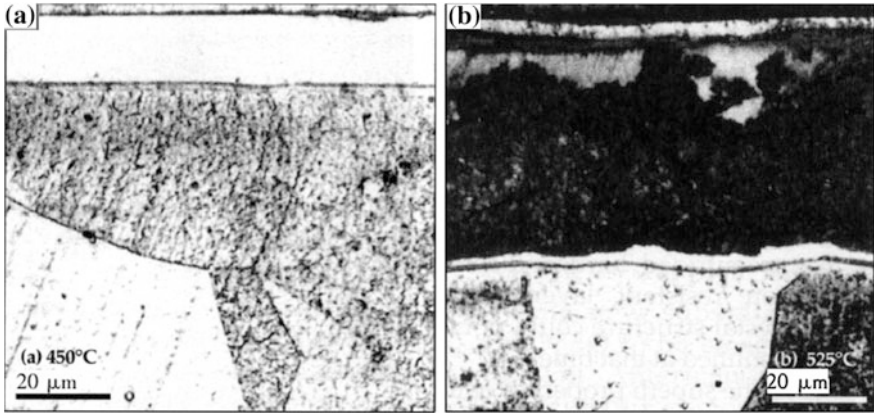


Fig. 5 AISI316 stainless steel nitriding at 450 °C (a) and 525 °C (b)

#### 4 Analysis of the Sensitive Factors

We analyzed kind of aspects those maybe the cause of RCCA nitriding pipe surface corrosion, including raw material, machining, storage, and application environment and so on.

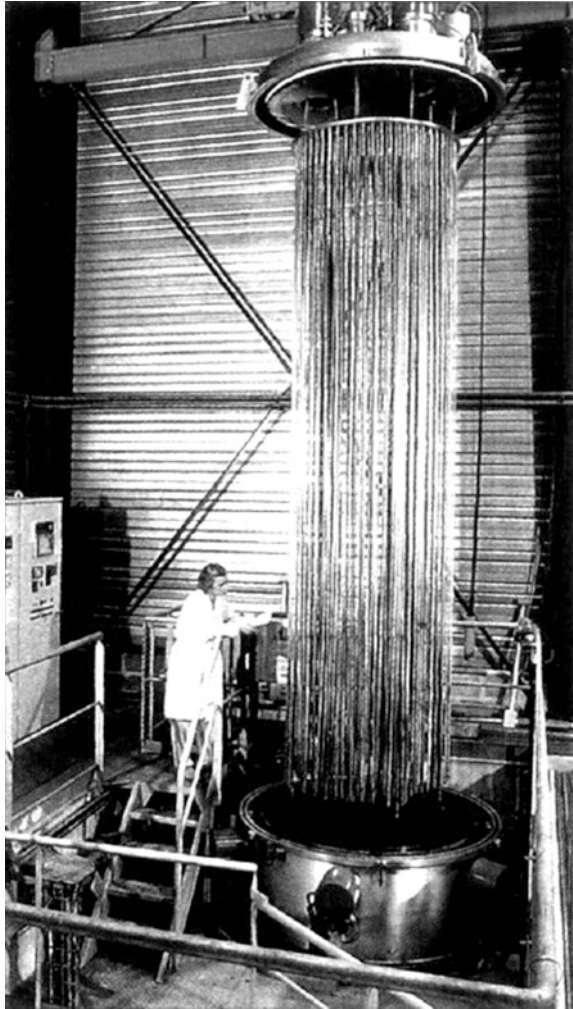
Sensitivity factor in raw material is ion nitriding process temperature. If the temperature control is not good, relatively high temperature ( $\geq 500$  °C) ion nitriding, 316L stainless steel nitrided to form a nitride layer is composed of different phases, these phases of composite structure containing:  $\gamma'$ -Fe<sub>4</sub>N,  $\epsilon$ -Fe<sub>2</sub> · <sub>3</sub>N, CrN, Cr<sub>2</sub>N, austenite ( $\gamma$ ) and ferrite ( $\alpha$ ), such a nitride layer is very high hardness (about 1400 HV), wear resistance is better; however, because CrN separate out, resulting in 316L stainless steel corrosion resistance decreased significantly, as shown in Fig. 5b.

In manufactory, manufacture is sustained and stable; reread the production records such as as-built documentation, found no significant anomalies, so machining is no problem.

Sensitivity factors in storage include: Temperature, humidity, pH value, dissolved oxygen, water conductivity, and so on. These factors mainly related to storage environment of nuclear power plant, all of these factors in the control of programs. But under the same program requirements, old nuclear power plant did not find RCCA nitriding tube surface corrosion. But In principle, these factors can promote RCCA nitriding pipe surface corrosion. so sensitivity factors in storage are not the most critical, they are just accessorial sensitivity factors.

We have found RCCA nitriding tube surface corrosion before use, so application environment is OK.

**Fig. 6** Application Nivox2 process austenitic stainless steel rod



## 5 The Process Deduction of Control Rod Surface Erosion

- The control rod surface corrosion of new fuel storage room (dry storage)

In the nitriding process of control rod tube, CrN precipitates at the grain boundary cause adjacent areas chromium depletion. This raises the cladding tube surface corrosion sensitization. In the case of an appropriate temperature, humidity, causing rod surface corrosion flecks. These corrosion products can be erased with

absorbent cotton cloth; but may appear in the same position again. Because the absorbent cotton cloth only takes away the corrosion products, there still have some corrosive materials. In addition, during the dry storage if not found some surface corrosion, does not mean it will not be; corrosion may occur when RCCA put in the spent fuel pool.

- The control rod surface corrosion of Spent fuel storage pools (wet storage)

In the factory, after the completion of the fuel assembly manufacturing, each FA needs to implement the control rods thrusting force checking, then transported to nuclear power plant. In the plant, each FA needs to implement the control rods thrusting force checking again. In thrusting force checking and transportation process, due to the mutual friction, the zirconium oxide film of guide tube can be peeling off. In the plant, mating control rod assembly of the fuel assembly is placed in the spent fuel pool. Due to reduce the surface corrosion resistance of the control rod nitriding tube, the complete dense oxide film cannot form on the control rod nitriding tube surface. Between the guide tube (Zr-4) and the control rod nitriding tube (316L), the original cell reaction is formed, resulting in electrochemical corrosion.  $\text{Fe}^+$  ions are released in the surrounding space when etching. The presence of  $\text{Fe}^+$  ions and the consumption of dissolved oxygen will slow down further corrosion. Guide tube water hole is in a relatively open space, the spent fuel pool water is in a state of flow; so the water hole near the guide tube is conducive to further spread of  $\text{Fe}^+$  ions in the water and continues to add new dissolved oxygen. This has resulted in more obvious traces of corrosion on control rod corresponding guide tube water hole.

After the above work, through metallographic analysis and experiment, manufacturer show that the residual nitriding layer is still greater than the thickness of the technical requirements. So they were loaded in QF cycle 1.

## 6 Conclusion

1. The temperature of Ion nitriding process is the most sensitive factor of RCCA nitriding pipe surface corrosion; temperature, humidity, pH value, dissolved oxygen, water conductivity are accessorial sensitivity factors. Raw material suppliers should strictly control the control rod ion nitriding process, avoid the temperature control is lax, so that the CrN separated out.
2. Compare with wet storage, RCCA surface corrosion in dry storage is significantly lighter, should try to reduce the wet storage time.
3. In view of the guide tube inside oxide film can be broke during the thrusting force checking, I suggest that cancel RCCA thrusting force checking after transported to nuclear power plant, it just as supplement checking after accelerometer out-of-tolerance.

4. I suggest manufacturer to increase the rechecking of imported raw materials, advancing raw materials localization; To strengthen the control rod nitriding tube quality supervision and tracking of raw materials.

## References

1. Zhuzu Chang, Xu Wen, Wang hong. Carburizing and nitriding heat treatment new process at home and abroad (III) [J] heat treatment technology and equipment, 2013, 34 (6): 1-9

# The Corrosion Protection of Drum Strainer in Fuqing Nuclear Power Plant

Gujian Ma and Xingbao Zhao

**Abstract** Long-term exposed to seawater, the drum strainer is easily corroded by water, moist air and other factors. The drum strainer of Fuqing Nuclear Power Plant Unit 2 was corroded during the time of installation and debugging. The reason of the corrosion includes carbon coating damaging, iron pollution in stainless steel, the cathodic protection system failed to put into operation in time, and human factors. By repairing coating, pickling, and passivating stainless steel can effectively eliminate the corrosion defects; timely commissioning of cathodic protection systems, strengthen the quality controlling of the equipment acceptance, and the process of installation and debugging can significantly reduce the risk of corrosion.

**Keywords** Drum strainer · Corrosion · Coating repairing · Pickling and passivating · Cathodic protection · Quality control

## 1 Introduction

Drum strainer is one of the water treatment equipment of circulating water filtration system (CFI) in nuclear power plant. It consists of the skeleton, stainless steel mesh, driving device, sealing device, flushing system, lubrication system, maintenance platform, cathodic protection devices, electrical control system, and so on. The drum strainer is used to intercept and remove the dirt from the seawater whose diameter is larger than that of the mesh ( $\Phi 3$  mm), ensuring normal operation of the equipments, such as cycling pumps, essential service water system pumps and condensers. As the drum strainer exposures in seawater long term, affected by seawater, moist air and other factors, it is easily to be corroded.

---

G. Ma (✉) · X. Zhao  
Fujian Fuqing Nuclear Power Co. Ltd, Fuqing 350318, China  
e-mail: magj@fqnp.com

X. Zhao  
e-mail: zhaoxb@fqnp.com

**Table 1** Material list of the drum strainer

Components	Material
The drum strainer mesh	316L
skeleton	Q345
Bolts of the mesh	A4-70
Bolts of the skeleton	A4-70
Bolts of the basic	Q345
Chief axis	42CrMo
Bearing block	QT450-10
Base plate of the bearing block	QT450-10
Wheel hub	ZG270-500

## 2 Corrosion Defects

The drum strainer of Fuqing Nuclear Power Plant Unit 2 was corroded during the time of installation and debugging. The coating of the skeleton appears breakage partly and rusts on the surface; the bolts of the skeleton and the stainless steel mesh are also corroded seriously. The coating of the equipment may peel off and some parts may even experience corrosion failure, affecting the safety of system seriously when the corrosion protection treatment is not put to use timely.

The main components of the drum strainers in Fuqing Nuclear Power Plant Unit 1 and 2 are made of seawater corrosion-resistant material, carbon steel equipment use a proper anti-corrosion measures. The chief axis of the drum strainer uses 42CrMo and the skeleton structure are made of Q345, coated with coal tar epoxy anti-corrosion coatings. Stainless steel mesh use 316L steel. The material of the drum strainer is shown in Table 1.

## 3 Corrosion Analysis

### 3.1 Less Protection During the Installation

1. Coating damage: there exists coating damage caused by the bump on the skeleton, and some coating thickness is less than that of the requirements. Drum strainer skeleton exposures in wet and high salinity environment, the coating is easily damaged with high risk of corrosion. Once the coating is damaged, the seawater enters the coating and contact with the steel body in directly, it is not only cause corrosion of the metal strongly, but also erodes carbon steel body surrounding coatings gradually, even make some corrosion pits holes in a short time.
2. Iron pollution in stainless steel: during the installing of the drum strainer, iron filings tarnish on the mesh which comes from scaffolding and welding. If the iron filings have not been removed promptly, it will produce iron pollution. The



corrosion resistance of stainless steel is up to the completeness and compactness of passive film on it. However, iron filings damage this film and make the passive state into active state. In this corrosive environment, iron pollution may induce galvanic corrosion, pitting corrosion, stress corrosion and so on, have a bad effect on safety and reliability of stainless steel equipment [1].

### ***3.2 The Cathodic Protection System (CPA) Failed to Put into Operation Timely, Causing Galvanic Corrosion***

The components of the drum strainer are made of different materials, such as stainless steel, carbon steel, and cast steel. Even though the anti-corrosion coating are coated on the surface of the carbon steel and cast steel, there exists a large potential difference between the interconnected parts, on the other hand, the sea-water is strong electrolyte solutions. These factors have led to risk of galvanic corrosion. To minimize the risk of galvanic corrosion, design has explicitly requested the use of CPA, but the CPA system was not put into operation timely and there is no temporary additional sacrificial anodes, causing corrosion of the connection parts of dissimilar materials.

### ***3.3 Human Factors***

The people of installation and debugging are lack of corrosion protection knowledge and experience, failure to identify the various aspects of the corrosion risk and take effective measures, causing corrosion defects of the drum strainer indirectly.

## **4 Treatment and Prevention**

### ***4.1 Strengthen the Protection of Site Equipment, Avoid the Destruction of Finished Products***

Carbon Steel Coating: The surface of the equipment should be cleaned when the installation is completed. Once the coating is damaged, it should be repaired in time to avoid corrosion deeply. Repair process:

1. Surface pretreatment: using the steel wire wheel and the steel wire brush for surface treatment after removing the oil and dust. The manual rust cleanliness should meet the requirements of GB/T8923-88 ST3. Painting should be finished within 2 h. If the surface is back to rust before painting, the surface should be retreated;

2. Coating: using SIGMACOVER 280LT primer and SIGMACOVER 300LT topcoat for repairing which is original design coating. Coating time interval and coating requirements should follow the instruction manual.
3. Quality inspection: after patching the film, the coating should be flat, smooth, cannot have cracks, leakage, flow, wrinkling, depression, bubbles, and other defects. It should have no significant difference between the patch area and the surrounding area. Film thickness inspection shall be carried out according to GB/T13452.2: 80 % sampling point thickness is not less than the specified thickness and 20 % sampling points thickness is not less than 80 % of the specified thickness.

Stainless steel components: after the installation is completed, the drum strainer should be cleaned by the demineralized water, removing the iron filings, and halogen ions on the surface of stainless steel. In the course of the inspection, the stainless steel components should be in need of pickling and passivation in time when it is found rust. Pickling and passivation process:

1. Surface pretreatment: removing the oil and dust. If there is a lot of oil on the surface, it can be taken alkali wash, and when the alkaline wash is finished, the surface should be washed clean by the demineralized water.
2. Pickling passivation process: according to the requirements of the specification, the pickling and passivation cream should be painted on the surface of stainless steel mesh and stay the necessary time. The cotton is used to wipe the rust and oxide before the pickling and passivation cream is drying. The wiping should not stop until the surface appears silver white. Then wash the surface by the demineralized water.
3. Quality inspection: After pickling passivation process, the surface should be uniform silver white with no obvious traces of corrosion and scarring. With phenolphthaleone check the residual liquid on the surface, pH value should be neutral. Furthermore, the blue point test should be carried out to ensure the accuracy of the results. The reagent used for the blue point test is made of 1 g  $K_3[Fe(CN)_6]$ , 3 ml (65 %\_85 %)  $HNO_3$ , and 100 ml water (for immediate use). The reagent should be impregnated with a filter paper, then attach the filter paper on the surface where is to be checked, within 30 s to observe the surface blue point. The surface of the PH is not qualified if it appears blue points. It should be noted that this test should be carried out after the surface is dry and the reagent must be rinsed after the test.

## ***4.2 CPA System Should Be Put into Operation in Time***

The CPA system should be put into operation as far as possible with the installation and debugging at the same time. Temporary sacrificial anode block should be added if the CPA system can not be put into operation timely, ensuring the drum strainer is

under the cathodic protection. Checking the operating status of the system regularly after the CPA system is put into operation. The normal protection potential range of the CPA system of the drum strainer is 250 to  $-50$  mV in Fuqing Nuclear Power Plant Units 1 and 2. Once the point data is found abnormal, notifying the relevant departments of the power plant to process and record, ensuring the normal and stable operation of the CPA system.

### ***4.3 Strengthen Quality Control of Equipment Acceptance, Installation, and Debugging***

1. It shall check whether the technical documents and inspection records are complete or not. Focus on whether the equipment is in good condition. Quality sampling should be performed if it is necessary, for example, random checking the coating thickness. Ensuring equipment acceptance is qualified.
2. Construction personnel should be strictly in accordance with the construction plan to carry out the work during installation and debugging. Furthermore, we should also pay attention to protect equipment and prevent foreign matter from entering the drum strainer. Civilized and safe construction should be conducted.
3. Quality control personnel should focus on the surface treatment of coating repairing, primer and topcoat painting during the installation, and debugging. The surface cleanliness of the drum strainer should be sampling after the installation is completed to reduce the risk of corrosion.

## **5 Summary and Recommendations**

As the drum strainer exposures in seawater long term, affected by seawater, moist air, and other factors, it is easily to be corroded. Corrosion defects occurred during installation and debugging of unit 2 in Fuqing nuclear power plant, the reasons of corrosion include coating damage, Iron pollution in stainless steel, the CPA system failed to put into operation in time and human factors. By coating repairing, pickling passivation can effectively eliminate corrosion defects; strengthen the quality controlling of the equipment acceptance and the process of installation and debugging can significantly reduce the risk of corrosion.

Peer nuclear power plant operation experience shows that corrosion inspection and treatment of the drum strainer have become an essential work every year. Even though the time window is tight, the workload is big, and the quality of corrosion treatment is high, it does not mean that the corrosion protection of the drum strainer is “the first and also the last deal” during the overhaul. The corrosion protection of drum strainer should be well planned during the designing,

manufacturing, installation, debugging, and operating, taking effective measures to achieve prevention. Finally, reach the goal of prevention as primary, treatment as secondary.

1. Project participating ensures good quality control in the manufacturing stage;
2. The corrosion treatment of the drum strainer during installation and debugging should be made a detailed record. Checking the anti-corrosion effect regularly provides experience feedback for corrosion inspection and treatment during the overhaul.
3. It should purchase an appropriate number of components for replacing in an emergency.

## References

1. Kadry Scifedine. Corrosion analysis of stainless steel [J]. *European Journal of Scientific Research*, 2008, 22 (4):508–516

# The Development of HOLLY Code and Single-Point Ex-core Detectors Calibration Method

WenHuai Li and Chao Wang

**Abstract** Since the Core Protection System (CPS) and Core Monitoring System (CMS) rely on the ex-core power range detectors to monitor the in-core power distribution, ex-core detectors have traditionally been calibrated monthly or quarterly using multi-points Movable In-core Detectors (MID) flux maps technique that is based on operational information from the current cycle. The HOLLY Code has been developed for six-section ex-core detector calibration, which is based on LOCA Surveillance System (LSS) in PWR. A simple model of LSS (sim-LSS) to monitor in-core fine axial power distribution using six-section ex-core detectors per channel has been developed for HOLLY test and qualification. The calibration parameters include the GK parameters for in-core power level and axial offset, the transfer-sensitivity matrix parameters for six-section in-core power distribution, and so on. The results of HOLLY code and sim-LSS code are reasonable and satisfying. Based on the HOLLY Code, a new single-point calibration method has been developed by replacing an actual power oscillation that would be produced in the core in multi-points calibration, with a simulation of an oscillation using predictive core neutronics solution model. The results of single-point calibration method are in accord with multi-points calibration results which are generated from real core oscillation measurement.

**Keywords** HOLLY · LSS · Single-point · Flux map · Ex-core calibration

## 1 Introduction

The six-section ex-core detector for PWRs has been developed for the LOCA Surveillance System (LSS) [1]. This ex-core detector has four neutron detectors which are axially arranged outside the reactor vessel and makes online measurements of the axial power distribution. Each detector monitors the power of the axial

---

W. Li (✉) · C. Wang  
China Nuclear Power Technology Research Institute, Shenzhen, China  
e-mail: liwenhuai@cgnpc.com.cn

quarter with its center at the same elevation as that of the detector's center, and the axial power distribution is reproduced from the signals of the six detectors using a transfer-sensitivity matrix technique.

In the conventional PWRs, the axial imbalance ( $\Delta I$ ) between the upper half and lower one of the core can be only measured with the two-section ex-core detector which consists of two axially arranged sections. These two signals are used to give readouts for reactor power level  $Pr$  and axial power difference  $\Delta\Phi$ , on the basis of calibration coefficients  $\alpha$ ,  $K_U$  and  $K_L$ , which may be set separately for each Power Range Channel.

Thus for a given Power Range Channel  $k$  ( $k = 1-4$ )

$$Pr(k) = K_U(k)I_U(k) + K_L I_L(k) \quad (1)$$

$$\Delta\Phi(k) = \alpha(k)[K_U(k)I_U(k) - K_L I_L(k)] \quad (2)$$

where  $I_U$  and  $I_L$  are the current signals (in mA), corresponding to the upper half and lower one of the six-section detector reading.  $Pr$  and  $\Delta\Phi$  are expressed in %FP,  $K_U$  and  $K_L$  are expressed in %FP/mA,  $\alpha$  is a dimensionless coefficient. The calibration coefficients  $\alpha$ ,  $K_U$  and  $K_L$ , are checked monthly during normal operation as follows.

In case of six-section detector system, however, the axial power distribution can be monitored and local maximum linear power can be calculated from the distribution. Therefore the plant capability such as the plant operating LOCA power margin can be considerably improved using the six-section detector system.

The six-section signals above mentioned are used in the LSS to provide the core average axial power distribution  $P(z)$ , on the basis of  $[TS]$  matrix, which may be set separately for each Power Range Channel ex-core detector. Thus for a given Power Range Channel  $k$  ( $k = 1, 4$ ), the LSS system performs the following calculations:

$$P_J = [COR][TS][V] \quad (3)$$

where  $[COR]$  is a radial correction matrix, depends on control rod position, and  $[TS]$  is a transfer-sensitivity matrix expressed in %FP/V.  $V$  is the six-section detector signals.  $P_J$  is six section-wise powers.

The  $[TS]$  matrix is the matrix result of sensitivity term  $[S]$  and a transfer term  $[T]$ . The  $[S]$  term is mostly related to the sensitivity of each section, including the electronics, while the  $[T]$  term represents the transfer of neutrons from the core to the ex-core detectors.

During normal operation,  $[TS]$  matrix is updated monthly for the  $[S]$  term and quarterly for the  $[T]$  term. The  $[COR]$  matrix value is determined online by the LSS computer, on the basis of the theoretical data, calculated for each of the up to ten rodged configurations.

Using a constant geometrical matrix, the six integrated power values  $P_J$  could be converted into fine mesh local power  $P(z)$  values, the active fuel height is divided into equivalent segments. The LSS computer determines the rodged configuration for each axial measurement point, and considers at this location, the corresponding

value of  $F_{xy}(z)$ . On the basis of the average axial power distribution  $P(z)$  and the axial distribution of the radial peaking factor  $F_{xy}(z)$ , the LSS computer calculates the axial power density distribution  $PL(z)$  in fine mesh points (expressed in W/cm). The comparison between the axial power density distribution  $PL(z)$  and the LOCA limit  $DLOC(z)$ , allows to determine the minimum LOCA margin  $MLOC$ .

## 2 Calibration Code: HOLLY

The main objectives of the HOLLY computer codes are: To determine calibration coefficients and matrix for each Power Range Channel of the Nuclear Instrumentation System (RPN), in order to provide readouts for power level, axial power difference, and average axial power distribution. Determination of calibration coefficients and matrixes for the ex-core detectors is made on the basis of processed in-core measurements obtained during flux mapping operation. The HOLLY code is relied on a processed flux map data file which generated by MAPLE code [2].

### 2.1 Determination of GK Coefficients

For each Power Range Channel  $k$  ( $k = 1-4$ ), the determination of GK ( $\alpha$ ,  $K_U$  and  $K_L$ ) coefficients is based on the relation between the In-core and the Ex-core axial offset values as

$$AO_{ex} = a + b AO_{in} \quad (4)$$

On the other hand, a global sensitivity term may be determined as

$$I_U + I_L = KW \quad (5)$$

where  $I_U$  and  $I_L$  are the current signals described in the above,  $W$  is a reference heat balance power,  $AO_{in}$  is the axial offset issued from flux map results.  $AO_{ex}$  is the ex-core axial offset value determined with the equivalent upper and lower sections currents.

So we can get that

$$\alpha = \frac{1 - \left(\frac{a}{100}\right)^2}{b} \quad K_U = \frac{1}{K\left(1 + \frac{a}{100}\right)} \quad K_L = \frac{1}{K\left(1 - \frac{a}{100}\right)} \quad (6)$$

When several flux maps and reference heat balances power level are considered,  $a$ ,  $b$ , and  $K$  coefficients may be determined with least-squared fitting method. Thus the  $\alpha$ ,  $K_U$ , and  $K_L$  coefficients are then determined as before. The  $\alpha$ ,  $K_U$ , and  $K_L$  coefficients values have to be set into the Nuclear Instrumentation System (RPN).

These coefficients are determined when calibration is performed with several measurements for different axial power distribution.

## 2.2 [TS] Matrix Determination

Difference with expression (3), we consider

$$[X] = [S][T]P_J^* \quad (7)$$

where  $P_J^*$  is the in-core power corresponding to the  $J$  section, and  $X$  is the reconstructed signal. Thus for  $n_k$  measurements, we obtain the following system:

$$X(i, n_k) = \sum_J S(i)T(i, J)P_J^*(J, n_k) \quad (8)$$

where  $i, J$  are the ex-core detector section number or the corresponding in-core section number, and  $n_k$  is the flux map number.

The  $[S]$  and  $[T]$  matrix have to be determined by minimizing deviations between  $X$  and  $V$ . That minimization is done with a conjugate gradient algorithm. When several measurements for different axial power difference values are considered, the sensitivity term ( $S$ ) and the transfer term  $[T]$  may be determined. When, only one measurement is considered, only the sensitivity term  $[S]$  may be determined, and the transfer term  $[T]$  is keeping its previous values.

The  $[T]$  term represents the transfer of neutrons from the core to the detectors, and the basic global transfer model used between a core sixth section and an ex-core detector section is an exponential function,  $t = e^{-H/L}$ , where  $H$  is the height of the ex-core detector section and  $L$  is the exponential constant or length.

## 2.3 HOLLY Application

The acceptance criteria are

$$|\Delta 1 = W - \text{Pr}(k)| < \varepsilon 1 \quad (9)$$

$$|\Delta 2 = \Delta \Phi_{\text{in}} - \Delta \Phi(k)| < \varepsilon 2 \quad (10)$$

where  $\varepsilon 1$  is error included in the high nuclear flux reactor trip set-point.  $\varepsilon 2$  is error using in over-temperature and over-power  $\Delta T$  protection set-points function.

A simple model of LSS (sim-LSS) to monitor in-core fine axial power distribution using six-section ex-core detectors per channel has been developed for HOLLY test and qualification. Using the flux map measurement of Lingao Nuclear



Power Plant (NPP) in China, the calibration data has been made and applied in sim-LSS code to compare differences between the ex-core detectors reconstructed power distribution and in-core flux map measured power distribution.

The flux map measurement data of core xenon transient status while rods movement at Middle of Cycle (MOC) from cycle12 is used to verify the HOLLY code. The comparison of the axial offset between in-core measurement and ex-core measurement is shown in Fig. 1. The maximum deviation of power level  $\Delta I$  in ex-core channel 1 is 0.63 %, in channel 3 is 0.58 %. The maximum deviation of axial offset in channel 1 and channel are all 0.07. These deviation results satisfy the acceptance criteria.

The comparison of the axial power distribution between in-core measurement and ex-core measurement for channel 1 at different axial offset condition is shown in Fig. 2. The maximum axial power distribution deviation at all axial offset condition for channel 1 is  $-2.38\%$ , for channel 3 is  $-2.41\%$ . The results are well within the uncertainty evaluation of axial power distribution in LSS.

**Fig. 1** Comparison of axial offset between in-core and ex-core measurement

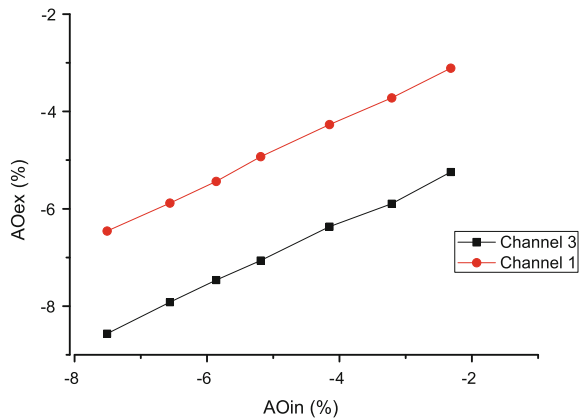
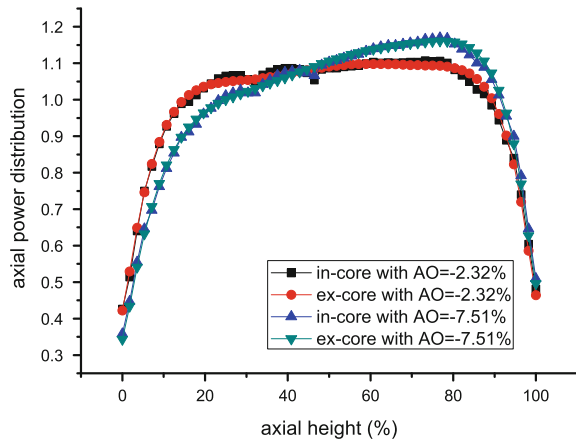


**Fig. 2** Comparison of axial power distribution between in-core and ex-core measurement



### 3 Improved Single-Point Ex-core Calibration Method

Ex-core detectors have traditionally been calibrated using a multi-point calibration technique that is based upon analysis of operational information from previous cycles or the current cycle. Multi-point calibration generally involves running movable detectors (i.e., in-core detectors) through instrumentation thimbles in some of the fuel assemblies to generate data. The collection of this data occurs at multiple frequent points during an intentionally induced axial power oscillation in the core. The data is then processed to produce multiple maps of core power distribution, each of which is referred to as a flux map. Together with the response of the ex-core detectors and the axial information from the flux map results, coefficients are derived to calibrate the ex-core detectors using HOLLY code.

Among other disadvantages, multi-point calibration is time-consuming and labor and cost-intensive. Specially, to complete the data collection, utilities are forced to spend time at low power levels, to introduce xenon oscillations in the core, or both. This undesirably requires additional plant personnel and lost power generation. Also infrequently performed in-core flux map measurement would result in premature malfunction, such as an in-core sensor becoming stuck in the core. So it is desirable to minimize the frequency with which the in-core detectors must be inserted into core.

The single-point calibration generally involves replacing an actual power oscillation that would be produced in the core, with a simulation of an oscillation, using a predictive neutronics solution model. Since the ex-core calibration coefficients essentially represent the relationship between in-core measurement power distribution and ex-core current reading. An improved single-point calibration method is developed for six-section detector calibration, which involved in three calibration step, including design coefficient generation, coupling coefficient generation, single flux map correction.

#### 3.1 Design Coefficient Generation

Because of the ex-core detector locations, which are symmetrically positioned around the periphery of the vessel, each ex-core detector provides corresponding flux information on the adjacent quadrant of the core. In each quadrant of the core, different assembly has different impact on ex-core responding. The fuel region more adjacently to ex-core locations has larger weight.

This calculation provides the relationship between the core average axial offset, and the weighted peripheral six-section axial power distribution.

$$P_{pp}^i = K^i \times AO_{in} + K_0^i \quad (11)$$

where  $P_{pp}^i$  is the  $i$ th section weighted peripheral axial power,  $AO_{in}$  is the core average axial offset,  $K^i$  is the  $i$ th section slope constant for converting core average axial offset to peripheral six-section axial power distribution.  $K_0^i$  is the offset constant for converting core average axial offset to peripheral six-section axial power distribution.

The weighted peripheral axial power could be expressed as

$$P_{pp}^i = \sum W(x, y, z, i)P(x, y, z) \quad (12)$$

where  $W(x, y, z, i)$  is the three-dimensional weighted matrix for each detector, while  $P(x, y, z)$  is the in-core three-dimensional power distribution.

The core average axial offset and the weighted peripheral axial six-section power is preferably determined by a series of rod maneuvers or a series of xenon oscillation calculations using the neutronics model at the required burnup of the calibration. The rod maneuvers and xenon oscillations are used to change the axial offset in the design calculation, and the design coefficient  $K^i$  and  $K_0^i$  are determined for each type of burnup. Each axial section of each ex-core quadrant location has an equation of expression (12).

### 3.2 Coupling Coefficient Generation

The coupling coefficients are the relationship between the raw ex-core detector six-section and the peripheral weighted core axial six-section power. Using the results of processed flux maps during an axial xenon oscillation, the coupling coefficient can be derived during the initial implementation of a state point. In future single-point analysis, the same coefficients can be used, since the coupling coefficient is mostly dependent on the core geometry and detector replacement, within barely influent by core burnup.

$$[V]_6 = [CM]_{6 \times 6} [P_{pp}]_6 \quad (13)$$

where  $[V]$  is six-section ex-core measurement current,  $[CM]$  is the coupling coefficient, a six by six matrix, which each quadrant location detector has unique one.  $[P_{pp}]$  is weighted peripheral axial six-section power.

### 3.3 Single Flux Map Correction

Using the design coefficient and coupling coefficient could establish the relationship between the in-core axial power and ex-core six-section readings. By providing a single-point flux map where a true measurement is known, this allows the constant value  $K_0^i$ , to be normalized.

After the correction of designed coefficients, one can simulate the in-core three-dimensional power distributions and ex-core measurement readings at the same time. Additional information could be set into HOLLY code combine with single-point flux map to determine the GK coefficients and TS matrix in LSS.

## 4 Application of Single-Point Method

The flux map measurements from cycle 12 of Lingao NPP are applied in the single-point ex-core calibration method qualification. Using the BOL flux map measurements to generate the coupling coefficient, using the EOL core neutronics solution model to calculate the design coefficient, using the EOL single-point flux map to normalize the design coefficient, we can simulate the in-core power distribution and ex-core measurement current for EOL in the same time, which will set to the HOLLY code to generate the calibration coefficient such as GK parameter and TS matrix. The results of EOL comparison between single-point ex-core calibration method and traditional multi-point ex-core calibration method were made.

Relations of in-core axial offset and ex-core axial offset at EOL are shown in Fig. 3. The curve fits of single-point simulated in-core axial offset and ex-core measurement axial offset points in channel 1 and channel 3 are coherent with the multi-point measurement points curve fits, which indicates that the simulated GK parameters are equivalence with measured GK parameters.

The comparison results of ex-core reconstructed axial power distribution between using single-point TS matrix and using multi-point TS matrix are shown in Fig. 4. The maximum deviation of axial power distribution is 5 % that occurred in-core peripheral area, which is not quite safety concern.

**Fig. 3** Comparison of axial offset curve fit between single-point and multi-point method

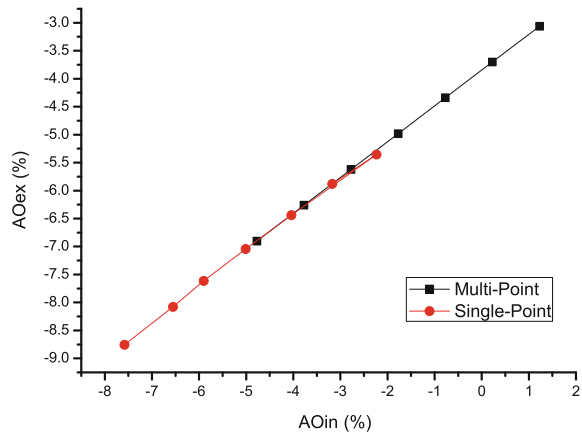
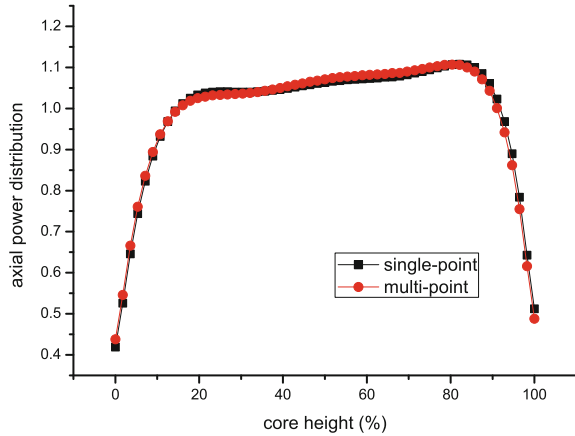


**Fig. 4** Comparison of axial power distribution between single-point and multi-point method



## 5 Conclusion

The HOLLY Code has been developed for six-section ex-core detector calibration, which is based on LOCA Surveillance System (LSS) in PWR. The calibration parameters include the GK parameters for in-core power level and axial offset, the transfer-sensitivity matrix parameters for six-section in-core power distribution, and so on. The results of HOLLY code are reasonable and satisfying.

Based on the HOLLY Code, a new single-point calibration method has been developed by replacing an actual power oscillation that would be produced in the core in multi-points calibration, with a simulation of an oscillation using predictive core neutronics solution model. The improved single-point calibration method is developed for six-section detector calibration, which involved in three calibration step, including design coefficient generation, coupling coefficient generation, and single flux map correction. The results of single-point calibration method are in accord with multi-points calibration results which are generated from real core oscillation measurement.

**Acknowledgments** The authors would like to extend their sincere appreciation to the development team of the COCO code. Appreciation also goes to Dr. Li Cai for her valuable suggestions and comments.

## References

1. ZHANG HONG. "CORE POWER DISTRIBUTION MEASUREMENT AND DATA PROCESSING IN DAYA BAY NUCLEAR POWER STATION," *Nuclear Science and Engineering*, **17(01)**, pp. 1–11, (1997)
2. Haoliang Lu, Kun Mo, Wenhui Li, et al. "DEVELOPMENT AND PRELIMINARY VERIFICATION OF THE 3D CORE NEUTRONIC CODE: COCO," *PHYSOR 2012*, Knoxville, Tennessee, USA, April 15–20, paper 383, (2012)

3. Wenhui Li, Haoliang Lu, Jिंगgang Li, et al. "DEVELOPMENT OF A NEW FLUX MAP PROCESSING CODE FOR MOVABLE DETECTOR SYSTEM IN PWR," *M&C 2013*, Sun Valley, Idaho, USA, May 5–9, 2013

# The Reasons for the Frequently Exceeded Pressure Drop of Resin Bed in Steam Generator Blowdown System

Shunlong Yang, Heng Liu, Hui Liu, Huaqiang Wu, Xiangmeng Hu, Kunfeng Yang, Jun Deng and Dawei Zhang

**Abstract** Steam generator blowdown (APG) system is a very important system for the steam generator water purification in PWR. However, the frequently exceeded pressure drop of resin bed in the APG system may cause excessive steam generator blowdown cut-off, or blowdown rate reducing, so that the steam generator water cannot be purified in optimization approach. At the same time, the real exceeded pressure drop of resin bed may also lead to the broken of resin, and then pollute the secondary water and block the related equipment of secondary cycle. So, these issues always bother the safety and stability of the system in operation. The frequent replacement of resin bed will increase unnecessary solid waste and economic losses. In order to find the main reasons for the frequently exceeded pressure drop of resin bed, the resin pressure drop in power station, the secondary water chemistry, the theoretical calculation for pressure drop, the deigned device structure and parameters, and the online instrument failure were be analyzed in this paper. After the theoretical analysis and the maintenance of resin bed during the outage, the main reasons for the frequently exceeded pressure drop of resin bed were be found, the blocked water cap of the resin bed.

**Keywords** Pressure drop · Resin bed · Steam generator blowdown system · Secondary water chemistry

## 1 Introduction

Steam generator blowdown (APG) system in nuclear power plant is used to ensure the water quality of steam generator (SG) secondary side, according to the set of continuous blowdown of SG secondary side. After cooling, APG water is treated by filters and resin beds, and is sent into condenser or conventional island waste

---

S. Yang (✉) · H. Liu · H. Liu · H. Wu · X. Hu · K. Yang · J. Deng · D. Zhang  
Fujian Ningde Nuclear Power Co., Ltd., Ningde, Fujian, China  
e-mail: shunlongyang@163.com

© Springer Science+Business Media Singapore 2017  
H. Jiang (ed.), *Proceedings of The 20th Pacific Basin Nuclear Conference*,  
DOI 10.1007/978-981-10-2317-0\_25

247

discharge system (SEL). Therefore, the resin beds of APG system bear the purification task of the APG water, and even the secondary water [1].

However, the exceeded pressure drop of APG resin bed appeared frequently since the units N1/N2 of Ningde Nuclear Power were put into operation, expressed as the relevant online instruments excessive. This issue triggered a series of work, such as isolating, calibrating, cleaning water cap of resin bed, and so on. However, after correlation processing and analyzing, this phenomenon has not been effectively alleviated.

If the exceeded pressure drop of APG resin bed is real, the following risks may be present. First, induce the resin breakage. Broken resin within the secondary relevant systems will lead to water pollution of the second loop, urge water quality exceeded seriously in SG, and even cause the unit retreat. Second, broken resin may cause related valves and pipes of secondary system blockage, and even cause the security risk. Finally, the resin bed which is in a long-term excessive pressure drop may cause damages to the instrument and related equipment.

According to the feedback of reference station [2], the exceeded pressure drop in the APG system was also occur frequently, which caused APG flow cut-off for sometimes, or caused the APG flow at a sub-healthy situation for a long time (maximum blowdown flow is  $70 \text{ m}^3/\text{h}$ ). This appearance resulted in impurity ions content higher in secondary system, so that the CPI index cannot achieve a good situation.

Therefore, the exceeded pressure drop in the APG system frequently affects the normal operation of the system, increases the consumption of the resin and solid waste production, and aggravates the risk of water quality deterioration at the same time. Thus, it is necessary to find out the defects accurately and take corresponding countermeasures, according to the abnormal phenomena and the characteristics of the equipment.

## 2 The Issue for the Frequently Exceeded Pressure Drop of Resin Bed in APG System

### 2.1 Introduction of Steam Generator Blowdown System

Figure 1 shows a simple flow chart of APG system. As Fig. 1 is shown, SG blowdown water, after cooling and decompression, is filtered by two fine filters 001FI and 002FI (pore size  $5 \mu\text{m}$ , maximum differential pressure 0.25 MPa), and then goes into the processing circuit with two parallel resin beds; each line has a half of maximum blowdown flow rate ( $70 \text{ m}^3/\text{h}$ ), namely  $35 \text{ m}^3/\text{h}$ ; in addition, each resin bed line is equipped with a cation bed (001DE or 002DE) and an anion bed (003DE or 004DE). Pressure drop meters, APG021/022/023/024LP, are respectively used to measure the APG001/002/003/004DE pressure drop, and the maximum pressure drop for one each resin bed is 0.15 MPa. APG025LP is used to



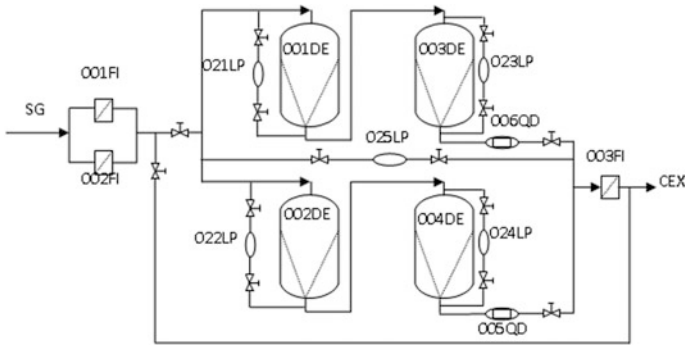


**Fig. 1** Simple flow chart of APG system

measure the total pressure drop of the two lines, and the allowed maximum pressure drop for this pressure meter is 0.25 MPa. Flowmeters, 006QD and 007QD are used to control and monitor the balance in two blowdown flow lines. Finally, the APG water goes into the drain line after filtered by 003FI (pore size 5 μm, maximum pressure 0.25 MPa), and then goes into condenser or SEL.

## 2.2 *The Issue for the Frequently Exceeded Pressure Drop of Resin Bed in APG System*

Since the units N1 and N2 of Ningde Nuclear Power were put into operation, the exceeded pressure drop of APG resin bed appeared frequently in units N1 and N2. Figure 2 shows respectively the pressure drop trend of 1APG001DE, 1APG004DE, 1APG025LP, 2APG002DE, 2APG004DE, and 2APG025LP.

The following phenomena can be seen from Fig. 2.

1. The exceeded pressure drop of APG resin bed appeared frequently in units N1 and N2.
2. The pressure drop of APG resin bed emerges different kinds of phenomena after replacement of the new resin, the pressure drop decreases, increases or keeps constant, as it can be seen from Table 1.
3. APG023LP and APG024LP in unit N2 appeared 0 or the upper limit value of meter, but in unit N1, these meters were in a stable condition.
4. APG025LP in unit N2 exceeded the corresponding standard for a long time, but it was relatively stable in unit N1.

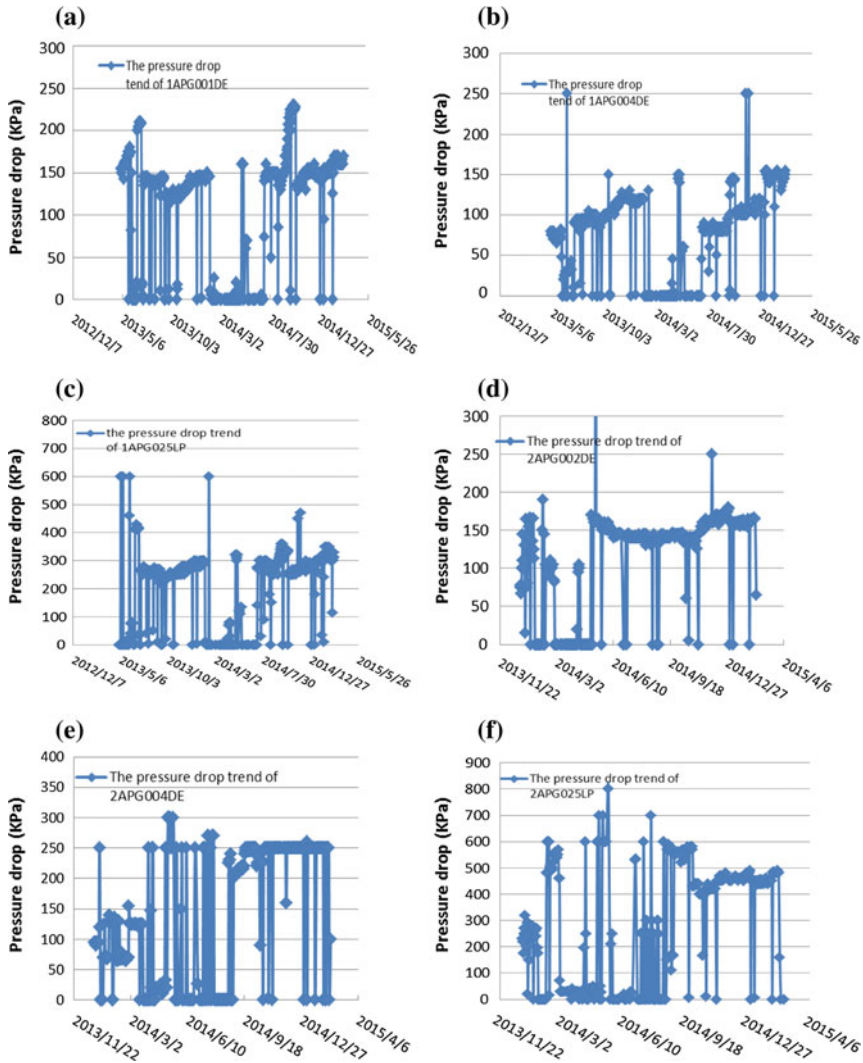


**Fig. 2** The pressure drop trend of 1APG001DE (a), 1APG004DE (b), 1APG025LP (c), 2APG002DE (d), 2APG004DE, (e) and 2APG025LP (f)

**Table 1** Different kinds of phenomena of pressure drop in units N1 and N2 after replacing the new resin

Phenomenon	Time	Remark
Increase after replacing resin	7	Increase and exceed the corresponding standard for 5 times
Steady after replacing resin	8	Steady and exceed the corresponding standard for 4 times
Decrease after replacing resin	9	Decrease and exceed the corresponding standard for 4 times

### **3 The Possible Factors and Treating Processes for the Frequently Exceeded Pressure Drop of Resin Bed in APG System**

#### ***3.1 Possible Factors 1, the Secondary Water Chemistry Was in Poor Condition or the Resin Was in Block***

If some impurities were in the secondary system, it may cause some block. Table 2 shows the WANO chemical index (CPI) of units N1 and N2. It can be seen from Table 2 that the second circuit water quality is perfect. The other, from the warehouse records, it can be seen that the resin used in desalt bed is in the period of validity. At the same time, it also can be seen that the resin is not blocked when the resin is not effective. So, the possibility of this factor is very low.

Remark, CPI, Fe, and Cu contents in feed water system, Cl, SO<sub>4</sub>, and Na contents in APG system.

#### ***3.2 Possible Factors 2, the Meters of APG021/022/023/024/025LP Are Abnormal***

In order to find out the possible reasons of the meters, the calibration works were carried out from 2014.5.1 to 2015.3.1, and found that only one times was damaged and the two times were zero drift during a total of 30 times. During overhaul, desalt water was flushed into the meter pipeline, and it was found that some pipelines were blocked by apron; however, this phenomenon was very singular. So, the possibility of this factor is middle.

#### ***3.3 Possible Factors 3, the Flow Was Uneven Due to the Blockage of APG006/007QD***

If APG006/007QD was blocked, uneven flow distribution would be got in the resin bed, which may contribute to the frequently exceeded pressure drop of resin bed. This phenomenon also can be seen in reference plants. The on-site inspection was carried out and found that it was not in the flow jam situation for APG006/007QD. APG003FI was also checked to make sure in a good condition.



### 3.4 Possible Factors 4, the Water Caps of Resin Bed Are Blocked

As we all know [3], water cap is the only way for the blowdown water in and out the resin bed; so, if water cap is blocked, it will result in the exceeded pressure drop and this phenomenon will be more and more serious, unless the blockage is cleared artificially. The model of water cap used in units N1 and N2 is all-welded stainless steel which is wired T-shaped. The gap width of water cap is  $0.2 \pm 0.02$  mm. The careful inspection to the resin bed was carried out during the outage; obviously, foreign body was not found on the water cap; however, the water cap gaps were blocked at varying degree. The partial enlarged view of water cap is shown in Fig. 3, which was washed before and after. Comparing with the two images of Fig. 3, it can be seen that the water cap gaps were clogged by tiny foreign body before flushing. After washing, the surface of water cap was clean and bright, and

**Fig. 3** The partial enlarged view of water cap washed before (a) and after (b)

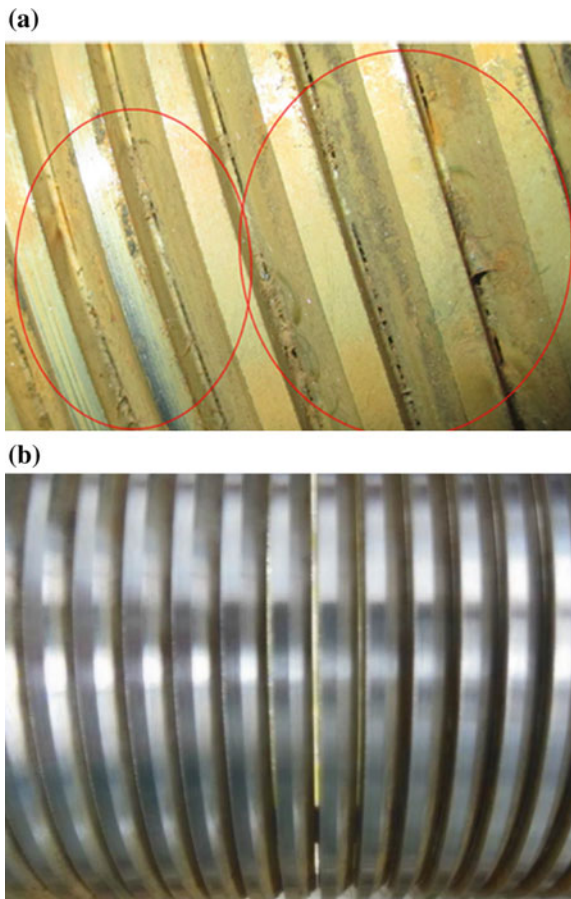


**Table 3** The reasons for the frequently exceeded pressure drop of resin bed in APG system

Number	Possible failure modes	Supporting evidence	Opposing evidence	Credibility
1	The secondary water chemistry is in poor condition or the resin was in block	None	The second circuit water quality is perfect	Low
2	The meters are abnormal	Meter failure and part of the meter pipeline failure during outage	Low failure rate during the daily operation	Middle
3	The flow was uneven	The feedback of the reference plant	None	Low
4	The water caps of resin bed are blocked	The water cap gaps were clogged by tiny foreign body	None	High
5	The designed parameters of the resin bed are unreasonable	The theoretical calculation of the resin bed	The feedback of the reference plant	Low

the water cap gap is clearly visible. The tiny foreign body appeared soft and floc, which was initially suspected to be water-soluble paper.

### ***3.5 Possible Factors 5, the Designed Parameters of the Resin Bed Are Unreasonable***

According to clarification of designer, the pressure drop of resin bed refers to the total pressure drop after the resin bed installed, which is based on operating temperature (typically 40–50 °C) during normal operation, the filling height of resin layer, flow, pressure drop characteristics of common resins, and other parameters. So, the upper limit presser drop value for each resin bed is 0.15 MPa. 0.25 MPa is set as the total pressure drop (APG025LP), which is considered a response of the operator's margin.

As we all know, pressure drop of resin bed can be obtained according to the theoretical characteristic curve, which is provided by resin manufacturers. So, the pressure drop of the resins can be calculated, which is 0.08 MPa or so. Therefore, if the pressure drops of water cap and pipeline are not in considered, the design value meets the requirements.

## 4 Conclusions

From the above analysis and phenomena, it can be seen that the reasons for the frequently exceeded pressure drop of resin bed in APG system are various. After investigating step by step, pressure drop of resin bed in units N1 and N2 is stable currently. The possible reasons are summarized in Table 3.

## References

1. Xuehong Yao, Daya Bay Nuclear Power, 1999, 03
2. Laixi Huang, Daya Bay Nuclear Power, 2002, 01
3. Qiya Yan, Guanqiong Yu, Applied Technoloyg, 2014, 07

# The Research of High-Voltage Auxiliary Power System Neutral Point Grounding Modes Between the Nuclear Power Plant and Conventional Fossil Fuel Power Plant

HouRong Pan and Yunfeng Zhang

**Abstract** Having induced the grounding modes of the high-voltage auxiliary power system neutral point in the large-scale nuclear power plant and the conventional fossil fuel power plant, having analyzed determining principles, commonly used grounding modes, requirements of related codes, determining methods of the neutral point grounding modes, having done the research of nuclear power plant and conventional fossil fuel power plant auxiliary power system's different characteristics leading to different demands of the grounding modes, and having done the research of the main nuclear power plants and the partial fossil fuel power plants high-voltage auxiliary power system neutral point grounding modes' selection and calculation with the practical engineerings, also having put forward optimal design schemes, at last, a conclusion works out: high-voltage auxiliary power system neutral point grounding modes directly affect the running of the auxiliary power system and even affect the security of the nuclear safety and the operation of the power plant. First, choose the suitable grounding mode according to the calculation result of capacitive current. Then, choose more conducive grounding mode to the operation of power plant according to the operation of technology equipments, the power requirement from the configuration, the connection of auxiliary power, and the cut from the accident of auxiliary power. I hope this article can play a role for reference on the selection of the auxiliary power system grounding modes. Currently, in power plants, the application of the extinction coil in high-voltage auxiliary power system neutral point is less experienced. As some power plants which are under-construction will be putting into operation one after another, a whole set of perfect security arrangements and operating experiences will also be accumulated inevitably.

---

H. Pan (✉) · Y. Zhang  
Hebei Branch Electric and I&C Dept, China Nuclear Power  
Engineering Co., Ltd, Hebei, Shijiazhuang, China  
e-mail: panhr@cnpe.cc

Y. Zhang  
e-mail: zhangyfe@cnpe.cc



**Keywords** Nuclear power plant · Fossil fuel power plant · Neutral point · Grounding mode · Nuclear safety · Capacitive current

## 1 Introduction

Affected by the Fukushima incident in Japan, nuclear power is a clean and efficient energy once stagnant development. With the increasing development of China's industrialization process, environmental degradation is worse in some parts of the region, and environmental pressure increases rapidly, such as the large area of fog and haze in 2013 is irrefutable evidence. Restart nuclear power is the trend. But after the nuclear power plant project approved to restart, its access threshold is improved, and the requirements of technology and safety indicators must reach the international level of the three generations of nuclear power units. At present our country has been put into operation for most of the M310 units, in the construction including WWER-1000 improved, AP1000, and other third-generation units. Recently, our country developed a 1000 MW level with independent intellectual property rights of the third generation of nuclear power brand "Hualong 1."

The grounding mode of the high-voltage auxiliary power system of power plant relates to the safe operation of power plant, the continuity of power supply, and other important issues, in professional technology aspect at the same time, also involves auxiliary power system overvoltage and insulation coordination, relay protection, grounding design, and many other fields. At present put into production or in construction of domestic nuclear power units and conventional fossil-fired power plant in different ways of high-voltage auxiliary power system, neutral point grounding continuously improves the capacity of power plant; auxiliary electrical capacitance currents are more; influence of safe operation of the auxiliary power system is greater. Although there are rules and regulations on the grounding mode of neutral point, the choice of most suitable for plant operation of grounding mode and implementation plan is still controversial. Besides, the determination of resistor connected way and resistance also needs in the actual project, through the analysis and calculation, after comprehensive consideration of various factors.

There are conclusions of determination principles and methods of power plant high-voltage auxiliary power system neutral point, and findings of nuclear power plants and conventional fossil-fired power plants of high-voltage auxiliary power system neutral point grounding mode. We study and draw the design requirements and design optimization, and then analyze to improve the safety of equipments and reliability of power supply, and apply to the following localization of nuclear power plant design, for the choices of nuclear power plant high-voltage auxiliary power system neutral point grounding mode to provide reference in the future.

## 2 Principles for Determining the Neutral Point Grounding Mode

Most of the faults of power plant high-voltage auxiliary power system are caused by single-phase grounding, so that the generator outage occurred frequently, often burn circuit breakers, switch cabinets, mutual inductor, transformers, cables, and other equipments, even the occurrence of burning generatrix, the unit stopped several hours, directly cause economic losses. With the increase of capacity of generating units in power plant, the increasing high-voltage auxiliary power system load and high-voltage cables, there have been a corresponding increase in, resulting in, high-voltage auxiliary power system of the single-phase grounding fault current which increases, directly affecting the power plant safety, reliability, continuous and equipment insulation level, and single-phase capacitor current of equipment damage.

Due to the heat capacity of power equipments in power plant, auxiliary power system is relatively low. Therefore, we should limit single-phase grounding fault current magnitude to prevent burning; at the same time, equipment which fault cannot restore should be as soon as possible withdraw from the operation, to prevent the expansion of the equipments damage or malfunction. In order to ensure the reliability of its operation, it can be automatically eliminated to prevent the failure of the power supply reliability; when there is occurrence of unrecoverable faults, the fault equipment must be isolated as soon as possible, so as not to affect the normal power supply. Therefore, it is important to identify and isolate the ground fault branch.

According to the above factors, the basic principle of the neutral point grounding mode of power plant auxiliary power system is determined:

1. The minimum impact to continuous power supply is single-phase grounding fault, and equipments of auxiliary power system can continue to run for a long time.
2. When the single-phase grounding fault occurs, the sound phase of a low-voltage multiple occurs, not to destroy the power system insulation level, so that there is a development of interphase short circuit.
3. When the single-phase grounding fault occurs, the fault current can be limited to the minimum level to the motor, cable, etc.
4. To minimize the impact of inter-plant equipments.
5. Grounding equipments are easy to order, and the grounding protection is simple, and the investment is small.

### **3 Regulation, Standard Requirements**

#### **3.1 Nuclear Power Plant**

(NB/T20051-2011 Nuclear power plant power system design code)

As specified in the specification 5.2.2.2.1 pressure water reactor nuclear power plant medium voltage auxiliary power system neutral point grounding mode: when the medium voltage auxiliary power system grounding capacitor current is 10 A and below, it should be the neutral point grounding mode in order to be able to run continuously, and allowed within the time limit with single-phase grounding fault conditions, to gain time for handling fault, and this time the need for insulation of continuous monitoring system. When the grounding capacitance current is higher than 10 A, the security and availability of the nuclear power plant can be met, and other grounding modes are available. The specification is RCC-E-2002 (The pressurized water reactor nuclear power plants nuclear island equipments design and construction rules) for the development of reference, combined with the domestic nuclear power plant design, construction, and operation experience in the preparation, for reference to France 900 MW series of pressurized water reactor nuclear power plant design of nuclear power plant.

#### **3.2 Fossil-Fired Power Plant**

##### **3.2.1 (GB 50660-2011 Large- and Medium-Sized Fossil-Fired Power Plant Design Code)**

The 16.3.2 section provides the following way of the neutral point grounding mode of the high-voltage auxiliary power system of fossil-fired power plant:

1. The neutral point grounding mode of high-voltage auxiliary power system of fossil-fired power plant can be used in the form of non-grounding, and grounding with grounding resistance.
2. When the grounding capacitance current of high-voltage auxiliary power system of fossil-fired power plant is in the following 10 A, the neutral point can be used in the form of a non-grounding mode, and can also be used with high resistance grounding mode. When using the high resistance grounding method, the total current of the single-phase grounding fault is less than 10 A, and give an alarm to protection, all above should be based on the reasonable choice of grounding resistance.
3. When the grounding capacitance current of high-voltage auxiliary power system of fossil-fired power plant is in the 7 A above, the resistance grounding mode can be used in the resistance. Grounding resistance should make when single-phase grounding fault occurs, the resistive current is not less than capacitive current, and single-phase grounding fault current total value that protection device for accurate and sensitive action on the trip.

### 3.2.2 (DL/T620-1997 Over Voltage Protection and Insulation Coordination for AC Electric Device)

The 3.1 provisions of the specification are as follows:

1. The design of high resistance grounding system should conform to the standards of  $R_0 \leq X_{C0}$ , to limit transient overvoltage due to arc grounding fault. Generally the grounding fault current is less than 10 A.  $R_0$  is a system equivalent zero sequence resistance, and  $X_{C0}$  is a system for each phase of distribution capacitance.
2. A low resistance grounding system attempt to obtain adequate current for fast and selective relay protection, grounding fault current is generally used for 100–1000 A. For general system, limit transient overvoltage  $(R_0/X_0) \geq 2$ .  $X_0$  is the equivalent zero sequence inductive reactance of system.

Content above and DL/T5153-2002 (Thermal power plant with electric design technical requirements) are consistent with the requirements.

## 4 The Methods of Determining the Mode of Neutral Point Grounding

### 4.1 Capacitance Current Calculation

To determine the neutral point grounding mode, the current flowing through the neutral point is first calculated. General calculation method is the maximum capacity of a plant with a station transformer or auxiliary transformer connected to the power supply network of single-phase grounding capacitor current and according to this determines the grounding mode, the selection of equipment and setting relay protection.

The capacitance of the high-voltage power system is mainly based on the capacitance of the cable. The calculation of total capacitance of the cable according to the capacitance relates to the grounding of various cables, and the total capacitance of system is calculated by multiplying the total capacitance of the cable by 1.25. Single-phase grounding capacitive current can be obtained by formula (4.1):

$$I_c = \sqrt{3}U_e\omega C \times 10^{-3} \quad (4.1)$$

Type:  $\omega = 2\pi f_e$

$I_c$ —the capacitance current of single-phase grounding (A);  
 $U_e$ —the rating line voltage of auxiliary power system (kV);  
 $\omega$ —angular frequency;

$f_c$ —rating frequency (Hz);

$C$ —per phase resistance to earth of auxiliary power system ( $\mu\text{f}$ ).

The capacitance current of single-phase grounding of 6–10 kV cables can be calculated by the following formula:

Line of 6 kV cables:

$$I_c = \frac{95 + 2.84S}{2200 + 6S} U_e \quad (4.2)$$

Line of 10 kV cables:

$$I_c = \frac{95 + 1.44S}{2200 + 0.23S} U_e \quad (4.3)$$

Its  $S$ —cross section of cables ( $\text{mm}^2$ ).

#### 4.2 According to the Calculation Results of the Capacitance Current

For the methods of determining mode of neutral point grounding of high-voltage auxiliary power system by the calculation results of capacitance current, contrastive study of neutral point grounding mode is shown in Table 1.

**Table 1** Neutral point grounding modes of high-voltage auxiliary power system of domestic nuclear power plant and fossil-fired power plant

Type of plants	The name of the project	Grounding mode
Fossil-fired power plant	200 MW and below	Non-grounding or grounding by arc suppression coil
	300 MW and above	Grounding by resistance
Nuclear power plant	The first and second phase of the Qinshan project, Dayawan project, The first and second phase of the Lingao project	Non-grounding
	The first phase of the Tianwan project, Sanmen project	Grounding by resistance
	The first phase of the Fuqing project, Fangjiashan project	Non-grounding in normal time, grounding by arc suppression coil when single-phase grounding

## 5 Contrastive Study

Limited information and space, the following comparative study is only for the current domestic M310, WWER, AP1000 nuclear power units and 300 MW and above of conventional fossil-fired power units, and study is about the grounding mode of high-voltage auxiliary power system.

### 5.1 Situation Analysis

At present, neutral point grounding modes of high-voltage auxiliary power system of domestic nuclear power plant and fossil-fired power plant are shown in Table 1.

### 5.2 Contrastive Study

From Table 1, we can choose the grounding mode by meeting the requirements of calculation of capacitor current, the mode of non-grounding can be used in the following 10 A; while the capacitor current is 10 A above, we can only use the mode of grounding by arc suppression coil or resistance. Different grounding modes of single-phase grounding fault occur, and take different fault measures, non-grounding, high resistance grounding, and arc suppression coil grounding at the time of the first single-phase grounding fault which is only alarm without tripping, and resistance grounding mode trip directly, which directly affects the operation of the mode of auxiliary power plant, and nuclear safety and operation safety of the nuclear power plants and fossil-fired power plant. It is believed that the selection of the grounding mode and the operation mode of the power plant process equipment is closely related to the requirements of the power supply, the service power of the plant and the exchange of power accident. Typical wiring diagram of high-voltage auxiliary power system of M310, WWER1000, AP1000, and fossil-fired power units of 300 MW and above is shown in Figs. 1, 2, 3 and 4.

#### 5.2.1 Power Supply Requirements of Process Equipment Configuration and Operation

The biggest difference of nuclear power plants and conventional fossil-fired power plants is that the load classification and nuclear power plants with nuclear safety and the safety of equipment and related equipment, to meet the requirements of “defense in depth”, needs to set up emergency shutdown installations, containment isolation, emergency installations of cooling core heap and heat discharge, and safety features of preventing radioactive substances to the surrounding

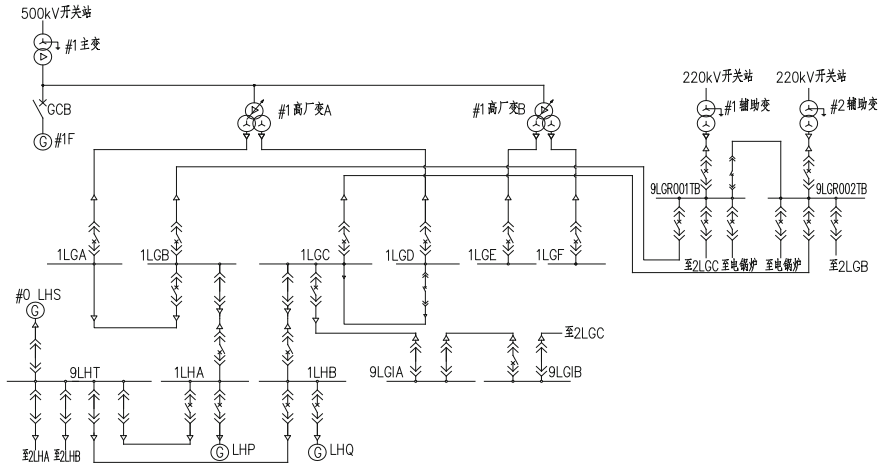


**Fig. 1** Typical wiring diagram of high-voltage auxiliary power system in the M310

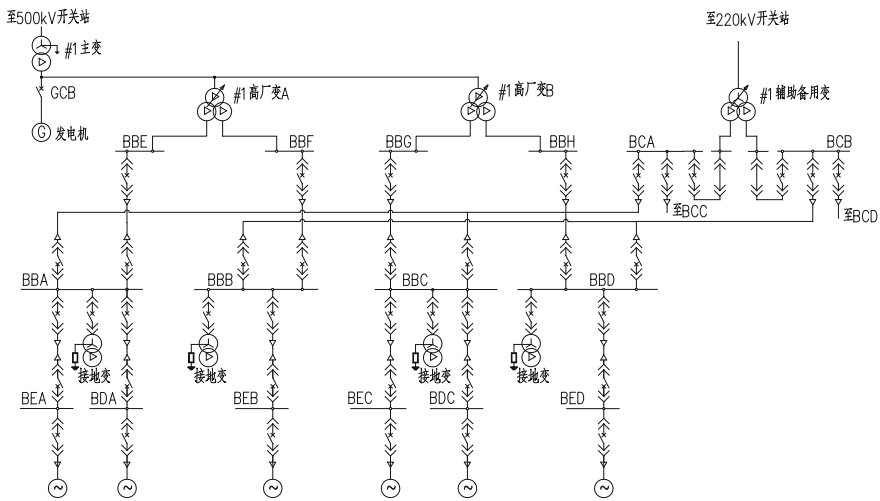


**Fig. 2** Typical wiring diagram of high-voltage auxiliary power system in the WWER1000

environment. Fossil-fired power equipment only includes safety equipment, and no nuclear safety-related equipment.

1. M310 and WWER1000

The M310 and WWER1000 are in the presence of medium voltage power load, in any working condition (the whole plant, the design reference accident) to ensure that these loads are reliable power supply. Without normal power supply, emergency power supply is supplied by emergency diesel engine to the special safety

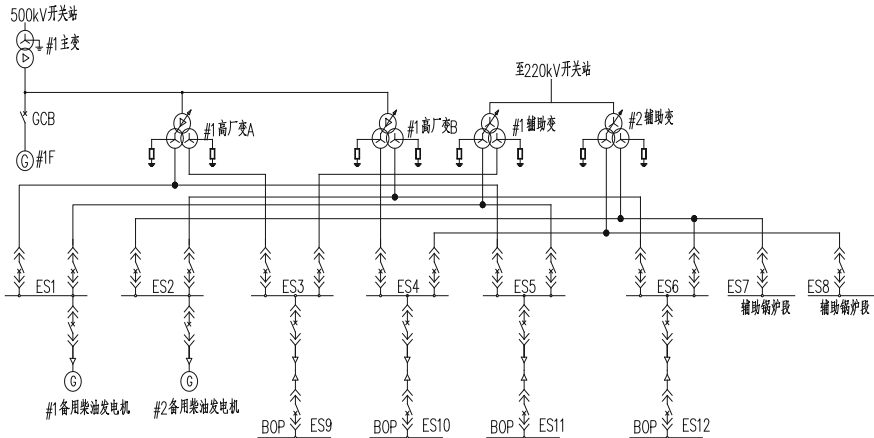


**Fig. 3** Typical wiring diagram of high-voltage auxiliary power system in the AP1000

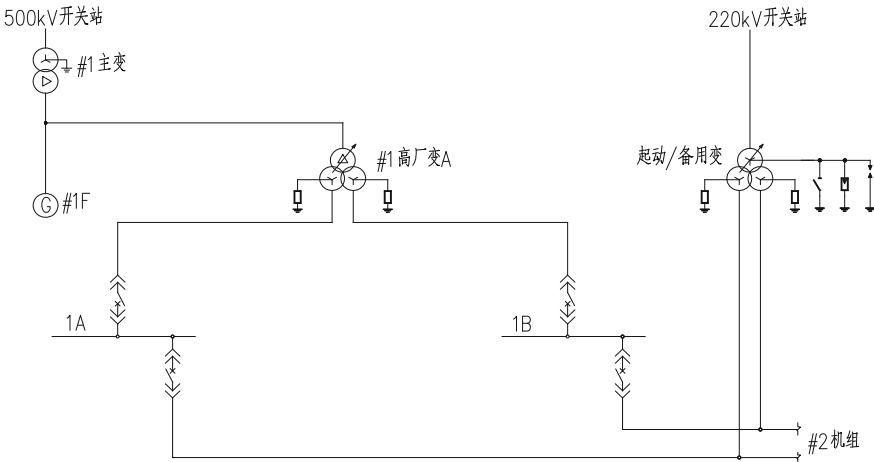


**Fig. 4** Typical wiring diagram of high-voltage auxiliary power system in 300 MW and above of fossil-fired power units

facilities. M310 emergency power supply system of diesel engine is a neutral point ungrounded system, and when the first single-phase grounding fault occurs, the action on the signal, without tripping, also can ensure continuous power supply time, WWER emergency power supply system of diesel engine with high resistance grounding; when first single-phase grounding fault occurs, the situation is as same as the M310, also moves to the signal. From the above setting, we can find that the M310 and WWER types need to maintain the operation of the medium voltage auxiliary power supply system. The emergency power supply system can meet the needs of losing continuous power supply and ensure the safety of nuclear power.



## 2. AP1000

AP1000 maintains reactor core cooling and containment isolation and heat output safety function no longer depend on AC power supply system of both inside and outside the plant, and compared with M310 and WWER1000, AP1000 has no emergency medium voltage load, in addition to main pump circuit breaker, it pumps power when the heap shutdown, and the rest of the AC power has safety-related functions of executing the cutting main system for non-security level.

One resecting a circuit of 6 kV bus line. From Table 2, if most of the loops of 6 kV bus jump back due to single-phase grounding fault, the unit output has no effect, and only the resection of wind machine and other few load need to reduce the unit load. With the continuous expansion of the power grid capacity, the output of the unit has little effect on the system, but the sudden failure of the 300 MW and the above units has a greater impact on the system.

Based on the above analysis, from the view of the process and equipment configuration and operation mode, requirements of power supply should ensure nuclear safety defense in depth and the safety of the equipment; when single-phase grounding fault occurs, it has the highest reliability requirements of the M310 units for medium voltage auxiliary power supply, the mode of neutral point grounding by non-grounding or arc suppression coil grounding, fault action in signal in favor of nuclear safety facilities of power supply. Emergency diesel engine power supply system is a neutral point non-grounding system; the fault of single-phase grounding is able to meet the requirements of continuous power supply. The reliability requirements of medium voltage auxiliary power supply of WWER are also higher; in the normal operation, the mode of neutral point grounding is resistance grounding, and the grounding protection action is tripping, but due to emergency diesel engine using high resistance grounding, reliability also meets the requirements. Medium voltage AC system of AP1000 has no nuclear safety requirements. The mode of neutral point grounding is resistance grounding, and the grounding protection action is tripping. And 300 MW and above conventional fossil-fired power only has equipment safety requirements, the mode of neutral point grounding

**Table 2** The unit output with resecting a circuit of 6 kV bus line

The name of the loop	The unit output/%
Circulating water pump	Summertime 60, Wintertime 100
Condensate pump	100
Coal mill, mill exhauster	100
Belt conveyor	100
Induced draft fan, pressure fan, primary air fan	70
Forepump	100
Open circulating water pump	100
Mortar pump	100
Low-voltage power supply of main plant and auxiliary shop	100

is resistance grounding, and the grounding protection action is tripping. The portion of loop tripping on the output of electric power has certain influence, but compared with non-grounding, single-phase grounding may cause bus short-circuit fault, and cause the unit shutdown; this harm is much smaller and more to ensure the safety of the device.

### 5.2.2 Leading for Service Power

Unit plant equipments of M310 reactor only by main power outside the factory, it is single supply, standing load from main and auxiliary power supply outside the factory, it is dual power supply; WWER1000 and AP1000 unit load from main and auxiliary power supply outside the factory, respectively, in the shutdown process, load power supply by main and auxiliary power supply outside factory, and the emergency diesel generator power supply. Whether it is on the unit and standing load or emergency power supply reliability is higher than the M310. 300 MW and above of the unit load from the high-voltage station transformer and the high-voltage start/standby transformer each lead a power, the power to continue the process of the security load in addition to the above two power supplies. The power supply of diesel generator set the reliability of the unit and the load power supply is higher than M310. Auxiliary power device of M310 unit is with a single power supply, if WWER high-voltage station transformer has failure, it can switch to standby power, but still need to stop. AP1000 unit load is at least with two power supplies, when there is a failure to continue to operate, while the fossil-fired power unit load has two power supplies, when one failure can be switched to another power to continue to run. From the view of ensuring the continuous and stable operation, the safety of the main equipment power plant, and improving the operation time of the power plant, the M310 unit has the highest requirements for power supply. That is why many different grounding modes can suit neutral point of high-voltage auxiliary power system of units.

### 5.2.3 Results of Factory Power Accident

M310 reactor and WWER1000 reactor are with double heap layout, four sets of high-voltage station transformer and two auxiliary transformers in two sets; capacity of auxiliary transformer of the M310 is smaller than the single-station transformer; capacity of auxiliary transformer of the WWER1000 and single-station transformer is basically the same. The AP1000 reactor type uses a single heap layout and sets two high-voltage station transformers and two auxiliary transformers of same capacity and number.

In the type of the M310, when the power supply is switched to the standby power supply, the unit needs to stop. While in the WWER1000, when switch to standby power supply, turbine generator set down to load but to maintain the load required by 40 % power of reactor, only to stop the pile. From the current

understanding of operating mode of the AP1000, when switching to the standby power supply, the unit can take power under generation operation, but the actual practice has not yet run experience; still need to further implement the project. Fossil-fired power units are usually in the event of single-phase grounding fault when cutting off equipments, even if losing the power of the medium voltage bus, auxiliary power system can be quickly switched to the standby power supply, in the premise of ensuring the safety of equipment, basically does not affect the operation of power plant or load operation. Thus, when M310 high-voltage auxiliary power fault occurs, switching to auxiliary power directly into the shutdown state, to maintain the continuity of power supply is very important and necessary, and WWER and AP1000 plants with switching service power are not directly shut-down; there may be power back in operation as soon as possible; power supply continuity requirements are lower than the M310, and it is suitable for the resistance grounding mode, the selection of resistance grounding of fossil-fired power units, switching service power rapidly when single-phase grounding fault happens, which can satisfy the need of safety equipment, and also can meet the requirements of the power plant runs continuously.

#### **5.2.4 Summary**

From the above three aspects' analysis, M310 units in single-phase grounding fault timely keep continuous operation for a period of time as soon as possible to eliminate the fault. WWER and AP1000 can occur after the single-phase to ground fault occurs in the immediate tripping protection equipment safety, also on nuclear safety has little effect or no effect. When single-phase grounding fault of separate circuit of fossil-fired power units happens, it trip immediately, to the power plant output, and it does not affect or less affected, mainly to meet the needs of safety equipment.

### **5.3 Engineering Application**

According to high-voltage auxiliary power system neutral point grounding mode of the actual project of nuclear power plant and conventional fossil-fired power plant, to do one by one comparison research, and put forward the design optimization program. M310 nuclear power units in Fuqing nuclear power plant, WWER nuclear power units in Tianwan nuclear power plant No. 3 and No. 4, AP1000 nuclear power units in Sanmen nuclear power plant are taken as examples. A case study of fossil-fired power units is the 300–1000 MW unit designed by in a number of electric power design institutes.

### 5.3.1 Grounding Mode and Arc Suppression Coil Grounding Mode

#### 1. Grounding scheme

In the first phase of the Fuqing project, the high-voltage station transformer A and auxiliary transformer supply, capacitive current of the auxiliary power system nearly 13 and 17 A, and in accordance with the requirements of the RCC-E, which neutral point should take non-grounding mode, in order to achieve with grounding fault operation for a period of time, there is a greater risk. According to EPRI test results of arc self-extinction behavior with single-phase grounding fault, in the neutral point grounding mode, capacitive current is more than 10 A, arc is difficult to extinguish and has not meet the reliability requirements; and in the event of single-phase grounding, such a large capacitive current will probably soon by the single-phase grounding develop phase to phase short circuit. For example, a  $2 \times 300$  MW power plant hopper turbine circuit in 6 kV flat cable dragged improper, on the rail turbine wheels rolling off, resulting in phase A unstable grounding (Yellow cable core wire ablate, found at the scene) and generate intermittent arc grounding fault, non-fault phase B and C overvoltage. At this point, the switch cabinet in test position of a fan circuit corresponding to the vertical bus C support insulator is weak and under voltage breakdown occurs, resulting in heterogeneous (A, C) two grounding points to short-circuit in the 6 kV IIA section system. In the case of two points to ground, turbine loop through the large fault current bucket, A fuse blowing, contactor tripping, bucket turbine circuit grounding fault clearing, and 6 kV bus phase C grounding fault still exists, due to phase C of the bus connection failure cannot be eliminated, the metal vapor arc generated by the faults began to spread, causing static contact phase to phase short circuit of switch cabinet bus side. After phase-to-phase fault, high-voltage station transformer over current protection act, switch of the 6 kV IIA section of the inlet wire of power supply is tripped, the 6 kV IIA section of bus power loss. The fault ends. The whole failure process is only about 4–5 min. From the point of view of the failure process, the single-phase grounding fault is the basic reason for the development of the fault. If the fault is still used in the non-grounding mode, it cannot guarantee the reliable operation of the medium voltage system. And due to reasons described in 4.2.1, the M310 unit because of the plant with operation requirements, as much as possible with a ground fault operation for a period of time is needed, and low resistance does not satisfy this requirement; so the neutral point grounding mode makes comprehensive transformation, and finally determine the neutral point by eliminating arc circle (with adjustable) grounding capacitive current compensation and grounding line selection device method, normal fire extinguishing coil offline, the single-phase grounding fault quickly into the arc suppression coil compensation capacitance current, if it is permanent fault, fault line selection, but also greatly improve the personal safety protection.

## 2. Calculation of arc suppression coil capacity

It should adopt the way of compensation operation. The capacity of arc suppression coil is generally calculated by the following formula:

$$Q = 1.35I_c \frac{U_c}{\sqrt{3}} \quad (5.1)$$

Type:

$Q$ —compensation capacity (kVA);

$U_c$ —rated line voltage (kV) of the auxiliary power system;

$I_c$ —capacitive current (A) of the auxiliary power system.

## 3. Existing problems

Although the fire arc suppression coil grounding mode has its own advantages, such as through the capacitive current compensation, slowing the rise speed of recovery voltage, it is advantageous to the connected arc extinguished, reduces the occurring probability of the intermittent arc grounding over voltage and the most instantaneous grounding fault automatically disappear. The grounding system with arc suppression coil and non-grounding system belongs to the category of ineffective grounding, and it can take 2 h of fault. But the grounding by arc suppression coil also has inherent defects, neutral point via arc suppression coil grounding divided into over compensation and under compensation, the so-called over compensation refers to the compensation way of inductive current which is greater than the volume of current; so-called under compensation refers to the compensation way of inductive current which is less than the capacitance current. In practice, the compensation method is adopted to prevent the operation mode from being changed, the capacitance current is reduced, and the arc suppression coil is in the resonance point. Arc suppression coil is close to full compensation operation, and it will enlarge the displacement voltage of neutral point; it is the “unreal grounding” phenomenon. Need to pay attention to arc suppression coil in domestic and international power plant auxiliary power system is rarely used. It is understood only in certain 200 MW steam turbine factory in Guangdong electrically neutral point and part of 100 MW and below the small units used is also a lack of a wide range of operating experience, in the actual application process; grounding mode of operation is relatively complex; grounding protection is also more complex; fire arc suppression coil through the contactor can be fast and reliable investment; and failure probability of the devices and the neutral point displacement is too limit problem remains to be further understood tracking.

#### 4. Design optimization

For the capacitive current of the medium voltage auxiliary power system more than 10 A, but also want to take a neutral point of non-grounding mode operation, the following measures can be taken to reduce the capacitive current to 10 A.

Which is not directly related to the production of the power plant load, such as factory before the district office buildings, dormitories, and so on load not by the plant with power supply, replaced by public power supply.

Using the new technology of medium pressure casting bus instead of cable lines, can effectively reduce the capacitive current, the technology currently in the nuclear power plants built by China Guangdong nuclear power has been successfully applied.

For the long medium voltage load of individual cable lines, the method of setting the isolation transformer is adopted to reduce the capacitance current of the auxiliary power system.

### 5.3.2 Resistance Grounding Mode

#### 1. Detailed classification

The traditional classification is divided into two types, which are high resistance grounding and low resistance grounding. With the development of resistance grounding technology, three kinds of grounding modes, which are high resistance, middle resistance, and low resistance, are gradually developed. The grounding fault current is less than 10 A in high resistance grounding fault. Low resistance grounding fault current is generally 100–1000 A. Which does not give the definition of resistance of 30–300 A interval, according to the relevant literature, such as Table 3 (system voltage is 6.3 kV).

#### 2. The resistance value of grounding resistance calculation

Our country still has no standard to make clear regulation to the choice of neutral point resistance.

The choice of neutral point resistance value must be according to the specific conditions of power plant; it is necessary to consider the factors restrict the gap arc light grounding overvoltage and ratio of relay protection sensitivity, on the lines of communication interference, touch voltage and step voltage, analysis and comparison, according to the comprehensive effect of the best original in choice.

Neutral point resistor direct access system resistance calculation formula is as follows:

**Table 3** Resistance grounding resistance division

The resistance division	High resistance	Middle resistance	Low resistance
Resistance range ( $\Omega$ )	>300	10–300	<10
Earth fault current IR (A)	IR < 10	10 < IR < 600	600 < IR < 1000

$$R_N = \frac{U_c}{\sqrt{3}I_R} \quad (5.2)$$

Type:

$R_N$ —the resistance value of a resistor direct access (K);

$U_c$ —rated line voltage (kV) of the bus bar of the high-voltage power plant;

$I_R$ —grounding resistive current (A), should not be less than the grounding capacitance current of the system.

### 3. Selection of grounding resistance in neutral point high resistance grounding mode

Control of single-phase grounding fault current is less than 10 A.

Generally according to  $I_R = (1-1.5) I_C$  to choose, calculation according to the 6.3 kV of medium voltage station voltage, grounding resistance to take 300–500  $\Omega$  or so.

In high resistance grounding mode, for capacitive current below 7 A, at present, whether nuclear power plant and conventional fossil-fired power plant, high-voltage auxiliary power system adopt the cable network, so capacitance current in large power plant basically are more than 7 A, high resistance grounding mode is not used.

### 4. Selection of resistance

$$I_R = U_{ph}/R_n \quad (5.3)$$

$$K = I_R/I_c \quad (5.4)$$

$R_n$ —neutral point resistance;

$U_{ph}$ —rated phase voltage;

$I_R$ —the current flowing through the  $R_n$  in single-phase grounding fault;

$I_c$ —power grid capacitance current.

#### A. To limit the arc grounding over voltage requirements

The principle of neutral point grounding with resistance to limit the arc grounding over voltage is the role of the energy consumption of resistance, when the single-phase grounding fault happens, the fault arc from dying to reign takes half a cycle of the time; in this half a cycle, charge of non-fault grounding capacitor will be released to the earth through the neutral point grounding resistance  $R_N$ , the speed of capacitor charge discharge is associated with  $K$  value ( $R_N$ ), with the

$K$  value increasing, arc over voltage is reduced accordingly. But arc over voltage ratio decreased and the  $K$  value of the relationship is not linear relationship, when the  $K$  value is greater than 4, then increase  $K$ ; the effect of decrease of arc voltage is not obvious. At home and abroad lots of experiments and calculations of many research institutions and researchers show that, when the  $I_R = I_C$ , the ratio of intermittent arc over voltage can limit in less than 2.6 times. The ratio of intermittent arc over voltage can limit in less than 1.8 times when the  $I_R = 4I_C$ , generally selected  $I_R = (1-4)I_C$  can meet the requirements to limit the overvoltage of the intermittent arc.

#### B. To ensure the sensitivity of relay protection

From the point of view of the sensitivity of relay protection, the bigger the  $K$  value (the smaller the  $R_n$ ), the better, however, the microcomputer protection generally has the function of zero sequence protection, and the current starting value is quite small (0.01 A). Whether in the middle or low resistance grounding system, the single-phase grounding fault current is much larger than that of each line, and it can meet the sensitivity of zero sequence protection generally.

#### C. From the consideration of personal safety

Neutral point through a small resistance connected to distribution network in the single-phase grounding fault and the fault point grounding potential rise caused by fault grounding short-circuit current is relatively large, and there may be resulted in the step voltage and the contact voltage exceeds the allowable value. If the person is close to the point of failure or contact with the failure of electrical equipment may cause casualties. So from the lower step and touch voltage angle of the fault point, neutral grounding resistance is as possible.

#### D. Consideration from the point of reducing the fault point grounding short-circuit current

Single-phase grounding short-circuit current of fault point is larger, the fault of equipment failure, the more damage, considering the reduced single-phase grounding fault current of equipment damage and the value of neutral point grounding resistance is the bigger, the better.

In summary, the choice of neutral point grounding resistance is a comprehensive technical and economic problem, according to the specific conditions of various plants and analysis comparison of characteristics of electrical comprehensive and makes selection of the best solution.

Previous years, China's Motor Function Association High-pressure Committee Organization held repeatedly neutral point grounding technology seminar, the experts basically formed a consensus, in the premise of meeting the reduction of the intermittent arc grounding over voltage, choose the bigger resistance of neutral grounding resistance.



E. The value of grounding resistance

In 6 and 10 kV auxiliary power systems, the usual capacitive current is rarely more than 40 A. Therefore, neutral point access grounding resistance, the resistive component of the current limit value can be controlled at about 40 A; specific values also depend on the requirements of the system capacitive current size and sensitivity of protecting equipment. It should be explained that the single-phase grounding current of the system is still limited by the duration of the fault, so that the core of the burn can be prevented from occurring in the motor or transformer. For this should be satisfied: single-phase grounding current is less than or equal to  $100t - 0.4$  【6】. The relationship between single-phase grounding current (A) and arc duration  $t$  (s) is proposed. If the fault removal time to take 1 s, the single-phase grounding current of system should be less than 100 A, take 0.2–0.3 s, the single-phase grounding current of system should be less than 200 A; this value can be regarded as the upper limit of single-phase grounding current. It can be seen that when grounding by medium resistance, the single-phase grounding current is recommended in 40–200 A, and should not be too large. Personally think that the grounding current value from capacitive current is about four times of the value can limit intermittent arc over voltage ratio in less than 1.8 times, for the safe operation of cables and equipment is very favorable. The value of resistance current is mostly in the above range, as shown in Table 4.

In the first phase of the Sanmen nuclear power plant, resistance is 6.06/1000 A. In addition to the Sanmen nuclear power plant using neutral point grounding by low resistance, the above resistance grounding of nuclear power plants and fossil-fired power units are taken in a large number of medium resistance. In the Sanmen

**Table 4** Resistance/Single-phase grounding current

Fossil-fired power plants	CSCEC	Henan Xinyang power plant 2 × 300 MW	100 Ω/40 A (6 kV)
		Qinghai Huadian Datong power plant 2 × 300 MW	40 Ω/100 A (6 kV)
		The first phase of the Shanxi Fugu power plant 2 × 1000 MW	60 Ω/100 A (10 kV)
		The fourth phase of the Tianjin Zhouxian power plant 2 × 1000 MW	60 Ω/100 A (10 kV)
	CPECC	Tianjin Lingang power plant 2 × 350 MW	18.2 Ω/200 A (6 kV)
	GEDI	Shanwei power plant 2 × 600 MW	40 Ω/100 A (6 kV)
		Datang Chaozhou Sanbaimen power plant 4 × 600 MW	40 Ω/100 A (6 kV)
	Nuclear plants	CNADRI	Tianwan No. 3, 4 power plant 2 × 1000 MW
ECADI		The first phase of the Sanmen power plant 2 × 1250 MW	6.06 Ω/1000 A (10 kV)

nuclear power plant, the main reason of grounding by low resistance is the regulations of the IEEE 142 standard, the star-type wiring equipment, such as transformer and motor, should protect the 90 % winding, 10 % winding approach to the neutral point is still not protected, around single-phase grounding current of only terminal 10 % at close to 100 A. To ensure the sensitivity of single-phase grounding protection, electrical equipment external single-phase grounding fault current to reach about 1000 A to meet the requirements, while the domestic standard only on the 100 MW dynamo stator set protection area of not less than 90 % grounding protection requirements of electric machine and transformer requirements of single-phase grounding protection, different with the standard requirements.

### 5. Optimization of the design

Grounding by low resistance, because the single-phase grounding current is too large, will bring the following problems:

- A. Fire camp. A single-phase grounding fault occurs in a cable trench or cable tunnel where a current arc of 600 A or more may burn the other cables. Channeling along channel.
- B. Endanger personal safety.  
Single-phase to ground potential or motor enclosure voltage will rise sharply. The contact voltage and step voltage and weak electronic equipment insulation are likely to exceed the standard.
- C. Large volume, supplies more, and the price of resistor is high.
- D. May cause malfunction of transformer differential protection.

The current of single-phase grounding fault flow through the neutral point resistance of transformer. When the current is too large to exceed the range of differential protection of the transformer, the differential protection will act to cut off the power circuit and expand the accident. Therefore, it is recommended to limit the use of low resistance grounding mode.

Personally think AP1000 units in the building. After the introduction of digestion and absorption, for neutral point grounding resistance and grounding fault current, it can be combined with the domestic standards, operation of power plant, and localization process of equipment for further optimization, such as manner of resistance grounding or eliminating arc suppression coil grounding.

## 6 Conclusion

Neutral point grounding mode of high-voltage auxiliary power system of nuclear power plant and fossil-fired power plant will directly affect the operation mode of power plant and the impact of the nuclear power plants and fossil-fired power plant nuclear safety and operation safety, first of all, according to the calculation results

of capacitive current can meet the specification requirements of grounding mode, and then according to the requirements of power supply from configuration and operation mode of process equipment of power plant, the connecting guide of service power supply, switch results of accident of auxiliary power system, and other requirements, choose more conducive to the operation of the power station grounding mode, it cannot be generalized.

Through the analysis and research on the neutral point grounding mode of high-voltage auxiliary power system in large nuclear power plant and fossil-fired power plant, it can enlighten and draw lessons from the selection of grounding mode for nuclear power unit in the future.

Application of fire arc suppression coil in the mode of neutral point of auxiliary power system of power plant is lack of experience, nearly 2 years, with nuclear power plants put into operation one after another will gradually accumulated a set of perfect safety measures and experience of operation.

## References

1. NB/T 20051-2011 Design criteria of power system for nuclear plant
2. GB 50660-2011 Code for design of large and medium sized thermal power plant

# The Research of Selecting Scope of Maintenance Rule in the Key System of New Nuclear Power Plant

Chaojun Li, Jiaxu Zuo, Yan Chen, Wei Song and Peng Zheng

**Abstract** The American nuclear power plants achieved good economic benefits after the United States applied the maintenance rule, and the technology transfer documents of AP1000 nuclear power introduced from the United States also have the contents related to the maintenance rule. This article introduces the content and implementation of the maintenance rule, emphasis on the first step of maintenance rule “Selecting the scope”. Take the chemical and volume control system (CVCS) of a new nuclear power plant, for example, first, we analyze the components of CVCS if they are safety-related, if they are, the components belong to the scope of the maintenance rule. If the component is non-safety-related, we will analyze if it is relied upon to mitigate accidents or transients or is used in plant emergency operating procedures (EOPs), or the failure of it could prevent safety-related structures, systems, and components (SSCs) from fulfilling their safety-related function, or the failure of it could cause a reactor scram or actuation of a safety-related system. The component will belong to the maintenance rule if it meets one of these. We list the components of the CVCS that belong to the maintenance rule by this way. The study of selecting the scope will lay a foundation for introducing the maintenance rule into the nuclear power plant and carrying out the maintenance rule next step in China.

**Keywords** Maintenance rule · Nuclear power plant · AP1000 · Selecting the scope · Chemical and volume control system (CVCS)

## 1 Introduction

The nuclear power plants implement the maintenance rule and get the benefit in the United States. The performance indicators of NRC, the Institute of Nuclear Power Operations (INPO), and the World Association of Nuclear Operators (WANO)

---

C. Li (✉) · J. Zuo · Y. Chen · W. Song · P. Zheng  
Nuclear and Radiation Safety Center of MEP, Beijing, China  
e-mail: lichaojun86@126.com

show the performance of the American nuclear power plants continues to rise in recent years and remains the leading level in the world. In addition to the overhaul optimization and other technical improvements, the implementation of maintenance rule also played a significant role on the operation of nuclear power plants. In order to us the good practice of foreign countries for reference and make better use of the maintenance rule technology, it is necessary to research the application of maintenance rule in the new nuclear power plants in China. Selecting the scope is the first step of maintenance rules, and in order to introduce the maintenance rule technology in our nuclear power industry we research the scope screening of maintenance rule.

## **2 Related Contents of the Maintenance Rule**

### ***2.1 Main Contents of the Maintenance Rule***

The nuclear power plant maintenance is clearly important in protecting public health and safety. Therefore, the NRC published in the Federal Register (56 Fed. Reg. 31324) its final Maintenance Rule entitled, "Requirements for Monitoring the Effectiveness of Maintenance at Nuclear Power Plants." on July 10, 1991.

The contents of maintenance rules include: paragraph (a) (four terms), namely (a)(1), (a)(2), (a)(3) and (a)(4); paragraph (b), namely (b)(1) and (b)(2). Paragraph (b) of 10 CFR 50.65 requires the scope of the maintenance rule include safety-related and non-safety-related SSCs. The paragraph (a) and paragraph (b) can be defined as follows [1, 2, 5].

1. Paragraph (a)(1) of 10 CFR 50.65 requires that power reactor licensees monitor the performance or condition of SSCs against licensee-established goals in a manner sufficient to provide reasonable assurance that such SSCs are capable of fulfilling their intended functions. Such goals are to be established commensurate with safety and, where practical, take into account industry-wide operating experience. When the performance or condition of an SSC does not meet established goals, appropriate corrective action must be taken.

Paragraph (a)(2) of 10 CFR 50.65 states that monitoring as specified in Paragraph (a)(1) is not required where it has been demonstrated that the performance or condition of an SSC is being effectively controlled through the performance of appropriate preventive maintenance, such that the SSC remains capable of performing its intended function.

Paragraph (a)(3) of 10 CFR 50.65 requires that performance and condition monitoring activities and associated goals and preventive maintenance activities be evaluated at least every refueling cycle provided the interval between evaluations does not exceed 24 months. The evaluations must be conducted taking into account, where practical, industry-wide operating experience. Adjustments must be

made where necessary to ensure that the objective of preventing failures of SSCs through maintenance is appropriately balanced against the objective of minimizing unavailability of SSCs because of monitoring or preventive maintenance. In performing monitoring and preventive maintenance activities, an assessment of the total plant equipment that is out of service should be taken into account to determine the overall effect on performance of safety functions.

Paragraph (a)(4) of 10 CFR 50.65 requires that before performing maintenance activities (including but not limited to surveillances, post-maintenance testing, and corrective and preventive maintenance), the licensee shall assess and manage the increase in risk that may result from the proposed maintenance activities. The scope of the assessment may be limited to SSCs that a risk-informed evaluation process has shown to be significant to public health and safety.

Paragraph (b) of 10 CFR 50.65 states that the scope of the monitoring program specified in Paragraph (a)(1) is to include safety-related and non-safety-related SSCs as follows.

1. Safety-related structures, systems, and components that are relied upon to remain functional during and following design basis events to ensure the integrity of the reactor coolant pressure boundary, the capability to shut down the reactor and maintain it in a safe shutdown condition, or the capability to prevent or mitigate the consequences of accidents that could result in potential offsite exposure comparable to the guidelines in 10 CFR, as applicable.
2. Non-safety-related structures, systems, or components:
  - (i) That are relied upon to mitigate accidents or transients or are used in plant emergency operating procedures (EOPs); or
  - (ii) Whose failure could prevent safety-related structures, systems, and components from fulfilling their safety-related function; or
  - (iii) Whose failure could cause a reactor scram or actuation of a safety-related system.

## ***2.2 The Implementing Procedure of the Maintenance Rule***

Figure 1 is the implementing procedure of the maintenance rule in the American nuclear power plants, and the implementation process includes the following aspects [3, 4]: selecting the scope of SSCs included in the scope of MR, judging the risk significant, establishing performance criteria, monitoring performance and defining corrective objectives, mutual conversion of (a)(1) and (a)(2), risk assessment and management of maintenance activities, and periodical evaluation. The implementation of the maintenance rule adopts the risk significant criterion the same as that of the risk-informed categorization, which reflects the consistency of the American nuclear regulations. For the high safety significant SSCs in the risk significant criterion belong to the important risk in the MR, and should use the

specific performance criteria. The low safety significant SSCs should exempt from the special handling requirements regulated in 10 CFR 50.69 [6].

### 3 Selecting the Scope of the Maintenance Rule

#### 3.1 The Procedure of Selecting Scope of the Maintenance Rule

The screening criteria mainly depends on functional importance and failure consequences of the SSCs, and make the safety significant SSCs but not all the equipment under the monitoring of maintenance rules. Paragraph (b) of MR defines the scope of monitoring. Figure 2 is the procedure of selecting scope of the Maintenance Rule.

In order to determine whether the SSCs belong to the scope of MR or not, we can apply the following methods:

The Final Safety Assessment Report (FSAR), the list of master equipment, etc.

The nuclear power reactor licensees must determine the scope of MR by following principles. According to the requirement, the scope of MR is limited to the SSCs directly affect the operation of nuclear power plant. The safety system may not perform safety functions only, and it also perform additional function, such as a system used to perform the function of transporting water and also provides safety function. According to the FSAR, the licensees define which non-safety-related SSCs are relied to mitigate the consequences of accident or transient, and the SSCs will belong to the MR if the answer is positive, such as: condensate storage tank, fire extinguishing systems, transport system supply boric acid for refueling water storage tank, etc.

The MR focus on the safety function of SSCs, and differentiate the safety SSCs and non-safety SSCs is the basis for determining whether the SSCs belong to the MR scope. For the SSCs not belong to the MR scope, the licensees should keep on maintain appropriate maintenance and define the maintenance contents according to the impact of these SSCs on power generation and economy.

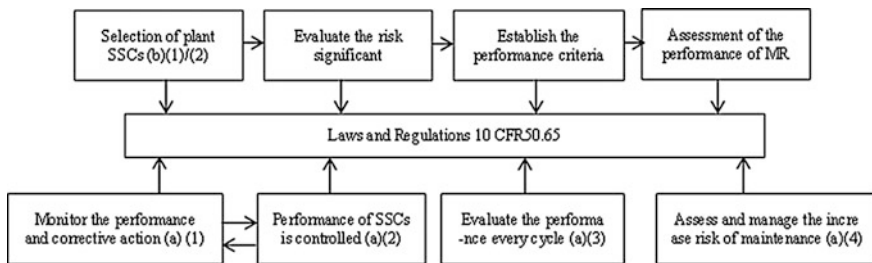


Fig. 1 The implementing procedure of maintenance rule

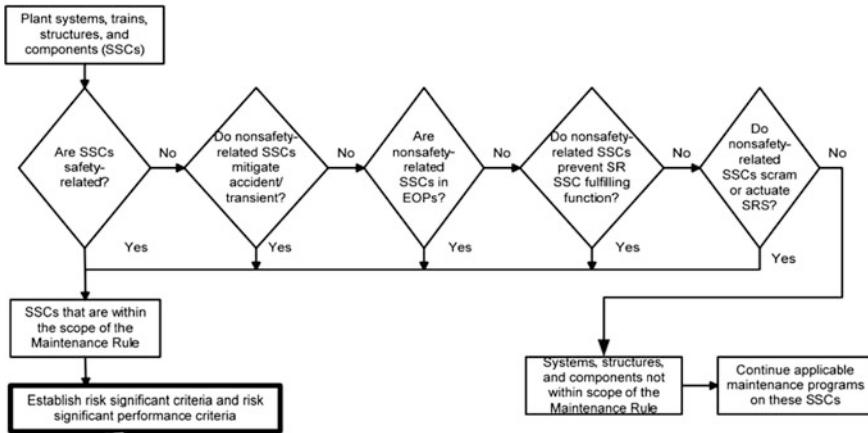


Fig. 2 The procedure of selecting scope of the maintenance rule

### 3.2 The Application of Selecting the MR Scope of the Chemical and Volume Control System (CVCS) in the New Nuclear Power Plant

In order to lay the foundation of applying the MR technology in the new nuclear power plants, we take the CVCS of new nuclear power plant as an example to research the first step of MR and learn how to select the scope.

The CVCS of new nuclear power plant includes regeneration heat exchangers, desalination, filter, tank, supply pump and associated valves, pipes, instrumentation components [7]. There are three main functions of CVCS, namely: volume control, chemical control, and reactivity control. Figure 3 is a flowchart of CVCS in new nuclear power plant.

According to the screening process of the MR, the following can be drawn:

1. The function of purifying the reactor coolant system is non-safety function, at the same time, there is no mitigative function for accident or transient, and this function is not used in emergency operating procedures, and it will not prevent the implementation of safety-related SSCs, and it will not trigger the safety system or shutdown. Therefore, this function not belongs to the scope of MR and the related SSCs do not fall within the scope of MR.
2. The function of controlling the reactivity by adjusting the capacity of boron is the safety-related functions, and the boric acid storage tank, supply pump A/B, water filter, regenerative heat exchanger belong to this functional scope. Therefore, the related SSCs fall within the scope of MR and should be monitored at the train level.



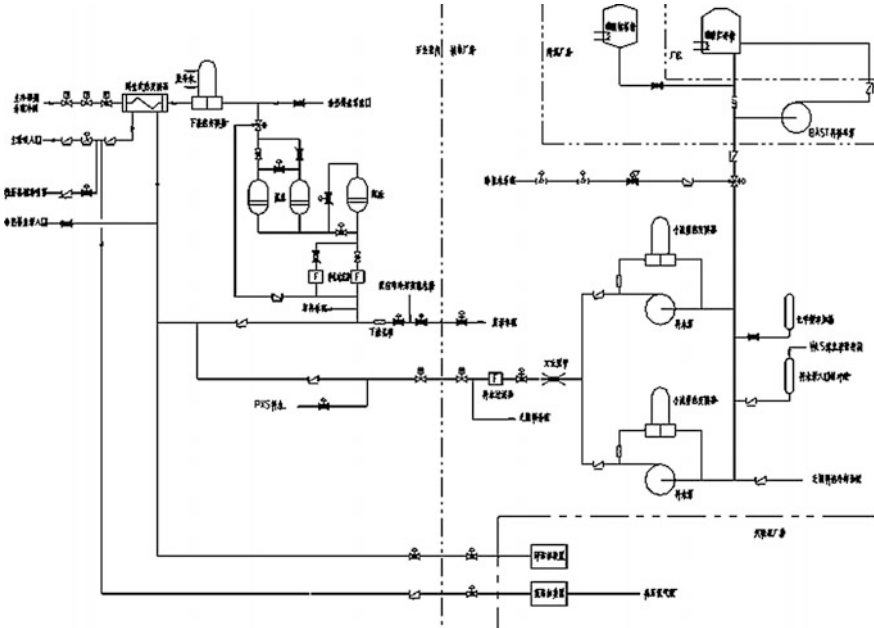


Fig. 3 The flow chart of CVCS in new nuclear power plant

3. Maintaining the capacity of pressurizer at a design value is non-safety-related function, but when the capacity of pressurizer deviates from the setting value that will lead to an emergency shutdown of the reactor, therefore, the related SSCs fall within the scope of MR and should be monitored at the plant level. The boric acid storage tank, supply pump A/B, water filter, regenerative heat exchanger belong to this functional scope.
4. Discharge the excess coolant to the radioactive waste system is a non-safety-related functions. The discharging heat exchanger, mixed bed A/B, cation bed and discharged plate belong to this functional scope.

As there are many components in the CVCS, we list the major key components fall within the scope of MR in this scope screening, and we will not discuss the other components.

According to the paragraph b(1) and b(2), the SSCs belong to the MR should be monitored, and we should carry out the most stringent standards if the monitoring of certain components belongs to the plant level and train level. Such as the boric acid storage tank, supply pump A/B, water filter, regenerative heat exchanger belong to the plant level and train level, and we should monitor these components under the train level.

## 4 Conclusions

We introduce the implementation process and the scope screening methods and processes of MR in this paper, and take the CVCS of new nuclear power plant as an example to research the scope screening of MR, in order to lay a foundation for implementing the MR technology for the next phase.

After the new nuclear power plant into the commercial operation, and according to the implementation of MR in the American nuclear power plants, we can improve the rules of maintenance management system gradually, draw up the maintenance rule management program and other supporting documents, manage risk maintenance activities, optimize the list of overhaul, reduce repair times, and improve quality of the overhaul and operating performance of the plant.

## References

1. 10 CFR 50.65, Requirements for Monitoring the Effectiveness of Maintenance at Nuclear Power Plants. 1991
2. NUMARC 93-01 Rev.2, Industry Guidelines for Monitoring the Effectiveness of Maintenance at Nuclear Power Plants[R]. 1996
3. Regulatory Guide 1.160(Rev.2), Monitoring the Effectiveness of Maintenance at Nuclear Power Plants. 1997
4. Regulatory Guide 1.182, Assessing and Managing Risk before Maintenance Activities at Nuclear Power Plants. 2000
5. Zou Weixiang. The application of the maintenance rule in US nuclear power plant[J]. China Electric Power Education (Chinese), 2013(26):215–218
6. USNRC 10CFR50.69. Risk-Informed Categorization and Treatment Structures, Systems and Components for Nuclear Power reactors. 2004
7. Lin Chengge. Advanced pressurized water reactor nuclear power technology of passive safety [M], Beijing: Atomic Energy Press (Chinese), 2010

# The Research on the Model of Condense Regenerate Heater Under Off-design Conditions

Quan Wang, Rongyi Huang and Wei Chen

**Abstract** The paper defined the heat transfer characteristic coefficient (HTCC) of condense regenerate heater, and obtained the relationship between HTCC, and feedwater flow and power outlet, and then present the model of condense regenerate heater under off-design conditions based on the characteristics coefficient; the model is used for the calculation of outlet temperature and heater temperature difference. The parameters of the model needed are the data on the base operation rather than the heater structure and complicate calculation of heat transfer coefficient; the heater outlet water temperature can be calculated by the steam pressure and turbine power outlet. The simplicity and good accuracy of model are proved by the regenerate heater calculation of 330 MW unit under off-design conditions, which shows the potential value for engineering application.

**Keywords** Condense regenerate heater · Heat transfer characteristic coefficient (HTCC) of heat transfer · Characteristic model under off-design conditions

## 1 Introduction

Regeneration is the important method to increase the thermal efficiency of power plant. Condense regenerate heater is the surface heater without steam cooler and drain cooler. The temperature difference of the regenerate heater which has the significant index is one of the three main effective elements [1, 2] of power plant for the importance of heat balance calculation and unit performance monitoring and optimization [3]. Therefore, it is important to research the regulation of regenerate

---

Q. Wang (✉) · R. Huang · W. Chen  
China Nuclear Power Engineering Co. Ltd., Beijing, China  
e-mail: wangquana@cnpe.cc

heater under off-design loads for the unit equipments monitoring and thermal diagnoses in power plant.

The regenerate heater calculation under off-design conditions is usually based on the traditional heat transfer equation. The heat transfer coefficient is needed for the calculation of outlet water temperature and temperature difference of regenerate heater [4–6]. Some researchers obtained the heat transfer coefficient of regenerate heater under the rated condition first. And based on that, the heat transfer coefficient under off-design conditions is calculated by fitting [7] or modifying [8–10] on the transfer coefficient under rated condition with a few principles, and then the regenerate heater parameters can be consequently obtained. The calculation process of heat transfer coefficient needs numerous heater structure parameters such as area, flow paths, tube side and shell side structure, the diameter of inside and outside pipe, pipe material, and so on, one or more of that need to be estimated by empirical formula. Any data above losing would cause that the heat transfer coefficient could not be calculated or errors increase. Furthermore, with the long operation, the heat transfer coefficient is changing constantly because of the thermal resistant and heat exchange area resulted by that such as scaling, wear, pipe blockage, or water level change [5]. Therefore, the traditional heat transfer equation is suitable for design and check calculation, rather than for the calculation and monitor of outlet water temperature when unit operation and test.

Due to the phase change heat transfer of condensing regenerate heater, the heat from extraction steam on shell side transferred to the feedwater on pipe side and condensed, and in this process, the working fluid on shell side remains as the same as saturation temperature. The paper defined the heat transfer characteristic coefficient of condense regenerate heater, and based on that presented the calculation principle and model of condense regenerate heater under off-design conditions. The model could calculate the outlet water temperature and temperature difference of regenerate heater under off-design conditions by the parameters of rated condition more quickly and simply than the traditional model. The novel calculation method is validated with a turbine unit regenerative system. The conclusion shows that the novel model is accurate and effecters provide the reliable basis for monitoring and diagnose of regenerate heater thermal efficiency.

## 2 Characteristic Model Under Off-design Conditions

The steam cooler and drain cooler are not installed on condense regenerate heater, so the steam temperature remains as the same as the saturation temperature in the heat exchange and condense process (see Figs. 1 and 2).

**Fig. 1** Flow diagram of condense regenerate heater

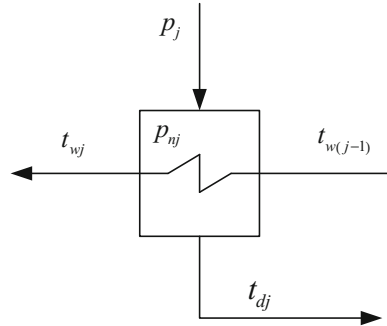
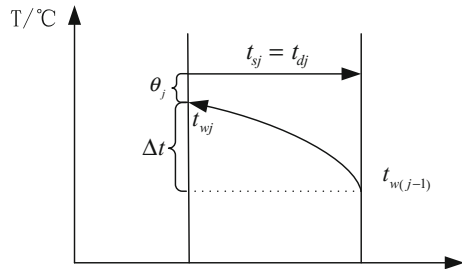


**Fig. 2** Heat exchange process diagram of condense regenerate heater



The traditional equation of condense regenerate heater temperature difference is:

$$\theta_j = t_{sj} - t_{wj} = \frac{t_{wj} - t_{w(j-1)}}{\exp\left(\frac{K \cdot F}{D_{wj} \cdot c_p}\right) - 1} \tag{1}$$

where

#j representatives the #j regenerate heater;

$t_{sj}$  is the saturation temperature corresponding to the steam pressure on shell side, °C;

$\Delta t$  is the temperature increase of feedwater in #j, °C;

$t_{wj}$ ,  $t_{w(j-1)}$  are the outlet and inlet temperatures of #j, respectively, °C;

$K$  is the overall heat transfer coefficient of #j,  $W/(m^2 \cdot °C)$ ;

$F$  is the heat transfer area of #j,  $m^2$ ;

$D_{wj}$  is the feedwater flow of #j, t/h;

$c_p$  is the water-specific heat capacity at constant pressure,  $kJ/(kg \cdot °C)$ , which is constant as 4.1868.

The equation of overall heat transfer coefficient  $K$  is

$$K = \frac{1}{\frac{1}{h_1} + \frac{\ln(d_2/d_1)}{\lambda} + \frac{1}{h_2}} \quad (2)$$

where

$h_1$  is the heat transfer coefficient of shell side,  $W/(m^2 \text{ } ^\circ\text{C})$ ;

$h_2$  is the heat transfer coefficient of pipe side,  $W/(m^2 \text{ } ^\circ\text{C})$ ;

$\lambda$  is the thermal conductivity of pipe material,  $W/(m^2 \text{ } ^\circ\text{C})$ ;

$d_1$  and  $d_2$  are the inner and outer diameters of pipe, m.

It can be concluded from Eq. (2) and engineering experience that the overall heat transfer coefficient is affected by the smallest one of pipe side, shell side, and pipe materials. As  $h_1$  and  $\lambda$  are much bigger, the small  $h_2$  is the major element for overall heat transfer coefficient, which means  $K \propto h_2$ . And the forced flow in the heater is on the turbulent state, so it could get the equation between  $h_2$  and Reynolds number  $Re$  is  $h_2 \propto Re^{0.8}$ ; then the  $Re$  is affected by the feedwater flow  $D_{wj}$ , which means  $Re \propto D_{wj}$ . Finally, we get the relationship between overall heat transfer coefficient  $K$  of regenerate heater and feedwater flow  $D_{wj}$ :  $K \propto D_{wj}^{0.8}$ .

If according with Eq. (1) to calculate the temperature difference of condense heater, then the overall heater structure document of the heater is needed for the  $K$  and heat transfer area  $F$ . However, if the  $K$  and  $F$  were considered as an integrated, they are only related to the thermal parameter of heater. After all, when the heat transfer process changes, the overall coefficient is only related to the feedwater flow, and the heat transfer area  $F$  and water-specific heat capacity at constant pressure remain as constant.

Then  $[(K \cdot F)/(D_{wj} \cdot c_p)]$  in Eq. (1) is considered as integrated and defined as heat transfer characteristic coefficient (HTCC). The HTCC on rated condition (design condition or test condition, marked as "o") is concluded as below according to the logarithmic temperature difference equation of heat transfer:

$$\left( \frac{K \cdot F}{D_{wj} \cdot c_p} \right)^o = \ln \left( \frac{t_{wj}^o - t_{w(j-1)}^o}{t_{sj}^o - t_{wj}^o} + 1 \right) \quad (3)$$

When the regenerate heater condition changes, we could get the ratio of the HTCC of condition change before and after according to the parameters above relations:

$$\frac{\left(\frac{K \cdot F}{D_{wj} \cdot c_p}\right)^o}{\left(\frac{K \cdot F}{D_{wj} \cdot c_p}\right)} = \frac{K^o}{K} \cdot \frac{D_{wj}}{D_{wj}^o} = \left(\frac{D_{wj}^o}{D_{wj}}\right)^{0.8} \cdot \frac{D_{wj}}{D_{wj}^o} = \left(\frac{D_{wj}^o}{D_{wj}}\right)^{-0.2} \tag{4}$$

Therefore, we got the principle of the HTCC that the feedwater flow is considered as comparison standard parameter.

The trend of feedwater flow is same as that of unit power, so Eq. (4) is deduced as below:

$$\frac{\left(\frac{K \cdot F}{D_{wj} \cdot c_p}\right)^o}{\left(\frac{K \cdot F}{D_{wj} \cdot c_p}\right)} = \left(\frac{D_{wj}^o}{D_{wj}}\right)^{-0.2} = \left(\frac{P_{el}^o}{P_{el}}\right)^{-0.2} \tag{5}$$

Then the HTCC of condense regenerate heater under off-design condition is

$$\left(\frac{K \cdot F}{D_{wj} \cdot c_p}\right) = \left(\frac{K \cdot F}{D_{wj} \cdot c_p}\right)^o \cdot \left(\frac{P_{el}}{P_{el}^o}\right)^{-0.2} \tag{6}$$

The principle of HTCC is obtained, which is based on the plant power as comparison standard parameter. The outlet water temperature of condense regenerate heater under off-design condition is deduced by Eqs. (1) and (6):

$$t_{wj} = \frac{t_{sj} \cdot \left\{ \exp \left[ \left(\frac{K \cdot F}{D_{wj} \cdot c_p}\right)^o \cdot \left(\frac{P_{el}}{P_{el}^o}\right)^{-0.2} \right] - 1 \right\} + t_{w(j-1)}}{\exp \left[ \left(\frac{K \cdot F}{D_{wj} \cdot c_p}\right)^o \cdot \left(\frac{P_{el}}{P_{el}^o}\right)^{-0.2} \right]} \tag{7}$$

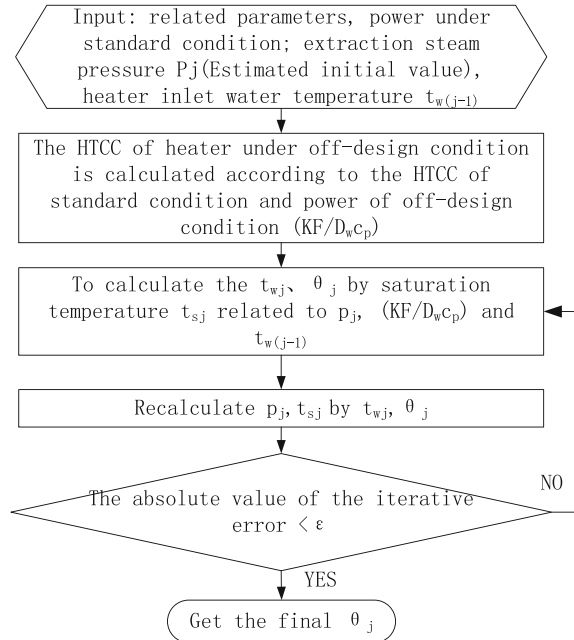
Based on the HTCC model under off-design condition, the calculation diagram of temperature difference refers as Fig. 3.

### 3 Calculation Example of Condense Heater Under Off-design Condition

The temperature difference of regenerate heater is calculated with the 330 MW power plant. The #1 and #2 heaters are the condense heaters and the design data is shown in Table 1.

Nine design conditions (100 %THA condition, constant pressure 75 % condition, constant pressure 50 % condition, slide pressure 75 % condition, slide pressure 50 % condition) are considered as standard conditions by Eqs. (4) and (5) as the standard parameter. Then the temperature difference of #1 & #2 heaters is

**Fig. 3** Calculation diagram of condense regenerate heater under off-design condition



calculated by the model presented by this paper. The results are compared with the actual data of the unit under the corresponding conditions which are shown in Tables 2 and 3.

According to the calculation, it indicates that the results obtained by the feed-water flow as standard parameter and plant power as standard parameter are basically consistent with each other, which shows the correctness of Eq. (5).

In addition, the heater temperature difference of design data is the same as each other under different conditions which are obviously unreasonable.

It also indicated that the temperature difference under a certain condition is not completely the same as the corresponding data of design condition, because of the heat transfer effect get worse by scaling and so on, so the real temperature difference is little bigger than the design data.

If the calculation condition is quite different with the standard condition, then the heat process is also quite different with the corresponding conditions, which causes the calculated temperature difference error a little bigger relatively. When the calculation condition is close to the standard condition, it can get more accurate results.



**Table 1** Design data of heater for a 330 MW unit

	Condition	Power $P_{d1}/(\text{kW})$	Feedwater flow $D_{w1}/(\text{t/h})$	Extraction steam pressure $p_j/(\text{MPa})$	Outlet temp $t_{w1}/(\text{°C})$	Inlet temp $t_{w(-1)}/(\text{°C})$	Saturation temp $t_g(\text{°C})$	HTCC	TD	
									$\theta_j(\text{°C})$	
1# heater	100 %	330,220	648.6	0.0231	60.27	33.6	63.2	2.3096	2.937	
	CP 75 %	247,601	483.8	0.0174	54.12	33.9	57.1	2.0600	2.959	
	CP 50 %	165,049	335.6	0.0122	46.76	34.3	49.8	1.6431	2.992	
	SP 75 %	247,632	492.4	0.0177	54.48	33.6	57.4	2.0865	2.962	
	SP 50 %	165,180	338.8	0.0123	46.95	34.3	49.9	1.6636	2.966	
2# heater	100 %	330,220	648.6	0.0635	84.39	60.3	87.4	2.2025	2.997	
	CP 75 %	247,601	483.8	0.0471	76.85	54.1	79.8	2.1533	2.986	
	CP 50 %	165,049	335.6	0.0324	67.94	46.8	70.9	2.1062	2.935	
	SP 75 %	247,632	492.4	0.0479	77.3	54.5	80.3	2.1669	2.952	
	SP 50 %	165,180	338.8	0.0327	68.16	47	71.1	2.1091	2.929	

*TD* temperature difference; *CP* constant pressure; *SP* slide pressure

**Table 2** Calculation results of heater under off-design conditions (feedwater flow  $D_w$  as the standard parameter)

	Off-design	Design TD	Standard	100 %	CP 75 %	CP 50 %	SP 75 %	SP 50 %
	Condition		Actual TD	Cal. TD	Cal.TD	Cal.TD	Cal.TD	Cal.TD
1# heater	100 %	2.937	3.318	–	4.239	7.006	4.106	6.862
	CP 75 %	2.959	2.828	2.006	–	5.042	2.861	4.932
	CP 50 %	2.992	–	1.110	1.686	–	1.626	2.922
	SP 75 %	2.962	2.949	2.079	3.063	5.209	–	5.097
	SP 50 %	2.966	1.856	1.129	1.714	3.037	1.653	–
2# heater	100 %	2.997	3.168	–	3.559	4.280	3.488	4.254
	CP 75 %	2.986	2.693	2.488	–	3.631	2.923	3.608
	CP 50 %	2.935	–	1.954	2.378	–	2.324	2.915
	SP 75 %	2.952	2.952	2.514	3.015	3.664	–	3.641
	SP 50 %	2.929	1.870	1.966	2.390	2.949	2.337	–

There is not CP 50 % condition in actual operation

**Table 3** Calculation results of heater under off-design conditions (turbine power  $P_{el}$  as the standard parameter)

	Off-design	Design TD	Standard	100 %	CP 75 %	CP 50 %	SP 75 %	SP 50 %
	Condition		Actual TD	Cal. TD	Cal.TD	Cal.TD	Cal.TD	Cal.TD
1# heater	100 %	2.937	3.318	–	4.230	7.076	4.126	6.949
	CP 75 %	2.959	2.828	2.011	–	5.103	2.882	5.007
	CP 50 %	2.992	–	1.090	1.657	–	1.610	2.931
	SP 75 %	2.962	2.949	2.066	3.041	5.245	–	5.145
	SP 50 %	2.966	1.856	1.103	1.677	3.028	1.630	–
2# heater	100 %	2.997	3.168	–	3.552	4.335	3.506	4.323
	CP 75 %	2.986	2.693	2.494	–	3.688	2.945	3.677
	CP 50 %	2.935	–	1.921	2.334	–	2.300	2.925
	SP 75 %	2.952	2.952	2.500	2.992	3.696	–	3.685
	SP 50 %	2.929	1.870	1.923	2.337	2.939	2.303	–

## 4 Conclusion

The paper presented the HTCC model of condense regenerate heater based on the regular relationship between HTCC and unit power, and the correctness and effect is proved by the operation parameters. Finally it concluded that

1. In this model, the results calculated by feedwater flow as standard parameter and unit power as standard parameter are basically consistent, so either of the two

parameters could be used as standard parameter according to the actual situation in engineer project.

2. When the unit power decreased, the feedwater flow would decrease, which caused the heat load decreased, the heat exchanged adequately, and thus the temperature difference decreased; conversely, when the unit power increased, the temperature difference would increased.
3. The less the standard condition and calculation condition, the less difference the heat transfer state of heater. Therefore, the selection principle of standard condition in the novel model is that the standard conditions could be one or more of the design condition or test condition under different power rates, when the model is applied under off-design condition, and it is recommended to use condition which is close to that off-design condition as the standard condition.

The model presented by this paper is simple and accuracy without complex calculation, structure parameter, and water flow of heater. The calculation under off-design condition just related to a few parameters such as extraction steam pressure, unit power of standard condition, extraction steam pressure, unit power, and heater inlet water temperature under off-design condition, which shows the potential value for engineering application.

## References

1. WANG Pei-hong, SU Zhi-gang, WANG Quan, Recent Research Progress in Performance Analysis, Monitoring and Optimization of the Thermal Power Station[J], East China Electric Power, 2010(10):1517–1521
2. ZHU Fang, WANG Pei-hong, etc, Research on optimization arithmetics for regeneration parameters[J], East China Electric Power, 2008(07):71–73
3. WU Zheng-yong, WANG Pei-hong, General Calculation Model on the Influence of Terminal Temperature Difference on Heat Economy of Unit[J], Turbine Technology, 2008(03):226–229
4. LI Yong, MA Guanghui, A Method for Evaluating Thermal Economic Performance of Low-pressure Feedwater Heaters[J], Proceedings of the CSEE, 2012(20):20–26
5. LU Guo-dong, Research of Regenerative Systems' Variable Condition Character of Coal-fired Power Plant[D], North China Electric Power University, 2008
6. YU Shu-mei1, LIU Jia-qi1, etc, Research of Reference Value for Variable Condition Terminal Difference in Regenerative Heater[J], Power Equipment, 2010(03):169–171
7. YANG Tao, XU Jian-qun, etc, Varying Condition Characteristic Calculation Model of Feedwater Heater Based on Dimensional Analysis[J], Turbine Technology, 2013(05):326–330
8. LU Guo-dong, ZHANG Chun-fa, etc, Research on the Partial Load Property of Standard Number of the Temperature Difference of Heater with Steam-cooling Segment[J], Turbine Technology, 2008(02):126–127
9. DING Chang-fu, GUAN Xin-yuan, etc, Simple Calculation Model of Heater Terminal Temperature Difference based on Operating Parameters[J], Power Station Auxiliary Equipment, 2011(03):7–9
10. CAO Zuqing, Turbine characteristic on off-design conditions[M]. Water Resources and Electric Power Press, 1991

# The Study of Extending AP1000 Spent Fuel Racks' Storage Capacity

Yu Zhang, Weidong Rong, Shiwei Wang, Zheng Zheng  
and Wenbin Wei

**Abstract** Haiyang nuclear power plant spent fuel racks' storage capacity was reduced to 75 % of initial design storage capacity because the criticality analysis of the spent fuel racks' region 2 did not meet the requirement of the HAD 102/15-2007. Thus the whole operation cycle of the spent fuel racks was cut from the designed 18 to 13.5 years. In according to the current storage quantity of spent fuel assembly in Chinese nuclear power plant and the spent fuel assembly transport capacity, it is almost impossible that the spent fuel assembly was transported only after a few years storage. Based on the above conditions, this article provides the Monte Carlo criticality calculation model of fuel assembly and spent fuel storage racks used by MCNP5 and confirms the validity of these models. Furthermore, this article provides the method of extending the spent fuel racks' region 2 storage capacity by appropriate spent fuel assembly distribution. Finally, this article provides the design improvement of AP1000 spent fuel storage racks for the future construction. The calculation results demonstrate that these methods will effectively improve the current spent fuel racks' storage capacity and it will be very important for the future spent fuel storage management and spent fuel racks' design improvement in Haiyang nuclear power plant.

**Keywords** Criticality analysis · MCNP · Fuel assembly arrangement

## 1 Introduction

The spent fuel racks of Shandong Nuclear Power Company (SDNPC) unit 1 are designed and fabricated by HOLTEC and when the SDNPC reviewed the report of criticality analysis for Haiyang AP1000 spent fuel racks, they found that the criticality analysis of region 2 did not consider some assumption requirements in HAD102/15-2007 which resulted that the region 2 could not meet the requirements

---

Y. Zhang (✉) · W. Rong · S. Wang · Z. Zheng · W. Wei  
Shandong Nuclear Power Company, Haiyang 265112, China  
e-mail: jianghong@cnpe.cc

of HAD102/15-2007. The conflicts are mainly the following two aspects: (1) the credits of burnup and soluble boron are both applied in the criticality analysis of AP1000 spent fuel racks' region 2, while the HAD102/15-2007 requires that the burnup credit and the soluble credit cannot be applied in the same storage area; (2) The double contingency principle precludes the necessary of considering the simultaneous occurrence of multiple accident conditions in 10CFR50.68, while the HAD102/15-2007 requires that the spent fuel pool should be subcritical in the condition of undergoing two unlikely independent and concurrent incidents or postulated accidents. Coupling with these two aspects, the new requirements of the criticality analysis are to ensure the effective neutron multiplication factor ( $K_{\text{eff}}$ ) is less or equal to 0.95 under pure water (considering boron dilution accident in the spent fuel pool).

HOLTEC provides the '3-out-of-4' proposal to meet the requirements of HAD102/15-2007. The strategy is that three of each four storage racks in region 2 will be used to store the fuel assembly and the remaining one is blocked by the Cell Blocker, and thus the storage capacity will be reduced by about 25 %, which will result the cycle time of shipping the spent fuel assembly out of the spent fuel pool will change from 18 to 13.5 years.

Actually, the shipment of spent fuel which just goes through a less interval will bring a series of problems. The direct affect is that the shipping cask design of the radiation shield, heat conduction and critical calculation will change and the process of reprocessing of the spent fuel may be not applicative. Besides, according to the current spent fuel shipping and disposing capacity in China, and simultaneously considering the amount of the spent fuel in current China running nuclear power plant [1–3], the situation will be that there is no storage racks in spent fuel pool but the spent fuel assembly cannot be shipped out. At that time, the owner may build another spent fuel pool or purchase additional storage facility. HOLTEC say that they have a passive nature cooling spent fuel storage facility, but its price is very expensive and the owner need to modify the lifting equipments in spent fuel pool and purchase the transport tools.

Base on the above problems, this article provides the method of extending AP1000 spent fuel racks' storage capacity. The objective of this method is to ensure that with the burnup credit and by appropriate spent fuel assembly arrangement, the effective neutron multiplication factor ( $K_{\text{eff}}$ ) is less or equal to 0.95 with the storage rack 100 % loaded with spent fuel assembly. The essence of this method is to make the best of some conservative assumptions. To achieve this objective, the Monte Carlo criticality calculation model of fuel assembly and spent fuel storage racks is produced using MCNP5 and confirmed with HOLTEC design report. Furthermore, this article provides the design improvement of AP1000 spent fuel storage racks for the future construction. This article will be very important for the future spent fuel storage management and spent fuel racks' design improvement in SDNPC.

## 2 Method

### 2.1 Input Data

The design parameters for the AP1000 spent fuel racks' region 1 and region 2 that are used in this analysis are given in Fig. 1a, b.

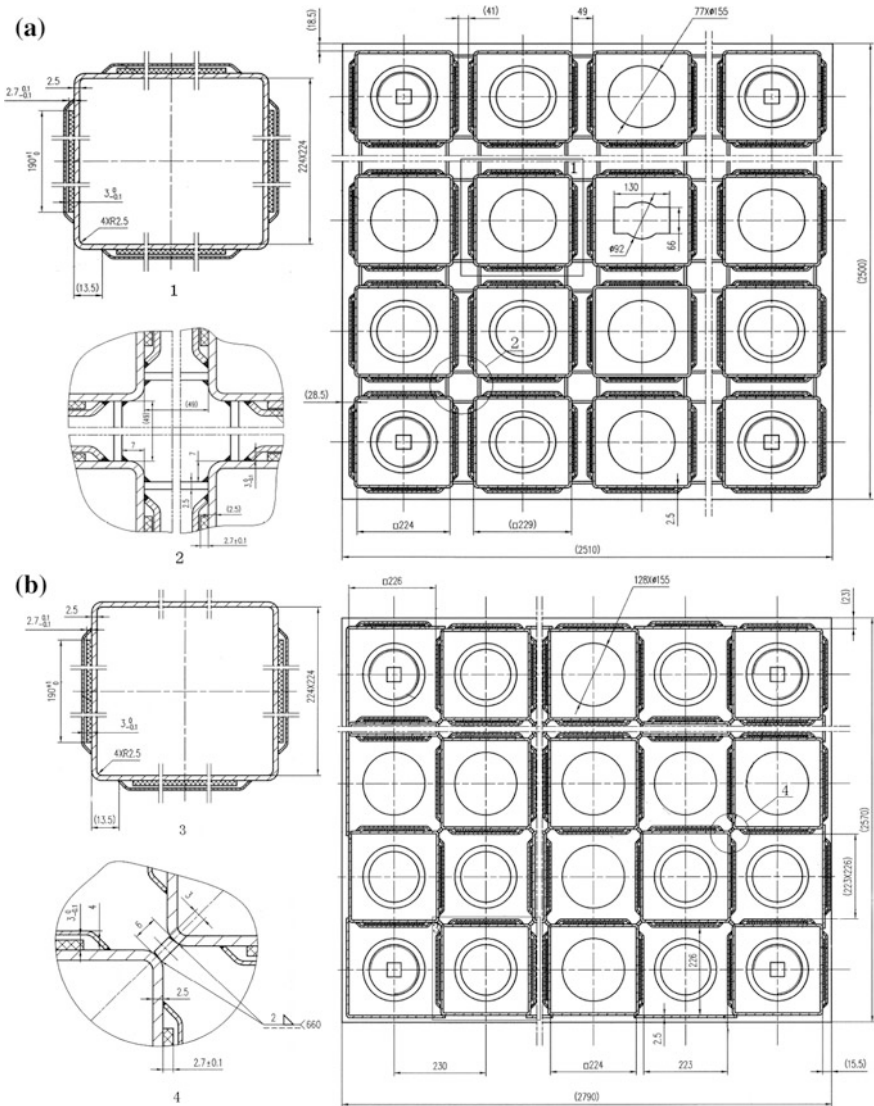


**Fig. 1** AP1000 spent fuel storage racks' design parameters

The region 1 storage cells are composed of stainless steel boxes separated by a water gap, with fixed neutron absorber panels centered on each side. The material of the neutron absorber is ceramics called Metamic and it is covered by stainless steel sheathing supports. The inside surface of the steel walls defines the fuel assembly storage cells and the outside surface of the sheathing supports defined the whole storage cell boundary. There is water inside the storage cells and among the storage cells. The region 2 storage cells are composed of stainless steel boxes with a single fixed neutron absorber panel centered on each other attached by stainless steel sheathing. The stainless steel boxes are arranged in an alternating pattern which means two storage cells use the same neutron absorber and the steel sheathing such that there is no water among each storage cell.

The rod array of AP1000 fuel assembly is  $17 \times 17$ , and the active fuel length is 168 in. There are 24 control rod thimble tubes and 1 instrument tube. The fuel rod is composed of pellets, ZIRLO cladding. The model material and components used in this analysis are given in Table 1.

## 2.2 Assumptions and Uncertainty

In order to ensure the real reactivity in spent fuel pool is always lower than the calculation reactivity, the following conservative assumptions and uncertainty are used:

1. The temperature of the moderator (pure water) is 4 °C (the density is 1 g/cm<sup>3</sup>), and actually the normal operation temperature will be 20 °C. Thus this assumption will introduce additional positive reactivity because of the negative temperature coefficient under the configuration of the spent pool design.
2. The structural materials in fuel assembly which will absorb neutron such as grid, vane, and tab are instead by water. This assumption will introduce additional reactivity because water will enhance the slowing of the neutron.
3. The total reflection boundary conditions are used in the analysis, and thus means that the effective multiplication factor of an infinite radial array of single storage cell or the whole storage area ( $12 \times 11$ ) is calculated.
4. The length of neutron absorber panels is set the same as the active fuel length. This is conservative as the neutron absorber is actually longer than the active fuel length.

**Table 1** Model material and components

Material (density)	Components (%)
Metamic (2.6349 g/cm <sup>3</sup> )	B-10: 0.04440, B-11: 0.19821, C: 0.06739, Al: 0.69000
ZIRLO™ (6.56 g/cm <sup>3</sup> )	Nb: 0.01, Sn: 0.01, Fe: 0.0011, O: 0.0013, Zr: 0.9776
Stainless steel	Los Alamos National Laboratory
Pellet (10.4668 g/cm <sup>3</sup> )	U-235:4.95, 3.046 (Model verification), 0.74–4.2712
Water	Los Alamos National Laboratory

5. The presence of burnable absorbers (WABA, IFBA, control rod) in the fresh fuel assemblies is neglected and replaced by water.

The normal geometric parameters of spent fuel racks and fuel assemblies are used in the model. The maximum  $K_{\text{eff}}$  ( $k_{\text{eff}}^{\text{max}}$ ) is determined from the MCNP5 calculated  $K_{\text{eff}}$  ( $k_{\text{eff}}^{\text{mncp}}$ ), the biases ( $\Delta k_{\text{eff}}^{\text{bias}}$ : the calculated bias and the temperature bias), and the applicable uncertainties and tolerances ( $\sigma$ : bias uncertainty, calculated uncertainty, rack tolerances, fuel tolerances) using the following formula:

$$k_{\text{eff}}^{\text{max}} = k_{\text{eff}}^{\text{mncp}} + (1 + 5\%) \Delta k_{\text{eff}}^{\text{bias}} + \sqrt{\sum_i \sigma_i^2}$$

where the biases directly use the design value (MCNP4a) and was increased by 5 % for additional conservatism. The rack tolerances and the fuel tolerances directly use the maximum design value.

### 2.3 The Fuel Assembly Arrangement of the Region 2

The advanced first core (AFC) used 157 fuel assemblies is a typical low leakage pattern including five kinds of deferent enrichment fuel assemblies (A–E) including 16 “A” fuel assemblies, 49 “B” fuel assemblies (for the reloaded cycle there is always one “B” fuel assembly in the core), 28 “C” fuel assemblies, 36 “D” fuel assemblies, and 28 “E” fuel assemblies. The storage cells array of AP1000 spent fuel racks' region 2 is  $12 \times 11$ ; so there are total 132 storage cells (there are three regions in 2 areas and each one is  $12 \times 11$ ). Now the problem is that how to arrange the 132 storage cells using 157 fuel assemblies to ensure that the  $K_{\text{eff}}$  is less or equal to 0.95. The principle is to give priority to the low enrichment fuel assemblies to be symmetrically loaded into the  $11 \times 11$  storage cells of region 2 and to fill the remaining 11 storage cells with high enrichment “E” fuel assemblies. According to this principle the 132 storage cells of region 2 will be loaded by all A/B/C/D fuel assemblies and only 4 E fuel assemblies.

### 2.4 The Design Improvement of Region 2

The objective of design improvement of region 2 is to ensure with the using of the whole storage cells in the spent pool the spent fuel assemblies shall never be shipped outside until 11 operation cycles. One applicative method is to increase the thickness of the neutron absorber panels. With the thickness increasing, the whole size of the region 2 will increase which will conflict with the modular architecture of the spent fuel pool. Thus the thickness of the absorber panels cannot



be arbitrarily value and it is the optimization result between the storage requirements and the size of the spent fuel pool module.

Another method is to enhance the B-10 component in the METAMIC material by increasing the enrichment of the B-10 (the fabricating cost will be a significant care) or improving the percent of  $CB_4$ . The sintering of boron carbide ceramics and its application has been extensively studied in China [5–8]. This article chooses the boron carbide and aluminum oxide ceramics (the enrichment of B-10 is the same with the value of HOLTEC design report: 18.3 %) to calculate the percent of  $CB_4$  to meet the criticality requirements with the different fuel assembly burnups.

### 3 Result and Analysis

#### 3.1 Module Verification

Figure 2a, b shows the pictures of basic calculation models used in MCNP5. These pictures were created with the two-dimensional plotter in MCNP and clearly indicate the explicit modeling of fuel rods in each fuel assembly. The calculation model for the region 1 racks (A) consists of a single cell with reflective boundary conditions through the centerline of water gaps, thus simulating an infinite array of region 1 storage cells. The calculation model for the region 2 racks (B) consists of a single cell with reflective boundary conditions through the centerline of the composite of materials between the cells, thus simulating an infinite array of region 2 storage cells. The MCNP5 criticality parameters are that a minimum of 10,000 histories were simulated per cycle, a minimum of 100 cycles were skipped before averaging, a minimum of 100 cycles were accumulated, and the initial source was

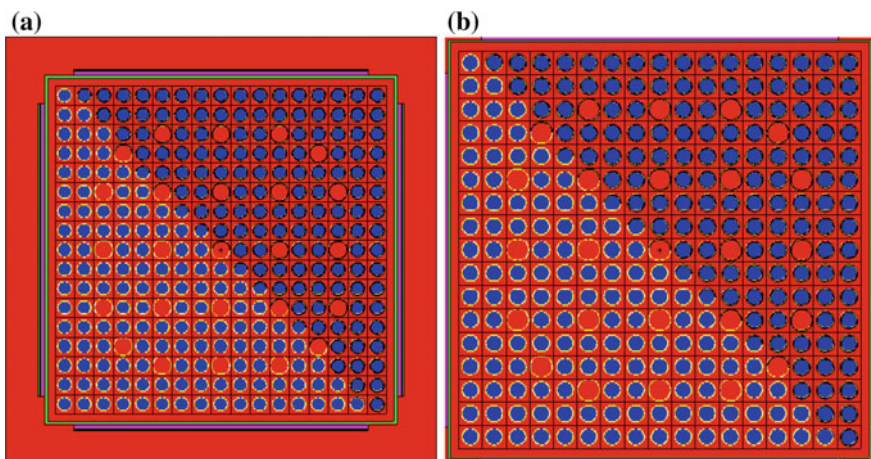


Fig. 2 MCNP5 calculation model for region 1 (a) and region (b)

**Table 2** Module verification with the design value (without uncertainty)

Items (enrichment)		$K_{eff}$	$\sigma$	$\Delta$
1 Fresh fuel	MCNP5 (4.95)	0.9075	0.0009	0.0023
	Design value (4.95)	0.9052	0.0006	
2 Burnup 10GWD/tU	MCNP5 (3.046) <sup>a</sup>	1.0241	0.0006	0.0279
	Design value (3.0)	0.9962	0.0007	

<sup>a</sup>There is no 3.0 wt% enrichment fuel assembly so the nearest enrichment is used

specified as uniform over the fueled regions (assemblies). The calculation results of MCNP5 compared with the HOLTEC design value are given in Table 2. The results show that the calculated  $K_{eff}$  with the MCNP5 model has a very small deviation with the design value. The relative bigger deviation for region 2 is because that there is no 3.0 wt% enrichment fuel assembly in AFC and the nearest value is 3.046 wt% which is the enrichment of “C” fuel assembly. The MCNP5 value is a little bigger than the design value which means that you will get a little more conservative  $K_{eff}$  value using the MCNP5 model. As for the uncertainty and biases, the MCNP5 model will directly use some maximum values of the design model, and thus the basic MCNP5 calculation models are enough accurate and conservative to perform the further calculation.

### 3.2 Extending Region 2 Storage Capacity

The fuel assembly arrangement of up-left region 2 and the burnup versus enrichment curve (loading curve) are given in Fig. 3. The design burnup in the loading curve is burnup used by HOLTEC design calculation. It is obtained by the interpolation method to keep the  $K_{eff}$  less or equal 1.0 using the basic region 2 model in pure water. It means if you put the fuel assemblies in region 2 with the burnup versus enrichment above the loading curve, any arrangement will never make the region 2 super critical. The MCNP5 burnup is the burnup versus enrichment (the average enrichments of the fuel assembly and its isotope component are from AP1000 nuclear design report [9]) used in this article region 2 arrangement. The criticality calculation result is shown in Table 3. This means if you load the region 2 with the pattern of Fig. 3, the  $K_{eff}$  will be less than 0.95 (0.9474) although using the more conservative biases and uncertainty value in Table 3. The key factor to get the lower criticality is that the higher enrichment fuel assemblies (C and D) are separated with the lower enrichment fuel assemblies (A and B) to prevent some small sub-regions becoming super critical. If you put some higher enrichment fuel assemblies adjacent, you will find that the  $K_{eff}$  will not be a decreasing trend after 100 effective cycles accumulated. The discharge burnup is the final unloaded burnup of the fuel assemblies in the unclear design report. There is also a large margin between the discharge burnup and the calculation burnup, so if you put the

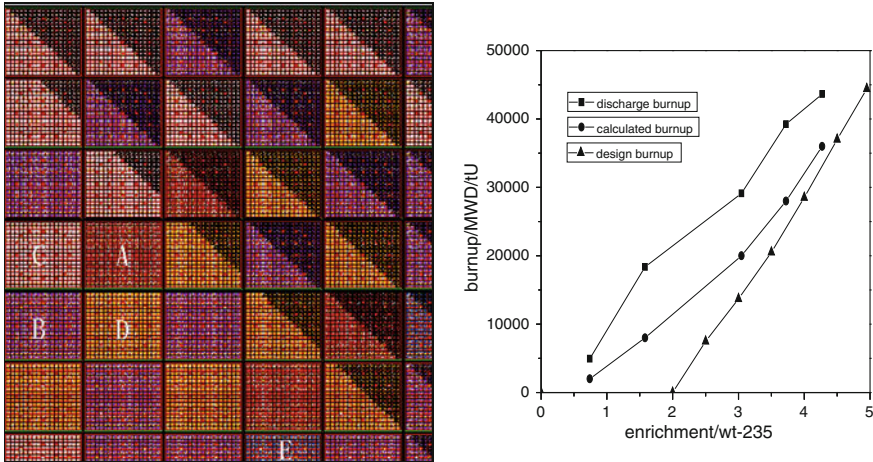


Fig. 3 The arrangement of region 2 and loading curve

Table 3 The criticality result of region 2

Item	Component	Result
Uncertainty	Bias uncertainty (95 %/95 %)	0.0090 (MCNP4a)
	Calculation statistics (95 %/95 %, $2 \times \sigma$ )	0.0012
	Rack tolerances	0.0026 (the maximum value in MCNP4a)
	Fuel tolerances	0.0075 (the maximum value in MCNP4a)
Bias	Temperature bias	0.0049 (the maximum value in MCNP4a)
	MCNP5 bias	0.0012 (MCNP4a)
MCNP5 calculated $K_{eff}$	0.9289	
Maximum $K_{eff}$	0.9474	

Note The margin of the calculated burnup is big enough to consider the burnup uncertainty

actual fuel assemblies in the region 2, you will get a lower  $K_{eff}$  than the calculation value.

The first cycle of AP1000 core is the typical low leakage pattern and it is very similar with the equilibrium cycle. The remaining reactivity of the first cycle fuel assemblies is also similar with the equilibrium cycle fuel assemblies. So for the following unloaded fuel assemblies, we can also use the appropriate arrangement and loading curve to make the whole region 2 available.

### 3.3 Design Improvement of Region 2

#### 3.3.1 Increase the Thickness of Absorber

The criticality analysis is performed using the basic region 2 model with different absorber thickness. Figure 4 shows the curve of the  $K_{eff}$  versus the increment of the absorber thickness with various burnups of 3.046 wt% enrichment fuel assembly. As we know, the  $K_{eff}$  decreases with the increase of the thickness. In order to meet the 11-cycle storage interval requirement, the whole region 2 can mostly sustain 22 storage cells losses that is the size requirement A in Fig. 4. This means the whole region 2 mostly releases 2 rows storage cells to accommodate the absorber thickness increase. In this condition, there is no spare storage cell in case of any storage cell damaged and other work requirement. The size requirement B is the case of reducing 11 storage cells, thus the remaining 11 storage cells will be the spare cells. For 3.046 wt% fuel assemblies, with the 10GWD/tU calculated burnup, the criticality and size A requirements will be met with the 0.4 in. increment. When the burnup is increased to 14GWD/tU, the increment will only be 0.3 in. for size A and the burnup is increased to 18GWD/tU, and the increment will reduce to 0.2 in. for size B. According to nuclear design report, the discharge burnup of 3.046 wt% fuel can up to 28GWD/tU, which is conservative enough for size B.

As for other enrichment fuel assemblies, we can use the similar method to find the increments of each enrichment versus its burnup (the loading curve). On this basis, we need to consider the economic benefit to determine an optimized neutron absorber size.

#### 3.3.2 Improve B-10 Component

The criticality analysis is performed using the basic region 2 model with different percent  $CB_4$  in  $CB_4$  and  $Al_2O_3$  ceramics with the density of  $2.4422 \text{ g/cm}^3$  (97 %

**Fig. 4** The curve of  $K_{eff}$  versus the absorber thickness for 3.046 wt% fuel assembly

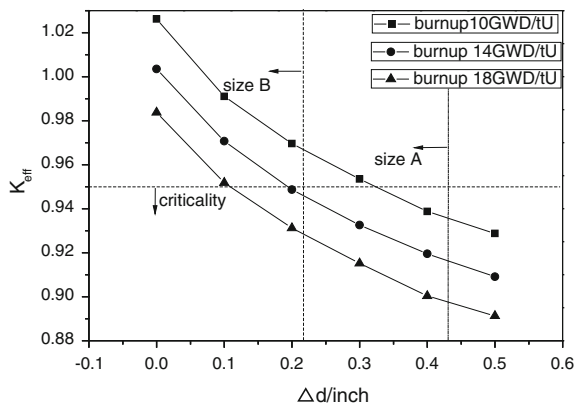
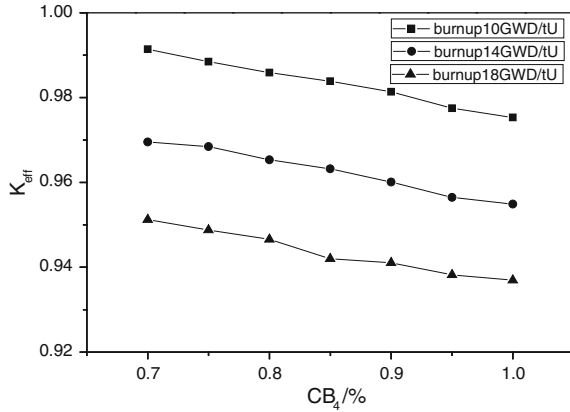


**Fig. 5** The curve of  $K_{\text{eff}}$  versus the percent of  $\text{CB}_4$  for 3.046 wt% fuel assembly



theory density). Figure 5 shows the curve of the  $K_{\text{eff}}$  versus the percent of the  $\text{CB}_4$  with various burnups of 3.046 wt% enrichment fuel assembly. Compared with the increase of absorber thickness, the  $K_{\text{eff}}$  does not show a significant reducing with the improvement of  $\text{CB}_4$ . When the burnup is 10 GWD/tU, although the percent of the  $\text{CB}_4$  is large enough, the  $K_{\text{eff}}$  is still bigger than 0.95. When the burnup is up to 18GWD/tU, the percent of  $\text{CB}_4$  shall be more than 85 % to meet the criticality requirement. Besides, the  $K_{\text{eff}}$  is related to the material density. For 10GWD/tU, when the density reduces from 100 % theory density to 97 %, the  $K_{\text{eff}}$  increases from 0.97181 to 0.97218. So, when we use this new material, we need not only to meet the requirement of  $\text{CB}_4$  component but also to reach the definite sintered density.

## 4 Conclusions

This article studied the extending of AP1000 spent fuel storage racks by the methods of appropriate fuel assembly arrangement, increasing the absorber thickness and the  $\text{CB}_4$  percent in new material. The results show that the appropriate fuel assembly arrangement and burnup will make the whole region 2 available and for 3.046 wt% enrichment fuel assembly with 18GWD/tU, increasing the 0.2 in. absorber thickness or using new absorber material with more than 85 %  $\text{CB}_4$  component and no less than 97 % theory sintered density, the 11 cycles' storage interval will be kept. The calculation results demonstrate that these methods will effectively improve the current spent fuel racks' storage capacity and it will be very important for the future spent fuel storage management and spent fuel racks' design improvement in Haiyang nuclear power plant.

## References

1. Zhang H. The Market of Spent Fuel Transport Hopes to Open. *Energy* [J], 2014(03) 65–67
2. Zhou Y S, Qian J H. The Challenge and Suggest of Chinese Spent Fuel Reprocessing. *Chinese Unclear Industry* [J], 2013(10) 27–29
3. Zhu J, Liu W. Pay Attention to the Development of Spent Fuel Reprocessing Capacity. *Chinese Unclear Industry* [J], 2014(03) 38
4. HOLTEC. Criticality Analysis for Haiyang AP1000 Spent Fuel Storage Racks
5. Li G, Jian M, Wang M I, Wang G C, Liu X Z Research Progress in Neutron Absorbers Materials for Reactor Spent Fuel Storage and Transportation Applications. *Materials Review* [J], 2011(25) 111–113
6. Wang L S, Bian F Y, Chu W F, Yin B Y. The Position of  $CB_4$  in Neutron Materials and its Application. *Materials Science and Engineering of Powder Metallurgy* [J], 2000(5), 113–120
7. Wang L, Chen D M, Zhang H, Tong J F. Structure and Mechanical Properties of Dandified Boron Carbide Ceramics by SPS. *Rare Metal Materials and Engineering* [J], 2009(38) 529–532
8. Yang L L, Xie Z P, Liu W L, Wei H k, Zhao L, Song M. New Progress in the Preparation of Sintering and Application of Boron Carbide Ceramics. *Journal of Ceramics* [J], 2015(36) 1–8
9. AP1000 nuclear design report

# Valves Maintainability Study on Nuclear Power Plant Design Stage

Xiaohu Yang, Jiao Deng, Hong Jiang, Lifei Yang and Wen Chen

**Abstract** To improve the valve maintainability and reduce the maintenance cost on nuclear power plant operation stage, this paper puts forward a method for valves maintainability evaluation and optimization on the nuclear power plant design stage. The main content of the method are: (1) Analyzing the valve's preventive maintenance requirement with RCM (Reliability Centered Maintenance) to get the valve maintenance strategy list. (2) Analyzing the unit operational modes in which the valve can exit operation without violating relevant functional requirements and the required unit operational modes for the valve maintenance strategy implementation to get the comprehensive maintenance window of the valve. (3) Comprehensively considering the space layout of the valve, radiation protection, and other factors to analyze whether the implementation of the maintenance strategy is accessible. (4) Analyzing the system layout, isolation conditions, type and the connection modes of the valve to ensure that the technical condition can meet the valve maintenance strategy implementation requirements.

**Keywords** Valves · Nuclear power plant design stage · Maintainability

## 1 Introduction

Maintainability refers to the product features which facilitate maintenance. Maintainability analysis is an important content of maintenance program and has been applied to evaluate the users' satisfaction degree of various related factors in maintenance progress. The Advanced LWRs Utility Requirements Document (URD) [1] has clearly required the nuclear power plant to carry out the Reliability Assurance Program (RAP) during the design of the standard ALWR plant.

IAEA has issued a guidance document to support the development of nuclear power plant reliability assurance program. The RAM model (reliability, availability,

---

X. Yang · J. Deng (✉) · H. Jiang · L. Yang · W. Chen  
Suzhou Nuclear Power Research Institute, Shen Zhen, Guang Dong, China  
e-mail: dengjiao@cgnpc.com.cn

and maintainability) in the guidance document covers the equipment maintainability analysis. With important function and a large number, the valve's controllability and reliability in the nuclear power plant has strict requirements and has been stettered with various rigid nuclear safety principles. It makes the maintenance works of the valves very complicated. To guarantee the nuclear safety and industry safety during the maintenance of valves, it has strict requirements on the plant system status and environment in which the maintenance activities are to be performed, including system isolation requirements, radiation protection, and industrial safety requirements. It greatly weakens the valves' maintainability. However, few of the existing maintainability evaluation models involve maintainability studies on the nuclear power equipment and the valves' maintainability evaluation on nuclear power plant design stage are still in blank [2–4]. Thus, it's necessary to evaluate and optimize the valves' maintainability on nuclear power plant design stage to improving the maintainability and reducing the operation and maintenances cost of the valves.

## 2 Valve Maintainability Evaluation Methods

Figure 1 shows the valve maintainability evaluation and optimization process on nuclear power plant design stage. The detailed evaluation process is discussed in the following sections.

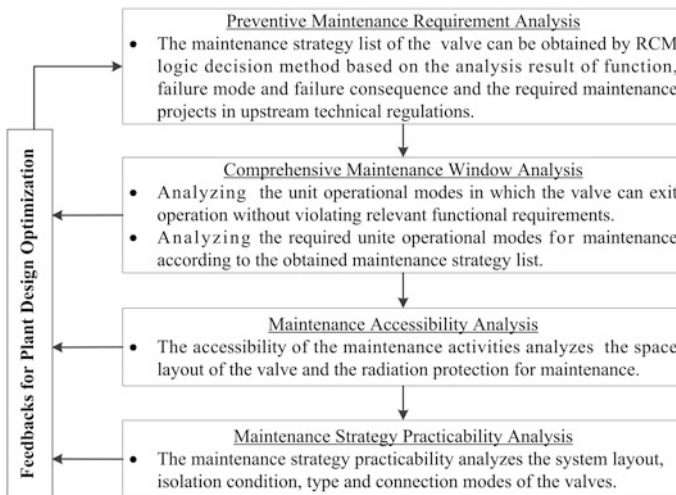


Fig. 1 Valve maintainability evaluation process



## ***2.1 Preventive Maintenance Requirement Analysis***

RCM (Reliability Centered Maintenance) is a systematic engineering approach to determine the equipment preventive maintenance requirements and optimize maintenance rules. This evaluation method first analyzes the valves preventive maintenance requirements by RCM methods.

First, analyze the function and performance criteria of the valves to set preventative maintenance goal and reference the equipment classification results of the valves as the criteria to determine its maintenance activities.

Second, analyze the failure modes that possibly cause the valve's function failure by referring the fault template database to obtain the major failure modes and considering the failure modes ever appeared or has not occurred in the same or similar type of valves. Then, analyze the subsequent influence and consequence of each failure modes happened to the unit, system and equipment. Based on the analyzed failure consequence and the plant operation and maintenance experience, the maintenance strategy of each failure modes can be obtained by RCM logic decision. According to the valve equipment classification result, the required maintenance projects in sub-item technical regulations can be interpreted.

Finally, the maintenance strategy list of the valve can be obtained by summarizing the above analyzed maintenance strategies.

## ***2.2 Comprehensive Maintenance Window Analysis***

The comprehensive maintenance window of the analyzed valve refers to the unit status that allows the valves to exit for conducting maintenance activities.

Based on the thermodynamics and reactor physical properties, the normal operation of the pressurized water reactor power plant is divided into six operational modes such as RP, NS/SG, NS/RRA, MCS, RCS and RCD [5]. For different operational modes, the system has different operation limits and conditions and has different status requirements for the valve with specific functions.

Firstly, analyze the unit operational modes in which the valve can exit operation without violating relevant functional requirements. Such unit operational modes can be defined as the functional exiting modes of the valve. Second, according to the obtained maintenance strategy list, the unit operational modes for the maintenance activities can be confirmed by analyzing the required unit, system and equipment status for maintenance strategy implementation. Then, the comprehensive maintenance window of the valve can be obtained by estimating whether the functional exiting modes of the valve can satisfies the required unit operational modes for the implementation of the maintenance strategy.

### ***2.3 Maintenance Accessibility Analysis***

Maintenance accessibility refers to the difficulty to approach the equipments and parts that need to repair. As an important factor of maintainability evaluation, maintenance accessibility directly affects the equipment maintainability evaluation results.

For general equipment, good maintenance accessibility assures adequate inspection, test, repair, and replacement space. However, there are special requirements for nuclear power plant valves' maintenance accessibility evaluation. It could be summarized from the following two aspects.

First, judge whether the space layout of the valves can meet the maintenance requirement. Space layout refers to the relative position between the valve and its actuator or the adjacent equipments. The space distance and space location design of the adjacent equipments in maintenance working area influences the comfortability, convenience and safety of the valve's maintenance, and directly influences the efficiency of the maintenance works. The space layout of the valves requires that the maintenance working space should be designed on the basis of human body dimension, and should be larger than the required minimum working space. So that the maintenance staffs can keep a comfortable working posture and see their own operation motion during the maintenance works to avoid interference or collision with the adjacent equipments. Thus, the valve's space layout design must conclude maintenance areas for inspection, test, repair, and replacement.

Second, for the valves maintenance accessibility, whether the radiation protection can meet the maintenance requirement is also an important aspect to considering. The primary circuit and its pressure-retaining boundary constitute the secondary shielding barrier of the pressurized water reactor. The primary circuit valve not only performs its major functions, but also undertakes the radioactive inclusive function. The leakage of the primary coolant system valves is likely to cause local radioactive pollution, and the pollution level during the maintenance of the valves can be more serious. Thus, plant must be equipped with radiation protection facilities to ensure the maintenance environment under a normal radiation level. For the valves installed in high radiation level areas, the plant must provide sufficient space for radiation shielding. Furthermore, for some special valves in the primary circuit, we can layout the actuators of the valves can be installed in low radiation level areas through transmission mechanism to reduce the personal radiation exposure during the operation and maintenance of the valves.

### ***2.4 Maintenance Strategy Practicability Analysis***

Maintenance strategy practicability analysis is to confirm whether the maintenance technical condition satisfies the maintenance requirements through analyzing the system layout, isolation condition, type, and connection modes of the valves.

System layout refers whether the system is equipped with supportability facilities for the maintenance activities. For example, to facilitate the testing and quickly locating the failure of valves, the system must be equipped with appropriate monitoring point to provide a good failure testing condition; to perform leakage test for valves, the system must be equipped with additional testing line for leak tightness testing; to debug the valve performance, the system must be equipped with corresponding temporary debugging pipelines.

Furthermore, to avoid potential system or equipment failure caused by incorrect operation during the maintenance of valve, the nuclear power plants reactor design should pay attention to human factors engineering. This includes the following aspects:

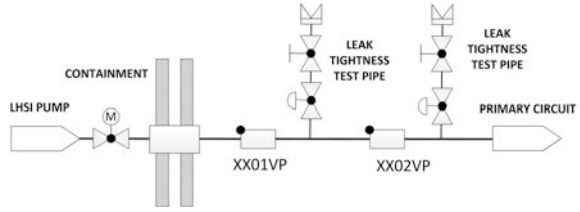
- Equipping thorough error prevention measures and identification marks to avoid installation error;
- Providing appropriate maintenance environment through sound absorption and vibration damping measures to keep the sound level of the workplace acceptable;
- Keeping an appropriate working environment temperature;
- Providing different intensity of illumination in different work conditions to ensuring an appropriate lighting.

The valve isolation error during its maintenance has severe consequences to plant safety, equipment, and personal safety. So system design must satisfy the isolation condition for valve maintenance. The valves should be equipped with isolation valves in the upstream and downstream to isolate it from the system. For valves with significant functions, we can add isolation valve to realize double isolation requirements in its upstream. If the valve cannot be isolated on line, the system should have redundancy design. The operation condition, frequency and ease of operation and performance of different types of valves should be taken into consideration for better selection and configuration of valves. A reasonable selection of the valve type, the material of its key parts and the type of actuators ensures the stability operation of the system and reduces the failure rate of valves. In addition, the connection mode between the valve and the pipeline will directly affect the probability of valve leakage and the efficiency of valve disassembly and reinstallation.

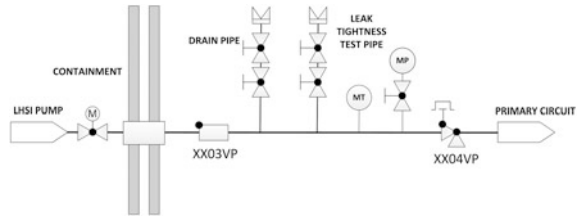
### 3 Case Study

Figure 2 shows the flow diagram of low head safety injection (LHSI) pipeline in a certain nuclear power plant in service. As shown in Fig. 2, as a containment mechanical penetration isolation valve, the regulation (Periodic Test Surveillance Program of The Safety Related Systems and Equipment) requires leak tightness test to verify the sealing of XX01VP during the overhaul of the plant. Since the two

**Fig. 2** The flow diagram of low head safety injection pipeline in a certain nuclear power plant in service



**Fig. 3** The flow diagram of low head safety injection pipeline in a new designed nuclear power plant



check valves on the downstream (XX02VP and the check valve in RCP system) of XX001VP have no isolation function, the primary circuit is required to stay on a certain pressure level as the leak tightness test isolation boundary. Thus, the maintainability of XX01VP is regarded as poor. As the isolation boundary of the primary circuit, the regulation also requires leak tightness test for XX02VP, and the primary circuit is required to stay on a certain pressure as the isolation boundary for the leak tightness test as well. Thus, XX02VP is also regarded as poor maintainability.

Figure 3 shows the flow diagram of low head safety injection pipeline in a new designed nuclear power plant. As show in Fig. 3, in order to improve the maintainability of the containment mechanical penetration isolation valve XX03VP, the check valve XX04VP is designed with a hand wheel. Closing XX04VP by hand wheel provides isolation boundary for the leak tightness test of XX03VP. Thus, the leak tightness test (XX03VP) can be implemented under RCD mode (Reactor Complement Decharge) which improves its maintainability. In addition, as a primary circuit isolation valve, two pressure and temperature measuring instrument (MT, MP) are installed on the upstream of XX004VP. They monitor the leakage of XX04VP in the daily operation of the plant and improve its maintainability.

## 4 Conclusions

This paper studies the valve maintainability on nuclear power plant design stage. A valves maintainability evaluation and optimization methods is obtained through analyzing the valves preventative maintenance requirement, comprehensive

maintenance window, maintenance accessibility, and maintenance strategy practicability. It provides significance guideline for system design and valve selection from the perspective of maintenance during the nuclear power plant design stage.

## References

1. S. Swilley, *Advanced Nuclear Technology Advanced Light Water Reactor Utility Requirements Document, Revision 12*, 2013 Electric power Research Institute, Inc. December 2013
2. Feng Bing, Zhang Jingping, Research on weapon system maintainability design evaluation method. *Acta Armamentarii, Journal of China Ordnance*, 2003(24):222–225
3. Zhao Yi, Zhou Lin, A New Kind of Maintaining Evaluation Model which Considering the Maintaining Attributes, *Journal of Projectiles, Rockets, Missiles and Guidance*, 2004(24): 408–410
4. Tao Fenghe, Yu Yongli, The establishing model of the system maintainability in the engineering development phase of the materiel, *Machinery Design & Manufacture*, 2006 (7):98–99
5. He Yu, Pu Jilong, Gao Ligang, etc. *900 mw PWR nuclear power plant system and equipment*, Atomic Energy Press, Bei Jing, 2005

**Part II**  
**Supply Capability and Quality Control**

# An Improved Welding Process of Instrumentation Tubes on Nuclear Reactor Pressure Vessel

Ruifeng Guan, Hong Chen, Bin Zhang and Wenbin Zhong

**Abstract** Because of the importance of the weld seam which the instrumentation tubes weld on the nuclear reactor pressure vessel, the organization and the welding feature of nickel base alloy were expounded, and the influence factors of the welding quality and welding precision were expounded. An improved welding technology which the instrumentation tubes weld on the reactor pressure vessel was discussed. The welding results show that welding which was based on the welding parameters and welding requirements determined by welding procedure qualification can ensure the welding quality to meet the design requirements; Use water cooling device and anti-deformation tooling to assist welding, and adjust welding sequence or take correction according to the monitoring results of the welding deformation which can effectively reduce welding deformation and ensure the welding precision.

**Keywords** Reactor pressure vessel · Instrumentation tubes · Nickel base alloy · Shielded metal arc welding · Welding assistant measures

## 1 Introduction

Reactor pressure vessel (abbr. RPV) is thick wall equipment which is used under high temperature, high pressure, and long-term exposure. It is the most important part of the reactor coolant pressure boundary, besides RPV cannot be replaced during the whole service life of nuclear power plant. Therefore, the manufacture of RPV is one of the most important things among nuclear power plant equipment [1]. There are 50 instrumentation tubes welded on the RPV's lower dome, which used for neutron fluence rate measurement catheter to pass through. Due to the importance, its nickel base alloy material and welding structure, the welding of the

---

R. Guan (✉) · H. Chen · B. Zhang · W. Zhong  
China Nuclear Power Engineering Co., Ltd, Shenzhen City Guangdong Province, China  
e-mail: guanruifeng@cgnpc.com.cn

instrumentation tubes and lower dome is always one of the key technologies in manufacturing process.

## 2 Weldability Analysis

### 2.1 Base Metal and Welding Material

For seal welds between instrumentation tubes and RPV's lower dome, nickel base alloy shall be buttered on the bevels of lower dome, followed by filling up the fillet chamfers with nickel base alloy. So, actually the welding between instrumentation tubes and lower dome is welding between nickel base alloys.

Inconel 690 is high nickel base alloy. Because it has very low corrosion rate and excellent stress corrosion resistance in high temperature water, and it also has high strength, good metallurgical stability and processability, it is widely applied in the main equipment of nuclear island [2]. But Inconel 690 has a weakness that the weldability is not good, it is easy to produce solidification crack in welding. The main chemical elements of Inconel 690 include S, P, Si and other impurity elements, Mn, Nb, Al, Ti and other alloying elements, N, H, O and other gas elements [3]. The main chemical composition is shown in Table 1.

The weld microstructure using Inconel 690 electrode is single phase of austenite, the structure of buttering is slender columnar crystal, and the direction is perpendicular to the fusion line, the structure of weld zone is dendritic crystal. In addition, there is brittle intermetallic compound TCP phase appeared in the weld, such as S phase, Laves phase, which will adversely affect mechanical property and corrosion resistance of the weld metal, and increase hot cracking susceptibility of weld [2]. So it make more difficult to weld between instrumentation tubes and lower dome.

Furthermore, the welding precision of instrumentation tubes is very high, but nickel base alloy has big thermal expansion coefficient, and the thickness of instrumentation tube wall is thin, which made that it is easy to produce welding deformation in welding process. In addition, instrumentation tube and lower dome composes single J groove as Fig. 1. Because of the asymmetry of single J groove, it made different deposited metal amount in different position in welding process, which causes thermal stress is uneven in different position. This is the main reason of welding deformation. Therefore, it is one main and difficult technical point to control the welding deformation of welding between instrumentation tubes and lower dome.

**Table 1** Main chemical composition of Inconel 690 (wt%)

C	Mn	Si	Ti	S
0.014-1.04	≤ 0.15	≤ 0.50	≤ 0.50	≤ 0.01
P	Ni	Cr	Fe	
≤ 0.015	≥ 58	28-31	7.00-11.00	



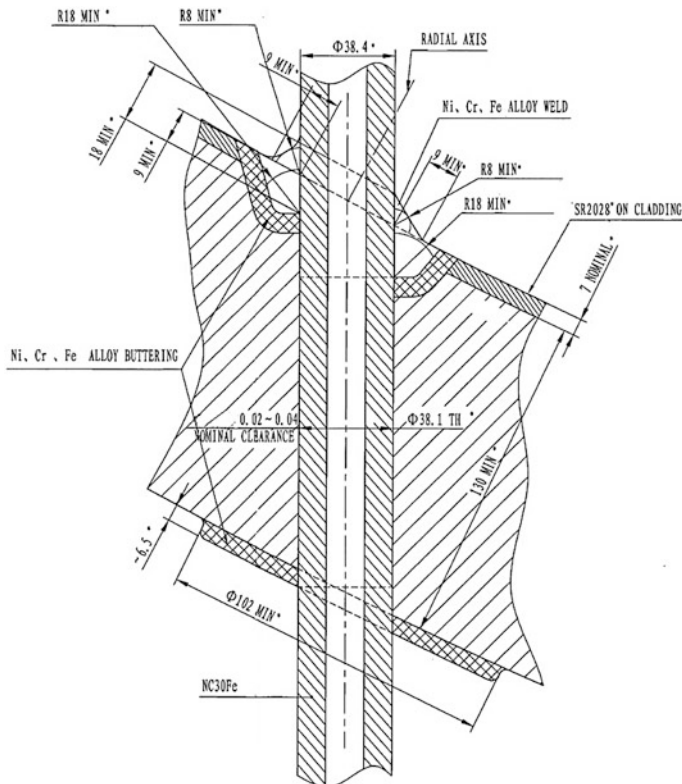


Fig. 1 Typical view of welding of instrumentation tubes

## 2.2 Welding Technology

As the traditional welding method, because shielded metal arc welding (abbr. SMAW) uses the simplest welding equipment, and it does not need shielding gas, it just uses the soldering material coated on the outside of the electrode to provide environmental protection for arc and weld pool, it is widely used in the manufacture of mechanical equipment. Under the effect of arc, soldering material can prevent oxidation of weld pool by decomposing CO, CO<sub>2</sub>, and metal vapor to isolate from the surrounding air. Meanwhile, soldering material will decompose and form a layer of viscous slag which covered the hot melt droplets to play a protective role in the droplet cooling process. In this paper, Inconel 152 electrode was used to welding between instrumentation tubes and lower dome using SMAW.

### 3 Welding Process

#### 3.1 Welding Preparation

Because of the importance of seal welding between instrumentation tubes and RPV's lower dome, it needs to use protective casing to wrap instrumentation tubes to prevent spatter and pollution, and use acetone to clean the welded surface to ensure no oil pollution and other impurities. In addition, the interpass temperature shall be lower than 225 °C to ensure welding performance; therefore a water cooling device which has grade A water pass through was arranged under the lower dome to decrease interpass temperature using water circulation.

#### 3.2 Execution of Fillet Welds

In order to control the welding deformation, especially for welding on the single J groove which have relatively large asymmetry on the edge of lower dome, 23# to 50# instrumentation tubed were chosen to use relevant anti-deformation tooling. The anti-deformation tooling was assembled and spot welded on the lower dome before instrumentation tubes assembly. The tolerance fitting of instrumentation tube and lower dome is clearance fit whose nominal clearance is 0.02–0.04 mm, so it needs to spot weld instrumentation tube to ensure position precision after assembly. In order to increase the symmetry of welding to decrease welding deformation, 50 instrumentation tubes were divided into four regions to weld, which is shown as

Fig. 2 Sketch of welding division

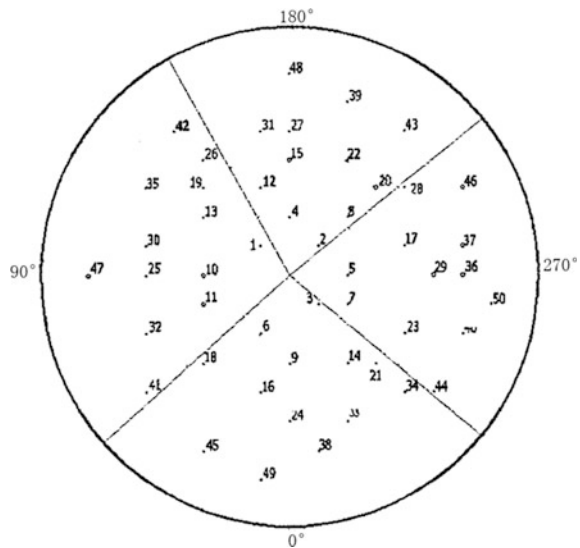


**Fig. 3** Schematic diagram of welding process

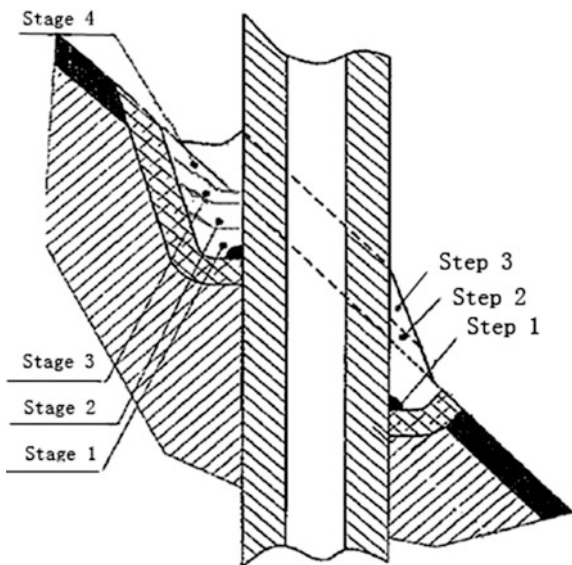


Fig. 2, and the tubes in the symmetric regions were welded at the same time. The welding process between instrumentation tubes and lower dome can be divided into three steps included root pass, filling pass in the groove and final pass, which is shown as Fig. 3.

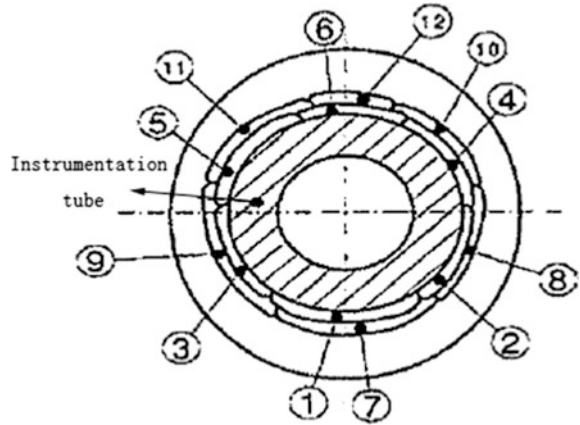
### 3.2.1 Root Pass

Root pass which was always used  $\Phi 2.5$  mm electrode to weld is shown as step 1 in Fig. 3. When root pass's welded closed to the position spot welded in assembly, it need to use rotary burrs to slightly polish the spot welding line and make it smooth in order to meet the requirement of welding surface. Besides the overlap joint of welding shall be checked and slightly polished as needed in order to ensure good overlap and smooth transition in the welding process. It needs to perform liquid penetrant examination after finished root pass's welding.

### 3.2.2 Filling Pass

Filling pass can be divided into four stages shown as stage 1–4 of step 2 in Fig. 3. Each stage just welded less than three layers to ensure that welding height is about 10 mm. The welding sequence is shown in Fig. 4. It shall not weld continuously in the same position and the instrumentation tube needs to be welded symmetry to ensure uniform welding stress in different position. In order to make the molten weld can shrinkage free to reduce welding residual stress, it shall be welded from tube side

**Fig. 4** Diagram of welding sequence of filling pass



to outside, and welded from the bottom of single J groove to up. Electrode of different sizes was used in welding filling pass according to different welding position, that  $\Phi 2.5$  mm electrode was used in welding the position close to the instrumentation tube, and the position outer the instrumentation tube can use  $\Phi 2.5$  or  $\Phi 3.2$  mm electrode depended on the distance from the edge of groove. The welding interpass temperature shall be controlled strictly and the instrumentation tubes shall be welded alternately in the same region to avoid excess temperature.

The cleanliness of welded surface is important so that vacuum cleaner was used to clean the dust and slag before welding. In addition, the welding arc shall be stopped slow and outward to avoid electrode touching the instrumentation tube. The overlap joint of welding, especially the overlap joint on the position of narrow groove, need to be checked and slightly polished as needed to ensure good overlap and smooth transition. The position back of instrumentation tube, especially the instrumentation tube on the outboard lower dome, needs to be welded flat before next layer's welding. The single J groove needs to be filled and make the interpass welding almost flat to the stainless steel cladding of lower dome when welding of stage 3 finished. The welding shall be 1–2 mm higher than the stainless sell cladding of lower dome when welding of stage 4 finished, and the welding can be overlapped the nickel based alloy buttering 1–2 mm with smooth edge. Visual examination and liquid penetrant examination shall be performed for every third layer weld maximum.

### 3.2.3 Final Pass

Final pass which includes four welding layers is shown as step 3 in Fig. 3. In this step it shall keep special focus on that final pass shall not be welded over the edge of stage 4 of filling pass. In the first two layer of final pass, the angle between

**Table 2** Key parameters of welding

Step.	Electrode type	Electrode size/mm	Welding current/A
1	Inconel 152	2.5	55–70
2, 3	Inconel 152	2.5	45–70
		3.2	75–100

electrode and cladding is  $30^{\circ}$ – $45^{\circ}$ , the amount of overlap is about 50 %, and the welding shall be smooth without dent. In the third layer, the angle between electrode and cladding is  $70^{\circ}$ – $80^{\circ}$  and smooth transition shall be formed between layers. In the last layer, the angle between electrode and cladding is  $15^{\circ}$ – $25^{\circ}$  to ensure no undercut. In addition, sample plates were used to measure the thickness and shape of welding, so it should weld more than it need in final pass to ensure polishing allowance. Visual examination and liquid penetrant examination also shall be performed for every third layer weld maximum and the final welding surface.

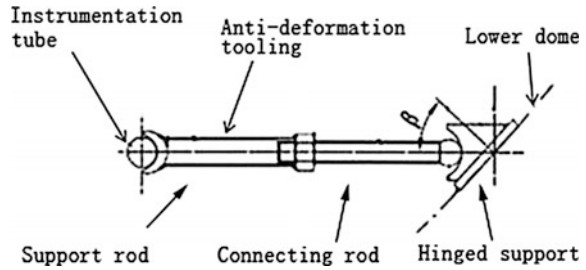
The key parameters of welding between instrumentation tubes and RPV's lower dome which was accepted by welding procedure qualification are shown as Table 2. Qualified weld with good welding surface and welding structure can be received using the welding parameters. Preheating and postheating are not required for the welding of fillet welds, and stress relieving heat treatment is not required for the fillet welds between instrumentation tubes and lower dome, however, the fillet welds can undergo the stress relieving heat treatment of sub-assembly regarding to the rules of cumulative stress relieving heat treatment.

### 3.3 *Welding Assistant Measures*

#### 3.3.1 *Use of Water Cooling Device*

The cooling rate has a great influence on the welding quality. Increasing the cooling rate is beneficial to the refinement of the microstructure, and it can decrease the sensitivity of the hot cracking to some extent. In addition, local rapid cooling of welding metal in the trail of molten weld pool can reduce welding hot cracking effectively, and reduce welding stress and deformation. Forced cooling of base metal on either side of molten weld pool can also reduce welding stress and welding deformation, reduce grain growth in weld metal zone and avoid brittle fracture [2]. Therefore, the water cooling device which lets grade A water pass through the instrumentation tube circulatory was used to increase cooling rate. The water temperature difference between inlet and outlet was adjusted in less than  $5^{\circ}\text{C}$ . This water cooling device can control the interpass temperature lower than  $90^{\circ}\text{C}$  to improve the microstructure of weld metal, so that it can reduce the probability of

**Fig. 5** Structure sketch of anti-deformation tooling



hot cracking occurrence of nickel-based alloy weld and ensure the quality of seal weld between instrumentation tubes and RPV's lower dome.

### 3.3.2 Use of Anti-deformation Tooling

According to the extent of the asymmetry of single J groove, 23# to 50# instrumentation tubes were chosen to use relevant anti-deformation tooling to assist welding. The structure sketch of anti-deformation tooling is shown as Fig. 5. It is composed of three main parts include hinged support, connecting rod, and support rod. The connecting rod is connected with hinged support using hinge axis, so that it can be rotated to adjust the direction of the anti-deformation tooling. The supporting rod is connected with connecting rod using screw thread, so that it can be adjusted length of anti-deformation tooling by adjusting the extent of tightening. There is a cambered support head at the end of the supporting rod, which surface is required very smooth to ensure contacting well with instrumentation tube.

At the time of installation, first the direction and length of each anti-deformation tooling needs to be calculated precisely according to the position of each instrumentation tubes. Second, hinged support was spot welded on the stainless steel cladding of lower dome. Finally, the direction and length of anti-deformation tooling was adjusted according to the earlier calculations after instrumentation tube assembly. At the moment the cambered support head was contact instrumentation tube well. The welding deformation will be greatly reduced because of the supporting force providing by the anti-deformation tooling during the welding process.

### 3.3.3 Deformation Monitoring of Welding Process

In the welding process, the welding sequence was adjusted real time dynamically by welding deformation monitoring, even that forced adjustment was performed as needed, so that the welding deformation can be reduce effectively.

Before welding of each layer, a pre-deformation of instrumentation tube whose direction is  $5^{\circ}$ – $15^{\circ}$  towards to the center of the lower dome's circle was set, so that

the instrumentation tube can be straightened automatically during welding. Angle optical inclinometer was used to check the perpendicularity of instrumentation tube during welding. According to the welding deformation and welding deformation direction measured by angle optical inclinometer, it can use hammering to adjust, or use anti-deformation measure that welds on the opposite deformation direction, and if necessary, some of the weld metal on the opposite deformation direction can be polished to help to weld. Dummy rods are used to check the linearity of instrumentation tube during welding process. It should let the dummy rod vertical freefall through the instrumentation tube without shaking or forcing by hand, and it is acceptable if the dummy rod can pass through.

### **3.4 Welding Results**

After taking above welding process, the results of dimension test, visual examination and penetrant examination show that good welding quality can be obtained and welding deformation can be controlled effectively. The visual examination and penetrant examination's results are good, and the position of instrumentation tubes after welding is less than R3 which is required according drawing. When dummy ball was used to check the roundness, a  $\Phi 15$  mm stainless steel ball can pass through all 50 instrumentation tubes freely. When dummy rod was used to check the cylindricity, a  $\Phi 14$  mm stainless steel rod, whose length is 900 mm, straightness is 0.2 mm, can also pass through all 50 instrumentation tubes freely. The welding results between instrumentation tubes and lower dome meet the requirements of technical specification.

## **4 Conclusions**

Since the chain fission reaction is occurring in the RPV, the quality of seal weld between instrumentation tubes and RPV's lower dome is very important, and any crack is not acceptable in welding process to prevent nuclear leakage accident. Besides as the channel of the neutron fluence rate measurement catheter passed through, the welding deformation shall be controlled strictly. Therefore, it is very important to develop an advanced scientific nickel base alloy welding process.

An improved welding process was discussed in this article. The results show that it can ensure the welding quality and precision well using anti-deformation tooling to assist welding, welding according to the welding requirements strictly, monitoring the welding deformation during the welding process and adjusting real time dynamically even that forced adjusting.

## References

1. Shi Yaixin, Tian Hongzhi. Property requirements and technological measures of a based metal for reactor pressure vessels with an expected 60-year life [J]. *Power Equipment*, 2012, 26(2): 134-137.
2. Yang Zhipeng, Wu Yidang, Liu Mingyu. Welding technology and process optimization of housing penetrations of reactor pressure vessel [J]. *Metal Processing*, 2012, 22: 41-43.
3. Zhang Qixian, Wu Shaobin, Liu Mingyu, et al. Study on weldability of domestic heat transfer tube used in nuclear steam generator [J]. *Hot Working Technology*, 2012, 41(23): 159-162.



# Analysis of the Development of Nuclear Power Plant Construction Management Model and Management of Engineering Company and Owners

Keteng Ma and Bin Hou

**Abstract** With the development of nuclear power industry in China, the nuclear power plant construction project management model has also been under constant evolution and development based on absorbing the advanced international experience. Through the research and comparison of the several major construction management models introduced in domestic China, the author in this dissertation analyzes the status of various management modes in nuclear power construction, and simply describes the advantages of EPC (Engineering, Procurement, and Construction) model under the new situation. In addition, this dissertation also makes analysis and discussion of the division of labor and cooperation problems between engineering company and owners under EPC model.

**Keywords** Nuclear power plant · EPC model

The nuclear power is an economical, reliable and clean energy, and it will not pollute the atmosphere, or emit the greenhouse gases. Currently, the nuclear power generation in China has accounted for less than 3 %, which is far below world average power generation of 10.2 %. After summing up the lessons of Fukushima, Japan, China has made various improvements for the second generation of nuclear power technology, and China has launched its own research and development of third-generation nuclear power technology. This year is the restarting year of the coastal nuclear power plant construction in China since the Fukushima accident, and China's inland nuclear power plant construction is also brewing for the restarting. According to China's medium- and long-term nuclear power development plan (2005–2020), the total installed capacity of nuclear power plants in mainland China by 2020 will reach 58 million kilowatts, with 30 million kilowatts to be under construction. Meanwhile, China's nuclear power industry strategy of

---

K. Ma (✉) · B. Hou  
China Nuclear Power Engineering Co., Ltd, Beijing 100083, China  
e-mail: makt@cnpe.cc

going global has also been constantly advancing, with the advent of the era of large-scale development of China's nuclear power; it has been faced with the new issue and challenge of how to further improve the level of nuclear power plant construction project management [1].

## **1 Project Management Model of the Current Nuclear Power Plant Construction**

Since the industrial development in China was started in the 1980s, the nuclear power construction has been started later, and the nuclear power industry system as a whole is weak, coupled with the long nuclear power plant construction period, large project difficulty; high-quality requirements, strict quality assurance system; deep degree of specialization, the complexity of docking system and other characteristics, China's nuclear power construction has primarily taken the way of development of nuclear power as introduction—digestion—absorption—another innovation.

The early development of nuclear power is mainly for the multi-contract model or fewer contract/sub-island procurement model. With the development of nuclear power industry, especially with the establishment and development of the general contractors of nuclear power construction, the EPC model has gradually become the mainstream of construction of nuclear power.

### ***1.1 Multi-contract Model***

The owners are responsible for signing all kinds of the procurement contracts such as engineering design, equipment procurement, civil construction, installation, etc., and they independently undertake the project management, and coordination tasks among contractors; each contractor is only responsible for the management within the scope of contracted contract, such as Qinshan Phase II. The corresponding organization management model is as shown in Fig. 1.

### ***1.2 Single Contract/Sub-island Procurement Model***

The respective contracting of design construction and procurement tasks is conducted in accordance with the nuclear island, conventional island, BOP, etc., the owners are responsible for contract bidding and management, they undertake the coordination tasks independently. Each contractor is responsible for the management of contracted portion. For example, Sanmen Nuclear Power Plant belongs to

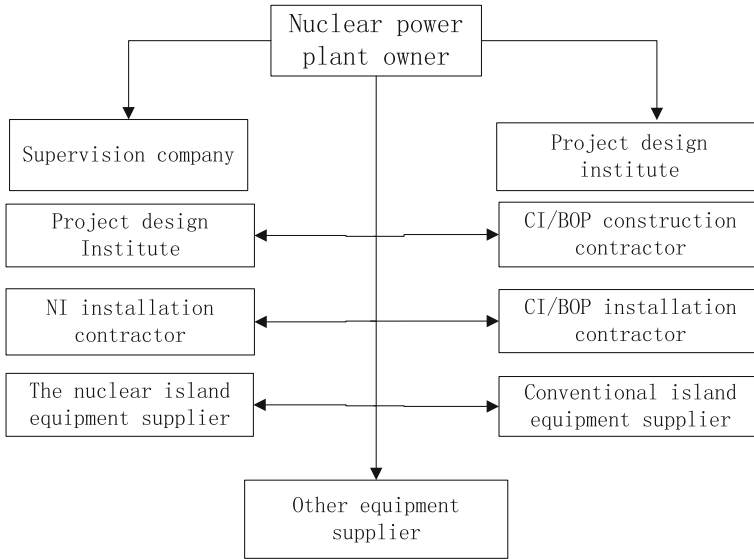


Fig. 1 Diagram of multi-contract management model

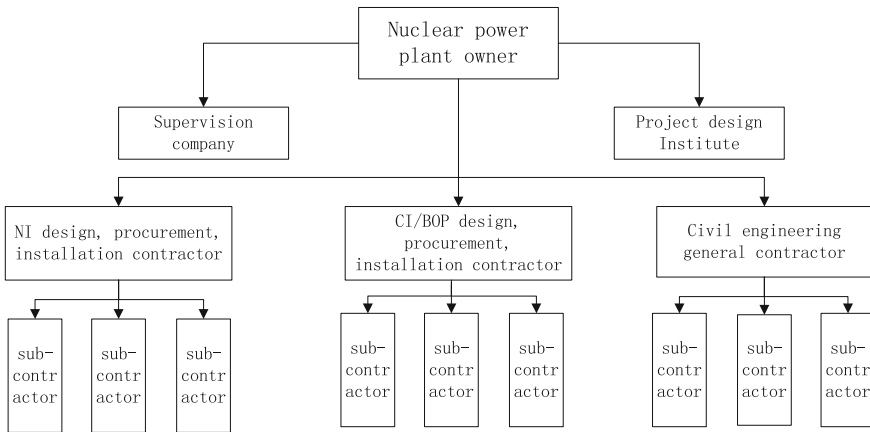
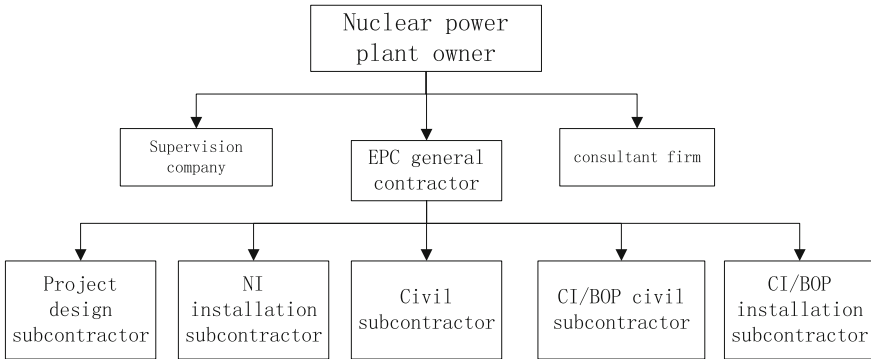


Fig. 2 Diagram of single contract/sub-island procurement model

typical single contract management model, of which, the nuclear island is contracted by China Nuclear Power Engineering Co., Ltd through the EPC model; conventional island and BOP are managed by Sanmen Nuclear Power Plant, the construction is carried out by ZTPC (Zhejiang Thermal Power Company) through EPC model. In addition, unit No. 1/2/3/4 of Hongyan River Nuclear Power Plant, unit No. 1/2 of Taishan Nuclear Power Plant and others are for such project management model as the single contract/sub-island procurement model. The corresponding management model is as shown in Fig. 2.



**Fig. 3** Diagram of nuclear power project EPC model

### 1.3 EPC Model

With the development of China's nuclear power construction industry, digestion and absorption of nuclear power technology, experience in the nuclear power construction and accumulation of nuclear power construction personnel, EPC model has gradually become the main model of nuclear power construction management. Under the EPC model, the owners will hand off the design, procurement, and construction work as a whole to a qualified contractor [2, 3]. In this model, the owners focus on the global positioning, and they taking into account the optimization of the overall effectiveness of the investment project, thus to control project schedule, quality and cost from the height of the entire project. The general contractors are responsible for all design, procurement of the project, contracting and management of the total construction contract, and they are also responsible for coordinating various subcontractors. For example, unit No. 1–4 of Yangjiang Nuclear Power Plant is conducted by China Nuclear Power Engineering Co., Ltd through EPC model; and also unit No. 1/2 of Guangxi Fangchenggang Nuclear Power Plant; unit No. 1/2 of Fangjiashan Nuclear Power Plant, unit No. 1–6 of Fuqing Nuclear Power Plant, unit No. 1/2 of Hainan Nuclear Power Plant are conducted by China Nuclear Power Engineering Co., Ltd through EPC model. The corresponding management model is as shown in Fig. 3.

## 2 Pros and Cons of Each Management Model

### 2.1 Multi-contract Management and Single Contract/Sub-island Management

In the early construction of China's nuclear power, the nuclear power construction foundation was weaker, together with the shortage of nuclear power technology and

talent pool, and there is no contracting unit with the formation of capability in EPC model. Thus such contract model has made a significant contribution in starting development of China's nuclear power, with the advent of large-scale development of nuclear power; this model has been unable to meet the sustainable development of the nuclear power industry, such as the following aspects:

1. It is not conducive to marketization and specialization of the project management. The owners need to invest a lot of time and efforts to manage the construction work, but also they require a lot of professional staffs that are proficient in the technology, construction, economics, law, management, and others to meet the three controls of the project. Once the project was completed, the experience accumulated from the project also cannot be fully absorbed and digested, which is not conducive to accumulation and heritage of nuclear power construction management experience.
2. In view of the one-time and unique project features, once there is completion of the construction project, the construction management team is also disbanded, thus it is unable to form and maintain a professional project construction management team.

With the scale development of the nuclear power plant, and under the condition of gradual formation of various units' capability in EPC model, the single contract/sub-island EPC model has also made a certain contribution within a certain period. Under this model, the nuclear power companies only undertake the functions of investment and financing, construction inspection, risk management and others, each general contractor and subcontractor implement the professional management of the project implementation process, respectively. This model has effectively promoted the nuclear power design and project management autonomy, and promoted the level of domestic equipment manufacturer, thereby reducing the costs and risks of owners.

### **3 Advantages of EPC Model**

EPC is currently the more advanced project management model in international, and is mainly divided into Engineering, Procurement, and Construction; Design-Bid-Build, Design-Build; Construction Management, Build-Operate-Transfer, as well as Project Management Contractor, etc., while the current mainstream for nuclear power plant construction project contracting is EPC model. Namely, the professional nuclear engineering companies carry out EPC model for nuclear power project construction. Such model mainly has the following advantages:

1. It is conducive to make unified planning, coordination and organization, together with full process control of each subcontractor's work content. Since implementation of the whole project process of is undertaken by a contractor, the general contractor is responsible for management of all subcontractors, thus

it reduces the administrative burden of the owners, and the owners can control the overall schedule, fees and costs.

2. The integration contracting of design, construction, and procurement reduces the project cost. It is estimated that 90 % of the engineering cost has been confirmed at the design phase, the impact of the construction phase on the investment accounts for only about 5 %. EPC model solves the problems of construction and design difficult to be coordinated, contradiction of cost and the use function under the traditional model, the construction and design are deeply interlinked, thus the cost and construction period can be minimized as possible under the condition of meeting the contract requirements. At the same time, the unified planning, management and coordination of design, construction and procurement is conducive to control the quality, schedule, and cost of the entire process.
3. It is conducive to create a professional and high-quality EPC team. Under EPC model, the professional contractors undertake the project management throughout the construction, the contractors can learn from the rich experience of a reference power plant. Such contracting model can greatly reduce and avoid the occurrence of the same type of risks during the project implementation process, thereby improving the project quality, shortening the construction period and reducing the project costs.

#### **4 The Division of Labor and Coordination Problems Between Engineering Company and the Owners Under EPC Model**

With the development of China's nuclear power industry, EPC model has gradually become mainstream project contracting model of China's nuclear power construction based on learning from the advanced experience of foreign countries. However, EPC model in China has yet not been called as EPC in true sense due to the influence of the big owner management thinking. In the following, the author will discuss about the nuclear power EPC issues by taking the management and collaboration between the owner and engineering company of a Nuclear Power Plant under EPC model:

##### ***4.1 Unclear Rights and Liabilities***

1. Procurement rights and liabilities are not clear. Currently, most of EPC contract of China's nuclear power project adopted two types of fixed-price or cost-plus contract, no matter what type of EPC contract is adopted, it is not the EPC model in true sense, there is also the case of owners deeply involved in the full cycle of engineering equipment procurement, such as owners jointly sign the

- equipment procurement contracts, participation in the payments of the general contractors for subcontractors, participation in management of the contract execution, etc. The extending of the rights of owners results in weakness of general contracting procurement, and construction management, unclear liabilities, delayed decision-making time, which thus affect the construction progress.
2. Although the joint office model has certain advantages, and it can solve the human resource problem of the project management within a period of time, the in-depth involvement of the owners will have adverse impact on EPC corporate management, program flow control and others; weakening the rights of the owners, making it difficult to effectively use the nodes to conduct the rewards and punishments for engineering contracting enterprises.

#### ***4.2 More Business Controversies, Long Decision-Making Process and Inefficient***

The total price of EPC contract equipment is often determined at a later stage of the project. Meanwhile, engineering companies and owners have inconsistent perspective of dealing with the issues, especially for the emergency procurement. In order to ensure on-site construction schedule, the field equipment issues are solved at the first time, the general contractor release the procurement without the in-depth investigation and identifying the responsible party, thus to ensure project progress, and there will be more followed controversies and wrangling in identifying the liabilities and business negotiations, thereby affecting the signing and payment of changes of the emergency procurement contract, and the treatment of the field equipment issues.

Meanwhile, the more in-depth involvement of the owners makes the management of EPC enterprise difficult to be implemented, in particular the numerous technical renovation items.

#### ***4.3 More Major Technical Renovation***

Technical renovation refers to improvement and upgrading of inappropriate portion after all systems, equipment and others are transferred to the owners, in order to improve economic efficiency and reduce costs, or based on the actual situation at the scene. However, due to the more in-depth involvement of the owners and the impact of the open-ended contracts, during installation process, the owners propose more technical renovation items based on operating experience of nuclear power plants, causing a large number of design changes. Meanwhile, the technical renovation interlinks to the normal construction process, which results in the rework, reloading and other massive work, affecting construction management, construction

progress. If the technical renovation involves items for foreign purchases, and then the longer procurement cycle also affects the normal node schedule.

#### ***4.4 Management Losses Between Owners and Engineering Companies Are Large***

Owners and the management personnel of the engineering companies are overlapped, especially in procurement management, both owners and engineering companies have staff to manage the same contract, which results in waste of the personnel and unclear responsibilities, leading to the prevarication, slow progress in dealing with issues and others. For example, the contract changes, contract payments, and others need the reapproval of the owners after the approval of the engineering companies, if the owners disagreed with the results of the engineering companies, and the latter are also required to make full explanation. The above processes not only increases workload of the owners, but also results in the repetitive work of the engineering companies.

### **5 Experience References and Improvements**

Advantages of EPC model lie in EPC enterprise's control over engineering design, procurement and construction, but the in-depth involvement of the owners in project management, damage efficiency increase internal friction, unclear rights and liabilities, affecting the construction progress. Therefore, according to the above problems, the improvements in the subsequent nuclear power plant EPC management should be made as follows:

1. In the early construction of the nuclear power plant, there should be scientific budget of the EPC costs of the nuclear power plant, and the fixed total price contract should be signed;
2. The owners control the overall quality objectives, progress goals and investment objectives, and they should not participate in the actual site construction management. There should be the development of assessment methods for key control over a variety of large nodes, and implementation of the rights, clear penalties and indicators clearly that should be strictly enforced.
3. Engineering companies need to strengthen the experience feedbacks. In particular the design department should learn and absorb the outstanding schemes of technical renovation of the same type of nuclear power plants, and put them into practice of the general contracting contract at pre-stage of the project.
4. Engineering company's general contracting responsibilities should be strengthened, and there should be the maximum grant of management authority to the engineering company to ensure the priority of efficiency.



## 6 Conclusion

Currently, nuclear power engineering EPC construction management mode has played an important role in nuclear power construction project management, but it is still in its infancy in domestic market. With the maturing EPC model, gradual accumulation of EPC experience, the management of EPC enterprises will become increasingly scientific and perfect through engineering practice, the rights and obligations between EPC enterprises and the owners will be gradually clear.

## References

1. Wu Yongzhong, *Research on Development Strategy of China Nuclear Power Engineering Co., Ltd.* [D]. Beijing, 2013.
2. Cheng Pingdong, Sun Hanhong, *Nuclear Power Project Management* [M], Beijing, China Electric Power Press, 2006.
3. Yu Fei, Liu Haibo et al. *Research on Existing Problems and Countermeasures of Nuclear Power Engineering EPC Site Management* [J], Beijing, People's Yangtze editorial department, 2015.

# Components Qualification for the Safe Operation of Nuclear Power Plants

Holger Schmidt, Martin Betz, Ingo Ganzmann, Achim Beisiegel,  
Thomas Wagner, Emmanuel Peter, Darryl Gordon and Gong Yufeng

**Abstract** AREVA operates a worldwide unique thermal hydraulic platform to ensure high safety standards in the nuclear industries. This platform is operated as an accredited test and inspection body according to ISO 17025 and 17020 to grant a high and independently confirmed quality standard. The accreditation also ensures the independency of the organization and confidentiality to the individual stakeholders, as for example research centers, utilities, components suppliers, engineering companies, and vendors. Especially for nuclear power plants it is very relevant to consider that reliability depends on the integrity of its components during its life time—from design through construction, operation, and maintenance. For example, a typical nuclear power plant (NPP) has 1000–2000 large valves and 7500–12,500 small valves, of which about 200–400 are designated Safety Class 1. These safety-related components require a higher level of diligence in ensuring that they function properly. The qualification of these Safety Class 1 components is relevant for reactor new builds but also for installed plants. Because replacing worn or malfunctioning safety-related components, especially those that were designed and manufactured decades ago by now-defunct manufacturers, is a challenge,

---

H. Schmidt (✉) · M. Betz · I. Ganzmann

AREVA—Thermal Hydraulics and Components Testing, Paul-Gossenstr.100,  
91052 Erlangen, Germany  
e-mail: test-labs@areva.com

A. Beisiegel · T. Wagner

AREVA—Thermal Hydraulics and Components Testing, Seligenstädter Strasse 100,  
63791 Karlstein, Germany

E. Peter

AREVA—Thermal Hydraulics and Components Testing, 30 Boulevard de L'Industrie,  
71205 Le Creusot, France

D. Gordon

AREVA—Thermal Hydraulics and Components Testing, 3315 Old Forest Road,  
Lynchburg, VA 24501, USA

G. Yufeng

AREVA—Thermal Hydraulics and Components Testing, Keysur International F11,  
Tower a, Millennium Plaza, no. 72, Beijing 100037, China

qualification programs for new components have been developed. As regulations have changed over the years, so have the requirements for component qualification. This paper explains newly established qualification tasks, the corresponding testing infrastructure, and the state of the art of testing technology. By way of example, the paper describes the program and possible sequence of qualifying NPP safety-related valves. Depending on the design and operational conditions, such a qualification program may include testing containment environmental effects, sealing capability, end loading, seismic performance, and proper functioning under various conditions, such as high-energy pipe rupture, thermal shock, particle-loaded fluids, to name a few.

**Keyword** Component qualification

## 1 Introduction

Ensuring that safety and regulatory standards are met in new nuclear plant projects or large modification projects at existing nuclear plants requires the qualification of any new or modified components. The use of qualified components to ensure safety functions is valid for instrumentation and control components as well as for all safety-related mechanical components, which include in-core components like control rods and all relevant components outside the core, such as pumps and valves. The general philosophy is for all of these components to undergo a rigorous qualification process, even though the codes and standards they must meet differ from component to component or plant to plant. Additionally, a previously qualified component that is being used in a new application must undergo a qualification process to ensure that it will have the desired performance in the new application. This need has become evident as the industry's level of safety knowledge has increased over the years and the push for power uprates, extended lifetimes, and new plant designs has led to new requirements and new applications for plant equipment. If it is not possible to confirm the required functioning of a component based on engineering work and previously performed qualification tests, it becomes necessary to perform new qualification programs, including the appropriate qualification tests. Because the requirements are so stringent, sub-suppliers often have difficulty in performing the qualification testing in-house. To address this critical supply chain issue, AREVA decided to open its testing and qualification facility to all stakeholders in the nuclear industry, including utilities, authorities, research centers, component manufacturers, or engineering companies. To meet the high safety and qualification standards required by these stakeholders, AREVA's testing and qualification facility has been accredited to the ISO 17025 and ISO 17020 standards. This accreditation also ensures the independence of the facility and confidentiality of the individual stakeholders. Because the various stakeholders have different qualification requirements, a flexible infrastructure and accreditation have been established. This means that, as long as the tests and qualifications are

**Table 1** Accredited measuring range

Measurement	Measuring range
Temperature	0–1100 °C
Pressure	10 Pa to 40 MPa
Volume flow	0.1 l/h to 100,000 m <sup>3</sup> /h
Mass flow	0.005 kg/h–4000 kg/s
Force	1 N–10,000 kN
Torque	1 Nm–50,000 Nm
Length	1 μm–10 m
Velocity	1 mm/s–100 m/s
Acceleration	0.5–1000 g
Current	1 μA–85,000 A
Voltage	1 mV–4 kV
Electrical power	up to 20 MW
Effective power	up to 420 kW
Mass	0.005 g–3000 kg
Insulation resistance	50 kΩ–200 TΩ

based on the basic infrastructure and the measurement signals are in the accredited range (see Table 1), the accreditation is valid. Although accreditation is always the responsibility of the local governmental-linked organization, acceptance by the International Laboratory Accreditation Cooperation (ILAC) ensures that laboratory quality meets worldwide standards.

Using safety-related valves as an example, this paper examines a typical qualification process required to ensure the proper functioning of equipment in a new or modified nuclear power plant.

## 2 Qualification Concept—Using the Example of Safety-Related Valves

The purpose of the qualification is to demonstrate that the component fulfills its design function until the end of its scheduled operational time and in the event of accident conditions. Therefore, it is necessary to analyze the entire life cycle of the component and the related parts of the components that can fail. From this analysis, specific tests will be determined. In a typical nuclear power plant (NPP), about 200–400 valves are safety related with very different requirements. A sample structure for a test program to qualify safety-related valves is presented below.

### 2.1 Containment Environmental Effects and Aging

In the case of electrically operated valves, the functioning of the actuators has to be demonstrated. To consider the entire lifecycle, a set of tests are commonly

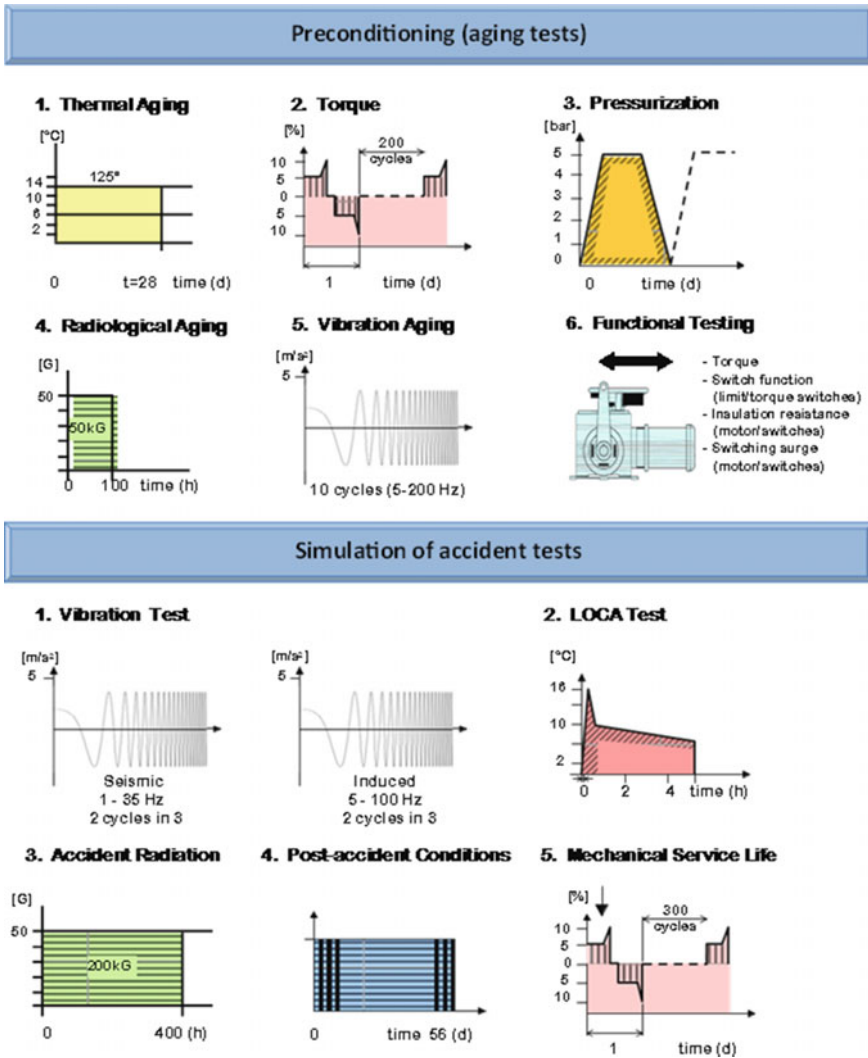


Fig. 1 Steps of an actuator qualification

performed (Fig. 1). These tests can be split into aging tests, accident condition tests, and post-accident tests. The aging test simulates component operation until the end of life. This test can include thermal, operational, pressurization, radiation, and vibration aging. These aging processes have to be reduced in time scale. Therefore, higher temperature rates and respectively higher dose rates are applied, which will have a similar effect as full-time operation at lower levels. In addition, open/close cycles and containment pressure tests are performed, using applied torque and vibration aging.

Following the aging part of the qualification program, accident conditions are applied. Typically, it is assumed that an earthquake has occurred, which may cause the accident directly or indirectly. Therefore, related vibration tests are performed, followed by a loss of coolant accident (LOCA) test, which represents the containment atmosphere following a break in the primary coolant system boundary. This typically involves sharp increases in pressure and temperature under high humidity and related water chemistry. For this purpose, testing setups as shown in Fig. 1 are necessary to control the appropriate ambient conditions. To avoid the installation of a radiation source in the containment atmosphere test vessel, the actuator is typically placed in a second test step in front of a radiation source to represent the assumed increased radiation during an accident. Depending on the requirements of the valve, it is often the case that the valve has to be activated in the post-LOCA phase. Therefore, it is a typical requirement that the actuator has to withstand a post-LOCA atmosphere, which can be realized in a test vessel similar to that used in the LOCA atmosphere tests, but at lower pressure and temperature levels. Finally, the actuator has to be capable of applying the defined torque and performing the intended safety function of the device.

## **2.2 Sealing Capability**

During the different test sequences of a valve, it is a common requirement to show that the valve fulfills one of the original requirements, which is sealing. For example, after the different aging steps (as described in Sect. 2.1) or after function tests, the valve is connected to test devices to check for leakage, as shown in Fig. 2 (left photo is the test device; middle sketch is the test setup; right photo shows the device connected to a test valve). Leak tightness testing consists of two applications: testing for tightness against water or against a gas. In the case of water-tightness, the device is first flooded via a relief valve on top of the device. This ensures that no air is remaining in the piping, which could affect the measurement. In the second step, the valve is closed and, via a pump, the pressure is increased up to the operational tightness measurement point. Mini flow rate devices will detect any flow past the valve. In a similar way, the gas tightness is tested—gas from a bottle (typically, nitrogen) is applied on the testing side.

## **2.3 End Loading—Seismic Qualification**

During the course of operation of the nuclear plant, the valve must be designed to survive various design basis earthquake events. The earthquake events can cause the valve to experience a variety of loads from movement of the valve relative to its mounting in the piping system and the motion of the valve actuator. The seismic test involves mounting the valve on a seismic shake table in a manner that simulates

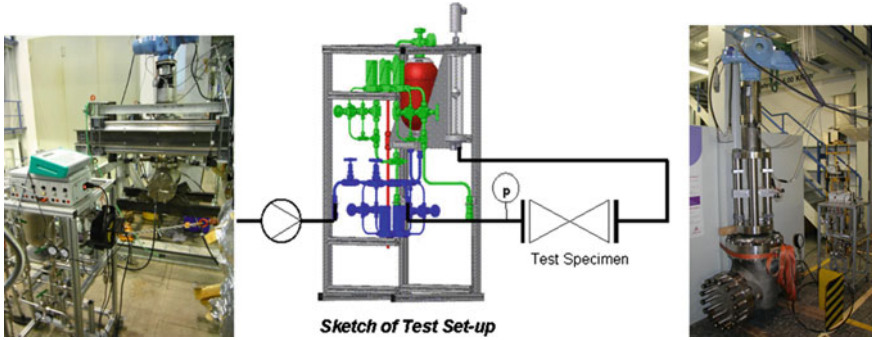


**Fig. 2** Leakage measurement device—(left photo: test device; middle sketch: test setup; right photo: device connected to test valve)

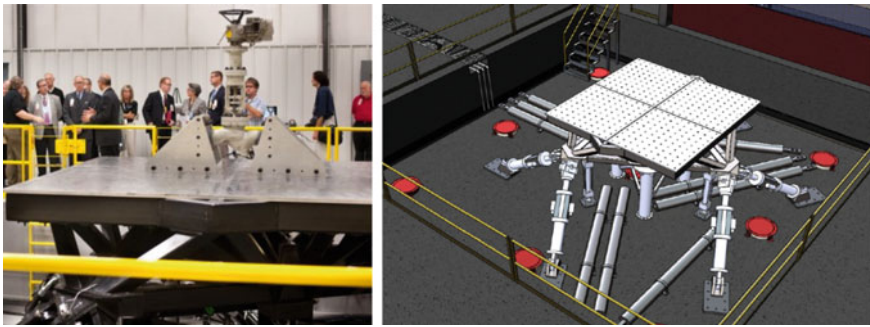


**Fig. 3** Left Shake table with a test valve; right sketch actuator arrangement of the shaker table

the installed condition. A series of tests will be used to replicate the motion that the valve will experience at a specific location within the nuclear plant. Five tests are performed to simulate the levels of an operational basis earthquake (OBE) followed by a test to simulate a safe shutdown earthquake (SSE) event. During the earthquake events, the valve is functionally tested to ensure that operation is not affected by the earthquake-induced motion. It is possible to perform the seismic test with the valve in various positions, open or closed, or in motion from one state to another. For pressure relief valves, the valve is tested with pressure applied to ensure that the motion does not result in release of the pressure. This testing provides evidence that the valve will continue to perform the intended safety function during and following an earthquake event. In Fig. 3 on the left is shown, how a valve can be fixed on a shaker table and on the right the arrangement of the actuators of a 6-dimensional shaker table. The multidimensional movement capability of the shake table allows adjusting the loads to the expected loads coming from the pipes or other support structures.

## 2.4 Functional Qualification

As the different types of valves have to ensure different functions, the types of tests to demonstrate the functioning have to be different as well. In addition, it is sometimes necessary (or reasonable) to perform different tests for one valve type to consider different aspects of the function. For example, for safety valves, one option is to test the opening and closing characteristics in one test campaign. Additional tests demonstrate the behavior under full flow conditions.

In any case, it is important to analyze the different possible operating modes of the valve and define test programs representing these operations. For this purpose, a setup of different test facilities is necessary. Typical functioning requirements and the related test facilities are described below.

### 2.4.1 Cycling

Cycling tests determine whether a valve closes and opens under operational conditions. AREVA operates two facilities to perform this type of testing; the main design concept is the same for both, but they have different maximal flow rates. Assuming operational velocities of 5 m/s, it is possible to use the KOPRA—APS loop for valve diameters of up to 150 mm. A sketch of this loop is shown in the left part of Fig. 7. The pressure in the loop can be adjusted with a pressurizer, and the fluid temperature is controlled via a cooler in the bypass over the pump. The loop is designed in such a way that valves of different diameters can be installed in parallel. During the tests, the valve will be opened and closed – typically up to 1000 times. An additional bypass around the pump ensures a continuous run during the cycling tests. For valves with diameters bigger than 150 mm, AREVA operates the KOPRA KVA loop. Figure 4 shows a photo and the isometry of the pipe layout of this loop.

### 2.4.2 High-Energy Pipe Rupture—Outflow

One function of valves in NPPs is to seal pipes in case of a pipe rupture. A typical valve for this application is the main steam isolation valves behind the steam generators. In the case of a pipe rupture of the main steam line, this type of valve closes to prevent a quick emptying of the steam generator. In this scenario, very high flow rates—up to the speed of sound—can occur. Figure 5 shows a sketch and a photo of the very large valve test platform known as GAP, which is capable of simulating this kind of scenario. For this purpose, the GAP has a big vessel, which acts as an accumulator. This accumulator is filled with saturated water (via a 22 MW boiler) at a pressure above the operational pressure of the test valve (indicated in Fig. 7 as a test specimen). Outflow is established by quickly opening the valves. When the testing flow conditions are reached, closing of the valve is



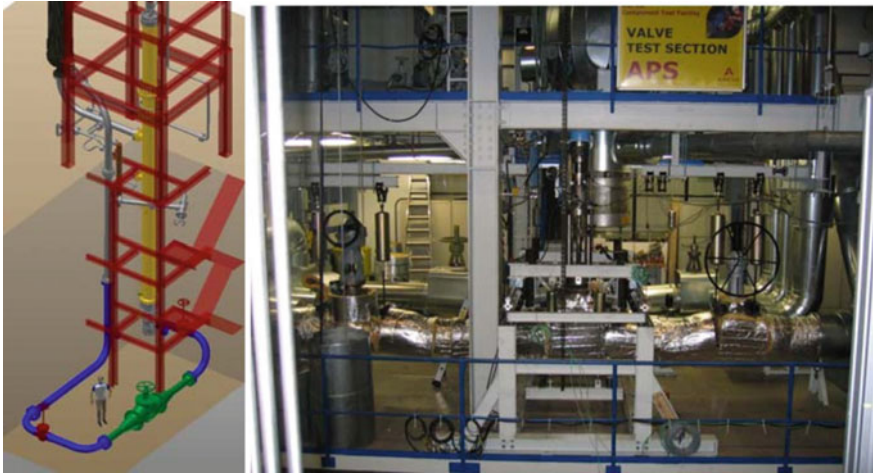


Fig. 4 Isometry and photo of the KOPRA KVA loop

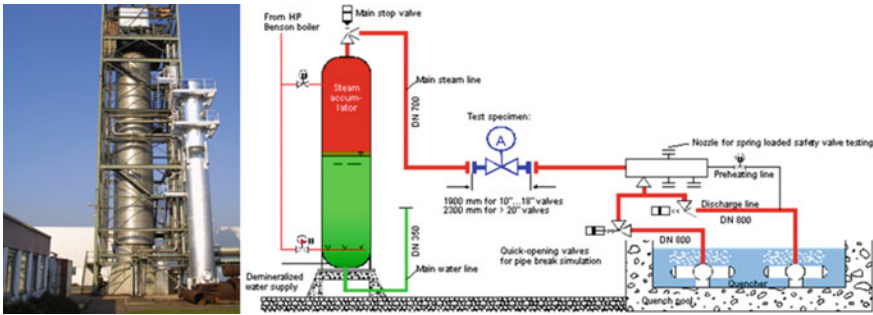


Fig. 5 Left Photo of the accumulator of the GAP; right Sketch of the GAP

initiated. The accumulator has an additional pipe at the bottom, which can be connected to the test specimen (green line in Fig. 5). In this case, water will go through the test specimen. Such an arrangement is also used to test main feed water insulation valves.

Figure 6 shows as an example of a test run with a water steam mixture flowing through the test object. The main objective was to demonstrate that the valve closes in the appropriated time. For this purpose steady-state flow conditions have been established while the valve is open. An indicator for the proper establishment of the flow condition is the almost constant flow conditions at about 8.5 s with a total mass flow above 4000 kg/s and a pressure above 75 bar. The closing time of the valve can be derived from the measurement of the mass flow rates, which reaches a value of 0 kg/s within less than 2 s.

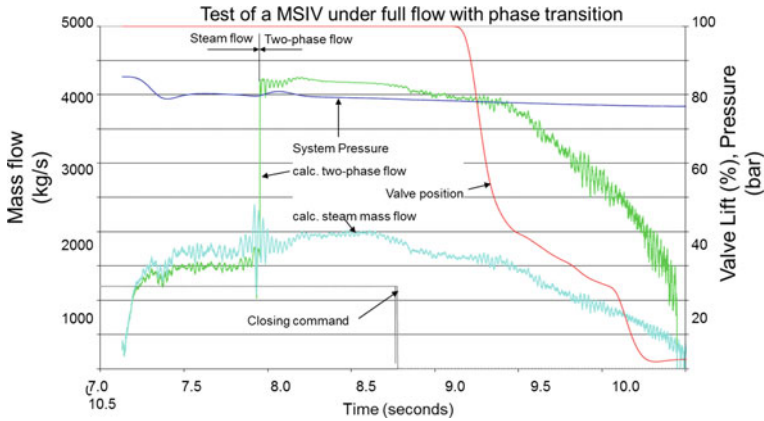


Fig. 6 Typical transient conditions during a flow interruption test

### 2.4.3 Set Pressures

For safety valves, especially the pressurizer safety valves or their pilot valves, it is important to test and/or adjust the set pressure and the closing pressure. The KOPRA APS can be used for this purpose. By limiting the lift of the valve, lower flow rates can be achieved, with the consequence that smaller sized vessels, compared to the GAP, can be used. Another benefit is that the energy consumption is also significantly lower than that for the GAP.

The safety valve test section is shown on the right in Fig. 7. It consists mainly of two pressurizers connected via a valve to the test valves, which can be pilot valves or direct safety valves. The KOPRA is designed in such a way that it can be used for newly designed/manufactured valves as well as for valves that have been in service in an NPP. Thus, the steam going through the silencer can be sent in a condensation chamber that is closed and can accumulate a certain level of contamination. This leads to an application suitable for outage optimization. In this particular case, the one set of valves is adjusted prior to the outage in the test facility to replace the current set in the plant. By this measure, one gets the valves already adjusted for operating condition without affecting the outage’s critical path.

Figure 8 shows a typical transient flow diagram of a set pressure test. The lift has been limited to 2.2 mm, as it is not important to demonstrate the full flow capability, which could be tested, for example, with the GAP or another similar loop for higher pressures. In this case pilot valves have been tested. Therefore, the pressure before the valve as well as the pressure in the control volume for opening the main valve is of relevance. Both values are shown in Fig. 8. The opening and closing time can be derived from the plot of the lift and the opening and closing pressure.

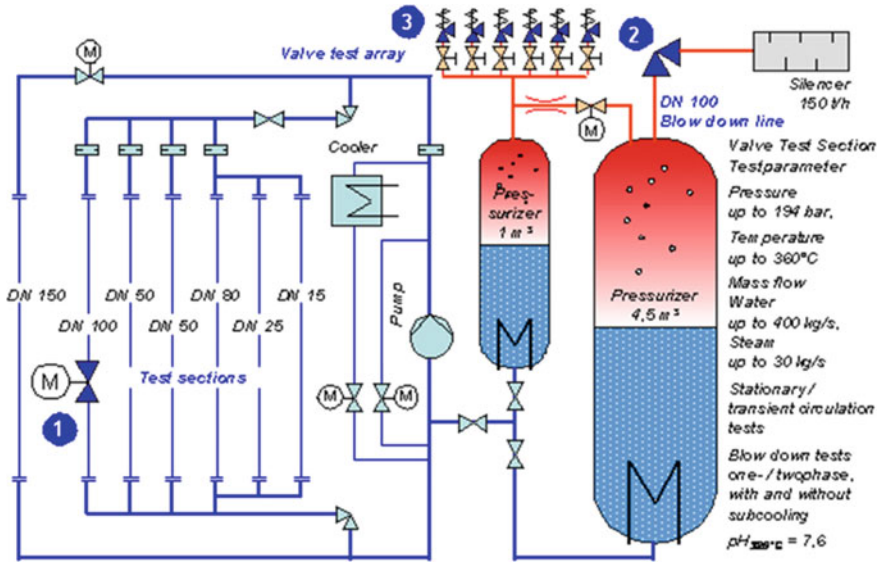


Fig. 7 Sketch of the KOPRA APS (Cycling section is on the left and safety valve adjustment is on the right)

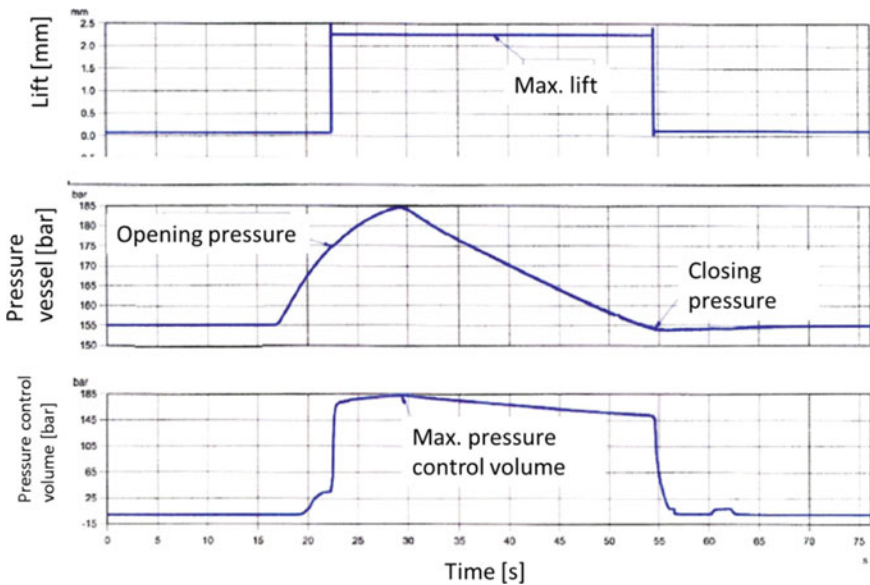
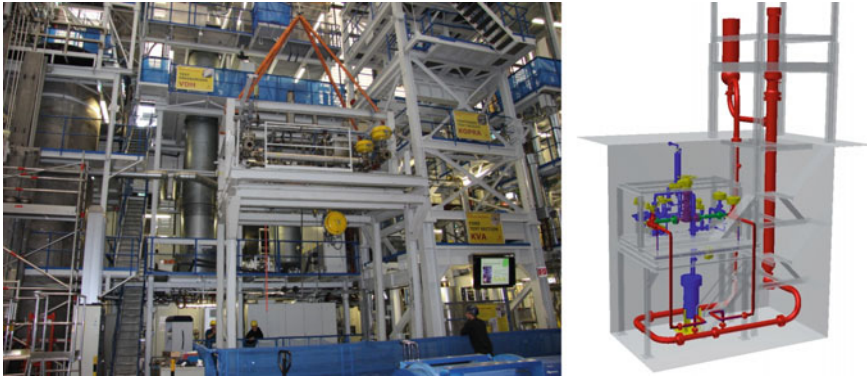


Fig. 8 Pressure transient during set-pressure tests



**Fig. 9** *Left* Photointegration of a connection unit between a cold and hot loop with the test specimen; *right* piping scheme of the connection unit between the cold and hot loop

#### 2.4.4 Thermal Shock

Thermal transients can occur in NPP, such as during transients, when water has been cooled down in the part of a piping system that was switched off. When this switched off part is reconnected to the system, the water can be pulled out by hot water. This can lead to a quick change of the inner surface of the affected valve, causing deformation due to restrained thermal expansion. Testing such valves requires a loop with both cold- and hot water loop. The valve has to be installed between the two loops. In Fig. 8 on the left is shown, how such an additional test structure has been moved between a cold and hot supply loop. As shown in the pipe layout scheme in Fig. 9 on the right this additional structure has been moved into a pit—to ensure in the case of an opening of a flange during a thermal transient, that no persons will be hurt. The flow through the test valve is feed either from the hot or cold loop. Specific safety aspects must be considered, because not only the valve itself will be shocked, but also parts of the connecting loop. Because temperatures can rise as high as 220 K, the design of the valve and connecting loops must ensure that no cracks can occur. As shown flow in scheme in Fig. 10 consists the loop in additional a capture vessel, which collects the thermal plug going through the test specimen, to avoid, that the loop itself will reach a temperature in between the two.

#### 2.4.5 Particle-Loaded Fluids

It is a common design requirement for NPP that, in the case of a LOCA, water be sucked from the sump through sieves back into the core to ensure cooling. The entire chain of components in the related piping system must be properly qualified. This can require—in addition to the above-mentioned tests (thermal shock and cycling)—tests that consider whether the valve will properly close even if the water contains a certain amount of debris. Therefore, a loop like the one shown in Fig. 11

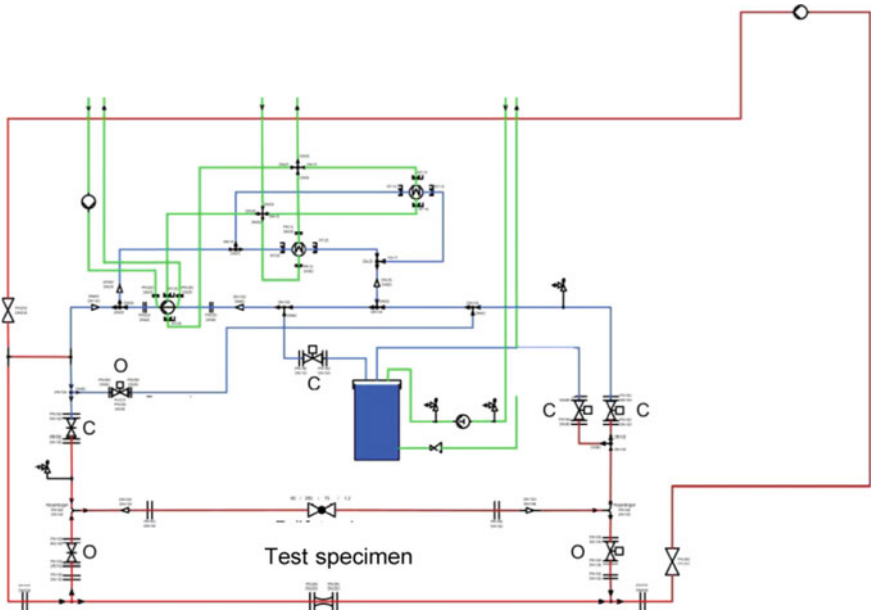
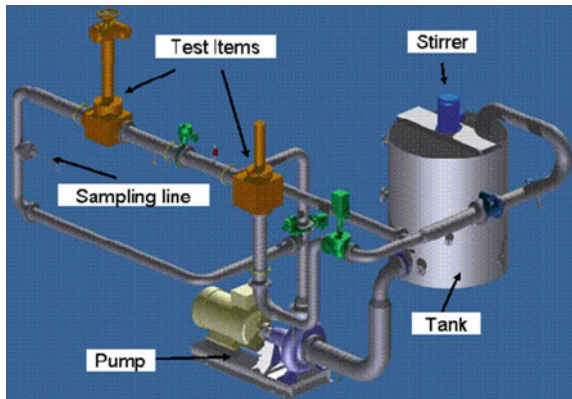


**Fig. 10** Setup of the sketch of a thermal shock loop—blue lines indicate the cold loop; red lines indicate the hot loop

**Fig. 11** Valve test section for particle-loaded water



must be used. Such a loop contains a vessel where the debris has to be prepared. Special attention is required to ensure that the concentration remains within specification inside the loop and during its operation. If the test goal is to check that the proper closing of different valves in the loop do not influence each other, it is possible to install a series of valves in one test, as long as they follow the same test specification.

### 3 Conclusions

To qualify safety-related components, it is important to understand their operation throughout the entire life cycle of the components, including different applied loads, which may cause failures. This understanding is the basis for analyzing the reliability of the components, whether they are new components or existing components being used in a new application. In many cases, engineering analysis alone is not adequate to qualify the components. Sometimes, it is necessary to perform adequate tests in a qualification program. A qualification program requires the appropriate testing infrastructure and a qualified testing team. Accreditation of the program by a recognized test/inspection organization is a very good indicator of the program's ability to fulfill essential requirements in a variety of applications to ensure the performance of safety-related nuclear qualification tests.

### References

1. Ganzmann I., W. Herr, H. Schmidt, W. Stecher, D. Walter, K. Umminger, A. Beisiegel, M. Wich, P. Dolleans, T. Muller; AREVA's Thermo-Hydraulic Platform qualified as test and inspection body VGB Power Tech (2011).
2. IEEE Standard 323, Standard for Qualifying Class 1E Equipment for Nuclear Generating Stations.
3. IEEE Standard 344, Recommended Practices for Seismic Qualification of Class 1E Equipment for Nuclear Generating Stations.
4. ASME NQA-1, Quality Assurance Requirements for Nuclear Facility Applications.

# How to Build EQ System for Safety Classed Electrical Equipment Under the Modal of AE

Shiquan Zhan

**Abstract** Qualification of nuclear safety electrical equipment is an important part of ensuring the safety of nuclear power. This paper begins with the description of equipment qualification on the basis of practical experience and its evaluation, it analyzes the existing problems in nation's current equipment qualification work while researching the experience of the United States, France and Japan and other countries, to identify common features used in equipment qualification systems in these countries. Combining the status of Chinese nuclear power under EPC mode, the paper puts forward the basic idea of how to construct equipment qualification system.

**Keywords** Nuclear safety electrical equipment · Qualification · Equipment classification · Prototype

## 1 Introduction

As China actively implements its nuclear power and related nuclear power technology localization strategy, nuclear safety will be raised to a very important position and equipment qualification is a crucial step in ensuring nuclear power plants' safety and their stable operation. Meanwhile, the domestic nuclear power plant construction pattern has undergone tremendous change, it transforms from the previous owner + institute model to EPC mode. In order to ensure the safe operation of nuclear power plants, it is imperative to develop suitable methods for the current mode of nuclear safety electrical equipment qualification.

---

S. Zhan (✉)

Testing Center of China Nuclear Power Engineering Co., Ltd., Beijing, China  
e-mail: zhansqa@cnpe.cc

S. Zhan

No. 117 of Xisanhuan Road, Haidian District, Beijing, China

© Springer Science+Business Media Singapore 2017

H. Jiang (ed.), *Proceedings of The 20th Pacific Basin Nuclear Conference*,

DOI 10.1007/978-981-10-2317-0\_34

This paper analyzes the current national equipment qualification system and any existing problems, combining the practical experience and understanding of our lab, the paper explores the issues in constructing qualification system, its executing standards and required technology.

## **2 Introduction of Nuclear Power Electrical Equipment Qualification**

### ***2.1 General Methods and Purpose***

Generally, methods of analyzing, testing, or both in combination are used to ensure the nuclear safety equipment and any safety-related equipment in both normal and abnormal operating conditions still maintain security features as specified in the design; also maintain functional design needs under accident conditions and seismic conditions (or after).

The purpose of conducting qualification for nuclear safety equipment is to prove that the equipment in their lifetime (e.g., 60 years) can reliably operate and perform its safety function under a variety of expected operating conditions and unexpected accident conditions.

Nuclear Safety Regulations specifies that only equipment passed equipment qualification are allowed to use in nuclear power plants.

### ***2.2 The Process of Qualification***

Generally include the following steps:

1. First, analyze the safety functions of Nuclear Power Plants' main system, categorizing equipment into different safety ratings according to its actual safety function. Make a list identifying all equipment required to undergo qualification in accordance with its safety rating.
2. Then select particular devices from a large number of devices of similar structure as a representative prototype. Selection criteria can be based on types, load capacity, and size difference. Devices should be chosen as one from each different manufacturers or one device of each different types; for different load capacity and dimensions, selection should be made based on the conservative requirement of qualification, and device with the most demanding qualification requirements should be selected.
3. Make qualification programs to conduct qualification tests of selected prototypes.
4. Evaluate qualification test results.



Since the nuclear safety equipment qualification method is carried out according to equipment grading, how to identify the equipment needed to carry out an accurate classification is the basis for a reasonable qualification of the quality of equipment. Below is a brief introduction of nuclear safety electrical equipment classification according to RCC-E standards.

### ***2.3 Classification of Equipment***

According to RCC-E specification, any nuclear safety-related electrical equipment are all 1E grade, 1E grade electrical equipment are categorized into the following three types:

Type K1: Install on the inside of the containment, should maintain its safety function under normal working condition, under accident condition and seismic loading condition.

Type K2: Install on the inside of the containment, should maintain its safety function under normal working condition and under seismic loading condition.

Type K3: Install on the outside of the containment, should maintain its safety function under normal working condition and under seismic loading condition.

Basis for classification of electronic equipment is its installation position and specific safety function, such as type K1 and K2 equipment are installed inside the containment, and will perform safety functions under accident conditions; while type K3 equipment are installed on the outside of the containment, it runs only under normal operating conditions and seismic loading conditions.

## **3 Analysis of Domestic Status Quo**

With the acceleration of Chinese localization of nuclear power equipment, it also exposes many problems in the existing system of nuclear safety electrical equipment qualification, not only institutional issues, also issues in the area of relevant standards and technology.

At present, domestic equipment qualification are controlled by the equipment manufacturer who is responsible for equipment development and the preparation of qualification standards and documents, and then entrust the qualification to the United Association of Chinese machinery, China Nuclear Energy Association, and other units of local to convene industry experts to conduct professional qualifications on the selected prototypes.

The main problem of this approach can be summarized in the following.

### ***3.1 Qualification System Is Inadequate, Leading to Unregulated Equipment Qualification that Lacks Authority***

In current practice, there is a need to prepare factory equipment qualification syllabus. Since factory qualifications lack technology consistency, there should be different standards of syllabus put in place in line with the conditions of its equipment use and required function. If the syllabus cannot satisfy the specific practical need of a nuclear power plant, it will impact on the effect of qualification conducted and will result in unnecessary waste of society resources.

Current national laboratory resources for qualifications are relatively scattered, some qualification equipment lack the required capability to satisfy an adequate qualification, there is some level of difficulty to rely on manufacturers to find the suitable laboratory. Sometimes the test is done, but not recognized by the industry.

In addition, after prototype equipment pass qualification, problems may occur during its mass production process, the variances between single piece production and mass production should be resolved.

All of the above problems occur as result of inadequate equipment qualification system, caused by unclear responsibility and unstandardized methods.

### ***3.2 The United States and France Uses Two Parallel Sets of Standards, Resulting in the Same Device Performing Under Inconsistent Accreditation Standards, Making It Difficult to Judge in Nuclear Power Plant Equipment Purchasing***

Generally used domestic standard are the French standard and the American standard. When equipment manufacturers doing equipment development, it often uses an approach of “covering both standards” to save costs. As such, some manufacturers blindly adopt higher parameters to increase the difficulty of development; while some manufacturers adopt a standard that can be found and conducted by domestic testing devices. Even if the equipment is of the same type, different manufacturing factories adopt different qualification criteria and methods, and all “prototype equipment” passes experts’ qualifications.

Regardless of the accuracy, both practices have brought a great deal of difficulty to the nuclear power plant in equipment purchasing.

### ***3.3 Standards for Qualification Testing Device Construction Is not High and Some Departments Can Only Partially Meet the Requirements of Qualification Standards***

Some existing domestic testing stands were built during the second phase of the Qinshan nuclear power engineering, subject to domestic technology limitation, these testing stands lack the ability to meet the demand of nuclear power plants with new reactor, mainly reflected in radiation testing, vibration and seismic testing stands, and so on.

In addition, the mechanical properties of the main stand was built in the equipment manufacturing factory, its testing capabilities are not the same.

### ***3.4 Lack of Professional Technical Team and Lack of Understanding of Test Methods Impacts the Result of Equipment Qualification to Be Scientific and Authoritative***

The basis for equipment qualification is to be familiar with the safety function of infrastructures in nuclear power plants, as well as their installation requirements and storage conditions, normal operating conditions, abnormal conditions and accidental conditions through tests to verify whether the device is able to perform its functions.

However, most testing personnel in domestic testing institutions are part-time, or transferred from other fields, lacks familiarity and knowledge of nuclear power plants. In addition, in the education of nuclear power, there is no equivalent professional course for the field, which resulted in the lack of comprehensive knowledge of equipment qualification by testing personnel, some even lack of relevant practical work experience.

Some technicians of equipment manufacturers are not familiar with the field of nuclear power, thus it is very difficult for them to write an outline of nuclear power plants to meet the specific needs of a particular nuclear power plant.

Therefore, the lack of knowledge of the technical team affects the scientific basis of an equipment qualification and its authority.

## **4 Qualification System and Experience in Foreign Countries**

### ***4.1 The Case Study in the United States***

#### **1. System, responsibility and recognition**

U.S. Nuclear Regulatory Commission (NRC) proceeds review on nuclear safety, to issue an operation permit to electrical power company (or AE) and require the electrical power company (or AE) to ensure that the safety grade equipment used by the nuclear power plant has been identified, or to be identified.

Specific qualification work can be done by the equipment manufacturer or third party qualification agencies (such as the WYLE laboratory).

#### **2. Regulations and standards system**

Since February 1974, the United States Nuclear Power Engineering Committee (NPEC) issued a nuclear power plant 1E class equipment qualification standard IEEE323 revision, the Nuclear Regulatory Commission also continuously released a guide RG1.089 specific safety critical electrical equipment environment qualification, NUREG-0588, federal regulations 10CFR-PART50.49, and other types of equipment qualification standards.

#### **3. Laboratory construction**

In the United States, the nuclear grade equipment qualification laboratory is divided into two levels, namely the equipment manufacturing plant laboratory and laboratory of professional equipment qualification company.

In the United States there are a number of professional qualification companies engaged in equipment qualification, they have a high level of technology, experienced, engaged in design consulting, equipment in service inspection and fault diagnosis, and other engineering services. Such as WYLE laboratory, it can complete the full equipment qualification of IEEE323, IEEE344 and IEEE382, and other provisions of.

### ***4.2 The Case Study in France***

#### **1. System, responsibility, and recognition**

For EDF, under the administration of French Government Energy Administration, as the owner exclusive, ARENVE serves as the general contractor.

In terms of nuclear security, EDF is responsible for the government.

In terms of equipment qualification, AREVA is responsible for EDF.

## 2. Regulations and standards system

In terms of nuclear safety grade equipment qualification, RCC-E provides K1, K2, and K3 type qualification procedures.

In addition to RCC-E, France also use the general industrial standard NF, UTE. The IEEE or ANSI standard is used for the non-covered parts of RCC-E and French industrial standard.

## 3. Laboratory construction

Mainstream qualification laboratory in France is the National Laboratory, in addition there are several laboratories belonging to the manufacturing plant, with a smaller scale.

The National Laboratory, part of them belongs to Atomic Energy Commission (CEA), the rest part of them belongs to EDF. The qualification test system is made up of these laboratories in France.

# 4.3 *The Case Study in Japan*

## 1. System, responsibility and recognition

Electric power company to take all nuclear power plants nuclear security responsibility, Ministry of international trade and industry (MITI) reviews the nuclear safety applications and issue the license, Nuclear power plant license will be issued by the Prime Minister.

### Contractor

The Contractor shall be responsible for the electric power company in accordance with the contract, such as the general contractor of the pressurized water reactor is Mitsubishi Co., Mitsubishi Co has a manufacturing plant and a research institute, with the equipment to improve the function of the test bench, environmental testing, and seismic test bed.

Mitsubishi's equipment subcontractor is responsible for MITSUBISHI, they all have test bed.

In the equipment qualification test, the power companies and the general contractor proceeds scene observation and guidance, but the responsibility is not transferred.

The validity of the test results will be recognized as following, subcontractor is recognized by the general contractor, the general contractor (including the Subcontractor is recognized by the general contractor) is recognized by the power company. Finally, the power company proceeds relevant security review, approval procedures from Ministry of international trade and industry (MITI).

## 2. Regulations and standards system

The design and construction of nuclear power plants are equivalent to the U.S. Standard, and the quality of its qualification of nuclear safety grade equipment is also according to the U.S. standards, such as IEEE323 and IEEE344.

## 3. Laboratory construction

Japanese equipment qualification laboratory is divided into two levels, one is the factory's laboratory, one is the National Laboratory, and Japan has no professional equipment qualification company.

## 4.4 *Summary*

From the cases research of the United States, France and Japan, we can found that the equipment qualification in the country in terms of the approach is not the same, according to their national conditions, they set up a sound system of qualification, regulations and standards, the establishment of a test facility. Their successful experiences can be summed up in the following aspects:

### 1. Specialized authority and a complete system of recognition.

Whether it is the United States, France or Japan, they have an authority responsible for the equipment qualification, have an organization to supervise and proceed level recognition. This constitutes a complete system of equipment qualification, to ensure the quality of the authority and objectivity of the qualification.

### 2. Right regulations and standards system

The first level of qualification standards issued by the nuclear safety supervision department, such as IEEE323, France's test methods, procedures, regulations and standards, they formed a complete qualification of the standard system. All qualification works have the laws and regulations to follow.

### 3. Strength of the laboratory

Whether it is a national laboratory, or laboratory of equipment manufacturer, it has played its due role in the qualification system.

## 5 **Qualification System Under the EPC Mode**

Under the EPC mode, the owner of the nuclear power plant is responsible for the safety of the nuclear power plant, the general contractor shall be responsible to the owner, and the subcontractor shall be responsible to the general contractor. Therefore, in the design of nuclear equipment qualification system, we should draw

lessons from the United States, France and Japan and other countries' experience, but also to combine the actual situation of our country.

Specific programs are as follows.

### ***5.1 Organization, Responsibility, and Recognition System Design***

General contractor for the construction of nuclear power plants is responsible for the equipment qualification, establish the professional qualification organization, namely "nuclear materials and equipment qualification center," in charge of equipment research and materials qualification technology research, establish a professional laboratory; draw up qualification test procedures, proceed qualification test, issue the qualification evaluation report according to the test results.

Qualification organization can have their own laboratory, or cooperate with other professional laboratories or listing.

Qualification organization will be recognized and supervised by State Nuclear Safety Bureau, the owner and the engineering company expert committee or "the Nuclear Grade Equipment Qualification and Accreditation Committee."

### ***5.2 Standard System***

1. The general standard of the first level: IEEE323 and RCC-E, or use national standard, etc.
2. The professional qualification standard of the second level: Using the United States IEEE standards or our national standards, Energy Bureau standard, approval by the nuclear power plant owners and the National Nuclear Safety Agency.
3. The qualification test procedure of the third level: issued by relevant qualification centers, and recognized by the engineering company expert committee, "the Nuclear Grade Equipment Qualification and Accreditation Committee" or the relevant professional accreditation.

### ***5.3 Supervision Mechanism of Qualification***

According to our national conditions and the actual situation of our companies, we should adopt the three levels of supervision mechanism.

1. Nuclear Safety Bureau's approval for the owner;
2. Nuclear power plant owners' approval for the engineering company;
3. Engineering company's approval for qualification organization.

#### **5.4 Laboratory Capacity Construction**

Due to the domestic laboratories distribution is scattered, some of the laboratories in the Universities, some in research institutions; some are located in the equipment manufacturing plants.

And each laboratory can only assume one or several qualification tests. According to this, laboratory can use the method of cooperation or listing, give listing license to one test in one laboratory. It has not only played the advantages of the domestic professional laboratories, but also avoided the repeated construction of the test equipment which caused great waste to the social resources.

### **6 Conclusion**

In the process of localization and localization of nuclear power technology in our country, there is a serious shortage of qualification of nuclear grade equipment, which will affect the safety of nuclear power in our country. Therefore, it is urgent to design and establish the quality evaluation system of nuclear grade equipment in our country.

Through the study found that the qualification system in the United States, France and Japan and other countries have following features: (1) specialized authority and a complete system of recognition; (2) right regulations and standards system; (3) strong laboratories.

Therefore, in view of the problems in our country's nuclear grade equipment qualification system, we should proceed from the following aspects of the construction of the nuclear grade electrical equipment quality qualification system under the mode of general contracting:

1. Organization, responsibility and recognition system design;
2. Standard system construction;
3. Construction of supervision mechanism for quality qualification;
4. Laboratory capacity construction.

And the state nuclear safety authorities, nuclear power plant owners and engineering companies must take the approval and supervision responsibilities to qualification organizations and professional laboratories.



## References

1. HAF 601 Administrative Regulations for Design, Manufacture, Installation of Civil Nuclear Safety Equipment
2. GB/T 12727-2002 Nuclear power plants-Electrical Equipment of safety system-Qualification
3. RCC-E (Version of 1993.1) Design and Construction Rules for Electrical Equipment of PWR Nuclear Islands
4. IEEE 323-2003 IEEE Standard for Qualifying Class 1E Equipment for Nuclear Power Generating Stations

# Modal Analysis of Anchored Cylindrical Liquid Storage Tanks

Zimin Zhan

**Abstract** The eigenfrequencies of anchored cylindrical liquid storage tanks are investigated with different methods in this paper. Several liquid storage tanks are modeled using finite element software ANSYS. Three methods are applied to analysis the natural frequencies of these liquid storage tanks: formula method, added-mass method, and fluid-solid coupling method. The results show great consistencies. Formula method provides the most conservative result in the three; added-mass method is the most widely used and easy to setup; and fluid-solid coupling method provides better accuracy. Mode shapes of the tank-liquid coupling system can be divided in three types: Liquid sloshing, beam vibration, and circle wave. The influence of liquid volume to frequencies is also analyzed. Results from this investigation could be used for evaluation of anti-seismic performance of anchored cylindrical liquid storage tanks.

**Keywords** Liquid storage tanks · Modal analysis · Added-mass · Fluid-solid coupling

## 1 Introduction

Seismic response of anchored storage tank for liquid has long been of interest to structural engineers. Early research was mainly focused on experiment studies [1]. In 1960s, Housner developed a simplified mechanical analog model for analytic calculation, which was further improved in Haroun-Housner model. In 1970s finite element method was employed in the computation of response, which greatly improved the accuracy of result. However, in most research, only lateral motion of the tank is considered that limited their applicability [2, 3].

The aim of present study is to compare nonlinear time integration method for calculation of seismic response of filled anchored storage tank with analytical

---

Z. Zhan (✉)  
China Nuclear Power Engineering Co. Ltd., Beijing, China  
e-mail: zhanzm@cnpe.cc

formula and added-mass method. Three anchored cylindrical liquid storage tank models of different sizes were studied for comparison. And both lateral and vertical motions are taken into account.

## 2 Physical Modeling

Three groups of sizing parameters of tanks are listed in Table 1. Finite element models are built using ANSYS. Illustration of the models is shown in Fig. 1. Material of tank is Q235 steel. Its properties are listed in Table 2. Physical properties of liquid filled in tank are assumed to be the same as water.

## 3 Modal Analysis of Coupled System

Three approaches are used for calculation of eigenmodes of the tank-liquid coupling system: analytical equations, mass-added FEM, and FSI FEM.

Three types of mode shape are of main interest, the longitudinal vibration mode, liquid sloshing mode, and the radial vibration mode as shown in Figs. 2, 3 and 4.

Mode shapes of large storage tanks are mainly radial modes with dense distributed eigenfrequencies. Sloshing of liquid weakly affects frequencies of coupled system; the denser the density the lower the coupled frequency, but the mode shape remains the same.

The longitudinal vibration modes dominate the dynamics response of tank under seismic load. The liquid sloshing modes and radial modes are difficult to be excited, thus are less important. Only frequencies of longitudinal modes are calculated in this paper.

**Table 1** Sizing parameters of three tank models

Model name	Volume of tank V (m <sup>3</sup> )	Radius R (m)	Tank height H (m)	Wall thickness T (mm)
T1	1000	6	9.52	5
T2	2000	7.25	12.69	7
T3	10,000	14.25	15.85	16
Model name	Floor thickness <i>t</i> (mm)	Height of liquid <i>h</i> (m)	Mass of tank M (ton)	Volume of liquid V <sub>1</sub> (m <sup>3</sup> )
T1	5	8.42	18.52	951
T2	6	11.49	39.54	1896
T3	8	14.65	218.31	9335

**Fig. 1** Illustration of tank model

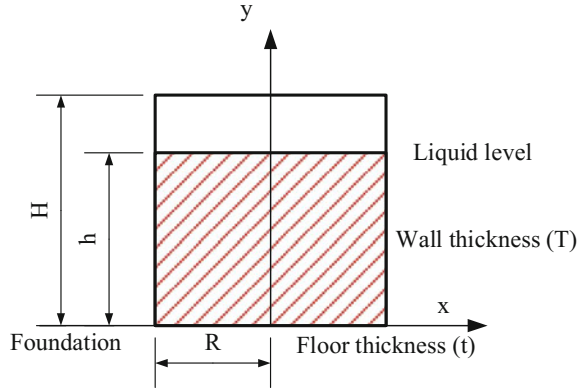
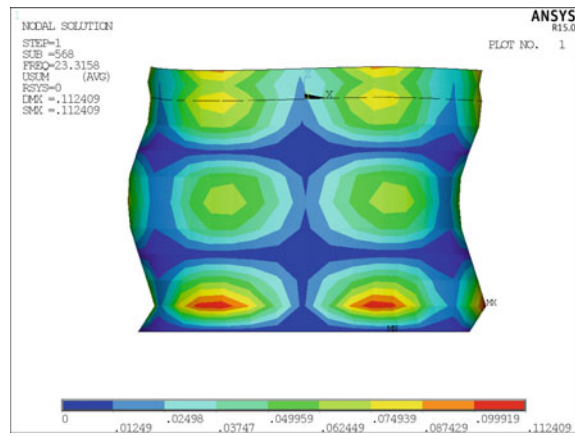


**Table 2** Material properties of Q235

Material	Density (kg/m <sup>3</sup> )	Young's module E (GPa)	Poisson ratio	Yield stress (MPa)	Tensile strength (MPa)
Q235	7850	210	0.3	235	360

**Fig. 2** Longitudinal vibration mode



### 3.1 Analytical Formula Method

For circular tanks, first frequencies of tank could be calculated using variational principles by following Equation [1].

$$f_m = \frac{1}{2\pi} \sqrt{\frac{ET}{\rho_1 R^3} \left( \alpha_m \frac{R}{h} \right) \frac{I_1 \left( \alpha_m \frac{R}{h} \right)}{I_0 \left( \alpha_m \frac{R}{h} \right)}}$$

Fig. 3 Liquid sloshing mode

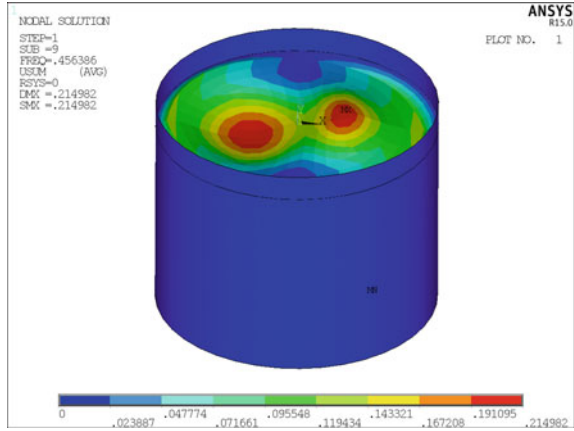


Fig. 4 Radial vibration mode

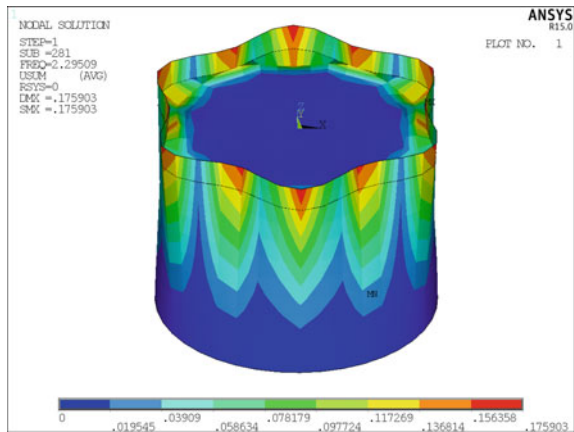


Table 3 Frequencies calculated by equation in Hz

Order	T1	T2	T3
1st	8.193	6.551	5.205
2nd	18.562	15.322	10.909
3rd	24.982	20.787	14.472

Where  $f_m$  is the  $m$ th frequency (Hz),  $I_0$  and  $I_1$  are Bessel functions of zero order and first order.  $E$  is the Young's module,  $T$  is wall thickness of tank.  $\rho_1$  is density of liquid,  $R$  is radius of tank,  $h$  is height of liquid,  $\alpha_m = (m - 1/2)\pi$ . The results of first three modes are listed in Table 3.

**Table 4** FEM models used in mass-added simulation

Model	Element size	Number of elements	Number of nodes	Mass
T1	300	7435	7500	969.5
T2	400	6671	6732	1935.5
T3	600	9207	9284	9553.3

**Table 5** Frequencies calculated by mass-added method in Hz

Order	T1	T2	T3
1st	7.65	6.03	5.09
2nd	17.01	13.47	11.71
3rd	23.13	18.22	15.37

### 3.2 Mass-Added Method

The mass-added method models liquid as the mass elements attached on tank walls. The tank walls are modeled with ANSYS SHELL181 elements. Number of nodes and elements of different models are listed in Table 4.

Reduced methods are used for modal analysis, which couples DOFs of each layer to a center point and retains only a lateral and a vertical DOF to extract only longitudinal modes. The first three eigenfrequencies are calculated and listed in Table 5.

### 3.3 Fluid-Solid Coupling Method

For fluid-solid coupling method, tank walls are modeled with ANSYS SHELL63 elements, and liquid with FLUID80 elements. Reduced methods are applied for modal analysis. DOF of z-direction on fluid surface and radial direction DOF on the interface of fluid and solid are taken as master DOFs while remaining is taken as slave DOFs. The results are listed in Table 6.

For comparison, the frequencies calculated by three methods are presented in Table 7. All three methods give consistent frequency values.

In summary, all three methods are capable for eigenfrequency calculation. Analytical formula are able to deal with tanks of simple geometry. When tank shape becomes more complex, only mass-added method and fluid-solid coupling method are feasible. The mass-added method is easy to apply and faster than the fluid-solid coupling method, but the later one gives more accurate results.

**Table 6** Frequencies calculated by Fluid-Solid coupling method in Hz

Order	T1	T2	T3
1st	7.18	5.15	3.50
2nd	17.35	14.91	9.81
3rd	23.32	19.53	11.98

**Table 7** Frequencies calculated by different methods

Model	Modal order	Results from equation	Results from mass-added method	Results from fluid-solid coupling method	Values taken form [2]	Values taken form [3]
T1	1st	8.19	7.65	7.18	7.03	7.34
	2nd	18.56	17.01	17.35	17.22	17.39
	3rd	24.98	23.13	23.32	22.35	21.47
T2	1st	6.55	6.03	5.15	5.11	5.25
	2nd	15.32	13.47	14.91	13.95	13.43
	3rd	20.79	18.22	19.53	18.43	18.10
T3	1st	5.21	5.09	3.50	4.71	3.36
	2nd	10.91	11.71	9.81	10.80	10.19
	3rd	14.47	15.37	11.98	13.67	11.99

## 4 Conclusion

For tanks with simple geometry, analytical formula, mass-added method and fluid-solid coupling method could give similar result. When tank shape becomes more complex, only numerical methods are feasible. The mass-added method is easy to apply and faster than the fluid-solid coupling method, but the later one provides more accurate results.

## References

1. G Chen, R Xing. History of storage tank anti-seismic research, Science & Technology Information, 2009, Vol. 33: 812–814
2. D Pan, M Deng. Modal analysis of storage tank using ANSYS. Western prospecting engineering, 2008, Vol. 5: 52–54
3. C Song, L Jiang. Modal analysis of anchored open containers. Low temperature architectural techniques, 2011, Vol. 8: 74–75

# Quality Control of Application Research on Supervision Planning of Hualong #1 Emergency Diesel Generator

Junxiao Li and Wenxi Ge

**Abstract** In this paper, the selection of witness points in quality plan, key points in equipment supervision as well as supervision risks have been investigated through the supervision planning of EDG used in Hualong #1 nuclear unit, the third generation with proprietary intellectual property right of China, adhering to the principles of ‘Key supervision for key equipment’ and ‘Enhanced control on weak points’. The aim of this work is to enhance the efficiency and improve the quality control in supervision. And this paper can be used as a beneficial reference for the improvement of supervision efficiency and quality management of NPS.

**Keywords** Hualong #1 · Nuclear power station (NPS) · Emergency Diesel Generator (EDG) · Structural characteristics · Equipment supervision · Key and difficult points in equipment supervision · Quality plan · Supervision risk

## 1 Introduction

The Purchase Department has paid high intention to equipment supervision, and has established a specialized branch—Equipment Supervision Branch, which is dedicated to the quality control of equipment manufacturing process, since the establishment of China Nuclear Power Engineering Co., Ltd (CNPE). Over the past ten years, under the great support of leaders from various levels, the Equipment Supervision Branch has undergone a series of bold explorations and continual improvements, also accumulated a vast amount of experience in equipment supervision, on the basis of careful and sound supervision practice, as well as adhering to the nuclear spirit of “A career is above everything, the responsibility is more important than everything, strict fine into everything, and enterprising make

---

J. Li (✉) · W. Ge  
China Nuclear Power Engineering Co., Ltd (CNPE), Beijing, China  
e-mail: cnpe-lijx@163.com

W. Ge  
e-mail: gewx-cnpe@163.com



everything”, and in accordance with the QA requirements of “Everything has its rules, everything has its evidences, everything is due to responsibility and everything is due to supervision”. Meanwhile, with the accumulation of supervision practices in former projects, a great amount of supervision experience has been feedback to the latter projects, which provides valuable data and information for carrying out risk analysis in equipment supervision. Thus, a positive circle has been formed through accumulated supervision experience. As a result, the effectiveness of equipment supervision and management level has been continually improved and enhanced.

The analyses and descriptions of supervision planning for EDG at Hualong #1 are given below.

## **2 Planning of Equipment Supervision**

The EDG is classified as Supervision Grade 1 (JZ1) according to the ‘Equipment Supervision Program’ and ‘List of Equipment Supervision Grading’. The contract, references, scope of supervision, staffing, selection of witness points, analysis of key and difficult points in supervision, analysis of supervision risks and supervision planning are given below.

### **2.1 Contract [1]**

The Procurement Contract for EDG was signed on December 30, 2013. The Contract covers five EDGs, one of them is used for nationalization, and the rest is for Units 5&6, two for each unit.

### **2.2 References**

HAF003 Code on the Safety of Nuclear Power Plant Quality Assurance  
HAD003.03 Quality Assurance in the Procurement of Items and Services for Nuclear Power Plants  
CP03G9001 Technical Specification of EDG  
RCC-E 2005 PWR Nuclear Power Plant Electrical Equipment Design and Supervision rules  
RCC-M 2002+2002 Supplements PWR Nuclear Power Plant Electrical Equipment Design and Supervision Rules  
ISO 9001 Quality Management System  
FQZ210AR025CPMB06CT Procurement Contract on Fuqing Nuclear Power Station Units 5&6 for EDG and Auxiliary Power Source

### **2.3 Main Parameters of EDG [2]**

Diesel Engine Model: 12PC2-6B, Four Stroke, V type, Turbo changer  
Rotation 600 rpm  
Power 8640 kW  
Rated voltage 6.6 kV  
Rate frequency 50 Hz  
Noise  $\leq 113$  dB  
Nuclear safety 1E  
QA grade QA1

### **2.4 Composition of Diesel Engine**

Diesel Engine, the core of EDG, is a set of highly complicated integrated, modularized equipment. It is composed mainly of diesel engine, generator, connecting units and common base supports, and the medium-voltage emergency AC power is composed of EDG, auxiliary system of diesel engine, generator excitation and protection system, instrument and control system, medium-voltage connection terminal box/cabinet, including such auxiliary equipment as neutral wiring box/cabinet and phase box/cabinet, and traveling automatic synchronizer.

## **3 Supervision Scope and Work**

In accordance with the requirements of technical specification, the EDG shall undergo qualification test, which is to be followed by the supervision personnel. The subsequent work shall not proceed without the approval of the qualification test report.

### **3.1 Prerequisites Check**

#### **3.1.1 Design Document**

Check the list of design document which includes working drawings, technical specification, and technical conditions, and prepared by the equipment supplier, for the sorts, quantity and revision of design documents.

The equipment supplier shall submit the list of design documents for the design performed by the supplier; check if the documents are approved.

Checking if issues related to design liaison, design review meeting minute and technical drawings are solved.

Check if CR/TA is answered and if DEN is complete.

Check if design interfaces are closed.

Check if corrective actions initiated by NNSA are closed.

### **3.1.2 Process Documents**

Check if various process documents (weld data package, process qualification, bent pipe process qualification, expansion connecting process qualification) are approved, and if anything missing from the list of weld process qualification.

Check if manufacturing process rules meet the inspection requirements.

Check if manufacturing process rules meet the manufacturing requirements.

Check for the preparation, reviews, approval, and revisions of the above documents. Check if the process documents or process card are issued to workshop.

### **3.1.3 Quality Plan**

Check for the preparation, review, approval, and revision of quality plan.

### **3.1.4 Others**

Check if preparation and modification of Index of Engineering Documents (IED) conforms to the requirements of work commencement.

Check if the project quality assurance program (PQAP) is approved by CNPE. Check for completeness of the PQAP and the list of procedures. Check if the supplier organization chart and its duties and responsibilities are in conformity with the PQAP. Check if the PQAP is submitted to CNPE for filing.

Check if the CAR, OBN or corrective actions issued by CNPE, Owner or NNSA are closed or acceptable, to prevent adverse effect on work commencement.

## ***3.2 Receiving Acceptance of Main External Purchased Parts and Raw Material***

Receiving acceptance and reinspection of raw material, external purchased parts used as structural materials and parts of diesel engine is needed. First, check the quality certificate of material and parts and require the supplier to strictly carry out the receiving acceptance; Second, the supplier is required to perform re-inspection, if necessary, as per the Contract and ‘Technical Conditions for Re-inspection of

Nuclear Grade Metal Material', and the supervision should witness, review and confirm the re-inspection.

The externally purchased parts include mainly crank, connecting rod, and cylinder liner, etc.

### ***3.3 Quality Control of Main Parts for EDG***

#### **3.3.1 Quality Control of Cast and Forged Parts**

The engine body (cast blank)

Mechanical property: check if tensile strength and shock work is acceptable, with attention focused on 1) the representativeness of test results of mechanical property and selected test specimen and 2) such defects as abscess and blowhole is liable to occur due to its structural complicatedness.

Cylinder cover (cast blank)

Mechanical property and hardness: check if tensile strength hardness is acceptable. Only one stretching specimen shall be taken from each part in this process. If specimen is unacceptable, the re-inspection shall be rejected. (over half specimens taken in each lot are unacceptable, all parts in said lot shall be rejected).

Connecting rod

The receiving inspection of Forged blank shall be focused on whether the inspected item is complete, effective, and acceptable, as per technical requirements, and check if the documentation and data is legible and effective, especially, if number of parts is in conformance with that of connecting rod.

#### **3.3.2 Supervision of Machining Process**

The following process shall be supervised: finishing of cylinder liner, cylinder cover and engine body, bearing cover as well as fine bored crankshaft hole, camshaft hole and cylinder hole, etc.

#### **3.3.3 Quality Surveillance of NDE**

Qualifications of NDE personnel shall be checked for its validity. Two examiner of Grade II shall be assigned for each examination item. Check if NDE monitoring equipment and instrument, provided by the supplier, is perfect and within calibration period. The supervision personnel, responsible for NDE of each parts, shall check for relevant operation rules and procedures.

Main parts to be examined include crankshaft, camshaft, piston skirt, piston top, connecting rod, and common base.

### 3.3.4 Assembly of Diesel Engine Parts

Cylinder cover assembly: check the valve for its air-tightness, settlement, and clearance.

Piston-connecting rod assembly: check the alignment of oil hole or groove, on connecting rod sleeve, with oil hole on connecting rod.

The connecting rod number shall correspond to that of connecting rod cover. Each connecting rod bolt corresponds to bolt hole, and attention shall be focused on consistency of bolt and whole number during assembly.

Crankshaft and bearing cover assembly: the number of crankshaft cover and crank hole shall be identical, and ensure that crank bolt stretching, and axial clearance, after assembly of crankshaft, meets process requirements.

Assembly of piston, connecting rod, and cylinder liner: check the size of piston, cylinder liner and connecting rod tile hole before assembly. In measuring connecting rod tile size and assembling crankshaft and connecting rod, the connecting rod bolt shall be tightened fractionally, and tightening torque and angle (tighten up to a certain torque, then rotate at a certain angle) shall comply with process requirements. Bolt tightening line shall be aligned at a time. Reversion is prohibited if the line is exceeded in tightening. The proper way is to retightening after being loosened.

Installation of camshaft: camshaft is worked into work-piece in installing, and camshaft and hole is to be applied with oil to avoid scraping camshaft bearing sleeve. Axial clearance is monitored to meet process requirements after the camshaft has been put into location. In adjusting camshaft, check if crankshaft and camshaft is positioned to be accurate, and if the accuracy meets process requirements. Attention should paid to that if any movement occurs to camshaft and gear in tightening camshaft gear bolt. Reposition and assembly shall be carried out if any movement is observed.

Assembly of crankshaft gear and shock absorber: after expansion and thrust pressure reaches required pressure in synchronism, the expanded oil pressure is released, while the thrust oil pressure is required to maintain in required retention time.

Assembly of cylinder cover: cylinder cover stretching or tightening torque and angle (tighten up to a certain torque, then rotate at a certain angle) shall meet process requirements.

Oil injection pump and lateral control mechanism: prior to installation of oil injection pump, proper thickness of adjusting washer is selected in accordance with the measured results.

Exhaust manifold: the joint of charger tank and exhaust manifold shall be clean. Before assembly, the junction surface shall be applied with sealer. Check if one-way valve of charger lubricant system is properly installed.

### 3.3.5 Single Diesel Engine Test

Single diesel engine test includes running-in test and performance test. The running-in test is a key link in detecting and removing quality problem existed in diesel engine assembly. Before test, the supervisor ensures that test operators have completed pre-test preparations according to the Test Program. Before start-up, the static test of diesel engine shall meet safety protection requirements, and alarming and shutdown unit shall be set and inspected, with trigger point kept in test record, to confirm all sensor signal on test bench are normal, with the aim of preventing the diesel engine from any damage caused by assembly quality problem. Performance test, a verification of basic performances possessed the diesel engine, includes, at least, the one required by related standard and technical specifications in delivery performance delivery inspection.

### 3.3.6 Quality Control of Generator

Generator set, an important and key equipment of Grade 1E, is being manufactured in France. The supervision work is undertaken by the European office of CNPE, the supervision staff of which is responsible for quality control of the generator according to related requirements.

### 3.3.7 Test and Delivery Inspection of EDG

EDG delivery inspection items consist of

Visual inspection

Insulation resistance measuring

Insulation dielectric strength test

Start-up property check

Phase sequence check

Functional inspection of indication unit for control panel and electrical panel

Non-load voltage setting range check

Protection unit action reliability check

Measuring of voltage and frequency transient adjusting ratio and recovery time

Voltage and frequency fluctuation ratio measuring

Continual operation test at rated working conditions

Measuring of oil consumption ratio

Measuring of temperature rise for generator winding

Measuring of linear voltage wave sine deformation ratio

Vibration test

Delivery acceptance: check for the quality of hardware and software (as-build document)

## 4 Equipment Supervision Mode and Manpower Allocation

The EDG belongs to supervision grade of JZ1, according to 'List of Equipment Supervision Grading for Fuqing Units 5&6'. The supervision personnel have been dispatched for quality control.

According to actual conditions one supervisor is dispatched and stationed in the supplier. The generator is being manufactured in France, where the European Office of CNPE is held responsible for quality control of imported parts and components for the generator set.

## 5 Selection of Witness Points

### 5.1 Selection of Witness Points for Diesel Engine

No.	Parts or activities	Supervision items	Type of witness points (H/W/R)	Remarks
1	The diesel engine body (cast blank)	Analysis of chemical composition before furnace	R	
		Mechanical property	W	
		Hardness (HBW)	W	
2	The diesel engine body (finishing)	Hydraulic test	H	
		Final inspection	W	
3	Crankshaft	Magnetic particle examination MT	W	
		Main size measuring	W	
4	Camshaft	Material inspection	R	
		Mechanical property	R	
		Magnetic flaw detecting	W	
		Final inspection	W	
5	Cylinder cover (cast blank)	Analysis of chemical composition before furnace	R	
		Chemical composition	R	
		Mechanical property	W	
		Hardness	W	
6	Cylinder cover (finishing)	Hydraulic test	H	
		Final test	W	

(continued)

(continued)

7	Piston skirt	Material inspection	R	
		Chemical composition	R	
		Ultrasonic defect detecting	W	
		Detecting of hardness, mechanical performance	W	
		Dye penetrant examination	W	
		Shape finishing	R	
		Dye penetrant examination of inside-skirt	W	
		Final inspection	W	
		Graphite treatment of skirt	R	
8	Piston head	Ultrasonic defect detecting	W	
		Inspection of mechanical performance	W	
		Finishing of external cylindrical, ring groove, end surface	R	
		Dye penetrant examination	W	
		Final inspection	W	
9	Connecting rod	Forged blank receiving inspection	W	
		Ultrasonic defect detecting	W	
		Weighing and recording	R	
		Magnetic flaw detecting	W	
10	Cylinder linear (cast blank)	Analysis of chemical composition before furnace	R	
		Mechanical property	W	
		Hardness	R	
11	Cylinder linear (finishing)	Prerequisites check	W	
		Final inspection (Report)	W	
		Close of quality plan	W	
12	The public base	PT+UT Flaw detecting	W	
		Leakage test	W	
		PT+UT Weld flaw detecting	W	
13	Diesel pipeline	Quality records	R	
14	Diesel partial/general assembly	Assembly of cylinder cover	W	
		Assembly of piston-connecting rod element	W	
		Assembly of camshaft and bearing cover	W	
		Assembly of piston, connecting rod, and cylinder sleeve	W	
		Crank arm check	W	
		Hydraulic test of water system	W	
		Completeness inspection and visual inspection of diesel engine	W	

(continued)



(continued)

15	Diesel Single test	Test of diesel engine	H	
		Check of preparedness before test	W	
		Running-in test	W	
		Acceptance test	H	
		After-test inspection	H	

## 5.2 Selection of Witness Points for Generator

No.	Parts or activities	Supervision items	Type of witness points (H/W/R)	Remarks
1	Rotator assembly	Dynamic balance	W	
2	Motor test	Generator test	W	
		Exciter test	W	
		Permanent magnet motor test	W	
		Complete machine test	W	
3	Motor	Review of End of Manufacturing Report	W	

## 5.3 Selection of Witness Points for EDG

No.	Parts or activities	Supervision items	Type of witness points (H/W/R)	Remarks
1	Assembly of EDG	Check of certificate for coupling	R	
		Check of certificate for material and parts	R	
		Check of coaxiality of engine and generator	R	
2	Test and acceptance of EDG	Check of preparedness before test	W	
		Delivery inspection of EDG	H	
		After-test check	H	

*Note* The number of witness points may be increased or decreased according to the quality trend and characteristics during execution of the project

## **6 Analysis of Key and Difficult Points for Equipment Supervision**

### ***6.1 Casting of Diesel Engine, Cylinder Liner, and Connecting Rod***

Diesel engine, cylinder sleeve, connecting rod are liable to abscesses during forging process according to previous experience, therefore, quality control of forging process should be enhanced.

In case of sub-contracting of cylinder sleeve, connecting rod, the supplier is required to strengthen quality control and management to its sub-contractor.

Crankshaft is to be produced by overseas supplier, which is required to enhance management of its sub-contractor in quality control, receiving inspection and re-inspection.

### ***6.2 Assembly of Diesel Generator Set***

Checking certificates of material for coupling, and reviewing documents that prove coupling conformity of diesel engine with generator.

Checking quality certificate of material and parts, to ensure that quality plan for diesel engine is implemented and all related witness points have been signed. Reviewing the quality documents and certificates for air start-up valve, pre-lubrication oil pump, cooling water pump, preheater, fuel cooler, air start-up piping and parts, lubricating oil, fuel pipe and parts; Review the NDE report for start-up air pipe and parts.

Coaxiality of diesel engine and generator shall be inspected, to ensure that the coaxiality of diesel engine and generator, after they have been located in test bench, conforms to the process documents.

### ***6.3 Test of Diesel Engine***

Test operators have completed pre-test preparatory document and records according to the Test Program prior to test, and check if the test environment meets the requirements for diesel test conditions. The check list of electrical units and its functions for EDG shall be reviewed before initial start-up. Before test, all sensor signal is to be checked to be normal and without alarming signal.

EDG test includes, as a general rule, the following: power verification test, speed controller test, start-up test, vibration measuring, loading test, margin test, under-load test, non-load test and 50 % load test, etc.

Power verification test: EDG shall operate at a load of 100, 75, 50, 25, and 110 %, respectively, for a time interval stipulated in the Test Program, and check if the operating parameters of diesel engine and generator conform to the requirement of the Test Program.

Speed controller test: when the generator load decreases from 100 %, gradually or abruptly, to 0 %, check if the static and dynamic maximum rotating speed meet the requirements of the Test Program.

Start-up test: If the air storage tank is not filled any more, and at 10 pre-heatings, check if the engine start-up (5 times at Side A, and 5 times at Side B) time meet the requirements of the Test Program.

Vibration measuring: under a working condition of 100 % load, check if the vibration value, measured at a point designated by the Test Program, is in conformity with the Test Program.

Loading test: check if EDG dynamic and static parameters conform to the Test Program under loading conditions, in accordance with the loading sequence and as specified in the Test Program.

Margin test: check if operating parameters is in conformity with the Test Program when the load is increased to designed maximum after the time limit specified by start-up signal.

Under load test: check if the operating parameters conform to the requirements of the Test Program under 10 % load and within the specified time by the Test Program.

Non load test: check if the operating parameters conform to the requirements of the Test Program under 0 % load and within the specified time by the Test Program.

50 % load test (after non-load test): check if frequency drop and voltage deviation conform to the requirements of the Test Program after non-load test, when the load is increased to 50 %. Attention shall be given to the occurrence of any alarming signal abnormal parameters.

Run post-test checks according to the Test Program.

## **7 Analysis of Supervision Risk**

### **7.1 Case No. 1**

Manufacturing phase: Charger burnout.

Risk: Quality issue with Charger.

Control measures: Problem charger is segregated after packing.

Cases: April 21, 2014, SNMD performed adjustment test of 4LHP 5870051L. When loading to 800 kW, abnormal noise occurs in the diesel engine. As unloading (A2 high-pressure charger rotates at about 20,000 rpm), abnormal rotation drop of A1 high-pressure charger was found, while A1 high-pressure charger rotates normally. Restart was made after the diesel engine and charger was checked and no abnormal conditions were found. A2 charger rotation was not found; when the

engine run A2 high-pressure charger remained unmovable after repeated check of the electrical system.

## **7.2 Case No. 2**

Manufacturing phase: Oil piping non-return valve reversed.

Risk: Many non-return valves are installed in the piping system of diesel engine, especially in the lubrication oil piping system. The non-return valve is small in diameter and volume, same connecting size, with small indication for flow direction. If the non-return valve is reversed in assembly, it will cause damages to some parts of diesel engine due to improper lubrication.

Control measures: Problem charger is segregated after packing As for the defects, the supervisor issued a communication notice, requiring the supplier work out a detailed check scheme of thoroughly checking all charger oil system, checking, testing, and confirming all non-return valves in order to eliminate all other potential quality problem. The supplier was required to enhance technical training and management, to improve professional skills, to prevent from the occurrences of similar problem. The supervisor is required to enhance routine site check, and to push related working and inspection personnel to strictly and carefully check and verify the assembly of non-return, sign, and verify the check records.

Cases: On April 23, when replacing A2 high-pressure charger, and assembly of the diesel engine, it is found the Oil piping non-return valve was reversed.

## **7.3 Case No. 3**

Manufacturing phase: Casting of the diesel engine.

Risk: Casting defects with the diesel engine.

Control measures: Casting process should be strictly controlled, and welding training strengthened. Repair welding performed after weld process qualification is acceptable.

Cases: Abscess was found inside camshaft hole after completion of casting of the diesel engine body; repair welding of defective area was unacceptable.

## **7.4 Case No. 4**

Manufacturing phase: Connecting rod bolt.

Risk: Cracks occurred during connecting rod bolt manufacturing process.

Control measures: The supplier was required to carry out related analysis, replace the bolt, and to perform MT for connecting rod bolt.

Cases: Cracks were found during the assembly process of connecting rod bolt after delivery.

## 8 Conclusions

As described above, it is important to make the supervision of the manufacturing process of nuclear equipments, which have a higher quality requirements and complicated process. The supervision of manufacturing process for domestic equipments, especially for specific structural characteristics and with difficulties in researches, is more essential. In order to do a better equipment supervision job, it is critical to carry out a supervision planning before the manufacturing of contract equipments.

Making the analyses of equipment risks, it is essential to recognize and grasp accurately the main and important points in equipments supervision, according to the structural characteristics and difficulties of equipments. Meanwhile, combine the feedbacks from former projects, thus making the comprehensive analyses. Taking the priority control of supervision in equipment supervision process in conformity with the principle of “key equipments, key supervision” and “weak links, strengthen control”. On the basis of supervision for Fuqing NPP, Fangjiashan NPP, Hianan NPP equipment, the supervision planning has been implemented on the subsequent projects, and obtained good effects. The supervision planning has attained better results, improved supervision efficiency and quality control, heightened the supervision effectiveness, as well as nuclear equipment quality, and thus provided beneficial references.

## References

1. FQZ210AR025CPMB06CT Procurement Contract on Fuqing Nuclear Power Station Units 5&6 for EDG and Auxiliary Power Source
2. CP03G9001 Technical Specification of EDG

# Quality Control of Sub-suppliers in EDG

Wang Wei

Abstract ■■■

Keywords ■■■

## 1 EDG/Quality Management System/Sub-supplier/Supply Chain/Safety

After Fukushima accident, Emergency Diesel Generator (EDG) is becoming more critical for safety operation of NPP. As we know, safety operation of EDG plays an important role for the safety operation in NPP. In this case, we spend more time in studying how to get more reliable EDG for the NPP. The Quality Control EDG becomes our main topic in our study.

## 2 Foreword

As we know, EDG system contains fuel system, lubrication oil system, cooling system, air-starting system, intake and exhaust air system, and other supporting electric and control equipment (see Fig. 1). EDG system contains about 400 equipment, and more than 10,000 parts and material. In this case, it is not possible to have one manufacturer to build a complete EDG system. Therefore, we have dozens of sub-suppliers to build a complete EDG system. Only if the quality of all equipment and materials is reliable, the complete EDG system will be reliable. In this case, the quality control of each sub-supplier becomes more critical. (Figure 2 shows the percentage comparison of the supplied equipment manufactured by main contractor and sub-suppliers).

---

W. Wei (✉)

CNPE Procurement Department, 117# Xisanhuanbeilu, Beijing, People's Republic of China  
e-mail: wangweic@cnpe.cc

### Components & boundaries 部件和边界

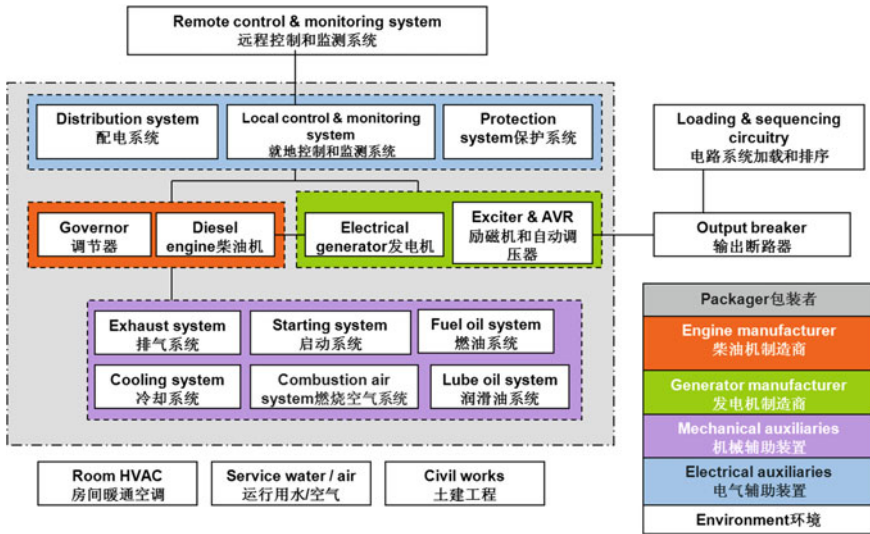
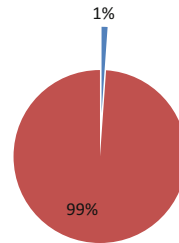


Fig. 1 EDG system

Fig. 2 Percentage comparison of the supplied equipment

### Equipments for EDG system

■ main contractor ■ sub-supplier



CNPE should take full responsibilities for the safety during the time of building the NPP. Therefore, according to IAEA Safety Standards GS-R-3 “*The Management System for Facilities and activities*,” we should build a management system to ensure all requirements are not considered separately from the safety requirement, and put all parties in the supply chain (as mentioned in Fig. 3) into this management system.

In order to ensure the quality and keep the time schedule, each party in the supply chain should establish his own management system, improve the management system timely based on the lessons learnt. Based on that, we mainly control each step before manufacturing, such as reviewing the Qualification Report of sub-suppliers from the contractors, reviewing the design and test documents,

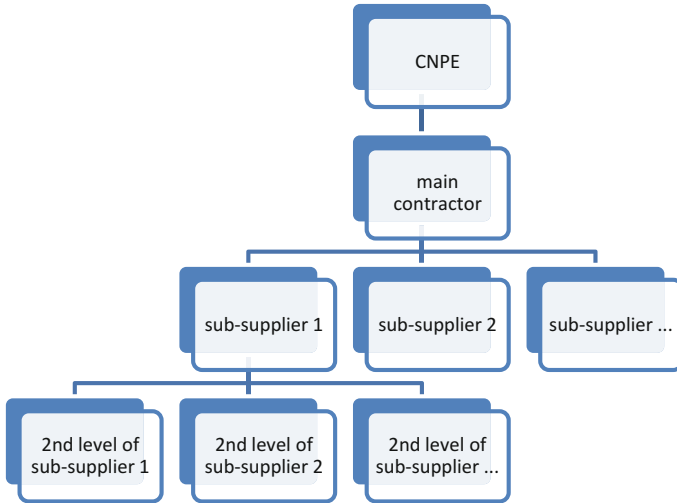


Fig. 3 Supply chain

checking the precondition before manufacturing, and make deeply inspection during the manufacturing till release shipment.

### 3 Quality Management System Established

In case of the characteristic of EDG system, we should establish a complete control system including all suppliers, who involve in EDG system. In order to let the complete system run properly, we must have efferent control of each party, and each party should play his own role sufficiently.

Therefore, each party should properly

- control the quality of himself,
- control the quality of his supplier
- audit the quality control process of suppliers to the sub-suppliers

Based on that, we can see each party will have at least two parties involve in the quality control in the process, as IAEA request Defence in depth and Safety margin.

In order to establish an efficient management system, we

- grade all equipment
- define all necessary document.
- evaluate the manpower.



### 3.1 *Grade All Equipment*

According to the safety requirement of the NPP Designer, the EDG designer prepared the equipment classification of the quality assurance class for all equipment. Based on that, with regarding the significance and complexity of the product and consider the maturity and the reference of the manufacturer, we grade all equipment in different levels for the quality control.

- For the complex equipment which have longer manufacturing duration time, the quality control level will be high than the quality assurance class.
- If the manufacturer has the similar products manufactured in the same time, and the manufacturing capability is nearly exhaust, the quality control level will be higher.
- If the products will be manufactured only by the automatic machinery, the quality control level will be lower.
- The quality control level also changed according to the reference of the manufacturers.

Based on all these, we have four quality control levels

- JZ1: complete quality inspection in manufacturing period.
- JZ2: periodical inspection during manufacturing
- JZ3: quality inspection according to the quality plan.
- JZ4: only factory shoptest.

Since most of the EDG suppliers are the sub-suppliers, the quality control class becomes very important for quality control of all the sub-suppliers. Hereafter, I make an example for that.

**Example 1 The bolt of conrod were found crack during OPI before assembly (raise the quality inspection level)**

Quality assurance class of the conrod is QNC, which means no need for the inspection during the whole process of manufacturing. But we raise the quality control after we found the defect in the previous project.

**Description:**

- Because one type of GENSET is only assembled in China local company and all assembled parts (SKD) are delivered from European.
- During the OPI in China, we found some bolts of conrod were cracked by the inspectors.

**Solution:**

- The manufacturer prepared the trouble shooting and the analysis report
- All conrod were checked by the third party and the defected parts were taken out
- The manufacturer make better quality control in order to prevent from the similar issue happening again.
- Exchanged all defected conrod.

### **Lessons learnt**

- The supplier reinforced the quality control of the sub-suppliers, and reinforced the quality control of the material incoming check.
- We added the quality check point before shipping of SKD. This earned better quality for next delivery materials.
- We raised the quality control level for this point in all project now.

### **Example 2 silencer manufacturing (lower the quality control level)**

The silencer design as QA2 and the quality control level should be JZ2 as periodical inspection during manufacturing.

During two projects execution and 10 similar products manufacturing, the products have no quality defect and have no delay for delivery.

With this good reference, we decided to lower the quality control level to JZ4 as only factory shop test before release for shipment. This also saves our manpower to put into more critical products.

## ***3.2 Define All Necessary Document***

When we receive a new project, we hold a kick-off meeting directly. We will check by all parties for all necessary documents for the validity.

With the kick-off meeting held, all the detailed project execution methods and communication way is settled in the meeting, and the management system of the sub-suppliers is also established

## **4 Quality Management System Process of Sub-suppliers**

In the management system process of the sub-supplier, we

- Evaluate the sub-suppliers,
- Review the documents of sub-suppliers,
- Inspect the quality during the manufacturing process.

### ***4.1 Evaluate the Sub-suppliers***

Based on the regulation of our company, all important sub-suppliers, which quality assurance class is higher than QA3, can be used in the project only after the approval of our company. During the review process, we mainly review the

evaluation reports which the supplier submitted to us. The main review points are the following:

- Check the completeness of the evaluation report prepared by sub-supplier
- Check all related qualification certificate of the sub-supplier
- Check the capacity of the design and manufacturing of sub-supplier
- The reference of the sub-supplier
- The evaluation record of the supplier to the sub-supplier
- Analysis if the sub-supplier can follow the requirement of the contract.

For the safety-related equipment supplier, we will review the quality assurance procedure of the project.

Here is the example for our reviewing the evaluation report in one project.

**Example: Sub-supplier: XXX for the expansion tank manufacturer**  
**Reviewing process:**

- The report was complete.
- They have the qualification certificate of HAF 601 and other certificate of pressure vessel.
- The manpower and machinery are qualified for the product.
- The suppliers audition report shows nothing negative
- They are one the main suppliers in petrol field, and new suppliers in NPP field. But in the previous project showed a lot of problem of the company.
  - Bad project management. This created the delay of the previous project.
  - Bad quality control management: the process of the manufacturing was not following the procedure. There was no improvement when we gave them the notice for the quality failure.
  - The document management was very bad. Invalid documents were used in the manufacturing.
  - This means the company has bad management system in the quality control.

Review result:

- We refused the manufacturer been the sub-suppliers for the expansion tank.
- We ask the supplier to improve his own audition process for the sub-suppliers.

## ***4.2 Document Control***

During the project execution, we must guarantee that the documents are properly controlled.

- We reviewed the design documents to be sure that the documents are mating the requirement of the contract.

- We checked the documents which are submitted by supplier if all documents are following the correct process by preparing, reviewing, and approval by supplier and his sub-suppliers
- We checked if the valid documents used in the manufacturing process of sub-suppliers.

### 4.3 *Inspection During the Manufacturing*

In order to have the final satisfied product, the strict inspection during the manufacturing is very important. This inspection should not only come from one party but also from all related parties and better with third party.

#### ***Manufacturing kick-off***

In order to have same understanding by all inspectors from all parties and check the preparation for the manufacturing starting, the manufacturing kick-off meeting is necessary. We will check the following:

**Manpower:** checked the qualification for all related staffs who involve in the process

**Machinery:** checked the qualification and the evaluation for the manufacturing equipment, test equipment, and checked the storage for manufacturing device.

**Material:** checked if all material used for the product have been prepared.

**Document:** check if all documents are valid and the valid documents are used in the workshop.

**Condition:** checked if the manufacturing condition and the storage is fitting the requirement of the contract.

#### ***Quality control during the manufacturing:***

All the inspections by all parties should strictly follow the request of the contract document and related standards to check all manufacturing process in order to ensure the quality of the products.

We also gathered all the lessons learnt from our own projects and other project and put into our quality control system.

Here is the example for the quality control and put back into the quality control system.

**Example: Surface defect of the valves during the OPI on NPP site.**

#### **Description:**

During OPI, we found the rust on the surface and debris inside the valve (Fig. 4).

#### **Solution:**

All defect valves were sent back to the manufacturers, repaired, and tested before released for shipping.



**Fig. 4** Surface and debris inside the valve

**Lesson learnt:**

- Put the strict surface check request into the quality control process
- The manufacturer changed the manufacturing procedure to avoid the rust during the transportation and storage.
- The contractor changed the quality control system to improve the quality control process of the sub-suppliers.

## **5 Measurement, Assessment, and Improvement**

The effective of the quality management system should be measured to confirm the ability to achieve the requirement of the contract and NPP design. All the process should be monitored and assessed by self or other. Therefore, the lesson learnt helps us to find the shortage and non-conformity to improve the quality control system.

Here is the example for us to improve our quality control system.

**Example: The blades broken of the fans in fan cooler:**

**Description:**

The broken blades of fans in fan cooler were found in a NPP project. After the accident analysis, the reasons for the accident are

- Poor quality of the manufacturing
- Shortage of the system design.

The supplier of the fan is the supplier of the fan cooler manufacturer and sub-supplier of EDG. For us, it is the third-level supplier. The EDG contractors and we did involve in the manufacturing of the fan manufacturing.

**Solution:**

Change all blades of the fan for all NPP sites. Recalculate the system design.

**Lessons learnt:**

- This is shown that the quality control chain was broken. One supplier is out of control in the quality management system.
- The manufacturer of fan cooler should reinforce the quality control of suppliers
- The contractors should reinforce the quality control of sub-suppliers.
- Improve our quality control system.

**Improvement:**

- Add more stage of equipment and material classification. Each supplier should grade their equipment till material.
- Each level of the suppliers should control their suppliers according to classification level in order to avoid that one material or product is failed for quality control by other parties.
- Each level of the suppliers should also review the sub-suppliers to order that each supplier is effectively controlled.
- The action of improvement will be monitored and the effectiveness of the improvement will be checked in the completeness.

## 6 Conclusion

Since the complexness and variousness of the EDG system, the quality management system is not possible to be established and executed by only one party. It needs all parties, who involved in the supply chain, to take their own responsibilities in the process. Each party in the supplier chain should play their own roles in the system. This is the only chance to keep quality of each material used in EDG system be controlled. When the quality of each material and product have been effectively controlled, the complete EDG system will be satisfactorily safe.

## References

1. IAEA GSR 4 “*Safety Assessment for facilities and Activities*”
2. IAEA GS-R-3 “*The Management System for Facilities and activities*”
3. HAD003-08 Quality” Assurance during product manufacturing”
4. CNPE-MSW-6100-1302 “*grading during equipment inspection*”
5. CNPE-MSW-6100-1312 “*the management of quality inspection*”
6. CNPE-MSW-6100-1609 “*quality assurance system in procurement of product*”

# Research on Identification Test for Sealing Performance of Equipment on Containment Pressure Boundary

Xiao-xuan Wang

**Abstract** The characteristics of sealing material for equipment on containment pressure boundary may be changed under the high temperature and high pressure and high irradiation conditions caused by accident. This will result in loss of containment tightness. So we need to perform the identification test to verify that the equipment under accident conditions can keep the seal function. In view of the identification, standard for design basis accidents and serious accidents is different, cannot cover each other, and therefore should be identified respectively. Influence factors for identification and mainly consider the normal condition of thermal aging, normal condition of irradiation aging, mechanical aging, accident condition of thermal environment, the accident condition of irradiation aging, accident conditions of chemical environment, etc. And assume that seal material in the life of the final suffered a design basis accident or serious accident. When evaluating the test results, the acceptance value should be between the leakage rate limit and intact seal leakage rate, ensure enough design margin, and guarantee the evaluation test pass.

**Keywords** Sealing · Identification test · Aging

## 1 Introduction

Containment pressure boundary equipment consists of personnel airlock, equipment hatch as well as various mechanical and electrical penetration assemblies. As an important integrated part of the containment pressure boundary, they penetrate the reactor containment. Seal structure (including sealing materials) performance is essential to ensure the sealing performance of equipments. Under high temperature,

---

X. Wang (✉)

China Nuclear Power Engineering Co. Ltd, Beijing 100840, China

e-mail: wangxx@CNPE.cc

X. Wang

Nuclear Island Mechanical Equipment Design,

Harbin Engineering University, Harbin 150001, China

© Springer Science+Business Media Singapore 2017

H. Jiang (ed.), *Proceedings of The 20th Pacific Basin Nuclear Conference*,

DOI 10.1007/978-981-10-2317-0\_38



high pressure and high irradiation effect from accident conditions, high temperature and irradiation effect would cause embrittlement and rupture of rubber materials while moist, steam, and other factors would cause decomposition of rubber materials. These factors may cause serious consequences such as seal failure and uncontrollable release of radioactive substances.

There are a number of factors to affect sealing and it is difficult to evaluate them using a simple and effective calculation model. In this case, it is required to design the seal structure based on existing engineering experience and then verify the whole seal structure (including sealing materials) by means of type identification test to certify sealing performance under accident conditions. But existing domestic and foreign standards specify no relevant requirements for sealing identification of the containment pressure boundary equipment. The technical specification for equipment only proposes a small number of principle requirements and it is short of complete and specific identification methods. Based on the identification method of electrical penetration assembly and actual equipment characteristics, some parameters get modified and some test contents are added in this paper to fill the gap of research field.

## 2 Objectives of Identification Test

Objectives of the whole identification test could be divided into three aspects based on the gradually progressive principle. First, find out the seal structure (including sealing materials) which can maintain sealing function under accident conditions. Then, acquire sealing material manufacturer, treatment process, formula and other information by means of confirming rubber product model to ensure product quality. Finally, obtain the corresponding relation between performance indicators of rubber materials and sealing performance in the identification test. These indicators (such as hardness, tear resistance, compression set, aging resistance, and so on) could be used for quality control in the future procurement of sealing materials. Among the objectives, it is the most basic and most important for the identification test to ensure reasonable selection of sealing materials and reasonable seal structure design and perform sealing function under normal condition, in the accident and after the accident.

In order to accomplish this objective, two aspects shall be considered. First, select appropriate sealing materials. Required sealing function can be realized only when sealing materials still have sufficient resilience under accident conditions. Specifically, sealing materials shall be considered in the following aspects:

- (a) Sealing materials shall have strong tear resistance to prevent release of radioactive substances arising from tearing seal rings under accident condition. If the seal ring suffers radial cracks and even damage under pressure loads due to lack of strong tear resistance, the sealing performance would be damaged.

- (b) Sealing materials shall have the lower compression set. The compression set is a key indicator of rubber products and mainly affects rubber resilience. If its value is lower, the resilience and sealing performance would be better.
- (c) Sealing materials shall be resistant to irradiation. As irradiation dose increases, sealing materials would be gradually hardened with compression set rise, resilience loss and sealing performance drop. Therefore, it is required to maximize selection of the sealing materials which still have the lower compression set and good sealing performance after withstanding accident irradiation dose.
- (d) Sealing materials shall have the higher operating temperature. Selected rubber materials shall be able to run for a long time at the temperature under accident condition.
- (e) Sealing materials shall be highly resistant to aging and able to maintain required sealing performance within the expected service life.

Second, determine a reasonable seal structure size to ensure that the seal ring can reach an appropriate magnitude of interference. It is very important for seal structure design process to control the magnitude of interference. If the magnitude of interference is too low, the seal ring cannot reach initial condition for sealing so as to result in the leakage rate exceeding the standard; if the magnitude of interference is too high, the seal ring would be excessively compressed so as to cause resilience reduction and easily result in the leakage rate exceeding the standard under pressure. The seal structure size shall be preliminarily determined based on previous engineering experience and the literature [1] and an appropriate magnitude of interference shall be selected. Scheme selection shall be conducted based on test results to optimize the design of seal structure.

### **3 Introduction to Identification Test**

#### ***3.1 Basic Principles of Identification Test***

The occurring of various accidents is random in the nuclear power plant. Therefore, the nuclear power plant shall be deemed to have accidents at the end of seal ring service life and consider corresponding aging from the conservative perspective. The seal ring shall be able to withstand ambient condition of design basis accident or severe accident once and maintain required sealing function after reaching the expected service life.

In order to ensure the identification test shows adequate representation, parameters of the identification test, such as aging and accident irradiation dose, shall take 10 % of theoretical calculating value as the additional identification margin according to requirements of the literature [2].

### 3.2 *Basic Approach of Identification Test*

#### (a) Determining test parameters

It is required to determine test parameters by analyzing ambient conditions of the nuclear power plant under normal operation and accident condition, including expected life of sealing rings, thermal aging and mechanical aging parameters, accident condition type required for consideration, temperature and pressure under accident condition, hydrochemistry environment, irradiation dose rate, accumulated dose, post-accident allowable leakage rate limit and allowable leakage rate limit of the identification test, etc.

#### (b) Design seal structure and sample parts

It is required to preliminarily determine groove dimensions, magnitude of interference for sealing rings as well as dimensions of simulated sample parts and tooling based on previous engineering experience and the literature [1]. Due to limitation of test conditions, full-scale simulated parts cannot be tested. Therefore, simulated sample parts and tooling in a reduced size could be used under the premise of ensuring the sample parts have the same local structure (including groove depth, width, groove spacing, surface roughness, seal ring dimensions and tolerance, etc.) and initial sealing state (including pretightening state, magnitude of interference, etc.) with actual equipment.

#### (c) Determining contents of identification test

Based on specific identification test conditions, the identification test under the design basis accident (DBA) adopts the irradiation test mode of low dose rate + long time and that under severe accident (SA) adopts the mode of high dose rate + short time. For rubber materials, the identification test is divided into DBA and SA based on damage mechanism of the above two of irradiation test modes.

In order to achieve traceability of test data in case of test failure, the identification test is divided into items test and integrated test, which can acquire individual test data to achieve data traceability and comprehensively consider influences of various factors in the accident to ensure the test conclusion is convincing enough.

### 3.3 *Contents of Identification Test*

Based on the above basic principle and basic approach, the whole identification test is divided into four stages by test time sequence

- **The first stage: determination test in initial condition, including three tests**

- ① Determination of sealing material properties. The primary purpose is to acquire parameters of the seal ring in initial condition and use them for comparison with parameters of the seal ring subject to aging. The

determination involves tensile strength, elongation, shaw hardness, tensile strength and compression set.

- ② Compacting force test. It is required to acquire the compression quantity (Q) of the seal ring in initial condition under different compacting forces (F) using the counter weight method under normal atmospheric conditions and measure the leakage rate under different compression quantities (Q) in order to obtain the magnitude of interference required for the equipment building the initial sealing state and use it for evaluating the sealing performance of the equipment under some operating conditions (such as earthquake and negative containment pressure).
- ③ Leakage rate test. It is required to compress the seal ring to the setting interference under ambient temperature conditions in order to determine the leakage rate of O-ring in initial condition under accident pressure.

• **The second stage: DBA integrated test, including three tests in sequence**

- ① Aging test. It assumes that the seal ring has been used for 7 years at 50 °C and accelerates thermal aging to simulate the state of seal ring at the end of life. In addition, mechanical aging shall be considered for door body seal ring and dynamic seal of personal airlocks.
- ② DBA irradiation test. The dose rate specified in the literature [3] shall be adopted to determine the state of seal ring under DBA irradiation dose. Accumulated dose includes that under normal operation and DBA condition.
- ③ DBA integrated test. Temperature, pressure and hydrochemistry environment under DBA condition are simulated to verify whether sealing materials and seal structure can withstand DBA condition and reach required sealing performance.

The leakage rate and physical parameters shall be measured after each test is finished.

• **The third stage: SA item test, including four test in sequence**

- ① Aging test. It is similar to the aging test at the second stage and used to simulate the state of the seal ring at the end of life.
- ② SA irradiation test. The dose rate under SA shall be adopted to determine the state of seal ring under SA irradiation dose. Accumulated dose includes that under normal operation and SA condition.
- ③ SA thermal condition test. It is used to determine the state of seal ring under SA thermal conditions.
- ④ SA chemical immersion. It is used to determine the state of seal ring under SA hydrochemistry environment. The test adopts chemical components of atmosphere or spray water under SA.

The leakage rate and physical parameters shall be measured after each test is finished.

- **The fourth stage: SA integrated test, including three tests in sequence**

- ① Aging test. It is the same as the aging test at the third stage.
- ② SA irradiation test. It is the same as SA irradiation test at the third stage.
- ③ SA integrated test. Temperature, pressure, and hydrochemistry environment under SA condition are simulated to verify whether sealing materials and seal structure can withstand SA condition and reach required sealing performance.

The leakage rate and physical parameters shall be measured after the third test is finished.

## 4 Determination of Key Parameters

### 4.1 *Determination of Temperature and Time for Thermal Aging Test*

- ① Based on previous engineering experience, the expected life of rubber seal ring is about 5 years. Considering 10 % of usage margin and design margin for a replacement cycle, the extreme life shall be 7 years.

- ② Determining thermal aging base time

It is specified in the literature [3] that, the test time below  $\tau$  (thermal aging base time) could be selected for special equipment replaced at regular intervals, provided that a reasonable evidence.

Before selecting and determining the test time below  $\tau$ , the selection basis of the thermal aging base value shall be determined and then the test time can be adjusted by the replacement cycle.

As specified in the literature [3], the thermal aging base value is 135 °C for 950 h. Normal aging time shall be calculated by the formula to determine the temperature for normal operation (50 °C).

$$\text{Normal operating life: } \tau_0 := 950 \text{ h} \cdot 2^{\left(\frac{135-50}{10}\right)} = 39.236 \text{ year}$$

According to calculation results, the design life is 39 years (almost 40 years). The result complies with the requirements of M310 NPP for design life. Therefore, the thermal aging base time shall be 950 \* 7 years/39 years for the seal ring.

- ③ Calculating thermal aging time

The thermal aging time could be reduced by raising test temperature, but it shall not be less than 100 h according to standard requirements.

$$\begin{aligned} \text{Test temperature } \theta &:= 135 \\ \text{Aging test time: } \tau &:= \left(950 \cdot \frac{7}{39}\right) \text{h} \cdot 2^{\left(\frac{135-\theta}{10}\right)} = 170.513 \text{ h} \end{aligned}$$

Thus, the thermal aging test of seal type identification shall be conducted based on 171 h@135 °C.

## ***4.2 Calculation of Irradiation Rate and Accumulated Dose Under Severe Accidents***

The irradiation dose rate changes with the time under severe accidents. But the irradiation dose rate cannot be changed when the seal ring is placed in the fixed position near the radioactive source for radiation aging of the identification test. Therefore, the average dose rate shall be calculated based on calculation data provided by the reactor specialty.

For the seal ring of containment pressure boundary equipment, it is installed on the edge of containment.  $\gamma$  irradiation dose rate in this position could be that in the border position of sphere model or cylinder model for the containment, half of the irradiation dose rate in the atmospheric center of containment. Correspondingly, the accumulated irradiation dose rate is also half of that in the center position. For  $\beta$  irradiation dose rate, it could be calculated based on semi-infinite cloud model. At some time after severe accidents, the irradiation dose rate under the semi-infinite cloud model is about half of that under the infinite cloud model; at all time, the accumulated dose is half of that under the infinite cloud model.

$\gamma$  and  $\beta$  rays can cause different hazards to rubber materials under shielding conditions. Due to lack of relevant test supports, the dose rate and accumulated dose shall be calculated conservatively by direct superposition and shall consider 10 % identification margin.

$\gamma$  irradiation dose rate drops to the lower level and has no big change after 24 h from severe accidents. Therefore, the calculation time of  $\gamma$  irradiation dose rate shall be up to 24 h after accidents. The calculation time of accumulated dose shall be up to 720 h, namely 30 days after accidents. It far exceeds the requirements of 15 days for resistance to severe accidents, as shown in Fig. 1.

Under severe accidents,  $\beta$  has a change pattern of irradiation dose rate similar to that of  $\gamma$  ray. Therefore, the calculation time for average irradiation dose rate of  $\beta$  shall be up to 24 h after accidents. The calculation time for  $\beta$  accumulated dose also shall be up to 720 h, as shown in Fig. 2.

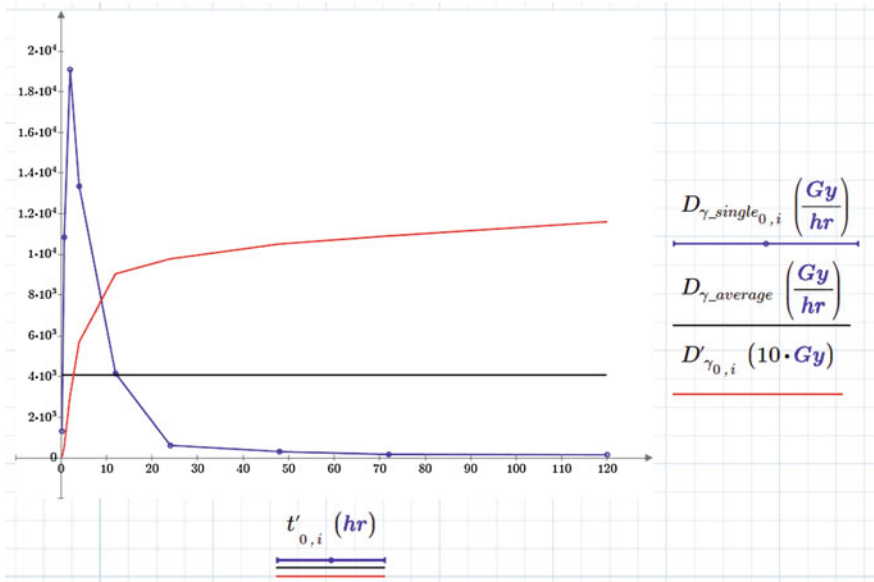


Fig. 1 Change pattern and average of  $\gamma$  irradiation dose rate

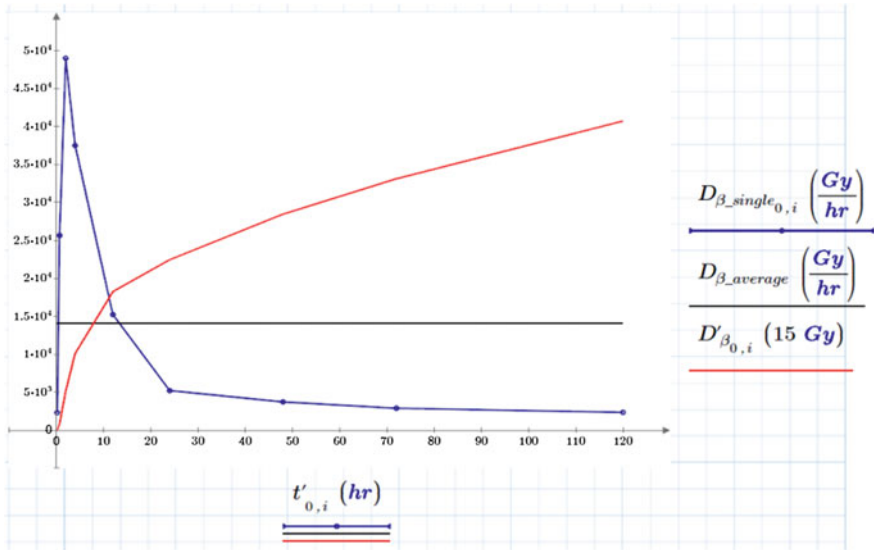


Fig. 2 Change pattern and average of  $\beta$  irradiation dose rate

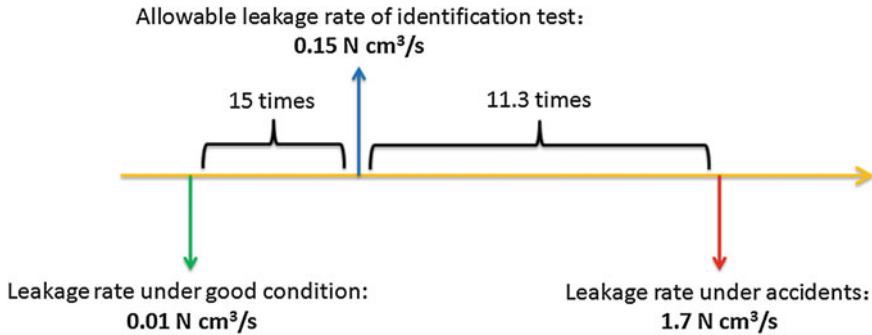


Fig. 3 Allowable leakage rate of identification test

### 4.3 Determining Allowable Leakage Rate of Identification Test

For determining allowable leakage rate of identification test, it shall be considered that the compression set and resilience drop after aging of the seal ring. If the leakage rate of the seal ring in initial condition is taken as the limit value to determine whether the seal ring passes the test, it would be deemed too conservative. In addition, the identification test simulates influences of various ambient conditions rather than actual operating conditions on the seal ring. If the allowable limit value of the containment is used for determining whether the seal ring passes the test, it would be deemed too aggressive. A balance point shall be obtained between the above two aspects to avoid excessive conservativeness and keep a larger margin, as shown in Fig. 3.

## 5 Conclusions

The identification test partly takes the identification method of electrical penetration assembly. Some parameters get modified based on actual equipment characteristics and test contents are added to finish research and development of the entire test method. The approach of identification test could be used to guide the identification test of seal structure for other equipment in order to fill the gap of research field. Characteristics of the identification test are shown as follows:

- (a) It is divided into item test and integrated test, which can acquire individual test data to achieve data traceability and comprehensively consider influences of various factors in the accident to ensure the test conclusion is convincing enough.



- (b) The identification at the DBA stage adopts the same parameters such as the irradiation dose rate, accumulated dose, and integrated test curve with the identification of electrical penetration assembly.
- (c) Thermal aging time and temperature parameter are modified based on expected life of the seal ring, the calculation method of irradiation dose rate, and accumulated dose under severe accidents is proposed and the allowable leakage rate of the identification test is determined to fill the gap of domestic research.

According to detection results of physical parameters, radiation aging is the primary cause for compression set rise and resilience drop of sealing materials. Therefore, great emphasis shall be laid on the radiation aging of sealing materials to be selected.

## References

1. GB/T 3452.3-2005, Housing Dimensions for O-ring Elastomer Seals in Hydraulic and Pneumatic Applications [S]
2. GB/T 12727-2002, Nuclear Power Plants - Electrical Equipment of the Safety System – Qualification [S]
3. EJ/T 1197-2007, Method and Ambient Condition of Qualification Test for Safety - related Electrical Equipment of Nuclear Power Plants [S]

# Research on Problems of Ultrasonic Test for Reactor Vessel Internal During Manufacturing Process

Yingpeng Liao

**Abstract** This topic starts from one of the most common non-destructive testing methods: ultrasonic testing. Connecting tightly with the reactor vessel internal manufacturing process, some typical ultrasonic tests have been listed in the essay; the reasons why these tests should be executed at that certain period of time and actual problems confronted during these processes have been issued as well. The problems mentioned include austenitic stainless steel plate, forging piece, and those happened during RVI machining processes, which can help NDT engineers comprehend criterion better and can be used as a feedback for technical preparations and quality surveillance during RVI manufacturing processes.

**Keywords** RVI · Ultrasonic test · Outlet nozzle · Stainless steel plate · Forging part

## 1 Introduction

As one of the eight main components in nuclear power plant, reactor vessel internal (abb:RVI) plays an important role both during the normal operation and emergency shutdown periods. Generally speaking, reactor internal is composed of two basic structures: Core support structures (CSS) and internal structures (IS). Core support structures provide direct support or restraint of the core, whereas internal structures are all structures within the reactor vessel other than core support structures, fuel, blanket assemblies, control assemblies, and instrumentation (see Fig. 1).

---

Y. Liao (✉)

China Nuclear Power Engineering Co., Ltd., Shenzhen, Guangdong province  
People's Republic of China  
e-mail: liaoyingpeng@cgnpc.com.cn

Y. Liao

China Nuclear Power Engineering Company (CNPEC), Yang Guang Avenue  
in Jiang Xia District, Wuhan City, Hubei Province, China

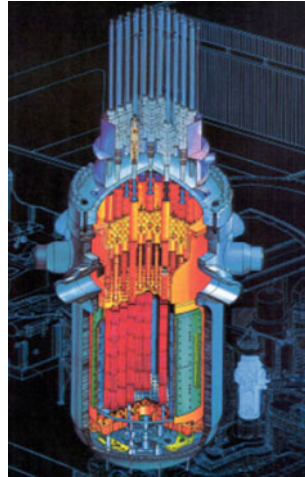


Fig. 1 Control assemblies and instrumentation

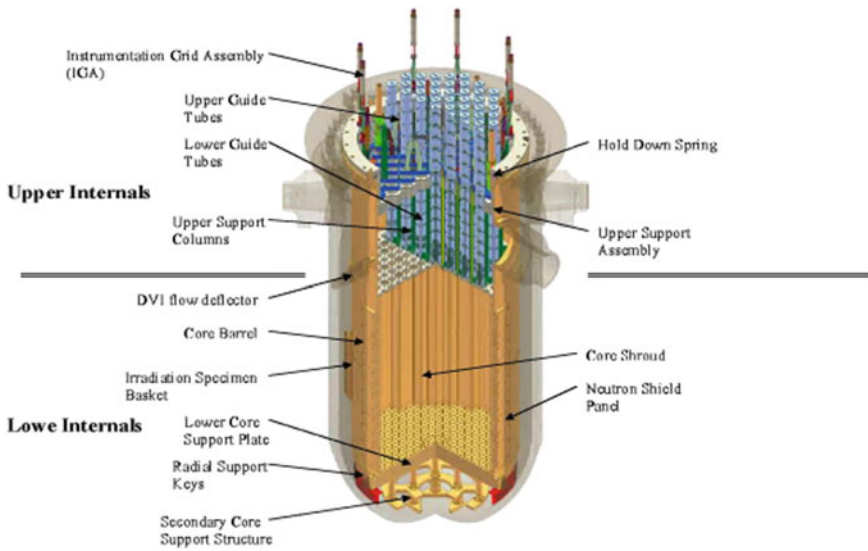


Fig. 2 Functional performance RVI

Upper internals and lower internals are the two main parts to form RVI as a whole; here is the functional performance RVI plays in the plant (see Fig. 2):

- Provide support and alignment for the fuel assemblies;
- Direct coolant to fuel assemblies;
- Provide guidance for the control rods;

- Provide support and alignment for instrumentation;
- Provide radiation shielding for the reactor vessel;
- Transmit loads from the reactor internals to the vessel;
- Accommodate differential thermal expansion with respect to vessel;
- Provide cooling flow to the reactor vessel head plenum;

RVI is made from stainless steel considering the influence both from the weight it appears and the function it plays to shield the radioactive ray. The main processes to complete RVI manufacturing include steel plate rolling, welding, outlet nozzle, machining/welding, core support plate, and final machining of the whole barrel. There are varieties of ultrasonic tests RVI should undergo during different periods of the full manufacturing cycle, including the raw material period when this equipment is just steel plate, forged pieces or iron bars. The following instances may elaborate.

## 2 Examples

### 2.1 UT on Outlet Nozzle Forged Parts

For each CPR1000 nuclear plant, there are three outlet nozzles in the upper shell ring of RVI, directing the coolant to the fuel assemblies (see Fig. 3).

These nozzles are all forged (family:3a, see NF-A04-308 for details) of Z2 CN 19-10 with controlled nitrogen content austenitic stainless steel and should undergo ultrasonic test for the whole bulk; according to the technical specification, it is recommended to implement UT after the machining and property heat treatment. According to the measured data from forged parts supplier, the inner and outer diameters of the nozzle are 716.2 and 1115.7 mm, respectively (see Fig. 4 for semifinished product).

Using a 45° oblique probe, testing operator scanned the whole volume from the external circle and no flaw was found, and then the forged parts were delivered from the sub-contractor to the main contractor.

After the final machining, these three outlet nozzles had been welded in the upper cylinder of RVI. Once UT report from the raw material supplier was reviewed by owner accidentally, and they pointed out using only 45° oblique probe is incorrect and there are blind zone for sure according to the dimension of the forged parts.

**Fig. 3** Three outlet nozzles in the upper shell ring of RVI

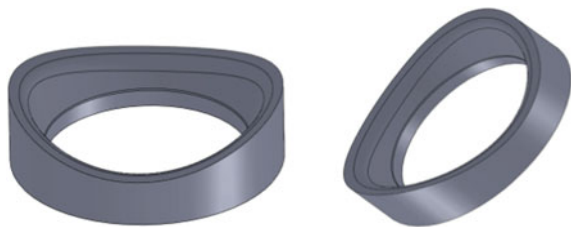


Fig. 4 Semifinished product

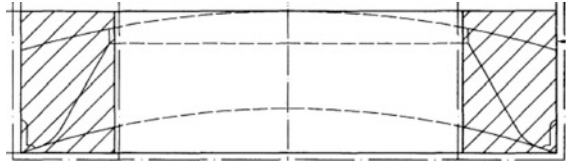
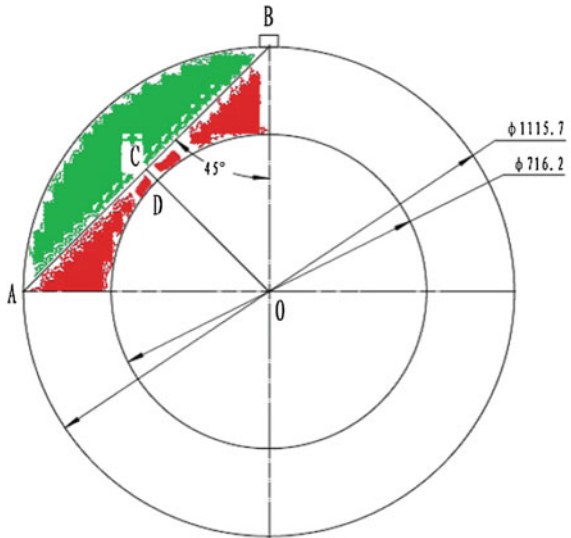


Fig. 5 Dimension of the forged parts



$$OB=1115.7/2=557.85, OD=716.2/2=358.1, OC=557.85*\sin45^\circ =394.52 > OD$$

See Fig. 5 for details.

Take the second quadrant for example: the green zone can be tested using only a 45° oblique probe, whereas the red zone is totally untested under this circumstance. That means ultrasonic test in the raw material factory cannot be a convincing evidence to prove the forge pieces are flawless.

Problem like this is not uncommon in RVI manufacturing processes. According to incomplete statistics later, the same question had been found in other nuclear power project like HONG YANHE, FANG CHENGGANG, and YANGJIANG. After scanning with small-angle probe (refer to NF A 04-308 and RCC-M MC2320), these forge pieces were accepted eventually (see Fig. 6 for details).

## 2.2 UT on Stainless Steel Plate

Thicknesses of plates used in RVI are 60 mm or plus. According to the specifications issued by designer, all these plates should undergo ultrasonic test, and the

**Fig. 6** Scanning with small-angle probe



criterion of this test is NF EN 10307S<sub>3</sub> and E<sub>4</sub>; besides, welds should undergo the same test compared with the edge of the plate.

When the quality level is S<sub>3</sub>, UT comprises continuous examination along the lines of a grid made of a 100-mm square parallel to the edges of the flat product, or along with parallel or oscillating lines distributed uniformly over the area, giving the same degree of control. See excerpt from EN 10307 for details (Fig. 7).

After cutting and baiting, possibly the old inner parts of the plate may become the new edges, and these parts should be one-hundred percent tested like the edges already existed. Scanning in terms of grid is forbidden in this situation, no matter how compact the grid is (see Fig. 8).

And for those whose thickness is greater than 60 mm, zone width for edges is 75 mm (Fig. 9).

There is no difficulty for plates supplier to execute 100 % UT test for the edges; the question is RVI manufacturers sometimes ignore providing their groove drawing to sub-contractors, which means plates' suppliers have no idea which parts

**13.3.2 Quality class S<sub>2</sub> and S<sub>3</sub> flat product**

Scanning comprises continuous examination along the lines of a grid made of a 100 mm square parallel to the edges of the flat product, or along with parallel or oscillating lines distributed uniformly over the area, giving the same degree of control.

**Fig. 7** Excerpt from EN 10307 [1]

**14.2 Testing the edges**

The test consists of scanning the total area of the edges (or areas to be welded according to sketches) where discontinuities were located defined in 8.3 under the same conditions as for flat product body (14.1).

**Fig. 8** Scanning in terms of grid

**Table 2 — Zone width for flat product edges**

Thickness of the flat product <i>t</i> mm	Zone width mm
$6 \leq t < 50$	50
$50 \leq t < 100$	75
$100 \leq t \leq 200$	100

**Fig. 9** Zone width

may become the new edges ready for welding, and then it is not surprised to see why the lack of 100 % scanning for the new edges is that common in many steel plates suppliers for RVI.

Meanwhile, according to EN 10307, both flat product and flat-bottomed hole should be used to adjust the curve in order to eliminate the quantitative deviation caused by attenuation (Fig. 10).

Plates rolling and welding had finished by the time these two problems were exposed to RVI manufacturer and the owner. After in-depth discussion among the designer, purchaser, and NDE professionals, RVI manufacturer had to retest the welds to prove that the “new edges” were defectless, 18 dB beyond the reference sensitivity was coercive to avoid the so-called “-18 dB zone” in order to guarantee the accuracy (Figs. 11 and 12 show the sensitivity setting and retesting processes).

**2.3 UT Housing of Energy Absorber**

Energy absorber is an important part of RVI, which can support the lower internal weight and buffer the force both in regular and emergency situation. Energy absorber consists of absorber axis and housing, and both of these two components can be turning to form their final dimensions from a stainless steel bar or pipe. If the original shape is a pipe, everything will be ok as long as purchase orders and

For each type of probe, curves shall be used giving:

- a) the change in the amplitude of the back-wall echo as a function of the thickness of the flat product;
- b) the change in the amplitude of the echo of the flat-bottomed hole as a function of its depth, for holes of diameter:

Fig. 10 Quantitative deviation

Fig. 11 Sensitivity setting

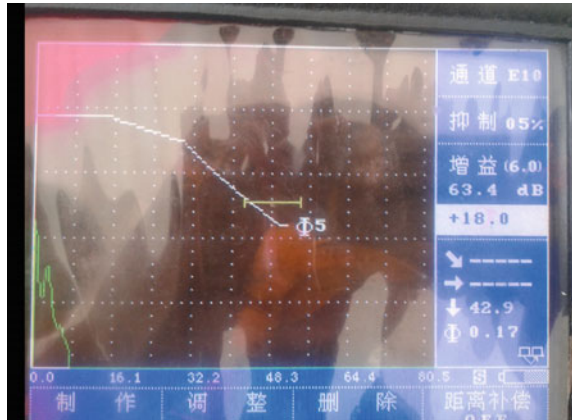


Fig. 12 Retesting processes



specifications are strictly obeyed by material suppliers; but if the products are machined from a bar, there are easily overlooked questions in regulations and actually, and they were ignored in deed by manufacturers.



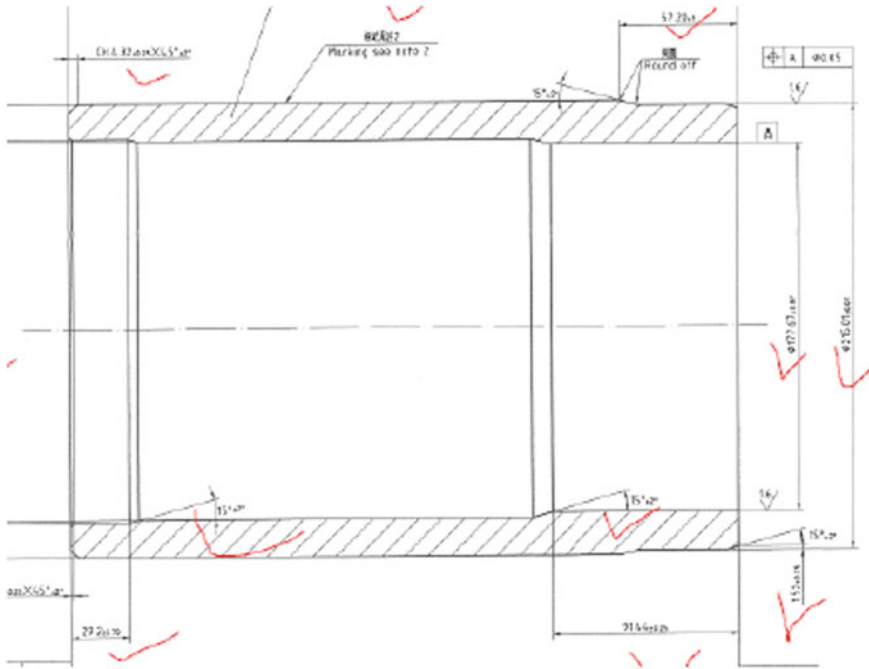


Fig. 13 The inner and outer diameters of housing

The inner and outer diameters of housing are 177.67 and 215.01 mm, respectively; the ratio between OD and ID is 1.21 (see Fig. 13).

According to NF-A04-308, forged parts are classified into 3 families; solid bars belong to family 1a, whereas hollow cylindrical parts obtained by extrusion, wire drawing or boring belong to family 3a. If 1a-family forged parts have been machined into corresponding 3a parts through boring, when the ratio between OD and ID is equal to or less than 1.6, an oblique-wave ultrasonic test should be imposed over the whole cylindrical outside surface, even if the 1a-family bars have already been tested before boring (see excerpt from NF-A04-308) (Fig. 14).

For conservative consideration, RVI designers and owners always require the most strict and comprehensive test been carried out on the products. Although material suppliers and manufacturers had clarified that the quality of forged bars was under control, they had to retest the housing surface again to make their conclusion credible (see Fig. 15).

The same incidents happened in different nuclear power projects, reflecting that there is still a long way to go for technicians and quality involved engineers to comprehend regulations thoroughly and clearly.

### 9 - REFERENCE NOTCH METHOD

Transverse wave examination using the echo reflected by a reference notch applies only to hollow cylindrical parts from families 3a and 3b whose ratio of outside diameter over inside diameter is at least equal to 1,6.

Fig. 14 Excerpt from NF-A04-308 [2]

Fig. 15 Retest the housing surface



## 3 Conclusions

The three examples above are typical problems confronted in RVI manufacturer processes. Some of them, like plates and forged pieces testing questions for instance, can even be used as feedbacks for other main equipments in nuclear island like RPV/SG, etc. Most of these problems have been detected at very late period of the manufacturing circle, adding the difficulties to address them for missing the best problem-solving time. So for projects like nuclear power stations, each person involved, especially those technicians and quality surveillances, should comprehend the regulations and specifications clearly. Last but not the least, communications and discussions with designers and owners can help solve the problems effectively and efficiently.

## References

1. NF EN 10307-2001 <Non-destructive testing-Ultrasonic testing of austenitic and austenitic-ferritic stainless steels flat products of thickness equal to or greater than 6 mm (reflection method)>
2. NF-A04-308-88 <STEEL FORGINGS ULTRASONIC TESTING Inspection methods-Limits of testing>

# Risk Analysis on Holes Machining and Inspecting of RVI as One of the Main Equipments in Nuclear Island

Yingpeng Liao

**Abstract** As one of the main equipments in nuclear island, Reactor Vessel Internal (abb: RVI) provides space for nuclear fuel assemblies installment and location, steers CRDM (Controlling Rod Drive Mechanism, one of the main equipments in nuclear island) to control the start-up, power adjustment, and shutdown of the reactor, leads a channel for coolant to the reactor core and dominates the rate of flow to assure the normal running of the first circle in the reactor, shields RPV (Reactor Pressure Vessel, another main equipment in nuclear island) from radiation, and supports the reactor both during normal and emergency conditions as well. There are series of screw holes and pinholes in the surface of RVI, ensuring the accurate positioning of baffles and formers (which points out the foundation of the functions RVI operates in the core mentioned above). These holes are with different dimensions and diverse types, which making machining them a tough task to accomplish. This essay focuses on the machining and dimension inspection processes of these holes, establishing a risk-prevention system to distinguish the technical risks, and formulating corresponding actions to control the final quality. Besides, the machining processes, dimensional testing technology and modularization management mentioned in this essay can be used as a beneficial feedback for technicians and quality surveillances involved in the nuclear power field as well.

**Keywords** RVI · Holes machining · Risk-prevention system · Modularization management

---

Y. Liao  
China Nuclear Power Engineering Co. Ltd., Shenzhen  
GuangDong Province, People's Republic of China

Y. Liao (✉)  
China Nuclear Power Engineering Company (CNPEC)  
Quality Surveillance Engineer, Yang Guang Avenue in  
Jiang Xia District, Wuhan City, Hubei Province, People's Republic of China  
e-mail: liaoyingpeng@cgnpc.com.cn

# 1 Introduction

As one of the eight main components in nuclear power plant, Reactor Vessel Internal (abb:RVI) plays an important role both during the normal operation and emergency shutdown periods. Generally speaking, RVI is composed of two basic structures: Core support structures (CSS) and Internal structures (IS): Core support structures provide direct support or restraint of the core, whereas Internal structures are all other structures within the reactor vessel except core support structures [1].

Divided by spacial relations, upper Internals and lower Internals are the two main parts to form RVI as a whole, here is the functional performance RVI plays in the plant (see Figs. 1 and 2).

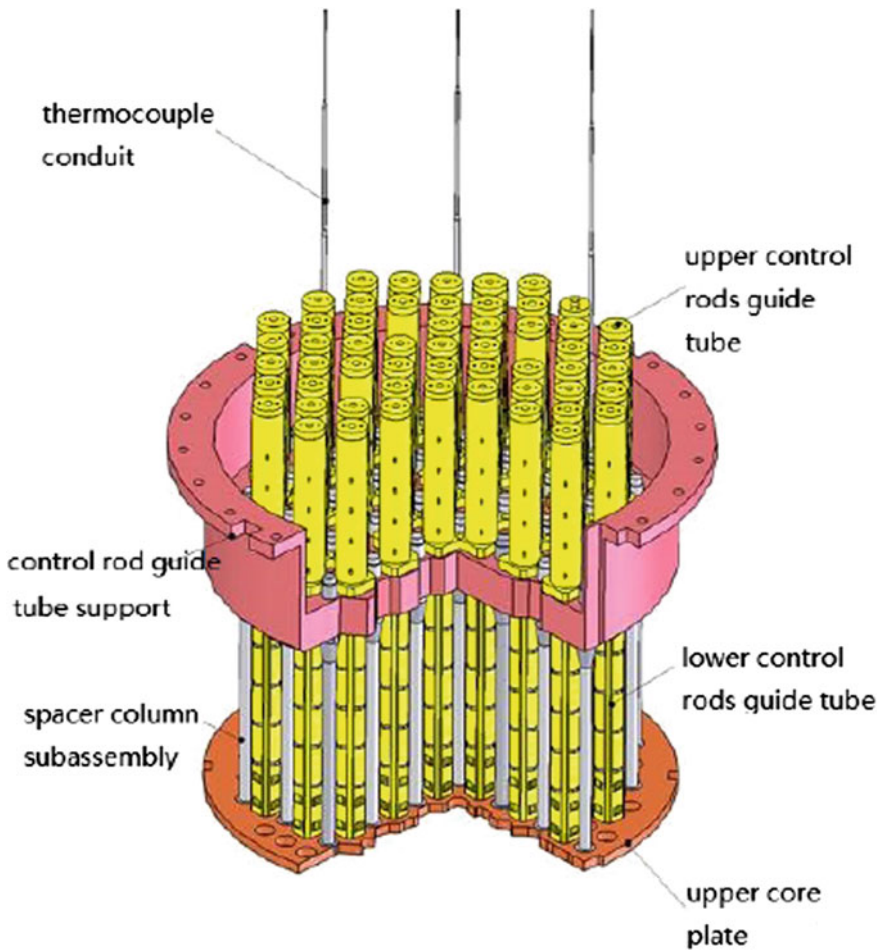


Fig. 1 Functional performance RVI

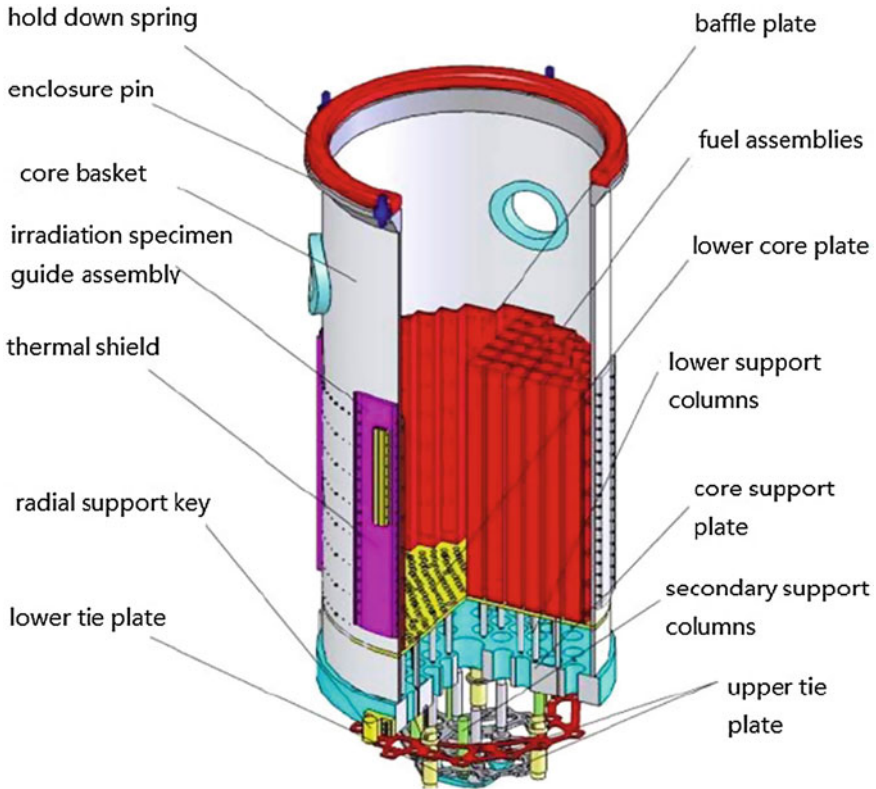


Fig. 2 Alignment for the fuel assemblies

- Provide support and alignment for the fuel assemblies;
- Direct coolant to fuel assemblies;
- Provide guidance for the control rods;
- Provide support and alignment for instrumentation;
- Provide radiation shielding for the reactor vessel;
- Transmit loads from the reactor internals to the vessel;
- Accommodate differential thermal expansion with respect to vessel;
- Provide cooling flow to the reactor vessel head plenum;

Baffles and formers assemblies are connected with RVI in the form of bolts and pins, forming a compact space for fuel assemblies location. The machining of screw holes and pinholes is a tough task to accomplish for every RVI manufacturer for the requirements of huge quantities, different sizes, and high accuracy of these holes. History tells that positional or dimensional errors have already happened in nuclear power projects like HONG YANHE, NING DE, and FANG CHENGGANG, and once incidents like this occur, they can easily become the problems influencing the



**Fig. 3** System runs

first-grade milestone in nuclear power site. After a detailed analysis, reasons that may cause the machining errors had been summarized as follows:

- Dislocation has already existed in rough machining period for holes in baffle-former assemblies and holes in RVI;
- Adjusting the center repeatedly in holes-matching period aggravates the tiny deviations in former previous stages;
- Tool/cutter wear;
- Other reasons like human errors;

To protect the product quality and ensure that each reasons been recognized above can be prevented ahead, we establish a risk-prevention system, formulating precautions for every potential risks. See Fig. 3 for details about how this system runs.

## 2 Implementations

### 2.1 Before Machining

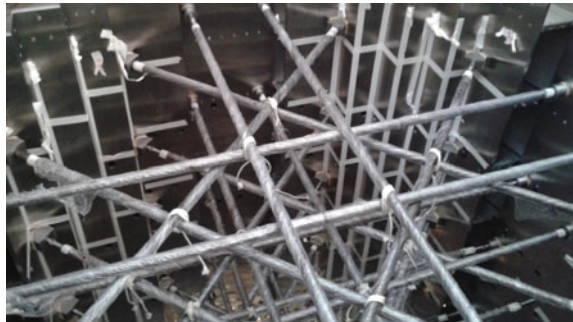
Making sure the baffle-former assemblies are correctly located in RVI is the priority to do before final match-machining and inspection. If oversize of the holes has already existed in spare parts, then it is indispensable to confirm that these errors have no influence with final machining or can be removed by further operations. We made this risk on the checking lists (see part of the lists in Fig. 4) and completed the very first step before final machining.

As there are large vibrations during match-machining process [2], baffle-former assemblies should be tightly fixed in RVI with temporary jigs, this is another vital preparation we should be aware of before machining (see Fig. 5 for details).

		一象限 (0° ~ 90° 区间) (参见: 图NPC-44200-07-00(3012) 剖面AA)																
周向 (0° +) →	轴向高度 ↓	3	8.5	14.75	18.25	25.25	29.25	34.5	39.75	47	50.25	55.5	60.75	64.75	71.25	75.25	81.5	87
243.6		23	23	25	22	10	20	25	23	22	24	22	40	30	22	24	20	24
803.1		42	23	28	30	12	① 36-60	40	25	27	23	37	45	30	30	30	24	20
1325.1		25	20	24	40	25	20	35	20	25	25	25	60	25	30	25	25	25
1847.1		28	21	29	15	10	30	45	40	29	36	38	30	30	29	30	25	28
2369.1		40	22	30	30	18	28	40	35	25	30	35	60	38	30	30	23	24
2891		30	28	30	15	11	30	42	42	28	29	45	30	38	30	30	27	35
3413		40	22	25	15	15	30	40	35	25	30	40	30	35	30	25	26	30
3936	【1】 20	25	29	10	10	30	40	25	24	20	30	30	30	30	28	29	22	27
		二象限 (90° ~ 180° 区间) (参见: 图NPC-44200-07-00(3012) 剖面AA)																
周向 (90° +) →	轴向高度 ↓	3	8.5	14.75	18.25	25.25	29.25	34.5	39.75	47	50.25	55.5	60.75	64.75	71.25	75.25	81.5	87
243.6		22	20	25	25	17	27	20	20	30	20	20	15	15	10	15	10	30
803.1		20	23	25	26	30	28	20	20	30	40	28	18	22	20	15	10	40
1325.1		20	20	20	25	25	30	15	10	30	15	15	10	10	15	25	10	38
1847.1		30	22	22	26	27	30	20	15	38	20	25	20	22	20	20	40	40
2369.1		26	19	23	30	25	23	22	25	30	15	30	13	15	15	18	10	30
2891		30	24	26	30	29	30	22	22	38	25	25	35	20	22	20	45	45
3413		30	20	26	24	29	28	20	20	30	55	20	18	20	20	18	15	35
3936		28	22	22	26	25	28	15	30	35	② 30-70	25	29	17	17	18	35	【2】 22

Fig. 4 Checking lists

Fig. 5 Vital preparation



According to the drawing issued by designer, there are 544 screw holes and 16 pinholes in the surface of RVI, all are used to fix baffle-former assemblies and should be match-machining altogether with holes in baffle-former assemblies. Screw holes are evenly distributed in eight layers of RVI surface, whereas pinholes, on the other hand, are scattered only in the first and the fourth layer counted from top to bottom. Specifically speaking for the first and the fourth layer, 68 screw holes are arranged a circle and pinholes are distributed among them with certain degree relations unsymmetrically, that's may be the point apt to be ignored by technicians and operators because of empiricism (see Fig. 6). That is a risk about drawing digestion and should be annihilated at the very beginning.

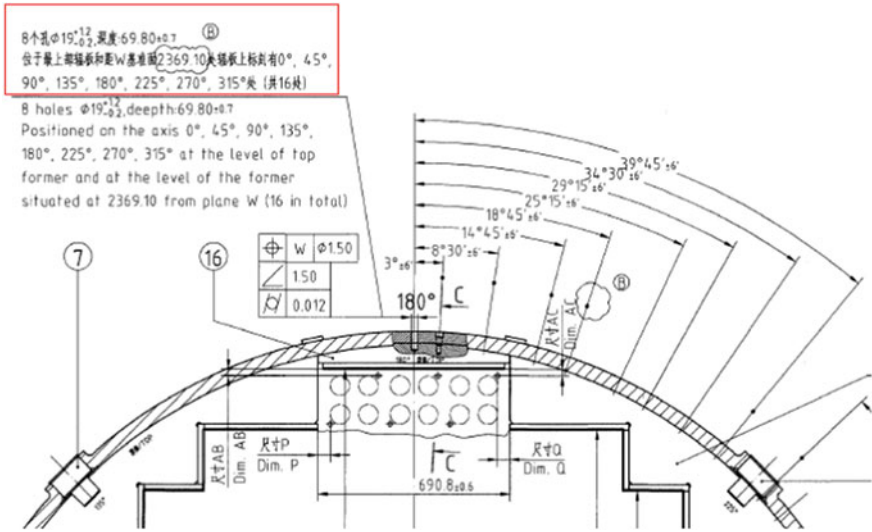


Fig. 6 Technicians and operators

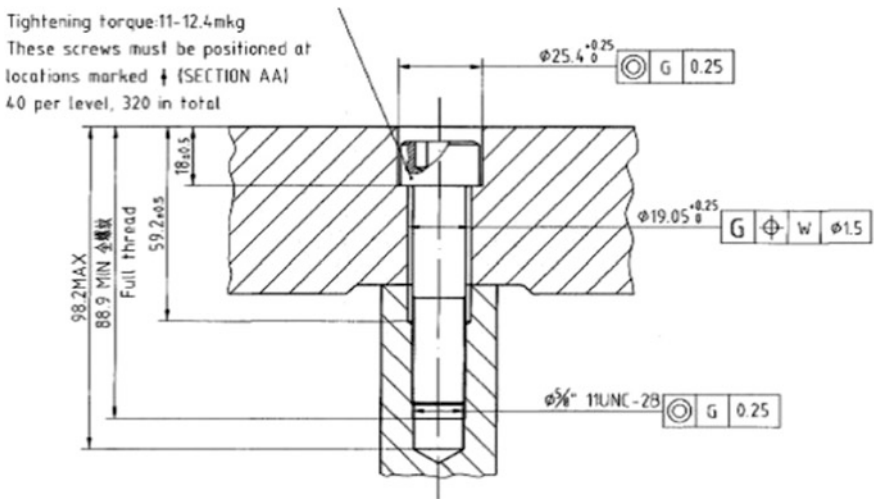


Fig. 7 Inner diameters

## 2.2 Machining

To make the bolts tightly fixed, screw holes are designed in the form of step holes with the bigger and smaller inner diameters 25.4 and 19.05 mm, respectively (see Fig. 7).

Pinholes, on the other side, have a 19 mm inner diameter with a depth of 69.80 mm (see Fig. 6), which means these holes cannot be machined with one



single knife tool at a time. Changing knives means engine bed must transform working conditions continuously between power on and power off, and each time we resume machining process, the priority is to check if the center found in the last circle is still there or not. To confirm the stability of the engine bed, some holes had been drilled in samples before formal machining (see Figs. 8 and 9).

Tool wear is another issue worthy our concern. If the drill wears, two cutting edges are not symmetrical to the axis of the drill bit that may possibly cause dislocation, angulation, or oversize of the holes. Effect of cutting force on the drill bit can be decomposed into axial force along the way drill feedings and the rotating force which can cut material from the base metal. Each component of the force will change if the drill wears after long-time service (see Fig. 10).

**Fig. 8** Stability of the engine bed



**Fig. 9** Formal machining



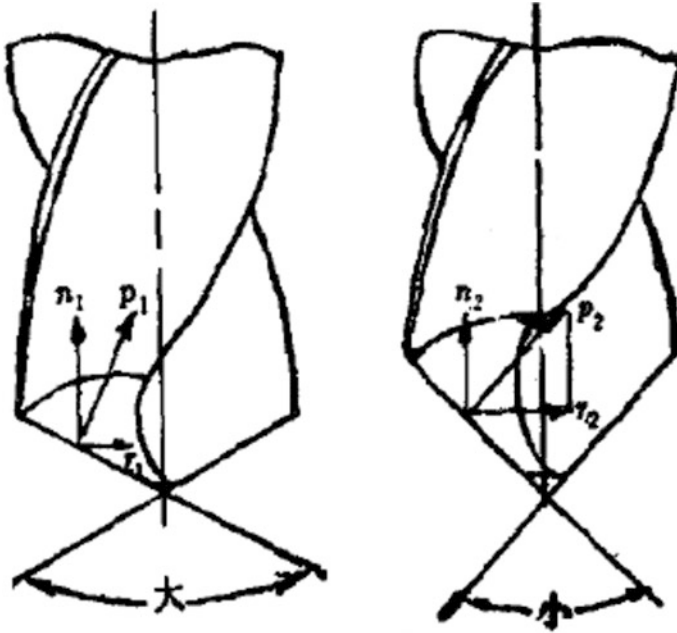
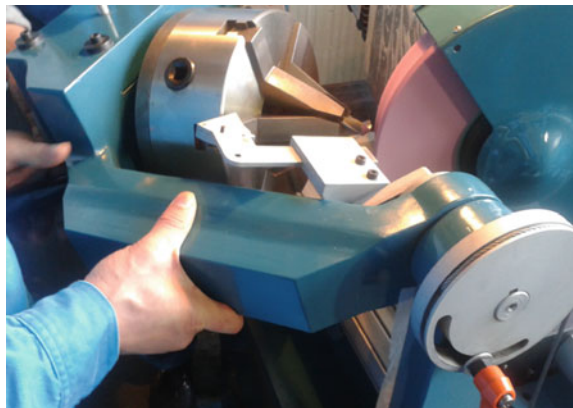


Fig. 10 Drill wears

Fig. 11 Periodic inspection



A new tool can be used to drill 50 holes at most before the first grinding. But in prolonged manufacturing processes, workers may not be aware of the exact numbers of the holes machined, that is the reason why batches of holes been wrongly machined in RVI manufacturing history in other nuclear power projects. To avoid this systematic errors, we made periodic inspection and kept records for the usage of every drill (see Figs. 11 and 12).

**Fig. 12** Kept records



**Fig. 13** Screw tap



**Fig. 14** Feeding process alignment



Besides, the selection and inspection of screw tap are equally important for they directly influence the assembly relations of bolts and holes. For the original hole is deep according to the drawing, we chose a sleeve set in the front side of the screw tap to make the feeding process alignment (see Figs. 13 and 14).

**Fig. 15** Preparations and experiments



**Fig. 16** Coaxiality inspection



### **2.3 After Machining**

It is mentioned above that screw holes are all step holes for precise location, the coaxiality of each hole is the most important factor that may directly influence the assembling of the holes and accurate location of baffles and formers. Besides conventional measuring tools, we made special tools for this inspection one by one, especially after the completion of the first hole machining, which can both verify the effectivity of the tool and the quality of machining after all these preparations and experiments (see Figs. 15 and 16 for details about coaxiality inspection).

### **3 Conclusions**

Seven risk factors had been recognized and more than 10 precautions had been executed during the whole machining and inspecting processes in this RVI manufacturing activities of YANG JIANG nuclear power project, unit 4. A risk-prevention system had been established and each activity involved can be regarded as a module to react in a certain period of time. The benefit is, with a preliminary planning, technicians, quality surveillances and engineers could both see the process as a whole or decompose every single activity into a spare part, which may do great help to control risks, and the result turned out that no non-conformity happened in this whole machining process, which may be a beneficial feedback for RVI manufacturing.

### **References**

1. BLX4420001DNNP44DS <Reactor Vessel Internals Equipment specification>
2. BLX44200043DNNP44DS <The lists of key dimensions of RVI>

# The Disbonding Mechanism Research of Submerged Arc Stainless Steel Strip Cladding

Chengdong Yang, Weibao Tang and Maolong Zhang

**Abstract** The disbonding mechanism of submerged arc stainless steel strip cladding has been studied. The results reveal that hardened layer has been found in transition zone of the welding joint, and the average thickness of the hardened layer is 25  $\mu\text{m}$ . The hardened layer with higher hardness and lower toughness is lath martensite. Type-II grain boundary and porosity appeared in transition zone and martensite layer, respectively, is the internal cause for disbonding. Numerical simulation results indicate that the residual stress improving with the number of the cladding layers increasing, and the residual stress reach to 380 MPa when cladding six layers. Type-II grain boundary as the crack source expands inducing the disbanding, greater residual stress is the external cause for disbanding.

**Keywords** Stainless steel · Submerged arc stainless steel strip cladding · Hardened layer · Type-II grain boundary

## 1 Introduction

It is considered that the nuclear power is the most important developmental direction of energy for its cleaning, sustainable ability of power supplying and less constrained by geographic position [1–5]. Steam generator is the critical equipment of nuclear island, and its function in primary side of nuclear power station is translating the heat of heating medium to secondary side, providing the pressurized steam which dehumidified by steam-water separator for turbine. It is well know that high temperature steam within steam generator will erode the inner surface. In order to improve the ability of corrosion resistance, inner surface cladded by stainless steel is widely used for the steam generator during manufacturing. Submerged arc stainless steel strip cladding has advantages of high deposition rate, high efficiency,

---

C. Yang (✉) · W. Tang · M. Zhang  
Shanghai Electric Nuclear Power Equipment Co., Ltd.,  
Shanghai 201306, China  
e-mail: cdyang@sjtu.edu.cn

better welding appearance, dimensional stability, and without arc radiation; therefore, this technology has been extensively used for stainless steel cladding [6–9]. During the process of submerged arc stainless steel strip cladding, cracks and even disbanding may be happened. Cracks and disbanding has terrible effect for safety performance within the nuclear power station service cycle, and the safety performance is the lifeline that the nuclear power must be ensured. So it has great significance to research the disbanding mechanism of submerged arc stainless steel strip cladding, as it could reveal the disbanding mechanism and optimizes the cladding technology, then preventing the cracks and disbanding, improving the properties of the cladding joint.

In this paper, experiment of submerged arc stainless steel strip cladding has been conducted. Then the microstructure and properties of the transition zone was investigated. Simultaneously, numerical simulation has been used to predict the residual stress of the interface. The disbonding mechanism of submerged arc stainless steel strip cladding has been studied.

## 2 Strip Cladding Experiment

The base metal used for strip cladding is low alloy steel SA508Gr3C12, while the cladding materials are EQ308L and EQ309L stainless steel, the dimension of band-electrode is  $60 \times 0.5$  mm. The welding flux of EQ308L and EQ309L is RECORD INT120 Q5 and RECORD INT101 Q5 respectively. EQ308L and RECORD INT120 Q5 was used for the first layer cladding, the other layers were clad by EQ309L and RECORD INT101 Q5. Three cladding layers were conducted for the left side of the sample, correspondently, six cladding layers were implemented for the right side.

Chemical composition of base metal and filler material is shown in Table 1, whereas Table 2 shows the strip cladding parameters. Post-heat treatment was implemented after the inner surface cladding has been finished, then macroscopic crack has been found in the welding joint. Figure 1 shows the disbanding sample, the crack was expanded form the right side to the left side. Rigorous ultrasonic inspection results reveal there are many welding defects. Another obvious phenomenon in Fig. 1 is that the interface far from six cladding layers area without crack. Exampling from the initial position to the end position of the crack, then the

**Table 1** Chemical composition of base metal and filler metal (wt%)

Material	Elements								
	C	Si	Mn	P	S	Ni	Cr	Mo	Cu
SA508Gr3C12	0.2	0.3	1.3	0.015	0.004	0.7	0.15	0.5	0.1
EQ308L	0.02	0.35	2	0.02	0.015	10.5	20.5	0.04	0.15
EQ309L	0.02	0.35	2	0.02	0.015	13	24	0.04	0.15

**Table 2** Parameters of submerged arc stainless steel strip cladding

Layer	Welding way	Filler metal	Dimension (mm)	Welding current (A)	Welding voltage (V)	Welding speed (mm min <sup>-1</sup> )	Preheating temperature (°C)	Inter pass temperature (°C)
First layer	SAW	EQ309L	60 × 0.5	840–850	32–35	190–200	230–250	230–250
Other layers	SAW	EQ308L	60 × 0.5	820–830	30–33	195–205	/	230–250

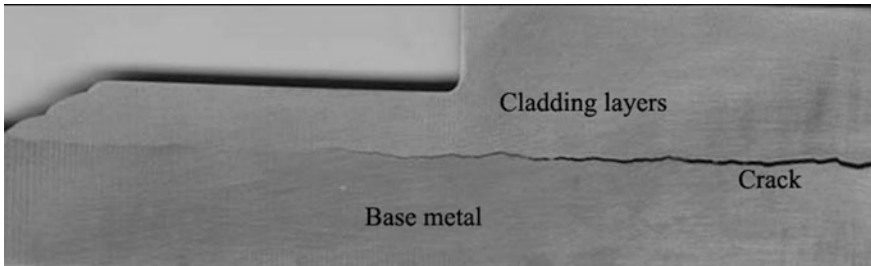


**Fig. 1** Disbonding sample

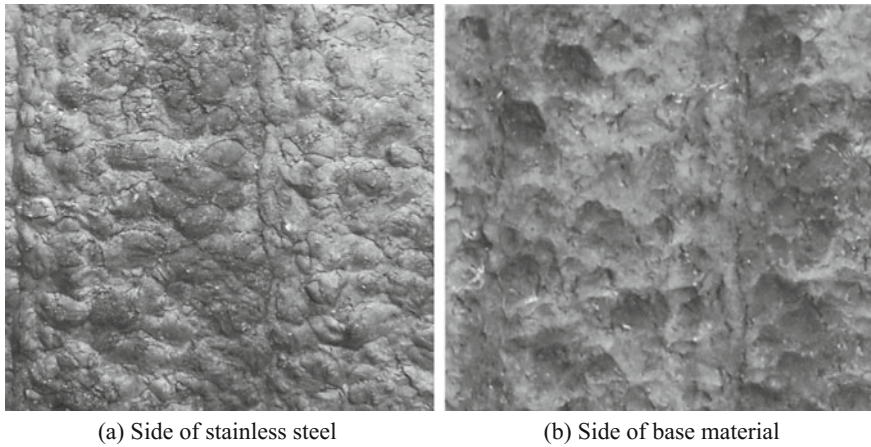


**Fig. 2** Disbonding interface

sample divided into clad and base metal completely, the disbonding surface topography of clad and base metal shown as Fig. 2. Dense embossments distributed in side of the clad, and the corresponding depressions appeared in base metal side. Apparently, the disbanding surface does not has the characteristics of laceration.



### 3 Disbonding Mechanism Analysis

#### 3.1 Microstructure and Properties of Transition Zone

Metallographic examination has been conducted for the welding joint, and the microstructure of each zone is shown in Fig. 3. Figure 3a–c show the microstructure of clad, transition zone, and base metal separately.

Figure 3a clearly indicates that the microstructure of clad is dendritic austenite, and the growing direction of dendritic austenite is against the welding direction. Figure 3c shows the microstructure of base metal is bainite. The transition zone is located between clad and base metal, for the reason of element diffusing, microstructure near both sides of fusion line is different of the clad and base metal, which termed “buffer layer,” shown as Fig. 3b. EDS (energy dispersive spectroscopy) was used to inspect the main elements of the base metal, transition zone and clad, the scanning position and results is shown in Fig. 4. The vertical red line in Fig. 4a is fusion line, the area nearest both sides of the fusion line is transition zone, base metal at the left side while right side is clad. The horizontal yellow line

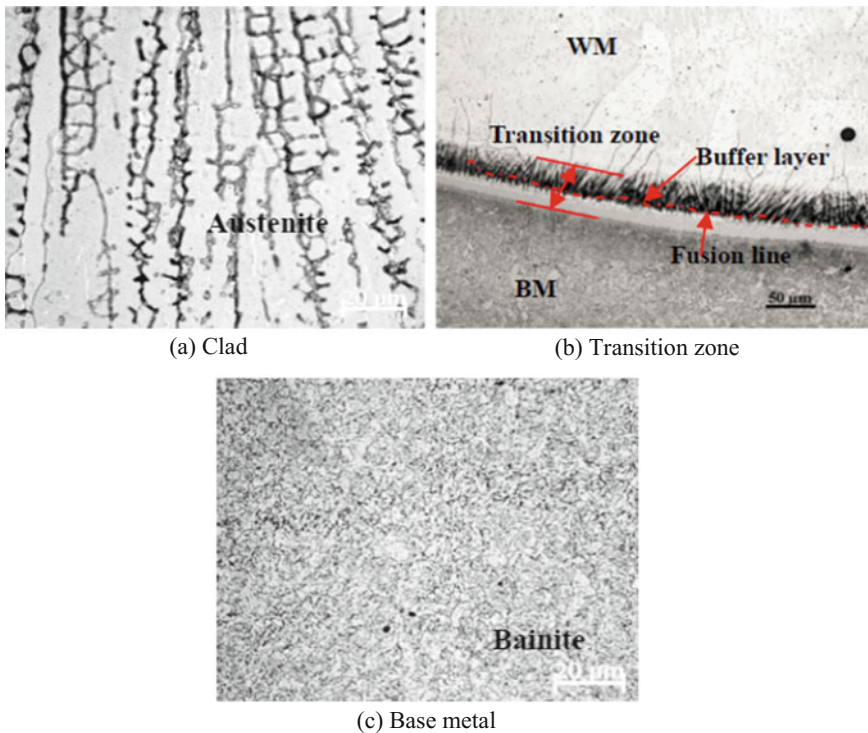


**Fig. 3** Microstructure of welding joint

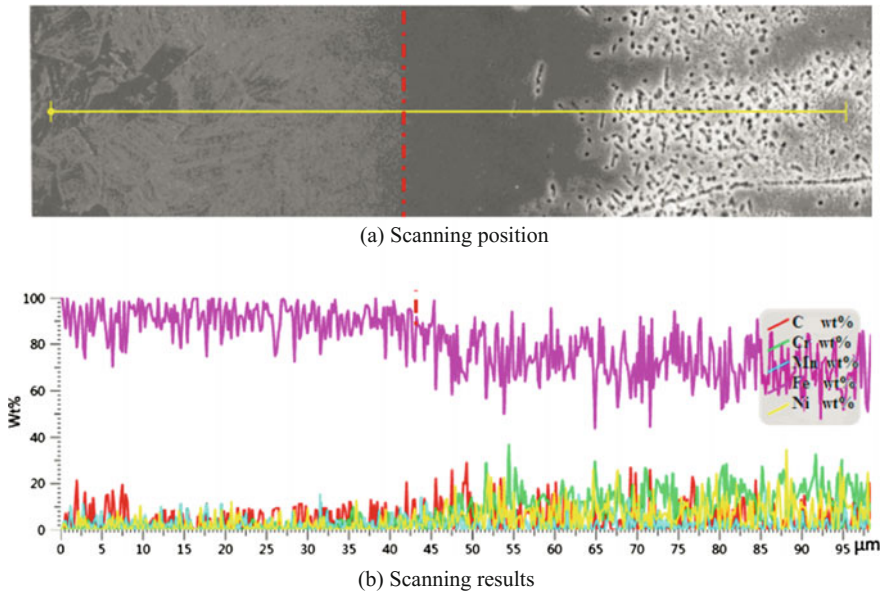


Fig. 4 EDS line scanning

represents the EDS scanning position. Figure 4b shows the EDS results of line scanning.

Comparing the chemical composition of low alloy base metal SA508Gr3C12 and austenitic stainless steel filler metal EQ308L, EQ309L in Table 1, SA508Gr3C12 has higher C content while lower Ni, Cr content, the C, Ni, Cr content is 0.2, 0.7, 0.15 %. Conversely, EQ308L and EQ309L has lower content of C and higher content of Ni, Cr, the C, Ni, Cr content of EQ308L and EQ309L is 0.02, 10.5, 20.5 and 0.02, 13, 24 %, respectively. Figure 4b indicates the content of main elements in base metal, transition zone and clad. An apparent characteristic of Fig. 4b is that the content of C in transition zone is higher than the clad, simultaneously the content of Ni, Cr are higher than the base metal. This phenomenon can be illustrated by element migrating, the C migrates from base metal to transition zone, while Ni and Cr migrate from the filler metal to transition zone.

The microstructure of transition zone is shown as Fig. 5. Figure 5a indicates that Type-II grain boundaries appearing in this area. During the process of stainless steel cladding, in situations in which the base metal is ferritic at temperatures near the melting point and the weld metal is austenitic, normal epitaxial growth may be suppressed. This can result in the formation of Type-II grain boundaries that run roughly parallel to the fusion boundary [10]. These are in contrast to the Type-I grain boundaries that result from columnar growth from base metal grains into the weld metal and are oriented roughly perpendicular to the fusion boundary [11].

In order to confirm the microstructure of buffer layer, SEM (scanning electronic microscope) was used to analyze and the result of SEM is shown in Fig. 5b. It is

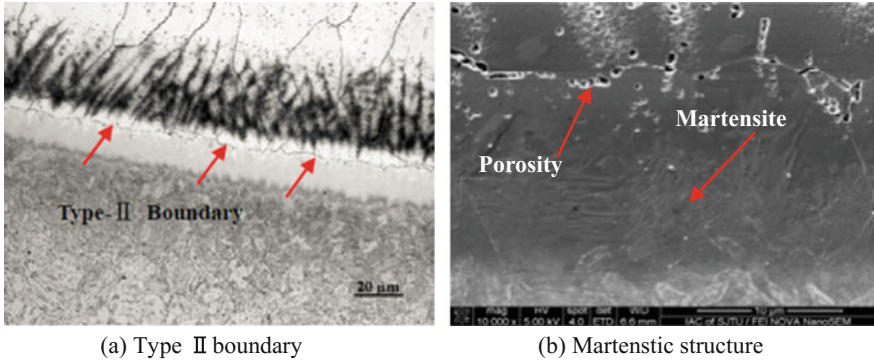


**Fig. 5** Microstructure of transition zone

obviously that the microstructure of buffer layer is lath martensite according SEM result. The C content of base metal is 0.2 %, whereas the content of C in filler metal is 0.02 %. In condition that the base metal has higher carbon content than the weld metal, carbon will diffuse (or migrate) from the HAZ (heat affected zone) to the fusion zone during welding or PWHT (post welding heat treatment). This can potentially result in a narrow martensitic region at the fusion boundary that exhibits high hardness. Furthermore, if the weld metal is high in chromium and the base metal has little or no chromium, the tendency for carbon to migrate from the HAZ into the weld metal during PWHT is very high [12, 13]. According to Table 1, the Cr content of weld metal is 10.5–13 %, and the content of Cr in base metal is 0.15 %. Comparing to the base metal, the weld metal has much higher chromium content, as a result, high tendency of carbon migrating from HAZ to weld seam will be induced consequentially during cladding. The martensitic region was generated in transition zone for the reason of carbon migrating. The thickness of martensite layer was measured and the measurement result demonstrates that the thickness is 25  $\mu\text{m}$ . Another characteristic of Fig. 5b is that there is much porosity on the lath martensite. Type-II grain boundaries in transition zone and porosity in lath martensite is the internal cause for cracking and disbonding.

Micro hardness of transition zone has been measured, the load is 50 g. Figure 6a, b shows the measurement position and result. Measurement result illustrates that the highest micro hardness of hardened zone is 550 HV, which is two times as the base metal and three times as the weld zone. A phenomenon for the micro hardness curve is that the hardness has a minor decrease area in heat affected zone, this can be explained by the carbon migrating and the increasing of  $\delta$  ferritic content. Meanwhile, Nano mechanical properties of each zone has been tested, Table 3 illustrates the tested results, the hardness of weld metal, base metal, hardened zone and buffer layer is 2.46, 3.10, 4.84, 2.99 HV. Distinctly, the hardened zone has the highest hardness of the welding joint, in which is agreement with the micro hardness Measurement result. The residual plastic deformation of weld metal, base metal, hardened zone and buffer layer is 325.2, 248.8, 212.5, 266.6 nm.

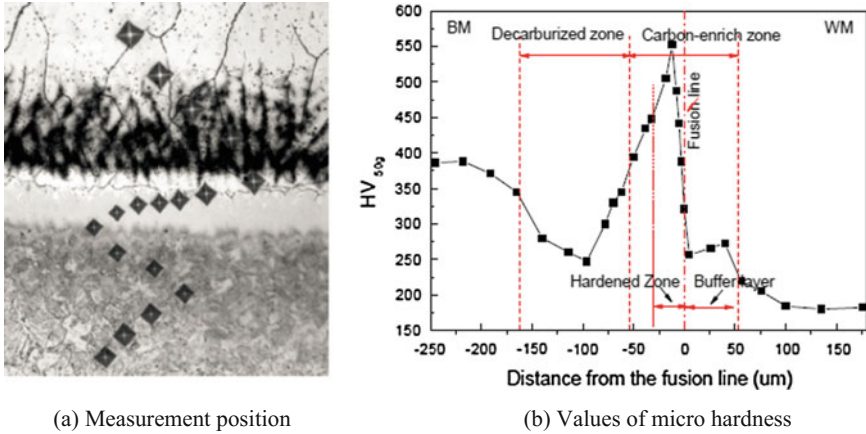
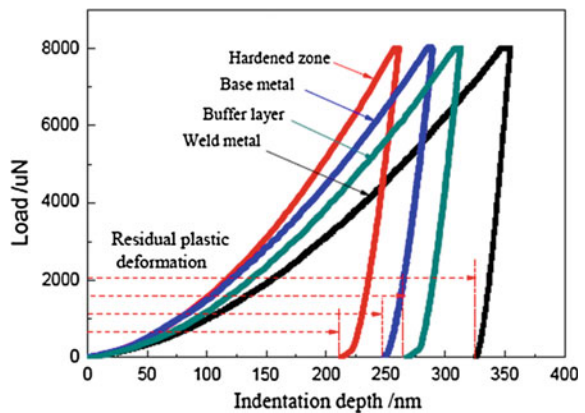


Fig. 6 Micro hardness of transition zone

Table 3 Nano mechanical properties for different zone

Property	Sub-zone			
	Weld metal	Base metal	Hardened zone	Buffer layer
Hardness (HV)	2.46	3.10	4.84	2.99
Young's modulus (GPa)	194.5	174.1	188.3	172.37
Residual plastic deformation (nm)	325.2	248.8	212.5	266.6

Fig. 7 Curve of load and Indentation depth



Higher hardness implies lower plastic, comparing to weld metal, base metal, and buffer layer, the residual plastic deformation of hardened zone decreases 53.0, 17.1, and 25.4 %, respectively. Figure 7 shows the curve of load and indentation depth, it confirms that the hardened zone has the minimal residual plastic deformation.

The higher hardness and lower plastic of hardened zone lead to the lower ability of strain resistance, furthermore, Type-II grain boundary and porosity appeared in transition zone and martensite layer, so the welding joint is easy to happen cracking and even disbonding under large stress.

### 3.2 Numerical Simulation

In this section, the three-dimensional numerical simulation was carried out by using the software ANSYS to research the effect of the cladding layers to the residual stress. Figure 8 shows the finite element model of the cladding. Figure 8a illustrates the geometric model which contents six layers, the first layer, second layer and third layer includes four bead respectively, while the fourth layer includes three bead, the fifth layer contents two bead, and the sixth layer has only one bead. Considering that the temperature gradient of welded zone and heat affected zone is very high, the meshes in these zones are fine, whereas the meshes far away from the welded zone are coarse. The element size around the weld region is 2 mm in both welding and thickness direction.

The heat transfer near the weld molten pool zone is mainly dominated by heat radiation, while in the further place surface is dominantly heat convection. Considering the common effects of radiation and surface heat convection, the formula of compound heat conduction coefficient is shown below [14].

$$h = \frac{\varepsilon_{em} \sigma_{bol} (T^4 - T_{amb}^4)}{(T - T_{amb})} + h_{con} \tag{1}$$

where  $h$  is the compound heat conduction,  $\varepsilon_{em}$  is the radiation coefficient,  $h_{com}$  is the convection coefficient,  $\sigma_{bol}$  is the Stefan–Boltzmann constant,  $T$  is the temperature variable, and  $T_{amb}$  is the surrounding temperature.

Numerical simulation result is shown as Fig. 9. The stress curves demonstrate that the stress in base metal is tensile stress, at the range of 5–13 mm near the fusion line, tensile stress has changed very little. Within the area from base metal to weld metal near the fusion line, the tensile stress decreases dramatically, and the tensile stress

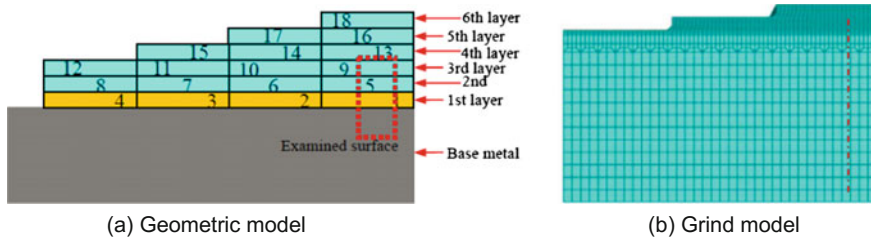
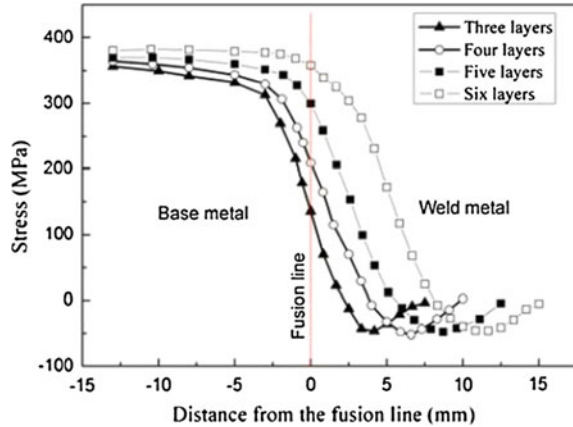


Fig. 8 Finite element model

Fig. 9 Residual stress



even changes into compressive stress. With the distance from the fusion line in weld metal increasing, the stress changes into tensile stress again. Different cladding layers have different distance for this changing. The stress on fusion line indicates that the residual stress of interface improving with the number of cladding layers increasing, the residual stress reach to 380 MPa when cladding six layers, which is greater than the interfacial bonding strength between the clad and the base metal.

Type-II grain boundary and porosity appeared in transition zone and martensite layer, furthermore, the hardened layer has higher hardness and lower toughness. The residual stress of interface improving with the number of cladding layers increasing, when the residual stress greater than the interfacial bonding strength, Type-II grain boundary as the crack source expands inducing the disbonding. The greater residual stress of the welding joint is the external cause for the disbanding of submerged arc stainless steel strip cladding.

## 4 Conclusions

The disbonding mechanism of submerged arc stainless steel strip cladding has been studied, and the major findings are summarized as follows.

- (1) The hardened layer has been found in transition zone of the welding joint, and the average thickness is 25  $\mu\text{m}$ . The hardened layer with higher hardness and lower toughness is lath martensite.
- (2) Type-II grain boundary and porosity appeared in transition zone and martensite layer, respectively, is the internal cause for disbonding.
- (3) The residual stress improving with the number of the cladding layers increasing, and the residual stress reach to 380 MPa when cladding six layers, which is greater than the interfacial bonding strength. Greater residual stress is the external cause for disbanding.

**Acknowledgments** This work is supported by Science and Technology Commission of Shanghai Municipality under Grant No. 14DZ2250300, Shanghai, P.R. China.

## References

1. Corner, A., Venables, D., Spence, A., Poortinga, W., Demski, C., Pidgeon, N. Nuclear power, climate change and energy security: exploring British public attitudes [J]. *Energy Policy*, 2011. 39(9): 4823–4833
2. Toth, F.L., Rogner, H.-H. Oil and nuclear power: Past, present, and future [J]. *Energy Economics*, 2006. 28(1): 1–25
3. van der Zwaan, B.C., Nuclear energy: tenfold expansion or phase-out? [J] *Technological Forecasting and Social Change*, 2002. 69(3): 287–307
4. Carelli, M.D., IRIS: A global approach to nuclear power renaissance [J]. *Nuclear News*, 2003. 46(10): 32–42
5. Pacala, S., Socolow, R. Stabilization wedges: solving the climate problem for the next 50 years with current technologies [J]. *Science*, 2004. 305(5686): 968–972
6. Lu, S. P., Kwon, O. Y., Kim, T. B., Kim, K. H. Microstructure and wear property of Fe–Mn–Cr–Mo–V alloy cladding by submerged arc welding [J]. *Journal of Materials Processing Technology*, 2004. 147(2): 191–196
7. Kuo, I., Chou, C., Tseng, C., Lee, I. Submerged Arc Stainless Steel Strip Cladding–Effect of Post-Weld Heat Treatment on Thermal Fatigue Resistance [J]. *Journal of materials engineering and performance*, 2009. 18(2): 154–161
8. Jinya, K., Hiroyuki, N., Makoto, D., Mitsuyuki, N., Kunio, O., Assessments of residual stress due to weld-overlay cladding and structural integrity of reactor pressure vessel [J], *Proceeding of the ASME 2010 pressure vessels & piping division/K-PVP conference*, 2010, Bellevue, Washington, USA. 1–7
9. Susan, P., Solveig, R., Leif, K., Ann-Charlotte, G. Contributed papers electroslag and submerged arc stainless steel strip cladding [J], *Anti-corrosion methods and materials*. 1998, 45(1): 41–47
10. Matsuda, F. Nakagawa, H. Simulation test of disbanding between 2.25 %Cr-1 %Mo steel and overlaid austenitic stainless steel by electrolytic hydrogen charging technique [J], *Transactions of JWRI*, 1984, 13(1): 159–161
11. Dupont, J. N. Kusko, C. S. Martensite Formation in Austenitic/Ferritic Dissimilar Alloy Welds [J], *Welding Journal*, 2007, 86(2): 51s–54s
12. Lundin, C. D. Dissimilar Metal Welds-Transition Joints Literature Review [J], *Welding Journal*, 1982, 61(2): 58s–63s
13. Dupont, J. N. Lippold, J. C. Kiser, S. D. *Welding Metallurgy and Weldability of Nickel-Base Alloys* [M]. Shanghai Scientific and Technological Literature Press. 2014
14. Abid M, Siddique M. Numerical simulation to study the effect of tack welds and root gap on welding deformations and residual stresses of a pipe-flange joint. *International Journal of Pressure Vessels and Piping*, 2005, 82(11): 860–871

# Welding Process and Welding Consumable of Generation III Nuclear Island Main Equipment

Ju-wen Yang, Shuang-yan Li, Mao-long Zhang, Li-li Wang  
and Wen-yang Zhang

**Abstract** The structural features of generation III nuclear island main components are introduced. Described the welding processes, welding filler metal classification and welding filler metal special requirement for products in detail, and discuss about the Storage requirement and apply requirement of welding filler metal in briefly. These introductions will be help to lay a solid foundation for the subsequent III generation nuclear equipment.

**Keywords** Generation III nuclear · Nuclear island main equipment · Welding filler metal · Welding process

As the security is the premise of nuclear power development, in addition to building some generation II plus nuclear power units, more and more advanced generation III nuclear power units which are safer and more economical are starting to build in the world. Sanmen nuclear power units and Haiyang nuclear power plants which are under construction in China are based of AP1000 technology which is the advanced generation III nuclear power technology designed by Westinghouse (USA).

The AP1000 technology is designed by Westinghouse on the basis of AP600. The AP1000 technology is a two-loop advance passive pressurized water reactor (PWR) that uses a simplified, innovative, and effective approach to safety. The AP1000 nominal net electrical output is 1117 megawatt electric (MWe). The AP1000 plant has a design life of 60 years based on the service life of the reactor vessel. The main safety system of AP1000 plant uses the passive design. Compared with the generation II plus CPR1000 nuclear power products, the structure of the

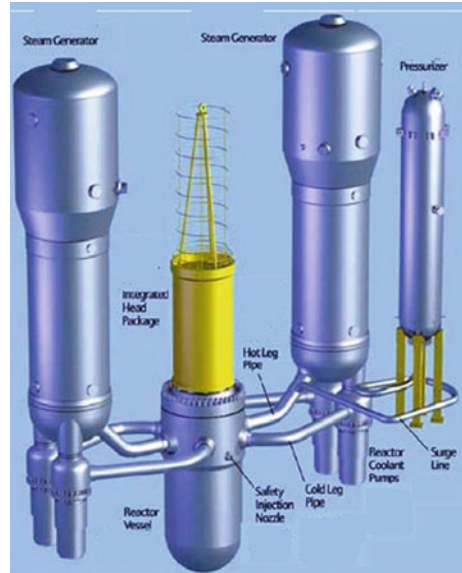
---

J. Yang (✉) · S. Li · M. Zhang · L. Wang · W. Zhang  
Shanghai Electric Nuclear Power Equipment Co., Ltd., Shanghai 201306, China  
e-mail: yangjw@shanghai-electric.com

J. Yang · S. Li · M. Zhang · L. Wang · W. Zhang  
Shanghai Engineering Research Center of Nuclear Power Equipment Welding  
and Examination, Shanghai 201306, China



**Fig. 1** Schematic diagram of AP1000 nuclear island main equipment structure



AP1000 nuclear power products is larger, heavier, more stringent, and more complex in material and manufacturing requirements.

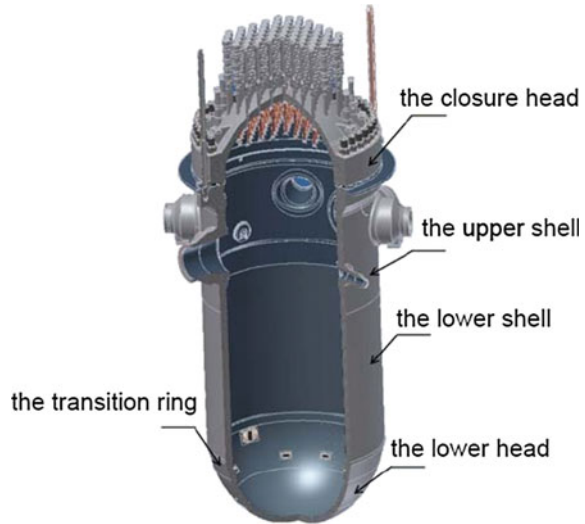
The AP1000 nuclear power plant is designed, fabricated, examined, and tested in accordance with the applicable construction code, which is the 1998 Edition through 2000 Addenda of the ASME Boiler and Pressure Vessel Code, Section III, “Rules for the Construction of Nuclear Power Plant Components”, plus the NRC requirements and exceptions to that version of the ASME Code specified in the U.S. Code of Federal Regulations, 10 CFR 50.55a and any applicable ASME Code cases. The island main equipments of AP1000 nuclear power plant mainly include the reactor pressure vessel, the steam generator, the pressurizer, etc. This article mainly introduces welding process and welding consumable of AP1000 nuclear island main equipments. The AP1000 nuclear island main equipments layout structure is as shown in Fig. 1.

## 1 Nuclear Main Equipment Structure and Material

### 1.1 The Reactor Pressure Vessel (RPV)

The reactor pressure vessel is a vertical cylindrical container. The reactor pressure vessel is divided into the closure head component and the containers component; these two components are sealed by two O-rings and connected by 45 sets main bolts. The reactor pressure vessel structure is shown in Fig. 2. Container components include the upper shell, the lower shell, the transition ring, and the

**Fig. 2** Schematic diagram of AP1000 reactor pressure vessel structure



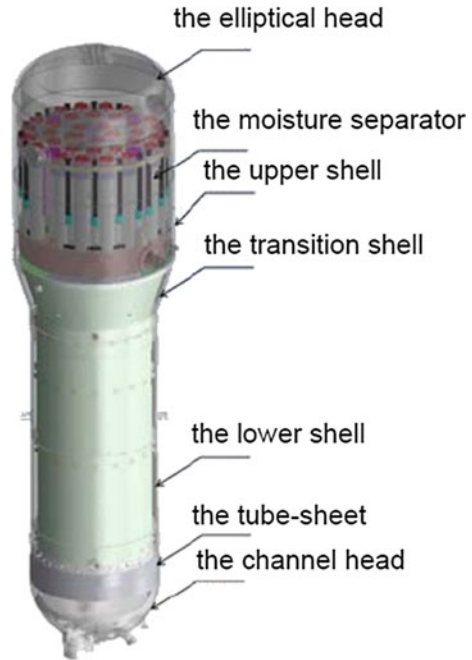
hemispherical lower head. The forging materials of container components are SA-508Gr. 3Cl.1. The inner surface of container components is clad with austenitic stainless steel welding materials for corrosion resistance. The upper shell, the lower shell, the transition ring, and the lower head are connected with low-alloy steel welding materials and the welding process is narrow gap submerged arc welding (SAW). The closure head components are hemispherical and integrated structure is consisting of the following main components:

- A. One-piece head forging of flange and dome
- B. Internal cladding and cladding on the mating surface
- C. 69 control rod drive mechanism (CRDM) assemblies
- D. One vent pipe
- E. Eight Quickloc instrument nozzles.

## 1.2 The Steam Generator (SG)

The steam generator is a vertical shell and U-tube evaporator with integral moisture separating equipment. The steam generator is mainly divided into the upper component and the lower component, the steam generator structure is as shown in Fig. 3. The upper component includes the upper shell, the elliptical head, the moisture separator, the feedwater nozzle, etc. The lower component includes the transition shell, the lower shell, the tube-sheet, the tube bundle, the channel head. The forging materials of the upper shell, the lower shell, the elliptical head, the channel head, the tube-sheet, the transition shell, the feedwater nozzle are SA-508

**Fig. 3** Schematic diagram of AP1000 steam generator structure

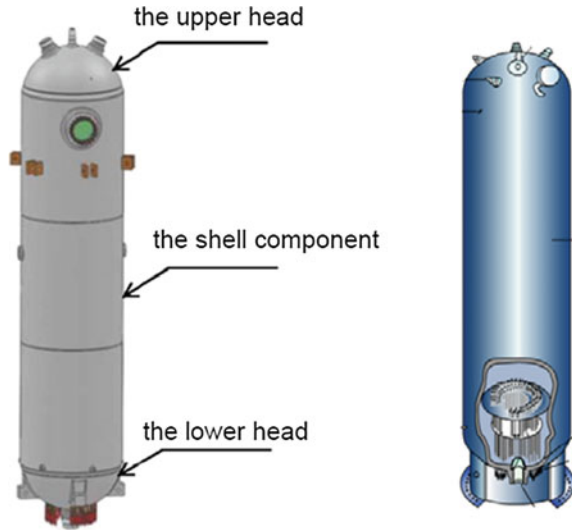


Gr. 3 Cl.2. The inner surface of the channel head is clad with austenitic stainless steel welding materials for corrosion resistance. The surface of the tube-sheet is clad with 690 nickel-based alloy for corrosion resistance. The elliptical head, the upper shell, the transition shell, the lower shell, the tube-sheet, and the channel head are connected with low-alloy steel welding materials, the welding process is shield metal arc welding (SMAW) and narrow gap SAW. The tube bundle is composed of 10,025 pcs 690 nickel-based alloy tube U-bends for which the nominal wall thickness is 1.01 mm. The tube bundle is the weakest part of the primary pressure boundary, and the chemical composition of tube U-bends shall be in high requirement control. Tube U-bends and the tube-sheet after deep hole drilling is connected with hydraulic expansion process and melt sealing welding process to prevent the secondary water to enter the gap between the tube U-bends and tube-sheet.

### 1.3 Pressurizer

The pressurizer is electric heating vertical cylindrical structure. The pressurizer is mainly divided into the upper head, the shell component, and the lower head. The pressurizer structure is as shown in Fig. 4. The forging materials of the upper head, the shell component, and the lower head are SA-508 Gr.3Cl.2. The inner surface of

**Fig. 4** Schematic diagram of AP1000 pressurizer structure



the upper head, the shell component, and the lower head are clad with austenitic stainless steel welding materials for corrosion resistance. The upper head, the shell component, and the lower head are connected with low-alloy steel welding materials, the welding process is SMAW and narrow gap SAW.

## 2 Welding Process

### 2.1 The Welding Process for the Reactor Pressure Vessel

#### 2.1.1 The Welding Process for the Shell Girth Weld

The reactor pressure vessel is the thick wall and large equipment; it requires a high quality welding joint. The conventional welding method is difficult to get a high quality welding joint, so narrow gap SAW is used for welding the shell girth weld, such as the girth weld between the upper shell and the lower shell. The groove shape is U-shaped, the groove bevel angle is  $1^\circ$ , U-radius is R11. The welding position is flat, the welding materials classification is F9P4-EG-F2N and the wire diameter is 4.0 mm. First step is to perform SAW at the outer wall of circular seam, second step is perform back gouging, final step is to continue SAW at the inner wall of circular seam.

Narrow gap SAW is used for welding the saddle-shaped weld, such as the girth weld between the outlet nozzle and the upper shell. There is no angle groove, the gap width is 38 mm. The welding position is flat, the welding materials classification is F9P4-EG-F2N and the wire diameter is 4.0 mm. First step is perform

SAW at the outer wall of circular seam with scaleboard, second step is remove the scaleboard and perform back gouging, finally step is continue SAW at the inner wall of circular seam.

### **2.1.2 The Welding Process for Inner Surface of the Shell, Nozzle, and Closure Head**

SAW is used for cladding the inner surface of the shell, nozzle, and closure head. The welding position is flat, the welding materials classification is EQ309L/EQ308L/flux, and the strips size is  $60 \times 0.5$  mm and  $30 \times 0.5$  mm.

### **2.1.3 The Welding Process for Nozzle to Safe-End**

The weld between nozzle and safe-end is very important for the reactor pressure vessel, because it is very close to the core activity area and shall bear high temperature and high pressure during the nuclear power plant working. Therefore, the weld between nozzle and safe-end shall have the characteristics of high plasticity, high toughness, high corrosion resistance, high neutron irradiation resistance, enough fracture toughness, and enough fatigue resistance.

For the reactor pressure vessel, nozzle to safe-end is mainly the inlet nozzle to the safe-end, the outlet nozzle to the safe-end, the DVI nozzle to the safe-end.

First step is to perform hot wire TIG buttering at the inlet/outlet/DVI nozzle surface (base metal is SA508 Gr.3Cl.1), the welding position is flat, the welding materials classification is ERNiCrFe-7A and the wire diameter is 1.2 mm. Second step is to perform PWHT for the nozzle with buttering. Final step is to perform narrow gap automatic TIG, welding the butt weld between the inlet/outlet/DVI nozzle and the safe-end (base metal is SA182F316LN), the groove shape is U-shapes, the groove bevel angle is  $3.5^\circ$ , U-radius is R5, the gap width is 20–23 mm, the welding position is horizontal, the welding materials classification is ERNiCrFe-7A and the wire diameter is 0.9 mm.

### **2.1.4 The Welding Process for $\Omega$ Seal Weld in Closure Head**

There have total 69 canopy weld seams (also called  $\Omega$  seal weld) of the control rod drive mechanism in closure head, the base metal is SA182 F304LN, the thickness of the base metal is 2.29–2.41 mm.

Automatic GTAW is used for welding these canopy weld seams. The  $\Omega$ -shaped groove bevel angle is  $37.5^\circ$ , the gap width is 0.8–1.4 mm. The welding machine is the special equipment which is made by Jiangsu Huasheng Company because the welding space is narrow and the welding position shall be horizontal. The welding material classification is ER308L and the wire diameter is 0.9 mm.

### **2.1.5 The Welding Process for Quickloc Weld**

Narrow gap automatic GTAW is used for welding the weld for the Quickloc instrument nozzle (base metal is SA182 F304) to head weld build-up connection, the groove shape is U-shaped, the groove bevel angle is  $3^\circ$  at the head weld build-up, the groove bevel angle is  $4^\circ$  at the Quickloc instrument nozzle, the gap width is 20–23 mm. The welding machine is the special equipment which is made by POLYSOUDE Company, the welding position is horizontal, the welding materials classification is ERNiCrFe-7A and the wire diameter is 0.9 mm.

## **2.2 The Welding Process for the Steam Generator**

### **2.2.1 The Welding Process for the Shell Girth Weld**

SMAW and Narrow gap SAW is used for welding the shell girth weld, such as the girth weld between the elliptical head and the upper shell. The groove shape for SMAW is V-shaped, the groove bevel angle is  $30^\circ$ . The groove shape for SAW is U-shaped, the groove bevel angle is  $1^\circ$ , U-radius is R11. The welding position is flat, the welding materials classification is E9018-G for SMAW and F9P4-EM2-M2 for SAW. The diameter of E9018-G is 3.2, 4.0, and 5.0 mm. The diameter of wire EM2 is 4.0 mm. First step is to perform SMAW at the inner wall of circular seam, second step is to perform back gouging and the final step is to perform SAW at the outer wall of circular seam.

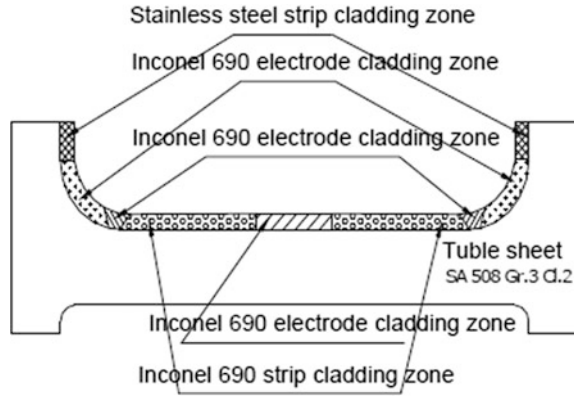
Narrow gap SAW is used for welding the saddle-shaped weld, such as the main feedwater nozzle to the shell D. The groove shape is double-U. The welding position is flat, the welding materials classification is F9P4-EM2-M2 and the wire diameter is 4.0 mm.

### **2.2.2 The Welding Process for Surface of the Tube-Sheet, Inner Surface of the Nozzle and the Channel Head**

The tube-sheet base material is SA-508Gr.3Cl.2 with thickness 783 mm. The schematic diagram of tube-sheet cladding area is as shown in Fig. 5. SAW is used for cladding the tube-sheet surface (except the center area) cladding, the welding materials classification is EQNiCrFe-7A and flux, the size of strip EQNiCrFe-7A is  $60 \times 0.5$  mm. SMAW is used for cladding the center area and the corner area of the tube-sheet, the welding materials classification is ENiCrFe-7 and the diameter of it is 2.4, 3.2, and 4.0 mm.

SAW is used for cladding the upright part of the tube-sheet, inner of inlet nozzle and inner of outlet nozzle, the welding materials classification is EQ309L/EQ308L and flux, the size of strip EQ309L and EQ308L is  $30 \times 0.5$  mm.

**Fig. 5** Schematic diagram of tube-sheet cladding area



SAW is used for cladding the inner of the channel head, the welding materials classification is EQ309L/EQ308L and flux, the size of strip EQ309L and EQ308L is  $60 \times 0.5$  mm.

### 2.2.3 The Welding Process for the Tube to the Tube-Sheet

The size of the U-tube is  $\Phi 17.48 \text{ mm} \times 1.01 \text{ mm}$ , there is total 10,025 pcs U-tubes will be weld to the tube-sheet with nickel-based alloy 690 cladding weld, it is the thick plate and thin tube welding, the tube to the tube-sheet welding joint is as shown in Fig. 6. Greater demands are being placed on the welding process for the tube to the tube-sheet to avoid burn-through or excessive defects at root or bad weld shape in the all-position welding. Considering all these factors, TIG without filler metal is used for welding the seal weld of the tube to the tube-sheet, the welding machine is the special equipment which is made by Polysoude Company, and the shielding gas is mixture gas with helium and argon. Cleanliness shall be controlled before welding and after welding, the tube to the tube-sheet seal welding is as shown in Fig. 7. When the tube welding to the tube-sheet, the end of the tube shall be sit flush with tube-sheet cladding surface. Each welding seam shall be brushed by the stainless steel wire brush for remove the black oxide and then the welding seam surface shall be grinding by cloth wheel or cleaning by the white cotton cloth.

### 2.2.4 The Welding Process for Nozzle to Safe-End

For the steam generator, nozzle to safe-end is mainly the inlet nozzle to the safe-end, the PRHR nozzle to the safe-end.

First step is perform hot wire TIG buttering at the inlet/PRHR nozzle surface (base metal is SA508 Gr.3Cl.2), the welding position is flat, the welding materials classification is ERNiCrFe-7A and the wire diameter is 1.2 mm. Second step is to perform PWHT for the nozzle with buttering. Final step is to perform automatic

**Fig. 6** Schematic diagram of tube-tube-sheet welding joint

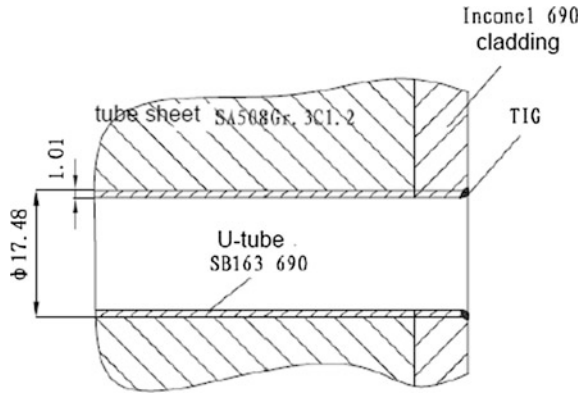


**Fig. 7** Tube-tube-sheet welding



TIG welding the butt weld between the inlet nozzle and the safe-end with base metal SA336 F316LN) or the butt weld between the PRHR nozzle and the safe-end with base metal SB564 UNS N06690, the groove shape is U-shape, the welding position is flat, the welding materials classification is ERNiCrFe-7A and the wire diameter is 0.9 mm.

Overlap shall be controlled during the welding, each bead and each layer shall be clean during the welding.

### 2.2.5 The Welding Process for the Divider Plate to the Stainless Steel Cladding Layer Inside Channel Head

The materials of the divider plate are nickel-based alloy SB168 UNS N06690. K-shaped groove and SMAW welding process is used for welding the divider plate to stainless steel cladding layer inside channel head, the welding material is ENiCrFe-7.



Symmetrical, segmentation and alternately welding sequence shall be used during welding the divider plate to stainless steel cladding layer inside channel head in order to control the welding deformation.

## **2.3 The Welding Process for Pressurizer**

### **2.3.1 The Welding Process for the Shell Girth Weld**

SMAW and narrow gap SAW is used for welding the shell girth weld, such as the girth weld between the upper head and the upper shell. The groove shape for SMAW is V-shaped, the groove bevel angle is 30°. The groove shape for SAW is U-shaped, the groove bevel angle is 1°, U-radius is R11. The welding position is flat, the welding materials classification is E9018-G for SMAW and F9P4-EM2-M2 for SAW. The diameter of E9018-G is 3.2, 4.0, and 5.0 mm. The diameter of wire EM2 is 4.0 mm. First step is to perform SMAW at the inner wall of circular seam, second step is to perform back gouging and the final step is to perform SAW at the outer wall of circular seam.

Narrow gap SAW is used for welding the saddle-shaped weld, such as the girth weld between the manway pad and the upper shell. There is no angle groove, the gap width is 38 mm. The welding position is flat, the welding materials classification is F9P4-EG-F2N and the wire diameter is 4.0 mm. First step is to perform SAW at the outer wall of circular seam with scaleboard, second step is to remove the scaleboard and perform back gouging and the final step is to continue SAW at the inner wall of circular seam.

### **2.3.2 The Welding Process for Inner Surface of the Shell and the Head**

SAW is used for cladding the inner surface of the shell and the head. The welding position is flat, the welding materials classification is EQ309L/EQ308L/flux, and the strips size is 60 × 0.5 mm.

SAW is used for cladding the inner surface of the electric heater area in the lower head, the cladding thickness shall be not less than 64 mm. The welding position is flat, the welding materials classification is EQNiCrFe-7A/flux, and the size of strip EQNiCrFe-7A is 60 × 0.5 mm.

### **2.3.3 The Welding Process for Nozzle to Safe-End**

For the pressurizer, the nozzle to safe-end is mainly spray nozzle to safe-end, surge nozzle to safe-end, safety nozzle to safe-end.

First step is to perform hot wire TIG buttering at the spray/surge/safety nozzle surface (base metal is SA508 Gr.3Cl.2), the welding position is flat, the welding

materials classification is ERNiCrFe-7A and the wire diameter is 1.2 mm. Second step is to perform PWHT for the nozzle with buttering. Final step is to perform automatic TIG welding the butt weld between the surge/safety nozzle and the safe-end with base metal SA182 F316LN) or the butt weld between the spray nozzle and the safe-end with base metal SB564 UNS N06690, the groove shape is U-shaped, the welding position is flat, the welding materials classification is ERNiCrFe-7A and the wire diameter is 0.9 mm.

### **2.3.4 The Welding Process for Electric Heater Sleeve**

Manual GTAW is used for welding the electric heater sleeve (base metal is SA 182 F316LN) to the lower head with nickel-based alloy 690 welding material. The groove shape is J-shape, the welding materials classification is ERNiCrFe-7A and the wire diameter is 1.2/2.0 mm.

Manual GTAW is used for welding the electric heater sleeve (base metal is SA 182 F316LN) to the heater. The groove shape is V-shaped, the welding materials classification is ER316L and the wire diameter is 2.0 mm.

## ***2.4 The Preheat and Interpass Temperature Requirement***

Preheat and interpass temperature shall meet the following provision which base of design requirements and the engineering experience:

- A. For welding P-3 materials, a preheat temperature of 150 °C minimum is required, the interpass temperature shall be between 150 and 250 °C. This preheat shall be established prior to welding and maintained until welding is completed. After the weld has been completed, the preheat shall be maintained until either an intermediate or a full post-weld heat treatment has been performed or, as an alternate, the weld temperature may be maintained at the temperatures 250–400 °C for a minimum of 4 h after which the temperature may be lowered to ambient prior to performing post-weld heat treatment.
- B. For weld overlay cladding and buttering, a preheat temperature of 121 °C minimum is required, the interpass temperature shall be between 121 and 177 °C. For the SMAW and GTAW processes, the preheat may be lowered to room temperature if the deposited thickness is a minimum of 5.0 mm. For multi-arc, strip, or other high heat input automatic welding processes, the minimum preheat shall be maintained for the first and second layers. After all layers of the weld overlay cladding that require preheating are completed or the final cladding is completed, the preheat may be lowered to ambient temperature prior to performing post-weld heat treatment when the weld is maintained at the temperature 250–400 °C for a minimum of 4 h after welding.

### 3 Welding Material

#### 3.1 Classification and Type

Welding material selection is important for weld quality. Determine classification and type of the welding materials which will be used in the nuclear main equipment according to the structure characteristics of the nuclear main equipment, the base metal type, and the design requirements, the information of welding material is as shown in Table 1.

#### 3.2 Special Requirements

Compare with CPR1000 project, AP1000 project has more special requirements in welding materials which are used in main equipment, mainly reflected in the minimum PWHT holding time, chemical composition, mechanical properties of the deposited metal, welding materials storage and using, etc.

##### 3.2.1 Minimum PWHT Holding Time

According to the product manufacturing process, the maximum PWHT holding time is 16 h for the steam generator, 18 h for the reactor pressure vessel and 8 h for the pressurizer. Consider the remaining PWHT time at shipment and remaining PWHT time at nuclear power local site for repairs or alterations or replacement; the AP1000 design requires the minimum PWHT holding time for the welding

**Table 1** Welding material classification and type for nuclear main island equipment

Classification	Type	
Carbon steel welding material	Electrode	E7018
	Wire/rod	ER70S-6
Low-alloy steel welding material	Electrode	E8018-B2/E9018-G
	Wire/flux	F9P4-EM2-M2 F9P4-EG-F2N
	Wire/rod	ER80S-B2/ER100S-1
Stainless steel welding material	Strip/flux	EQ308L/EQ309L
	Electrode	E308L/E309L
	Wire/rod	ER308L/ER309L/ER316L
Nickel base alloy welding material	Strip/flux	EQNiCrFe-7A
	Electrode	ENiCrFe-7
	Wire/rod	ERNiCrFe-7A

materials used in the steam generator that shall not be less than 48 h, the minimum PWHT holding time for the welding materials used in the reactor pressure vessel and the pressurizer shall not be less than 40 h.

### 3.2.2 Chemical Composition

Beside the elements of oxygen (O), nitrogen (N), hydrogen (H), the elements of sulfur (S) and phosphorus (P) are the most harmful impurities in the weld. Sulfur (S) is in the form of FeS and MnS in the weld, FeS can be infinitely dissolved in the liquid iron, but the solubility in the solid iron is only 0.015–0.02 %; FeS will be separated out a lot when molten pool solidification and FeS will be membranous distributed in the grain boundary and it will weakened the connection between the grain. The low melting FeS (melting point 985 °C) in the weld is the important reasons cause solidification cracking (the main form of hot crack) [1]. Base of design requirements and the engineering experience, the sulfur (S) content of the welding materials which will be used in the pressure boundary shall be less than 0.010 %.

Phosphorus (P) is prone to intergranular segregation during the crystallization process, it will cause high phosphorus content in some areas and cold-brittle transition temperature raises, then will cause cold crisp phenomenon; final it will cause the impact toughness, especially low temperature impact toughness is drastically reduced. Irradiation will increase the vacancy concentration, strengthened the diffusion, induce phosphorus (P) and interstitial atom interaction, and accelerated the thermal segregation. Phosphorus (P) atoms diffuse into the grain boundary will cause a large number of phosphorus (P), nickel (Ni), manganese (Mn) enriched grain boundary segregation, and it will cause  $T_{NDT}$  raise, and finally will increase the tendency of irradiation embrittlement [2]. Base of design requirements and the engineering experience, phosphorus (P) content of the welding materials which will be used in the pressure vessel core area shall be less than 0.010 %.

Copper (Cu) is precipitation strengthening element which can improve the yield strength of the material and play a role in strengthening the weld [3], at the same time copper (Cu) is the element that increases the tendency of irradiation embrittlement. Base of design requirements and the engineering experience, copper (Cu) content of the welding materials which will be used in the pressure vessel core area shall be less than 0.06 %.

Nickel (Ni) is an effective element to expanding the austenitic phase, refining the grain, spheroidized carbide, ensure comprehensive performance and improve the hardenability. But nickel (Ni) is easy to form low melting eutectic with sulfur (S), phosphorus (P), titanium (Ti), niobium (Nb) and so on. It will promote the formation of hot crack [2]. Nickel (Ni) will increase the tendency of irradiation embrittlement. Base of design requirements and the engineering experience, nickel (Ni) content of the welding materials which will be used in the pressure vessel core area shall be less than 0.85 %.

In order to facilitate the maintenance of nuclear power plant and reduce the harm of emission elements to human body, the cobalt (Co) is not allowed to add and the cobalt (Co) content shall be controlled in the materials which are used in the nuclear power plant because cobalt (Co) will increase activation cross-section. Base of design requirements and the engineering experience, the cobalt (Co) content of the nickel-based alloy welding materials and stainless steel welding materials shall be less than 0.05 % when used in the reactor pressure vessel and shall be less than 0.10 % when used in the steam generator or the pressurizer.

### 3.2.3 Mechanical Properties of Deposited Metal

AP1000 has divided cladding into structural cladding and non-structural cladding.

AP1000 design requirements for mechanical properties of the stainless steel structural cladding deposited metal is as shown in Table 2. The existence of sigma phase in austenitic stainless steels may significantly reduce their ductility and toughness. The sigma phase is formed in the temperature range between 565 and 925 °C. Factors contributing to the rate of formation of sigma phase include the amount of ferrite, time in the sigma phase transformation range, prior cold working, variation in composition due to progressive solidification, high chromium content, and the presence of ferrite stabilizing elements, particularly molybdenum, columbium, and titanium. 309L welding material have high chromium content and high ferrite content, and 309L deposited metal shall suffer more than 40 h PWHT in the temperature range between 595 and 620 °C, these reasons will cause sigma phase transformed a lot, so the plasticity and impact toughness of 309L deposited metal are poor, the elongation of 309L deposited metal is usually less than 10 %. Because of the above reason and considering 309L is only used as a transition layer on the product, finally the joint tensile test instead of all weld metal tensile test and the joint tensile test requirement is as shown in Table 2.

Nickel-based alloy 690 strip EQNiCrFe-7A and flux is used for cladding the tube-sheet of the steam generator and the electric heater sleeve area of the pressurizer. Nickel-based alloy 690 wire ERNiCrFe-7A with diameter 1.2 mm is used for buttering the nozzle inner surface. These cladding parts or buttering parts are considered to be the structural cladding parts. AP1000 design requirements for mechanical properties of the nickel-based alloy 690 structural cladding deposited metal is as shown in Table 2.

### 3.2.4 Storage and Apply

#### Storage

For low-hydrogen welding materials, covered electrode and rod shall be suitably packaged to ensure against humidity. Extra-low hydrogen welding materials shall be supplied with sealed package. All low-hydrogen SMAW electrodes and

**Table 2** Mechanical properties for stainless steel and nickel base welding material use for cladding

Classification	Type	Tensile properties		
		Tensile strength (MPa)	Yield strength (MPa)	Elongation (%)
Strip/flux	EQ308L EQ309L	≥ 550	≥ 345	≥ 35
Electrode	E308L E309L	≥ 550	≥ 345	≥ 35
Wire/rod	ER308L ER309L ER316L	≥ 550	≥ 345	≥ 35
Strip/flux	EQNiCrFe-7A	≥ 550	≥ 310	≥ 30
Electrode	ENiCrFe-7	≥ 550	≥ 310	≥ 30
Wire/rod	ERNiCrFe-7A	≥ 550	≥ 310	≥ 30

<sup>a</sup>It is not application for joint tension

extra-low hydrogen SMAW electrodes and SAW fluxes shall be stored in unopened hermetically sealed containers until ready for use. After opening, the consumables shall be stored in ovens between 107 and 177 °C unless a different temperature range is recommended by the consumable manufacturer.

### Apply

Only low-hydrogen type consumables shall be used when welding carbon, low alloy steel, martensitic stainless steels, or other steels susceptible to hydrogen embrittlement or cracking.

The electrode shall be kept in a portable electrode barrel with an electric heating function. SMAW consumables shall only be exposed to the atmosphere for a maximum of 2 h unless the consumable has the optional AWS designator “R” for moisture resistance. Then a 9 h limit shall apply. SAW flux may be removed from heated storage for use up to 4 h provided that the flux hopper used in production is covered with suitable protection from moisture and other contaminants.

Consumables shall also not be exposed to moisture (air/atmosphere) in excess of the manufacturer’s recommendations if the recommendations are less than that allowed above. As an alternative to the above exposure limits, the consumable manufacturers recommended that exposure limits may be used to provide that the consumable manufacturer has demonstrated by testing that the consumable will not exceed the required hydrogen limits when exposed to the maximum time/temperature/humidity limits that are recommended.

## 4 Conclusion

AP1000 technology is one of the mainstream of the generation III of nuclear power technology. Safety and economical are the biggest characteristic of AP1000 technology. The structure of the AP1000 nuclear power products is larger, heavier, more stringent and more complex in material and manufacturing requirements.

Based on digesting and absorbing the AP1000 technology, the AP1000 main island equipments such as steam generator, pressurizer, reactor pressure vessel were successful manufactured by independent. It helped us to master and form a set of welding process technology and welding materials technology which met the requirement of AP1000 technology. The mature and advanced welding process technology which used in AP1000 nuclear power equipment manufacture will provide rich experience for CAP1000 project, and also will lay a solid foundation for the follow-up CAP1400 project which designed by independent.

**Acknowledgments** This work is supported by Science and Technology Commission of Shanghai Municipality under Grant No. 14DZ2250300, Shanghai, P.R. China.

## References

1. Welding Society, Chinese Mechanical Engineering Society. Welding Handbook [M], Beijing, China Machine Press, 2011
2. Qiu Tian, Improvement of design life of reactor pressure vessel 60 years based on irradiation embrittlement, Cheng Du, Nuclear Power Engineering, 2013
3. Zhang Yi, Influence of the alloying elements on weld properties, Inner Mongolia: Inner Mongolia Petrochemical Industry Press, 2000
4. LI Zhengcao, Irradiation Embrittlement Mechanisms and Relevant Influence Factors of Nuclear Reactor Pressure Vessel Steels, Shenyang City, Liaoning Province, Science Press, 2014

## Author Biography

**Yang Ju-wen** (1983–), Male, Zhe Jiang Province, China, Bachelor, Welding Engineer, mainly engaged in welding technology of nuclear equipment.

# **Part III**

## **Fuel Cycles**



# Application of Man–Machine System Analysis in the Process Control of Nuclear Fuel Manufacturing

Xiaolin Gu and Shibo Wang

**Abstract** Nuclear fuel is the first barrier for safety operation of the nuclear power plant. High quality of the fuel is the foundation for their good performance in the reactor. Generally, the process of fuel manufacturing includes several steps, chemical conversion, pellets preparation, fuel elements and fuel manufacturing. The process control of the nuclear fuel manufacturing is implemented in the means of person, machine, material, methods, environment and metering, thus to ensure the quality of fuel and to ensure the nuclear security. The target of the implementation of the process control is to set the whole processes under control and no issues occurred that can lead to the process failure. The article discusses the Key points to realize the controlled fuel manufacturing process, based on the theory of man-machine system analysis and fuel manufacturing. Meanwhile, it also gives the actions taken according to the key points to prevent human error, equipment malfunction and the process failure. Different practices of the process control are compared to demonstrate that there are different choices to realize the process control due to different approaches of fuel manufacturing. All the means taken is useful and effective to prevent the malfunction of the processes. The paper also gives the good experiences about the manufacturing process control, such as establish of management procedures to prevent the mis-operation, implement of prevent repair and maintenance to ensure the reliability of equipments etc.

**Keywords** Man-machine system analysis · Nuclear fuel · Process control · Failure · Prevent

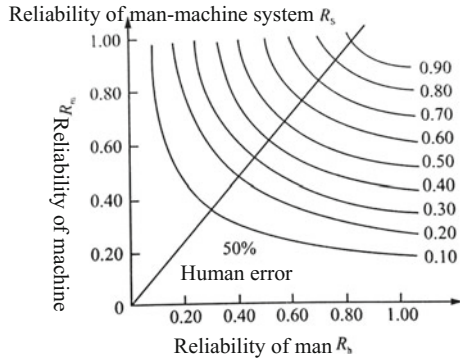
---

X. Gu (✉) · S. Wang  
China North Nuclear Fuel Co., Ltd., Baotou, China  
e-mail: gu730530@sina.com

© Springer Science+Business Media Singapore 2017  
H. Jiang (ed.), *Proceedings of The 20th Pacific Basin Nuclear Conference*,  
DOI 10.1007/978-981-10-2317-0\_43

453

**Fig. 1** Reliability of man-machine system



## 1 Overview

It is well known that the nuclear fuel is the first barrier for the safety operation of the nuclear power station. The quality of the fuel is such important to assure the nuclear safety. The fuel manufacturing process is a complex system that operating through man, machine, environment, and their interactions. The process of fuel manufacturing will be realized following the designed process and management requirements if the man, machine, and environment fit well, and then the quality of fuel is assured. The article describes the major points chosen to perform the process control during the nuclear fuel manufacturing to avoid the human error, malfunction of machine, and management failure based on the man-machine system analysis principle. Change “settle the problem” to “prevent the occurrence” and thus to ensure the quality of process control and products.

## 2 Man-Machine System Analysis and Process Control of the Fuel Manufacturing

### 2.1 Man-Machine System Analysis

Man-machine system is a working system which realizes the designed functions that dominated by man, and coordinated and interacted on the machine he controlled. Based on the different characteristic of man and machine, the investigation was conducted to get the proper function distribution, thus to avoid the unsafe behavior of man, and the unsafe situation of the machine. The reliability of the system is ensured by the reliability of man and machine. Figure 1 shows the reliability of man-machine system.

It is know from the figure that, to raise the reliability of man-machine system, the reliability of man and machine must be raised at the same time. Data from the statistic shows that, the reason for the event in industry, 85 % is direct or indirect

due to person factor. The risk for the system can be effectively reduced if the human error, the major reason for the system, is prevented and precautioned.

## ***2.2 Approaches to Improve the Reliability of Man–Machine System***

### **(a) Man**

Strictly obey the procedure and rule is the basic approach to avoid the human error. Improve the working condition and establish the proper environment; perform the technical training to improve the comprehensive ability of the employee. Make them aware of the situation of the item that they operated with to avoid the possible risk, such as design, manufacturing defects and reliability, etc.

### **(b) Machine**

Distinguish the not acceptable units and materials based on the safely operating of operator, which means to reach the tentative safety through improvement of design. Normal means includes, reduce the complex degree to the minimum level, raise the reliability of the units or components in the mechanical system, take full consideration of backup system during design, check the status during operating, change the units or parts that wearing or near the expire date on time.

## ***2.3 Man–Machine System Analysis and Process Control of Nuclear Fuel Manufacturing***

The process of nuclear fuel manufacturing is a comprehensive system that associated function by people, machine, material, processes, environment, and metrology. The process of manufacturing and all the management functions taken to realize the process control build up the process of the fuel manufacturing. The process of manufacturing requires the qualified person to implement the manufacturing and inspection of the fuel with accepted materials through the proper running of the equipments under the defined processes parameters. To avoid human error and malfunction of equipments are the key points in this part. To avoid the management process failure is the key point.

### **(a) Avoid of human error.**

- First, the standard or requirement for the task must be clearly defined, since it is the reference of the working.
- Second, the necessary basic conditions must be provided, including the relative operating and safety and quality training, good equipments, accepted materials, etc.
- Avoid cross-operation during design.

- Take full considering of sequence of implement.
- Cross-check, self-check, and inspections shall be designed in the system.
- The tools and means to avoid human error must be established and implement to prevent and reduce the effect of human error to the process control of fuel manufacturing.

(b) Avoid the malfunction of the equipments

- This part is closely related with people. The potential hazards that may have threat to life and health in the system must be distinguished.
- Analyze that if the advanced equipments is too much requirement for people to operate, since the high level operating requirement out of the ability of operator leads incorrect manipulation and malfunction of the system.
- Necessary alarm symbols, interlocks, emergency stop, and human–computer interaction interface shall be built into the system when the system is designed.
- The routing observation must be conducted to verify the status of operating, especially the key components, to perform the daily and preventive maintenance of the equipments.

(c) Avoid the management process failure

To avoid the management process failure of the fuel manufacturing process, the input, process and output shall be under controlled.

The input includes the design control, purchase and supplier management, etc. Several manage processes shall be implemented and under controlled in the process, includes the organization, responsibility and authorization, training, item control, process parameters control, inspection and tests, nonconformance control, corrective action process, control of records, and audit. For the output of the process, we shall pay more attention to the delivery of the products and technical services to the power plant.

To avoid the management process failure, relative procedures must be established and implemented based on the status of fuel manufacturer. And the tool of process failure mode and effects analysis (PEMEA) shall be used to distinguish the risk. All the means for avoiding of management process failure shall be recorded in written procedures.

### **3 Application Examples of Man–Machine System Analysis in Nuclear Fuel Manufacturing Process Control**

#### ***3.1 Avoid the Human Error***

(a) Establish the suitable environment for working.

- Build comprehensive sets of guides, regulations and procedures, standards to avoid the human error.

Fig. 2 Route card

压水堆核燃料元件厂		AFA3G 导向管组件流通卡				TQR/YS-0191-01 Rev: 00		
流通卡号		图纸号/版本		技术条件/版本				
专项管理 操作卡号		接收代码表		版本( )				
专项管理号		调整批号		PC 管理号		蒸汽批号		
PC 卡 编号	开始管理试样:		开始管理试样:					
	结束管理试样:		结束管理试样:					
系名称	接收代码	设备编号	适用文件	版本	操作内容	结果	执行人	日期
01	( )				制作 PC 样及自校	<input type="checkbox"/> 合格 <input type="checkbox"/> 不合格	20	..
02	( )					<input type="checkbox"/> 完成		
03	( )				蒸汽吹扫、检查	<input type="checkbox"/> 完成	20	..
04	( )					<input type="checkbox"/> 完成		
05	( )				压扁	<input type="checkbox"/> 合格 <input type="checkbox"/> 不合格	20	..
06	( )					<input type="checkbox"/> 完成		
07	( )					<input type="checkbox"/> 合格		
08	( )					<input type="checkbox"/> 合格		
09	( )					<input type="checkbox"/> 合格		
10	( )				漂洗	<input type="checkbox"/> 完成	20	..
11	( )					<input type="checkbox"/> 完成		
12	( )					<input type="checkbox"/> 合格		
13	( )				表面状态 过程自校	<input type="checkbox"/> 合格 <input type="checkbox"/> 不合格	20	..
14	( )					<input type="checkbox"/> 完成		
15	( )					<input type="checkbox"/> 合格		
16	( )				表面状态 尺寸自校	<input type="checkbox"/> 合格 <input type="checkbox"/> 不合格	20	..
17	( )					<input type="checkbox"/> 完成		
18	( )					<input type="checkbox"/> 合格		
19	( )				专项管理操作卡	<input type="checkbox"/> 完成	20	..
20	( )					<input type="checkbox"/> 完成		
21	( )					<input type="checkbox"/> 完成		
22	( )					<input type="checkbox"/> 合格		
23	( )				流通卡自校	<input type="checkbox"/> 合格 <input type="checkbox"/> 不合格	20	..
24	( )					<input type="checkbox"/> 完成		

系名称填写人:

备注:

- Initiate the report process without punishment. The question attitude shall be carried out during the working. Confirm the reference documents before starting the work; make sure that well understanding of the requirements in the reference documents.
  - When there is doubt, suspend the working till solved.
- (b) Ensure the correctness and suitability of the reference documents.
- Route cards, parameter cards, and operation orders are used to realize the traceability, since each step of operation is defined in the cards; it is a good mode to avoid lack of some steps. See Fig. 2 as example, the route card for guide thimble assembly fabrication.
- (c) Attach importance to each human error occurred and transfer into experience feedback system to prevent the similar error reoccur. That is the root cause of analysis and corrective actions requirement in the quality management system.

**Fig. 3** Two hands operating at tacking station



**Fig. 4** Emergency stop button



**Fig. 5** Alarm light for malfunction

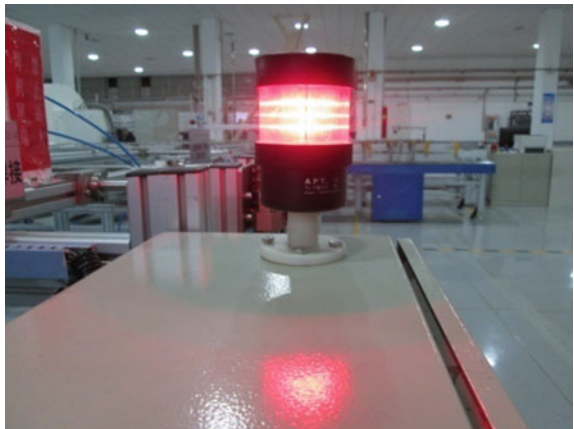
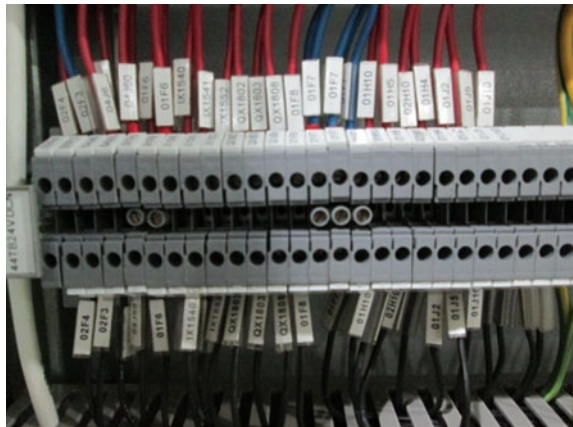




Fig. 6 Information confirm block in computer

Fig. 7 Pipe identification



### 3.2 Avoid the Malfunction of the Equipments

- (a) Improve the safety status of the man-machine system to ensure the reliability of the system.
  - Apply standardized modes for the design as much as possible, thus to reduce the cost of repairing and change of components compared with production.
  - Make the operators obey the operating procedures to properly implement the operating; maintenance, repairing, and grasp the skill of primary determine the reason of the malfunction of the equipments through proper training.

- (b) Take full consideration of the operating of people to avoid the malfunction of the equipment and the effect onto the products. For example,
- the tacking station needs the operator to press the buttons by two hands at the same time to implement the tack welding. See Fig. 3.
  - Equipment has several emergency buttons that located near the operator for easy reach for the case of emergency. See Fig. 4.
  - On the frame of the equipment, alarm light appliances are designed to remind the operator of malfunction. See Fig. 5.
  - Block of confirm will show on the screen of computer to ask for confirm of the information. See Fig. 6.
  - When the parameters are out of the setting range, it will alarm, etc.
- (c) Make the record of maintenance in such table to avoid missing of some steps during the maintenance or repair work.
- (d) The identification of electrical cycle or gas flow is clearly identified to avoid the misconnect. See Fig. 7.
- (e) Implement the obvious label for maintenance or repair work, and make authorized people to monitor to avoid the accident of misoperating.

### 3.3 Avoid the Management Process Failure

The process failure mode and effects analysis (PEMEA) can be applied to avoid the management process failure. It is well known that human error is the main reason of process failure. PEMEA is a comprehensive technology to analyze and distinguish the possible failure mode during the processes and manufacturing, and the effect onto the products if the failure occurred. And obtain actions to reduce or prevent the risk for the manufacturing to make the quality under control and get improved.

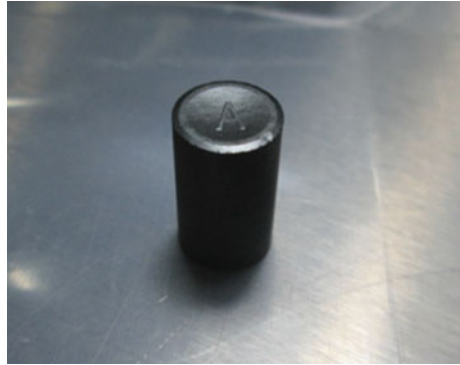
- (a) Purchase and supplier manage
- Perform the supplier assessment before the contract signing to assess the aptitude and ability.



Fig. 8 Status of inspection and test



**Fig. 9** Enrichment identification



- During the production of the purchased material, implement the surveillance on site of supplier;
  - Perform the source inspection and receiving inspection. Implement the audit regularly to assess the running status of the supplier.
- (b) Item control
- Establish the rules of items control.
  - Use different colors to distinguish different products for the customer or different type of items.
  - Implement physical identifications of the items as much as possible.
  - Make area label to identify the different status. Implement the status of inspection and test to avoid the mixing of different lot of items. See Fig. 8 for example.
  - Define characteristics or symbols to distinguish the different enrichment of pellets on the surface of punches of pellet pressing, in order to imply the enrichment management of the pellets. See Fig. 9.
  - Implement the QA release on the materials for production, semiproducts, and final products.
- (c) Process control
- List all manufacturing and examination items in the fuel manufacturing process by documents, and quality control points are set in the documents includes R, document review point, W, witness point of process, and Hold point, not only for the manufacturer, but also for the customer.
  - Implement the confirm step on the key processes, such as skeleton manufacturing, fuel assembly, and the final inspection of the assembly or bundle.

All the actions shall be put into experience feedback system after implementing to ensure the long-term effectiveness.

## **4 Summary**

Man, machine, and environment are inalienable parts in the fuel manufacturing system. All the means and actions implemented are aimed to avoid the human error, malfunction of machine and management process failure, and change the solving of problem to prevent the occurrence of event. Establish the institutionalized human factor analyzes and experience feedback system is a reliable way to improve the reliability of the system and ensure the quality of the fuel assembly.

# Decisioneering on Short- to Long-Term Nuclear Energy System Strategies DANESS v7.1

Luc Van Den Durpel

**Abstract** DANESS provides a simulation environment enriching the decision-making process on short- to long-term intra-nuclear options. Short-term ones being essentially nuclear fuel cycle optimisation with longer term options the increasing synergies one may envisage in keeping nuclear energy as competitive as possible while responding to a multitude of constraints and criteria within the economic, environmental and socio-political sustainability space. Deciding upon and communicating on the various options during the early planning for nuclear energy use, while performing R&D and investment options evaluation, through operational optimisation and fuel cycle options and waste management evaluations, all demand a holistic view on the performance of such time-evolving nuclear energy systems. DANESS, i.e. Dynamic Analysis of Nuclear Energy System Strategies, has been under continuous development during the last 10 years with increasing functionalities and simulation performance embedded in what's now being version 7.1 of DANESS. This paper provides an overview and refers to applications of DANESS v7.1.

**Keywords** Nuclear energy · Simulation · Sustainability · Dynamic analysis · System dynamics · Economics · Waste management · Fissile material management · Recycling · Nuclear scenarios

## 1 Introduction

Whatever nuclear energy system, composed of at least one nuclear reactor, its fuel and associated nuclear fuel cycle, spans a century-long activity with licensing, construction, operation and final waste management being some of the central activities. For newcomer countries, assessing the fuel cycle options available from the international market is already important to assess operational and economic risks associated to nuclear energy use. For larger nuclear power parks, investment analysis

---

L. Van Den Durpel (✉)  
Nuclear-21.Net, Groenstraat 35, 9250 Waasmunster, Belgium  
e-mail: vddurpel@nuclear-21.net

of fuel cycle options and the operational and programmatic optimisation of both reactor park and associated fuel cycle are as important to keep the nuclear option as competitive as possible. Additionally, transitioning towards more advanced nuclear energy systems, including recycling options, demand surely the capacity to assess the nuclear energy system performance over many decades and even up to one century or beyond. For instance, the operational management of used fuels presents already multiple options where an appropriate and trusted technical-economic assessment tool brings clear value in decisioneering on such options. Above all, considering nuclear being a sustainable energy option to address energy supply assurance and climate change, a larger and surely international nuclear energy system with multiple hundreds of nuclear reactors and a variety of nuclear fuel cycle as well as ultimate waste management options becomes increasingly complex to seek local, if not global, optimisation. This optimisation is addressing multiple facets by a variety of stakeholders on economic, environmental and socio-political grounds.

To assess the various technical-economic options in nuclear energy systems, covering both the shorter-term operational decisions as the longer term strategic investment decisions, asks for simulation tools covering the various physical, economic and socio-political facets. Such simulation tools need to fit the decisioneering framework and needs from utilities, governments, waste management agencies and stakeholders at large.

DANESS, i.e. Dynamic Analysis of Nuclear Energy System Strategies, is such a decisioneering simulation tool allowing to address the mass-flows and inventories in time-evolving nuclear energy systems as well as the economic performance of such systems and the various short- to longer term options available [1–7].

The latest version, available since early 2016, is a completely overhauled version of DANESS embedded into a complete nuclear energy system decisioneering framework. This paper provides a description of DANESS v7.1 and example applications.

## 2 Simulation Models for Decisioneering Purposes

Nuclear energy systems codes have, ideally, to respond to a number of criteria to be considered trustworthy by the different stakeholders in their decisioneering on nuclear energy systems

- (a) *Appropriate level of technical detail*, i.e. the ‘physics’ needs to be right which means that the basic phenomena such as mass-flow balances of various system components has to be sufficiently correct. ‘Sufficiently’ meaning that the level of detail has to be matched to the questions being assessed and this level of ‘sufficiently’ to be clear and well communicated.
- (b) *Understandable* by providing the level of assessment details according the stakeholder needs. For instance, an energy economist would like to see the

typical economic criteria/indicators while relying ‘blindly’ on the correct mass-flow and isotopic composition calculations that do have an impact on nuclear system scenarios (economic) performance; vice versa, a waste management manager would strongly appreciate mass-flows, inventories and composition of the to be managed waste well calculated and trusting on the economics to be addressed correctly as well. This means, among others, that such codes need to relate to internationally renown assessment methodologies but above all have to represent the system scenarios results in appropriate format to the user/stakeholder.

- (c) *Transparent and verifiable in the modelling and results-analysis* ensuring that users/stakeholders can easily trust these codes by facilitating the understanding of the results especially in comparative assessment between nuclear energy system options. This also means that verification and validation of the code is important.
- (d) *Interactive*, i.e. aligned with the dynamics of the decisioneering process as such. Nuclear energy system simulation codes need to be able to provide trustworthy results in rather short ‘interactive’ mode, i.e. less than a few minutes calculation time, allowing to use such codes as part of the learning and sometimes educational process with stakeholders to assess system options. More lengthy in-depth calculations can be considered once such system simulation codes have reduced the options space for in-depth simulations.

Additional though optional considerations are

- (e) *Open source* codes are increasingly common practice in various domains though less in the industrial (nuclear) domain where the verification/validation of codes is crucial to ensure the trustworthiness but also the confidentiality that may be required of certain detailed assessment sub-models and associated data;
- (f) *Database support* is surely an important consideration but not crucial as such from the modelling perspective. Databases with technical-economic characteristics or attributes of the system components are very helpful in speeding up the use of such simulation codes and the use of verified/validated input data;
- (g) *Modular architecture* allowing co-development is very useful though not as such conditional to the usefulness of simulation codes.

Since the early days of development, DANESS focused on criteria (a) and (b) and increasingly developed (c) and (d), by significantly strengthening (a), while using a modular architecture approach (g) and database-support (f). DANESS decided not to be open source but to be modular by providing users and developers the possibility to develop proprietary or detailed sub-models that can be integrated within DANESS while ensuring overall reliability and validation of DANESS.

DANESS is based on the system dynamics simulation package STELLA Professional/iThink [8] where close collaboration between the development teams from iseesystems and DANESS have been ensuring continued strengthening of functionalities in line with the above development criteria.

Today, version 7.1 of DANESS (using STELLA Professional v1.0.3 in 64-bit mode and/or iThink 10.1.2) in full-fledged mode simulating a 100-year nuclear energy system with 20 reactor families (with ‘unlimited’ number of reactors per family) and 20 fuel type families with full mass-flow analysis takes less than 5 min on modern laptop-configurations which has been set as upper-limit to criterion (d).

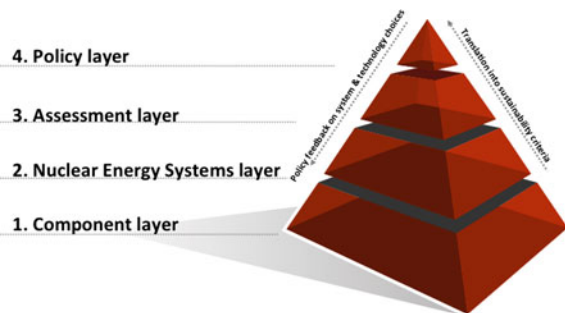
### 3 Daness Architecture

The basic architecture of DANESS is sketched in Fig. 1 showing four interactive model-layers with each of these layers embedding modular structure including specific sub-models.

The ‘*Component*’-layer simulates the various components of a nuclear energy system, e.g.:

- Nuclear reactors with varying degrees of detail on fuel management, i.e. with choice among
  - database or used-specified fresh and spent fuel compositions for the basic DANESS version;
  - a LWR-UOX/MOX and FR-oxide/metallic fuel analytical sub-model and including REPU and Pu equivalence models;
  - a one-point kernel core sub-model;
  - a detailed depletion code using JEF-3.2 neutron data library.
- Nuclear fuel cycle infrastructure from mining until final (geological) disposal of radioactive waste and ‘all’ fuel cycle steps being represented including transport of materials. Again, different levels of detail are possible using specific sub-models
  - While in the basic version, a transfer-function is used on mass-flows and inventories;

**Fig. 1** DANESS basic architecture



- Specific sub-models per fuel cycle facility type are available detailing the facility-specific process-steps allowing for more specific and/or realistic modelling of constraints and facility performance (e.g. decay heat limitations on input/output).

The ‘*Nuclear Energy Systems*’-layer combines the various components into systems and scenarios, i.e.:

- Systems being composed of nuclear reactors and their fuel types that, themselves, are to be integrated in nuclear fuel cycles composed of various fuel cycle facilities. This allocation of fuel cycle facilities to fuel types and those to reactor types can be time-dependent or function of calculated variables specified by the user;
- Scenarios then define the time-evolution of these systems matching various objectives and/or constraints, e.g.:
  - Nuclear energy demand or nuclear reactor park evolutions;
  - Minimal economic costs and/or risks;
  - Limited interim storage periods for spent fuel;
  - Minimal separated fissile material inventories,
  - And many other objectives functions that can be user-defined in the full-fledged version of DANESS.

The ‘*Assessment*’-layer translates the mass-flows, inventories, isotopic compositions, cash-flows and other calculated variables from the previous two layers into assessment criteria and indicators. Those criteria and indicators typically being used within the ‘*Policy*’-layer feeding back into systems deployment decisions which will be executed in the ‘*Nuclear Energy Systems*’-layer. Predefined sets of criteria and indicators are available based on the Generation-IV [9] and the IAEA-INPRO [10] sustainability assessment methodologies. An additional set of criteria and indicators is based on the proprietary Nuclear-21.Net [11] assessment methodology for intra-nuclear options assessment specifically addressing short-term industrial Decisioneering includes the use of real options models to assess decisional flexibility.

The ‘*Policy*’-layer finally translates, iteratively with user or using specific sub-models, the criteria and indicators back into decisional processes simulating objective functions for the nuclear energy system that will impact the scenarios, for instance

- Increasing certain reactor types or fuel cycle options to improve competitiveness or to reduce overall fissile/fertile material inventories;
- Spent fuel interim storage durations impacting economics, mass-balances and waste management options;
- Impact of technology development options per reactor and/or fuel and/or fuel cycle facility.

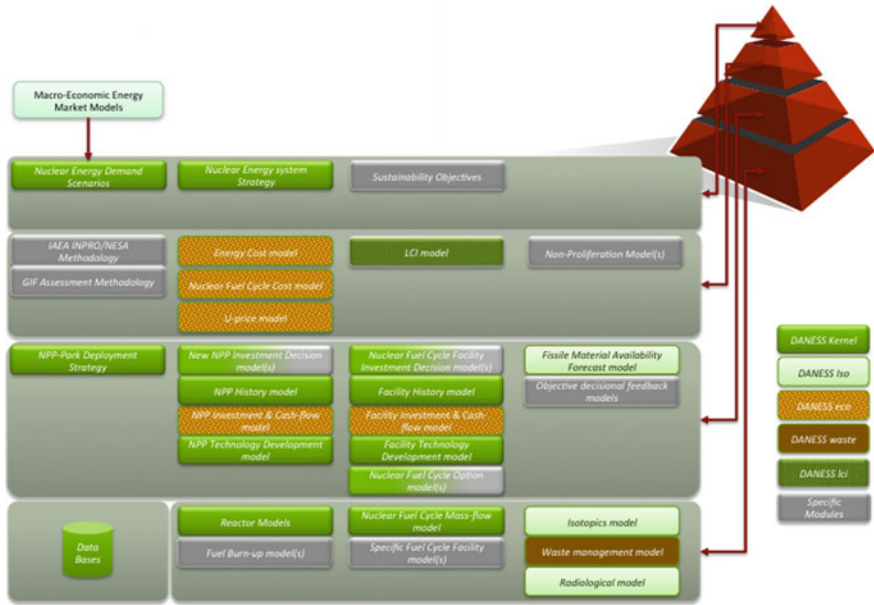


**Fig. 2** Overview of the 29 main models within DANESS (more detailed information on [www.daness.net](http://www.daness.net))

This set of functions per layer is accomplished by a DANESS-model composed of 29 fully integrated (sub-)models (see Fig. 2) with additional sub-models that can be connected or plugged-in according to the user's requirements to enter into more analysis detail.

Especially the capability to connect or integrate more detailed sub-models representing specific technology options or more detailed process-sheets for, for instance, fuel cycle facilities, is a very important feature based on the modularity of DANESS. A library of detailed sub-models is available where users may also develop their own specific detailed sub-model(s) that may remain proprietary and/or shared with other DANESS-users. This library of sub-models relates mostly to fuel cycle facilities such as more detailed reprocessing flowsheets (aqueous and pyro), geological repository footprint analysis, life cycle analysis and proliferation risk metrics analysis as well as specific sub-models detailing radiological aspects in the nuclear fuel cycle.



## 4 Daness Features

DANESS is a fully parameterised model which allows to simulate nuclear energy systems on world, region, country, utility, or even reactor-per-reactor basis with input-sheets describing the nuclear energy system as such. A library of country nuclear energy system cases has been established for DANESS where historic data on reactor park development, nuclear fuel cycle development and anticipated development or deployments is embedded in databases interfacing with DANESS [11]. DANESS users may obviously establish their own specific/proprietary set of simulation cases that may go hand-in-hand with the use of specific (proprietary) sub-models.

As a basic case, DANESS allows to simulate in parallel an ‘unlimited’ number of nuclear reactors grouped into 20 reactor families (each of which are fully parameterisable) combined with 20 fuel families (again unlimited number of fuel batches) and using again a selection of 52 fuel cycle technologies, services or facilities making up the entire nuclear energy system. Though, paralleling multiple DANESS-cases allows to simulate even the largest nuclear energy systems in full depth, i.e. per reactor and fuel type, while allowing intra-nuclear transfers between reactors and fuel cycle facilities, f.i. used fuel pool-to-pad operations and pad-to-repo operations. The relations between reactors, fuels and fuel cycle facility use may hereby be time-dependent by user-specification or as a result of the objective functions defined in the ‘Policy’-layer. Each reactor as well as each fuel cycle facility follows a life cycle from licensing, construction, operation and shut-down up to decommissioning allowing to take into account the inherent dynamic aspects of nuclear energy system deployment scenarios. This is also important in the economic, specifically cash-flow, analysis providing a detailed reactor/facility-specific cash-flow analysis during the entire lifetime of such components.

The nuclear reactors’ in-core fuel management can be detailed according simulation needs, i.e. use of tabled fresh/spent fuel compositions or calculated values based on specific depletion sub-models as mentioned before. DANESS v7.1 continues to use a 111 isotopes-list, i.e. 57 actinides and decay chain nuclides, 52 fission and activation products and two lumped short-lived and long-lived fission/activation product groups. This list of isotopes is adequate for most applications of DANESS but may be changed and/or expanded to a larger set of isotopes if required by certain detailed assessment requirements. The in-core fuel management sub-models are an analytical model, a one-point core model or a more detailed depletion code using JEF-3.2 nuclear data and where verification has been undertaken with reactor physics models.

Uranium and Plutonium equivalence models have been implemented in recycling schemes to provide the prefabricated fresh fuel compositions responding to available separated fissile material inventories. While DANESS comes with standardised values for the parameters for these sub-models, users may implement their own set of parameters to simulate specific reactor models and fuels. A database with

reactor, fuel and fuel cycle facility technologies is associated to DANESS based on publicly available assessment studies of nuclear energy systems.

An important feature of DANESS is the detailed assessment capability of back-end fuel cycle operations. The user may choose to track used fuel batches during a few years or, rather exceptional in multi-decade nuclear energy system studies, to track each individual batch of used fuel until final management. This latter option demands especially a lot of data-management that renders this option only used in very specific detailed assessment studies. Though, as a standard, the time-period of cooling of used fuel in at-reactor pools keeps the fuel-batch history where this used fuel history is then lumped together per month time-steps and per fuel type.

Multi-parameter uncertainty and sensitivity analysis is made possible. Various distributions of parameters can be defined external to and then imported in DANESS which is then operating in batch-mode running multiple hundreds of cases resulting into distributions of key variables and allowing, in post-processing, single-value deterministic or, for multiple parameters, joint sensitivity analysis.

A typical nuclear energy system simulation, whatever number of reactors and fuels, spanning a one-century one-month time-step takes less than 5 min on modern PC or Mac platforms.

Specific sub-models of highest importance are

- Full-fledged fuel cycle mass-flow analysis with full isotopic follow-up allowing to adapt the timing of operations in the nuclear fuel cycle;
- Fissile material equivalence models for recyclable materials as Pu and reprocessed U in various reactors, specifically LWR-MOX and REPU in PHWR recycling;
- Detailed management of used fuel in At-Reactor and interim storage facilities, being wet or dry, and optimisation of used fuel management options with respect to used fuel management provisioning, uncertain futures and technical-economic optima;
- Economic decision-making on fuel cycle options.

## 5 Daness Databases and Results Visualisation

DANESS is data-intensive both in input as in output. To facilitate the usability of DANESS by a variety of user profiles, various tools have been developed and further integrated with DANESS v7.1 (see Fig. 3), i.e.

- *DANESS Attributes-Database* that provides a detailed set of data per country, province, region, utility, and fuel cycle facility of the historic and current mass-flows and inventories in the nuclear energy systems as well as the characteristics or attributes for the technologies used within the system's

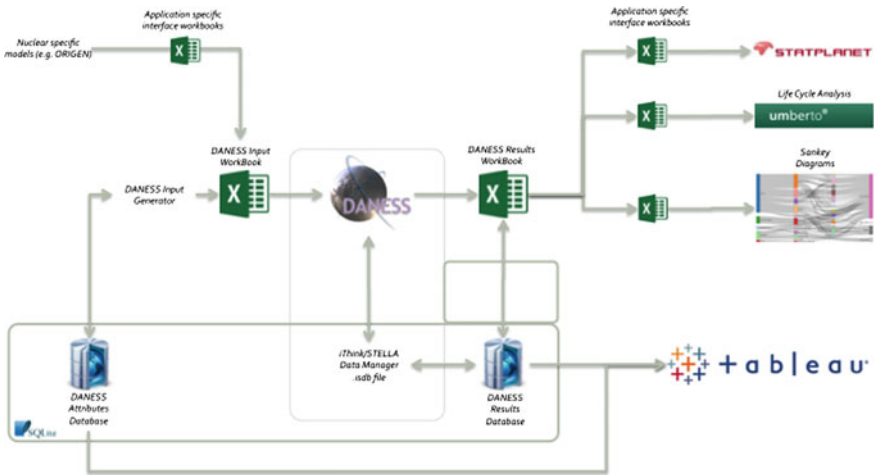
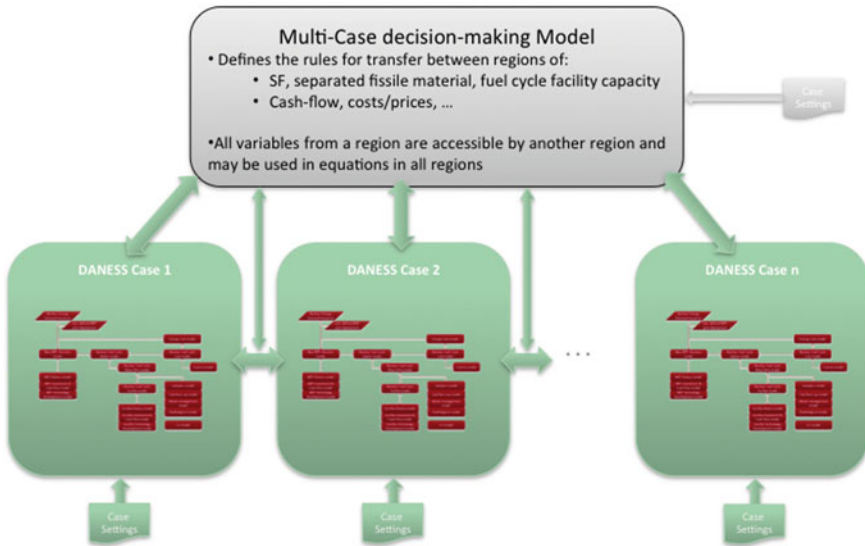


Fig. 3 Input and output to DANESS

components. This Attributes database is as such independent of DANESS-use and is used for other assessment studies as well;

- A *DANESS Input-Generator* facilitating the set-up of a DANESS simulation case. This Input-Generator connects to the Attributes Database as well as the DANESS Results Database allowing to recover settings from different cases and to set-up comparative assessment cases (for instance for uncertainty and sensitivity analysis). The Input-Generator results into an MS-Excel input-sheet typically used by all previous and this version of DANESS. A major development has been the smooth integration of DANESS results with a variety of *data-visualisation tools* but primarily with the Tableau-software [12] rendering the analytics of DANESS results a lot more interactive even allowing on-line publication via web-server and tablet;
- Other interface app’s have been developed to export DANESS-data into sankey-diagram software, life cycle analysis and another geo-data visualisation package StatPlanet [13].

Finally, DANESS can be customised to a specific user-profile by locking the graphical user interface within a specific set of accessible parameters or settings such that less-experienced DANESS-users can use DANESS in a more restricted framework, e.g. educational use, commercial services, ...



**Fig. 4** Multi-regional nuclear energy system simulation by running multiple DANESS-cases in parallel

## 6 Multi-Case Nuclear Energy System Modelling

A unique feature of DANESS v7.1 made possible with the advances of the STELLA Professional and iThink developments since the last two years is to perform simulations with multiple DANESS-cases in parallel, e.g. multi-region, multi-utility, multi-country (see Fig. 4).

This unique feature is very important especially in the new modular structure of DANESS where individual DANESS-cases can be combined together into a 'macro-case' with mass and cash flowing within and between the DANESS-cases. A 'Multi-Case Decision-Making'-model governing these intra-case (e.g. intra-regions) exchanges. This feature is extremely helpful when synergies between (e.g. national) nuclear energy systems are to be investigated though relying on validated individual DANESS-cases providing all the detailed information per DANESS-case (e.g. region, country, utility, ...). Typical application of this functionality is reported in [6, 14, 15].

## 7 Daness-Cases Database

Various levels of detailed nuclear energy system models have already been developed for a number of countries using or intending to use nuclear energy (see Fig. 5). These nuclear energy system models are based on a collection and analysis

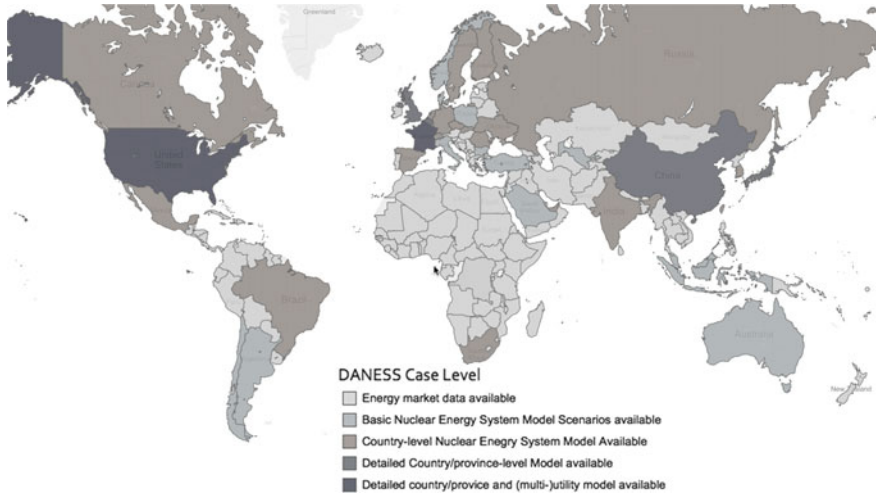


Fig. 5 Available country/utility-specific nuclear energy systems models

of publicly available information and, where appropriate when proprietary models used, based on users provided information. These world, region and country-specific models are now updated annually. These models can be detailed to reactor-specific level or utility-level and be configured for specific assessment needs.

## 8 Example Application: Chinese Nuclear Energy System

As an example of application, reported in more detail in [16], the time-evolving Chinese nuclear energy system has been simulated from the first reactor on with full detail per reactor and fuel being used or projected to be used. In addition, full geographic positioning of reactors, interim storage facilities and future fuel cycle facilities was taken into account allowing, in more in-depth analysis, also to analyse the transport needs for the various nuclear materials throughout the Chinese nuclear energy system.

Based on public data on expected reactor and fuel cycle options, some fuel cycle options relating to the time-evolving reactor park have been assessed specifically focusing, in the short-term, on avoiding saturation of at-reactor used fuel pools and thus timing the deployment of interim storage facilities and/or reprocessing capacity.

Figure 6 provides snapshots of the geographic distribution (shown on province level for sake of readability) of the reactor park (year 2030) and the used fuel inventories over time in Fig. 7. Figure 8 indicates the regional distribution of used fuel inventories beyond at-reactor pool capacity by the year 2030, and this requires

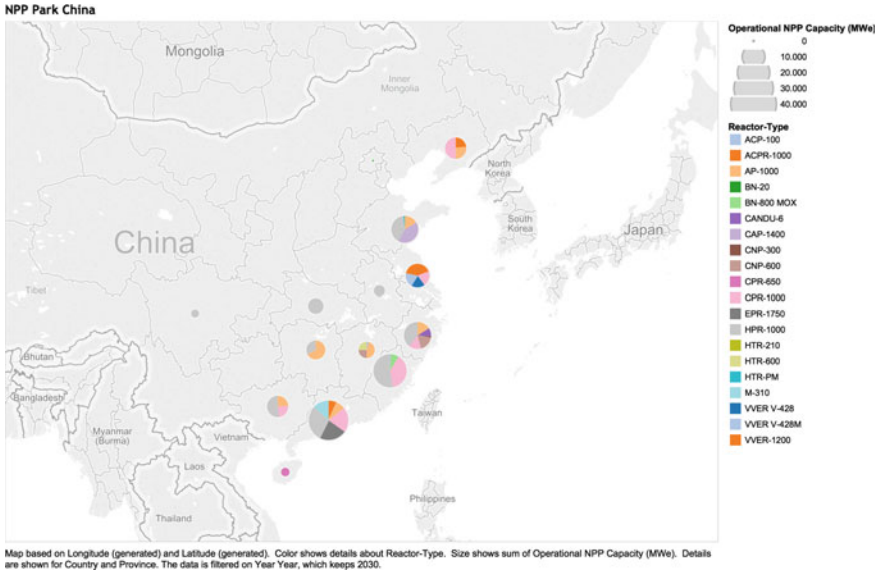


Fig. 6 Chinese nuclear reactor park by the year 2030

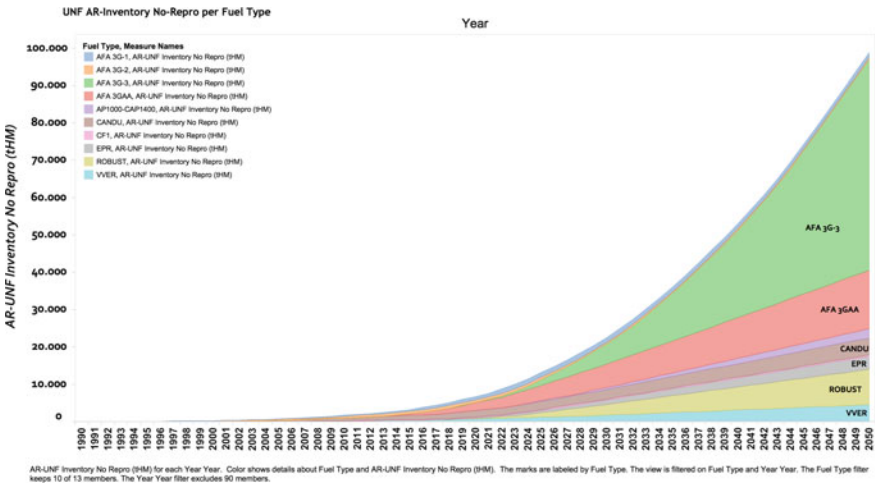
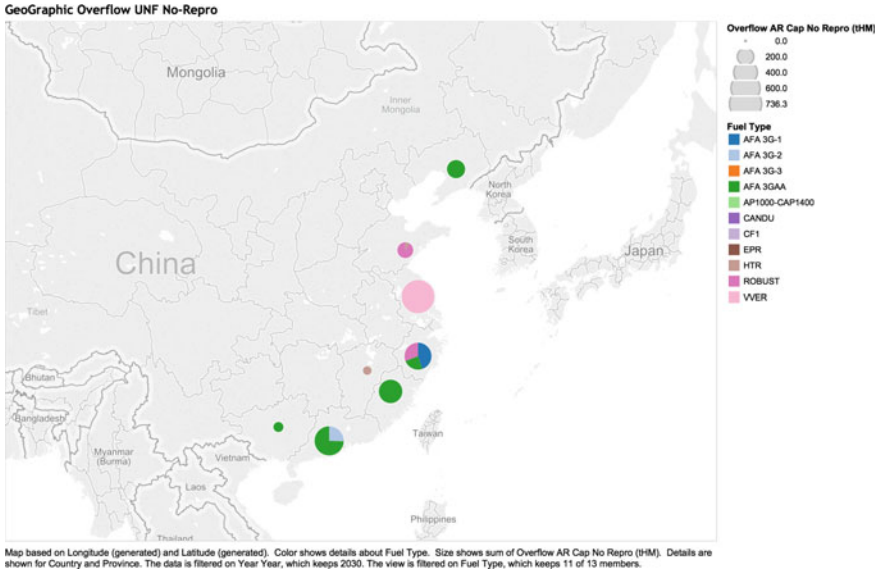


Fig. 7 Chinese used fuel inventory build-up

timely decisions to transfer the used fuel to other facilities. A more in-depth analysis is available in [16].



**Fig. 8** Used fuel inventories requiring evacuation from at-reactor used fuel pools by the year 2030

## 9 Future Developments

The two main developments envisaged for DANESS during the coming year 2015–2016 are to further detail and documents the detailed process flowsheets for, specifically, back-end fuel cycle facilities and recycling schemes, next to, though fully complementary to this, the coupling with other assessment tools valuing the flexibility in nuclear energy systems specifically regards fuel cycle options. A real options models NROM have been developed and is currently being applied to specific cases to assess the flexibility in the (back-end of) the fuel cycle especially relating to used fuel management options given the various technical-economic uncertainties and even unknown timing of operations.

## 10 Conclusions

DANESS has recently been known as a major overhaul of its model kernel and especially also the process up-stream and down-stream of running DANESS-cases. A very important added value being the coupling with regularly updated databases for region/country/utility-specific cases and the analysis of DANESS results next to further detailing the process flowsheets specifically for recycling shemes demands precise modelling of materials' compositions impacting facility flowsheets.

From DANESS v7.1, supported by a shared development roadmap with STELLA Professional/iThink-developers, a more performing dynamic analysis model for nuclear energy system strategies is made available as an essential tool for nuclear energy system decisioneering.

## References

1. L. Van Den Durpel, A. Yacout, D. Wade, H. Khalil, “DANESS, *Dynamic Analysis of Nuclear System Strategies*”, in GLOBAL 2003 Meeting, November 16–20, 2003, New Orleans, LA, USA
2. L. Van Den Durpel, D. C. Wade, H. Khalil, A. Yacout, “*Dynamic Analysis of Nuclear Energy System Strategies for Electricity and Hydrogen Production in the USA*”, in GLOBAL 2003 Meeting, November 16–20, 2003, New Orleans, LA, USA
3. A. M. Yacout, R. N. Hill, L. Van Den Durpel, P. J. Finck, E. A. Schneider, C. G. Bathke and J. S. Herring, “*Dynamic Analysis of the AFCI Scenarios*”, PHYSOR 2004, Chicago, Illinois, April 25–29, 2004
4. A. M. Yacout, L. Van Den Durpel, D. C. Wade, and H. Khalil, “*Scenarios for the Expanded Use of Nuclear Energy*”, 2004 International Congress on Advances in Nuclear Power Plant (ICAPP’04), Pittsburgh, PA USA, June 13–17, 2004
5. L. Van Den Durpel, “*Dynamic Analysis of Nuclear Energy System Strategies: DANESS v7*”, Global2015, September 20–24 2015, Paris, France
6. L. Van Den Durpel, “*Globally sustainable nuclear energy systems with regional competitiveness*”, Global2015, September 20–24 2015, Paris, 2015
7. DANESS, [www.daness.net](http://www.daness.net)
8. STELLA Professional—iThink, Iseesystems, [www.iseesystems.com](http://www.iseesystems.com), USA
9. Generation-IV, [www.gen-4.org](http://www.gen-4.org)
10. IAEA, INPRO, “*INPRO Guidance for the Application of an Assessment Methodology for Innovative Nuclear Energy Systems—INPRO Manual—Overview of the Methodology*”, IAEA-TECDOC-1575 rev. 1, 2008
11. Nuclear-21.Net, [www.nuclear-21.net](http://www.nuclear-21.net)
12. Tableau-software, [www.tableau.com](http://www.tableau.com)
13. StatPlanet, [www.statsilk.com](http://www.statsilk.com)
14. D. Wade, L. Van Den Durpel, A. Yacout, Ph. Finck, H. Khalil, “*A multi-regional analysis of nuclear energy systems: Synergies between regions, reactors and fuel cycles*”, Global2005
15. A. Yacout, L. Van Den Durpel, D. Wade, P. Finck, “*Scenarios for the Expanded use of nuclear energy*”, ICAPP2004, June 13–17 2004, Pittsburg, USA, 2004
16. L. Van Den Durpel, C. Oosterlee, L. Grzelak, “*Fuel Cycle Flexibility Assessment of the Chinese Nuclear Energy System: Real Options Valuation of Scenarios*”, this conference, PBNC2016, Beijing, China



# Determination of Boron in ThO<sub>2</sub> Powder by ICP-AES After Matrix Separation Using Solvent Extraction

He Shuhua, Li Xiaoyun, Han Ling, Luo Yan, Cao Changqing and Lin Jun

**Abstract** Thorium-based nuclear reactors use thorium as fuel through breeding to uranium-233. The analysis of boron level in thorium fuels is essential due to the stringent specifications for boron. A method has been developed for the determination of trace boron in high-purity ThO<sub>2</sub> powders. About 0.4000 g of ThO<sub>2</sub> powder was added to a mixture of 4 mL concentrated HNO<sub>3</sub> and a few drops of 0.5 % HF, then dissolved in a microwave digester. The solution was then heated to evaporate surplus HNO<sub>3</sub> and HF, and then an amount of 3 M HNO<sub>3</sub> was added and the solution was subsequently used for the chemical separation. By spiking a known amount of boron before the evaporation process, it was observed that recoveries of boron were near 100 % in this open heating step. 50 % (v/v) tri-*n*-butyl phosphate (TBP) using carbon tetrachloride as the diluent was used as the extractant. The number of extractions was optimized to reduce the thorium concentration in the aqueous phase to avoid spectral interference of thorium in the determination of boron by inductively coupled plasma-atomic emission spectroscopy (ICP-AES). The results of blank experiments showed that the limit of detection of the developed method was about 0.03 µg B/g ThO<sub>2</sub>. Samples of a high-purity ThO<sub>2</sub> powder (ThO<sub>2</sub> > 99.99 % by weight) were analyzed, and the results showed that the boron level was about 0.24 µg/g ThO<sub>2</sub> and that the relative standard deviation (RSD) was about 10.5 % ( $n = 6$ ). By spiking 0.10 µg boron (corresponding to 0.25 µg/g ThO<sub>2</sub>) into the ThO<sub>2</sub> powders before digestion, it was found that the recoveries were in the range of 88–108 % ( $n = 6$ ). These results indicated that the proposed method could meet the requirements for the determination of trace boron in high-purity ThO<sub>2</sub> powders.

**Keywords** Boron · Trace analysis · TBP extraction · Thorium dioxide · ICP-AES

---

H. Shuhua · L. Xiaoyun · H. Ling · L. Yan · C. Changqing (✉) · L. Jun  
Shanghai Institute of Applied Physics, CAS, Shanghai, China  
e-mail: caochangqing@sinap.ac.cn

© Springer Science+Business Media Singapore 2017  
H. Jiang (ed.), *Proceedings of The 20th Pacific Basin Nuclear Conference*,  
DOI 10.1007/978-981-10-2317-0\_45

477

## 1 Introduction

Thorium is convertible to fissile uranium-233 by absorbing slow neutrons so that it can be used as nuclear fuel. The Chinese Academy of Sciences (CAS) initiated a research and development project for thorium molten-salt reactor in 2011. And relevant studies are developing rapidly in China in the recent years.

The same as the uranium fuels, boron has a stringent specification in thorium fuels due to its high thermal neutron absorption cross section. As a result, it is important to develop efficient and relatively simple method to determine trace boron in thorium fuels. The determination of trace boron in a solid with techniques such as inductively coupled plasma-atomic emission spectrometry (ICP-AES) or inductively coupled plasma-atomic mass spectrometry (ICP-MS) is usually carried out after the dissolution of the solid samples. However, direct analysis of trace boron is very difficult due to the interferences of the matrix element of thorium in the dissolved aqueous samples. Therefore, chemical separation and pre-concentration of boron is necessary.

Solvent extraction employing organic extractants such as 2-ethylhexyl hydrogen 2-ethylhexyl phosphonate [1], cyanex 923 [2] and tributyl phosphate (TBP) [3] have been used to separate thorium and the impurities including boron. However, 2-ethylhexyl hydrogen 2-ethylhexyl phosphonate and cyanex 923 are not readily available for many laboratories while TBP is a commercial one which is widely used in reprocessing of used nuclear fuel [4]. Simbolon [3] used TBP–kerosene (7:3 v/v) as an extraction solvent in extracting thorium nitrate from its impurities, and boron, among other elements, was determined by ICP-AES after the matrix separation. However, the detection limit for boron was reported to be 0.5 ppm, which is not suitable for the purpose of quality control of nuclear-grade thorium compounds.

In this study, TBP-CCl<sub>4</sub> (1:1 v/v) was employed to separate boron and thorium after the dissolution of thorium dioxide by concentrated nitric acid and a few drops of 0.5 % HF, and boron concentrations were also analyzed by ICP-AES. The method performance parameters, such as the limit of detection (LOD), repeatability and recovery, were evaluated using the proposed measurement procedure.

## 2 Experimental

### 2.1 Reagents

Concentrated nitric acid (HNO<sub>3</sub>) of ultrapure grade was obtained from Suzhou Crystal Clear Chemical Co., Ltd. Boron standard solution was purchased from AccuStandard. A sample of high-purity thorium dioxide powder was prepared by the Engineering Research Center for the Separation and Purification of Res and Thorium at Changchun Institute of Applied Chemistry, Chinese Academy of

Sciences (CAS). All the other reagents like TBP, HF and CCl<sub>4</sub> were of analytical grade. High-purity ionized water with negligible boron content, was made by a Millipore ultrafiltration system and was used for the preparation of all the solutions.

## 2.2 Procedure

Before used, TBP-CCl<sub>4</sub> (1:1 v/v) was washed twice with same volume of deionized water, and then was pre-equilibrated with 3 M HNO<sub>3</sub>. The reason for pre-equilibration is to keep the nitric acid molarity of the aqueous phase nearly constant during the extraction processes.

Thorium dioxide powder of about 0.4000 g was dissolved by the mixture of 4 mL concentrated HNO<sub>3</sub> and two or more drops of 0.5 % HF, by digesting for 30 min at 140 °C in a MDS-8G microwave digestion system (Sineo Microwave Chemistry Technology (Shanghai) Co., Ltd.).

The solution was evaporated at 150 °C on an electric hot plate to get rid of surplus HNO<sub>3</sub> and trace HF, then it was transferred to a 50 mL plastic tube by approximately 5 mL solution of 3 M HNO<sub>3</sub>. This aqueous phase containing about 70 g/L thorium was contacted with 20 mL TBP-CCl<sub>4</sub> (1:1 v/v) for three times. For each extraction, the plastic tube was put on an XW-80A mixer (Shanghai Precision & Scientific Instrument Co., Ltd.) and vibrated for 1 min. After the repeated extraction, the obtained aqueous phase was transferred and diluted to 10.00 mL using deionized water, and then analyzed by ICP-AES (PerkinElmer Optima 8000).

The emission spectral intensities at 249.772 nm were used to calculate the boron concentration in the solution and accordingly in the thorium dioxide powder. At the selected wavelength, the interference of thorium could be corrected by using Multicomponent Spectral Fitting (MSF) for spectral overlap correction when the thorium concentration in the solution was below 20 mg/L.

## 3 Result and Discussion

### 3.1 Temperature Used in the Evaporation Process

One of the main concerns of the trace boron determination is that significant amount of boron may be lost during the pre-treatment processes, especially in evaporation processes at high temperatures. To evaluate whether the process of HNO<sub>3</sub> evaporation leads to a loss of boron, standard solutions containing 0.10 µg boron were added to 4 mL concentrated HNO<sub>3</sub> with two drops of 0.5 % HF, and the resulted solutions were evaporated at 230 °C until the volume of the solution was in the range of 0.1–0.2 mL, which was then transferred and diluted to 10.00 mL using deionized water and then the boron concentration was analyzed by ICP-AES.

**Table 1** Boron concentration and recovery after the evaporation process

Sample number	Boron concentration (ppb)	Recovery (%)
1	10.3	103
2	10.8	108
3	10.9	109
4	9.52	95
5	10.5	105
6	10.2	102
7	11.0	110
8	9.90	99

The results of 8 replicates are given in Table 1. It shows that the recovery of boron was between 95 and 110 %, which reasonably indicates that the loss of boron in this process was not significant. To avoid loss of boron and ensure proper evaporation rate, 150 °C was recommended for the evaporation process. According to our experience, to avoid the further loss of the boron, it must be noted that the dissolved solution should not be dried completely in the evaporation process.

### 3.2 Thorium Remained in the Aqueous Phase

As stated in the introduction, the main reason for separating the matrix thorium from the aqueous phase is that thorium has a very rich line emission spectrum which may overlap the signals of the measurand, i.e., boron in the present study. Therefore, it is important to reduce the concentration of thorium to a quite low level in the 10.00 mL diluted solution submitted to ICP-AES analysis. The preliminary experiment results showed a level of 20 mg/L thorium was sufficient to eliminate the interference of thorium on the boron determination, and that the number of contacts should not be less than 3. Table 2 shows the thorium concentration, which was also analyzed by ICP-AES, in the 10.00 mL diluted solution in three parallel samples when the number of contacts was 3 and 4, respectively. The results show that the thorium concentration in the aqueous phase was quite stable after a given number of contacts, and that 3 contacts were adequate to ensure that the concentration of thorium was reduced to below 15 ppm. For reducing thorium concentration 4 contacts would be better, but more extractants are needed, so it is not economical and environmentally friendly. As a result, 3 contacts were used in the

**Table 2** Thorium concentration in the 10.00 mL diluted solution after 3 or 4 contacts

Number of contacts	Thorium concentration (ppm)		
	3	12.2	12.9
4	1.31	1.49	1.59

subsequent experiments. It could be calculated from Table 2 that more than 99.9 % of thorium was extracted from the aqueous phase by 3 contacts using 20 mL TBP-CCl<sub>4</sub> (1:1 v/v) each time.

### 3.3 Limit of Detection of Boron

Limit of detection (LOD) of an analytical procedure is essential for trace element analysis. In order to determine the limit of detection, 11 replicate measurements of the reagent blanks were carried out, in which the entire measurement procedure was performed, but no thorium dioxide was added. The limit of detection of a given measurement procedure could be estimated by  $3 \times$  standard deviation (3 sigma) [5, 6]. As shown in Table 3, the limit of detection of boron was about 0.03  $\mu\text{g/g}$  at the sample size of 0.4000 g, which is low enough for the boron determination in thorium dioxide powders of nuclear grade. To calculate the limit of quantification (LOQ), which can be defined as the lowest concentration of the analyte that can be determined with an acceptable precision [6], we can multiply the standard deviation by ten and get a value of approximately 0.11  $\mu\text{g/g}$ . However, both the limit of detection and the limit of quantification calculated in the above should be taken as indicative values for trace analysis [5]. It is more relevant in the present case of trace boron analysis, since its detection limit is closely dependent on the experimental conditions, such as the reagent blanks, the boron content in the atmosphere at the laboratory, the blank level of the ICP-AES equipment, and so on. As a result, to obtain a low level of the limit of detection of boron, all the reagents, especially the water and the nitric acid used, should be with negligible boron content.

**Table 3** Results of 11 replicate measurements of reagent blanks and the LOD of boron

Sample number	Boron content in the 10.00 mL diluted solution (ppb)	Corresponding boron content in ThO <sub>2</sub> ( $\mu\text{g/g}$ )
1	2.04	0.051
2	1.42	0.036
3	0.95	0.024
4	1.36	0.034
5	0.96	0.024
6	1.52	0.038
7	0.83	0.021
8	1.65	0.041
9	1.73	0.043
10	1.90	0.048
11	2.18	0.055
3 sigma	1.30	0.030

### 3.4 Repeatability and Recovery

Precision and trueness are important performance characteristics for an analytical procedure. Precision, which is usually expressed as standard deviation or relative standard deviation, is a measure of how close results are to one another obtained under stipulated conditions; while trueness, which is expressed quantitatively as “bias”, is a measure of the closeness between a test result and the accepted reference value [5, 6]. In this study, the precision under repeatability conditions, i.e., with the same analyst with the same equipment in a short period of time, was evaluated. And because of the absence of certified reference materials (CRMs), the standard addition method was used to evaluate the bias of boron determination at a level of about 0.25 ppm for the present method [5, 7]. To determine the repeatability of the method, 6 replicate measurements were made for the thorium dioxide sample. At the same time, standard addition experiments were carried out by adding standard boric acid solution containing 0.10  $\mu\text{g}$  boron to the thorium dioxide sample before dissolution. The results are showed in Table 4. According to the results, the average boron content of the  $\text{ThO}_2$  sample was about 0.24  $\mu\text{g/g}$ , and the corresponding relative standard deviation (RSD) was about 10.5 %. As for the boron recovery, the average was about 98.7 % and the corresponding RSD was about 8.3 % for 0.25  $\mu\text{g/g}$  boron addition. Since the recovery is not significantly different from unity, it could be concluded that there was no significant loss of boron during both the extraction and the evaporation processes and that the bias of the present method was low.

Up to now, there is no standard specification for thorium dioxide powders. If we refer to the standard specifications for uranium dioxide, such as ASTM C776-06 (2011), the total equivalent boron content (EBC) should not exceed 4.0  $\mu\text{g/g}$  U for thermal reactor use [8]. If the same value is set for nuclear-grade thorium compounds, it could be concluded that by employing the present method, the boron in nuclear-grade thorium dioxide could be measured and that results with good quality could be obtained. However, in the future, studies on the analyses of (certified) reference materials when they are available are necessary.

**Table 4** The results of replicate measurements of the  $\text{ThO}_2$  samples and the recovery experiments

	Boron content in the $\text{ThO}_2$ sample ( $\mu\text{g/g}$ )	Boron added ( $\mu\text{g/g}$ )	Boron recovered ( $\mu\text{g/g}$ )	Boron recovery (%)
1	0.25	0.25	0.27	108
2	0.21	0.25	0.22	88
3	0.22	0.25	0.23	92
4	0.28	0.25	0.26	104
5	0.22	0.25	0.27	108
6	0.26	0.25	0.23	92
Average	0.240		0.247	98.7
RSD	10.5 %		8.3 %	

## 4 Conclusions

A simple measurement procedure using common chemicals has been developed for the analysis of trace boron in thorium dioxide. The method based on microwave sample digestion, the separation of thorium base using TBP-CCl<sub>4</sub> and ICP-AES detection is established for determination of trace boron in high-purity ThO<sub>2</sub>. The results of the standard addition experiments showed that when the spiking level was 0.25 µg/g, the recovery was approximately unity and the corresponding RSD was about 8.3 %, which indicated the developed method would be precise and accurate. The method can be used for the characterization of thorium dioxide of nuclear grade.

## References

1. Gopalkrishnan, M., et al., *Determination of trace impurities in uranium, thorium and plutonium matrices by solvent extraction and inductively coupled plasma atomic emission spectrometry*. Talanta, 1997. **44**(2): p. 169–176
2. Kulkarni, M.J., et al., *Chemical separation and inductively coupled plasma–atomic emission spectrometric determination of seventeen trace metals in thorium oxide matrix using a novel extractant—Cyanex-923*. Analytica Chimica Acta, 1998. **370**(2–3): p. 163–171
3. Simbolon, S., *Analysis of boron, cadmium and iron in thorium nitrate by ICP-AES method after matrix separation using tributyl phosphate*. Jurnal Teknologi Bahan Nuklir, 2013. **8**(2): p. 105–117
4. Kim, J.S., et al., *A Brief Review on Solvent Extraction of Uranium from Acidic Solutions*. Separation and Purification Reviews, 2011. **40**(2): p. 77–125
5. Magnusson, B. and U. Örnemark, *Eurachem Guide: The Fitness for Purpose of Analytical Methods—A Laboratory Guide to Method Validation and Related Topics*. 2nd ed., 2014
6. Thompson, M., S.L. Ellison, and R. Wood, *Harmonized guidelines for single-laboratory validation of methods of analysis (IUPAC Technical Report)*. Pure and Applied Chemistry, 2002. **74**(5): p. 835–855
7. Thompson, M., et al., *Harmonized guidelines for the use of recovery information in analytical measurement*. Pure and Applied Chemistry, 1999. **71**(2): p. 337–348
8. ASTM C776–06(2011), *Standard Specification for Sintered Uranium Dioxide Pellets*, 2011: ASTM International, West Conshohocken, PA

# Development and Validation of Methodology for Depletion Analysis of FHR at Equilibrium State

Haibo Tang, Jianlong Han, Xiangzhou Cai and Jingen Chen

**Abstract** Fluoride salt cooled High temperature Reactor (FHR) attracts particular attention in the world because of its excellence in high power density and low operation pressure. However, it is difficult to simulate the discharge burnup of FHR at equilibrium state because of the changes of fuel element and fuel pebble position. At present, there are three methods used to estimate the attainable burnup of FHR: full core method, equilibrium bed method and infinite uniform bed method. These methods including refueling or searching equilibrium state consumes more computation time. Based on the infinite uniform bed method, this work introduces a new method to estimate the discharge burnup without needing to search equilibrium state. The obtained results from the new method are validated with those from the infinite uniform bed method in MOCUP and full core method in VSOP. It shows that the developed method can be used to estimate the discharge burnup in pebble-bed reactor.

**Keywords** FHR · Depletion analysis · Equilibrium state · Discharge burnup

## 1 Introduction

The Fluoride salt cooled High temperature Reactor (FHR) [1–4] is a pebble-bed reactor cooled by fluoride salt and moderated by graphite. This new reactor concept has been receiving particular attention in the world because of its excellence in high power density and atmosphere pressure, especially the potential of thorium fuel utilization with high burnup.

Assessment of performance for equilibrium fuel cycle is an objective in reactor design, which can ensure a reactor obtaining the upper limit of fuel burnup. And the

---

H. Tang · J. Han · X. Cai · J. Chen (✉)  
Shanghai Institute of Applied Physics, CAS Innovative Academies in TMSR Energy System,  
Shanghai, China  
e-mail: chenjg@sinap.ac.cn



FHR loaded with fuel pebbles is an ideal reactor to attain a very high burnup. However, the equilibrium state depletion analysis in FHR is a difficult problem because of fuel pebbles movement and fuel composition change. In the design code for a reactor, the fuel pebble position and the fuel composition in the fuel pebble should be predicted and represented. Massimiliano Fratoni et al. developed a full core method [5, 6] which simulates all pebbles movement and fuel composition change in a reactor during the operation time. It obtains the equilibrium state discharge burnup with continuous or batch refueling mode. Another possibility is to describe the pebble movement as a laminar flow and thus it can be approximated by flow channels, which has been used within VSOP [7, 8]. These full core methods can provide a precise description for neutronics for movable pebbles but requires much more computation time. Other two methods developed by Massimiliano Fratoni et al., i.e., the infinite uniform bed method [5, 9, 10] and the equilibrium bed method [5], which simulate a single fuel cell irradiated by neutron flux in a typical reactor. In the infinite uniform bed method, all pebbles are assigned with the same composition, and the depletion calculation is performed under the constraint of a constant flux. And in the equilibrium bed method, the same fuel composition is also assigned to all the pebbles in the simulated subset, except one fresh pebble placed in the center of the subset. And the fresh pebble is depleted while the other pebbles maintain their set compositions. For these three equilibrium depletion analysis methods, the most important procedure is to search the equilibrium system, including flux, material composition, power and  $k_{\text{eff}}$ , which will take a great deal of computation time.

This work presents a new method for FHR equilibrium state depletion analysis based on the infinite uniform bed method without needing to search the equilibrium state. In this method, the equilibrium burnup can be deduced from the residence time of pebbles staying in the equilibrium core. The residence time is obtained by calculating the depletion of the fuel pebble with MCNP. Once the residence time is obtained, the discharge burnup at equilibrium state is determined. This method facilitates the calculation of FHR discharge burnup with reliable precision.

With this method, the discharge burnup of FHR with seed fuel of low enriched uranium is estimated. Section 2 gives the detailed information on the developed methodology. The results of validation and application of the developed method in a FHR are given in Sect. 3. The discussion and conclusion are presented in Sect. 4.

## 2 Methodology

For FHR, the total reactivity of the full core is made up of the reactivity of each pebble at different burnup level. The burnup level at equilibrium state is a function of residence time of the pebble in the core. To evaluate the  $k_{\infty}$ , neutron fission and absorption of the fuel pebble are considered. For the entire core, the reactivity

$k_{\infty, \text{core}}$  is the sum of the reactivity of each pebble in the core, which can be written as:

$$k_{\infty, \text{core}} = \frac{\sum_{i=1}^N F_i}{\sum_{i=1}^N A_i} = \frac{\sum_{i=1}^N \frac{F_i}{A_i} A_i}{\sum_{i=1}^N A_i} = \sum_{i=1}^N k_{\infty, i} \frac{A_i}{\sum_{i=1}^N A_i}, \quad (1)$$

where  $F_i$  and  $A_i$  is the number of fission and absorption neutrons of pebble  $i$ , respectively.  $N$  is the total number of pebbles in the core. At equilibrium state, pebbles are well mixed in the core. Therefore, it is reasonable to assume that the fraction of neutrons absorbed by each pebble is constant. Then Eq. (1) can be rewritten as:

$$k_{\infty, \text{core}} = \frac{\sum_{i=1}^N k_{\infty, i}}{N}. \quad (2)$$

For pebble  $i$ , the  $k_{\infty, i}$  associates with its burnup level. Then Eq. (2) can be written as a function of burnup level:

$$k_{\infty, \text{core}} = \frac{\sum_{i=1}^N k_{\infty, \text{pebble}}(\text{BU}_i)}{N}, \quad (3)$$

where  $\text{BU}_i$  is the burnup level of pebble  $i$ , which is a function of residence time.

Since the pebbles are uniformly distributed in the equilibrium core, the neutron spectrum is strongly determined by the average fuel composition, and the neutron flux is constant at equilibrium state. Thus, the burnup level corresponds only to the residence time  $t$  [5]. Equation (3) can be written as a function of the residence time in the core:

$$k_{\infty, \text{core}} = \frac{\sum_{i=1}^N k_{\infty, \text{pebble}}(t_i)}{N}, \quad (4)$$

where  $t_i$  is the residence time of pebble  $i$ . If  $T$  is the total residence time, then:

$$\frac{1}{N} = \frac{T}{N} = \frac{\Delta t}{T}, \quad (5)$$

where  $\Delta t$  is an average depletion step. Equation (4) becomes:

$$k_{\infty, \text{core}} = \sum_{i=1}^N k_{\infty, \text{pebble}}(t_i) \frac{\Delta t}{T}. \quad (6)$$

When  $N \rightarrow \infty$ , thus  $\Delta t \rightarrow 0$ , and Eq. (6) can be written as:

$$k_{\infty, \text{core}} = \frac{1}{T} \int_0^T k_{\infty, \text{pebble}}(t) dt. \quad (7)$$

If  $P_{\text{NL}}$  is the neutron non-leakage probability from the finite core, then

$$k_{\infty, \text{core}} = \frac{k_{\text{eff}, \text{core}}}{P_{\text{NL}}} = \frac{1}{T} \int_0^T k_{\infty, \text{pebble}}(t) dt, \quad (8)$$

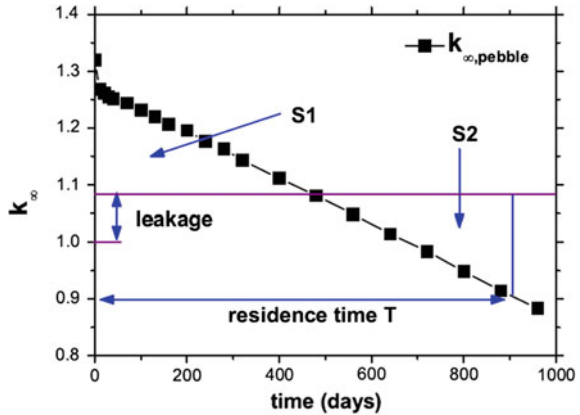
where  $k_{\text{eff}, \text{core}}$  is the reactivity of the full core. The residence time  $T$  can be obtained from Eq. (8), which means the sum of the reactivity of each pebble in whole residence time equals the reactivity of the full core at equilibrium state.  $k_{\text{eff}, \text{core}} = 1$  and  $P_{\text{NL}}$  is constant, and the solution of Eq. (8) relies on the evolution of  $k_{\infty, \text{pebble}}(t)$ , i.e., the fuel depletion simulation. Once the residence time  $T$  is determined, the burnup level and the fuel composition can be obtained from the fuel depletion analysis.

In the fuel depletion analysis, in order to simplify the calculation some approximations are introduced. Keeping the value of flux constant and keeping power constant are two standard approximation methods, which are often used in depletion analysis [11]. Nuclide evolution using these two kinds of approximation are quite different over a long time step, which would lead to different isotope depletions: a nuclide density undergoes an evolution as a nonlinear function of residence time for a constant flux and as a linear function for a constant power [11]. However, the fuel composition evolution is similar under an irradiation at a certain burnup level for the above two approximation methods. That means the two approximations are equivalent in fuel burnup analysis.

In this work, a constant power approximation is adopted in the fuel depletion analysis to simplify the solving of Equation (8) with a graphic illustration for  $k_{\infty, \text{pebble}}(t)$  evolution, which is shown in Fig. 1. The  $k_{\infty, \text{pebble}}(t)$  evolution of a fuel pebble under a constant power is drawn, and the value of  $1/P_{\text{NL}}$  is also presented. Equation (8) predicates that at a certain time  $T$ , the in-closed area of  $k_{\infty, \text{pebble}}(t)|_0^T$  with the  $X$  axis is equal to  $T/P_{\text{NL}}$ , namely, the area of S1 equals that of S2. Once the residence time  $T$  is achieved, the burnup and fuel component can be obtained from the depletion analysis. It should be noted that, the residence time  $T$  is a pseudo parameter which would not exactly correspond to the real residence time of a pebble in the core.

This method can save significantly computation time since one does not need to search the equilibrium state of the core [9]. As assumed previously, all pebbles are well mixed in the equilibrium core and the neutron absorption is constant for each pebble. In particular this method does not consider the difference between one pebble neutron spectrum and the real one of the full core [9]. And the assumption in the deduction of Eq. (2) points out that the neutron absorption of each pebble in the core is equivalent, which implies that the developed method can only be applied to a core loaded with only one kind of fuel in each pebble.

**Fig. 1** Depletion calculation and residence time estimation



### 3 Validation of the Developed Method

In order to validate the developed method, several core designs are taken as references [9, 12] which evaluate the burnup of different cores but all loaded with fuel pebbles. Considering the restriction of the developed method, four PB-AHTR designs calculated with the infinite uniform bed method and one PBMR-400 design calculated with VSOP [12] are adopted for comparison. The reference designs are named Designs A, B, C, D and E, and the related design parameters are listed in Table 1.

In the present calculation, the mean power of one pebble is the core power averaged by the number of fuel pebbles in the core. The depletion calculation of  $k_{\infty, \text{pebble}}(t)$  is performed with MCNP5 coupled with ORIGEN2. And the non-leakage probability  $P_{NL}$  is taken from the MCNP5 simulation of the core at the Beginning Of Life (BOL). In the calculation, a single hexagonal prism model with reflective boundary conditions is used, as shown in Fig. 2. The pebble is surrounded by liquid flibe salt ( $\text{LiF-BeF}_2$ ) for the PB-AHTR designs and by gaseous helium for the PBMR-400 design. The volume fraction of the pebble in the hexagonal prism is same as the designed value in Refs. [9, 12]. The pebble diameter

**Table 1** Parameters for various core designs

Property	Design A	Design B	Design C	Design D	Design E
	PB-AHTR	PB-AHTR	PB-AHTR	PB-AHTR	PBMR-400
Power density ( $\text{MW/m}^3$ )	10.2	10.2	20	40	1.19
Total core power (MWth)	2400	600	2400	2400	400
Core diameter (cm)	684	431	547	408	200/370
Core active length (cm)	640	405	514	408	1100
Leakage (%)	3	6	4	6	15.6
Reference burnup (GWd/tHM)	129	113	122	113	92.5
Developed method (GWd/tHM)	128	109	120	114	89.5

is 6 cm and the fuel sphere with diameter of 5 cm contains thousands of fuel TRISO kernels within graphite matrix. The diameter of TRISO is 425  $\mu\text{m}$  for PB-AHTR and 500  $\mu\text{m}$  for PBMR-400 with  $C/HM = 360$ . More detailed information on fuel pebbles can be seen in Refs. [9, 12].

The leakage probability values are used to calculate the  $P_{NL}$  as shown in Eq. (8). The evolution of  $k_{\infty, \text{pebble}}(t)$  with constant power used in the graphical representation of Eq. (8) is shown in Fig. 3.

The spectrum comparison of fuel pebble for Design A at BOL and End Of Life (EOL) is shown in Fig. 4. The methodology is based on a single pebble model neglecting the effect of the neighboring pebbles. This effect is negligible for low enriched uranium because the neutron spectrum of the pebble does not change drastically during the whole residence time. One can see that the difference of the spectrum for the prism fuel model and that for the whole core model at both BOL and EOL is not significant, which implies that the burnup calculation for a whole core model can be represented approximately by a prism fuel model simulation.

**Fig. 2** Schematic of hexagonal prism model for pebble simulation and depletion calculation

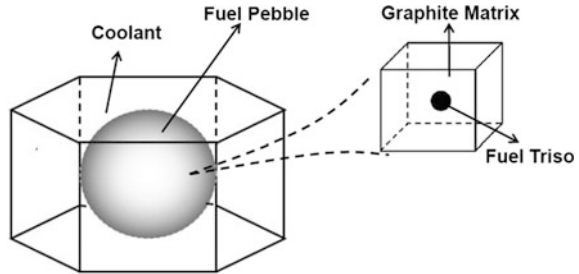


**Fig. 3** Depletion evolution with constant power that is used in the discharge burnup estimation

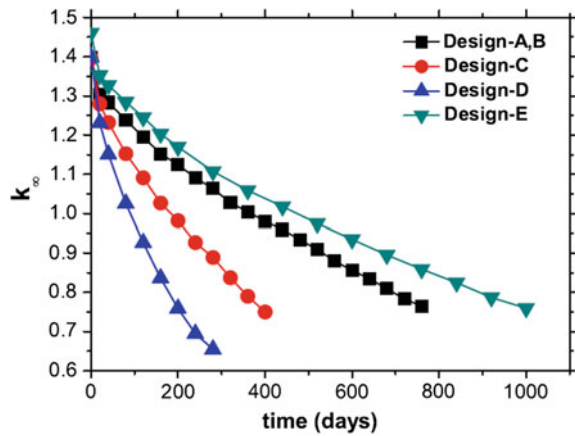
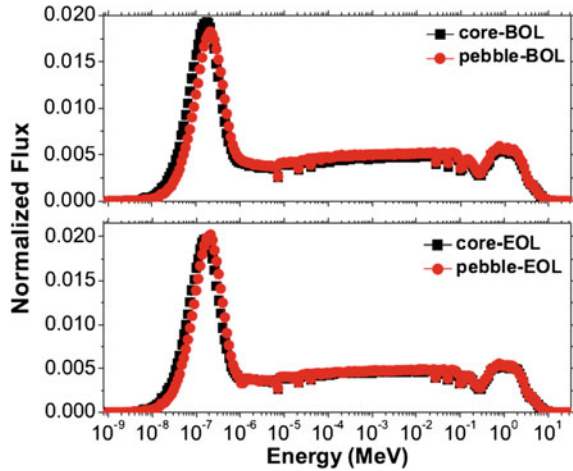


**Fig. 4** Comparison of the spectra at BOL and EOL of hexagonal prism model (Design A) and whole core



The new evaluated burnup for the references are listed in the last line of Table 1 and the reference values are also presented for comparison. It can be seen that the newly evaluated burnup values are very close to those counterpart values taken from the references. The minor difference might come from several aspects: constant power approximation in the  $k_{\infty, \text{pebble}}(t)$  depletion analysis, namely, the approximation significantly simplifies the calculation but may be inconsistent with a real reactor; the difference of the neutron spectra between the single pebble model (see Fig. 2) and full core model, which is neglected in this method because of low enriched uranium fuel used in the five models, while the neutron spectrum is sensitive to nuclides' macroscopic cross section; the attainable discharge burnup is a function of residence time in this method, which is very sensitive to the leakage probability, while the values of leakage probability used to calculate the  $P_{NL}$  in Eq. (8) is adopted at BOL instead of equilibrium state; and based on the assumption that pebbles are mixed well in equilibrium core, so that the neutron absorption of each pebble is equivalent.

## 4 Conclusions

A facilitative method for scoping analysis of the attainable burnup of pebble-fueled reactors is developed in this work. This method can save much more computation time since the procedure of searching the equilibrium state of the core is not required. The results for several core designs of PB-AHTR and PBMR-400 are compared to validate the developed method. The comparison reveals the rationality of the new method, and it is workable for estimating the discharge burnup of pebble-fueled reactors.

However, in this method, in order to simplify the calculation and obtained the equilibrium discharge burnup quickly, we have assumed that the neutrons absorption of each pebble is equivalent in equilibrium state, and over the residence time the power of fuel pebble can be treated as constant; the effect of neighboring pebbles and the spectrum difference of a single pebble and a full core were also neglected. These simplifications have effects on the equilibrium discharge burnup estimation, but the methodology can provide a reliable depletion calculation for pebble-bed reactor.

**Acknowledgments** This work is supported by the Chinese TMSR Strategic Pioneer Science and Technology Project under Grant No. XDA02010000.

## References

1. Todd Allen, et al., *Fluoride-Salt-Cooled, High-Temperature Reactor (FHR) Subsystems Definition, Functional Requirement Definition, and Licensing Basis Event (LBE) Identification White Paper*. 2013
2. Todd Allen, et al., *Fluoride-Salt-Cooled, High-Temperature Reactor (FHR) Methods and Experiments Program White Paper*. 2013
3. Todd Allen, et al., *Fluoride-Salt-Cooled High Temperature Reactor (FHR) Materials, Fuels and Components White Paper*. 2013
4. D.T. Ingersoll, et al., *Status of Preconceptual Design of the Advanced High-Temperature Reactor (AHTR)*. ORNL, 2004
5. Fratoni, M., *Development and applications of methodologies for the neutronic design of the Pebble Bed Advanced High Temperature Reactor (PB-AHTR)*. ProQuest Dissertations And Theses; Thesis (Ph.D.)—University of California, Berkeley, 2008
6. Massimiliano Fratoni and Ehud Greenspan, *Equilibrium Core Composition Search Methodologies for Pebble Bed Reactors*. NUCLEAR SCIENCE AND ENGINEERING, 2010. **166**: p. 1–16
7. Andre Xhonneux, et al., *Progress on the development of a new fuel management code to simulate the movement of pebble and block type fuel elements in a very high temperature reactor core*. Nuclear Engineering and Design, 2014. **271**: p. 370–378
8. H.J. Rütten, K.A. Haas, and C. Pohl, *Computer Code System V. S. O. P. (99/11) Update 2011 of V.S.O.P(99)-Version 2009 CODE MANUAL*. 2009
9. Massimiliano Fratoni, Ehud Greenspan, and P.F. Peterson, *NEUTRONIC AND DEPLETION ANALYSIS OF THE PB-AHTR*. Global 2007, Boise, Idaho, September 9–13, 2007
10. Massimiliano Fratoni, Ehud Greenspan, and P.F. Peterson, *NEUTRONIC DESIGN OF THE PB-AHTR*. Nuclear Engineering and Design, 2009. **239**(8): p. 1531–1543
11. James J. Duderstadt and Louis J. Hamilton, *Nuclear Reactor Analysis*. John Wiley & Sons, Inc., New York, 1976
12. Mulder, E. and E. Teuchert, *Characteristics of a different fuel cycle in a PBMR-400 for burning reactor grade plutonium*. Nuclear Engineering and Design, 2008. **238**(11): p. 2893–2897

# Effects of Compressing Strength of Core Ball on Crushing Strength of Spherical Fuel Element

Jiucheng Tian, Ming Gao, Wenjie Yu, Yu Zhang and Huimin Shi

**Abstract** The spherical fuel element (pebble fuel) for high temperature gas-cooled reactor (HTGR) is the fourth-generation nuclear fuel element with completely independent intellectual property rights. The most notable feature of pebble fuel is its inherent safety, which is guaranteed by the four coating layers serving as its major security barrier and the external matrix graphite. The pebble fuel is composed of inner core and nonfuel zone, the former is composed of coated uranium dioxide particles and matrix graphite powder and molded by quasi-cold isostatic pressing (CIP) technique, while the nonfuel zone is matrix graphite shell wrapping on the core pebble by CIP again. After subsequent processes of low temperature carbonization, lathing and high temperature purification, spherical fuel elements complying specific performance requirements can be obtained. Currently, as the first fuel element production line supplying fuel for HTR power plant in the world, the HTR fuel element plant of China North Nuclear Fuel Co., Ltd. has completed its process technology development. The molding characteristics of spherical fuel elements is “composite quasi-cold isostatic pressing” of both fuel zone and nonfuel zone. Fuel particles and matrix graphite powder will be mixed up uniformly and premolded into core pebble using CIP, then by adding matrix graphite powder wrapping the core pebble to use CIP again for nonfuel zone creation. Through specific process, matrix graphite powder, the main raw material for spherical fuel elements, has certain composition of artificial graphite, natural graphite, and phenolic resin. In the production process of spherical fuel element, some destructive tests on graphite pebble without fuel particle but prepared by the same process for fuel pebble are required, among which the crushing strength is one of the most important testing items. For each batch of fuel pebbles, the crushing strength on directions both axial and perpendicular to the molding direction is tested. The results of the trial production of matrix graphite spheres indicate that compressing strength of the core pebble directly affects crushing strength of graphite pebble. Compressing strength of core ball depends both on the characteristics of matrix graphite powder including particle morphology, particle size distribution, content of

---

J. Tian (✉) · M. Gao · W. Yu · Y. Zhang · H. Shi  
China North Nuclear Fuel Co., Ltd., Baotou, China  
e-mail: 13847250253@163.com



phenolic resin, and the compressing pressure. In this paper, major study efforts are concentrated on the effect of matrix graphite powder characteristics on core ball compressing strength in order to discover the relations between powder characteristics and the crushing strength of substrate graphite sphere.

**Keywords** Spherical fuel element · Substrate graphite sphere · Core ball · Compressing strength · Crushing strength

## 1 Introduction

The matrix graphite materials for spherical fuel elements serve three primary functions: moderating material for fission neutrons; transferring fission heat from coated fuel particles to the surface of elements; structural material protecting coated fuel particles from being damaged by external forces. Matrix graphite spheres, whose manufacturing processes and raw materials must be identical to those of the spherical fuel elements except for being devoid of any coated fuel particles, are used as specimens substituting the fuel pebbles for high temperature gas-cooled reactor nuclear fuel elements destructive testing. Matrix graphite spheres are produced for every batch of pebble fuel products in order to obtain most of the performance of the fuel pebbles while being tested for various items.

Matrix graphite powder is molded into spherical billets by first premolding the core pebble and then being pressed with additional matrix graphite powder for nonfuel zone formation. After subsequent processes of heat treatment, lathing etc., matrix graphite pebbles with the same diameter as fuel pebbles can be obtained, as is shown in Fig. 1.

The composition of the matrix materials for making high temperature gas-cooled reactor spherical fuel element includes natural graphite powder and artificial graphite powder. Due to the anisotropic properties of graphite single crystal, the  $\alpha$ -direction thermal conductivity is several hundreds times of that of c direction. The degree of anisotropy of matrix graphite is the most important factor affecting its

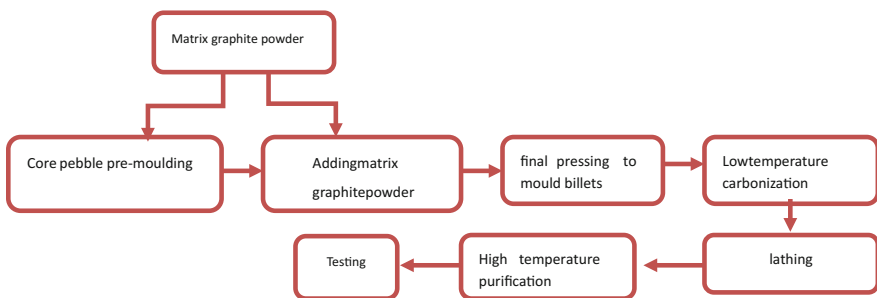


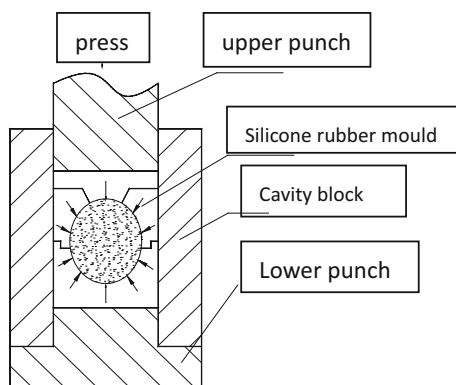
**Fig. 1** Matrix graphite ball manufacturing process

irradiational dimension change anisotropism, thus being major consideration in fuel element forming methods selection. Polycrystalline graphite anisotropy degree is defined as the ratio of the thermal expansion coefficients in the directions perpendicular and parallel to the crystal grain preferred orientation, i.e.,  $\alpha_{\perp}/\alpha_{\parallel}$ , which is  $\leq 1.3$  for matrix graphite, and (2–4) for the flake small sample molded using ordinary steel sheet molding method. As a result, the preparation of the spherical fuel elements must adopt the isotropic isostatic pressing method rather than ordinary steel molding method. It is reported early in 1957 the method of pressing fuel pebbles in the steel mold using elastic mold, namely the cold quasi(half) isostatic pressing methods, which is referred to SH Repression for short. The pressing process is conducted by pouring powder into special silicone rubber mold first, then putting the silicon rubber mold into the steel mold, while being pressurized with punch, rubber flows like liquid under high pressure, resulting in three-dimensional quasi-isotropic pressing (Fig. 2). Silicone rubber mold consists of three parts: the head, upper mold, and lower mold. In order to get the spherical shape, the design of silicon rubber mold cavity is vital, ellipsoid shape is preferred (Fig. 2). The ratio of the ellipsoid of the major axis and minor axis is affected by apparent density of pressed powder, the hardness of silicone rubber and other factors. The pressing process of substrate graphite sphere includes core pebble pressing and nonfuel area preforming, both are implemented using the cold isostatic pressing in mold made of silicone material.

## 2 Analysis of Relations Between the Strength of Core Ball and Matrix Graphite Ball Crushing Strength

The process of pressing substrate graphite sphere is first core ball premolding, which is followed by adding coating graphite powder need for nonfuel zone before being pressing again to bind the graphite layer of nonfuel zone with the core pebble to form an entity. It is difficult to measure the strength of the graphite core ball due

**Fig. 2** Schematic diagram of cold (half)isostatic pressing



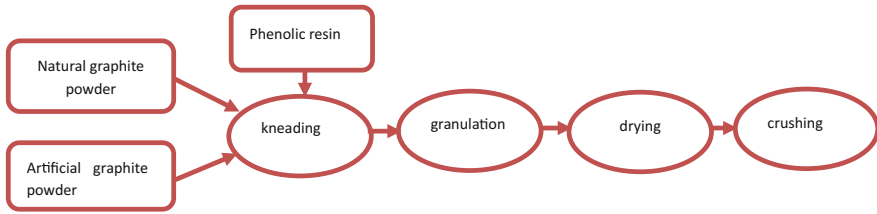


**Fig. 3** Matrix graphite powder manufacture process

to its overall low strength. Therefore, during the trial production, core ball pressure represents core strength by ensuring that equipment parameters are constant.

## ***2.1 Analysis of Morphology and Particle Size Distribution of Matrix Graphite Powder Used for Trail Production***

As the main raw material of spherical fuel elements, the performance of matrix graphite powder depends on the performance of raw materials and preparation process. Matrix graphite powder is prepared by mixing natural graphite, artificial graphite powder, phenolic resin, and ethanol solution according to specific composition. The main process is as shown in Fig. 3.

### **2.1.1 Analysis of Morphology of Matrix Graphite Powder Used for Trail Production**

Natural graphite powder has flaky morphology and relatively smooth edges and corners, while the morphology of artificial graphite powder is irregular polygonal ribbed. After the above preparation process, its main body morphology is between the sheet and polygon shape showing little change, as shown in Fig. 4.

In the process of powder preparation, increasing molding pressure resulting in decreasing gap space and increasing compact density, and powder particles gradually start to produce mechanical meshing force and the stress between atoms by mutual wedging with each other and connections, meanwhile the compact intensity of ball billet increases gradually. For flake graphite powder structure, however, the phenomenon of particle rearrangement will appear in early stage, the graphite particles with various original direction will “dump” along the layers in the direction normal to the pressing, and the contact area between particles increases gradually, and the friction also increases, especially by cold isostatic pressing method, the pressure in the direction of vertical pressing comes from the side of the cylinder liner, the lateral pressure transferred to the compact through silicone mold deformation. While friction is relatively large regarding small elastic force of

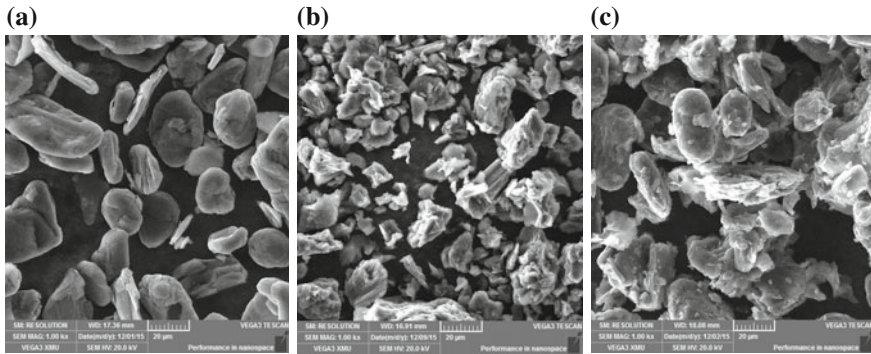


**Fig. 4** **a** Natural graphite powder morphology (1000×) **b** artificial graphite powder morphology (1000×) **c** matrix graphite powder morphology (1000×)

silicone mold deformation, resulting in the lateral pressure from the direction of vertical pressing is less than pressing force, thus the compact intensity of graphite ball in the direction of the vertical pressing is relatively small. The results of experiments proved that the size shrinkage of graphite ball billet after compacting in the suppressing direction is significantly greater than that in the vertical direction, and the crushing strength parallel to the pressing direction is greater than that in the vertical direction.

### 2.1.2 Analysis of particle Size Distribution of Matrix Graphite Powder Used for Trail Production

Typically, if powder particle size compositions are different, its behavior will be not consistent in the compacting process. In general, finer powder has poorer flow ability thus having difficulty to fill cavity, and it will become easier to form a bridge. Because finer powder has relatively lower apparent density, the filling volume in them old is larger, inevitably leading to an increased cavity height. In this case, both the moving distance of punch and the internal friction force among the powder will increase in the pressing process, and the loss of powder during pressing will also increase, affecting density distribution uniformity and the strength of the compact further.

Matrix graphite powder particle size has direct relation with the particle size distribution of raw materials and grinding process, etc. Under the premise of other process unchanged, matrix graphite powder and its raw materials are grinded and sieved with Type FZ-450 cone crusher, at a rotating speed of 3000 rpm and sieving mesh size of 1.5 mm, before conducting laser particle size analysis. The specific granularity distribution result is shown in Fig. 5.

It can be seen that the average particle size and  $D_{50}$  value of natural graphite powder and artificial graphite powder have little difference, but artificial graphite

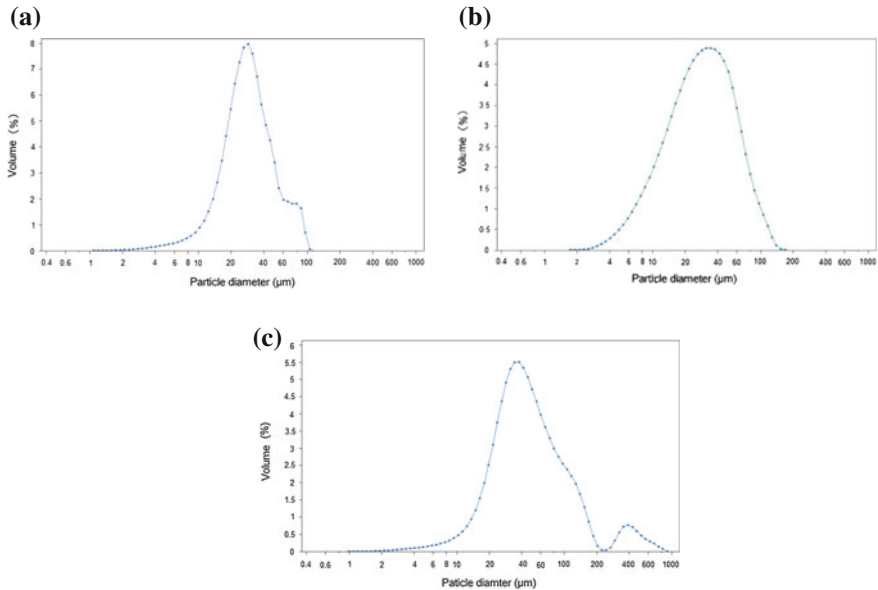


**Fig. 5** a Natural graphite powder particle size distribution b artificial graphite powder particle size distribution c matrix graphite powder particle size distribution

powder has larger percentage of particles with diameter more than 100 microns and less than 10 microns in the relatively more when compared to the natural graphite powder, and its overall particle size distribution is relatively wider. After the preparation of matrix powder, both of its average particle size and  $D_{50}$  value increase, maximum particle size is larger than 1000 microns, particle size distribution becomes much wider. Relatively, the larger the particles in test powder, the wider the particle size distribution and the higher the apparent density. Because there is a part of the larger particles, part of the small particles will fill the voids, test powder apparent density is relatively high, about  $0.54 \text{ g/cm}^3$ . Normally, compared with coarse powder of the same shape, formability of fine powder is poorer, for the reasons that fine powder particles have more contact points between each other, resulting in more contact area and smaller pore. Under the same pressure, large pore is easier to collapse than the producing larger dislocation sliding distance, and has higher compression ratio. The compaction properties of powder of no single particle size will be better, because it is easy to fill into the pores between the larger particles by small particles. Therefore, the compact density and strength increase while the elastic aftereffect decreases obtaining high density and high strength compact. Consequently, appropriate particle size distribution of matrix graphite powder, will guarantee a reasonable particle size collocation, somehow affecting the crushing strength of matrix graphite ball.

## 2.2 Core Ball Compacting Pressure Range Determination

The above matrix graphite powder is used for compacting test, core ball compression uses the silicon mold whose cavity is ellipsoidal. Usually, the apparent density of flake powder is relatively small to irregular and spherical shape powder, leading to increasing powder contact area, poorer powder flow ability, and higher friction between powder particles, thus powder pressing force is small in the deformation of soft mold. The result of test shows that the core ball cannot be molded into shape or breaks instantly on touch when core ball pressure is below 2.4 MPa. When the pressure increased to more than 6.0 MPa, core ball shape is better, but a little bit too dense, when conducting the final compacting process after coating matrix graphite powder in nonfuel area, the interface for core ball and nonfuel zone is obvious in some moderate cases, More severely, the “skinning” phenomenon will appear (see Fig 6).

## 2.3 The Pattern of Core Ball Pressing Pressure Affecting crushing Strength of Matrix Graphite Ball

In trail productions, experiments were conducted varying core ball pressure while maintaining other conditions unchanged, such as same matrix graphite powder low temperature carbonization, lathing and high temperature purification process parameters. The core ball forming pressure range is from 2.4 to 6.0 MPa, using cylindrical silicon mold with ellipsoidal inner cavity. In order to ensure the firm combination of core ball and nonfuel area, the cavity surface of mold for core ball

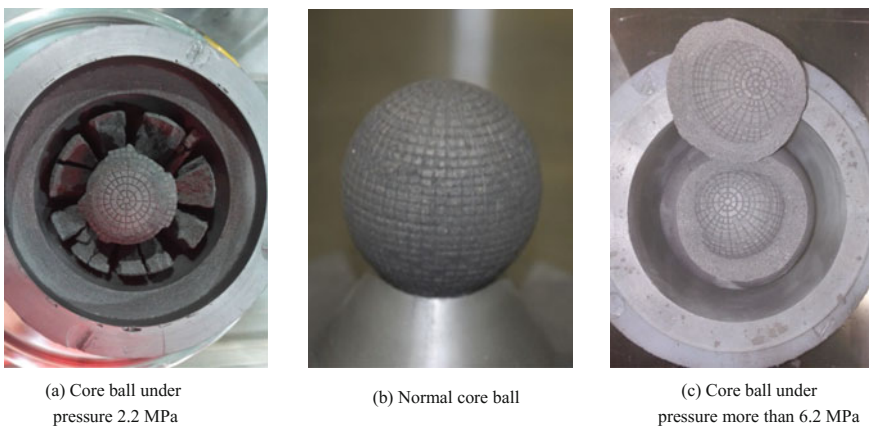


Fig. 6 Two matrix graphite powder particles size distribution

pressing is intertwined transverse and longitudinal shape, which increases the adhesion between the nonfuel area graphite layer and the core ball after compact ends. The press machine is one-way downward press. After compacting and subsequent process, the crushing strength will be tested.

The inspection equipment for crushing strength is the universal material testing machine, whose range is from 0 to 100 kN, accuracy is 0.01 kN. In the detection process, first placing graphite ball on the machine's level stage, then adjust the direction of the suppression, level of pressure head on the press will be downward at a speed of 1 mm/min until the sphere is crushed. Matrix graphite ball of different core ball pressure crushing strength test results are shown in Table 1 and Fig. 7.

Through data analysis, when matrix graphite powder and subsequent preparation process are constant, matrix graphite ball crushing strength increases with the core ball pressure, and reached maximum at 4.0 MPa. When the core ball pressure increase continued, crushing strength began to decline to a certain range of values and remained relatively stable. Through an analysis of crushed samples, it is found that the interface of core ball and no fuel zone becomes gradually obvious when

**Table 1** The results of detection about crushing strength at different pressures

Serial number	Core ball pressure (MPa)	Crushing load (kN)					Average
1	2.4	15.9	15.9	16.3	16.3	16.9	16.3
2	3.0	17.0	17.1	17.1	17.2	17.3	17.1
3	3.6	17.3	17.5	17.6	17.8	17.8	17.6
4	4.0	19.3	19.6	20.1	21.0	21.1	20.2
5	4.6	18.2	17.9	18.5	18.3	18.0	18.2
5	5.0	16.9	17.3	17.5	17.8	17.9	17.5
6	5.6	16.4	16.5	16.6	17.0	17.1	16.7
7	6.0	16.1	16.3	16.5	16.8	17.0	16.5

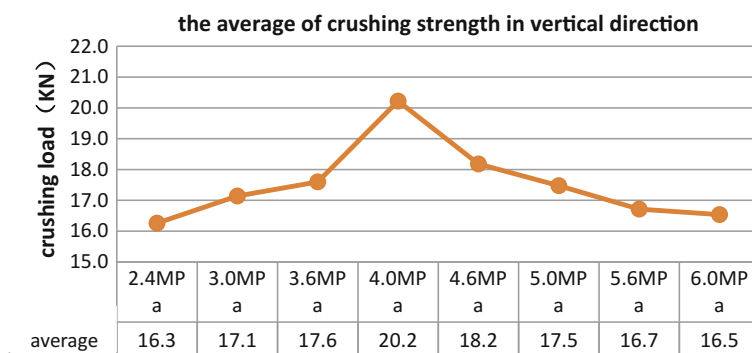


**Fig. 7** The crushing strength average change trend chart in different pressures

core ball pressure is greater than 4.0 MPa and increasing, the peeling phenomenon will appear when pressure is close to or more than 6.0 MPa. With a reduced pressure good combination between the soft core ball and nonfuel area graphite layer is obtained, however, the isostatic pressed spheres have lowered core ball strength and overall strength.

### 3 Conclusion

Substrate graphite spheres whose compacting process is the same as spherical fuel elements can be used for performance test instead of using pebble fuels. Conducting ball billet compact while maintaining constant material properties and powder preparation parameters, the graphite core ball needs to be pressed twice, the strength of core ball would be closely linked to the strength of the graphite pebble. If the core ball strength is too high, the ability to secondary deformation resistance will be diminished in the final pressing, and that will cause internal crack; if core strength is too low, formability would be unacceptable, and it will be difficult to complete subsequent process like the process of graphite powder's package. At the same time, when the pressure of compact core and peripheral drops, a certain pressure of premolding can appropriately increase core strength, and the overall compact intensity is improved. By the test, it is proved that if matrix graphite core ball is molded at a pressure of 4.0 MPa, the crushing strength of the matrix graphite ball could be improved.

### Bibliography

1. Chunhe Tang. The high temperature gas cooled reactor nuclear fuel element. Beijing: chemical industry press, 2009
2. Jianming Ruan, Peiyun Huang. Powder metallurgy principle. Beijing: mechanical industry press, 2012.3
3. Jun He, Yanwen Zou, Tongxiang Liang etc. HTR—10 spherical fuel element manufacturing j. nuclear power engineering, 2002 (23) 2, 60–62



# Flow Effect on Core Burnup in a Molten Salt Reactor

Jianhui Wu and Jingen Chen

**Abstract** The molten salt reactor (MSR) adopts the fissile materials dissolved in fluoride salt as fuel. In the core, nuclear fission occurs in the fuel salt, while only nuclear decay happens when the fuel salt flows to the outer-loop. It would make the core burnup to perform differently from that in the reactor adopting solid fuel. To simulate the fuel salt circulates through the core and outer-loop, an auxiliary code based on three-dimensional (3-D) diffusion code CITATION is developed. In the core burnup calculation, accurately evaluating nuclide density of  $^{135}\text{Xe}$  is important because of the large neutron absorption cross section.  $^{135}\text{I}$  is the main source of  $^{135}\text{Xe}$ , which should also be precisely assessed. In this paper, the flow effect on nuclide density of  $^{135}\text{I}$  and  $^{135}\text{Xe}$  is investigated at various flow speeds, core to outer-loop volume ratios, as well as core power scales. The result shows that the nuclide density of  $^{135}\text{I}$  decreases significantly when the fuel salt flow is considered due to nuclide decay of  $^{135}\text{I}$  in the outer-loop. At low core power scale, the flow effect on nuclide density decrease of  $^{135}\text{Xe}$  is apparent, which results in hundreds of pcm increase of the core reactivity, because the nuclide decay of  $^{135}\text{Xe}$  in the outer-loop is considerable comparing with the  $^{135}\text{Xe}$  generation in the outer-loop resulting from  $^{135}\text{I}$  nuclide decay. It is mitigated as the core power scale is increased which increases the nuclide density of  $^{135}\text{I}$  and the nuclide generation of  $^{135}\text{Xe}$  in the outer-loop, which decreases the effect of  $^{135}\text{Xe}$  nuclide decay in the outer-loop on the  $^{135}\text{Xe}$  nuclide density.

**Keywords** Molten salt reactor • Liquid fuel • Flow effect • Burnup • Nuclide density

---

J. Wu · J. Chen (✉)

CAS Innovative Academies in TMSR Energy System,  
Shanghai Institute of Applied Physics, CAS, Shanghai, China  
e-mail: chenjg@sinap.ac.cn

## 1 Introduction

As one of the Generation IV reactor concepts, the R&D of Molten Salt Reactor (MSR) is carried out in worldwide. The Molten Salt Reactor Experiment (MSRE) with power of 8 MW successfully operated from 1956 to 1968 by the Oak Ridge National Laboratory (ORNL) [1]. The favorable experiences were gained for later R&D of MSR. In Europe, the Molten Salt Fast Reactor (MSFR) addresses the concept for Thorium–Uranium (Th-U) fuel cycle breeding with an intermediate/fast neutron spectrum in the core [2–4]. The MOlten Salt Actinide Recycler & Transmuter (MOSART) developed in Russian Federation aims to transmute transuranic elements (TRU) [5, 6]. The Thorium Molten Salt Reactor Nuclear Energy System (TMSR) and FUJI molten salt reactor (FUJI MSR) are the thermal neutron spectrum molten salt reactor, which are studied in China and Japan, respectively. They strive for realizing effective thorium utilization based on Th-U fuel cycle.

The MSR adopts nuclear fuel dissolved in fluoride salt coolant as fission element. In the core, the fission occurs in the fuel salt which then flows out to the exchanger, where the heat is transferred to the second loop salt. The most important effect caused by the salt flow is the delayed neutron precursor loss, which reduces the delayed neutron fraction of the core and brings challenges to the core safety control. The recent studies found that the fuel flow affects the delayed neutron precursor significantly, especially for long lived nuclides [7]. Different approaches were developed for trying to evaluate the fraction of delayed neutron of the core accurately [8–10].

The other important effect resulting from salt flow is nuclide evolution. Different from that in a reactor adopting solid fuel, in which the fuel is fixed and the nuclide evolution is only under the neutron irradiation condition, the fuel salt of MSR, which entrains fissile materials and fission products (FP), experiences neutron flux exposure as it flows through the core, while undergoes only nuclide decay when the fuel salt flows out to the outer-loop of core. These two conditions occur alternatively when the fuel salt continuously circulates the primary loop system. On the other hand, the additional online refueling and reprocessing make the nuclide evolution more complicated. Since there is no neutronic calculation tools dedicated to MSR and it is considered that the flow cycle time (a few tens of seconds) is too short that the nuclide decay in the outer-loop can be negligible for nuclide evolution calculation, most of the studies adopts the same tools as that in the reactor using solid fuel for solving the Bateman equation to obtain general nuclide evolution as shown in Eq. (1) [11–16].

$$\frac{dN_i}{dt} = \sum_j N_j \Phi \Delta \sigma_{j \rightarrow i} - \sum_j N_i \Phi \Delta \sigma_{i \rightarrow j} + \sum_j N_j \lambda_j \Delta \sigma_{j \rightarrow i} - N_i \Delta \lambda_i, \quad (1)$$

where the nuclide transmutation at neutron flux  $\Phi$  (the first and second terms at the right side of equation) and decay (the third and fourth terms at the right side of

equation) are considered. To simulate online reprocessing and feeding, the terms of  $\lambda_i^{\text{reprocess}} N_i$  and  $A_i$  are added as expressed in Eq. (2) [14, 15].

$$\frac{dN_i}{dt} = \sum_j N_j \Phi \Delta \sigma_{j \rightarrow i} - \sum_j N_i \Phi \Delta \sigma_{i \rightarrow j} + \sum_j N_j \lambda_j \Delta \sigma_{j \rightarrow i} - N_i \Delta \lambda_i - \lambda_i^{\text{reprocess}} N_i + A_i, \quad (2)$$

where  $\lambda_i^{\text{reprocess}}$  is the effective removal time constant and  $A_i$  denotes the fuel feeding rate.

In addition, to take the flow effect into account, some efforts have been made for improving the simulation of nuclide evolution in the previous MSR studies. Fratoni et al. and Rodriguez-Vieitez et al. revised the Bateman equations (see Eqs. (1) and (2)) by dividing the neutron flux term with a factor of 2, which accounts for the fact that the fuel salt is exposed to the neutron flux only approximately one half of the reactor operation time [17–20]. In the MSFR reactor system, due to the highly turbulent flow, short fuel cycle time (4 s) and relative slow change of the nuclide density with time, the fuel salt is considered to be homogeneously mixed for all time. Frima et al. [21] modified the Bateman equations by only considering time dependence of nuclide density and then volume averaging over the entire primary loop. In the study conducted by Doligez et al. [15], a system of nuclide evolution differential equations performed in the core and reprocessing unit are established to couple with the materials evolution in the core and reprocessing unit. These studies however did not accurately describe the nuclide evolution behavior of MSR as they overlooked the nuclide decay occurred at the part of primary loop outside core, which would possibly misestimate the nuclide density.

In thermal reactors,  $^{135}\text{Xe}$  is an important nuclide due to its very large neutron absorption cross section ( $2.7 \times 10^6$  barn at 0.025 eV). The nuclide density of  $^{135}\text{Xe}$  poses a significant impact on core reactivity, which should be evaluated accurately.  $^{135}\text{I}$  has a much smaller absorption cross section (8 barn at 0.025 eV), but its half-time (6 h) is short resulting in the most decay of  $^{135}\text{I}$  to  $^{135}\text{Xe}$ , which occupies major part of the  $^{135}\text{Xe}$  nuclide density. Accurately assessing the nuclide density of  $^{135}\text{I}$  is also important for a MSR. In the MSRE studies, much effort has been made for trying to predict the  $^{135}\text{Xe}$  behavior accurately at equilibrium state [22–26]. A model functioning  $^{135}\text{Xe}$  diffusion among fuel salt, helium bubble and graphite was developed. However, the research revealed that much work is still needed for evaluating the  $^{135}\text{Xe}$  behaviors.

The purpose of this paper is to investigate the fuel salt flow effect on fuel burnup. First, an auxiliary code based on the 3-D diffusion code CITATION is developed. It is applied to simulate the fuel salt circulating core and outer-loop considering the actual core flow speed. Online reprocessing and feeding are not involved, which will be engaged in our future study. Then, the flow effect on nuclide density of  $^{135}\text{I}$  and  $^{135}\text{Xe}$  is evaluated at various flow speeds, core to outer-loop volume ratios, and core power scales.

## 2 Calculation Methodology and Core Flow Modeling

### 2.1 Neutronic Calculation

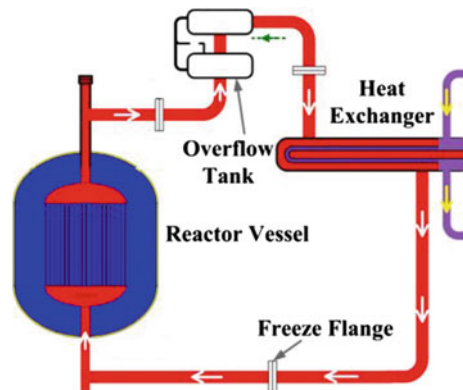
The code systems for neutronic calculation are composed of DRAGON and CITATION. The cell depletion calculation is executed for preparing macroscopic cross sections and diffusion coefficients by using DRAGON code which is based on collision probability techniques [27]. It adopts 67 energy groups from the WIMS-D data based on the ENDF/B-VII library. At the end of calculation, the overall cell is homogenized and condensed to 12 energy groups. The core depletion calculation is implemented by using the 3-D diffusion code CITATION based on cell macroscopic cross section [28]. Finally, the neutron flux and power distribution over the core are obtained.

### 2.2 Core Flow Modeling

The fuel salt flows through the core, goes out to the pipes and pump, reaches to the heat exchanger, where the heat is transferred to the second loop, and then returns to the core as shown in Fig. 1 The primary loop system can be modeled as the core and outer-loop including pipes, pump and heat exchanger as shown in Fig. 2. Nuclide decay occurs throughout the whole primary loop system, but nuclear fission occurs only in the core. The system is axially divided into a number of subregions. The nuclide composition and macro cross section at each subregion circulate clockwise to simulate the fuel salt flow. The code applied in traditional solid fuel reactor burnup calculation is inappropriate and an auxiliary code based on CITATION is developed.

The calculation flow chart is shown in Fig. 3. Cell burnup calculation based on DRAGON code prepares macroscopic cross section (Macro XS), nuclide density

**Fig. 1** Molten salt reactor primary loop system



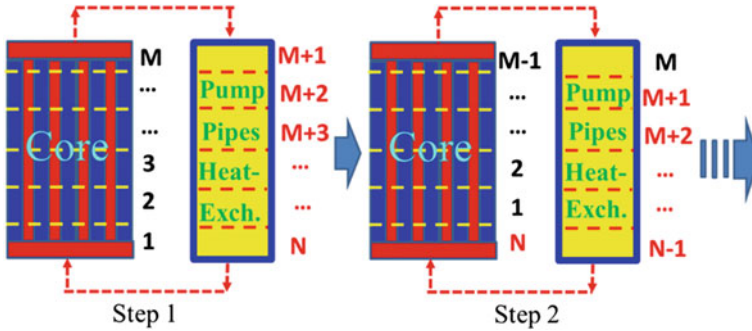


Fig. 2 Fuel salt flow modeling

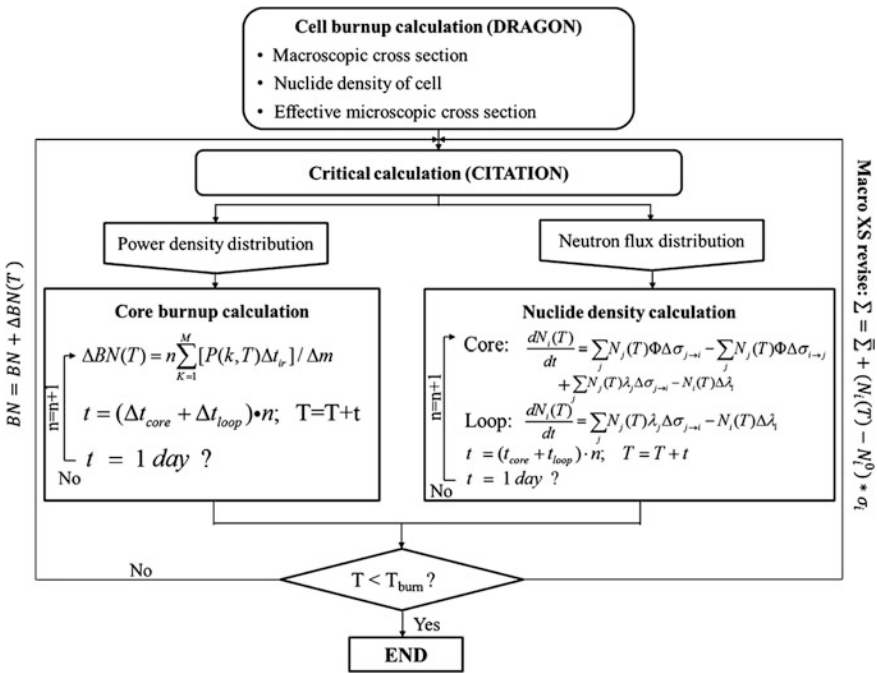


Fig. 3 Calculation flow chart

( $N_i^0$ ), and effective nuclide microscopic cross section ( $\sigma_i$ ). The critical calculation based on the CITATION code is executed first. The power and neutron flux are extracted from the calculation results for burnup and nuclide density evaluation, respectively. The core burnup is deepened as the fuel salt continuously circulates through the core, which can be expressed as Eq. (3).

$$\Delta BN(T) = n \sum_{k=1}^M [P(k, T) \Delta t_{\text{ir}}] / \Delta m, \quad (3)$$

where  $n$  is the number of the flow cycle during 1 day which is the time interval for critical calculation.  $M$  is the number of subregions in the core.  $P(k, T)$  is the power at subregion  $k$  and burnup time  $T$ . It is assumed to be unchanged during the time interval (1 day) of critical calculation.  $\Delta t_{\text{ir}}$  is the time for the salt passing through one subregion in the core.  $\Delta m$  is the heavy metal weight of one subregion.

The nuclide density of  $^{135}\text{I}$  and  $^{135}\text{Xe}$  changing with burnup is calculated, respectively, based on the neutron flux from critical calculation. Equations (4) and (5) are the basic equations for calculating nuclide density changes with time in the core.

$$\frac{dN_{\text{I}}(t)}{dt} = \gamma_{\text{I}} \sum_{\text{f}} \phi - \lambda_{\text{I}} N_{\text{I}}(t), \quad (4)$$

$$\frac{dN_{\text{Xe}}(t)}{dt} = \gamma_{\text{Xe}} \sum_{\text{f}} \phi + \lambda_{\text{I}} N_{\text{I}}(t) - (\lambda_{\text{Xe}} + \sigma_{\text{a}}^{\text{Xe}} \phi) N_{\text{Xe}}(t), \quad (5)$$

where  $\gamma_{\text{I}}$  and  $\gamma_{\text{Xe}}$  are the fission production ratio of  $^{135}\text{I}$  and  $^{135}\text{Xe}$ , respectively.  $\lambda_{\text{I}}$  and  $\lambda_{\text{Xe}}$  are the corresponding decay constant.  $\phi$  denotes the neutron flux of the core.  $\sum_{\text{f}}$  is the fission cross section.  $\sigma_{\text{a}}^{\text{Xe}}$  indicates the neutron absorption cross section of  $^{135}\text{Xe}$ . The above two equations can be rewritten as Eqs. (6) and (7) when the fuel salt flows through the outer-loop where the neutron flux can be neglected.

$$\frac{dN_{\text{I}}(t)}{dt} = -\lambda_{\text{I}} N_{\text{I}}(t), \quad (6)$$

$$\frac{dN_{\text{Xe}}(t)}{dt} = \lambda_{\text{I}} N_{\text{I}}(t) - \lambda_{\text{Xe}} N_{\text{Xe}}(t). \quad (7)$$

During the first flow cycle, the nuclide density of  $^{135}\text{I}$  and  $^{135}\text{Xe}$  after passing through the first subregion in the core can be evaluated by Eqs. (8) and (9), respectively, which are obtained by integrating Eqs. (4) and (5).

$$N_{\text{I}}^{1,1}(T) = \frac{\gamma_{\text{I}} \sum_{\text{f}} \phi_1}{\lambda_{\text{I}}} [1 - \exp(-\lambda_{\text{I}} \Delta t_{\text{ir}})], \quad (8)$$

$$\begin{aligned} N_{\text{Xe}}^{1,1}(T) &= \frac{(\gamma_{\text{I}} + \gamma_{\text{Xe}}) \sum_{\text{f}} \phi_1}{\lambda_{\text{Xe}} + \sigma_{\text{a}}^{\text{Xe}} \phi_1} \{1 - \exp[-(\lambda_{\text{Xe}} + \sigma_{\text{a}}^{\text{Xe}} \phi_1) \Delta t_{\text{ir}}]\} \\ &+ \frac{\gamma_{\text{I}} \sum_{\text{f}} \phi_1}{\sigma_{\text{a}}^{\text{Xe}} \phi_1 + \lambda_{\text{Xe}} - \lambda_{\text{I}}} \{\exp[-(\lambda_{\text{Xe}} + \sigma_{\text{a}}^{\text{Xe}} \phi_1) \Delta t] - \exp(\lambda_{\text{I}} \Delta t_{\text{ir}})\}. \end{aligned} \quad (9)$$

Then, the nuclide density of  $^{135}\text{I}$  and  $^{135}\text{Xe}$  after passing through the other subregion in the core can be calculated iteratively by Eqs. (10) and (11).

$$N_{\text{I}}^{1,i}(T) = \frac{\gamma_{\text{I}} \sum_f \phi_i}{\lambda_{\text{I}}} [1 - \exp(-\lambda_{\text{I}} \Delta t_{\text{de}})] + N_{\text{I}}^{1,i-1} \exp(-\lambda_{\text{I}} \Delta t_{\text{ir}}), \quad (10)$$

$$N_{\text{Xe}}^{1,i}(T) = \left[ N_{\text{Xe}}^{1,i-1}(T) - \frac{(\gamma_{\text{I}} + \gamma_{\text{Xe}}) \sum_f}{\lambda_{\text{Xe}} + \sigma_{\text{a}}^{\text{Xe}} \phi_i} - \frac{\lambda_{\text{I}} \left( N_{\text{I}}^{1,i-1}(T) - \frac{\gamma_{\text{I}} \sum_f \phi_i}{\lambda_{\text{I}}} \right)}{\lambda_{\text{Xe}} + \sigma_{\text{a}}^{\text{Xe}} \phi_i - \lambda_{\text{I}}} \right] \times \exp[-(\lambda_{\text{Xe}} + \sigma_{\text{a}}^{\text{Xe}} \phi_i) \Delta t_{\text{ir}}] + \frac{(\gamma_{\text{I}} + \gamma_{\text{Xe}}) \sum_f}{\lambda_{\text{Xe}} + \sigma_{\text{a}}^{\text{Xe}} \phi_i} + \frac{\lambda_{\text{I}} \left( N_{\text{I}}^{1,i-1} - \frac{\gamma_{\text{I}} \sum_f \phi_i}{\lambda_{\text{I}}} \right)}{\lambda_{\text{Xe}} + \sigma_{\text{a}}^{\text{Xe}} \phi_i - \lambda_{\text{I}}} \exp(-\lambda_{\text{I}} \Delta t_{\text{ir}}). \quad (11)$$

There is no neutron flux when the fuel salt flows out to the outer-loop. The nuclide density of  $^{135}\text{I}$  and  $^{135}\text{Xe}$  can be assessed by conducting Eqs. (12) and (13).

$$N_{\text{I}}^{1,i}(T) = N_{\text{I}}^{1,i-1}(T) \exp(-\lambda_{\text{I}} \Delta t_{\text{de}}), \quad (12)$$

$$N_{\text{Xe}}^{1,i} = N_{\text{Xe}}^{1,i-1} \exp(-\lambda_{\text{Xe}} \Delta t_{\text{de}}) + \frac{\lambda_{\text{I}} N_{\text{Xe}}^{1,i-1}}{\lambda_{\text{I}} - \lambda_{\text{Xe}}} [\exp(-\lambda_{\text{Xe}} \Delta t) - \exp(-\lambda_{\text{I}} \Delta t_{\text{de}})], \quad (13)$$

where  $\Delta t_{\text{de}}$  is the time for fuel salt passing through one subregion in the outer-loop.

As the fuel salt returns to the core, Eqs. (10) and (11), followed by Eqs. (12) and (13), are conducted alternatively.

The critical calculation is carried out again when the depletion time is accumulated to be 1 day. The burnup is called for interpolating macro cross section. The nuclide density is returned to revise the macro cross section as expressed in Eq. (14).

$$\sum = \overline{\sum} + (N_i(T) - N_i^0) \sigma_i, \quad (14)$$

where  $\overline{\sum}$ ,  $N_i^0$ , and  $\sigma_i$  are the macro cross section, nuclide density, and effective microscopic cross section of nuclide  $i$ , respectively, which are all from the cell burnup calculation.

### 2.3 Calculation Method Verification

To verify the calculation method, the cell burnup calculation with irradiation and decay being performed in turn is constructed as shown in Fig. 4. The time interval is 864 s. The power is set to 52.25 W during the irradiation period, while it decreases to zero as the time shifts to decay. It expects to simulate the fuel salt irradiated in core and decayed in outer-loop when the fuel salt circulates through the primary loop system. Meanwhile, the normal cell burnup calculation with no decay is also investigated. The nuclide density of  $^{135}\text{Xe}$  is evaluated based on the burnup calculation by using SCALE6 which was developed at ORNL for reactor criticality calculation and safety analysis. Figure 5 shows the result of  $^{135}\text{Xe}$  nuclide density changing with burnup. It can be seen that the  $^{135}\text{Xe}$  density of both two cases agrees well, although there is a small difference which might be caused by the different energy groups (67 energy groups for Dragon and 383 energy groups for SCALE6).

## 3 Calculation Result and Analysis

### 3.1 Core Description

The configuration of the MSR core depicted in Fig. 6 comprises of an active core region and a graphite reflector. The fuel assembly with the MSRE-like fuel channel, which is exhibited in Fig. 4a and labeled by the lattice in the active core region, is adopted. The graphite reflector located at the core top and bottom has the thickness of 40 cm, respectively, for reducing neutron leakage. The fuel salt density is  $2.6313 \text{ g/cm}^3$  (at the operation temperature of  $610 \text{ }^\circ\text{C}$ ) with the enrichment of 16 % for  $^{235}\text{U}$  and 99.95 % for  $^7\text{Li}$ . The parameters of the core and fuel assembly are summarized in Table 1.

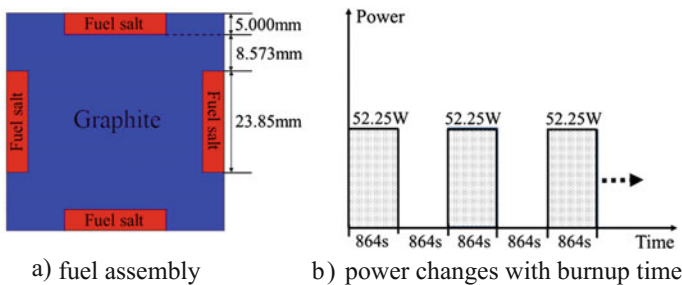


**Fig. 4** Model for calculation method verification



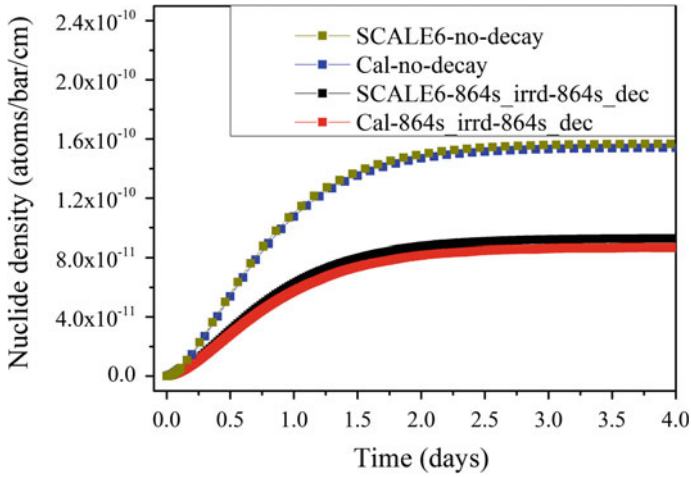


Fig. 5 Nuclide density of Xe-135 changing with burnup

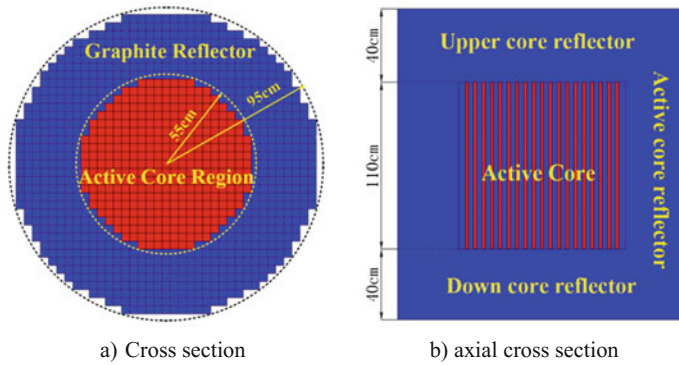


Fig. 6 Configuration of the MSR core

Table 1 Parameters of the core and fuel cell

Number of fuel assembly	348
Graphite thickness (axial/radial) (cm)	40.0/40.0
Core diameter/height (cm)	190.0/190.0
Length of fuel assembly (cm)	5.1
Length/width of fuel channel (cm)	2.385/0.5
Fuel salt density (g/cc)	2.6313
Fuel salt composition (mol %)	68 %LiF-28 %BeF <sub>2</sub> -0.1 %ThF <sub>4</sub> -3.9 %UF <sub>4</sub>
U-235 Enrichment (%)	16
Li-7 enrichment (%)	99.95

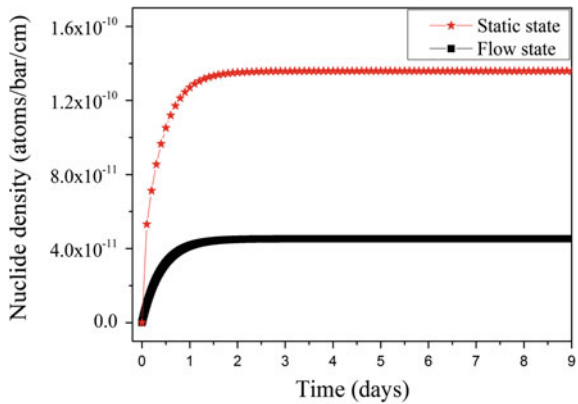
### 3.2 $^{135}\text{I}$ and $^{135}\text{Xe}$ Nuclide Density

#### 3.2.1 Fuel Salt at Static and Flow State

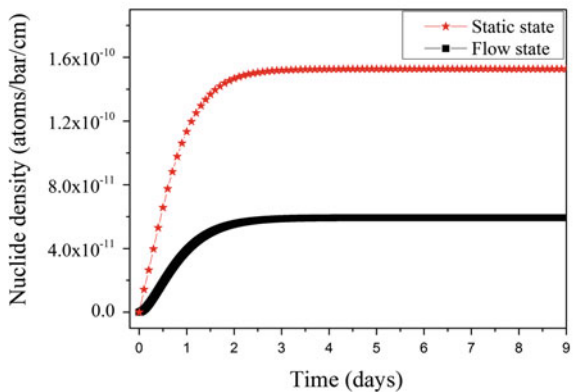
To evaluate the flow effect on  $^{135}\text{I}$  and  $^{135}\text{Xe}$  nuclide density, the fuel salt at static and flow state are investigated. The core power of 2 MW which is taken from MSR experimental prototype of SINAP (Shanghai Institute of Applied Physics), is selected for calculation. In the case of flow state, the fuel salt is assumed to stay 10 s in the core, while 20 s in the outer-loop. The core is axially divided into 10 subregions and the outer-loop is subdivided into 20 regions. It should be noted that the study on the cases with the other different flow time will be presented later in this paper.

At a flow state,  $^{135}\text{I}$  is generated in the core, but its decay occurs in both the core and outer-loop as expressed in Eqs. (4) and (6). It makes the nuclide density of  $^{135}\text{I}$  less than that at the static state as shown in Fig. 7a. Generally, the decrease of  $^{135}\text{I}$

**Fig. 7** Nuclide density of  $^{135}\text{I}$  and  $^{135}\text{Xe}$  changing with burnup



a) nuclide density of  $^{135}\text{I}$



b) nuclide density of  $^{135}\text{Xe}$

nuclide density caused by the fuel salt flow decays to  $^{135}\text{Xe}$  at the outer-loop, where  $^{135}\text{Xe}$  decay also occurs at the same time as shown in Eq. (7). With the time accumulation,  $^{135}\text{Xe}$  reveals a smaller nuclide density than that at the static state, which can be seen from Fig. 7b.

On the other hand, the decrease of equilibrium nuclide density of  $^{135}\text{I}$  and  $^{135}\text{Xe}$  due to the fuel salt flow is significant as given in Fig. 7. It can be explained by the law of  $^{135}\text{I}$  and  $^{135}\text{Xe}$  nuclide evolution at the flow state. In order to analyze conveniently, the core and outer-loop are treated as one region, respectively. The nuclide density of  $^{135}\text{I}$  from the core at the  $n$ -th flow cycle can be calculated by Eq. (15), which is derived from Eqs. (10) and (12).

$$N_{\text{I}}^{n, \text{core}}(T) = \frac{\gamma_{\text{I}} \sum_{\text{f}} \bar{\phi}}{\lambda_{\text{I}}} [1 - \exp(-\lambda_{\text{I}} \Delta t_{\text{ir}})] + N_{\text{I}}^{n-1, \text{core}}(T) \exp[-\lambda_{\text{I}} (\Delta t_{\text{de}} + \Delta t_{\text{ir}})], \quad (15)$$

where  $\bar{\phi}$  is the average neutron flux in the core.

The nuclide density of  $^{135}\text{I}$  achieves an equilibrium state as the burnup time accumulates which indicates the density at the  $n$ -th flow cycle ( $N_{\text{I}}^{n, \text{core}}(T)$ ) equals that at the  $(n-1)$ -th flow cycle ( $N_{\text{I}}^{n-1, \text{core}}(T)$ ). Hence, Eq. (15) can be rewritten to Eq. (16).

$$N_{\text{I}}(\infty) = \frac{\gamma_{\text{I}} \sum_{\text{f}} \bar{\phi}}{\lambda_{\text{I}}} [1 - \exp(-\lambda_{\text{I}} \Delta t_{\text{ir}})] / [1 - \exp(-\lambda_{\text{I}} (\Delta t_{\text{de}} + \Delta t_{\text{ir}}))], \quad (16)$$

where the first term at the right side is the equilibrium nuclide density at the static state. From Eq. (16), it can be seen that the flow effect on the equilibrium nuclide density of  $^{135}\text{I}$  is determined by the stayed time in the core ( $\Delta t_{\text{ir}}$ ) and outer-loop ( $\Delta t_{\text{de}}$ ). In this calculation,  $\Delta t_{\text{ir}}$  and  $\Delta t_{\text{de}}$  are assumed to be 10 s and 20 s, respectively. The calculation result shows that the equilibrium  $^{135}\text{I}$  nuclide density decreases almost two-thirds than that at static state.

Based on the equilibrium nuclide density of  $^{135}\text{I}$ , the function (Eq. (17)) for evaluating the equilibrium nuclide density of  $^{135}\text{Xe}$  can be elicited according to Eqs. (5) and (7).

$$N_{\text{Xe}}(\infty) = N_{\text{Xe}}^{\text{static}}(\infty) \frac{(\Delta t_{\text{de}} + \Delta t_{\text{ir}})A}{B \Delta t_{\text{de}} + \Delta t_{\text{ir}}} - \frac{\gamma_{\text{I}} \sum_{\text{f}} \bar{\phi}}{(\lambda_{\text{Xe}} + \sigma_{\text{a}}^{\text{Xe}} \bar{\phi})} \cdot \frac{(\Delta t_{\text{de}} + \Delta t_{\text{ir}})A - \Delta t_{\text{ir}}}{B * \Delta t_{\text{de}} + \Delta t_{\text{ir}}}, \quad (17)$$

where  $A = [\lambda_{\text{Xe}} / (\lambda_{\text{Xe}} + \sigma_{\text{a}}^{\text{Xe}} \bar{\phi})]$ ,  $B = \frac{[1 - \exp(-\lambda_{\text{I}} \Delta t_{\text{ir}})]}{[1 - \exp(-\lambda_{\text{I}} (\Delta t_{\text{de}} + \Delta t_{\text{ir}}))]}$ . The  $N_{\text{Xe}}^{\text{static}}(\infty)$  is the equilibrium nuclide density at the static state, which is  $\frac{(\gamma_{\text{I}} + \gamma_{\text{Xe}}) \sum_{\text{f}} \bar{\phi}}{\lambda_{\text{Xe}} + \sigma_{\text{a}}^{\text{Xe}} \bar{\phi}}$ . It can be seen that the flow effect on equilibrium nuclide density is determined by  $\Delta t_{\text{ir}}$ ,  $\Delta t_{\text{de}}$ , and neutron flux ( $\bar{\phi}$ ). By inputting  $\Delta t_{\text{ir}} = 10$  s and  $\Delta t_{\text{de}} = 20$  s, the decrease of equilibrium  $^{135}\text{Xe}$  nuclide density is around two-thirds than that at the static state.

### 3.2.2 Flow Effect at Various Flow Speeds

The volume of core is assumed to be the same as that of the outer-loop. The time for the fuel salt passing through the core and outer-loop can be considered as the same due to the constant volume flux in the primary loop system. The flow speed decreases by 15 times when the staying time of fuel salt in the core/outer-loop changes from 5 to 75 s. Figure 8 gives the equilibrium nuclide density of  $^{135}\text{I}$  and  $^{135}\text{Xe}$  at various speeds. It shows that the variation is quite small. The phenomenon can be explained by the unchanged ratio of the nuclide generation time to the nuclide decay time over a burnup period at various speeds.

### 3.2.3 Flow Effect at Various Core to Outer-Loop Volume Ratios

The fuel salt staying time in the core is fixed to 10 s, while in the outer-loop is changed from 5 s to 35 s. It denotes the core to outer-loop volume ratio is decreased by 7 times since the volume flow is kept constant. The calculation result is given in Fig. 9. The equilibrium nuclide density of both  $^{135}\text{I}$  and  $^{135}\text{Xe}$  decreases with the increase of volume of the outer-loop. As given in Eq. (16), the equilibrium nuclide density of  $^{135}\text{I}$  is inversely proportional to the staying time in the outer-loop. It is complicated to see the influence of core to outer-loop volume ratio on  $^{135}\text{Xe}$  equilibrium nuclide density according to Eq. (17). But the phenomenon illustrated in Fig. 9 can be explained by the nuclide decay time extending when the outer-loop volume increases, which results in the increase of  $^{135}\text{Xe}$  nuclide disappearance.

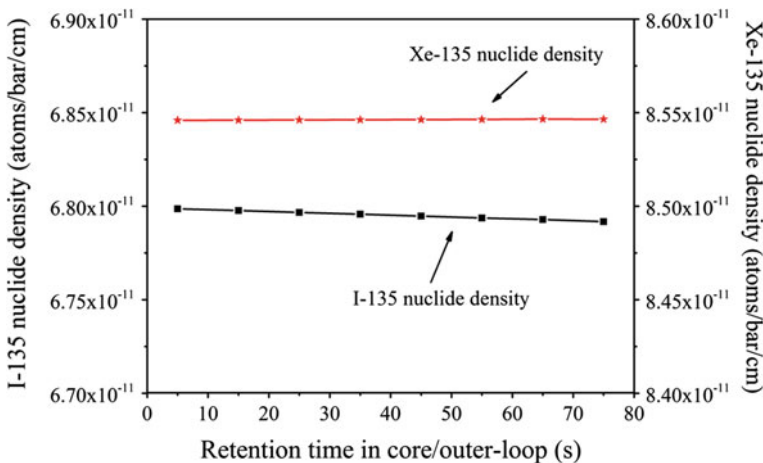
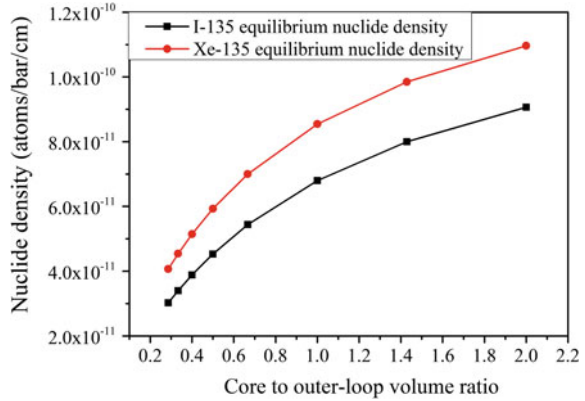


Fig. 8 Nuclide density of  $^{135}\text{I}$  and  $^{135}\text{Xe}$  changing with flow speed

**Fig. 9** Nuclide density of  $^{135}\text{I}$  and  $^{135}\text{Xe}$  changing with core to outer-loop volume ratio



### 3.2.4 Flow Effect at Various Core Power

The core power of 10, 100, and 1000 MW are also adopted for calculation. As introduced in Sect. 3.2.2, the flow speed makes no influence on the flow effect under the MSR normal operation condition (with flow cycle time being a few tens of seconds) at the flow state, the fuel salt staying time in the core and outer-loop are set to be 10 and 20 s, respectively. The flow effect on nuclide density of  $^{135}\text{I}$  and  $^{135}\text{Xe}$  at 10 and 100 MW are similar to that at 2 MW. It behaves differently at 1000 MW due to the large power scale, which gives a much larger  $^{135}\text{I}$  nuclide density than  $^{135}\text{Xe}$ , as shown in Fig. 10. The nuclide density of  $^{135}\text{Xe}$  at the static state gradually declines rather than keeping constant after about 1.5 days. It can be explained by the increase of neutron flux ( $\phi$ ) and the unchanged power with the burnup. The reduction of fissile nuclide is significant, which presents the remarkable decrease of macro fission cross section ( $\sum_f$ ), with the burnup due to the large power scale. To keep the power ( $\eta \sum_f \phi$ ) unchanged, the neutron flux ( $\phi$ ) would increase with the burnup. As expressed in Eq. (5), the  $^{135}\text{Xe}$  nuclide density would decrease because of the unchanged  $\sum_f \phi$  and the raised neutron flux ( $\phi$ ). Unlike the static state,  $^{135}\text{Xe}$  generated in the outer-loop due to the  $^{135}\text{I}$  decay is continuously injected to the core. It would make up the  $^{135}\text{Xe}$  nuclide decrease due to the neutron flux increase as illustrated in Fig. 10. On the other hand, compared with the  $^{135}\text{Xe}$  nuclide generation in the outer-loop, the  $^{135}\text{Xe}$  decay can be neglected due to the much larger  $^{135}\text{I}$  nuclide density ( $7.0 \times 10^{-08}$  atoms/barn/cm) than the  $^{135}\text{Xe}$  nuclide density ( $6.9 \times 10^{-10}$  atoms/barn/cm). As a result, the flow effect on the  $^{135}\text{Xe}$  nuclide density is small as illustrated in Fig. 10. The performance of  $^{135}\text{I}$  nuclide density changing with the burnup time is the same as that at 2 MW because of the unchanged  $\sum_f \phi$ .

Figure 11 shows the nuclide density of  $^{135}\text{I}$  and  $^{135}\text{Xe}$  changing with the salt flow speed as well as the core to outer-loop volume ratios at different power scale.

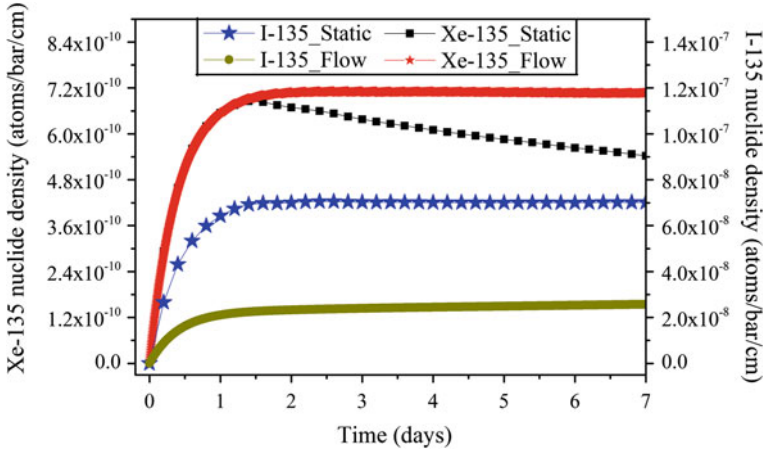


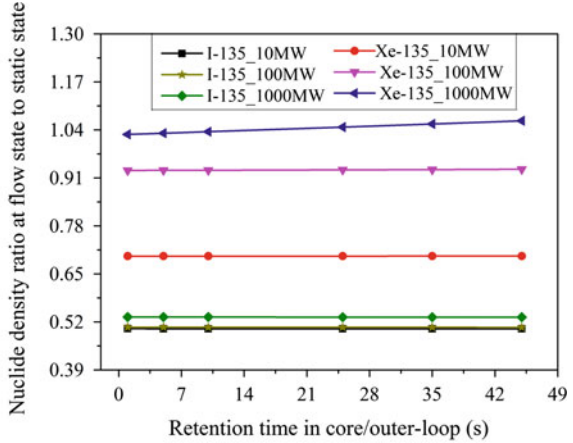
Fig. 10 Nuclide density of  $^{135}\text{I}$  and  $^{135}\text{Xe}$  at 1000 MW

The vertical coordinate of the figures indicates the equilibrium nuclide density at the flow state to that at the static state except at 1000 MW, which is the maximum nuclide density. As illustrated in Fig. 11a, the speed has a quite small influence on the nuclide density of  $^{135}\text{I}$  and  $^{135}\text{Xe}$ . It is because of the unchanged ratio of nuclide generation time to decay time when the core to outer-loop volume ratio is fixed. By changing the core to outer-loop volume ratio, the  $^{135}\text{I}$  nuclide density ratio at flow state to static state is almost the same at different power scale, but the flow effect on the nuclide density of  $^{135}\text{Xe}$  is mitigated as the power increases as shown in Fig. 11b. The phenomenon can be explained by the increase of  $^{135}\text{I}$  nuclide density, which increases the  $^{135}\text{Xe}$  generation in the outer-loop and makes the effect of  $^{135}\text{Xe}$  decay in the outer-loop be mitigated.

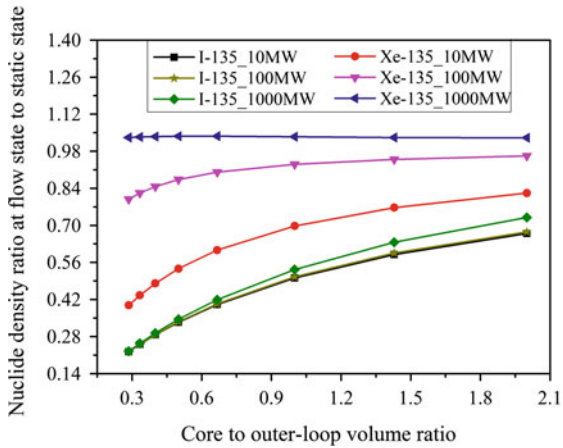
### 3.3 Flow Effect on Core Reactivity

Figure 12 shows the flow effect on the core reactivity increases at equilibrium state at various power scales except at 1000 MW, where the core reactivity decrease is estimated at the burnup of the 4th day. Generally, the flow effect on the core reactivity is proportional to the amount of  $^{135}\text{Xe}$  nuclide decrease and the neutron flux. By increasing the core power scale, the flow effect on the  $^{135}\text{Xe}$  nuclide density decrease is mitigated, but the neutron flux is increased. The integrated factors make the flow effect on reactivity is nonmonotonic with the core powers as shown in Fig. 12. In the case with the core to outer-loop volume ratio being 1 and 2, the flow effect on reactivity achieves a maximum value at 10 MW rather than 2 MW. It can be explained by the relatively larger neutron flux although the  $^{135}\text{Xe}$  nuclide decrease is smaller than that at 2 MW.

**Fig. 11** Nuclide density of  $^{135}\text{I}$  and  $^{135}\text{Xe}$  at different power scale



a) Different salt flow velocity



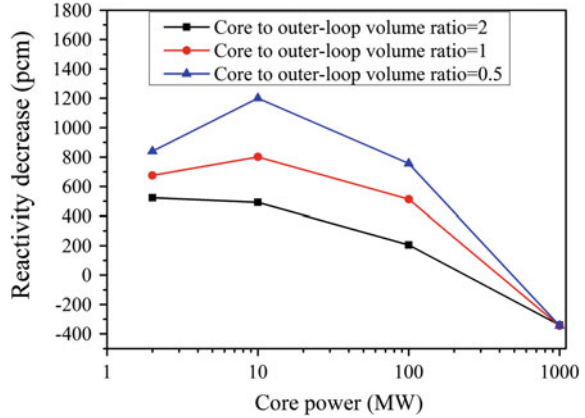
b) different core to outer-loop volume ratio

## 4 Conclusion

In this work, the flow effect on the nuclide density of  $^{135}\text{Xe}$  and  $^{135}\text{I}$  is investigated at various fuel salt flow speeds, core to outer-loop volume ratios and core powers. To simulate the fuel salt flow, an auxiliary code based on CITATION is developed. The calculation method is demonstrated by conducting the cell depletion calculation with the irradiation and decay alternatively performed. A core similar to MSRE is adopted for the calculation. The results achieved can be summarized as follows:

- The nuclide density of  $^{135}\text{I}$  decreases significantly when the fuel salt flow is considered. It becomes even less when the core to outer-loop volume ratio decreases. The phenomenon can be explained by the nuclide decay time

**Fig. 12** Flow effect on core reactivity at various core powers



extension resulting from the fuel salt flowing out to the outer-loop. The performance of flow effect on  $^{135}\text{I}$  nuclide decrease at various powers is almost the same.

- The  $^{135}\text{Xe}$  nuclide density is decreased when the flow effect is taken into account at relatively low power. The nuclide density decrease is inversely proportional to the core to outer-loop volume ratio. The flow effect is mitigated as the core power increases due to the increase of  $^{135}\text{I}$  nuclide density, which increases the  $^{135}\text{Xe}$  generation at the outer-loop and makes the effect of  $^{135}\text{Xe}$  decay at the outer-loop decrease. The nuclide density of  $^{135}\text{Xe}$  increases at very large core power scale such as 1000 MW when the fuel salt flow is taken into account.
- The flow speed has a quite small influence on the  $^{135}\text{I}$  and  $^{135}\text{Xe}$  nuclide density decrease at the flow state. It is because the ratio of nuclide decay time to nuclide generation time keeps unchanged at different flow speeds due to the constant volume flow.
- The core reactivity is increased at low power scale, where the  $^{135}\text{Xe}$  nuclide is decreased when the fuel salt flow is considered. But it is decreased at very large power scale due to the increase of  $^{135}\text{Xe}$  nuclide density.

Online refueling and bubbling are not considered. It will be incorporated in the calculation during the future work. On the other hand, the flow effect on the other nuclide density such as  $^{149}\text{Pm}$ ,  $^{149}\text{Sm}$ , and  $^{233}\text{Pa}$  which have large neutron absorption cross sections will be conducted in the future.

**Acknowledgments** This work is supported by the Chinese TMSR Strategic Pioneer Science and Technology Project under Grant No. XDA02010000 and the Frontier Science Key Program of the Chinese Academy of Sciences under Grant No. QYZDY-SSW-JSC016.



## References

1. Haubenreich, P.N. and Engel, J.R., *Experience with the molten-salt reactor experiment*. Nuclear Applications & Technology, 1970. **8**: p. 118–136
2. Mathieu, L., Heuer, D., Brissot, R., et al., *The thorium molten salt reactor: Moving on from the MSBR*. Progress in Nuclear Energy, 2006. **48**(7): p. 664–679
3. Mathieu, L., Heuer, D., Merle-Lucotte, E., et al., *Possible Configurations for the Thorium Molten Salt Reactor and Advantages of the Fast Nonmoderated Version*. Nuclear Science and Engineering, 2009. **161**: p. 78–89
4. Serp, J., Allibert, M., Beneš, O., et al., *The molten salt reactor (MSR) in generation IV: Overview and perspectives*. Progress in Nuclear Energy, 2014. **77**: p. 308–319
5. Ignatiev, V.V., Feynberg, O.S., Zagnitko, A.V., et al., *Molten-salt reactors: New possibilities problems and solutions*. Atomic Energy, 2012. **112**(3): p. 157–165
6. Ignatiev, V., Feynberg, O., Gnidoi, I., et al., *Molten salt actinide recycler and transforming system without and with Th-U support: Fuel cycle flexibility and key material properties*. Annals of Nuclear Energy, 2014. **64**: p. 408–420
7. Zhang, D., Qiu, S., Liu, C., et al., *Steady state investigation on neutronics of a molten salt reactor considering the flow effect of fuel salt*. Chinese Physics C, 2008. **32**(8): p. 624–628
8. Mattioda, F., Ravetto, P., and Ritter, G., *Effective delayed neutron fraction for fluid-fuel systems*. Annals of Nuclear Energy, 2000. **27**(16): p. 1523–1532
9. Guerrieri, C., Cammi, A., and Luzzi, L., *A preliminary approach to the MSFR control issues*. Annals of Nuclear Energy, 2014. **64**: p. 472–484
10. Carlo Fiorina, M.A., Antonio Cammi, Claudia Guerrieri, Jiri Krepel, Lelio Luzzi, Konstantin Mikityuk, Marco Enrico Ricotti. *Analysis of the MSFR core neutronics adopting different neutron transport models*. in *ICONE20-POWER2012*. 2012. Anaheim, California, USA
11. Nuttin, A., Heuer, D., Billebaud, A., et al., *Potential of thorium molten salt reactors-detailed calculation and concept evolution with a view to large scale energy production*. Progress in Nuclear Energy, 2005. **46**(1): p. 77–99
12. Heuer, D., Merle-Lucotte, E., Allibert, M., Doligez, X., Ghetta, V., *Simulation tools and new developments of the molten salt fast reactor*. Revue Générale Nucléaire: Tous les numéros 2010. **6**: p. 95–100
13. Delpéch, S., Merle-Lucotte, E., Heuer, D., et al., *Reactor physic and reprocessing scheme for innovative molten salt reactor system*. Journal of Fluorine Chemistry, 2009. **130**(1): p. 11–17
14. Aufiero, M., Cammi, A., Fiorina, C., et al., *An extended version of the SERPENT-2 code to investigate fuel burn-up and core material evolution of the Molten Salt Fast Reactor*. Journal of Nuclear Materials, 2013. **441**(1–3): p. 473–486
15. Doligez, X., Heuer, D., Merle-Lucotte, E., et al., *Coupled study of the Molten Salt Fast Reactor core physics and its associated reprocessing unit*. Annals of Nuclear Energy, 2014. **64**: p. 430–440
16. Yu, C., Li, X., Cai, X., et al., *Analysis of minor actinides transmutation for a Molten Salt Fast Reactor*. Annals of Nuclear Energy, 2015. **85**: p. 597–604
17. Fratoni, M., Barnes, D., Greenspan, E., et al., *Design and Analysis of Molten Salt Reactor Fueled by TRU from LWR*, in *PHYSOR 2004*. 2004: Chicago, Illinois
18. Fratoni, M. and Greenspan, E., *Transmutation capability of molten salt reactors fueled with TRU from LWR*, in *ARWIF-2005*. 2005: Oak-Ridge, TN
19. Becker, B., Fratoni, M., and Greenspan, E., *Feasibility of a critical molten salt reactor for waste transmutation*. Progress in Nuclear Energy, 2008. **50**(2–6): p. 236–241
20. Rodriguez-Vieitez, E., Lowenthal, M.D., Greenspan, E., et al., *Transmutation Capability of once-through critical or sub-critical molten-salt reactors*, in *Proceedings of the Seventh Information Exchange Meeting on Actinide and Fission Product Partitioning and Transmutation*. 2002: Jeju, Republic of Korea
21. Frima, L.L.W., *Burnup in a molten salt fast reactor*, in *Department of Radiation Science and Technology*. 2013, Delft University of Technology

22. Haubenreich, P.N., Engel, J.R., Prince, B.E., et al., *MSRE design and operations report part III. Nuclear analysis*. ORNL, 1964, ORNL TM-730
23. Engel, J.R. and Prince, B.E., *The Reactivity Balance in The MSRE*. ORNL, 1967, ORNL-TM-1796
24. Kedl, R.J. and Houtzeel, A., *Development of a model for computing  $^{135}\text{Xe}$  migration in the MSRE*. ORNL, 1967
25. Scott, D. and Eatherly, W.P., *Graphite and Xenon behavior and their influence on molten-salt reactor design*. NUCLEAR APPLICATIONS & TECHNOLOGY, 1969. **8**: p. 179–189
26. Engel, J.R. and Steffy, R.C., *Xenon Behavior in the Molten Salt Reactor Experiment*. ORNL, 1971, ORNL-TM-3464
27. Marleau G., H.e.A., Roy R., *A User guide for dragon version5*. École Polytechnique de Montréal, 2014, IGE-335
28. Fowler, T.B. and Vondy, D.R., *Nuclear reactor core analysis code: CITATION*. Oak Ridge National Lab., Tenn., 1969, ORNL-TM–2496

# Key Parameter Measurements of the Low-Pressure Gas Discharge Plasmas Used for Studying the Ion Extraction Process

Heping Li, Qihui Chu, Xin Wang, Peng Wang, Junjie Chai  
and Zhanxian Li

**Abstract** Extraction of the target isotope ions in the laser photoionized plasmas is one of the key processes in the atomic vapor laser isotope separation. The key plasma parameters, including the electron number density, the temperatures of electrons and heavy species, may have significant influences on the characteristics of the ion extraction process. In recent years, the ion extraction simulation facility has become an important tool to study the ion extraction mechanisms. In the present paper, a low-pressure, alternating-current (AC) gas discharge experimental setup is developed. Based on this gas discharge plasma source, the electrical and optical measurements are conducted for studying the features of the argon discharge plasma jet under different operating conditions. In particular, a collisional-radiative model is established for argon plasmas and is used for the derivation of the electron temperature and number density based on the measured spectral line-intensity ratios, while the gas temperature is obtained by fitting the recorded optical emission spectra of the plasma jet ranging from 334.5 to 337.5 nm using SPECAIR. The preliminary experimental results show that both the power input and driving frequency of the power supplies have significant influences on the number density and temperature of electrons in the expanded plasma jet region with constant chamber pressures of  $(6.0\text{--}9.0) \times 10^{-2}$  Pa. The measured key plasma parameters, including the temperature and number density of electrons and the gas temperature, of the argon plasma jet are, on the order of magnitude, close to those of the laser photoionized plasmas in the laser isotope separation process, which provides a good basis for the ion extraction simulation experiments.

---

H. Li (✉) · Q. Chu  
Department of Engineering Physics, Tsinghua University, Beijing 100084, China  
e-mail: liheping@tsinghua.edu.cn

X. Wang · Z. Li  
College of Mechanical Engineering, North China University of Science and Technology,  
Tangshan 063009, China

P. Wang · J. Chai  
Research Institute of Physical and Chemical Engineering of Nuclear Industry,  
Tianjin 300381, China

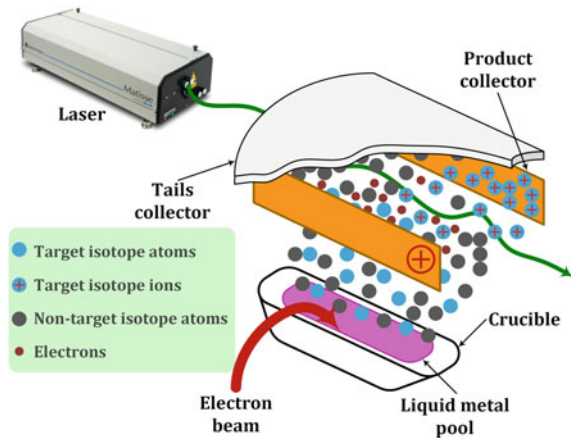
**Keywords** Ion extraction process • Low-pressure gas discharge • Plasma jet • Optical emission spectroscopy • Collisional-radiative model

## 1 Introduction

During the past few decades, isotope separation by a laser-induced selective ionization in the atomic metal vapor phase has attracted much attention of the researchers due to its potentially high efficiency and large separation factor compared with other existing isotope separation methods, e.g., the electromagnetic method, gas diffusion method and the centrifugal separation method. However, there still exist lots of difficulties for promoting the actual applications of this isotope separation technique from the lab-scale prototype to the large-scale commercial facility at the present time. A complete atomic vapor laser isotope separation process is illustrated in Fig. 1, which is composed of three subprocesses, i.e., the metal atomization subprocess to form an atomic vapor beam moving with a macroscopic velocity, laser photo-ionization subprocess to obtain target isotope ions and electrons with remaining neutral un-target isotope atoms, and the ion extraction subprocess to collect the target isotope ions [1].

Among the preceding subprocesses, there are many factors influence the transportation characteristics of the isotope ions, especially the ion extraction time and efficiency, in the ion extraction subprocess, including the initial electron number density and energy of the laser-induced metal plasmas [2–6], the type of the collection electrodes, the amplitude and waveform of the externally applied electric field [7–12], the species diffusion [13, 14], inelastic collisions, and the ion sputtering on the electrode surface [15–18], etc. In the foregoing experimental studies (e.g., [7–9, 11, 12]), the laser-induced metal plasmas are usually necessary with a very complicated and expensive laser system. Recently, studies on the ion

**Fig. 1** Schematic of laser isotope separation process



extraction process based on a ion extraction simulation facility using a gas discharge plasma source have been reported [14, 19]. The advantages using these simulated ion extraction facilities exist not only in the low capital cost, but also in providing a possible wide plasma parameter (e.g, electron number density and temperature, gas temperature) window for investigating, as well as for optimizing, the actual ion extraction process. In Ref. [14], a YAG quadruple-frequency pulse laser is used to ion air enclosed in a quartz tube at a pressure of 1 Pa for obtaining a plasma with an electron number density of  $10^8$  to  $10^9$   $\text{cm}^{-3}$ . While a Xe inductively coupled plasma (ICP) source driven at a frequency of 300 MHz and a chamber pressure of  $4 \times 10^{-4}$  Torr ( $\sim 5 \times 10^{-2}$  Pa) was employed in [19] for studying the resonant effect of the applied radio frequency electric field on the ion extraction characteristics, in which the electron number density and temperature are on the magnitude of  $10^{10}$   $\text{cm}^{-3}$  and 8 eV, respectively.

In this paper, a low-pressure alternative-current (AC) gas discharge plasma source is established to provide a platform for investigating the ion extraction process. The optical emission spectroscopy (OES) method is employed to study the variations of the key plasma parameters, which are referred to the electron number density, the temperatures of electrons and heavy species in this study, under different operating conditions.

## 2 Experimental Setup

As shown in Fig. 2, the ion extraction simulation platform consists of the vacuum system, plasma producing system and the ion extraction and collection system. The vacuum system is used to achieve a required low pressure environment for the gas discharges and the ion extraction and collection. The vacuum chamber includes a cylindrical main chamber with the inner diameter and length of 700 and 900 mm, respectively, and an auxiliary cubic chamber which is connected with the main chamber with a dimensional size of  $750 \times 400 \times 250$   $\text{mm}^3$ . The coaxial type plasma generator is located inside the auxiliary chamber and the plasma jet is issued from the torch nozzle and enters the main chamber. Two pump units, consisting of one mechanical pump (BeiYi WooSung Vacuum, TRP-60) and one molecular pump (JiuTai Vacuum, JTFB-1600) for each unit, are employed to achieve a background pressure less than  $5 \times 10^{-4}$  Pa and a working pressure on the magnitude of  $10^{-2}$  Pa which depends on the mass flow rate of the plasma working gas. The ion collection electrodes are positioned on top of the plasma torch nozzle exit as shown in Figs. 2 and 3. The electrode gap spacing can be automatically controlled ranging from 0 to 140.0 mm via stepper motors using a PLC (Programmable Logic Controller); while the declination angle between the electrodes is adjusted manually between  $0^\circ$  (a parallel electrode configuration) and  $60^\circ$  before experiment. The area of the collection electrode can be adjusted according to the size and number of the Faraday cups in the ion extraction experiment. In this study, the width and height of each collection electrode are 145.0 and 240.0 mm, respectively.

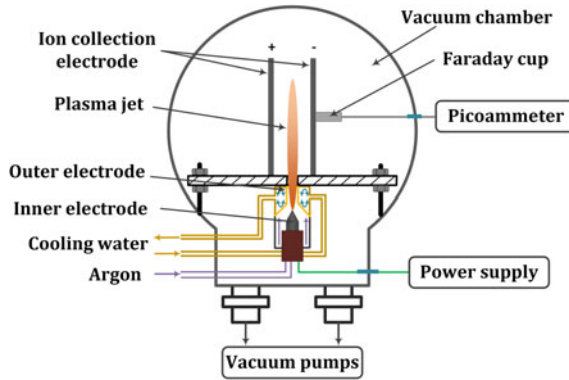


**Fig. 2** Schematic of the ion extraction simulation platform

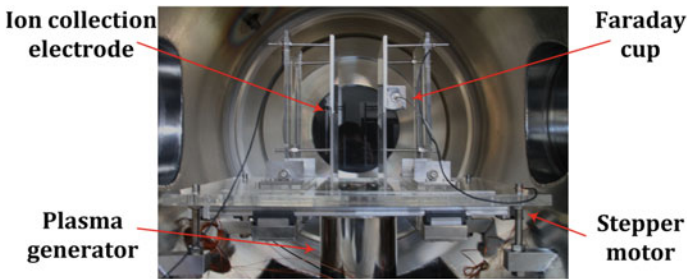


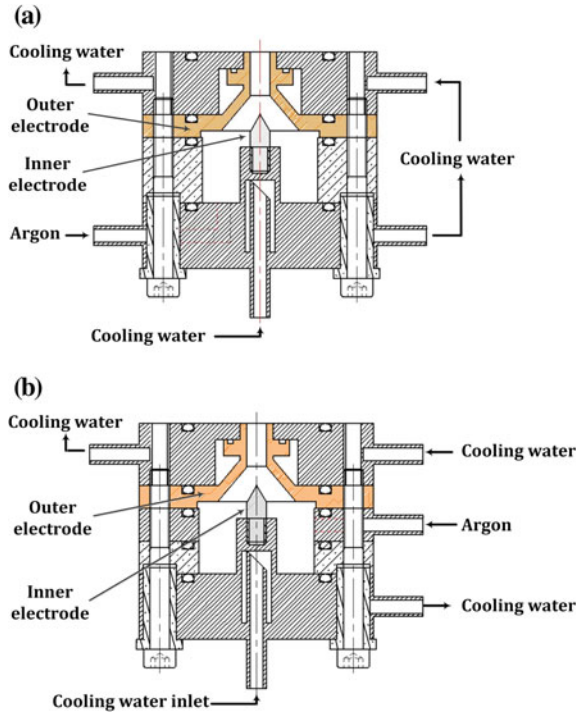
**Fig. 3** Picture of the main part of the experimental setup

And these two stainless steel electrodes are placed in parallel with a gap spacing of 80.0 mm.

In this study, two types of coaxial type plasma generators are used to produce a stable plasma jet driven by a kilo-Hertz (Fig. 4a) or a radio frequency (RF) (Fig. 4b) power supply. The inner and outer electrode materials are molybdenum and copper, respectively, and there exist no dielectric barrier layers between electrodes. The diameter of the inner electrode is 6.0 mm with a 60° conical tip, and the annular electrode gap spacing is fixed at 3.0 mm. The kilo-Hertz (10–30 kHz) and RF (13.56 MHz) power supplies are used to produce the stable discharges. Such type of plasma generator has been employed to produce warm [20] and cold plasmas [21] at atmospheric pressure. Under low pressure conditions, the argon discharge plasmas would show a significant non-equilibrium feature and expand significantly at the downstream of the torch nozzle exit.

During discharges, the electrodes are cooled by a circulating water and the mass flow rate of the plasma forming gas (99.99 % or better of argon) is controlled by the mass flow controllers (Beijing Sevenstar Electronics Co. Ltd., D07-7K). The values of the discharge voltage and current are measured using a high voltage probe

**Fig. 4** Schematics of the plasma generator **a** for kilo-Hertz driven discharges; **b** for RF driven discharges



(Tektronix P6015 A) and a current probe (Tektronix TCP202), respectively, and recorded on a digital oscilloscope (Tektronix DPO4034). The discharge images are taken by a digital camera (Canon EOS 7D). The optical emission spectra of the plasma jet are recorded by a spectrometer (Avantes AvaSpec-3648) using a fiber probe. During experiments, the optical fiber is located on a two dimensional precision translational stage (GCD-202100 M and GCD-203100 M, China Daheng Group, Inc.) with a positioning precision of 0.01 mm. To obtain the spatially resolved spectra of the plasmas, a convex lens with a focal length of 250 mm is located between the discharge chamber and the optical fiber which have a spatial resolution of 3.0 mm. Therefore, the spectrometer records the integrated value of the emitted intensity of the plasma jet along the light path.

### 3 Experimental Results and Discussions

In this study, the electron number density ( $n_e$ ) and temperature ( $T_e$ ) of the plasma jet are determined based on the collisional-radiative model (CRM) [22], while the gas temperature ( $T_h$ ) is obtained by matching the SPECAIR code-simulated spectrum with the experimental result of the nitrogen band ranging from 334.5 to 337.5 nm

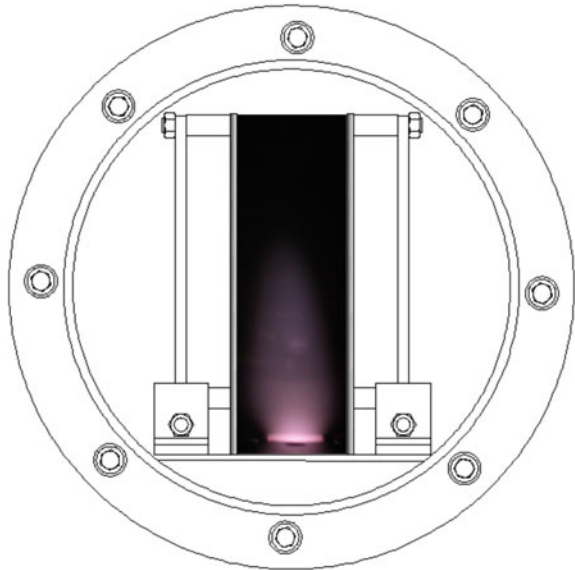
[23]. The detailed descriptions on these OES methods can be referred to Refs. [22, 23] and the papers cited therein.

### 3.1 Discharges Driven by a Kilo-Hertz Power Supply

A typical discharge image of the expanded plasma jet for the case with the total argon mass flowrate of  $\dot{m} = 71.4$  mg/min, power input of  $P_{\text{in}} = 8.2$  W, driving frequency of  $f = 26$  kHz and chamber pressure of  $p = 6.0 \times 10^{-2}$  Pa is shown in Fig. 5 with an exposure time of  $t_{\text{exp}} = 1/30$  s. It is seen from Fig. 5 that the plasma jet expands at the downstream of the torch nozzle exit due to the low chamber pressure. The derived three key plasma parameters, i.e.,  $T_h$ ,  $T_e$  and  $n_e$ , at 3.0 cm away from the nozzle exit along the geometrical axis of the plasma generator are 600 K, 2.47 eV and  $1.65 \times 10^{10}$  cm $^{-3}$ , respectively. These experimentally measured values indicate that, on one hand, the plasma jet deviates from the local thermodynamic equilibrium (LTE) state significantly; and on the other hand, the values of  $T_e$  and  $n_e$  of the produced plasma jet are close to those of the photoionized plasmas in the laser isotope separation process [10, 11] or those of the ICPs in [19]. In addition, our experimental results show that the variation of the gas temperature ( $T_h$ ) is very small. Thus, we will focus on the variations of  $T_e$  and  $n_e$  in the following subsections.

The variations of the electron number density and temperature with the power input at 3.0 cm away from the nozzle exit along the geometrical axis of the plasma generator are shown in Fig. 6 with other parameters being unchanged

**Fig. 5** Typical image of the plasma jet  
 ( $\dot{m} = 71.4$  mg/min,  
 $P_{\text{in}} = 8.2$  W,  $f = 26$  kHz,  
 $p = 6.0 \times 10^{-2}$  Pa,  
 $t_{\text{exp}} = 1/30$  s)





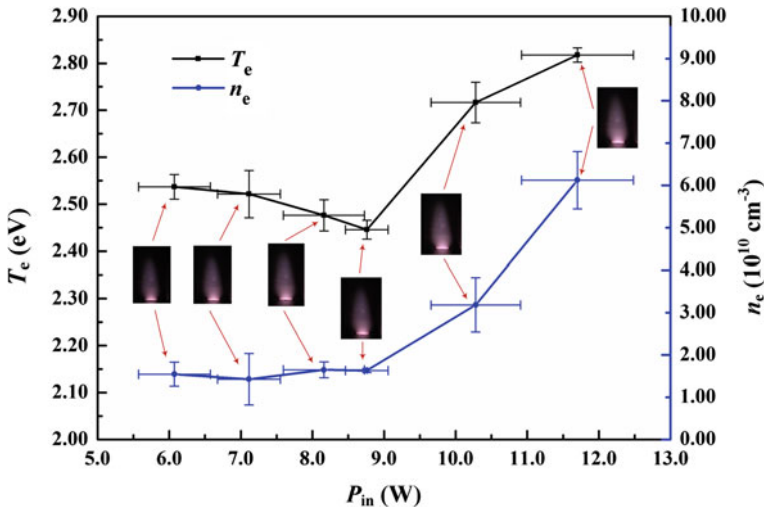


**Fig. 6** Variations of the electron number density and temperature with the power input ( $\dot{m} = 71.4 \text{ mg/min}$ ,  $f = 26 \text{ kHz}$ ,  $p = 6.0 \times 10^{-2} \text{ Pa}$ ,  $t_{\text{exp}} = 1/30 \text{ s}$ )

( $\dot{m} = 71.4 \text{ mg/min}$ ,  $f = 26 \text{ kHz}$ ,  $p = 2.1 \times 10^{-2} \text{ Pa}$ ). It is seen that: (i) for the cases with lower power input (e.g., lower than 9.0 W in this study), the influences of the power input on both  $n_e$  and  $T_e$  are small; (ii) while with the further increase in the power input (e.g., higher than 9.0 W), both the electron number density and temperature increase significantly, which results very possibly from the higher energy deposition to the free electrons from the external electric field, and the subsequent energy transfer from the electrons to heavy particles via the elastic and inelastic collisions between them.

### 3.2 Discharges Driven by a RF Power Supply

For the RF glow discharges, the issued plasma jet from the torch nozzle exit diffuses much more significantly than that of the kilo-Hertz driven discharges. The experimental observations show that the expanded RF plasma jet occupies most space of the main chamber, as shown in Fig. 7.

The influences of the power input on the electron number density and temperature are provided in Fig. 8. Compared with the measured results presented in Fig. 6 for the kilo-Hertz driven gas discharge plasmas, we can see that: (i) Although the electron number density increases with increasing in the power input, the maximum value of  $n_e$  ( $1.36 \times 10^{11} \text{ cm}^{-3}$ ) for the RF discharge plasmas is about twofold of that of the kilo-Hertz driven discharges ( $6.12 \times 10^{10} \text{ cm}^{-3}$ ) due to the higher RF power input. (ii) The influence of the RF power input on the electron temperatures is smaller than that of the kilo-Hertz driven gas discharge plasmas

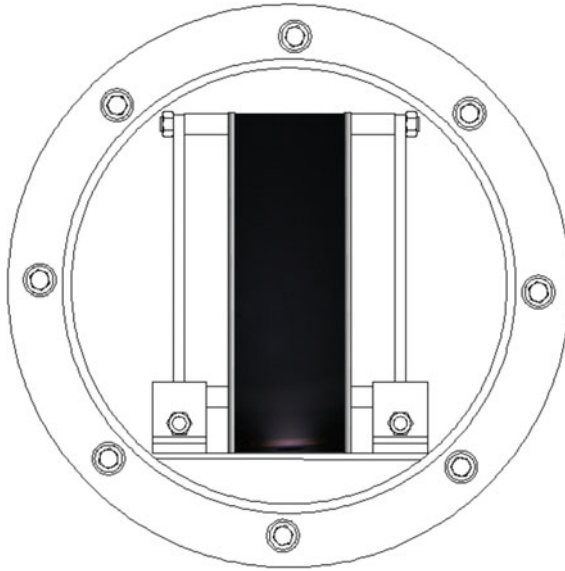


**Fig. 7** Typical image of the plasma jet ( $\dot{m} = 87.4$  mg/min,  $P_{in} = 127.0$  W,  $f = 13.56$  MHz,  $p = 9.0 \times 10^{-2}$  Pa,  $t_{exp} = 1$  s)

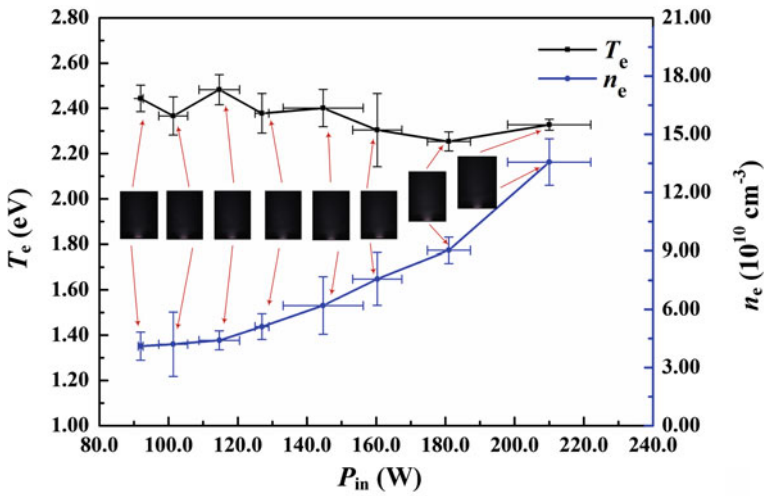


**Fig. 8** Variations of the electron number density and temperature with the power input ( $\dot{m} = 87.4$  mg/min,  $f = 13.56$  MHz,  $p = 9.0 \times 10^{-2}$  Pa,  $t_{exp} = 1$  s)

(Fig. 6) with a maximum relative change of 7.8 %. The reasons lead to this phenomenon is not clear at the present time, and the numerical and experimental studies concerning the influences of the driving frequency of the power supply on the characteristics of the plasma jets are indispensable in our future research.

## 4 Conclusion

In this paper, an ion extraction simulation facility is established based on a low-pressure gas discharge plasma source for investigating the influences of the key plasma parameters, especially the electron number density and temperature, on the characteristics of the ion extraction process. As a preliminary study, the influences of the power input on the key plasma parameters are studied experimentally using the optical emission spectroscopy method. The experimental results show that, on one hand, the produced plasma jet can be used to simulate the photoionized plasmas in the laser isotope separation process with the values of  $n_e$  and  $T_e$  close to, on the order of magnitude, those of the laser-induced metal plasmas; and on the other hand, the values of  $n_e$  and  $T_e$  can be adjusted by varying the operating parameters (e.g., the power input and driving frequency of the power supplies), which provides a wide parameter window for investigating the influences of  $n_e$  and  $T_e$  on the ion extraction features more conveniently compared with the usage of the actual laser isotope separation facilities.

## References

1. H.-P. Li, P. Wang, X. Wang, W. You, J.-J. Chai, Z.-Y. Li, Advances on the atomic vapor laser isotope separation process-(I): Theory, *High Voltage Engineering*, 2015, 41(9): 2825–2836 (In Chinese)
2. M. Widner, I. Alexeff, W. D. Jones, and K. E. Lonngren, Ion acoustic wave excitation and ion sheath evolution, *Physics of Fluids*, 1970, 13(19): 2532–2540
3. F. F. Chen, Decay of a plasma created between negatively biased walls, *Physics of Fluids*, 1982, 25: 2385–2387
4. K. Okano, Theory of ion-extraction time from a plasma by a static electric field, *Journal of Nuclear Science and Technology*, 1992, 29(7): 601–607
5. K. Yuan, P. Xu, P. Yu, and J. Wang, Investigation of ion extraction in laser isotope separation, *Chinese Journal of Atomic and Molecular Physics*, 1993, 10(3): 2839–2843 (In Chinese)
6. M. Yan, C. Ying, D. Wang, and X. Zhu, Two-dimensional numerical simulation of collisionless ion collection, *Journal of Tsinghua University (Sci. and Tech.)*, 1996, 36(6): 5–10 (In Chinese)
7. K. Yamada, T. Tetsuka, and Y. Deguchi, Ion extraction characteristics by an electric field on laser-produced barium plasma, *Journal of Applied Physics*, 1990, 67(11): 6734–6741
8. K. Yamada, T. Tetsuka, and Y. Deguchi, Ion extraction characteristics on a barium plasma produced between grounded parallel plate electrodes and a positively biased upper plate electrode, *Journal of Applied Physics*, 1991, 69(12): 8064–8071

9. K. Yamada, and T. Tetsuka, Ion extraction characteristics on a barium plasma produced between alternately biased parallel plate electrodes, *Journal of Nuclear Science and Technology*, 1993, 31(4): 301–307
10. H. Kurosawa, S. Hasegawa, and A. Suzuki, Ion extraction from a laser-ionized plasma produced between parallel plate cathodes and an anode above them, *Journal of Applied Physics*, 2002, 91(8): 4818–4823
11. R. Nishio, K. Yamada, K. Suzuki, M. Wakabayashi, Ion transport from laser induced metal plasma to ion extraction electrodes, *Journal of Nuclear Science and Technology*, 1995, 32(3): 180–190
12. T. Matsui, K. Tsuchida, S. Tsuda, K. Suzuki, T. Shoji, Ion extraction characteristics from photoionized plasma by radio-frequency resonance method, *Journal of Nuclear Science and Technology*, 1997, 34(9): 923–929
13. V. A. Gundienvkov, A. N. Tkachev, S. I. Yakovlenko, Characteristic time of ion extraction from a plasma bunch in laser isotope separation, *Quantum Electronics*, 2004, 34(6): 589–595
14. Z. Cao, W. Zhang, C. Bao, Distribution characteristics of ion collection during ion extraction from laser-induced plasma, *Journal of Chinese Mass Spectrometry Society*, 2007, 28(1): 5–11 (In Chinese)
15. R. Chen, Experimental research of ion extraction in atomic vapor laser isotope separation, Master Thesis, Tsinghua University, 2005 (In Chinese)
16. J. Xiong, D. Wang, Simulation of 2-D ion extraction with collision, *Journal of Tsinghua University (Sci. and Tech.)*, 1999, 39(10): 48–51 (In Chinese)
17. H. Zhu, D. Wang, Ion collection simulation by  $j \times B$  scheme with collision and sputtering, *Atomic Energy Science and Technology*, 2003, 37(5): 467–470 (In Chinese)
18. A. G. Zhidkov, Simulation of ion extraction from laser-induced plasma by electromagnetic fields, *Physics of Plasmas*, 1998, 5(2): 541–549
19. T. Matsui, K. Tsuchida, S. Tsuda, K. Suzuki, and T. Shoji, Ion extraction from plasma by using a radio frequency resonant electric field, *Physics of Plasmas*, 1996, 3(12): 4367–4375
20. Z.-B. Wang, G.-X. Chen, Z. Wang, N. Ge, H.-P. Li, and C.-Y. Bao, Effect of a floating electrode on an atmospheric-pressure non-thermal arc discharge, *Journal of Applied Physics*, 2011, 110: 033308
21. W.-T. Sun, G. Li, H.-P. Li, C.-Y. Bao, H.-B. Wang, S. Zeng, X. Gao, and H.-Y. Luo, Characteristics of atmospheric-pressure, radio-frequency glow discharges operated with argon added ethanol, *Journal of Applied Physics*, 2007, 101: 123302
22. A. Bogaerts, R. Gijbels and J. Vlcek, Collisional-radiative model for an argon glow discharge, *Journal of Applied Physics*, 1998, 84(1): 121–136
23. C. O. Laux, T. G. Spence, C. H. Kruger, and R. N. Zare, Optical diagnostics of atmospheric pressure air plasmas, *Plasma Sources Science and Technology*, 2003, 12: 125–138

## Author Biographies

**Li He-Ping** is a faculty with the Department of Engineering Physics of Tsinghua University, P.R. China. His current research interests are laser isotope separation and plasma science and technology.

**Chu Qiu-Hui** is a graduate student with the Department of Engineering Physics of Tsinghua University, P.R. China. Her current research interests are nuclear science and technology.

**Wang Xin** is a graduate student with the College of Mechanical Engineering of North China University of Science and Technology, P.R. China. His current research interests are plasma science and technology.

**Wang Peng** is an engineer with the Research Institute of Physical and Chemical Engineering of Nuclear Industry, P.R. China. His current research interests are laser spectroscopy.

**Chai Jun-Jie** is a senior engineer with the Research Institute of Physical and Chemical Engineering of Nuclear Industry, P.R. China. His current research interests are laser spectroscopy.

**Li Zhan-Xian** is a faculty with the College of Mechanical Engineering of North China University of Science and Technology, P.R. China. His current research interests are mechanical and electrical integration technologies.

# Online Nondestructive Testing of Gadolinium Containing Fuel Rods

Liu Ming, Yuan Ping and Zhang Lei

**Abstract** The determination of nuclear fuel pellets in  $Gd_2O_3$  and abnormal core blocks by the method of eddy current testing, the factors affecting the detection process were analyzed and processed, through the design of standard bar detection on equipment performance is verified. From the result of the verification, the eddy flow detection method in the detection speed of 4.4 m/min case for precision measurement of  $Gd_2O_3$  content in gadolinium fuel pellets is higher than 0.5 % (absolute value), the credibility of 95 % can distinguish the difference of  $Gd_2O_3$  content, the 1 % single fuel rods in the mixing core piece, credibility is 100 %.

**Keywords** Fuel rod · Eddy current testing · Gadolinium content · Ferromagnetic material · Standard stick

## 1 Introduction

Use of burnable poison on neutron absorption, in order to reduce the initial reaction of reactor, flattening of neutron flux, and power density, avoid just refueling in due to excessive and fission violent, which occurred in the fault, at the same time by balancing reactor core reactivity also prolongs the time of each refueling, greatly saves the operation cost of nuclear reactors with pressurized water reactor nuclear power plant fuel consumption increase, in the fuel assembly in adding a certain content of burnable poison fuel rods. And the current widely used as burnable poison fuel rods containing gadolinium fuel rod, due to the element gadolinium neutron absorption ability is very strong, the excess GD will lead to the decline of the reactor power. Therefore, in the fuel rod manufacturing process must strict control of nuclear fuel rods of gadolinium content. The content of  $Gd_2O_3$  in the  $UO_2$  fuel core of the nuclear reactor is approximately from 2 to 8 % and 1 %, in the form of  $Gd_2O_3$  in the nuclear fuel core. In the production line, the fuel core block

---

L. Ming (✉) · Y. Ping · Z. Lei  
Zhengzhou Branch Company of China Nuclear Power Engineering Co., Ltd, Beijing, China  
e-mail: liuming@cnpe.cc

into zirconium alloy cladding tube, at both ends of the welding end plug package consisting of fuel rod, each nuclear fuel rods may contain several kinds of gadolinium content of the core block. Therefore, it is necessary a method and apparatus to online nondestructive detection of nuclear fuel rods in  $Gd_2O_3$  content and identify mixed with different content of abnormal core block.

## 2 The Basic Structure and Composition of the Fuel Rods Containing Gadolinium

The basic structure of the fuel rod containing gadolinium is shown in Fig. 1, which is composed of a Zr-4 alloy cladding tube, a  $Gd_2O_3$  fuel core, a spring, and an end plug. Prior to the sintering of the gadolinium containing fuel core,  $Gd_2O_3$  was uniformly mixed with  $UO_2$  powder in the form of powder, and  $Gd_2O_3$  was evenly distributed in the solid solution of the fuel core after the core was sintered. At the same time in the production process of gadolinium containing fuel rods, various trace amounts of iron magnetic impurities may be mixed into the fuel core, the content of only 10–200 ppm or so, its components are Fe, Ni, Co, and its alloys. The composition and physical properties of the fuel rods containing gadolinium are shown in Table 1.

The physical properties of gadolinium and uranium are shown in Table 2.

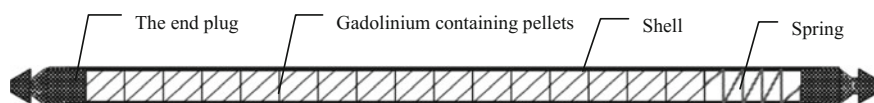


**Fig. 1** Schematic diagram of the fuel element containing gadolinium

**Table 1** Composition and physical properties of GD containing fuel rods

Component	Magnetization intensity (emu/g-oe)	Magnetic moment (emu/g, 7.5 koe)	Relative permeability	Mass ratio in the core (%)
$Gd_2O_3$	$1.47 \times 10^{-4}$	$1.1 \times 10^{-2}$	15	2–8
$UO_2$	$8.74 \times 10^{-6}$	$6.5 \times 10^{-2}$	1.0	92–98
Fe	$3.03 \times 10^{-2}$	$1.52 \times 10^{-2}$	5000	0.01
Zirconium	$1.34 \times 10^{-6}$	$8.5 \times 10^{-4}$	1.0	–

**Table 2** Physical properties of U and Gd

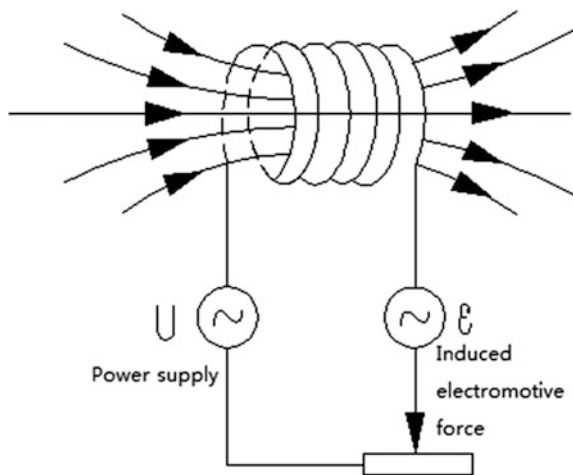
Element	Density ( $kg/m^3$ )	Magnetic susceptibility	Magnetization intensity ( $A/M$ )
Gd	$7.89 \times 10^3$	$4.8 \times 10^3$	1.168
U	$1.9 \times 10^4$	1.67	0.163

Through the analysis of the physical, chemical, and nuclear properties of gadolinium element, the method of  $Gd_2O_3$  content detection is three methods, which are thermal neutron transmission method, X-ray fluorescence analysis, and eddy current testing technology. Thermal neutron transmission method is not suitable for online detection because of the large influence of the  $UO_2$  absorption thermal neutron in the nuclear fuel core, which has great influence on the detection results. X-ray fluorescence analysis method because of Gd on its own characteristics of X-ray has a strong absorption, while the existence of fuel cladding on the intensity of radiation caused some attenuation. In the case of meeting the requirements of the detection accuracy, the detection speed is only 1.2 dm/min, it is difficult to meet the requirements of online detection. And eddy current testing technology using electromagnetic induction principle, measurement of Gd content in the core block of reaction or induction to detect the size of the coil impedance or voltage, to determine the detection method of Gd content. Because of the advantages of high detection speed, high sensitivity, noncontact detection, non radioactive hazard, etc., it has become the only effective means to detect the Gd content of nuclear fuel element.

### 3 Detection Principle

The theoretical basis for the detection of gadolinium content and its uniformity of the gadolinium containing fuel rods is electromagnetic induction. As shown in Fig. 2, in the probe coil through to a certain frequency alternating current, when the current in the coil is changed, due to self inductance, coil itself will produce electromotive force (EMF) and the magnitude of the electric potential:

Fig. 2 Self inductance phenomenon





$$\varepsilon = -\frac{d\Psi}{dt} = -L\frac{dI}{dt} = -\mu_0 \times \mu_r \times \frac{N}{l} \times \pi \times r^2 \times \frac{dI}{dt} \tag{1}$$

Among them:

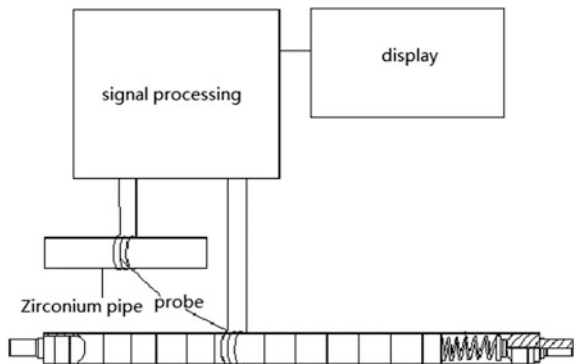
- $\varepsilon$  Electromotive force, V;
- $\mu_0$  Vacuum permeability, W/(A m);
- $\mu_r$  Relative magnetic permeability of magnetic medium in coil;
- $N$  Coil turns;
- $l$  Coil length, m;
- $r$  Coil radius, m;
- $\frac{dI}{dt}$  Instantaneous value of current in the coil, A.

The detection principle of the Gd content in the fuel rod core is shown in Fig. 3, which is composed of a zirconium tube, a fuel rod to be tested, an eddy current transducer, a signal transmitting and processing system, a data acquisition, and processing system. A total of two coils are connected to the two ends of the bridge circuit, as shown in Fig. 4. Before testing, the first two coils were placed in a and to be detection of nuclear fuel element rod package exactly the same shell material and size (inner and outer diameter and wall thickness) of zirconium alloy cladding tube, when the excitation signal detection and comparison coils with identical, the two coils in equilibrium state, regulating circuit, and the output signal of the bridge is zero, then remove the detection coil of zirconium tube.

Detection containing gadolinium fuel rod uniform into the detection coil were detected, due to the fuel rods is provided with the core block resulted in two coils in different magnetic permeability, therefore, self-induced electromotive force generated by the two coils is different and break the balance of the bridge, the output terminal of the output of an unbalanced voltage signal, that is, two coil inductance electromotive force difference. Signal is collected by the data acquisition card, after A/D conversion, amplification, noise reduction and other processing, the results on the display in real-time display.

After the A/D conversion peak processing, the amplitude of the output signal is:

**Fig. 3** Schematic diagram of detection



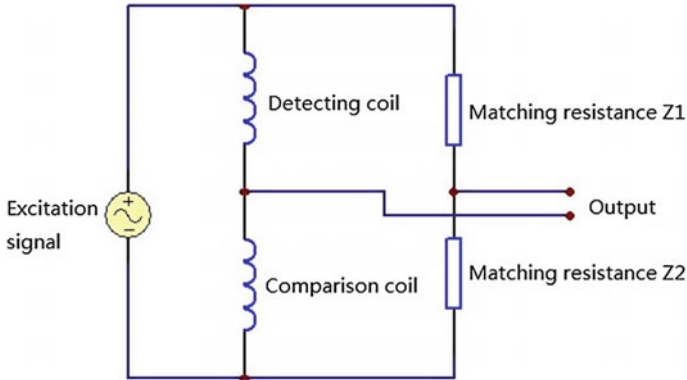


Fig. 4 Bridge circuit

$$\begin{aligned} \varepsilon' &= -I_0 \times \mu_0 \times \mu_{r1} \times \frac{N}{l} \times \pi \times r^2 \\ &= -I_0 \times \mu_0 \times (\text{Gd}\% \times \mu_{\text{Gd}} + \text{U}\% \times \mu_{\text{U}}) \times \frac{N}{l} \times \pi \times r^2 \end{aligned} \tag{2}$$

Among them:

- $I_0$  Maximum current in a coil;
- $\mu_{r1}$  Relative permeability of the core in the coil;
- Gd% Mass percent content of gadolinium oxide;
- $\mu_{\text{Gd}}$  Relative permeability of gadolinium oxide;
- U% Mass percent content of uranium oxide;
- $\mu_{\text{U}}$  Relative permeability of uranium oxide.

From Table 1 can know, gadolinium oxide, relative permeability of approximately 15, the relative permeability of uranium oxide is approximately 1.0, the permeability of gadolinium is much larger than the uranium, so you can think core block gadolinium content changes, effects of variation of uranium content of coil inductance electromotive force unchanged, that is:

$$I_0 \times \mu_0 \times (\text{U}\% \times \mu_{\text{U}}) \times \frac{N}{l} \times \pi \times r^2 = C \quad (\text{constant}) \tag{3}$$

The amplitude of the output signal is:

$$\varepsilon' = -C - I_0 \times \mu_0 \times \text{Gd}\% \times \mu_{\text{Gd}} \times \frac{N}{l} \times \pi \times r^2 \tag{4}$$

According to (4), the output signal amplitude and the content of gadolinium oxide linear relationship, according to the signal amplitude and gadolinium content

of linear regression equation, and the standard bar production standard curve. Along with gadolinium fuel rod axial direction distribution and utilization difference exceeding discriminant method, can determine the fuel rods is mixed with the anomaly core block; at the same time, the whole fuel rods measuring voltage for an average value and standard curve comparison, we can get fuel rods of gadolinium content through the size of the measuring signal amplitudes.

## 4 Key Technologies and Solutions

### 4.1 *The Elimination of the Influence of the Shell on the Test Results*

The Zr-4 alloy coated with Gd containing fuel rod is a non magnetic conducting material with a resistivity of about  $7 \times 10^{-7}$  ohm meter. Fuel rods in the detection process, the package shell will produce eddy current, due to the trend of the effect of skin effect, the magnetic lines of force generated by the detection coil most is bound in the cladding, enable gadolinium containing core block of magnetic field coils are greatly reduced, thus cladding are lowering the detection sensitivity, on the other hand the eddy currents are generated after and the detection coil is produced by mutual inductance, generated by a coil a large transformer electromotive force (far outweigh the GD containing pellets are caused by self-induced electromotive force generated by the detection coil), leading to a system output signal-to-noise ratio is very low, it is difficult to distinguish gadolinium content difference of 1 % of the core block.

In order to reduce and eliminate the cladding in gadolinium containing core block fuel rod gadolinium content detection process, on the one hand the increase within the coil current was increased by the coil in the magnetic field intensity, accompanied by decreasing the excitation frequency of the detection coil to reduce the cladding tending to skin effect, the magnetic field of the coil can fully penetrate to the core block location and be able to effectively detect. On the other hand detection system through the use of the two coils, a detection, a compared respectively. The arms of access four arm bridge circuit, fuel rods of the same type of cladding implantation compared coil, through mutual inductance electromotive force and the detection coil reverse connection and offset the cladding eddy current induced, thus greatly improving the signal-to-noise ratio of the system. Table 3 the detection results of different kinds of core blocks in the fuel rods were compared

**Table 3** Comparison of the eddy current values of the core values of the output of the detector when the coil is inserted into the package

Gadolinium content (%)	0	3	5	7	10
Do not insert the package shell	322	324	327	330	333
Insert package	81	102	119	136	162

between the coils and the fuel rods (Adjust the parameters, the best data measured in the signal is not saturated).

### 4.2 *Effect of Iron and Nickel Impurities on the Detection Results*

Due to fuel rods containing trace amounts of impurities such as iron, nickel, and their relative permeability to than GD at least two orders of magnitude in the detection process because pellets of iron and nickel impurities caused by eddy current probe output a enough to completely submerged Gd<sub>2</sub>O<sub>3</sub> detection signal voltage signal, so we must try to eliminate iron and nickel impurity interference and influence.

Any substance in the magnetic field by the role of the magnetic field will show a certain magnetism, this phenomenon is called magnetization. According to the effect of magnetic materials for magnetic field can be in material is divided into three categories and is delivered to field weakening material called diamagnetic substance; slightly enhanced the magnetic material called for paramagnetic substances, gadolinium and uranium belongs to the paramagnetic material; make the magnetic field strongly increased said is made of ferromagnetic material. The magnetization curves of paramagnetic substances and ferromagnetic substances are shown in Fig. 5. Iron and nickel are ferromagnetic materials. [The mathematical expression of the effect of the magnetic field on the magnetic field is shown in the formula (5).] In the use of the principle of electromagnetic induction using eddy current method to detect the content of gadolinium, when the iron and nickel content is slightly larger, can make the magnetic field increased dramatically, the detection results greatly affected.

$$B = \mu_0 H + \mu_0 H' = \mu_0 H + \mu_0 \chi_m H = \mu_0 (1 + \chi_m) H = \mu_0 \mu_r H = \mu H \quad (5)$$

(Form in,  $H'$  is Change of magnetic field after magnetization of substance;  $\mu_0$  is Vacuum permeability;  $\chi_m$  is Magnetic susceptibility;  $\mu_r$  is Relative permeability, Its size is  $\mu_r = 1 + \chi_m$ ;  $\mu$  is Absolute permeability of medium).

Can be seen from the ferromagnetic material properties in a magnetic field and the magnetization curve, the permeability of the ferromagnetic materials the magnetizing field is increased to a maximum value, then gradually began to decline with and eventually reached a steady, and corresponding magnetic induction intensity increased to a maximum value and eventually reach the saturated state. And paramagnetic material is no such characteristic, no matter how big magnetic field, will not make its magnetic induction intensity reached saturation.

According to the characteristics of ferromagnetic materials, we design outside of the test coil magnetic field and a DC steady magnetic field, the purpose is through with a constant magnetic field can the core block contains iron, magnetic material saturated, so that by detecting the fuel rods of eddy current testing waveform amplitude can truly reflect the level of the core block of gadolinium content. And

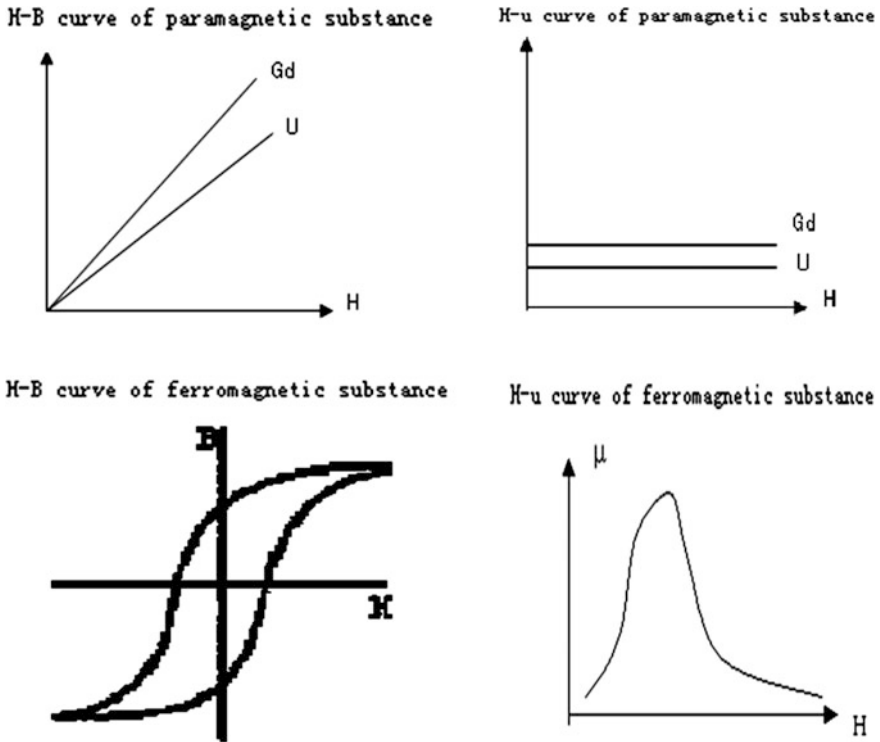


Fig. 5 Magnetization curve of paramagnetic substance and ferromagnetic substance

applied is a DC steady magnetic field and through a lot of experiments we identified when the applied magnetic field direction and the detecting coil magnetic field perpendicular to the direction of, and be detected fuel rods driving in the same direction, not to high frequency alternating magnetic field detection coil impact, detection of gadolinium content nor any effect. By this measure will fuel pellets of iron and nickel iron magnetic material on the detection result effect was completely eliminated, fuel level detecting the amplitude of the waveform, and core block of gadolinium content completely proportional relationship, by detecting the waveform can reflect the test fuel rods in the core block of gadolinium content and distribution.

### 4.3 Oscillation Frequency Selection of Eddy Current Sensor with Gd Content

First according to the theoretical study, Gd content detection of eddy current sensor oscillation frequency is high, detection sensitivity is higher and higher, but penetration depth of the magnetic field in the fuel rods in the smaller, containing GD

core block of coil magnetic field effect is small, but if frequency is too low, detection sensitivity and resolution will decrease. To this end, according to the diameter of the gadolinium containing fuel core and the diameter of the casing pipe. By Monte Carlo simulation, the calculated frequency of eddy current sensor using the Gd content detection should be the best in 4–15 kHz. Finally through repeated experiments to determine the best frequency of Gd content detection eddy current sensor is 7–12 kHz.

### 5 Composition of Testing Equipment

On line nondestructive testing device for containing fuel rod as shown in Fig. 6, mainly includes the magnetic saturation device, cooling system, a mechanical transmission device, automatic control system, the eddy current probe part, physical instrumentation, data acquisition, and processing software.

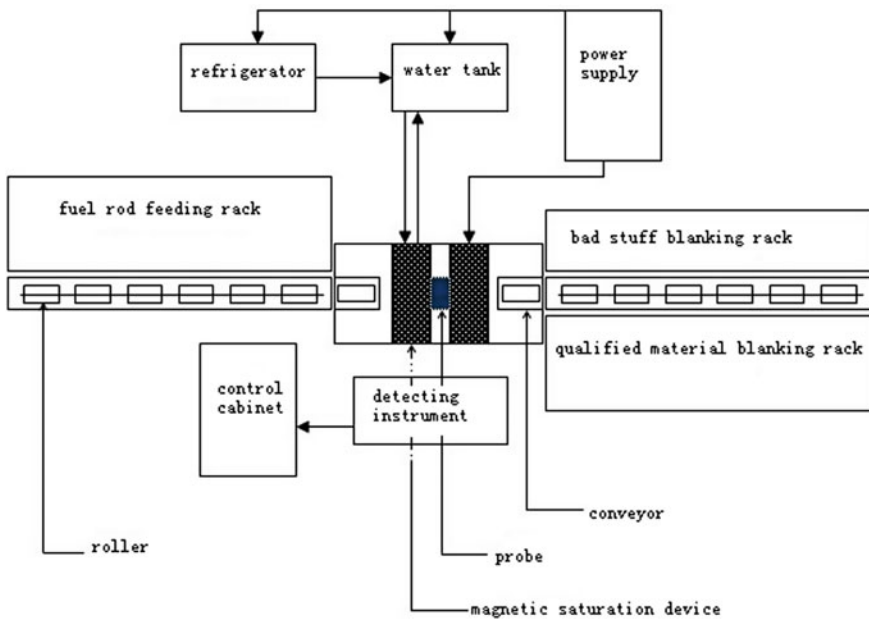


Fig. 6 The flow chart of the eddy current testing equipment for the gadolinium content of gadolinium containing fuel rods

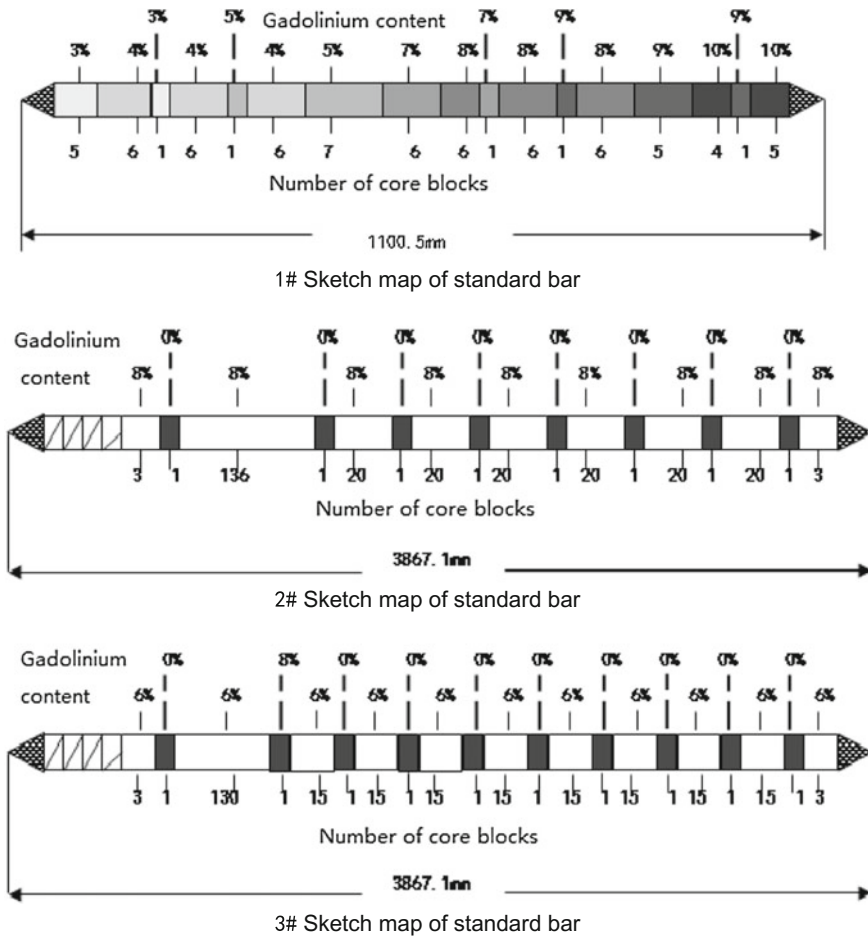


Fig. 7 Schematic diagram of the standard bar containing gadolinium

## 6 Design and Fabrication of a Standard Bar Containing Gadolinium

In order to establish the calibration curve of gadolinium content measurement of gadolinium containing fuel rods, and to verify the sensitivity and reliability of the equipment, we designed three kinds of standard. The distribution of the core block in the standard bar is shown in Fig. 7. The number of core blocks in the standard bar is shown in Table 4.

**Table 4** The number of core blocks in 1#, 2# and 3# standard bars

1# Standard bar			2# Standard bar			3# Standard bar		
Block type	Nominal gadolinium content (%)	Number of core blocks	Block type	Nominal gadolinium content (%)	Number of core blocks	Block type	Nominal gadolinium content (%)	Number of core blocks
Abnormal block	3.0	5	Matrix core	8.0	62	Matrix core	6.0	250
Abnormal block	4.0	18	Abnormal block	0.0	8	Abnormal block	0.0	9
Abnormal block	5.0	8				Abnormal block	8.0	1
Abnormal block	7.0	7						
Abnormal block	8.0	18						
Abnormal block	9.0	6						
Abnormal block	10.0	9						



## 7 Results and Discussion

### 7.1 Evaluation Index of Testing Equipment

Evaluation of GD containing fuel rod gadolinium content detection device of the main technical index is in a certain detection rate and can measure the whole rod containing gadolinium fuel rods absolute value of gadolinium oxide content accuracy and can detect fuel rods mixed with gadolinium content in the one exception block core block relative deviation of minimum value and test results of the confidence probability. The faster the detection rate, the higher the detection accuracy, the smaller the confidence probability, the better performance of the equipment. Used in the reactor containing gadolinium fuel rods in the gadolinium oxide content is 2–8 %, index of testing equipment requirements under certain detection speed and fuel rods gadolinium content average measurement accuracy is better than 0.5 %, detection results of confidence probability is 95 %, to distinguish between fuel rods of gadolinium content relative deviation is less than 1 % of the single mixture pellets and test results of the confidence probability is 95 %.

### 7.2 Results and Treatment

#### 7.2.1 Regression Equation for Calculation of Gadolinium Content

Using 1# standard bar in various types of gadolinium containing core blocks of the nominal value of gadolinium content  $M$  (3, 4, 5, 7, 8, 9, and 10 %). The regression equation is established to calculate the value of the signal with the amplitude of  $A$  in the corresponding detection parameter:

$$A = a * M + b \quad (6)$$

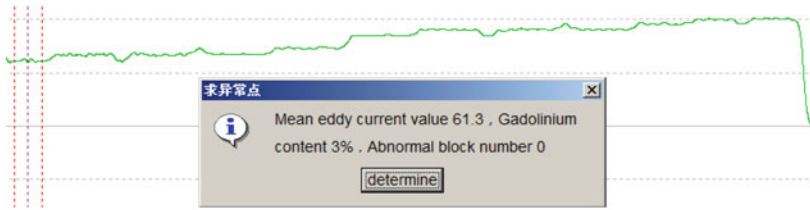
The calculation equation for the gadolinium content  $M$  is:

$$M = (A - b)/a \quad (7)$$

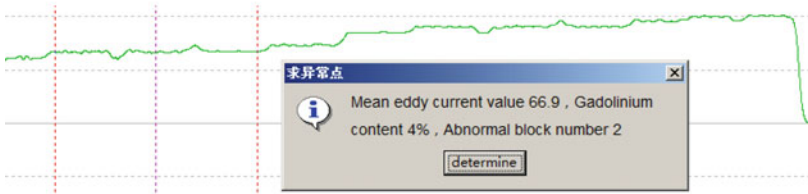
Among them:  $a$ ,  $b$  is the scale factor.

#### 7.2.2 Treatment of 1# Standard Bar Test Results

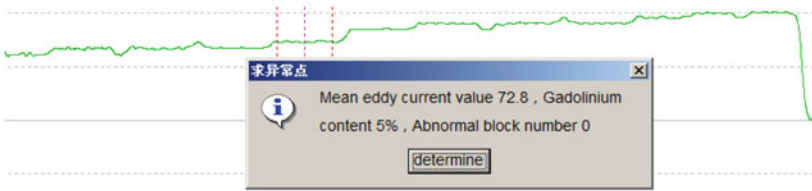
In order to verify the detection sensitivity of the device, the 1# fuel rod is measured, and the measurement results are analyzed in order to verify the sensitivity of the detection device to the 1 % core block of the gadolinium content. Figures 8 for the



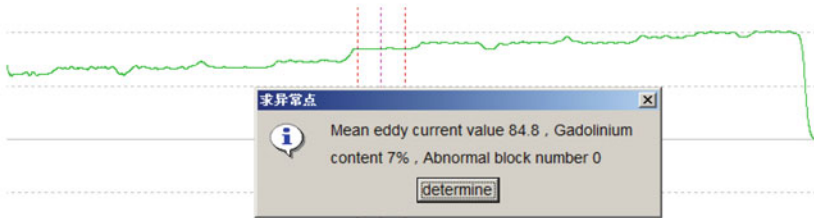
The first part of the signal analysis results



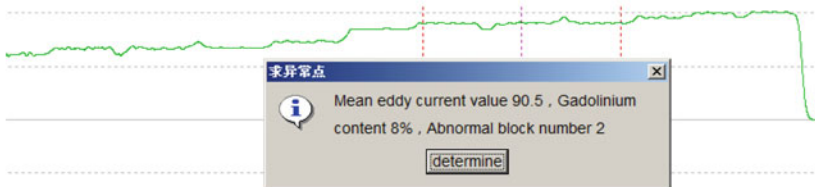
Second part of the signal analysis results



Third part of the signal analysis results

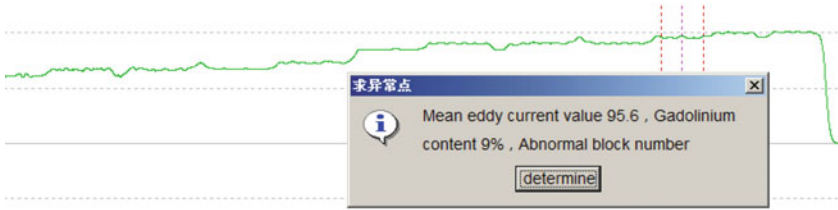


Fourth part of the signal analysis results



Fifth part of the signal analysis results

Fig. 8 Analysis of 1# standard bar test results



Sixth part of the signal analysis results



Seventh part of the signal analysis results

Fig. 8 (continued)

treatment of 1# standard bar test results, in which the horizontal coordinates for the rod length, longitudinal coordinates for the signal amplitude. The scope of the red expansion box in the graph is the data analysis area, and the pop-up window is the result of the data analysis. The first part of the signal analysis results

From Fig. 8, we can see that the test results are in good agreement with the actual distribution of the core, and the detection accuracy is better than 0.1 %. The test equipment not only can accurately pick out the 1 %  $Gd_2O_3$  content of the core, and can accurately calculate the content of  $Gd_2O_3$  in the sectional area.

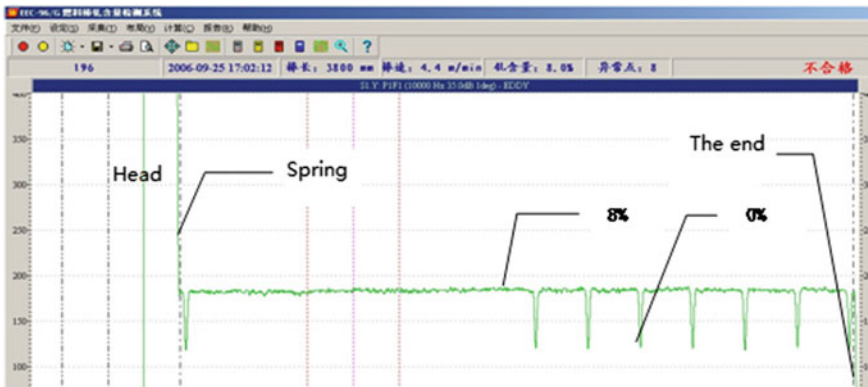


Fig. 9 2# Standard bar test signal



Fig. 10 3# Standard bar test signal

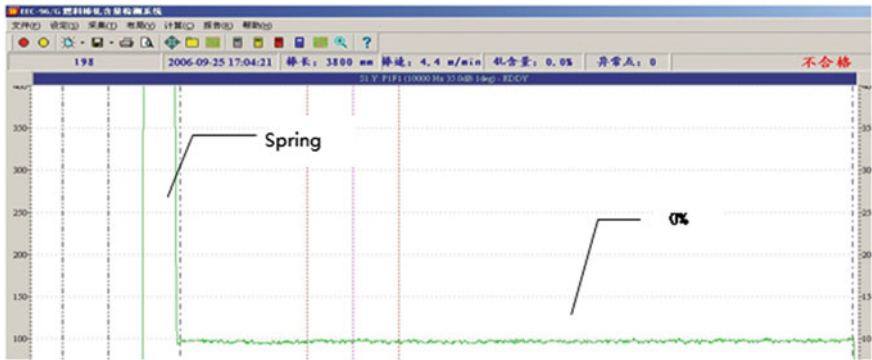


Fig. 11 Non gadolinium based fuel rod test signal

### 7.2.3 Detection Results of 2#, 3# Standard Bar and Non-gadolinium-containing Fuel Rods Are Automatically Detected

Through the automatic detection process of 2#, 3# standard rod and a non-gadolinium-containing fuel rods for automatic cycle measurement, the detection rate of 4.4 m/s, Each fuel rod test time is about 1 min (time of up and down). Device to automatically print and file the test results for each fuel rod.

2#, 3# standard bar and the detection signal of Non gadolinium containing fuel rod as shown in Figs. 9, 10 and 11, the horizontal axis is vertical rod length, amplitude of signal.

**Table 5** Measurement data and treatment results of 2#, 3# and non-gadolinium-containing fuel rods

Measuring times	0 %			6 %			8 %		
	Relative voltage value	Calculation value of gadolinium content	Abnormal block	Relative voltage value	Calculation value of gadolinium content	Abnormal block	Relative voltage value	Calculation value of gadolinium content	Abnormal block
1	1655.0	0.0 %	0	1713.1	6.0 %	10	1739.9	8.0 %	8
2	1654.2	0.0 %	0	1712.9	6.0 %	10	1740.3	8.0 %	8
3	1653.5	0.0 %	0	1712.9	6.0 %	10	1739.4	8.0 %	8
4	1653.4	0.0 %	0	1712.9	6.0 %	10	1739.8	8.0 %	8
5	1653.6	0.0 %	0	1712.7	6.0 %	10	1739.2	7.9 %	8
6	1653.7	0.0 %	0	1712.3	5.9 %	10	1739.3	7.9 %	8
7	1653.2	0.0 %	0	1712.9	6.0 %	10	1739.3	7.9 %	8
8	1655.0	0.0 %	0	1713.9	6.0 %	10	1740.3	8.0 %	8
9	1654.4	0.0 %	0	1713.1	6.0 %	10	1740.0	8.0 %	8
10	1653.4	0.0 %	0	1712.8	6.0 %	10	1739.7	8.0 %	8
11	1653.5	0.0 %	0	1713.5	6.0 %	10	1739.5	8.0 %	8
12	1653.6	0.0 %	0	1713.0	6.0 %	10	1739.9	8.0 %	8
13	1653.5	0.0 %	0	1713.3	6.0 %	10	1739.7	8.0 %	8
14	1653.6	0.0 %	0	1713.1	6.0 %	10	1739.4	8.0 %	8
15	1653.5	0.0 %	0	1713.2	6 %	10	1739.9	8.0 %	8
16	1652.5	0.0 %	0	1712.5	5.9 %	10	1739.6	8.0 %	8
17	1653.6	0.0 %	0	1713.1	6.0 %	10	1739.7	8.0 %	8
18	1653.5	0.0 %	0	1713.3	6.0 %	10	1739.7	8.0 %	8
19	1653.4	0.0 %	0	1712.4	5.9 %	10	1738.9	7.9 %	8
20	1653.2	0.0 %	0	1712.8	6.0 %	10	1739.4	7.9 %	8

(continued)

**Table 5** (continued)

Measuring times	0 %			6 %			8 %		
	Relative voltage value	Calculation value of gadolinium content	Abnormal block	Relative voltage value	Calculation value of gadolinium content	Abnormal block	Relative voltage value	Calculation value of gadolinium content	Abnormal block
21	1653.2	0.0 %	0	1712.8	6.0 %	10	1739.4	8.0 %	8
Average value	1653.643	0		1712.976	5.985714		1739.633	7.97619	
Standard deviation	0.581009	0		0.364561	0.035857		0.351188	0.043644	
Voltage difference between 0 % and	0			59.33			85.99		
Equation	$Y = 10.55 * X + 1652.85$								
Reliability	$R = 0.9978898$								

From Figs. 9, 10 and 11 detection signal can clearly will end, tail, spring, the core block signal integrity is displayed, the standards of 2# and 3# best mixed core material block signal and the substrate core block signal is clearly distinguished.

Table 5 processing results of the test data of three standard bars.

## 8 Conclusion

System at the scene through the detection of a variety of core blocks of gadolinium content, the equipment on the content of the  $Gd_2O_3$  content of the core block can be achieved in the detection of the ability to achieve the following technical indicators:

- (1) The measurement accuracy of the  $Gd_2O_3$  content of the fuel pellets is higher than 0.5 % (absolute), and the reliability is 95 %.
- (2) A single mixed core with a difference of 1 % in the  $Gd_2O_3$  content of the fuel rods was able to be distinguished, and the reliability was 100 %.
- (3) In the meeting (1) (2) under the condition that the speed of detection of single nuclear fuel rods is greater than 4400 mm/min.

## References

1. Yang Shiwei. Eddy current nondestructive testing. Liaoning educational audio and video publishing house, 1998
2. Liu Bao, Xu Yanlin etc. Eddy current testing technology and its development. Weapon Industry Automation, 2006
3. Tian Daicai etc. Eddy current testing signal processing technology. Nondestructive testing, 2006

# Optimization of Thorium Utilization in Fluoride Salt-Cooled High-Temperature Reactor (FHR)

Xiaoxiao Li, Jingen Chen and Yonghan Fang

**Abstract** Preliminary neutronics analysis of thorium utilization in Fluoride salt-cooled High-temperature Reactor (FHR) has been carried out using a similar reactor model and fuel composition as the one researched in UC Berkeley. Compared with uranium-based fuels, thorium-based fuel (i.e., Th<sub>2</sub>/U<sub>3</sub>) shows a deeper burnup but a lower conversion ratio (CR) and a smaller temperature coefficient of reactivity (TCR). To improve the TCR, the weight ratio of the fissile material (U-233) and the fertile nuclide (Th-232) and the geometry of the TRISO and/or pebble are investigated. The higher the proportion of Th-232 in the Th<sub>2</sub>/U<sub>3</sub> fuel, the higher the CR and TCR can be obtained. On the other hand, a harder spectrum is also contributive to the improvement of the TCR through the geometry optimization of TRISO and/or pebble. These two optimization approaches can be conducted to balance the burnup, TCR, and CR to realize efficient and safe utilization of thorium in FHR.

**Keywords** Thorium · FHR · C/HM · TCR · Burnup

## 1 Introduction

Thorium–uranium fuel cycle possesses obvious advantages [1], involving better breeding capacity particularly in thermal/epithermal spectra and lower radiotoxicity of nuclear waste within 10,000 years after shutdown. In addition, to deliver on potential performance of thorium, especially its high-temperature stability, thorium was tested and taken as nuclear fuel in High-Temperature gas-cooled Reactors (HTRs) [2–4]. The Fluoride salt-cooled High-temperature Reactor (FHR) [5, 6] is essentially the same as a HTR, which contains TRISO particles moderated by graphite but is cooled by molten salt instead of helium gas. Most of the researches

---

X. Li · J. Chen (✉) · Y. Fang  
CAS Center for Excellence in TMSR Energy System,  
Shanghai Institute of Applied Physics, CAS, Shanghai, China  
e-mail: chenjg@sinap.ac.cn



on FHRs have been concentrated in uranium-based fuel [7, 8] while that in thorium-based fuel is only in the beginning stage [9–11].

The neutronic characteristics of thorium utilization were preliminarily analyzed with a whole-core model of pebble bed FHR in our previous work [9]. By comparing the thorium-based fuel to the uranium one, it can be conducted that the  $^{232}\text{Th}/^{233}\text{U}$  fuel system (Th2/U3 for short) has the highest initial  $k_{\text{eff}}$  and deepest burnup due to the smaller resonance absorption of Th-232 and the higher effective number of fission neutrons of U-233 especially in thermal and epithermal spectrum region. Since the reactor model and the fuel composition used in our previous work [9] are similar as the one researched in UC Berkeley based on uranium fuel [8], there are two drawbacks for Th2/U3 in such FHR, i.e., low conversion ratio (CR) and small temperature coefficient of reactivity (TCR). According to the analyses in our previous work [9], approaches to optimize CR and TCR can be conducted by adjusting such as the weight ratio of fissile material and fertile nuclide (i.e., the U-233 weight fraction (w%) for Th2/U3, defined as U-233 w%) and neutron spectrum. The neutron spectrum corresponding to the ratio of moderator to heavy metal (C/HM) can be adjusted in two ways, i.e., modifying the number of TRISO coated particles and changing the fuel kernel radius. The former way using a fuel kernel radius of 0.25 mm offers an opportunity to alter C/HM without making changes to the TRISO itself.

The description of the FHR core, fuel pebble, TRISO-coated fuel particle, fuel composition, and nuclear analytical tool are presented in Sect. 2. Optimizations of the U-233 weight fraction and the TRISO geometry to improve CR and TCR are given in Sect. 3. Conclusions are summarized in Sect. 4.

## 2 Methodology

### 2.1 Geometric Properties

The present study on the use of Th2/U3 in FHR is based on a whole-core design in reference [9]. Both the diameter and the height of the active zone have the same value of 5.06 m. The active zone is filled with fuel pebbles in a regular hexagonal lattices with a packing factor of 60 % while the remaining 40 % filled with molten salt, and surrounded by a graphite reflector with thickness of 0.5–1 m [12]. The molten salt area filled with FLiBe (66 mol%  $^7\text{LiF}$ –34 mol%  $\text{BeF}_2$ ) is located below the active zone. The density of FLiBe is  $1.90 \text{ g/cm}^3$  [8] (assumed operation temperature of 1050 K), and the abundance of Li-7 in FLiBe is 99.995 %.

Each pebble is composed of a fuel zone with radius of 2.5 cm and a fuel-free graphite shell with thickness of 0.5 cm. The former part is formed by a graphite matrix with density of  $1.6 \text{ g/cm}^3$  in which several thousands of TRISO-coated fuel particles are embedded and uniformly distributed within a hypothetical six prismatic crystal lattice. The latter part is made of pure graphite with density of  $1.6 \text{ g/cm}^3$ .

**Table 1** Description of fuel pebble and TRISO coatings

Item	Size	Material
<i>Fuel pebble</i>		
Fuel zone radius	2.5 cm	Graphite matrix
Fuel-free zone thickness	0.5 cm	Graphite
Pebble packing factor	60 %	
<i>TRISO coatings</i>		
Fuel kernel radius	0.25 mm	UO <sub>2</sub> + ThO <sub>2</sub> (variable: U-233 w%)
Porous carbon buffer layer thickness	95 μm	Graphite
Inner pyrolytic carbon layer thickness	40 μm	Graphite
Silicon carbide layer thickness	35 μm	SiC
Outer pyrolytic carbon layer thickness	40 μm	Graphite
TRISO packing factor	Variable	

Each TRISO-coated fuel particle consists of a fuel kernel surrounded by four coating layers [13, 14], i.e., a Porous Carbon Buffer layer, an Inner Pyrolytic Carbon layer, a silicon carbide layer, and an Outer Pyrolytic Carbon layer. The fuel kernel contains a mixture of UO<sub>2</sub> and ThO<sub>2</sub>, and U-233 is the only isotope in the uranium of UO<sub>2</sub>. The thickness of the TRISO coating layers has a linear relation with the fuel kernel radius to ensure the retention of all the fission products and make very little influence upon neutronics [15].

The geometrical parameters used for the fuel pebble and the TRISO-coated fuel particles are summarized in Table 1. The purpose of this work is to improve CR and TCR by altering neutron spectrum through changing C/HM without modifying the core geometry. Therefore, possible variations in the fuel design are fuel kernel radius, number of fuel particles corresponding to C/HM, graphite matrix diameter (the fuel zone of pebble). For simplicity, only the second case is chosen in this work without making changes to TRISO and pebble themselves. Furthermore, U-233 w% in fuel kernel is adjusted to optimize CR and TCR through the competition between the fission ability of U-233 and the capture ability of Th-232.

## 2.2 Neutronics Simulation Tool

The calculation including criticality and burnup for a whole FHR core is performed using the SCALE code package [16] which is an inclusive modeling and simulating tool applicable for nuclear criticality and safety analysis. Considering the FHR-specific phenomenon, a DOUBLEHET module is used to treat the resonance self-shielding effect and the double heterogeneous nature [17, 18], which is capable of handling all the layers of the TRISO-coated fuel particles and the whole pebble at once [12]. Time-dependent cross-section processing reveals the fuel composition variation during burnup based on the ENDF/B-VII library with 238-group. Moreover, the burnup calculation is carried out under a constant

power of 1000 MWth and a large enough number of nuclides (388 nuclides) are monitored in trace quantities. Considering the calculation accuracy, the burnup steps with a smaller time are required particularly at the original irradiation to achieve an equilibrium concentration of much of fission products. Furthermore, raising the order of burnup steps as the increasing depletion is also needed to save computation time [19]. For each burnup step, 50 cycles are skipped and a total of 200 cycles with 2000 neutrons per cycle are applied. The average computation time of one burnup step is around 15 min with a single-core computer.

### 3 Results and Discussions

Three-dimensional Monte Carlo neutronics calculations are performed to study the characteristics of the FHR core with Th2/U3. The influences of the U-233 weight fraction (U-233 w%) and C/HM upon TCR and burnup are investigated for six different U-233 weight fractions, between 7.5 and 20 %, and for four different C/HM ranging from 100 to 400.

#### 3.1 The Influence of U-233 w% and C/HM upon Spectrum

Spectrum factor (unit: eV) is defined as the energy of average lethargy of fission, which can be used to characterize the neutron energy spectrum. The larger the spectrum factor, the harder the spectrum becomes. Figure 1 gives the variation of the spectrum factor with the U-233 weight fraction for different C/HM. Under the same U-233 weight fraction, the spectrum factor becomes larger with the decreasing C/HM, and it is clear that the U-233 weight fraction is of great importance for the spectrum factor especially for a lower C/HM. To find out the reason for this trend, the difference of the neutron fractions between the highest C/HM (i.e., 400) and the lowest C/HM (i.e., 100), defined as  $\Delta$ , is presented in Fig. 2. The three values ( $\Delta_1$ ,  $\Delta_2$ , and  $\Delta_3$ ) correspond to thermal, intermediate, and fast neutron regions, respectively, and the positive (negative) value represents

**Fig. 1** Spectrum factor for the FHR core as a function of U-233 weight fraction for different C/HM

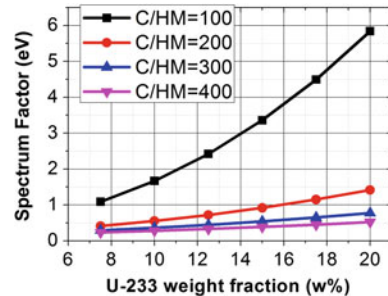
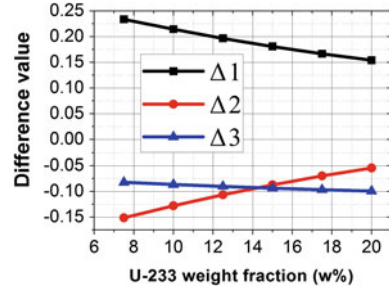


**Fig. 2** Difference of neutron fraction between highest C/HM (i.e., 400) and lowest one (i.e., 100) versus U-233 w%



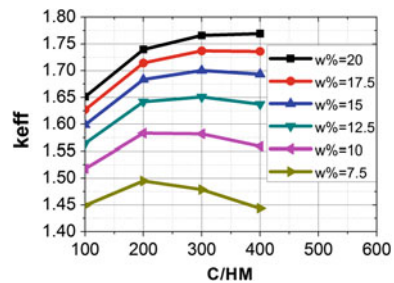
raising (reducing). It can be seen that the differences of the thermal and intermediate neutron ranges are more evident while that of the fast one is less significant along with the increase of the U-233 weight fraction. That is to say, the evolution of the spectrum factor as a function of the U-233 weight fraction mainly depends on the competition of  $\Delta 1$  and  $\Delta 2$ . For the higher U-233 weight fraction, the higher the difference between the absolute value of  $\Delta 1$  and  $\Delta 2$ , the more significant change of the spectrum factor is.

Besides, with the same C/HM, the spectrum factor tends to be larger with the increase of the U-233 weight fraction, and the U-233 weight fraction is more significant to the spectrum factor for a higher U-233 weight fraction. The reason for such trends is same as described above.

### 3.2 The Influence of U-233 w% and C/HM upon $k_{eff}$

The initial  $k_{eff}$  and the conversion ratio (CR) from Th-232 to U-233 are two competitive factors during burnup, which determine the depth of burnup. A deeper burnup can be obtained with a higher initial  $k_{eff}$  and a larger CR. The  $k_{eff}$  is plotted as a function of C/HM for different U-233 weight fractions in Fig. 3. For all weight fractions of U-233, the increase of C/HM from 100 to 400 initially leads to an increase of  $k_{eff}$  when the fuel pebbles is for the under-moderated condition and then to a decrease as the fuel pebbles become over-moderated due to a larger C/HM.

**Fig. 3**  $k_{eff}$  for the FHR core as a function of C/HM for different U-233 weight fractions



The value of  $C/HM$  at which the transition from under-moderated to over-moderated occurs also increases as the U-233 weight fraction rises.

It is worth mentioning that the value of  $C/HM$  with 200, denoted as  $C/HM200$ , is an interesting point in Fig. 3.  $C/HM200$  almost corresponds to the transition point for the lower U-233 weight fraction (7.5 %). In addition, the evolutions of  $k_{\text{eff}}$  with  $C/HM$  for the higher U-233 weight fractions ( $\geq 10\%$ ) are almost parallel before  $C/HM200$  and show different evolution trends after this point. It can be analyzed from the perspective of six-factor formula, but it will not be discussed here. Furthermore,  $C/HM200$  is also a dividing point in the trend of TCR with the increase of the U-233 weight fraction, which will be discussed in detail in Sect. 3.3.

### 3.3 The Influence of U-233 w% and C/HM upon TCR

The TCR has been determined for the Th2/U3 fueled pebbles in a whole FHR core. Therefore, the separate  $k_{\text{eff}}$  value can be obtained by changing the temperature of the pebbles, the moderator, the coolant, and the reflector, respectively. A negative TCR is necessary for safe operation of a reactor. The total TCR with negative values for the whole FHR core is plotted as function of the U-233 weight fraction for different  $C/HM$  in Fig. 4. It can be seen that a wider choice of the U-233 weight fraction is available for a lower  $C/HM$  to obtain a negative TCR.

Under the same U-233 weight fraction, a lower  $C/HM$  leads to a stronger negative TCR which is chiefly determined by the fuel TCR (FTCR) and coolant TCR (CTCR). In all cases, FTCR is negative and reduces as  $C/HM$  rises. Likewise, the same law can be found in the trend of the coolant coefficient of reactivity (CTCR). FTCR and CTCR for two different U-233 weight fractions (10 % and 20 %) and for different  $C/HM$  (100, 200, 300, and 400) are given in Table 2. Moreover, FTCR decreases and CTCR increases with the increase of the U-233 weight fraction. TCR decreases with the increasing U-233 w% for lower  $C/HM$  (i.e., 100) due to the greater reduction of FTCR than the smaller enhancement of CTCR. Instead, TCR increases with the increase of U-233 w% for higher  $C/HM$  (i.e.,  $\geq 200$ ) due to the inverted variation of FTCR and CTCR.

**Fig. 4** TCR for FHR core as a function of the U-233 weight fraction for different  $C/HM$

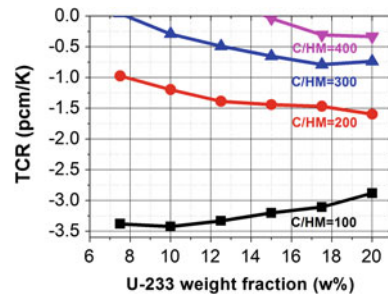


**Table 2** FTCR and CTCR for the FHR core

C/HM	100	200	300	400
U-233 w% = 10				
FTCR	-3.22	-1.58	-0.97	-0.8
CTCR	-1.03	0.3	0.52	1.27
U-233 w% = 20				
FTCR	-2.26	-1.47	-0.97	-0.97
CTCR	-1.2	-0.23	-0.15	0.17

### 3.4 The Influence of U-233 w% and C/HM upon Burnup

The burnup calculations are performed for four different C/HM by varying the number of TRISO coated particles, and for six different U-233 weight fractions, from 7.5 to 20.0 % and presented in Fig. 5. It is found that the burnup deepens with the increasing U-233 weight fraction and the decreasing C/HM. For all C/HM, the burnup increases gradually and obtains a saturated value at the point with the U-233 weight fraction of about 12.5 %.

Two dimensions are used to explain the trends in Fig. 5. First, Fig. 6 shows the evolution of  $k_{eff}$  and CR for the FHR core with the U-233 w% of 12.5 for four different C/HM. It can be seen that the FHR core with a lower C/HM possesses a higher CR during depletion and thus the  $k_{eff}$  decreases more slowly with burnup and then a deeper burnup can be obtained even with a smaller initial  $k_{eff}$ . Second, Fig. 7 gives the evolution of  $k_{eff}$  and CR for the FHR core with C/HM of 200 for four different U-233 weight fractions. It is evident that the FHR core with a higher U-233 weight fraction has a lower CR and then the  $k_{eff}$  displays a rapider decline with burnup but a deeper burnup is achieved due to a much larger initial  $k_{eff}$ . In short, a deeper burnup can be realized through a higher CR with a small difference of initial  $k_{eff}$  (see Fig. 6), but it does not work for a large difference of initial  $k_{eff}$  (see Fig. 7).

Based on the above discussions, a deeper burnup can be obtained with appropriate initial  $k_{eff}$  and CR by varying either C/HM or the U-233 weight fraction. Furthermore, a similar burnup can be achieved for the FHR core with a higher

**Fig. 5** Burnup for FHR core as a function of the U-233 weight fraction (w%) for different C/HM

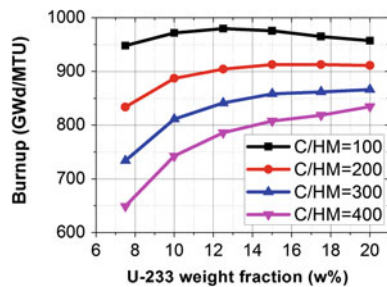


**Fig. 6** Evolution of  $k_{\text{eff}}$  (*top*) and CR (*bottom*) with the burnup of U-233  $w\% = 12.5$  for different C/HM

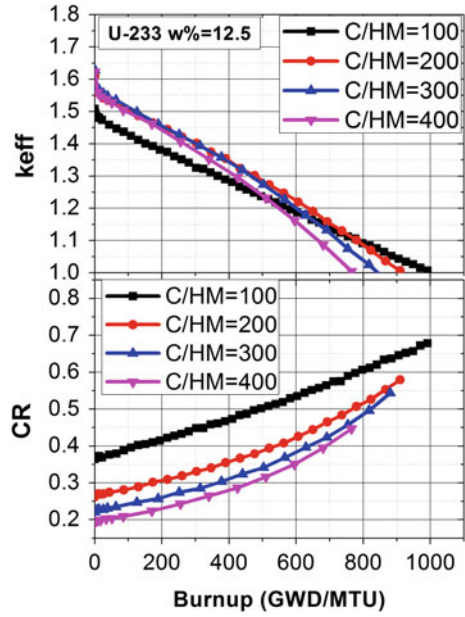
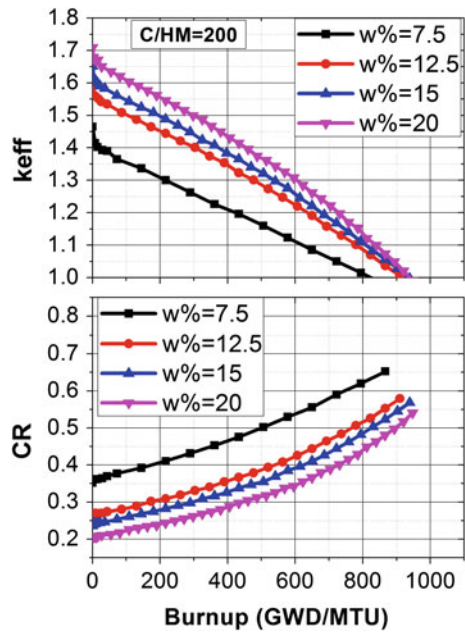


**Fig. 7** Evolution of  $k_{\text{eff}}$  (*top*) and CR (*bottom*) with the burnup of C/HM = 200 for different U-233 weight fractions



U-233 weight fraction for different C/HM. All of such phenomena can be explained from the perspective of neutron balance or the six-factor formula, and it is not discussed here.

## 4 Conclusions

In order to improve the TCR for thorium-based fuel (Th2/U3), the influences of the U-233 weight fraction and the number of TRISO-coated particles (corresponding to C/HM) upon neutronics for a FHR core are investigated, including the spectrum, the initial  $k_{\text{eff}}$ , the TCR, and the burnup. The conclusions drawn from the above analysis are shown as below:

- A harder spectrum shows a larger spectrum factor. The lower the C/HM, the higher the U-233 weight fraction, the larger spectrum factor can be achieved. The U-233 weight fraction is of great importance for the spectrum factor with low C/HM while the C/HM is more significant for the spectrum factor when U-233 weight fraction becomes greater.
- An improved TCR can be obtained by reducing C/HM. As the U-233 weight fraction increases, the negative TCR tends to be a larger value for the FHR core with a higher C/HM ( $\geq 200$ ) but trends toward a smaller value for the one with a lower C/HM (e.g., 100).
- A deeper burnup can be achieved for the FHR core with a lower C/HM and/or a higher U-233 weight fraction, which displays a relatively higher initial  $k_{\text{eff}}$  and/or a comparatively better conversion ratio benefited from a harder spectrum.

From the aspects of improved TCR and deeper burnup, a FHR core with C/HM of 200 and U-233 weight fraction of 12.5 % is recommended for the optimization of thorium utilization. Multizone with different C/HM is also required to improve the conversion ratio of thorium. Moreover, elaborate fuel pebble arrangement and fuel pebble recycling are expected to obtain a deeper burnup.

**Acknowledgments** This work is supported by the Chinese TMSR Strategic Pioneer Science and Technology Project under Grant No. XDA02010000 and the Frontier Science Key Program of the Chinese Academy of Sciences under Grant No. QYZDY-SSW-JSC016.

## References

1. IAEA, "Thorium fuel cycle—Potential benefits and challenges", IAEATECDOC-1450, International Atomic Energy Agency (2005)
2. Baumer and I. Kalinowski, "THTR commissioning and operating experience", *Energy*, 16(1–2):p 59 (1991)
3. A.L. Habush and A.M. Harris, "330-MW(e) Fort St. Vrain high-temperature gas-cooled reactor", *Nuclear Engineering and Design*, 7(4):p 312 (1968)



4. Ming Ding and Jan Leen Kloosterman. "Thorium utilization in a small long-life HTR. Part I: Th/U MOX fuel blocks", *Nuclear Engineering and Design*, 267, p 238 (2014)
5. Ingersoll, DT et al., "Tatus of preconceptual design of the advanced high-temperature reactor (AHTR)", Department of Energy (2004)
6. Fluoride-Salt-Cooled High Temperature Reactor (FHR) Materials, Fuels and Components White Paper, Facilitators, UW Madison and Facilitators, MIT (2013)
7. Fratoni, Massimiliano, "Development and Applications of Methodologies for the Neutronic Design of the Pebble Bed Advanced High Temperature Reactor (PB-AHTR)", ProQuest (2008)
8. Fardin, EV1 François-Paul and Koenig, EV1 Fabien, "Preliminary study of the Pebble-Bed Advanced High Temperature Reactor", GA Master Thesis Project, (2006)
9. Li, X.X., et al., "Analysis of thorium and uranium based nuclear fuel options in Fluoride salt-cooled High-temperature Reactor", *Progress in Nuclear Energy*, 78:p 285 (2015)
10. Zhu, G. F., "Investigation on Thorium used in Pebble-Bed Fluoride Salt-cooled High Temperature Reactor", Doctoral thesis Project for CAS, (2015)
11. Holcomb, David E., et al., "Fluoride salt-cooled high-temperature reactor technology development and demonstration roadmap", ORNL/TM-2013/401, ORNL, Oak Ridge, TN (2013)
12. G. Ilas, et al., "On the few-group cross-section generation methodology for PBR analysis", *Annals of Nuclear Energy*, 33(11-12):p 1058 (2006)
13. Jeffrey J. Powers, Brian D. Wirth, "A review of TRISO fuel performance models", *Journal of Nuclear Materials*, 405 (1):p 74 (2010)
14. J. Wang, "An Integrated Performance Model for High Temperature Gas Cooled Reactor Coated Particle Fuel", Doctoral Thesis, Massachusetts Institute of Technology (2004)
15. F.J. Wols, et al., "Fuel pebble design studies of a high temperature reactor using thorium", High temperature Reactor Conference (2012)
16. ORNL, "Scale: a Comprehensive Modeling and Simulation Suite for Nuclear Safety Analysis and Design", ORNL/TM-2005/39, Oak Ridge National Laboratory (2011)
17. Williams M. L., et al., "Recent Enhancements to the SCALE 5 Resonance Self-Shielding Methodology". *Transactions of the American Nuclear Society*, 92 (2005)
18. Schultz, R.R., et al., "Next Generation Nuclear Plant Methods Technical Program Plan", INL/EXT-06e11804. Idaho National Laboratory (2010)
19. Allen K, Knight T., "Destruction rate analysis of transuranic targets in sodium-cooled fast reactor (SFR) assemblies using MCNPX and SCALE 6.0", *Progress in Nuclear Energy*, 52(4): p 387 (2010)

# Preparation of Zr-Doped ThO<sub>2</sub> Ceramic Microsphere By Sol–Gel Method

He Huang, Jun Lin, Yan Chao, Peng Wang, Fengxia Wang,  
Changqing Cao and Zhiyong Zhu

**Abstract** Recently, there has been increasing interest in thorium as a potential fuel for next-generation nuclear reactors because its abundant reserve in the earth's crust is three times higher than uranium. The usage of thorium will save uranium resources considerably. In this paper, Zr-doped ThO<sub>2</sub> ceramic microsphere was prepared via external gelation process. Appropriate calcining and sintering programs were set on the basis of Thermal Gravity Analysis (TG) curve of microsphere drying in the air. Dense Zr-doped ThO<sub>2</sub> microspheres with density higher than 90 % TD were obtained with a series of doping concentration. The appearance of the product was investigated by microphotography. Homogeneity analysis of the Zr-doped ThO<sub>2</sub> microsphere was studied by Energy-dispersive spectrometer (EDS). The microstructure of the sintered Zr-doped ThO<sub>2</sub> microsphere was characterized by scanning electron microscopy (SEM), X-ray diffractometry (XRD), etc. The results of microphotography showed that the prepared Zr-doped ThO<sub>2</sub> microsphere exhibited good sphericity and uniformity with diameter of 830 μm. The influence of doping concentration and sintering temperature on grain size and microstructure was discussed.

**Keywords** Thorium · Nuclear fuel · Sol–gel · External gelation

## 1 Introduction

There has been a recent resurgence of thorium as a potential fuel for generation IV nuclear reactors. Thoria (ThO<sub>2</sub>) has been investigated as fuel matrix over the last three decades [1, 2]. Baena et al. [3] synthesized uranium dioxide and thorium dioxide doped with gadolinium oxide via both dry route and semidry route. The main conclusion that can be drawn from these studies is that ThO<sub>2</sub> can dissolve

---

H. Huang · J. Lin (✉) · Y. Chao · P. Wang · F. Wang · C. Cao · Z. Zhu  
Shanghai Institute of Applied Physics, Chinese Academy of Sciences,  
Shanghai, China  
e-mail: linjun@sinap.ac.cn

large concentrations of metal oxide while still maintaining its face-centered cubic crystal structure. The solubility of the  $M^{x+}$  in  $\text{ThO}_2$  varies with temperature and is much higher for the heavier  $M^{x+}$  compared to that of the lighter ones.

At the present time, as the advanced and newer generation nuclear reactors developed increasingly, how to dispose the nuclear waste safely has been got more attention by researchers [4]. Considering the public acceptance and safety, scientific communities are devoted to search for appropriate matrixes for disposing the nuclear wastes environmentally friendly [5, 6]. The Rock-like oxide (ROX) fuel is a sort of inert matrix fuels and consists of mineral-like compounds such as yttria stabilized zirconia (YSZ), spinel ( $\text{MgAl}_2\text{O}_4$ ), and corundum ( $\text{Al}_2\text{O}_3$ ), which have stable chemical and physical behaviors in disposal environments. Yttria-stabilized zirconia is the most hopeful candidate for the inert matrix because of its high stability against both neutron and fission fragments irradiations and high melting temperature ( $\sim 2960$  K) [7]. High ability to accommodate actinides and lanthanides in its lattice is also a high advantage property. Irradiation stability of stabilized zirconia was demonstrated by Berman et al. [8]. Although spinel shows good stability against neutron irradiation, it seems not to be very stable against high energy fission fragments. It is preferable to localize fission fragments damage to a small region to avoid swelling and degradation of thermal conductivity.

As an inert matrix-based fuel, the rock-like oxide fuel has an excellent performance to transmute Pu, and the spent fuel is less toxic than the MOX spent fuel [9, 10]. A ROX fuel core has several problems such as lower fuel temperature and void coefficients and a large power peaking factor [11]. To solve these problems,  $\text{ZrO}_2$  is added to Thoria matrix. Zr-doped Thoria can improve the thermal properties and enhance the chemical stability [12].

## 2 Experiments

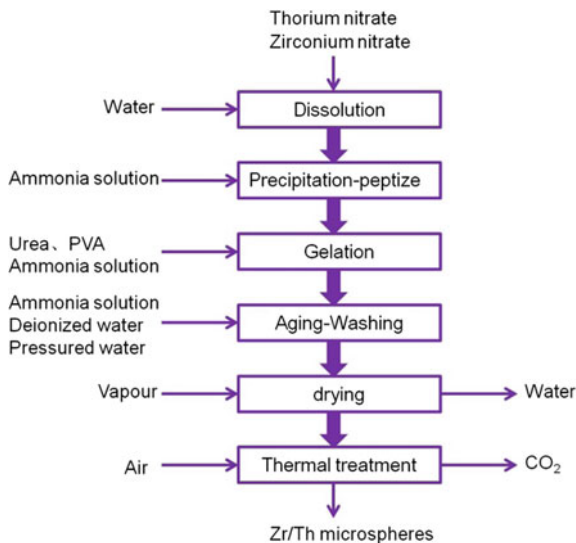
### 2.1 Fabrication Process

The Zr-doped  $\text{ThO}_2$  microsphere was fabricated on the base of external gelation technology. The fabrication process was showed as Fig. 1.  $\text{Th}(\text{NO}_3)_4 \cdot 4\text{H}_2\text{O}$  was synthesized by Changchun Institute of Applied Chemistry, Chinese Academy of Sciences.

### 2.2 Sol Preparation

The ammonia solution (12 M) was added to a 100 mL 1.2 M mixed solution of Th and Zr nitrates corresponding to the composition  $\text{Th}_{1-x}\text{Zr}_x\text{O}_2$ , reacted gently at 60 °C. After pH reached 3.7–4.0, 0.03 g/mL urea was added. Urea,  $\text{CO}(\text{NH}_2)_2$ , was also added into the bulk solution to obtain good mechanical property of the gel spheres.

**Fig. 1** Flow sheet item of the applied external gelation process for Zr-doped ThO<sub>2</sub>



### 2.3 Gelation and Dispersion

Microspheres were created, using an injection pump and a hollow needle to introduce the bulk sol solution as drops in a column filled with ammonium hydroxide. Pinhole diameter of the hollow needle, feeding rate, frequency, and amplitude of the vibration generator and the height of the ammonia area should be controlled carefully.

### 2.4 Aging and Washing

The gel microspheres were aged in a 12 M ammonia solution. Afterward, the gel microspheres were filtered and washed with 0.01 M ammonia solution to remove impurities such as ammonium nitrate and urea. At last, microspheres were washed several times with distilled.

### 2.5 Drying, Calcination, and Sintering

The prepared gel microspheres were placed in a corundum crucible and then dried in an oven for 3 h at 200 °C. Air-dried particles were brown due to carbon decomposed from PVA. Calcination was carried out in air atmosphere from room temperature to 650 °C for 5 h with ramp rate of 1 °C/min. Finally, samples were sintered at 1350 °C for 3 h with heating rate of 3 °C/min.

## 2.6 Characterization

The crystallographic phase was characterized with X-ray diffraction (XRD) at room temperature with Cu-K $\alpha$  radiation. The microstructure was measured by scanning electron microscopy (SEM). And the Energy-Dispersive Spectroscopy (EDS) was used to identify the elements. The particle size and sphericity distribution was determined by a laser particle size analyzer (Sympatec GmbH, Germany).

## 3 Results and Discussion

Gelation occurred successfully only when sol was formed properly. Reaction temperature and pH of feed sol and concentration of metal nitrate solution were the key factors for the gelation behavior of feed solution. The quality of the gel was studied depending on the pH and the mole concentration of thorium solution, as shown in Fig. 2.

Ammonium hydroxide reacted with hydrogen ion to neutralize and form the metal ion polymer  $(Th(OH)_n)^{n+}$ . Low metal concentration or neutralization results in fragile polymer molecular network skeleton, which would too soft for external gelation process. While higher metal concentration would lead gel sphere cracked during processing. If sol reaction was not completed, aging time would be too long. It was found that when reaction temperature was higher than 60 °C, milky white precipitate was acquired rather than sol. When reaction temperature was too low, it would be time-consuming for sol preparation. Therefore, 60 °C was the suitable temperature for sol preparation. The high-quality gel spheres were white and elastic.

Investigations of the sintered particles by optical microscopy exhibits good sphericity with smooth surface, as shown in Fig. 3. The diameter distribution was determined by a laser particle size analyzer, and the size distribution is displayed in Fig. 4. The average diameter is 830  $\mu\text{m}$ . The diameter difference between the minimum and maximum value is less than  $\pm 8\%$  over all particles. Average sphericity is 0.945 with standard deviation of  $\pm 2\%$ .

**Fig. 2** Gelation field diagram for thorium

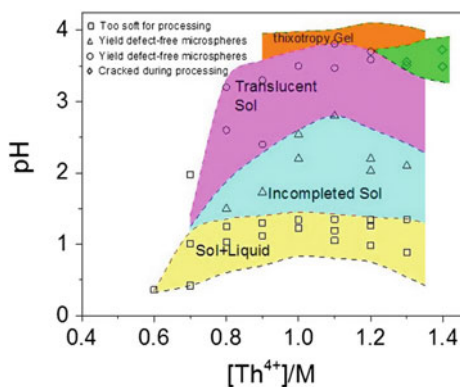


**Fig. 3** Microscopy of sintered microspheres

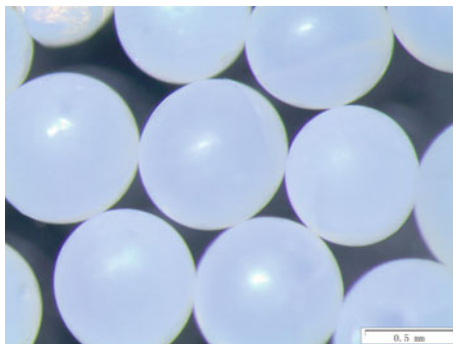
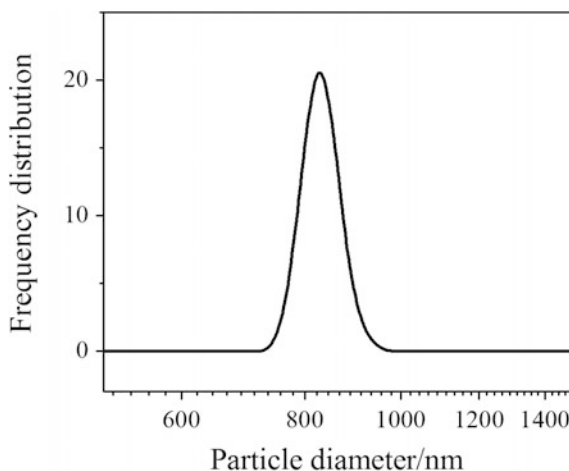


**Fig. 4** Diameter and sphericity distribution for sintered microspheres



The SEM pattern of sintered microsphere is shown in Fig. 5, and no obvious cracks and nicks are found. The grain sizes differ from 100–800 nm. In order to confirm the homogeneity of thorium and zirconium, EDS were performed. Figure 6 shows a good homogeneity of each element.

XRD patterns of Th<sub>1-x</sub>Zr<sub>x</sub>O<sub>2</sub> ( $x = 0.005, 0.015, 0.025, 0.45$ ) series were recorded and analyzed as shown in Fig. 7. Pure ThO<sub>2</sub> crystallizes as fluorite structure which is evident by the presence of superlattice peaks at  $2\theta \approx 28(111), 32(200), 46(220), 54(311), 57(222)$ , etc. [13]. Figure 5a–f exhibits the XRD patterns of fluorite phase for the compositions corresponding to  $x = 0.0–0.45$ . The diffraction peaks shift toward lower angle on doping (Fig. 6b) which clearly indicates the lattice cell parameters of the doped fluorite increase as the concentration of tetravalent zirconium ion is increased. Th<sub>0.55</sub>Zr<sub>0.45</sub>O<sub>2</sub> is found to be a mixture of fluorite ThO<sub>2</sub> and mixed ZrO<sub>2</sub>, which is in accordance with earlier studies [14].

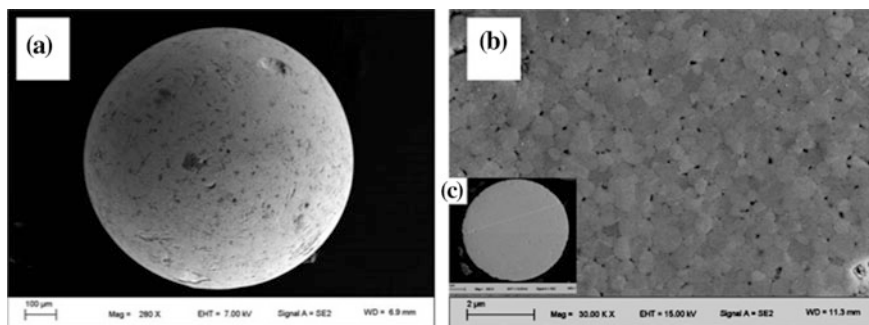


Fig. 5 SEM micrographs of  $\text{Th}_{0.985}\text{Zr}_{0.015}\text{O}_2$

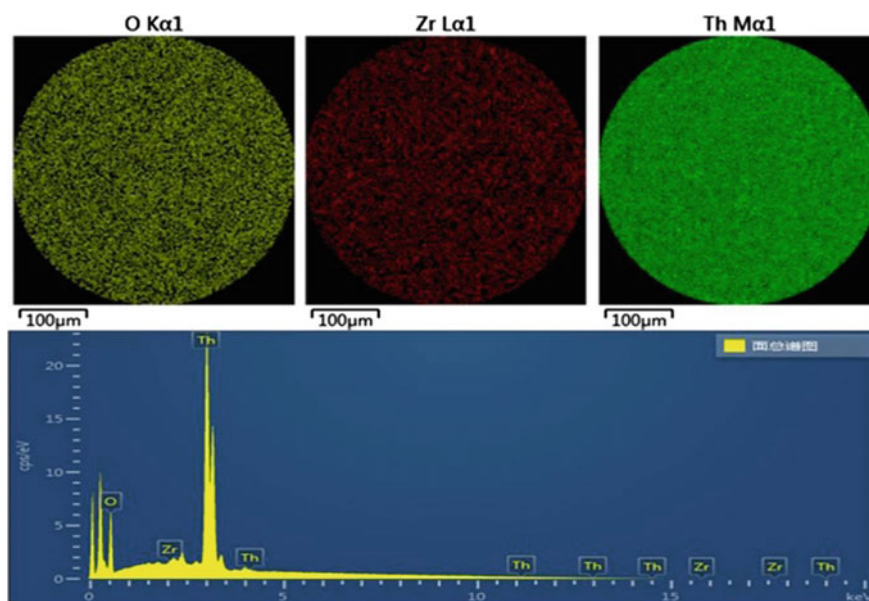
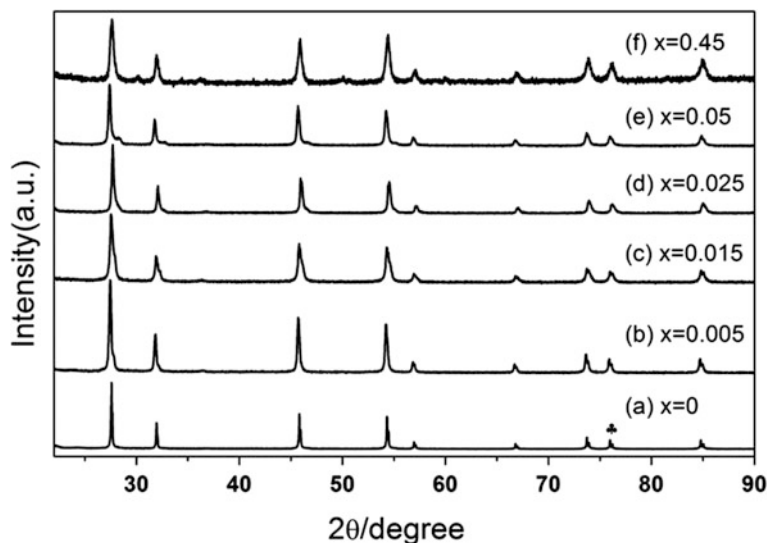


Fig. 6 EDS of cross-sectional views of sintered spheres

## 4 Conclusion

This study introduced the preparation of  $\text{ZrO}_2$ -based IMF by an external gelation technology. Gelation of Zr, Th nitrate mixtures was conducted successfully. The sintered spheres consisted of a uniform fluorite type phase as Zr was lower than 1.5 mol%. The sintering temperature of 1350 °C is suitable for the preparation of



**Fig. 7** X-ray diffraction patterns from sintered spheres, Th<sub>1-x</sub>Zr<sub>x</sub>O<sub>2</sub>, with  $x = 0, 0.005, 0.015, 0.025, 0.05,$  and  $0.45$

ThO<sub>2</sub>/ZrO<sub>2</sub> composite ceramic fuel with high density and strength, uniform grain sizes as well as good microstructure.

**Acknowledgments** This study was supported by the Strategic Priority Program of the Chinese Academy of Sciences with grant No. XDA02030000 and XDA02030200, and the Frontier Science Key Program of the Chinese Academy of Sciences (Grant No. QYZDY-SSW-JSC016).

## References

1. M. Lung, A Present Review of the Thorium Nuclear Fuel Cycles, EUR 17771, European Commission, Luxembourg, 1997
2. D. Das, S.R. Bharadwaj, Thoria-based Nuclear Fuels, Springer-Verlag, London, 2013
3. Angela Baena, Thomas Cardinaels, Benedict Vos, Koen Binnemans, Marc Verwerft, Journal of Nuclear Materials 461, 2015, 271–281
4. H. Kleycamp, J. Nucl. Mater. 275,1999, 1
5. G.J. McCarthy, W.B. White, R. Roy, B.E. Scheetz, S. Komarzeni, D.S. Smith, D.M. Roy, Nature 273, 1978, 216
6. A.E. Ringwood, S.E. Kesson, N.G. Ware, W. Hibberson, A. Major, Nature 278, 1979, 219
7. T. Yamashita, K. Kuramoto, H. Akie, Y. Nakano, N. Nitani, T. Nakamura, K. Kusagaya, T. Ohmichi, 39(8), 2002, 865–871
8. R. M. Berman, M. I. Bleiberg, W. Yeniscavich, J. Nucl. Mater., 2, 1960, 129
9. Akie, H., Muromura, T., Takano, H., Matsuura, S.: Nucl. Technol., 107, 1994, 182
10. Shelley, A., Akie, H., Takano, H., Sekimoto, H.: Nucl. Technol., 131, 2000, 197
11. Akie, H., Takano, H., Muromura, T., Nitani, N.: Prog. Nucl. Energy, 29, 1995, 345



12. K. Idemitsu, T. Arima, Y. Inagaki, S. Torikai, M.A. Pouchon, Manufacturing of zirconia microspheres doped with erbia, yttria and ceria by internal gelation process as a part of a cermet fuel, *Journal of Nuclear Materials* 319, 2003, 31–36
13. Michael Aizenshtein, Tatiana Y.Shvareva, and Alexandra Navrotsky, *J. Am. Ceram. Soc.*, 93 (12), 2010, 4142–4147
14. V. Grover, A.K. Tyagi, *J. Nucl. Mater.* 305, 2002, 83

# R&D Base for Nuclear Fuel Manufacturing—CNNFC

Wang Shibo

Abstract ■■■

Keywords ■■■

## 1 General Status

China North Nuclear Fuel Co., Ltd. (abbreviated as CNNFC) was built in 1958, which is one of the important members of China National Nuclear Corporation. CNNFC located in Baotou, Inner Mongolia, is the main research and production base of nuclear material, nuclear fuel elements in China, and made important contribution to the national defense and peaceful use of atomic energy.

CNNFC is a nuclear fuel manufacturer which is able to produce all kinds of nuclear fuel fulfills the customer's needs, and provides service related with nuclear fuel in China. CNNFC has nuclear fuel R&D facilities, has a research institute of nuclear materials and nuclear fuel, four nuclear fuel elements production lines, a uranium conversion production line and an independent inspection center, supplies nuclear fuel elements for PWR and PHWR power plant and all of research reactors in China, will supply nuclear fuel to AP1000 PWR power plant and HTGR nuclear power plant in the future. More than 10 years, the nuclear fuel elements supplied by CNNFC run very well in the reactors, satisfied by all the customers.

After nearly 60 years of development, CNNFC has made brilliant achievements in the field of nuclear materials and nuclear fuel research and fabrication. With the rapid and large-scale development of nuclear energy in recent years, the production, R&D, and human resources system made great progress, the capacity of nuclear fuel elements increased continuously, is able to provide reliable and high-quality nuclear fuel for the nuclear power plant with the development of nuclear power industry in China.

---

W. Shibo (✉)

China North Nuclear Fuel Co.,Ltd., Baotou, China

e-mail: jianghong@cnpe.cc

## 2 Introduction of the Nuclear Manufacturing Lines for NPP

There are four nuclear fuel manufacturing lines in CNNFC. Two production lines are operating and the other two are under construction. CANDU plant and Cobalt adjust rod assembly production line, PWR fuel plant are the two lines operating, the product is CANDU-6 bundle, Cobalt adjust rod assembly, and AFA3G fuel assembly. The CANDU plant put into production in 2003, and PWR fuel plant put into production in 2010. The AP1000 fuel production line and HTR-PM fuel production line are under construction. In 2016, these two production lines will complete the commissioning and qualification, and then put into production.

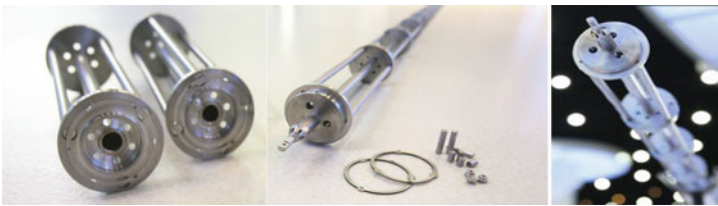
The following figure shows the construction starting time of the four fuel production lines in CNNFC.



- CANDU PLANT the line has been running with the design capacity of 200TU per year since 2003. It is the first fuel production line built in CNNFC. And this CANDU plant is the unique production line for the fabrication of CANDU-600 nuclear fuel in China. It includes chemical conversion line using ADU process, pellets preparation, subassembly manufacturing, end cap welding, and end plate welding process using pressure resistance welding; and the machining of the end caps, spacers, bearing pads, etc. Many developments for the equipments had been carried out to achieve the automation of the operating, especially the welding. Till now, there are more than 128,000 bundles delivered to TQNPC in Haiyan, Zhejiang province. Bundles had good performance in the reactor. The quality reached the international most advanced level.



- Cobalt adjust rod assembly for CANDU reactor has been independently developed and manufactured by CNNFC, which replaced the stainless steel rod assembly which is used for adjusting neutron flux and producing  $^{60}\text{Co}$ . By now the market share in the mainland of  $^{60}\text{Co}$  from assemblies manufactured by CNNFC reaches 60 %.



- PWR fuel—AFA3G FAs manufacture line has been constructed since 2006 and finished in 2008; the design capacity is 200TU per year. In 2010, the PWR fuel plant completed the commissioning and qualification, and then put into normal production. The whole manufacture line consists of several processes, the chemical conversion (ADU process and IDR process), pellets preparation, fuel rod welding, fuel assembly, and components manufacturing. Innovations and improvements were implemented for the production line to get more effectiveness, good operating, and less cost. Till now, 492 fuel assemblies had been manufactured and they get good performance in the reactor.



- AP1000 FAs manufacture line which is operated by China Baotou Nuclear Fuel Co., Ltd. (abbreviated as CBNF), which is the subcompany of CNNFC. The design capacity of 400TU per year construction started on 28th, and another 400TU interface was designed and reserved. Now the production line is commissioning. The manufacturing line transfers the technology of AP1000 fuel assembly manufacturing from Westinghouse Electric Company, especially the IFBA pellet preparation & inspection, fuel rod welding, skeleton swaging, and fuel assembly. Most of the main equipments have been introduced from Westinghouse, and other equipments are purchased from internal and external supplies. The line will complete the qualification in 2016. The production line will produce the reload for SanMen and HaiYang nuclear power station in 2017 in China.
- HTR-PM fuel plant. The production line started the construction on March 16, 2013. The design capacity is 300,000 spheres per year. The production line is based on the fuel manufacturing technology of Institute of Nuclear and New Energy Technology, Tsinghua University, has proprietary intellectual property right of China. The plant will produce the fuel for ShiDaoWan nuclear power station after the commissioning and qualification. MHTGR has become the main development direction of HTGR technology in the world.

Nuclear Safety Culture is that assembly of characteristics and attitudes in organizations and individuals which establishes that, as an overriding priority, nuclear plant safety issues receive the attention warranted by their significance.

CNNFC focus on customers' satisfaction and an open, honest quality culture was established. The quality management system has been established and operated properly in CNNFC. The whole process of nuclear fuel manufacturing is under control through all the actions and means defined. The safely operation of the nuclear power station is the start point and goal of our nuclear safety work.

### 3 Summary

With the rapid development of China's nuclear power industry and the continuous progress of the world nuclear industry, CNNFC will continue to improve the industrial R&D capabilities and manufacturing capacity, the product quality and optimize the services.

CNNFC is always to commit to creating value for customers, to realize the perspective of achieving the nuclear industry scale, independent, international development. By 2020, CNNFC will reach the capacity of 200TU/year for CANDU fuel, 200TU/year for AFA3G fuel, 800TU/year for AP1000 fuel, and larger capacity for HTGR fuel elements as the request. By the successful cooperation with international corporations, such as Westinghouse, AREVA NP, and Cameco, CNNFC will be the top-ranking base of nuclear materials research and nuclear fuel elements production, and one of the best nuclear fuel fabrication companies around the world.

# Research and Discussion of Development of Reliability Program About Nuclear Fuel Cycle

Hong Shen, Xiaowei Yang, Chunlong Zhang and Yuntao Liu

**Abstract** Different types of systems and equipment for the nuclear fuel cycle facilities are complex and difficult to maintain, used in the special environment, which inclusive medium is radioactive and corrosive fluids or gases. Safe and stable operation of the equipment will be directly affected. Higher reliability program is guarantee for safety of nuclear fuel recycle. This thesis analyzes the reality and problems of nuclear fuel recycle. We also provide some solutions for those problems.

**Keywords** Nuclear fuel recycling · Reliability · Development direction

## 1 Introduction

Industry of nuclear fuel recycling is an important basic for development of nuclear power in China. Accelerate the development of nuclear power projects in the country; making the nuclear fuel cycle facilities has been an unprecedented development. Nuclear fuel cycle includes uranium exploration, Uranium enrichment, nuclear fuel element fabrication, reprocessing, and treatment and disposal of radioactive waste [1]. Different types of systems and equipment for the nuclear fuel cycle facilities are complex and difficult to maintain, used in the special environment, which includes medium is radioactive and corrosive fluids or gases, electromechanical devices, and electrical components will be directly affected [2]. Thus, how to improve the quality of equipments is a key step for nuclear fuel cycle.

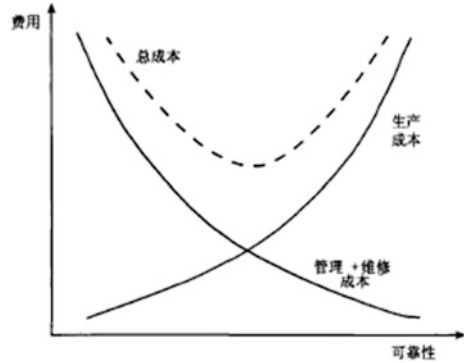
---

H. Shen · X. Yang (✉) · C. Zhang · Y. Liu  
Nuclear and Radiation Safety Center, MEP, Beijing 10082, China  
e-mail: YangXiaowei@chinansc.cn

© Springer Science+Business Media Singapore 2017  
H. Jiang (ed.), *Proceedings of The 20th Pacific Basin Nuclear Conference*,  
DOI 10.1007/978-981-10-2317-0\_54

573

**Fig. 1** Reliability—cost curves



Reliability is the ability that the product and the system complete the required function under specified conditions and within the time prescribed. Reliability is closely related to the security and economy; the relationship shown in Fig. 1.

## 2 The Current Situation and Issues of the Reliability of Nuclear Fuel Cycle Facilities in China

### 2.1 *Reliable Work Still in Primary Level with Narrow Scope in Reliable Technology Using*

The concept of reliability originated in the USA. In 1960s, many researches, and promotion and application were conducted in the field of reliability and maintainability by DOD and NASA, which formed and released many standard norms, regulations, and manuals in the technical criterion of engineering reliability. In 1974, after Three Mile Island accident in the USA, the USA strengthens the safety and reliability of the nuclear power station establishing NSAC and INPO. The former focuses on the accelerated aging of studied devices and the fault from redundant safety system, while the latter studies the evaluation technics of human factors and probabilistic safety analysis and is in charge of the analysis of the reliability data. NRC specially formed the outline guiding the work of the reliability in the nuclear power station. It was required clearly by (The outline of the reliability in the nuclear power station) that all nuclear power stations in Canada must form (The outline of reliability) and conduct the corresponding reliability work. Russia also attaches much importance in the basic reliability work. In Russia, devices of uranium separation are in a meticulous and thorough way. Many experiment stations for various types and elements are established, and many researches on the increasing of reliability are conducted, which gets much convincing data. In recent years, the theory of reliability has been perfected while the

relating technics have been appeared in endlessly. The exploitation and application of computer software provide a good solution for the reliability calculation of complicated systems, which reduces the manly calculation in large extent. In addition, with the enlargement of the reliability extent, based on some traditional concept of reliability, it has been combined with maintainability, safety, security, and testability and becomes a comprehensive issue. In the field of nuclear industry [3], PSA has been studied deeply and developed from a static PSA to a dynamic one. In order to improve the accuracy of analysis of PSA, human reliability analysis techniques, complex systems FTA, GO analysis methods, and other techniques have new development and applications.

In the middle 1990s, eliable technology is used in nuclear field. There are many kinds of nuclear fuel cycle facilities but only a few have started the research work of reliable, such as centrifugal machine established some experiment terrace, started the environmental stress sift, reliable testify, and the accelerate experiment. Nowadays, the reliable skill prefers to solve the equipments reliability. However, in the running of system, all kinds of random fault and instant fault happen frequently which caused the hidden danger in the safety running of equipment. So how to solve these problems from the reliable angle waits for deeper research. In general, the reliable work of nuclear fuel cycle started late and still in the primary level with narrow scope, and has not form a set of RMSTS thinking method to start work.

## ***2.2 Lack of Reliability Standards and Norms***

Although uranium isotope separation device has been carried out some research of reliability tests, but test methods, test data processing, and other aspects are still lacking of the guidance of mature technological standards. At present, the nuclear industry has only issued seven technological reliability standards, which means more work of reliability has not formed into experience or even has not been carried out.

## ***2.3 Lacking of Basic Data Accumulation***

The accumulation and analysis of the reliability data is the foundation of the reliability design. Nowadays, the level of using the reliability in the nuclear fuel circulation equipment various a lot; the needed project data has not finished. The Uranium Isotopes established the reliability data base but not complete. It is difficult to collect the data because of lacking of equipment (e.g., reprocessing, and treatment and disposal of radioactive waste) which still in the accumulation progress



and the foreign data is hard to get, so it will take a long time to accumulate data and start the work of reliability test and verify.

#### ***2.4 Reliability Design Analysis System Has not Been Established***

Reliability design is primary link to determine the reliability of systems and equipment. Design of nuclear fuel cycle facilities have not been changed from a conventional design for the reliability design analysis, design work on the reliability of the program, the basic content and basic methods are poorly understood. The reliability of the basic system design analysis has not been established.

#### ***2.5 Failing to Carry Out Effective Reliability Tests***

Reliability engineering appliance is not deep enough which lacks of means and necessary testing equipment. It has not carry out effective reliability tests and validation tests specifically in nuclear fuel cycling facilities.

#### ***2.6 Reliability Management System Is not Perfect, the Responsibility Is not Clear***

Reliability management system of the nuclear fuel cycle has not been established which lacks the necessary means. Reliability objectives and responsibilities are not clear. Lacking of understanding of the reliability, practical work often succumb to the facility performance, economic factors, making it difficult to carry out effectively.

### **3 Developing Direction of Reliability Work in China**

Technology of reliability has been researched and applied in the research of the model of nuclear fuel cycling facilities, but the application is not deep. Combine the technology of reliability and engineering practice. Established the system of reliability design and analysis and reliability test [4] and evaluation to improve the reliability of nuclear fuel cycling system is the focus of future work Fig. 2.

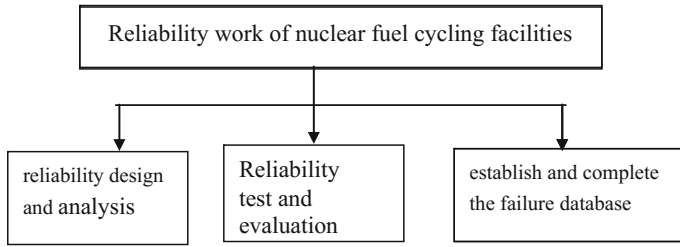
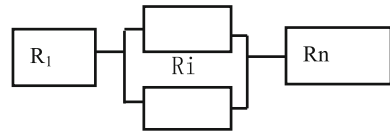


**Fig. 2** Work block diagram of reliability

**Fig. 3** The diagram of reliability system



### 3.1 *Appliance of Reliability Designed Analyzing Method*

Reliability designing method believes that all designed equipment and components have a certain probability of failure, but which can not exceed the allowable value formulated by the technological condition. Thus, it can express the probability of failure or reliability quantitatively during the function of products and compensate the limitations of conventional designing method. To predict, design, and analyze the reliability of nuclear cycling system, we must analyze the functions of systems and the relationship of equipments and establish reliability models. A complex system can be viewed as a plurality of cells (equipment, subsystem) consisting of series-parallel (Fig. 3). If the entire series-parallel system to work, it must require all units to work simultaneously, generous rate of reliability of the system is calculated as a multiplication laws.

The failure rate that is the key to reliability design can be controlled within a certain range. General equipment failure rate can be selected from the relevant profile. The basic components of some of the equipment failure rate (see Table 1). These values can be applied to the equipment with these parts.

### 3.2 *Reliability Test and Evaluation*

Reliability testing includes various environment tests, enhancing reliability tests, and identify reliability tests [5]. We analyze if it reach the good by testing identify system, if it is correct and reasonable by system reliability model and reliability allocation. We can collect all kinds of statistics then make the rules to evaluate the reliability testing.

**Table 1** Component failure rate

No.	Names of parts	Failure rate $\lambda G/10^{-5} \text{ h}^{-1}$
1	Roller bearings	0.2–2.5
2	Gear light load	0.01–0.10
3	Common axis	0.01–0.05
4	Vane wheel	2.8
5	Pump housing	2.8
6	Pins and bond	1
7	Motor	1
8	Rubber sealing component	0.002–0.1
9	Screws, bolts	0.0005–0.012

### 3.3 Established Failure Database and Fault Tree

We need to establish and complete the failure database of various facilities which provide basic data for the design and analysis of reliability. Reliability and event systems are inseparable; it requires a combination of event sequence analysis (Fig. 4).

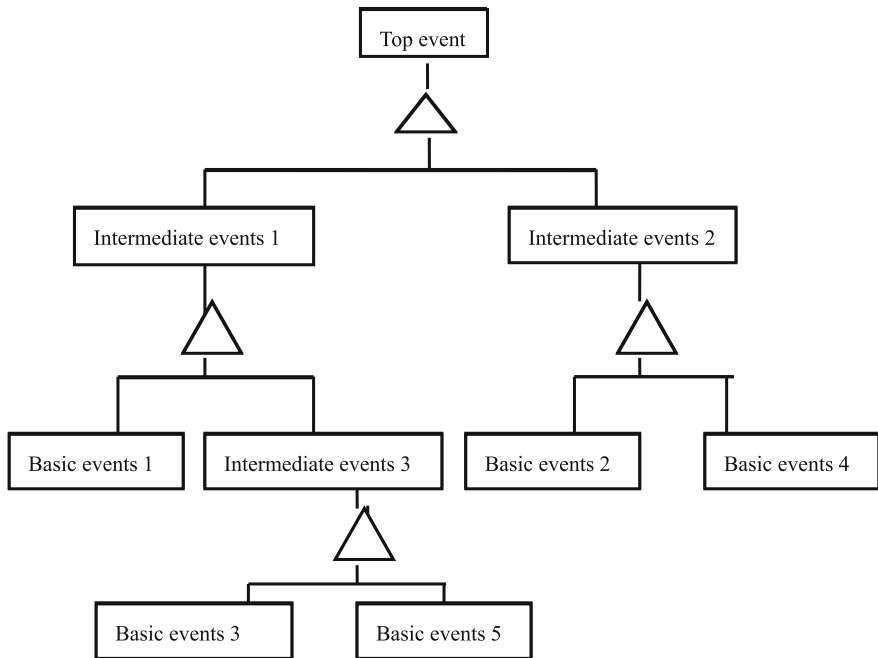


**Fig. 4** Fault tree

### ***3.4 Established Reliability of Management Systems***

In addition to technical concerns, we should be concerned about the reliability of the management system in practical application process, in order to implement the reliability.

## **4 Conclusion and Recommendations**

Reliability of nuclear fuel cycle facilities is a complicated systematic project, which needs more professional skills and accumulations. We could use the different strategy and personal training plans to rebuild the basic ability of reliability program. We could make approaches to suit for nuclear fuel recycling by basic working and deep researching. We could improve the design of nuclear fuel recycling and make a guarantee for develop the nuclear fuel cycle.

## **References**

1. LIAN Peisheng. Nuclear Energy Industry [M]. Beijing. Atomic Energy of a Press.2002
2. HUYan. Reliability Design Encyclopedia [M]. Beijing China Standard Press. 2006
3. Yang Weiming. General maintenance type of reliability [M]; Beijing. Defense Industry Press. 1995
4. JIA Jianguo, YANG Yu. Reliability Integrated Planning Analysis and Fault Diagnosis System [J] Application Research of Computers 2012. 29(3)
5. WU Fengfeng. Thinking of The reliability of China's nuclear industry status quo [J] Nuclear Standards and Metrology. 2011 vol 1

# Role and Position of PHWR in Nuclear Fuel Cycle in China

Zhenhua Zhang, Gang Qiao and Shen Fan

**Abstract** Although the closed nuclear fuel cycle strategy has been adopted in China, there are still some issues existing in the developing strategy, such as ignoring the utilization of recycled uranium, just depending on the U–Pu fuel cycle, etc. Because of the high neutron economy, simple fuel bundle design, and on-power refueling, PHWR could use recycled uranium economically and efficiently, and could be the breakthrough of nuclear utilization of thorium. It is suggested that developing PWRs, reprocessing plants and FRs with matched number of PHWRs to utilize the Recycled Uranium, close the U–Pu fuel cycle, and develop Th–U fuel cycle as the backup measure of the U–Pu cycle, which would guarantee the continual development of nuclear energy.

**Keywords** Closed fuel cycle · PHWR · Recycled uranium · Thorium · Role

## 1 Status Quo Development of Nuclear Fuel Cycle in China

In the “Mid-Long Term Development Plan for State’s Nuclear Power of China (2005–2020)” [1] issued in 2007, China put forth the specific requirements of “adhering to the technical line of closed nuclear fuel cycle” and “developing nuclear fuel industry with appropriate advance.” However, at present, the closed nuclear fuel cycle industry is still in the starting phase in China. Reprocessing is an obvious restricting factor in the development of closed cycle industry. The development of reprocessing industry has been lagged behind the actual demand because on one hand, in the nuclear energy development in the initial period, China attached importance to the development of nuclear power technologies, but the development of closed nuclear fuel cycling technologies was neglected, and on the other hand, the economic performance of reprocessing is not so attractive.

---

Z. Zhang · G. Qiao · S. Fan (✉)  
Third Qinshan Nuclear Power Company, Haiyan, Zhejiang, China  
e-mail: fans@cnp.com.cn

**Table 1** Utilization rate of natural uranium resource

Cycle form	Utilization efficiency (kWh/kg NU)	Increase as compared with once-through type
Once-through	42,000	–
Plutonium recovery and utilization*	47,000	12 %
Recovery of both uranium and plutonium*	55,000	30 %

*Note* The table shows the data of one cycle

\* If the nuclear fuel is recycled more than one cycle, it is hard to calculate the utilization rate of NU. So only one cycle is considered for the utilization rate

To increase the economic performance of reprocessing industry, all products in reprocessing process must be utilized as far as possible. Among the reprocessing products, highly radioactive wastes account for about 5 %, which should be disposed geologically; about 1 % of plutonium can be recovered to be used in fast reactors as an important strategic resource; however, no recycling for use has been considered for the recovered uranium, accounting for 94 % of the reprocessing products, instead, cost must be paid to properly store it. Actually, use of recovered uranium can provide many benefits: first, the economic performance of closed fuel cycle can be substantially increased; second, the utilization rate of natural uranium resource can be greatly increased. Table 1 shows the utilization rate of natural uranium resource under various conditions; the utilization of recovered uranium can raise the utilization rate of natural uranium resource by a further about 20 % on the basis of utilizing the recovered plutonium.

Furthermore, in the current nuclear fuel cycle in China, only the uranium–plutonium cycle system has been taken into account. As China has rich thorium reserves, out research on utilization of nuclear energy of thorium resource and appropriate development of thorium–uranium fuel cycle technology can serve as supplement to the uranium–plutonium fuel cycle technology, conducive to ensuring the sustainable and healthy development of nuclear energy.

## 2 Researches on the Utilization of Recovered Uranium and Thorium Resource

### 2.1 Researches on Utilization of Recovered Uranium

The international nuclear energy circle has fully realized the significance of utilizing recovered uranium, and trials have been made. To use recovered uranium in pressurized water reactor (PWR), it should be enriched again, but the radioactive level after enrichment can be about 80 times as maximum that of natural uranium fuel, resulting in complicated fuel fabrication processes and poor economic performance. Therefore, although there has been no major technical problem in

**Table 2** Comparison of using recovered uranium with PHWR and PWR

	PHWR	PWR
Re-enrichment	Not required	Required
Radioactivity level	2–3 times	About 80 times
Fuel fabrication, transport and use	Minor change	Major change
U-235 to compensate extra neutron depletion of U-234 and U-236	Very low	About 0.3–0.5 %
Fuel economic performance	Lower than the current fuel cost	3–4 times

utilizing recovered uranium in PWR for years, and a number of countries have used recovered uranium fuel either on long-term basis or trial basis, due to the economic performance of fuel and political factors, recovered uranium fuel has not been extensively used in PWR.

AECL in Canada and KAERI in Korea have done a lot of work on using recovered uranium in pressurized heavy water reactor (PHWR). AECL succeeded in the trial making of recovered uranium fuel bundles, but no substantial application has been conducted. Korea tried on directly using spent PWR fuel, which is known as DUPIC (Direct Use of spent PWR fuel in CANDU) by skipping over the spent fuel reprocessing; however, as the series processes of DUPIC fuel manufacturing, transport and loading are accompanied with high radioactivity, and also due to other technical issues, the development has been stopped now.

According to domestic and international research practice, PHWR is more advantageous over PWR in using recovered uranium, as detailed in Table 2. In general, using recovered uranium in PHWR is technically feasible and can produce obvious economic benefits.

## ***2.2 Research of Thorium Resource Nuclear Energy Utilization***

Internationally, the research and development on using nuclear energy of thorium was started in the 1970s, after that, due to successive new uranium mines being discovered and the reduction of uranium product price, and the negative impact of the Chernobyl nuclear accident in 1986 on the use of nuclear energy, most of countries suspended the research and development on using thorium fuel. In the 1990s, some developed countries became interested again in thorium fuel, mainly for three purposes: first, the thorium–uranium fuel cycle can effectively consume weapon class plutonium and plutonium for civil use, second, the thorium–uranium cycle produces much less long life actinium-series nuclides than uranium–plutonium cycle, and third, nuclear fuel U-233 produced in the thorium–uranium cycle contains a certain amount of U-232, and its decay products radiate high-energy  $\gamma$ -ray, conducive to prevention of nuclear proliferation.

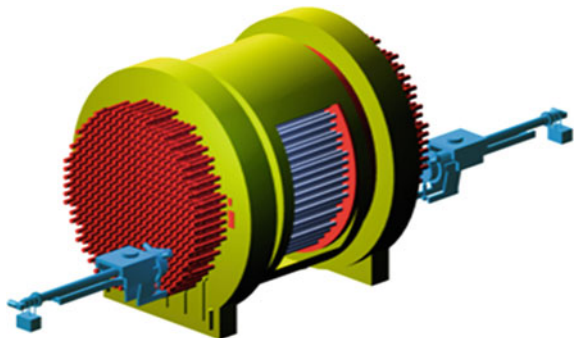
In China, the research work on using thorium for nuclear energy has also experienced ups and downs in a period of 40 years, and research work has been carried out on thorium thermal neutron breeder reactor, aqueous reprocessing for thorium–uranium cycle and basic research on thorium–uranium cycle. Some research data have shown that it is possible to realize thermal reactor proliferation of thorium–uranium cycle through using thorium resource in PHWR and the associated reprocessing facilities. In December 2008, the National Energy Administration (NEA) of China organized an expert symposium in nuclear utilization of thorium resource. The symposium proposed that giving the outstanding advantages of PHWR and fast reactor breeding zone in nuclear utilization of thorium resource; the state should make use of the feature of PHWR in flexible fuel management, and strive to make breakthrough in the application of thorium resource in PHWR in conjunction with the favorable conditions of international cooperation.

### 3 Technological Advantages and Development Results of PHWR

#### 3.1 *Brief Introduction to PHWR*

PHWR is one of the three main commercial nuclear power reactor types in the world, the CANDU reactor developed in Canada is the main reactor type in PHWR nuclear power plants in service, and the Third Qinshan Nuclear Power Co., Ltd has imported two CANDU units from Canada. The core structure is as shown in Fig. 1, consisting of fuel channels and calandria arranged horizontally, heavy water is used as moderator and coolant, with pressure pipes containing fuel and coolant under high temperature and high pressure, and calandria containing moderator under low temperature and low pressure, isolated from coolant. CANDU reactors have the features of high neutron utilization rate, flexible fuel management, and high inherent safety.

**Fig. 1** The core of CANDU reactor





A CANDU reactor can use natural uranium, slightly enriched uranium, recovered uranium, and thorium as fuel. Also, in a CANDU reactor, the adjustor rods that regulate core power distribution remain in the core during normal operation. If Co-59 is used for adjustor rods, Co-59 becomes isotope Co-60 after absorbing neutron, so that scaled production of isotope Co-60 can be realized. In addition, in a CANDU reactor, heavy water is used as moderator and coolant, the isotope deuterium can absorb neutrons under neutron radiation, to produce isotope tritium. These technological advantages of CANDU reactors can be summarized as “tritium, cobalt, uranium, and thorium.”

With the above-mentioned advantages, PHWR also has the disadvantages of complicated systems, high tritium radiation level, large amount of spent fuel, and the need of interim unit refurbishment by replacing pressurized pipes. On process systems, as heavy water is used as coolant and moderator, and it is quite expensive, extra systems to collect, clean and upgrade heavy water are provided for a PHWR, as compared with a PWR, the systems are more complicated and work load is higher. For the high tritium radiation level, on one hand, the operation practice of the two PHWR reactors at Qinshan has demonstrated that the existing protection provisions are sufficient to protect the working personnel, the public and the environment, on the other hand, tritium removal facility can be provided, to keep the tritium radiation in the unit at a low level. For the large amount of spent fuel, today, mature spent fuel dry storage technology has been developed, and associated spent fuel dry storage facilities are constructed for all CANDU units, so that long-term safe storage of spent fuel can be realized at a fairly low cost. For interim refurbishment of units, up to date, interim replacement of pressurized pipes, and other associated refurbishment work has been successfully implemented for a number of units, and refurbishment will be done for a number of units, and practice shows that the interim refurbishment technology for CANDU units are mature in technology and feasible economically. Therefore, although the technological disadvantages of CANDU reactors may produce some effect on the economic performance of units, they can be overcome with the existing technical means, and the overall economic performance can be guaranteed, that is why Argentina and Romania are preparing to build new PHWR units, and Canada, Korea, and Argentina have approved to replace pressurized pipes for unit refurbishment.

### ***3.2 Advanced Fuel Technology Development Results for PHWR***

#### **3.2.1 Use of Recovered Uranium in PHWR [2]**

The U-235 enrichment of spent fuel from a PHWR is normally 0.8–1.4 %, higher than that of natural uranium. There are two feasible plans to use in PHWR the uranium recovered after reprocessing of PHWR spent fuel: mixing the recovered

uranium with depleted uranium into a fuel equivalent to natural uranium fuel, abbreviated as natural uranium equivalent fuel; and using the recovered uranium directly, equivalent to low-enrichment uranium. Directly using recovered uranium can produce better result, however, to use it in the existing CANDU units, there will be great difficulties in design and licensing, and it will also require very high project investment. In conjunction with the foundation of industries associated with PHWR in China, it is appropriate to take natural uranium equivalent fuel plan as the first choice.

TQNPC, jointly with a number of domestic and overseas entities, organized the research work on using recovered uranium in PHWR according to the above-mentioned technical roadmap. In March 2010, after sufficient analysis and justification and obtaining approval by the National Nuclear Safety Administration (NNSA), natural uranium equivalent fuel was loaded in two channels of Unit 1, to start the in-core test following the management process flow of natural uranium fuel. The test was completed in March 2011, and then under water inspection and hot cell inspection were performed for the natural uranium equivalent spent fuel. In this demonstration test, a series of processes for natural uranium equivalent fuel, including fabrication, in-core test and post-radiation inspection, were checked, getting through the technical line for application of recovered uranium in PHWR. After the demonstration test, TQNPC immediately started the development work for using natural uranium equivalent fuel in a whole PHWR reactor. At present, work on physical calculation, safety analysis, purchasing of recovered uranium, and production line renovation is going on smoothly, and it is expected that use of recovered uranium in a whole reactor can be realized at the end of 2016.

### **3.2.2 Using Thorium Resource in PHWR Reactors**

To implement the proposal at the meeting of NEA on December 11, 2008 on using thorium resource nuclear energy, TQNPC started the associated research work on using thorium resource in PHWR reactors together with Nuclear Power Institute of China, China North Nuclear Fuel Co., Ltd. and AECL in 2008. In October 2009, the preliminary feasibility study report on thorium fuel PHWR was issued. The report proposed that low enriched uranium be used as drive fuel to realize the nuclear energy utilization of thorium resource, on the basis of the existing enhanced CANDU6 reactor and high performance CANFLEX fuel technology, and this can promote the development of critical technologies associated with the nuclear energy utilization of thorium resource while saving natural uranium resource. Relevant experts praised this plan highly, believing that it was feasible technologically, with enhanced safety features and good expected economic performance, and could be implemented in projects in a short period of time.

### ***3.3 Development of Advanced Fuel CANDU Reactor [3]***

To use recovered uranium more economically and with higher efficiency and steadily push ahead the use of thorium resource in PHWR, TQNPC has developed advanced fuel CANDU reactor (AFCR) in cooperation with domestic and overseas research entities. It is based on the enhanced CANDU6 reactor developed in Canada, fully incorporates the experience of Fukushima, and has achieved higher safety performance, to meet the technological requirements of G3 nuclear power units; it can also use and recycle uranium fuel and thorium fuel; therefore, good economic performance can be expected. In terms of engineering maturity, the enhanced CANDU6 reactor has passed the safety review of three phases by Canadian Nuclear Safety Commission, and conditions are ready to carry out further work in conjunction with site.

In November 2014, China Nuclear Energy Association organized experts of the industry to review the technical plan of advanced fuel CANDU reactor, it was concluded in the review that the advanced fuel CANDU reactor is feasible technologically with good safety performance, while retaining the production capacity of tritium and cobalt, it also has good fuel flexibility; therefore, it is in line with the overall nuclear energy development strategy of China, with good prospects of development.

## **4 Position of PHWR in the Development of Closed Fuel Cycle in China**

With the joint efforts by TQNPC and relevant domestic and overseas research and development entities, large scale use of recovered uranium in PHWR will soon be realized, and it has become an extensive common view that PHWR can be used as a breakthrough in nuclear utilization of thorium resource. In conjunction with the advantages of PHWR in using recovered uranium and thorium resource and the status quo development of closed nuclear fuel cycle in China, research and plan have been made for the near, medium, and far term implementation strategy of closed nuclear fuel cycle in China and the possible role of PHWR.

### ***4.1 Proposal on Implementation Strategy for Closed Nuclear Fuel Cycle***

In the near term, efforts should be made to complete a closed nuclear fuel small cycle system with a pilot plant as the center, by taking into account the conditions of reprocessing industry, the research and development of using recovered uranium in PHWR and development status quo of fast reactor in China, to get through the

technical line. In the meantime, the research work on using thorium resource nuclear energy should be started.

In the medium term, a large closed nuclear fuel cycle system of commercial scale based on big reprocessing plant should be built. A big reprocessing plant of 200–800t/a and associated MOX fuel plant will be built, to supply fuel to demonstration fast reactor, and AFCR reactor matching with big reprocessing plant will be built, to realize the use of recovered uranium from the big reprocessing plant. According to a preliminary estimation, a 200t/a reprocessing plant can process spent fuel from 8 PWR's of 1000 MW class, recovering plutonium about 2t, sufficient for two fast breeder reactors, and recovering uranium about 190t, for use by three PHWR reactors.

In the far term, technological development for closed fuel cycle of fast reactor breeding cycle will be completed, to realize industrialized development of fast reactor breeding system, and gradually realize the transition from thermal reactor closed cycle to fast reactor closed cycle. The thorium–uranium cycle technology has basically become mature, and can be used as an effective supplementary and backup means too uranium–thorium cycle. In the meantime, the isotope tritium in PHWR can be used as nuclear fuel in the research and development and testing of fusion reactors.

#### ***4.2 Position of PHWR in Closed Nuclear Fuel Cycle***

The above-mentioned development strategy for closed nuclear fuel cycle has taken into full account the development orientation of closed nuclear fuel cycle in China and the existing condition of coexistence of PWR, PHWR and fast reactors, and is therefore feasible. PHWR reactor, with its good neutron economic performance, high fuel flexibility and ability to produce isotope in large scale, will play an important role in the nuclear energy and nuclear technology industrial development in China in near and medium terms, and a summary has been made as shown in Table 3.

### **5 Conclusions and Suggestions**

China has made clear the technical strategy of nuclear closed fuel cycle. The uranium and plutonium recovered in spent fuel reprocessing plant account, respectively, for about 94 and 1 %; today, the cycle system of PWR-FBR only takes into account the recycling of plutonium, but large amount of recovered uranium has not been effectively used. Using the recovered uranium from reprocessing plant as a nuclear energy resource to realize the closing of nuclear fuel cycle, it can

**Table 3** Role of PHWR in the development of nuclear energy and nuclear technology industry

Period	Position of PHWR
Near term (–2020)	Directly use recovered uranium, to raise the utilization rate of uranium resource and increase economic performance of reprocessing Carry out research on nuclear utilization of thorium resource as a test platform Produce cobalt isotope in large scale
Medium term (2020–2030)	Further use recovered uranium Realize nuclear energy use of thorium resource, and open up new source of nuclear fuel Carry out research on thorium–uranium cycle, to reduce pressure in the development of fast breeder reactors Produce cobalt isotope in large scale
Far term (2030–)	Generate power by using the recovered uranium accumulated in PWR operation Thorium–uranium cycle as the backup means of uranium–plutonium cycle Produce cobalt isotope in large scale Produce isotope tritium to provide nuclear fuel for the development of fusion reactors

substantially increase the utilization rate of uranium resource and economic performance of fuel cycle.

For years, China has done a lot of research work on the use of recovered uranium in existing PHWR units, the results show that PHWR is a realistic and effective way to use recovered uranium from reprocessing plant and the technology is feasible, the full core use of recovered uranium in the existing PHWR reactor can be realized in near term. To make full use of recovered uranium, PHWR should be developed to match the reprocessing capacity, and this will be effective in realizing the closed cycle of nuclear fuel. As the first step, to match with the 200t/a reprocessing plant in China, it can be considered at appropriate time to build two new PHWR units.

As China has rich thorium resource, and there are still some technical difficulties in the development of closed cycle of uranium–plutonium fuel, the research of nuclear utilization of thorium and thorium–uranium fuel cycle can be promoted by the research and development and application of thorium fuel PHWR, as a backup means for uranium–plutonium cycle, to ensure the mid-long term development of fission nuclear energy industry.

Given the advantages of PHWR in using recovered uranium and thorium resource, also, China and Canada have carried out much research and development work on using recovered uranium and thorium in PHWR, and have started the development of AFCR with intellectual property rights shared by them. The role of PHWR in the closed nuclear fuel cycle system of China should be taken into full account and scientific positioning be made, and the coordinated development of PWR, reprocessing, FBR and PHWR should be taken into account, to ensure the large scale and sustainable development of the nuclear power industry in China.

## References

1. China National Development and Reform Commission, Mid-Long Term Development Plan for State's Nuclear Power of China (2005–2020), 2007 June
2. Z. Meng, S. Fan, G. Qiao etc., “Application Report on Utilizing NUE Fuel in Third Qinshan Nuclear Power Plant”, Third Qinshan Nuclear Power Company, Haiyan, Zhejiang, China, 2013 December
3. D. Popov, C. Cottrell, M. Boubcher etc., “Technical and Commercial Summary Report of an Advanced Fuel Candu Reactor(AFRCR) in CHINA,” Candu Energy Inc., Mississauga, Ontario, Canada, 2014 October

# Shielding Calculation Model and Simplified Analysis of the Spent Fuel Pool

Yaoquan Zhou, Pinghui Zheng, Xiuge Ma, Puzhong Zhang and Lin Qiu

**Abstract** According to the storage mode of the spent fuel assemblies in the spent fuel pool and shielding calculation model of some nuclear power plant spent fuel pool, appropriate improvement and optimization can be made for the relevant shielding calculation model according to the detail conditions. Some simplified methods can be adopted based on the symmetry principle and equivalence principle. The calculation model and analysis method can provide reference for the shielding calculation and simplified analysis of other nuclear power plant spent fuel pool. Similarly, it can be applied in other cases that involve a large numbers of the same type and neatly arranged radiation storage sources, such as shielding calculation and analysis for solid radioactive waste storage facilities and repositories.

**Keywords** Nuclear power plant · Spent fuel pool · Shielding calculation model · Simplified analysis

## 1 Introduction

The radioactive source term of spent fuel assemblies is dominant in the source terms of reactor core, which is the main source term that decides the shielding thickness of reactor refueling cavity pool, spent fuel pool, and shipping cask. The spent fuel pool needs to store a large number of spent fuel assemblies in a long time period. The radioactivity of spent fuel assemblies is very high, especially when they are unloaded from the core after shutdown in a short time. Therefore, the shielding design of spent fuel pool is extremely important to ensure that the workers are protected under a low level of radiation exposure. The shielding calculation model of the spent fuel pool will have a direct influence on the accuracy of the calculation results, thus impact on the choice of shielding materials, thickness, and cost of building. It is vital to simplify the model and ensure the accuracy of calculation, due

---

Y. Zhou (✉) · P. Zheng · X. Ma · P. Zhang · L. Qiu  
China Nuclear Power Engineering Co., Ltd, Beijing, China  
e-mail: zhouyaoquan@sina.com

to the reason that the spent fuel pool stores many spent fuel assemblies, and every assembly is divided into upper structures, fissile part and lower structures with different material constitution and radioactivity in each part, and every part of the assembly has to be considered as an individual radioactive source term.

Based on the storage mode of the spent fuel assemblies in the spent fuel pool and shielding calculation model of some nuclear power plant, the shielding calculation model of spent fuel pool is improved and optimized, and some simplifying method for the calculation is analyzed. Also the weakness of the shielding building around the spent fuel pool is analyzed and some feasible measures are recommended.

## 2 Calculation Location

The calculation locations for the shielding design of spent fuel pool include: under pool bottom, behind side walls of the pool, behind strobes, above surface of the pool and the operating floor [1, 2]. A type of the spent fuel pool which stores spent fuel assemblies in two regions is illustrated in Fig. 1.

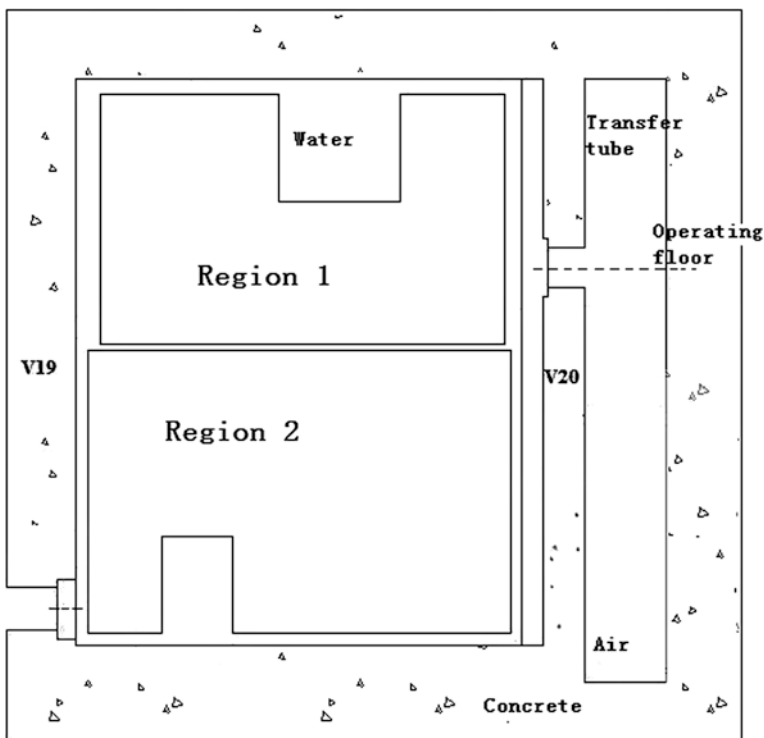


**Fig. 1** Top view of spent fuel pool storing spent fuel assemblies in different regions



### 2.1 Under Pool Bottom

In order to calculate dose rate of the room under pool bottom, contribution of 37 assemblies distributed symmetrically is considered and dose receiving point is right below the No. 1 assembly [2], which can be seen in Fig. 2.

If the model is based on 37 spent fuel assemblies, there will be 111 radioactive sources and the calculation model will be extremely complicated, and it is easy to make mistakes due to the tremendous computing work. According to the symmetry principle, only 13 spent fuel assemblies need to be considered in the model, as can be seen in Fig. 3.

However, there remain 39 radioactive sources to define the model based on 13 spent fuel assemblies, and the model is still complicated. From further analysis and investigation, we can see that according to the equivalent principle, only No. 5, No. 9, and No. 10 assemblies are essential as radioactive resources in the calculation. Set 5 dose points under No. 1–5 assemblies as A, B, C, D, E, and assume that the dose rate contributions to A, B, C, D, E of No. 5 assembly are 5A, 5B, 5C, 5D, 5E, No. 9 assembly are 9A, 9B, 9C, 9D, 9E, and No. 10 assembly are 10A, 10B, 10C, 10D, 10E, respectively. The contribution to dose point A of No. 1 assembly is the same as the contribution to E of No. 5 assembly (5E). Similarly, the contributions to dose point A of No. 2–10 assemblies are the same as 5B, 9C, 10B, 5A, 5D, 10A, 5D, 9A, 10A. The calculation model will be greatly simplified and the improvement will shorten the input data and computing time, and will decrease the possibility of making mistakes. The final dose rate calculation result is equal to the contribution of No. 1 assembly plus four times the contributions of No. 2–10 assemblies:

$$5E + 4(5B + 9C + 10B + 5A + 5D + 10A + 5D + 9A + 10A)$$

Fig. 2 Calculation model under pool bottom

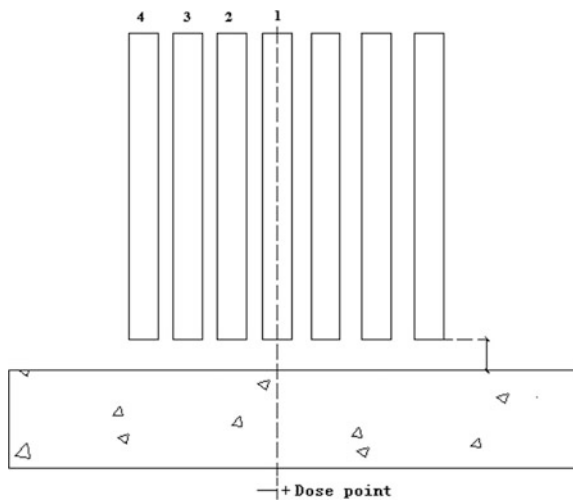


**Fig. 3** Simplified calculation model under pool bottom

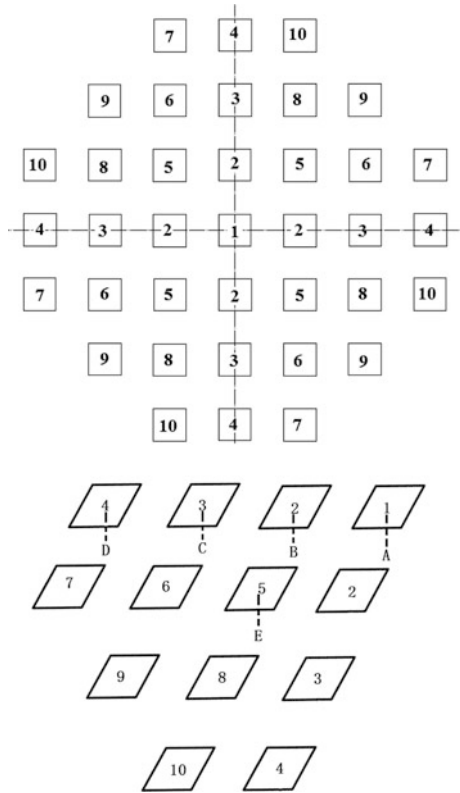


**Table 1** The contributions of No. 1–10 assemblies to the dose points under pool bottom

Assembly No.	1	2	3	4	5
Dose rate (mSv/h)	7.57E-05	7.30E-05	6.60E-05	5.08E-05	7.03E-05
Contribution (%)	12.23	11.80	10.67	8.21	11.37
Contribution to total dose rate (%)	3.37	3.25	2.94	2.26	3.13
Assembly No.	6	7	8	9	10
Dose rate (mSv/h)	6.37E-05	4.92E-05	6.37E-05	5.74E-05	4.92E-05
Contribution (%)	10.29	7.94	10.29	9.27	7.94
Contribution to total dose rate (%)	2.83	2.19	2.83	2.55	2.19

The contributions of No. 1–10 assemblies to the dose points are listed in Table 1, taking AFA-3G assemblies cooled 4 days after shutdown under 18-month refueling cycle condition of some reactor as an example.

## 2.2 Behind Side Walls and Strobes

Dose rate contribution of 22 spent fuel assemblies is considered when calculating dose rates of room behind side walls of the pool. As can be seen in the calculation model in Fig. 4, the dose rate contribution of assemblies outside No. 16 assembly is negligible, and the 22 assemblies are placed in two rows with 11 assemblies in each row.

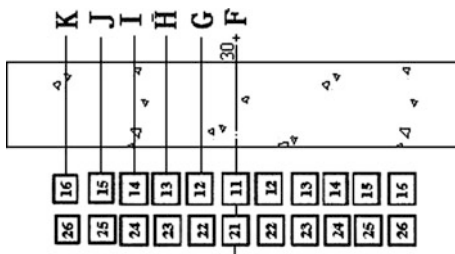
If the model is based on 22 spent fuel assemblies, there will be 66 radioactive sources and the calculation model will be complicated. From further analysis, we can see that according to the symmetry principle, only No. 11 and No. 21 assemblies are essential as radioactive resources in the calculation. Set 6 dose points of No. 11–16 assemblies behind side walls as F, G, H, I, J, K. The dose points are located at the center plane of the spent fuel fissile part. The contribution to dose point F of No. 12 assembly is the same as the contribution to G of No. 11 assembly. Similarly, the contributions of No. 13–16 assemblies are the same as contribution to dose points H, I, J, K of No. 11 assembly.

Assume that the dose rates of No. 11 assembly to dose points F, G, H, I, J, K are 11F, 11G, 11H, 11I, 11J, 11K, and the dose rates of No. 21 assembly to dose points F, G, H, I, J, K are 21F, 21G, 21H, 21I, 21J, 21K. The final dose rate result is the contribution of No. 11 and No. 21 to dose point F plus the 2 times the contribution of No. 11 and No. 21 to dose points G, H, I, J, K:

$$11F + 21F + 2(11G + 11H + 11I + 11J + 11K + 21G + 21H + 21I + 21J + 21K)$$

There are two strobes between the spent fuel pool and fuel transfer tube, spent fuel pool and cask loading pits, respectively, on the upper part of the concrete wall. The strobes will not open until the reactor needs to load and unload the fuel or transfer the fuel. When the strobes are open, two sides of the gate will be connected and the assemblies are transferred through the strobes under water. When the reactor is under normal operation conditions, the strobes are closed and there is no water behind the gate, namely there is no water in the transfer tube or cask loading pits. The strobes are made of thin stainless steel and its shielding ability is negligible, so the shielding design of the strobes is a weakness and the dose rate behind the strobes needs to be calculated.

Fig. 4 Calculation model behind side walls of the pool



The method and model of calculating dose rate behind the strobes is similar to the calculating behind side walls. Because of the shielding ability of the thin strobes is weaker than the thick concrete walls, contribution of more rows of assemblies should be taken into consideration based on the analysis. An improved assemblies' arrangement is illustrated in Fig. 5. As shown in Fig. 5, there are two more rows with 9 assemblies in row 3 and 7 assemblies in row 4, considering that the contribution of assemblies far away in the oblique direction is negligible and the model is not too complicated to lead to an accurate result.

In cautious consideration, several dose points are set at different heights to calculate the dose rate distribution of the location. The contributions of assemblies to the dose points are listed in Table 2, taking AFA-3G assemblies cooled 4 days after shutdown under 18-month refueling cycle condition of some reactor as an example.

As the strobes are usually made of 8 mm thickness stainless steel, the shielding ability lessened greatly. In order to avoid the high radiation to the maintenance personnel behind the strobes, two measures can be taken to reduce the dose rate:

- (1) Store spent fuel assemblies with long cooling time and low radioactivity in front of the strobes.

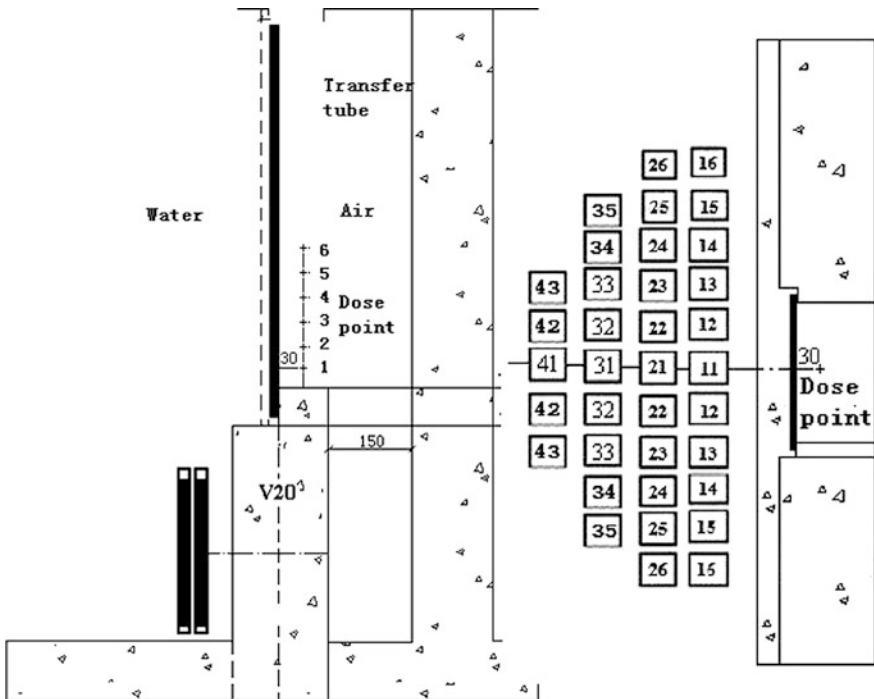


Fig. 5 Dose points behind strobes

**Table 2** The contributions of each assemblies to the dose points behind the strobes

Assembly No.	11	12	13	14	15	16
Dose rate contribution (%)	7.20	6.98	5.45	3.48	1.90	0.9
Assembly No.	21	22	23	24	25	26
Dose rate contribution (%)	9.20	9.78	7.84	5.25	3.04	1.55
Assembly No.	31	32	33	34	35	
Dose rate contribution (%)	5.82	6.37	5.15	3.55	2.14	
Assembly No.	41	42	43	44		
Dose rate contribution (%)	2.88	3.31	2.78	2.08		

- (2) Vacate several shelves near the strobes and do not store spent fuel assemblies with radioactivity.

If the dose rates behind the side walls are rather high, the same measures mentioned above can be taken to reduce the dose rates.

### 2.3 Above Surface of the Water and the Operating Platform

Single spent fuel assembly in processing of transferring or operating is considered when calculating dose rate above the surface of the water. The operator may come near the surface of the water and spent fuel assembly on the crane, so it is necessary to ensure that the operator is under a low level of radiation exposure. The relevant dose points are illustrated in Fig. 6.

In order to research the dose rate distribution above the surface of the water, several dose points were located at different distances deviation from the assembly axes. The results of the calculation show that the dose rate distribution is affected by the shape of the radiation source and shielding water thickness. The dose rates above the surface of the water in relating to deviation from the assembly axes with 262 cm thickness water are shown in Fig. 7.

According to Fig. 6, the maximum shielding water thickness above the spent fuel assemblies is limited by the height of floor under the strobes. In order to make the dose rate above the surface of the water satisfy the requirements, the water thickness could be increased if the height of the pool bottom cannot change.

There is no water when the assembly is not transferred. When the worker is operating the spent fuel assemblies on the operating platform, the assembly should not be too closed to the strobes to ensure that the worker is under a low level of radiation exposure.

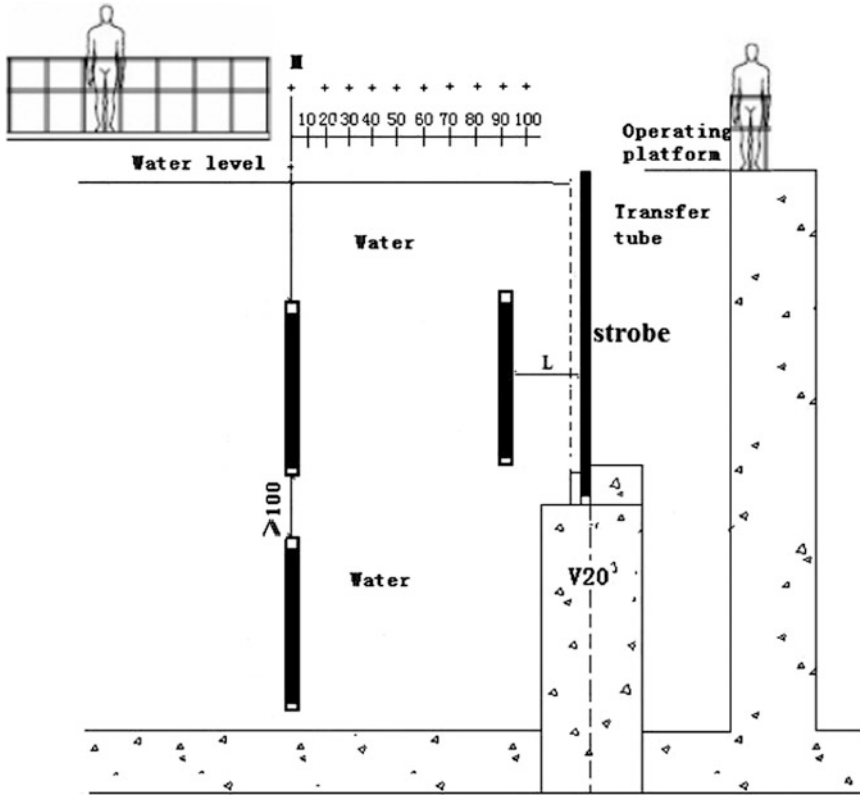


Fig. 6 Dose points above the surface of the water and the operating floor

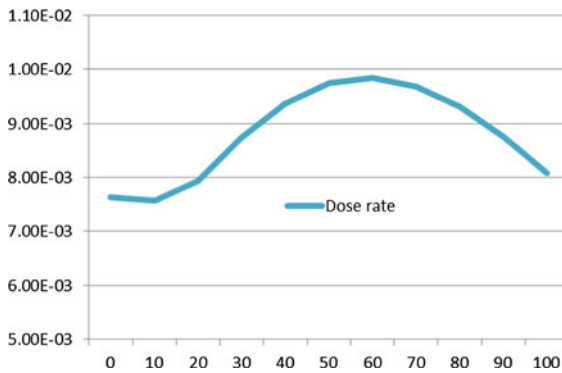


Fig. 7 Dose rates deviation from the assembly axes above the surface of the water

### 3 Conclusions

Based on the analysis of shielding calculation for the spent fuel pool bottom, side walls, strobes, water surface, and operating floor of some nuclear power plant, the model of spent fuel pool is improved and optimized at some locations. At the same time, some simplifying method for the calculation is adopted according to the symmetry and equivalent principle, so that the model is greatly simplified and the improvement decreases the input data and computing time, and reduces the possibility of making mistakes. The calculation model, simplified method, and optimization analysis will be applicable to other spent fuel pools, as well as shielding calculation model of a large number of regularly arranged radioactive sources, e.g., regularly arranged solid radioactive waste drums.

Relatively, the shielding ability of the strobes is weakness. In order to avoid the high radiation irradiating to the maintenance personnel behind the strobes, two measures can be taken to reduce the dose rate in this zone: either store spent fuel assemblies with long cooling time and low radioactivity in front of the strobes, or vacate several shelves near the strobes and do not store spent fuel assemblies with radioactivity.

The maximum shielding water thickness on the spent fuel assemblies is limited by the height of floor under the strobes. In order to decrease the dose rate above the surface of the water, the water thickness could be increased to satisfy the requirements in some cases. There is no water when the assembly is not transferred, in order to ensure that the worker is under a low level of radiation exposure, the assembly should not be too closed to the strobes when the worker is operating the spent fuel assemblies on the operating platform.

### References

1. Beijing Institute of Nuclear Engineering, 2007, Nuclear island shielding design report of Qinshan Nuclear Power Phase II expansion project
2. Ling Ao nuclear power station units 1&2, 2000, Radiation shielding design report calculations in fuel building and around transfer tube

# PBNC—2016 Technology Evolutions in MOX Fuel Reprocessing Plants

Christopher Dane

**Abstract** A backlog of approximately 23,500 tons of used nuclear fuel will be waiting for reprocessing in 2030 in China. France has a long history with fuel recycling with the first plant commissioned in La Hague in 1966 and later with its Melox plant that started MOX fuel production in 1995 in an industrial scale. With a huge growth in nuclear Energy in and the willing to achieve self-sufficiency of most aspects of the fuel cycle, China expects to reprocess fuel and have its first 800 tons/year commercial reprocessing plant ready by 2030. How will the evolution of technology and standards of the last two decades make China's reprocessing plant more competitive? Is the supply chain expertise used for the past plants up to date and ready to face this challenge? Parts of the process are the intellectual property of the supply chain like ROBATEL which designed and fabricated essential components of the plants of la Hague and Melox. Like for instance the decanter centrifuge systems or the centrifugal extractors, and to the capacity question, the answer is yes.

**Keywords** ■■■

## 1 Introduction

The first fuel treatment plant was built in La Hague and commissioned in 1966 originally for military purposes, it rapidly moved to civil use after 1969. Later in the 70s after the first oil shock, Government decided to invest massively in the nuclear energy with the intent to reprocess spent fuel; leading to the high level of nuclear energy (58 reactors producing about 78 % of the French electricity) in the French electricity mix we have today, and the most developed spent fuel reprocessing program in the world so far.

---

C. Dane (✉)

Business Development, ROBATEL Industries, 12 Rue de Genève,  
69741 Genas Cedex, France  
e-mail: jianghong@cnpe.cc



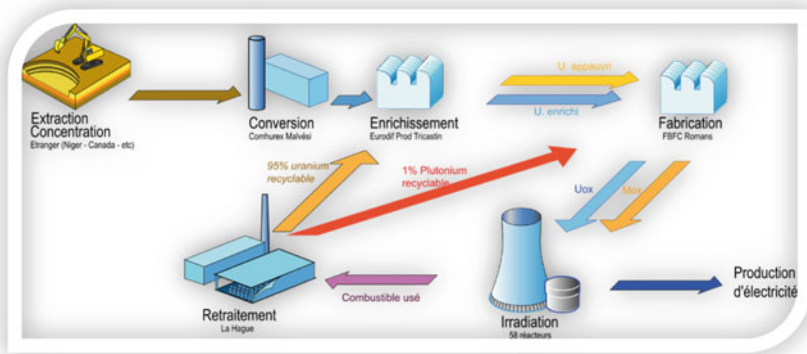


**Fig. 1** Nuclear fuel cycle in France

The French nuclear fuel recycling activities take place in three different locations being La Hague plant on one hand for reprocessing and the plants of Marcoule and Pierrelatte, respectively for the fabrication of the MOX fuel and for the enrichment of uranium oxide.

So far the plants have treated 50,000 tons of spent fuel, mainly UNGG and UOX. The spent fuel treatment is set at around 1050 tons/year in La Hague.

The production of MOX fuel is in the order of 120 tons per year, saving about 900t of natural uranium annually (out of a consumption of 8400t annually) and serving 22 reactors out of 58 (Fig. 1).

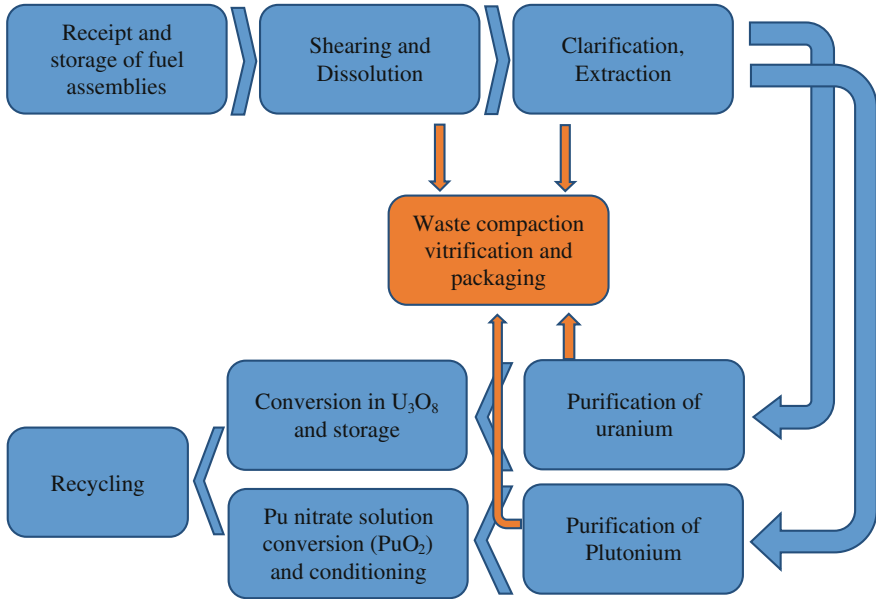
With a program of over 200 future operating reactors, China will be the world's largest nuclear energy producer and will potentially hold a third of the world's power plant units, also bringing the reprocessing needs to another scale.

## 2 Overview of the Current Separation Process

After about 4 years in a reactor, the spent fuel still holds 96 % of recyclable fuel: 95 % of uranium, 1 % of plutonium, and 4 % of fissions products and actinides.

The current spent fuel treatment process is the PUREX, extracting the plutonium and the uranium from the spent fuel and separating these recyclable/valuable components from the fission products and minor actinides.

The treatment is performed in many steps. From cutting of the fuel assemblies to the conditioning of the recycled uranium and plutonium.



First, the spent fuel assemblies are sheared into small sections, separated from their ends. The pieces of the pins containing the fuel are collected and transferred to a dissolution unit separating the cladding from the irradiated fuel.

The cladding and other irradiated metals are collected in the compacting workshop, compressed for volume reduction and packaged as radioactive wastes (Fig. 2).

The dissolution units were initially discontinuous type dissolvers as for instance at the ATI workshop or at the UP2-400 plant. This technology has limited capacity and was replaced by the continuous type rotating wheel dissolver that are implemented in the UP2-800 and UP3 plants in La Hague (Fig. 3).

After this first recovering phase, the dissolved irradiated fuel is clarified and purified. The first extraction cycle mainly prevents later equipment in the process from plugging. In this several techniques were implemented starting with the sand filtration in the UP1 plant, and a pulsed filter at ATI and APM. This technique had limited efficiency due to filter reliability and maintenance requirements. The UP2-400 plant used one ROBATEL DPC-800 centrifuge and the latest UP3 and UP2-800 plants are equipped with specific four centrifuges ROBATEL DPC-900.

*Note:* Other Nuclear facilities using ROBATEL centrifuges: Marcoule (1 × DPC-900), Rokkasho-Mura (2 × DPC-900), Thorp (1 × DPC-800) (Fig. 4).

In UP3 and UP32-800, once clarified, uranium and plutonium are extracted, partitioned and purified using annular pulsed columns and/or mixer-settler cascades. The last plutonium purification cycle is performed by a centrifugal extractor. These three liquid–liquid extraction technologies have each their advantages and



**Fig. 2** Fuel assembly cutting unit and compacting unit—La Hague

drawbacks in efficiency, dimensions, ability to deal with solids, solvent residence time...

The latest technology, the centrifugal extractor was developed by ROBATEL, for the purification of plutonium. This technology has the advantage to be very compact, the residence time is limited to a few seconds, resulting in a significant reduction of solvent radiolysis, a much reduced material inventory and a very fast achievement of chemical equilibrium (Fig. 5).

The final stage is the conversion of the Uranium and the Plutonium in  $\text{PuO}_2$  and  $\text{U}_3\text{O}_8$ , their conditioning and interim storage prior to being used in recycled fuel assemblies.

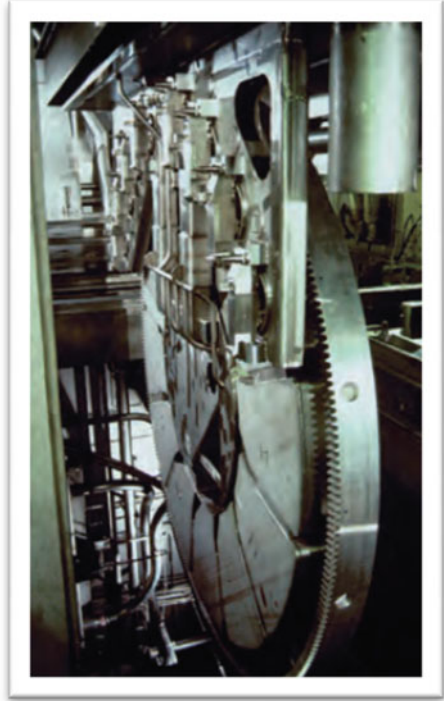
The uranium can be used for the fabrication of fresh fuel pellets where the Plutonium is sent to the Melox plant in Marcoule for the fabrication of MOX fuel.

The Chinese reprocessing plants will have the choice between several proven technologies that have been developed for many years and that are now up and running efficiently and very reliable.

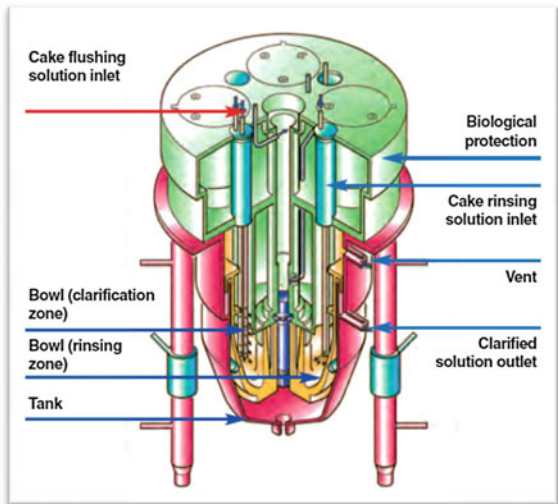
### **3 Overview of the Recycled Fuel Fabrication Process**

The MOX fuel is a mix of depleted uranium oxide and plutonium oxide. Typical MOX fuel contains 8.65 % of plutonium.

**Fig. 3** Rotating-wheel dissolvers used in the UP3 and UP2-800 plant, at La Hague



**Fig. 4** Schematic of the ROBATEL DPC-900 centrifuge



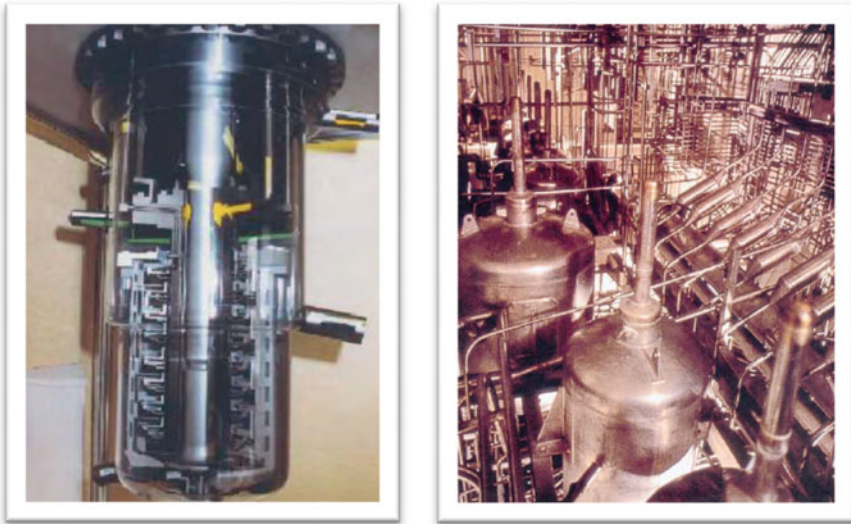


Fig. 5 ROBATEL centrifuge extractor (left) and La Hague plant pulsed column heads (right)

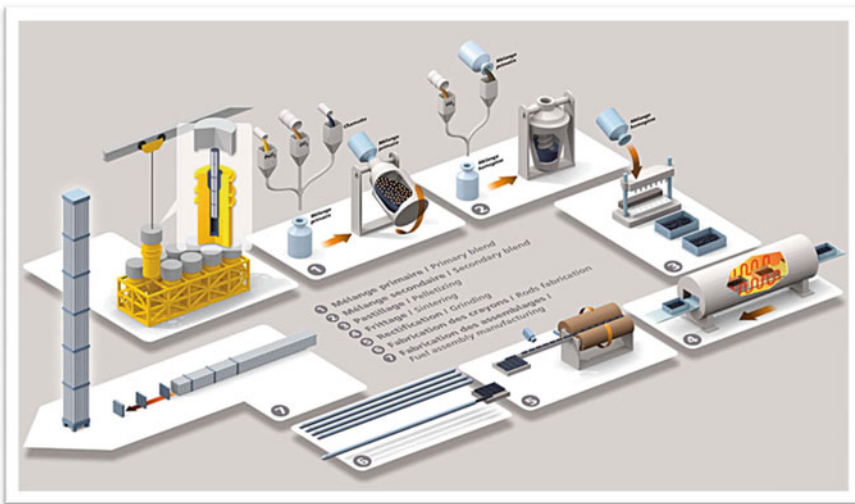


Fig. 6 MOX fuel fabrication process at AREVA plant in Marcoule (image from website [AREVA.com](http://www.aveva.com))

Use of MOX fuel started in 1987 in France. Since then, over 3000 MOX fuel assemblies were loaded into nuclear reactors corresponding to the recycling of around 80 tons of plutonium and a saving of over 8000 tons of natural uranium (Fig. 6).

The fabrication process implemented in France is called the MIMAS (“micronized masterblend”).

The MOX fuel fabrication is close to the fresh uranium oxide UOX fuel in principle. It takes place in 7 main steps:

1. The production of the primary mix, in which the plutonium content is around 30 %. This mix is composed of depleted uranium oxide, plutonium oxide, and crushed MOX pellets that have been rejected.
2. The production of the secondary mix: uranium oxide is added to the primary mix to achieve the requested plutonium content, depending on the reactor’s needs; between 5 and 12.5 %.
3. The pellet fabrication: after a homogenization step, the powder is transferred in a press where it is compacted in the form of pellets.
4. The sintering: the pellets are then cooked in an oven to a temperature achieving 1700 °C.
5. The Grinding: in order to obtain the requested diameter to fit in the fuel pins, the pellets are grinded. The pellets that do not meet the requirements are rejected and sent back to step 1 to be reused in the process.
6. The insertion in the pins: the pellets are loaded inside the pin cladding to constitute the MOX fuel pins.
7. The assembling: the pins are installed in their dedicated structures to form the MOX fuel assemblies.

Each of these steps enclose numbers of quality checks to verify the chemistry, isotopic content, the structure, the geometry, density, etc.

Excepted for the last step where the fuel is contained in the pins, all the steps of the process is performed inside gloveboxes, these gloveboxes are designed and built around the processes involved in the MOX fabrication.

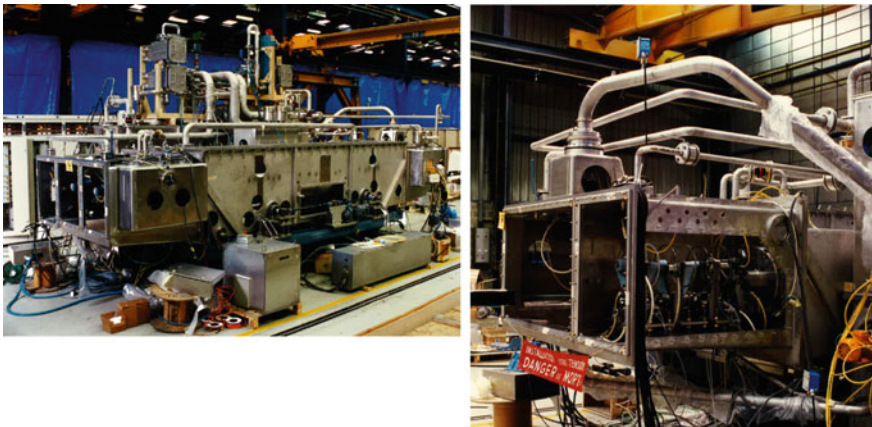


**Fig. 7** MOX fuel pin decontamination Glovebox being assembled prior to commissioning

At several stages of the MOX fabrication process, Robatel, and others from the French supply chain have highly contributed to this project.

ROBATEL has fabricated for instance the filter pre-clogging glovebox and its process, the fuel pin decontamination glovebox, among others is also one of ROBATEL' realization (Fig. 7).

## 4 Conclusion

The spent fuel treatment plants and the MOX fuel fabrication plant have evolved during the years to optimize their capacity, making the processes cleaner and safer. Taking the opportunity to use special processes like centrifugal technologies from ROBATEL that were offered by the supply chain.

The French nuclear industry has always been supported by successive French governments. This commitment to nuclear energy allowed the industry to build a strong sector that is internationally recognized for its technology, quality, safety, and research and development. The nuclear industry directly employs over 125,000 people in around 2500 companies, of any size.

China's nuclear development is unprecedented. It is a challenge for the world nuclear industry, opening new opportunities to develop even more efficient processes using the latest technologies. The reprocessing plants foreseen in China will drastically increase the fuel recycling capacity, potentially setting new standards in fuel cycles locally but also internationally.

## References

1. Treatment and recycling of spent nuclear fuel—Actinide partitioning—Application to waste management—CEA
2. The Nuclear fuel cycle «Le cycle du combustible nucléaire»—CEA (Marcoule)

# The First AP1000 Fuel Fabrication Line in China

Shuangqing Shi and Zhigang Wang

**Abstract** The purpose of this paper is to present a description about the first AP1000 fuel fabrication line in Baotou, China. Owned by China Baotou Nuclear Fuel Corporation (CBNF), the facility construction was started in March, 2012. A capacity of 400 TU/year of fabrication from IFBA pellet fabrication through final fuel assembly, as well as manufacturing of core components, have been designed in the project, space for another 400 TU/year has been reserved. Manufacturing process development has been performed, manufacturing of key process equipments have been studied and localized. Since the completion of the civil work and equipment installation, the project has come into the qualification stage, and the entire line is scheduled to be qualified in 2016 by manufacturing of four fuel assemblies. Under the AP1000 Technology Transfer Contract, Westinghouse has been involved in depth in the project and playing an important role during the plant design stage and the process qualification stage. The first reload fuel fabrication is expected to be scheduled in 2017.

**Keywords** AP1000 · Fuel · Fabrication line · CBNF

## 1 Project Background

China Baotou Nuclear Fuel Corporation (Hereinafter referred to as CBNF) was founded in 2008, with RMB 600 million of registered capital. 50 % of the shares are owned by China North Nuclear Fuel Corporation (Hereinafter referred to as CNNFC), 35 % are owned by State Nuclear Power Technology Corporation (Hereinafter referred to as SNPTC) and 15 % are owned by China Jianzhong Nuclear Fuel Corporation.

CBNF has been designated by SNPTC as the Nominated User to receive and use the AP1000 fuel fabrication technology under the contract frame between SNPTC

---

S. Shi (✉) · Z. Wang  
China Baotou Nuclear Fuel Co.,Ltd, Baotou, China  
e-mail: shishuangqing@cbnf-ap1000.com



and Westinghouse for AP1000 nuclear technology transfer. CBNF is now in the process of establishing an AP1000 fuel fabrication line, and it will be fabricating and supplying AP1000 fuel for AP1000 nuclear power plants in China.

## 2 Project Description

Taking the advantage of the CNNFC existing resource, such as land area, chemical conversion and pelletizing technology, auxiliary power supply and machining technology, the AP1000 fuel fabrication line at CBNF starts from IFBA pellet coating through the final fuel assembly, as well as the associated core components fabrication. The fuel fabrication covers the processes of IFBA pellet coating, fuel rod fabrication, Inconel/Zirlo grid manufacturing, skeleton manufacturing, nozzle assembly, final fuel assembly, and packing. The associated core components fabrication includes manufacturing processes for black control rod assembly, gray control rod assembly, wet annular burnable absorber assembly, neutron source assembly, and thimble plug assembly. Related inspection systems are also equipped for manufacture of fuel assembly and associated core components. Although the facility constructed has a space for fabrication capacity of 800 TU/year, the fabrication line is equipped for a capacity of 400 TU/year for the first phase.

CNNFC will be responsible for the chemical conversion, pelletizing and manufacturing of most of the components, such as strap punching, nozzle casting, and small components, as well as the related inspection for its fabrication.

## 3 Project Status

### 3.1 Project Approval

- AP1000 fuel fabrication line project initiating report was approved by State Administration of Science, Technology and Industry for National Defence, PRC (SASTIND) on Jan. 25th, 2011.
- Sub-License agreement between SNPTC and CBNF was signed on Mar. 11th, 2011. CBNF became the nominated user for AP1000 fuel manufacturing.
- AP1000 fuel fabrication line project feasibility study report was approved by SASTIND on Dec. 8th, 2011.
- Preliminary safety analysis report and environmental impact report for AP1000 fuel fabrication line project passed the review of NNSA.
- AP1000 fuel fabrication line project construction permit was obtained from National Nuclear Safety Administration (NNSA) on Mar. 26th, 2012.
- Nuclear material permit for CBNF was issued by SASTIND on Apr. 21st, 2014.

### 3.2 Project Progress

#### 3.2.1 Construction and Installation

- The construction started from Mar. 28th, 2012, and was capped by the end of 2012.
- Equipment installation started from Apr. 15th, 2013, and ended in Apr. 2014.
- Auxiliary system testing started from Jul. 2013, and ended in Oct. 2013.
- Qualification phase started from Jul. 2014 up to date.

### 3.3 Qualification

To ensure product quality, the equipment, process and software affecting quality shall be qualified before formal production starts. The qualification was planned based on the following principles:

- Equipment and its programmable logic controller (PLC) shall be qualified before process qualification to ensure that they meet the process need.
- Laboratory shall be qualified before process development in order to provide inspection data to support process development and process qualification.
- Process development shall be made before process qualification to find out the parameter range to meet the product requirement.
- Individual process shall be qualified to make acceptable product.
- The entire fabrication line was divided into 11 process lines with several individual processes in each.
- Each process line shall be qualified to reduce the risk of production qualification.
- The entire fabrication line shall be qualified to demonstrate that it will be running and all supporting systems will be working as expected.

Based on such qualification principles, the qualification sequence was determined as Fig. 1:

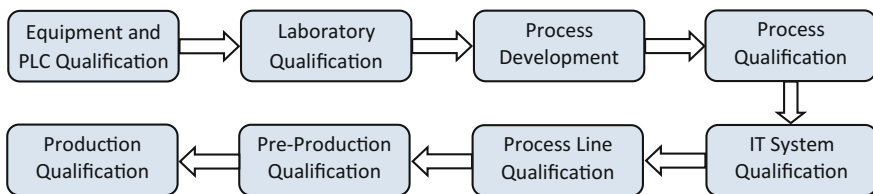


Fig. 1 Qualification plan

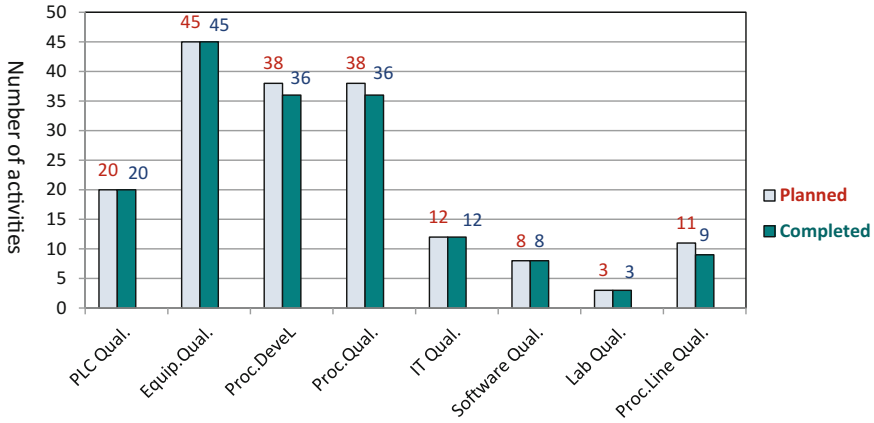


Fig. 2 Qualification progress status

The qualification progress status is shown in Fig. 1. It is expected that all qualification effort will be completed by mid of 2016, and the production line will be ready for fuel fabrication by the end of 2016 (Fig. 2).

## 4 Technology Transfer

Under the frame of the Technology Transfer Contract by SNPTC/Westinghouse, and the Sub-License Agreement by SNPTC/CBNF, as the Nominated User, CBNF has been working with SNPTC and Westinghouse for the AP1000 fuel fabrication technology transfer. The current target for this technology transfer is to enable CBNF to manufacture and supply AP1000 fuel assemblies for the first 2 reloads of the Chinese-based AP1000 Nuclear Power Plants.

The technology transfer is executed through four major channels:

- Technical Documentation
- Technical Service–Training Program
- Technical Service–Consultation
- Living License.

### 4.1 Technical Documentation

Westinghouse has delivered a data pack for AP1000 fuel fabrication. The delivery scope covers product drawing, product specification, material specification, process specification, inspection specification, manufacturing and quality plan, operating

procedure, inspection procedure, maintenance procedure, and quality program documents as well.

## ***4.2 Technical Service—Training Program***

A total of 174 man/month training was defined in the contract. The training includes UO<sub>2</sub> powder fabrication, UO<sub>2</sub> pelletizing, fuel component manufacturing, nonfuel bearing core component manufacturing, fuel rod manufacturing, final fuel assembly, quality control and laboratory testing, plant management system, quality assurance, and supply chain management.

Up to date, 166 of the 174 man/month training have been performed in Westinghouse Columbia Fuel Fabrication Facility. The remaining 8 man/month flexible training will be performed at a later date.

## ***4.3 Technical Service—Consultation***

Base on the contract, Westinghouse will provide 108 man/month China-based consultation, and 58 man/month US-based support for the areas of plant design, data pack consulting, qualification, quality system, supply chain development, first 2 reload fuel manufacturing.

Under such a consultation and support frame, Westinghouse has been involved in this project since the very beginning of the project.

- The Plant Design has incorporated valuable suggestions by Westinghouse to establish a more scientific and reasonable process flow.
- Each qualification plan has been reviewed by Westinghouse before the execution.
- Qualification activities have been witnessed by Westinghouse.
- Each qualification report has been reviewed by Westinghouse before the approval of qualification.

The normal production will be started after the production qualification. Based on the Technology Transfer Contract, Westinghouse will provide surveillance and then certification for each of the first reload fuel assembly product.

# **5 Management System**

## ***5.1 Environmental Management System***

An environmental management system has been established at CBNF. This system has been audited and certified to be in conformity with ISO 14001:2004 Standard on Dec. 08, 2015.

## **5.2 Occupational Health and Safety Management System**

CBNF has established an occupational health and safety management system. This system has been audited by Westinghouse. On Dec. 08, 2015, the occupational health and safety management system was certified to be in conformity with OHSAS 18001:2007 Standard.

## **5.3 Quality Management System**

The quality management system has been established based on HAF 003 and ISO 9001:2008 Standard. This system has also incorporated the requirements of Westinghouse quality management system. The quality management system has been certified to be in conformity with ISO 9001:2008 Standard on July 7, 2015.

Under the technology transfer frame, Westinghouse has performed a program audit in 2014 and an implementation audit in 2015 to CBNF's quality management system. The final effectiveness audit by Westinghouse will be performed during the final production qualification stage before this AP1000 fuel fabrication line is certified by Westinghouse.

# **6 Development of Key Technology and Equipment**

Aiming to establish a world-class AP1000 fuel plant with high degree of automation, a systematic study combining with comprehensive scientific research and process test on the AP1000 fuel fabrication technology was performed, multiple key technologies have been mastered, and some of the related key equipments have been developed.

- **IFBA Coating Technology and Equipment**

IFBA pellet preparation is one of the most key technologies for AP1000 fuel. Some of the AP1000 pellets need to be coated with a layer of  $ZrB_2$  as the Integral Fuel Burnable Absorber (IFBA) for the control of reactivity in reactor. A direct current magnetron sputtering method is being used for this process. A high vacuum multi-targets magnetron sputtering coater has been successfully developed in China and the test shows that the coat on the pellet meet the product requirement.

- **Nozzle Precision Casting Technology**

AP1000 fuel Nozzles are designed to be manufactured by casing plus machining, such that natural chambers are created to reduce the pressure drop, debris risk is minimized and less material is used.

The mechanisms for alloy melt flow and defect creation were studied, the pouring system configuration design and process parameters were optimized. Multiple rounds of tests were performed to verify the feasibility of the process. At the same time, study on the cast machining and nozzle inspection was also performed. Finally, sample products for top and bottom nozzles were produced.

**• Grid Welding Technology and Equipment**

The first localized grid laser welder has been successfully developed. For laser welded grid, the effect of welding frequency, power and pulse number on the welding quality were studied, and the laser welding process and inspection method for AP1000 grid were established. For brazed grid, the effect of brazing temperature, vacuum, brazing paste viscosity, and paste amount on the brazing quality were studied, and the brazing process for AP1000 fuel end grid was developed.

**• Skeleton Bulging Technology and Equipment**

After a systematic study to the skeleton bulging process and equipment, using the Westinghouse equipment as a reference, based on the skeleton product specification, the first localized AP1000 fuel skeleton bulging equipment was developed. Bulging parameters were worked out to created correct bulging position and strength to meet the product requirement. The bulging process is now qualified.

**• Digitalized Information Technology System**

The requirement survey and design for the Enterprise Resource Planning System, Manufacturing Execution System and Laboratory Information

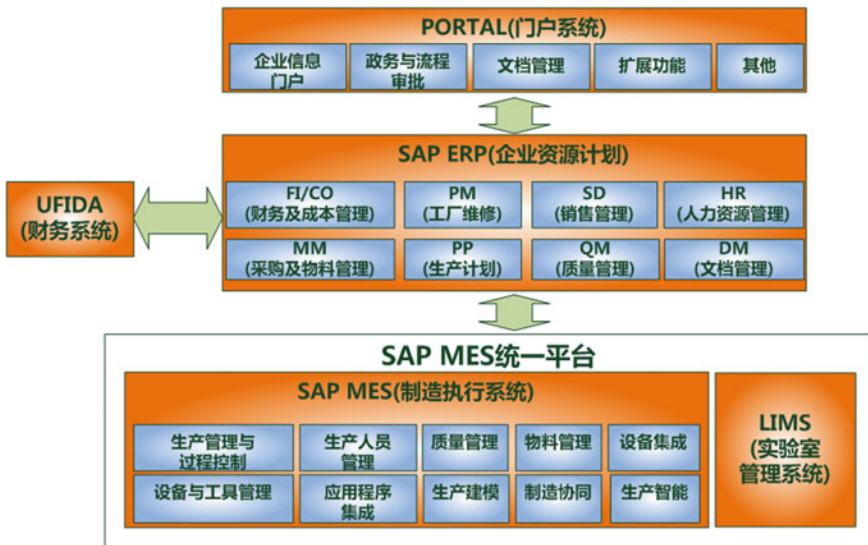


Fig. 3 Information system

Management System were completed, the systems have been developed. The systems enable the AP1000 production line to have a integrated data process and automation control, including process control, test and inspection management, quality management, item control, and traceability (Fig. 3).

## 7 Closings

There are many unique designs for AP1000 fuel assembly, which are resulting in unique manufacturing processes. Some of the designs lead to some relatively simple processes for manufacturing, for example, skeleton bulging, however, some of other designs lead to complicated process for manufacturing, IFBA coating is an example, and oxide coating is another one. Generally speaking, compared with other similar nuclear fuel design, AP1000 fuel manufacture needs more complicated processes, more difficult process control, and more multiple qualifications. But AP1000 will also bring much more significant economic benefit to the Nuclear Power Plants.

# The Important Aspects on the Protection of Occupational Exposure of the Spent Nuclear Fuel Reprocessing Facility

You Wei, Long Lin, Tian Yingnan, Mi Aijun and Gao Guiling

**Abstract** Taking the importance of protection of occupational exposure in the spent nuclear fuel (SNF) reprocessing facility into account, based on the international and domestic key technologies of design and construction and commercial operation experiences this paper preliminarily concluded several important aspects on radiation protection design including significant system and pipeline layout, radiation shielding calculation and analysis, radiation monitoring design, and so on. Some suggestions to the protection of occupational exposure of SNF reprocessing facility are made as well.

**Keywords** Radiation shielding · Radiation monitoring · Criticality accident · Reprocessing facility

## 1 Introduction

Over the years clean and economical nuclear power has evolved as viable alternative to conventional routes of energy production, and has been widely developed all over the world. In order to ensure the sustainability of nuclear energy, it is necessary to establish a complete matching system of nuclear fuel cycle.

For long-term nuclear power production, there are two fuel cycle options that are of relevance and under consideration, namely the once through cycle with permanent disposal of spent fuel and the closed fuel cycle with reprocessing and recycle of uranium and plutonium. France, Britain, Russia, India, and Japan and other countries adopt the mode of nuclear fuel closed cycle, China also adopt the mode, and has enter in the field of reprocessing of spent fuel arising from power reactor by way of design, erection, and commissioning of a reprocessing plant at LanZhou. Table 1 shows the reprocessing plants operating and planned in different nations.

---

Y. Wei (✉) · L. Lin · T. Yingnan · M. Aijun · G. Guiling  
Radiation Safety Design, CNPE, Beijing, China  
e-mail: youwei@cnpe.cc



**Table 1** Reprocessing plants operating and planned in different nations

Country	Location	Scale	Rated Capacity (Metric tons/yr)	Remark
China	Lanzhou	Pilot plant	–	Hot test at 2010
France	1. La Hague UP2-800	Commercial	850	
	2. La Hague UP3	Commercial	850	
India	1. Kalpakkam Reprocessing Plant (KARP)	Demonstration	100	
	2. Lead Minnicell Facility (LMF)	Pilot plant	n/a	
	3. Power Reactor Fuel Reprocessing Plant (PREFRE)	Demonstration	100	
	4. Fast Reactor Fuel Reprocessing Plant*	Commercial	n/a	
Japan	1. Rokkasho Reprocessing Plant	Commercial	800	
	2. JNC Tokai Reprocessing Plant	Demonstration	210	
Russia	1. Research Institute of Atomic Reactors (RIAR)	Pilot plant	1	
	2. RT-1, Combined Mayak	Commercial	400	
U.K.	1. BNFL B205	Commercial	1500	
	2. BNFL THORP	Commercial	1200	

Radiation protection of occupational exposure is always an important consideration at nuclear fuel cycle facilities, special attention should be paid to ensure operation safety of system and worker safety in the operational process [1]. Not only the external exposures, but also the potential internal exposures caused by releases of radioactive material should be carefully controlled to adhere to the operational dose limits. Based upon the content above, this paper concluded several important aspects on protection of occupational exposure including radiation source, significant system and pipeline layout, radiation shielding calculation and analysis, and radiation monitoring design [2, 3].

## 2 Safety Criteria

The radiological exposure of the workers is estimated considering the different operational situations in accordance with the safety criteria. Safety criteria are the objectives for the maximum exposure of the workers during the different operational situations. For the workers, GB18871-2002 recommends the following objective in normal operation: 20 mSv on average during a period of 5 years without exceeding 50 mSv during one year. The safety criterion for the Chinese facility is set to 15–18 mSv per year under normal operating conditions. Under

**Table 2** Guidance values for restricting exposure of emergency workers

Tasks	Guidance value
Actions to avert a large collective dose	<100 mSv
Life saving actions	<500 mSv This value may be exceeded under circumstances in which the expected benefits to others clearly outweigh the emergency worker's own health risks, and the emergency worker volunteers to take the action and understands and accepts this health risk
Actions to prevent severe deterministic effects and actions to prevent the development of catastrophic conditions that could significantly affect people and the environment	<500 mSv

accidental situations, GB18871-2002 indicates a value of 50 mSv which is set for the Chinese facilities for the accidental radiological impact on the workers for one accident within the design basis. Meanwhile, guidance values for restricting exposure of emergency workers are also recommended, as shown in Table 2.

### 3 Reprocessing Process and Radiation Source

The technology for reprocessing spent nuclear fuel (SNF) and for fuel recycle has been developing for many years and relevant information may be found in the publicly available literature. The THORP chemical separation plant was designed and constructed during the 1980s and early 1990s with a nominal capacity of 1200 metric tons of initial heavy metal (MTHM) of SNF per year, which is the largest reprocessing plant of operating facilities in the world. The Fig. 1 shows an overview of the process chemistry of the chemical separation facilities in the THORP at Sellafield [4].

Because the reprocessing is to deal with the spent fuel with high burn up level, the activity of radioactive materials in the spent fuel is high and type of nuclides is very complex. In comparison with nuclear power plant, radiation sources in reprocessing plant is more complicated in open situation; for the different steps involved in the process, such as head-end treatment co-decontamination, scrubbing of organic stream with nitric acid, partitioning of uranium and plutonium, further purification of uranium and plutonium streams to obtain U and Pu of desired purity, treating the used solvent and waste management, radioactive materials in the spent fuel are distributed in different radioactive system and building, thus it is more probable that worker could contact a large amount of the radioactive material during the equipment maintenance and serving, and therefore type, activity, and strength

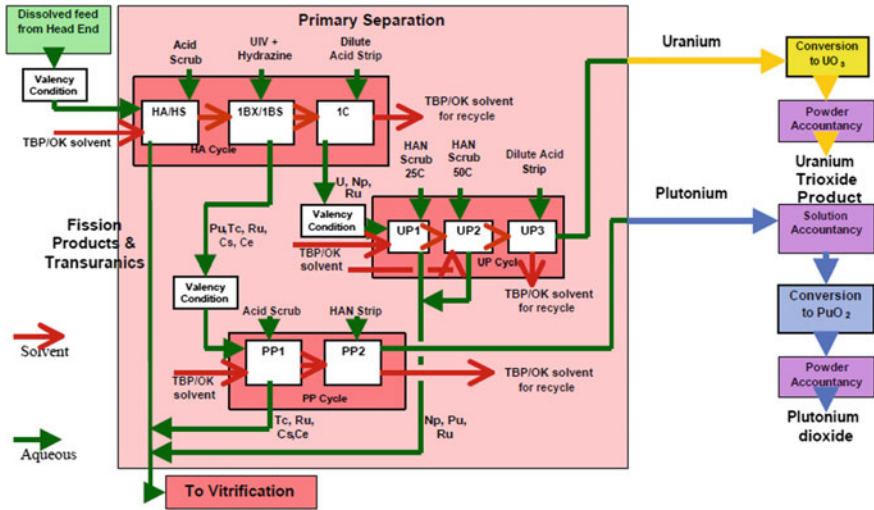


Fig. 1 THORP chemical process flowsheet

spectrum characteristic of radiation sources in different process need to be noticed carefully.

### 4 System Layout and Radiation Zoning

In order to ensure the security of the staff, reasonable layout of plant and equipment is needed to limit the exposure of site personnel, so that radiation doses of staff could meet the requirements of the dose control limits. For the layout of facility, areas in facility should be divided into radioactive areas and nonradioactive areas. The layout of radioactive areas should be relatively concentrated; at the same time, overall access should be set for those areas. In the radioactive area, changing areas should be set to prevent the spread of contamination during maintenance and normal operation between radioactive areas and nonradioactive areas.

As for the layout of radioactive equipment, equipment with different radioactivity levels should be placed in different areas. Because individual high radioactivity level of equipment will increase the radiation protection requirements of the entire equipment areas, high radioactivity level of equipment should be placed in separate areas.

Radioactive pipeline Laying should be based on activity concentration and environmental conditions; it should be avoided in-line accumulated fluid for the outdoor radioactive pipeline. Shielding thickness of pipe gallery and trench should be design based on the radioactivity level of pipeline.

## 5 Radiation Shielding

Shielding is one of the important measures to reduce the external exposure.

Shielding design should assure occupational exposure of personnel accord with the principle of ALARA during the operation of facility. According to the requirement of the level of radiation, radiation zoning, character of operation and size of space, choose suitable shielding material and shield Settings, consider reasonable margin to calculate and determine the thickness of the shield.

Based on the nature of the radiation (whether beta and bremsstrahlung, neutrons and gamma rays, or gamma rays only are produced), the shielding properties of materials, space, and weight limitations, the appropriate materials for a shield should be chosen for every shield.

According to different design objects, shielding calculation methods including Point Kernal Integral and Monte Carlo method generally are chosen to solve the neutron, photon, or neutron/photon coupling transport problems, evaluated parameters should be used in the calculation to ensure the calculation accuracy and conservative.

Criticality safety is another dominant safety issue for the nuclear fuel reprocessing facility [5]. Because of the diversity of technologies and processes, the materials of interest to nuclear safety are more distributed throughout the facility. Because of the different form, such as bulk, distributed, and mobile forms, fissile materials could be easily accumulated in some parts of the equipment or release form the facility as a result of equipment leakage.

Nuclear criticality safety must be ensured and to prevent the potentially exposures of gamma and neutron to workers and then the subsequent release of fission products from equipment and building. Thus, first engineering designs of the facility need to ensure sub-criticality in all areas where possible ‘criticality safe designed equipment,’ second relevant preventive measures should be taken to protect safety of workers, at last reduce the release of fission products from the facility and protect the safety of public and environment.

Since 1953, the number of international nuclear criticality accidents reported sum up to 22 [6]. Table 3 summarizes the statistics of the service conditions of preventive measures for those criticality accidents. The most useful preventive measure for reducing the criticality accident consequence is enough shield structure [7].

**Table 3** Statistics of the service conditions of preventive measures for those criticality accidents

Preventive measures	The number for success	The number for no success
Appropriate operation regulation	1	9
Preferred equipment geometry	1	–
Better safety auxiliary equipment	1	1
Enough iron or concrete shield	3	–

**Table 4** Classification of the total fission number of criticality accidents

Magnitude for total fission number	The number for criticality accident	Ratio (%)
$10^{15}$	2	11
$10^{16}$	1	5
$10^{17}$	12	63
$10^{18}$	3	16
$10^{19}$	1	5

During the preliminary design stage of reprocessing facility, it is difficult to do the detail calculation for every criticality accident and analyze corresponding consequence; however, the general wall thickness of facility, namely shield thickness should be determined first. Fortunately the following semi-empirical equations could be used for estimated gamma dose and neutron dose calculations of criticality accident [8].

$$D_{\gamma} = 2.1 \times 10^{-22} N d^{-2} e^{-3.4d} \quad (1)$$

where  $D_{\gamma}$  is the prompt gamma dose (Sv),  $N$  is the number of fissions, and  $d$  is the distance from source (km).

$$D_n = 7 \times 10^{-22} N d^{-2} e^{-5.2d} \quad (2)$$

where  $D_n$  is the prompt neutron dose (Sv),  $N$  is the number of fissions, and  $d$  is the distance from source (km).

For the equations above, the number of fissions during nuclear criticality accident is the most key parameters. Total numbers of fission for international 19 nuclear criticality accidents reported are estimated and the results can be seen in Table 4.

In the table magnitude of  $10^{17}$  for total fission number is the most frequently observed, and magnitude of  $10^{19}$  is the largest value for all of those criticality accidents. Based on the recommended different number of fission from the first burst, dose reduction factors for concrete, exposure time, and the dose limitation of workers, the approximate and conservative thickness of shield could be obtained.

## 6 Radiation Monitoring

Though a reprocessing plant is intrinsically stable and not susceptible to rapid fluctuations from normal conditions, radiation levels shall be monitored so that any abnormal conditions would be detected and workers may be evacuated, it is also necessary to maintain normal operation of system and safety of public and the environment [9, 10]. Figure 2 shows the content of radiation monitoring corresponding to the design of reprocessing facility.

Gamma radiation monitoring of area should be designed and installed in various locations of the plant in order to monitor the ambient radiation levels of areas,

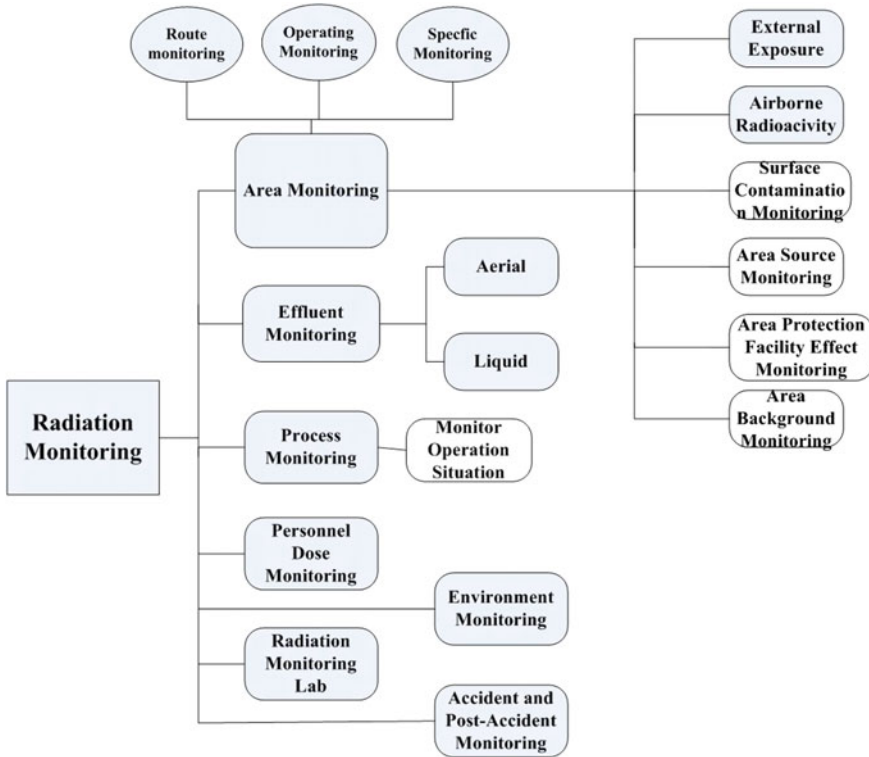


Fig. 2 Content of radiation monitoring corresponding to the design of reprocessing facility

where the staff often pass by or enter. In addition, these areas could include personnel access and the place where the staff need enter under accident conditions.

For the operating related to Beta ray, such as a higher risk of contamination through the glove box operation of uranium product, and high pollution areas or opened the sealed equipment for maintenance, in addition to the measurement of gamma radiation levels, beta external exposure levels should also be monitored.

Under normal conditions, neutron monitor should be set up in areas with neutron irradiation risks, including plutonium working box and plutonium product library.

Airborne radioactive concentration of workplace should be monitored at potential areas to continuously monitor the ambient air for any suspended airborne radioactivity. Besides, airborne activity levels are monitored in every shift as well as during any specific operations in contaminated areas.

All operating personnel who may be occupationally exposed to radiation at levels that are significant for the purposes of radiation protection shall be issued Thermo Luminescent dosimeters and their doses are well recorded and assessed.

In addition, it is postulated that there exists a probability of criticality accident in reprocessing facility; hence, it is necessary to have criticality monitors and alarm

device at strategic locations for initiating immediate evacuation of personnel in the vicinity, such as head-end treatment, co-decontamination, and purification of plutonium. Criticality accident last for a very short time, for example, 1 ms, meanwhile, the radiation source strength will be very high, both of them will failure the “normal” radiation monitor, criticality monitors and alarm device need to response quickly and generate alarm signal. At the same time, considering the dose assessment and personnel protection, as well as key data acquisition, the neutron and gamma dose monitoring should also be designed for staff.

## **7 Key Problems**

### **7.1 Radiation Source**

In comparison with nuclear power plant, radiation sources in reprocessing plant is more complicated in open situation; for the different steps involved in the process, such as head-end treatment co-decontamination, scrubbing of organic stream with nitric acid, partitioning of uranium and plutonium, further purification of uranium and plutonium streams to obtain U and Pu of desired purity, treating the used solvent and waste management, radioactive materials in the spent fuel are distributed in different radioactive equipment, system, and building [11]; meanwhile the achievement of criticality depends on the mass of fissile material present and its distribution among the components of the system, since radiation source in different part and step of process should be analyzed reasonably.

### **7.2 Dose Assessment**

Though critical accident consequence was given by a simplified method, but the possibility of criticality accident for the different steps and equipment involved in the process should be analyzed individually, and the design should protect the safety of workers, appropriate evacuation routes, and regrouping areas should also be identified.

### **7.3 Public Influence**

After criticality accident a large amount of fission product will release from the equipment chamber into the building and then the environment, since how to define the source term released and assess the safety of public is a necessary task.

## 8 Conclusion

China is still on the initial stage of the field of reprocessing of spent fuel; radiation protection design in the SNF reprocessing facility should be paid attention in order to assure the normal and safe operation of facility. Several important aspects on radiation protection design including significant system and pipeline layout, radiation shielding calculation and analysis, radiation monitoring are summarized in the paper, and the results is benefit for the following construction and operation of SNF reprocessing facility.

## References

1. IAEA Safety standards, Safety of Nuclear Fuel Cycle Facilities, Safety requirements No. NS-R-5(Rev. 1).
2. RUAN Zhongyuan, CAO Jingwei, LIU Longyun, YANG Zhangzhong, LEI Fuan, and WEN Wen, Analysis of Spent Nuclear Fuel Reprocessing Facilities' Safety Features upon Reviewing the Exxon Reprocessing Plant, Nuclear Safety, Dec. 2013, Vol. 12, S1.
3. LI Jinying, SHI Lei, HU Yantao, Some considerations on the construction of a spent nuclear fuel reprocessing plant in China, Journal of Nuclear and Radiochemistry, Aug. 2011, Vol. 33, No. 4.
4. C. Burrows, C. Phillips, A. Milliken, The Thermal Oxide Reprocessing Plant at Sellafield-Lessons Learned from 10 Years of Hot Operations and their Applicability to the DOE Environmental Management Program, WM'06 Conference, February 26–March 2, 2006, Tucson, AZ.
5. LI Ruirou, XU Yunqi, Accident Safety Analysis Method Study for Spent Fuel Reprocessing Plant, Nuclear Safety, 2012, No. 3.
6. Liu Xinhua, Liu Hua, Wang Deqiang and Li Bing, Experience and Lessons From Criticality Accidents In Nuclear Fuel Plants Abroad, Radiation Protection, Jan 2002, Vol 22 No. 1.
7. LV Dan, GAO Mingyuan, LIU Binbin, XU Yunqi, Statistics and Analysis of Critical Accidents of the Foreign Spent Fuel Reprocessing Plant, Nuclear Safety, Mar. 2014, Vol. 13, No. 1.
8. Assumptions Used for Evaluating the Potential Radiological Consequences of Accidental Nuclear Criticality in a Fuel Reprocessing Plant, Regulatory Guide 3.33, Revision 2, Jan 1998.
9. V. Meenakshisundaram\*, V. Rajagopal, R. Santhanam, S. Baskar, U. Madhusoodanan, S. Chandrasekaran, S. Balasundar, K. Suresh, K.C. Ajoy, A. Dhanasekaran, R. Akila, and R. Indira, Operation experiences in radiation protection in fast reactor fuel reprocessing facility.
10. Sadaaki FURUTA and Kenjiro MIYABE, Radiation Protection Feature and Research at Nuclear Fuel Cycle Engineering Laboratories, JAEA.
11. P.K. Dey, Spent fuel reprocessing: An overview, INSAC 2003.



# The Method to Ascertain Time-Control Parameters of Reverse Fluidic Device Based on Level Feedback of Supply Tank

Bao Yin, Liu Yu and Guo Xiao-Fang

**Abstract** Reverse fluidic device (RFD) is a kind of maintenance-free equipment which is used for radioactive liquids (nuclear fuel) transportation (Smith and Lewis in Design of a pulsed-mode fluidic pump using a venture-like reverse flow diverter. OAK Ridge National Laboratory Press, Tennessee, 1987 [1]). The parameters of system are difficult to be measured. In addition, every phase of cycle operation is a nonlinear process (Fallows et al. in Applications of power fluidic technology in nuclear waste processing plants. Tucson, AZ, 2005 [2]). So the control method of RFD is hard to be ascertained. By the research of traditional method to ascertain time-control parameters, a new method based on level feedback of supply tank is suggested. The time-control parameters to be ascertained by this method are used for RFD system operation. System can stably operate for a long time. Meanwhile, the method can eliminate the influence of different initial levels on system operation. As a kind of maintenance-free equipment, reverse fluidic device (RFD for short) can be used for radioactive liquid transportation at spent nuclear fuel plant (Rajeev et al. in fluidic pump development studies. Indira Gandhi Centre for Atomic Research, 2002 [3]). The control method of RFD is one of the most important key points at engineering application for purpose of system long-time steady operation by some measuring and control methods. Now instruments on the market cannot be used for liquid level real-time measurement of RFD and cannot be maintained or replaced. In addition, every phase of RFD cycle operation is a nonlinear process (Priestman and Tippetts in Fluid Control 16(4):19–39, 1986 [4]). So it is very difficult to ascertain a safe, reliable, and steady control method of RFD. In this paper, by the analysis of RFD transportation characteristics and the research of traditional method to ascertain time-control parameters, a new method based on level feedback of supply tank is suggested, and time parameters ascertained by this new method are used in RFD system control to verify its effectiveness.

**Keywords** Reverses fluidic device · Time-control parameter · Level feedback

---

B. Yin (✉) · L. Yu · G. Xiao-Fang  
Fluidic Device and Automation, China Nuclear Power Engineering Co., Ltd., Beijing, China  
e-mail: pumu100@sina.com

# 1 Revers Fluidic Device (RFD)

## 1.1 The Structure of Reverse Fluidic Device (RFD) System

RFD system consists of a controller, a jet pump pair, isolation valves, pressure transmitters, a charge vessel, the RFD, and the discharge tube [5]. RFD has advantages of non-moving parts, simple structure, good sealing, steady working, and maintenance-free [6]. The pressure head of RFD outlet port is higher enough and RFD would not heat and dilute liquid (Fig. 1).

## 1.2 RFD System Operating Principle

Through measuring two level signals and the pressure signal of charge vessel, and interlocking to control the two solenoid valves open and close, RFD system can operate with three-phase level-control method steadily and automatically at non-radioactive environment [7]. The operation cycle includes three phases: suction phase, drive phase, and vent phase. These phases are then repeated to produce a cyclic operating process [8–10].

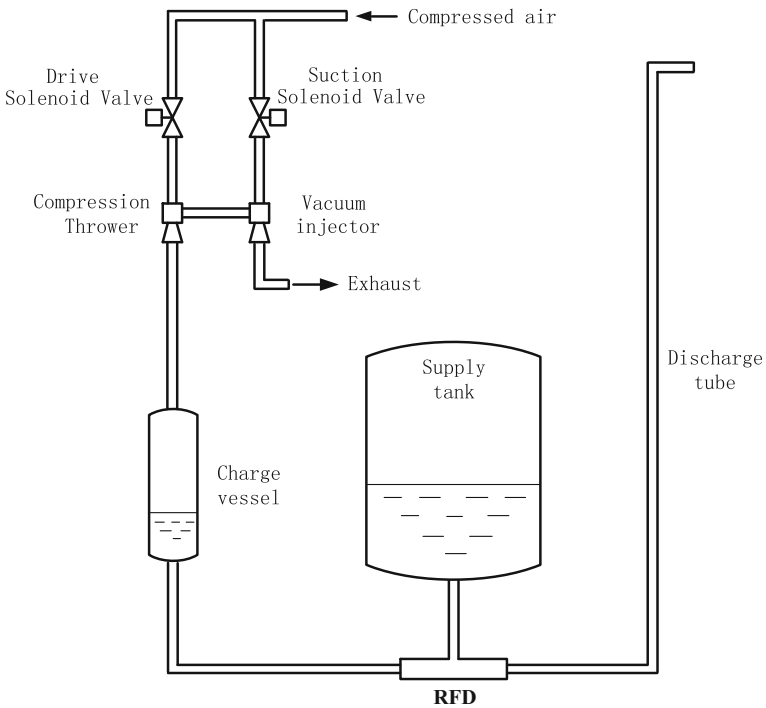
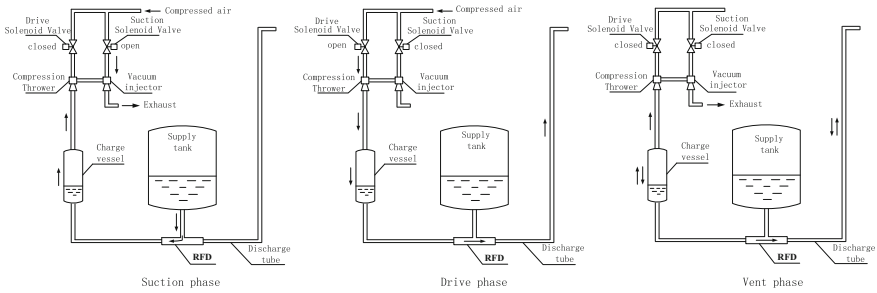


Fig. 1 Reverse fluidic device (RFD) system



**Fig. 2** Operating principle of RFD system

a. Suction phase

The process starts from suction phase by opening suction isolation valve. Vacuum injector work and generate vacuum pressure in charge vessel. Liquid passes from the supply tank, through the RFD to refill the charge vessel. The liquid level of charge vessel rapidly rises. They exhaust discharge into ventilation system. This phase continues until the charge vessel is full (Fig. 2).

b. Drive phase

When the level of charge vessel reaches the present value, suction isolation valve is closed and drive isolation valve is opened. The drive phase start. As a result, compressed air is passed to the charge vessel which forces the liquid through the RFD, where more liquid is sucked from the supply tank, and on to delivery through the discharge tube. The liquid level of charge vessel rapidly falls. This phase continues until the charge vessel is nearly empty.

c. Vent phase

When the level of charge vessel reaches to another preset value, drive isolation valve is close too. The vent phase start. Pressed air in charge vessel begins to discharge. Because of energy releasing, outflow in discharge tube reduces until it is zero. Then suction isolation valve is open again, and another cyclic action starts.

### 1.3 Control Technical Characteristics of RFD System

RFD system is a kind of maintenance-free equipment which is used at radioactive environment. So there is hardly any instrument that can measure and detect the level of the charge vessel and be maintained and replaced. In addition, every phase of RFD system cyclic operating process is a complex nonlinear process. It is difficult to set up a mathematical model. So it is highly difficult to ascertain a safe, reliable, and steady control method of RFD system.

## 2 Control Method of RFD System

According to the control technical characteristics and operating principle of RFD system at non-radioactive environment, using a non-contact measuring method instead of traditional level instrument to interlock control valves is the key issue of RFD system in the engineering application.

### 2.1 Time-Control Method of RFD System

Time-control method of RFD system is a three-phase control method of RFD system using time parameters instead of level parameters to interlock control valves. The time parameters of time-control method are obtained by collecting and calculating large amounts of time data of test system. After that, writing these time parameters into control system program, RFD system can operate with time-control method automatically.

### 2.2 The Method to Ascertain Time-Control Parameters of RFD System Based on Fixed Level of Charge Vessel

To ascertain time-control parameters of RFD system, traditional method is to convert fixed level parameters of charge vessel into time parameters. The method is as follows:

#### A. Preparation

- Measure the level value of charge vessel by instrument at non-radioactive environment.
- Preset the upper limit level  $h1$  as the event of suction phase finish and to preset the lower limit level  $h2$  as the event of drive phase finish.
- Preset limit pressure value  $p0$  as the event of vent phase finish.

#### B. Initial suction time

- To start RFD system, open the suction isolation valve. System is in initial suction phase ①.
- Close the suction isolation valve when the level of charge vessel reaches  $h1$ . Initial suction phase finishes.
- Note the initial suction time  $\Delta t1$ .

## C. Drive time

- Meanwhile, open the drive isolation valve. The drive phase ② starts.
- Close the drive isolation valve when the level of charge vessel reaches  $h_2$ . Drive phase finishes.
- Note the drive time  $\Delta t_2$ .

## D. Vent time

- Meanwhile, the vent phase ③ starts.
- Open the suction isolation valve when the pressure of charge vessel decline to  $p_0$ . Vent phase finishes.
- Note the vent time  $\Delta t_3$ .

## E. Suction time

- Meanwhile, a new suction phase ④ starts.
- Close the suction isolation valve when the level of charge vessel reaches  $h_1$  again. Suction phase finishes.
- Note the suction time  $\Delta t_4$ .

## F. Repeat

- Repeat the above steps  $n$  times.
- Get the time data sets  $\{\Delta t_{1i}\}$ ,  $\{\Delta t_{2i}\}$ ,  $\{\Delta t_{3i}\}$ , and  $\{\Delta t_{4i}\}$ .

## G. Calculation

- Calculate the average of these data sets.
- Figure out the time-control parameters of RFD system which are the initial suction time  $t_1$ , the drive time  $t_2$ , the vent time  $t_3$ , and the suction time  $t_4$ .

$$t_1 = \frac{\sum_{i=1}^n \Delta t_{1i}}{n}, \quad t_2 = \frac{\sum_{i=1}^n \Delta t_{2i}}{n}, \quad t_3 = \frac{\sum_{i=1}^n \Delta t_{3i}}{n}, \quad t_4 = \frac{\sum_{i=1}^n \Delta t_{4i}}{n}$$

### 3 The Method to Ascertain Time-Control Parameters of RFD System Based on Level Feedback of Supply Tank

#### 3.1 Principle

Traditional method is to convert fixed level values of charge vessel into time parameters. But due to the movement of charge vessel liquid level, the pressure head of RFD each port would change likewise. If using the time parameters ascertained by fixed level of charge vessel at different levels of charge vessel, the

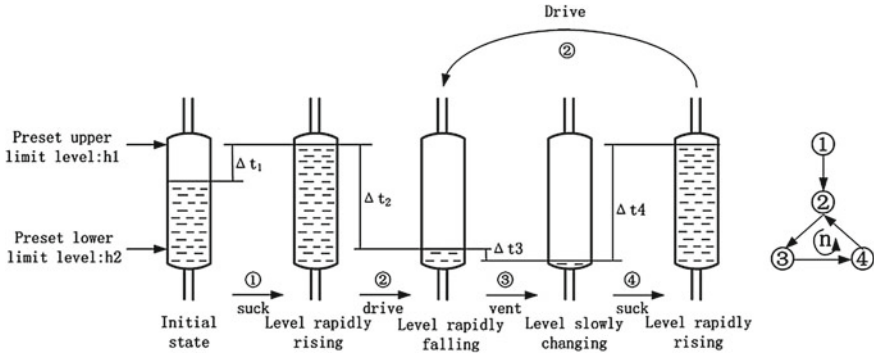


**Fig. 3** The method to ascertain time-control parameters of RFD system based on fixed level of charge vessel

RFD system would run unsteadily. In addition, considering the different initial levels of charge vessel for various RFD systems, the RFD system would run unsteadily also if using the time parameters ascertained by traditional method (Fig. 3).

The basic principle of the method that ascertain time-control parameters of RFD system based on level feedback of supply tank is to convert real-time level values of charge vessel into time parameters instead of fixed level values.

**A. Preparation**

- Put the bottom of charge vessel with the same height of supply tank.
- Measure the level values of charge vessel  $H$  and supply tank  $L$ .  $H$  and  $L$  are equal in initial state.

**Fig. 4** The initial level relationship

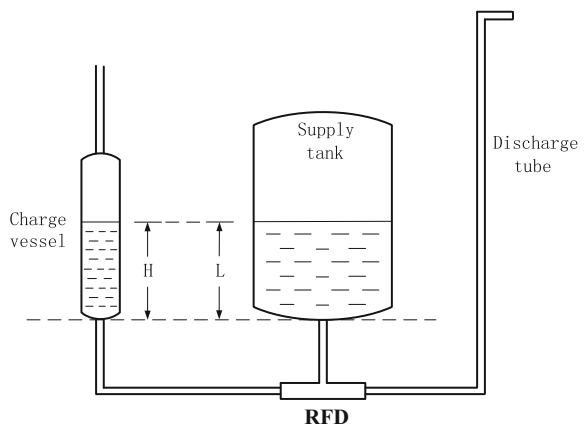
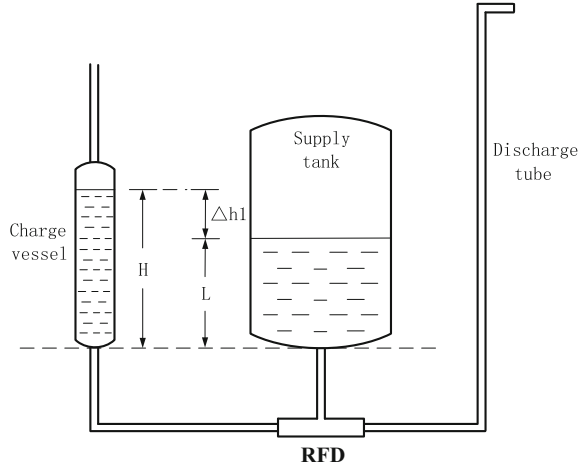


**Fig. 5** The first suction time parameter



- Preset the upper limit level difference  $\Delta h1$  as the event of suction phase finish and the lower limit level difference  $\Delta h2$  as the event of drive phase finish.
- Preset limit pressure value  $p0$  as the event of vent phase finish (Fig. 4).

**B. Initial suction time**

- To start RFD system, open the suction isolation valve. System is in initial suction phase.
- Close the suction isolation valve when the level of charge vessel  $H$  reaches  $L + \Delta h1$ . Initial suction phase finishes.
- Note the initial suction time  $\Delta t1$  (Fig. 5).

**C. Drive time**

- Meanwhile, open the drive isolation valve. The drive phase starts.
- Close the drive isolation valve when the level of charge vessel  $H$  reaches  $L - \Delta h2$ . Drive phase finishes.
- Note the drive time  $\Delta t2$  (Fig. 6).

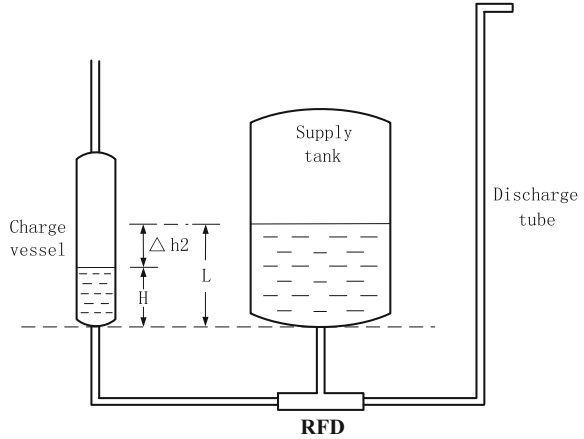
**D. Vent time**

- Meanwhile, the vent phase starts.
- Open the suction isolation valve when the pressure of charge vessel declines to  $p0$ . Vent phase finishes.
- Note the vent time  $\Delta t3$ .

**E. Suction time**

- Meanwhile, a new suction phase starts.
- Close the suction isolation valve when the level of charge vessel  $H$  reaches  $L + \Delta h1$  again. Suction phase finishes.

**Fig. 6** The drive time parameter



- Note the suction time  $\Delta t_4$ .

F. Repeat

- Repeat the above steps  $n$  times.
- Get the time data sets  $\{\Delta t_{1i}\}$ ,  $\{\Delta t_{2i}\}$ ,  $\{\Delta t_{3i}\}$ ,  $\{\Delta t_{4i}\}$ .

G. Calculation

- Calculate the average of these data sets.
- Figure out the time-control parameters of RFD system which are the initial suction time  $t_1$ , the drive time  $t_2$ , the vent time  $t_3$ , and the suction time  $t_4$ .

$$t_1 = \frac{\sum_{i=1}^n \Delta t_{1i}}{n}, \quad t_2 = \frac{\sum_{i=1}^n \Delta t_{2i}}{n}, \quad t_3 = \frac{\sum_{i=1}^n \Delta t_{3i}}{n}, \quad t_4 = \frac{\sum_{i=1}^n \Delta t_{4i}}{n}$$

## 4 Validation Test

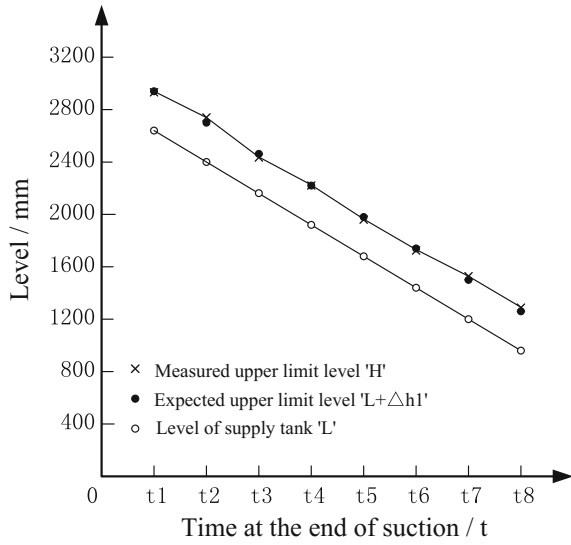
In order to verify the effectiveness of this method at engineering application, we make the validation test on complete RFD test system (includes online detection instrument). To verify the stability, reliability, and adaptability, 96 batches of simulated liquid are transported by time-control method whose time parameters are ascertained by this new method.

(1) Stability

At all the 96 batches of simulated liquid transport process, no breakdown happened (the level of charge vessel down to zero). All the 96 batches of simulated liquid are transported effectively.



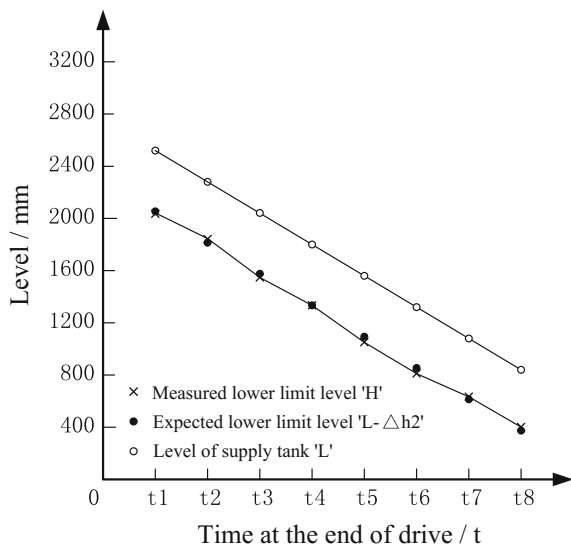
**Fig. 7** The reliability analysis of upper limit level



(2) Reliability

Every suction phase upper limit level value of charge vessel H is measured to compare with expected upper limit level value  $L + \Delta h1$  (the preset upper limit level difference  $\Delta h1 = 400$  mm). As shown in Fig. 7, the real-time upper limit level values ascertained by this method are good agreement with theoretical values. So the time parameter at suction phase is reliable.

**Fig. 8** The reliability analysis of lower limit level



Every drive phase lower limit level value of charge vessel H is measured to compare with expected lower limit level value  $L - \Delta h_2$  (the preset lower limit level difference  $\Delta h_2 = 500$  mm). As shown in Fig. 8, the real-time lower limit level values ascertained by this method are good agreement with theoretical values. So the time parameter at drive phase is reliable.

### (3) Adaptability

The initial levels of these 96 batches of simulated liquid are random. But the initial suction time of all batches is the same. So we validate that RFD system can transport effectively regardless of the initial level of supply tank.

## 5 Conclusion

In this paper, by the analysis of RFD transportation characteristics and the research of traditional method to ascertain time-control parameters, a new method based on level feedback of supply tank is suggested. The new method is to convert real-time limit level values of charge vessel into time parameters instead of traditional method that convert fixed level limit values into time parameters. By validation test, this method can realize RFD system effectively transportation. Meanwhile, this method can eliminate the influence of different initial levels on system operation and the influence of the liquid level changes of supply tank on the time parameters. So the method to ascertain time-control parameters of RFD system based on level feedback of supply tank can effectively applied in the engineering application of RFD system.

## References

1. Smith G V, Lewis B E. Design of a pulsed-mode fluidic pump using a venture-like reverse flow diverter [R]. Tennessee: OAK Ridge National Laboratory Press, 1987.
2. P. Fallows, M. Williams, P. Murray, Applications of power fluidics technology in nuclear waste processing plants [C], WM'5 Conference, February 27–March 3, 2005, Tucson, AZ.
3. R. Rajeev, C.V. Joyakin and S.B. Koganti, Fluidic pump development studies[R], Indira Gandhi Centre for Atomic Research, 2002.
4. Priestman G H, Tippetts J R. Characteristics of a Double-Acting Fluidic Pump With Hot and Cold Water [J]. Fluid Control, 1986, 16(4): 19–39.
5. Tesar V. Pump for extremely dangerous liquids [J]. Chemical Engineering Research and Design, 2011, 8(7): 940.
6. Li Jiangyun, Xu Ruliang, Wang Leqin. Reversible fluid converter device optimization design and application, China mechanical engineering [J], 2003. Vol. 14(23): 1994–1998.
7. Jiao Lei, Yin Junlian, Chen Zhongnan, design parameters on the properties of eddy diodes pump test research [J], journal of engineering thermal physical, 2010. Vol. 31(4): 593–596.
8. Li Jiangyun, Wang Jian, Hu Shaohua. Based on numerical simulation of reverse flow diverter (RFD) optimized design method [J]. Journal of Wuhan University: Engineering, 2010, 43(6): 747–751.

9. H.M. Shaw. Application of power fluidics in British nuclear reprocessing plants [R]. BNFL, 1995, 11.
10. Y.F. Fan, Experimental Study on the Performance of Reverse Flow Diverters and Pneumatic Pulsed Fluidic Pump Used in Nuclear Industry [M]. Beijing, Tsinghua University, 2008.

# The Microstructure and Characteristic Analysis of USW Welding

Pengbo Ji and Junfeng Sun

**Abstract** The welding process of cladding tube and end plug is a key process of PWR fuel assembly manufacture. The welding seam of cladding tube and end plug is the weakest part of the whole fuel rod. The life of assembly and safety of reactor is directly influenced by the quality of welding seam, so the fuel plant has very high requirements on the quality of welding seam. And choosing proper weld method is important to the manufacture. The USW welding of AFA 3G fuel rod is a new project in China until now. This thesis analyses the USW welding process through the history of USW welding and formation of welding joint. And based on large numbers of experiments, the influences of different welding parameter on the metallography, burst test, and corrosion test are analyzed and studied in details. This analysis and study provides the theoretical base for controlling of fuel rod end plug welding process to manufacture the qualified fuel rods.

**Keywords** Fuel rod · Pressure resistance welding (USW) · Microstructure · Welding characteristic

## 1 Foreword

The USW welding of AFA 3G fuel rod is a new project in China until now. Comparing with traditional fuel rod welding process, the main advantage is that it does not need to seal the hole of top end plug and inspect the welding quality. Comparing with the traditional ultrasonic or X ray welding seam inspection, it cuts the production cost and reduces the environment pollution.

---

P. Ji (✉) · J. Sun  
China North Nuclear Fuel Co. Ltd, Baotou 014035, China  
e-mail: 14213481@qq.com

© Springer Science+Business Media Singapore 2017  
H. Jiang (ed.), *Proceedings of The 20th Pacific Basin Nuclear Conference*,  
DOI 10.1007/978-981-10-2317-0\_61

639

## 2 Brief Introduction of USW

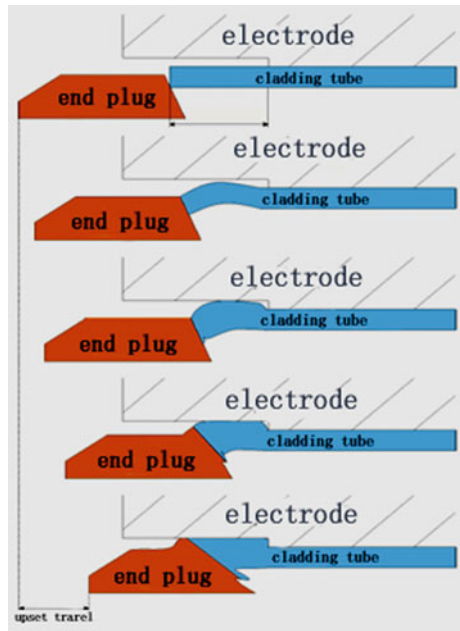
### 2.1 The Developing History of USW

The pressure resistance welding was first developed for the fuel rod welding in Erlangen Lab of Siemens Company in the late 1960s. Pressure resistance welding was used in the fuel rod manufacture in Siemens Company in the late 1970s, and it first applied to the PWR fuel reload in 1979. In 2001, the AREVA NP experts validated that USW welding was the best choice for fuel rod welding. Now, American Richland Fuel Plant and Lynchburg Fuel Plant, Belgium Dessel Fuel Plant, French Romans Fuel plant, and German Lingen Fuel Plant are all using USW welding to manufacture the fuel rods.

### 2.2 Forming Process of Welding Joint

In a pressure resistance welding cycle, joint formation process consists of three successive parts: prepressing, electrifying to heating, and cooling crystallization (see Photo 1) [1].

**Photo 1** Forming process of welding joint



- (a) Prepressing Stage  
 Characteristic of machine-electric process for prepressing stage:  $F > 0, I = 0$ . Its function is removing part of contact surface roughness and oxide film under pressure, and forming a physical contact point.
- (b) Electrifying to Heating Stage  
 Characteristic of machine-electric process for electrifying to heating stage:  $F > 0, I > 0$ . Its function is forming plastic ring and nugget under thermal and mechanical force, growing along with heating until reaching needed nugget size.
- (c) Cooling Crystallization Stage  
 Characteristic of machine-electric process for cooling crystallization stage:  $F > 0, I = 0$ . Its function is to make the nugget cooling crystallization under the action of the pressure, finally forming the welding seam.  
 Note: “ $F$ ” is force, “ $I$ ” is current.

### 2.3 Welding Equipment

Taking the top end plug welding as an example, schematic diagram of welding chamber is shown in Photo 2.

In the process of USW, the material of welding zone is heated by welding current. The end plug electrode gives a constant axial upsetting force to push the end plug moving toward the cladding tube to form the upset. The dimension of upset is determined by the cladding tube electrode, just like the forging die in the forging process.

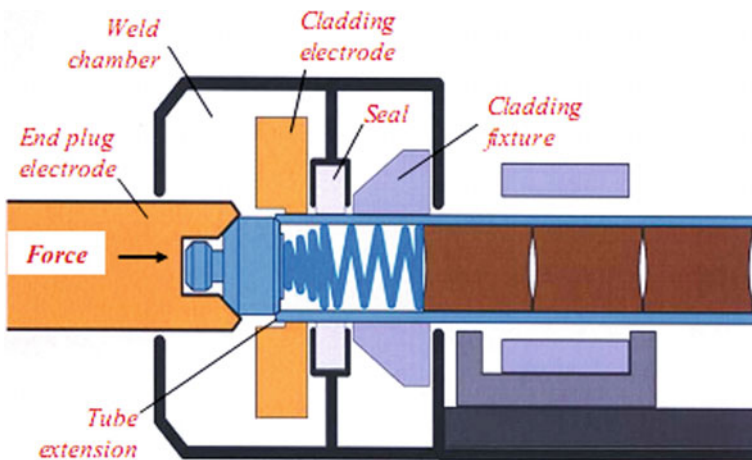
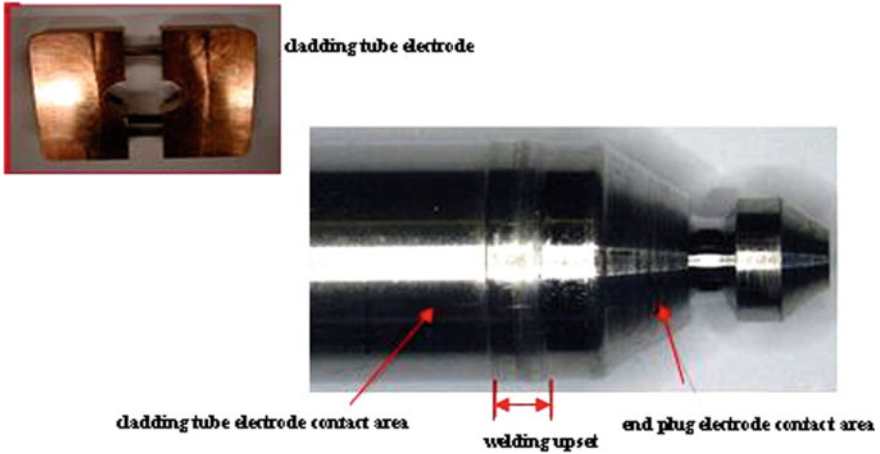


Photo 2 Schematic diagram of welding chamber



**Photo 3** Photo of USW cladding tube electrode and welding seam

In fact, USW welding is heating and upsetting forming process on the welding zone. Photo 3 is the Photo of USW cladding tube electrode and the fuel rod welding seam.

### 3 Microstructure and Characteristic Analysis

#### 3.1 Test Scheme and Inspection Result

##### 3.1.1 Preparation of Test Material

Use Zr4 end plug and M5 PC tube as test material. Check the dimension and appearance according to inspection specification, and results fulfill the specification.

##### 3.1.2 Selection of Variable Parameter and Collection of Results

According to the performance of equipment, two variable parameters are combined as listed in Chart 1, i.e., different welding current matching with different electrode pressure. The inspection results of samples are listed in Chart 2.

**Chart 1** Variable welding parameters

Parameter	Value							
Welding current (A)	8000	9000	10,000	11,000	12,000	13,000	14,000	15,000
Electrode pressure (N)	2800	2900	3000	3100	3200	–	–	–

**Chart 2** Summary of inspection results

Current (A)	Inspection	Force (N)				
		2800	2900	3000	3100	3200
8000	Burst test	NOK	NOK	NOK	NOK	NOK
	Metallography	–	–	–	–	–
	Corrosion test	OK	OK	OK	OK	OK
9000	Burst test	NOK	NOK	NOK	NOK	NOK
	Metallography	–	–	–	–	–
	Corrosion test	OK	OK	OK	OK	OK
10,000	Burst test	OK	OK	OK	OK	OK
	Metallography	OK	OK	OK	OK	OK
	Corrosion test	OK	OK	OK	OK	OK
11,000	Burst test	OK	OK	OK	OK	OK
	Metallography	OK	OK	OK	OK	OK
	Corrosion test	OK	OK	OK	OK	OK
12,000	Burst test	OK	OK	OK	OK	OK
	Metallography	OK	OK	OK	OK	OK
	Corrosion test	OK	OK	OK	OK	OK
13,000	Burst test	OK	OK	OK	OK	OK
	Metallography	OK	OK	OK	OK	OK
	Corrosion test	OK	OK	OK	OK	OK
14,000	Burst test	OK	OK	OK	OK	OK
	Metallography	OK	OK	OK	OK	OK
	Corrosion test	OK	OK	OK	OK	OK
15,000	Burst test	OK	OK	OK	OK	OK
	Metallography	OK	OK	OK	OK	OK
	Corrosion test	NOK	NOK	OK	OK	OK

### 3.2 The Analysis of Inspection Results

#### 3.2.1 Burst Test

Specification of Inspection

Requirement: Weld strength is judged to be sufficient if the following requirements have been met.



- Bursting of sample occurs outside the initial junction of cladding tube and end plug (welding contact surface).
- A minimum burst force is achieved.

Testing: Burst test shall be performed at room temperature, and check with eyes.

### Test Equipment and Inspection Method

- (1) Equipment: Electronic universal tester.
- (2) Inspection method.

Burst test is the most effective method to check the mechanical strength of welding seam. Actually, it is the pressure resistance test of welding seam. Therefore, a specially designed burst test device is used. Put the welding sample, which has soft plastic stick inside, into test fixture and apply pressure onto plastic stick to make it extrude and deform until the welding sample is broken, as shown in Photo 4.

### Test Results

According to the specification of burst test, the results are as follows:

When welding current is 8000 A, the rupture positions of burst test specimens are at the initial junction of cladding tube and end plug (welding contact surface).

When welding current is 9000 A, the rupture positions of burst test specimens are at the initial junction of cladding tube and end plug (welding contact surface).

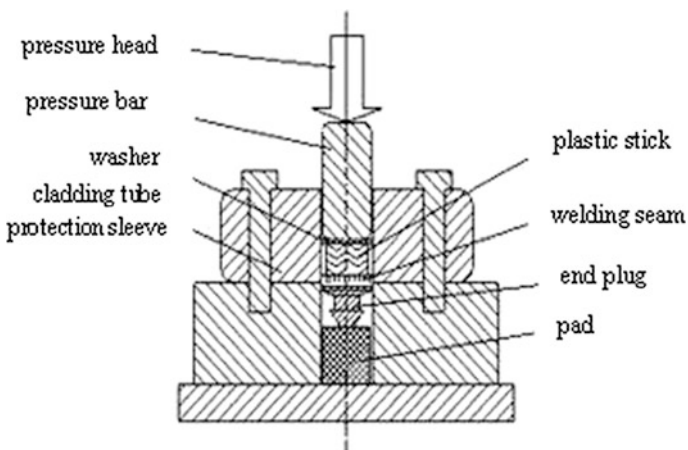


**Photo 4** Burst test equipment

When welding current is 10,000–15,000 A, the rupture positions of burst test specimens are not at the initial junction of cladding tube and end plug (out of welding contact surface). And the bursting force values are larger than required value.

### The Analysis of Results

When welding current is 8000–9000 A, the rupture positions of samples are all located at welded joints. It can be concluded as low welding current makes bonding strength of weld is not enough. That means, the low welding current cause the insufficient heat of joint and the plastic deformation does not concentrate.

### 3.2.2 Metallographic Inspection

#### Specification of Inspection

Requirement: The welding seam must be free of discontinuities and show integrated nugget along the initial junction of cladding tube and end plug (welding contact surface).

Testing: After the burst test, longitudinal micro-sections shall be removed from the weld and examined at 50-times magnification to check the insufficient interface bonding.

#### Test Device and Test Method

- (1) **Equipment:** metallurgical microscope
- (2) **Test method:**

#### Sampling

Metallographic samples are from burst test.

#### Cutting

Longitudinal cut the burst sample, and take half as metallographic samples for testing (the other half is put into the autoclave as corrosion sample). Sample length is about 40 mm. Cutting method is shown in Photo 5.

Because of the need for anodic oxidation, samples are not enchased.

**Photo 5** Cutting method of sample

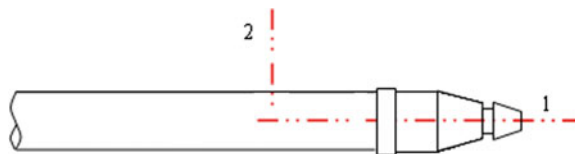


**Chart 3** The steps and parameters of grinding and polishing

Step	Granularity	Time
1	P600 SiC sand paper	Until rubdown
2	P1200 SiC sand paper	Complete remove the grinding trace which is from last step
3	P2500 SiC sand paper	Complete remove the grinding trace which is from last step
4	3 $\mu\text{m}$ polishing liquid, polishing cloth	3 min
5	1 $\mu\text{m}$ polishing liquid, polishing cloth	3 min

### Grinding and polishing

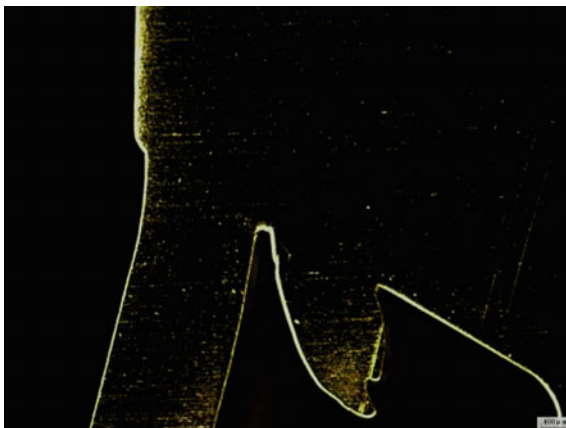
In order to get in line with the requirements of the metallographic inspection plane, the samples need to be ground for 3 times and polished for 2 times. The parameters of grinding and polishing are shown in Chart 3.

### Inspection and Analysis of Welding Quality

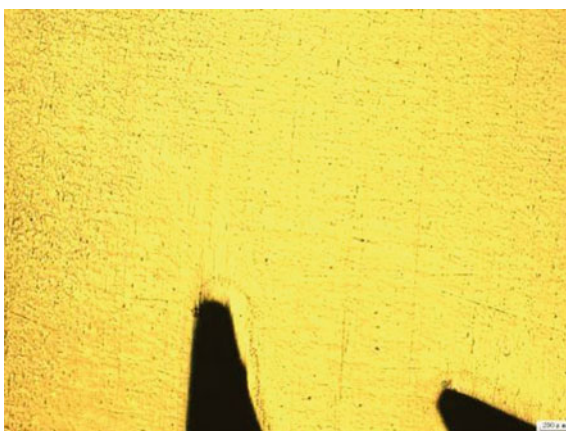
The sample is placed under the microscope. Using the bright field method and dark field method and 50 $\times$ , 100 $\times$ , 200 $\times$ , 500 $\times$  magnification, inspect the welding area of samples for which the welding current is 10,000–15,000 A (see Photos 6, 7, 8, 9, 10, 11, 12, and 13). There is no lack of fusion, crack, and other defects in welding zone.

**Photo 6** 50 $\times$  bright field

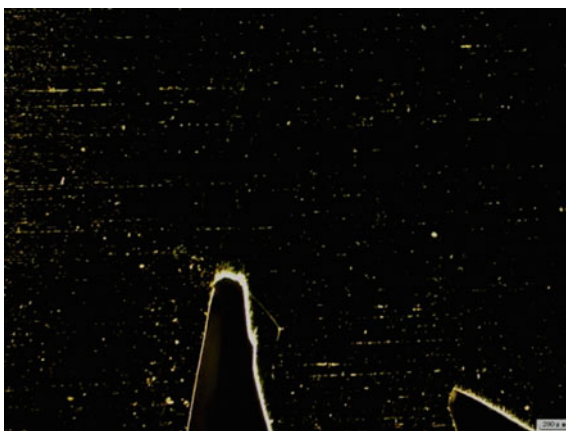
**Photo 7** 50× dark field

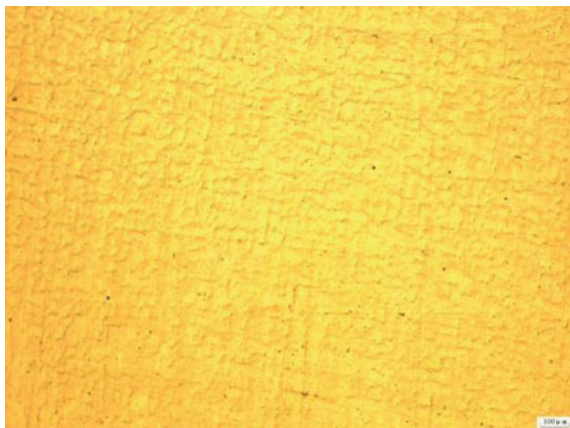
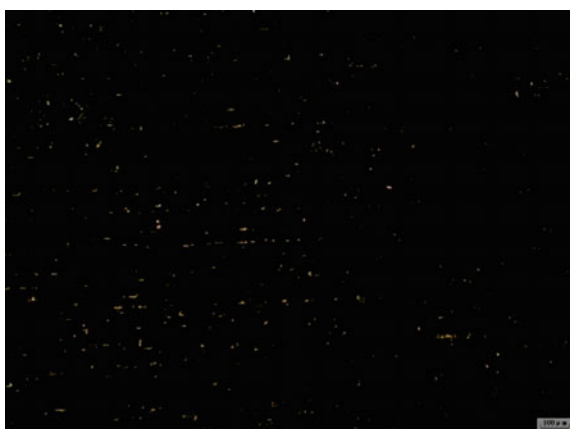


**Photo 8** 100× bright field

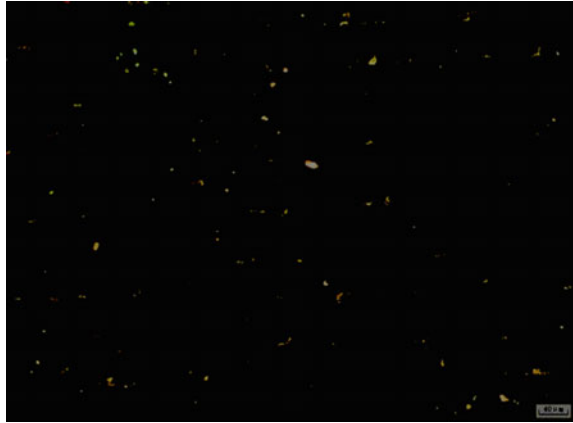


**Photo 9** 100× dark field



**Photo 10** 200× bright field**Photo 11** 200× dark field**Photo 12** 500× bright field

**Photo 13** 500× dark field



### Inspection and Analysis of Grain

In order to further examination of grain morphology combination characteristic in weld area, perform the chemical polishing, and anodic oxidation for the samples. Then place the samples under the microscope to check, using polarized light observation method, in 50×, 100×, 200×, 500×, 1000× magnification (see Photos 14 and 18). Observation results show that the samples have the integrity welding seam zone, heat affected zone, stress deformation zone, and parent metal equal grain zone (Photo 14), and weld zone presents complete grain combination, while welding current is 10,000–15,000 A (Photos 15, 16, 17, and 18).

In this series of photos, we found that there is a thin line at weld joint zone. Analysis of reasons: Metallurgical combination can increase the oxide absorption ability of zirconium alloy. Metallographic examination will find that there is a very

**Photo 14** 50× polarized light

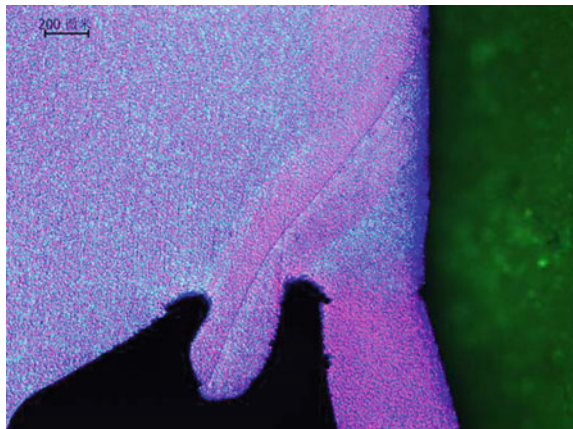


**Photo 15** 100 $\times$  polarized light

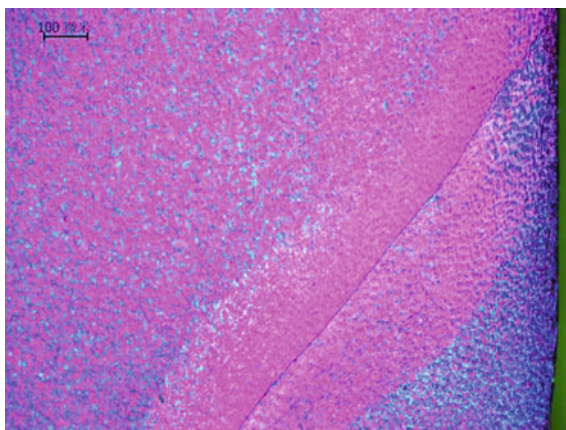


**Photo 16** 200 $\times$  polarized light

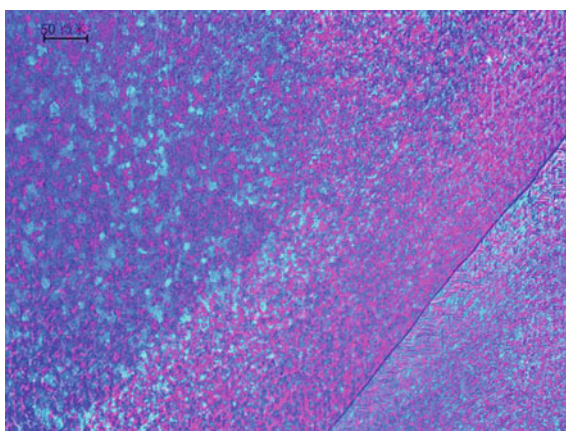


**Photo 17** 500 $\times$  polarized light

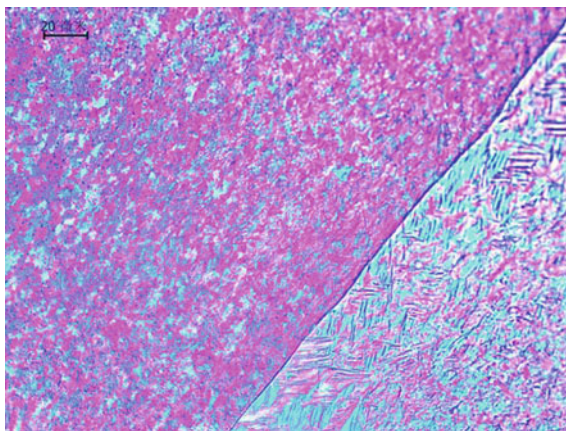
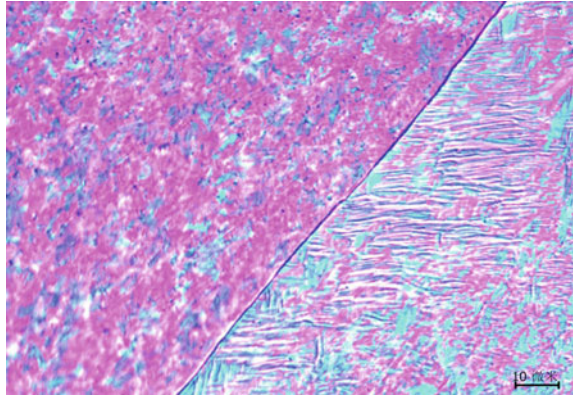


**Photo 18** 1000× polarized light



fine line at the original boundary of joint for the welding seam of different materials, called “welding line.” The welding line is composed of small oxide. During the preparation of metallographic specimen, the oxide is varying degrees by corrosion. Dash-dotted line can be observed under the microscope, but burst tests have proved that the existence of welding line does not affect the weld mechanical strength.

### 3.2.3 Corrosion Test

#### Specification of Inspection

Requirement: All the surface of welding seam shall be uniform black, no corrosion trace.

Testing: The sample shall be subjected to an autoclave test in pressurized water conditions according to ASTM G2.

#### The Analysis of Results

According to relevant inspection procedure, perform the water corrosion test. When welding current is 8000–14,000 A, routine observation surface (outside surface) of sample is uniform black oxide film (see Photo 19), and the inside surface of the sample (metallographic grinding surface) is uniform black oxide film (see Photo 20).

When the welding current is 15,000 A and electrode pressure is 2800 and 2900 N, all the corrosion samples have white corrosion mark (see Photo 21) and it does not meet requirements. Analysis of reasons: when high current matches with



**Photo 19** Outside surface of corrosion sample



**Photo 20** Inside surface of corrosion sample

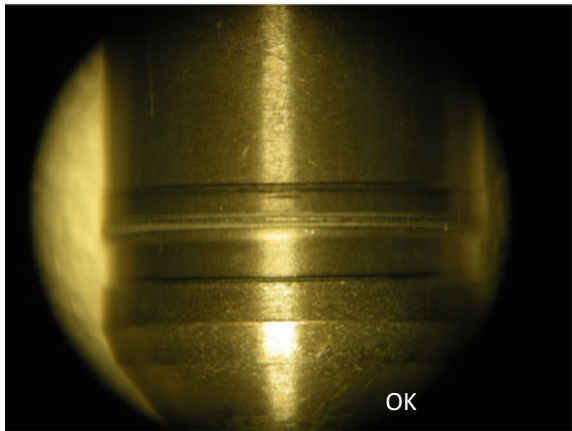
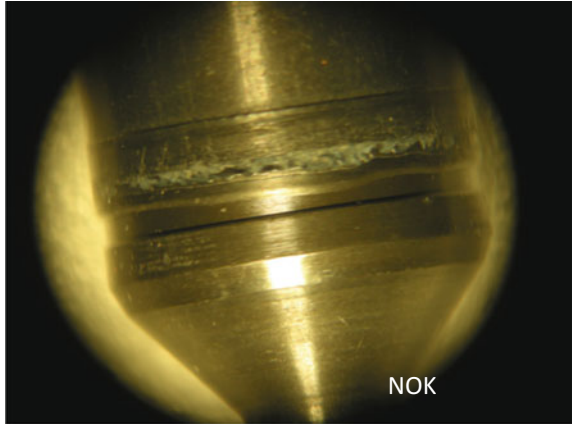


low electrode pressure, because of low electrode pressure and high welding current, the contact resistance of end plug, and cladding tube increases. Meanwhile, the resistance heat increases. There is high heating power at the welding joint and it cannot loss the heat in time during cooling crystallization stage. It makes that the welding seam is oxidized.

## 4 Conclusions

- (1) The low current welding process is easily to cause insufficient heat of the joint and plastic deformation is not concentrated, which causes weld bonding strength is not enough.
- (2) Using the Zr4 end plugs and M5 cladding tubes, there is a “welding line” at weld joint boundary. Burst tests have proved the existence of “welding line” does not affect the mechanical strength of welding seam.

**Photo 21** The corrosion picture of welding seam



- (3) When high current matches with the low electrode pressure, the weld seam is easy to have white corrosion due to oxidation in the corrosion test.

### Reference

1. City of Beijing-1990- *“Pressure welding” Engineering Industry Press, Zhao Xihua*

# Ultrasonic Test for Typical Defect of Zirconium Alloy Tube used in Nuclear Fuel Assembly

Jiangwu Ou

**Abstract** The zirconium cladding tube is the main component of PWR nuclear fuel assembly, and as the first protective barrier to prevent radiation production escaping, it is significant to environmental protection. After cladding tube production, a non-destructive testing is required, ultrasonic inspection is a main method. Through the analysis of the types of defects in the process of manufacturing, design, and production, artificial defects different in length, width, depth, and angles, both vertical and horizontal orientation, simulate analysis of the ultrasonic response to different component of defect. Aiming at the typical defects found during the inspection, develop inspect items, such as longitudinal, transverse defect, with longitudinal and transverse position defect, density defect, surface roughness, etc. Adopt metallographic anatomical analysis for some typical defects, and measure the actual shape and size to verify the inspection results.

**Keywords** Cladding tube · Ultrasonic test · Typical defect

## 1 Introduction

The zirconium cladding tube is the main component of PWR nuclear fuel assembly, and it has direct contact with the pellets, under high pressure, high temperature, high humidity, high irradiation, and cyclic flow erosion environment, high quality of cladding tube is required. At present PWR nuclear power plant, the cladding tube's outer diameter is about  $\Phi 9-11$  mm, wall thickness is about 0.4–0.8 mm, and belongs to the thin-wall tube in the classification. In the nuclear safety system, for cladding tube manufacturing, testing, retesting process need non-destructive testing, ultrasonic inspection is an efficient automated method with high detection sensitivity, high speed, and harmless to human body.

---

J. Ou (✉)

CNNC Jianzhong Nuclear Fuel Co., Ltd, Yibin 644000, Sichuan, China  
e-mail: 769383615@QQ.COM

In the process of rolling cladding tubes, the main defects generated are crack, pit, folding, surface scratch, etc. Ultrasonic inspection has high detection rate to this kind of area-type defect. Reference to the ASTM811 for the detection of thin-walled tube, take the water immersion ultrasonic line-focusing method, two vertical and two horizontal channels work parallel, defects of different types and directions can be detected, and there is an improvement the detection reliability. Designed and produced artificial defects with differences in length, width, depth, and angles, both vertical and horizontal orientation, debug the ultrasonic inspection equipment, simulate analysis of the ultrasonic response to different components of defect. Detect tubes with natural flaws and artificial defects, adopt metallographic anatomical analysis for some typical defects, and measure the actual shape and size to verify the inspection results.

## 2 Defects of Zirconium Alloy Cladding Tube

Cladding tube is obtained by perforator method and high speed extrusion method. Perforator method is used in piercing with the roller rolling, high speed extrusion method is a direct extrusion in an extruder, this method of processing tube has high size precision. The main defects in cladding tube are cracks, folding, and inclusions [1].

Longitudinal cracks—due to the improper heat treatment and machining.

Transverse cracks—due to the violent rolling, excessive heat, or cold processing.

Surface scratch—due to the process of catheter and the shape of the die-bad.

In the detection procession, not only unqualified tubes with defect signal higher than rejection line are removed, but also defects significantly higher than the average noise are concerned.

## 3 Water Immersion Ultrasonic Line-Focus Detection

Water immersion ultrasonic line-focus detection is placed along the longitudinal wave probes in water, acoustic beam obliquely incident to the water/tube interface, when the incident angle in a certain range, can obtain the pure shear wave [2]. Cladding tube belongs to the small diameter tube, general use of focus probe, there are line-focus and point-focus probe, generally use the line-focus probe. In order to detect small defect, choose high frequency to improve the inspection sensitivity. Automatic inspection equipment in general have two longitudinal and two horizontal parallel detection channels, probe mounted in rotating head, tube pass through the rotating head, longitudinal and transverse detection mode as shown in Fig. 1.

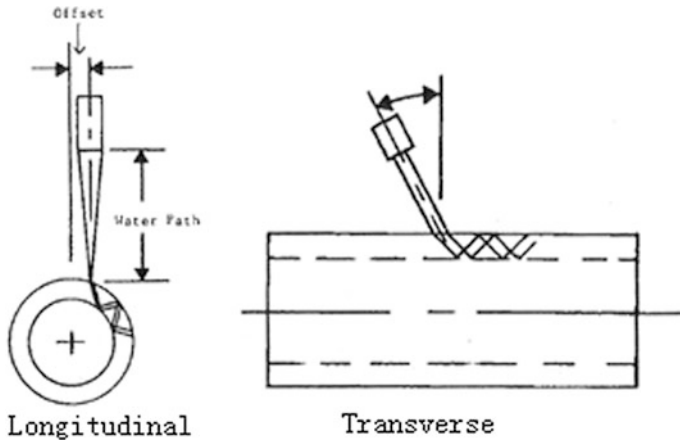


Fig. 1 Detection mode

According to the provisions of ASTM B811, for the thin-wall tube ultrasonic inspection, need to engrave longitudinal and transverse groove defects both in the tube inner surface and the outer surface [3]. The purpose of this paper is to test the detection ability for small defect, so produced specification of  $2.0 \times 0.1 \times 0.05$  mm (length  $\times$  width  $\times$  depth) defects in a qualified tube as the standard defect tube, with inner and outer longitudinal defects, inner and outer transverse defects. For the groove defect shape, on the basis of the current craft there are V-groove, U-groove,  $\Pi$ -(flat) groove defects [4]. Standard defect and artificial defect used herein are U-groove defects. This article takes the standard detection method of ASTM B811, for the ultrasonic line-focus probe, the frequency is 10 MHz, the effective beam length 5 mm ( $-3$  dB, EBL), the effective beam width 0.5 mm ( $-3$  dB, EBW). After debugging the ultrasonic inspection system, standard defects acoustic amplitude value records are shown in Fig. 2.

#### 4 Design and Test of the Artificial Defects

Design and produce different lengths, widths, depths of the longitudinal and transverse artificial U-groove defects, also produce a set of the same size but have different angles of U-groove shape defects, simulate analysis of the ultrasonic response to different components of defect.

4.1 produced 3 sets of longitudinal defects in the same test tube, the specification of defects are shown in Table 1, the ultrasonic testing results are shown in Fig. 3.

For longitudinal defects:

- (1) When the defect length  $<$  the effective beam length (5 mm), when the defect length increases, the acoustic amplitude value increases; when defect

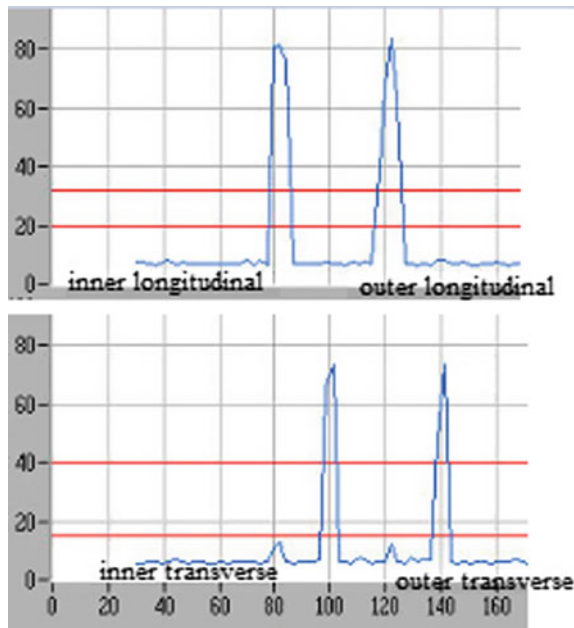


Fig. 2 Standard defects records

Table 1 Longitudinal defects (length × width × depth)

Different lengths (mm)	Different widths (mm)	Different depths (mm)
1.5 × 0.08 × 0.05	3.0 × 0.05 × 0.05	1.5 × 0.08 × 0.035
2.2 × 0.08 × 0.05	3.0 × 0.07 × 0.05	1.5 × 0.08 × 0.050
3.0 × 0.08 × 0.05	3.0 × 0.08 × 0.05	1.5 × 0.08 × 0.070
5.0 × 0.08 × 0.05	3.0 × 0.11 × 0.05	1.5 × 0.08 × 0.100
7.0 × 0.08 × 0.05	3.0 × 0.16 × 0.05	1.5 × 0.08 × 0.130

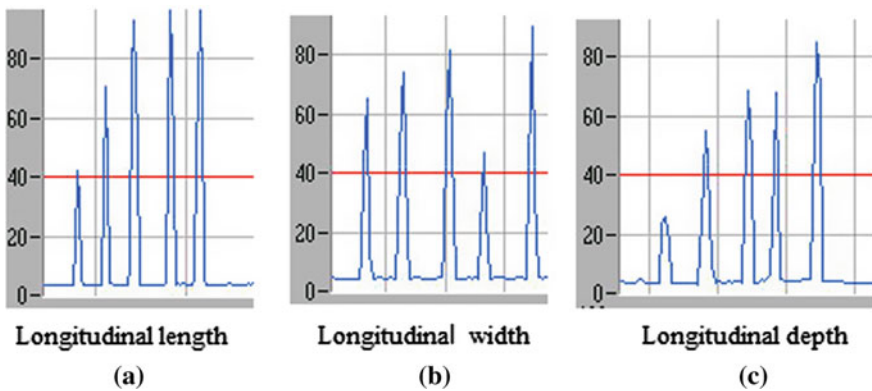
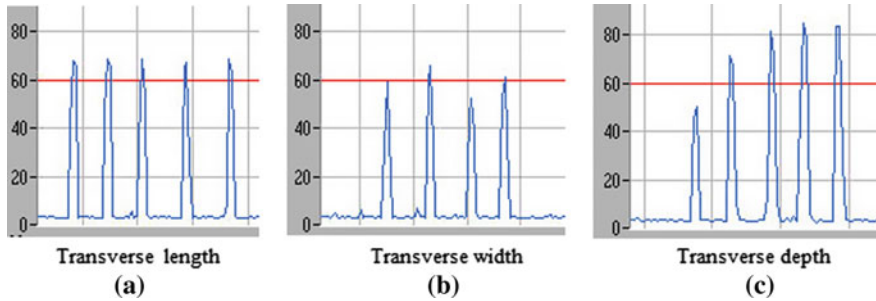


Fig. 3 Longitudinal defects amplitude records

**Table 2** Transverse defects (length × width × depth)

Different lengths (mm)	Different widths (mm)	Different depths (mm)
1.5 × 0.11 × 0.07	3.0 × 0.05 × 0.05	2.5 × 0.07 × 0.03
2.5 × 0.11 × 0.07	3.0 × 0.08 × 0.05	2.5 × 0.07 × 0.05
3.0 × 0.11 × 0.07	3.0 × 0.11 × 0.05	2.5 × 0.07 × 0.07
5.0 × 0.11 × 0.07	3.0 × 0.16 × 0.05	2.5 × 0.07 × 0.08
7.0 × 0.11 × 0.07	–	2.5 × 0.07 × 0.10



**Fig. 4** Transverse defects amplitude records

length ≥ EBL, the defect length increases, no more increase in echo amplitude, as shown in Fig. 3a;

- (2) When the defect width < 2 × depth (3.0 × 0.11 × 0.05 mm), the echo amplitude of defects increases with the width increase; when width near more than 2 × depth, echo amplitude will be the lowest value, as shown in Fig. 3b;
- (3) With increase in the depth, the echo amplitude value increases, as Fig. 3c shown.

4.2 produced 3 sets of transverse defects in the same test tube, the specification of defects are shown in Table 2, the ultrasonic testing results are shown in Fig. 4. For transverse defects:

- (1) The length of defects are greater than the effective beam width (0.5 mm), so the echo amplitude is basically the same, for the standard artificial transverse defects, in general its length is about 3 × to 10 × of EBW, as shown in Fig. 4a;
- (2) The echo amplitude of different widths of defects were basically the same, but when the width is nearly more than 2 × depth (3 × 0.11 × 0.045 mm), the echo amplitude is low than others, but not that obvious in the longitudinal case, as shown in Fig. 3b;
- (3) The depth increases when the echo amplitude value increase, as shown in Fig. 4c.

For the width near more than 2 × depth, amplitude record is the lowest value, both longitudinal and transverse detection. In this case, the cross section of

U-shape groove defect is semicircular, the acoustic beam scattering in the circular curved surface is most serious, The defect signal reflected back to be received by the probe decreases, so the echo amplitude value is lower [5].

4.3 Produce a set of the same size ( $2.5 \times 0.07 \times 0.05$  mm) but have different angles of U-groove shape defects in the range of 200–300 mm, from the center line of the tube with  $15^\circ/30^\circ/45^\circ/60^\circ/75^\circ$ , the specification of defects are shown in Table 3, the ultrasonic testing results are shown in Fig. 5.

**Table 3** Defects with angles

Different angles ( $l \times w \times d$ ) (mm)	
0°	$2.5 \times 0.07 \times 0.05$ (longitudinal)
15°	$2.5 \times 0.07 \times 0.05$
30°	$2.5 \times 0.07 \times 0.05$
45°	$2.5 \times 0.07 \times 0.05$
60°	$2.5 \times 0.07 \times 0.05$
65°	$2.5 \times 0.07 \times 0.05$
75°	$2.5 \times 0.07 \times 0.05$
90°	$2.5 \times 0.07 \times 0.05$ (transverse)

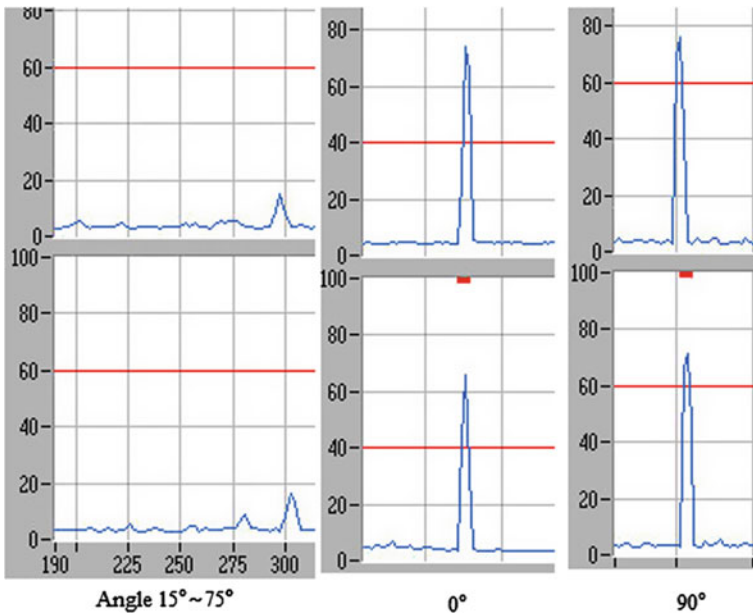


**Fig. 5** Inclined defects amplitude records



For defects with angle:

The longitudinal channels and the transverse channels making lower or obscure echo amplitude value to them; while for the defect  $0^\circ$ ,  $90^\circ$ , respectively, inspected by the longitudinal and transverse channel.

### 5 Application Experiments

During the natural defect tube testing, obtain longitudinal defects, transverse defects, with vertical and horizontal position defect, densely defects and abnormal noise, set them as typical defects items for tube ultrasonic inspection. Specific examples of amplitude records are shown in Fig. 6.

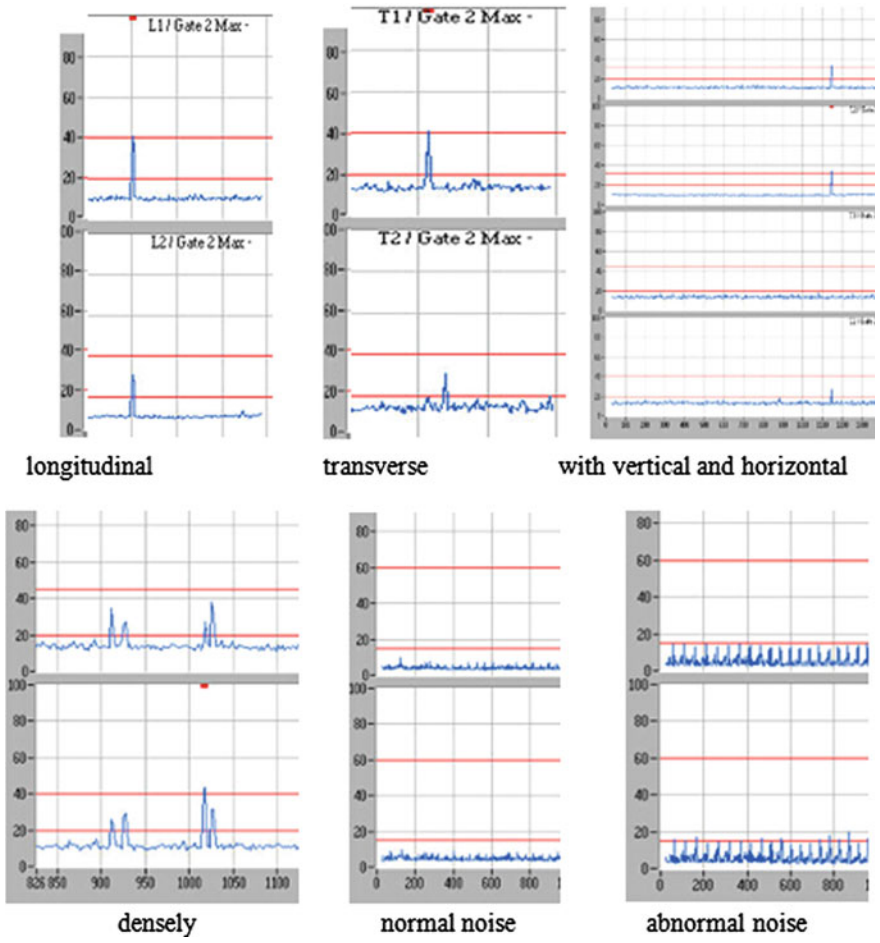
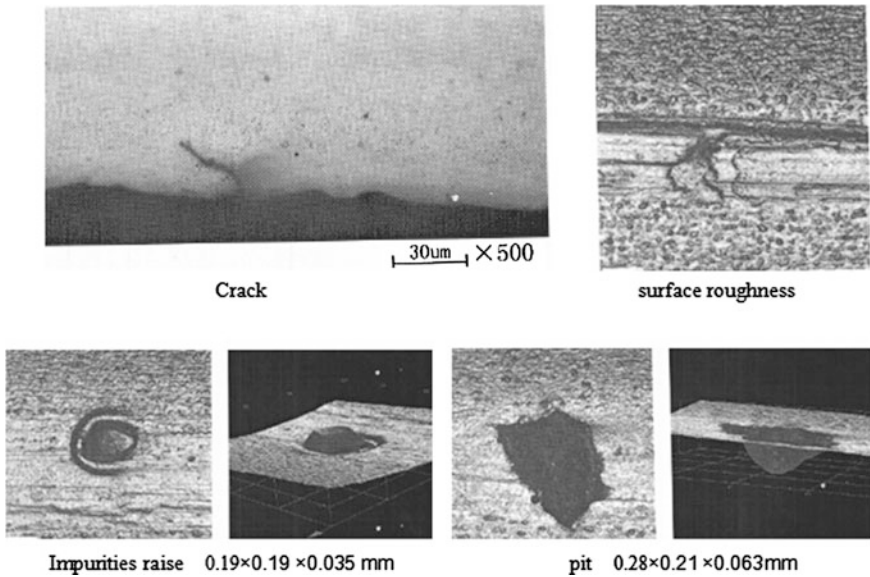


Fig. 6 Example of typical nature defects amplitude records



**Fig. 7** Example of metallurgical analysis for natural defects

After testing, and obtaining the typical defects, take optical microscopy and anatomy method to measure its actual size, confirms the ultrasound test results, Specific examples are shown in Fig. 7.

Through the practical analysis:

- (1) Only detected in the longitudinal channels substantially be longitudinal cracks; only detected in the transverse channels substantially be transverse cracks. Both detected by vertical and horizontal channels substantially be diagonal cracks or point bulge, pits.
- (2) For natural defect, because its shape is irregular, there is always a part of echo signal reflected back, the scattering wave caused by the interaction of sound beam and the defect partly received by probe formatting the signal of defects [6].
- (3) The abnormal noise caused by improper polishing, pickling, or long straight scratch.

## 6 Conclusions

- (1) After testing the typical longitudinal and transverse artificial defects as well as the experiment of nature defects test, tiny defects can be detected.

Water immersion ultrasonic line-focus method is applicable to the zirconium cladding tube automatic inspection, with high precision and sensitivity.

- (2) The type of defect, size, orientation, affect the echo amplitude. When width is nearly more than 2 times of the depth, echo height is the lowest value, both longitudinal and transverse detection. In this case, the cross section of U-shape groove defect is semicircular, acoustic beam scattering in the circular curved surface is most serious.
- (3) Ultrasonic inspection is not sensitive to the artificial defect with angles. With the angle relation, only a small part of reflect signal backtrack to be received by probe. Also, there are some differences in the detection results and its actual defect size.

## References

1. DENG HUI, LIN SHUQING, Ultrasonic testing second edition. Beijing: The Chinese Labor and Social Security Publishing House, 2008
2. HE YAN, GUO CHONGXIONG, ZHANG LONG, Thin-walled steel ultrasonic immersion testing [J], physical testing, 2003, (04)
3. ASTM B 811-02(2007) Standard Specification for Wrought Zirconium Alloy Seamless Tubes for Nuclear Reactor Fuel Cladding
4. JB/T4730.3-2005 Nondestructive testing of pressure equipments—Part3: Ultrasonic testing
5. YING CF, TRUELL R. Scattering of a plane longitudinal wave by a spherical obstacle in an In-tropically elastic soiled [J]. J. Appl-phys. 1956.27(9):1086–1097
6. KOLKOORI SR, RAHMAN MU, CHINTA PK, et al. Ultrasonic field profile evaluation in acoustically in homogenous anisotropic materials using 2D ray tracing model: Numerical and experimental comparison[J]. Ultrasonics, 2013(53):396–411

## Author Biography

**Ou Jiangwu** Male, born in 1991, graduated in University of South China. Since July 2012 working in the Laboratory of Physical and Chemical, CJNF. Engaged in Zirconium alloy and Stainless steel alloy material ultrasonic testing, such as tubes, bars, etc.

**Part IV**  
**New Technology and New Applications**

# A Deconvolution Algorithm for Gamma Spectrum Based on Energy Resolution Calibration

Rui Shi, Xianguo Tuo, Honglong Zheng, Huailiang Li  
and Junyu Zhou

**Abstract** A deconvolution algorithm with response function based on energy resolution calibration was presented. A  $^{152}\text{Eu}$  gamma spectrum was detected by a  $\text{LaBr}_3(\text{Ce})$  scintillator. The energy resolution calibration was best fitted by a square root of a quadratic function, based on which the detector response matrix was constructed connected with the energy, and the boosted Gold deconvolution algorithm was applied. The deconvolution results are better than the fixed response function with a constant standard deviation.

**Keywords** Deconvolution · Detector response matrix · Energy resolution calibration ·  $\text{LaBr}_3(\text{Ce})$  scintillator · SNIP background elimination

---

R. Shi

Chengdu University of Technology, Chengdu, Sichuan 610059, China  
e-mail: shirui0601@126.com

R. Shi · X. Tuo · H. Zheng

Sichuan University of Science & Engineering, Zigong, Sichuan 643000, China  
e-mail: 965998755@qq.com

X. Tuo (✉) · H. Zheng · H. Li

Fundamental Science on Nuclear Wastes and Environmental Safety Laboratory,  
Mianyang, Sichuan 21010, China  
e-mail: tuoxg@cdut.edu.cn

H. Li

e-mail: leehl@swust.edu.cn

J. Zhou

Sichuan Central Station of Radiation Environmental Monitoring, Chengdu  
Sichuan 61139, China  
e-mail: yagamizero@foxmail.com

© Springer Science+Business Media Singapore 2017

H. Jiang (ed.), *Proceedings of The 20th Pacific Basin Nuclear Conference*,  
DOI 10.1007/978-981-10-2317-0\_63

## 1 Introduction

Gamma spectrum analysis always is a significant work in  $\gamma$  spectrum detection. The gamma spectrum analysis consists of qualitative and quantitative analysis. The qualitative analysis is about nuclide identification by energy calibration, and the quantitative analysis is to calculate the peak area and contents of nuclide. To sum up, there are two categories about the methods of peak area calculation. First and also the easiest method is sum of each channel's counts, but this method is only suitable for a single peak. Second is function fitting method that is fitting the spectrum data with a function and obtaining the peak area by integral of this function. This method is complicated but suitable for overlapping peaks [1]. The fitting function is also called detector response function [2]. For the limited resolution detector like NaI(Tl), LaBr<sub>3</sub>(Ce), the overlapping peak is a common situation, then the peak decomposition is essential.

From the signaling system point of view, the spectrum is the convolution by input impulse signal with the detector response function. Therefore, in theory, we can invert out the input radiation signal through deconvolution. In 1997, the Morhac et al. [3] employed the Gold deconvolution algorithm into gamma spectrum unfolding, which is an iteration algorithm proposed by Gold [4] in 1964. There are some other deconvolution algorithms such as Richardson–Lucy algorithm [5], maximum a posteriori deconvolution algorithm [6], and so on. In essence, these deconvolution algorithm is to solve an equation set with ill-posed problem using iteration algorithm [7], so the construction of the detector response matrix is the most important. For the gamma spectrum, the resolution FWHM will increase along with the energy increase. The purpose of this work is to improve the accuracy of gamma spectrum deconvolution by constructing a detector response matrix based on establishing the relationship of FWHM with energy.

## 2 Gold Deconvolution Algorithm

The detection system can be seen as a signaling system, shown as Fig. 1.

So the gamma spectrum  $y(x)$  is the convolution by input gamma ray function  $f(x)$  with the system's response function  $h(x)$ , and in ideal conditions, the  $f(x)$  is a  $\delta$  function.

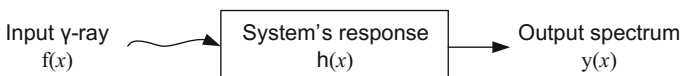


**Fig. 1** Simplified signaling system of detector

$$y(x) = h(x) * f(x) = \int_{-\infty}^{+\infty} h(x - t)f(t) dt \tag{1}$$

For a discrete system

$$y(i) = \sum_{k=0}^{N-1} h(i - k)f(k), \quad i = 0, 1, 2, \dots, N - 1 \tag{2}$$

where  $N$  is the length of  $f$  and  $h$  vectors. In matrix form we have

$$y = Hf$$

$$\begin{bmatrix} y(0) \\ y(1) \\ y(2) \\ \vdots \\ \vdots \\ \vdots \\ h(N-1) \\ 0 \\ 0 \\ \vdots \\ y(2N-2) \\ y(2N-1) \end{bmatrix} = \begin{bmatrix} h(0) & 0 & 0 \cdots \\ h(1) & h(0) & 0 \cdots \\ h(2) & h(1) & h(0) \cdots \\ \vdots & \vdots & \vdots \\ \vdots & \vdots & \vdots \\ h(N-1) & h(N-2) & h(N-3) \cdots \\ 0 & h(N-1) & h(N-2) \cdots \\ 0 & 0 & h(N-1) \cdots \\ \vdots & \vdots & \vdots \end{bmatrix} \begin{bmatrix} f(0) \\ f(1) \\ f(2) \\ \vdots \\ \vdots \\ f(N-1) \end{bmatrix} \tag{3}$$

Let us assume that we know the response and the output vector (spectrum) of the above given system. The deconvolution represents solution of the overdetermined system of linear equations, i.e., the calculation of the vector  $f$ .

The goal of the deconvolution methods is to improve the resolution in the spectrum and to decompose multiplets. From all the methods studied the Gold deconvolution (decomposition) proved to work as the best one [8, 9]. It is suitable to process positive definite data (e.g., histograms) [10].

In detail the method is described in [3].

$$y = Hf$$

$$H^T y = H^T H y$$

$$A = H^T H, \quad y' = H^T y \tag{4}$$

$$f_i^{(n+1)} = \frac{y'_i}{\sum_{m=0}^{N-1} A_{im} f_m^{(n)}}, \quad i = 0, 1, 2, \dots, N - 1$$

where  $n$  is the iterations times, and the initial values  $f^{(0)} = [1, 1, \dots]^T$ .

Equation (3) is the Gold algorithm of deconvolution. It is an extension of Van Cittert's iterative method [8]. The advantage of Gold's method is that the solution  $f$  is positive. But, the method is not able to concentrate the peak into the  $\delta$ -function. In 2011, Morháč et al. [11] presented a high-resolution deconvolution algorithm in which a boosting coefficient was introduced to concentrates the area of the peak completely into one channel. The detail of this algorithm was elaborated in Ref. [11].

### 3 Response Matrix Construction Based on Resolution Calibration

The detector response function can be simplified as a full-energy peak function after the elimination of background. In order to simplify the calculation process, a simple Gaussian where  $n$  is the iterations times, and the initial values function can be used as the detector response function [12].

With the increase of energy, the energy resolution of the detector become poor, that is the full width of half maximum (FWHM) of peak increases [13, 14]. Therefore, one can consider to construct a detector response matrix based on establishing the relationship of FWHM with energy.

The energy resolution is determined by three factors [15]: the statistics of the charge-creation process, the uncertainty in charge collection process, and the electronic noise. A simplified energy resolution model connected with energy following the equation [16]:

$$\eta^2 = \left( \frac{\text{FWHM}}{E} \right)^2 = a + \frac{b}{E} \quad (5)$$

Equation (5) indicate that the square of energy resolution  $\eta^2$  has linear relationship with the reciprocal of the energy  $1/E$ . So one can figure the  $1/E$  as the  $x$  axis and  $\eta^2$  as  $y$  axis and fitting out the parameters  $a$  and  $b$ . But according to our experiment data, in fact,  $\eta^2$  is quadratic polynomial relationship with  $1/E$ . So Eq. (5) can be changed as

$$\eta^2 = \left( \frac{\text{FWHM}}{E} \right)^2 = a + \frac{b}{E} + \frac{c}{E^2} \quad (6)$$

When  $c$  approaches to 0, Eq. (6) is same as (5).

So the relationship of FWHM with energy  $E$  is expressed as



$$FWHM = \sqrt{a \cdot E^2 + b \cdot E + C} \tag{7}$$

And the standard deviation  $\sigma$  of Gaussian function is

$$\sigma(E) = \frac{1}{2.355} FWHM = \frac{1}{2.355} \sqrt{aE^2 + bE + C} \tag{8}$$

For the discrete gamma spectrum data, each channel corresponds to different energy. The detector response function with Gaussian function is expressed as

$$h_m(i, \sigma_m) = \frac{1}{\sqrt{2\pi}\sigma} \exp\left(-\frac{(i - u)^2}{2\sigma_m^2}\right), \tag{9}$$

$i = 0, 1, 2, \dots, N - 1. m = 0, 1, 2, \dots, N - 1$

which indicates that different energy has different response function. So Eq. (2) is changed as

$$\begin{bmatrix} y(0) \\ y(1) \\ y(2) \\ \vdots \\ \vdots \\ \vdots \\ \vdots \\ \vdots \\ \vdots \\ y(2N - 2) \\ y(2N - 1) \end{bmatrix} = \begin{bmatrix} h_1(0, \sigma_1) & 0 & 0 & \dots \\ h_1(1, \sigma_1) & h_2(0, \sigma_2) & 0 & \dots \\ h_1(2, \sigma_1) & h_2(1, \sigma_2) & h_3(0, \sigma_3) & \dots \\ \vdots & \vdots & \vdots & \vdots \\ h_1(N - 1, \sigma_1) & h_2(N - 2, \sigma_2) & h_3(N - 3, \sigma_3) & \dots \\ 0 & h_2(N - 1, \sigma_2) & h_3(N - 2, \sigma_3) & \dots \\ 0 & 0 & h_3(N - 1, \sigma_3) & \dots \\ \vdots & \vdots & \vdots & \vdots \end{bmatrix} \begin{bmatrix} f(0) \\ f(1) \\ f(2) \\ \vdots \\ \vdots \\ \vdots \\ f(N - 1) \end{bmatrix} \tag{10}$$

in which the response matrix is consisted with different response function based on resolution calibration.

### 4 Background Elimination

Background elimination is an essential process for quantitative spectral analysis. On the other hand, the background affects the accuracy of the deconvolution unless the background can be removed from the measured spectrum [17]. SNIP ( Statistics sensitive Nonlinear Iterative Peak-clipping) algorithm has been proved as the most

efficient to eliminate the background of a spectrum [18–20]. Morháč improved the SNIP algorithm based on a clipping operation with the window adjustable automatically to the width of identified peak regions and proposed smoothing in iteration process, and the detail has been demonstrated in Ref. [18].

## 5 Results and Discussion

The LaBr<sub>3</sub>(Ce) scintillators, with good energy resolution (3.2 %@662 keV) and very high light output (~60,000 photons MeV) and fast principal decay constant (~25 ns), are paid more and more attention in the field of radiation detection and have the potential instead of NaI(Tl) detector [21]. However, the energy resolution of the LaBr<sub>3</sub>(Ce) scintillator is still poor compared with the HPGe detector so that the overlapping peak is exist. In this work, in order to test the new Gold deconvolution algorithm base on the resolution calibration, a <sup>152</sup>Eu gamma source was detected by a LaBr<sub>3</sub>(Ce) scintillator detector. The background was eliminated according to the improved Gold algorithm proposed by Morháč in Ref. [18].

### 5.1 Energy Resolution Calibration

Several independent peaks are chosen to calibrate energy resolution, shown in Table 2. There are some other resolution calibration fit functions except for the

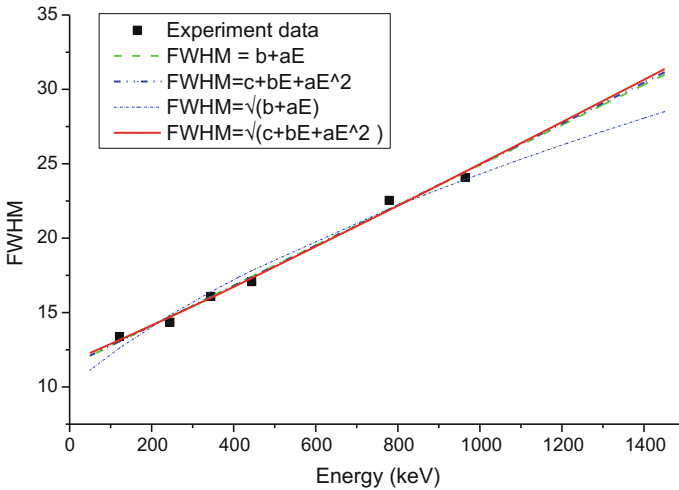


Fig. 2 Energy resolution calibration using four fit functions

**Table 1** Fitted functions with their coefficients of determination

Fitted FWHM functions	$R^2$
$FWHM = b + aE$	0.9912
$FWHM = c + bE + aE^2$	0.9912
$FWHM = \sqrt{b + aE}$	0.9811
$FWHM = \sqrt{c + bE + aE^2}$	0.9914

function (7). Four different functions have been involved in resolution calibration to compare [15, 22]: a linear function ( $FWHM = b + aE$ ), a quadratic polynomial ( $FWHM = c + bE + aE^2$ ), a square root of a linear function ( $FWHM = \sqrt{b + aE}$ ), and a square root of a quadratic function ( $FWHM = \sqrt{c + bE + aE^2}$ ) that is function (7). The fit results are shown in Fig. 2, and the accuracy of the fit was evaluated with the coefficient of determination  $R^2$ , shown in Table 1.

From the results of Table 1, the relationship that the best fit for the experimental data is  $FWHM = \sqrt{c + bE + aE^2}$ . This function also has a friendly mathematical form. When uses this function to calibrate the energy resolution, one can firstly fit energy resolution  $\eta^2$  with reciprocal of the energy  $1/E$  according to the Eq. (6) to determine the coefficients  $a, b, c$ .

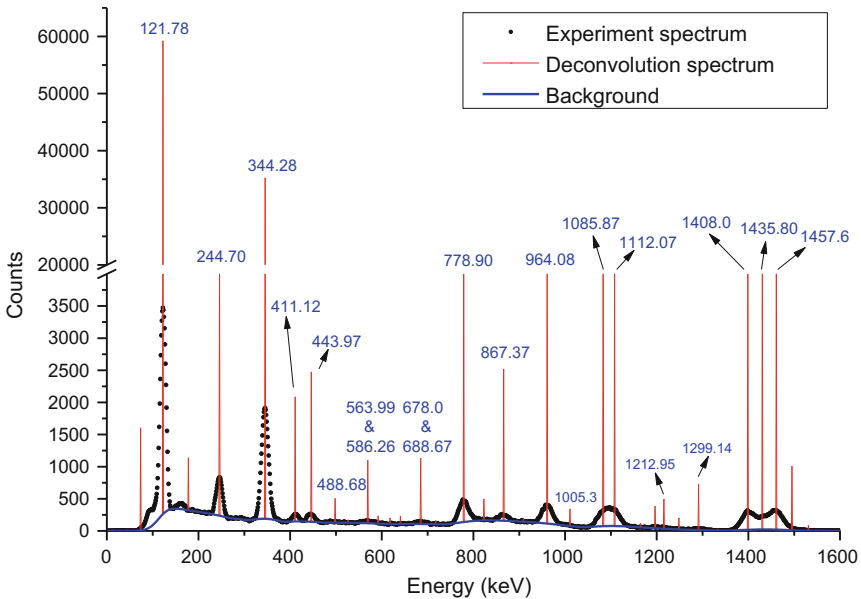


**Fig. 3**  $^{152}\text{Eu}$  experimental spectrum and deconvolved spectrum using Gold deconvolution algorithm based on energy resolution calibration, in which the background was eliminated by improved SNIP algorithm proposed by Morháč in Ref. [10]

**Table 2** Independent peaks and their FWHM used to calibrate energy resolution. The comparison of the peak position of experiment and deconvolution, the peak area of experiment and deconvolution

Energy (keV)	FWHM	Experimental peak position	Deconvolved peak position	Experimental peak area	Deconvolved peak area	Peak area error (%)
121.7817	13.3950	106	106	47,291	58,740	-0.2421
244.6975	14.3536	215	216	8820	11,060	-0.2540
344.2785	16.0862	303	303	28,837	34,890	-0.2099
443.9650	17.0750	391	393	1989	2325	-0.1689
778.9040	22.5400	685	687	8116	8481	-0.0450
964.0790	24.0775	849	848	7311	7610	-0.0409

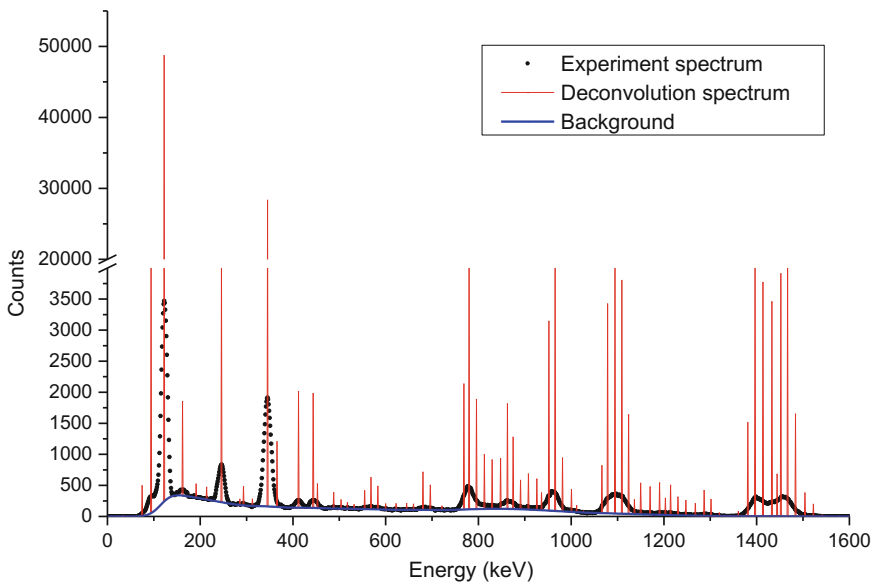


**Fig. 4**  $^{152}\text{Eu}$  experimental spectrum and deconvolved spectrum using Gold deconvolution algorithm with the Gaussian response function using a constant standard deviation

## 5.2 Deconvolution Based on Energy Resolution Calibration

According to the matrix Eq. (10), the response matrix with Gaussian response function based on resolution calibration can be constructed. The results of deconvolution are shown in Fig. 3. The peak position and area of experiment and deconvolution are shown in Table 2.

From the results of Table 2, we can see that the peak position difference between deconvolution and experiment is within  $\pm 2$  channels. This demonstrates that the deconvolution algorithm is accurate for peak position. However, the deconvolved peak area is larger than the experimental peak area calculated by total peak area

(TPA) algorithm [15], especially at low energy, nevertheless, the deconvolved peak area error based on the experimental peak area is decrease with the energy increase. This is caused by the incomplete background elimination of low energy scattering by SNIP algorithm.

For comparison, the response matrix with the Gaussian response function having a constant standard deviation was carried out. In this work, we use the 121.78 keV peak's standard deviation as an example and the results are shown in Fig. 4.

From Fig. 4, we can see that, in low energy region, the deconvolution result is good, but in high energy region there are many sundry peaks appearing, which demonstrates that using this constant standard deviation for deconvolution is only suitable for the low energy not for the high energy. However, from Fig. 3, we can see that, when the response matrix was constructed based on resolution calibration, the results are apparently better than the Fig. 4. All characteristic peaks are converged to  $\delta$  functions. In addition, the overlapped peaks can be separated such as 1085.87 and 1112.07 keV, but 563.99 and 588.26 keV and 678.00 and 688.67 keV cannot be separated possible reasoned by the counts insufficient. On the other hand, it is worth noting that the radioactivity of  $^{138}\text{La}$ -1435.8 keV emitted from  $\text{LaBr}_3(\text{Ce})$  materials can be completely identified, and this is very important for the  $\text{LaBr}_3(\text{Ce})$  detector's  $\gamma$  spectrum analysis.

## 6 Conclusions

In this study, we presented a deconvolution algorithm with response function based on energy resolution calibration. There have developed several deconvolution algorithms so far, and we just highlight the Gold algorithm and a  $^{152}\text{Eu}$  gamma spectrum was used to test.

For energy resolution calibration, four different functions have been involved, and the best fit function for our experimental data is a square root of a quadratic function. Based on the energy resolution calibration, the detector response matrix was constructed connected with the energy. The background is eliminated by the improved SNIP algorithm with the window adjustable automatically to the width of identified peak regions. The deconvolution results are better than the fixed response function with a constant standard deviation. Additionally, this algorithm of response matrix's construction is also suitable for another deconvolution algorithm. Furthermore, the Monte Carlo simulation is another good method to constructed response function and it is a good idea for further researching.

**Acknowledgments** This work has been supported by the National Natural Science Foundation of China (No. 41374130, 41374112) and National Projects Major Scientific Instruments and Equipment Development of China (No. 2012YQ180118).

## References

1. LI Zhe. X-ray Detector Response Mechanism and Applied Modeling Technology (Ph.D Thesis). Chengdu: Chendu University of Technology, 2013. (in Chinese).
2. Li Z, Zhang Y, Sun S, et al. A semi-empirical response function for Gamma-ray of Scintillation detector based on physical interaction mechanism[J]. arXiv preprint arXiv:1407.0799, 2014.
3. Morháč M, Kliman J, Matoušek V, et al. Efficient one- and two-dimensional Gold deconvolution and its application to  $\gamma$ -ray spectra decomposition[J]. Nuclear Instruments and Methods in Physics Research Section A: Accelerators, Spectrometers, Detectors and Associated Equipment, 1997, 401(2): 385–408.
4. R. Gold. An iterative unfolding method for matrices, in: Mathematics and Computer Research and Development Rep. ANL-6984. Argonne National Laboratory. Argone, III. 1964.
5. Lucy L B. An iterative technique for the rectification of observed distributions[J]. The astronomical journal, 1974, 79: 745.
6. Olofsson T, Stepinski T. Maximum a posteriori deconvolution of sparse ultrasonic signals using genetic optimization[J]. Ultrasonics, 1999, 37(6): 423–432.
7. Morháč M. Deconvolution methods and their applications in the analysis of  $\gamma$ -ray spectra[J]. Nuclear Instruments and Methods in Physics Research Section A: Accelerators, Spectrometers, Detectors and Associated Equipment, 2006, 559(1): 119–123.
8. Bandžuch P, Morháč M, Krištiak J. Study of the Van Cittert and Gold iterative methods of deconvolution and their application in the deconvolution of experimental spectra of positron annihilation[J]. Nuclear Instruments and Methods in Physics Research Section A: Accelerators, Spectrometers, Detectors and Associated Equipment, 1997, 384(2): 506–515.
9. Beatham N, Orchard A F. The application of Fourier transform techniques to the problem of deconvolution in photoelectron spectroscopy[J]. Journal of Electron Spectroscopy and Related Phenomena, 1976, 9(2): 129–148.
10. Morháč M, Matoušek V. Complete positive deconvolution of spectrometric data[J]. Digital Signal Processing, 2009, 19(3): 372–392.
11. Morháč M, Matoušek V. High-resolution boosted deconvolution of spectroscopic data[J]. Journal of Computational and Applied Mathematics, 2011, 235(6):1629–1640.
12. Li Z, Tuo X G, Shi R, et al. A statistical approach to fit Gaussian part of full-energy peaks from Si (PIN) and SDD X-ray spectrometers[J]. Science China Technological Sciences, 2014, 57(1): 19–24.
13. Zhe L I, Xianguo T U O, Rui S H I, et al. Analytic fitting and simulation methods for characteristic X-ray peaks from Si-PIN detector[J]. Nuclear Science and Techniques, 2013, 24(6): 60206–060206.
14. Zhe L, Xian-Guo T, Jian-Bo Y, et al. Statistical distribution based detector response function of a Si (PIN) detector for  $K\alpha$  and  $K\beta$  X-ray[J]. Chinese Physics C, 2013, 37(1): 018202.
15. K. Debertin, R. Helmer, Gamma- and X-ray Spectrometry with Semiconductor Detectors, North- Holland, Amsterdam, 1988.
16. Pang J F. Gamma Energy Spectroscopy Analysis 3, 1990. (in Chinese).
17. Lei L, Xian-Guo T, Ming-Zhe L, et al. High-resolution boosted reconstruction of  $\gamma$ -ray spectra [J]. Nuclear science and techniques, 2014, 25(5).
18. Morháč M. An algorithm for determination of peak regions and baseline elimination in spectroscopic data[J]. Nuclear Instruments and Methods in Physics Research Section A: Accelerators, Spectrometers, Detectors and Associated Equipment, 2009, 600(2): 478–487.
19. Ryan C G, Clayton E, Griffin W L, et al. SNIP, a statistics-sensitive background treatment for the quantitative analysis of PIXE spectra in geoscience applications[J]. Nuclear Instruments and Methods in Physics Research Section B: Beam Interactions with Materials and Atoms, 1988, 34(3): 396–402.
20. Morháč M, Matoušek V. Peak clipping algorithms for background estimation in spectroscopic data[J]. Applied spectroscopy, 2008, 62(1): 91–106.

21. Shah K S, Glodo J, Klugerman M, et al. LaBr3: Ce scintillators for gamma-ray spectroscopy [J]. Nuclear Science, IEEE Transactions on, 2003, 50(6): 2410–2413. [22] G. Gilmore, J. Hemingway, Practical Gamma-Ray Spectrometry, Wiley, New York, 1995.
22. G. Gilmore, J. Hemingway, Practical Gamma-Ray Spectrometry, Wiley, New York, 1995.

# A Potential Way of Co-60 Production in CANDU6 Reactors

Jinqi Lyu, Mohammad Abdul Motalab, Younwon Park and Yonghee Kim

**Abstract** In addition to electricity generation, CANDU6 reactors are used to produce Co-60, which is an important radioactive nuclide used in many industrial areas. In this study, an innovative way of producing Co-60 in CANDU6 reactors is introduced. Unlike the conventional Co-60 production scheme using the adjuster rods in CANDU6 reactors, the central fuel element is replaced by Co-59 together with graphite or SiC in this study and Co-60 is obtained after the fuel bundle is discharged. To improve the generic safety of the Co-loaded CANDU6 core, the CANFLEX fuel is also considered and compared with the standard fuel bundle. To investigate such a new and innovative Co-60 production scheme in CANDU6 reactors, various lattice depletion studies are performed to determine the possible amount of Co-59 loading and to derive an optimal material composition in the center pin of a fuel bundle. Through the lattice depletion analysis, the achievable fuel burnup is evaluated and the possible Co-60 production capacity has also been calculated with several neutronic assumptions. For the lattice analysis, the fuel discharge burnup is calculated based on the nonlinear reactivity theory. Coolant void reactivity is also evaluated and compared with that of the standard CANDU6 lattice. Lattice power distribution is also evaluated for different cases. All the neutronic analyses are performed with the continuous-energy Monte Carlo code Serpent in this work.

**Keywords** Co-60 · CANDU6 · Serpent · Coolant void reactivity · CANFLEX

---

J. Lyu · M.A. Motalab · Y. Kim (✉)

Department of Nuclear and Quantum Engineering, KAIST, Daejeon, South Korea

e-mail: yongheekim@kaist.ac.kr

J. Lyu

e-mail: lyujq@kaist.ac.kr

M.A. Motalab

e-mail: motalab@kaist.ac.kr

Y. Park

BEES Inc., Daejeon, South Korea

© Springer Science+Business Media Singapore 2017

H. Jiang (ed.), *Proceedings of The 20th Pacific Basin Nuclear Conference*,

DOI 10.1007/978-981-10-2317-0\_64



## 1 Introduction

Co-60 is a high intensity gamma-ray emitter, which has fundamental applications in medical, industry, and many other fields. The basic technology for Co-60 producing was developed by MDS Nordion and Atomic Energy of Canada Limited (AECL) in 1946 by using a research reactor at the AECL Chalk River Laboratory. In their experiments, a Co-59 target was introduced into a research reactor where the Co-59 atom absorbed one neutron and then became Co-60. The same technology was adapted and applied in a CANDU6 power reactor. The standard CANDU6 reactor has 21 so-called adjuster rods which are fully inserted into the core during normal operation. The stainless steel adjuster rods are replaced with neutronicallly equivalent Co-59 adjusters to produce Co-60. With high neutron flux and optimized fuel burnup, CANDU6 reactors have a high Co-60 production rate in a relatively short time [1].

In some Canadian CANDU6 reactors, some or all the adjuster rods are removed from the core to maximize the uranium utilization [2]. Meanwhile, the roles of the adjuster rods are nowadays rather vague since nuclear reactors cannot be quickly restarted after a sudden reactor trip due to more stringent regulations, which indicates that adjuster rods may be removed for other purposes of the reactor [3].

Dr. Park Y.W. proposed an idea of Co-60 production by using the CANDU6 fuel bundle, instead of the adjuster rods [4]. In this work, an innovative way of producing Co-60 in CANDU6 reactors is introduced. The fuel in central element is replaced by a Co-59 target, and Co-60 is obtained after the fuel bundle is discharged. To get higher production of Co-60, different target models are considered and compared with the conventional Co-60 production method using the adjuster rods. The necessary reactivity loss is calculated to get the same discharge burnup as conventional CANDU6 reactors. Coolant void reactivity (CVR) and lattice power distribution of different models are also studied. All the neutronic analyses are performed with the continuous-energy Monte Carlo code Serpent in this work [5].

## 2 Analysis Models and Methods

### 2.1 Analysis Models

Figure 1 shows a single fuel lattice comprised of the standard 37-element fuel bundle. Standard fuel and lattice design parameters are used in this work. The fuel and coolant temperatures are derived for 100 % power conditions. In this study, two kinds of Co-59 targets are considered, either cylindrical or thin annulus shape. In order to derive a favorable target configuration, four kinds of models are considered, which are shown in Table 1.

**Fig. 1** Standard CANDU6 fuel bundle with 37 fuel elements

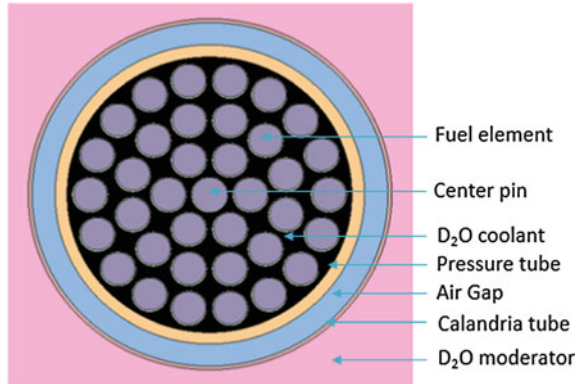


**Table 1** Co-59 target models

Fuel type	Case no.	Center pin	Volume fraction of Co-59
Standard	1	Fuel (UO <sub>2</sub> )	Not available
	2	Co surrounded by C	2.70 %
	3	Co surrounded by SiC	2.70 %
	4	C surrounded by Co	2.70 %
CANLFEX	5	Co surrounded by C	2.70 %

Case 1 is simply the standard fuel design without any Co-loading in the central element. Figure 2 shows the conventional fuel pin structure filled with natural UO<sub>2</sub> in Case 1. In Cases 2 and 3, the UO<sub>2</sub> fuel in the center pin is replaced with a cylindrical Co-59 target surrounded by graphite (C) and SiC. As shown in Fig. 3, in these two cases, the radius of Co-59 cylindrical is 0.1 cm, which means Co-59 occupies 2.7 % of the total volume of the original natural uranium fuel in Case 1. For comparison, an annular Co-59 target is considered in Case 4, as shown in Fig. 4, in which Co-59 target surrounds the center graphite and the volume fraction of the annular Co-59 target is also 2.7 %. It is expected that the annular Co-59 target will absorb more neutrons since its self-shielding effect can be quite smaller than in the compact cylindrical target in Cases 2 and 3. It should be noted that the central pin should design such that it can withstand the high coolant system pressure.

The CANFLEX fuel design, as shown in Fig. 5, is also considered in this study for comparison since CANFLEX fuel design can improve the operating and safety margin as well as the economics of CANDU6 reactors [6]. The center pin structure is similar to that of Case 2, except the radius of Co-59 and graphite. In order to get

**Fig. 2** Structure of the center fuel pin of Case 1

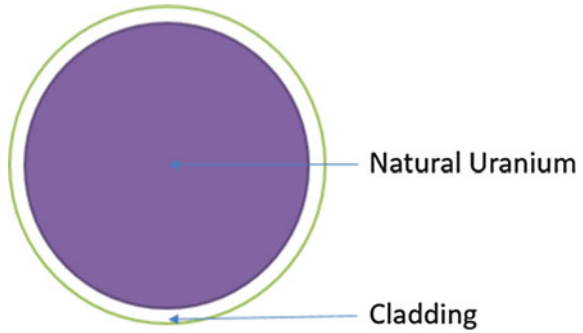


**Fig. 3** Structure of the center pin in Case 2 and 3

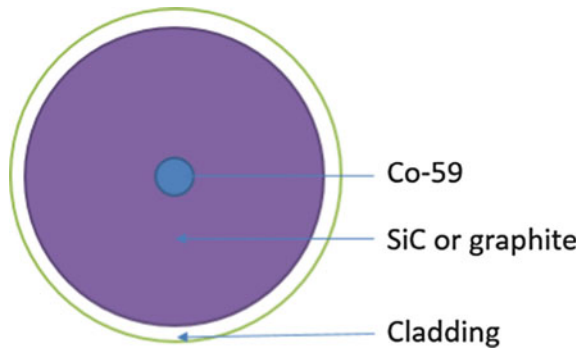
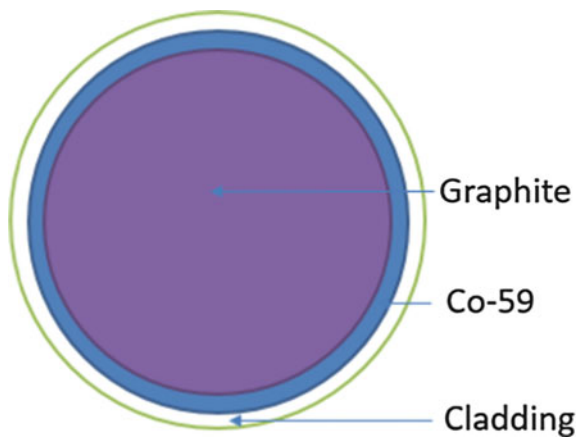
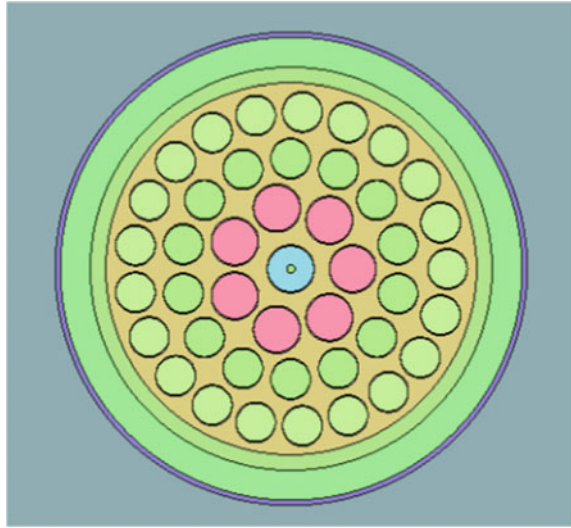


**Fig. 4** Structure of the center pin in Case 4



the same volume fraction of Co-59, the radius of Co-59 target is adjusted to 0.1045 cm, which is a little larger since the radius of the pins in the inner two rings is also larger than that of the standard CANDU6 fuel bundle.

**Fig. 5** Configuration of CANFLEX fuel bundle



## 2.2 Analysis Methods

In this study, the analysis is done for a 3-D single lattice geometry in both Figs. 1 and 5. Infinite multiplication factor is calculated by the Serpent code as a function of burnup with the ENDF/B-VII.1 nuclear data library. In the Monte Carlo calculations, the number of the neutron histories is 50,000 in each cycle and the total number of cycles is 400 including 100 inactive ones. The standard deviation of the infinite multiplication factor during the depletion ranges from 22 to 40 pcm.

In CANDU6 lattice analysis, the approximate discharge burnup is determined by the nonlinear reactivity model:

$$\int_0^{B_d} (\rho_{(B)} - \rho_{\text{loss}}) dB = 0 \tag{1}$$

where  $\rho_{(B)}$  is the lattice reactivity as a function of burnup;  $\rho_{\text{loss}}$  is the reactivity loss due to the leakage and parasitic capture in CANDU6;  $B_d$  is the fuel discharge burnup [7]. In typical CANDU6 core, the reactivity loss is calculated to be about 4.3 % or 4300 pcm.

## 3 Results and Discussions

### 3.1 Multiplication Factor and Discharge Burnup

Figure 6 shows the evaluation of the infinite multiplication factor values over the fuel burnup for the five cases in Table 1. It indicates that replacing the fuel in the

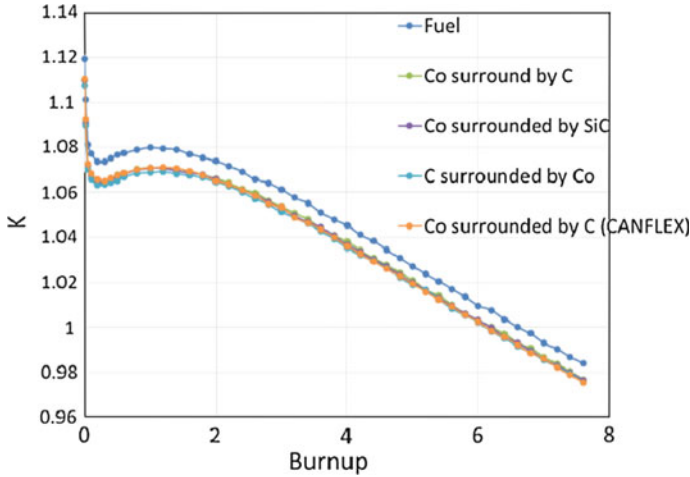


**Fig. 6**  $K_{inf}$  value as a function of burnup

center pin with a Co-59 target does reduce the multiplication factor quite noticeably. This is simply because a nonfuel Co-59 absorber replaces the central fuel.

It is worthwhile to note that the absorption cross section of Co-59 is much higher than that of natural uranium in thermal and resonance energy range, as shown in Fig. 7. The relatively high neutron capture cross section of Co-59 results in a small Co-59 volume in the central pin. Due to the reduced reactivity over the burnup period, the achievable discharge burnup is also smaller than that of standard CANDU6 fuel bundle if all the other core designs are the same. The achievable discharge burnup of the fuel are summarized Table 2 for several values of the reactivity loss. In this study, the reactivity loss in the CANDU6 core can be reduced by removing some of the adjuster rods. The total reactivity worth of the 21 adjuster rods in a typical CANDU6 core is assumed to be about 1200 pcm, which is considered to be an underestimation of the actual worth. In Table 3, the required reactivity loss to achieve the conventional fuel burnup of 7200 MWD/tU is provided and corresponding number of adjuster rods to be removed is also given. In Table 3, it is simple assumed that the adjuster rod worth is proportional the number of the rods.

Table 2 shows that discharge burnup of  $\sim 7.2$  GWd/MTU, which is the normal discharge burnup of CANDU6 reactors nowadays, can be achieved by reducing the reactivity loss in the Co-loaded cases. According to Table 3, desired discharge burnup can be obtained in the Co-loaded cases by removing some of the adjuster rods in the whole core. It is important to note that limited amount of Co-59 can be loaded into the central pin without compromising the fuel discharge burnup. In the following analysis, the discharge burnup is 7.2 GWd/MTU and the mid-burnup is 3.6 GWd/MTU for all cases.

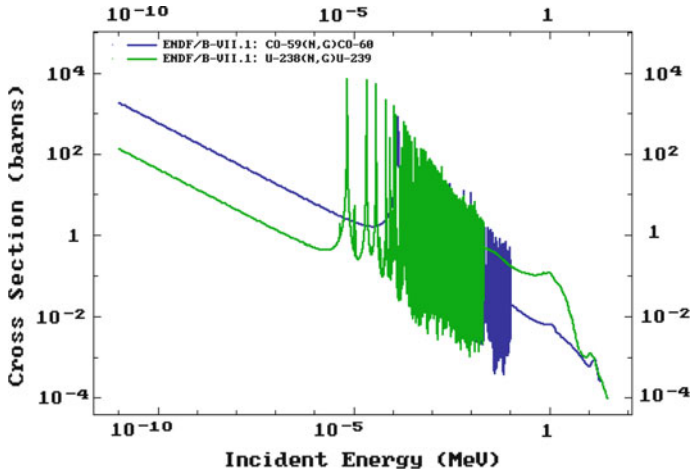


Fig. 7 Capture cross sections of Co-59 and U-238

**Table 2** Discharge burnup with different reactivity loss

Bundle type	No.	$\rho_{loss}$ (pcm)		
		4300	3700	3100
		$B_d$ (GWd/MTU)		
Standard	1	7.19	8.00	8.80
	2	6.24	7.08	7.89
	3	6.16	7.00	7.81
	4	6.01	6.86	7.67
CANLFEX	5	6.13	6.96	7.77

**Table 3** Necessary reactivity loss for the same fuel burnup

Fuel bundle	No.	$\rho_{loss}$ (pcm)	No. of removed adjustor rods
Standard	1	4293	0
	2	3611	12
	3	3552	13
	4	3448	15
CANLFEX	5	3522	14

### 3.2 Co-60 Production Capacity

Nowadays, in the standard CANDU6 core loaded with natural uranium, the so-called 8-bundle fuel shifting is used for the daily fuel management and about 1.9 channels are reloaded every day. This indicates that about 15 fuel bundles are discharged from the core in one day. Therefore, the Co-60 production capacity can

**Table 4** Production of Co-60

Fuel type	No.	Per bundle (gram)	Per year (gram)	Radioactivity produced per year (curies)
Standard	1	0	0	0
	2	0.542	3164.5	3.5E+06
	3	0.543	3171.9	3.5E+06
	4	0.677	3954.0	4.3E+06
CANLFEX	5	0.602	3518.5	3.9E+06

be easily calculated with the Co-60 mass at the discharge burnup of 7200 MWD/MTU. The results of Co-60 production analysis are shown in Table 4.

From Table 4, it is clear that the maximum amount of Co-60 can be achieved in Case 4, i.e., annular Co-59 target surrounding a graphite cylinder. This is mainly because the thermal neutron flux can be higher at the edge of center pin than in the central region of the pin. In addition, it is also mentioned that Co-target surrounding SiC cylinder produces slightly smaller amount of Co-60 since the neutron capture by Si is noticeably higher than that of C.

As shown in Table 4, the Co-60 production in terms of activity per year is over 3.5 million curies every year, which is much higher than that produced in a CANDU6 reactor core in Qinshan Nuclear Power Plant, around 3 million curies per year [8]. From the standard CANDU6 reactor analysis, it is recalled that fuel residence time is about a year and it is expected the residence time of the Co-target is also quite similar to a year.

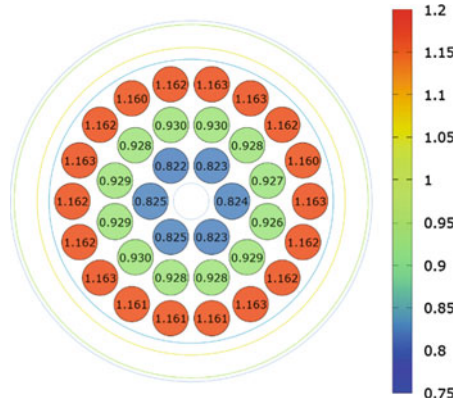
### 3.3 Coolant Void Reactivity

As is well known, the CANDU6 reactor has a strongly positive CVR due to its unique fuel channel design, and it is an outstanding safety concern of CANDU6 reactors. It is also known that the CVR can be reduced substantially by loading a strong neutron absorber in the central region of the fuel bundle, just like the Co-59 target in this study. To see the impacts of the Co-59 loading in the fuel bundle, the CVR values were also evaluated for both the fresh and mid-burnup conditions of the fuel bundle. It should be noted that the mid-burnup condition well represents the actual equilibrium core of the CANDU6 reactor. The CVR evaluation results are given in Table 5.

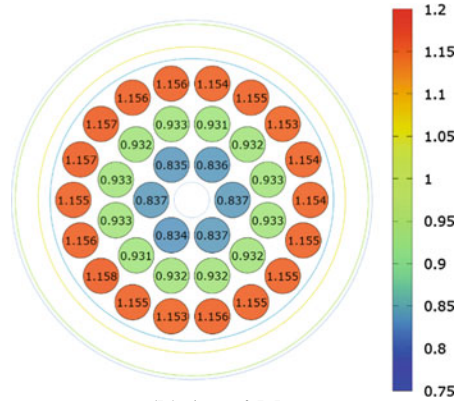
**Table 5** Impacts of Co-loading on the CVR

Fuel type	No.	CVR (Fresh)	CVR (Mid-burnup)
Standard	1	16.982	14.995
	2	16.415	13.889
	3	15.725	12.374
	4	16.172	12.925
CANLFEX	5	17.442	14.130

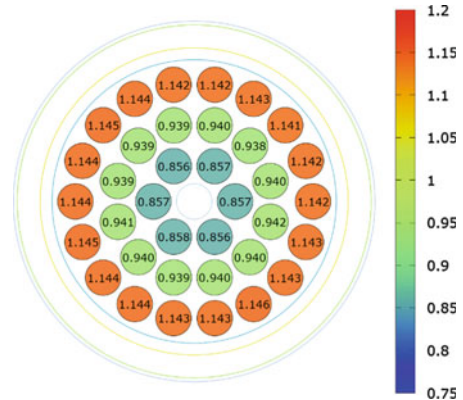
**Fig. 8** Normalized power distribution in Case 2



(a) At zero burnup



(b) At mid-burnup



(c) At discharge burnup



From Table 5, it is obvious that the Co-59 loading does reduce CVR both at zero burnup and mid-burnup. Coolant voiding causes a slight increase of thermal flux in the center of the lattice, simply because more thermal neutrons, produced in the moderator region, are able to reach the central region of the fuel bundle in the case of coolant loss so that more thermal neutrons are absorbed by Co-59. However, Case 3 has lower CVR than Case 4, where Case 4 maximized Co-59 capture by reducing spatial self-shielding. Because Si has much higher capture cross section than C, Case 3 model central pin has higher thermal capture cross section than Case 2 and 4. Although cross section of Si and C is very small compared to Co-59, its volume fraction is 97.2 % in the central rod and thermal capture by Si is not small.

It should be mentioned that the CVR of CANFLEX fuel design is slightly bigger than that of the standard fuel design, which is obvious in Case 2 and Case 5 in Table 5. It is because that in general, the CANFLEX fuel design has a slightly higher CVR than the standard fuel design since it has  $\sim 5\%$  larger coolant area than standard fuel design. The relatively higher central power is also partially responsible for the slightly higher CVR in the CANFLEX design.

### 3.4 Power Distribution in Fuel Bundle

Normalized pin power distribution in the Co-loaded fuel bundle in all cases is also analyzed at zero burnup, mid-burnup, and discharge burnup conditions. Figure 8 shows the resulting power distributions for Case 2, in which the fuel in the center pin is replaced by a Co-59 surrounded by graphite. It is shown that the peak power decreases with depletion. It is because that the fissile isotopes in outer rings deplete faster than those in inner rings. The spatial self-shielding of the fuel bundle becomes weaker with depletion, and the normalized power in the inner rings tends to increase with burnup. Although the bundle power profiles in other cases are not given here, the trend is similar to those in Fig. 8.

Table 6 shows the power peak at BOL (beginning of life), MOL (mid of life) and EOL (end of life) of the five cases. It is clear that replacing the fuel with the Co-59 target slightly increases the peak power in the fuel bundle. One can also note that the peak power is noticeably lower using the CANFLEX design. It is mainly because that CANFLEX fuel bundle has more fuel pins and it

**Table 6** Burnup-dependent power peaks

Fuel type	No.	BOL	MOL	EOL
Standard	1	1.141	1.136	1.124
	2	1.163	1.158	1.146
	3	1.163	1.157	1.145
	4	1.166	1.160	1.146
CANFLEX	5	1.151	1.148	1.133

provides a smaller linear power than the standard one. Additionally, the bundle power distributions are flattened in CANFLEX by introducing two types of fuel elements.

## 4 Conclusions and Future Works

This study introduces an innovative method for Co-60 production in the CANDU6 core. In this new scheme, the central fuel element is replaced by a Co-59 target together with graphite or SiC and Co-60 is obtained after the fuel bundle is discharged. It has been shown that the new method can produce significantly higher amount of Co-60 than the conventional Co production method in CANDU6 reactors without compromising the fuel burnup by removing some of the adjuster rods in the whole core. The CVR is noticeably reduced when a Co-59 target is loaded into the central pin of the fuel bundle. Meanwhile, the peak power in a fuel bundle is just a little higher due to the central Co-59 target than in conventional CANDU6 fuel design.

In future study, the Co-59 target design will be optimized to maximize the efficiency of Co-60 production in CANDU6 and more detailed analyses will be performed to characterize the new Co-60 production scheme.

## References

1. Y. Kim, Donny H., (2012) "A High-Fidelity Monte Carlo Evaluation of CANDU6-6 Safety Parameters," PHYSOR 2012, Knoxville, Tennessee, USA April 15–20
2. Malkoske G R, Nordion M D S, Slack J, et al. CO-60 PRODUCTION IN CANDU6 POWER REACTORS, The 13th pacific basin nuclear conference. Abstracts. 2002
3. D. Gho, et al, (2007). "Feasibility Study on Optimization of Adjustor System for CANDU6", KHNP report, A07NJ23
4. Y.W. Park, "Manufacturing Method of Isotopes using CANDU6 Type Reactor" Korean Intellectual property office,10-1502414, 2015
5. Leppanen, J., 2013. Serpent—A Continuous-energy Monte Carlo Reactor Physics Burnup Calculation Code User's Manual. VTT Technical Research Centre of Finland
6. Hartanto D, Kim Y, Venneri F. Neutronics evaluation of a super-deep-burn with Hartanto D, Kim Y, Venneri F. Neutronics evaluation of a super-deep-burn with TRU Fully Ceramic Microencapsulated (FCM) fuel in CANDU6. *Progress in Nuclear Energy*, 2015, 83: 261–269
7. Driscoll, Michael J., Thomas Joseph Downar, and Edward E. Pilat. The linear reactivity model for nuclear fuel management. American Nuclear Society, 1990
8. Tang Jiongran, Independence Research Succeed in Co-60 Producing for CANDU6 Reactor, Process Report on China Science & Technology, 2009

# Base-Isolation Technology Investigation for SMR Nuclear Island Building

Chen Jian and Ma Jia

**Abstract** The application of Lead-Rubber Bearing base-isolation technology was studied in this paper, including base-isolation method scheme, selection of seismic isolation devices, determination of isolation structure models, etc. Taking one SMR nuclear safety-related building for example, the influence on isolation effectiveness of buildings from various spaces and various hysteretic models for the isolation layer were investigated based on the dynamic analysis of isolation structures. The study shows that: (1) the application of isolation measures can significantly increase the structure's natural vibration period, reduce the dynamic response of the superstructure, and amplify the structure's horizontal displacement, but the story displacements are small; (2) the bilinear model for isolation bearing has a more actual isolation effectiveness, it should be pay more attention in design.

**Keywords** SMR · LRB · Isolation structures · Equivalent linear model · Bilinear model

## 1 Introduction

Base-isolation technology has been applied widely and accumulated mature experience after nearly forty years of development. It has also obtained favorable benefits both on economy and on society. However, there is fewer application of base-isolation technology in structural design of NPPs, especially in China; it is empty for the engineering application of base-isolation technology for nuclear safety-related building. Theoretically, the application of base-isolation technology can improve the reliability and safety of nuclear power building. Therefore, standard design can be realized without caring of the value of earthquake during the seismic design of primary structures and facilities. Consequently, the speed of design and construction can be accelerated and the cost can be reduced [1]. However,

---

C. Jian (✉) · M. Jia  
China Nuclear Power Engineering CO., Ltd., Structure Analysis, Beijing, China  
e-mail: Chenjian@cnpe.cc

considering of the particularity and complexity of nuclear structures and the incomplete of related criterions, the attitude toward the application of base-isolation technology for nuclear power buildings from leading countries including America, Japan, and France is still prudential. Accordingly, there is a great necessity to develop the investigation on base-isolation technology for nuclear power buildings. The self-designed SMR and Hualong One proposed the subject of base-isolation technology prospectively under which this paper is just set. Based on a certain site, taking one nuclear island building for example, the research was developed on base-isolation method scheme, selection of the seismic isolation device, determination of isolation structure model, etc. And then, dynamic analysis of isolation structures was carried out. The technical sustain on standard design and site adaption for new type of nuclear plant was provided through this investigation.

## **2 Base-Isolation Method Scheme**

### ***2.1 Description of Project***

The description of ground motion at the site: The PGA of ultimate safety ground motion (SL2) is 0.50 g in horizontal direction and 0.33 g in vertical direction.

Necessity of base-isolation: the peak acceleration (SL2) exceeds 0.3 g which is the standardized design value. In order to meet the standard design of structures and nuclear-related facilities, base-isolation technology should be adopted so as to decrease the earthquake action.

The location of isolation layer: the isolation layer locates at the bottom of foundation.

### ***2.2 Description of Isolation Devices***

The seismic isolation device can be divided into two types, seismic isolation device and damping device. Seismic isolation device is used to provide large deformation and prolong the natural period, so as to decrease the earthquake action on super-structure. Damping device is used to provide vibratory decay damping force so as to restrict structural displacement. Based on the aim of seismic isolation, the following essential performance should be considered when choosing of isolators: enough vertical bearing capacity and vertical stiffness, smaller horizontal stiffness and proper damping decay characteristic, isolator durability, fire resistance, and other related characteristics [2–5]. Lead-Rubber Bearing (LRB) is adopted in this paper for base-isolation technology investigation of nuclear power building. Because of the heavier weight, larger stiffness, larger earthquake action, and more restrict displacement requirement of nuclear power structures compared with normal civil

structures, large diameter isolators are considered for using. The related parameters of LRB are as follows:

Effective diameter  $D$ : 1000 mm;  
Total thickness of rubber layers  $tr$ : 162 mm;  
Vertical bearing capacity  $P$ : 7850 kN;  
Vertical stiffness  $Kv$ : 6929 kN/mm;  
1st shape factor  $S1$ : 41.7; 2st shape factor  $S2$ : 6.17;  
Horizontal equivalent stiffness 4539 kN/m;  
Equivalent damping ratio  $\zeta = 21.6 \%$ ;  
Pre-yield stiffness  $K1 = 29,240$  kN/m;  
Post-yield stiffness  $K2 = 2924$  kN/m;  
Yield force  $Qy = 261.7$  kN.

### **2.3 Arrangement of Isolators**

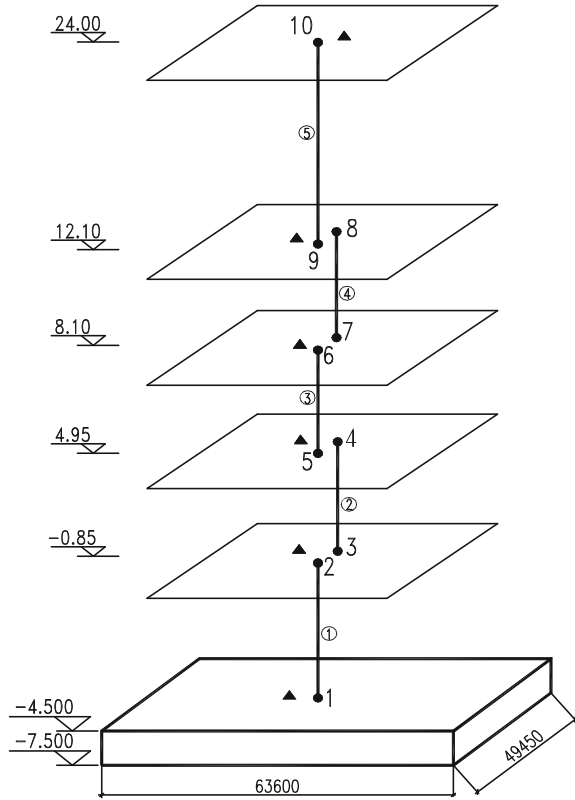
Based on the estimation of bearing capacity, detailing requirement of installation and maintain space, three kinds of uniform arrangement of isolators are considered preliminarily:  $2.5 \text{ m} \times 2.5 \text{ m}$ ,  $3.0 \text{ m} \times 3.0 \text{ m}$ , and  $3.5 \text{ m} \times 3.5 \text{ m}$  of spaces. Because of the uniform arrangement of isolators, the stiffness center of isolators is located at the center of base plate which is closed with the quality center of overlying structures. So the influent of torsion caused by eccentric can be decreased. Checking calculation of vertical bearing capacity of isolators is carried out to verify the preliminary feasibility of these three kinds of arrangement. Through checking calculation, the two spaces  $2.5 \text{ m} \times 2.5 \text{ m}$  and  $3.0 \text{ m} \times 3.0 \text{ m}$  can meet the preliminary design requirement.

## **3 Computational Models**

### **3.1 Model of Superstructure**

Compared with isolation layers, the stiffness of overlying structures is very large because of the thick concrete wall and thick concrete floor. So lumped mass stick model is adopted in this paper. Meanwhile because of the complexity of structure configuration, the stiffness center and quality center are not coincident, so torsion effect should also be taken into account, which is the considering of two horizontal linear displacements and one angular displacement of floor. Therefore, the model of superstructure adopts lumped mass stick model considered with prejudicial torsion effect (Fig. 1).

**Fig. 1** Lumped mass stick model



### 3.2 Model of Isolation Layer

In order to confirm the mechanical model of isolation layer, linear elastic model is adopted in vertical tension–compression hysteretic model, while nonlinear constitutive model and equivalent linear model are adopted in horizontal. Equivalent bilinear model is adopted to indicate nonlinear constitutive model approximately.

## 4 Time History Analysis

### 4.1 Finite Element Model of Building

ANSYS is adopted in this paper to establish the lumped mass stick computational model of the building. Every isolator is composed of three combine elements in X, Y, and Z direction. For equivalent linear model, Combin14 linear spring element is adopted to modify the X, Y, and Z direction of isolator. For bilinear model,

Combin40 element is adopted to modify the *X* and *Y* direction of isolator, while Combin14 element is adopted to modify the *Z* direction of isolator.

### 4.2 Modal Analysis

The first two steps of modal analysis results of isolation structure are listed in Table 1. As space is limited, first two vibration modes of the isolation structures in horizontal direction of equivalent linear model at the space of 3.0 m × 3.0 m are shown in Fig. 2. Based on the vibration modes, it can be seen that the mode shape of superstructure is nearly rigid body motion because its stiffness is much larger than that of the isolator layers, which is coincident with the result of academic analysis in isolation system. The data in Table 1 shows that the horizontal natural periods increase significantly after using isolation for both equivalent linear model and bilinear model. The natural period is 6–15 times larger than nonisolation structure. The larger the space of LRB isolators, the larger the period increased. From the basic principle of isolation structures, the aim of prolonging the structural natural period is achieved.

**Table 1** First two vibration modes of the isolation structures

Mode shapes	Natural period of isolation structure (s) (equivalent linear model)		Natural period of isolation structure (s) (bilinear model)		Natural period of nonisolation structure (s)
	LRB space 2.5 m × 2.5 m	LRB space 3.0 m × 3.0 m	LRB space 2.5 m × 2.5 m	LRB space 3.0 m × 3.0 m	
1	1.390	1.679	0.552	0.665	0.0899
2	1.389	1.679	0.551	0.665	0.0877

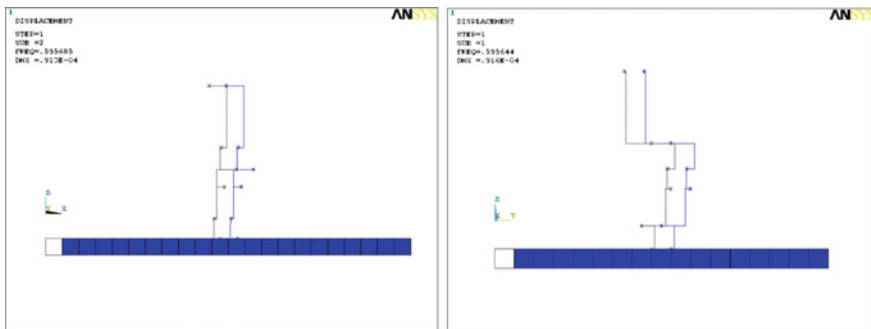


**Fig. 2** First two vibration modes of the isolation structures in *H* direction

### 4.3 Ground Motion

Dynamic time history analysis is adopted in this isolation analysis. Three single groups (two in horizontal and one in vertical) of mutual orthogonal and statistic independently manual time histories are achieved by fitting from RG1.60 standard response spectra. The total duration of time history is 25 s. The stable period duration of ground motion is 8 s. The time step length of time history is 0.01 s. The total time step is 2500 steps. The PGA is 0.50 g in horizontal direction, and 0.33 g in vertical.

### 4.4 Dynamic Response of Isolation Structure

#### 4.4.1 Acceleration Response Analysis

##### (1) Equivalent linear model

As space is limited, only list the result of structural response in X-direction below. Figures 3 and 4 show the comparison of accelerations in X-direction for space 3.0 m at bottom layer and top layer, respectively. As can be seen from the figures, the structural acceleration response decreases significantly for isolation structure. Figure 5 shows the comparison of peak values of accelerations at each floor of isolation structure under two kinds of isolator spaces and the same condition of nonisolation structure. Figure 6 shows the comparison of seismic reduction factors (seismic reduction factor = response with isolation/response without isolation). As can be seen from the figures: Peak values of accelerations response at each floor above isolation layers are nearly the same, which is coincident with the conclusion that the overlying structure is rigid body motion generally. The maximum seismic reduction factor is located at bottom layer, which is about 0.5. The higher the

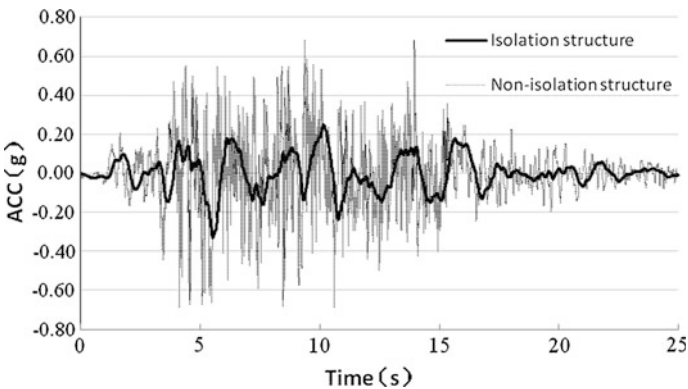


Fig. 3 Accelerations in X-direction at bottom layer



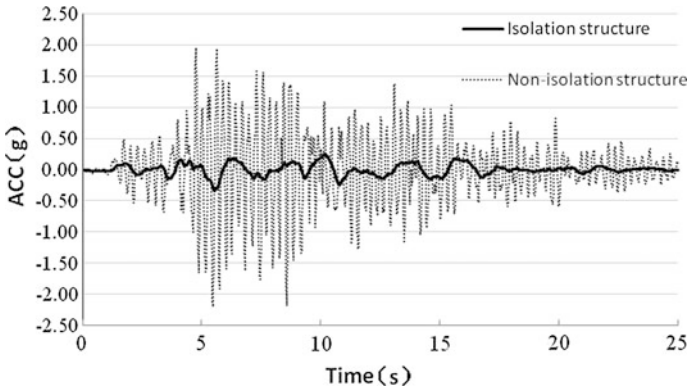


Fig. 4 Accelerations in X-direction at top layer

Fig. 5 Peak values of accelerations for different isolator spaces

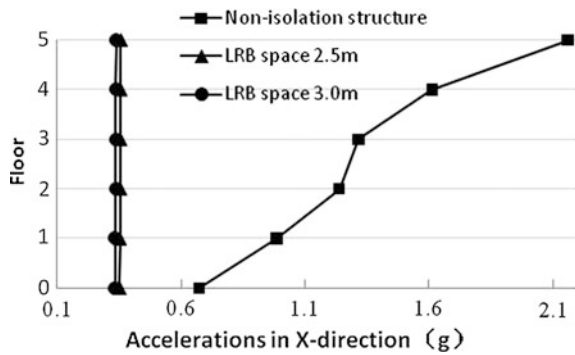
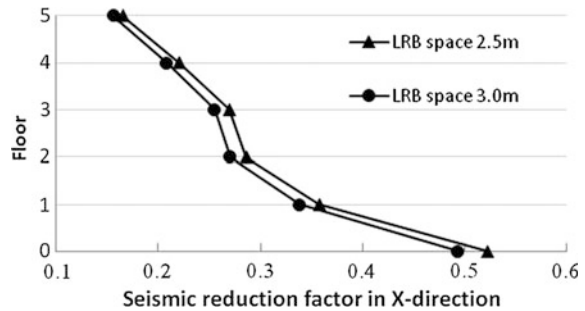


Fig. 6 Seismic reduction factors for different isolator spaces



elevation is, the more significant the factor is. The seismic reduction factor is about 0.15 at top layer. As increasing of isolator space (from 2.5 to 3.0 m), stiffness of isolation layer, peak values of accelerations response and seismic reduction factor decrease. That means the effect of isolation is more significant.

(2) Bilinear model

Figures 7 and 8 show the comparison of accelerations in X-direction for space 3.0 m at bottom layer and top layer, respectively, in bilinear model. Figures 9 and 10 show the comparison of peak values of accelerations and seismic reduction factors at each floor under the same condition. The analysis result of bilinear model shows the same trend as equivalent linear model: Peak values of accelerations response at each floor are nearly the same. The maximum seismic reduction factor is located at bottom layer, which is about 0.5. The higher the elevation is, the more significant the factor is. The seismic reduction factor is about 0.15 at top layer. As increasing of isolator space (from 2.5 to 3.0 m), peak values of accelerations response and seismic reduction factor decrease. That means the effect of isolation is more significant.

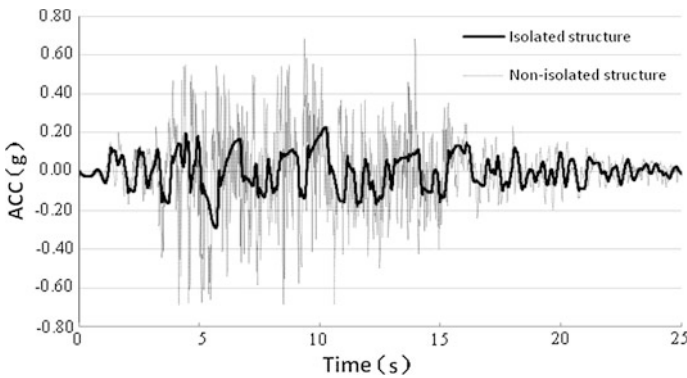


Fig. 7 Accelerations in X-direction at bottom layer

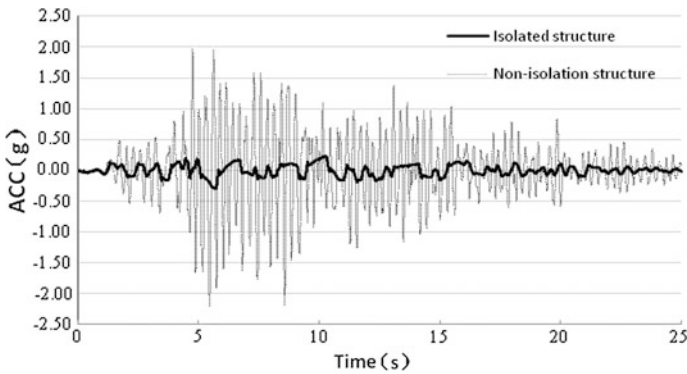
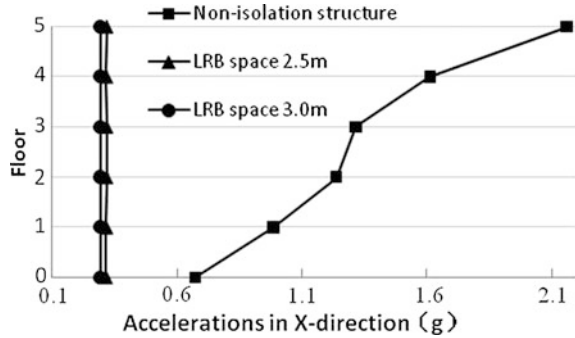
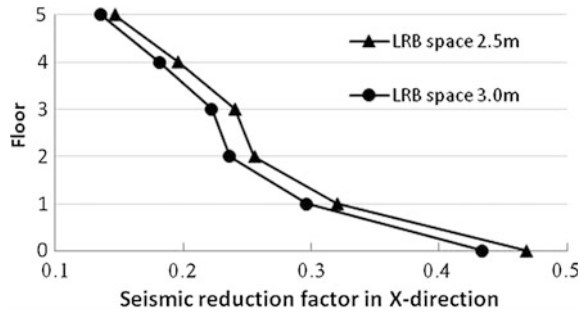


Fig. 8 Accelerations in X-direction at top layer

**Fig. 9** Peak values of accelerations for different isolator spaces



**Fig. 10** Seismic reduction factors for different isolator spaces



**4.4.2 Displacement Response Analysis**

(1) Equivalent linear model

Figures 11 and 12 show the comparison of displacements in X-direction and story displacements in equivalent linear model. Compared to nonisolation structure, the rigid body motion of overlying structure in isolation system is larger. The maximum displacement in X-direction is 187.6 mm, which is far larger than the maximum displacement of nonisolation structure at top layer of 45.9 mm. Although there are large displacements of isolation structure, but the story displacements of overlying structure are very small because of its rigid body motion (Fig. 12), which is of great benefit to structure. As increasing of isolator space (from 2.5 to 3.0 m), stiffness of isolation decreases and the displacements of overlying structure increases significantly (increased about 40–50 %). The analysis result of displacement shows the opposite trend as acceleration result. It can be concluded that, the structural period will be increased and achieve favorite isolation effect when decreasing the structural stiffness. But the disadvantage is the increasing of structural displacement, which can be weakened by installation damping devices. Consequently, it is necessary to choose proper stiffness and damping in order to achieve ideal effect of isolation.

**Fig. 11** Peak values of horizontal displacement for different isolator spaces

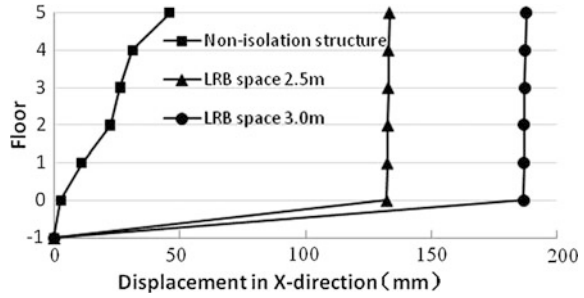
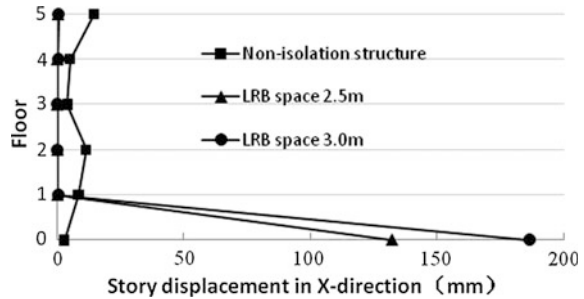


**Fig. 12** Story displacements for different isolator spaces



(2) Bilinear model

Figures 13 and 14 show the comparison of displacements in X-direction and story displacements in equivalent bilinear model. The analysis result of bilinear model shows the same trend as equivalent linear model: The rigid body motion of overlying structure in isolation system is relatively large. The maximum displacement in X-direction is 221.6 mm, which is far larger than the maximum displacement of nonisolation structure at top layer of 45.9 mm. As the result of rigid body motion, the story displacement of overlying structure is quite small (Fig. 14). As increasing of isolator space (from 2.5 to 3.0 m), stiffness of isolation decrease, and the displacements of overlying structure increase significantly (increased about 50–80 %). It can be seen, the displacement of isolation structure is very sensible to the stiffness of isolation layer. Consequently, it is necessary to balance the effect of isolation and restriction of displacement during isolation designing.

**4.4.3 Dynamic Response Comparison Between Equivalent Linear Model and Bilinear Model**

Figures 15 and 16 show the comparison results of structural dynamic response between equivalent linear model and bilinear model.

It can be seen from the comparison: peak displacements of bilinear model increase 5–8 % than equivalent linear model at the LBR space of 2.5 m and

**Fig. 13** Peak values of horizontal displacement for different isolator spaces

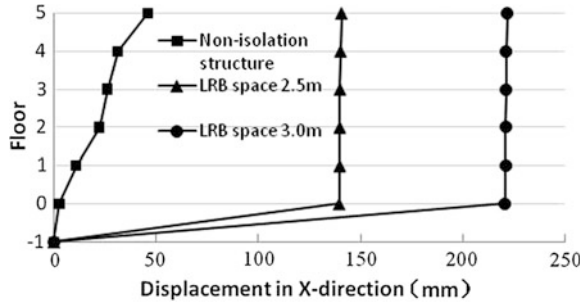


**Fig. 14** Story displacements for different isolator spaces

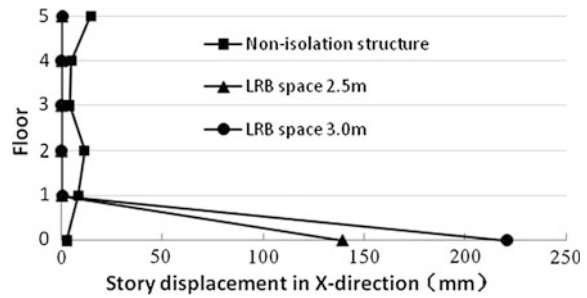


**Fig. 15** Displacements in X-direction for different isolator spaces

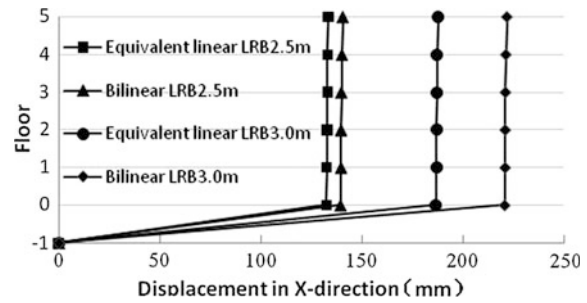
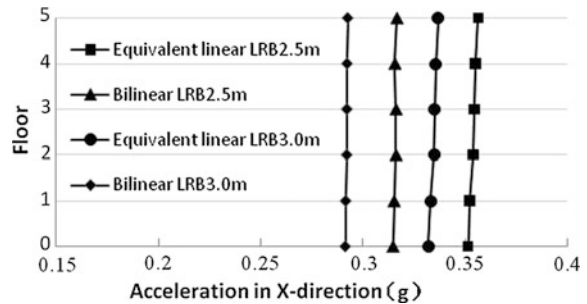


**Fig. 16** Accelerations in X-direction for different isolator spaces



increase 18 % at the space of 3.0 m. It can be concluded that, the influence of stiffness of isolation layer is obvious to the displacement of isolation structure. For acceleration response, peak values of bilinear model are smaller than equivalent linear model. Also, the reduction extent of both kinds of LRB space is nearly the same, which is about 10–16 %. Accordingly, the sensitivity on acceleration of LRB space is weaker than displacement.

## 5 Conclusions

Taking one SMR nuclear safety-related building for example, LRB base-isolation technology was studied in this paper, including base-isolation method scheme, determination of isolation structure model, dynamic response analysis of isolation structure, etc. Conclusions are listed as follows:

- (1) After using of LRB base-isolation technology, the natural period of isolation building can be extended to 15 times larger than nonisolation structure. The horizontal acceleration responds can be decreased significantly, and the seismic reduction factor can reach up to 0.15–0.50. With wonderful seismic reduction effect, the horizontal displacements of isolation structure increase significantly. Because of the rigid body motion of overlying structure, the story displacements are quite small, which could be beneficial for structural design.
- (2) The model of superstructure adopts lumped mass stick model considered with prejudicial torsion effect, which can meet the requirement of engineering design. For determination of isolation structure model, the result of bilinear model is more closed to actual stress condition, while equivalent linear model is good for its faster calculation speed and lower cost of computation. Consequently, it is suggested that equivalent linear model can be adopted at the phase of base-isolation method scheme, while bilinear model and other modified model can be adopted at the phase of final design because it is more coincident with actual hysteretic characteristic. The problem of large displacement can be settled by tectonic methods or by installing damping devices.
- (3) Combined the earthquake characteristic of nuclear power structure, isolators of large diameter, and large space should be adopted preferably during base-isolation method scheme designing. Convenience for construction and maintenance should also be taken into account.
- (4) The effect of isolator stiffness on structural displacement is more sensible than the effect of acceleration. Consequently, it is necessary to balance the relationship between the effect of isolation and restriction of displacement synthetically during engineering design.

## References

1. XIE Lili, ZHAI Changhai. A prospective study on applicability of base isolation in nuclear power plants [J]. *Journal of Earthquake and Engineering Vibration*, 2012, 32 (1): 1–10.
2. ZHOU Fulin. *Shock Attenuation Control for Engineering Structure* [M]. Beijing: Seismological Press, 1997.
3. DANG Yu, DU Yongfeng. *Base-isolation Structure Design and Construction Guide* [M], Beijing: China Water and Power Press, 2007.
4. GB20668.3-2006 *Rubber Isolation Bearings for Buildings* [S].
5. CECS 126: 2001 *Technical specification for seismic-isolation with laminated rubber bearing isolators*[S].

# Conceptual Design of High Temperature Water-Cooled Divertor Plasma-Facing Unit for Fusion Reactor

Xin Mao, Xuebing Peng, Xiaobo Chang, Xinyuan Qian and Ping Liu

**Abstract** Tokamak, a type of fusion experimental device, is considered as the most promising device on which net fusion power could be outputted for electricity production, i.e., the fusion reactor. Divertor, as one of the core components in Tokamak, has to sustain very high heat flux from high temperature plasma, up to tens of MWs, so that the design of divertor plasma-facing unit (PFU) is quite important. Up to now, the most advanced mature PFU technology is the ITER W/Cu PFU, which is a monoblock structure with tungsten, Cu and CuCrZr as the plasma-facing material, interlayer and heat sink, respectively. However, due to high activation of Cu element by neutron irradiation, CuCrZr is not appropriate for the material of heat sink anymore for future fusion reactor. In the paper, a design of PFU with a low activation material (named CLAM, China Low Activation Martensitic steel) as the heat sink was proposed based on ITER monoblock structure, i.e., W/CLAM PFU. With the temperature operation window as the design limit, thermal analysis of W/CLAM PFU was done initially with the same structural dimensions as ITER monoblock. Then the structural dimensions were optimized for the purpose of improving the heat loads removing capability, more than  $10 \text{ MW/m}^2$ . As a consequence, thermal stresses were calculated for the W/CLAM PFU, where stress in CLAM heat sink was found beyond the material limit. The issue was discussed and the solution was preliminary proposed. This can provide the necessary theoretical basis for improvement of heat flux handling capacity to divertor PFU in future application.

**Keywords** Fusion reactor · Divertor PFU · CLAM heat sink · Optimization · Ansys

---

X. Mao (✉) · X. Peng · X. Chang · X. Qian · P. Liu  
Institute of Plasma Physics, Chinese Academy of Sciences,  
Shushanhu Road 350, Hefei 230031, Anhui, PR China  
e-mail: maixin@ipp.ac.cn

X. Chang · X. Qian  
School of Nuclear Science and Technology,  
University of Science and Technology of China,  
Jinzhai Road 96, Hefei 230026, Anhui, PR China



## 1 Introduction

Tokamak, for instance ITER, is a most likely realization form for future fusion reactor. As one of the core components in Tokamak device, divertor, whose main role is related to power exhaust and impurity control, is a transitional zone between the high temperature plasma and materials, so that the divertor plasma-facing unit (PFU) design is very critical.

The operating power of future fusion reactor is very great, to reach thousand megawatt order of magnitude, such as CFETR or DEMO. It could be foreseen that the heat flux on surface of divertor PFCs, which consists of PFUs and its support bodies, is as high as  $10 \text{ MW/m}^2$  in steady state. Consequently, material selections of divertor at Tokamak operation are required strictly, especially for divertor PFU to withstand higher heat load.

So far, the most advanced mature PFU technology is the ITER W/Cu PFU, which is a monoblock structure with tungsten, Cu and CuCrZr as the plasma-facing material, interlayer and heat sink, respectively. Tungsten is considered as the most suitable armour material due to its refractory nature, good conductivity and low sputter yield. Then copper, which owns excellent thermal conductivity [ $305 \text{ W/(K m)}$ ] and high ductility, is used as transition layer material. According to investigation [1], two materials have been identified as the most promising for a DEMO water-cooled divertor, CuCrZr and RAFM. The current heat sink material mostly employs CuCrZr, whereas owing to high activation of Cu element by neutron irradiation, CuCrZr is not appropriate for the material of heat sink anymore for future fusion reactor.

The ITER design concept represents a promising solution also for DEMO PFUs. Therefore, a design of PFU with a low activation material (CLAM) as the heat sink was proposed based on ITER monoblock structure, i.e., W/CLAM PFU. This paper mainly presents the conceptual design progress of high temperature water-cooled divertor PFU. Section 2 describes material limiting condition and CLAM steel properties. Then the progress regarding divertor PFU conceptual design is detailed and taken on in Sect. 3. Finally, Sect. 4 gives conclusion.

## 2 Material Limiting Condition and Clam Steel Properties

The allowable temperatures of tungsten, copper, and CuCrZr are 1300, 550 and  $350 \text{ }^\circ\text{C}$ , respectively, whose other related properties are described in ITER SDC-IC [2].

CLAM is a candidate as structural material for plasma-facing components, blanket and divertor of future reactors, for its negligible irradiation-induced swelling even at high doses and its relatively small thermal expansion in comparison to austenitic stainless steel. CLAM was developed in China upon the results and experience of the other reduced activation ferritic martensitics (RAFM)s, such as

**Table 1** The mechanical properties of CLAM steel [7]

Temperature (°C)	Ultimate tensile strength (MPa)	Yield strength (MPa)	Total elongation (%)	Allowable temperature (°C)
25	670	512	25	300–550
400	554	447	17	
500	493	417	15	
600	373	327	19	

EUROFER97 [3], F82H [4], JLF-1 [5], and ORNL 9Cr-2WVTa [6], which were widely studied in the world. The mechanical properties of CLAM steel are presented in Table 1.

### 3 Design of High Temperature Water-Cooled Divertor PFU

The divertor is the component with the highest steady-state heat loads in Tokamak device. In design of divertor structure, the peak incident heat flux is one of the “most significant” parameters, because it will determine the thermal gradient (and relevant thermal stress) in the PFU. It will also prominently contribute to determine the wall heat flux and the margin to critical heat flux. Consequently, the primary design direction of high temperature water-cooled divertor PFU is to improve thermal load-carrying capability of monoblock, and its anticipated target is at least 10 MW/m<sup>2</sup>.

#### 3.1 Thermal Analysis of W/CLAM PFU with ITER Monoblock Dimensions

The ITER Divertor PFU is designed by adopting the pipe lining and water cooling structure. As shown in Fig. 1, PFU is made up of three kinds of materials: tungsten, copper, and copper alloy (CuCrZr) from the outside to the inside. A swirl tape (twist ratio of 2 and thickness of 0.8 mm) was inserted inside the tube to promote turbulence.

Thermal analysis of W/CLAM PFU established in Ansys was done initially using the identical structural dimensions with ITER monoblock, and the heat sink material CuCrZr is replaced with CLAM steel. The mesh (see Fig. 2) of monoblock model is composed by linear hexahedral elements for a total of 58,560 nodes and 177,404 elements. In particular a size element of 1 mm in the coolant flow direction was used, while in the heat flow direction 1.4 mm for the W armour and 0.25 mm

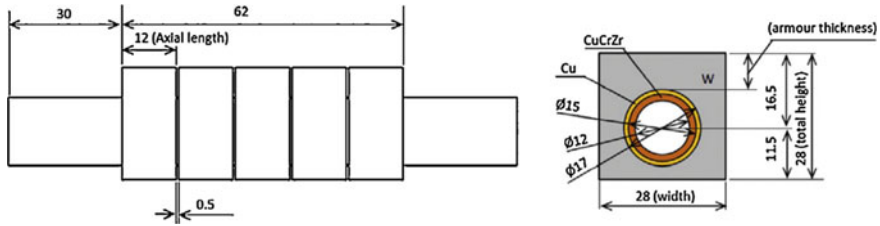
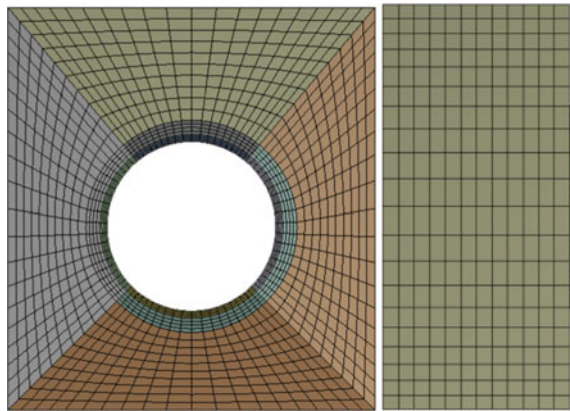


**Fig. 1** ITER monoblock geometry [8] (armour thickness of 8 mm). *Nota bene* the twisted tape is not shown

**Fig. 2** Mesh used for thermal analysis



for the copper were used (to have at least four elements along copper thickness in order to correctly simulate its thermal–mechanical behavior).

These thermal analyses were performed for the steady state using the heat transfer coefficient (HTC) calculated with the empirical correlation as a function of  $T_{wall}$ . HTC between water and heat sink tube is calculated using the SIEDER–TATE correlation for forced convection regime and the THOM–CEA correlation for subcooled boiling regime [9, 10].

For the thermal analysis, the loads and boundary conditions are as follows (Fig. 3). First, heat flux was applied on the top surface of tungsten tile. Second, HTC obtained by formulas is located at the inner wall of CLAM pipe. Third, the hydraulic parameters are pressure of 15.5 MPa, temperature of 300 °C, and velocity of 10, 15, or 20 m/s.

The calculated results indicate that, within the temperature limits of three materials, maximum handling heat fluxes of monoblock structure for different water velocities are 3.28, 3.38, and 3.43 MW/m<sup>2</sup>, respectively.

The max temperature in the W armor is predicted to reach 790 °C (see Fig. 4), while 550 °C in the Cu interlayer and 505 °C in the CLAM tube, respectively.

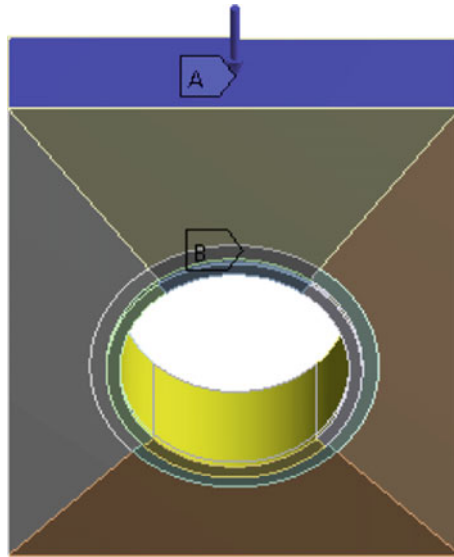


Fig. 3 Locations of heat load (a) and heat transfer coefficient (b)

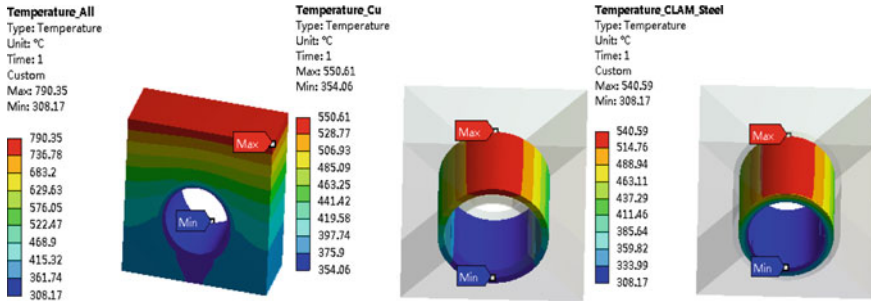
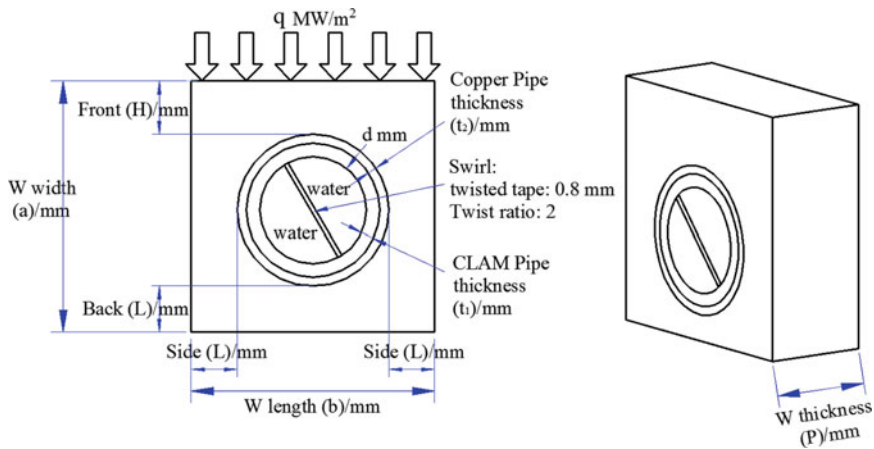


Fig. 4 Temperature distribution of tungsten (left), copper (middle), and CLAM pipe (right)

### 3.2 Design Optimization of Divertor PFU

#### (a) Parameters optimized process

From the aforementioned analyses, when the heat sink material is CLAM steel, max handling heat flux of monoblock is less than  $4 \text{ MW/m}^2$ , which is far from the expected target heat flux of  $10 \text{ MW/m}^2$ . The geometry of monoblock needs to be optimized. With respect to max heat load handling capacity of monoblock and allowable temperature of three materials, seven parameters of monoblock are optimized by controlling variable method in which one parameter is changed, and



**Fig. 5** Parametric design of monoblock geometry

**Table 2** The initial selected values

Design values
$d = 12, 10, 8, 7, 6, 5$ mm
$L = 5.5, 4.5, 3.5, 2.5$ mm
$t_1 = 0.4, 0.5, 0.6$ mm
$t_2 = 0.5, 0.7, 1, 1.2, 1.5$ mm
$H = 3, 5, 7, 9$ mm
$P = 4, 6, 9, 12$ mm
$V = 10, 15, 20$ m/s

the other parameters are fixed. The seven parameters,  $d$ ,  $L$ ,  $t_1$ ,  $t_2$ ,  $H$ ,  $P$ , and  $v$ , are shown in Fig. 5. According to the relevant experience of diverter [11], the initial values of these parameters about monoblock geometry are shown in Table 2.

The underneath example illustrates parameters selected process. For  $d$ , the constant parameters are  $P(12$  mm),  $v(10$  m/s),  $t_1(0.4$  mm),  $t_2(0.5$  mm),  $L(2.5$  mm),  $H(5$  mm), and the changeable parameter  $d(12, 10, 8, 7, 6, 5$  mm). Heat load handling capacity of monoblock structure is decreased with the increase of  $d$  from the computational statistics of  $d$ , nevertheless magnitude of the reduction is very small, about 1 %. The technical limitation in fabrication is taken into account in the meantime. As a result,  $d(7$  mm) has been chosen. For  $P$ , all the parameters are  $d(7$  mm),  $v(10$  m/s),  $t_1(0.4$  mm),  $t_2(0.5$  mm),  $L(2.5$  mm),  $H(5$  mm), and  $P(12, 9, 6, 4$  mm). In accordance with max heat flux handling ability of this model,  $P(4$  mm) would be used.

The selected process of another five parameters is the same as  $P$  and  $d$ . Eventually, the optimal values of seven parameters is the following (Table 3).

**Table 3** The optimal values of divertor PFU geometry

$V$ (m/s)	$d$ (mm)	$t_1$ (mm)	$t_2$ (mm)	$L$ (mm)	$H$ (mm)	$P$ (mm)
20	7	0.4	0.5	2.5	5	4

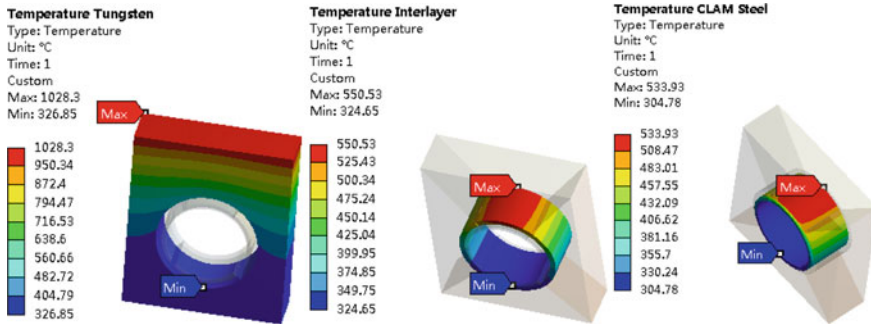


**Fig. 6** Temperature distribution of tungsten (*left*), copper pipe (*middle*), and CLAM steel pipe

(b) Thermo-mechanical assessment at the optimal monoblock structure

The optimal value of all the parameters was obtained in the thermal analyses. Compared with the boundary conditions of Sect. 3.1 analysis, only the incident heat flux and HTC value were different in this thermal analysis. Figure 6 shows the temperature distribution of tungsten, copper together with CLAM steel at the optimal parameters and it points out that the maximum temperature of three materials is below temperature limit subjected to the max heat flux  $10.12 \text{ MW/m}^2$ .

The stress analysis is done with the temperature field data obtained from the previous thermal analysis. Its boundary conditions involved thermal condition and pressure (15.5 MPa) applied to all the bodies and the inner wall of CLAM pipe, respectively, the bottom face of tungsten tile constrained in the vertical direction normal to the heat-loaded surface and three rotations, the environment temperature set to  $22 \text{ }^\circ\text{C}$  (see Fig. 7), and two-load step imposed on all the bodies (preheating and plasma operation). The stress results of the optimal monoblock are shown in Fig. 8.

From Fig. 8, max stress of tungsten tile is approximately 407 MPa which is below the allowable limit (3 Sm of tungsten at  $1028 \text{ }^\circ\text{C}$  is 627 MPa) in ITER SDC-IC. Max stress of 671 MPa in CLAM pipe is found at preheating. This value is too high for the material (3Sm of CLAM at  $300 \text{ }^\circ\text{C}$  is 575 MPa).

At preheating, the position of maximum stress is indicated in the middle of the inner wall surface to CLAM pipe (Fig. 8, middle). First, the thermal expansion coefficient of three materials is different, in which Copper is largest, and three kinds of materials extrude inwards at the same time, so that the inner wall strain of CLAM pipe reaches peak. Hence, the stress at the max strain place is also maximal in the

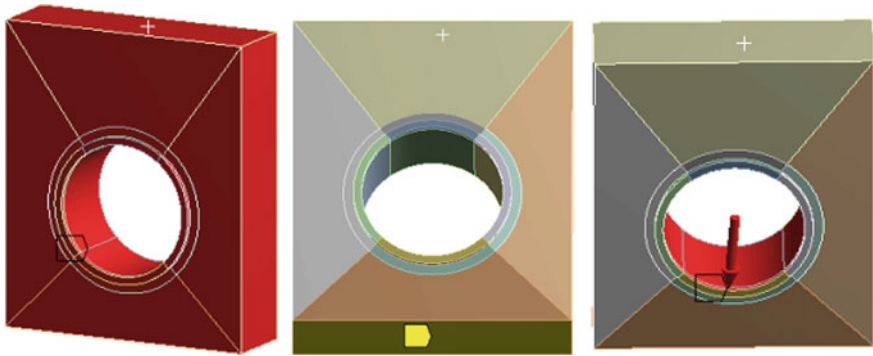


Fig. 7 Locations of thermal condition (left), remote displacement (middle), and pressure (right)

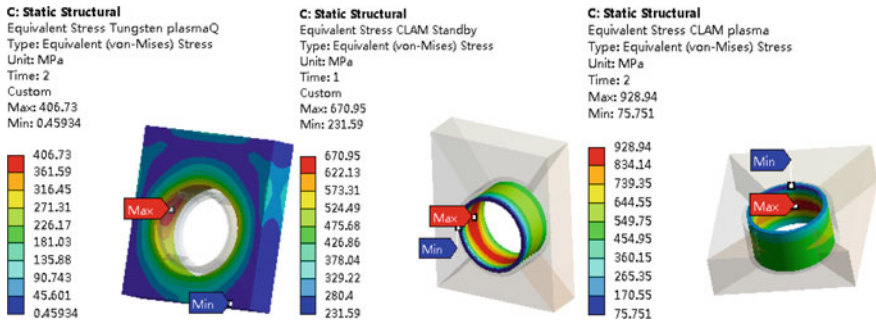


Fig. 8 Stress distribution of tungsten (left), CLAM pipe stress at preheating (middle), and plasma operation (right)

framework of linear elastic analysis. Besides, there is no expanding space for the middle part of CLAM pipe on account of the restriction of monoblock structure.

At plasma heating, the max stress is located at the upper part of the CLAM inner wall (Fig. 8, right). Due to existing temperature gradient on monoblock (Fig. 6, left), three materials (tungsten, copper, and CLAM) produce volume swelling which results in larger thermal stress. Then the compressive stress and tensile stress would be emerged in CLAM pipe higher and lower temperature zone separately. The outer wall of CLAM pipe comes into contact with the plastic material copper in the radial direction. When the bearing stress on copper pipe exceeds a certain value, copper pipe would produce plastic deformation in order to decrease the local stress of CLAM steel. Meanwhile, the inner wall of CLAM pipe bends inwards, and structure expansion would generate the greater stress. In the axial direction, the centre material of CLAM pipe has not space of expansion in order to come about the larger stress at the middle part. Moreover, the reason that max stress position turns up not the bottom but the top of CLAM pipe is the top thermal gradient which is more than the bottom.

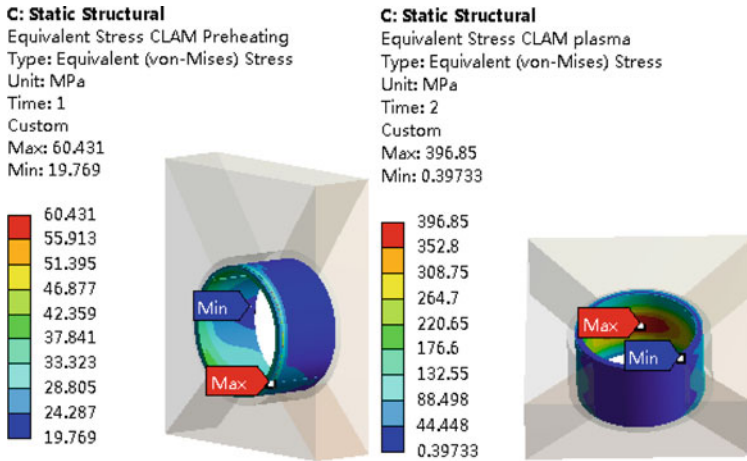


Fig. 9 Stress distribution of CLAM pipe with the environment temperature 300 °C

Above all, it is necessary to search for solutions that how to reduce stress of CLAM steel pipe.

### 3.3 Solution of Reducing CLAM Pipe’s Stress

It was considered that the environment temperature was changed from 22 to 300 °C. Figure 9 illustrates stress calculation results of CLAM tube at the environment temperature 300 °C. Then maximum stress of CLAM tube, which is lower than 3 Sm value, is obviously cut down. The main reason might be that PFU has no volume expansion which would not produce stress in the preheating stage.

## 4 Conclusions

Geometrical optimization and thermo-mechanical analysis were performed for W/CLAM PFU model using the empirical heat transfer correlation and design rules of ITER SDC-IC code. Major results are as follows: (1) Max handling heat flux of Divertor PFU (CLAM steel as heat sink material) at the optimal parameters is 10.12 MW/m<sup>2</sup> in steady state, attaining the due goal. (2) It turned out that the environment temperature has a great impact on max stress of CLAM pipe. (3) The other stress reduction methods of CLAM steel pipe at the optimal monoblock structure will be investigated further.



## References

1. Antonella Li-Puma, Marianne Richou, Philippe Magaud, et al., Potential and limits of water cooled divertor concepts based on monoblock design as possible candidates for a DEMO reactor, *Fusion Engineering and Design* 88 (2013) 1836–1843
2. P. Smith, G. Kalinin, D. Acker, et al., ITER STRUCTURAL DESIGN CRITERIA FOR IN-VESSEL COMPONENTS (SDC-IC), G 74 MA 8 01-05-28 W0.2
3. M. Rieth, M. Schirra, A. Falkenstein, et al. EUROFER 97 Tensile, Charpy, Creep and Structural Tests [PDF]. Forschungszentrum Karlsruhe GmbH, Karlsruhe in Germany 2003
4. A.-A.F. Tavassoli, J.-W. Rensman, M. Schirra, et al. Materials design data for reduced activation martensitic steel type F82H [J]. *Fusion Engineering and Design* 61–62 (2002) 617–628
5. Huailin Li, Arata Nishimura, Zaixin Li, et al. Low cycle fatigue behavior of JLF-1 steel at elevated temperatures [J]. *Fusion Engineering and Design* 81 (2006) 241–245
6. R.L. Kluch, M.A. Sokolov, N. Hashimoto. Mechanical properties of unirradiated and irradiated reduced-activation martensitic steel with and without nickel compared to properties of commercial steels [J]. *Journal of Nuclear Materials* 374 (2008) 220–228.
7. Qun-ying Huang, Chun-jing Li, Yan-fen Li, et al., R& D status of China low activation martensitic steel [J]. *Chinese Journal of Nuclear Science and Engineering*, 2007, 1: 008.
8. T. Hirai, F. Escourbiac, S. Carpentier-Chouchana, et al., ITER tungsten divertor design development and qualification program [J]. *Fusion Engineering and Design*, 2013, <http://dx.doi.org/10.1016/j.fusengdes.2013.05.010>
9. Marshall T D, Youchison D L, Cadwallader L C. Modeling the Nukiyama curve for water-cooled fusion divertor channels [J]. *FUSION TECHNOLOGY*, 2001, 39(2; PART 2): 849–855
10. F. Escourbiac. “High Heat Flux and Critical Heat Flux (CHF) Tests in Support to ITER HHFC”, Dec. 10–12, 2008 (<http://aries.ucsd.edu/raffray/IHHFC/presentations/Escourbiac.pdf>)
11. Marianne Richou, Antonella Li-Puma, Eliseo Visca., Design of a water cooled monoblock divertor for DEMO using Eurofer as structural material, *Fusion Engineering and Design* 89 (2014) 975–980

# Corrosion Resistance of Oxide Dispersion Strengthened Steel in Supercritical Water

Kaiju Yin, Wu Tang, Hao Wang, Xiaofeng Hong, Shaoyu Qiu, Rui Tang and Yong Chen

**Abstract** The oxidation behavior of 9Cr-ODS and MA956 oxide dispersion strengthened (ODS) steel exposed to supercritical water at 500–600 °C and 25 MPa were examined. For comparison, a non-ODS steel (9Cr) was also examined. The oxidized samples were characterized by scanning electron microscopy/energy and gravimetry. The oxide films were rather porous in 9Cr steel, while the porosity in 9Cr-ODS almost could not be observed. A three-layered oxide films formed on 9Cr-ODS steel, which was composed of an outer oxide layer, an inner oxide layer, and an internal oxide zone which was featured by gradual variation of alloying elements and oxygen from the oxide to the matrix, the  $\text{Cr}_2\text{O}_3$  in internal oxide zone play a key role of oxidation behavior. The kinetic data of 9Cr and 9Cr-ODS steels showed that oxide films formation obeyed a parabolic rate law. The oxidation rate of MA956 was lowest, the 9Cr-ODS steel lower than 9Cr.

**Keywords** Oxide dispersion strengthened (ODS) steel · Supercritical water · Oxide films · Corrosion kinetic

The supercritical water reactor (SCWR) design has been selected as one of the reactor concepts for future Generation IV nuclear reactor systems, because of its simplified design, smaller volume, and higher thermal efficiency than current light water reactors. As SCWR will operate above the supercritical point of water, it is expected to be more corrosive to structural materials that are commonly used in pressurized water reactor. Thus, the corrosion behavior of in-core used structure material has become a major obstacle to the practical application of SCWR.

---

K. Yin (✉) · W. Tang  
State Key Laboratory of Electronic Thin Films and Integrated Devices,  
University of Electronic Science and Technology of China,  
Chengdu 610054, P.R. China  
e-mail: yinkj1975@163.com

K. Yin · H. Wang · X. Hong · S. Qiu · R. Tang · Y. Chen  
Laboratory of Science and Technology on Reactor Fuel and Materials,  
Nuclear Power Institute of China, Chengdu 610041, P.R. China

Ferrite-martensitic (F/M) ODS steels have been identified as candidates for core structure components in SCWR. F–M steels exhibit good high-temperature strength and creep resistance, low swelling and activation under irradiation, low susceptibility to stress corrosion cracking, and modest corrosion resistance. The addition of rare metal oxide particle ( $Y_2O_3$ ,  $Th_2O_3$ , etc.) improved the strength and corrosion behavior of the material simultaneously [1–3].

Ohtuska's [4, 5] research revealed that the uniform distributed oxide particles in the base metal of ODS steel can inhibit the motion of dislocations and the slide of grain boundaries, slow down the diffusion of metal atoms, and increase the corrosion resistance of the base metal in high temperature conditions. Meanwhile, the addition of rare metal oxide particles can improve the high temperature mechanical properties effectively, the improvement effect is maintained until the temperature is close to the melt point of the alloy. Cho's [6, 7] research showed that the oxide dispersion strengthened F/M steels had a better corrosion resistance in SCW compared to ordinary F/M steels. The improvement attributes to two reasons, the first is the segregation of rare metal oxides in grain boundaries and in the interface of oxide and base metal; the second is the better adhesion of oxides with base metals in ODS steels. As the design life time of SCWR is as long as 60 years, the oxide films characteristic, corrosion kinetics, and oxide evolution mechanism of ODS steel need to be further investigated.

The corrosion behavior and corrosion kinetics of 9Cr-ODS steel and high chromium ODS steel in supercritical water were studied in this research. The experiment results were compared to a non-ODS 9Cr steel. SEM/EDX were used to characterize the morphology and microstructure of the oxide films. Furthermore, the mechanism of why ODS steel has an improved corrosion behavior compared to non ODS steel was also discussed.

## 1 Experiment

The chemical compositions of 9Cr-ODS, MA956, and 9Cr are given in Table 1. The distribution of oxide particles in 9Cr-ODS and MA956 is shown in Fig. 1.

The corrosion coupon dimensions are 40 mm × 20 mm × 1.5 mm and each coupon has a small hole for securing it in the autoclave. The corrosion coupons were mechanically polished down 1 μm using SiC paper and diamond paste, and then washed 10 min in acetone solutions by ultrasonic. Exposure tests were

**Table 1** Nominal compositions of 9Cr-ODS, 9Cr, and MA956 in wt%

Material	C	Si	Mn	Ti	Ni	Cr	Al	W	V	Y	Fe
9Cr-ODS	0.10	0.15	0.44	0.15	0.004	9.0	–	2.0	0.2	0.5	Bal.
9Cr	0.10	0.15	0.44	0.15	0.004	9.0	–	2.0	0.2	–	Bal.
MA956	0.006	0.10	–	0.50	–	19.24	5.01	–	–	0.5	Bal.

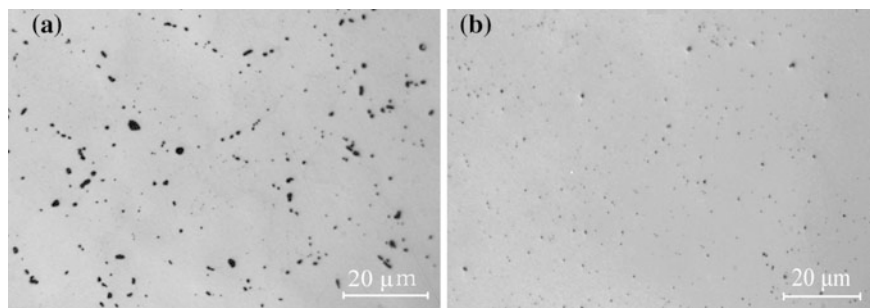


**Fig. 1** OM image of oxide dispersion particle in ODS, **a** image of oxide dispersion particle in 9Cr-ODS and **b** image of oxide dispersion particle in MA956

**Table 2** Test conditions for SCW exposure

Parameters	Conditions
Temperature (°C)	(500–600) ± 5
Pressure (MPa)	25 ± 0.5
Dissolved oxygen ( $\mu\text{g kg}^{-1}$ )	<10 (deaerated)
Water conductivity ( $\mu\text{S/cm}$ )	0.1
pH	Neutrality (RT)
Exposure time (h)	~ 1000
Sampling period (h)	200, 400, 600, 800, 1000

conducted over the temperature range of 500–600 °C and at pressure of 25 MPa. Exposure times were 200 h in each experiment. The time dependence of oxidation was studied at 500 and 600 °C with exposure times of 200, 400, 600, 800, and 1000 h. The weight gain of corrosion coupons was measured immediately after completion of the test. A summary of experiment at conditions is given in Table 2. SEM and EDS were used to analyze the surface morphology, cross sectional morphology, microstructure, and element distribution of the oxide films.

## 2 Results

### 2.1 Surface Oxide Morphology

9Cr, 9Cr-ODS, and MA956 were tested under the condition of 500 °C/25 MPa for 800 h. The morphology of the oxide films is shown in Fig. 2.

After SCW exposure, the surfaces of the three test materials are covered by polygonal crystal, among which, the surfaces of 9Cr and 9Cr-ODS steel are fully covered, but MA956 is partially covered. There are significant differences in the oxide films morphology between 9Cr and 9Cr-ODS. There are many holes in the

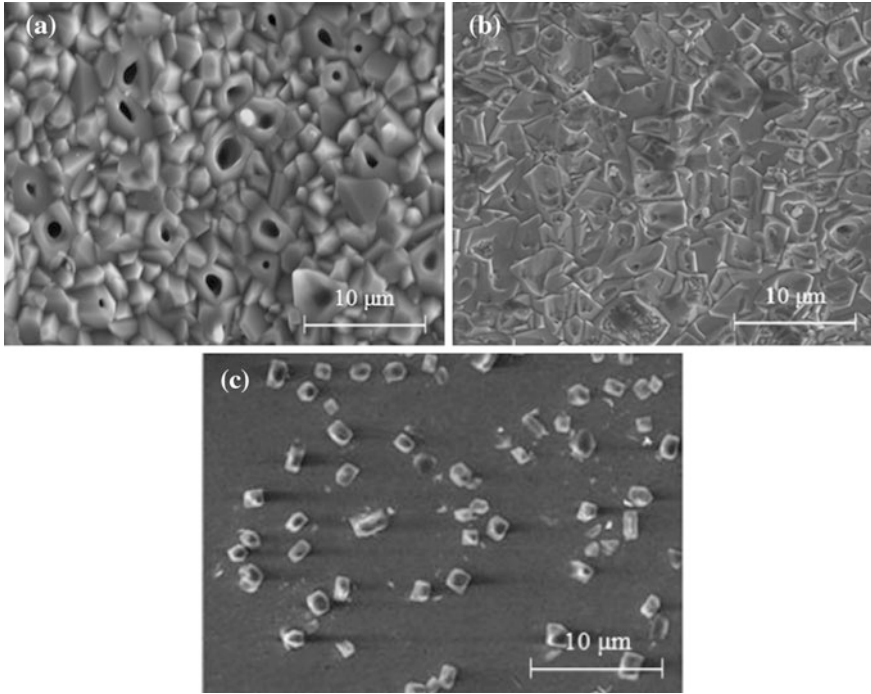


**Fig. 2** SEM images of the surface morphology of the 9Cr **a**, 9Cr-ODS **b** and MA956 **c** exposed to SCW under a pressure of 500 °C/25 MPa for 800 h

oxide films of 9Cr, few holes in 9Cr-ODS, and no hole in MA956. The growth of the oxide films of Fe–Cr alloys is controlled by the outward diffusion of cations and the inward diffusion of oxygen ion. The holes, cracks, and grain boundaries provide express ways for the diffusion of cations and oxygen ions. The plenty holes with a larger diameter than the other two material in the oxide films of 9Cr steel make the diffusion of cations and oxygen ions more quickly, thus the corrosion rate of 9Cr is higher. The significant difference in the morphology of test material after SCW exposure reveals that the addition of oxide dispersion particle  $Y_2O_3$  changed the corrosion behavior of the material distinctly.

## 2.2 Cross-Sectional Analysis

Oxide morphology was investigated on cross-section samples using SEM. Figures 3 and 4 show cross-section images of 9Cr and 9Cr-ODS steel coupons exposed to SCW for 1000 h.

The oxide films of 9Cr steel consist of two layers, an outer layer and an inner layer. The outer oxide layer is about 7  $\mu\text{m}$  thick, while the inner layer is about 6  $\mu\text{m}$

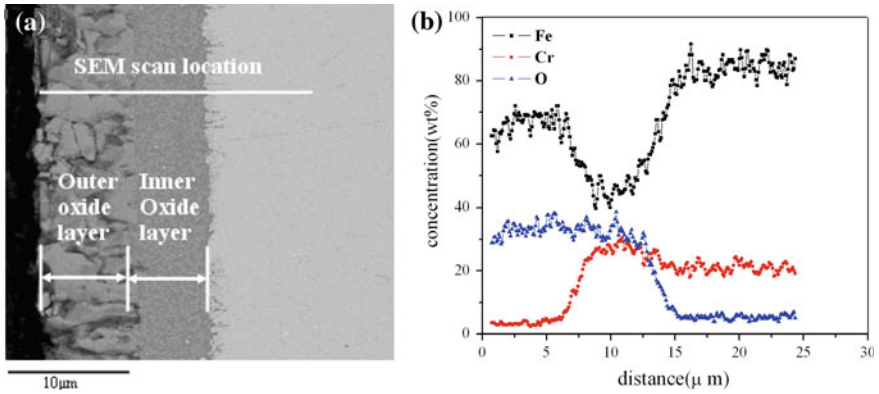


**Fig. 3** The oxide of the sample exposed to SCW at 500 °C/25 MPa for 1000 h. **a** Cross-sectional SEM image and **b** composition profiles of elements of Fe, Cr, O

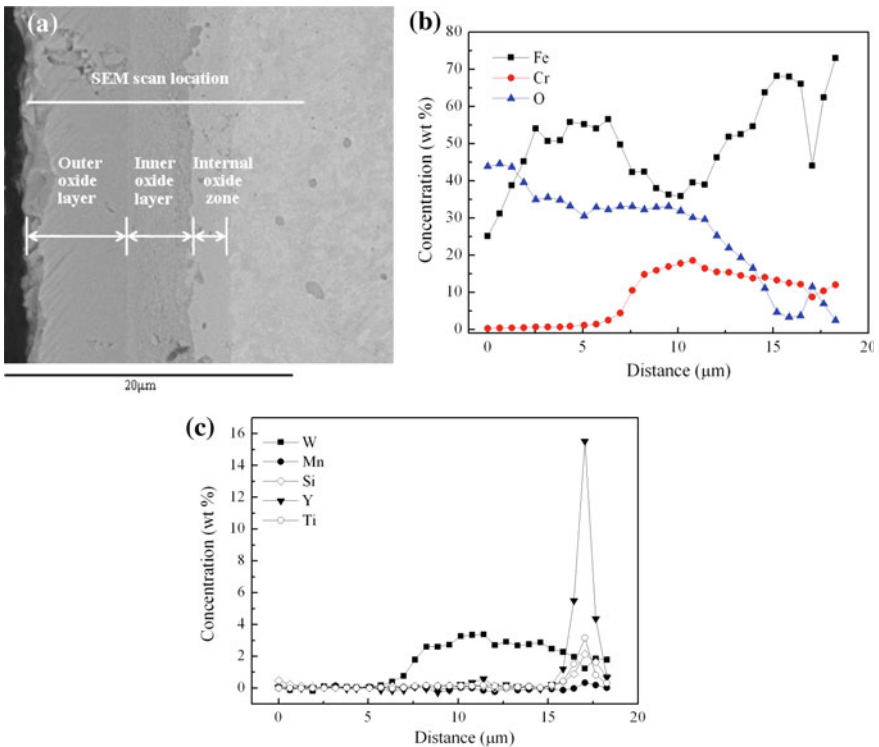


**Fig. 4** The oxide of the sample exposed to SCW at 500 °C/25 MPa for 1000 h. **a** Cross-sectional SEM image, **b** composition profiles of major elements of Fe, Cr, O, and **c** trace elements of W, Mn, Si, Y, and Ti

thick. The outer layer of 9Cr contains a significant amount of chromium. The oxide films of 9Cr-ODS steel consist of three layers, an outer oxide layer with a thickness of 6 μm, an inner oxide layer with a thickness of 4 μm and an internal oxide zone with a thickness of 2 μm. The outer oxide layer is rich in Fe but poor in Cr. The internal oxide zone is characterized by a gradual transition in the element content from oxide film level to base metal level.

The trace element atomic composition vs. depth profiles taken on the oxidized 9Cr-ODS cross sections using EDS are shown in Fig. 4c. Figure 4c indicates that tungsten enriched in the inner layer of oxide films, and no explicit enrichment of Y in the oxide films. There is a sudden increase of Y where the depth reaches to 17 μm, as a Y<sub>2</sub>O<sub>3</sub> particle lies in the scanning line of EDS. Figures 3 and 4 reveals that with the addition of dispersed Y<sub>2</sub>O<sub>3</sub> particle, there is a change in the oxide structure of 9Cr-ODS exposed in SCW. The oxide film of 9Cr is thicker than that of 9Cr-ODS after same exposure time (1000 h), which indicates that the 9Cr-ODS has a better corrosion resistance in SCW conditions.

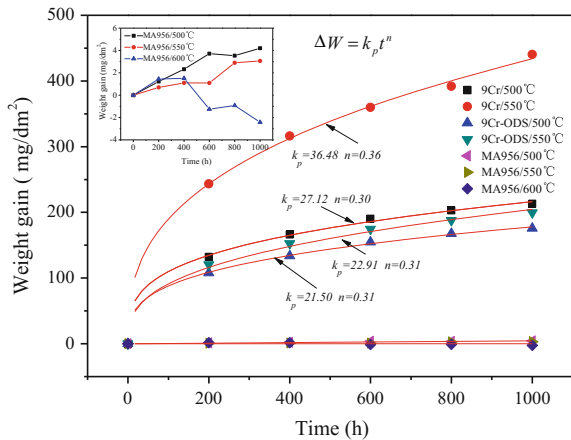
### 2.3 Temperature Dependence of Oxidation

Temperature has a great influence on the oxidation rate of 9Cr, 9Cr-ODS, and MA956 in SCW as shown in Fig. 5. The temperature dependence can be fit by an Arrhenius equation:

$$\Delta W = k_p t^n \tag{1}$$

$$k_p = k_0 \exp(-Q/RT) \tag{2}$$

**Fig. 5** Weight gain as a function of exposure time obtained from the 9Cr, 9Cr-ODS and MA956 exposed to SCW at 500–600 °C/25 MPa



where  $\Delta W$  is the weight gain,  $Q$  is the activation energy of the oxidation reaction (J/mol),  $k$  is oxidation rate constant ((mg/dm<sup>2</sup>/h)),  $R$  is the gas constant (8.314 J/mol K)  $t$  is the time in h,  $1/n$  is the time exponent, and  $T$  is the temperature (K). In Fig. 5, the corrosion rate of 9Cr and 9Cr-ODS increases as the increase of temperature in 500 and 550 °C SCW, the corrosion kinetics follow the parabolic law. The weight gain of MA956 in 500–600 °C SCW is very small. Weight loss of MA 956 is observed in 500, 550 and 600 °C SCW from the figure in the top left of Fig. 5 which indicates the breaking off oxide film had happened.

When compare the corrosion behavior of 9Cr, 9Cr-ODS, and MA956 in SCW, MA956 has the best corrosion resistance, while 9Cr has the worst and 9Cr-ODS in the middle. 9Cr-ODS and 9Cr have the same base metal and the element concentrations, but an addition of dispersed rare metal oxide (0.5 %) make the corrosion resistance of 9Cr-ODS increased significantly. This phenomenon is more obvious when the temperature increases. The corrosion rate of 9Cr is 2.5 times higher than that of 9Cr-ODS in 550 °C. Because of the addition of dispersed rare metal oxide and aluminum element, MA956 has the best corrosion resistance.

### 3 Discussion

The comparison of oxide film structure and corrosion kinetics of 9Cr, 9Cr-ODS in SCW conditions reveals that the addition of dispersed rare metal (Y) oxide makes the corrosion resistance of material increased significantly. The oxide films of 9Cr steel formed in SCW conditions consist of two layers, an outer layer and an inner layer. The oxide films of 9Cr-ODS steel consist of three layers, an outer oxide layer, an inner oxide layer, and an internal oxide zone.

The TEM research on 9Cr-ODS films formed in SCW done by Chen [8] revealed that the Cr<sub>2</sub>O<sub>3</sub> exist in the internal oxide zone with the form of discontinuous belt-shaped oxides. As the diameter of Y is relatively higher, its solution in oxide is lower, which makes it easier to segregate in the grain boundaries. The segregation of Y in grain boundaries makes it difficult for the diffusion of Cr<sup>3+</sup>.

In Fe–Cr alloys, the growth process of film is controlled by the outward diffusion of positive ion and the inward diffusion of oxygen. As the segregation of Y in grain boundaries prevents the diffusion of Cr<sup>3+</sup>, i.e., the progress of positive ions' outward diffusion through oxide film is suppressed, which leads to the increase of the corrosion resistance of 9Cr-ODS. There is a significant difference between 9Cr and 9Cr-ODS in their oxide film structures after exposed to SCW conditions, the oxide film of 9Cr contains a large number of mini holes while the holes in the oxide film of 9Cr-ODS is much less and smaller than that of 9Cr. These mini holes play an important role in the evolution of the oxide film growth of the Fe–Cr alloys. As is mentioned above, the growth process of film is controlled by the outward diffusion of positive ion and the inward diffusion of oxygen. In the process of diffusion, the holes, cracks, and grain boundaries provide express ways for the diffusion of cations and oxygen ions [9]. The larger amount of mini holes with a larger diameter



in the oxide films of 9Cr steel make the diffusion of cations and oxygen ions more quickly, thus the corrosion rate of 9Cr is higher which leads to a relatively worse anti-corrosion behavior.

MA956 and 9Cr-ODS both belong to the ODS type, but the anti-corrosion behavior of MA956 is superior to that of 9Cr-ODS, which is attributed to the addition of Al with the weight percent of 5 % in MA956. The addition of Al forms a protective oxide film of  $\text{Al}_2\text{O}_3$  in SCW conditions. In the other hand, the weight percent of Cr in MA956 is as high as 19.24 %, which forms a continuous protective film of  $\text{Cr}_2\text{O}_3$ . The protective film of  $\text{Cr}_2\text{O}_3$  increases the anti-corrosion behavior of the material. The oxidation behavior of single crystal MA956 (1 1 1) and (1 1 0) done by Czyska [10] revealed that in the early stage of the oxidation of MA956, the oxide film growth is not controlled by the inward diffusion of oxygen, otherwise it is controlled by the outward diffusion of Al from the interface of oxide film toward and base metal toward the interface of gas and oxide film. Particles of  $\text{Y}_2\text{O}_3$  will prevent the diffusion of positive ions through the grain boundaries of oxide film and base metal, which lead to a good anti-corrosion behavior of MA956 in SCW conditions.

## 4 Conclusion

The research on the oxide film surface morphology, oxide film structure, and corrosion kinetics of 9Cr, 9Cr-ODS, and MA956 in 500–600 °C/25 MPa SCW revealed that the addition of dispersed  $\text{Y}_2\text{O}_3$  changed the corrosion behavior of those materials in SCW conditions and improved the anti-corrosion properties.

- (1) The oxide film of 9Cr contains a large number of mini holes, but the holes in the oxide film of 9Cr-ODS is obviously less and smaller which leads to a decrease of diffusion express ways and finally improves the anti-corrosiveness.
- (2) The oxide films of 9Cr steel formed in SCW conditions consist of two layers, an outer layer and an inner layer. The oxide films of 9Cr-ODS steel consist of three layers, an outer oxide layer, an inner oxide layer, and an internal oxide zone. The  $\text{Cr}_2\text{O}_3$  in the internal oxide zone plays a key role in the increase of anti-corrosiveness.
- (3) The corrosion rate of 9Cr and 9Cr-ODS increases as the increase of temperature, the corrosion kinetics follow the parabolic law. The anti-corrosiveness of 9Cr-ODS is obviously superior to that of 9Cr. MA956 has the best anti-corrosiveness which is attributed to the high Cr content and the addition of Al.

**Acknowledgments** This research is sponsored by the National Key Scientific Research Program (2011ZX06004-009-0102) of China.

## References

1. Wolfgang Hoffelner, *Materials for Nuclear Plants*. 2013, 249: 309–357
2. G.R. Odette, M. J. *Annu. Rev. Mater. Res.*, 2008, 38: 471–503
3. R. Lindau, A. Moslang, M. Schirra, et al. *Journal of Nuclear Materials*, 2012, 307–311: 769–772
4. S. Ohtuska, S. Ukai, M. Fujiwara, et al. *Mater. Trans.* 2005, 46 (3): 1–8
5. S. Ukai, S. Mizuta, T. Yoshitake, et al. *J. Nucl. Mater.* 2000, 283–287: 702–710
6. H. S. Cho. *J. Nucl. Mater.* 2004, 329–333
7. V. de Castro, T. Leguey, A. Munz, et al. *Journal of Nuclear Materials*, 2009, 386–388: 449–452
8. Yun Chen, Kumar Sridharan, Shigeharu Ukai, et al. *Nuclear Materials* 2007, 371: 118–128
9. Kaiju Yin, Shaoyu Qiu, Rui Tang, *Supercritical Fluids*, 2009, 50: 235–239
10. Czyska-Filemonowicz, K. Szot, A. Wasilkowska, et al. *Solid State Ionics*, 1999, 117: 13–20

# Design of a Thin-Film Neutron Detector Used for Personnel Dosimeter

Wenming Xia, Junjun Gong and Junjun Chen

**Abstract** Semiconductors used for neutron detector are always coated by a thin-film, which is used to convert free neutrons into charged particles. The thin-film commonly used in such detectors utilize the  $^{10}\text{B}(n, \alpha)^7\text{Li}$  reaction, the  $^6\text{Li}(n, \alpha)^3\text{He}$  reaction, or the recoil proton reaction. The detection efficiency of these detectors coated with single thin-film varied with the energy of neutrons. So the energy response performance of personnel dosimeter with these detectors is not satisfactory. The purpose of the article is designing a suitable neutron detector for personnel dosimeter. In order to overcome the disadvantage of the energy response performance the neutron detectors are coated by a single thin-film. In these designs a neutron personnel dosimeter detector fabricated with three silicon diodes are coated by two different thin-films. One silicon diode is uncoated and will be used to subtract the response to gamma rays of the coated silicon diodes. The response of each silicon diodes coated by different thin-films are calculated with Monte Carlo code MCNPX. The total personnel dose rate results will be obtained by summing-up each response of the coated silicon diodes multiplied with different gain factors.

**Keywords** Neutron detector · Personnel dosimeter · MCNPX · Energy response

## 1 Introduction

The accurate neutron personnel dosimetry has become a research hotspot these years [1]. Semiconductors were used as active detectors for neutron personnel dosimeter. The most familiar format of these detectors is a semiconductor detector added with a convertor which could convert neutrons to charged particles. The

---

W. Xia (✉) · J. Gong · J. Chen  
Department of Nuclear Energy Science and Engineering,  
Naval University of Engineering, Nuclear Detection and  
Radiation Protection, Box 125 No. 717 Jiefang Avenue,  
Wuhan, Hubei, China  
e-mail: jianghong@cnpe.cc

convertors always contain  $^{10}\text{B}$ ,  $^6\text{Li}$  or  $^1\text{H}$ . For  $^{10}\text{B}$ , the  $^{10}\text{B}(n, \alpha)^7\text{Li}$  reaction was utilized to detect neutrons [2–4]; for  $^6\text{Li}$ , the  $^6\text{Li}(n, \alpha)^3\text{H}$  reaction was utilized to detect neutrons; and for  $^1\text{H}$ , the recoil protons produced by the neutron was utilized to detect neutrons. Some familiar reactive material used for the thin-film neutron convertors were: pure  $^{10}\text{B}$ ,  $^6\text{LiF}$ , pure  $^6\text{Li}$ , and  $^{10}\text{B}_4\text{C}$ .

## 2 Design of Thin-Film Neutron Detectors

$H_p(d)$  was devised as the operational quantity by the International Commission on Radiation Units and Measurement (ICRU) for personnel dosimetry, which is the dose equivalent in ICRU (soft) tissue at an appropriate depth,  $d$ , below a specified point on the human body. The specified point is usually given by the position where the individual dosimeter is worn. For the assessment of effective dose a depth  $d = 10$  mm is recommended. For monoenergetic neutrons at energy  $E$ , the personnel dose equivalent can be determined by

$$H_p(10) = \Phi h_{p,\text{slab}}(E)$$

where  $\Phi$  is the monoenergy neutron fluence and  $h_{p,\text{slab}}(E)$  is conversion coefficients for  $H_p(10)$  as a function of energy [5]. The values of  $h_{p,\text{slab}}(E)$  were show in Fig. 1.

As shown in Fig. 1,  $h_{p,\text{slab}}(E)$  is a highly nonlinear function in energy wherein relatively low dose equivalent per unit neutron fluence ( $\sim 10$  pSv  $\text{cm}^2$ ) is observed at energies below 10 keV followed by an early two order-of-magnitude increase

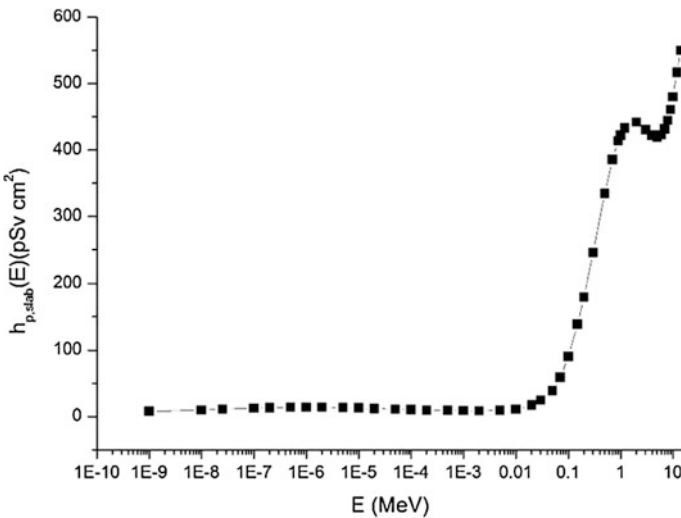


**Fig. 1** Fluence-to- $H_p(10)$  conversion curve devised by ICRP74

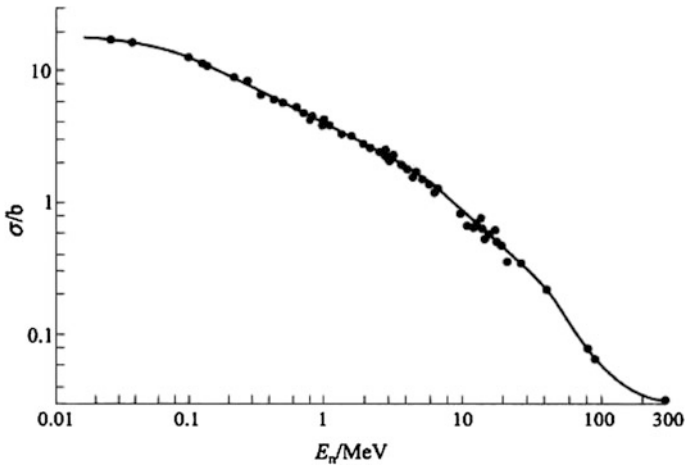
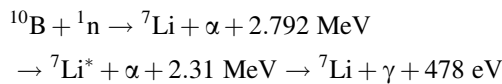


Fig. 2 Cross-section of <sup>1</sup>H recoil of neutron

(~ 600 pSv cm<sup>2</sup>) between 10 keV and 1 meV. The reactive materials contain <sup>10</sup>B or <sup>6</sup>Li used to detect neutron utilize nuclear interaction have big thermal cross-section, but the cross-section becomes small with the increase of the energy. The thermal cross-section is 3840 barns. In a common workplace, the energy of neutron was always a broad spectrum from thermal neutron to about 10 meV. Thin-films contain <sup>1</sup>H used for neutron converters can convert neutrons to protons by nuclear recoil. The cross-section of nuclear recoil of neutron and <sup>1</sup>H is shown in Fig. 2, and is about 1 to 10 barns from 0.01 to 10 meV.

This work uses <sup>10</sup>B<sub>4</sub>C and polyethylene as the thin-film reactive material, the <sup>10</sup>B<sub>4</sub>C was coated on the silicon base plate. The density of <sup>10</sup>B<sub>4</sub>C is about 2.52 g/cm<sup>3</sup>. When a <sup>10</sup>B nucleus captures a thermal neutron, it produces two charged particles through one of the following reactions:



The energy of  $\alpha$  particles produced by reactions above were 1.78 meV (6 %) and 1.47 meV (94 %), respectively. Range of  $\alpha$  particles with energy of 1.47 meV in <sup>10</sup>B<sub>4</sub>C is about 3.5  $\mu\text{m}$ . So, the <sup>10</sup>B<sub>4</sub>C layer coated on the silicon base plate need not be bigger than 3.5  $\mu\text{m}$ .

Because the thickness was enslaved to the technology of making the thin-film neutron convertor; the thinnest <sup>10</sup>B<sub>4</sub>C layer coated on the silicon base plate is 10  $\mu\text{m}$ . So, the thickness of <sup>10</sup>B<sub>4</sub>C layer in this work is 10  $\mu\text{m}$ .

The thickness of polyethylene thin-film was selected by using the MCNPX program [6]. The simulated detectors were Si PIN diodes with 0.3 mm thickness and 10  $\times$  10 mm<sup>2</sup> active area combined with polyethylene films with different thicknesses coated on their surfaces. Each simulation run consisted of the emissions

**Fig. 3** Computing model of the neutron detectors with polyethylene thin-films as neutron converters

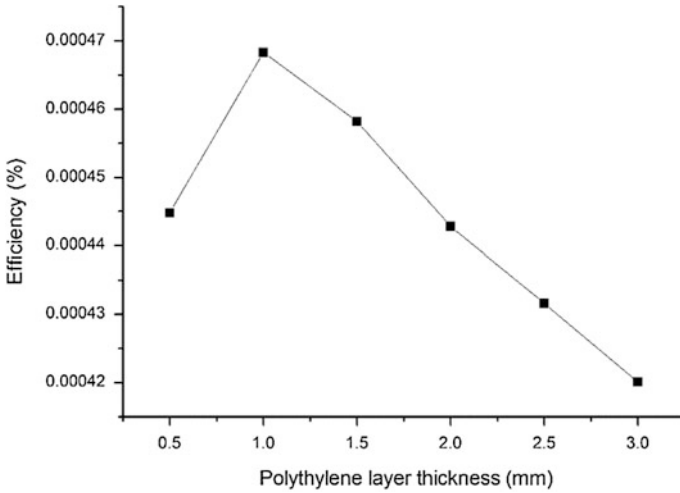
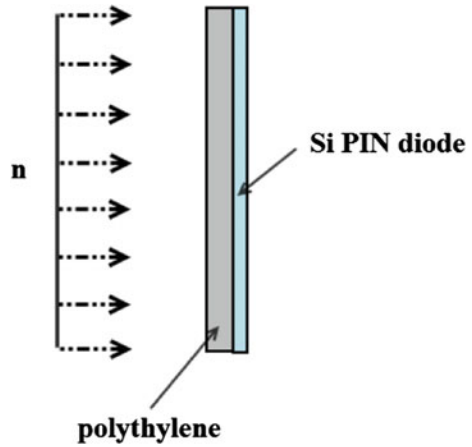


**Fig. 4** Detection efficiency of Si PIN diodes with different thickness of polyethylene layers (1 meV neutron)

of  $10^7$  monoenergetic neutrons with 1 meV energy, focused directly on the front side of the detector, as shown in Fig. 3. The computing results were shown in Fig. 4. It can be observed from this figure that simulated maximum efficiency can be got when the converter layer thickness is 1 mm.

Photograph shown in Fig. 5 were the thin-film neutron converters and the Si PIN diodes prepared for the personnel dosimeter prototype.

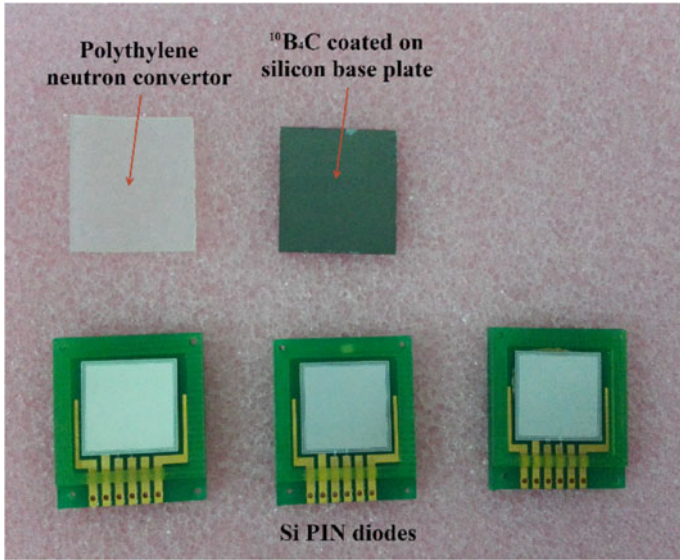


Fig. 5 Photograph of thin-film neutron converters and Si PIN diodes

### 3 Computing of the Gain Factor

Because the Si PIN diodes were also sensitive to photons, so a Si PIN diode of the same type was added to the personnel dosimeter to subtract the photon response of Si PIN diodes coated with thin-film neutron converters.

There are two Si PIN diodes with different neutron converters used to detect neutrons in different energy ranges. In order to get the personnel dose rate results, the response of two Si PIN diodes should be multiplied with different gain factors, as shown in following:

$$H_p(10) = g_B M_B + g_P M_P$$

where  $M_B$  and  $M_P$  denote the number of counts on the Si PIN diodes with different neutron converters, and  $g_B$  and  $g_P$  denote the gain factors of the Si PIN diodes.

The gain factors could be got by simulation or experiments. At the design stage in this work, the gain factors were got by simulation with MCNPX. Two simulation run consisted of the emissions of neutrons from <sup>241</sup>Am-Be and <sup>252</sup>Cf neutron sources.  $M_B$  and  $M_P$  of each neutron source were got by simulation, and the gain factors can be got by solving a binary linear equation group.

## 4 Conclusions

The detector of a personnel neutron dosimeter was designed in this work. The detector utilizes two different reactive materials as the neutron converters of Si PIN diodes. One is polyethylene, another is  $^{10}\text{B}_4\text{C}$ . Thickness of the thin-films was selected by MCNPX simulation. The Si PIN diodes have different response to the same neutron fields. The counts of each Si PIN diodes multiplied with different gain factors and stacked up to get the personnel dose rate results of the dosimeter. The gain factors were got by MCNPX simulation.

This work is still in progress and will be the basis for developing the personnel dosimeter prototype that we will carry out this year.

## References

1. D. T. Bartlett, R. J. Tanner, D. J. Thomas. Active Neutron Personal Dosimeters: A Review of Current Status. *Radiation Protection Dosimetry*, Vol. 86, No. 2, pp. 107–122 (1999)
2. M. Luszik-Bhadra. A Prototype Personal Neutron Dosimeter with One Silicon Diode. *Radiation Protection Dosimetry*, Vol. 96, Nos 1–3, pp. 227–229 (2001)
3. C. Guardiola, C. Fleta, D. Quirion, et al. First investigations of a silicon neutron detector with a carborane converter. 2011 JINST 6 P11001
4. D. S. McGregor, R. T. Klannb, J. D. Sandersc, et al. Recent Results From Thin-Film-Coated Semiconductor Neutron Detectors. X-Ray and Gamma Ray Detectors and Applications IV, *Proceedings of SPIE*, Vol. 4784 (2002)
5. ICRP, Conversion Coefficients for Use in Radiological Protection Against External Radiation, Publication 74, International Commission on Radiological Protection, *Annals of the ICRP*, 26, no. 3/4, Pergamon Press, Oxford, 1996
6. J.S. Hendricks et al. eds., Monte Carlo N-Particle Transport Code System for Multiparticle and High Energy Applications, version 2.6.0, Los Alamos National Laboratory, NM, LA-UR-08-2216 (2008)



# Development and Verification of Liquid-Fueled Molten Salt Reactor Analysis Code Based on RELAP5

Chengbin Shi, Maosong Cheng and Guimin Liu

**Abstract** Liquid-fueled molten salt reactor is the only reactor system using liquid salt as fuel in the six generation IV advanced reactor systems, which can be characterized by remarkable advantages and competitiveness in nuclear safety, economical efficiency, natural resource protection, sustainable development, and proliferation resistance of nuclear energy. Each country in the world is carrying out research on the molten salt reactor, and system analysis is an important research content. RELAP5 code is the best estimation code of pressurized water reactor. In this paper the neutronics and thermal hydraulics models in the RELAP5 are extended, so as to develop a system analysis code for liquid-fueled molten salt reactor. Then the code is verified using molten salt reactor experiment (MSRE) experimental benchmarks. The results indicate that the computational results coincide well with MSRE experimental benchmarks, and preliminary verifies the validity of the extended system analysis code.

**Keywords** RELAP5 · Liquid-fueled molten salt reactor · MSRE · Code verification

## 1 Introduction

The molten salt reactor (MSR) is one of the six advanced reactor concepts identified by the Generation IV International Forum (GIF) as a candidate for cooperative development. The study on the molten salt reactors was first carried out at the Oak Ridge National Laboratory (ORNL) in the projects of the Aircraft Reactor Experiment (ARE) [1] and the Molten Salt Reactor Experiment (MSRE) [2]. Based on the experience of running MSRE, ORNL then published the Molten Salt Breeder Reactor (MSBR) conceptual design [3]. The research of MSR in Japan started from

---

C. Shi · M. Cheng (✉) · G. Liu  
Shanghai Institute of Applied Physics, Chinese Academy of Sciences,  
Shanghai 201800, China  
e-mail: chengmaosong@sinap.ac.cn

1980s, and the FUJI concept was published referred to the MSBR design [4]. Besides, in Russia, a new molten salt reactor concept, named the Molten Salt Actinide Recycler and Transmuter (MOSART), has been developed for burning transuranium plutonium and minor actinides [5]. In January 2011, Chinese Academy of Science launched a strategic pilot science and technology special project “Thorium Molten Salt Reactor Nuclear Energy System (TMSR),” aiming at developing both solid and liquid-fueled molten salt reactors [6].

Up to now, the characteristics of molten salt reactor have been studied by different researchers with various computational codes. The Cinsf1D code in one-dimension geometry using two-energy-group diffusion and a spatial dimension neutronic model was developed by Lecarpentier and Carpentier [7]. Krepel et al. [8, 9] extended the DYN1D/DYN3D code for liquid-fueled molten salt reactors, in which the neutron diffusion models were employed for neutrons calculation. Wang et al. [10] analyzed the fluid dynamic of the MOSART core with the code SIMMER-III by extending the thermo hydraulic and neutronic models. Guo et al. [11] developed the safety analysis code by considering the delayed neutron precursors both in the reactor core and the external loop.

The RELAP5 code is the thermal hydraulic best estimate code for pressurized water reactor, which was originally developed by Nuclear Regulatory Commission (NRC). In this work, the point kinetic model including the flow effect of liquid-fueled molten salt reactor and the thermal hydraulic model with internal heat source were embedded into the RELAP5 code. Then the dynamics of the MSRE were simulated to verify the validity of the extended RELAP5 code.

## 2 Physical Models and Solution Methods

### 2.1 Neutronics Model

According to the conservation law, the neutron equation of the reactor core can be written as

$$\frac{dn(t)}{dt} = \frac{\rho(t) - \beta_{\text{eff}}}{l} n(t) + \sum_{i=1}^6 \lambda_i c_i(t), \quad (1)$$

where  $n$  is the neutron density;  $\rho$  is the reactivity;  $\beta_{\text{eff}}$  is the portion of effective delayed neutron precursors;  $l$  is the neutron lifetime. Delayed neutron precursors in the liquid-fueled molten salt reactor flow with the liquid fuel in the primary loop, which is different from the traditional solid fueled reactor. Considering that delayed neutron precursors decay in the primary loop and flow back into the reactor core again, the delayed neutron conservation equation can be expressed as

$$\frac{dc_i(t)}{dt} = \frac{\beta_i}{l} n(t) - \left( \lambda_i + \frac{1}{\tau_c} \right) c_i(t) + \frac{\exp(-\lambda_i \tau_l)}{\tau_c} c_i(t - \tau_l), \quad (2)$$

where  $\beta_i$  is the portion of neutron fraction of group  $i$ ;  $\tau_c$  is the time of delayed neutron precursors staying in the core;  $\tau_l$  is the time of delayed neutron precursors staying in the external loop. The second term in the right side of Eq. (2) indicates the reduced delayed neutron precursors due to the decay and flow effect of fuel salt, and the third term in right side of Eq. (2) indicates the delayed neutron precursors flow back into the core. From Eqs. (1) and (2), the reactivity bias  $\Delta\rho_0$  can be obtained by setting the left side of the above equations to zero. The reactivity bias due to the liquid fuel flow in steady state can be expressed as

$$\Delta\rho_0 = \sum_{i=1}^6 \beta_i \left[ 1 - \frac{\lambda_i}{\lambda_i + \frac{1}{\tau_c} (1 - \exp(-\tau_l \lambda_i))} \right] \quad (3)$$

Reactivity feedback can be induced by temperature change, void fraction, power change. However, in this work, only reactivity feedback due to temperature change of fuel and graphite is taken into account. Therefore, reactivity feedback can be expressed as

$$\rho(t) = \Delta\rho + \rho_{\text{fuel}} + \rho_{\text{graphite}} \quad (4)$$

$$\rho_{\text{fuel}} = \alpha_{\text{fuel}} (T_{\text{fuel}} - T_{0,\text{fuel}}) \quad (5)$$

$$\rho_{\text{graphite}} = \alpha_{\text{graphite}} (T_{\text{graphite}} - T_{0,\text{graphite}}), \quad (6)$$

where  $\rho_{\text{fuel}}$  is the reactivity feedback of fuel salt in reactor core;  $\rho_{\text{graphite}}$  is the reactivity feedback of graphite in reactor core;  $T_{\text{fuel}}$  is the average temperature of fuel salt in reactor core;  $T_{0,\text{fuel}}$  is the initial temperature of fuel salt in reactor core;  $T_{\text{graphite}}$  is the average temperature of fuel salt in reactor core;  $T_{0,\text{graphite}}$  is the initial temperature of fuel salt in reactor core;  $\alpha_{\text{fuel}}$  is the feedback coefficient of fuel salt;  $\alpha_{\text{graphite}}$  is the feedback coefficient of graphite.

## 2.2 Thermal Hydraulic Model

For single-phase molten salt, liquid and vapor phase conservation equation need to be calculated, respectively, while vapor phase fraction sets to be a minimal value in the RELAP5.

Two-phase mass conservation equation can be written as following:

$$\frac{\partial}{\partial t} (\alpha_g \rho_g) + \frac{1}{A} \frac{\partial}{\partial x} (\alpha_g \rho_g v_g A) = \Gamma_g \quad (7)$$

$$\frac{\partial}{\partial t} (\alpha_f \rho_f) + \frac{1}{A} \frac{\partial}{\partial x} (\alpha_f \rho_f v_f A) = \Gamma_f, \quad (8)$$

where  $\alpha$  is the fraction of fluid,  $\rho$  represents the density,  $v$  is the speed of fluid flow, the subscript  $f$  and  $g$  represent the liquid and the vapor phase, respectively, the terms in the right side of Eqs. (7) and (8) indicate the generation rate of vapor  $\Gamma_g$  and liquid  $\Gamma_f$ . The overall continuity consideration requires that the liquid generation term needs to be the negative to the vapor generation.

Based on the assumption that the Reynolds stresses, the universally covariance terms, interfacial momentum storage, and phasic viscous stresses are neglected, the phasic pressures are assumed equal, the interfacial pressure is assumed equal to the phasic pressures, the interface force terms consist of both pressure and viscous stresses, and the normal wall forces are assumed adequately modeled by the variable area momentum flux formulation, two-phase momentum conservation equations can be written as following:

$$\begin{aligned} \alpha_g \rho_g A \frac{\partial v_g}{\partial t} + \frac{1}{2} \alpha_g \rho_g A \frac{\partial v_g^2}{\partial x} &= -\alpha_g A \frac{\partial P}{\partial x} + \alpha_g \rho_g B_x A - (\alpha_g \rho_g A) \text{FWG}(v_g) \\ &+ \Gamma_g A (v_{gl} - v_g) - (\alpha_g \rho_g A) \text{FIG}(v_g - v_f) \\ &- C \alpha_g \alpha_f \rho_m A \left[ \frac{\partial (v_g - v_f)}{\partial t} + v_f \frac{\partial v_g}{\partial x} - v_g \frac{\partial v_f}{\partial x} \right] \end{aligned} \quad (9)$$

$$\begin{aligned} \alpha_f \rho_f A \frac{\partial v_f}{\partial t} + \frac{1}{2} \alpha_f \rho_f A \frac{\partial v_f^2}{\partial x} &= -\alpha_f A \frac{\partial P}{\partial x} + \alpha_f \rho_f B_x A - (\alpha_f \rho_f A) \text{FWG}(v_f) \\ &- \Gamma_g A (v_{fl} - v_f) - (\alpha_f \rho_f A) \text{FIG}(v_f - v_g) \\ &- C \alpha_f \alpha_g \rho_m A \left[ \frac{\partial (v_f - v_g)}{\partial t} + v_g \frac{\partial v_f}{\partial x} - v_f \frac{\partial v_g}{\partial x} \right], \end{aligned} \quad (10)$$

where  $P$  is the pressure,  $B_x$  is the acceleration of body force, FWG is the wall friction drag coefficient, FIG is the interface friction drag coefficient, the terms in the right side of Eqs. (9) and (10) denote the pressure gradient, the body force, wall friction drag, momentum transfer due to interface mass transfer, interface frictional drag, and force due to virtual mass, respectively.

With the simplification of neglecting the Reynolds heat flux, the universally covariance terms, the interfacial energy storage, and internal phasic heat transfer, two-phase energy conservation equations can be written as following:

$$\begin{aligned} \frac{\partial}{\partial t} (\alpha_g \rho_g U_g) + \frac{1}{A} \frac{\partial}{\partial x} (\alpha_g \rho_g U_g v_g A) &= -P \frac{\partial \alpha_g}{\partial t} - \frac{P}{A} \frac{\partial}{\partial x} (\alpha_g v_g A) + Q_{wg} + Q_{ig} \\ &+ \Gamma_{ig} h_g^* + \Gamma_w h_g' - Q_{gf} + \text{DISS}_g + S_g \end{aligned} \quad (11)$$

$$\frac{\partial}{\partial t}(\alpha_f \rho_f U_f) + \frac{1}{A} \frac{\partial}{\partial x}(\alpha_f \rho_f U_f v_f A) = -P \frac{\partial \alpha_f}{\partial t} - \frac{P}{A} \frac{\partial}{\partial x}(\alpha_f v_f A) + Q_{wf} + Q_{if} - \Gamma_{ig} h_f^* - \Gamma_w h_f' + Q_{gf} + \text{DISS}_f + S_f, \quad (12)$$

where the  $Q$  is the heat transfer rate,  $h$  is the phasic enthalpy, DISS is the dissipation term, and  $S$  is the source term. Due to the fluid salt acting as both fuel and coolant, this paper add new internal heat source terms ( $S_g$  and  $S_f$ ) based on the original energy conservation equations, and create new control volume with internal heat source in RELAP5 code.

### 2.3 Solution Methods

The thermal hydraulics and the neutronics models are solved separately in RELAP5 code, where the solution of the thermal hydraulic model adopts semi-implicit method for pressure–velocity linked equations. Noticing that the third term in the right side of Eq. (2) contains the retarded term, this equation belongs to the delay differential equation, which can be solved by a special fifth-order Runge–Kutta method [12, 13].

The coupling process of thermal hydraulic module and point kinetic module in RELAP5 code is shown in Fig. 1. The thermal hydraulic module gets the reactor power data calculated by point kinetic model, and then carries out flow and heat transfer calculation, which works out the temperature and density of coolant and moderator of each segment. The point kinetic module gets the temperature and density data of coolant and moderator calculated by thermal hydraulic model, and processes feedback calculation. Thus, reactor power can be calculated from neutron flux.

## 3 Code Verification

In June 1965, the Oak Ridge National Laboratory processed the zero power reactor physics experiment of MSRE, and tested the response of reactivity to flow rate in fuel pump start-up and coast-down transients with the reactor critical [14]. In the late running period of MSRE, ORNL carried on the nature circulation experiment with the U-233 fuel, which made sure the residual heat removal character of MSRE primary system [15].

This paper verifies the expanded code using the MSRE fuel pump start-up, fuel pump coast-down and natural circulation experiment data. MSRE data using in verification is listed in Tables 1 and 2.

The comparison of calculation result and experiment data of fuel pump start-up and coast-down transient is shown in Fig. 2. As the fuel pump starts up, a portion of

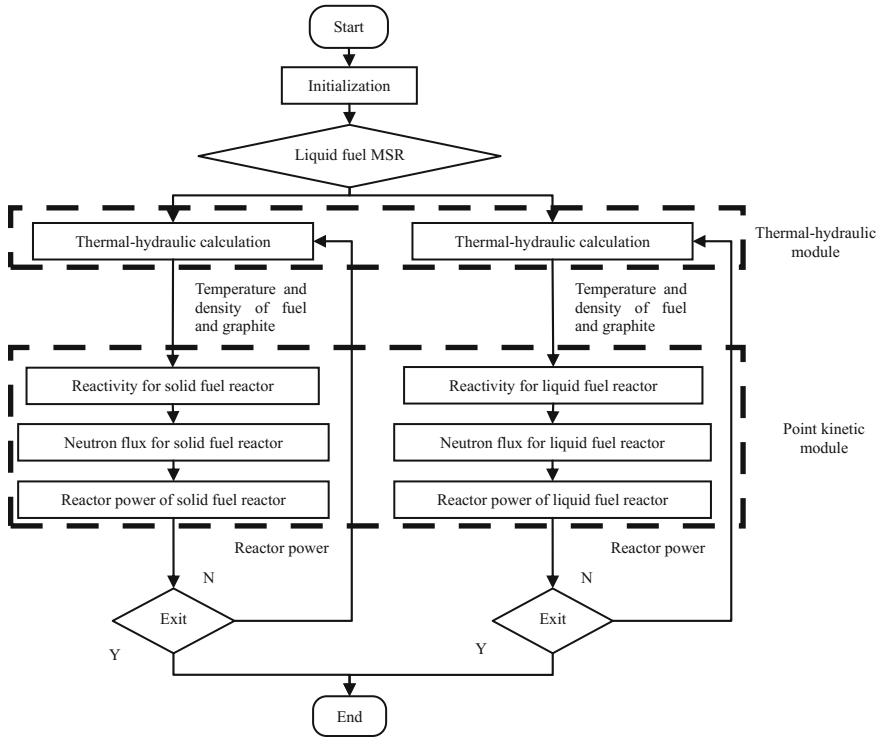


**Fig. 1** Flow chart of the point kinetic module coupling with the thermal hydraulic module

**Table 1** MSRE parameter [16, 17]

Parameter	U-235	U-233
Reactivity coefficient of fuel salt $\alpha_{\text{fuel}}/(\text{pcm/K})$	-8.46	-9.54
Reactivity of graphite $\alpha_{\text{graphite}}/(\text{pcm/K})$	-4.68	-5.76
Neutron lifetime $l/s$	0.000240	0.00040
Effective delayed neutron fraction $\beta_{\text{eff}}$	0.006661	0.002894
Fuel salt density $\rho_{\text{fuel}}/(\text{kg/m}^3)$	2263.0	2263.0
Specific heat of fuel salt $c_{p\_fuel}/(\text{J}/(\text{kg K}))$	1982.5	1982.5

**Table 2** Delayed neutron data in MSRE [17]

Group	U-235		U-233	
	$\lambda/s^{-1}$	$\beta_{\text{eff}}/10^{-5}$	$\lambda/s^{-1}$	$\beta_{\text{eff}}/10^{-5}$
1	0.0124	22.3	0.0126	23.76
2	0.0305	145.7	0.0337	85.76
3	0.111	130.7	0.139	71.90
4	0.301	262.8	0.325	82.14
5	1.14	76.6	1.13	15.79
6	3.01	28	2.5	10.03

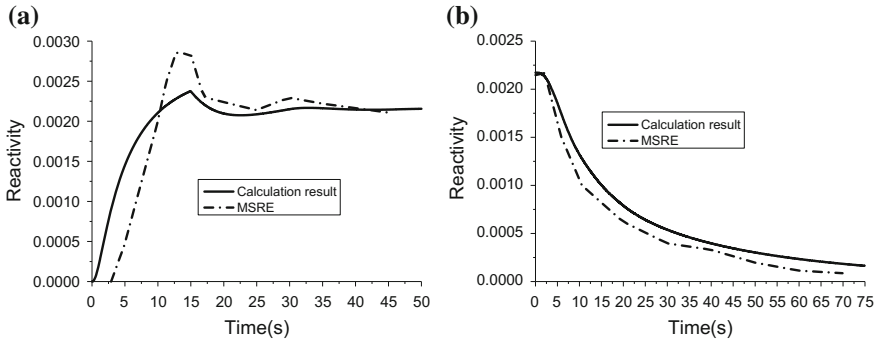


**Fig. 2** Reactivity inserted during fuel pump start-up (a) and coast-down (b) transients

delayed neutron precursors flows outside of the core following the fuel salt (Fig. 3a), which leads to reactivity lost. Reactivity will be compensated by withdrawing a control rod, so as to keep reactor critical. As the fuel pump coast down, the portion of delayed neutron precursors flowing outside the core decreases because the fuel speed reduces (Fig. 3b), which results in the reactivity rise. In order to keep reactor power at a constant level, negative reactivity will be inserted in the core by adjusting a control rod.

The comparison of calculation result and experiment data of natural circulation benchmark is shown in Figs. 4 and 5. During the natural circulation transient the fuel pump was turned off. The only source of fuel salt flow rate was natural circulation due to temperature difference between core inlet and outlet. Initially the power of reactor was only 4 kW, flow rate of fuel salt was almost zero with the reactor equilibrium. Transient experiment was driven by gradually increasing the heat removal rate in the heat exchanger, keeping the core critical and waiting for the system to be steady state before the next motion. Increasing heat removal rate in heat exchanger led to the decreasing of temperature at the core inlet, which

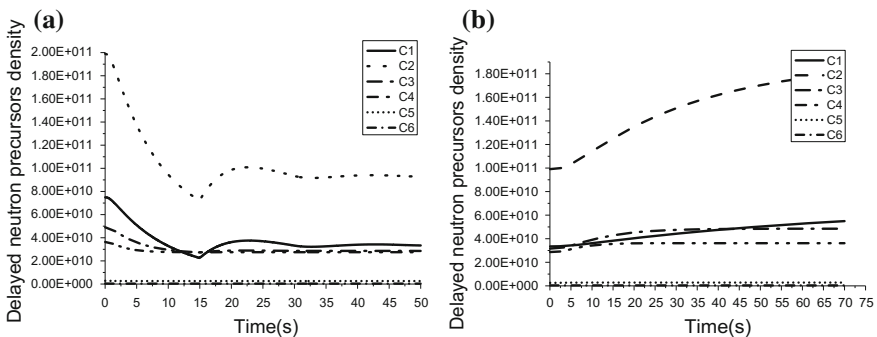


**Fig. 3** Density of delayed neutron precursors in the core during fuel pump start-up (a) and coast-down (b) transients

**Fig. 4** Reactor power during the nature circulation transient

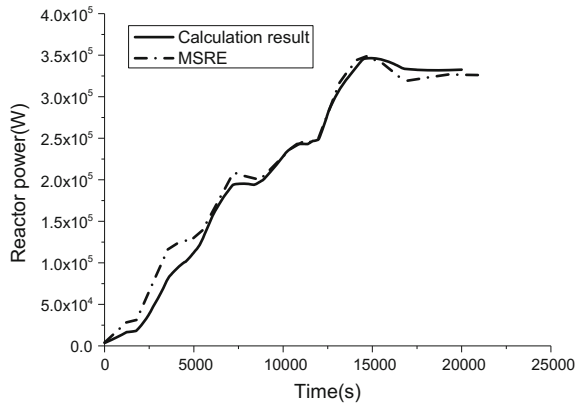
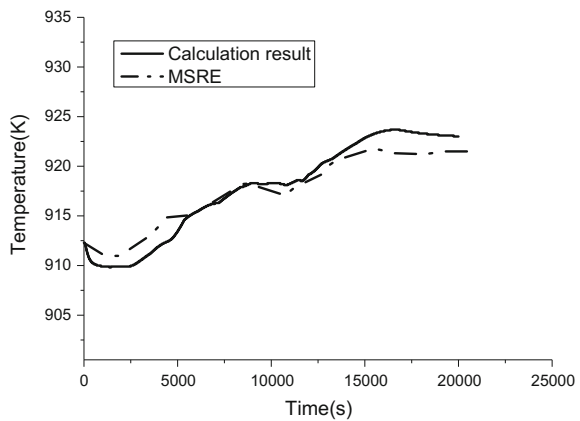


**Fig. 5** Core outlet temperature during the natural circulation transient



caused the reactivity rising due to the negative temperature feedback of fuel salt and graphite. This in turn caused the reactor power to increase. Both the decrease of temperature at core inlet and the increase of temperature at core outlet raised the temperature difference between core inlet and outlet, resulting in the higher flow rate of fuel salt due to nature circulation.

The calculation results coincide well with experimental data of three benchmarks above, which verifies the validity of the model and the extended RELAP5 code.

## 4 Conclusions

Liquid fuel molten salt reactor is special due to its fuel flow effect, so the thermal hydraulic and point kinetic models are different from traditional solid fuel reactor.



Based on the original structure of original RELAP5 code, new thermal hydraulic and point kinetic models for liquid fuel molten salt reactor were added, and the corresponding solving method was extended. Using the MSRE pump start-up, pump coast-down, and natural circulation experiments as the benchmarks, the validity of liquid fuel molten salt reactor models and modified system analysis code were verified. The results indicate that extended RELAP5 code is suitable to the system safety analysis of liquid fuel molten salt reactor system.

## References

1. Bettis E.S., Schroeder R.W., Cristy G.A., et al., 1957. The aircraft reactor experiment-design and construction. *Nucl. Sci. Eng.* 2, 804–825
2. Rosenthal M.W., Kasten P.R., Briggs R.B., 1970. Molten-salt reactors-history, states, and potential. *Nucl. Appl. Technol.* 8, 107–117
3. Robertson R.C., 1971. Conceptual design study of a single-fluid molten-salt breeder reactor. Oak Ridge National Laboratory. ORNL-4541
4. Furukawa K., Arakawa K., Erbay L.B., et al., 2008. A road map for the realization of global-scale thorium breeding fuel cycle by single molten-fluoride flow. *Energy Convers. Manag.* 49, 1832–1847
5. Ignatiev V., Afonichkin V., Feynberg O., et al., 2006. Progress in integrated study of molten salt actinide recycler and transmuter system. In: *Proc. Ninth Information Exchange Meeting on Actinide and Fission Product Partitioning and Transmutation*, France, September 25–29, 2006, Nuclear Energy Agency
6. Jiang M., Xu H., Dai Z., 2012. Advanced fission energy Program - TMSR Nuclear Energy System. *Bulletin of the Chinese Academy of Sciences.* 27 (03), 366–374
7. Lecarpentier D., Carpentier V., 2003. A neutronic program for critical and non-equilibrium study of mobile fuel reactors: the Cinsf1D code. *Nucl. Sci. Eng.* 143, 33–46
8. Krepel J., Grundmann U., Rohde U., 2005. DYN1D-MSR dynamics code for molten salt reactors. *Ann. Nucl. Energy.* 32, 1799–1824
9. Krepel J., Grundmann U., Rohde U., 2007. DYN3D-MSR spatial dynamics code for molten salt reactors. *Ann. Nucl. Energy.* 34, 449–462
10. Wang S., Rineiski A., Maschek W., 2006. Molten salt related extensions of the SIMMER-III code and its application for a burner reactor. *Nucl. Eng. Des.* 236, 1580–1588
11. Guo Z., Zhang D., Xiao Y., et al., 2013. Simulations of unprotected loss of heat sink and combination of events accidents for a molten salt reactor. *Ann. Nucl. Energy.* 53, 309–319
12. Hayashi H., 1996. Numerical solution of retarded and neutral delay differential equations using continuous Runger-Kutta methods. Graduate Department of Computer Science, University of Toronto. 13–22
13. Cohen E.R., Hetrick D.L., Homing W.A., 1958. A survey of nuclear reactor kinetics. Second United Nations International Conference on the Peaceful Uses of Atomic Energy, March 7, 1958
14. Prince B.E., Ball S.J., Engel J.R., et al., 1968. Zero-power physics experiments on the molten salt reactor experiment. Oak Ridge National Laboratory. ORNL-4233
15. Rosenthal M.W., Briggs R.B., Kasten P.R., 1969. Molten-salt reactor program semiannual progress report. Oak Ridge National Laboratory. ORNL-4396
16. Robertson R.C., 1965. MSRE Design and Operation Report, Part I, Description of Reactor Design. Oak Ridge National Laboratory. ORNL-TM-728
17. Auwerda G.J., 2007. Computational modeling of a molten salt reactor. TU Delft

# Emergency Strategy Research of MSLB Accident with Loss of Passive Residual Heat Removal for Small Modular Reactor

Yuqi Wang, Aimin Yu and Tao Tang

**Abstract** This paper researched the behavior of main steam line break (MSLB) accident with loss of passive residual heat removal (PRHR) of small modular reactor (SMR) in case of full power with RELAP5-3KEYMASTER code. Cooldown and depressurization by the mode of automatic depressurization system (ADS) and passive core cooling system are calculated post-accident. The variation of main parameters post-accident and the accident advancement and results have been analyzed. Operation intervention is given and the effects with it are discussed. And the emergency strategy for development and verification of emergency operating procedures (EOP) is given.

**Keywords** MSLB · PRHR · Emergency strategy · Intervention · RELAP5

## 1 Introduction

As a design basis accident, main steam line break (MSLB) may greatly threats nuclear reactor safety, especially in the condition of double-ended guillotine break [1]. During the accident, secondary steam discharge into atmosphere or containment, which lead to rapid depressurization and subcooling of primary side of reactor coolant system (RCS). Aiming at emergency strategy related to MSLB of conventional pressurized water reactor (PWR), plenty of work has been done [2–4].

---

Y. Wang (✉) · A. Yu · T. Tang  
China Nuclear Power Engineering Co., Ltd., Beijing, China  
e-mail: wangyuqi0705@163.com

A. Yu  
e-mail: yuam@cnpe.cc

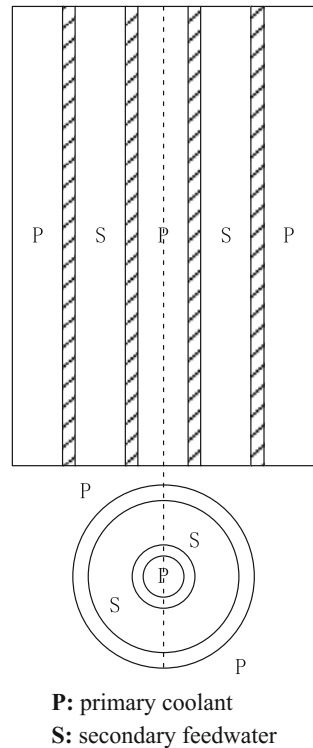
T. Tang  
e-mail: tangtao@cnpe.cc

A. Yu  
Xi'an Jiaotong University, Xi'an, Shanxi, China

Small modular reactor (SMR) is a new type of generation III+ reactor which has not been in commercial operating. Compared to conventional PWR, the most significant difference of SMR is integration design. 4 canned motor primary pumps are directly connected to reactor pressure vessel. And 16 once through type steam generators (OTSGs) are radially arranged inside reactor pressure vessel. Once through type steam generator tube include two pipes. Secondary feedwater flow upward in the annulus between inner and outer pipe, and primary coolant flow downward in the inner pipe and outside of outer pipe, as shown in Fig. 1. Superheated steam from 16 steam generators flows into main steam line, then is used for turbine drive. It also employs a series of passive safety systems to ensure the core integrity. As the only heat sink passive residual heat removal system (PRHR) plays an important role during SMR MSLB. So, it is of great significance to study the SMR MSLB emergency strategy in case of loss of PRHR.

In the present study, the response of SMR MSLB accident with loss of PRHR is simulated and analyzed using RELAP5-3KEYMASTER. The break is located in front of the main steam isolation valve (MSIV). Detail information about accident sequence and operator intervention will be discussed in the following.

**Fig. 1** Flow diagram of OTSG



## 2 Calculation Model and Hypothesis

### 2.1 Calculation Model

A preliminary model based on RELAP5 [5] code for SMR has been developed which represents all of major primary, secondary and passive safety system components. Some auxiliary systems, such as chemical and volume control system and residual heat removal system (RHR), are also included in the model and the nodalization is shown in Fig. 2.

All important parameters, such as pressure, temperature and water level, are displayed dynamically in the 3KEYMASTER [6, 7] interface. According to parameter trends during the accident, operators can execute some manual action, such as valve open/close, pump control and flow adjust, etc.

Prior to conducting analysis of MSLB transients, a steady-state run should be performed to validate the model. The steady-state value and rated value are listed in Table 1. It shows that calculated value agree well with the rated value, and the

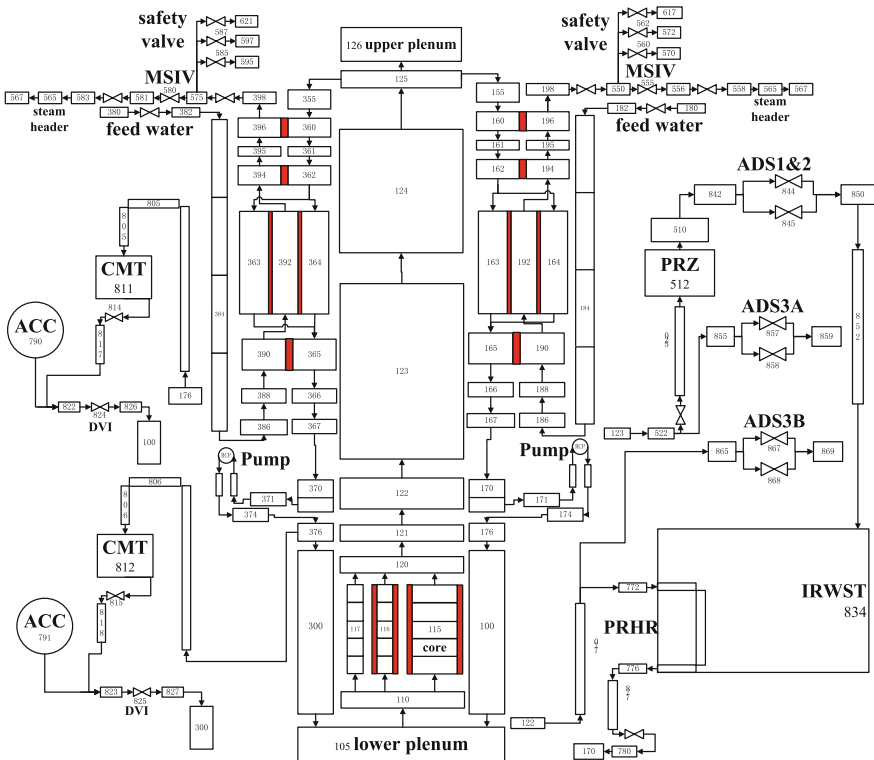
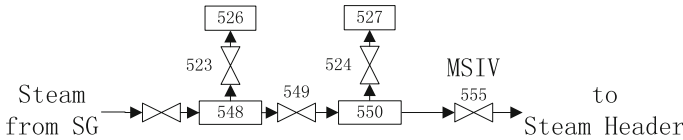


Fig. 2 Model nodalization

**Table 1** Steady-state results of full power for SMR

Parameters	Rated value	Calculated value	Relative error/%
Rated thermal power (MWt)	310.0	309.758	0.078
RCS pressure (MPa)	15.0	15.099	0.660
Primary average temperature (°C)	303.0	304.541	0.509
Core flow (kg/s)	1353	1354.15	0.085



**Fig. 3** Break nodalization

relative error between them is less than 1 %, which means that transient simulation based on the steady-state results is reasonable and believable.

Figure 3 indicates the double-ended guillotine break modeling of main steam line. In steady-state operation, valve 549 is open, and valve 523 and 524 are close. The break is assumed to open instantly when valve 549 is close, and valve 523 and 524 open at the same time.

### 2.2 Hypothesis

Before MSLB accident occurs, the plant is in full-power operation. Offsite power is available during the accident. Maximum value at the end of life is adopted for moderator density coefficient and Doppler temperature coefficient. The protection setpoint and time delay assumed in the analysis are listed in Table 2.

## 3 Description of Emergency Strategy

As mentioned above, the only heat sink, namely PRHR is unavailable during MSLB accident. The emergency strategy of this accident concerns the following three aspects:

1. Guarantee removal of core decay heat.
2. Radioactive release should be as low as possible.
3. Avoid frequent opening of pressurizer (PZR) safety valve, since it may result in failure of safety valve.

**Table 2** Protection setpoints and time delay

Function	Setpoint	Time delay/s
“S” signal	SG steam pressure low signal	5
Core inlet temperature low signal	260 °C	–
Reactor trip	After “S” signal	1
Main steam isolation	After “S” signal	5
Main feedwater isolation	After “S” signal	5
CMT actuation	After “S” signal	5
ADS 1 open	Manually	–
ADS 2 open	After ADS 1 open	70
ADS 3 open	After ADS 2 open and CMT level less than 20 %	240
Reactor coolant pump trip	After “S” signal	15
Start-up feedwater system in service	After reactor trip	0
Start-up feedwater isolation	After core inlet temperature low signal	0

To meet these requirements, the reactor should enter “feed-bleed” mode before primary pressure ascends to opening setpoint (16.9 MPa) of pressurizer safety valve. Subsequent actions include actuating safeguards, manually opening ADS1, controlling important primary parameters and transiting to NS/RHR mode, as depicted in Fig. 4.

## 4 Simulation Results and Analysis

After double-ended break occurs in the main steam line, steam discharges rapidly through the break, which leads to primary depressurization and subcooling. 10.07 s after the break, “s” signal results in isolation of main steam and main feedwater. 165.82 s later, core inlet temperature low signal is generated and results in isolation of start-up water. Following these automatic action, primary average temperature increases gradually. Meanwhile, RCS pressure also increases and leads to frequent opening of PZR safety valve.

Figures 5 and 6 illustrate different parameter trends in condition of with or without operator intervention. As shown in these two figures, primary average temperature, RCS pressure and intact SG steam pressure all decrease quickly when operator manually opens ADS 1 and establishes “feed-bleed” mode. The operator intervention successfully avoids frequent opening of PZR safety valve, and reduces the probability of failure of PZR safety valve.

When RCS pressure drops to ACC pressure setpoint, ACC isolation valves open and 50 °C cold water injects into reactor core. ACC injection not only decreases

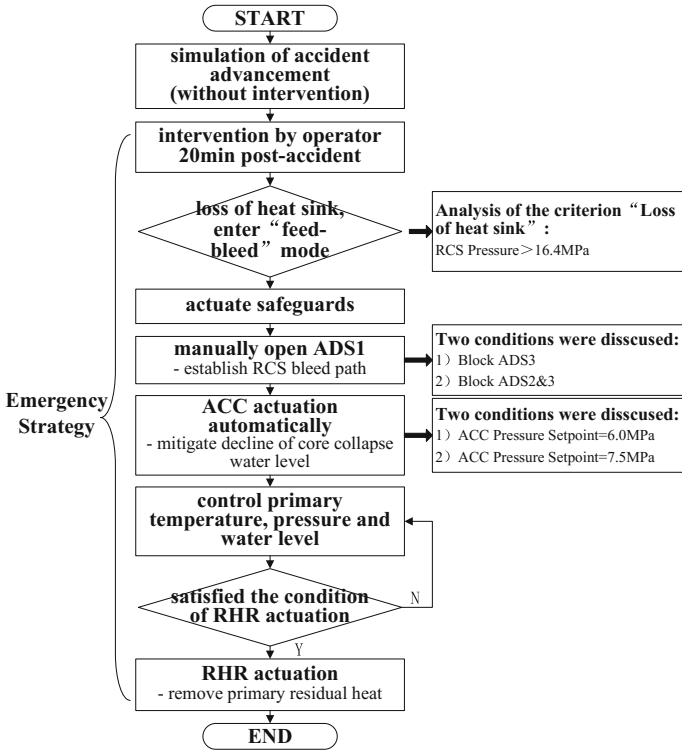
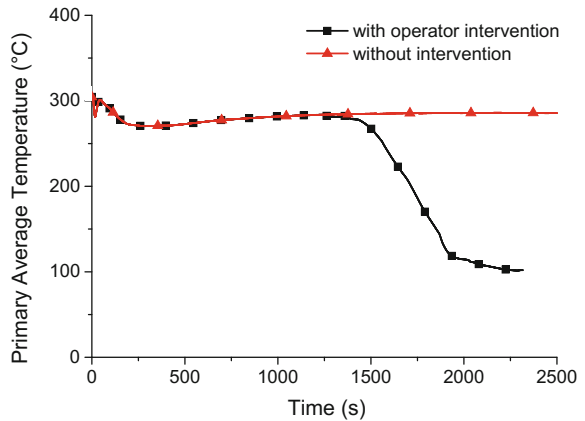
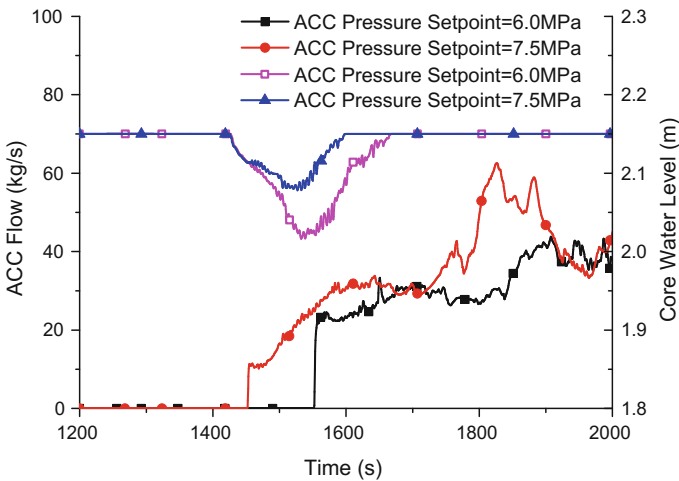
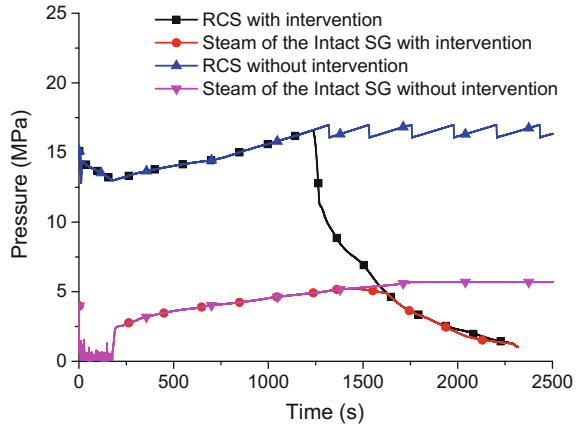


Fig. 4 Emergency strategy analysis flow chart for MSLB accident with loss of PRHR

Fig. 5 Evolutions of primary average temperature versus time



**Fig. 6** Evolutions of RCS and intact SG pressure versus time



**Fig. 7** Evolutions of ACC flow and core water level versus time

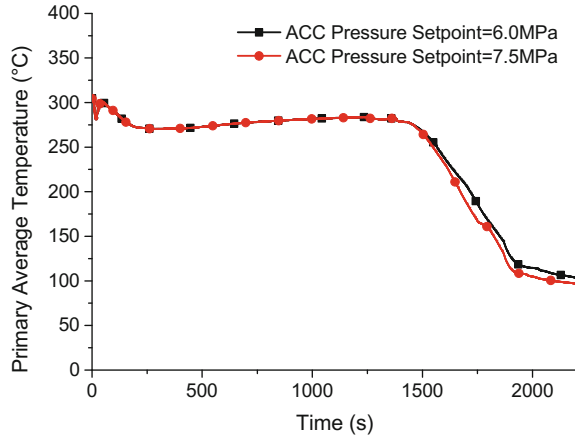
primary temperature but also compensates loss of reactor inventory, as shown in Figs. 7 and 8.

Furthermore, it indicates in Fig. 7 that in the transient process, if ACC pressure setpoint ascends from 6.0 to 7.5 MPa, ACC injection time advances from 1552.3 to 1452.1 s, and minimum core collapse water level increases from 2.01 to 2.08 m. Therefore, appropriately increasing ACC pressure setpoint will help to mitigate the consequence of SMR MSLB accident with loss of PRHR.

According to ADS design features, ADS stages 1&2 vent to sprayers immersed in the in-containment refueling water storage tank (IRWST), and ADS stage 3 vents



**Fig. 8** Evolutions of primary average temperature versus time



directly to containment. Once ADS stage 1 opens manually, ADS stage 2&3 will also open with some time delay, which means primary radioactivity vents to containment and pollutes the equipments located in containment. So, it is necessary to study the effect of blocking of ADS stage 2 or ADS stage 3. Event sequences of two conditions, namely blocking ADS stage 3 (No. 1 sequence) and blocking ADS stage 2&3 (No. 2 sequence) are listed in Table 3.

**Table 3** Events sequence

Events	No. 1 sequence (s)	No. 2 sequence (s)
MSLB with Loss of PRHR	0.00	0.00
“S” signal appear	5.07	5.07
Reactor trip and start-up feedwater system open	6.07	6.07
Main feedwater and main steam isolate	10.07	10.07
Water of CMT inject	10.07	10.07
Reactor coolant pump trip	20.07	20.07
Start-up feedwater isolate	175.89	175.89
RCS pressure reach 16.4 MPa, so enter “feed-bleed” mode	1187.50	1187.50
Open ADS 1 manually	1232.88	1232.88
ADS 2 open	1302.88	–
Water of ACC inject	1449.59	2249.34
Satisfy the condition of RHR actuation, and transit to NS/RHR mode	1845.01	5044.38

**Fig. 9** Evolutions of RCS pressure versus time

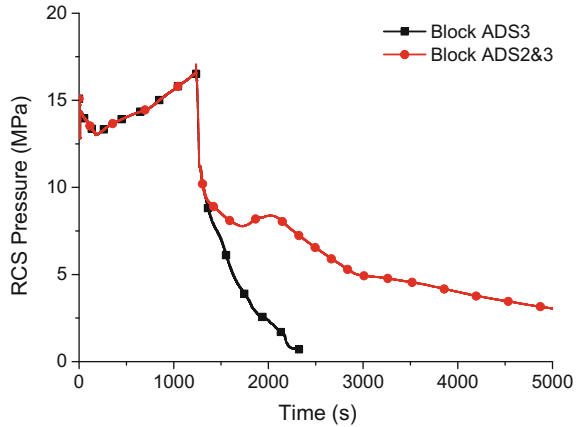
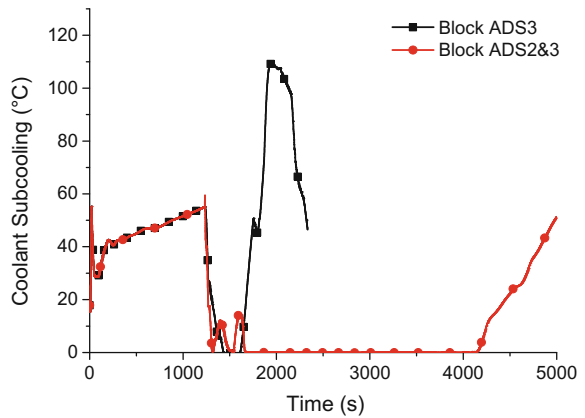


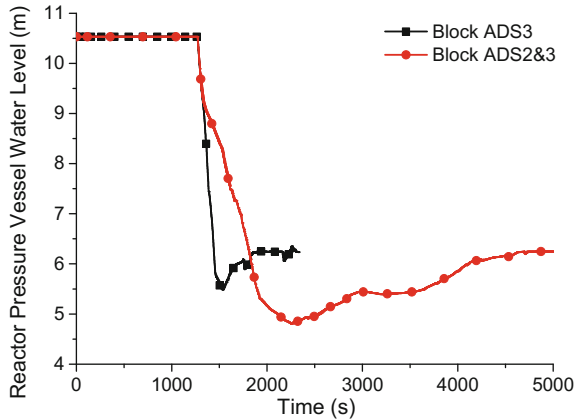
**Fig. 10** Evolutions of coolant subcooling versus time



It indicates in Fig. 9 that in the condition of blocking ADS stage 3, RCS pressure decreases by nearly 15 MPa in 20 min. Compared with the condition of blocking ADS stage 2&3, the RHR operates 3200 s earlier. The operation of RHR means that heat sink is rebuilt in primary side, which is helpful to remove decay heat and re-establishes subcooling of reactor core, as depicted in Fig. 10.

In the condition of blocking ADS stage 2&3, as illustrated in Fig. 11, ACC operating time delayed by nearly 800 s, and reactor pressure vessel water level increasing time delayed by about 3000 s. Consequently, the emergency strategy of SMR MSLB accident with loss of PRHR should only block ADS stage 3, which not only meet the requirement of primary depressurization, but also avoid radioactivity release to containment.

**Fig. 11** Evolutions of reactor pressure vessel water level versus time



## 5 Conclusions

Emergency strategy of SMR MSLB accident with loss of PRHR is studied based on RELAP5-3KEYMASTER. Main conclusions obtained in present study are summarized as follows:

1. Properly combination of ADS and ACC can effectively remove decay heat of reactor core and obviously mitigate the consequence of SMR MSLB accident with loss of PRHR.
2. According to special design features of SMR, the “feed-bleed” mode operating setpoint should be “RCS pressure increases to 16.4 MPa”. The new setpoint can avoid frequent opening of PZR safety valve and reduce the probability of failure of PZR safety valve.
3. Appropriately increasing of ACC pressure setpoint can effectively mitigate the consequence of SMR MSLB accident with loss of PRHR.
4. After opening ADS stage 1 manually, blocking ADS stage 3 can not only meet the requirement of primary depressurization but also avoid radioactivity release to containment. However, blocking ADS stage 2&3 is inadvisable because it delays the ACC operating time and increases the risk of core uncovering.

## References

1. YU Erjun, LI Jigen. Nuclear Safety of Nuclear Power Plants[M]. Beijing: Atomic Energy Press, 2010: 125
2. SUN Jiliang, YU Erjun. Main Steam Line Break(MSLB) Accident Analysis for Qinshan Power Plant(QNPP) with RELAP5/MOD2[J]. Atomic Energy Science and Technology, 1993, 27(4): 304–308

3. YU Erjun. Analysis for Postulated Main Steam Line Break Accident in Qinshan Nuclear Power Plant[J]. Atomic Energy Science and Technology, 1989, 23(5): 15–22
4. SHEN Caifen, ZHANG Hong, LIU Changwen. Major Steam Line Break Accident Analysis[J]. Nuclear Power Engineering, 1999, 20(4): 326–328
5. RELAP5/MOD3.3 code manual volume I: Code structure, system models, and solution methods[R]. Washington DC: NRC, 2001: 15
6. 3KEYMASTER User Guide: Relay modeling tool[R]. MD: WSC, 008
7. 3KEYMASTER User Guide: Transmitter modeling tool[R]. MD: WSC, 2006

# Evaluation and Analysis of Forced Convection Heat Transfer Correlations for Supercritical Carbon Dioxide in Vertical Tubes

Sheng-hui Liu and Yan-ping Huang

**Abstract** The objective of our research is to improve fundamental knowledge of the way to develop heat transfer correlation (HTC) for supercritical carbon dioxide (SCCO<sub>2</sub>). According to literature review, most of the existing SCCO<sub>2</sub> heat transfer correlations were extended from subcritical by three modification methods, i.e. thermo-physical modification, dimensionless number modification and segment function modification. Based on different modification method, this paper also presents an analysis of 17 heat transfer correlations developed for supercritical fluids (SCFs) flowing in vertical bare tubes. The results show that thermo-physical modification performs better within the low Nusselt number (Nu) range ( $\sim <400$ ), dimensionless number modification performs better over the whole range of Nu, and that segment function modification performs better within the high Nu range ( $\sim >400$ ). The analysis on the structure of the correlations based on heat transfer evaluation was also carried out.

**Keywords** Supercritical carbon dioxide · Heat transfer correlation · Forced convection · Nuclear reactor engineering

## 1 Introduction

Recently there has been raised interest in SCCO<sub>2</sub> driven by the need to develop innovative nuclear reactors which can compete in terms of cost, safety and reliability with other types of power generation plant. As a natural constituent of the biosphere, CO<sub>2</sub> is a non-flammable working fluid, safe, non-toxic, abundant in reserves, low thermo-physical critical point, easy-compress in the vicinity of pseudo-critical point and with no long-term effects on health and the environment. It also has preferable

---

S. Liu · Y. Huang (✉)

CNNC Key Laboratory on Nuclear Reactor Thermal Hydraulics Technology,  
Nuclear Power Institute of China, Chengdu, Sichuan, China  
e-mail: hyanping007@163.com

chemical stability and outstanding neutron physics performance within the medium design temperature of nuclear reactor. It is thought to have the potential to improve the economics of nuclear power generation by taking advantage of three particular benefits associated with using SCCO<sub>2</sub>. These are, improved cycle efficiency with Brayton cycle, compact size due to the high pressures involved, and reduced complication due to absence of phase change. To realize the absorbing goal, all these basic issues, such as reactor physics, thermal hydraulics, fuel and structure material, reactor system and equipment, reactor control and some other problems associated with SCCO<sub>2</sub> have priority to be dealt with, of which forced convection heat transfer of SCCO<sub>2</sub> is one of the most urgent subjects to be studied.

Results from heat transfer experiments with CO at supercritical pressure have sometimes exhibited striking features. This is not surprising in view of the strong dependence of the thermo-physical properties on temperature and pressure, a consequence of which is that the momentum and energy equations become non-linear. Up to now, a perfect theory or analysis method has not been created, which fully takes into account of thermo-physical properties variation, to predict normal and abnormal heat transfer of supercritical carbon dioxide. Heat transfer correlation based on experiment now is almost the main solution to predict heat transfer performance in SCCO<sub>2</sub> engineering. According to different modification methods, the present paper has induced and evaluated forced convection heat transfer correlations for SCCO<sub>2</sub> under typical operating conditions, based on experimental results.

## **2 Review of Typical Forced Convection Heat Transfer Correlations**

Complexly, convection heat transfer would often be affected by lots of parameters, i.e. channel geometry, flow state, properties of working fluid, boundary conditions, etc. Common research methods for convection heat transfer include theoretical analysis, experimental investigation as well as numerical simulation. While heat transfer correlation derived from analogy principle is most important one of heat transfer research methods. There are mainly two types of heat transfer correlation, i.e. Nusselt (Nu) type and Stanton (St) type. There are two branches of the Nu type, which are often called Dittus–Boelter (D-B) type and Petukhov–Kirillov (P-K) type. The former derives from analogy analysis and experimental data, while the latter from boundary layer theory and some mathematical analysis. To extend to SCFs heat transfer, considerable modifications of the subcritical heat transfer correlations are needed, which were summarized as thermo-physical modification, dimensionless number modification and segment function modification in this paper. The intension of the three modification methods will be expounded in the following context. The relationship between subcritical and supercritical convection heat transfer correlation is shown in Fig. 1.

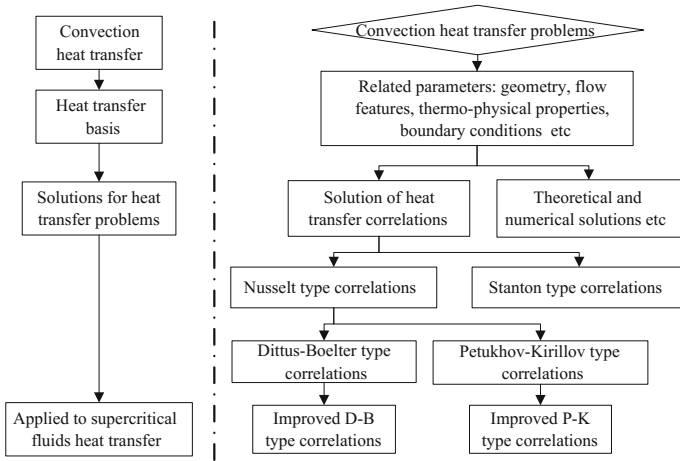


Fig. 1 Logic relationships of subcritical and supercritical convective HTCs

In the following, this paper will make a close review of the heat transfer correlations for  $\text{SCCO}_2$  forced convection according to different modification methods. However, for completeness of the correlation review it was decided to have a glance at the D-B correlation and P-K correlation firstly.

In 1930, Dittus and Boelter conducted a research on the performance of automobile tube radiator, and put forward the prototype of D-B correlation [1]. After several improvement, the most popular and long-standing D-B correlation was developed [2], which is as follows:

$$\text{Nu}_b = 0.023Re_b^{0.8}Pr_b^n \tag{1}$$

where  $n$  is suggested as a value of 0.4 or 0.3 corresponding heated or cooled. This correlation should be used with the fluid Prandtl number not smaller than 0.6 and medium bulk and wall temperature.

In 1958, Petukhov and Kirillov published the well-known P-K correlation [3], which is based on the boundary layer theory.

$$\text{Nu}_b = \frac{(f/8)Re_bPr_b}{1.07 + 12.7\sqrt{f/8}(Pr_b^{2/3} - 1)} \tag{2}$$

$$f = (1.82 \lg Re_b - 1.64)^{-2}$$

Under forced convection heat transfer, the density, viscosity, specific heat and other thermodynamic and transport properties of supercritical fluids often vary obviously along radial and axial directions, which have a good possibility to affect the heat transfer directly or indirectly. For instance, under some experimental

conditions the local specific heat becomes larger, which may strength the heat transfer; the radial and axial variation of density is likely to reform the flow field and change the heat transfer indirectly, which have been summarized as buoyancy effect and acceleration effect. The present paper will name thermo-physical properties as the first-level influences, which effect heat transfer directly, and buoyancy and acceleration the secondary-level influences which effect heat transfer indirectly.

## 2.1 Thermo-physical Properties Modification

The idea of thermo-physical properties modification is preliminarily to integrate the first-level influences into supercritical heat transfer correlations, which often present as the ratio of thermo-physical properties between bulk fluid and wall vicinity.

Krasnoshchekov and Protopopov [4] put forward the following forced convection heat transfer correlation for supercritical carbon dioxide, which is based on the P-K heat transfer correlation, and has taken into account of dynamic viscosity, heat conductivity and specific heat (K-P-1959):

$$\text{Nu}_b = \text{Nu}_{P-K} \left( \frac{\mu_b}{\mu_w} \right)^{0.11} \left( \frac{k_b}{k_w} \right)^{-0.33} \left( \frac{\bar{c}_p}{c_{p,b}} \right)^{0.35} \quad (3)$$

$$\bar{c}_p = \frac{i_w - i_b}{T_w - T_b}$$

Swenson et al. [5] carried out an experimental investigation on supercritical convection heat transfer, which was performed in upward flow of water inside 9.4-mm ID vertical tube with a length of 1830 mm. Data points lie within a wide range of thermodynamic parameters—pressures ranging from 22.7 to 41.3 MPa, mass flow rates from 0.2 to 2.0 mg/(m<sup>2</sup> s), wall heat flux from 0.2 to 2.0 MW/m<sup>2</sup>. Based on the D-B heat transfer correlation, Swenson et al. compiled the test data with wall temperature as characteristic temperature. Taking into account of radial density variation, they developed the heat transfer correlation for supercritical water (S-1965):

$$\text{Nu}_w = 0.00459 R e_w^{0.923} \overline{Pr}_w^{-0.613} \left( \frac{\rho_w}{\rho_b} \right)^{0.231} \quad (4)$$

$$\overline{Pr}_w = \frac{\bar{c}_p \mu_w}{k_w}, \quad \bar{c}_p = \frac{i_w - i_b}{T_w - T_b}$$

Jackson and Fewster [6] (2004) developed an improved D-B type heat transfer correlation for SCCO<sub>2</sub>, which integrated the effect of radial density variation (J-F-2004):



$$Nu_b = 0.0183Re_b^{0.82}\overline{Pr}_b^{0.5}\left(\frac{\rho_w}{\rho_b}\right)^{0.3} \tag{5}$$

Gupta et al. [7] developed three new heat transfer correlations for SCCO<sub>2</sub> in bare tubes. Specialized for normal and enhancement heat transfer model, Sahil Gupat et al. rejected the experimental data over deterioration region. Based on the D-B type correlation, they derived the following semi-empirical correlation (S-G-2013-b/f/w):

$$Nu_x = CRe_x^{n_1}Pr_x^{n_2}\left(\frac{k_w}{k_b}\right)^{n_3}\left(\frac{\mu_w}{\mu_b}\right)^{n_4}\left(\frac{\rho_w}{\rho_b}\right)^{n_5}$$

where the subscript *x* represents different characteristic temperature. Gupta et al. adopted wall temperature *T<sub>w</sub>*, bulk-fluid temperature *T<sub>b</sub>* and film temperature *T<sub>f</sub>*(= (*T<sub>b</sub>* + *T<sub>w</sub>*)/2) as characteristic temperature, respectively. Based on experimental data and fitting technique they achieved three new heat transfer correlations:

$$Nu_b = 0.01Re_b^{0.89}\overline{Pr}_b^{-0.14}\left(\frac{k_w}{k_b}\right)^{0.22}\left(\frac{\mu_w}{\mu_b}\right)^{-1.13}\left(\frac{\rho_w}{\rho_b}\right)^{0.93} \tag{6}$$

$$Nu_f = 0.0043Re_f^{0.94}\left(\frac{k_w}{k_b}\right)^{-0.52}\left(\frac{\rho_w}{\rho_b}\right)^{0.57} \tag{7}$$

$$Nu_w = 0.0038Re_w^{0.96}\overline{Pr}_w^{-0.14}\left(\frac{k_w}{k_b}\right)^{-0.75}\left(\frac{\mu_w}{\mu_b}\right)^{-0.22}\left(\frac{\rho_w}{\rho_b}\right)^{0.84} \tag{8}$$

### 2.2 Dimensionless Numbers Modification

The essence of dimensionless numbers modification is to integrate the secondary-level influences into heat transfer correlation, so as to make it more rational and accurate.

Kurganov and Ankudinov [8] researched the phenomenon of normal and deteriorated heat transfer of CO<sub>2</sub>. Taking into account the inlet effect and buoyancy effect, they developed a complex heat transfer correlation (K-1985):

$$\frac{Nu_b}{Nu_n} = \begin{cases} 1, & \tilde{K} \leq 1 \\ \tilde{K}^{-m}, & \tilde{K} > 1 \end{cases} \tag{9}$$

$$Nu_n = \frac{f_n/8Re_b\overline{Pr}_b}{1 + 900/Re_b + 12.7\sqrt{f_n/8}\left(Pr_b^{2/3} - 1\right)}$$

$$f_n = f_0 \left( \frac{\rho_w}{\rho_b} \right)^{0.4}, \quad f_0 = [0.55 / \lg(Re_b/8)]^2, \quad \overline{Pr}_b = \frac{\overline{c_p} \mu_b}{k_b}$$

$$\tilde{K} = \left( \frac{f_n^0}{F} + g_d \frac{Gr_n}{Re_b^2} \right) \frac{1}{f_n [1.0 - \exp(-Re_f/30,000)]}$$

$$f_n^0 = \frac{8q_w \beta_b}{Gc_{p,b}}, \quad Gr_n = \frac{g \rho_b^2 d^3}{\mu_b^2} \left( 1 - \frac{\rho_w}{\rho_b} \right)$$

$$g_d = \begin{cases} 1 & \text{upward flow} \\ -1 & \text{downward flow} \\ 0 & \text{horizontal flow} \end{cases}$$

$$m = 0.55 \{ 1 - \exp[-x/(50d)] \}$$

$$F = 1 - 0.8 \exp \left[ -3.0 \left( \frac{q_w \beta_b}{Gc_{p,b}} \frac{d/(4x)}{\ln(\rho_{in}/\rho_b)} \right)^2 \right]$$

Kim and Kim [9] conducted an experiment in a vertical tube with SCCO<sub>2</sub> to investigate the influence of acceleration and buoyancy effects on turbulent convection heat transfer. Based on their analysis, Dong Eok Kim and Moo Hwan Kim built a D-B type heat transfer correlation (D-M-2010):

$$Nu_b = 0.226 Re_b^{1.174} Pr_b^{1.057} \left( \frac{\rho_w}{\rho_b} \right)^{0.571} \left( \frac{\overline{c_p}}{c_{p,b}} \right)^{1.032} Ac^{0.489} Bu^{0.0021} \quad (10)$$

$$q^+ = \frac{q_w \beta_b}{Gc_{p,b}},$$

$$Ac = \frac{q^+}{Re_b^{0.625}} \left( \frac{\mu_w}{\mu_b} \right) \left( \frac{\rho_b}{\rho_w} \right)^{0.5},$$

$$Bu = \frac{Gr_q}{Re_b^{3.425} Pr^{0.8}} \left( \frac{\mu_w}{\mu_b} \right) \left( \frac{\rho_b}{\rho_w} \right)^{0.5}$$

Kim and Kim [10] found that the acceleration effect was obvious under their experimental conditions. Analyzing the distribution of shear stress and the variation of thermo-physical properties, they developed another heat transfer correlation for CO<sub>2</sub> (D-M-2011):

$$Nu_b = 2.0514 Re_b^{0.928} Pr_b^{0.742} \left( \frac{\rho_w}{\rho_b} \right)^{1.305} \left( \frac{\mu_w}{\mu_b} \right)^{-0.669} \left( \frac{\overline{c_p}}{c_{p,b}} \right)^{0.888} (q^+)^{0.792} \quad (11)$$

### 2.3 Segment Functions Modification

Previous studies show that the flow, thermal and some other physical field vary dramatically under supercritical conditions. Each item in heat transfer correlation should be formed differently according to different distribution of physical field. Now, the effect of physical field distribution to heat transfer is mainly integrate into correlations by segment functions modification, which often refer to the relationship between wall temperature  $T_w$ , bulk-fluid temperature  $T_b$  and pseudo-critical temperature  $T_{pc}$ .

Bringer and Smith [6] (1957) attempted to optimize supercritical forced convection heat transfer correlation by redefining the characteristic temperature of Reynolds number. According to different thermal field, Bringer and Smith adopted bulk-fluid temperature, wall temperature and pseudo-critical temperature as characteristic temperature respectively, and developed the following CO<sub>2</sub> forced convection heat transfer correlation (B-S-1957):

$$Nu_b = 0.0375Re_x^{0.77} Pr_w^{0.55} \tag{12}$$

where the characteristic temperature of  $Re_x$  is  $T_x$ , which is defined as:

$$T_x = \begin{cases} T_b & \text{if } \frac{T_{pc}-T_b}{T_w-T_b} < 0 \\ T_{pc} & \text{if } 0 \leq \frac{T_{pc}-T_b}{T_w-T_b} \leq 1 \\ T_w & \text{if } \frac{T_{pc}-T_b}{T_w-T_b} > 1 \end{cases}$$

Krasnoshchekov [11] optimized the P-K correlation based on experimental investigation. Taking into account different thermal property under different thermal field, Krasnoshchekov developed a new correlation (K-1966):

$$Nu_b = Nu_{P-K} \left( \frac{\rho_w}{\rho_b} \right)^{0.3} \left( \frac{c_p}{c_{p,b}} \right)^n \tag{13}$$

$$n = \begin{cases} 0.4 & \text{if } T_b < T_w < T_{pc} \text{ or } T_w > T_b > 1.2T_{pc} \\ 0.4 + \frac{0.2(T_w/T_{pc}-1)}{1-0.5(T_b/T_{pc}-1)} & \text{if } T_{pc} < T_b < 1.2T_{pc} \\ 0.4 + 0.2(T_w/T_{pc} - 1) & \text{if } T_b < T_{pc} < T_w \end{cases}$$

Yamagata and Nishikawa [12] studied the flow and heat transfer characters of supercritical water experimentally, and built a correlation which is able to predict heat transfer over enhancement region preferably (Y-1972):

$$Nu_b = 0.0135Re_b^{0.85} Pr_b^{0.8} F_c \tag{14}$$

$$F_c = \begin{cases} 1.0 & \text{if } E \geq 1 \\ 0.67Pr_{pc}^{-0.05} (\bar{c}_p/c_{p,b})^{n_1} & \text{if } 0 \leq E \leq 1 \\ (\bar{c}_p/c_{p,b})^{n_2} & \text{if } E \leq 0 \end{cases}$$

$$n_1 = -0.77(1 + 1/Pr_{pc}) + 1.49$$

$$n_2 = 1.44(1 + 1/Pr_{pc}) - 0.53$$

$$E = \frac{T_{pc} - T_b}{T_w - T_b}$$

Jackson [6] (2002) developed a new heat transfer correlation for CO<sub>2</sub>. Jackson brought radial distribution of density and specific heat into this new correlation, which also took it into account that the effect of thermal field to specific heat distribution (J-2002):

$$Nu_b = 0.0183Re_b^{0.82}Pr_b^{0.5} \left(\frac{\rho_w}{\rho_b}\right)^{0.3} \left(\frac{\bar{c}_p}{c_{p,b}}\right)^n \tag{15}$$

$$n = \begin{cases} 0.4 & \text{if } T_b < T_w < T_{pc} \text{ or } T_w > T_b > 1.2T_{pc} \\ 0.4 + \frac{0.2(T_w/T_{pc}-1)}{1-0.5(T_b/T_{pc}-1)} & \text{if } T_{pc} < T_b < 1.2T_{pc} \\ 0.4 + 0.2(T_w/T_{pc} - 1) & \text{if } T_b < T_{pc} < T_w \end{cases}$$

Jackson [13] (2008) modified his correlation further, and publish the following one (J-2008):

$$Nu_b = 0.022Re_b^{0.8}Pr_b^{0.4} \left(\frac{\rho_w}{\rho_b}\right)^{0.3} \left(\frac{\bar{c}_p}{c_{pb}}\right)^n \tag{16}$$

$$n = \begin{cases} 0.4 & \text{if } T_b < T_w < T_{pc} \text{ or } T_w > T_b > 1.2T_{pc} \\ 0.4 + \frac{0.2(T_w/T_{pc}-1)}{1-0.5(T_b/T_{pc}-1)} & \text{if } T_{pc} < T_b < 1.2T_{pc} \\ 0.4 + 0.2(T_w/T_{pc} - 1) & \text{if } T_b < T_{pc} < T_w \end{cases}$$

Son and Suh [14] experimentally studied the heat transfer features of SCCO<sub>2</sub> in a vertical tube. Based on conventional correlation and taking into account thermo-physical properties variation, the difference of wall shear between mix convection and forced convection as well as buoyancy effect, Hyung M. Son and Kung Y. Suh developed a complex correlation (H-K-2012):

$$Nu = Nu_0 \left(\frac{\rho_w}{\rho_b}\right)^{m_1} \left(\frac{\bar{c}_p}{c_{pb}}\right)^{m_2} \left(\frac{\mu_w}{\mu_b}\right)^{m_3} \left| 1 - \frac{10^4 \bar{G}r_b}{Re_b^{2.7} Pr_b^{0.5}} \right|^{m_4} \tag{17}$$

$$Nu_0 = \frac{(f/8)RePr}{1 + 3.4f + (11.7 + 1.8Pr^{-1/3})(f/8)^{1/2}(Pr^{2/3} - 1)}$$

$$f = (1.82 \lg Re - 1.64)^{-2}$$

$$\overline{Gr_b} = \frac{(\rho_b - \bar{\rho}^{int})d^3 g}{\rho_b^2}$$

Hyung M. Son et al. used optimization method of operational research (OR), and the target function is defined by the sum of temperature difference at each point (between prediction value and test data), the minimum of which is the final optimization solution. Son et al. organized experimental condition by  $q/G$  (unit:  $J/kg$ ), and there exist four optimal numbers, i.e.  $m_1, m_2, m_3$  and  $m_4$  under each experimental condition. With fitting technology, they achieved the following functions:

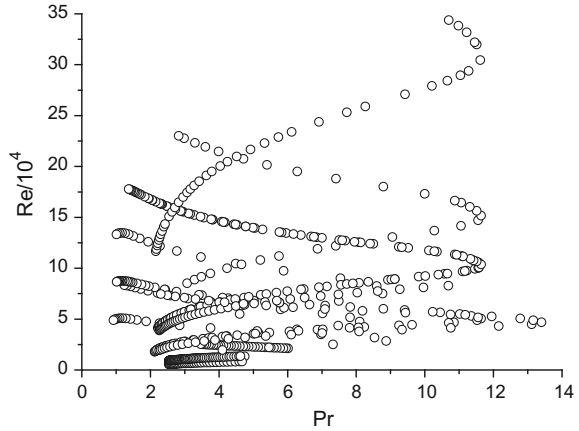
$$m_2 = \begin{cases} 0.4 & \frac{T_b}{T_{pc}} < \frac{T_w}{T_{pc}} \leq 1 \text{ or } 1.2 \leq \frac{T_b}{T_{pc}} \leq \frac{T_w}{T_{pc}} \\ 0.4 + 0.2\left(\frac{T_w}{T_{pc}} - 1\right) & \frac{T_b}{T_{pc}} \leq 1 < \frac{T_w}{T_{pc}} \\ 0.4 + 0.2\left(\frac{T_w}{T_{pc}} - 1\right)[1 - 0.5\left(\frac{T_b}{T_{pc}} - 1\right)] & 1 < \frac{T_b}{T_{pc}} < 1.2 \text{ or } \frac{T_b}{T_{pc}} < \frac{T_w}{T_{pc}} \end{cases}$$

$$m_3 = 0.62 - 9.02 \times 10^{-2} \left(\frac{q}{G}\right) + 9.51 \times 10^{-4} \left(\frac{q}{G}\right)^2 - 3.22 \times 10^{-6} \left(\frac{q}{G}\right)^3 + 3.53 \times 10^{-9} \left(\frac{q}{G}\right)^4$$

$$m_4 = \begin{cases} -2.44 - 1.54 \times 10^{-2} \left(\frac{q}{G}\right) - 1.11 \times 10^{-4} \left(\frac{q}{G}\right)^2 & 46.57 \leq \frac{q}{G} \leq 151.82 \\ -13.40 - 1.03 \times 10^{-1} \left(\frac{q}{G}\right) - 2.08 \times 10^{-4} \left(\frac{q}{G}\right)^2 & 151.82 \leq \frac{q}{G} \leq 212.40 \\ -13.41 - 1.06 \times 10^{-1} \left(\frac{q}{G}\right) - 1.08 \times 10^{-4} \left(\frac{q}{G}\right)^2 & 212.40 \leq \frac{q}{G} \leq 334.88 \end{cases}$$

Comparing the above correlations, most of them are derived from subcritical forced convection heat transfer correlation by modification. And the modified correlations often show dazzling forms or shapes, which just illustrate the complexity of supercritical heat transfer, especially in the pseudo-critical region. As developed based on experiment, the existing supercritical correlation are usually called semi-empirical correlation, with a limited application. Recently, a better scheme to solve supercritical convection heat transfer has not been found, and a well-agreed idea about how to develop a perfect supercritical heat transfer correlation is badly needed.

**Fig. 2** Distribution of Reynolds and Prandtl numbers of selected experimental cases



### 3 Correlation Evaluate and Analysis

Based on the published experimental data [15–18], this paper evaluated the correlations (3–17). Getting rid of the data existing obvious errors, 782 points were accepted, which involve the following experimental conditions: tube diameters ranging from 2 to 9 mm, pressures from 8 to 8.8 MPa, mass flow rates from 197 to 1200 kg/(m<sup>2</sup> s), heat fluxes from 6.5 to 190 kW/m<sup>2</sup>, bulk-fluid Reynolds numbers from  $5 \times 10^3$  to  $3.4 \times 10^5$ , bulk-fluid Prandtl numbers from 0.92 to 13.4, upward flow of CO<sub>2</sub>. The distribution of bulk-fluid Reynolds and Prandtl numbers related to the 782 points are presented in Fig. 2.

The differences between the predicted values and test data are shown in Table 1, which indicated the correlation D-M-2010 and D-M-2011 have the highest accuracy, 73.27 and 84.63 % within a margin of error of  $\pm 30$  % respectively. The scatter plots of the experimental Nu versus the predicted ones are shown in Figs. 3, 4, 5, 6 and 7, among which Figs. 3 and 4 is on thermo-physical properties modification, Fig. 5 on dimensionless number modification, Figs. 6 and 7 on segment function modification.

Comparing Table 1 with Fig. 3, 4, 5, 6 and 7, it's concluded that S-G-2013-b/w/f correlations (by thermal properties modification) perform well within the lower Nu region ( $\sim < 400$ ), poorly within the higher Nu region ( $> 400$ ), which deviate from the overall tendency of the test data obviously. The possible explanation is that bulk-fluid temperature, wall temperature and averaged temperature are close to each other within the lower Nu region, and therefore the modified correlations haven't been changed profoundly compared to the D-B correlation, resulting in a good accuracy. However in the higher Nu region, bulk-fluid temperature, wall temperature and averaged temperature are different each other greatly, and the modified correlations have been changed profoundly compared to the D-B correlation, resulting in a poor prediction ability. Maybe we can preliminarily propose that one should think it time and again on the proper limits of modification before trying to build a

**Table 1** Evaluation of Nu based on upper heat transfer correlations

Correlations	The percentage of predictions within fixed deviations from test data/%				Modification method
	Within $\pm 20$ %	Within $\pm 30$ %	Within $\pm 40$ %	Within $\pm 50$ %	
K-P-1959	19.18	25.58	34.53	40.66	Thermal properties
S-1965	41.05	50.64	62.28	75.58	Thermal properties
J-F-2004	26.21	40.54	48.59	55.24	Thermal properties
S-G-2013-b	45.14	56.27	65.09	78.52	Thermal properties
S-G-2013-w	30.82	46.80	63.81	78.13	Thermal properties
S-G-2013-f	45.14	61.89	75.96	84.14	Thermal properties
K-1985	14.45	21.61	30.43	42.33	Dimensionless number
D-M-2010	56.14	73.27	87.98	95.52	Dimensionless number
D-M-2011	64.58	84.53	93.86	94.63	Dimensionless number
B-S-1957	15.86	20.46	23.53	28.64	Segment function
K-1966	30.69	40.41	47.31	54.48	Segment function
Y-1972	13.43	21.48	30.05	39.39	Segment function
J-2002	27.62	40.54	48.85	55.88	Segment function
J-2008	35.68	43.22	51.15	57.67	Segment function
H-K-2012	27.75	36.57	47.57	51.79	Segment function

**Fig. 3** Comparison of calculated results by correlation 3&5 with experimental data (—)

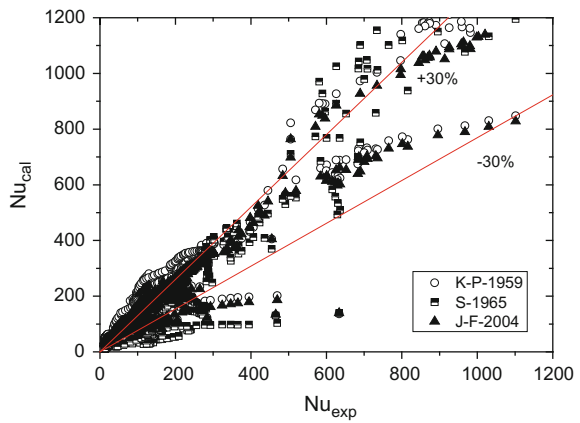


**Fig. 4** Comparison of calculated results by correlation 9&11 with experimental data (▢)

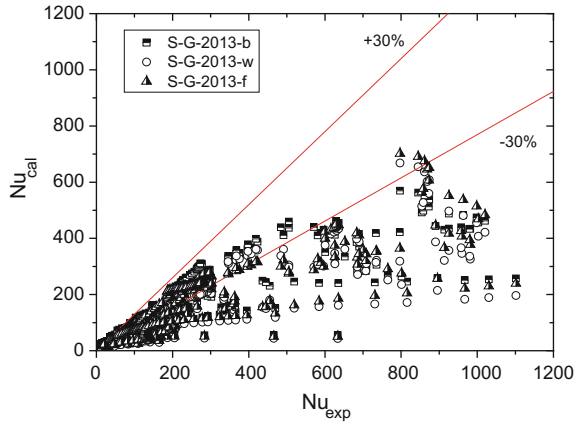


**Fig. 5** Comparison of calculated results by correlation 6&8 with experimental data

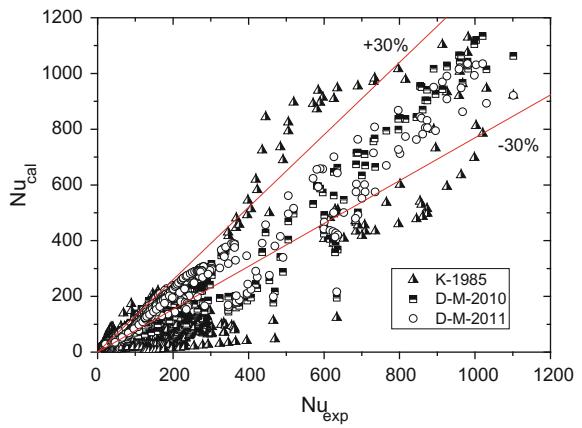


**Fig. 6** Comparison of calculated results by correlation 12&14 with experimental data (▢)

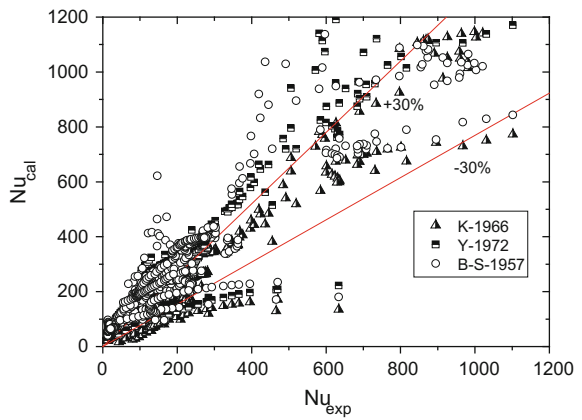




**Fig. 7** Comparison of calculated results by correlation 15&17 with experimental data (□)

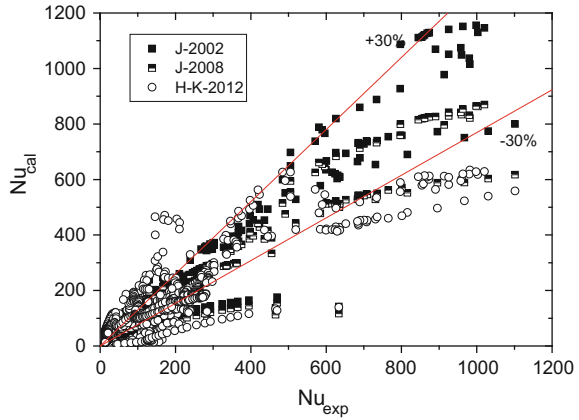
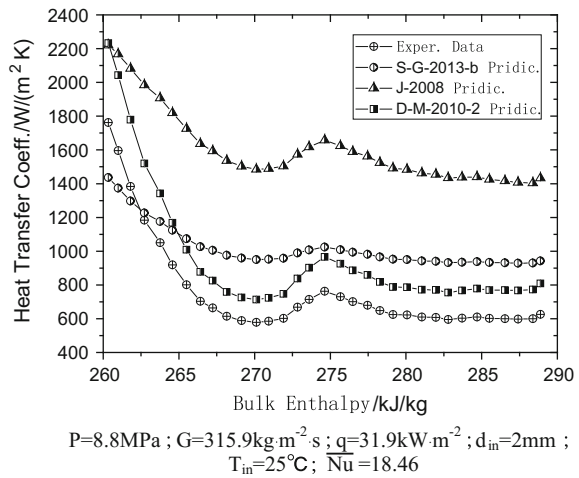


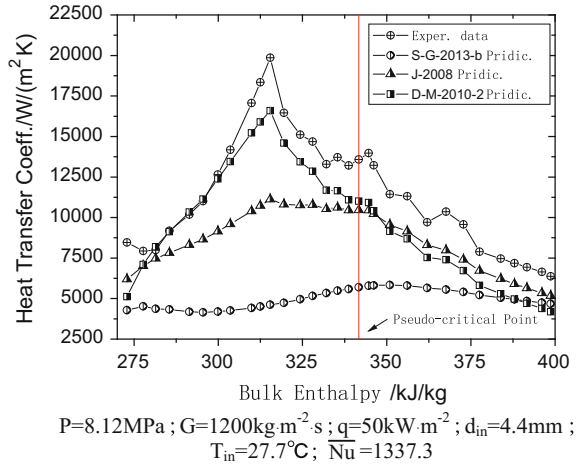
**Fig. 8** Comparison of heat transfer coefficient calculated by correlations with experimental data along the enthalpy at bulk fluid in the case of low Nu



supercritical heat transfer correlation by modification. In addition, J-2002 and J-2008 correlations (by segment function modification) perform better within the higher Nu region than the others. As improved by the three modification methods, most of them are able to predict the tendency of heat transfer to some extent, except for S-G-2013-b/w/f correlations.

To evaluate the performance of the reviewed correlations under specific experiment conditions, this paper studied S-G-2013-b correlation, J-2008 correlation and D-M-2011 correlation with two typical conditions, i.e. a high Nu condition and a low one, which were shown in Figs. 8 and 9. As we can see, the predictions are much higher deviated from experimental data in the low Nu condition, while opposite in the high Nu condition. Heat transfer at supercritical pressure is mainly characterized by the thermal physical properties which vary strongly, especially

**Fig. 9** Comparison of heat transfer coefficient calculated by correlations with experimental data along the enthalpy at bulk fluid in the case of high Nu



near the pseudo-critical point, and cause the equations for conservation of mass, momentum and energy nonlinear obviously, resulting in coupling of heat transfer with flow and more complex heat transfer phenomenon. Under fixed condition, enhancement or deteriorated heat transfer may occur, which make it difficult to predict heat transfer performance. At the recovery stage with unstable flow and great randomness, the unknown heat transfer model is difficult to predict with ordinary experimental study, as a result the prediction accuracy is poor too, which is shown in Fig. 9.

In experimental study, we often can only achieve wall temperatures, bulk-fluid temperatures, overall pressure differences and so on, but not some local parameters that we are interested. Unfortunately, supercritical carbon dioxide heat transfer has a more tight relationship with local thermal and flow field than subcritical state; maybe we have to work hard to explore how to extort thermal gradient and some other interesting information from wall temperature, bulk-fluid temperature and some other easily measured experimental parameters, which is certainly difficult. What is more, study is limited to the correspondence of inner field structure and boundary conditions. Now the accessible modification methods, i.e. thermo-physical properties modification, dimensionless numbers modification and segment functions modification, are aimed at integrating different level features or effects of supercritical fluid into heat transfer correlations. But here we come across an unsolved problem whether the three modifications overlap in a way or not. So we cannot be too careful to develop a new supercritical heat transfer correlation using more than one of them. In addition, the test data reduction skill has to be improved, so as to develop more advanced modification methods. For an instance, some researchers have recommended studying supercritical fluid heat transfer by importing neural network from artificial intelligence, which has a strong adaptation capacity to the kernel of supercritical fluid, i.e. thermo-physical properties variation. Someone also propose to reduce test data and develop heat transfer correlations

with the idea successive approximation or feedback. Exceptionally, the residual between experimental data and prediction values is a kind of important data resource, but no one studied.

## 4 Conclusions

Via collecting and analyzing forced convection heat transfer correlations for SCCO<sub>2</sub> flowing in tubes under heated condition, this paper made a many-sided evaluation of them, and concluded as follows:

1. Available forced convection heat transfer correlations for carbon dioxide were mainly developed by thermo-physical properties modification, dimensionless numbers modification and segment functions modification. Thermo-physical modification performs better within the low Nu range ( $\sim < 400$ ), dimensionless number modification over the whole range of Nu, and segment function modification within high Nu range ( $\sim > 400$ ). Among the correlations evaluated, D-M-2011 correlation has the highest accuracy, 84.63 % of the predictions within a margin of error of  $\pm 30$  % comparing with experimental data.
2. The evaluated correlations perform poorly in the enhancement and deteriorated heat transfer as well as the recovery stage of deteriorated heat transfer. Suitable multi-modification using the three methods may further improve prediction accuracy of these correlations.
3. There exist many-sided reasons for the poor performance of those correlations: the heat transfer mechanism in the pseudo-critical region is not clear enough, and we have not create a efficient mathematic model to control it; the sensitivity of thermo-physical properties to temperature and pressure, due to lower critical point, makes it more difficult to measure and determine basic parameters.

**Acknowledgments** This project is support by the National Science Fund for Distinguished Young Scholars (No. 11325526).

## References

1. F. W. Dittus, L. M. K. Boelter. Heat transfer in automobile radiators of the tubular type[J]. Int. J. Heat Mass Transfer, 1985, 12:3–22
2. Yang Shi-ming, Tao Wen-quan. Heat Transfer: Higher Education Press, 2006
3. P. B. S. Kirillov. About heat transfer at turbulent fluid flow in tubes[J]. Thermal Engineering, 1958, 4:63–68
4. K. E. A, P. V. S. Heat transfer at supercritical region in flow of carbon dioxide & water in tubes[J]. Thermal Engineering, 1959, 12:30–36
5. H. S. Swenson, J. R. Caever, C. R. Kakarala. Heat transfer to supercritical water in smooth-bore tube[J]. J. Heat Transfer, 1965, 477–484

6. Huang Yan-ping, Liu Guang-xu, Wang Jun-feng, Lu Fa. Evaluation of heat transfer correlations for supercritical carbon dioxide in circular tubes under heating conditions[J]. Nuclear Power Engineering, 2014, 35:1–5
7. S. Gupta, E. Saltanov, S. J. Mokry, I. Piro, L. Trevani, D. McGillivray. Developing empirical heat-transfer correlations for supercritical CO<sub>2</sub> flowing in vertical bare tubes[J]. Nuclear Engineering and Design, 2013, 261:116–131
8. V. A. Kurganov, V. B. Ankudinov. Calculation of normal and deteriorated heat transfer in tubes with turbulent flow of liquids in the near-critical and vapour region of state[J]. Thermal Engineering, 1985, 32:332–336
9. D. E. Kim, M. H. Kim. Experimental study of the effects of flow acceleration and buoyancy on heat transfer in a supercritical fluid flow in a circular tube[J]. Nuclear Engineering and Design, 2010, 240:3336–3349
10. D. E. Kim, M.-H. Kim. Experimental investigation of heat transfer in vertical upward and downward supercritical CO<sub>2</sub> flow in a circular tube[J]. International Journal of Heat and Fluid Flow, 2011, 32:176–191
11. K. E. A, P. V. S. Experimental study of heat exchange in carbon dioxide in the supercritical range at high temperature drops[J]. Teplofizika Vysokikh Temperatur, 1966, 4:389–398
12. K. Yamagata, K. Nishikawa. Forced convective heat transfer to supercritical water flowing in tubes[J]. Int. J. Heat Mass Transfer, 1972, 15:2575–2593
13. Y.-Y. Bae, H.-Y. Kim, D.-J. Kang. Forced and mixed convection heat transfer to supercritical CO<sub>2</sub> vertically flowing in a uniformly-heated circular tube[J]. Experimental Thermal and Fluid Science, 2010, 34:1295–1308
14. H. M. Son, K. Y. Suh. Experimental heat transfer to supercritical carbon dioxide flowing upward vertical tube with highly conducting surroundings[J]. Nuclear Engineering and Design, 2012, 250:573–584
15. D. E. Kim, M. H. Kim. Two layer heat transfer model for supercritical fluid flow in a vertical tube[J]. The Journal of Supercritical Fluids, 2011, 58:15–25
16. H. Kim, H. Y. Kim, J. H. Song, Y. Y. Bae. Heat transfer to supercritical pressure carbon dioxide flowing upward through tubes and a narrow annulus passage[J]. Progress in Nuclear Energy, 2008, 50:518–525
17. J. K. Kim, H. K. Jeon, J. S. Lee. Wall temperature measurement and heat transfer correlation of turbulent supercritical carbon dioxide flow in vertical circular/non-circular tubes[J]. Nuclear Engineering and Design, 2007, 237:1795–1802
18. Li Zhi-hui, Jiang Pei-xue. Experimental investigation of heat transfer in vertical tubes for supercritical carbon dioxide under high Reynolds number[J]. Nuclear Power Engineering, 2008, 29:41–45

# Experimental Study on the Effects of Temperature and pH on the Deposition of Corrosion Products in Fusion Reactor

Yan Ma, Jinyun Lei, Xin Xu, Yun Fu, Yixue Chen  
and Arslan Muhammad

**Abstract** Deposition of corrosion products increases radiation in primary coolant loops of reactor. The effects of temperature and pH on the deposition of corrosion products in fusion reactor were experimentally investigated. Experimental conditions are that the highest temperature is 150 °C, the range of pH is 7.00–10.50 and the flow rate is 5.667–5.696 m<sup>3</sup>/h. Magnetite particles with 99.5 % purity are used to simulate corrosion products in this experiment. State of loop was made stable by heating and pressurizing. Thickness of deposition in primary and test pipelines is determined by oxide skin thickness gauge (model OMD-100), with accuracy of 0.1 μm. The experimental results indicate that a higher value of pH is more profitable for reducing deposition of corrosion products in primary coolant loops, and the temperature of 140 °C should be focused because there exists maximum value of deposition thickness. Higher value of pH is benefit for corrosion products transport from fusion reactor core to steam generator. Furthermore, there exists an appropriate pH, such as pH = 9.00, which can make the deposition thickness get smallest in primary pipelines on the whole. In addition, higher curvature causes larger flow resistance, which makes corrosion products easier to deposit.

**Keywords** Temperature and pH · Deposition · Corrosion products · Fusion reactor

## 1 Introduction

In the phases of running of fusion reactor, it is proved that corrosion products are the most important influencing factor to source item analysis. Since the corrosion products could be activated when the coolant flows through the reactor core [1], the deposition of corrosion products will increase radiation in primary coolant loops of

---

Y. Ma (✉) · J. Lei · X. Xu · Y. Fu · Y. Chen · A. Muhammad  
School of Nuclear Science and Engineering, North China Electric Power University,  
Beijing, China  
e-mail: 983449231@qq.com

reactor. The factors affecting deposition are basically less well understood [2]. Results obtained point out the impact of the main water chemistry parameters (e.g. water temperature and pH) on ACP production, transport and deposition [3]. Therefore, the deposition and migration behavior of corrosion products is examined in this experiment.

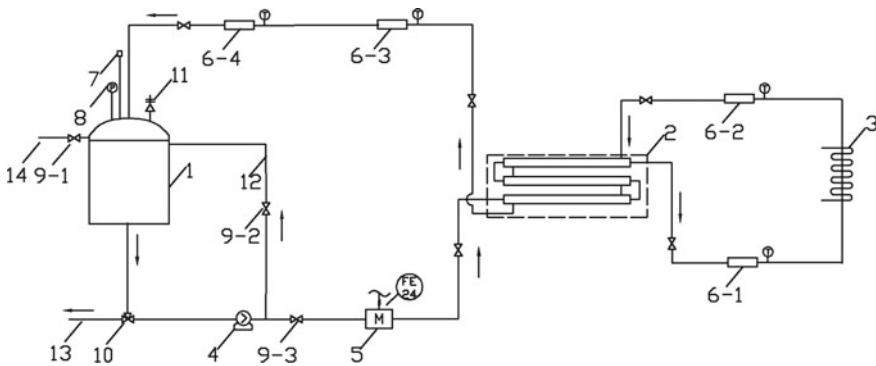
Objective of this experiment is to study the effects of temperature, pH, and curvature on the deposition of corrosion products. To study behavior of deposition thickness with temperature, pH, and curvature, all experimental results are well analyzed.

## 2 Experimental Methods

### 2.1 Experimental Loop

Figure 1 shows the schematic diagram of the experimental loop.

The simulation experiment loop is self-established according to ITER [4, 5]. In the experiment loop, the electric heater is used to simulate fusion reactor core, the double-pipe heat exchanger is used to simulate steam generator and the water tank is used to simulate pressurizer. The whole experimental loop is full of pure water. When the experiment is in process, 15 g magnetite ( $\text{Fe}_3\text{O}_4$ ) particles are added into the water tank. With the drive of the centrifugal pump, these particles would deposit in primary and test pipelines. State of loop was made stable by heating and pressurizing.



- 1-water tank; 2-double-pipe heat exchanger; 3-electric heater;  
 4-centrifugal pump; 5-vortex flow meter; 6-test pipelines;  
 7-thermometer; 8-pressure gage; 9-ball valves; 10-three-way  
 valve; 11-safety valve; 12-bypass; 13-drainage pipe

**Fig. 1** Schematic diagram of the experimental loop

### 2.2 Measuring Method

For fusion structure materials, the low activity materials, such as ferrite-martensite steel, are mostly studied at present. The application of ferrite-martensite steel is expected to become the first fusion structure material [6]. Therefore, Fe<sub>3</sub>O<sub>4</sub> particles, diameter 5 μm, with 99.5 % purity are used to simulate corrosion products in this experiment.

Thickness of deposition in primary and test pipelines is determined by oxide skin thickness gauge (model OMD-100), with accuracy of 0.1 μm. The measuring instrument is developed by Beijing Constel Technology INC.

The mechanism of measuring deposition thickness is taking advantage of the inherent magnetism of Fe<sub>3</sub>O<sub>4</sub>. By inducing magnetic field, the scale thickness gauge can transfer magnetic signals into electric signals. Voltage values obtained are used to determine the transforming relationship with deposition thickness.

Through the calibration of instrument, the fitted transforming equation is established (Eq. (1)):

$$y = -15.08458e^{-\frac{x}{44.67965}} + 14.93835 \tag{1}$$

where y is the deposition thickness, x is the measured voltage. The related coefficient is 0.99762.

According to calculations of heat transfer [7, 8], all the measuring points are basically arranged. After the loop is stable, the deposition thickness of all the measuring points is obtained by the measuring instrument.

Figure 2 shows the working principle of the oxide skin thickness gauge.

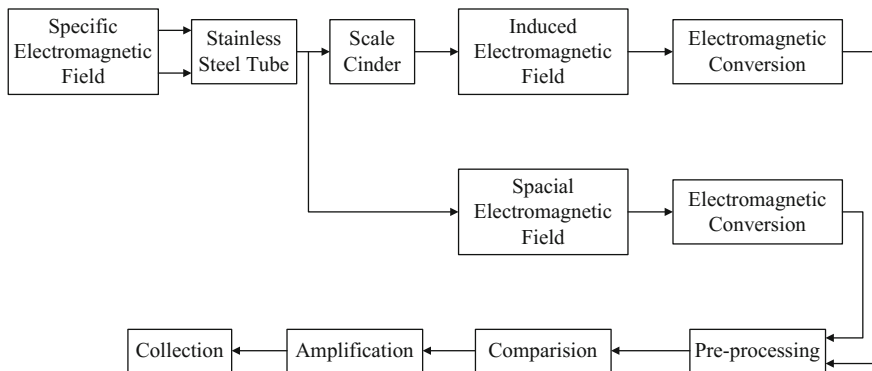


Fig. 2 The working principle of the oxide skin thickness gauge

### 2.3 Experimental Conditions

Most of the pressurized water reactors in the world are using high purity lithium hydroxide of  $^7\text{Li}$  as pH control agent [9]. Based on this, lithium hydroxide with 98 % purity is also adopted to adjust pH values in this experiment.

Conditions of the experiment are shown in Table 1. The experiment can simulate the deposition of corrosion products in primary cooling circuit in ITER.

## 3 Results and Discussion

### 3.1 Temperature and pH

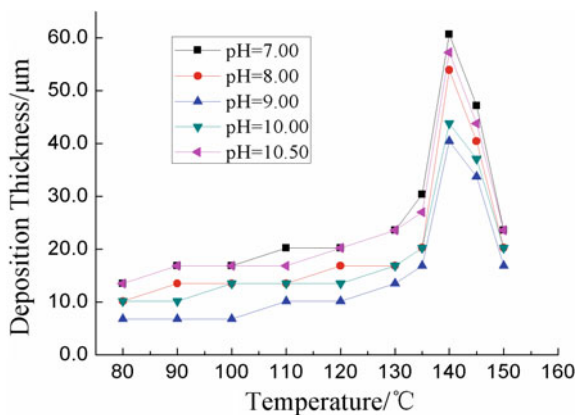
Figure 3 shows that for each pH value, when pH remains constant, with increase in temperature, thickness of deposition also increases. Initially thickness of deposition increases gradually but after sometime it increases rapidly and gets peak at 140 °C. After reaching to the peak, these curves start to decrease linearly.

Another important observation of this experiment is that for each temperature, when temperature remains constant, pH ranges from 7.00 to 9.00, higher the value of pH, lower will be the thickness of corrosion products deposits. However, when pH increases from 9.00 to 10.00, the law of the deposition gets changed. It exactly

**Table 1** Experimental conditions

Parameter	Range of parameter
Temperature (°C)	80–150
pH (at 25 °C)	7.00–10.50
System pressure (MPa)	0.48–0.50
Flow rate (m <sup>3</sup> /h)	5.667–5.696

**Fig. 3** Effects of temperature and pH on the deposition thickness of Fe<sub>3</sub>O<sub>4</sub> (primary pipelines, particle diameter = 5 μm, pH = 7.00–10.50)





suggests that there exists an inflection point of pH between 8.00 and 10.00, which can reverse the law of the deposition.

The results indicate that temperature and pH can influence the solubility of  $Fe_3O_4$  directly, which influence the deposition further.

Another important observation is that the results indicate that keeping an appropriate pH, such as  $pH = 9.00$ , can make the deposition thickness get smallest in primary pipelines on the whole, which is benefit for the running of fusion reactors. In other words, pH is not the bigger the better.

### 3.2 Curvature

The experimental loop contains 4 test pipelines, 2 of them are horizontal bends, and the other 2 are vertical U-shaped bends. At each test pipeline, there are 3 measuring points of different curvature:  $0.000$ ,  $0.010$  and  $0.027 \text{ mm}^{-1}$ . Table 2 shows the parameter of test pipelines.

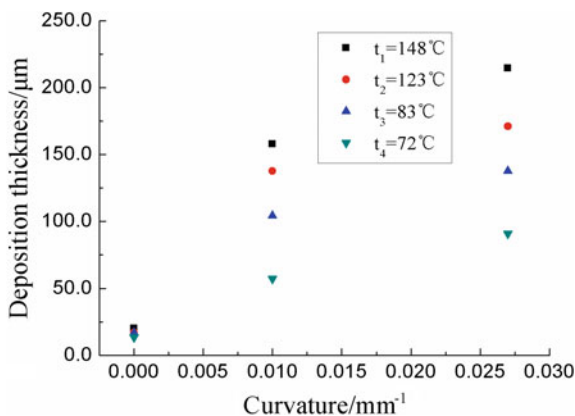
Deposition thickness at all 12 measuring points is measured. Figure 4 shows the results when  $pH = 7.00$ .

Figure 4 shows that the deposition thickness increases with increasing curvature. It validates that higher curvature causes larger flow resistance, which makes corrosion products easier to deposit. Thus the curvature of  $0.027 \text{ mm}^{-1}$  needs to be focused for its' maximum value of deposition thickness. During recondition of

**Table 2** Parameter of test pipelines

Types of test pipelines	Radius of curvature/mm	Curvature/ $\text{mm}^{-1}$
Straight pipe	$\infty$	0.000
Bent pipe	100.0	0.010
Bent pipe	37.5	0.027

**Fig. 4** Effects of curvature on the deposition thickness of  $Fe_3O_4$  (test pipeline, particle diameter =  $5 \mu\text{m}$ ,  $pH = 7.00$ )



fusion reactors, all bend pipes need to be carefully checked in order to clean up deposited corrosion products.

## 4 Conclusions

1. When temperature remains constant, higher value of pH is more profitable for reducing deposition of corrosion products in primary coolant loops. It is beneficial for corrosion products transport from fusion reactor core to steam generator.
2. pH is not the bigger the better. There exists an inflection point of pH between 8.00 and 10.00, which can reverse the law of the deposition.
3. There exists an appropriate pH, such as  $\text{pH} = 9.00$ , which can make the deposition thickness get smallest in primary pipelines on the whole.
4. The temperature of  $140\text{ }^{\circ}\text{C}$  should be focused because there exists maximum value of deposition thickness.
5. Higher curvature causes larger flow resistance, which makes corrosion products easier to deposit.

## References

1. Lu Daogang, Yuan Bo, Wu Licun, et al. Research on the deposition model of particle-like corrosion product in SG tubes of PWR. *Annals of Nuclear Energy*, 2015, 81: 98–105
2. Mikko Vepsäläinen, Timo Saario. Magnetite Dissolution and Deposition in NPP Secondary Circuit. Research Report VTT-R-09735-10
3. L. Di Pace, G. Cambi, D.G. Cefrigo, E. Sobrero, M. Costa. Activated Corrosion Products in ITER First Wall and Shielding Blanket Heat Transfer System. 0-7803-2969-4/95/\$4.000 IEEE, 1995
4. ITER Technical Basis, International Atomic Energy Agency, VIENNA, 2002
5. V. Massaut, On the erosion-corrosion in ITER, water chemistry and the PACTITER code development, EFDA-CSU Garching -Field Safety & Environment, 2005
6. YU Xingzhe, SONG Yueqing, CUI Shun, et al. Status and Progress of Research on Structural Materials for Fusion Reactors. *Materials Review*, 2008, 22 (2): 68–72 (in Chinese)
7. Ran Chunyu. Calculations of Temperature Drop and Heat Release in Hot Water Heating Pipes. Jilin Institute of Architecture & Civil Engineering (in Chinese)
8. Yang Shiming, Tao Wenquan. *Heat Transfer*. 4th ed. Beijing: Higher Education Press, 2006 (in Chinese)
9. Han Yande. *Water Chemistry Of Nuclear Power Plant*, 1st ed. Beijing: Atomic Energy Press, 2010 (in Chinese)

# Large-Fluence Laser-Driven Ion Beam for Inertial Fusion Ignition

Suming Weng, Zhengming Sheng, Masakatsu Murakami, Min Chen, Lule Yu and Jie Zhang

**Abstract** As a prospective approach for inertial confinement fusion, fast ion ignition may achieve high gain with low driver energy and simple target fabrication. However, studies show that fast ion ignition requires an ion beam with extremely large energy fluence and high quality. In comparison with conventional accelerators, laser-driven ion accelerators have advantages of compact size, high density, and short bunch duration. Nevertheless, it is still challenging to simultaneously enhance the yield and quality of laser-driven ion beams for fast ion ignition. In this work, we propose a scheme to address this challenge. First, the ions of a target can be uniformly accelerated in hole-boring radiation pressure acceleration by matching the laser intensity profile with the target density profile. Second, the oscillation of the electric field for ion acceleration can be effectively suppressed by using two-ion-species targets. Particle-in-cell (PIC) simulation demonstrates that almost all ions in a solid target of a few microns can be uniformly accelerated to relativistic speeds by using our scheme. The resulting ion beam with large energy fluence and high quality may drive fusion ignition and more generally create matter with unprecedented high-energy density.

**Keywords** Inertial confinement fusion · Fast ion ignition · Laser-driven ion acceleration · Laser hole-boring · Radiation pressure acceleration · Laser pulse shaping

---

S. Weng (✉) · Z. Sheng · M. Chen · L. Yu · J. Zhang  
Department of Physics and Astronomy, Shanghai Jiao Tong University,  
Shanghai, China  
e-mail: wengsuming@sjtu.edu.cn

M. Murakami  
Osaka University, Osaka, Japan

## 1 Introduction

Inertial confined fusion driven either by heavy ion beams or by high power lasers requires fast heating of a compressed target to a sufficient high temperature [1]. Currently, it is still challenging to achieve such a fast heating by the ion beams from conventional accelerators. On the other hand, the high power lasers cannot deposit their energy directly in the compressed fusion targets. However, with the development of ultrashort high power lasers, laser-driven acceleration of high-energy ion beams has been received significant interest because of its various potential advantages in terms of high-energy density, short duration, and compact size in contrast to conventional accelerators [2, 3]. This may promise novel ion sources in applications including fast ion ignition [4], hadron therapy [5], proton imaging [6], and neutron generation [7].

Motivated by these applications, many novel mechanisms have been proposed to accelerate ions over the last decades [2, 3]. However, there are still a few pivotal issues to be solved or improved for the large-scale application of laser-driven ion beams in practice. Among these issues, enhancing the yield and quality of laser-driven ion beams attracts particular attention.

In this paper, we will propose a hole-boring radiation pressure acceleration (RPA) scheme using the temporally tailored pulse, which is capable of generating monoenergetic ions with a large fluence for inertial confinement fusion. Further, we will show that in the hole-boring RPA the energy spread of ion beam can be effectively reduced by using a two-ion-species target.

## 2 Laser-Driven Large-Fluence Monoenergetic Ion Beam

### 2.1 Uniform Laser Hole Boring in Inhomogeneous Plasmas

According to the piston model for the hole-boring of a circularly polarized (CP) laser pulse in a uniform plasma [8, 9], the laser front propagation velocity and the mean accelerated ion energy are given by

$$v_b = c\Pi/(1 + \Pi) \quad (1)$$

$$\varepsilon_i = 2m_i c^2 \Pi^2 / (1 + 2\Pi), \quad (2)$$

where the characteristic parameter  $\Pi$  is defined as

$$\Pi = a(Zm_e n_c / 2Am_p n_e)^{1/2}, \quad (3)$$

with the critical density  $n_c = m_e \varepsilon_0 \omega^2 / e^2$ , the dimensionless laser amplitude  $a = [I\lambda^2 / (1.37 \times 10^{18} \text{ W/cm}^2 \mu\text{m}^2)]^{1/2}$ , the ion mass in units of the proton mass  $A = m_i / m_p$ ,

the ionic charge state  $Z$ , the electron mass  $m_e$  and density  $n_e$ , and the laser wavelength  $\lambda$  and frequency  $\omega$ .

Now we consider the uniform hole boring of a laser pulse in inhomogeneous plasma [10]. For convenience, we assume that the semi-infinite plasma has a density profile  $n(x)$  in the space  $x \geq 0$  and the pulse with a temporal profile  $a(t)$  irradiates from the left side. Equations (1) and (2) suggest that a time-independent  $\Pi_0$ , i.e. a constant hole-boring velocity  $v_b$ , is essential for the monoenergetic ion beam generation in the interaction of a laser pulse with inhomogeneous plasma. With a constant  $v_b = c\Pi_0/(1 + \Pi_0)$ , the time  $t_s$  when the slice at the  $t'$  interval of the pulse catches up with the plasma can be calculated from  $ct_s = ct' + v_b t_s$ . Thus the instantaneous interface position can be calculated as

$$x' = v_b t_s = c\Pi_0 t'. \quad (4)$$

Combining Eqs. (3) and (4) gives the temporal intensity profile of the laser pulse to generate monoenergetic ion beam with inhomogeneous target density  $n(x)$  as [10]

$$a(t) = (2Am_p/Zm_e)^{1/2} \Pi_0 n_e^{1/2} (c\Pi_0 t). \quad (5)$$

Particularly, an exponential density profile  $n_0 \exp(x/L)$  is widely present in the pre-compressed fuel target for inertial confinement fusion [10] or the pre-plasma produced in the laser-plasma interactions [11]. In these cases, the temporally tailored laser profile can be simplified as

$$a(t) = a_0 \exp(t/2T_0), \quad (6)$$

where  $a_0 = \Pi_0(2Am_p n_0/Zm_e n_c)^{1/2}$ ,  $T_0 = L/c\Pi_0$ , and  $n_0$  is the electron number density at the front boundary of the target. From the acceleration region  $0 \leq x \leq x_{\max}$ , a total energy fluence of monoenergetic ions

$$F_i = \varepsilon_{i,0} \int_0^{x_{\max}} n(x) dx = \varepsilon_{i,0} L (n_{\max} - n_0), \quad (7)$$

can be generated by a tailored pulse rising from  $a_0$  to  $a_{\max} = a_0 \exp(x_{\max}/2L)$  within a duration of  $x_{\max}/c\Pi_0$ , where  $n_{\max} = n_0 \exp(x_{\max}/L)$  and  $\varepsilon_{i,0} = 2\Pi_0^2 m_i c^2 / (1 + 2\Pi_0)$ .

The efficient generation of monoenergetic ion beam by the hole boring of a tailored pulse has been verified by PIC simulations. The code employed is similar to that used in previous investigations [12]. In this simulation case, it is assumed that the laser pulse is circularly polarized with a wavelength  $\lambda = 1.06 \mu\text{m}$ , thus  $n_c = 9.92 \times 10^{20} \text{ cm}^{-3}$ . The plasma has a profile of  $20n_c \exp(x/20\lambda)$  rising from 20 up to  $200n_c$  over a distance of  $46\lambda$  and then remain uniform, and ions are deuterons. The spatial and temporal resolutions  $\Delta x = \lambda/512$  and  $t = \Delta x/c$  are used, and 800 weighted macroparticles per cell are initially allocated in the plasma region. Equation (6) suggests that a tailored pulse with  $a_0 = 49.63$  and  $T_0 = 154.44\lambda/c$  can

result in a stable hole-boring velocity  $v_b = 0.115c$  (i.e.  $\Pi_0 = 0.13$ ) and generate monoenergetic deuterons at a mean energy of 50 MeV.

Simulation results of such a tailored pulse with a duration of 350 laser wave cycles have been shown in Fig. 1. A nearly constant laser front propagation velocity of  $0.115c$  has been identified during the whole duration of interaction as shown in Fig. 1a. As a result, deuterons can be accelerated to momenta with a time-independent mean  $p_x = 0.23m_i c$  as illustrated in Fig. 1b. Moreover, these deuterons have a good quality of being monoenergetic, and such a good monoenergetic quality can be well maintained in the whole duration of the interaction. The energy spreads are always about 11.3 % as indicated by the energetic deuteron spectra at different times in Fig. 1c. Finally, Fig. 1d shows that a total deuteron energy fluence of  $2.82 \text{ GJ cm}^{-2}$  can be achieved by such a tailored pulse with a laser energy fluence of  $13.94 \text{ GJ cm}^{-2}$ . In other words, the conversion efficiency of this deuteron acceleration scheme is about 20.23 %, which is in a good quantitative agreement with the theoretical estimate 20.57 %. This efficient generation of a high fluence of monoenergetic deuterons may provide a promising approach to trigger the fast ion ignition of inertial confinement fusion [4]. In the

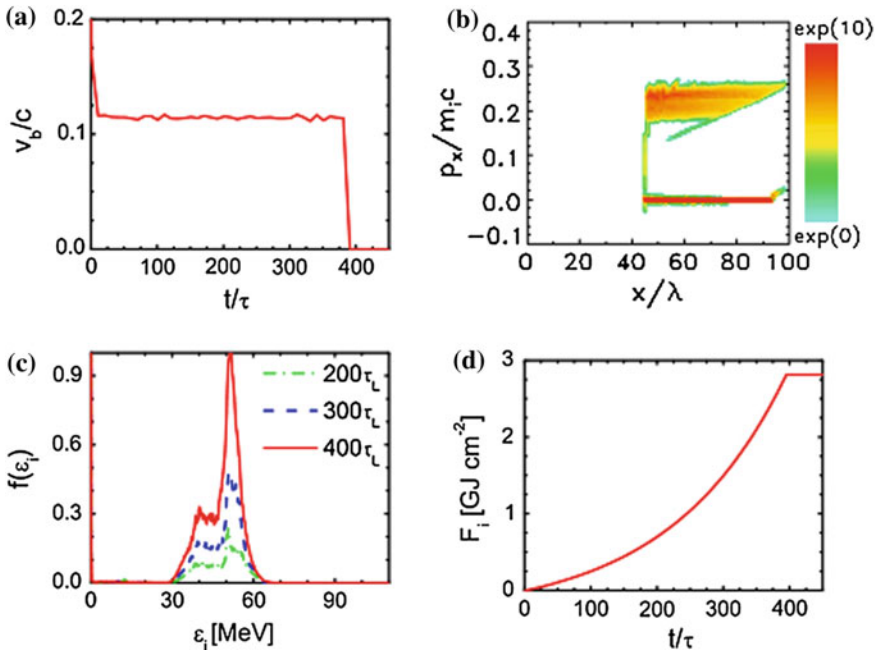


**Fig. 1** **a** Propagation velocity of the laser front, **b** deuteron momentum distribution, **c** energetic deuteron spectra at different times, and **d** energy fluence of deuterons produced in the interaction of a temporally tailored pulse with an inhomogeneous target. Simulation parameters are given in the text

case of multi-dimensions, the match between the tailored laser pulse and the target will be more complicated and was discussed in detail in Ref. [10].

On the other hand, target density modulation is recently proposed to achieve the hole-boring RPA of ion beams with high yield and high quality [13]. With the help of micro/nanofabrication techniques, it might be more practical to modulate the target density profile than the laser intensity profile. The density-modulated target permits its ions to be uniformly accelerated as a dense block by laser radiation pressure. In addition, the density-modulated target is half embedded in a substrate thick enough to keep the DM target cold enough for the high-quality hole-boring RPA. Particle-in-cell simulations demonstrate that almost all ions in a solid-density plasma of a few microns can be uniformly accelerated to about 25 % of the speed of light at an intensity around  $10^{22}$  W/cm<sup>2</sup>. The resulting dense block of well-collimated quasi-monoenergetic ions is interesting for the creation of astrophysical-like high-energy density conditions, as well as high pressure materials science. More importantly, it may be applied in the fast ignition of inertial confinement fusion [13].

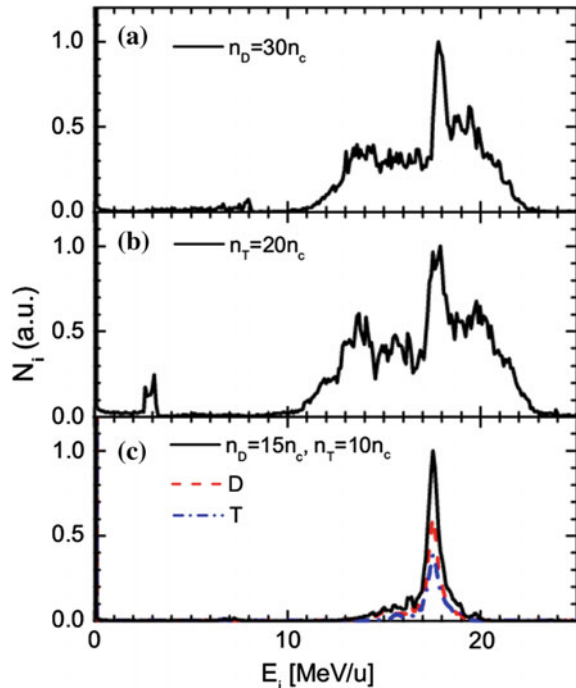
## 2.2 Reducing Energy Spread by Two-Ion-Species Targets

To show the effect of target composition, we have also performed PIC simulations using different targets: (a) pure deuterium target with  $n_D = n_e = 30n_c$ , (b) tritium target with  $n_T = n_e = 20n_c$ , and (c) DT target with  $n_D = 15n_c$ ,  $n_T = 10n_c$ , and  $n_e = 25n_c$ . The electron number density  $n_e$  varies in order to yield the same mass density  $\rho = 0.1$  g/cm<sup>3</sup> in all targets. For simplification, in all simulations of this section we assume that the laser amplitude rapidly rises as  $a \sin(\pi t/10\tau)$  in the first five cycles and then keeps constant with  $a = 50$ , where  $a$  and  $\tau = \lambda/c$  are the laser field amplitude and wave period, respectively. The simulation box is located at  $-10\lambda \leq x \leq 70\lambda$  and simulations start at  $t = -10\tau$ , where the laser pulse is launched from the left boundary  $x = -10\lambda$ . The targets with different compositions are all located in  $0 \leq x \leq 50\lambda$ , and each one is initially cold with a homogeneous density. The spatial and temporal resolutions  $\Delta x = \lambda/300$  and  $t = \Delta x/c$  are used, and 1200 macroparticles per cell are initially allocated for particles.

Figure 2 shows the energy spectra of ions accelerated from these three targets. Since the overall hole-boring dynamics are determined by the laser intensity and the target total mass density [14], it is reasonable that ions are roughly accelerated to the same velocity and hence the ion spectra from three targets are all peaked at the same energy per nucleon (17.55 meV/u) as predicted by Eq. (2). For the applied laser pulse  $a = 50$ , it is clear that the condition  $a < n_e/n_c$  fails for all targets. Therefore, the relativistic critical density increase may play some role in laser–target interaction as well as the hole boring RPA [12]. Consequently, it is expected that the resulting energy spectra should be quite broad. Indeed, this is true in the target with either pure deuterons or pure tritons. As shown in Fig. 2a, b, the accelerated deuterons or tritons are broadly distributed over the energy spectrum with the respective energy spreads

$\Delta E/E = 13.2$  or  $38.9\%$ , here  $\Delta E$  is the full width at the half maximum (FWHM) and  $E$  is the peak energy of the spectrum. However, the energy spectrum from the DT target surprisingly displays a favorable quality of being quasi-monoenergetic with a narrow spread  $3.7\%$  in Fig. 2c. It is important to note that the principle of reducing the energy spread in the hole-boring RPA by using two-ion-species target is essentially different from these in the target normal sheath acceleration (TNSA) or light-sail RPA. In the TNSA or light-sail RPA, the lighter ions such as protons are quickly separated from the heavier ions, then the heavy ion layer acts as a substrate to protect the lighter ions from the instabilities and thus provide a more stable accelerating field for generating quasi-monoenergetic lighter ions [15, 16]. Usually, the energy spread of the lighter ions monotonously decreases with its ratio and the quality of heavier ion beams is sacrificed in the TNSA or light-sail RPA using two-ion-species targets. In the hole-boring RPA with two-ion-species targets, however, it is clear that the respective spectra of lighter ions (deuterons) and heavier ions (tritons) are very similar as shown in Fig. 2c. They are almost peaked at the same energy per nucleon with narrow spreads  $3.2$  and  $3.7\%$ , respectively. In the hole-boring RPA, ions will be reflected (accelerated), separately in time, from the laser-plasma interface. Due to different charge-to-mass ratios, ions from a two-ion-species target will be distributed into more bunches and each bunch bears less charge [17]. Consequently, the oscillation of the longitudinal electric field for accelerating ions can be effectively suppressed

**Fig. 2** Ion energy spectra at  $t = 100\tau$  from PIC simulations. The laser amplitude is  $a = 50$  and targets are: **a** pure deuterium target with  $n_D = n_e = 30n_c$ , **b** tritium target with  $n_T = n_e = 20n_c$ , and **c** DT target with  $n_D = 15n_c$ ,  $n_T = 10n_c$ , and  $n_e = 25n_c$ . The respective spectra for deuterons (red dashed) and tritons (blue dash-dotted) from the DT target are also drawn in (c)





according to Poisson equation. As a result, the energy spread of ion beams generated in the hole-boring radiation pressure acceleration can be greatly reduced in the two-ion-species target such as TD targets. For interested readers, more details about the dynamics of the accelerated ions can be found in Ref. [17].

### 3 Conclusions

In conclusion, we have formulated the temporal profile of a laser pulse to achieve the hole boring at a constant velocity in an inhomogeneous plasma for the efficient generation of monoenergetic ion beams with a large energy fluence. For a deuterated target with an exponential density profile, simulation results indicate that monoenergetic deuterons can be efficiently generated by the hole-boring RPA using a temporally tailored intense CP pulse. In particular, the high conversion efficiency and the good monoenergetic quality of accelerated deuterons can be well maintained in the whole duration of interaction. Therefore, it is capable of generating a high fluence of monoenergetic deuterons efficiently using the temporally tailored pulse, which is particularly suitable for fast ion ignition.

Further, we have found that the energy spread of ion beams generated by the hole-boring RPA can be effectively reduced by using two-ion-species target. Unlike these by the TNSA or the light-sail RPA, the energy spread of fast heavier ions generated by the hole-boring RPA in a two-ion-species target is nearly as narrow as that of lighter ions, which may be beneficial to enhancing the energy conversion efficiency of laser pulse into useful ions for fast ignition of inertial confinement fusion.

### References

1. S. Atzeni and J. Meyer-ter-Vehn, *The Physics of Inertial Fusion: Beam Plasma Interaction, Hydrodynamics, Hot Dense Matter* (Clarendon Press, 2004)
2. H. Daido, M. Nishiuchi, and A. S. Pirozhkov, *Rep. Prog. Phys.* **75**, 056401 (2012)
3. A. Macchi, M. Borghesi, and M. Passoni, *Rev. Mod. Phys.* **85**, 751 (2013)
4. M. Roth *et al.*, *Phys. Rev. Lett.* **110**, 044802 (2013)
5. E. Fourkal, I. Velchev, J. Fan, W. Luo, and C. M. Ma, *Med. Phys.* **34**, 577–584 (2007)
6. M. Borghesi *et al.*, *Phys. Plasmas* **9**, 2214–2220 (2002)
7. P. A. Norreys *et al.*, *Plasma Phys. Control. Fusion* **40**, 175–182 (1998)
8. A. P. L. Robinson *et al.*, *Plasma Phys. Control. Fusion* **51**, 024004 (2009)
9. T. Schlegel *et al.*, *Phys. Plasmas* **16**, 083103 (2009)
10. S. M. Weng *et al.*, *Phys. Plasmas* **21**, 012705 (2014)
11. X. Ribeyre *et al.*, *Plasma Phys. Control. Fusion* **50**, 025007 (2008)
12. S. M. Weng *et al.*, *New J. Phys.* **14**, 063026 (2012)
13. S. M. Weng *et al.*, “Dense blocks of energetic ions driven by multi-petawatt lasers”, *Scientific Reports* **6**, 22150 (2016)

14. A. P. L. Robinson, D. H. Kwon, and K. Lancaster, *Plasma Phys. Control. Fusion* **51**, 095006 (2009)
15. T. P. Yu, A. Pukhov, G. Shvets, and M. Chen, *Phys. Rev. Lett.* **105**, 065002 (2010)
16. Y. Q. Cui *et al.*, *Phys. Plasmas* **20**, 024502 (2013)
17. S. M. Weng *et al.*, *Laser Part. Beams* **33**, 103–107 (2015)

# Lead Cooled Fast Reactor Core Physics Parameters Calculation Based on Monte Carlo Method

Yang Lyu

**Abstract** The lead cooled fast reactor (LFR), which has received more and more worldwide attention in recent years, was chosen as one of the Generation IV reactors by GIF. Using MCNP code, lead cooled fast reactor physics calculation model has been set up. Detailed calculation of several kinds of critical physics calculations has been established, including fuel elements, fuel assemblies, control rods, reflector and reactor pressure vessel. Then the three-dimensional models were developed for the whole core. The calculation results include the following core physics parameters: primary effective multiplication factor, power distribution, control system worth, reactivity coefficient. The results indicate that its physics characteristics of the LFR can satisfy the core design requirement; the power distributions are reasonable; the control system can meet the request for shutdown. The calculation results can provide necessary parameters for thermal hydraulic and transient analysis for lead cooled fast reactor.

**Keywords** LFR · MCNP · Core physics parameter · CR worth · Power distribution

## 1 Introduction

Lead cooled fast reactor (LFR) is one of the six most hopeful nuclear systems chosen by nuclear system technology route. When compared with other nuclear systems of the GEN IV technology, LFR system is best in sustainable development because of the ability of nonproliferation and physical protection. LFR's coolant is characterized by relative inertness so that the system can be safe and economical. Using lead or LBE as coolant, fast spectrum and closed nuclear fuel cycle, LFR can be designed into breeder reactor and burn reactor. Breeder reactor can be used to

---

Y. Lyu (✉)

Reactor Design and Safety Research Center, China Nuclear Power  
Technology Research Institute, Shenzhen, Guangdong, China  
e-mail: lv-yang@cgnpc.com.cn

produce electricity and breed nuclear fuel at the same time and its fuel type is uranium or thorium nitride. Burn reactor is used for evolution product of the spent fuel nuclear waste so that the fuel can be taken from spent fuel of PWR.

Based on the use of sequence of random numbers, MCNP method is used to obtain sample values for the problem [1]. Monte Carlo method imitates the particle flight path and different interactions between the neutrons and materials. By using the LFR core design as a reference case, the Monte Carlo MCNP code is used to develop an accurate description of the arrangement of LFR core [2, 3]. A three-dimensional model is developed for the whole core including all the fuel elements, coolant, control rods, safety rods and reflector assemblies. The following reactor core physics parameters are calculated for LFR: effective multiplication factor, power distribution, control system worth, shutdown margin, reactivity coefficient.

## 2 Reactor Core and MCNP Models

The LFR's fuel is  $\text{UO}_2$  and uses lead as coolant. The active zone adopts inhomogeneous description and the data library is ENDF b7u. Under normal conditions, the fuel temperature is 1200 K, cladding and lead are 600 K. The core is divided into the following zones from inner to outer:

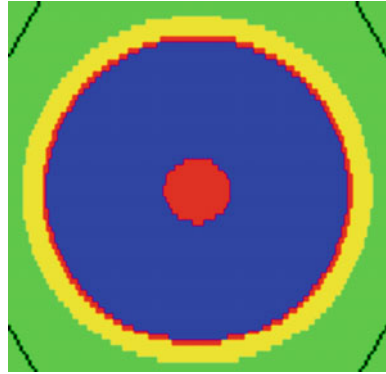
1. active zone, including inner fuel assemblies and outer fuel assemblies; this zone contains nuclear fuel and coolant;
2. control zone, including control rod assemblies and safety rod assemblies;
3. reflectors, contain side reflector assemblies; there are coolant circulation channels.

The inner and outer fuel assemblies use  $\text{UO}_2$ . The inner enrichment degree is 20 % while that of the outer is 25 %. There are two reasons for having chosen the enrichment degree above, one is that consider the aim to breed the nuclear fuel (which has been calculated for several kinds of enrichment), another is the values are normally used for fast reactors. The fuel pellet is hollow, inside the hole is helium. Through this design, it can increase linear power of the reactor and avoid the problem that the temperature might exceed the maximum allowable limit. The fuel assembly with central hole can also let the radial flux flatten.

The fuel pin includes upper plug, lower plug, insulator, gas plenum, spring and fuel pellet. The fuel assembly wrapper is hexagonal structure. There are 127 fuel pins inside, and tungsten device upside. By using MCNP code, the fuel pins and fuel assemblies can be modeled. Figures 1 and 2 have given some cross sections of the LFR models.

There are two independent control systems, control rod assemblies and safety rod assemblies. The control rod assemblies are used for normal control of the reactor and for SCRAM case. The safety rod assemblies are only used for SCRAM

**Fig. 1** Geometry model of fuel cell



case. Both CR and SR adopt B4C as absorber. The control rod assemblies are positioning into the outer zone, which has higher enrichment fuel to make the core power distribution flatten. When under SCRAM, the CR takes advantage of buoyancy effect of lead. Both of them are designed as pin type. The lead coolant flows through the pin gap to cool the assemblies. The MCNP model is shown in Fig. 3.

The reflector assemblies use  $ZrO_2$  as material and the wrapper has the same size with fuel assemblies. There are 127 reflector pins inside the wrapper used to reflect neutrons and shielding. There are also coolant channels inside and around reflector pins so that sedimentary from neutron irradiation can be decreased.

By using the MCNP repetition structure, the whole core of lead cooled fast reactor can be modeled. As shown in Figs. 4 and 5, the core adopts a homogeneous configuration in the radial direction that incorporates the annular rings of the inner and outer fuel assemblies. The control rod assemblies are put into the outer fuel assemblies which have higher enrichment. Meanwhile, the safety rod assemblies are put into the inner zone with high neutron flux. Outside the core zone are reflector assemblies, which can protect the vessel from neutron irradiation damage and decrease neutron leakage.

### 3 Core Physics Calculations

#### 3.1 $k_{eff}$ Multiplication Factor

The  $k_{eff}$  multiplication factor value has been calculated by running the MCNP calculation in the KCODE mode. The value obtained is  $k_{eff} = 1.04386 \pm 0.00048$ .

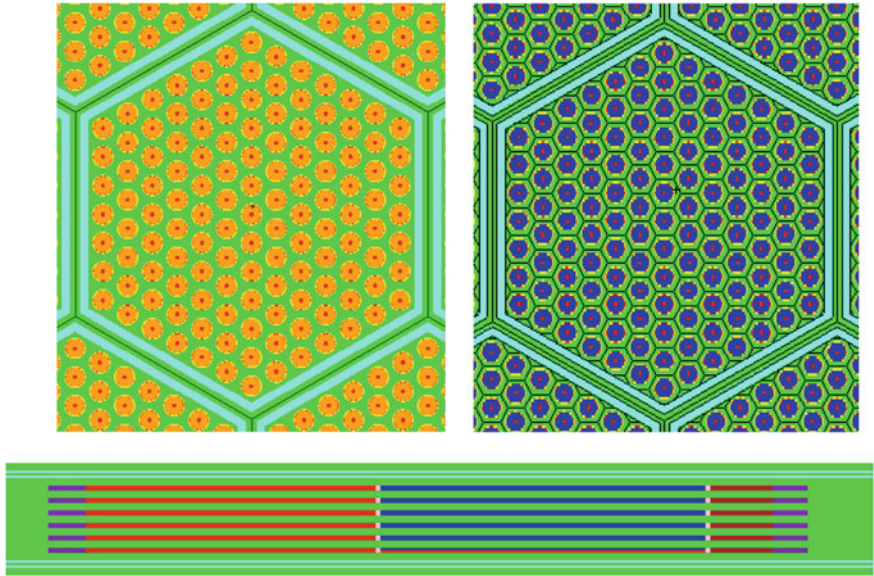


Fig. 2 Fuel assembly (inner and outer assembly)

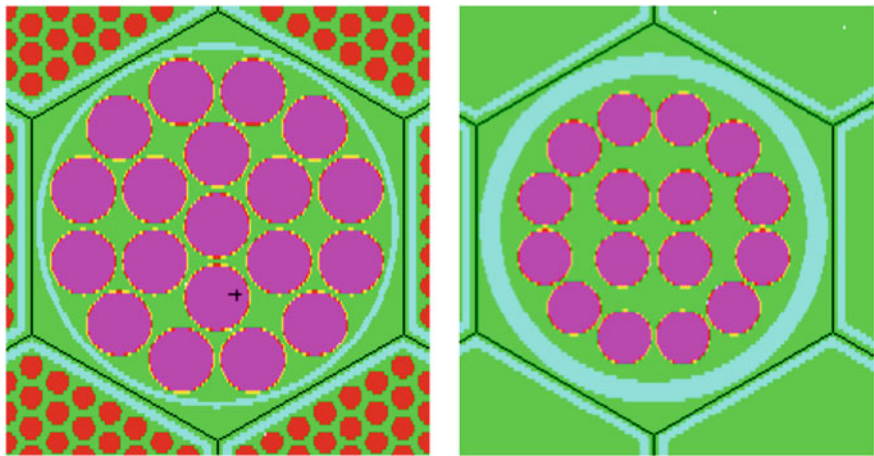
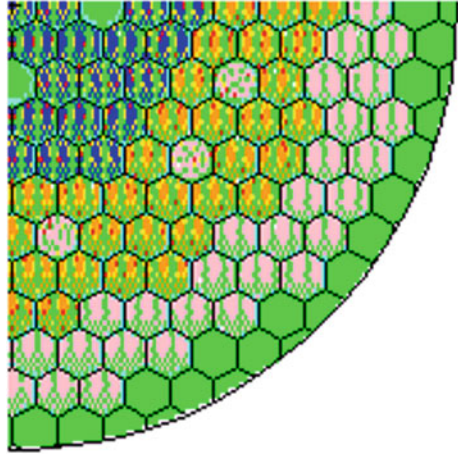
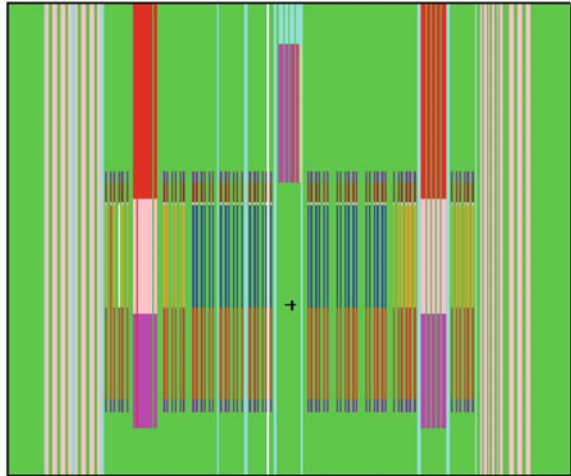


Fig. 3 Design of CR and SR (MCNP model)

**Fig. 4** Cross section of LFR core (1/4)



**Fig. 5** Axial section of LFR core (yz direction)



### 3.2 Power Distribution

The thermal power due to fission is calculated in the formula as follows:

$$P_{th} = n_f \langle E_f \rangle \tag{1}$$

where  $n_f$  is the calculated overall number of fission in the core and  $E_f$  is the average recoverable energy per fission. The number of fission should be multiplied with the energy per fission in order to obtain the overall core thermal power [4]. F7 card is used in LFR Monte Carlo calculations, which can get the fission energy deposition averaged over a assembly. The factor  $n_f$  can be calculated from MCNP result, the

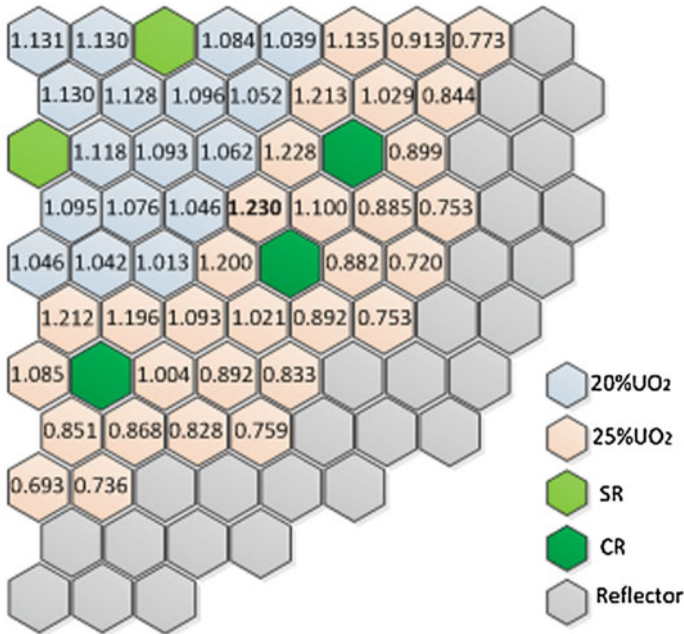


Fig. 6 Radial distribution factors of LFR

standard deviation is about 0.0036. The fission rate weighted average value  $E_f$  is chosen as 200 meV/fission. From the formula, the total core thermal power distribution can be calculated. Figure 6 displays the distribution of the power throughout the assemblies in LFR core.

From the results, the maximum value is between the inner fuel zone and outer fuel zone and is at the outer fuel zone fuel assembly. The maximum distribution factor is 1.230, which equals the ratio of the maximum power to the average power in the fuel assemblies.

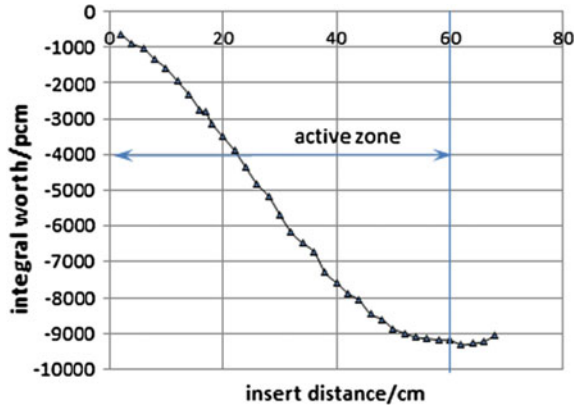
### 3.3 Anti-reactivity of Control Rod Assemblies

The reactivity worth of the control rod assemblies at the beginning of the fuel cycle is  $-9193$  ppm. The calculation results from all the situations of CR assemblies and SR assemblies are extracted from the core active zone. The total rod worth in different rod position is shown in Fig. 7.

From the figure, it can be inferred that the CR system can satisfy core control requirement well.



**Fig. 7** Reactivity worth of CR at different insert distance



### 3.4 Reactivity Effect

The increase of the coolant temperature into the core involves a decrease of its density, causing a decrease of the interactions between neutrons and coolant nucleus. It involves the three following effects: a spectral effect, an effect due to the leakages as well as an effect bound to the captures. The variation of the core reactivity depends on the competition between these three effects [5].

An increase of the fuel temperature has for consequence a higher thermal agitation provoking, for each isotope of the fuel, a broadening of the capture and fission resonances.

The fuel expansion is subdivided into axial expansion and radial expansion. In this research, only axial expansion is considered. Axial expansion has three major effects. The first effect is the decrease of the fissile nucleons concentration in the fuel which will bring negative effect on the reactivity. The second is the increase of the fissile core height with positive effect. The third is the increase of the coolant mass in the core due to the increase of the fissile core height. This effect corresponds with the effect of the increase of the coolant density, which results in negative effect.

By using MCNP code, several situations are simulated to calculate the reactivity effect factors above. When calculating the coolant temperature constant, the coolant densities are replaced by 11.00868 and 10.292 g/cm<sup>3</sup> and the fuel Doppler Effect is calculated by changing the fuel temperature. The fuel expansion considers the changing of fuel height and fuel density (Table 1).

From the table above, it can be inferred that in LFR, the coolant temperature constant is negative, which means that the occurrence of accidents will lead to an increase of coolant temperature. The LFR core has negative reactivity factor which brings better safety. The Doppler Effect coefficient is negative, which signifies that further to an increase of the fuel temperature, the Doppler Effect involves a decrease of the reactivity, and conversely a decrease of the temperature. The fuel expansion constant is negative, which manifests when the fuel cell is irradiation, the fissile

**Table 1** Calculated reactivity coefficients

	Coolant temperature/K	Coolant density g/cm <sup>3</sup>	Fuel height/cm	$k_{\text{eff}}$	Reactivity feedbacks
Coolant temperature constant	300	11.00868	–	1.04521	–0.65 pcm/K
	600	10.65	–	1.04386	
	900	10.292	–	1.04129	
Doppler constant of fuel	600	–	–	1.04617	–0.67 pcm/K
	900	–	–	1.04386	
	1200	–	–	1.04214	
	Fuel temperature/K				
Fuel expansion constant	600	10.482	59.817	1.04646	–0.76 pcm/K
	900	10.45	60	1.04386	
	1200	10.4166	60.192	1.04188	

core height will increase, and the core reactivity can insure the core under safety situation. Negative feedbacks during various voiding scenarios can guarantee that these scenarios will not jeopardize the safety of LFR in a neutronic point of view.

## 4 Conclusions

This paper models an LFR core by MCNP method. The  $k_{\text{eff}}$  multiplication factor, power distribution, reactivity effect factor and control system worth have been calculated.

By summarizing the results, it can be concluded that all these simulations above have proven that MCNP code is a valid tool to model critical mode of LFR core design. Significant negative coolant temperature constant, Doppler constant and fuel expansion constant give rise to a more stable core. The results can supply significant parameters to thermal hydronic analysis and safety analysis of future lead cooled fast reactor.

## References

1. LIU Li-min, ZHANG Da-lin, ZHANG Mei-yin. Calculation of Core Physics Parameter of Thorium Molten Salt Reactor with Solid Fuel. Atomic Energy Science and Technology, Vol 49, suppl, May 2015
2. FRATONI M. Development and applications of methodologies for the neutronic design of the pebble bed advanced high temperature reactor(PB-AHTR)[D]. Berkeley: University of California, 2009

3. CHAI Xiaoming, WANG Kan, YU Ganglin. Requirement of temperature dependent nuclear cross sections for MCNP calculation[J]. Nuclear Physics Review, 2006, 23(2):111-114
4. HE Ke-yu, HAN Wei-shi. Core Physics Design Calculation of Mini-type Fast Reactor Based on Monte Cado Method. Nuclear Power Engineering, Vol 28, No.4, Aug 2007
5. LIAO Yi-xiang, ZHANG Wen-xing, GONG Xue-yu. Application of MCNP Code in the Shielding Calculation of ADS. Atomic Energy Science and Technology, Vol 38, No.6, Nov 2004

# Neutron Activation Analysis of Candidate Materials for High-Temperature Reactors

Ramy Tannous, Chary Rangacharyulu, Dave Guzonas  
and Laurence Leung

**Abstract** A neutron activation study has been performed through exposing potential cladding materials for high-temperature reactors to neutrons at the low power research reactor of Saskatchewan Research Council in Saskatoon of Canada. These cladding materials included Stainless Steel (SS) 304, Alloy 600, and E-Brite. The activated samples were analyzed for induced activities of chromium (Cr), manganese (Mn), iron (Fe), nickel (Ni), and molybdenum (Mo) by high-resolution energy spectroscopy of the characteristic gamma rays. ( $n, \gamma$ ) transmission rates of selected isotopes have been established from the intensities of the characteristic lines.

**Keywords** Gen IV nuclear power reactors · Cladding materials · Neutron activation analysis, activity transport

## 1 Introduction

The current fleet of nuclear power reactors achieves about 30 % in thermal efficiency compared to over 45 % for supercritical fossil-fuel power plants. Improving the thermal efficiency would enhance the economic and sustainability characteristics of nuclear reactors. With the focus on these two characteristics, the Gen IV International Forum (GIF) was established to jointly support research and development of the next-generation nuclear reactor systems [1]. After reviewing over 100 potential candidates, six reactor concepts were selected for collaborative development. The technical goals of this collaborative development are to achieve enhanced sustainability, economics, safety, reliability, proliferation resistance, and

---

R. Tannous (✉) · C. Rangacharyulu  
Department of Physics and Engineering Physics, University of Saskatchewan,  
Saskatoon, SK, Canada  
e-mail: chary.r@usask.ca

D. Guzonas · L. Leung  
Canadian Nuclear Laboratories, Chalk River, ON, Canada

physical protection. Among the six selected next generation systems, Canada is focusing on the Supercritical Water-cooled Reactor (SCWR) [2, 3], as Canada has significant expertise in the design and operation of water-cooled reactors.

The various SCWR concepts are being developed for operation at supercritical pressures (about 25 MPa) and core-outlet temperatures ranging from 500 to 625 °C. The Canadian SCWR concept has a proposed core-outlet temperature of 625 °C, and thermal hydraulics analyses have shown that in some locations in the core, the fuel cladding temperature could reach a maximum of 800 °C during normal operation. Under these conditions, traditional zirconium-based alloys are no longer feasible for use as a fuel cladding and other materials have been examined as potential cladding candidates. Through an extensive assessment [4], it has been concluded that high-chromium content stainless steels or nickel-based alloys are the most feasible candidates for the cladding material, based on their good corrosion resistance and mechanical properties. However, as these alloys contain nickel, the strong neutron absorption characteristic of nickel has an adverse impact on power and burnup. Optimization of the nickel content in the material candidate requires an integrated approach between materials, reactor physics, and thermal hydraulics [5].

In an irradiated environment, nickel exhibits a unique physics property not common to most other materials. Natural nickel consists of 68 % in  $^{58}\text{Ni}$ , which is converted to  $^{59}\text{Ni}$  through neutron capture. This results in buildup of the  $^{59}\text{Ni}$  isotope, which is radioactive with a long half-life of 76,000 years. The  $^{59}\text{Ni}$  can be converted to  $^{56}\text{Fe}$  by an  $(n, \alpha)$  reaction, which has a positive Q value of 5.1 MeV. The degree of this artificial transmutation and its implication to the material integrity are the major concerns for using nickel-based alloys in a reactor core [6]. Other elements present in an alloy at low concentrations as impurities (e.g.,  $^{59}\text{Co}$ ) can also become neutron-activated, and if released by corrosion, can lead to high radiation fields downstream of the core [6]. Therefore, the behavior of potential fuel cladding alloys under irradiation must be carefully assessed.

In a previous study [7], six commercially available alloys with a nickel contents ranging from ~0 to 72 wt% were examined for their corrosion resistance. The alloys were selected to have roughly similar chromium content and low concentrations of other alloying elements. Initial theoretical assessments of thermal-hydraulic and irradiation properties were also carried out, with the goal of better understanding the effects of nickel content in candidate SCWR fuel cladding alloys on key performance criteria. As part of ongoing work, a fundamental study has been initiated to examine the neutron activation characteristics of several of these alloys by exposing them to neutrons at the low power research reactor of the Saskatchewan Research Council in Saskatoon of Canada. It is noteworthy that the experiment did not simulate the high radiation environments of the high-temperature reactors and the material samples were exposed over a relatively short duration. Nevertheless, the experiments provide some insights into the neutron activation characteristics needed to identify the relative performance of candidate alloys.

## 2 Principle of the Experiment

The growth of radioactivity induced through a process of continuous irradiation, such as neutron activation, is expressed as

$$A(t) = R \left[ 1 - e^{-t/\tau} \right], \quad (1)$$

where  $A(t)$  is the radioactivity at a time ' $t$ ' and ' $\tau$ ' is the mean life of the radioactive species. The constant rate of production of radioactive atoms,  $R$ , is defined as

$$R = \text{Neutron flux } (\phi) \times \text{No. of activation atoms } (N_a) \\ \times \text{Production cross-section } (\sigma) \quad (2)$$

The production cross section ( $\sigma$ ) is the physics parameter specific to the nuclear process contributing to the transmutation. The number of activation atoms is given by

$$N_a = x \frac{N_0 \rho}{A}, \quad (3)$$

where  $N_0$  is the Avogadro Number,  $\rho$  and  $A$  are the density and mass number of the element. " $x$ " is the fractional natural abundance of the target isotope which is irradiated. The flux is the number of neutrons/(cm<sup>2</sup> s) and is specified by the nuclear reactor facility.

In our experiment, we measured the activity,  $A(t)$ , of each isotope of interest. This data, along with the known mean life ( $\tau$ ) and the duration of irradiation, are enough to estimate the "R", the rate of transmutation of each measured activity.

The important feature is that, for a constant flux, the activity levels saturate to the value 'R'. Under steady-state reactor operation the activity reaches about 99.4 % of the saturation level after about five mean lives. This parameter can be determined experimentally for estimating the total time integrated transformation over arbitrary periods of constant irradiations. This offers a very convenient way to determine the total amount of transformation of the original composition to a different composition for each element using short-term, low flux measurements. In addition, the total number of transformations can be modeled for each alloy independently since the result depends on the product of the number of activation atoms (percentage weight of the target atoms of interest) and the production cross section, the physics parameter.

## 2.1 Materials

Table 1 lists compositions of various commercial alloys in the previous corrosion study [2]. These alloys consist of a range of nickel content from  $\sim 0\%$  for E-Brite to  $72\%$  for Alloy 600. Three of these alloys were selected for the neutron activation experiment at the low power research reactor: E-Brite and Alloy 600 (corresponding to the two bounding nickel contents of  $\sim 0\%$  and  $72\%$ , respectively), and SS 304. E-Brite contains molybdenum, which activates to  $^{99}\text{Mo}$  through neutron capture on  $^{98}\text{Mo}$  ( $24\%$  natural abundance), while SS 304 contains a significant amount ( $\sim 2\text{ wt}\%$ ) of manganese (natural element consists of  $100\%$  pure  $^{55}\text{Mn}$ ).

## 2.2 Experimental Method

The experiment was performed by neutron activation analysis using a high-resolution HPGe detector which had been energy and efficiency calibrated. Weighed alloys were irradiated under identical neutron flux irradiation conditions and irradiation times. The neutron source was the SLOWPOKE-2 research reactor of the Saskatchewan Research Council at Saskatoon in Canada [8]. It delivers neutron fluxes of up to  $10^{12}$  neutrons/cm<sup>2</sup>/s, and routinely operates at a flux of  $5 \times 10^{11}$  neutrons/cm<sup>2</sup>/s. The experimental logistics and the detector system resulted in measurements limited to gamma rays due to beta activities of a few hours and longer half-lives. As the shortest half-life of radioactivities of interest are of about 2.5 h (see below), the duration of irradiation was selected to be 10–30 min to ensure linear production rate and sufficiently high activities without saturating the detector system.

Photons of about 100 keV to several MeV were measured with the detector calibrated for photon energies and full energy peak detection efficiencies. The efficiency calibration was carried out for a wide range of energies from a measurement of radiations of 122 keV to 1.4 MeV energies from a  $^{152}\text{Eu}$  sealed source [9], kept in the same geometry as the experimental samples. From the activation measurements,

**Table 1** Compositions of alloys used to study the effects of nickel on corrosion under SCWR conditions [7]

Alloy name	Composition (wt%)							
	Ni	Fe	Cr	Al	Ti	Si	Mo	Mn
E-Brite	0.5 max	Bal	25–27	–	–	0.4 max	0.75–1.5	0.4 max
SS-304	9	Bal	18.5	–	–	0.75	–	2
SS-310	19–22	Bal	24–26	–	–	1.5 max	–	2 max
Alloy 800	30–35	39.5 min	19–23	0.15–0.6	0.15–0.6	–	–	–
Alloy 690	58	9.2	29	0.02	–	0.35	–	0.35
Alloy 600	72	6–10	14–17			0.5 max		1 max

**Table 2** Gamma ray emitting radioactive isotopes produced by neutron capture from the cladding material candidate alloys (half-lives, energies, and intensities obtained from the National Nuclear Data Center at <http://www.nndc.bnl.gov>)

Isotope	Half-life	Gamma ray energies (intensities), keV (%)
<sup>51</sup> Cr	27.7 days	320(9.9)
<sup>56</sup> Mn	2.6 h	846(99), 1032(0.04), 1238(0.04), 1811(27), 2113(14), 2523(1), 2598(0.02), 2657(0.65), 2959(0.3), 3369(0.17)
<sup>59</sup> Fe	44.5 days	142.6(1), 192.3(3), 1099(56), 1292(43)
<sup>60</sup> Co	5.3 years	1173(99.8), 1333(100)
<sup>65</sup> Ni	2.5 h	366(4.8), 1115(15.4), 1481(23.6), 1623(0.5)
<sup>99</sup> Mo	66 h	181(6), 739(12.3), 778(4.3)
<sup>99m</sup> Tc	6 h	140(89)

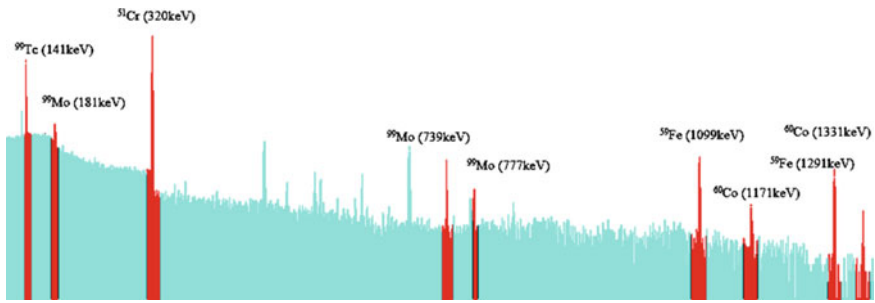
we identified the product isotopes as due to radiative neutron capture processes on atoms <sup>50</sup>Cr (4.4 %), <sup>55</sup>Mn (100 %), <sup>58</sup>Fe (0.3 %), <sup>59</sup>Co (100 %), <sup>64</sup>Ni (1 %), and <sup>98</sup>Mo (24 %), where the numbers in brackets are the natural abundances of the isotope of interest. Needless to say, neutron induced reactions on the other isotopes of elements occur but our gamma spectroscopy is not sensitive to those processes. Table 2 lists the gamma rays emitted due to the activation of the alloys by thermal neutron capture.

### 3 Results and Discussion

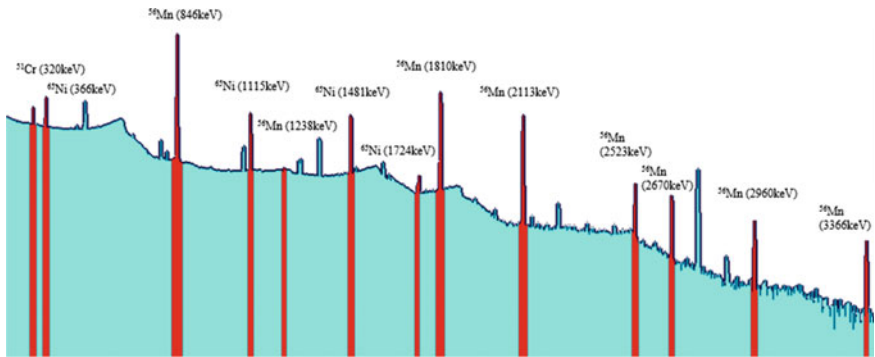
Figures 1, 2, and 3 illustrate the gamma ray spectra observed for the E-Brite and Alloy 600 samples, respectively. E-Brite is a ferritic stainless steel containing less than 0.5 wt% nickel. Decay radiations from <sup>99m</sup>Tc, <sup>99</sup>Mo, <sup>60</sup>Co, and <sup>59</sup>Fe are observed in Fig. 1. In contrast, Alloy 600 has a high nickel content (72 wt%) and a higher manganese content than E-Brite. As expected, gamma rays from nickel and manganese irradiation products were detected as shown in Fig. 2. The spectrum is dominated by the <sup>56</sup>Fe gamma rays arising from the <sup>56</sup>Mn decays of <sup>55</sup>Mn(*n*,  $\gamma$ )<sup>56</sup>Mn, as is the spectrum of SS 304 (Fig. 3), which contains slightly more Mn than Alloy 600. It should be remarked that even small amounts of manganese yield high levels of gamma radiations due to the fact that <sup>55</sup>Mn is 100 % in natural abundance and a cascade of gamma radiation emitted from each beta decay of the product nucleus <sup>56</sup>Mn.

Table 3 lists the estimated production rates (*R*) per 10<sup>8</sup> neutrons of various radioactive isotopes in the three samples. The spectra presented in Figs. 1, 2, and 3 together with the *R* values listed in Table 3 illustrate that the selected alloys become radioactive and undergo artificial transmutations. As a simple comparison, the activity of nickel for Alloy 600 is a factor of 8 stronger than that for SS 304,





**Fig. 1** Neutron activation gamma ray spectrum of the E-Brite sample. In addition to the marked lines of interest, gamma rays from the commonly observed interfering activities such as  $^{24}\text{Na}$  are seen



**Fig. 2** Neutron activation gamma ray spectrum of the Alloy 600 sample. In addition to the marked lines of interest, gamma rays from the commonly observed interfering activities such as  $^{24}\text{Na}$  are seen

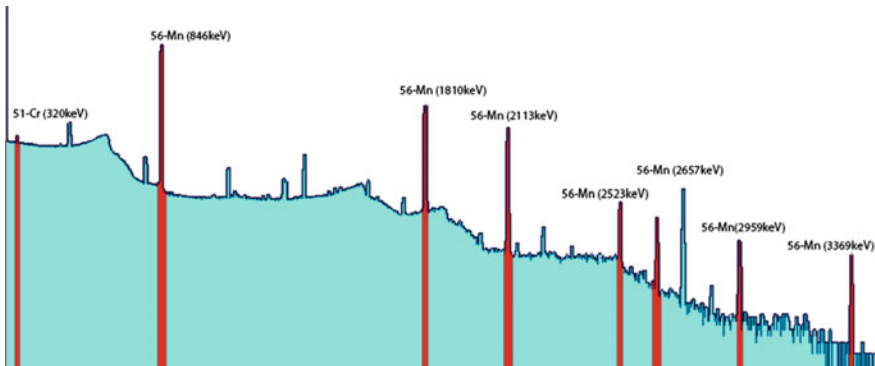


**Fig. 3** Neutron activation gamma ray spectrum of the SS 304 sample. In addition to the marked lines of interest, gamma rays from the commonly observed interfering activities such as  $^{24}\text{Na}$  are seen

**Table 3** Production rates ( $R$ ) per gram of material for  $10^8$  incident neutrons for various elements in Alloy 600, SS 304, and E-Brite

Radioisotope	E-Brite	SS 304	Alloy 600
55-Mn	0.87	40	7
59-Fe	0.005	0.01	0.0007
65-Ni	–	1	4
51-Cr	0.35	0.86	0.18
60-Co	0.0003	0.006	0.0005
99-Mo	0.016	–	–

consistent with the nickel element ratio shown in Table 1. In addition, the specific activities of chromium are consistent with the elemental compositions shown in Table 1. Significant amounts of  $^{60}\text{Co}$  are observed, suggesting that these as-received alloys would have the potential to produce high radiation fields on out-of-core piping should they be used in an SCWR [6]. These results are therefore applicable, with some confidence, in estimating the radioactivity levels and total number of transformations over a finite period of operation of a reactor in stable operating conditions. However, these measurements are insensitive to very short-lived radionuclides (say,  $t_{1/2} < 0.5$  h) or decays without photon emissions. Therefore, the influence of the  $^{59}\text{Ni}(n, \alpha)$  process, which is of concern with regard to the effect of nickel content on material performance, could not be established.

## 4 Conclusions

Exploratory measurements have been obtained to assess the effects of neutron activation of several alloys with a range of compositions relevant to the selection of a fuel cladding alloy for high-temperature reactors. The resulting activities are consistent with the compositions of the alloys tested and the known nuclear properties of the constituent elements. The experimental technique has been shown to have value for determining radiation levels and material transformations under an irradiated environment. While the current measurements are limited to gamma-emitting decays of finite lifetimes, this technique could be extended to other modes of decays and transformations.

**Acknowledgments** We thank Dr. Jeremy Pencer of the Canadian Nuclear Laboratories for very helpful discussions and extensive collaboration in the numerical and physical aspects of the simulations codes. We also thank Mr. Dave Chorney and Mr. Jeff Zimmer of the Saskatchewan Research Council for the reactor time and help with irradiations. This project is supported by the Sylvia Fedoruk Canadian Centre for Nuclear Innovation (SFCCNI—[www.fedorukcentre.ca](http://www.fedorukcentre.ca)), Canadian Nuclear Laboratories and the University of Saskatchewan, Canada.

## References

1. [https://www.gen-4.org/gif/jcms/c\\_9502/generation-iv-goals](https://www.gen-4.org/gif/jcms/c_9502/generation-iv-goals)
2. M. Yetisir, M. Gaudet, D. Rhodes, Development and Integration of Canadian SCWR Concept with Counter-flow Fuel Assembly, 6<sup>th</sup> International Symposium on Supercritical Water-Cooled Reactors (ISSCWR-6), March 3-7, 2013, Shenzhen, Guangdong, China, Paper ISSCWR6-13059
3. M. Yetisir, R. Xu, M. Gaudet, M. Movassat, H. Hamilton, M. Nimrouzi, J. Goldak, Various Design Aspects of the Canadian Supercritical Water-Cooled Reactor Core, 7<sup>th</sup> International Symposium on Supercritical Water-Cooled Reactors (ISSCWR-7) 15-18 March 2015, Helsinki, Finland paper # ISSCWR7-2072
4. D. Guzonas, M. Edwards and W. Zheng, Assessment of Candidate Fuel Cladding Alloys for the Canadian Supercritical Water-Cooled Reactor Concept, ASME J of Nuclear Rad Sci 2(1), 011016, 2015
5. M. Griffiths, The Effect of Irradiation on Ni-Containing Components in CANDU® Reactor Cores: A Review, AECL Nuclear Review, 2013, 2(1): 1-16, 10.12943/ANR.2013.00001
6. D. Guzonas, L. Qiu, Activity Transport in a Supercritical Water-cooled Reactor”, 6<sup>th</sup> International Symposium on Supercritical Water-Cooled Reactors, March 03-07, 2013, Shenzhen, Guangdong, China
7. C. Rangacharyulu, D.A. Guzonas, J. Pencer, A. Nava- Dominguez and L.K.H. Leung, An Integrated Approach to Selecting Materials for Fuel Cladding in Advanced High-Temperature Reactors, Proc. 19<sup>th</sup> Pacific Basin Nuclear Conference (PBNC-2014), Vancouver, Canada, 2014
8. <http://www.src.sk.ca/industries/environment/pages/slowpoke-2.aspx>
9. Be et al., Update of X-Ray and Gamma Ray Decay Data Standards for Detector Calibrations and Other Applications, Vol.1, Table 3, International Atomic Energy Agency Report, 2007. ISBN 92-0-113606-4

# Physics Analysis of Alternative Fuel Options for HTGR

Hangbok Choi, Robert Schleicher and Myunghee Choi

**Abstract** The modular high-temperature gas-cooled reactor (MHTGR) is known to be inherently safe because the fuel cannot fail even if all engineered safety systems, including decay heat removal and reactivity control, fail. In the event of a loss of cooling accident, even with failure of passive convective systems, core afterheat will safely be conducted to ground. However, it is also known that the MHTGR core is physically big when compared with current commercial reactors, the tri-isotropic (TRISO)-coated particle fuel is expensive and limits the uranium loading, and the reactor vessel is very large despite modest power output. Earlier economic evaluations indicate the truly inherently safe MHTGR has a weakness as a commercial product due to high cost. This study investigates the neutronic feasibility of a fuel alternative similar to the conventional pellet-type fuel, which can simplify the fuel fabrication process and reduce the enrichment of the fuel, while maintaining the accident-tolerant fuel (ATF) features. The neutronics performance of such a fuel concept has been evaluated for the amount of fuel loading, excess reactivity, and fuel cycle length, followed by thermal–mechanical performance and inherent safety analyses of such a design. The preliminary investigations have shown that it is feasible to construct a fuel cycle using uranium carbide (UC) fuel of  $\sim 5$  wt% enrichment.

**Keywords** HTGR · Fuel fabrication · Safety

---

H. Choi (✉) · R. Schleicher  
General Atomics, San Diego, CA, USA  
e-mail: Hangbok.Choi@ga.com

M. Choi  
IMSOL-X, San Diego, CA, USA

## 1 Introduction

Modular high-temperature gas-cooled reactor (MHTGR) has been shown to be inherently safe, in which it enables natural cool down of the reactor core after shutdown without any active cooling system. The inherent safety stems from the low power density, high thermal capacity of core structural components, high-temperature ceramic fuel and structural materials, and good thermal conductivity of the graphite moderator and reflector [1]. However, it is also known that the MHTGR core is physically big when compared with current commercial reactors. The manufacturing of tri-isotropic (TRISO) fuel is expensive, the fuel loading of TRISO-coated particle is limited, and the manufacturing of reactor vessel cannot be modularized. The key issue of such a reactor has been the high cost that seriously disadvantages this reactor in the nuclear market.

However, after three major nuclear disasters, safety is a driving force for advanced reactor and fuel development. For example, accident-tolerant fuels (ATFs) to prevent aggressive cladding–water chemical reaction are being researched for light-water reactors (LWRs) [2, 3]. For the water-cooled reactor, various materials have been investigated as candidates for the ATF and cladding based on their material properties, manufacturability, cost, etc. [4]. So far, silicon carbide (SiC) exhibits the best potential for providing high performance during normal and accident conditions owing to its low neutron capture, high melting point, resistance to neutron irradiation, inertness to water reaction, etc. [5]. The motivation of this work is to investigate options to reduce the MHTGR cost, especially for fuel fabrication, by adopting conventional fuel/cladding arrangement, while maintaining the inherent safety feature of the MHTGR. Specifically, a pellet-type fuel with SiC cladding is analyzed for a 450 MW(t) MHTGR [6] with regard to nuclear, thermal–mechanical, and safety features.

Some new MHTGR fuel/core features that can reduce the burden of high HTGR cost while retaining inherent safety include the following [7]:

- (a) The fuel must have a negative fuel temperature coefficient (FTC), which can be improved using more  $^{238}\text{U}$  in the fuel. This requires fuel concepts that can accommodate higher U-loadings and low  $^{235}\text{U}$  enrichment.
- (b) Adequate conductance between fuel and coolant as well as to the ultimate heat sink under accident conditions is required. The heat transport arrangement must consider the density, thermal properties, and composition flexibility.
- (c) The fuel assembly design is based on fuel rods with conventional fuel pellet concept that has a great cost advantage over the traditional TRISO fuel compact and enables much higher U-loading.
- (d) High heat capacity material is recommended for structural components to mitigate the temperature rise due to decay heat [8]. Graphite, silicon carbide, or beryllium compounds can be considered [9, 10].
- (e) The fuel cladding must retain hermeticity at high temperatures for long irradiation times.

## 2 Physics Analysis of Alternative Fuel Options

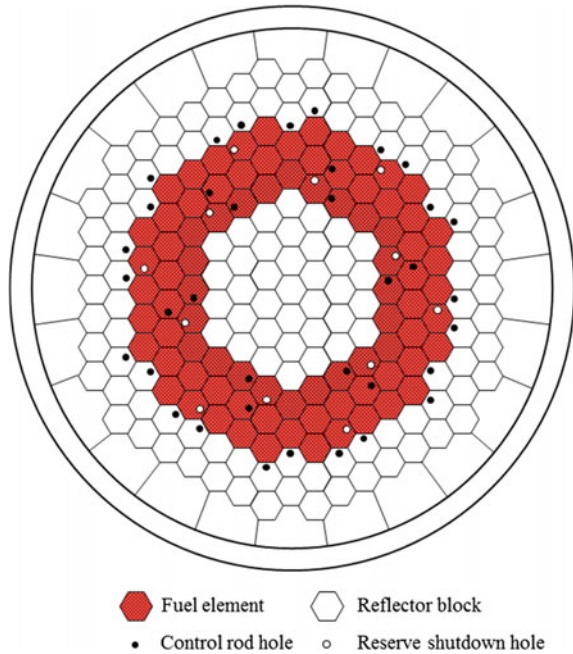
### 2.1 Base Core Model

The characteristics of 450 MW(t) MHTGR with prismatic fuel blocks are summarized in Table 1. The core design consists of an array of hexagonal fuel elements in a cylindrical arrangement surrounded by two rings of identically sized solid graphite replaceable reflector elements, followed by a region of permanent reflector elements, all located within a reactor pressure vessel. The core power density is 6.0 MW/m<sup>3</sup>. The annular core configuration provides maximum power rating while permitting passive core heat removal by maintaining the fuel temperature at ~1600 °C during a conduction cooldown event. The active core effective outer diameter of 4.2 m is sized to maintain a minimum reflector thickness of 1 m within a 7.2-m-inner-diameter reactor vessel. These dimensions allow for a lateral restraint structure between the reflector and vessel. The height of the core with ten elements in each column is 7.9 m, which allows a maximum power rating and axial power stability over the cycle. The core arrangement is shown in Fig. 1.

**Table 1** MHTGR core nuclear design parameters

Core power, MW(t)	450
Number of fuel columns	84
Thermal power density, MW/m <sup>3</sup>	6.0
Effective inner diameter of active core, m	2.31
Effective outer diameter of active core, m	4.17
Active core height, m	7.93
Number of fuel elements (10 per column)	
Standard	600
Control	120
Reserve shutdown control (RSC)	120
Number of control rods	
In-core	12
Outer reflector	24
Number of RSC channels in the core	12
Fissile material in kernel (19.8 % enriched U)	UC <sub>0.29</sub> O <sub>1.63</sub>
Fertile material in kernel (natural U)	UC <sub>0.29</sub> O <sub>1.63</sub>
Refueling interval, months	18
Core fuel loading, kg	
Initial core, LEU	1877
NU	1910
Reloads, LEU	1280
NU	500

**Fig. 1** MHTGR core arrangement



## 2.2 Fuel Element Model

Figure 2 shows the compared result of the fuel block model of the original MHTGR and the alternative ATF. The original MHTGR fuel block has 210 fuel holes, 108 coolant holes, and 6 burnable poison (BP) holes in the standard hexagonal block. The physical dimensions of both the original and ATF blocks are the same. The ATF block has 57 holes for the fuel rod (red) and coolant (blue) and 3 burnable poisons (BPs) (green) for the standard block. The control block has 47 fuel rods. The ATF option has been studied for both uranium dioxide ( $\text{UO}_2$ ) and uranium carbide (UC) with SiC composite cladding. The carbide fuel has a thermal conductivity that is about five times that of oxide fuel (16.5 vs. 2.9 W/m K), which allows for higher power density. The higher fuel density of UC when compared with  $\text{UO}_2$  (13.63 vs. 10.97  $\text{g/cm}^3$ ) also allows higher fuel loading for an extended fuel cycle. When encapsulated in a SiC–SiC composite cladding, which is being developed as ATF of the LWR, these fuels can be used for high-temperature reactor systems.

The reactivity of the fuel block was assessed by the MCNP6 code [11] and the sensitivity of fuel block  $k_{\text{inf}}$  to the fuel-to-moderator volume ratio is shown in Fig. 3. In this calculation, the fuel diameter was fixed at 0.836 cm with a cladding thickness of 0.95 mm. The  $^{235}\text{U}$  enrichment is 5 wt% for both oxide and carbide fuels, which is close to that of conventional nuclear fuel. Regarding the fuel density, 95 % theoretical density (TD) is used for the oxide fuel, while 80 % TD is used for the carbide fuel considering its irradiation behavior. As expected, the  $k_{\text{inf}}$  of the fuel

**Fig. 2** Comparison of MHTGR fuel block (original vs. ATF model)

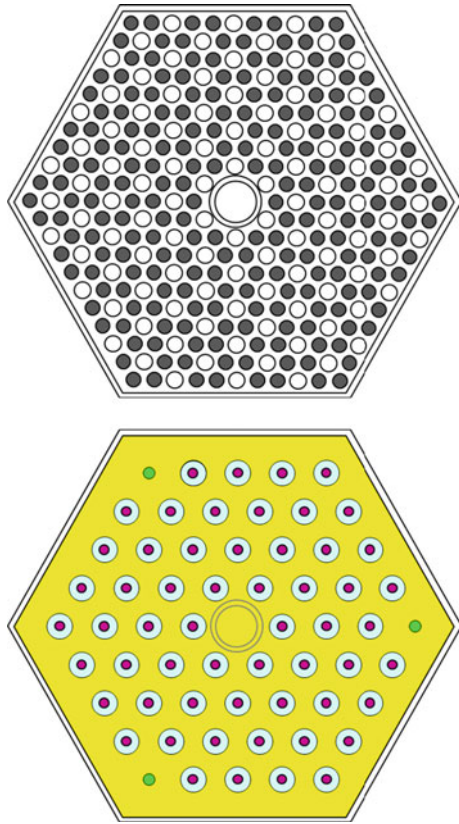
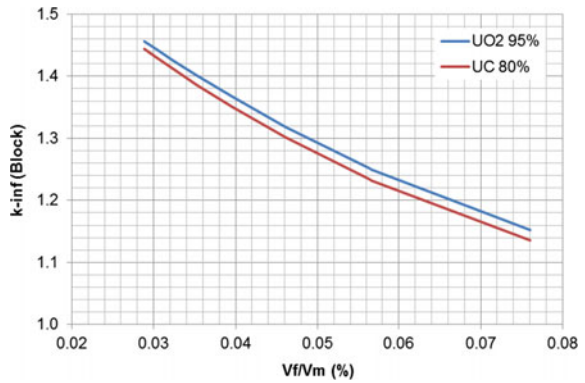


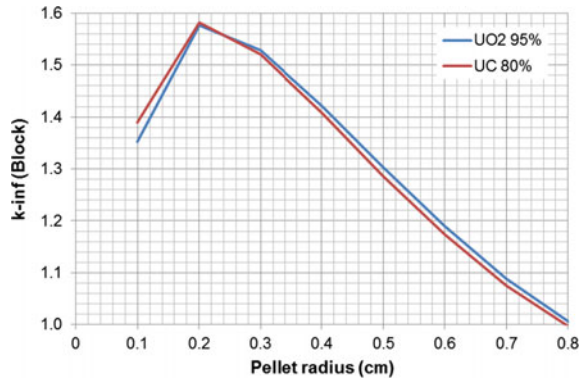
**Fig. 3** Sensitivity to fuel-to-moderator volume ratio



block decreases as the moderator volume ratio decreases. The sensitivity was also evaluated against the fuel pellet size. In this case, the fuel volume increases when the moderator volume decreases. As shown in Fig. 4, the fuel block excess reactivity is maximized when the fuel diameter is  $\sim 0.5$  cm. The results indicate that it



**Fig. 4** Sensitivity to fuel radius



is advantageous to reduce the fuel volume to obtain higher excess reactivity of the system to achieve a reasonable fuel cycle length.

### 2.3 Depletion Core

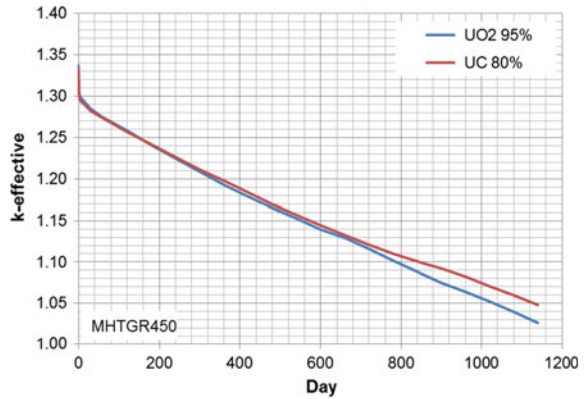
Table 2 summarizes the fuel loading of the core for two different fuel pellet sizes. Figure 5 shows the excess reactivity of the core when the pellet size is 0.836 cm in diameter. The single batch fuel cycle is ~4 years, while it could be ~1.5 years if the pellet size is 0.5 cm. The cycle length is still a variable that could be determined based on fuel enrichment, fuel loading, and number of batches depending on design requirements.

The volume fractions of fuel/cladding/gas/graphite are 1/1/19.6/78.5 and 2.7/1.5/19.6/76.2 for the larger and smaller pellet, respectively. The corresponding fissile loadings are ~9 and ~3 tons for the larger and smaller pellet cores, respectively, which are much higher than that of the original MHTGR core, i.e., ~0.4 tons. In this study, only two bounding cases of pellet size are used to produce thermal-mechanical and safety characteristics of such fuels in the MHTGR design.

**Table 2** Fuel dimension and core loading

Fuel	Pellet dia. (cm)	Coolant dia. (cm)	Fuel loading (tons)	
			<sup>235</sup> U	Uranium
UO <sub>2</sub>	0.836	2.4	8.8	175.7
	0.5	2.276	3.1	62.9
UC	0.836	2.4	9.4	188.9
	0.5	2.276	3.4	67.6

**Fig. 5** Depletion of MHTGR core with ATFs



### 3 Thermal–Mechanical Performance

The thermal–mechanical characteristics of the alternative fuel were analyzed by FEMAXI-6 code [12] updated for the carbide fuel and SiC cladding [13, 14]. For the oxide fuel, the existing property data of the FEMAXI-6 code is mostly used [15], while Preusser’s data [16] is mostly used for the carbide fuel. For the carbide fuel, it was assumed that there are no impurities such as sesquicarbide or oxygen. The fuel rod was selected from the inner fuel ring of the core, of which the linear power is the highest among three fuel rings. The boundary conditions were set to 450 and 850 °C for the coolant inlet and outlet temperature, respectively. Currently, only a small plenum volume is used for both the large and small pellet (0.5 cm diameter) rods. The flux depression in the fuel pellet was also considered even though the effect is very small. The thermal–mechanical analyses were conducted for the entire fuel height using axial power profile from the core calculation.

#### 3.1 Larger Fuel Rods

For the larger fuel rods (0.836 cm diameter), a relatively small fuel gap of 50 μm was used to minimize the temperature jump. Due to basic difference of thermal conductivity, the oxide fuel experiences much higher fuel temperature. The peak fuel temperatures during 500-day irradiation are 1850 and 1340 °C for the oxide and carbide fuels, respectively. For the oxide fuel, the fuel gap is immediately closed, while it is open until ~6 Gwd/t for the carbide fuel. The early gap closure of the oxide fuel is primarily due to the thermal expansion which is higher for the oxide fuel when the temperature is above 500 °C. The higher temperature of the oxide fuel also exacerbates the thermal deformation. Specifically the maximum thermal expansions are 78 μm and 58 μm for the oxide and carbide fuels, respectively. The swelling is higher for the carbide fuel, but is compensated by the densification effect.

The oxide fuel densification is based on FEMAXI-III model [17], which uses the maximum volume densification of 1 %. For the carbide fuel, however, it is 3.4 % based on Dienst's model [18]. Note that Dienst's model is based on 85 % TD carbide fuel. The maximum deformations of the pellet surface due to densification are  $-24$  and  $-44$   $\mu\text{m}$  for the oxide and carbide fuels, respectively, during the irradiation up to 15 GWd/t. As a result, the estimated circumferential stresses of the cladding are 195 and 180 MPa for the oxide and carbide fuels, respectively. These are still below the yield strength of monolithic SiC, i.e., 270 MPa [19].

### 3.2 Smaller Fuel Rods

For the smaller fuel rods (0.5 cm diameter), the fuel gaps were adjusted to 150 and 300  $\mu\text{m}$  for the oxide and carbide fuels, respectively, to reduce the stress on the cladding even though it increases the fuel temperature as shown in Fig. 6. The estimated peak fuel temperatures are 2470 and 1560  $^{\circ}\text{C}$  for the oxide and carbide fuels, respectively. For the oxide fuel, the maximum thermal expansion, densification, and swelling are 77,  $-17$ , and 28  $\mu\text{m}$ , respectively, while they are 37,  $-28$ , and 267  $\mu\text{m}$  for the carbide fuel. The swelling rate is very high for the carbide fuel, but is compensated to a certain extent by the creep compression ( $-88$   $\mu\text{m}$ ). The fuel gap of the oxide fuel is open during 500-day irradiation, while it is closed at  $\sim 6$  GWd/t for the carbide fuel. The adjustment of the fuel gap results in the maximum cladding circumferential stresses of 154 and 103 MPa for the oxide and carbide fuel, respectively, is as shown in Fig. 7.

**Fig. 6** Comparison of peak fuel temperatures for small fuel rods

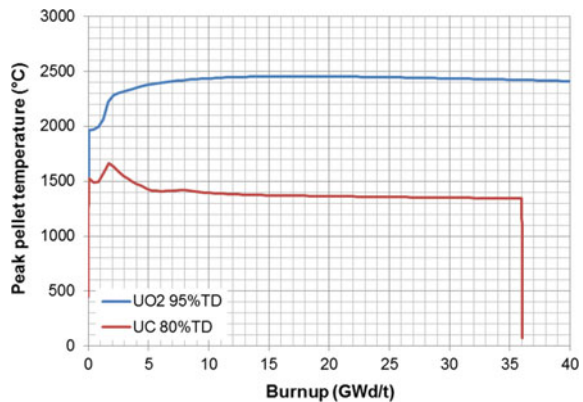
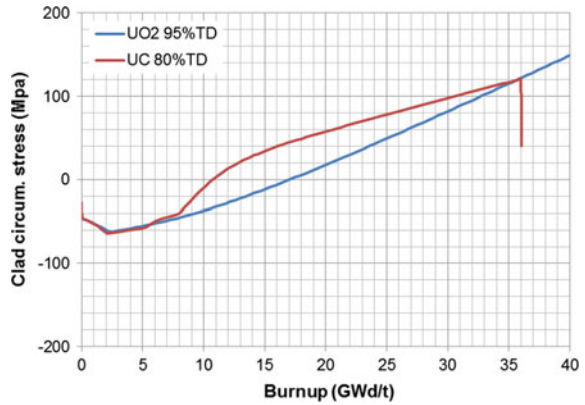


**Fig. 7** Comparison of circumferential stresses for small fuel rods



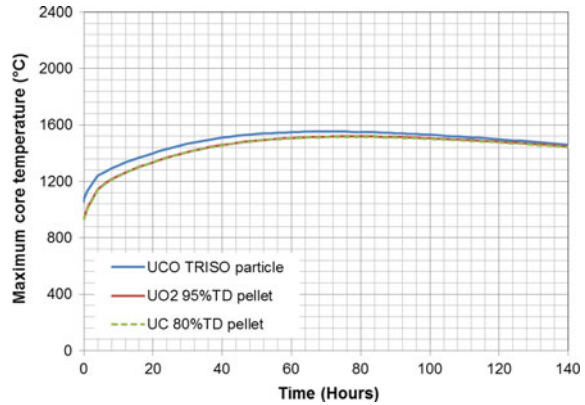
### 4 Conduction Cool down Capability

The depressurized conduction cooldown (DCC) of the MHTGR was assessed for the ATF by TAC2D code [20]. TAC2D simulates steady-state and transient temperature distributions of the reactor core and surrounding structure using two-dimensional finite difference equation formulated in terms of capacitance, heat generation, and heat flow paths to neighboring nodes. The materials used for the simulation are the active fuel, helium, SiC cladding, graphite, reactor vessel, etc. The DCC event assumes no credit taken for either active or passive engineered heat removal systems. The reactor is at 100 % steady-state power operations before the onset of event. All engineered safety systems fail upon a reactor shutdown (normal or trip). The primary system is immediately depressurized to atmospheric conditions. These instantaneous events establish the basis for the DCC, and all heat transfer is limited to conduction, radiation, and some natural convection in selected areas (none within the reactor). The ultimate heat sink is the ground.

Figure 8 illustrates the thermal response of the MHTGR loaded with ATFs. The maximum active core temperature is reached at around 70 h into the event, which is 1519 and 1515 °C for the oxide and carbide fuels, respectively. The peak core temperature of the original TRISO particle fuel MHTGR is 1553 °C. The result confirms that the conduction cooldown capability of the MHTGR is driven by the low core power density and high graphite volume. The estimated maximum temperature of the reactor vessel wall is below 500 °C.

The average volumetric heat capacity of the ATF core is  $2.6 \times 10^6 \text{ J/m}^3 \text{ K}$ , while the thermal conductivity is 17–37 W/m K. A study conducted by Sato et al. [21] on the Gas turbine high-temperature reactor (GTHTR) with TRISO-coated particle annular fuel compact [22] indicated that the fuel temperature limit of TRISO-coated particle is met if the thermal conductivity is greater than  $\sim 25 \text{ W/m K}$  when the volumetric heat capacity is  $2.6 \times 10^6 \text{ J/m}^3 \text{ K}$ . Therefore, it is believed that the result of MHTGR ATF transient is consistent with that of the similar study.

**Fig. 8** Active core temperature after DCC



## 5 Conclusions

The alternative ATF options have been investigated for the MHTGR based on conventional fuel fabrication method for both oxide and carbide fuels. In conclusion, the proposed ATF models at least show that it is feasible to apply the conventional fuel form and fabrication method to the MHTGR which satisfies fundamental design requirements of the neutronics, fuel thermal–mechanical, and safety performance. However, the proposed model is still premature and there is a technical gap to the practical application to the MHTGR. The conclusions and recommendations are as follows:

- Though the conventional pellet fuel fabrication process reduces the cost when compared with the coated particle fuel fabrication, the benefit could diminish if the fuel loading is too high. The uranium utilization should be improved by adjusting the enrichment and fuel loading.
- The carbide fuel exhibits better thermal performance for the fuel temperature. However, it should be noted that the uncertainties associated with the carbide fuel performance are relatively large when compared with those of the oxide fuel due to limited availability of carbide fuel property data.
- The fission gas releases of both oxide and carbide fuels are very high, which increases the internal pressure of the fuel rod. Though the stress of cladding is kept below the yield point, the fuel design needs to incorporate means to reduce the internal pressure and accommodate the chemical reactions.
- The conduction cooldown capability is basically dependent on the constituent material and its configuration. If the pellet-type fuel is used, the temperature limit during the conduction cooldown needs to change to that of the ATF, which could alter the material balance between the fuel and moderator.

**Acknowledgments** This work was supported by General Atomics internal funding.

## References

1. M. LaBar and A. Shenoy, W. Simon, E. Campbell, "The Gas Turbine-Modular Helium Reactor," *Nuclear News*, Vol. 46, pp. 2, 2003
2. F. Goldner, "Development Strategy for Advanced LWR Fuels with Enhanced Accident Tolerance," Nuclear Energy Advisory Committee Meeting, Washington D.C., U.S.A., June 12, 2012
3. D.M. Carpenter, "Assessment of Innovative Fuel Designs for High Performance Light Water Reactors," M.S. Thesis, Massachusetts Institute of Technology, 2006
4. K. Barrett, S. Bragg-Sitton, and D. Galicki, "Advanced LWR Nuclear Fuel Cladding System Development Trade-off Study," INL/EXT-12-27090, Idaho National Laboratory, September 2012
5. S. Ray, E. Lahoda, and F. Franceschini, "Assessment of Different Materials for Meeting the Requirement of Future Fuel Designs," 2012 Reactor Fuel Performance Meeting, Manchester, UK, September 2–6, 2012
6. R. A. Rucker, "450 MW(t) MHTGR Core Nuclear Design," DOE-HTGR-90237, General Atomics, September 1993
7. F.A. Silady, W.A. Simon, "Innovative Safety Features of the Modular HTGR," GA-A20789, General Atomics, April 1992
8. D. Chung, "Materials for Thermal Conduction," *Applied Thermal Engineering*, 21, pp. 1593–1605, 2001
9. S. Nishigaki, "Utilization of BeO in High Temperature Gas Cooled Reactor," *J. of the Atomic Energy Society of Japan*, Vol. 6, pp. 583–593, 1964
10. S.K. Kim et al., "Economic Viability of BeO-UO<sub>2</sub> Fuel Burnup Extension," *Nuclear Engineering and Technology*, Vol. 43, pp. 141–148, 2011
11. "MCNP – A General Monte Carlo N-Particle Transport Core, Version 5," LA-UR-03-1987, Los Alamos National Laboratory, April 2003
12. M. Suzuki and H. Saitou, "Light Water Fuel Analysis Code FEMAXI-6 (Ver. 1)," JAEA-Data/Code 2005-003, Japan Atomic Energy Agency, 2005
13. H. Choi, "Evaluation of Carbide Fuel Property Data and Models," Reactor Fuel Performance Meeting, TopFuel 2015, Zurich, Switzerland, Sept. 13–17, 2015
14. H. Choi, "LWR Fuel Behavior with SiC Cladding," 2013 ANS Annual Meeting, Atlanta, USA, June 16–20, 2013
15. D.L. Hagman and G.A. Reyman, "MATPRO-Version 11, A Handbook of Materials Properties for Use in the Analysis of Light Water Reactor Fuel Rod Behavior," NUREG/CR-0497, TREE-1280 Rev.3, 1979
16. T. Preusser, "Modeling of Carbide Fuel Rods," *Nuclear Technology*, 57, pp. 343–371, 1982
17. T. Nakajima et al., "FEMAXI-III: A Computer Code for the Analysis of Thermal and Mechanical Behavior of Fuel Rods," JAERI-1298, Japan Atomic Energy Research Institute, 1985
18. W. Dienst, "Swelling, Densification and Creep of (U,Pu)C Fuel Under Irradiation," *J. Nuclear Materials*, 124, pp. 153–158, 1984
19. L.L. Snead et al., "Handbook of SiC Properties for Fuel Performance Modeling," *J. Nuclear Materials*, 371, pp. 329–377, 2007
20. R. Boonstra, "TAC2D – A General Purpose Two-Dimensional Heat Transfer Computer Code," GA-A14032, General Atomics, July 1976
21. H. Sato et al., "Thermal analysis of heated cylinder simulating nuclear reactor during loss of coolant accident," *J. Nuclear Science and Technology*, 51, pp. 1317–1323, 2014
22. K. Kunitomi et al., "Reactor core design of Gas Turbine High Temperature reactor 300," *Nuclear Engineering and Design*, 230, pp. 349–366, 2004

# Preliminary Design of Oxygen Control and Purification System in Lead-Alloy Cooled Reactors

Xian Zeng and ShuBin Sun

**Abstract** Oxygen control and purification was required in reactor of Lead-Bismuth Eutectic (LBE) to slow down the corrosion of structural materials and at the same time avoid  $\text{PbO}/\text{Bi}_2\text{O}_3$  formation in the coolant. So a whole system that can measure and adjust the oxygen concentration and purify the coolant are essential for the reactor. The oxygen control system should supply adequate oxygen to compensate the loss by surface oxidation. The methodology for design of oxygen control and purification system is presented in this paper. Oxygen could be provided by the gas phase or PbO dissolution based solid mass exchangers. Every method for controlling oxygen has its special advantages and disadvantages. To design the required oxygen control system for LFR the expected amount of oxygen that was consumed by the steel oxidation is evaluated. This evaluation considers a realistic operation scenario and start-up of a reactor. Oxygen consumption under different operating scenario in the reactor was calculated. It can provide input parameters for the design of oxygen control system.  $\text{H}_2/\text{H}_2\text{O}/\text{Ar}$  was used to control the oxygen concentration and a reasonable oxygen partial pressure device was designed to control the oxygen concentration in LBE. This method can be used for controlling oxygen concentration and ensuring the safety of the reactor operation.

**Keywords** Lead-alloy cooled reactor · Oxygen control · Purification

---

X. Zeng (✉) · S. Sun

Reactor Design and Safety Research Center, China Nuclear

Power Technology Research Institute Co., Ltd(CNPRI), Shenzhen, China

e-mail: zengxian@cgnpc.com.cn

S. Sun

e-mail: sunshubin@cgnpc.com.cn

© Springer Science+Business Media Singapore 2017

H. Jiang (ed.), *Proceedings of The 20th Pacific Basin Nuclear Conference*,

DOI 10.1007/978-981-10-2317-0\_77

## 1 Introduction

The LBE and pure lead are usually used as the coolant in LFR and ADS. Pure lead/LBE has the advantages of a good neutron characteristics, good safety performance and good natural circulation abilities, etc. However, the coolant of LBE or pure lead will also bring some disadvantages such as the corrosion on the materials, the generation of Po (a highly poisonous substance), the capacity problems with the structure materials, etc. The LBE and pure lead corrosion is a physical or a physical–chemical process, involving species dissolution, oxidation and transport, chemical reactions and new phase formation. For protecting the structures from corrosion, oxygen should be filled through the coolant, but oxygen concentration ought not to be too high because high oxygen concentration will result in the generation of lead oxide which may block the channel. Therefore, we should control the oxygen concentration to ensure the safety of the reactor. Oxygen control includes the gas phase method and the solid phase method. In the procedure of designing oxygen control system, we must pay attention to the method of the oxygen concentration control, oxygen concentration automatic adjustment, the layout of the oxygen sensor.

The development of the oxygen control and purification is one of the critical issues for nuclear systems using the LBE and pure lead either as a coolant or as a spallation target [1]. It is essential to control the oxygen concentration in a reasonable range between the dissolution limit of the protective oxide film I and the solubility limit of oxygen [2, 3].

LFR and ADS designs of the LBE and pure lead-cooled nuclear reactors are common of pool-type reactors [4]. Up to now, it has been achieved to control oxygen concentration and purification of metal liquid on experiment loop facilities, but it has not been achieved in large pool-type reactors or ADSs. There are still lots of problems to be solved. First of all, it is the problem of oxygen control. Oxygen control and purification system in liquid lead or lead-bismuth in large-scale facilities is a real challenge. For instance the layout of the oxygen delivery system, the uniformity of oxygen concentration, the layout of the oxygen sensor and purification system are all need to be solved. To solve the problem of corrosion of large lead-based fast reactor, oxygen control and purification system is required. Because there is no oxygen control and purification system for large-scale facilities, the methodology for design of oxygen control and purification system is presented in this paper.

## 2 Methodology

For liquid metal coolant oxygen device acts an important role because of its contamination with the liquid and corrosion phenomenon when oxygen concentration is low. In the early stage excess of oxygen might be essential through more



dissolved oxygen in the liquid metal. Oxygen consumption is mainly because of the corrosion with structures materials. When the oxygen concentration is too low in LBE or pure lead coolant, the stainless steel will not form the oxide layer. The oxide layer must be kept over a minimum to guarantee sufficient resistance of the structural materials during the expected service lifetime. Meantime, when the oxygen concentration is too high, it will form PbO in the coolant. Lead oxide production may result in plugging due to mass transfer in a non-isothermal system. Therefore, oxygen control and purification system would be necessary for the start-up, restart, accident or maintenance phases. The following points that describe the requirements for operating a nuclear oxygen control and purification system would be detailed hereafter:

- The upper limit for oxygen concentration to avoid contamination formed by coolant oxides;
- The lower limit for oxygen concentration to enhance corrosion protection through the self-healing oxide layer;
- Reasonable arrangement of oxygen control system to minimize the issue of the homogeneity of the oxygen;
- High-efficiency of purification system to avoid products of corrosion, spallation and fission to plug the reactor core.

The methodology for design of oxygen control and purification system in lead-alloy cooled reactors was proposed according to experience of small- or medium-scale facility and loop test equipment, as shown in Fig. 1. Include the input parameters, definition of a reasonable oxygen concentration operating domain, calculation of oxygen consumption, oxygen delivery technology (oxygen sensors type, number of sensors, location of sensors, oxygen control pattern, location of oxygen delivery), purification technology.

## ***2.1 The Input Parameters***

Firstly, the information of lead-alloy cooled reactors must be provided, such as reactor power, coolant type, structural material, structure size, liquid metal properties (density, corrosion properties, viscosity), operating parameters (flow rate, flow conditions and coolant temperature ranges, coolant pressure), etc.

## ***2.2 Definition of an Oxygen Concentration Operating Domain***

There is a common agreement that the oxygen has to be controlled and maintained in a range that provides at high temperatures enough oxygen for scale formation and

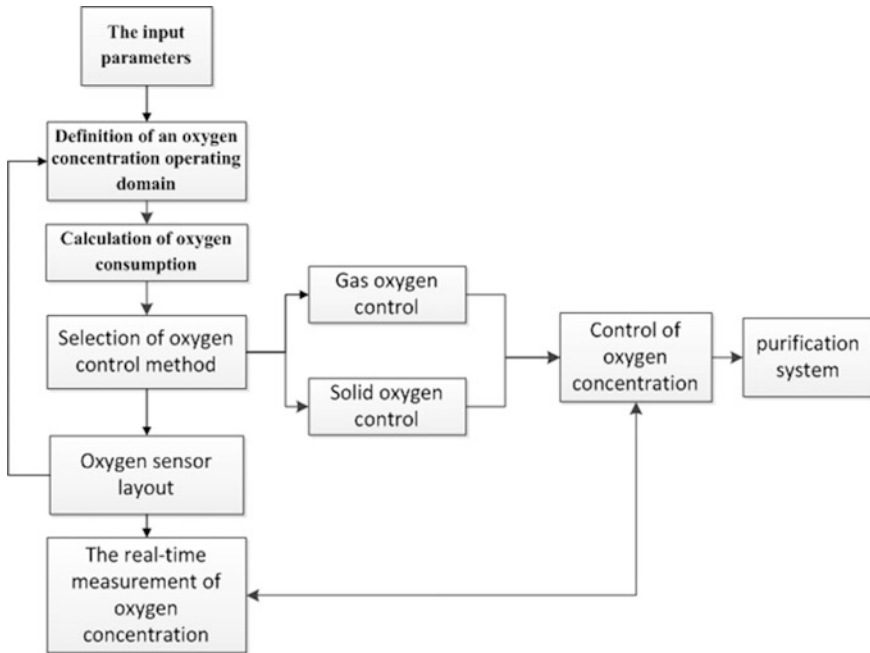


**Fig. 1** Design flow diagram of oxygen control and purification system

avoids the formation of PbO at the shutdown temperature. The upper limit of oxygen concentration was defined by the solubility of oxygen in LBE and pure lead coolant, giving a maximum allowable oxygen chemical concentration in the LBE and pure lead coolant. The following formulas define these limits for LBE and pure lead, for which stands for the dissolved oxygen chemical concentration expressed in weight percentage [1]:

- Lead (for  $300\text{ }^{\circ}\text{C} < T < 1100\text{ }^{\circ}\text{C}$ ):

$$\log C_{\text{O}(\text{wt}\%)}^{\max} = 3.23 - \frac{5043}{T(\text{K})}$$

- LBE (for  $400\text{ }^{\circ}\text{C} < T < 740\text{ }^{\circ}\text{C}$ ):

$$\log C_{\text{O}(\text{wt}\%)}^{\max} = 2.25 - \frac{4125}{T(\text{K})}$$

Define the iron concentration similar to the oxygen concentration it is equal to one when the iron is saturated in the solution, and define the minimum oxygen concentration required for effective corrosion protection for iron-based alloys, (wt %), the following formulas are derived:

- Lead:

$$\log C_{O(wt\%)}^{\min} = -\frac{3}{4} \log C_{Fe(wt\%)} + 2.38 - \frac{10618}{T(K)}$$

- LBE:

$$\log C_{O(wt\%)}^{\min} = -\frac{3}{4} \log C_{Fe(wt\%)} + 2.28 - \frac{10456}{T(K)}$$

The oxygen concentration areas of operation to ensure both no contamination, required for any system, and possible corrosion protection for higher operating temperature are similar for the liquid lead and the lead-bismuth eutectic [1]:

$$C_O^{\min} < C_O < C_O^{\max}$$

The operating specifications for oxygen are evaluated from Fig. 2 drawn with the previous relations illustrated for active control of iron-based structure, keeping

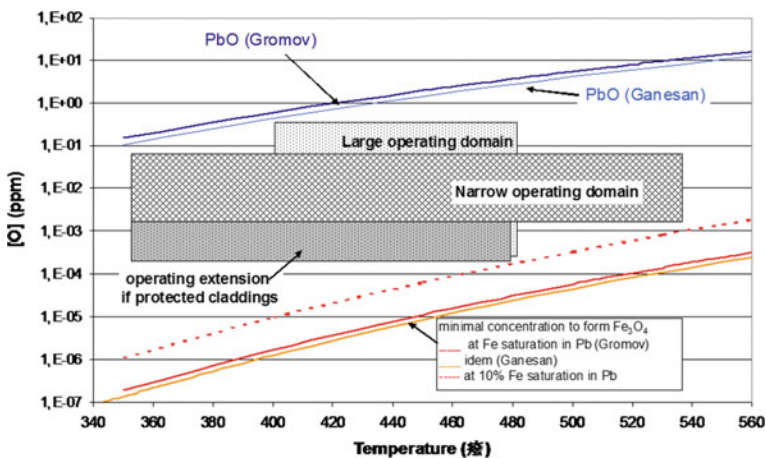


Fig. 2 Oxygen concentration operating domain specifications

in mind that for other non-ferrous structure materials, the specification for active oxygen control for corrosion protection would be less restrictive.

Simultaneously, it was not enough that Oxygen concentration operating domain was determined by the upper limit of oxygen concentration defined by the solubility of oxygen in lead alloys and the minimum oxygen concentration required for effective corrosion protection for iron-based alloys. In order to give a more appropriate range of oxygen concentration, We also need to consider the flow rate of heavy metal coolant, the thickness of the oxide layer, corrosion rate, Oxidation constant, etc.

### 2.3 Calculation of Oxygen Consumption

The main materials in contact with liquid metal inside reactor are the steels T91 and AISI136L. The scale growth relations derived from corrosion experiments for these steels are [5, 6]:

$$\delta_{S,T91}(t, T) = (-0987 + 2.54 \times 10^{-3}) \times \sqrt{t} \quad (420 \text{ }^\circ\text{C} < T < 550 \text{ }^\circ\text{C}) \quad (1)$$

$$\delta_{S,316L}(t, T) = (-0.31 + 8 \times 10^{-4}T) \times \sqrt{t} \quad (400 \text{ }^\circ\text{C} < T < 500 \text{ }^\circ\text{C}) \quad (2)$$

$$\delta_{S,316L}(t, T) = \text{oxide scale thickness } (\mu\text{m})$$

where  $t$  is the time (h) and  $T$  is the temperature ( $^\circ\text{C}$ ).

Equation (1) bases on numerous experiments on steel T91 mainly with LBE containing  $10^{-6}$  wt% of oxygen in the temperature range of 420–550  $^\circ\text{C}$ . Equation (2) describes the behavior of AISI316L under these conditions as determined from some experiments at 400  $^\circ\text{C}$ , 10,000 h (1  $\mu\text{m}$ ), 450  $^\circ\text{C}$ , 5000 h (3.5  $\mu\text{m}$ ) and 500  $^\circ\text{C}$ , 5000 h (6.9  $\mu\text{m}$ ). A homogeneous oxidation resulting in a continuous scale is assumed for 316L also which corresponds to an upper limit that could be achieved.

The amount of oxygen needed for formation of an oxide scale of  $\text{Fe}_3\text{O}_4$  with a thickness of  $\delta_s$  s:

$$w_{\text{O}} = 4 \times 10^{-4} \delta_s F \rho M_{\text{O}} / M_{\text{Fe}_3\text{O}_4}$$

$w_{\text{O}}$  is the weight of oxygen consumed (g),  $F$  is the surface area ( $\text{cm}^2$ ),  $\rho$  is the density of oxide scale, 5.2 ( $\text{g}/\text{cm}^3$ ),  $M_{\text{O}}$  is the atomic weight of oxygen, 16 (g),  $M_{\text{Fe}_3\text{O}_4}$  is the molecular weight of  $\text{Fe}_3\text{O}_4$ , 231.52 (g).

The growth rate of oxide scales on Al-alloyed surfaces is very low because of the low diffusion rates of oxygen in alumina that leads to thin stable oxide films with excellent protection properties. At 500–600  $^\circ\text{C}$  the scale thickness after 10,000 h exposure to Pb with  $10^{-6}$  wt% oxygen is still  $< 1 \mu\text{m}$ . Compared to the oxygen

needed by the non-alloyed structures inside the reactor it is only a minimal contribution that might be neglected.

## ***2.4 Oxygen Delivery Technology***

In large-scale facilities, oxygen delivery in liquid lead or lead-bismuth is a real challenge. The targeted oxygen content must be maintained at any time of operation in every part of the coolant. Oxygen delivery technology (Oxygen sensors type, number of sensors, location of sensors, oxygen control pattern, location of oxygen delivery) must be decided by oxygen concentration operating domain, oxygen consumption, coolant flow velocity, the homogeneity of the oxygen, anisothermal, technology maturity, etc.

## ***2.5 Purification Technology***

One of the most important impurities is oxygen. Besides oxygen, other main contamination sources include Fe mainly, Cr Ni, etc. metal element. If these impurities are not purified, they will block the channels and the core. Purification system needs to consider the following factors:

- The type of impurities (form, size and nature, concentration, etc ) influence the choice of the filtration method to trap impurities (surface filtration or deep bed filtration);
- The filter removal ratings;
- The type of filter medium;
- The required level of filtering.

## **3 Oxygen Control and Purification System**

Industrial scale systems like the planned ELFY (European Lead-cooled Fast Reactor) contain much more lead-alloy coolant and their oxygen transfer systems require special attention. LFR and ADS designs of heavy liquid metal cooled nuclear reactors are commonly of pool-type. The pool design has important active characteristic for nuclear reactor, namely the coolant has a large thermal inertia in the primary vessel, compact structure and a minimum of structures and components operating at the reactor core outlet temperature. The main equipment of the primary system was: reactor vessel and internal structures; steam generator and primary pump assembly; core; safety related DHR-1 (direct reactor cooling system); in-vessel fuel handling system and filter units. The Pb coolant flow path is

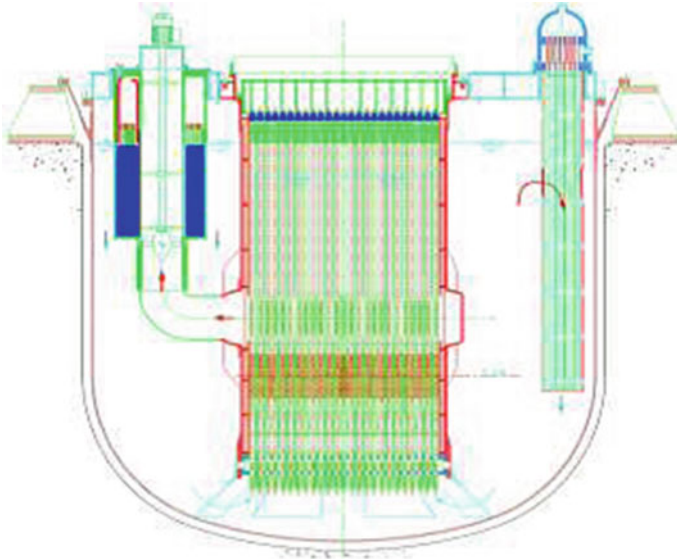


**Fig. 3** Reactor block

illustrated by lines with arrow heads in Fig. 3. Several features of the ELFR design are summarized in Table 1 [7].

The 400 and 480 °C, respectively, were the ELFR core inlet and outlet temperatures, allowing for a sufficient margin from the freezing point of the pure lead coolant in the vessel cold plenum, simultaneously, while decreasing the potential for structure material embrittlement (for structures material wetted by cold pure lead) and structure material corrosion (for structure component in hot molten pure lead). The maximum speed of the primary coolant was 2 m/s (10 m/s at the pump impeller) to limit erosion.

From Fig. 2, the upper limit corresponds to lead oxide PbO formation. This upper limit must be low enough to prevent lead oxide formation at cold shutdown (380 °C), even better with some margin (350 °C). The lower limit is defined by the minimum amount of oxygen necessary to form oxide layer.

According to our material corrosion criteria [8], as follows:

- Asymptotic Oxide layer:

$$0.1 \mu\text{m} \leq \delta_s \leq 70 \mu\text{m}$$

**Table 1** ELFR summary parameters

Power 1500 MW (th)	600 MW (e)
Core fuel	MOX (1st load)
Coolant temp.	400/480 °C
Core diameter	4.5 m
Core height	1.4 m
Maximum clad temp.	550 °C
Core breeding ratio-CBR	~ 1
Net efficiency	~ 42 %

- Corrosion rate:

$$R_C < 0.03 \text{ mm/yr}$$

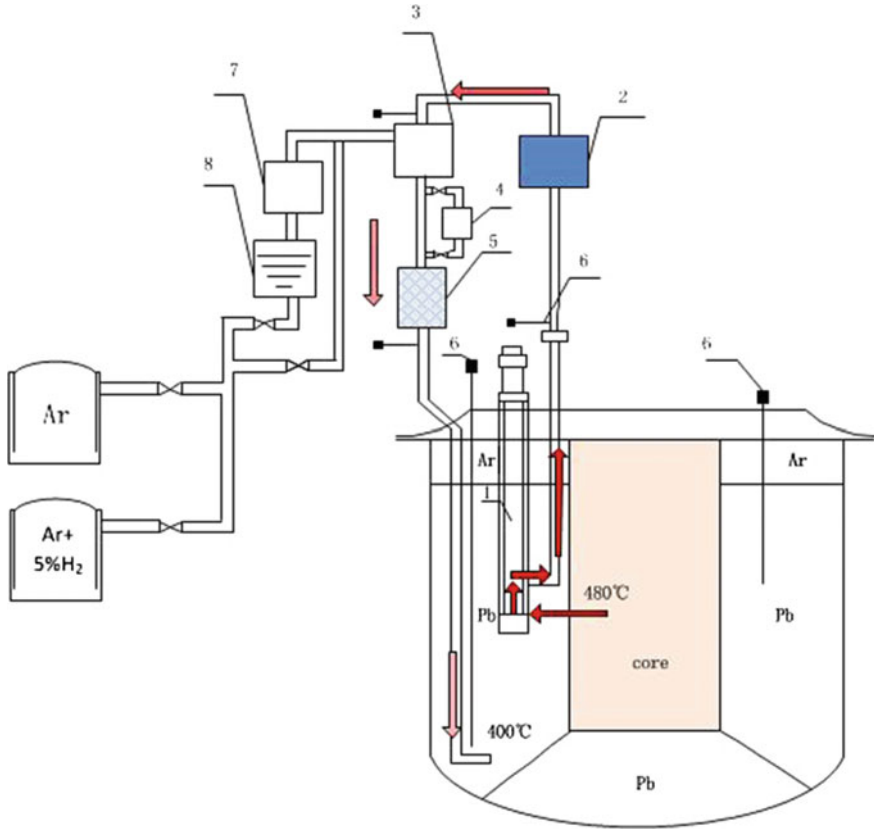
- Oxidation constant:

$$k_p \leq 1.72 \times 10^{-17} \text{ m}^2/\text{s}$$

The proposed ranges are between  $8 \times 10^{-2}$  and  $1 \times 10^{-3}$  ppm.

From Chap. 2, calculation of oxygen consumption was according to start-up, restart, accident or maintenance phases. During the first 3000 h about 30 kg of oxygen are needed to prevent the oxygen concentration in the liquid metal coolant from falling below the target concentration of  $10^{-6}$  wt%. This oxygen is mainly consumed by oxide formation on the surface of T91 steel structures while the contribution of 316L steel structures to the oxygen consumption is few percent only.  $1.6 \times 10^{-1}$  kg/h of oxygen would be needed in the first hour to satisfy the consumption of oxygen due to oxidation of the fresh metal surfaces in the reactor at 400 °C.  $3.7 \times 10^{-2}$  kg/h of oxygen was consumed in normal phase. The worst problem appears in the first 100 h since during that time 4.1 kg of oxygen must be delivered to the system to keep the oxygen above the target concentration of  $10^{-6}$  wt%.

Principally there are two options available to supply oxygen into the reactor coolant continuously; either via the gas phase or via PbO based solid mass exchangers. Gas oxygen control is a more mature method, which has been applied in the loop experiment. It is accepted that gases at equilibrium with the lead (e.g.  $\text{H}_2/\text{H}_2\text{O}$  mixtures) could not supply enough oxygen in large amount of lead because of the small driving force. One option for increasing gas phase supply would be the use of  $\text{Ar}/\text{O}_2/\text{H}_2\text{O}$  mixtures, but this method suffers severe drawbacks: lead oxide can be locally formed as the oxygen activity in the gas is much higher than the one for PbO formation, and efficient mixture of the gas and the lead must be found to



- 1—Auxiliary pump 2—Polonium purification device  
 3—Oxygen control cabinet 4—Solid oxygen control device  
 5—Purification device 6—Oxygen measuring device (sensor)  
 7—Gas mixing tank 8—Constant temperature water tank.

**Fig. 4** Sketch of oxygen control and purification system

increase the exchange area. However, the cover gas of the reactor will be in any case in direct contact with liquid pure lead and interact also with the oxygen dissolved there. Therefore, the cover gas should be used as a stabilizing background for the oxygen content and should be controlled as well. The most reliable and efficient method is Solid oxygen control, but it is not mature and there's less public information.

Oxygen control and purification system was preliminary structure of the circuit with oxygen control, coolant purification, gas purification, Po-removing device, etc.



In the outside of the reactor pressure vessel through the assist pump (1) the coolant was brought out in turn into the return piping, Po-removing device, (2) oxygen control box, (3) coolant purification and impurity removal device, after controlling of oxygen concentration adjustment, good coolant could be back into the pool-type. The oxygen control device uses gaseous oxygen control, with Ar/H<sub>2</sub> gas mixture to reduce the oxygen content in the coolant, if the oxygen content of the coolant is too low, you need to mixed gas by the constant temperature water tank configuration with required proportion of Ar/O<sub>2</sub>/H<sub>2</sub>O mixed gas and through the gas mixing tank mixing evenly after reverse through oxygen control box to regulate the oxygen concentration. In addition, the solid oxygen control loop with PbO particles is also provided. Consequently, about 8 oxygen control and purification systems are needed.

The location of oxygen supply must ensure that the parts are at highest temperature and therefore consume the most oxygen are all under operating conditions protected by the in situ formed oxide scales. The most critical regions regarding this are the core and the steam generator unit (Fig. 4).

## 4 Conclusions

LFR and ADS designs of heavy liquid metal cooled nuclear reactors are commonly of pool-type. Up to now, it has been achieved to control oxygen concentration and purification of metal liquid on experiment loop facilities, but it has not been achieved in large pool-type reactors or ADSs. The methodology for design of oxygen control and purification system in lead-alloy cooled reactors was proposed according to experience of small- or medium-scale facility and loop test equipment. Specific standards and guidelines for design of oxygen control and purification system in lead-alloy cooled reactors include the input parameters, definition of an oxygen concentration operating domain, calculation of oxygen consumption, oxygen delivery technology (oxygen sensors type, number of sensors, location of sensors, oxygen control pattern, location of oxygen delivery), and purification technology.

According to the methodology for design of oxygen control and purification system in lead-alloy cooled reactors proposed in the second chapter, preliminary design of oxygen control and purification system was provided for ELFY (European Lead-cooled Fast Reactor). Given the deepening of the research, the methodology will continue to be improved.

## References

1. Fazio, C., "Handbook on Lead-bismuth Eutectic Alloy and Lead Properties, Materials Compatibility, Thermal-hydraulics and Technologies". published by OECD, Paris, 2015

2. Zrodnikov, A. V., et al., "Heavy liquid metal coolant lead-bismuth and lead technology". *Atomic Energy* 2004, 97, (2), 534–537
3. Gromov, B. F., et al. In "Physical–chemical principles of lead-bismuth coolant technology", *Liquid Metal Systems. Material behaviour and physical chemistry in liquid metal systems 2.*, Karlsruhe; Borgstedt, H. U., Ed. Plenum Press, 1993; pp 339–343
4. Müller, G., Heinzl, A., Schumacher, G., Weisenburger, A., 2003. Control of oxygen concentration in liquid lead and lead–bismuth. *J. Nucl. Mater.* 321, 256–262
5. A. Weisenburger, C. Schroer, A. Jianu, A. Heinzl, J. Konys, H. Steiner, G. Müller, C. Fazio, A. Gessi, S. Babayan, A. Kobzova, L. Martinelli, K. Ginestar, F. Balbaud-Célerier, F. J. Martín-Muñoz, L. Soler Crespo; Long term corrosion on T91 and AISI 316L steel in flowing lead alloy and corrosion protection barrier development: Experiments and models; *J. Nucl. Materials*, 415, 2011, 260–269
6. Heinzl, A., Müller, G., Weisenburger, A. 2013. Corrosion behavior of austenitic steels in liquid lead containing 10–6wt% and 10–8wt% oxygen at 400–500°C. submitted to *J. Nucl. Materials*
7. E. Bubelis, K. Mikityuk, TEC008-2012, PLANT DATA FOR THE SAFETY ANALYSIS OF THEETDR (ALFRED), LEADER PROJECT
8. Zhang J, Hosemann P, Maloy S (2010) Models of liquid metal corrosion. *J Nucl Mater* 404:82–96

# R&D of the In-Vessel Materials for Future Magnetic Confinement Fusion Reactors at SWIP

Xiang Liu, Jiming Chen, Kaiming Feng, Pengfei Zheng, Youyun Lian, Penghuai Wang, Xiaoyu Wang, Yongjin Feng, Xuru Duan and Yong Liu

**Abstract** Materials are the foundation for realizing fusion reactors, in which the in-vessel materials, such as plasma-facing materials, structural materials, and functional materials, are more critical since they will be exposed to high flux of edge plasma, high heat load, and 14 MeV neutron irradiations. Therefore, good performances at high temperatures and low induced activation by neutrons are essential requirements for in-vessel materials. The existing industrial-grade materials can hardly satisfy all the requirements, and thus fine-grained tungsten alloys by oxides or carbides dispersion strengthening are developed as plasma-facing materials (PFM). Reduced activation ferritic/martensitic (RAFM) steel, named CLF-1, and its oxides dispersion-strengthened (ODS) alloy are fabricated for the purpose of application in ITER-TBM (Tritium Breeder Modules) and possible application in CFETR (China Fusion Engineering Testing Reactor). Additionally, advanced structural material, V-4Cr-4Ti alloy, and its dispersion-strengthened alloys, such as V-4Cr-4Ti-1.5Y-0.3Ti<sub>3</sub>SiC<sub>2</sub>, are also developed. Besides plasma-facing materials and structural materials, another key in-vessel material is functional material, such as beryllium pebbles as neutron multiplier and Li<sub>4</sub>SiO<sub>4</sub> pebbles as tritium breeder, and they are intensively studied and prepared. In this paper, the progress of W alloys as PFMs, CLF-1 (including ODS-CLF-1), and V-4Cr-4Ti alloy (including dispersion-strengthened V alloys) as structural materials, Be and Li<sub>4</sub>SiO<sub>4</sub> pebbles as functional materials is overviewed by focusing on the manufacturing technology, characterization, service evaluation, for example, neutron irradiation data, high heat load performances, plasma irradiation effects, etc. Through this research it is hoped to guide the development of fusion reactor materials.

**Keywords** W alloys · CLF-1 · V-4Cr-4Ti alloy · Be pebbles · Li<sub>4</sub>SiO<sub>4</sub> pebbles

---

X. Liu (✉) · J. Chen · K. Feng · P. Zheng · Y. Lian · P. Wang · X. Wang · Y. Feng · X. Duan · Y. Liu  
Center for Fusion Science, Southwestern Institute of Physics Chengdu,  
Sichuan, China  
e-mail: xliu@swip.ac.cn

# 1 Introduction

Development of materials is an important issue for the realization of future nuclear fusion reactors. A lot of efforts have been made on the R&D of fusion reactor materials in the world and a great deal of progress has been made although it is still far away to completely achieve it up to now. For the applications of fusion reactors, in-vessel materials or components must have low neutron-induced activation owing to safety and environmental friendly requirements. Therefore, only few choices are for the selection of in-vessel materials. As for plasma-facing materials (PFMs) or components, tungsten might be one of the best choices of PFMs due to its relatively low activation, perfect high-temperature performances, and low tritium retention; however pure W is brittle at room temperature and relatively high temperature since its DBTT is about 400 °C, thus inducing machining difficultly, and possible operation failure due to frequently crossover DBTT. On the other hand, owing to the quality degradation of re-crystallization, alloying of tungsten is paid more attentions in order to broaden its operation window, such as W-Ta solid solution-strengthened alloy, W-Y<sub>2</sub>O<sub>3</sub>, W-La<sub>2</sub>O<sub>3</sub>, and W-TiC dispersion-strengthened alloys [1–4]. In addition, tungsten coating may be adopted as the armor of first wall owing to relatively low-heat loads, in which CVD-W could be one of the best selections [5]. Bulk tungsten will be considered for applications of divertor chamber.

RAFM steel has been selected as the structural material of ITER-TBM, and several kinds of RAFM steel have been developed, for example, Eurofer 97 in Europe [6, 7], F82H in Japan [8, 9], and CLAM and CLF-1 in China [10, 11]. They have similar compositions and comparable performances. Their database is being established and the material specification or qualification is ongoing. Vanadium alloys, such as V-4Cr-4Ti, are considered as the basic structural material of next-generation fusion reactors, especially when be used for liquid blanket concept. V alloys for fusion applications are investigated in many countries, such as USA, Japan, Russia, France, and China [12–15]. SiC/SiC composite has better high-temperature performance and is thought of the structural material of fusion reactors as the long-range target of fusion reactors development [16].

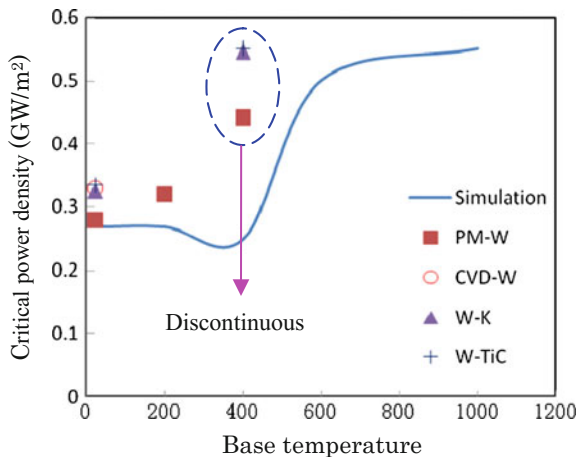
Besides plasma-facing materials and structural materials, another key material is functional materials, such as neutron multiplier and tritium breeding materials. Helium-cooled ceramic breeder test blanket module (HCCB TBM) is considered as the ITER-TBM in China [17], in which beryllium and Li<sub>4</sub>SiO<sub>4</sub> pebbles are developed as the neutron multiplier and tritium breeder of CN HCCB TBM, respectively. The fabrication and trial technologies are being developed at SWIP.

In this paper, the developments and main achievements of fusion reactor materials at Southwestern Institute of Physics (SWIP) are overviewed by focusing on the plasma-facing materials/components (PFMs/PFCs), structural materials, and functional materials.

## 2 Plasma-Facing Materials/Components

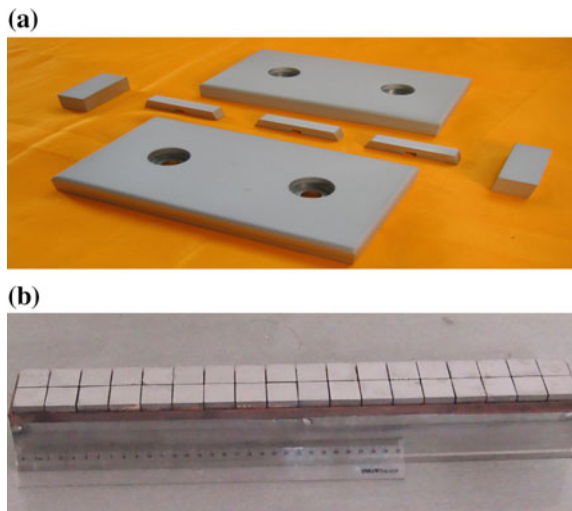
First, different grades of tungsten are being developed. Bulk tungsten includes pure tungsten with purity of 99.95–99.99 % by traditional powder metallurgy process, and its main properties complied with ITER specifications and solid solution-strengthened W-Ta alloy, oxides and carbides dispersion-strengthened W-Y<sub>2</sub>O<sub>3</sub> and W-TiC alloys are made by mechanical alloying and sintering processes, and then followed by hot rolling or forging treatments to get refined tungsten plates or rods. Commercial W-K alloy is also investigated owing to its perfect machinability. On the other hand, considering the good quality of chemical vapor deposition tungsten coating (CVD-W), it may be used for current fusion experimental devices or the low-heat load region of fusion reactors. A fast CVD technology with deposition rate up to 0.5 mm/h was developed by cooperated with Xiamen Tungsten & molybdenum Co. Ltd. [18, 19]. Transient heat loading experiments indicated that CVD-W coating and TiC dispersion-strengthened alloy show better thermal shock resistance abilities than pure tungsten, and CVD-W is more sensitive to the cracking suppression effects of elevated temperature owing to its columnar grain structure and high-temperature strength [19, 20]. In addition, it is also found that commercial W-K alloy (k content less than 100 ppm) has higher cracking threshold than pure tungsten [20, 21]; the reason could be owing to its good plasticity. Figure 1 indicates the cracking threshold of different W grades under 5 ms transient heat loading and solid line is the simulation result of ITER grade W by ABAQUS code based on the elastic–plastic fracture theory; more details can be found in Refs. [19, 20].

**Fig. 1** Critical power densities of different tungsten grades at elevated base temperature for 5 ms transient heat loading



Tungsten joining with CuCrZr heat sink has been developed by brazing technology at SWIP. One kind of Cu–Mn filler is adopted. In order to reduce the negative influence of high-temperature brazing, a fast brazing process following by fast cooling and aging treatment was developed; after this brazing cycle the strength loss of CuCrZr heat sink can be controlled within 20 % and no significant grain growth was observed [22]. Several joining technologies have been developed, for example, direct brazing, pure copper casting followed by brazing, and pure copper coating (by magnetron sputtering) followed by HIP (hot isostatic pressing). Figure 2 shows the specimen made by CVD-W-coated CuCrZr and brazing technique (pure copper casting + brazing). 2-mm CVD-W-coated CuCrZr with PVD-Cu as interlayer can endure 5 MW/m<sup>2</sup> heat flux for 1000 cycles, a small-scale CVD-W sample with graded W–Cu interface was even tested at a 11 MW/m<sup>2</sup> for 1000 cycles without failure, while brazed W/CuCrZr mockups can withstand 1000 cycles at a heat flux of 8 MW/m<sup>2</sup> [22, 23]. These well-developed technologies can provide a simple and economics method for the construction of W first wall and divertor in the current fusion experimental devices. In order to meet the harsh requirements of the generation fusion testing devices, for example, CFETR (China Fusion Engineering Testing Reactor) and DEMO reactors, the helium-cooled FW and divertor mockups are also being designed and investigated. Several kinds of fillers of Ti base, Ni base, and Fe base materials were developed and the joining technology and evaluation of W and CLF-1 steel are under investigations. In addition, a helium loop of maximal pressure 8 MPa was constructed and it can supply the helium coolant for a high heat load facility EMS-60 (60 kW Electron-beam Material testing Scenario) [22, 23], and thus the heat load evaluation and heat transfer tests of helium cooling mockups can be available soon.

**Fig. 2** Components by thick CVD-W coated CuCrZr alloy (a) and a brazed W/CuCrZr mockup (b)



### 3 RAFM Steel CLF-1

As to future fusion reactor, copper alloy cannot be adopted as heat sink materials owing to fast degradation of its performances by neutron irradiation and low activation consideration, and it has to be replaced by RAFM steel or other low activation structural materials, such as vanadium alloy and SiC/SiC composite. One kind of RAFM steels, named as CLF-1, has been developed with the purpose of the application of CN HCCB TBM and CFETR. CLF-1 steel was manufactured by vacuum induction melting followed with consumable electrode re-melting process; in this way, the content of oxygen was kept below 0.005 wt% and the radiological undesirable trace elements can be controlled to a low level as shown in Table 1. Compared with other RAFM steels, such as Eurofer 97 or F82H, CLF-1 has similar chemical compositions, but N is selected as a controllable element and has slightly higher content. Up to now, several 1-ton heats were produced and the heats were used in normalized (1253 K for 45 min) and tempered (1013 K for 1.5 h) states. The as-received normalized and tempered CLF-1 steel has a microstructure of fully martensitic with equiaxed prior austenitic grain size 13  $\mu\text{m}$ , and consists of thin plates of laths of  $300 \pm 100$  nm width, where M<sub>23</sub>C<sub>6</sub> (M = Cr, W, Fe) carbides distribute mainly along lath and grain boundaries and MX (M = Ta, V; X = C, N) particles distribute in matrix. The characterization of the 1-ton CLF-1 steel heat, including tensile, impact, creep, and fatigue properties, has been finished. For example, the ultimate tensile strengths (UTS) of CLF-1 steel at room temperature and 500 °C were about 680 and 450 MPa, respectively, and its DBTT is about -75 °C derived from the impact property test using V-notch specimens, which is comparable to the values of -70 °C for Eurofer 97 in the as-received condition (980 °C 27 min +760 °C 90 min) [24].

Thermal aging effect on the microstructure and mechanical properties was studied. No obvious degradation in tensile properties but a slightly DBTT shift of about 5 and 10 °C in impact properties has been observed after thermal aging up to 6000 h at 550 and 600 °C. Microstructure observation results show that thermal aging strongly affects the precipitation behaviors that M<sub>23</sub>C<sub>6</sub> carbide coarsens and agglomerates along the lath boundaries and prior austenitic grain boundaries but no obvious increase of the MX-type precipitates was observed. The coarsening and agglomeration of M<sub>23</sub>C<sub>6</sub> seems to be the reason of the impact properties deterioration after long-term thermal aging [25].

The high-temperature performance of creep resistance and fatigue behavior was studied. Creep test was conducted at 500, 550, and 600 °C, respectively, at different applied stresses. Generally, the minimum creep rate of CLF-1 steel was smaller and rupture time was longer compared with Eurofer 97 as shown in Fig. 3. The reason could be due to slightly higher nitrogen content, which induces the increase of the number of MX (mainly vanadium-rich nitrides) precipitates.

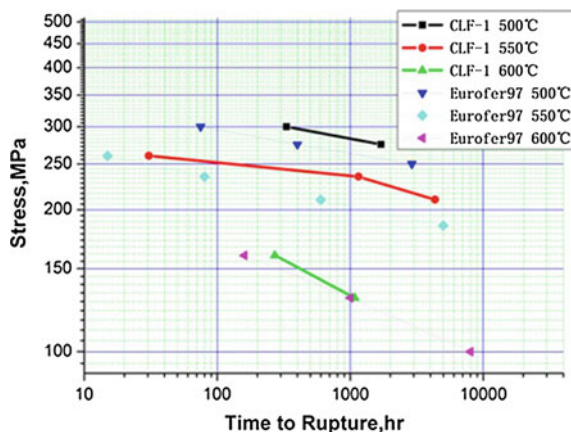
According to the qualification requirements of ITER-RAFM steel, 5-tons heats are being prepared. Neutron irradiation campaigns have been started and the first

**Table 1** The chemical composition of CLF-1 steel

Alloy element	Cr	C	W	Ta	Mn	V	N	Fe
Content control	8.5 ± 0.3	0.11 ± 0.015	1.5 ± 0.2	0.10 ± 0.03	0.5 ± 0.2	0.3 ± 0.1	0.02–0.035	Bal.
Impurity	S	P	Ti	B	Nb	O	Ni	Mo
Content control	<0.005	<0.005	<0.01	<0.005	<0.01	<0.005	<0.01	<0.01
Impurity	Cu	Al	Si	Co	As	Sn	Sb	Zr
Content control	<0.01	<0.03	<0.05	<0.01	As + Sn + Sb + Zr	<0.05		



**Fig. 3** Creep performances of CLF-1 at 500–600 °C, data Eurofer 97 for comparison



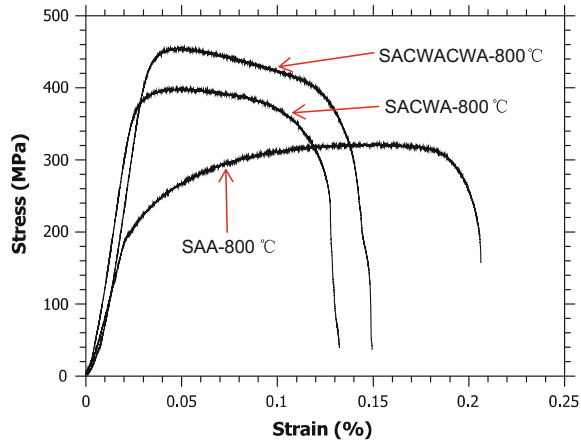
irradiation data with the dose of 1 dpa at 300 °C in the high flux engineering test reactor (HFETR, China) will be available by the end of 2014.

## 4 Vanadium Alloys

Vanadium alloys are considered as advanced structural materials, in particular for the liquid blanket concept, Li/V blankets. V-4Cr-4Ti has been widely investigated and is selected as the reference vanadium-based alloy for fusion application. An engineering scale ingot of V-4Cr-4Ti alloy with 30 kgs (called SWIP-30) has been prepared by electron-beam melting and then the ingot was canned with stainless steel for hot rolling and forging, 5-mm plates are achieved after final cold rolling. Heat treatment and cold working have significant influence on the mechanical properties of vanadium alloy. Figure 4 shows tensile tests of SWIP-30 plates at 800 °C after several typical heat treatments and combined cold working processes. It can be found that repeated cold working and aging treatments can strengthen the V alloy; here SAA means solid annealing and aging, SACWA means solid annealing followed by cold work and aging, and SACWACWA means solid annealing followed by twice cold work and aging treatments.

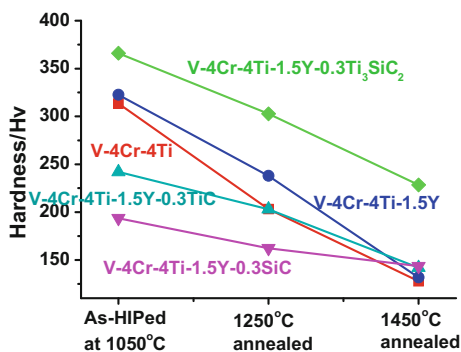
Similarly, V alloys can be strengthened by particle dispersion. Different particle species, such as  $Y_2O_3$ , SiC, or TiC, have been tried in mechanical alloying of vanadium alloys [26–29]; up to certain extent, all of them show good strengthening effects. In order to further increase the strengthening effect, the combined particle strengthening is investigated. Five kinds of V-4Cr-4Ti alloys are prepared, in which yttrium is used as the scavenger for O, N impurities and three kinds of carbides as

**Fig. 4** Tensile tests of V–4Cr–4Ti alloy after different thermal and mechanical treatments



dispersion strengthening particles. The necessary amount of Y is designed as 1.5 wt %, which is comparable with the amount used in previous study [30]. These powders are mixed to yield the compositions of V–4Cr–4Ti, V–4Cr–4Ti–1.5Y and V–4Cr–4Ti–1.5Y–0.3MC in an argon atmosphere (99.9999 %), where MC is one of the TiC, SiC, and Ti<sub>3</sub>SiC<sub>2</sub> carbides. During mechanical alloying process, the phase evolution of the powders is characterized by X-ray diffraction (XRD) analysis. The total milling time is determined by the XRD analysis, and it was found 140 h milling might be a good choice by which a completely alloying was achieved; meanwhile the impurity, especially W from the ball, can be controlled in a relatively low level. After canning the powders with steel capsules, HIPing is applied in a 150 MPa argon atmosphere at 1323 K for 3 h. Chemical compositions of the main interstitial elements such as C, O, and N are analyzed. Mass density is measured in a pycnometer. Annealing treatments at 1523 and 1723 K for 1 h are performed on the as-HIPed samples to dissolve different species of nano-particles, such as Ti-(C, O, N) and possibly yttrium compounds, respectively. Hardness of the five kinds of dispersion-strengthened V alloys is measured using as-HIPed and annealed samples as shown in Fig. 5; obviously, V–4Cr–4Ti–1.5Y–0.3Ti<sub>3</sub>SiC<sub>2</sub> alloy has the highest hardness, and it could be foreseen that V–4Cr–4Ti–1.5Y–0.3Ti<sub>3</sub>SiC<sub>2</sub> alloy will be with most efficient strengthening effect and the best thermal stability; this would widen its operation temperature margin. TEM and XRD observations indicated that TiC, SiC, and Ti<sub>3</sub>SiC<sub>2</sub> may not be completely dissolved during the MA process, but most Ti<sub>3</sub>SiC<sub>2</sub> additions may be refined and parts of Ti<sub>3</sub>SiC<sub>2</sub> additions may be decomposed in the present MA process. Thus nano Ti<sub>3</sub>SiC<sub>2</sub> particles act as the agent that hardens the V–4Cr–4Ti–1.5Y–0.3Ti<sub>3</sub>SiC<sub>2</sub> alloy, especially after annealing at 1723 K, and improve the thermal stability of V–4Cr–4Ti alloys. Further investigation is under way.

**Fig. 5** A relationship of the hardness for several kinds of V alloys with different annealed states



## 5 Functional Materials

Beryllium is considered as a neutron multiplier owing to its effective high neutron multiplication cross-section, high thermal conductivity, low density, and low activation properties. Since beryllium become brittle and swells under neutron irradiation, its use in the form of small pebbles offers the various advantages. In fact, within small pebbles the temperature differences are small, thus the stressed caused by thermal gradients and by different swelling rates are considerably reduced. Beryllium in its pebble form has been proposed in various blanket concepts. Also, pebble beds have been suggested as a functional material form for the TBM of ITER. On the other hand, Li-contained ceramic is selected as the tritium breeding material of solid blanket concept since tritium is the reaction products of Li and neutron. The material form options for the tritium breeders and neutron multiplier are pebble bed. Using pebble beds in breeder blanket has several advantages. First, bed characteristics can be tailored to obtain the required thermal characteristics. Second, the effective thermal conductivity can be controlled by adjusting bed characteristic. Third, tritium produced in the pebble beds can be easily removed by the purge gas.

Beryllium pebbles can be obtained by mechanical method, gas atomizing method, shot process and vacuum evaporation condensed method, and rotating electrode process (REP). The beryllium pebbles obtained by the REP have various advantages that they are not only smaller and more uniform in particle diameter but also higher in sphericity and smaller in surface roughness, compared with the one obtained by the other methods. The advantage of REP for producing pebbles is never in contact with other metals. This factor reduces the likelihood of contamination and makes possible the production of pebbles that is close to the electrode in cleanliness and composition. The REP method has been expected to be suitable for impurity control and mass production of beryllium pebbles. REP method was

adopted in China to produce beryllium pebbles [31]. Figure 6a shows the photos of beryllium pebbles with 1 mm diameter and a density of 98.9 % (compared with theory density); its impurity content mainly depend on the raw materials, and REP normally cannot introduce other impurities. In addition, the average sphericity of the beryllium pebbles is 0.994. Compression tests show that the 250 N will induce crack formation, but it did not broken till 2000 N load only a big crack parallel to the compressive force direction was observed. Meanwhile, the fracture properties of the beryllium pebbles are not affected by pebble size.

The  $\text{Li}_4\text{SiO}_4$  pebbles with the diameter 1.0 mm as shown in Fig. 6B were fabricated using the melt-spraying technique [31, 32]. These pebbles were conditioned by annealing at 1000 °C for 2 h to obtain the thermo-dynamically stable phase, lithium orthosilicate, and metasilicate and a homogeneous microstructure in all pebbles. Using the Hg-porosimetry a density of approximately 94 % T.D. (T. D. = 2.40 g/cm<sup>3</sup>) and an open porosity of 5.2 % were measured; while a closed porosity of 3.2 % was measured by He-pycnometry. SEM (Scanning Electron Microscopy) was used to study the microstructure of the pebble surface, see Fig. 2.  $\text{Li}_4\text{SiO}_4$  pebbles exhibit the known dendritic solidification microstructure due to rapid cooling. The pebbles were packed into a container made of stainless steel and tapped into place by hand. The packing ratio, which is the ratio of the total volume of pebbles to the volume of a pebble container, is about 60.5 %. A new technique TPS (Transient Plane Source method) was applied to measure the thermal parameters of tritium breeder pebble bed. Figure 7 shows the measured effective conductivity of the  $\text{Li}_4\text{SiO}_4$  pebble beds compared with the previous data obtained by hot wire method [33–36]. These results indicate that the effective thermal conductivity has the same trend of increasing thermal conductivity with the temperature increase. But the measured data are higher than the other previous experimental data especially at temperature 500 and 600 °C. The reason comes from the different measure methods. The contact areas between pebbles with sensor using TPS are larger than hot wire method.

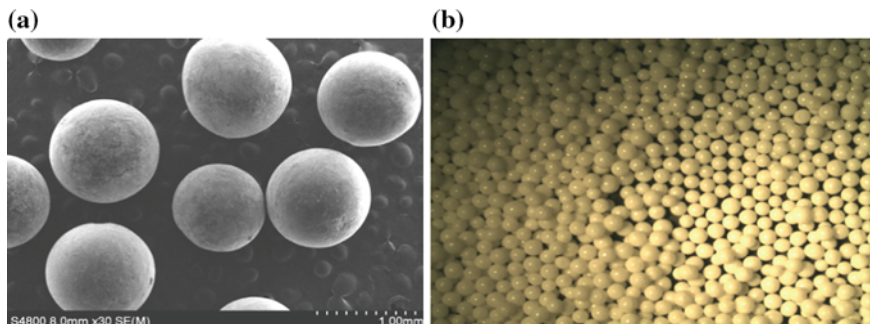
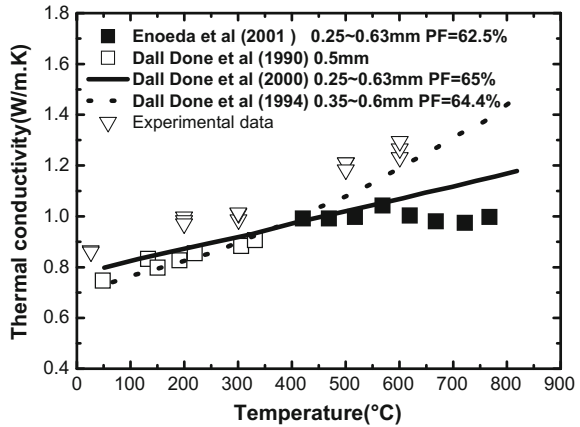


**Fig. 6** Photos of 1 mm beryllium (a) and  $\text{Li}_4\text{SiO}_4$  ceramic (b) pebbles

**Fig. 7** Thermal conductivity of  $\text{Li}_4\text{SiO}_4$  pebble beds and the comparison with other data



## 6 Conclusions

According to China fusion development strategy, fusion material study at SWIP is focusing on both the requirements in the near future, for example HL-2 M tokamak and ITER-TBM, and the long-term targets, such as CFETR and DEMO. In term of PFMs/PFCs, W-Ta, W- $\text{Y}_2\text{O}_3$ , W-TiC solid solution, or dispersion-strengthened alloys are being developed, and combined with well-developed fast CVD-W coating technology, it is hopeful to supply candidate materials for HL-2 M and CFETR, even beyond. W joining with CuCrZr alloy by fast brazing technology was developed and W brazed with RAFM steel for helium cooling mockups is being studied. As to structural materials, one kind of RAFM steel (CLF-1) has been developed and an equivalent property with Eurofer 97 is achieved. CLF-1 steel shows better creep and fatigue resistance capabilities than Eurofer 97 and F82H owing to slightly high N content. In addition, a 30 kg V-4Cr-4Ti heat was manufactured by melting technology and 5-6 mm plates were prepared, an optimized thermal-mechanical treatment (TMT) technique was obtained. Oxides and carbides dispersion-strengthened V alloys are also investigated by mechanical alloying (MA) and a kind of Y +  $\text{Ti}_3\text{SiC}_2$  co-combined particle dispersion-strengthened V-4Cr-4Ti alloy was found to have good strengthening effect and thermal stability. With respect to functional materials, beryllium and  $\text{Li}_4\text{SiO}_4$  pebbles, respectively, as neutron multiplier and tritium breeder were fabricated; basic features were measured; and the characterization is ongoing, and they will used for ITER-TBM.

## References

1. M. Rieth, S.L. Dudarev, S.M. Gonzalez etc, "A brief summary of the progress on the EFDA tungsten materials program" J. Nucl. Mater., 442 (2013) S173

2. S. Wurster, N. Baluc, M. Battabyal etc, "Recent progress in R&D on tungsten alloys for divertor structural and plasma facing materials" *J. Nucl. Mater.*, 442 (2013) S181
3. Zhangjia Zhou, Jun Tan, Dandan Qu, Gerald Pintsuik, Manfred Roedig, Jochen Linke, "Basic Characterization of oxide dispersion strengthened fine-grained tungsten based materials fabricated by mechanical alloying and spark plasma sintering", *J. Nucl. Mater.*, 431 (2012) 202
4. K. Tokunaga, H. Kurishita, H. Arakawa, etc, "High heat load properties of nanostructured, recrystallized W-1.1TiC" *J. Nucl. Mater.*, 442 (2013) S297
5. T. Tanabe, M. Akiba, Y. Ueda, K. Ohya, M. Wada, V. Philipps, "on the utilization of high Z materials as a plasma facing component" *Fus. Eng. Des.*, 39–40 (1998) 275
6. B van der Schaaf, F. Tavassoli, C. Fazio, E. Riegal, E. Diegele, R. Lindau, G. LeMarios, "The development of EUROFER reduced activation steel", *Fus. Eng. Des.*, 69 (2003) 197
7. R. Lindau, A. Moeslang, M. Rieth etc, "Present development status of EUROFER and ODS-EUROFER for application in blanket concepts" *Fus. Eng. Des.*, 75–79 (2005) 989
8. S. Jitsukawa, M. Tamura, B van der Schaaf, etc, "Development of an extensive database of mechanical and physical properties for reduced-activation steel F82H", *J. Nucl. Mater.*, 307–311 (2002) 179
9. A.-A.F. Tavassoli, J.-W. Rensman, M. Schirra, K. Shiba, "Materials design data for reduced activation martensitic steel type F82H" *Fus. Eng. Des.*, 61–62 (2002) 179
10. Q. Huang, N. Baluc, Y. Dai, S. Jitsukawa, A. Kimura, J. Konys, R.J. Kurtz, R. Lindau, T. Muroga, G.R. Odette, B. Raj, R.E. Stoller, L. Tan, H. Tanigawa, A.-A.F. Tavassoli, T. Yamamoto, F. Wan, Y. Wu, "Recent progress of R&D activities on reduced activation ferritic/martensitic steels", *J. Nucl. Mater.*, 442 (2013) S2
11. J.M. Chen, J.H. Wu, X. Liu, P.H. Wang, Z.H. Wang, Z.N. Li, X.S. Wang, P.C. Zhang, N.M. Zhang, H.Y. Fu, D.H. Liu, "Materials development for ITER shielding and test blanket in China", *J. Nucl. Mater.*, 417 (2011) 81
12. W. R. Johnson, J. P. Smith, *J. Nucl. Mater.* 258–263 (1998) 1425–1430
13. T. Muroga, T. Nagasaka, et al. *J. Nucl. Mater.* 307–311 (2002) 547–554
14. M. M. Potapenko, et al. Proc. IEA/JUPITER-II Workshop on Critical Issues of Vanadium Alloy Development for Fusion Reactor Applications, Dec 15–16, 2003, NIFS, Japan
15. Haiying Fu, Jiming Chen, Pengfei Zheng, et al., "Fabrication using electron beam melting of a V–4Cr–4Ti alloy and its thermo-mechanical strengthening study", *J. Nucl. Mater.*, 442 (2013) S336
16. Aljaz, Ivekovic, Sasa Novak, Goran Drazic, Darina Blagoeva, Sehila Gonzalez de Vicente, "Current status and prospects of SiCf/SiC for fusion structural applications", *Journal of the European Ceramic Society*, 33 (2013) 1577
17. K.M. Feng, C.H. Pan, G.S. Zhang et al. "Progress on design and R&D for helium-cooled ceramic breeder TBM in China", *Fus. Eng. Des.*, 87 (2012) 1138
18. Jiupeng Song, Yang Yu, Zhigang Zhuang, Youyun Lian, Xiang Liu, *J. Nucl. Mater.* 442 (2013) S208
19. Y.Y. Lian, X. Liu, Z.K. Cheng, J. Wang, J.P. Song, Y. Yu, J.M. Chen, ICFRM-16, to be published on *J. Nucl. Mater.*
20. X. Liu, Y.Y. Lian, L. Chen, etc, "Experimental and numerical simulations of ELM-like transient damage behaviors to different grade tungsten and tungsten alloys", PSI-14, Japan, Oral, to be published on *J. Nucl. Mater.*
21. Xiang Liu, Youyun Lian, Jiming Chen et al, 24th IAEA Fusion Energy Conference, 8–13 October 2012, San Diego, USA
22. Xiang Liu, Youyun Lian, Lei Chen, etc, "Tungsten joining with copper alloy and its high heat load performance", <http://dx.doi.org/10.1016/j.jnucmat.2014.07.041>
23. Youyun Lian, Xiang Liu, Xu Zengyu, Jiupeng Song, Yang Yu, *Fus. Eng. Des.* 88 (2013) 1694
24. R. Lindau, A. Moslang, M. Schirra, *Fusion Engineering and Design* 61–62 (2002) 659–664
25. Pinghuai Wang, Jiming Chen, Haiying Fu, Shi Liu, Xiongwei Li, Zengyu Xu, "Effect of N on the precipitation behaviours of the reduced activation ferritic/martensitic steel CLF-1 after thermal ageing", *J. Nucl. Mater.*, 442 (2013) S9

26. T. Sakamoto, H. Kurishita, S. Kobayashi, K. Nakai, High temperature deformation of V–1.6Y–8.5 W–(0.08, 0.15)C alloys, *Journal of Nuclear Materials* 386–388 (2009) 602–605
27. T. Furuno, H. Kurishita, et al. “Effects of grain size on high temperature creep of fine grained, solution and dispersion hardened V–1.6Y–8 W–0.8TiC”, *Journal of Nuclear Materials*, 417 (2011) 299–302
28. H. Kurishita, S. Oda, S. Kobayashi, K. Nakai, T. Kuwabara, M. Hasegawa, H. Matsui, “Effect of 2 wt% Ti addition on high-temperature strength of fine-grained particle dispersed V–Y alloys”. *Journal of Nuclear Materials*, 367–370 (2007) 848–852
29. T. Sakamoto, H. Kurishita, T. Furuno, T. Nagasaka, S. Kobayashi, K. Nakai, S. Matsuo, H. Arakawa, A. Nishimura, T. Muroga, “Uniaxial creep behavior of nanostructured, solution and dispersion hardened V–1.4Y–7 W–9Mo–0.7TiC with different grain sizes”. *Materials Science and Engineering: A*, 528 (2011) 7843–7850
30. P.F. Zheng, T. Nagasaka, T. Muroga, J.M. Chen, “Investigation on mechanical alloying process for vanadium alloys”, *Journal of Nuclear Materials* 442 (2013) 330–335
31. FENG Yongjin, FENG Kaiming, CAO Qixiang, ZHANG Jianli, HU Jin, “Current Status of the Fabrication of  $\text{Li}_4\text{SiO}_4$  and Beryllium Pebbles for CN HCCB TBM in SWIP”, *Plasma Science and Technology*, Vol. 15, No. 3, Mar. 2013
32. Y.J. Feng, K.M. Feng, Q.X. Cao, J. Hu, H. Tang, “Fabrication and characterization of  $\text{Li}_4\text{SiO}_4$  pebbles by melt spraying method”, *Fusion Engineering and Design* 87 (2012) 753–756
33. M. Enoda, Y. Ohara, N. Roux, A. Ying, G. Piazza, S. Malang, Effective Thermal Conductivity Measurement of the Candidate Ceramic Breeder Pebble Beds by the Hot Wire Method, *Fusion Technology* 39 (2001) 612–616
34. M. Dalle Donne, G. Sordon, Heat Transfer in Pebble Beds for Fusion Blankets, *Fusion Technology* 17 (1990) 597–635
35. M. Dalle Donne et al. Heat transfer and technological investigations on mixed beds of beryllium and  $\text{Li}_4\text{SiO}_4$  pebbles”, *Journal of Nuclear Materials* 212 (1994) 872–876
36. M. Dalle Donne, A. Goraieb, G. Piazza, G. Sordon, “Measurements of the effective thermal conductivity of  $\text{Li}_4\text{SiO}_4$  pebble bed”, *Fusion Engineering and Design* 49–50 (2000) 513–519

# Research on Ionizing Effects in $\gamma$ -Ray-Irradiated CMOS Pixel Image Sensor

Shou-Long Xu, Shu-Liang Zou and You-Jun Huang

**Abstract** Study of availability in radiation environment is presented for video monitoring system. Testing experiment has been completed by seven kinds of Image sensor module which include three kinds of digital image sensor module and four kinds of analog image sensor module. Radiation accident condition was simulated by  $\gamma$ -ray ionizing radiation environment where the dose rate at 16.63, 20.20 and 58.30 Gy/h. Availability has been studied by analyzing real time monitoring image quality parameters captured in  $\gamma$ -ray exposure environment. The primary image quality parameters include average gray level about dark image and synthetic brightness about color image. The most suitable image sensor module has been selected by image quality parameters comparison before and after irradiation. Experimental results show that, digital camera has minimum background noise, the radiation resistance of CMOS image sensor is better than CCD image sensor. Therefore, digital video monitoring system with CMOS image sensor has the best image quality parameters and slightest effect in  $\gamma$ -ray ionizing radiation environment where the dose rate is less than 58.30 Gy/h. Meanwhile, adequate light could reduce noise interference reduced by  $\gamma$ -ray for all types of video monitoring system. However, digital signal processing integrated circuit board has been destroyed when the accumulated dose reach to 88.40 Gy, but the CMOS image sensor integrated circuit board has normal working parameters. As a conclusion, digital video monitoring system with CMOS image sensor could be used for real-time monitoring in radiation accident condition, but the digital signal processing integrated circuit board need to be hardened by radiation hardened technology.

**Keywords** Video monitoring system • CMOS • Availability • Radiation Accident Condition •  $\gamma$ -ray • Radiation hardened

---

S.-L. Xu · S.-L. Zou (✉)  
University of South China, HengYang, Hunan, China  
e-mail: zousl2013@126.com

S.-L. Xu  
e-mail: 119242948@qq.com

Y.-J. Huang  
Nuclear Power Institute of China, ChengDu, Sichuan, China



## 1 Introduction

Video surveillance, as one of the real time information collection method, which could help people to make fast and effective emergency response measures by analyzing environmental information [1]. As the core devices of video monitoring system, image sensor and digital processing chips are all very sensitive to ionizing radiation [2–10]. Large amounts of radionuclides released from nuclear leakage accident, which could damage video surveillance equipment. In order to save costs and time, most of current electronic components ionizing radiation damage research use high dose rate to simulate the low dose rate. However, the sensitivity of different types of electronic components to the dose rate is different, even under the condition of the same total dose [11]. Because of the presence of the annealing effect, the change of damage is not completely linear under the low dose rate [12, 13]. In addition, with the improvement of image processing technology, a certain degree of interference caused by incident photons can be repaired by image processing [14]. Therefore, image sensor damage dose not represent the damage of entire module. Radiation damage conclusion of one type of module can't apply to all kinds of image sensor modules.

The traditional analog image sensor module integrate image sensor and digital processing chip in a motherboard, while the advanced digital image sensor can separate the image sensor from motherboard, and connect by FPC line. Thus, digital signal processing chip can be protected by shielder. Both the analog and digital image sensor modules have advantages and disadvantages. Clearer pictures can be captured by digital image sensor module but easy to lost signals when disturbed. Analog image sensor module has better anti-jamming capability but lower improving potential [15].

In recently, more research focused on the study of space application. They care more about radiation damage induced by proton and high energy particles. Different from space radiation,  $\beta$  and  $\gamma$  radionuclide and radioactive aerosol are the principal factors in nuclear accident environment. For equipment, damage from  $\alpha$  and  $\beta$  ionization radiation effect is stronger, but easy to protect. Therefore,  $\gamma$ -ray ionizing radiation becomes the main damage factor for devices.

Early research [16–19] has shown that, image sensor is sensitive to particle irradiation, which embodied the total ionizing dose effect [17]. After exposure to  $\gamma$ -ray, oxide trap charge generated near the  $\text{SiO}_2/\text{Si}$  surface due to holes captured by these radiation induced defects, and interface state generated at the  $\text{SiO}_2/\text{Si}$  surface due to the reaction between holes and hydrogen-containing defects or dopant complexes [3, 4, 10]. Dark current increase sharply under the combined effect of oxide traps charge and interface state [3, 4, 10].

In this paper, we studied and compared real time monitoring image parameters before and after radiation, which captured by different types of image sensor samples. In order to evaluate radiation damage effect, we analyzed average gray level of dark and nature light image.

## 2 Experiment Details

Seven types of commercial image sensor modules has been studied, the sample parameters as shown in Table 1.

All the samples were irradiated at room temperature (23 °C) by Co-60  $\gamma$ -ray source with energy of 1.17 and 1.33 meV, activity of radioactive source is 680 kBq. The radioactive source stored under the water. The rise time is about 100 s. Radiation dose rate is 16.63, 20.20 Gy/h and 58.30 Gy/h respectively. Experimental samples placed in a testing box which can isolate light from outside. D65 standard light source has been used as testing light source. Experimental parameters have been shown in Table 2. Light transmittance of camera lens has been tested by light transmittance taster before and after ionizing radiation, light source of the taster is standard illuminant C, the color temperature is 6774 K.

Each type of module has been equipped with the camera lens and filter. Lenses are made by glass material, and filters are made by plastic material. Attenuation multiple of light transmittance has been calculated by the formula as follow,  $T_0$  and  $T$  is the light transmittance before and after radiation damage.

$$\Delta T = \frac{T}{T_0} \times 100 \% \tag{1}$$

Average gray level of dark image ( $V_{mD}$ ) is an average value of the gray levels for all the pixels in a sensor under the condition of no illumination,  $V_{iD}$  is gray level for each different pixel,  $N$  is the total number of pixels in a sensor sample,  $m$  represents the average value of all the pixels,  $i$  represents the value of each pixel,  $D$  represents the dark image.

$$V_{mD} = \frac{1}{N} \sum_{i=1}^N V_{iD} \tag{2}$$

**Table 1** Parameters of experimental samples

No.	Module type	Image sensor type	Size (inch)	Resolution	DSP type
1#	Digital	OV9712 (CMOS)	1/4	1280 × 800	HI3518C
2#		AR0130 (CMOS)	1/3	1280 × 960	HI3518C
3#		SONYIMX 222LQJ (CMOS)	1/2.8	1984 × 1225	HI3516
4#	Analog	SONY811 (CCD)	1/3	976 × 582	EFFIO 4140
5#		SONY673 (CCD)	1/3	976 × 582	EFFIO 4140
6#		SONYIMX238 (CMOS)	1/3	976 × 582	FH8520
7#		MT9V139 (CMOS)	1/4	1305 × 1049	FH8510

**Table 2** Experimental parameters

Condition	Dose rate (Gy/h)	Time (h)	Accumulated dose (Gy)
Color image	16.63	0.35	5.82
	20.20	1	26.02
	58.30	1.07	88.40
Dark image	16.63	0.35	5.82
	20.20	1	26.02
	58.30	1.07	88.40
Without electricity	20.20	50	1010

Average color channel gray level of nature light image ( $I_{mL}$ ) is an average value of the gray levels (include R, G, B color channel) for the pixels in a sensor under the condition of illumination.  $I_{iL}$  is gray level of R, G or B color channel,  $N$  is the total number of pixels in one sensor sample,  $L$  represents the nature light image.

$$I_{mL} = \frac{1}{N} \sum_{i=1}^N I_{iL} \quad (m = R, G, B) \tag{3}$$

Brightness of the nature light image ( $R_{mL}$ ) is an evaluation function for the color deviation.  $I_{RL}, I_{GL}, I_{BL}$  are average value of R, G and B color channel gray levels,  $L$  represents the nature light image.

$$R_{mL} = 0.222I_{RL} + 0.707I_{GL} + 0.071I_{BL} \tag{4}$$

### 3 Result and Discussion

The camera lens light transmittance before and after radiation has been shown in Table 3, the filter transmittance drop slightly, which indicated that filter made by plastic material has strong radiation damage resistance. Light transmittance attenuation of 3.6 and 4 mm lens are similar at the same accumulated dose.

**Table 3** The camera lens light transmittance before and after radiation

Type	Accumulated dose $D$ (Gy)	Light transmittance before radiation $T_0$ (%)	Light transmittance after radiation $T$ (%)	Attenuation multiple $\Delta T$ (%)
Filter	88.4	23.73	23.01	96.97
Filter	1010	23.73	22.98	96.84
3.6 mm lens	88.4	10.2	9.1	89.22
4 mm lens	88.4	11.41	10.29	90.18
4 mm lens	1010	11.41	2.74	24.01

As result shown, decrease of camera lens light transmittance has little relationship with focal length. Radiation induced color centers generated in crystal structure of camera lens glass. These kinds of color centers can capture the visible light and make the camera lens glasses in coffee color, which induced visible light transmittance decreased. The camera lens light transmittance drop nearly 10 % at 88.4 Gy, but this level of affect can be adjusted by digital signal process device. However, light transmittance drop nearly 75 % at 1010 Gy, streaking, blur and noise appeared in the video images at this level of radiation damage.

The average gray level of each sample under the condition of no illumination has been shown in Fig. 1. CCD image sensors have lower background noise than CMOS image sensors, and digital modules are better than analog modules.

Figure 2 shows the average gray level of seven types of image sensor modules during the decline-rise-decline radiation resource process, the maximum dose rate was 16.63 Gy/h at the test point. With the radiation resource decline (during 0 to 100 s), dose rate began to decrease from 16.63 to 0 Gy/h, and the average gray level of each sample fall back to initial state. Gray level of each sample increased with the radiation resource rise up again (during 170 to 270 s, and dose rate from 0 to 16.63 Gy/h). Increasement of average gray level on digital modules was tardier than analog modules. As shown in Fig. 2, 3# sample is least affected by ionizing radiation damage. A valley appeared during radiation resource rising stage, this phenomenon might be induced by ionizing radiation interference combined with self-regulation of image sensor module. Because of the interference of the digital signal to the digital signal, several peaks appeared in digital image sensor modules.

Figures 3 and 4 shows the average gray level of seven image sensor module samples during radiation resource rising stage under the condition of no illumination. The maximum dose rate was 22.20 and 58.30 Gy/h respectively. Several peaks appeared during the process of average gray level increase. All the samples achieve stability at each dose rate level.

**Fig. 1** Dark image average gray level of each sample before radiation

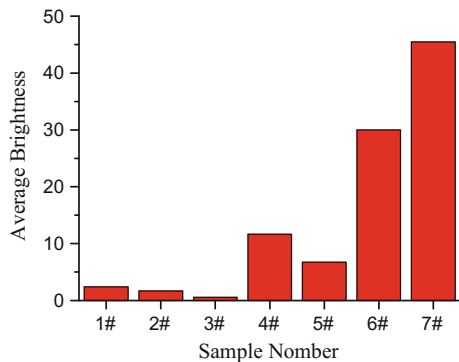
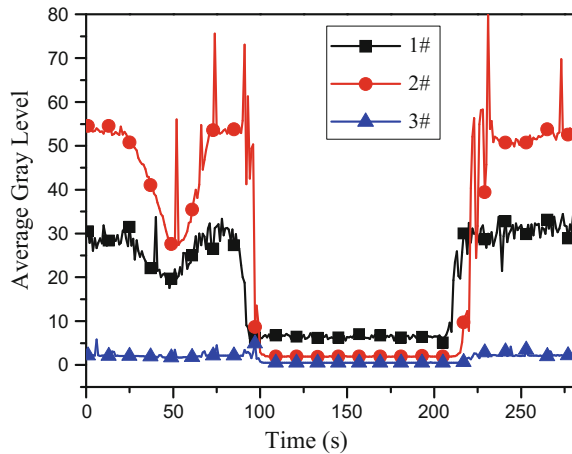
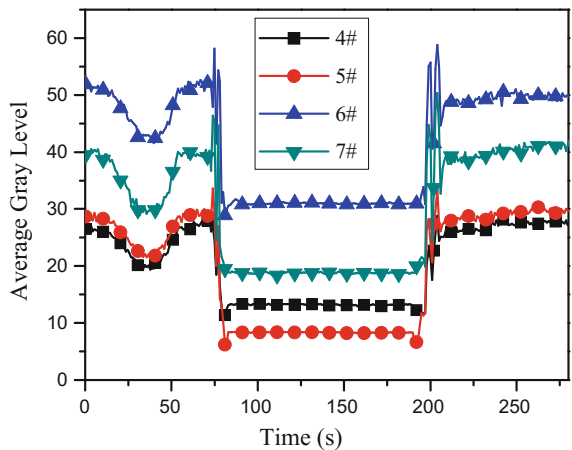


**Fig. 2** The average gray level of dark image during the resource declining and rising process (maximum dose rate is 16.63 Gy/h)



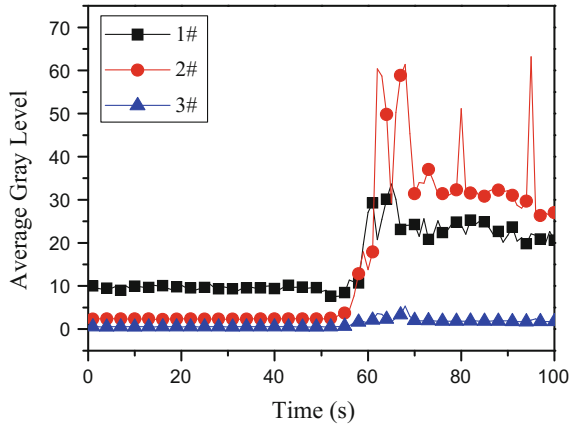
**(a)** Digital module



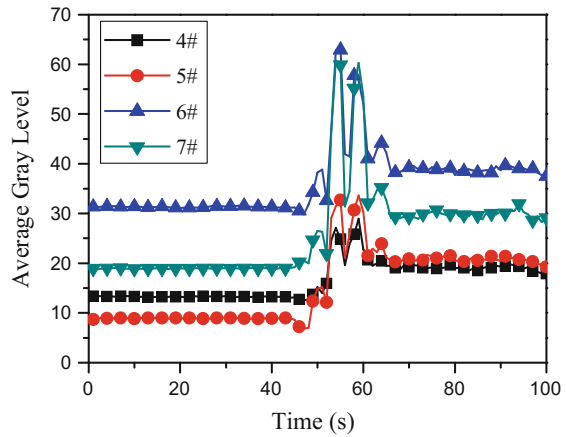
**(b)** Analog module

The average gray level of each sample at different dose rate has been shown in Fig. 5. Except 7# sample, the average gray level of all the other samples showed an increasing tendency with dose rate increase. However, the value at 20.20 Gy/h is smaller than the value at 16.63 Gy/h, which indicated that the relationship between the average gray level and dose rate is not simply linear. 7# sample have a higher background noise, parameters change in contrast to other samples. Incident photons improved the contrast ratio of image but also interference image quality.

**Fig. 3** The average gray level of dark image during the resource rising process (maximum dose rate is 20.20 Gy/h)



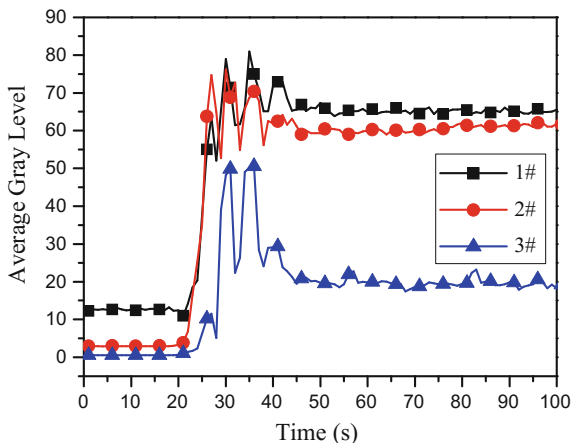
(a) Digital module



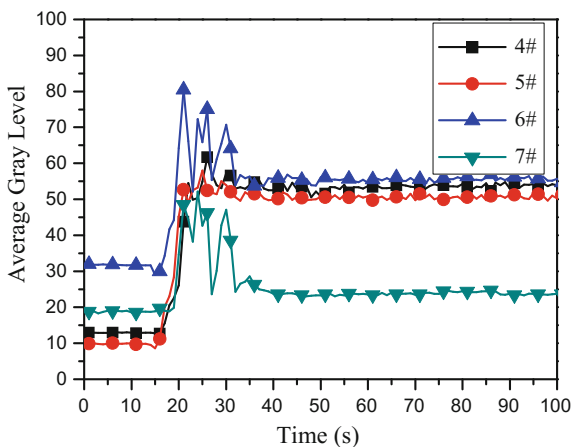
(b) Analog module

Image sensor module ionizing radiation damage mainly realized as the total ionizing dose effect, which induced digital devices failure. However, in view of annealing effect, devices are not damaged at low dose rate, but still disturbed by incident photons. When these photons incident into photosensitive element, electron hole pairs generated and induce trapped charge. Part of electrons enter into the depletion region of photodiode and become into signal current. With the average signal current increase, auto control system shortens the integration time, thus, the phenomenon of average gray level decrease happened. This can explain the decline of the average gray level from 16.63 to 20.20 Gy/h. However, 7# sample has a

**Fig. 4** The average gray level of dark image during the resource rising process (maximum dose rate is 58.30 Gy/h)



**(a)** Digital module

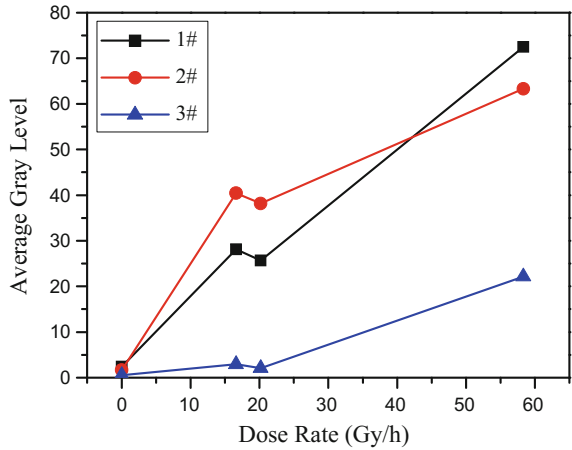


**(b)** Analog module

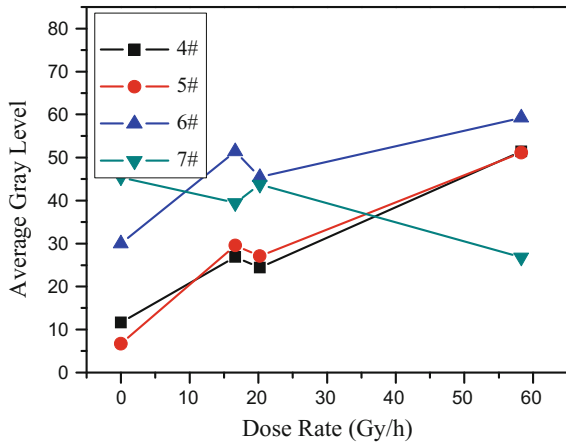
higher background noise. The regulation of integration time decreased the average gray level with dose rate increased. This kind of phenomenon is similar to irradiated by infrared light.

Figures 6, 7 and 8 shows the brightness changes under the condition of illumination. The maximum dose rate is 16.63, 20.20 and 58.30 Gy/h respectively. Radiation damage is quite week under the condition of adequate illumination at the dose rate less than 58.30 Gy/h. The image quality of all the modules has little damage at this level of dose rate, but some noise still appeared.

**Fig. 5** The average gray level of dark image at different dose rate



**(a)** Digital module



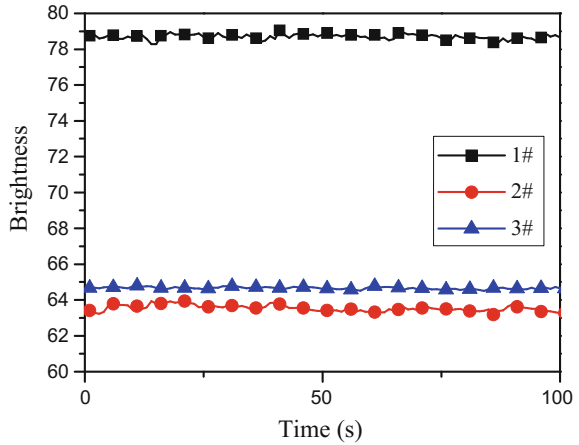
**(b)** Analog module

The brightness of each sample at different dose rate has been shown in Fig. 9. As shown in result, the relationship between brightness and dose rate is not linear. This might also be induced by ionizing radiation interference combined with integral time regulation of image sensors.

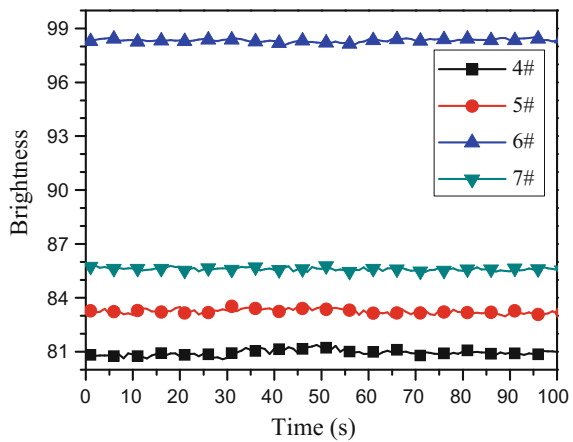
With amount of photons incident into depletion region of a pixel. Large numbers of electron hole pair generated in space charge region. Free electrons flow into potential well of photodiode and become into signal current. With total ionizing dose increase, electrons generated by radiation are far more than that of natural light. The amount of charge in the photodiode reaches saturation and overflows. Therefore, the light signal recorded by pixel unit is the maximum and also affects the surrounding pixels. When signals are reached or close to the maximum in one



**Fig. 6** The brightness of color image during the resource declining and rising process (maximum dose rate is 16.63 Gy/h)



(a) Digital module

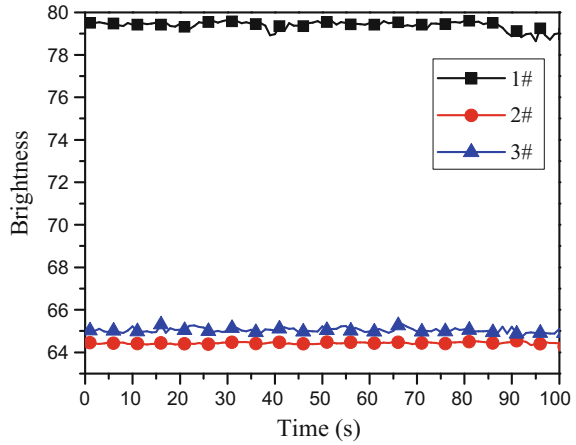


(b) Analog module

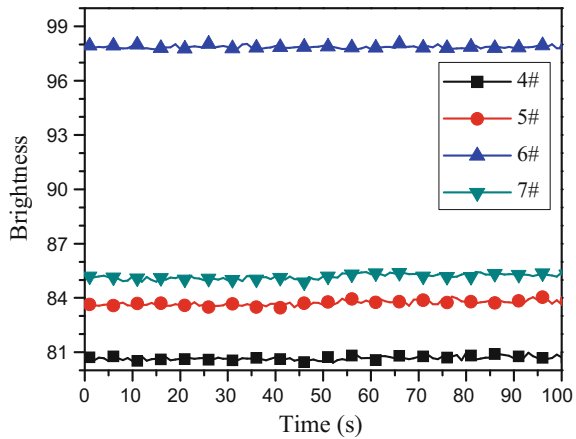
area, the output image of this region is white. The average gray level of images increased with the increase of white spot. The noises mainly induced by  $\gamma$ -ray are impulse noise and Gaussian noise. Signal to noise ratio can be improved under the condition of adequate illumination. Therefore, adequate light can effectively reduce the ionizing radiation interference.

Comparing with the curve diagram of dark and natural images before and after irradiation at different dose rate, CMOS image sensors have better radiation resistance than CCD image sensors. Meanwhile, digital modules have better anti-jamming capability than analog modules due to superior digital signal processing. Therefore, digital CMOS image sensor module is more suitable for radiation environment monitoring. However, the reliability of signal storage and

**Fig. 7** The brightness of color image during the resource rising process (maximum dose rate is 20.20 Gy/h)



(a) Digital module



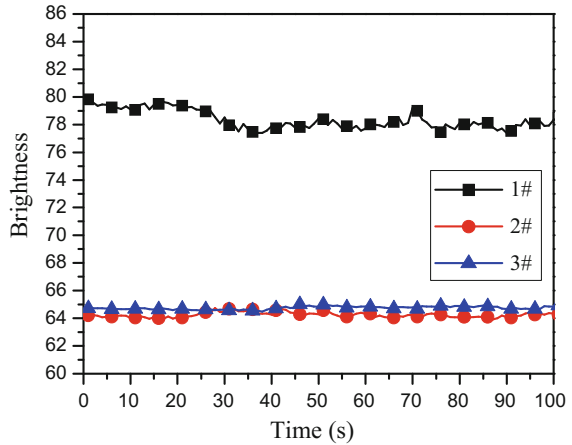
(b) Analog module

transmission mode of digital video module is lower when work in radiation environment.

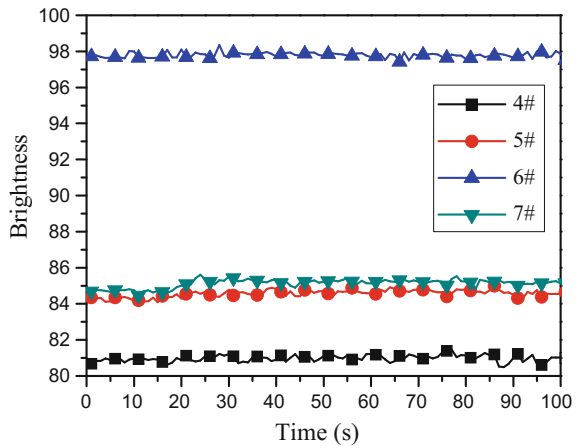
## 4 Conclusions

Parameters of seven types of image sensor modules have been study by several groups of  $\gamma$ -ray ionizing radiation experiments. Radiation resistance of these samples has been analyzed. On the basis of the results, we can reach the following conclusion:

**Fig. 8** The brightness of color image during the resource rising process (maximum dose rate is 58.30 Gy/h)



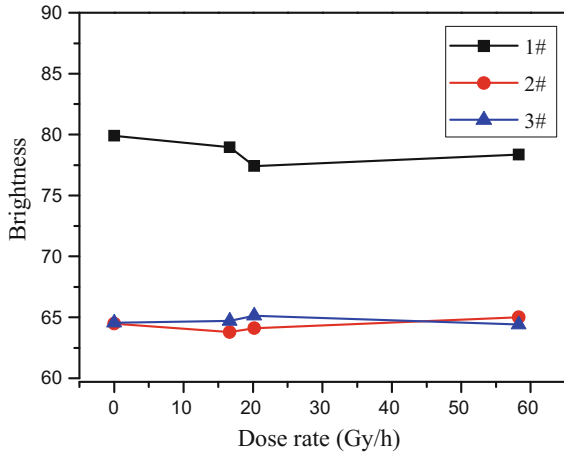
**(a)** Digital module



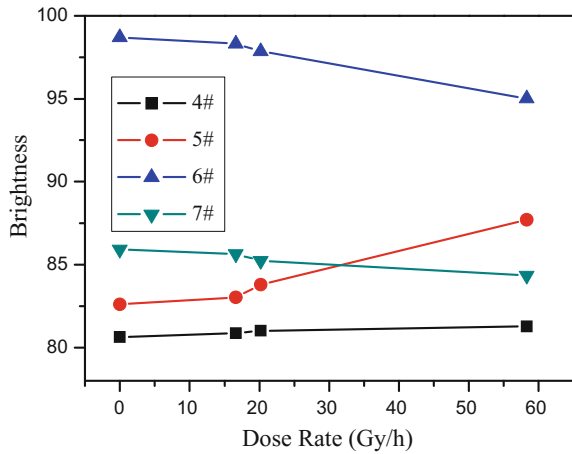
**(b)** Analog module

- (1) Radiation induced color centers generated in crystal structure of camera lens glass. With the total ionizing dose increase, the color center generation rate is faster than the annealing rate. Therefore, visible light transmittance decreased
- (2) The relationship between the average gray level and dose rate is not simply linear. The average gray level increased with the increase of dose rate as a whole, but the value decreased at 20 Gy/h.
- (3) Signal to noise ratio can be improved under the condition of adequate illumination.
- (4) Digital image sensor module with CMOS technology process is more suitable for real-time monitoring in radiation environment.

**Fig. 9** The brightness of color image at different dose rate



**(a)** Digital module



**(b)** Analog module

## References

1. Xiaoping h, Bin W, Jianyou L, et al. Application of the technology of digital video supervision in the nuclear emergency[J]. Atomic Energy Science and Technology, 2003, 37 (2): 182–184
2. Zujun W, Dongsheng L, Minbo L, et al. Radiation Damage Effects on the CMOS Active Pixel Sensors[J]. Semiconductor Optoelectronics, 2014, 35(6): 945–950, 982
3. Bo W, Yudong L, Qi G, et al. Total Dose Effects in 0.5  $\mu\text{m}$  CMOS Active Pixel Image Sensor [J]. Chinese Journal of Luminescence, 2015, 36(2): 242–248
4. Goiffon V, Estriebeau M, Marcelot O, et al. Radiation Effects in Pinned Photodiode Cmos Image Sensors: Pixel Performance Degradation Due to Total Ionizing Dose[J]. Nuclear Science, Ieee Transactions on, 2012, 59(6): 2878–2887

5. Shaoyang M. Research on Radiation Dose Rate Effect on the Performance of CMOS Image Sensor[D]. Harbin Institute of Technology, 2014
6. Gaillardin M, Goiffon V, Marcandella C, et al. Radiation Effects in Cmos Isolation Oxides: Differences and Similarities with Thermal Oxides[J]. Nuclear Science, Ieee Transactions on, 2013, 60(4): 2623–2629
7. Náfrádi G, Kovácsik Á, Pór G, et al. Radiation Damage of the Pco Pixelfly Vga Ccd Camera of the Bes System on Kstar Tokamak[J]. Nuclear Instruments and Methods in Physics Research Section A: Accelerators, Spectrometers, Detectors and Associated Equipment, 2015 (770): 21–28
8. Meng X, Kang A, Li J, et al. Effects of Electron and Gamma-ray Irradiation on Cmos Analog Image Sensors[J]. Microelectronics Reliability, 2003, 43(7): 1151–1155
9. Place S, Carrere J, Magnan P, et al. Radiation Effects on Cmos Image Sensors with Sub-2  $\mu\text{m}$  Pinned Photodiodes[J]. Ieee Transactions on Nuclear Science, 2012, 59(4): 909–917
10. Bo W, Yudong L, Qi Guo. Research on dark signal degradation in  $^{60}\text{Co}$   $\gamma$ -ray-irradiated CMOS active pixel sensor[J]. Acta Phys. Sin., 2014, 63(5): 313–319
11. Xiangti M, Aiguo K, Qiang H, Effect of Gamma-ray Irradiation on Output Characteristic of Color CMOS Digital Image Sensors[J]. Atomic Energy Science and Technology, 2004, 38 (S1): 231–235
12. Pengwei L, Qi G, Diyuan R, et al.. Radiation Damage Effect on Charge-Coupled Devices During  $^{60}\text{Co}$  Gamma Ray and Electron Irradiation[J]. Atomic Energy Science and Technology, 2010, 44(1): 124–128
13. Pengwei, Qi G, Diyuan R, et al. Annealing Effects of Charge Coupled Devices After  $^{60}\text{Co}$   $\gamma$  Irradiation[J]. Atomic Energy Science and Technology, 2010, 44(5): 603–607
14. Mei Y, Jianshan Z, Lei C. Preliminary study on effects of  $^{60}\text{Co}$   $\gamma$ -irradiation on video quality and the image de-noising methods [J]. J. Radiat. Res. Radiat. Process, 2011, 29(1): 53–57
15. Dong L. HD: Development direction of digital video surveillance system [J]. CHINA SECURITY & PROTECTION, 2009(Z1): 38–39
16. Goiffon V, Virmontois C, Magnan P, et al. Identification of Radiation Induced Dark Current Sources in Pinned Photodiode Cmos Image Sensors[J]. Nuclear Science, Ieee Transactions on, 2012, 59(4): 918–926
17. C Virmontois, V Goiffon, P Magnan, et al. Total ionizing dose versus displacement damage dose induced dark current random telegraph signals in CMOS image sensors[J]. IEEE Transactions on Nuclear Science, 2011, 58(6): 3085–3094
18. Náfrádi G, Czifrus S, Kocsis G, et al. Analysis of Dark Current Images of a Cmos Camera During Gamma Irradiation[J]. Fusion Engineering and Design, 2013, 88(12): 3169–3175
19. Goiffon V, Virmontois C, Magnan P, et al. Radiation Damages in Cmos Image Sensors: Testing and Hardening Challenges Brought By Deep Sub-micrometer Cis Processes[C]// Remote Sensing, [S.l.]: International Society for Optics and Photonics, 2010: 78261–78261

# Scheme Research of Mars Surface Nuclear Reactor Power

Chengzhi Yao, Shouzhi Zhao, Gu Hu, Jiachun Xie, Jian Guo  
and Jian Gao

**Abstract** As the nearest neighbor of earth, Mars has always been the first choice for space exploration and development of human beings. Landing on Mars, to establish a base and the development and utilization of resources is the primary goal of Mars exploration, but the establishment of Mars base needs to solve the problem of energy and power supply first. Nuclear reactor power system has the advantages of high power, long service life and environmental tolerance ability. It is an ideal energy solution option for Mars base and other deep space exploration missions. A brief analysis of the current status of energy that can be used for a Mars base is carried out. The design idea of 40 kWe nuclear reactor power for Mars surface is proposed. After the preliminary optimization design, scheme and overall design parameters of the nuclear reactor power are given. Finally, the power scheme is analyzed and demonstrated from the aspects of reactor physics, shielding, thermal and structure. The results show that the nuclear reactor power scheme is reasonable and feasible. It can meet the requirements of safety and lifetime.

**Keywords** Mars surface · Lithium heat pipe · Nuclear reactor power · Thermoelectric conversion · Stirling engine

## 1 Introduction

The earth's resources are becoming increasingly scarce, and the living environment is deteriorating since entering the twenty-first century. The demand for extraterrestrial resources and living space is becoming more and more obvious. With the development of space exploration technologies and urgent demand for resources exploitation, many countries have made their plans to develop deep space exploration in the next few years. As one of the eight planets in solar system, Mars is the closest planet to earth orbit, and its surface environmental characteristics are closest

---

C. Yao (✉) · S. Zhao · G. Hu · J. Xie · J. Guo · J. Gao  
China Institute of Atomic Energy, Beijing, China  
e-mail: yaochengzhi2006@163.com

© Springer Science+Business Media Singapore 2017  
H. Jiang (ed.), *Proceedings of The 20th Pacific Basin Nuclear Conference*,  
DOI 10.1007/978-981-10-2317-0\_80

to the earth. So Mars has been the first choice for human exploration and development of deep space. The United States, Russia, European Space Agency, and other countries and organizations have set up a recent Mars exploration program, is expected to achieve manned Mars flight in this century, and establish Mars base to develop and utilize the resources, energy and special environment of Mars.

The establishment of Mars base needs to solve the problem of power supply first. The total power requirements could range from 10 kWe to more than 100 kWe [1], and the electrical loads include landers, habitats, in situ resource utilization plants, mobility and construction equipment, and science experiments. The unique environment of Mars surface poses many challenges for power systems. Because of the great distance from the Sun and the attenuation through the atmosphere, insolation at the Martian surface is reduced, and the value decreases significantly with dust storms. The potentially corrosive, carbon dioxide atmosphere at Mars may also present problems for the power system. For the Mars, power systems must be highly reliable to assure steady and continuous power for crew safety. At present, the chemical power, solar power and radioisotope battery and nuclear reactor power can be used for Mars base. The combination of high power, difficult environmental conditions, and assured reliability making the nuclear reactor power system an advantageous option among the various power systems [2, 3].

Considering the nuclear reactor power characteristics mentioned above, a lithium heat pipe cooled modular fast reactor conceptual design has been developed to support future China manned Mars base application. The nuclear reactor power system has a solid reactor core and is designed to use dynamic Stirling conversion to produce 40 kWe electricity for up to eight years. Whole system efficiency is  $\sim 20\%$  and has a mass of  $\sim 3.2$  tons. Waste heat is rejected by potassium heat pipe radiator. The system has advantages of low mass, long lifetime, no pumped liquid coolant, and no single point of failure.

## 2 General Design Scheme

The Mars surface nuclear reactor power system adopts a lithium heat pipe cooled modular fast reactor, eight Stirling engines for thermoelectric conversion, potassium heat pipe radiator for waste heat rejection, the Martian regolith for shield. The reactor fuel is uranium dioxide ( $\text{UO}_2$ ), and reactor reactivity is controlled by rotating control drums. The reactor is designed to supply 210 kWt to the power conversion via lithium heat pipe, and is designed for a full-power lifetime of 8 years. The flow chart of nuclear reactor power system is shown in Fig. 1.

The nuclear reactor power system is placed on Mars surface as an integral, comprising reactor core (including shield), heat exchanger, Stirling engine, potassium heat pipe radiator, supporting structure and control unit. The general configuration of nuclear reactor power system is shown in Fig. 2.

The radiator is vertically arranged on Mars surface in order to reduce the influence of Mars dust adhesion and surface reflection of rock on the performance

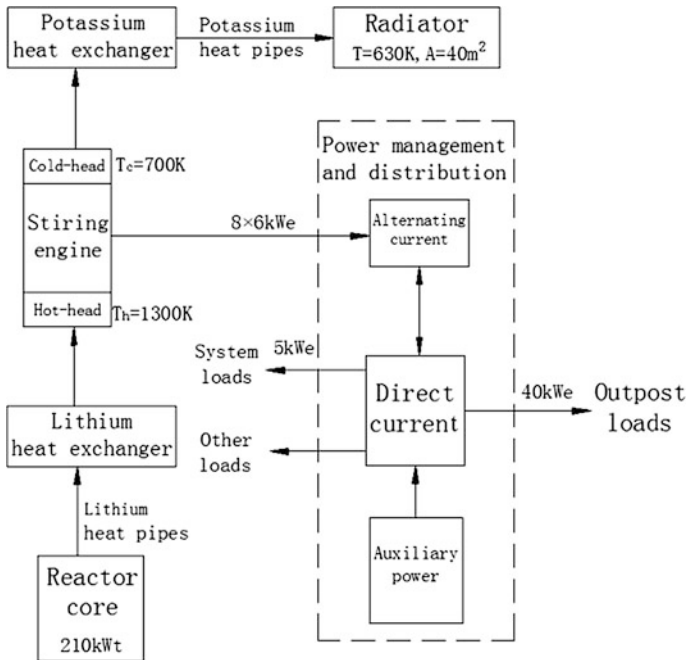


Fig. 1 Flow chart of nuclear reactor power system

of radiator. Four individual radiators are adopted to achieve better stability when the system is deployed on the windy Mars surface. Due to the large weight of radiator, multiple supporting rods are laid at the bottom of radiator. This scheme sets up two liquid metal heat exchangers, one is lithium heat exchanger which is placed between reactor core and Stirling engine, and the other is potassium heat exchanger which is placed between Stirling engine and radiators. The hot end and cold end of Stirling engine are separately placed in liquid metal lithium and potassium heat exchanger to realize heat transmission.

This scheme has advantages of high thermoelectric conversion efficiency, high reliability, small size, compact structure, and so on. The integrative design can reduce installation work of nuclear reactor power system on Mars surface. The adopting of heat pipes for reactor core cooling and waste heat rejection, which can avoid the problem of coolant freezing and thawing. The hot end and cold end of Stirling engine are immersed liquid metal of heat exchangers, which makes the connection of Stirling engine and heat pipe simple, avoids complicated connection problems, at the same time the thermal can be assigned to the eight Stirling engines evenly. In the case of given electric power, the thermal power of reactor core will reduce by introduce efficient Stirling engine, which will greatly reduce the volume and weight of power system. By using eight independent Stirling engines, four vertical radiators and plurality heat pipes, the single point failure problems of



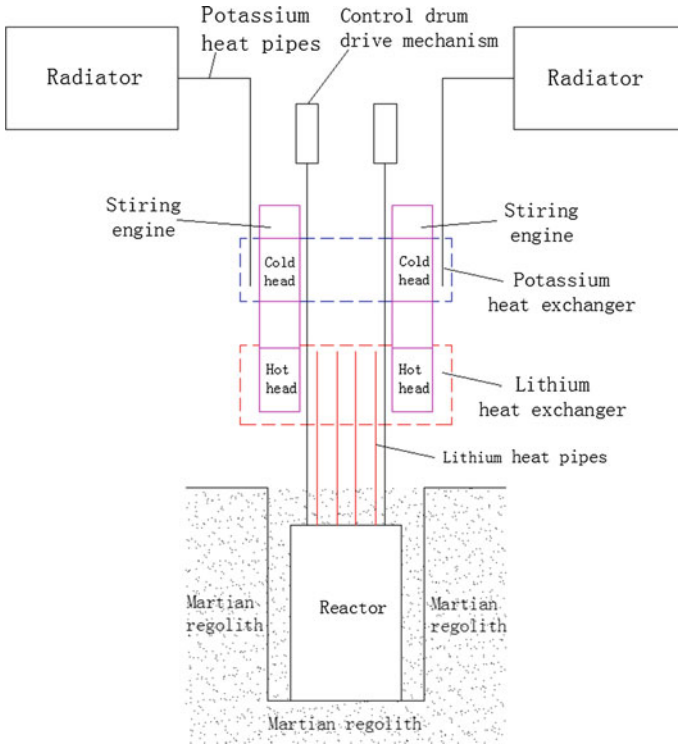


Fig. 2 General configuration of nuclear reactor power system

thermoelectric conversion, waste heat rejection and reactor core cooling system can effectively avoid. Meanwhile, the reliability of power system can be improved.

### 3 Preliminary Calculation

#### 3.1 Reactor Description

The reactor core consists of 156 fuel pins made up of 90 % enriched  $\text{UO}_2$ , and 61 heat pipes containing a lithium working fluid, arranged in a hexagonal lattice within a Mo-14 %Re monolith. The reactor core is 38 cm tall and 21 cm wide flat to flat, which is shown in Fig. 3. The fuel meat is assumed to be 95 % theoretical density, with a nominal 0.005 cm assembly gap between the fuel and Mo-14 %Re clad (cold/beginning-of-life (BOL)). The core uses a triangular pitch pin-lattice arrangement. A tie structure holds the pins axially and radially on one end, but allows the pins to float axially at the other end. The outer diameters of fuel element and heat pipe are the same. Every fuel element is adjacent to at least two lithium

heat pipes to avoid fuel destruction caused by single heat pipe failure. At each end of the fuel pin is a 5 cm long beryllium oxide (BeO) axial reflector. Below the bottom axial reflector is a 2 cm long fission gas plenum.

The fueled region is surrounded by BeO radial reflector and six control drums. The radial reflector is 51 cm in diameter, and the axial reflector is 5 cm in diameter, which are surrounded by a 0.2 cm thick MA-ODS956 alloy can. Each 14 cm diameter control drum contains BeO neutron reflector and boron carbide ( $B_4C$ ) neutron poison. The  $B_4C$  absorber is 1 cm thick, 38 cm long. Reactivity is controlled by rotating the control drums. The least reactive position is with the control drums turned in, i.e.  $B_4C$  closest to the reactor core. The control drum is contained in a MA-ODS956 alloy cylinder. Each control drum is powered by a dedicated motor and drive mechanism to permit angular position changes. A nominal 0.2 cm radial gap is between the control drums and reflector to prevent contact that might impede drum movement. In order to make sure that the reactor is subcritical in launch failure accident, the Mo-14 %Re alloy is chosen as core structure material, and a 0.01 cm thick  $Gd_2O_3$  is coated on Mo-14 %Re monolith and radial reflector can [4]. Re and  $Gd_2O_3$  are excellent spectral shift absorber materials [5], which have large absorption cross section for thermal neutron, but the absorption cross section is small for fast neutron. When the reactor fall into water or wet sand in launch failure accident, the materials can effectively absorb thermal neutron, which is conducive to the reactor under subcritical state. In order to reduce core heat dissipation and temperature effect on radial reflector layer performance, the axial and radial reflector segments are thermally insulated from the reactor core by 20 layers of molybdenum-zirconia multifoils insulation (2.2 mm total thickness) [6, 7].

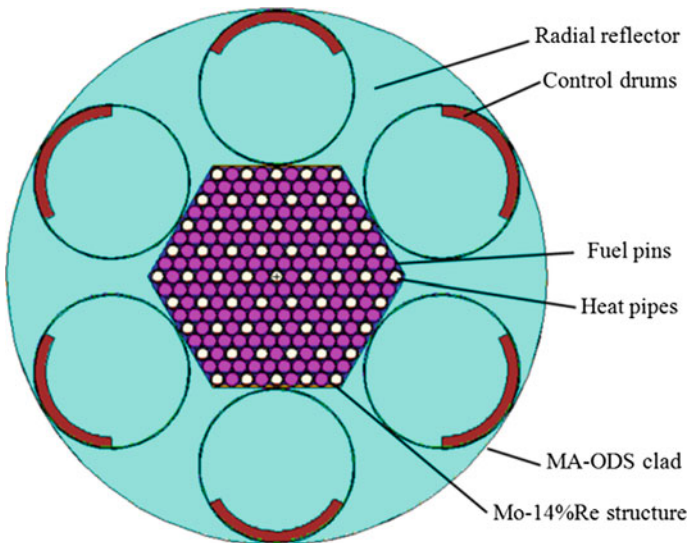


Fig. 3 Scheme of reactor core

### 3.2 Reactivity Design and Analysis

The reactivity design of the reactor core is focused primarily on maintaining sufficient criticality until end of life as well as having sufficient shutdown margin to ensure subcriticality in all nominal and credible off-normal configurations. An analysis is also performed to ensure sufficient operating margin in the event that one of the control drums becomes stuck in the least reactive position. All of the nuclear performance analysis is performed using MCNP. The main reactivity parameters of nuclear reactor are presented in Table 1. The reactor initial excess reactivity and control drum value are all satisfied design requirements. The reactor reactivity of warm state is slightly less than cold state, which is mainly caused by Doppler effect and expansion effect. This indicates that the reactor has an overall negative temperature coefficient of reactivity. It means that the reactor power will self-regulate to match the power demanded in a manner that keeps the reactor temperature essentially constant. Therefore the reactor has the inherent safety characteristic, it can inherently respond to any power conversion operational changes by automatically adjusting fission power.

As part of the analysis, the fluence and burnup of reactor core were studied also. In the current design, the core is main energy greater than 0.1 meV fast neutron. Over the eight years lifetime, the peak fluence of reactor core is expected to be  $6.58 \times 10^{21}$  n/cm<sup>2</sup>s, and the fast neutron mainly distribute at the center area of reactor core. The average fuel burnup is 9.51 GWd/tU, and the fuel burnup level is very low. The effective multiplication factor of the reactor at the end of life is more than 1.005, which indicates that the reactor reactivity can meet the requirements of eight years lifetime.

The radial relative power distribution of reactor is shown in Fig. 4. The radial power distribution is calculated with 1/6 core because of the reactor core is a regular hexagon. It can be observed that the power density of fuel element decreases slowly with the increase of radial distance, but it increases near the reflector, which is mainly due to the radial reflector to return a lot of neutrons. The axial power density distribution of fuel element is shown in Fig. 5, which is consistent with the distribution of neutron fluence rate, and its distribution is similar to the cosine curve. The maximum axial power density is near the center area of reactor core. From the concrete numerical value, the radial and axial power distribution of the fuel element is relatively flat, their peak-to-average power density is 1.16 and 1.2 respectively,

**Table 1** The reactivity parameters of nuclear reactor

Description	$k_{\text{eff}}$
Beginning-of-life, cold, all control drums turned out	1.02453
Beginning-of-life, warm, all control drums turned out	1.02178
Beginning-of-life, cold, all control drums turned in	0.82869
Beginning-of-life, cold, one control drums turned out	0.84728

the average power density of fuel element is  $25.2 \text{ W/cm}^3$  and the maximum power density is  $30.02 \text{ W/cm}^3$ .

### 3.3 Critical Analysis

National expectations for reactors require that any system that would be launched into orbit should not pose a significant risk to the environment or the public in case of a launch accident. Generally this requirement is interpreted to mean that the reactor being designed cannot go critical for any credible accident scenario. Ideally, under accident conditions, the safety margin would be large enough to allow for things to go worse than expected and still be safe. The reactor will be examined for three major accident scenarios: immersion in water, immersion in wet sand and immersion in dry sand [8]. These three accidents represent the credible worst case scenarios commonly examined for space reactor proposals. For these accidents, the design goal is for the reactor to maintain a multiplication factor of less than 0.98. The launch accident scenario analysis is presented in Table 2. In this analysis, seawater is assumed to have a density of  $1.025 \text{ g/cm}^3$  and consists of 96.9 wt% water ( $\text{H}_2\text{O}$ ) and 3.1 wt% salt ( $\text{NaCl}$ ). Sand is modeled as silica ( $\text{SiO}_2$ ) with a theoretical density of  $2.65 \text{ g/cm}^3$  and a porosity of 30 %, for an actual density of  $1.855 \text{ g/cm}^3$ . When the voids are completely filled with seawater, the resulting wet sand is 85.8 wt% silica and 14.2 wt% seawater and has a total density of  $2.1625 \text{ g/cm}^3$  [6].

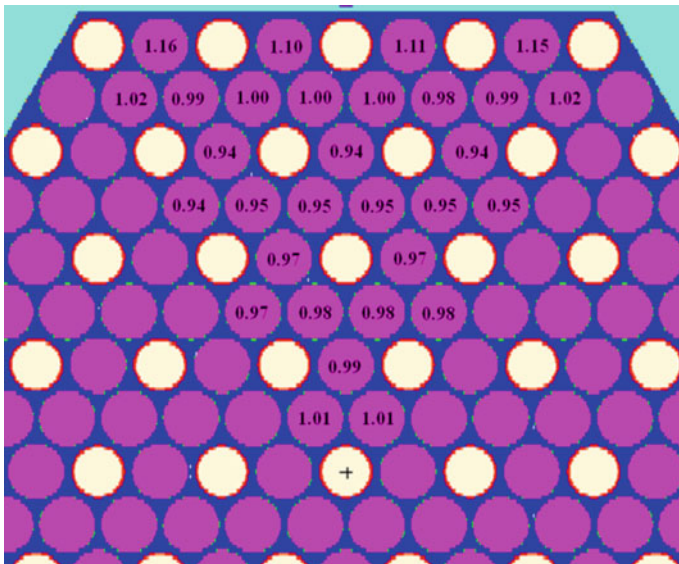
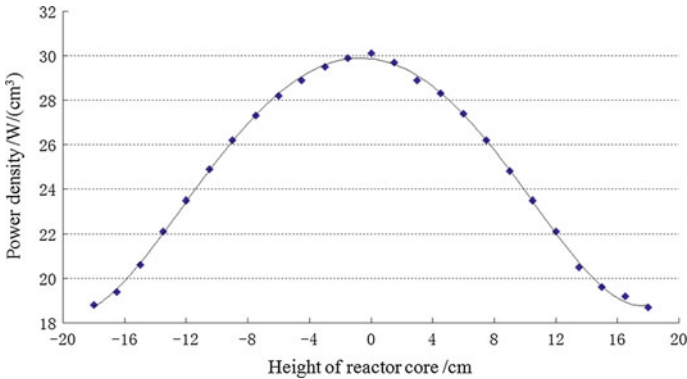


Fig. 4 Scheme of reactor core relative power distribution of 1/6 reactor core



**Fig. 5** Axial power distribution of reactor core

**Table 2** The critical parameters of nuclear reactor in different scenarios

Serial number	Scenario description	Reflector state	$k_{\text{eff}}$
A	Surrounded by dry sand, all control drums turned in	Existent	0.83411
B	Surrounded by dry sand, flooded with fresh water, all control drums turned in	Existent	0.92912
C	Surrounded by wet sand, all control drums turned in	Existent	0.83241
D	Surrounded by wet sand, flooded with fresh water, all control drums turned in	Existent	0.92783
E	Surrounded by fresh water, all control drums turned in	Existent	0.83194
F	Surrounded by fresh water, flooded with fresh water, all control drums turned in	Existent	0.92761
G	Surrounded by dry sand	Stripped	0.93013
H	Surrounded by dry sand, flooded with fresh water	Stripped	0.97732
I	Surrounded by wet sand	Stripped	0.81541
J	Surrounded by wet sand, flooded with fresh water	Stripped	0.91151
K	Surrounded by fresh water	Stripped	0.76112
L	Surrounded by fresh water, flooded with fresh water	Stripped	0.86665

It can be observed that all kinds of accident scenarios can meet the requirements of criticality safety; their effective multiplication factor is less than 0.98. The accident scenario of immersion in water with flooding of the core is worse than the core is not flooded with water, which indicates the water having outstanding moderating effect for neutron. In these accident scenarios, the dry sand accident case is worst, its effective multiplication factor is 0.92912 when the reflector is existent, and its effective multiplication factor is 0.97732 when the reflector stripped.

### 3.4 Thermal Analysis

An important aspect of the nuclear reactor power system design process is to ensure that component temperatures are within acceptable limits during normal operations and during possible fault scenarios where overheating may occur. Thermal analysis is designed to validate the reasonability of nuclear reactor power system. The peak temperature of fuel pin and clad are 1652 and 1402 K, respectively, which is less than the limit temperature of  $\text{UO}_2$  and Mo-14 %Re, which can meet the safety requirements. The heat transfer limit of lithium heat pipe is 301.34 kWt, which is more than power 210 kWt, so it can transfer the core heat safely and keep a margin of 43 %. The calculation results show that the heat pipe can meet the heat transfer requirement even if one heat pipe is disabled. The radiator can reject waste heat effectively even if considering a 3 % damage rate annually, and it has 58 % margin at the end of life.

### 3.5 Shielding Design

Shielding design is to ensure the radiation dose of personnel and equipment within permitted limit. Here the reactor is buried in a 150 cm depth Martian crater, and boron carbide ( $\text{B}_4\text{C}$ ) shielding material is arranged in core radial,  $\text{B}_4\text{C}$  and tungsten (W) shielding material are arranged at the top and bottom of core, as shown in Fig. 6.

$\text{B}_4\text{C}$  and W are used as shielding material because of the  $\text{B}_4\text{C}$  has outstanding absorption property, outstanding mechanical properties, low density and high

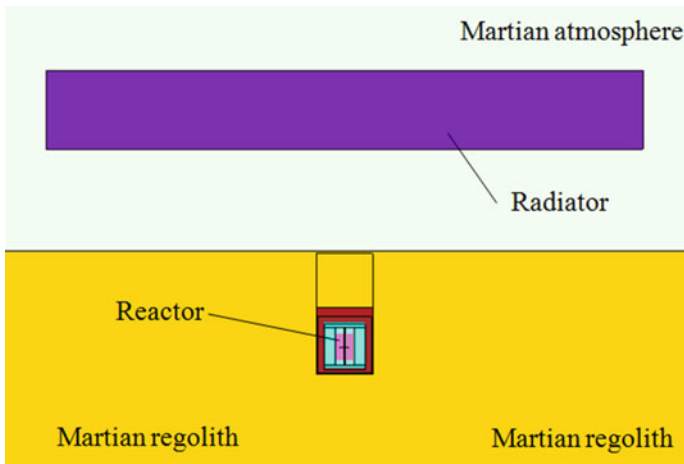
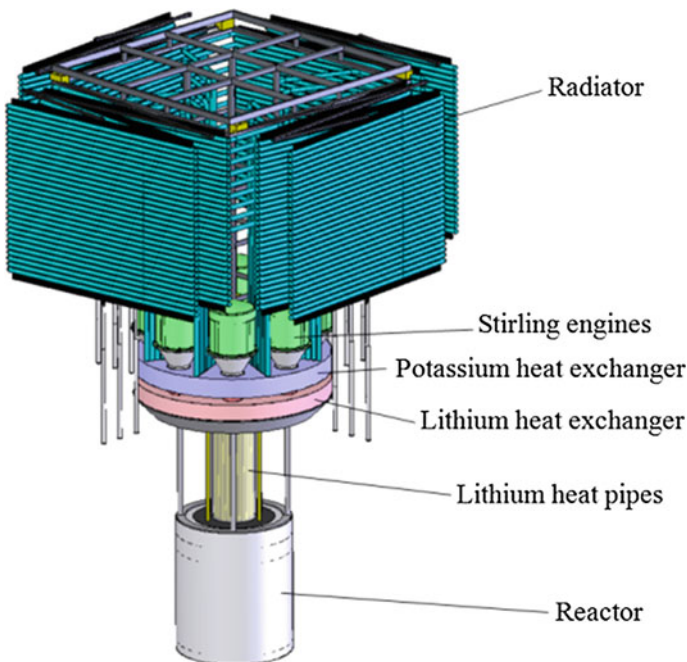


Fig. 6 Shielding calculation model of reactor

melting point. Meanwhile, the W is excellent shielding material because of the small probability of gamma ray scattering, so W is set up at the top of core to prevent gamma ray. Because of the large probability of neutron scattering,  $B_4C$  shielding material is arranged at the top, the radial and the bottom of the reactor core. The W is arranged on the outside of  $B_4C$ , which can obstruct the secondary photon generated by neutron and  $B_4C$  [9]. The calculation results show that the radiation dose from the reactor is 0.62 rem per year at a 100 m radius, the fast neutron fluence of Stirling engine is  $1.75 \times 10^{14}$  n/cm<sup>2</sup>, and the gamma dose is 4.3 Mrad, which can meet the requirements of dose limits [1, 10].

### 3.6 System Configuration and Mass Estimation

The overall structure of the nuclear reactor power on Mars surface is shown in Fig. 7. The power system is 3.8 m high, and the lithium heat exchanger is placed on the Mars surface. The maximum diameter of power system is 9.6 m when the four vertical radiators deployed. The folded state configuration of nuclear reactor power system is shown in Fig. 7, its maximum diameter is 2.8 m and the size can meet the transport and launch requirements. Table 3 shows the system mass distribution.



**Fig. 7** Folded state configuration of nuclear reactor power system

**Table 3** The mass estimate of nuclear reactor power

Item	Mass (kg)
Reactor Core	433
Shield	510
Lithium heat pipes	61
Support structures of heat exchanger	75
Lithium heat exchanger	174
Potassium heat exchanger	140
Stirling engine	288
Control drum actuators	84
Radiator	300
Support structures of radiator	119
Radiator drive motor	8
Power management and distribution module	173
Transmission cabling	180
Instrumentation and control system	98
Mass margin (20 %)	529
Total mass	3172

The total mass of nuclear reactor power system is about 3172 kg, and the specific mass is about 12 We/kg.

## 4 Conclusions

This paper presents a lithium heat pipe cooled modular fast reactor power system. The system is designed to have a thermal power of 210 kWt and use Stirling conversion module to produce over 40 kWe electricity for up to 8 years. Whole system efficiency is  $\sim 20\%$  and has a mass of  $\sim 3.2$  tons. Waste heat is rejected by potassium heat pipe radiator. The system has advantages of low mass, long lifetime, no pumped liquid coolant, and no single point of failure. The integrative design can reduce the installation work of nuclear reactor power system on Mars surface. The using of heat pipes for reactor core cooling and waste heat rejection, which can avoid the problem of coolant freezing and thawing. The hot end and cold end of Stirling engine are immersed liquid metal of heat exchangers, which makes the connection of Stirling engine and heat pipe simple, avoids complicated connection problems, at the same time the thermal can be assigned to the eight Stirling engines evenly. In the case of given electric power, the thermal power of reactor core will reduce by introduce efficient Stirling engine, which will greatly reduce the volume and weight of power system. By using eight independent Stirling engines, four vertical radiators and plurality heat pipes, the single point failure problems of thermoelectric conversion, waste heat rejection and reactor core cooling system can effectively avoid. Meanwhile, the reliability of power system can be improved. The final analysis results show that the power system scheme is reasonable and feasible.



## References

1. MASON L, POSTON D, QUALLS L. System concepts for affordable fission surface power [R]. Ohio: Glenn Research Center, 2008
2. SHALTENS R K. Future opportunities for dynamic power systems for NASA missions[C]// International Stirling Forum 2006. Osnabruck, Germany: [s. n.], 2007
3. RAN Xu, SHAN Jianqiang, ZHU Jizhou. Summary of space nuclear reactor power[J]. Foreign Nuclear Power, 2004, 25(5): 1–5 (in Chinese)
4. Steven A. Hatton, Mohamed S. El-Genk. Sectored compact space reactor (SCoRe) concepts with a supplementary lunar regolith reflector[J]. Progress in Nuclear Energy, 2009, 51: 93–108
5. KING J C, EL-GENK M S. Submersion criticality safety of fast spectrum space reactors potential spectral shift absorbers[J]. Nuclear Engineering and Design, 2006, 236: 238–254
6. KING J C, EL-GENK M S. Submersion-subcritical safe space (S4) reactor[J]. Nuclear Engineering and Design, 2006, 236:1759–1777
7. KING J C, EL-GENK M S. El-Genk. Solid-core, gas-cooled reactor for space and surface power[C]. Space technology and applications international forum, 2007:298–307
8. [CURTIS D, PETERS. A 50–100kWe gas-cooled reactor for use on Mars[R]. New Mexico: Sandia National Laboratory, 2006
9. BUSHMAN A, CARPENTER D M, ELLIS T S, et al. The Martian surface reactor: An advanced nuclear power station for manned extraterrestrial exploration, MIT-NSA-TR-003 [R]. [S. l.]: [s. n.], 2004
10. Fission Surface Power Team. Fission surface power system initial concept definition[R]. Ohio: National Aeronautics and Space Administration and Department of Energy, 2010

# Seawater Desalination Technology Route and Analysis of Production Capacity for Large Commercial Nuclear Power Plant

Hong-mei Yan, Cheng-yan Cao, Gang Bai and Wei Bai

**Abstract** This paper mainly elaborates the history and current situation of nuclear seawater desalination and the development and application of seawater desalination in China. For desalination technology of commercial nuclear power plants from large reactor, membrane desalination technology route is chosen through comparative demonstration of membrane and distillation desalination. And desalination production capacity based on ACP1000 reactor is analyzed in this paper as an example. It shows clearly that nuclear desalination has good economic and social benefits in the electricity and water shortage areas.

**Keywords** Nuclear power · Seawater desalination · Large reactor · Technology route · Production capacity

## 1 Introduction

Freshwater is necessary for survival and development of human. Along with the high-speed development of economic construction and improvement of people's living standards, water demand will keep increasing, freshwater supplies are particularly urgent in areas where are lack of freshwater resources.

There is about 1.386 billion cubic kilometers water storage on earth, 96.54 % of which stored in ocean, the seawater takes up more than 97 % of the earth's total water which is rich in resources. Development of marine economy, the utilization of marine advantage, application of desalination technology to meet the demand for freshwater is the most effective measure to make up for the shortage of freshwater resources, and also the best way to efficiently solve the crisis and has a very broad prospect.

Seawater desalination, producing freshwater from seawater, is a kind of technology that develops water resources for increment in water resources utilization.

---

H. Yan (✉) · C. Cao · G. Bai · W. Bai  
China Nuclear Power Engineering Co., Ltd, Haidian, Beijing, China  
e-mail: yanhm@cnpe.cc

Seawater desalination has lots of advantages including increasing the amount of total freshwater; high quality water production with more and more rational price; guaranteeing the coastal residents' and industrial users' demand for freshwater; supporting for the sustainable development of the local economy; bringing good social benefits. Besides, seawater desalination is also not affected by time and space.

The rise in energy prices is the biggest factor that affects seawater desalination, 60 % of seawater desalination cost comes from energy.

## **2 History and Current Situation of Seawater Desalination with Nuclear Power**

The three main stream technologies in the present seawater desalination field are multi-stage flash distillation (MSF), low-temperature multiple-effect distillation (MED) and reverse osmosis (RO).

Nuclear desalination refers to a kind of desalination technique that costs either electric energy or thermal energy generated by nuclear energy. Usually, RO process utilizes electricity, MSF and MED consume thermal energy or other low-temperature waste heat. The reliable and affordable energy is an important condition for desalination.

The actual experience of the world nuclear desalination mainly comes from Kazakhstan and Japan. The nuclear desalination plant in Kazakhstan was built in the 1970s. The nuclear desalination plants in Japan are based on the current three main desalination technologies, the first one was established in 1978.

Throughout the history of international nuclear desalination, water-cooled reactors have a good application history because of the advanced technology and complete configuration. There are two kinds of nuclear desalination programs, one has nuclear power generation and desalination coupled dual purposes, the other one has one single purpose of desalination.

Main results of the nuclear desalination research before 1970s had been collected in the sixth volume of papers of the 4th International Conference on the Peaceful Use of Atomic Energy in Geneva. They are briefly described as follows.

- (1) Energy is combined with water resource and listed into national policy. Many countries have put forward the coupling scheme for both nuclear power generation and seawater desalination to meet needs for power supply and desalted water supply. As for economic distribution, 75 % of energy is provided for power generation and 25 % of energy for seawater desalination. MSF and MED are selected for process. Steams are firstly supplied to steam turbine for the power generation and then transferred to seawater desalination by back-pressure turbine or through stage-by-stage steam extraction.
- (2) In response to increasing needs for water supply, possibility and technology are both studied for large-scale low-price seawater (or brackish water) desalination.

In consideration of energy economic efficiency, nuclear power is better than the fossil energy, which has dual purpose of power generation and seawater desalination and brings higher economic efficiency. And desalted water can be used for diverse purposes, including urban water supply, industrial water supply, and also domestic water supply. The larger scale of water supply is, and the lower desalination costs.

- (3) Applications of desalted water are tested. Unit area production of rice and wheat which are irrigated with desalted seawater can be increase 350 %. Moreover, it can be applied to chemical fertilizers to promote quality.

More than 100 reactor-years of experience in seawater desalination with nuclear power have been accumulated in the world so far, most which were possessed by the former Soviet Union and Japan. General conclusions on international are: desalination equipment has been commercialized, nuclear reactor technology is mature, and nuclear power stations with dual coupling purposes can be used throughout the world, single-purpose desalination technology, which is basically used for low-temperature heating reactor, and related technology is also mature.

### **3 Developments and Current Situation of Seawater Desalination in China**

There are 2.8 trillion  $\text{m}^3$  water resources in China, per capita freshwater resources of 2220  $\text{m}^3$ , which is 1/4 of the world average, ranks No. 121, showing a serious shortage of water resources. Desalination technology was described 2000 years ago. Modern desalination technology began in 1958, starting from electrodialysis; reverse osmosis technology came out in 1965; medium-sized distillation unit in 1975; The construction multi-stage flash desalination plant of 3000  $\text{m}^3$  per day was completed in 1986; seawater reverse osmosis desalination unit of 500  $\text{m}^3$  was completed in 1997 [2]. After that, reverse osmosis desalination unit with kiloton daily production and brackish water reverse osmosis desalination unit with million tons daily production have been built up one after another. Through a series of measures including water diversion projects, better water conservation efforts, wastewater reuse potential development and desalination extension, and the water tension has been relieved effectively.

The sea area of our country is vast with long coastline and abundant water, sufficient supply of freshwater by desalination technology has become an effective way to relieve the water crisis. The cumulative production capacity of desalination projects that have been built or is under construction is about 600,000 tons/day, the market capacity of the desalination within the next decade will increase five times more, which means that prospects are very optimistic.

After development of 40 years in China, the reverse osmosis desalination technology has become more perfect and made great progresses, and freshwater and energy costs have reached international standards. Compared with the thermal

method, reverse osmosis does not require a vapor source, needs low energy consumption (no phase change), short construction period, low investment, less area characteristics. Energy consumption of reverse osmosis is mainly utilized to overcome the osmotic pressure of concentrated water. With the continuous improvement of the reverse osmosis membrane materials, the development of ultralow pressure composite membrane, and the prices drop of membrane component, Seawater reverse osmosis (SWRO) systems has been brought into focus increasingly, now it has become a major competitor of distillation desalination systems.

SWRO with daily production of million tons has been in safe operation for more than a decade in China. Zhejiang Huaneng Yuhuan Power Plant: reaction sedimentation tanks + UF + RO, design scale is 36,000 m<sup>3</sup>/d, output water from the first stage reverse osmosis is used as production water in plant, output water from conditioning process after second stage reverse osmosis is used as domestic water. Qingdao Baifa Desalination Project: Mixed capable of precipitating + flotation + UF + RO, total designed production is 100,000 m<sup>3</sup>/d for municipal domestic water.

Most nuclear power plants in China have been built on the coast. There is shortage of freshwater for use in coastal areas, freshwater rivers barely meet the needs of large nuclear power plants. Desalination has been the best way to resolve the water crisis efficiently for the coastal nuclear power plant.

Nuclear desalination applications in China include: Liaoning Hongyanhe Nuclear Power Plant completed the commissioning and began operation in 2010; nuclear power plants with seawater desalination which have been built up or is under construction include Fujian Ningde nuclear power plant, Sanmen Nuclear Power Plant, Shandong Haiyang Nuclear Power Plant, Liaoning Xudapu Nuclear Power Plant. Reverse osmosis technology is adopted for seawater desalination in all these nuclear power plants.

## **4 Nuclear Desalination Technology Route and Analysis of Production Capacity**

### ***4.1 Technology Route and Main Technological Process of Seawater Desalination***

#### **4.1.1 Technology Route of Seawater Desalination**

The main technical development routes of nuclear desalination are: membrane method reverse osmosis desalination by using electricity generated from nuclear power; distillation method desalination by using steam generated from nuclear power.

Which technical development route should be adopted depends on specific conditions. The advantages should be fully developed. For example, power, waste heat, waste steam or some other sources generated by nuclear power is utilized for desalination. Desalination with single-purpose or multi-purpose of water, electricity and heat is chosen on realities. Economy, security and others aspects should also be considered in program design.

If seawater desalination technology is adopted in large nuclear power plant, the following problems should be considered as well:

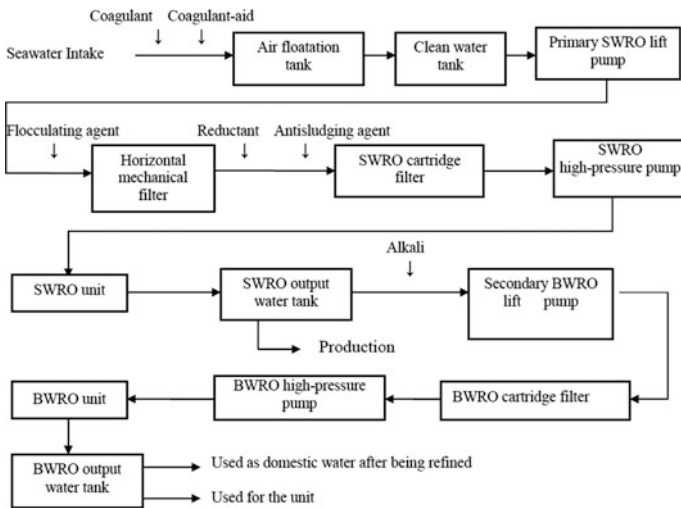
- (1) **Applicability:** since the distillation method needs suction of steam, large design modification of the second or the first loop of nuclear power plant may be involved. Thereby the risk is high and the method still needs argumentation. At present, it is recognized that thermal method desalination is more appropriate for thermal power plant. However, whether it is appropriate for large reactor nuclear power plant still needs study. No alteration for primary nuclear reactor is needed if membrane method is used.
- (2) **Security:** after Fukushima accident, research on nuclear power security has been actively carried out by nuclear power workers from different countries. The results of integrated safety examination on nuclear facilities in 2011 indicates that the nuclear power units including ones in operation and ones under construction in China basically meet the requirement of actual nuclear safety laws of China and the lasted standards of IAEA. That means the safety and quality of the nuclear power units are guaranteed. China is making great efforts to make sure that newly constructed nuclear power plants will actually eliminate the possibility of vast radioactive substance release in design. For seawater desalination technology, there is no doubt for security of seawater desalination with membrane method. There is possibility for seawater desalination with distillation method to cause pipe break which will lead to steam leak, thus there is potential risk that may cause spread of radioactive pollution. So distillation method desalination still needs to study. For example, as to air cooling style for nuclear power plant, EPRI regulates that direct air cooling is not recommended because the range of radioactive pollution may spread caused by steam break.
- (3) **Operation stability:** it is not easy to keep distillation method seawater desalination in operation stably and continuously in long term, which will cause the equipment to start up and stop frequently. However, the security and efficiency can be guaranteed only when the nuclear power plant can operate stably and continuously in long term under high load. The operation laws of seawater desalination units which are connected to nuclear reactor shall be in accordance with nuclear reactor, which means, keep operation stable in long term. Otherwise, it will cause unnecessary safety hidden troubles and affect the efficiency of the whole system [1].
- (4) **Maturity:** application of membrane method in large nuclear power plant is mature and there is similar performances in China, and no risk for it.

As above, as to large nuclear power plant, technology of membrane seawater desalination is mature, safe, reasonable and economic.

### 4.1.2 Process Flow Chart of System

Quality of water: qualities for living, production, and for nuclear power units' own use; output water from conditioning process after secondary stage reverse osmosis is used as domestic water, and water that comes from primary reverse osmosis is used for production.

Flow chart of the main technology is shown below.



Desalination capacity is analyzed based on ACP1000 reactor as follows.

## 4.2 Analysis of Seawater Desalination Production Capacity

China's annual total water consumption 614.18 billion m<sup>3</sup> in 2012, domestic water accounts for 11.87 % of that, industrial water accounts for 23.18 % and agricultural water accounts for 63.18 % (the amount of irrigation water accounts for more than 90 % of the total agricultural water), ecological water accounts for 1.77 %. From 2000 to 2012, compound annual growth rate of domestic water has been 2 %. Considering the future trends in water, demand for domestic water will be growing in the future for a very long period. Desalination program is designed on the 1:4 ratio of living and production (industry and agriculture). Design water temperature is 25 degrees centigrade temporarily.

Net output power of ACP1000 MWe single reactor power plant is 1060 MW; the maximum daily water consumption for single-unit nuclear power plant is 7000 m<sup>3</sup>/d (unit startup condition). Above capacity calculation refers to the secondary reverse osmosis water production.

Following design indexes are presented in the scheme based on technical features of RO-based seawater desalination system and requirements of users for water quality.

The power consumption of water output for the primary RO is 3.66 kWh per ton, the consumption for the secondary RO is 0.62 kWh per ton and 0.2 kWh for water transportation per ton. After conversion, comprehensive power consumption is 3.8 kWh per ton for production water and 4.89 kWh per ton for domestic water (the secondary RO production).

The intake and discharge of seawater do not account in the following analysis.

#### 4.2.1 Total Capacity of Power Plants

Net output power of the single reactor is utilized for the seawater desalination.

The ratio of living and production water is about 1:4, if all 1060 MWh electricity production is all used for the desalination process. After accounting, primary seawater reverse osmosis is about 6.47 million m<sup>3</sup>/d (25 °C), 5.06 million m<sup>3</sup>/d of which is directly used for the production of water; 1.41 million m<sup>3</sup>/d is used for secondary RO, the output is about 1.27 million m<sup>3</sup>/d, 7000 m<sup>3</sup>/d of which is used for the nuclear power plant. The water supply capacity of desalination plant is 6.33 million m<sup>3</sup>/d, the annual output is up to 2.3 billion m<sup>3</sup> per year.

#### 4.2.2 Water and Power Cogeneration

The analysis is based on a certain medium coastal city in northern China. The total water supply of this city in 2013 is about 142 million m<sup>3</sup>, production water accounts for 44.5 %, domestic water is 23.2 %, water population is 1.487 million, daily per capita domestic water consumption is 120 L, which is lower than the low limit of the average daily domestic water level 150 L/(person • d). In 2014, the urban population increased about 30,000 people, the annual water volume growth rate was 7 %, power generation increased 3.9 %. The proposed design of the program that uses nuclear desalination is shown as follows:

The nuclear power plant generates electricity out while providing outwardly 300,000 m<sup>3</sup>/d output water from desalination.

The ratio of the area living and production water is about 1:3, the design water capacity of primary seawater reverse osmosis is about 325,600 m<sup>3</sup>/d (25 °C), 240,000 m<sup>3</sup>/d of which is used directly for production; 85,600 m<sup>3</sup>/d is used for secondary reverse osmosis, and the water production is about 77,000 m<sup>3</sup>/d, 7000 m<sup>3</sup>/d of which is used for the nuclear power unit. The water supply capacity



of desalination plant is 300,000 m<sup>3</sup>/d, the annual output is up to 110 million m<sup>3</sup> per year. Domestic water demand is almost met to a great extent in this area.

The electricity consumption of 300,000 m<sup>3</sup>/d water is about 52 MW, power generation from desalination water in nuclear power plants is 1008 MW.

The two kinds of nuclear desalination capacity analysis above are based respectively on single-purpose and water and electricity cogeneration. Section 4.2.1 applies to the desert region that has very severe shortage of freshwater resources; Sect. 4.2.2 applies to the areas that have the shortage of available freshwater resources which is mainly used for power generation, and nuclear desalination supplement.

Nuclear desalination can not only solve the water problems of nuclear power plants, but also provides the local electricity and freshwater resources, guaranteeing the needs of electricity and freshwater for local residents and industrial users, supporting the sustainable development of the local economy, with good social benefits.

## 5 Conclusion

Along with the increasing promotion of desalination technology, it has more and more advantages using freshwater from seawater desalination as the water resource of nuclear power plants. Desalination technology is the best choice to meet freshwater needs of coastal nuclear power plants in the future.

Nuclear desalination technology is mature. For new nuclear power plants, seawater reverse osmosis membrane technology has certain advantages. The membrane nuclear desalination ratio is flexible, which brings good social and economic benefits for electricity and water shortage areas.

Desalination technology utilizing clean energy and renewable energy is the future development direction of the desalination industry. Nuclear desalination is the development trend of the world's desalination industry.

## References

1. GAO Cong-jie, CHEN Guo-hua editor. Seawater desalination technique & project manual. Beijing: Chemical industry press, 2004.2.
2. WANG Shi-chang editor. Seawater desalination project. Beijing: Chemical industry press, 2003.2.

# Structural Design and Verification of the CNFC-HTR New Fuel Transport Container

Ning Li, Hongjun Zhang and Xiaogang Xu

**Abstract** The CNFC-HTR new fuel transport container is specially developed for transport spherical new fuel elements of high-temperature reactors (HTR). This paper describes the structural design process of the CNFC-HTR new fuel transport container, as well as the experimental results of the container mechanical test, thermal test, and simulated transport test. In order to ensure the safety of the fuel elements under both normal conditions of transport and accident conditions of transport, and also to ensure that the elements meet the requirement of the acceleration limits during conventional transport, the container is designed with an outer container body and container lid with shock absorption material, and an inner container with neutron absorbing material. Based on the results of mechanical tests, the container structure is improved and verified through mechanical tests again to ensure that the structure of the container can keep the safety of the fuel element under both normal and accidental conditions of transport. The thermal test was conducted to ensure that the aluminum neutron absorbing material does not fuse at a high temperature and to ensure the criticality safety of the fuel elements. The result of the simulated transport test shows that elements, under the conventional transport conditions, fully meet the requirement of the acceleration limits. The CNFC-HTR new fuel transport container structure is reasonably designed and meets the type A (F) II-YELLOW package requirements of the IAEA Specific Safety Requirements No. SSR-6 and GB 11806, so that it can ensure the safety for transport spherical new fuel elements of HTRs.

**Keywords** New fuel transport container · HTR · Structural design · Verification test · Simulated transport test

---

N. Li (✉) · H. Zhang · X. Xu  
China Nuclear Power Engineering Co., Ltd, Beijing, China  
e-mail: lininga@cnpe.cc

© Springer Science+Business Media Singapore 2017  
H. Jiang (ed.), *Proceedings of The 20th Pacific Basin Nuclear Conference*,  
DOI 10.1007/978-981-10-2317-0\_82

873

## 1 Introduction

High-temperature reactor (HTR) is a new generation of nuclear power technology, and China is one of the few countries that master this kind of reactor technology. As research continues, HTR can also be applied to, besides electricity generation, aqua-thermolysis in hydrogen producing, desalination, oil refining, steel and non-ferrous metal smelting, district heating and other areas. Therefore, HTR has broad market prospects.

New fuel transport container is the key equipment in achieving the safety and reliability in providing fuel elements. HTR use spherical fuel elements containing UO<sub>2</sub> as fuel, the structure and size of which is completely different compared to other reactor types. The existing new fuel transport containers cannot be used to transport the new HTR fuel elements, and new fuel transport containers are needed.

## 2 Structural Design of the Container

The special geometry of the spherical fuel element requires that the spherical fuel elements be packed with plastic bags, made in a rod-like structure for easy operation by vacuuming and sealing, and then placed into an aluminum alloy tube bundle formed through welding the tube ends.

To support and fix the tube bundle, an outer basket will be designed. Outside the basket there will be cylindrical neutron absorbers in order to keep the new fuel sub-criticality and ensure critical safety during transport. Outside these neutron absorbers, a protective plate will be designed to protect the safety of the neutron absorbers during transport and handling of containers. The basket and the tube bundle serve as an inner container in order to load new fuel elements and guarantee their critical safety.

Taking into account the impact of transport accidents while ensuring the elements meet the requirement of the acceleration limits during conventional transport, the inner container is put in an outer container with shock absorption function; taking into account the fire accidents, the outer container also need to have fire resistant and heat insulation functions. Thus the outer container and container lid are made of stainless steel—a flame-retardant and cushioning material—stainless steel construction.

Based on the above-described design ideas, the container structure is completed as shown in Figs. 1 and 2, the container type model is CNFC-HTR new fuel transport container. The containers include an inner container and an outer container. The outer container includes an outer container barrel and container lid; the inner container includes an inner lid, a basket, and a tube bundle. The outer container barrel and the container lid are provided with a flame-retardant cushioning material, and the basket is designed with aluminum neutron absorbers. Bagged spherical fuel elements are placed in tube bundles for transport.

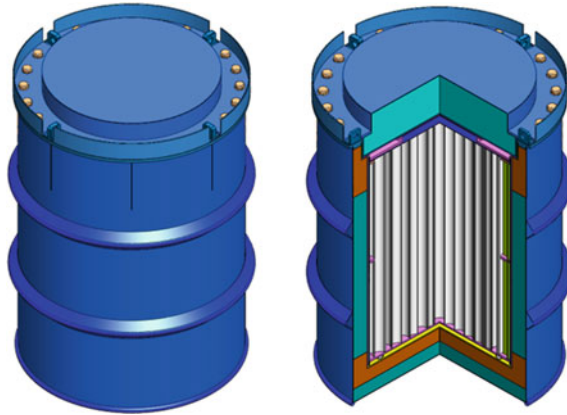


Fig. 1 Schematic diagram of the overall structure of the container

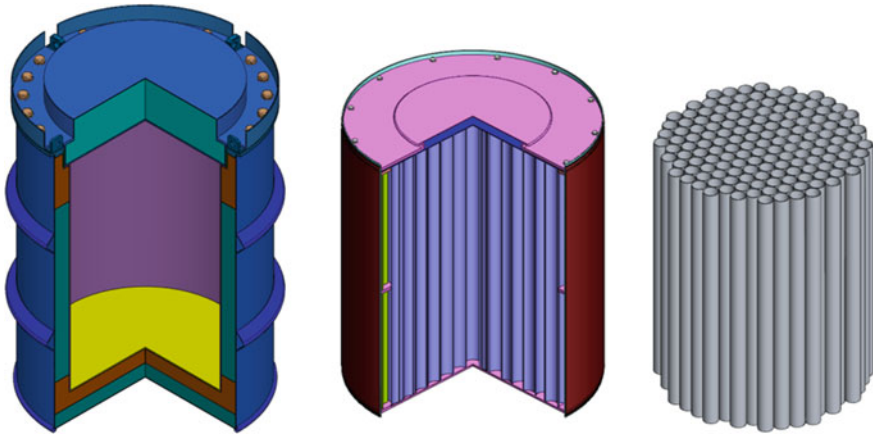
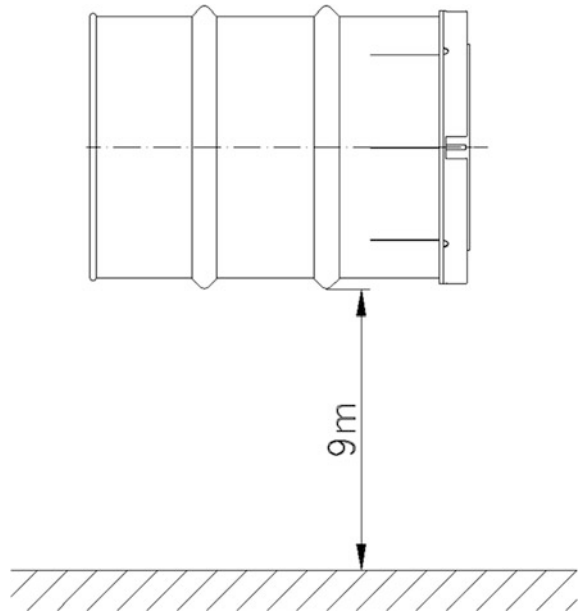


Fig. 2 Schematic diagram of the outer container, inner container, and tube bundle

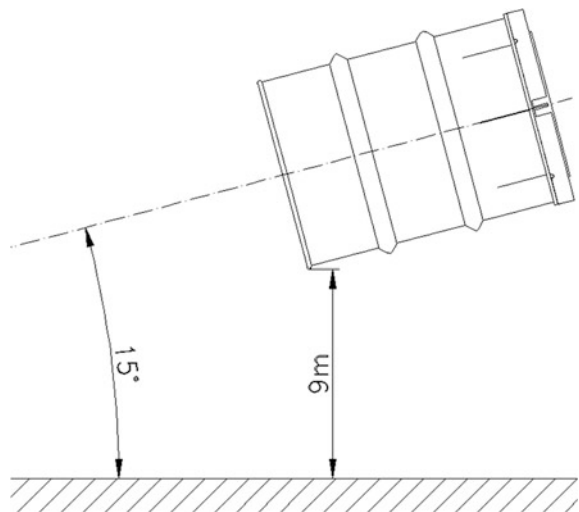
### 3 The Container Test

The test containers were manufactured after the container design completed. Container tests were carried out to verify whether the structural design of the vessel meets the design requirements. In accordance with the relevant requirements under IAEA SSR-6 and GB11806 for normal and accident conditions of transport, the mechanical tests are designed to be 9 m drops with different angles, and the drop posture are shown in Figs. 3, 4, 5 and 6.

**Fig. 3** 9 m horizontal drop diagram



**Fig. 4** 9 m 15° drop diagram



After the 9 m horizontal and 9 m 15° free-fall drop tests, the test container was disassembled. The outermost aluminum tubes holding fuel elements appeared axial damage, and fuel elements were partially damaged, as shown in Fig. 7.

**Fig. 5** 9 m vertical drop diagram

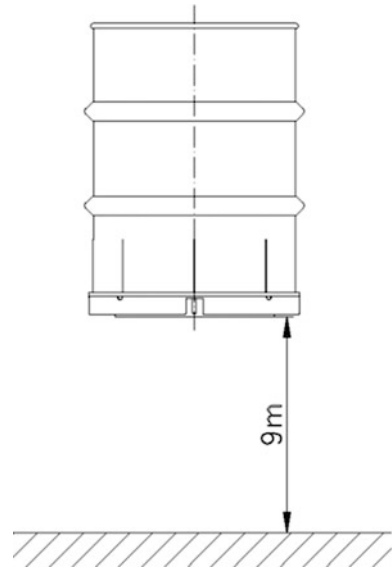
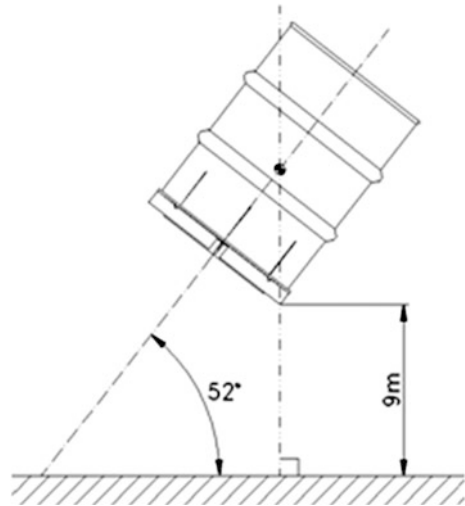


**Fig. 6** 9 m 52° drop diagram



#### 4 Structural Improvement of Container

After compare the test results with the calculation results of the container, the container structure have been improved by improving the external buffer structure of the outer container and filling cushioning materials in its interior, shown in Fig. 8. The number of support plate of the basket also increased in the inner container, shown in Fig. 9.

**Fig. 7** Axial breakages of aluminum tubes

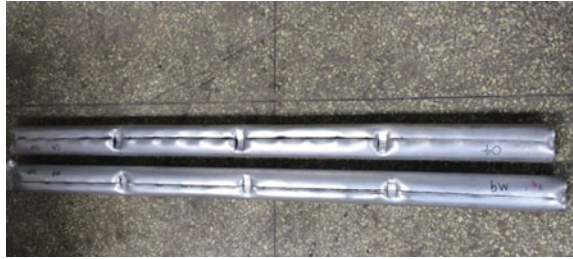


**Fig. 8** Outer containers before and after improvement

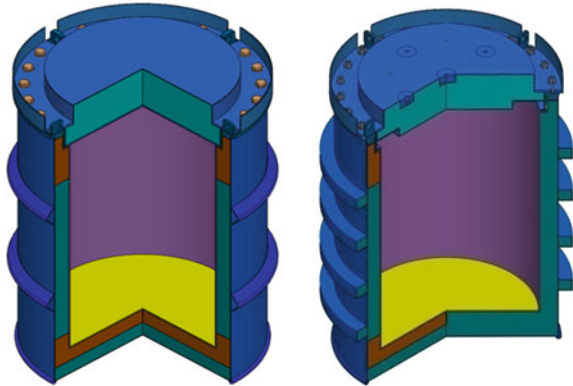
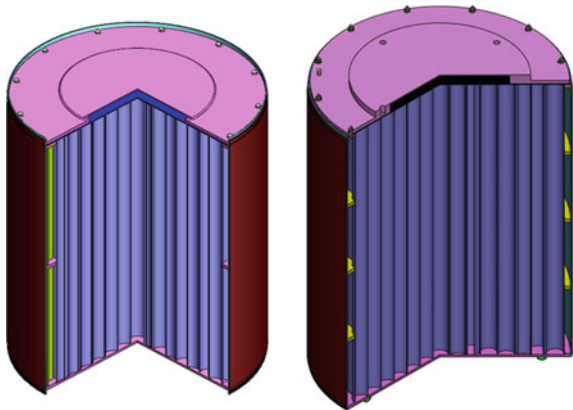


**Fig. 9** Inner containers before and after improvement



## 5 Tests After Improvement

The mechanical tests are designed to be 9 m drops with different angles ( $0^\circ$ ,  $90^\circ$ ,  $52^\circ$ ), shown in Fig. 10. After the free-fall drop tests, the thermal test ( $800^\circ\text{C}$ ) are conducted, shown in Fig. 11, then the test container was disassembled.

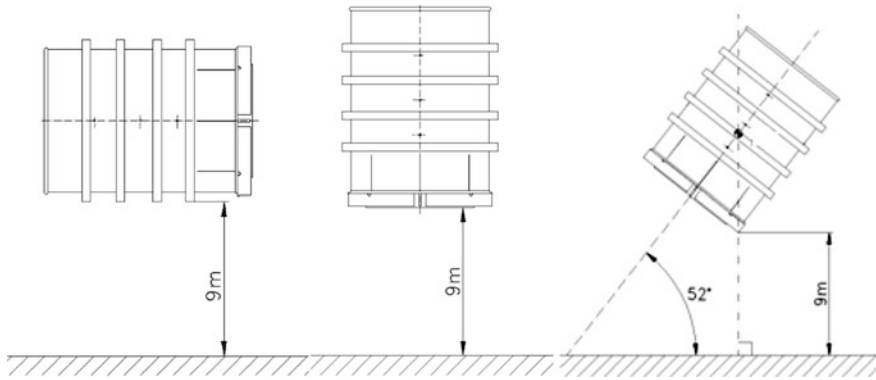


**Fig. 10** 9 m drop diagram

**Fig. 11** Thermal test



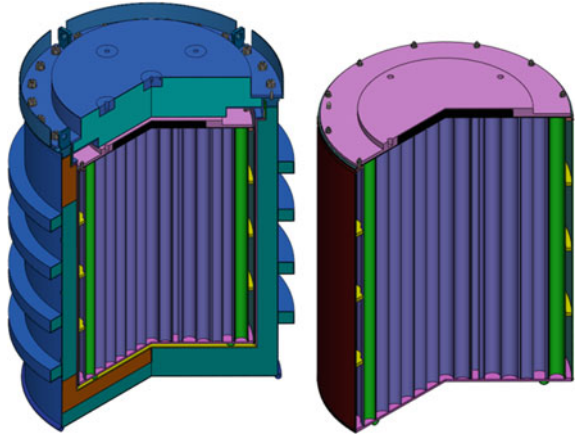
**Fig. 12** Lateral damage of the aluminum tubes



After being disassembled, the aluminum tubes bundle had no axial breakages. The damages occurred in the lateral position of the support plate, where there was breakage of the fuel elements, shown in Fig. 12. After the thermal test, the inner container remained below 100 °C, and the aluminum neutron absorbers and tube bundles did not melt, consistent with the criticality calculations.



**Fig. 13** Schematic diagram of the optimized container



## 6 Structural Optimization of the Container Structure

By comparing the results of the second test with the simulation results, the accuracy of the mechanical and thermal calculation model was confirmed. According to the results of tests, a protective tube was designed in the inner of the outermost aluminum tubes and converted the concentrated load acted on the tube bundle from the support plate into uniform load. By calculation, the deformation of the tube bundle was significantly reduced, and the fuel elements within the tube bundle will not be squeezed nor damaged, which can reach the design aims. The optimized inner container is shown in Fig. 13, the green part is the protective tube.

## 7 Simulated Transport Test

The simulated fuel elements were loaded in an optimized container and transported from fuel fabrication plant to nuclear power plant under actual transport conditions. There were acceleration measurements throughout the whole transportation process. The results showed that the acceleration of the fuel elements meets the limit requirement during the transportation. The method of container fixation on the transport vehicle is shown in Fig. 14.

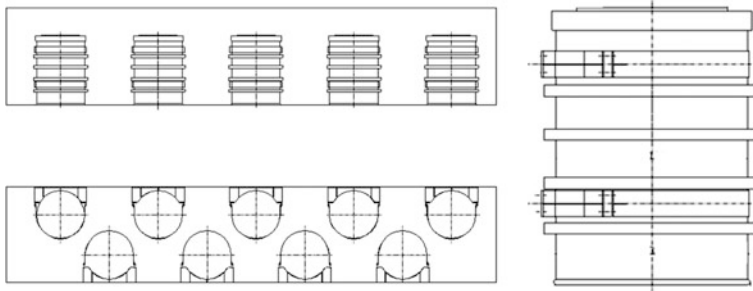


Fig. 14 The method of container transport fixation

## 8 Conclusion

According to the transport requirements for the HTR new fuel elements, the structure of the CNFC-HTR container has been designed and improved based on the test results. Relevant tests were conducted on the improved container and the container structure was optimized according to test results.

The optimized CNFC-HTR new fuel transport container structure is reasonably designed and meets the type A(F) II-YELLOW package requirements of the IAEA Specific Safety Requirements No. SSR-6 Regulations for the Safe Transport of Radioactive *Material* and GB 11806 *Regulations for the safe transport of radioactive material*, so that it can ensure the safety for transport spherical new fuel elements of HTRs and the normal operation of the HTR nuclear power plants.

# Structure Design of Calorimeter of EAST-NBI System Using Thermal Inertia with Cooling Water

Ling Tao, Chundong Hu and Yuanlai Xie

**Abstract** The calorimeter of Neutral Beam Injection (NBI) system of Experimental Advanced Superconducting Tokamak (EAST) must have better heat transfer ability to keep the system running stably and avoid thermal effect caused by a large number of high-energy particle deposition. The physical characteristics and engineering design factors of components were considered in the preliminary design of the structure. The calculation of surface softening temperature was carried out by numerical simulation of heat transfer, and the result verified the primary structure was suitable for the basic thermodynamic requirements of the target plate. This paper provides a reference for the safe and stable operation of EAST-NBI system.

**Keywords** Neutral beam injection · Calorimeter · High-heat flux components · Heat transfer structure

## 1 Introduction

As the major high-heat flux components inside the Neutral Beam Injection (NBI) system of Experimental Advanced Superconducting Tokamak (EAST), the calorimeter was used to measure and absorb the beam energy, from which the total ion beam energy when the magnet was off and the neutral beam energy when the magnet is on, and also the transient energy profile could be obtained. The structure design of components should not only meet the above requirements, but also have high performance of heat transfer in order to avoid thermal damage by long pulse beam power deposition by the high-energy particle [1, 2].

This paper studied the structural design of the calorimeter from the aspects of physical requirements, installation space requirements and condition orders, analyzed the shape layout, cooling pipe layout and major size and the flow rate of the cooling water, then the initial structure design was verified by the numerical calculation.

---

L. Tao (✉) · C. Hu · Y. Xie  
Institute of Plasma Physics, Chinese Academy of Sciences, Hefei, Anhui, China  
e-mail: palytao@ipp.ac.cn

## 2 Design Requirement

According to the working principle and engineering requirements of EAST-NBI system (as shown in Fig. 1), calorimeter should be able to measure the condition parameters on the working status and off the beam channel on the nonworking status, the design of the whole structure of it should consider the following aspects: the physical characteristics, spatial structure requirements, cooling performance requirements, and measuring requirements.

### 2.1 Physical Characteristics

The size of the beam extraction section of the ion source of EAST-NBI is  $120 \times 480 \text{ mm}^2$ , beam profile of the power is gaussian distribution in the X direction and Y direction, the beam power deposition on the calorimeter is also gaussian distribution in the X direction and Y direction by the physical analysis, the power distribution of the beam at the entrance is shown in Fig. 2. Due to the divergence angle of the extraction system itself and the charge effect of the particles, the beam extraction section of the beam is increased continuously, but the primary part of the power is still concentrated in the range of  $120 \times 480 \text{ mm}^2$ .

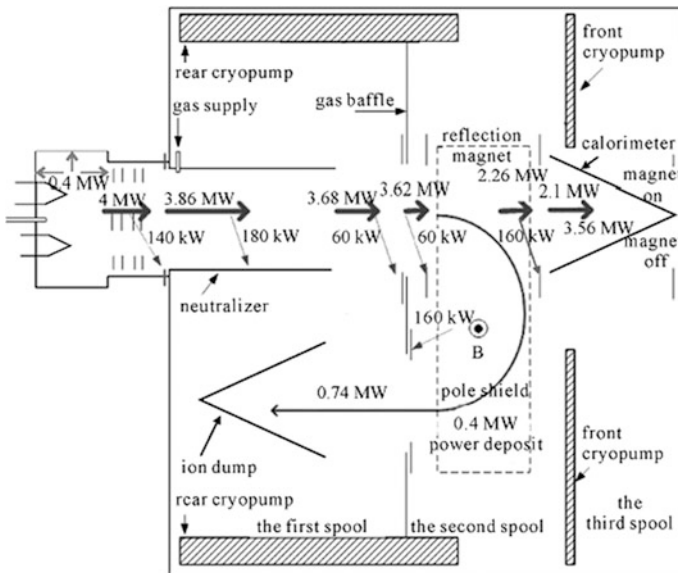
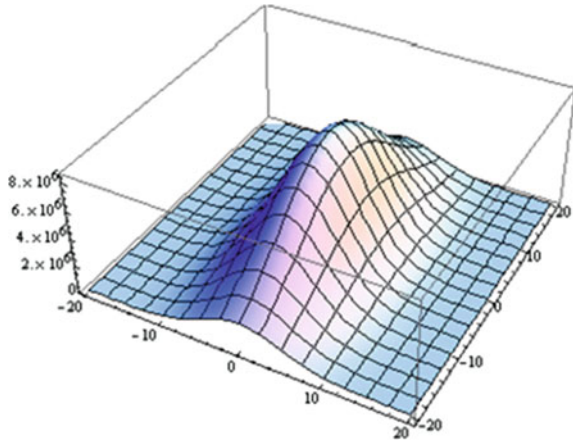


**Fig. 1** Schematic diagram of working schematic diagram and heat distribution of EAST-NBI system

**Fig. 2** Schematic diagram of power deposition value distribution on calorimeter of EAST-NBI system [3]



Therefore, within the space permitted range, the measurement section of the calorimeter should reach at least  $120 \times 480 \text{ mm}^2$ .

Besides, the target of the calorimeter of EAST-NBI must be able to achieve the measurement of beam parameters (beam power of 2–4 MW) and the corresponding measurement time of 0.5–1 s. According to the characteristic of beam power deposition in Fig. 1, if deflection magnet does not work, the ion beam power deposition on calorimeter is about 89 % of the extraction total power (90 % when do calculation), if deflection magnet works, the neutral beam power deposition on calorimeter is about 53 % of the extraction total power (60 % when do calculation).

## 2.2 Spatial Structure Requirements

The calorimeter was fixed in the third spool of vacuum chamber of EAST-NBI system. Considering the relative position of each component inside the NBI system, the spatial structure of calorimeter is as following: (1) two sets of beam energy were measured by two sets of calorimeter separately, the center line of calorimeter is parallel with beam path, and the angle between the two beam path is  $8^\circ 40'$  symmetry. (2) The longitudinal length (along the beam path direction) of the calorimeter plate must be less than 860 mm, and the height must be less than 1047 mm. There should be enough space for the beam to inject when the calorimeter was off-beam path. The narrowest length in the width of direction cannot be greater than 565 mm. (3) The length of single set of calorimeter at least meet the size of 480 mm along the beam path direction and 120 mm perpendicular to the beam path direction.

### **2.3 Condition Requirements**

(1) Calorimeter is fixed inside the vacuum chamber, the ultimate vacuum can reach the magnitude of  $1 \times 10^{-6}$  Pa. (2) Every periodic pulse time, severe thermal stress can be generated on the calorimeter plate under the periodic high heat load when the power is deposited. To ensure the system working on the normal condition, the maximum working temperature of the plate can not exceed the material softening temperature.

## **3 Structure Design**

According to the design requirement, the basic working principle of calorimeter is using thermal inertia with cooling water to calculate the power deposited.

### **3.1 The Selection of Materials**

Calorimeter was mainly used to measure the injection beam power and corresponding work pulse is generally in the second range, and power deposited on it is high, and therefore calorimeter should use good thermal conductivity material. In addition, in order to avoid the problem of sputtering and vacuum loss caused by the loss of material, the material should have small sputtering rate, with high mechanical strength and fatigue strength of material be satisfied at the meanwhile. At last, considering the economic, universal and other factor, the common copper (oxygen-free copper, OFC) was chosen as plate material.

### **3.2 Structure Design of the Plate of Calorimeter**

When calorimeter is on the beam path to calculate the beam parameters, beam pulse width of EAST-NBI system is shorter, generally limited in 0.5–1 s. In order to ensure the accuracy of the measurement, the plate using the thermal inertia of material is recommended. The heat energy generated by bombardment of the high-energy particle with the plate, and absorbed by the plate, and then be taken away by the cooling water in long enough beam pulse interval. Based on the above ideas, the structure of plate of calorimeter in EAST-NBI system is designed and analyzed as following.

### 1. Thickness of the plate

When the particle bombardment to the plate, the surface temperature will rise rapidly, and even lead to the surface melting. In order to ensure sufficient safety factor, the thickness of the target plate is calculated according to the assumption of absolute thermal conductivity without water cooling. Based on the infinite plate model [4], the thickness of the plate is  $L$ , the initial temperature is  $T_0$ , the temperature parameter of the copper plate is assumed constant, then the corresponding partial differential equation is

$$\frac{\partial T}{\partial t} = a \frac{\partial^2 T}{\partial x^2} \quad (1)$$

The initial condition and boundary condition

$$t = 0, \quad T = T_0 \quad (0 < x < L)$$

$$x = 0, \quad \frac{\partial T}{\partial x} = 0 \quad (0 < t < \tau); \quad x = L, \quad \lambda \frac{\partial T}{\partial x} = q''$$

Here,  $a$  is the thermal diffusion coefficient,  $T$  is the temperature of one point in the thickness direction,  $\tau$  is the pulse width,  $x$  is the distance from the heating surface to the heating surface,  $q''$  is the average power density on the plate.

By the separation of variables, the solution of this problem is

$$T = T_0 + 2 \frac{q''}{\lambda} \sqrt{a\tau} \sum_{x=0}^{\infty} \left\{ \operatorname{ierfc} \left[ \frac{(2n+1)L-x}{2\sqrt{a\tau}} \right] + \operatorname{ierfc} \left[ \frac{(2n+1)L+x}{2\sqrt{a\tau}} \right] \right\} \quad (2)$$

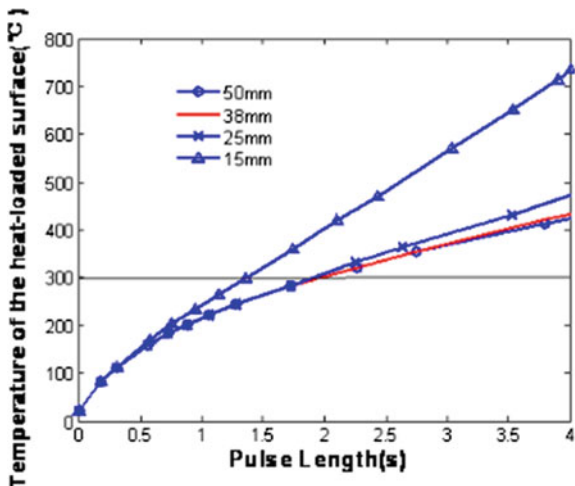
For the oxygen-free copper material target plate, when the thickness  $\delta$  is more than 15 mm, according to the formula  $t_{\text{diff}} = \delta^2/2a$ , the thermal diffusion time  $t_{\text{diff}}$  is 1 s, so for the beam for measurement with pulse width of 0.5–1 s, the formula 2 can be simplified as [5]

$$T = T_0 + 2 \frac{q''}{\lambda} \sqrt{a\tau} \frac{1}{\sqrt{\pi}} \quad (3)$$

By formula 3, the surface temperature rise of absorption plate of calorimeter depends on beam power and beam pulse width and physical parameters of target plate.

If the density of the deposited power was twice of the value of the average power per unit area, namely  $8.7 \text{ MW/m}^2$ , the temperature of the heat flux with different thickness (more than 15 mm) with the change of the pulse width time is shown in Fig. 3.

**Fig. 3** Temperature of the heat-loaded surface with different thickness



2. Plate of V shape

According to the requirements of physical properties, and the actual space allowance, target thickness, thermal expansion and contraction distance and beam transmission so far point of two targets point of contact should wait at the beam line factor were taken into account at the mean while, the shape of the calorimeter should design into by the two target plate splicing of V-shaped structures. This design can effectively increase the heat exchange area, and to multiple bounce absorption, reduce risk of ion sputtering rebound to other parts of the system. The open angle value of V-shaped structure is determined by the following formula:

$$P_b \times S = P_n \times (S \times \sin \alpha) \tag{4}$$

Here,  $P_b$  is the maximum power density that can withstand the target plate (assuming that the target plate is perpendicular to the beam),  $P_n$  is the peak power density for the deposition of the beam on the target plate,  $S$  is the area of the plate.

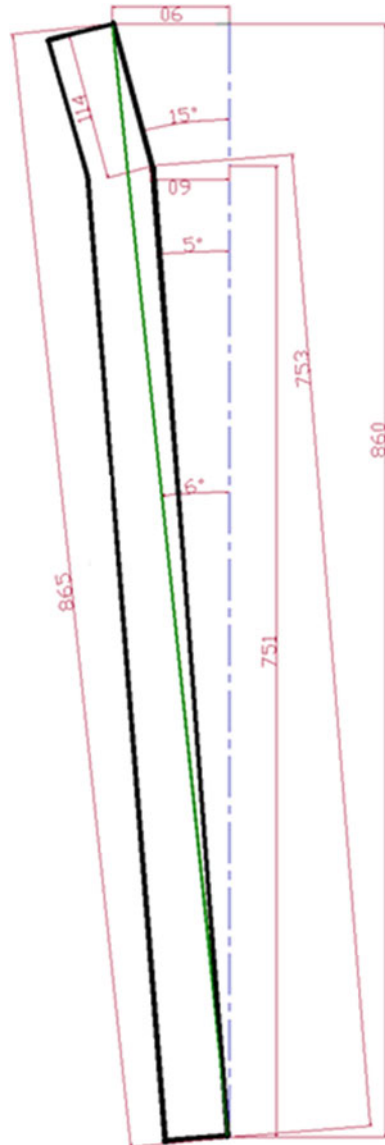
When the surface temperature reaches the soften, the temperature of the material of oxygen-free copper, the maximum heat flux deposited on the target plate surface is  $9.1 \text{ MW/m}^2$  with the pulse length of 1 s. The size of the beam extraction section is  $120 \times 480 \text{ mm}^2$ , and set 90 % of the extraction power about 4 MW was deposition in the target plate, so the peak power density under the average distribution of beam bombardment is  $42 \text{ MW/m}^2$  [6]. Then according to the V-shaped structure of the opening angle formula 4,  $\alpha$  can have maximum value  $12.5^\circ$  and the length of the plate along the beam direction is 405 mm.

Because of constant beam extraction section, the smaller the value of  $\alpha$  is, the smaller the maximum power density on the plate is. In the given space of the NBI system, the maximum length along the beam flow direction is 860 mm, the corresponding optimal angle of  $\alpha$  is  $6^\circ$  and the corresponding length is 865 mm, was



represented by the thin solid line in Fig. 4. In order to increase the heat exchange area in a limited space, as well as ensure an constant opening cross-section of  $180 \times 480$  mm, bending of the plate into 5 of  $\alpha$  and the angle between the plate and the center line is  $15^\circ$ , while ensuring that the length of the beam along the direction are the same, and ultimately design into V-shaped target plate structure, and identified by the solid line in Fig. 4. The actual length of the target plate is 867 mm.

**Fig. 4** Schematic diagram of V-shaped target board design



### 3. Cooling water flow

According to the principle of inertia cooling, assuming the energy is totally taken away by the cooling water, the maximum value of cooling water flow can be obtained according to the heat conduction and convection heat transfer mechanism. As requirements of the function, in order to get the energy deposited on the calorimeter, the cooling water circuit inside the two plates of V shape in one beamline should be connected in parallel to solve the whole, and the total inlet flow rate of cooling water can be expressed as

$$Q_{\text{total}} = q' \tau / (C_p \rho \Delta T t) \quad (5)$$

Here,  $q'$  is deposited power, be set to 1.2 MW (30 % of the extraction power of 4 MW),  $C_p$  is the specific heat of water and  $\rho$  is the density of water.  $\tau$  is the heating time in the pulse length and  $t$  is the cooling time of cooling water.

By formula 5, set 90 % of the extraction power about 4 MW was deposition in the target plate, measuring time was 1 s, and cooling time was 10 s, the total inlet flow rate of single plate for V-shaped calorimeter was 0.7 L/s.

### 4. Inner diameter and arrangement of cooling water pipe in target plate

In order to accurately show the accurate heat deposition value on the plate, the cooling pipeline of the calorimeter is arranged in tandem arrangement, single plate has one inlet and one outlet, the average power density on the plate is

$$q'' = q' / S \quad (6)$$

Here,  $S$  is set as  $480 \times 867$  mm. The heat flux density on the surface of the plate is 2 times that of the average heat flux value, that is,  $8.7 \text{ MW/m}^2$ .

$$\begin{aligned} \text{Pr} &= \mu C_p / \lambda_f, \quad \text{Nu} = hd / \lambda_f \\ \text{Nu} &= 0.023 \text{Re}^{4/5} \text{Pr}^{1/3}, \quad \text{Re} = 4\rho Q_x / (\pi d \mu) \end{aligned} \quad (7)$$

Here,  $d$  is the branch pipe diameter,  $C_p$  is the specific heat,  $\mu$  is dynamic viscosity coefficient,  $\lambda_f$  is thermal conductivity and  $\rho$  is the density of the water at the average temperature of  $60 \text{ }^\circ\text{C}$  under  $0.7 \text{ MPa}$  [7].

Assuming thermal energy was completely by taken by the cooling water inside the plate, and the wall temperature of the tube that direct contact with the cooling water should not exceed the saturation temperature under given pressure ( $438.1 \text{ K}$  corresponding to  $0.7 \text{ MPa}$ ), inlet temperature is equal to the total inlet temperature and set as  $30 \text{ }^\circ\text{C}$ , the outlet temperature was set according to the temperature rise of  $60 \text{ }^\circ\text{C}$ , so the qualitative temperature of cooling water is  $60 \text{ }^\circ\text{C}$ . At the temperature, the density of cooling water is  $983.2 \text{ kg/m}^3$ , kinematic viscosity is  $4.74 \times 10^{-7} \text{ m}^2/\text{s}$  thermal conductivity is  $0.644 \text{ W/(m K)}$ . By formula 7, we get  $L/d^{0.8} = 0.56$ .

According to the construction requirement of the cooling water circulation system, the maximum water supply pressure should not exceed  $0.7 \text{ MPa}$ , and back

pressure should at least 0.1 MPa reservation, so the corresponding maximum pressure drop is 0.6 MPa, the equivalent roughness of the inner wall of the cooling pipe is 0.1 mm. Assumed the pressure loss along the path is the same as the local pressure loss, and should not more than 0.3 MPa. As a result, the distance of the flow water in the plate is 1.9 m at least, the maximum flow rate is 31.7 m/s, the smallest diameter is 4.8 mm (set as 5 mm), the longest single row of tube is 800 mm, and at least two rows of layout.

Based on the above design process, the structure of calorimeter of EAST-NBI should meet the following sets: the length of single target plate is 867 mm, with width of 480 m and thickness of 15 mm at least. The layout of the cooling water tube is at least two rows, with minimum diameter of 5 mm for single tube. The opening angle of the V-shaped structure is  $5^\circ$ , and the plate was bending by angle of  $15^\circ$  with the center line. During practical manufacture process, in order to make the temperature more uniform after cooling, the number of row of cooling water tubes was increased into 18 within the width of the plate allowed.

## 4 Numerical Simulation

On the basis of the preliminary design of the target plate structure, the heat flow coupling analysis and optimization of the EAST-NBI calorimeter is carried out. Taking the following assumptions into account in the analysis on heat flux of coupled heat transfer in turbulent developing tube flow: (1) this section, the physical model only considers the target plates of the calorimeter, and the two plates are completely symmetrical; (2) the cooling water flow is incompressible flow; (3) the distribution of the entrance velocity and the inlet temperature is uniform; (4) the liquid boiling does not occur in the whole flow path; (5) Calorimeter is disposed in a vacuum chamber, regardless of the influence of radiation between the various power components within the NBI; (6) only the inner surface of the calorimeter under ion bombardment, in addition to the heat flow deposition surface has the energy deposition, the rest of the surface are adiabatic, no energy transfer abroad [4]; (7) the initial target plate temperature is the same with the space environment temperature.

In order to facilitate the software of fluent on the heat flow coupling analysis and optimization of the EAST-NBI calorimeter, the initial design of the calorimeter structure is simplified using internal hole instead of slot welding, neglecting the thermal contact resistance between the pipe and the copper, the main part of copper plate using the T-Grid mesh, the fluid region using the hex copper grid, the specific tube arrangement and mesh as shown in Fig. 5.

Thermodynamic parameters of oxygen-free copper were as follows: the specific heat is 390 J/kg K, the density of is 8930 kg/m<sup>3</sup>, the maximum surface temperature is 573 K (300°).

Assuming that deposited power on the calorimeter is the average distribution of peak power, the results were got and shown in Fig 6 by calculation. When the

**Fig. 5** Schematic diagram of the water pipe structure of the calorimeter plate in the Gambit

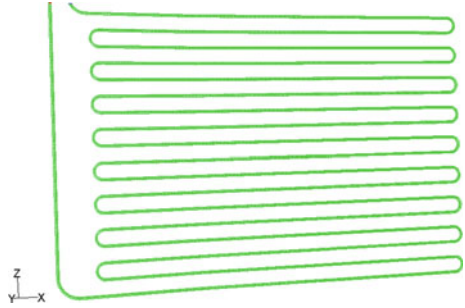
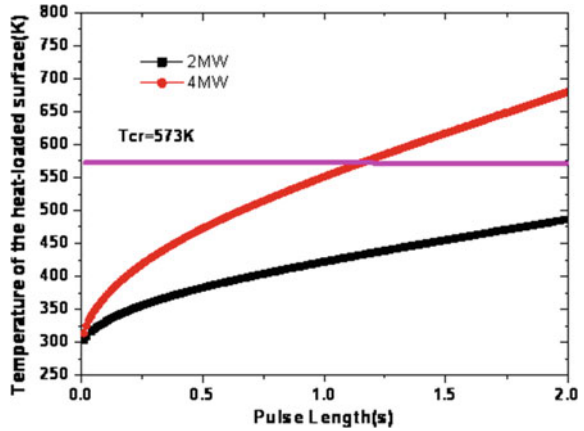


**Fig. 6** Curves of heat flux surface temperature with working pulse time under different beam extraction power conditions



extracting beam power is 2 MW, the longest working time for oxygen-free copper is more than 2 s by checking the maximum temperature with the softening temperature of the material, and when the power is 4 MW, the longest working time is 1.16 s, is higher than the design value of 0.5 s. Therefore, the preliminary design of the structure can better satisfy the basic physical design requirements.

## 5 Conclusions

The calorimeter is using for absorption and measurements of beam energy, and provide related measurement methods, the component design besides to meet the basic functional requirements must also be has better heat transfer ability, in order to avoid poor cooling effect, thermal stress and even functional component failure caused by a large number of high-energy particle deposition, to ensure the system to run for a long time.

In this paper, the physical characteristics and engineering design factors of components was considered in the preliminary design of the structure: the length of

single target plate is 867 mm, with width of 480 mm and thickness of 15 mm at least. The layout of the cooling water tube is 18 rows, with minimum diameter of 5 mm for single tube. The opening angle of the V-shaped structure is  $5^\circ$ , and the plate was bending by angle of  $15^\circ$  with the center line. The calculation of surface softening temperature was carried out from the point of view of numerical heat transfer, by assuming that deposited power on the calorimeter is the average distribution of peak power, and results show the primary structure of the primary structure was suitable for the basic thermodynamic requirements of the target plate. This paper provides reference for the design of other typical high-heat flux components, which provides a reference for the safe and stable operation of EAST-NBI system.

**Acknowledgments** This paper is supported by the Science Foundation of Institute of Plasma Physics, Chinese Academy of Sciences (DSJJ-15-GC02) and the National Natural Science Foundation of China (11605234).

## References

1. Zhu Shiyao. Principle of nuclear fusion [M]. Hefei: University of Science & Technology China press, 1992
2. Hu Chundong, Yuan Lai Xie, Ya Hong Xie. East long pulse development of neutral beam injector// Proc of Chinese Nuclear Society editor. China Nuclear Science and technology progress report: China Nuclear Society 2009 academic year will be the set. Beijing: Atomic Energy Press, 2009, 1 (6): 31–36
3. Liang Lizhen, Hu Chundong, Xie Yuanlai, et al. Calculation of beam intensity distribution for the neutral beam injection in EAST [J]. Plasma Science and Technology, 2011, 13(4): 502–505
4. Wang Fujun. The principle and application of computational fluid dynamics [M]. software - CFD Beijing: Tsinghua University press, 2004
5. Hong R, Colleratine A. Power flow measurements on the doublet neutral beam system [J]. Bulletin of the American Physical Society, 1982, 27: 11409–11412
6. Tao Ling. Design and research of high heat flux components in the long pulse high power neutral beam injection system [D]. Hefei: University of the Chinese Academy of Sciences, 2013
7. Tao Ling, Hu Chundong, Xie Yuanlai, et al. Engineering design of ion dump for EAST neutral beam injection system [J]. High Power Laser and Particle Beams, 2013, 25(10): 2687–2691 (in Chinese)

# Study of the Tritium Breeding Blanket in an Hybrid Fusion–Fission Transmutation System

Juan-Luis François, Cecilia Martín-Del-Campo and Aldo Fierro

**Abstract** The reactor studied in this work is the hybrid fusion–fission transmutation system (FFTS), which is a fusion–fission hybrid reactor with a central compact fusion neutron source (CFNS). It is based on the Tokamak concept, and it is surrounded by a zone made of transuranic elements obtained from reprocessing and recycling of spent fuel of light water reactors. High-energy neutrons, of fourteen MeV, are generated in the CFNS; they are produced by the deuterium–tritium reaction. In this study, the MCNPX Monte Carlo code was used to build up a model of the FFTS for studying the tritium breeding capability of the system. Tritium is produced from neutron capture in lithium, which is located in blankets specifically designed for this purpose. The tritium breeding ratio (TBR) is defined as the average number of tritium atoms bred per tritium atom burnt in the deuterium–tritium reaction. We must have  $TBR > 1$ , for a self-sustained fusion economy. In the first step of this work, the location of the lithium blankets was defined. Afterwards, different blanket materials were tested: natural lithium, enriched lithium in  ${}^6\text{Li}$ , different lithium alloys with neutron multipliers like lead and beryllium [ $\text{Li}_4\text{SiO}_4$ ,  $\text{LiTiO}_3$ ,  $\text{FLiNaBe}$ ,  $\text{FLiBe}$ ,  $\text{Pb-15.8Li}$  (Li-6 at 90 %)]. Finally, a study was carried out to determine the relationship between the width of the blanket and the tritium breeding. Concerning the blanket locations, we defined four: one in the central column of the FFTS, one in the upper and one in the bottom part of the fusion region of the system, and the last one in the external part of the fission region. This means that the first three blankets use high-energy neutrons from the deuterium–tritium reaction, and the fourth blanket uses neutron leaking from the fission reactions. The principal results show that the best option is the blanket with  $\text{Pb-15.8Li}$  with lithium enriched at 90 % in lithium-6 with  $TBR = 1.09$ . It was found that the blanket at the external part of the fission region has the higher tritium breeding capability. Regarding the blanket width, it was observed that most of the tritium breeding is carried out in the first 5 cm of the blanket, and beyond this width breeding is minimal; therefore, for the blanket it is more important to have a high view factor to neutrons (i.e., a big surface exposed to neutrons) than a deep region.

---

J.-L. François (✉) · C. Martín-Del-Campo · A. Fierro  
National Autonomous University of Mexico, Mexico, Mexico  
e-mail: juan.luis.francois@gmail.com

Finally, it is important to mention that the FFTS was critical during 1000 days that were simulated with MCNPX.

**Keywords** Hybrid fusion–fission • Compact fusion neutron source • Tritium breeding • Tritium blanket • Monte Carlo method

## 1 Introduction

Nowadays, investigations are under way with the goal of transmuting long lived isotopes from LWR spent fuel. One of them is related to the hybrid fusion–fission transmutation system, FFTS [1]; which has been theoretically designed based on experimental fusion reactors. The reactor analyzed in this investigation uses high energy neutrons obtained from the deuterium–tritium fusion reaction. The neutron source is in the center of FFTS, and is surrounded by a fuel region where the fissions occur.

The MCNPX (Monte Carlo N-Particle extended, version 2.6.0) [2] code was utilized in this study to build-up a model of the FFTS in order to analyze the tritium breeding capabilities in this type system. In Sect. 2, the description of the FFTS and the developed model are presented. The different study cases and the obtained results are showed in Sect. 3; and, finally, the conclusions are presented in Sect. 4.

## 2 Hybrid Fusion–Fission System

Since more than fifty years the development of thermonuclear fusion reactors has been underway with the hope of having a clean and sustainable source of energy. Nevertheless, the deployment of these systems has been very slow because of their complexity. Nowadays, the Tokamak fusion reactor is the most studied fusion technology; meanwhile the hybrid fusion–fission systems seem to be a more feasible technological option.

### 2.1 System Description

The FFTS is a concept proposed by the Institute for Fusion Studies, of the University of Texas at Austin, in 2009 [1], focused on the destruction of transuranic nuclear waste. The FFTS is a fusion–fission hybrid reactor with a central compact fusion neutron source (CFNS). It is based on the Tokamak concept, and it is surrounded by a zone made of transuranic elements obtained from reprocessing and recycling of spent fuel of light water reactors (see Fig. 1); this is a subcritical fission device. The fission zone can loaded with MOX (Mixed OXide) fuel.

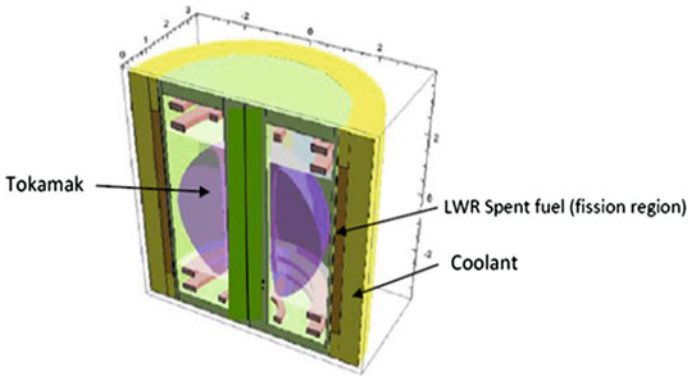
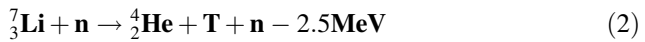


**Fig. 1** Fusion fission transmutation system

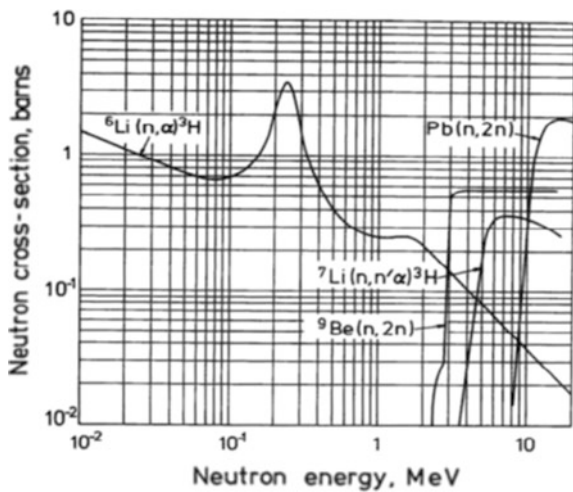
High energy neutrons, of fourteen MeV, are generated in the CFNS. They are produced by the deuterium-tritium reaction. The plasma in stable operation, inside the CFNS, forms a toroid (see Fig. 1).

Tritium is produced from neutron capture in lithium [through reactions (1) and (2)], which is located in blankets specifically designed for this purpose.



Reaction (1) is more likely to happen due to the highest neutron capture cross section of  ${}^6\text{Li}$  than  ${}^7\text{Li}$ , as can be seen in Fig. 2.

**Fig. 2** Capture cross section of selected isotopes [4]





The tritium breeding ratio (TBR) is defined as the average number of tritium atoms bred per tritium atom burnt in the deuterium-tritium reaction. We must have  $TBR > 1$ , for a self-sustained fusion economy.

Table 1 shows the materials of the fusion–fission system used in this study.

## 2.2 Fuel Description

In this work, the utilization of reprocessed fuel in the FFTS was studied in the form of (MOX). In our MCNPX model, the fuel and the sodium (coolant) were homogeneously mixed in rings (annular regions). This is a good approximation in fast reactors where the neutrons mean free path is large, compared with LWR. Table 2 shows the composition of the fuel-coolant. The MOX composition was obtained from [3]. This is a typical composition of the actinides obtained from the recycling of spent fuel from a boiling water reactor with a discharge burn-up of 48,000 MWd/t. For the MOX fuel, actinides were mixed with depleted uranium of 0.25 w/o, obtained from the tails of the enrichment process.

**Table 1** Materials description of the FFTS [1]

Structure	Material/density
Central column	Lead/11.34 g/cm <sup>3</sup>
Plasma	Deuterium-tritium/ $1.3 \times 10^{20}$ cm <sup>-3</sup>
Source	Neutrons (14 meV)
Void	O (21 %)-N (79 %)/ $1 \times 10^{-20}$ g/cm <sup>3</sup>
Coolant	Sodium/0.9291 g/cm <sup>3</sup>
Fuel	MOX (Table 2)
External cover	Lead/11.34 g/cm <sup>3</sup>

**Table 2** Fuel-coolant composition

MOX (at/b-cm)
<sup>235</sup> U/ $5.42 \times 10^{-5}$
<sup>238</sup> U/ $2.142 \times 10^{-2}$
<sup>238</sup> Pu/ $8.335 \times 10^{-5}$
<sup>239</sup> Pu/ $1.51 \times 10^{-3}$
<sup>240</sup> Pu/ $7.86 \times 10^{-4}$
<sup>241</sup> Pu/ $3.10 \times 10^{-4}$
<sup>242</sup> Pu/ $2.38 \times 10^{-4}$
<sup>237</sup> Np/ $1.70 \times 10^{-4}$
<sup>241</sup> Am/ $1.43 \times 10^{-4}$
<sup>243</sup> Am/ $5.93 \times 10^{-5}$
<sup>244</sup> Cm/ $1.96 \times 10^{-5}$
<sup>16</sup> O/ $4.95 \times 10^{-2}$
<sup>23</sup> Na/ $2.541 \times 10^{-2}$

### 2.3 Model

Simulations were carried out with the MCNPX-2.6.0 code. A total of one million neutron histories were simulated (5000 neutrons per cycle  $\times$  200 active cycles). Figs 3 and 4 show the MCPX model of the FFTS, the cross section and the lateral view, respectively. This is an approximate model where some structures (cables, detectors, etc.) are not modeled. From the center to the periphery the following elements can be identified: the central column (dark blue), surrounded by a void region (yellow), then the plasma (green), with the neutron source inside (in light blue). Afterwards, a void region surrounds the source (yellow). Then, the fuel region (in red) surrounded by a coolant zone (in orange), and finally the reflector (dark blue).

Based on this FFTS base model, four regions of lithium blankets were defined (see Fig. 5): one in the central column, one in the upper and one in the lower part of the fusion region of the system, and the last one in the external part of the fission region. This means that the first three blankets use high energy neutrons (14 meV) from the deuterium-tritium reaction, and the fourth blanket uses neutron leaking from the fission reactions (lower energy: 2 meV).

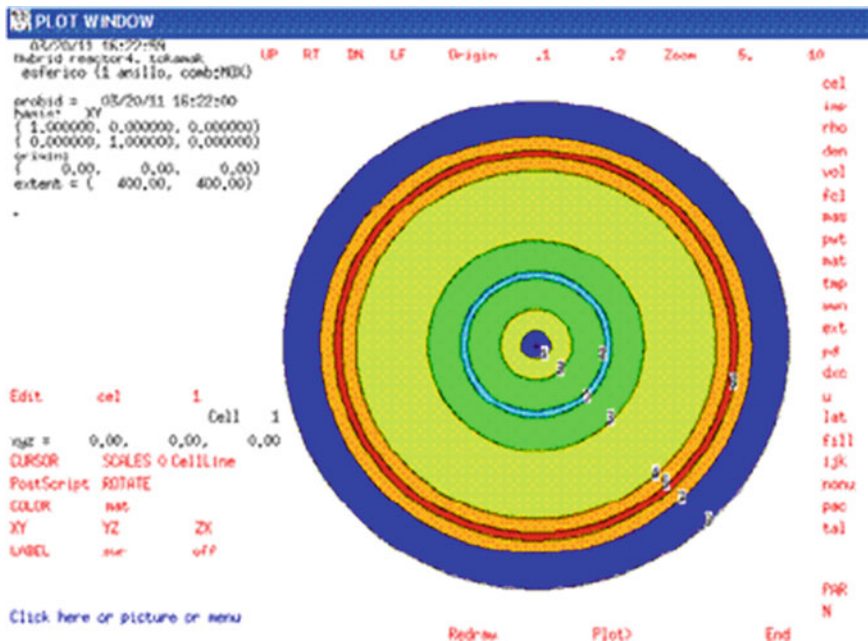


Fig. 3 Cross-sectional view of the MCNPX model (color figure online)

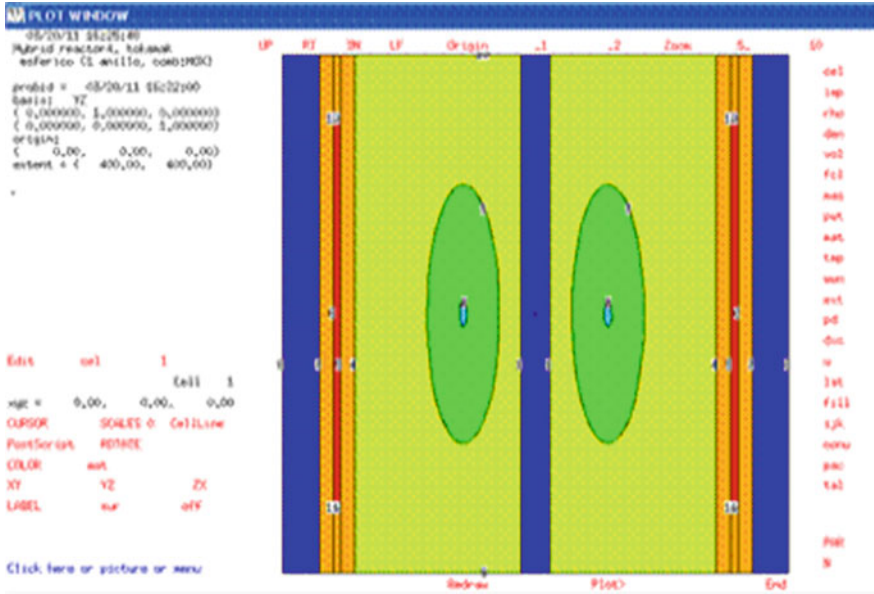
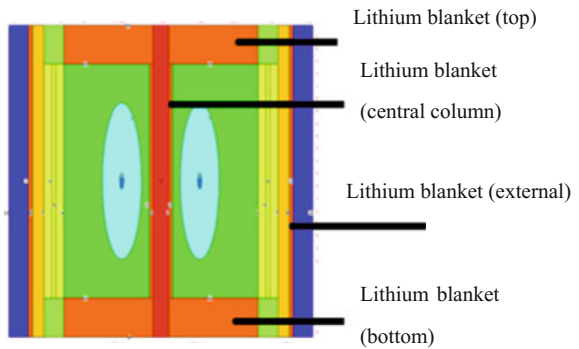


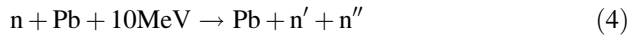
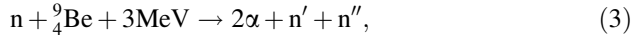
Fig. 4 Lateral view of the MCNPX model (color figure online)

Fig. 5 Lateral view of the MCNPX model with four regions of lithium blankets



### 3 Study Cases

Different blanket materials were tested: natural lithium ( ${}^6\text{Li}$ : 7.5 %,  ${}^7\text{Li}$ : 92.5 %), enriched lithium ( ${}^6\text{Li}$  at 90 %), different lithium alloys with neutron multipliers like lead and beryllium ( $\text{Li}_4\text{SiO}_4$ ,  $\text{LiTiO}_3$ ,  $\text{FLiNaBe}$ ,  $\text{FLiBe}$ ,  $\text{Pb-15.8Li}$ ). As their name suggests it, multipliers allow to produce more neutrons (that will be available for tritium breeding) through reactions like the following:



The neutron capture cross sections for Pb and  ${}^9\text{Be}$  are depicted in Fig. 2.

### 3.1 Results

Fig 6 shows the mass (grams) of tritium produced after 1000 days of operation of the FFTS for the studied blanket. Table 3 presents also the mass and the TBR as well. The effective neutron multiplication factor (at beginning of life) is also showed in this table, and it is worthy to say that the system remains critical along the 1000 days of operation for all the cases, as can be seen in Fig. 7, for the case with the Pb-15.8Li (Li-6 at 90 %) blanket, which was the case with better performance regarding tritium breeding.

Regarding the tritium production, it was found that, by far, the blanket at the external part of the fission region has the higher tritium breeding capability, as can be seen in Table 4 for the best case: Pb-15.8Li (Li-6 at 90 %). This can be due to the fact that the neutrons arriving at this region have lower energy (2 meV aprox.)

**Fig. 6** Mass of tritium produced

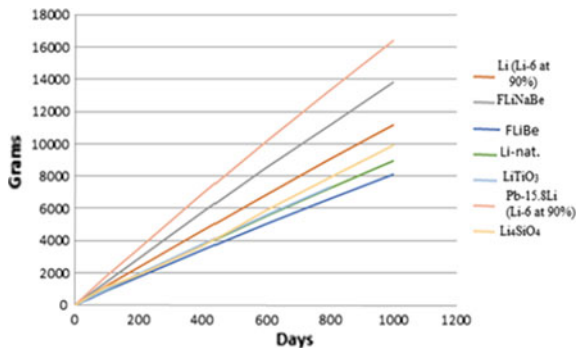


**Table 3** Results obtained for the studied blankets

Case	Blanket	K-eff (bol)	Tritium Prod. (g)	TBR
1	Li (natural)	1.06183	8742.2	0.582
2	Li (Li-6 at 90 %)	1.05687	11120.0	0.741
3	Li <sub>4</sub> SiO <sub>4</sub>	1.06268	9926.4	0.661
4	LiTiO <sub>3</sub>	1.06701	9167.5	0.611
5	FLiBe	1.06159	8120.0	0.541
6	FLiNaBe	1.03174	13785.2	0.919
7	Pb-15.8Li (Li-6 at 90 %)	1.00705	16381.2	1.092

than those that arrive to the other regions (14 meV approx.), and capture cross section of  ${}^6\text{Li}$  is higher at lower energy of the neutrons (see Fig. 2).

Concerning the relationship between the width of the blanket and the tritium breeding, a study was performed in which the total width of the external region of the best case: Pb-15.8Li (Li-6 at 90 %) was divided in 15 layer of 1 cm width each layer. The result is showed in Fig. 8, where it can be noticed that just with the first five layers the 90 % of the tritium is produced. Therefore, for the blanket it is more important to have a high view factor to neutrons (i.e., a big surface exposed to neutrons) than a deep region.

**Fig. 7** K-effective for the case with the Pb-15.8Li (Li-6 at 90 %) blanket

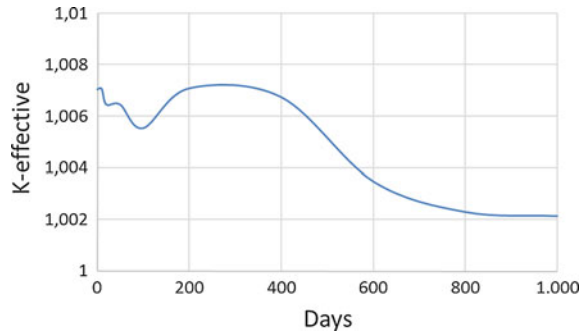
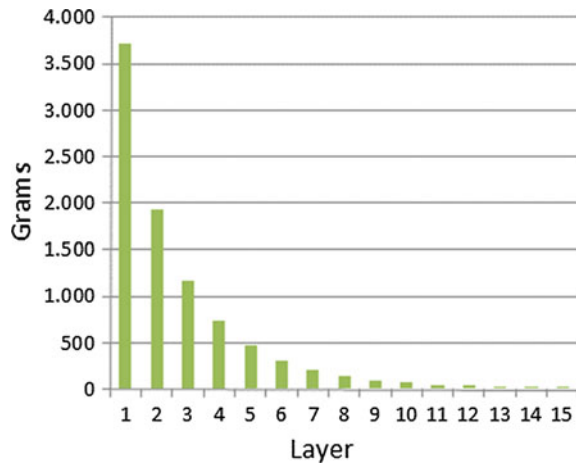


**Table 4** Tritium production by blanket region

Blanket region	Tritium production (g)	%
Central column	2028.85	12.4
Top	2688.34	16.4
Bottom	2688.34	16.4
External	8975.67	54.8

**Fig. 8** Tritium production in function of the blanket layer



## 4 Conclusions

With the development of a relatively simple model with MCNPX, interesting results were obtained for the study of the tritium breeding capabilities in a hybrid fusion–fission system.

Among the studied blankets, it was found that the best option was the blanket with Pb-15.8Li with lithium enriched at 90 % in lithium-6, with a TBR = 1.09. It was also found that the blanket at the external part of the fission region has the higher tritium breeding capability; this is explained by the fact that the neutrons arriving at this region have lower energy than those that arrive to the other regions.

Regarding the blanket width, it was observed that most of the tritium breeding is carried out in the first 5 cm of the blanket, and beyond this width breeding is minimal; therefore, for the blanket it is more important to have a high view factor to neutrons (i.e., a big surface exposed to neutrons) than a deep region.

## References

1. Kotschenreuther, M., Valanju, P.M., Mahajan, S.M., Schneider, E.A., “Fusion–Fission Transmutation Scheme - Efficient destruction of nuclear waste”, *Fusion Engineering and Design*, Vol. 84, 2009, pp. 83–88
2. Pelowitz, D. B., *MCNPX User’s Manual Version 2.6.0*, Los Alamos National Laboratory, Report LA-CP-07-1473, April, 2008
3. Guzmán, J. R., “Diseño y Optimización de Combustible Nuclear para el Reciclado de Combustible Gastado en Reactores de Agua en Ebullición”, Ph.D. Thesis, National Autonomous University of Mexico, 2008
4. JASON, “TRITIUM”, The MITRE Corporation, Report JSR-11-345, November, 2011

# Tagged Neutron Method Analysis: A Technique for Explosives Detection and Identification

Shi-wei Jing, Gui-fu Yang, Yong Guo, Huan-yu Li, Xuan Liu,  
Yan Zheng, Yu-lai Zheng, Qiang Wang and Guo-bao Wang

**Abstract** A laboratory prototype of the device for detection and identification of explosives hidden in luggage has been investigated. The device is based on the Tagged Neutron Method (TNM) by using D-T neutron generator. The unique advantage of the TNM method is to provide the image of the hidden object in three-dimension. At the same time, a large signal-to-background ratio provided by the TNM method significantly facilitates the identification of the hidden substances. The method of spectra analysis in our device is based on sequential analysis. In statistics, sequential analysis is statistical analysis where the sample size is not fixed in advance. Instead data is evaluated as it is collected, and further sampling is stopped in accordance with a predefined stopping rule as soon as significant results are observed. Thus a conclusion may sometimes be reached at a much earlier stage than would be possible with more classical hypothesis testing or estimation. It has been shown that explosive simulants of TNT and ammonium nitrate (300 g, respectively) shielded by 5 cm of dry milk powder or washing powder can be detected within 3 min. The type of explosives (TNT or ammonium nitrate) can be identified within 10 min.

**Keywords** Tagged neutron method (TNM) · D-T neutron generator · Explosives · LYSO detection system · Sequential analysis

---

S. Jing (✉) · Y. Zheng · Q. Wang · G. Wang  
China Institute of Atomic Energy, Beijing, People's Republic of China  
e-mail: jingsw504@nenu.edu.cn

S. Jing · G. Yang (✉) · H. Li · X. Liu · Y. Zheng  
Northeast Normal University, Jilin Changchun, People's Republic of China

Y. Guo  
Sichuan Police College, Sichuan Luzhou 646000, People's Republic of China  
e-mail: 953212427@qq.com

## 1 Introduction

The illicit trafficking of explosives through the conventional commercial networks (air, maritime and terrestrial) represents a real problem in preventing terrorist actions against civil populations and requires the development of large commercial payloads. There exist some explosive detection methods such as metal detection, neutron, X or gamma ray, electromagnetic, nuclear electric quadrupole moment, molecular particle, electrochemical, laser, terahertz [1–14].

Explosives (TNT, ammonium nitrate, etc.) are composed primarily of the chemical elements hydrogen, carbon, nitrogen, and oxygen. Compared with the commonly used X or gamma ray techniques, neutron technique is based on the principle that neutron can react with these elements and characteristic gamma rays become the symbol of the material. Although many innocuous materials are also primarily composed of these same elements, these elements are found in each material with very different elemental ratios and concentrations. It is thus possible to identify and differentiate, e.g., TNT from paraffin.

The main problem encountered in the nondestructive analysis of materials by neutron methods is a very high counting rate in the secondary radiation detection channels, caused by interaction of probing neutrons with the materials of the neutron source, the inspected object, and the materials of the environment. When the materials (e.g., sugar, melamine) with similar elemental ratio of C, O, N to explosives are placed with explosives, it is hard for a system to distinguish them. The false alarm rate would be very high.

The resulting very high level of background has until recently ruled out a wide use of neutron-based methods for detection of small amounts of hazardous materials hidden among other objects in passenger luggage, cargo containers, etc. The TNM [15–22] technique uses fast monochromatic neutrons with energy of 14.1 MeV produced in binary reaction  $d + t \rightarrow {}^4\text{He} + n$ . In this reaction, the  $\alpha$ -particle with the energy of 3.5 MeV flights back-to-back with the neutron (in c.m. system). By measuring the  $\alpha$ -particle trajectory the direction of the corresponding neutron is determined. These “tagged” neutrons interact with the interrogated object and can produce  $\gamma$  quanta in  $A(n, \gamma)A'$  reactions with energy spectra which are unique for each chemical element in the object. The characteristic  $\gamma$ -spectra could serve as “fingerprints” to identify the hidden substance. The prototype system has been developed using TNM technique. The choice of neutron generator and gamma detector, experimental setup design, data acquisition, algorithm study, and the measurement results are present in this paper.



## 2 Experimental Setup

### 2.1 The Choice of Neutron Source and Gamma Detector

The neutron generator and gamma detector are the key point of the TNM system. The ING-27 neutron generator produced by VNIA has the property of high output, long lifetime, and stable operation. The ING-27 neutron generator with nine  $10 \times 10$  mm  $\alpha$  detectors, which is 6.2 cm far from the target of the neutron generator, so the geometrical efficiency is about 0.2 %. The intrinsic efficiency for  $\alpha$  particle with 3 meV is about 100 %. The maximum neutron output is  $7 \times 10^7$  n/s and the suitable output can be adjusted during operation according to the experimental condition.

The characteristic  $\gamma$  rays of element C, O, N, through inelastic scattering reactions are registered by the LYSO detector with the scintillator of  $\phi 76$  mm and thickness 76 mm. Compared with NaI (Tl) and BGO detector, LYSO has higher energy resolution, higher efficiency at high energy, short light time and higher light output; compared with LaBr<sub>3</sub> (Ce) detector, the price of LYSO detector is relatively lower. The energy resolution of the gamma detector is 8 % at  $E_\gamma = 0.511$  MeV. The time resolution of the  $\alpha$ - $\gamma$  system is determined in the experiments with tagged neutron beam irradiating of  $142 \times 102 \times 65$  mm graphite block. The time resolution of the  $\alpha$ - $\gamma$  coincidence is about 1.7 ns. It determines mainly by the LYSO as the slowest element.

### 2.2 The Design of the Fast Electronics Coincidence Circuit

The localized suspected zone can be detected by  $\alpha$ - $\gamma$  coincidence method. The principle of  $\alpha$ - $\gamma$  coincidence was shown in Fig. 1. During the period of  $\alpha$ - $\gamma$  coincidence, by adjusting the delayed time  $t_6$ , the relation  $t_1 + t_2 + t_3 = t_4 + t_5 + t_6$  applied, where  $t_1$ : the time between the moment that a neutron produced and the moment that gamma ray produce;  $t_2$ : the time after the gamma ray is absorbed by gamma detector;  $t_3$ : the electronic time of gamma detector;  $t_4$ : the time between the moment that  $\alpha$  particles produce and the moment that they are absorbed by  $\alpha$  detector;  $t_5$ : electronic time of  $\alpha$  detector;  $t_6$ : the delayed time of delayed circuit. The parameters such as the speed of light (30 cm/ns), the distance between the sample and the neutron source, the speed of neutron (about 5.4 cm/ns for 14 meV), the speed of  $\alpha$  particle (3.5 meV), the distance between the target and the  $\alpha$  detector are known beforehand, so the  $t_1, t_2, t_4$  can be determined;  $t_3, t_5$  are the intrinsic time of gamma and  $\alpha$  detector, respectively. By adjusting the delayed time  $t_6$ , the coincidence detection can be realized. The time relation is shown in Fig. 1.

The electronics system for measurement is shown in Fig. 2. The procedure is like this: the fast signals from  $\gamma$  detector and  $\alpha$  detector pass through Constant Fraction Discriminator (CFD), served as the start signal and the stop signal for the

**Fig. 1** The time relationship of  $\alpha$ - $\gamma$  coincidence measurement

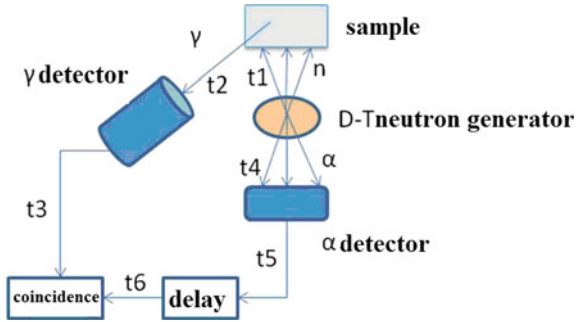
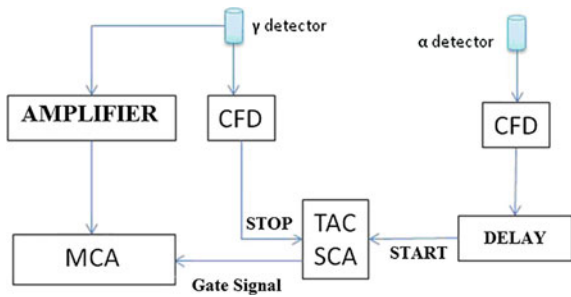


**Fig. 2** The electronics system of coincidence circuit



Time–Amplitude Converter (TAC), respectively. The output signal from TAC is then put into the Single Channel Analyzer (SCA). The upper and lower threshold of the SCA can be adjusted to make the peak of Time of Flight (TOF) in the spectrum. The output signal from SCA is served as the gate control for the Multichannel Analyzer (MCA). The MCA deals with the slow amplified signals from  $\gamma$  detector. After the logic procedure mentioned above, the spectra in MCA show the characteristic  $\gamma$  energy of elements of C, N, O, et al.

The schematic of the experimental setup is shown in Fig. 3. The main part of the equipment is like a big suitcase ( $93 \times 66 \times 47$  cm), composing of tagged particle neutron generator, LYSO detector, fast electronics with MCA, temperature control system. The suitcase main system is installed on a movable dolly, so it is easy to move the system to a suspicious luggage to detect. The control system (PC) is connected to the detection system through a network cable. Two  $\Phi 76$  mm  $\times$  76 mm LYSO detectors produced by Saint-Gobain Company were installed to two sides of the neutron generator. A block of iron 15 cm thickness is placed between the neutron source and the  $\gamma$ -ray detector. The distance between the interrogated object and gamma detector is varied within the range of 20–33 cm. The position of nine  $\alpha$  detectors is labeled as shown in Fig. 4, it is a view from a device in a direction to a sample under interrogation. The distance between the target and the outside of the luggage is 20 cm.

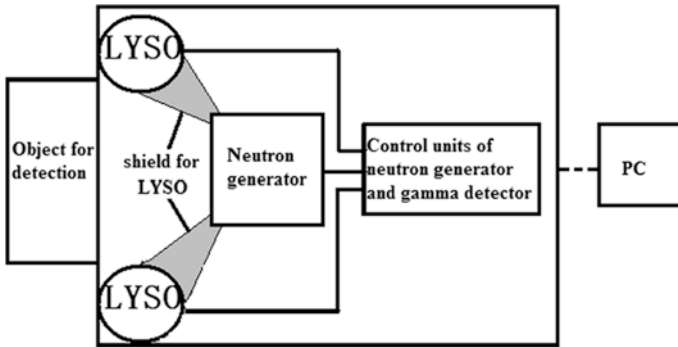
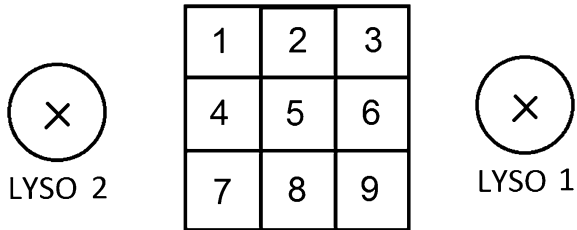


Fig. 3 The schematic of the experimental setup

Fig. 4 The label of  $\alpha$  and  $\gamma$  detectors



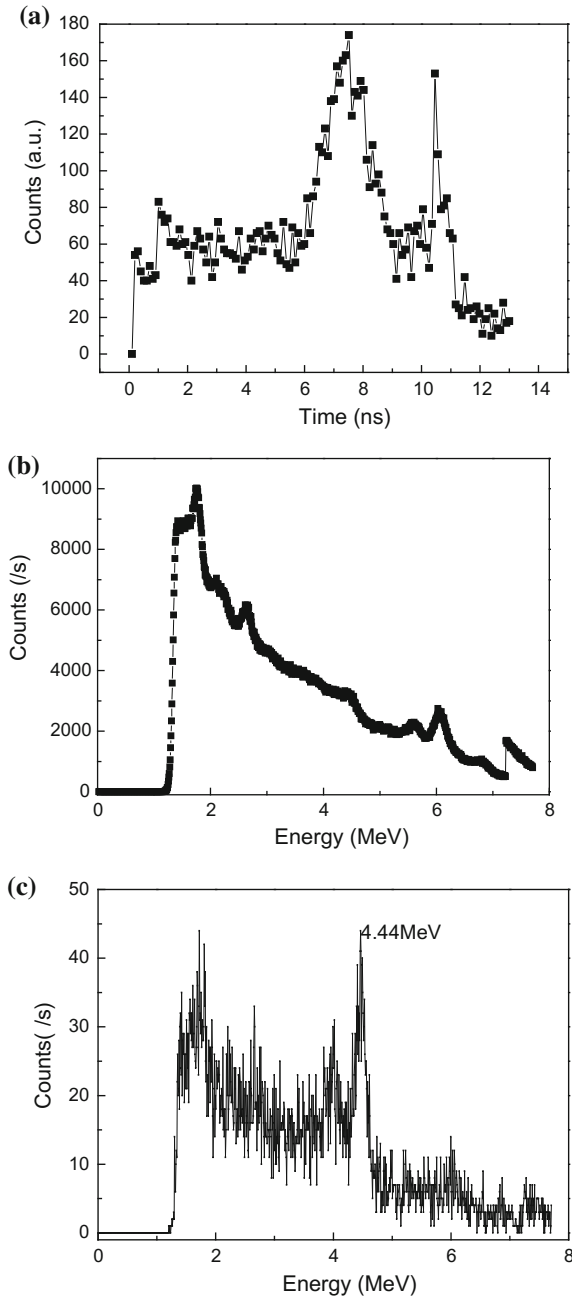
### 3 Experiment and Algorithm Study

#### 3.1 Time Calibration and Background Suppression

To illustrate the principal advantages of the TNM method, let us consider the time and energy distributions of characteristic gamma radiation from the interrogated substances, registered by the LYSO detector. A typical time-of-flight spectrum is shown in Fig. 5a. It has been collected for a sample of  $142 \times 102 \times 65$  mm graphite block, placed at 20 cm from the tritium target. The start of the time-of-flight measurement is given by the  $\alpha$  particle signal and the stop is given by the  $\gamma$  signal.

The two-peaks structure of the time spectrum superimposed on the flat background is clearly visible in Fig. 5a. The flat part of the spectrum corresponds to the accidental  $\alpha$ - $\gamma$  coincidences. The first peak corresponds to the detection of the prompt  $\gamma$  produced in the reactions  $A(n, n'\gamma)A$  for the interaction of the tagged neutrons with the sample. The second peak is caused by the neutrons scattered in the sample and detected by the LYSO counter later. The delay time of the second peak is about 4 ns. It corresponds to the time which is needed for a neutron to pass the distance of 20 cm between the sample and the detector with the velocity of 5 cm/ns. The clear separation of two peaks significantly improves the discrimination of the signal from the background. The Fig. 5b, c show the non-coincidence

**Fig. 5** The time and energy spectra of  $\alpha$ - $\gamma$  coincidence for graphite sample  
**a** time-of-flight spectrum;  
**b** non-coincidence energy spectrum;  
**c** coincidence spectrum



and coincidence  $\gamma$  energy spectra, respectively. One can see (Fig. 5c) a clear twin peak feature from the carbon line of 4.44 MeV with its single escape (SE). But the clear characteristic line of carbon shown in Fig. 5c cannot be seen in Fig. 3b because of the big background noise, which cannot be suppressed in no-coincidence circuit. This picture illustrates two main advantages of the TNM method. First, the knowledge of the time-of-flight provides the location of the spatial region under investigation. Second, the selection of the  $\alpha$ - $\gamma$  coincidences within a certain time interval drastically suppresses the background. Without the time selection the resulting  $\gamma$ -spectrum is superposition of the energy spectra from the interrogated substance (Fig. 5c) and the background from the scattered neutrons, like that shown in Fig. 5b. The background suppression is essential for enhancing the sensitivity needed to identify small mass objects.

### 3.2 *Some Typical Experimental Spectra*

To identify the hidden explosive the experiments are done as follows. First, the measurement of the background spectrum in the laboratory is performed. Second, the measurement of the reference spectrum of the not-shielded explosive is carried out. Third, the trial with the shielded investigated sample is performed. The process of identification is based on the comparison of the spectra of the investigated substances and the reference one.

The sample of 300 g TNT simulant ( $C_7H_5N_3O_6$ ) and 300 g Ammonium Nitrate ( $NH_4NO_3$ ) simulant is placed right in 5#  $\alpha$  pixel, respectively, which is 20 cm far from the front side of the system. The results of TNT and AMM (Ammonium Nitrate) are shown in Figs. 6 and 7, respectively. The characteristic  $\gamma$  spectra of C (4.44 MeV), O (6.13 MeV), and N (5.11, 2.31 MeV) are clearly shown in these figures. To demonstrate the potential of the method for identification of the explosives placed in between other objects, the sample of 300 g TNT was placed in a paper box of  $600 \times 400 \times 260 \text{ mm}^3$  which is 20 cm far from the tritium target. The width of the paper box along the neutron beam is 26 cm. Nine tagged neutron beams irradiate the paper box simultaneously. The sample is placed right in 5#  $\alpha$  pixel and behind 5 cm of dry milk powder and washing powder, respectively. The results are shown in Figs. 8 and 9. In general, the form of the difference spectrum depends on the difference between the chemical content of the hidden substance and the chemical content of the background substances such as dry milk powder and washing powder.

### 3.3 *The Method of Spectra Analysis*

The method of spectra analysis in our device is based on sequential analysis. In statistics, sequential analysis is statistical analysis where the sample size is not fixed

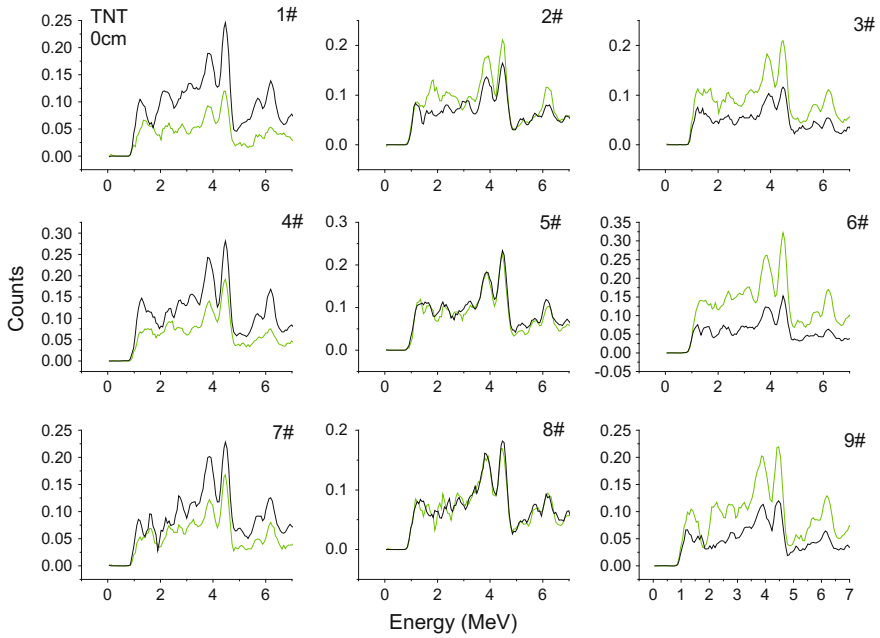


Fig. 6 The spectra of TNT sample by nine  $\alpha$  detectors and two  $\gamma$  detectors

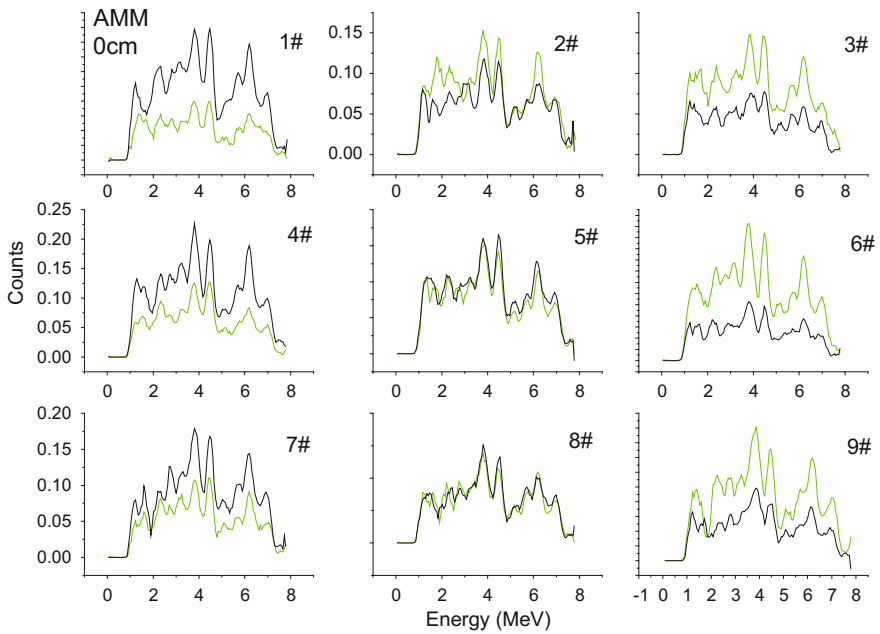
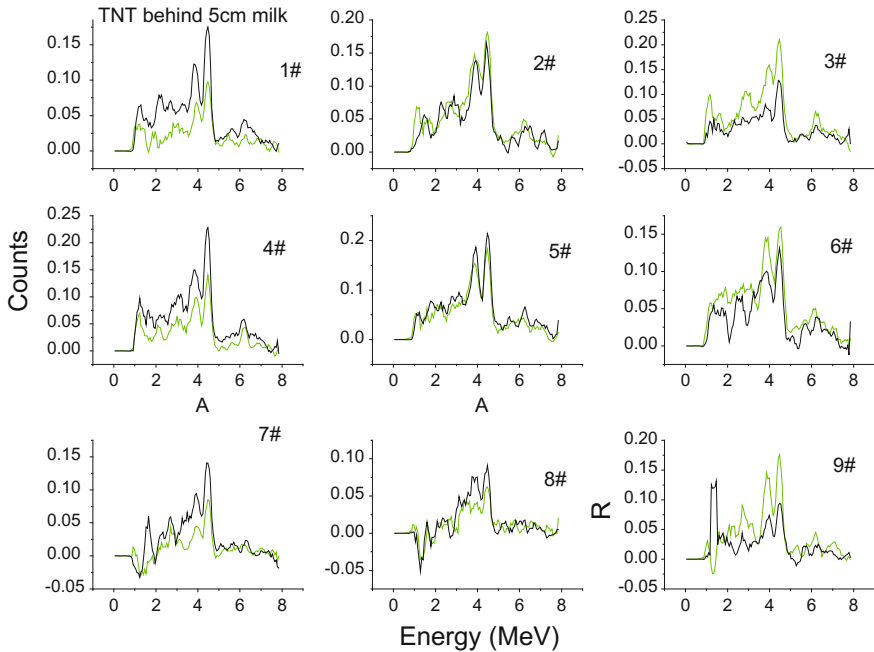


Fig. 7 The spectra of AMM sample by nine  $\alpha$  detectors and two  $\gamma$  detectors



**Fig. 8** The spectra of TNT sample behind 5 cm dry milk powder by nine  $\alpha$  detectors and two  $\gamma$  detectors

in advance. Instead data is evaluated as it is collected, and further sampling is stopped in accordance with a predefined stopping rule as soon as significant results are observed. Thus a conclusion may sometimes be reached at a much earlier stage than would be possible with more classical hypothesis testing or estimation.

Another key method is Pearson’s chi-squared test. It is a statistical test applied to sets of categorical data to evaluate how likely it is that any observed difference between the sets arose by chance.

First Step. Searching for space voxels filled with bulk.

Sequential analysis is used for searching bulk-containing space voxels. It is possible that several alpha-pixels would be just scanning empty space (if device is placed relative to a bag in a specific way). Or may be bulk is not filling all the distances device scans. We need to choose voxels filled with bulk.

It is done by two statistical hypothesis testing: hypothesis #1: spectrum looks like background one; hypothesis #2: spectrum looks like sum of background spectrum and pure spectrum of an explosive.

We have chosen voxels that more look like filled with bulk than empty ones (hypothesis #2). After that online background estimation starts.

Second step: Online background estimation.

Explosives have rather high density, which means that spectrum of an explosive would have much more counts (by any energies) than spectrum of any other

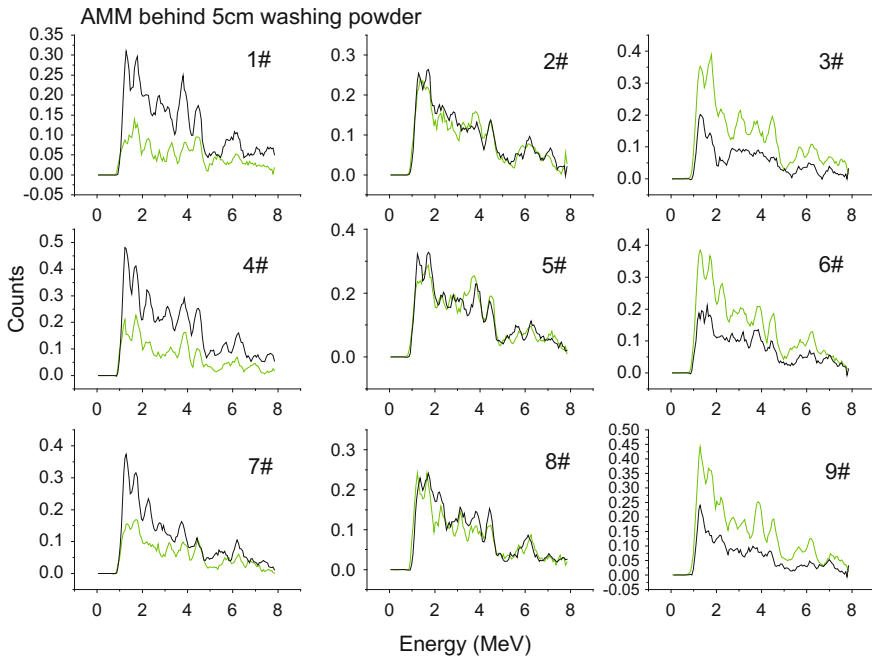


**Fig. 9** The spectra of AMM sample behind 5 cm washing powder by nine  $\alpha$  detectors and two  $\gamma$  detectors

popular substance (clothes, papers and so on). We need to find a voxel containing explosive by its high density. For that we estimate background spectrum for each voxel from the spectra of all the other voxels by recalculating them using specific factors (it is possible to calculate theoretical spectrum for one voxel using experimental spectrum of another one in assumption of uniform space filling). So, if there is a high density bulk in any voxel, it would be characterized by much more spectrum counts than it would be for uniform space filling case.

It is done by another two statistical hypothesis testing: hypothesis #1: spectrum looks like sum of background spectrum and estimated background (from the other voxels); hypothesis #2: spectrum looks like sum of background spectrum and pure spectrum of an explosive. This is done for all the voxels chosen in first step. Final (third) step starts only for those voxels that characterize by hypothesis #2.

Final step.

After voxels probably filled with bulk explosive have been chosen, Pearson's chi-squared test starts. It is used for comparison between measured spectrum and several library spectra (made a priori). If any voxels' spectra are similar to explosive ones than explosive is found, else not.



**Table 1** Detection results

Wrapping	Measurement types	Times of detection	Times of right result
Paper box	300 g TNT <sup>a</sup> behind 5 cm WP	10	10
	300 g TNT behind 5 cm Milk	10	10
	Only WP	5	5
	300 g AN behind 5 cm WP	10	9
	300 g AN behind 5 cm dry milk	10	10
	Only milk	5	5
Suitcase	Empty suitcase	5	5
	Suitcase full of sundries	5	5
	500 g AN in the suitcase full of sundries	10	10
	500 g TNT in the suitcase full of sundries	10	10

<sup>a</sup>TNT TNT simulant, AN ammonium nitrate simulant, WP washing powder, Milk dry milk

### 3.4 The Experimental Results

The experimental results are shown in Table 1. There are two experimental conditions. First, 300 g TNT and 300 g AMM simulant was placed in a paper box behind 5 cm of dry milk powder or 5 cm of washing powder, respectively. Second, 500 g TNT and 500 g AMM simulant was placed in a suitcase full of paper and water bottle, respectively.

## 4 Conclusions and Discussions

We have investigated the main parameters of the laboratory operational prototype based on the tagged neutron method (TNM) for the remote nondestructive identification of explosives, hidden in a suitcase or a paper box. In our experiments with neutron intensity of  $3 \times 10^7$  n/s, 300 g TNT or 300 g AMM shielded by 5 cm of washing powder or dry milk powder were detected within 3 min. The type of explosives (TNT or AMM) can be identified within 10 min. The result of any measurement made by TNM technique is a set of energy spectra distributed by space voxels. There is a unique spectrum for each distance, alpha detector and gamma detector. The shape (and number of counts) of each spectrum depends on chemical composition of a substance filling that space voxel. The main goal is to analyze spectra and find what chemical substance they are corresponding to. The algorithm in our system is like this: first, search for voxels filled with any bulk; second, estimate background for one from another voxels; third, if there is any density heterogeneity in some voxels, check them by spectrum shape analysis (Pearson's chi-squared test). The experiments have demonstrated that the TNM

method is superior compared with other techniques that use probing neutron irradiation, due to the facts that TNM has a higher signal-to-background ratio and therefore higher sensitivity.

## References

1. JIN Dazhi, TAN Xiaohua, DAI Jingyi, *et al.* Development of Neutron Detecting Latent Explosive [J]. Nuclear Physics Review, 2006, 23(1):70–72.
2. WANG Dong, HE Bin, ZHANG Quanhu. Simulation Study of Latent Explosive Detection by Using Neutron Back Scattering and Neutron Induced  $\gamma$ -ray Methods [J]. Atomic Energy Science and Technology, 2008, 42 (Suppl):318–321.
3. LI Xinnianm, GUO Junpeng, LUO Wenyun, *et al.* Detection of Hidden Explosives by Fast Neutron Activation Analysis [J]. Atomic Energy Science and Technology, 2008,42(4):343–347.
4. LU Shuhua. Detection of Explosives by Terahertz Spectroscopic Techniques[J]. Laser & Photoelectronics Progress, 2012, 49(040006):1–6. DOI:10.3788/LOP49.040006.
5. WANG Haidong, LI Yuanjing, YANG Yigang, *et al.* Study of explosive detection with PFTNA method and neural network [J]. Nuclear Electronics & Detection Technology, 2005, 25(4):384–387.
6. DING Wen, DOU Yuling, WANG Guobao, *et al.* Review on Detection Technology for Explosives[J]. Explosive Materials, 2011, 40(5): 33–37.
7. Hee-Jung Im, Byoung Chul Song, Yong Joon Park. Classification of materials for explosives from prompt gamma spectra by using principal component analysis [J]. Applied Radiation and Isotopes, 2009, 67: 1458–1462.
8. R. J. Evans, I. D. Jupp, F. Lei, D. Ramsden. Design of a large-area CsI (TI) photo-diode array for explosives detection by neutron-activation gamma-ray spectroscopy [J]. Nuclear Instruments and Methods in Physics Research A, 1999, 422: 900–905.
9. E. J. O. Ferreeira, V.R.Crispim, A. X. Silva. Detection of drugs and explosives using neutron computerized tomography and artificial intelligence techniques [J]. Applied Radiation and Isotopes, 2010, 68: 1012–1017.
10. D. Koltick, *et al.*, A neutron based vehicle-borne improvised explosive device detection system [J]. Nuclear Instruments and Methods in Physics Research B, 2007, 261: 277–280.
11. Vladivoj Valkovic, Davorin Sudac, Dario Matika. Fast neutron sensor for detection of explosives and chemical warfare agents [J]. Applied Radiation and Isotopes, 2010, 68: 888–892.
12. Robert C Runkle, Timothy A White, *et al.*, Photon and neutron interrogation techniques for chemical explosives detection in air cargo: A critical review [J]. Nuclear Instruments and Methods in Physics Research A, 2009, A603: 510–528.
13. Surender Kumar Sharma, Shrichand Jakhar, Rohit Shukla, Explosive detection system using pulsed 14 MeV neutron source [J]. Fusion Engineering and Design, 2010, 85: 1562–1564.
14. Tsahi Gozani, Dan Strellis. Advances in neutron based bulk explosive detection[J]. Nuclear Instruments and Methods in Physics Research B, 2007, 261: 311–315
15. C. Carascoa, B. Perota, S. Bernarda. In-field tests of the EURITRACK tagged neutron inspection system [J]. Nuclear Instruments and Methods in Physics Research A, 2008, 588: 397–405
16. C. Carascoa, B. Perota, G. Viesti. Photon attenuation and neutron moderation correction factors for the inspection of cargo containers with tagged neutrons[J]. Nuclear Instruments and Methods in Physics Research A, 2007, 582: 638–643

17. V. Valkovic, D. Sudac, S. Blagus. Fast neutron inspection of sea containers for the presence of “dirty bomb” [J]. Nuclear Instruments and Methods in Physics Research B, 2007, 263: 119–122
18. V. Valkovic, D. Sudac, J. Obhodas. The use of alpha particle tagged neutrons for the inspection of objects on the sea floor for the presence of explosives[J]. Nuclear Instruments and Methods in Physics Research A, 2013, 703: 133–137
19. Pesente, S, Nebbia, G, Lunardon, M, *et al.* Tagged neutron inspection system (TNIS) based on portable sealed generators[J]. Nuclear Instruments and Methods in Physics Research B 2005, 241: 743–747
20. Davorin, S, Dario, M, Vladivoj, V. Identification of materials hidden inside a sea-going cargo container filled with an organic cargo by using the tagged neutron inspection system [J]. Nuclear Instruments and Methods in Physics Research A, 2008, 589: 47–56
21. AN, Li, HE, Tie, GUO, Haiping, *et al.* Prompt  $\gamma$  Energy Spectrum by Associated Particle Technique [J]. Atomic Energy Science and Technology, 2010,44(Suppl):15–18
22. B. Perot, C. Carasco, S. Bernard. Development of the EURITRACK tagged neutron inspection system [J]. Nuclear Instruments and Methods in Physics Research B, 2007, 261: 295–298

# Using Traveling Wave Reactor (TWR) Technology to Provide Globally Scalable and Sustainable, Carbon-Free Energy

Kevan D. Weaver, John R. Gilleland and Robert Petroski

**Abstract** Energy security, reducing air pollution, and carbon emissions are topics of high importance to many countries throughout the world, particularly in Asia where energy use is expected to grow at 3.7 % per year, the highest growth rate in the world. According to the International Energy Agency (IEA), China alone is expected to account for almost one-fourth of world energy demand in the next 20 years. Although low-carbon options like wind and solar have seen large strides in deployment, growing by double and triple digits, the building of new coal plants still outpaces them all by orders of magnitude. In addition, most intermittent sources currently use fossil fuel generators as back up, lowering the potential gains that can be made in emission/carbon reduction goals. To further exacerbate this issue, worldwide electricity production is expected to double by 2040 to meet global needs, where coal is expected to play a major role in supplying that electricity unless an alternative can be found. Given the need to reduce the use of fossil fuels due to emissions/pollution/carbon concerns, and a desire for sustainable and globally scalable energy sources, an “all of the above” strategy for electricity generation has become an imperative. Nuclear power meets the requirements of a non-emitting source, and thus will need to be considered as part of the global energy strategy. However, nuclear energy in its current form has limitations, both perceived and real, regarding economics, waste, proliferation, and safety. In order to further improve on the current generation of reactors, TerraPower has developed the Traveling Wave Reactor (TWR), a near-term deployable and truly sustainable energy solution that is globally scalable for the indefinite future. As a fast reactor, the TWR allows up to a ~35-fold gain in uranium utilization when compared to conventional light water reactors (LWRs) using enriched fuel. Compared to other fast reactors, TWRs represent the lowest cost and lowest risk alternative: (1) they provide the energy security benefits of an advanced nuclear fuel cycle without the associated proliferation and cost concerns of fuel reprocessing; (2) they require less lifetime enrichment than LWRs, translating to a reduced number of enrichment plants that need to be built; (3) they produce less waste by volume than an LWR,

---

K.D. Weaver (✉) · J.R. Gilleland · R. Petroski  
TerraPower, LLC, Bellevue, WA, USA  
e-mail: kweaver@terrapower.com

resulting in less needed waste capacity requirements and reduced waste transportation costs; and (4) they require less uranium ore to be mined or purchased since natural or depleted uranium can be used directly as fuel. In addition to the benefits described above, the paper also describes the origins and current status of the TWR engineering, design, development, and test programs at TerraPower. Areas covered include the key TWR design challenges, and brief a description of the TWR-Prototype (TWR-P) reactor.

**Keywords** Fast reactor · SFR · Traveling wave reactor (TWR) · Sustainability · Scalable · Carbon-free · Low-carbon

## 1 Introduction

The current world population is approximately 7 billion, and is projected to increase to almost 9 billion by 2040, and then 10 billion by 2050. Unfortunately today, nearly 1.6 billion people have no access to electricity, and 2.4 billion people burn wood and manure as their main energy source. Access to affordable energy correlates strongly with quality of life and standard of living, where countries with access to vast energy supplies enjoy all of the economic and political benefits that come with controlling a highly sought after commodity. As more countries desire to have their economies and political influence increase (with the attendant increase in the standard of living), and populations continue to increase worldwide, global energy use will also need to grow. Energy use in Asia alone is expected to grow at 3.7 % per year, the highest growth rate in the world, with China leading the way by accounting for almost one-fourth of world energy demand in the next 20 years.

However, if history is any indication, most of this energy will be produced by sources that emit large amounts of air pollution and are carbon intensive. For example,  $\sim 2/3$  of the electricity in the U.S.,  $>1/2$  of the electricity in the European Union, and  $>4/5$  of the electricity in China is produced by fossil fuels (mainly coal and natural gas). Although low-carbon options like wind and solar have seen large strides in deployment, growing by double and triple digits, the building of new coal plants still outpaces them all by orders of magnitude. In addition, most intermittent sources currently use fossil fuel generators as back up, lowering the potential gains that can be made in emission/carbon reduction goals. To further exacerbate this issue, worldwide electricity production is expected to double by 2040 to meet global needs, where coal is expected to play a major role in supplying that electricity unless an alternative can be found. In addition, use of fossil fuels for electricity may see even larger increases if the transportation sector furthers its electrification (cars, trains, etc.). In order to meet greenhouse gas (GHG) reduction goals by 2040, more than 20 trillion kWh will need to be produced by non-fossil sources. To put that into perspective, the world currently consumes 17 trillion kWh, with the U.S. consuming roughly  $1/4$  of that total.

**Table 1** Avoidance of GHG emissions from the use of nuclear power as compared to fossil fuel

Average lifecycle GHG emissions (tonnes/GWh)		Emissions produced from generation 2518 TWh of electricity	Additional emissions avoided through use of nuclear electricity in place of fossil fuel
Lignite	1054	2654 million tonnes CO <sub>2</sub>	2581 million tonnes CO <sub>2</sub>
Coal	888	2236 million tonnes CO <sub>2</sub>	2163 million tonnes CO <sub>2</sub>
Oil	733	1846 million tonnes CO <sub>2</sub>	1773 million tonnes CO <sub>2</sub>
Natural Gas	499	1256 million tonnes CO <sub>2</sub>	1183 million tonnes CO <sub>2</sub>
Nuclear	29	73 million tonnes CO <sub>2</sub>	–

From 2011 data; Table courtesy of the World Nuclear Association

And it is not just about GHG emissions or CO<sub>2</sub>—there are severe consequences related to:

- Human health effects, where it has been estimated that >1,000,000 people die each year from coal particulates (20,000 in the U.S., and >300,000 in China alone) [1, 2];
- Direct environmental harm, with spills, pipeline breaks, coal impoundment failures (man-made ponds for storing toxic sludge from coal mining), drilling and mining effects; and
- Ocean acidification, where the lowering of ocean pH through simple CO<sub>2</sub> dissolving in seawater to form carbonic acid impedes calcification, severely altering the ocean’s food chains.

Given the need to reduce the use of fossil fuels due to emissions/pollution/carbon concerns, and a desire for sustainable and globally scalable energy sources, an “all of the above” strategy for electricity generation has become an imperative.

Nuclear power meets the requirements of a non-emitting source, is scalable at the terawatt (10<sup>12</sup> W) level, and thus will need to be considered as part of the global energy strategy. In 2011, nuclear power plants around the world supplied 2518 × 10<sup>9</sup> kWh (or 2518 TWh) of electricity (where in the United States nuclear energy accounts for roughly 2/3 of carbon-free electricity). Table 1 illustrates the additional emissions that would have been produced if fossil fuels (lignite, coal, and natural gas) had been used to generate the same amount of electricity as nuclear (in tonnes of GHG per GWh of electricity produced) [3]. Note that although oil and natural gas produce roughly half the GHGs as coal, they will still contribute to the production and increase of GHGs, just at a slower rate.

However, nuclear energy in its current form has limitations, both perceived and real, regarding economics, waste, proliferation, and safety. The Generation III and III+ nuclear reactors now coming into use have made significant strides in projected safety. In order to further improve on the current generation of reactors, TerraPower has developed the Traveling Wave Reactor (TWR), a near-term deployable and truly sustainable energy solution that is globally scalable for the indefinite future. The TWR is a sodium-cooled, fast neutron spectrum reactor. Compared to other fast

reactors, TWRs represent the lowest cost and lowest risk alternative: (1) they provide the energy security benefits of an advanced nuclear fuel cycle without the associated proliferation and cost concerns of fuel reprocessing; (2) they require less lifetime enrichment than LWRs, translating to a reduced number of enrichment plants that need to be built; (3) they produce less waste by volume than an LWR, resulting in less needed waste capacity requirements and reduced waste transportation costs; and (4) they require less uranium ore to be mined or purchased since natural or depleted uranium can be used directly as fuel.

## **2 Origins of Terrapower and the Traveling Wave Reactor (TWR)**

### ***2.1 Establishment of TerraPower***

The beginnings of TerraPower and its nuclear innovations are found in meetings held between Bill Gates, Nathan Myhrvold, Lowell Wood and experts during 2006 brainstorming sessions in Bellevue, Washington, USA. The central focus of the discussions was how to provide sustainable, scalable low-carbon energy for all the earth's inhabitants. It became clear that nuclear could play the needed central role in providing base load power in an environmentally and economically acceptable manner and on a relevant time scale.

The group also concluded that nuclear power could realize significant improvements by rigorous applications of twenty first century technologies, data and modeling capabilities. Nuclear power's unique potential and its need for improvements are consistent with the recently published conclusions of the global Ecomodernist group [4].

A small group, which eventually became TerraPower LLC, started organized activities in early 2007. The objective was to make improvements in as many areas of the nuclear enterprise as possible: safety, waste, efficiency, economics, weapons proliferation resistance, terrorist risk reduction and overall social acceptance. The group considered many types of reactors, including both existing and new concepts. As the assessments progressed it became increasingly apparent that the concept of the TWR offered improvements in all the above areas.

### ***2.2 The Traveling Wave Reactor (TWR)***

In the earliest versions of the TWR, waves that breed and in turn burn fissile material propagate in a cylindrical medium of depleted or natural uranium, where the wave appears to travel in the "lab" frame of reference. In 2007 several dozen fuels and coolants were considered to gain insights into which embodiment of the

concept might prove most practical. A sodium-cooled, fast neutron spectrum reactor utilizing metal uranium fuel was found to offer the most promise. This combination offered the thermal conductivity and cooling efficiency needed to support the required energy density in the core while maintaining realistic fuel and structural designs. Additional practical considerations of fuel shuffling and cooling system simplicity called for moving the fuel in the core rather than letting breed/burn waves travel within it, effectively changing the traveling wave to the fuel frame of reference.

The ability of the TWR to use depleted, natural, or low enriched ( $\leq 5\%$ ) uranium as reload fuel (all of which would be subcritical in any other sodium-cooled fast reactor), effectively extends the domestic reserves of both China and the United States by hundreds of years. This can be achieved without the need to first develop, fund and construct reprocessing facilities. After use of a low enriched core to start the first reactor, the long-term goal of an indefinite series of TWRs can be continued for hundreds of years without the need for any  $^{235}\text{U}$  enriched “starter”, or driver, fuel. The economic advantages of this highly efficient, simple once-through nuclear infrastructure can result in a cumulative savings of potentially trillions of dollars over the next 75 years if a large fleet of TWRs can be deployed. With advanced technological development and added cost, TWRs are also capable of reusing both their own used fuel and used fuel from LWRs, thereby eliminating the need for enrichment in the longer term and reducing the overall societal waste burden.

Safety is of course of paramount importance in the concept’s development. The advantages of a high temperature, low-pressure system, in the context of metal fuels and coolant offer inherent safety features well beyond those of current reactors. Nuclear waste from the TWR is approximately 1/5 that of current LWRs for each unit of electrical energy produced. Weapons proliferation risks are reduced because of the reduction in need for enrichment facilities, long-term isolation of the fuel in the nuclear island between infrequent decadal refueling outages, and the avoidance of reprocessing facilities.

All the above features of the TWR and its reduced infrastructure requirements simplify global deployment. A purchasing nation does not need to develop a complex and massive supporting network of facilities to ensure sustainability.

The TWR development program has been underway for approximately 9 years. Several hundred million dollars (USD) have been spent on a focused, tightly coordinated design and development effort. The commercialization of the TWR has three main components: design and construction of a first reactor that will serve to qualify full-scale TWR commercial fuels, components and systems [5]; commercial reactor designs and construction; and the integrated and focused technology development program to support these objectives on a sound and licensable basis.



### 3 TWR Engineering and Design

The TWR is a large sodium-cooled fast reactor (SFR) designed to supply large quantities of base load electricity to population centers. The TWR builds on successful U.S. and international experience with SFRs, with key innovations employed to allow extremely clean, safe and economic operation on a once-through fuel cycle without fuel reprocessing.

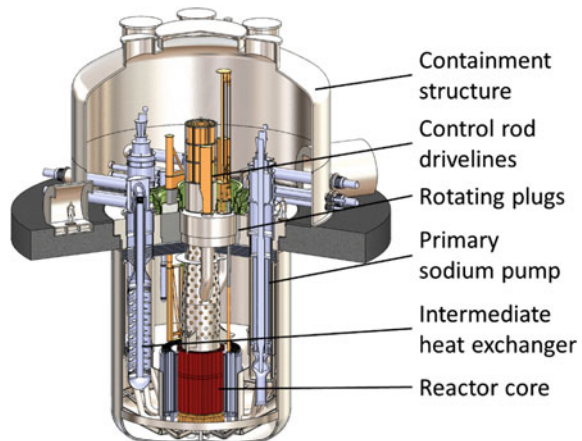
#### 3.1 Reactor and Plant Parameters

The TWR uses conventional sodium-cooled reactor architecture. Fission energy generated in the TWR core is transferred in series through the primary and intermediate loops to steam generators, which produce superheated steam. This steam powers a steam turbine generator set to produce electricity, and low temperature heat is rejected through a set of water-cooled vacuum condensers.

The intermediate loop acts as a barrier between the primary coolant loop and the high-pressure steam cycle, so that even if there is a leak or break in any of the components, the integrity of the core and primary coolant boundary can be ensured. An illustration of the TWR plant primary components and containment is shown in Fig. 1.

The TWR is a pool-type reactor, in which the primary system components (core, intermediate heat exchangers, and pumps) all reside in a large pool of atmospheric pressure sodium contained within a double-walled vessel. This arrangement has been employed in EBR-II in the United States, Phénix and SuperPhénix in France, BN-600 and BN-800 in Russia, CEFR in China, and PFBR in India. Using a pool has the advantage of reducing the amount of piping and space needed, providing a

**Fig. 1** Illustration of TWR components inside containment



large thermal inertia, and greatly reducing the likelihood and consequences of a coolant leak.

Designs for commercial TWRs have net power ratings ranging from 600 to 1200 MW electric. This range of power levels permits a gradual evolution from the first 600 MW prototype plant to larger units that achieve improved economies of scale. Core inlet and outlet temperatures are 360 and 510 °C, respectively, corresponding to a plant net efficiency of approximately 41 %; a significant improvement over the ~33 % efficiencies typical of current commercial light water reactors.

The TWR plant is being designed with consideration of construction, maintenance and operation, in order to minimize costs and maximize availability. The TerraPower design team includes highly experienced engineers, designers, and operators of past SFRs, using best practices drawn from over 1100 man-years of industry experience. To maintain appropriate design control, design, testing, fabrication, and software development activities are carried out within an ASME Nuclear Quality Assurance-1 (NQA-1) compliant program.

The TWR's overall core arrangement is typical of other SFRs, composed of hexagonal assemblies of wire-wrapped cylindrical fuel pins surrounded by an outer steel duct (see Fig. 2).

Control of core reactivity is accomplished through control rods that are inserted into the core, with a redundant bank of shutdown rods to ensure independent shutdown of the reactor.

A number of innovations have been employed in the fuel pins, fuel assemblies, and safety systems to achieve excellent safety and extremely good fuel utilization. Typical SFR designs require relatively high enrichment reload fuel (in many cases



**Fig. 2** TerraPower mock-up fuel assembly with wire-wrapped pins and wrapper/duct

>20 % transuranics or  $^{235}\text{U}$ ), and have a relatively low discharge burnup. This results in low utilization for a once-through fuel cycle, so a closed fuel cycle with fuel reprocessing is needed to reuse the fuel.

The TWR core design improves both achievable fuel burnup and the core's neutron economy to allow reload enrichments as low as zero, i.e., depleted uranium with near-zero fissile content. Key new technologies include:

- An optimized clad material
- A high uranium content metal fuel alloy
- A high burnup, low distortion fuel pin design
- An advanced, low distortion assembly duct
- A very low leakage core
- In situ, breed-and-burn fuel management scheme
- Systems that improve core inherent safety response

The combination of these technologies gives the TWR the unique ability to directly burn fissile fuel that's bred in the core, thus producing energy from unenriched uranium without relying on a separate reprocessing infrastructure. The corresponding once-through fuel utilization for a TWR is 170 GW-thermal days (70 GW-electric days) per ton of unenriched fuel. This corresponds to a waste reduction of 80 % relative to LWRs, and an improvement in uranium utilization that approaches  $35\times$  at breed-and-burn equilibrium.

### 3.2 *Safety Characteristics*

The TWR is designed to have an extremely high degree of safety, surpassing that of the present day fleet of light water reactors. Safe operation and response to accidents is achieved through a combination of several layers of protection:

- Systems that assure reactor shutdown, including control systems, inherent reactivity feedbacks, and passive shutdown systems
- Multiple heat removal pathways that rely on natural circulation of low pressure coolant to transfer decay heat to the atmosphere
- Multiple barriers that prevent radionuclides in the core from reaching the environment.

Many of these features are designed to operate in an inherent fashion, without requiring external power or operator actions.

During an accident, the normal route of full-power heat removal may become unavailable. Therefore, it is important to shut the reactor down, so that only a smaller amount of decay heat needs to be removed from the core. Shutdown is accomplished using a reactivity control system and a redundant standby shutdown system that insert neutron absorbers into the core to shut it down. Similar to existing

reactors, these systems function both automatically, e.g., if temperature or power exceeds a certain level, and extremely reliably.

The TWR core's natural reactivity feedbacks also help to shut the reactor down. The TWR, like other large sodium fast reactors, has a positive coolant temperature coefficient of reactivity: increasing coolant temperature alone causes the fission rate to increase. However, the other sources of feedback—including fuel temperature feedback, fuel axial expansion, and assembly radial bowing—act in the opposite direction and cause the net feedback to be negative, so the core tends to be self-stabilizing.

Together with the low operating temperature of the metal fuel, this quality allows the TWR to endure an “unprotected” loss of heat sink, a beyond-design-basis accident in which normal heat removal capability is lost and the reactor is not shut down by either the control rods or shutdown rods. In such a situation, the TWR core would stabilize itself at a near-zero power level and a slightly elevated average temperature. Note that no LWR could survive such an event.

In the case of an unprotected loss of flow, another extremely low likelihood event in which all coolant pumping is lost and the control and shutdown rods do not insert, natural feedbacks may not reduce core power quickly enough to counter the sudden loss of flow. In this scenario, a system that passively responds to loss of coolant flow can be used to quickly shut the core down. This approach is similar to the Gas Expansion Module (GEM) approach that was successfully demonstrated at FFTF for addressing the same type of event [6].

The primary reason that the TWR has enhanced safety relative to light water reactors is that it is simpler to remove decay heat from a large pool of low-pressure, high conductivity coolant than from highly pressurized water. The low pressure, large margin to coolant boiling, and redundant belowground vessels effectively eliminate the potential for a loss of coolant accident. The excellent heat transfer properties of sodium, and the use of high thermal conductivity metal fuel with low centerline temperatures, means it is possible to use simple natural circulation systems to reject all decay heat into the atmosphere.

In addition to the normal heat rejection pathway through the main condensers, decay heat removal can be accomplished via a separate high-pressure condenser system and a set of four separate Direct Reactor Auxiliary Cooling Systems (DRACS). Each DRACS consists of a simple natural circulation coolant loop, with one heat exchanger removing heat from the primary coolant, and another heat exchanger rejecting this heat to the atmosphere. Any two DRACS loops out of four are sufficient to remove enough decay heat to prevent core damage, making the DRACS a highly reliable and fully independent means of heat removal. Because heat is rejected to the atmosphere, an effectively limitless heat sink, decay heat removal can be assured for an indefinite period with no need for external power, makeup water, or operator actions.

The safety advantages of TWRs are borne out by Probabilistic Risk Assessments (PRA), which estimate a core damage frequency due to internal initiating events lower than of  $1 \times 10^{-8}$  per reactor year [7], a value several orders of magnitude lower than computed for currently operating reactors.

At these very low levels of risk, the primary hazard to the plant is due to very rare but catastrophic external events, primarily earthquakes. Such events are safeguarded against by seismically hardening the reactor and heat removal equipment, and by employing seismic isolation in high seismicity locations. Because the plant is designed to remain safely shut down without external assistance, the loss of supporting infrastructure associated with such an event would not endanger the plant.

With this very high level of safety, the TWR would continue the history of nuclear energy having a far lower health impact than any form of fossil fuel combustion [8].

## 4 TWR Development and Testing Programs

Work in the development and testing programs of the TWR is being performed to reduce the technical risk associated with the design, development, and deployment of the TWR. The programs can be divided into the following categories:

- Fuels and materials (e.g., fuel, cladding, duct, etc.)
- Other in-core and in-vessel systems and components (e.g., control rods, fuel handling machines, heat exchangers, etc.)
- Intermediate sodium systems and components (e.g., pumps, valves, steam generators, etc.)
- Balance-of-plant (BOP) systems and components (e.g., turbine generator, condensers, etc.)

The TWR systems, subsystems, and components were evaluated using a technology readiness assessment (TRA) process that was originally developed by the National Aeronautics and Space Administration (NASA) for evaluating and assigning technological maturity levels. The TRA rankings were used to provide guidance for the development, testing, and equipment qualification programs with regard to priority and technical risk reduction.

To date, TerraPower has contracted with more than 50 industrial, national laboratory, and academic institutions around the world to perform technology development work. This includes international collaboration with entities such as Kobelco (Kobe Steel) in Japan, and the Research Institute for Atomic Reactors (NIAR or RIAR) in Russia, as well as U.S. companies, many of the national laboratories, and universities.

In the sections below, work being performed in the fuels and materials area will be highlighted, as well as work being performed by TerraPower locally in Bellevue, Washington to support the other major categories described above.

## 4.1 Materials and Metal Fuel Development

In order to achieve a breed-and-burn equilibrium fuel cycle, where only depleted or natural uranium are needed as additional fuel, the fuels and materials will need to achieve high burnup and fluence—on the order of 30 % peak burnup for the fuel, and  $\sim 1.1 \times 10^{24}$  n/cm<sup>2</sup> fluence ( $\sim 550$  dpa) on cladding and in-core components. These burnups and fluences are far beyond what was achieved previously [9], which will require additional testing.

TerraPower has embarked on a fuels and materials development and qualification program, which includes fuel fabrication development, irradiation testing, and post irradiation examination (PIE) programs to provide information necessary for licensing and eventual construction of a TWR. The ferritic–martensitic stainless steel HT9 has been selected as the initial TWR fuel clad and assembly duct material because it: (1) has the largest body of irradiation data, (2) has demonstrated the best swelling performance when compared to austenitic stainless steel (Fig. 3), and (3) has an operating and fabrication history for use in fast reactors both as cladding and duct material.

However, historically there was variability in the swelling performance of HT9, as seen in Fig. 4.

As part of the development program, an optimized type of HT9 was developed by TerraPower to withstand even higher neutron damage with minimal swelling.

To help further reduce uncertainty, TerraPower is working with the University of Michigan to perform heavy ion irradiation of HT9 and other ferritic–martensitic stainless steel. An advantage of using heavy ions is the reduced time it takes to achieve high doses. To date, the TerraPower samples have received doses up to  $1.3 \times 10^{24}$  n/cm<sup>2</sup> (650 dpa), with very low swelling observed. A comparison of the swelling of historic and new/improved HT9 under heavy ion irradiation can be seen in Fig. 5, where the green bars are the optimized HT9 samples, and the others being historic HT9.

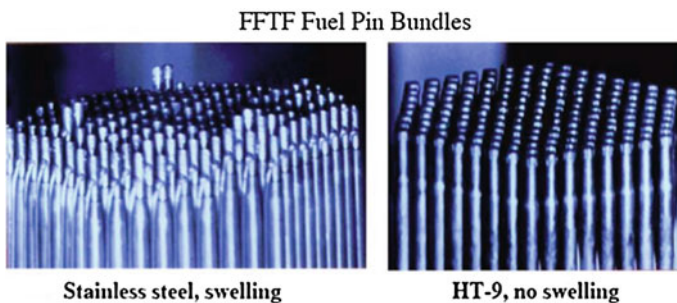


**Fig. 3** Irradiation induced swelling of SS316 and HT9 pins from FFTF (image courtesy Pacific Northwest National Laboratory)

**Fig. 4** Swelling behavior of different HT9 heats in FFTF

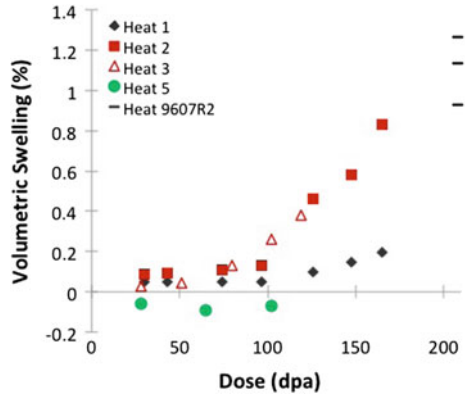
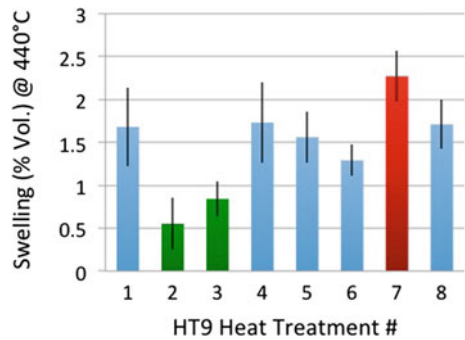


**Fig. 5** Reduced swelling behavior of optimized HT9 under heavy ion irradiation, as seen in samples 2 and 3 [10]



At the Idaho National Laboratory (INL), TerraPower is having work performed that ranges from post-irradiation exams (PIE) on historical Fast Flux Test Facility (FFTF) and Experimental Breeder Reactor II (EBR-II) metal fuel pins, to developing and constructing a pilot scale fuel fabrication facility. TerraPower is also having INL perform advanced fuel tests in the Advanced Test Reactor (ATR).

The BOR-60 reactor at RIAR (in Russia) is being used to irradiate materials specimens [11]. Irradiation rigs in the reactor contain a total of almost 1500 material specimens. BOR-60 will also be used to irradiate test pins to provide the fuel performance data needed for eventual licensing. The expectation is that the first test pins will begin irradiation in 2018, where the pilot fuel fabrication facility at INL will be used to make the test pins.

Finally, TerraPower contracted with AREVA to build a full size TWR dummy fuel assembly as a proof-of-fabrication test and for pressure drop testing (Fig. 6). This assembly demonstrated that tight tolerances could be handled from a fabrication standpoint, and is being used to benchmark thermal-hydraulic models.

**Fig. 6** Full-size TWR proof-of-fabrication fuel assembly



## ***4.2 Other Testing Programs***

TerraPower has recently started using  $\sim 10,000$  ft<sup>2</sup> ( $\sim 929$  m<sup>2</sup>) of dedicated laboratory space in Bellevue, Washington, USA for engineering testing, which is sufficiently large to handle full sized components. It also includes a flow test loop, and the ability to study mechanical, structural, vibration, integrated system, sodium, and materials behaviors. There are reconfigurable stations in the lab space, with a current setup that supports experiments for assembly and core design as well as specific functions of various plant systems (see Fig. 7).



**Fig. 7** TerraPower mechanical testing apparatus at the laboratory



## 5 TWR Prototype (TWR-P)

The commercialization plan for the TWR involves first building a 600 MWe (1475 MWt) prototype reactor called TWR-P, described in detail in [5]. The prototype will demonstrate the construction, operation, and maintenance of a commercial-size SFR with full-scale systems and equipment, including the core, pumps, heat exchangers, and steam turbine. The core of the prototype is based on established metal fuel technology, and will serve as a flexible platform for qualifying advanced fuels and materials that can be used in later units. TWR-P will thereby enable the deployment of subsequent generations of commercial TWRs.

## 6 Potential Role of Using the TWR for Global, Carbon-Free Energy Generation

In order to avoid the most severe outcomes of climate change, it will be necessary to keep global average temperatures from rising 2 °C (3.6 °F) relative to pre-industrial levels within the next generation, which in turn requires CO<sub>2</sub> levels to be reduced by 60–80 % below 1990 levels. As stated previously, the world currently consumes roughly 17 trillion kWh per year, and by 2040 this is expected to rise past 30 trillion kWh per year. If approximately 2/3 of energy consumption by 2040 needs to be carbon-free in order meet the climate change goals ( $\leq 2$  °C rise in temperature), then 20 trillion kWh will need to be carbon-free (fossil free) energy. Assuming nuclear power can produce the 20 trillion kWh per year of non-fossil generation by 2040, more than 2500 new nuclear plants will be required globally (assumes each nuclear plant can produce 1 GW, or 7.88 billion kWh per year at 90 % capacity factors). However, from the standpoint of diversification, it would be wise to include other carbon-free sources in the energy mix (e.g., renewables), where an assumption of 1/3 of the carbon-free energy comes from nuclear, or approximately 1250 new nuclear plants worldwide by 2040. The questions are whether this can be achieved in the given time frame, and what technology, or technologies, will be used.

Historically, nuclear can scale on the same order as coal, noting that coal currently accounts for ~40 % of electricity generation worldwide. Other fossil (gas and oil) accounts for another ~25 %. In the U.S., nuclear plant buildout peaked at 25–30 nuclear reactors per year, while at the same time other countries (e.g., France) were beginning a serious new build campaign, and China is already on this same track. In fact, China accounts for 40 % of nuclear new builds around the globe. The French program was able to increase its share of nuclear generation from <8 % in 1974 to >75 % by 1990. France is now the largest exporter of electricity in the world. Since 2005, France has exported up to 70 billion kWh each year, and EdF expects the exports to continue [12].

In addition to the expanding world need for more energy, the U.S. has an additional looming issue: whether to replace the eventual retiring nuclear plants with new nuclear, or something else (e.g., fossil). More specifically, most of the nuclear fleet in the U.S. will retire between 2030 and 2050, even with additional license extensions. If all the current nuclear generation in the U.S. were to be replaced by coal, an additional 700 million tonnes of CO<sub>2</sub> will be emitted per year (not accounting for growth). If replaced by combined cycle natural gas turbines (CCGT), an additional 350 million tonnes per year would be emitted. Although the use of CCGTs would only produce half the emissions of coal, because nuclear is zero emitting, it still results in a total increase in GHG emissions.

In the U.S., to just maintain nuclear's ~20 % share of the electricity generation by 2040 will require an additional 57 GW of installed nuclear capacity beyond the current 99 GW installed, for a total of 156 GW (assuming an average annual growth rate of 2 %). If this additional energy were produced by coal, it would result in an additional 1092 million tonnes of CO<sub>2</sub> in just 2040. For an annual growth rate of 1.5 %, an additional 40 GW would be needed beyond the current 99 GW, and there would still be an additional 973 million tonnes of CO<sub>2</sub> in 2040.

China is building the equivalent of approximately one large coal plant (1 GW) every week. Assuming each new plant will produce roughly 7 million tonnes of CO<sub>2</sub> per year, the result is an additional 350 million tonnes of CO<sub>2</sub> emitted from new coal plants each year. If this trend continues, and one includes an annual growth rate of 3.7 %, by 2040 there will be an additional 1841 coal plants in China producing 12,887 million tonnes of CO<sub>2</sub> per year. Clearly this will not be sustainable for the future, especially when considering GHG and particulate emissions, and the additional consequences of these emissions as outlined in Sect. 1, above.

Assuming 1250 new nuclear plants will need to be constructed between now and 2040 as described above, this results in the construction of  $\leq 55$  new nuclear plants worldwide per year—a number that has been shown to be achievable in the past (1970 through 1990), and the world is again approaching. In our assessment, the TWR would be fully capable of meeting the needs outlined above, but would operate at higher thermal efficiencies and require much less uranium and enrichment than the current fleet of LWRs. As mentioned in Sect. 3.1, the higher thermal efficiency of a TWR, due to its higher outlet temperature, contributes not only to higher uranium utilization, but also to lower water requirements. However, if the water requirements are limited due to siting considerations (e.g., arid locations), the high outlet temperatures of the TWR will allow it to be more efficient than LWRs when using dry cooling (i.e., the use of air instead of water at the condenser). Although this will reduce the thermal efficiency, it does make the TWR attractive for many more locations than current LWRs. Because the TWR is more uranium efficient than current reactors (LWRs), the current uranium resources, mined and depleted, would be more than sufficient to meet the estimated world power requirements, and would avoid 8750 million tonnes of CO<sub>2</sub> per year (also meeting the emissions goals set forth by the COP).

## 7 Conclusions

Given the ever increasing world population, and the need to deliver clean, sustainable energy to that population, the TWR is offered as a potential solution to providing carbon and emission free energy. As with other nuclear technologies, the TWR can readily scale to meet the growing demand—its high thermal efficiency

and high fuel utilization make it ideal for replacing retiring nuclear and coal plants, and for adding in needed extra capacity. Further, the TWR responds to the perceived and real limitations of nuclear energy in its current form regarding economics, waste, proliferation, and safety, by excelling in all these areas.

To date, the TWR development program has made good progress. Design activities have been carried out making use of extensive previous relevant data and experience, as well as utilization of twenty first century design tools and technologies. The required development activities are being managed through use of very detailed and formal technology readiness assessments. A matrix of tests and demonstrations have already been successfully carried out in key areas of materials and fuel development, and components. Approaches to licensing of the TWR have been outlined and are under discussion, which have, in turn, helped to shape the required development program.

The good technical progress to date, combined with economic and technical sensitivity studies, are confirming the great potential of the TWR to meet the growing need for energy while employing a carbon-free power source.

## References

1. Data from the World Health Organization and CDC, 1970–2011
2. Kharecha, P. A., and J. E. Hansen, “Prevented mortality and greenhouse gas emissions from historical and projected nuclear power,” *Environmental Science & Tech.* 47.9 (2013): 4889–4895
3. World Nuclear Association, <http://www.world-nuclear.org/nuclear-basics/greenhouse-gas-emissions-avoided.aspx>
4. Asafu-Adjaya, J., et al., “An Ecomodernist Manifesto,” available online at [www.Ecomodernist.com](http://www.Ecomodernist.com), April 2015
5. Hejzlar, P., et al., “TerraPower, LLC Traveling Wave Reactor Development Program Overview,” proceedings of the *International Congress on Advances in Nuclear Power Plants (ICAPP) 2013*, Jeju Island, Korea, 14–18 April, 2013
6. Waldo, J. B., A. Padilla Jr., D. H. Nguyen, and S. W. Claybrook, “Application of the GEM shutdown device to the FFTF reactor,” *Transactions of the American Nuclear Society*, v. 53, p. 312–313. American Nuclear Society and Atomic Industrial Forum joint meeting, Washington, DC, USA, 16–21 November 1986
7. Johnson, B. C., “Preliminary Results of the TerraPower–1 Probabilistic Risk Assessment,” proceedings of the *International Conference on Probabilistic Safety Assessment and Management (PSAM) 2012*, Helsinki, 25–29 June 2012
8. European Commission, “ExternE: Externalities of Energy: Methodology 2005 Update,” EUR 21951, Brussels, 2005
9. Weaver, K. D., J. Gilleland, C. Whitmer, G. Zimmerman, “High Burn–Up Fuels for Fast Reactors: Past Experience and Novel Applications,” proceedings of the *International Congress on Advances in Nuclear Power Plants (ICAPP) 2009*, Tokyo, Japan, 10–14 May, 2009
10. Hackett, M., G. Povirk, and J. Vollmer, “Materials Development for the Traveling Wave Reactor,” invited for proceedings of *The Metals, Minerals, and Materials Society (TMS) 2012 Annual Meeting*, Orlando, Florida, USA, 11–15 March 2012

11. Hilton, B. A., P. Hejzlar, D. G. McAlees, K. D. Weaver, S. A. Maloy, T. A. Saleh, M. B. Toloczko, "Traveling Wave Reactor: Material Requirements and Development Program," proceedings of *New Materials for Innovative Development of Nuclear Power Engineering Conference*, Dimitrovgrad, Russia, 24–27 March 2014
12. World Nuclear Association, <http://www.world-nuclear.org/information-library/country-profiles/countries-a-f/france.aspx>